

AD-A251 611



FINAL TECHNICAL REPORT
CONTRACT (N00014-87-C -0146)
OFFICE OF NAVAL RESEARCH

VANDERBILT UNIVERSITY FREE-ELECTRON LASER CENTER
FOR BIOMEDICAL AND MATERIALS RESEARCH

DTIC
ELECTE
MAY 26 1992
S A D

This document has been approved
for public release and sale; its
distribution is unlimited.

SUBMITTED BY:

Charles A. Brau
CHARLES A. BRAU
PRINCIPAL INVESTIGATOR

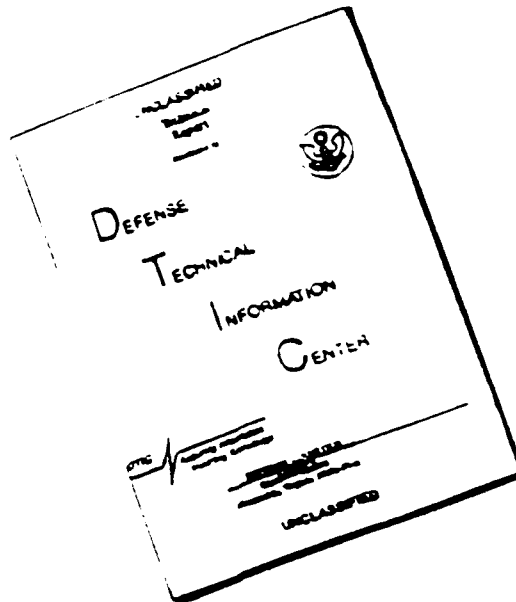
5/14/92
DATE

92 5 19 101

92-13422



DISCLAIMER NOTICE



THIS DOCUMENT IS BEST
QUALITY AVAILABLE. THE COPY
FURNISHED TO DTIC CONTAINED
A SIGNIFICANT NUMBER OF
PAGES WHICH DO NOT
REPRODUCE LEGIBLY.

FORWARD

During the period 2/1/87 to 1/31/91, Vanderbilt University, under Contract NO0014-87-C-0146 with the Office of Naval Research, developed a Free-Electron Laser Center, and carried out a program of research in medicine, biology, and materials science. The accomplishments of this effort are described in the final report.

The program may be divided into six projects, as follows:

I. Free-Electron Laser Construction and Operation under the direction of C. A. Brau, Department of Physics, College of Arts and Science. The objective of this effort has been to commission the free-electron laser and the optical beamline required to distribute the laser beam to the laboratories. Although the company supplying the free-electron laser ceased operations before the laser was completed, the installation and commissioning was completed by Vanderbilt personnel.

II. Mechanisms of Photon-Induced Damage in Optical Materials. The effort may be further subdivided into three efforts:

A. Desorption of Atoms and Molecules from Surfaces, under the direction of N. H. Tolk, Department of Physics, College of Arts and Science,

B. Nonlinear Effects of Lasers, under the direction of R. F. Haglund, Department of Physics, College of Arts and Science.

C. Interaction of Lasers with Defects in Optical Materials, under the direction of R. A. Weeks, Department of Materials Science and Engineering, School of Engineering.

III. Picosecond Spectroscopy of Biopolymers. Under the direction of G. S. Edwards, Department of Physics, College of Arts and Science, the objective of this research has been to examine the vibrational and electronic spectroscopy of important biopolymers, including DNA and RNA.

IV. Nonthermal and Selective Effects of Free-Electron Laser Irradiation of Tissue. Under the direction of R. H. Ossoff, Department of Otolaryngology, School of Medicine, the objective of this research has been to examine the effects of lasers on tissue, including the effect on wound healing.

V. Free-Electron Laser Based Studies of Biomembrane Dynamics and Drug Interactions. Under the direction of S. Fleischer, Department of Molecular Biology, College of Arts and Science, the objective of this research has been to understand the dynamics of membrane proteins, and how they are related to membrane function.

VI. Free-Electron Laser Applications in Neurosurgery. Under the direction of R. J. Maciunas, Department of Neurosurgery, School of Medicine, the objective of this effort has been to study the interaction of pulsed lasers with brain tissue, and to develop the techniques of stereotactic laser neurosurgery.

The close collaboration of researchers from so many Schools and Departments of the University has been a major factor in the success of the program, and will continue to be so as the program continues and expands to embrace researchers from around the world.

Accession For	
NTIS	CRA&I
DTIC	TAB
Unannounced	
Justification	
By <u>PA 195961</u>	
Distribution	
Availability Codes	
Dist	Avail and/or Special
<u>A-1</u>	<u>23</u>



INDEX

I. **Free-Electron Laser Construction and Operation**, C. A. Brau, Department of Physics & Astronomy, Vanderbilt University, Nashville, TN.

A. "Near-Monochromatic X-ray Beams Produced by the Free Electron Laser and Compton Backscatter", Frank E. Carroll, M.D., James W. Waters, Ph.D., Ron R. Price, Ph.D., Charles A. Brau, Ph.D., Carlton F. Roos, M.D., Norman H. Tolk, Ph.D., David R. Pickens, Ph.D, and W. Hoyte Stephens, MS., Vanderbilt University, Nashville, TN, Investigative Radiology, May 1990.

B." Generation of "Soft X-Rays by Using the Free Electron Laser as a Proposed Means of Diagnosing and Treating Breast Cancer", Frank E. Carroll, MD, Vanderbilt University Medical Center, Nashville, TN, Lasers in Surgery and Medicine 11:72-78 (1991).

C. "Tuneable Laser May Offer in Vivo Tissue Analysis", Frank E. Carroll, MD, Vanderbilt University Medical Center, Nashville, TN, Physics & Engineering, November 1989.

D. "Development of the Vanderbilt Compton X-Ray Facility", Wei Wei Andrews, MS, Frank E. Carroll, MD, James W. Waters, PhD., Charles A. Brau, PhD, Ron R. Price, PhD., David R. Pickens, PhD., Perry A. Tompkins, PhD, Carlton F. Roos, MD., Vanderbilt University, Nashville, TN.

E. "The Vanderbilt University Free-Electron Laser Center", C. A. Brau, Department of Physics & Astronomy, Vanderbilt University, Nashville, TN.

F. "The Vanderbilt University Free-Electron Laser X-Ray Facility", Perry A. Tompkins, Wei Wei Andrews, Charles A. Brau and James A. Waters, Frank E. Carroll, David R. Pickens, Ron R. Price and Carlton F. Roos, Vanderbilt University, Nashville, TN, (Conference on X-Ray Detector Physics and Applications.)

G. "The Vanderbilt Free-Electron Laser Center for Biomedical and Materials Research", N. H. Tolk, C. A. Brau, G. S. Edwards, G. Margaritondo and J. T. McKinley, Department of Physics & Astronomy, Vanderbilt University, Nashville, TN, 1991 SPIE Proceedings Reprint.

H. "Vanderbilt University FEL Center for Biomedical and Materials Research", G. S.

Edwards and N. H. Tolk, Department of Physics & Astronomy, Vanderbilt University, Nashville, TN. Elsevier Science Publishers B. V.

I. "The Vanderbilt University Medical Free-Electron Laser Program", C. A. Brau, Department of Physics & Astronomy, Vanderbilt University, Nashville, TN.

J. "Production of Near Monochromatic X-rays by The Vanderbilt Medical Free Electron Laser", Frank E. Carroll, M.D. Vanderbilt University Medical Center, Nashville, TN.

K.. "The Free Electron Laser: A Photon Factory for Science and Medicine", Richard F. Haglund, Jr., Department of Physics & Astronomy, Vanderbilt University, Nashville, TN.

Mechanisms of Photon-Induced Damage in Optical Materials

II. A. Desorption

1. "New Mechanism for Electron-Stimulated Desorption of Nonthermal Halogen Atoms from Alkali-Halide Surfaces", M. Szymonski, J. Kolodziej, P. Czuba, P. Piatowski, and A. Poradzisz, Institute of Physics, Jagellonian University, ul. Remonta 4, 30-059 Krakow, Poland, N. H. Tolk, Department of Physics and Astronomy, Vanderbilt, Nashville, TN, J. Fine, Surface Science Division, National Institute of Standards and Technology, Gaithersburg, Maryland 20899, submitted to Physical Review Letters.

2. "New Mechanism for the Desorption of Excited Atoms by Photon Bombardment of Alkali Halide Crystal," D. Liu, R. G. Albridge, A.V. Barnes, PhH. Bunton, C. S. Ewig, and N. H. Tolk, Vanderbilt University, Nashville, TN 37235, M. Szymonski, Institute of Physics, Jagellonian University, ul. Remonta 4, 30-059 Krakow, Poland, submitted to Physical Review Letters(4/4/91.)

3. "Generation of Excited CN Molecules Electronically Desorbed from Alkali-rich Surfaces", Jun Xu, Royal Albridge, Alan V. Barnes, Manfred Riehl-Chudoba, Akira Ueda, Norman Tolk, Center for Molecular and Atomic Studies at Surfaces, Department of Physics and Astronomy, Vanderbilt University, Nashville, TN, Dwight Russell and Paul Wang, Department of Physics, University of Texas, El Paso, TX , Elsevier Science Publishers B. V.(1991.)

4."Gas-Exposure Enhanced Na Emission from Na-Rich Surfaces", Jun Xu, Royal Albridge, Alan Barnes, Xinxing Yang, and Norman Tolk, Center for Molecular and

Atomic Studies at Surfaces, Vanderbilt University, Nashville, TN, Jan Xu, Oak Ridge National Laboratory, Oak Ridge, TN., accepted for publication 1.3.92: Applied Physics Letters.

II B. Nonlinear Effects

1. "Cu:Silica Nanocluster Composite Material With Picosecond Third-Order Nonlinear Optical Response", R. F. Haglund, Jr., L. Yang, R. H. Magruder, III, K. Becker, J. E. Wittig, R. A. Zuhr, Departments of Physics and Astronomy and Materials Science Engineering and Free-Electron Laser Center for Biomedical and Materials Research, Vanderbilt University, Nashville, TN, Solid-State Division, Oak Ridge National Laboratory, Oak Ridge, TN 37831, Submitted to Optics Letters, December 1991.

2. "Ultraviolet Laser Ablation of Halides and Oxides", R. F. Haglund, Jr., M. Affatigato, J.H. Arps and K. Tang, Department of Physics and Astronomy, Vanderbilt University, Nashville, TN, A. Niehof and W. Heiland, Fachbereich Physik, Universitat Osnabruck, W-4500 Osnabruck, Germany, Elsevier Science Publishers B. V. 1991.

3. "Production of Molecular Clusters of Lithium Niobate by Ultraviolet and Visible Laser Ablation", R. F. Haglund, Jr., K. Tang, Department of Physics and Astronomy, Vanderbilt University, Nashville, TN, and C. H. Chen, Chemical Physics Section, Oak Ridge National Laboratory, Oak Ridge, TN, Materials Research Society Symposium Proceedings, 245.

4. "Characterization of Surface Defects by Means of Laser-Induced Ga Emission from GaP Surfaces," Ken Hattori, Akiko Okano, Yasuno Nakai, Noriaki Itoh and Richard F. Haglund, Department of Physics, Nagoya University, Furo-cho, Nagoya 464-01, Japan and Department of Physics and Astronomy, Vanderbilt University, Nashville, TN, J. Phys: Condens. Matter# 7001-7006, Printed in UK.

5. "Effects of Oxygen Adsorption on Laser-Induced Sputtering from GaP (110) Surfaces", J. Kanasaki, H. Yamashita, A. Okano, K. Hattori, Y. Nakai, N. Itoh, Department of Physics, Faculty of Science, Nagoya University, Furocho, Chikusa-ku, Nagoya 464, Japan and R. F. Haglund, Jr., Department of Physics and Astronomy, Vanderbilt University, Nashville, TN, Surface Science Letters 257(1919) L642-L646 North-Holland, Elsevier Science Publishers B.V.

6. "Nonthermal laser sputtering from solid surfaces", Yasuo Nakai, Ken Hattori, Akiko Okano and Noriaki Itoh, Department of Physics, Nagoya University, Furo-Cho,

Nagoya 464001, Japan and Richard F. Haglund, Jr., Department of Physics and Astronomy, Vanderbilt University, Nashville, TN, Nuclear Instruments and Methods in Physics Research B58 (1919) 452-462 North-Holland, Elsevier Science Publishers B.V.

7. "UV Laser Ablation of Ferroelectrics", R. F. Haglund, Jr., H. H. Arps, K. Tang, Department of Physics and Astronomy, Vanderbilt University, Nashville, TN, and A. Niehof, W. Heiland, FB BarbarastraBe 7, Universitat Osnabruck, D-4500 Osnabruck, Germany, Materials Research Society Symposium Proceedings Vol. 210, 1991 Materials Research Society .

8. "Laser-Induced Fluorescence and Nonlinear Optical Properties of Ion-Implanted Fused Silica", K. Becker, L. Yang and R. F. Haglund, Jr., Department of Physics and Astronomy, Vanderbilt University, Nashville, TN, R. H. Magruder and R. A. Weeks, Department of Materials Science and Engineering, Vanderbilt University, Nashville, TN, R. A. Zuhr, Solid-State Division, Oak Ridge National Laboratory, Oak Ridge, TN, Nuclear Instruments and Methods in Physics Research B29/60 (1991), Elsevier Science Publishers.

9. "The Role of Valence-Band Excitation in Laser Ablation of KCl, Richard F. Haglund, Jr., Kai Tang, Patrick H. Bunton. Department of Physics and Astronomy, Vanderbilt University, Nashville, TN, SPIE Vol. 1441 Laser-Induced Damage in Optical Materials: 1919/127.

10. "Electronic Transitions in Surface and Near-Surface Radiation Effects, R. F. Haglund, Jr., M.H. Mendenhall and N.H. Tolk, Department of Physics and Astronomy and Center for Atomic and Molecular Physics at Surfaces, Vanderbilt University, Nashville, TN, G. Betz and W. Husinsky, Institut fur Allemeine Physik, Technische Universitat, A-1040 Vienna, Austria, Reprinted from Nuclear Instruments and Methods in Physics Research B.North-Holland Physics Publishing.

11. "Physics of Free-Electron-Laser Applications in the Visible and Infrared", Richard F. Haglund, Howard Schlossberg, Feature Editors, Physics of Free-Electron-Laser Applications in the Visible and Infrared, Free-Electron Lasers.

12. "The Role of Valence-Band Excitation in Laser Ablation of KCl", Richard F. Haglund, Jr., Kai Tang, Patrick H. Bunton and Lin-Jun Wang, Department of Physics and Astronomy, Vanderbilt, University, Presented at the XXII Symposium on Optical Materials for High-Power Lasers, Boulder, CO, October 1990. To be published in SPIE Proceedings Volume 1441.

13. "The Application of Lasers in Surface Science, Adriatico Research Conference, International Centre for Theoretical Physics, Trieste, Italy, August 23-27, 1988, Richard F. Haglund, Jr., Free-Electron Lasaser Center for Biomedical and Materials Research, Vanderbilt University, Nashville, TN. Foreign Trip Report to the Office of Naval Research.

14. "Scientific and Technological Applications of Free-Electron Lasers in Ultraviolet Photon-Stimulated-Desorption Spectroscopy", R. F. Haglund, Department of Physics and Astronomy and Free-Electron Laser Center for Biomedical and Materials Research, Vanderbilt University, Nashville, TN 37235.

15. "Laser Ablation" Mechanisms and Applications-Proceedings of a workshop held in Oak Ridge, Tn, USA 8-10 April 1991 J. C. Miller; R.F. Haglund, Jr.

II C. "Defect Formation in Fused Silicas Due to Photon Irradiation at 5 and 50 EV", P.W. Wang, D. L. Kinser, R.A. Weeks, Department of Materials Science and Engineering, Vanderbilt University, Nashville, TN, G. Escher, Sematech, Austin, Texas, R. F. Haglund, Jr., N. H. Tolk, Department of Physics and Astronomy, Vanderbilt University, Nashville, TN, D. G. Harris and P.M. Shay, Eds., Lasers '89:1020 (McLean, VA: S.T.S. Press 1990) Proceedings.

III. Spectroscopy of Biopolymers

A. "Sequence Dependence of Low-frequency Raman-active Modes in Muclei Acids" Glenn Edwards and Changle Liu, Department of Physics and Astronomy, Vanderbilt University, Nashville, TN, Physical Review A Vol. 44, Number 4,(August 15, 1991.)

B. "Prediction of Modes with Dominant Base Roll and Propeller Twist in B-DNA Poly(dA)-poly(dT)", L. Young, V. V. Prabhu, E. W. Prohofsky, Department of Physics, Purdue University, West Lafayette , Indiana 47907, G. S. Edwards, Department of Physics and Astronomy, Vanderbilt University, Nashville, TN, 1990 The Americal Physical Society.

C. "Low-frequency, Raman-active Vibrational Modes of Poly(dA poly(dT)", C. Liu and G.S. Edwards, Department of Physics and Astronomy, Vanderbilt University, Nashville, TN, S. Morgan and E. Silberman, Department of Physics, Fisk University, Nashville, TN, 1989 The American Physical Society.

D. "Applications of Free-Electron Lasers to Measurements of Energy Transfer in Biopolymers and Materials", Glenn Edwards, Bruce Johnson, John Kozub, Jerri Tribble, and Katrina Wagner, Vanderbilt University, Department of Physics and Astronomy, Nashville, TN, submitted to *SPIE*.

E. "Role of Immersion Refractometry for Investigating Laser Induced Effects in Cells", Jerri Tribble, John Kozub, Al Ali, Robert Ossoff, Glenn Edwards, Department of Otolaryngology, Department of Physics and Astronomy, Vanderbilt University, Nashville, TN. Accepted for Publication in Lasers in Surgery and Medicine.

F. "Role of Counterions in the Gigahertz Relaxation of Wet DNA", Glenn Edwards, Guangtaso Ying, and Jerri Tribble, Department of Physics and Astronomy, Vanderbilt University, Nashville, TN. Submitted to Physical Review A.

G. Far-Infrared Vibrational Modes of DNA, C. Liu and G. S. Edwards, Department of Physics and Astronomy, Vanderbilt University, Nashville, TN, S. Morgan, E. Silberman, Department of Physics, Fisk University, Nashville, TN.

H. " Pulsed-UV Induced Photochemistry of RNA-Protein Complexes", J. Kozub and G. S. Edwards, Department of Physics and Astronomy and S. Northington and W. LeSturgeon, Department of Molecular Biology, Vanderbilt University, Nashville, TN.

IV. Nonthermal Effects

A. "Nonthermal and Selective Effects of Free Electron Laser Irradiation of Tissue", Robert Ossoff, M.D., David L. Zealear, Ph.D., Debra Gonzalez, M. D. and Jerri Tribble, M.S. Department of Otolaryngology, Vanderbilt University Medical Center, Nashville, TN.

B. "Mechanisms of Laser-Tissue Interaction and Clinical Applications", Glenn Edwards, Robert Ossoff, Al Ali, John Kozub, and Changle Liu, Progress Report, May 1988.

C. "Role of Immersion Refractometry for Investigating Laser Induced Effects in Cells", Jerri Tribble, M. S., John Kozub, B.S., Al Ali, M.D., Robert Ossoff, M.D., Glenn Edwards, Ph.D., Department of Otolaryngology and Department of Physics and Astronomy. Accepted for Publication in Lasers in Surgery and Medicine.

D. "Canine Vocal Fold Fibroblasts in Culture: Expression of α -Smooth Muscle Actin

and Modulation of Elastin Synthesis". Caroline Broadley, Debra A. Gonzalez, Rhada Nair, Departments of Otolaryngology and Pathology, Vanderbilt University, Nashville, TN., to be submitted Laboratory Investigator, January 1992.

E. "KTP Laser-Induced Biomodulation of the Wound-Healing Process", Michael D. Kyzer, Al S. Aly, Robert H. Ossoff, Department of Otolaryngology, Vanderbilt University Medical Center. Submitted to Lasers in Surgery and Medicine.

F. "CO₂ Laser Micromanipulator Parallax Error Resolved", Jay A. Werkhaven, Jerri A. Tribble, Robert H. Ossoff, Department of Otolaryngology, Vanderbilt University, Nashville, TN. Submitted for publication Otolaryngology-Head & Neck Surgery.

G. "Lasers", Jay A. Werkhaven, M.D., Robert H. Ossoff, D.M.D., M.D., David Harris, M.D., In press book chapter H. L. Meyerhoff, D.H. Rice, Editors, Otolaryngology-Head & Neck Surgery, H. B. Saunders, Co.

H. "Multiphon Nuclei Acid Crosslinking Development of a Quantitative Approach", J. A. Tribble, M.S., W. Smithwick, B.S., M.D. Kyzer, B.S., G. S. Edwards, Ph.D., R. H. Ossoff, M.D., D.M.D., American Society for Laser Medicine and Surgery Abstracts, (September 3, 1991.)

I. "An Investigation of Laser-Induced Protein Synthesis by Cultured Fibroblasts", Debra A. Gonzalez, M.D., Jeffrey M. Davidson, PhD., David L. Zealear, Ph.D., Robert H. Ossoff, D.M.D., M.D., Vanderbilt University, Nashville, TN Poster. August 1990, Otolaryngology-Head and Neck Surgery.

J. "A Comparison of Vocal Fold and Skin Fibroblast Elastin Production in Tissue Culture", Debra A. Gonzalez MD, David L. Zealear, PhD., J.M. Davidson, PhD., Robert H. Ossoff, MD, DMD, August 1990 - Otolaryngology-Head and Neck Surgery.

K. "CO₂ Laser Micromanipulator Parallax Error Resolved, Jay Werkhaven, MD, Jerri Tribble, and Robert H. Ossoff, MD, DMD, Vanderbilt University, Nashville, TN, Otolaryngology-Head and Neck Surgery, August 1991.

L. "A New Endotracheal Tube for Co₂ and KTP/532 Laser Surgery of the Upper Aerodigestive Tract, Robert H. Ossoff, MD, DMD, Al Aly, MD, Nick Houchin, AAS, and Debra Gonzalez, MD, Vanderbilt University, Nashville, TN August 1991

M. "Fluorescence Detection and Identification in the Management of Acute Otitis

Media", L. Reinisch, Jay Werkhaven, Jerri Tribble, Vanderbilt University, Nashville, TN, The Nemours Children's Clinic, Jacksonville, Florida, January 10, 1992.

N. "An Investigation of the Potential for Laser Nerve Welding", Marjorie Korff, MD, Stephen W. Bent, BS, Michael T. Havig, BS, Mitchell K. Schwaber, MD, Robert H. Ossoff, M.D., David L. Zealear, PhD, Vanderbilt University, Nashville, TN. Presented at the Research Forum of the Annual Meeting of the American Academy of Otolaryngology-Head & Neck Surgery, Washington D.C., September 27, 1988.

O. "The Effect of Triton X-100 on Purple Membrane as Measured by Changes in the Dynamics", Jozsef Czege, Department of Radiology, Uniformed Services University, Bethesda, MD, Lou Reinisch, Department of Otolaryngology, Vanderbilt University Medical Center, Nashville, TN. Submitted Photochemistry and Photobiology, January, 1992.

P. "Laser Surgery in Otolaryngology: Basic Principles and Safety Considerations", Robert H. Ossoff, DMD, MD, FACS, Lou Reinisch, PhD., Department of Otolaryngology, Vanderbilt University Medical Center, Nashville, TN, (in press) Otolaryngology--Head and Neck Surgery, Second Edition, C. Cummings, ed. (C.V. Mosby, St. Louis, Missouri).

Q. "Photoinduced Ribonucleic Acid Crosslinking Using Visible and Infrared Wavelengths, Michael D. Kyzer, Jerri A. Tribble, Walter-G Wrobel, Robert H. Ossoff, Vanderbilt University Medical Center, Department of Otolaryngology, Nashville, TN, American Society for Laser Medicine and Surgery Abstracts 1990.

R. "A Study of De-Novo Protein Synthesis by Laser Irradiated Human Neutrophils" D. A. Gonzalez, J. Hurtig, J.M. Davidson, C. K. Broadley, R.L. Hoover, R.H. Ossoff, Departments of Otolaryngology and Pathology, Vanderbilt University Medical Center, Nashville, TN, American Society for Laser Medicine and Surgery Abstracts 1990.

S. "Vocal Cord Fibroblast Elastin Production in Tissue Culture, D.A. Gonzalez, R.R. Nair, R. H. Ossoff, J.M. Davidson, Depts. of Otolaryngology and Pathology, Vanderbilt University Medical Center, Nashville, TN, Association for Research in Otolaryngology 1990.

T. "An Investigation of the Potential for Laser Nerve Welding", M. Korff, MD, D.L. Zealear, PhD., M. Schwaber, MD, and R.H. Ossoff, DMD, MD, Vanderbilt University Medical Center, Nashville, TN, Scientific Sessions, Otolaryngology-Head and Neck Surgery, August 1988.

U. "Investigation of the Wavelength Dependence of Laser Induced Bacteriostasis". Jerry A. Tribble, MS, John A. Kozub, BS, Glenn F. Edwards, PhD, Al Aly, MD and Robert H. Ossoff, MD, Vanderbilt University, Nashville, TN Scientific Sessions-Otolaryngology -Head and Neck Surgery, August 1989.

V. "Advanced Microspot Microslad for the CO₂ Laser", Robert H. Ossoff, MD,DMD, Jay A. Werkhaven, MD, Joshua Raif,MSc,Martin Abraham, MSc, Nashville, TN and Allendale, New Jersey, Reprinted from Otolaryngology: Head and Neck Surgery, St. Louis Vol. 105, No. 3, pp. 411-414, September, 1991 (Copyright 1991 by the American Academy of Otolaryngology-Head and Neck Surgery Foundation, Inc.).

W. "The Use of the Laser in Head and Neck Surgery" Robert H. Ossoff, DMD,MD, Department of Otolaryngology, Vanderbilt University Medical Center, Nashville, TN, Dean M. Toriumi, MD, Department of Otolaryngology, Northwestern University School of Medicine, Chicago, Illinois, James A. Duncavage, MD, Department of Otolaryngology, Vanderbilt University Medical Center, Nashville, TN, Adv Otolaryngol Head Neck Surgery 1:217-240, 1987 Year Book Medical Publishers, Inc.

X. "Adult Subglottiscope for Laser Surgery", Robert H. Ossoff, DMD,MD, James A. Duncavage,MD, Vanderbilt University Medical Center, Nashville, TN, Annals of Otology, Rhinology & Laryngology, September-October 1988, Vol. 97 Number 5, Copyright 1988 Annals Publishing Company.

Y. "Laser Safety in Otolaryngology--Head and Neck Surgery: Anesthetic and Educational Considerations for Laryngeal Surgery, Robert H. Ossoff, DMD,MD, Supplement No. 48, August 1989, Vol. 99 No. 8 Part 2, American Laryngological, Rhinological and Otological Society, Inc.

Z. "KTP Laser-Induced Modulation of the Wound Healing Process, Michael D. Kyzer, Al S. Aly, Robert M. Ossoff, Vanderbilt University Medical Center, Nashville, TN, American Society for Laser Medicine and Surgery Abstracts 1989.

AA. " A Preliminary Study of the Effect of CO₂ Laser Radiation on Cultured Endothelium and on the Adhesion of Neutrophils to the Adhesion of Neutrophils to these Irradiated Cells", Al Aly, Caroline Kerr, Richard Hoover, Robert H. Ossoff, Vanderbilt University, Nashville, TN, American Society for Laser Medicine and Surgery Abstracts 1988.

BB. " A Histologic Comparision of Superpulse CO₂ Laser Tissue Effects, Jay

Werkhaven, Vanderbilt University, Nashville, TN. Bruce R. Maddem, Nemours Clinic, Jacksonville, Fla., David Kardatzke, University of Pittsburgh, Pittsburgh, PA, David M. Harris, Wenske Laser Center, Chicago, Ill., American Society for Laser Medicine and Surgery Abstracts 1990.

CC. "Interaction of Radiation with Cells and Cell Components", J. Tribble, J. Kozub, G. Edwards, K. Lane, A. Aly, and R. Ossoff, Vanderbilt University, Presented to the Fall, 1988 Mtg. of Tennessee Academy of Sciences.

DD. "The Effect of CO₂ Laser on Fibroblast Cultures" John F. Laurenzo, Al S. Aly, Jerry Davidson, Robert M. Ossoff, Achilles A. Demetriou, Vanderbilt University, Nashville, TN.

V. Biomembranes

A. "Dynamic Characteristics of Biomembranes and Membrane Proteins, J. Oliver McIntyre, Sidney Fleischer, Vandertilt University, Nashville, TN abstract - SDIO Fourth Annual Contractors' Meeting on Medical Free Electron Lasers, Sept. 22-24, 1989.

B. "Lipid-Dependent Membrane Enzymes Kinetic Modelling of the Activation of Protein Kinase C by Phosphatidylserine", Heinrich Sandermann, Jr. Insitut fur Biochemische Pflanzenpathologie, GSF Munchen, Newherberg Germany, Thomas M. Duncan, Department of Molecular Biology, Vanderbilt University, Nashville, TN, 1991 Elsvier Science Publishers B.V.

C. "Dynamic Characteristics of Biomembranes and Membrane Proteins", J. Oliver McIntyre and Sidney Fleischer, October 1987-December 1990 progress report.

VI. Neurosurgery

A. "Effects of Wavelength, Pulse Duration and Pulse Repetition Frequency of the Interactions and Desorption of Brain Tissue", M. Affatigato, R.J. Maciunas, R. F. Haglund, Jr., R. Carver, Departments of Physics and Astronomy and Neurosurgery, Vanderbilt University, Nashville, TN. (first draft -- for Publication JLMS)

B. "A New Device for Interactive, Image-Guided Surgery", Robert L. Galloway, Jr., Charles A. Edwards, Judith G. Thomas, Steven Schreiner, Robert J. Maciunas,

Departments of Neurosurgery, Biomedical Engineering, Vanderbilt University, Nashville, TN, SPIE, Vol. 1444 Image Capture, Formatting, and Display (1991).

C. "Simultaneous Graphics and Multislice Raster Image Display for Interactive, Image-Guided Surgery", Charles A. Edwards, II, Robert L. Galloway, Jr., Judith G. Thomas, Steve Schreiner, Robert J. Maciunas, Departments of Biomedical Engineering, and Neurological Surgery, Vanderbilt University, Nashville, TN 37232, SPIE, Vol. 1444 Image Capture, Formatting, and Display (1991).

D. "A Comparison of Three-Dimensional Surface Rendering Techniques", Judith G. Thomas, Robert L. Galloway Jr., Charles A. Edwards, II, Gerald L. Haden, Robert J. Maciunas, Departments of Biomedical Engineering, and Neurological Surgery, Vanderbilt University, Nashville, TN, SPIE Vol. 1444 Image Capture, Formatting, and Display (1991)

E. "An Intra-Operative Workstation for Interactive, Image-Guided Neurosurgery". R. Galloway, C. Edwards, V. Mandava, R. Maciunas, Departments of Biomedical Engineering and Neurological Surgery, Vanderbilt University, Nashville, TN, Annual International Conference on the IEEE Engineering in Medicine and Biology Society, Vol. 13, No. 3,(1991.)

F. "A Workstation Platform for Stereotactic Neurosurgical Planning", V. R. Mandava, R. J. Maciunas, J. M. Fitzpatrick, R. L. Galloway, C. R. Maurer, Vanderbilt University, Nashville, TN, Computers in Medicine, Annual International Conference of the IEEE Engineering in Medicine and Biology Society, Vol. 13, No. 3,(1991).

G. "Real-Time Assessment of Lung Microvascular Permeability: Use of a CO₂ Laser Aide Measurement of 1,2-Propanediol Concentration", L.E. Olson, R. L. Galloway, and T. R. Harris, Department of Biomedical Engineering, Center for Lung Research, Department of Neurosurgery, Vanderbilt University, Nashville, TN, Annual International Conference of the IEEE Engineering in Medicine and Biology Society, Vol. 13, No. 1,(1991.)

Special Report

Near-Monochromatic X-ray Beams Produced by the Free Electron Laser and Compton Backscatter

FRANK E. CARROLL, MD,* JAMES W. WATERS, PhD,† RON R. PRICE, PhD,*
 CHARLES A. BRAU, PhD,† CARLTON F. ROOS, MD,* NORMAN H. TOLK, PhD,†
 DAVID R. PICKENS, PhD,* AND W. HOYT STEPHENS, MS*

Carroll FE, Waters JW, Price RR, Brau CA, Roos CF, Tolk NH, Pickens DR, Stephens WH. Near-monochromatic x-ray beams produced by the free electron laser and Compton backscatter. *Invest Radiol* 1990;25:465-471.

The intense photon output of a free electron laser may be made to collide with its own high energy electron beam to create nearly monochromatic x-rays using Compton backscatter techniques. These x-rays can be used for imaging and non-imaging diagnostic and therapeutic experiments. The initial configuration of the Vanderbilt Medical Free Electron Laser (Sierra Laser Systems, Sunnyvale, CA) produces intense x-rays up to 17.9 keV, although higher energies are easily attainable through the use of frequency doubling methods, alteration of the energy of the electron beam and coupling to conventional laser inputs.

Key words: lasers; monochromatic x-rays; electron beams; free electron laser; Compton backscatter.

THE CREATION OF A powerful, tuneable, near-monochromatic source of "hard" x-rays would herald a new and exceptionally diverse generation of diagnostic medical imaging modalities, as well as opening the door to new therapeutic methods.

In diagnostic radiology, higher keV radiation is associated with the production of unusable, and objectionable scattered radiation; photons of lower keV energy may add little to the diagnostic information obtained, but contribute heavily to the radiation dose to the patient. If it were possible to select radiation of optimal energy for the job at hand, while eliminating those x-rays of higher and lower frequency, radiologists and other scientists could significantly enhance their ability to perform very high contrast/low dose imaging, accomplish in vivo trace element analysis, and achieve 3-D x-ray holographic imaging.

In 1986, Vanderbilt University was selected through a competitive grant process as the first dedicated Medical Free Electron Laser Facility to be funded by Congress through the Strategic Defense Initiative Organization. The principal investigators awarded this grant were a multidisciplinary investigative team comprised of physicians, physicists, biophysicists, molecular biologists, and engineers who work in very close collaboration on all facets of a unified inquiry into non-linear effects of radiation produced by this powerful, tuneable, and extremely fast laser.

The Free Electron Laser

The Free Electron Laser (FEL) uses a beam of relativistic electrons to amplify short wavelength radiation by stimulated emission. Electrons not bound to atoms (hence "free") are accelerated by one of any number of devices, such as a linear accelerator or Van de Graff generator, to multimillion electron volt energies, and are

From the *Department of Radiology and Radiological Sciences, Vanderbilt University Medical Center, and the †Department of Physics and Astronomy, Vanderbilt University.

Reprint requests: Frank E. Carroll, MD, Department of Radiology and Radiologic Sciences, Vanderbilt University School of Medicine, 21st and Garland Avenues, Nashville TN 37232-2675.

Received September 15, 1989, and accepted for publication, after revision, October 20, 1989.

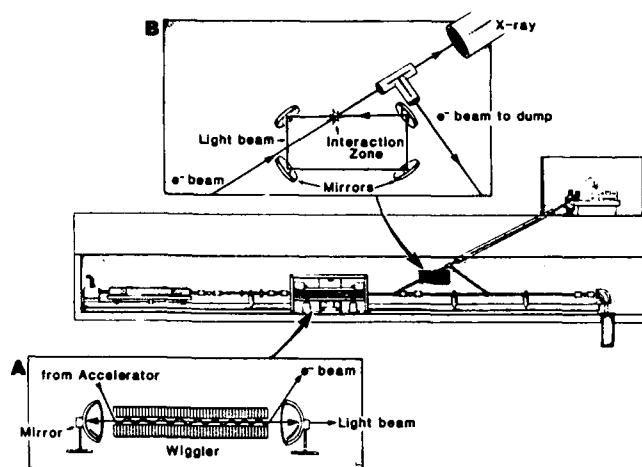


Fig. 1. The Free Electron Laser is a unique device among present lasers in that it is tuneable across the electromagnetic spectrum, extremely fast, and is extraordinarily powerful delivering gigawatts of power in pico or femtoseconds. Insert A shows the wiggler cavity of the FEL positioned to the right of and distal to the electron gun and linear accelerator. Insert B depicts the interaction zone of the Compton backscatter device. The x-ray photons are delivered to the imaging facility on the second floor of the Vanderbilt MFEL building.

then passed through an apparatus containing magnets of alternating north-south polarity (a wiggler). The electron trajectory describes an undulating or wiggling path through this device, interacting with the magnetic field to give off characteristic radiation, which is a function of the energy of the beam, the strength of the magnetic field and the periodicity of the magnets. The photons produced within the wiggler are reflected repeatedly by mirrors at the ends of the cavity and interact with the electron beam, amplifying the photon output (Fig. 1).¹ The FEL delivers an extremely high output in picosecond bursts that is tuneable across the infrared, visible and ultraviolet spectrum.

X-Ray Production by Compton Backscatter

In 1975, Piestrup et al³ showed that the momentum of a free electron beam may be modulated by interaction with laser light. To obtain significant energy exchange between an electron beam and light, it is necessary for the electrons to remain in an electric field of constant phase. This will occur in a medium that provides the proper refractive index, that maintains the phase velocity of the light's electromagnetic wave with electron velocity along the direction of motion of the electron. In a similar fashion, an electron beam may perform significant work on light photons. For some time now, high energy

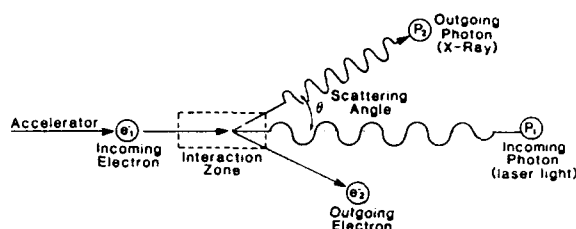


Fig. 2. Compton Backscatter yields a short wavelength x-ray photon for each collision/interaction between a near relativistic electron and a long wavelength light or infrared photon.

physicists have been creating gamma rays in the MeV to GeV range using the Compton backscatter (CB) phenomenon. Their technique involves the head-on collision of an intense beam of laser light with a high energy electron beam (Fig. 2). The incoming electron "collides" with an incoming photon, thereby losing energy, but at the same time imparting that energy to the incoming photon, scattering it backward at a higher energy.

More recently (in a patent filed in July of 1986), Luccio and Brill⁴ outlined a method and apparatus for producing x-rays which takes advantage of their first recognition that "photons of much lower energy than those ordinarily produced in nuclear physics research can be generated using the Compton backscatter effect by carefully controlling the energy level of the incoming electrons." Proposing a Microtron I electron source and a racetrack electron storage ring coupled to various "off the shelf" lasers, they provide a scheme that could potentially generate highly directional, tuneable, narrow bandwidth, polarized x-rays, which could conceivably cover a range of energies from 0.5 keV to 250 keV.

Coupling the FEL and Compton Backscatter

The electron beam of the FEL (Sierra Laser Systems, Sunnyvale, CA) is normally "discarded" in a beam dump after its exit from the wiggler cavity. We propose to use the residual electron beam (e-beam) from the FEL and make it collide with the FEL's own photon output to create tuneable, near monochromatic x-rays by Compton backscatter.

The configuration of the Medical Free Electron Laser/Compton Backscatter Device (FEL/CBD) presently under construction is seen in Figure 1. Once the electron beam has exited the FEL, the beam will be transported using bending and focusing magnets and evacuated beam lines to an interaction zone whose axis is aligned with a 12-in PVC x-ray beam pipe which penetrates the MFEL building structure from the downstairs shielded FEL vault to a "shirtsleeve" environment target room situated on the upper floor of the facility.

The light output of the FEL will be diverted by mirrors to the same interaction zone where it will collide "head-

For a more comprehensive discussion of the physics of FELs, the reader is referred to more complete texts.²

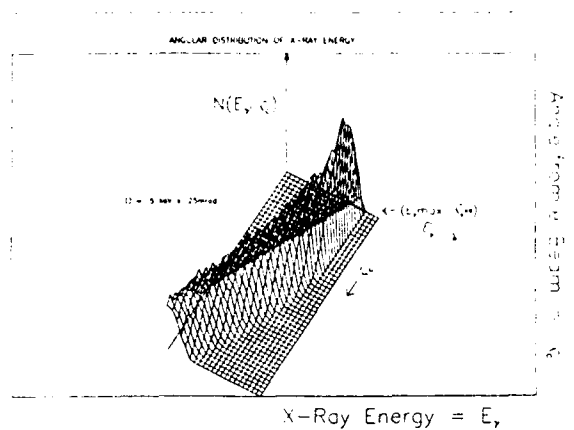


Fig. 3. Depicts the surface representing the distribution of x-ray energies and angles measured from the central electron beam direction. The figure was generated by the Monte Carlo program and resembles a mountain ridge, whose height is proportional to the probability of producing an x-ray with a given energy at a certain angle. The width of the ridge depends on the energy dispersion and angular divergence of the electron beam. The peak of the ridge is close to the maximum possible x-ray energy, 18 keV, and the axis of the electron beam. The quantity E_γ refers to the actual energy of an x-ray, while ζ_c refers to the angle measured from the central ray of the electron beam. Each rectangle on the plot represents an interval .5 keV by .25 mradian.

on" with the electron beam. It is here that the Compton backscatter occurs, allowing the creation of a cone of near monochromatic x-rays that will then be transported via the PVC x-ray beam pipe to the second floor target room. This beam exhibits a rather narrow scattering angle that does not exceed .01 radians.

Prior to its reaching the PVC beam pipe and after having interacted with the laser beam, the electron beam is again rotated and transported back to its original axis for disposal in the beam dump.

Photon Energy, Flux, and Distribution

In the case of photon scattering through 180° by a moving electron, the photon energy is increased by a factor $4\gamma^2$, where γ is the ratio of the electron's energy to its mass. In the present MFEL design, the electron energy is 43 MeV and the photon wavelength is 2μ , giving a maximum CB x-ray energy of 17.9 keV. The dependence of the laboratory energy on the angle and number of the backward scattered photons as measured from the electron is shown in Figures 3 and 4. A non-zero angle of incidence between the photon and electron beams has little effect on photon flux. There is very minimal displacement of the output curve when the incidence is $\approx 15^\circ$. This allows the interaction zone to be tilted somewhat so that the x-ray beam may exit the FEL/CBD without having to pass through the mirrors that focus the light beam at the electron beam. Lower keV

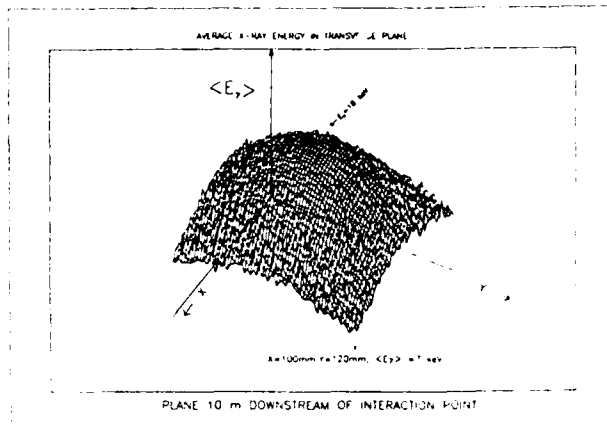


Fig. 4. This shows the surface representing the average x-ray energies at points in an arbitrary plane transverse to the central beam. The quantity $\langle E_\gamma \rangle$ is the average energy of all x-rays passing near a chosen point. In this calculation, E_γ is a function of the angle from the electron, so the scale of the figure is unimportant.

photons would be extensively attenuated if they needed to penetrate the interaction zone end mirrors while exiting the device.

The theoretical problem of photon-electron scattering has long been solved, the results being the Klein-Nishina formulas for the intensity and polarization of the scattered photons. In the energy regime of the MFEL, these formulas reduce to the classical ones of Thomson, in which the intensity is proportional to $(1 + \cos^2\theta_s)$, where θ_s is the scattering angle in the electron rest frame.

In practice, it is necessary to accept electrons in a cone of half-angle θ_c equal to a few milliradians, measured from the axis of the electron beam, because the probability for scattering into any range of angle is given by integrating the intensity over an element of solid angle which vanishes at $\theta_s = 0^\circ$ or 180° . Furthermore, because the beam has finite emittance (ie, the volume it occupies in phase space is not zero), all the electrons cannot be parallel, so at any fixed laboratory angle the observer sees photons scattered through a spectrum of angles from the directions of the electrons measured from the axis. The result is a spectrum of x-ray energies in the cone. Nearly monochromatic x-ray fluxes may be obtained by the selection of a portion of the cone for use (with the highest energy x-rays nearest the center of the cone) (Fig. 5).

The distributions of energies and angles in the laboratory system have been calculated by a Monte Carlo program. In the case of negligible beam emittance, the distributions in the proposed MFEL system are shown in Figure 6. In the Monte Carlo program, points in the electron phase space corresponding to positions and angles are generated uniformly over an ellipse with area E . In each slice of x-ray laboratory angle, the spectrum of x-ray energies can be calculated. In Table I, the mean and

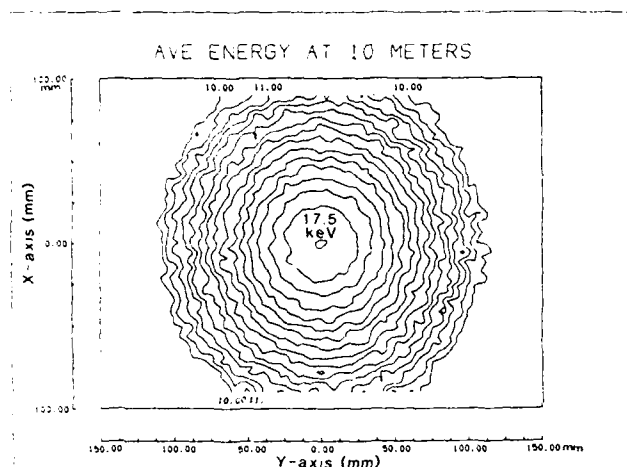


Fig. 5. An observer looking retrogradely into the x-ray beam would see concentric rings of near-monochromatic radiation as depicted in this energy plot. The irregularity of the rings is merely a reflection of the number of points plotted after Monte Carlo calculations.

rms of the x-ray energy at each laboratory angle are displayed for various choices of the electron beam radius. In fact, the energy distributions are not symmetric, being skewed toward the high end at small angles. For each beam waist the angle θ_c (max) for which 80% of the x-rays are above 15 keV has been calculated. For a waist of 20μ this angle is 5 milliradians. The entire x-ray energy spectrum, with beam energy resolution folded in, is shown in Figure 7. The spectrum of x-rays in the 5 milliradian cone is shown in the dashed histogram. The angular distribution is shown in Table 1 and Figure 8. The table shows the elements of the rate calculation for three possible beam waists, with the angular cut made to keep 80%

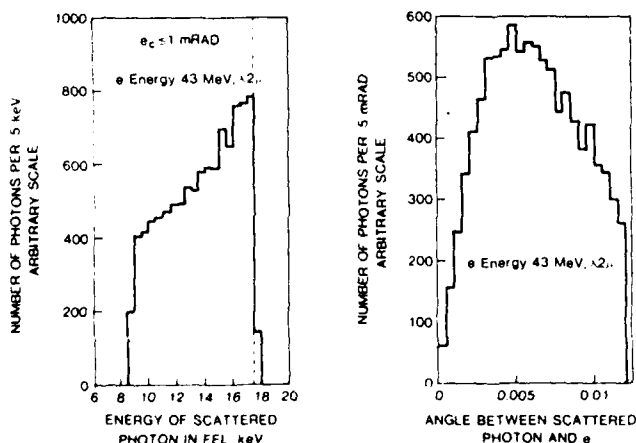


Fig. 6. X-ray energy and angular distributions obtained with an ideal electron beam and ideal photon beam.

TABLE 1. Rates in Cones with 80% of X-rays Above 15 keV*
(These figures refer to a "one-pass" system wherein electrons "see" light photons only once.)

r_b	15μ	20μ	50μ
θ_c max	4 mrad	5 mrad	6 mrad
L ($m^{-2}s^{-1}$)	5.0×10^{37}	2.8×10^{37}	4.6×10^{36}
σ_c ($\theta_c < \theta_c$ max) (m^2)	7×10^{-29}	1.1×10^{-29}	1.7×10^{-29}
Rate (photons/sec)	3.4×10^8	3.1×10^8	7.7×10^7

*where:

r_b is the radius of the beam

θ_c max is the maximum acceptance angle

L is the luminosity

σ_c represents the interaction cross-section

Rate refers to the x-ray photon production

of the x-rays above 15 keV, and the electron bunches colliding only once with the light photons.

Rate Calculations

Photon flux expressed as photons per second with angles less than θ_c is obtained from the product of incident intensity and a quantity called the cross section. The cross section σ_c is found by integrating the Compton scattering intensity divided by the incident intensity over the range of angle θ_c in the electron rest system corresponding to θ_c . In a colliding beam geometry the incident intensity is given by the luminosity, L , defined as

$$L = N_e \times N_\gamma \times f \div A$$

where

N_e is the number of electrons per bunch,

N_γ is the number of photons per bunch,

f is the frequency of intersection of the two bunches, and

A is the common area of the two bunches.

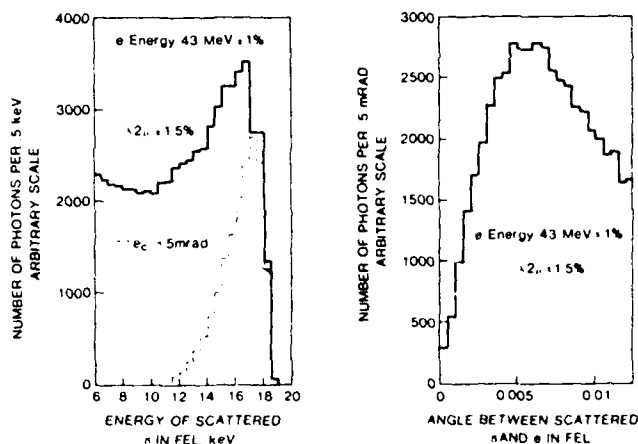


Fig. 7. X-ray energy and angular distributions obtained with the electron beam and photon beams coming from the Vanderbilt FEL.

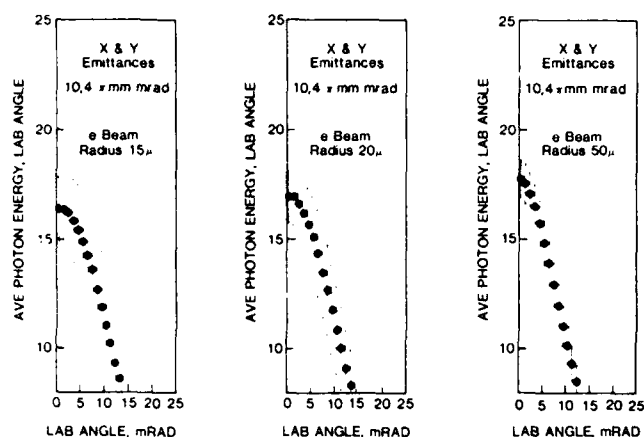


Fig. 8. The spread of x-ray energies delivered at various angles from the center of the electron beam. The various plots show the effect of changing the radius of the electron beam.

In the MFEL, the beam consists of micropulses of a few picoseconds duration at intervals of 350 picoseconds, spread over several microseconds (Fig. 9). Tentative parameters are a current of 20 A over 5 picoseconds, and a macropulse of 10 microseconds. Then $N_e = 6.25 \times 10^8$ electrons per micropulse. In a single pass system in which each micropulse of photons sees each micropulse of electrons once, the product $N\gamma f$ is the number of photons per second. For a beam of 6W and 2μ this product is $N\gamma f = 6 \times 10^{19}$ photons per second (since there are 1.7×10^6 micropulses per second and 3.5×10^{13} photons per micropulse).

The area depends on how tightly the beams are focused. The product of the radius of the beam times the angular divergence is equal to the normalized emittance γ_e . The MFEL $\pi\gamma_e$ is approximately 7π mm-mrad. As the area of the electron beam shrinks, the increasing divergence of the electrons results in a broader spectrum of x-ray energies at a given laboratory angle. By making the area of the beam small, one increases the rate, but the monochromaticity of the beam will be reduced. The effect of the beam divergence must be kept comparable to those of other uncertainties, such as the spread of beam energy, which is about 1%.

Higher Energy Photons from Backscatter

Although the original configuration of the FEL/CBD will yield x-ray photons at 17.9 keV, more energetic photons may be easily produced by any one or more of several methods.

Increasing the energy of the electron beam not only produces shorter wavelength radiation, but has the added benefits of creating a higher flux (more photons per second) that scatters at a smaller angle and is more monochromatic (narrower bandwidth). For example, an

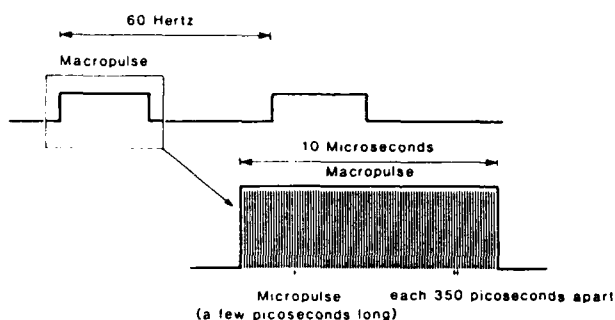


Fig. 9. The pulse structure of the FEL is programmable with the maximal repetition rate for macropulses at 60 Hz. Micropulses of a few picoseconds in length may be bunched together to form whatever macropulse one desires.

electron beam of 55 MeV produces light output from the FEL at 1.25μ . This combination of electron/photon interaction in the FEL/CBD will produce x-ray photons at 49 keV.

FELS may be operated at harmonics of the primary frequency but with a lower power output. This photon output may be used to generate higher keV x-rays with the FEL/CBD; or the primary frequency of the FEL can be doubled by passing its output through frequency doubling crystals after the light has left the FEL (both situations would reduce x-ray photon flux significantly).

High average power, ultrafast conventional lasers may also be used with the FEL/CBD both boosting photon flux and creating more energetic x-rays, given that the electron beam energy may remain fixed. One to two orders of magnitude increase in photon flux may also be achieved by causing multiple interactions between each electron pulse and each light pulse. Several methods of achieving this have been proposed. By including the lasing medium in one limb of a ring amplifier, and placing the interaction zone in one of the other limbs, a significant increase in light photon flux is created, such that the electron pulses "see" a much more intense light beam (Fig. 10).

Initial Use of the FEL/CBD

When radiation interacts with matter in the lower keV energy range, photoelectric effects can be used to great advantage to reduce scattered radiation, enhance natural tissue contrast, and establish the elemental composition of the tissue irradiated. As radiation energy increases, the amount of the x-ray beam that is absorbed continues to decrease until the energy of the photons slightly exceeds the binding energy of the inner K-shell electron. At that point, there is an abrupt increase in the absorption of the radiation beam called the "K-edge", something which is particularly pronounced in high atomic number absorbers.

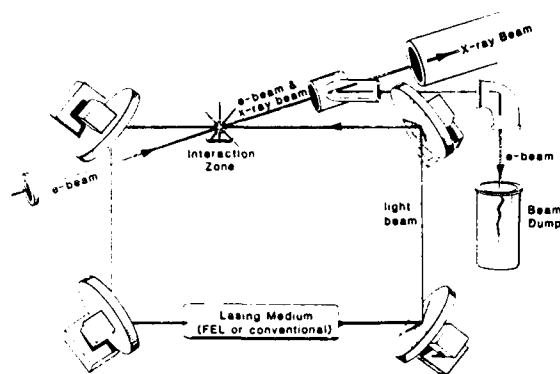


Fig. 10. Including the lasing medium in the ring cavity that contains the interaction zone markedly increases the photon flux "seen" by the electron beam thereby significantly boosting the x-ray flux exiting the interaction zone.

Among the atomic species most important in biological substances, hydrogen, carbon, nitrogen, oxygen, sodium, sulphur, chlorine, potassium, calcium and iron have discrete k-edges which are in the low keV energy range. Other substances such as copper, iodine, and barium have K-edges which are below 40 keV (Table 2). For maximal x-ray absorption, the energy of the x-ray beam should be as closely matched to the K-edge of the absorber as is possible.

There are a number of potential diagnostic uses for near-monochromatic x-radiation, among them the detection of breast cancer. At the present time, an accurate, noninvasive method for establishing the histologic characteristics of suspected malignancies within the breast is not available. Surgical excision of suspected lesions with microscopic examination of the excised tissue remains the only option when a suspected lesion is present. Surgical removal carries with it morbidity and often anguish for the woman involved. The cost in financial, social, and psychological terms for each "curable" cancer found dictates that the search for a more sensitive and specific screening tool than present-day mammography or diaphanography must be undertaken.

By illuminating the breast or any other tissue with discrete monochromatic beams of x-ray with keV energies between 0 and 40, one might take advantage of the photoelectric effect and the K-edges of the above mentioned "physiologic" atoms to perform elemental analysis of suspect biologic tissues. Utilization of multiple narrow lines of monochromatic radiation at various keV's in that range will allow elemental analysis and subtraction imaging in soft tissues. Our ultimate objective is to create a screening tool using the FEL/CBD, to simultaneously discover and histologically characterize intramammary lesions using near-monochromatic x-ray beams. This

technique will eventually be extended to other organ systems throughout the body.

Many factors are known concerning breast tumors which lend credence to our expectation that near-monochromatic x-ray beam elemental analysis and imaging stand an excellent chance for success. To some extent, it has already been shown by Johns et al⁹ that at 40 keV and below, there is a statistically significant difference in the attenuation coefficients for neoplastic and normal tissues in the breast. This difference becomes even more statistically significant below 30 keV.

There are also decided differences in the molecular and cellular composition of neoplastic tissues that discriminate them from normal tissues such as: polyploidy and differential DNA/RNA content than quiescent cell populations, neovascularization with higher blood flow, higher hyaluronidase activity than normal interstitial fluid, elevation in the water content of the interstitial spaces, higher hematocrit in the blood passing through tumors due to greater fluid leakage from the vessels, increased calcium content in the regions surrounding tumors (associated in some measure with the calcifications visible with plain film mammography), and a discrete variability in the diffusion gradients for nutrients and metabolic products in tumorous tissues, as well as necrosis within them. With such significant alterations in the regional biochemistry, cellular architecture, and elemental content, the absorption and transmission of multiple discrete monochromatic beams might be significantly altered relative to normal tissue.

The initial use of this device is centered on excised tissue samples, followed by tests on nude mice with human mammary carcinomas implanted in their soft tissues. First proofs are to be followed by application of this high contrast/low dose imaging modality to detection, analysis and treatment of breast lesions in humans.

Radiation Dose Considerations

The advantage of low-energy x-rays for producing images with high soft-tissue contrast has been recognized

TABLE 2. Some K-Edges of Importance

Element	K-Edge (keV)
Potassium	3.6
Calcium	4.0
Iron	7.1
Copper	9.0
Zinc	9.7
Gallium	10.0
Bromine	13.5
Technetium	21.0
Silver	25.5
Iodine	33.2
Xenon	34.5
Barium	37.4

for some time. This is due primarily to dominance of the photoelectric interaction, where the x-ray energy is absorbed without the creation of significant scattered radiation. This is in contradistinction to the Compton interaction which dominates at energies above 25 keV, and causes a reduction in contrast on the order of 3 to 6 times due to scatter.

Estimates have been made of the doses that might result from the use of narrow-beam low-energy monoenergetic beams relative to doses received from conventional film/screen x-ray mammography. Conventional systems deliver a dose of 0.06 rad with a skin entrance exposure of 0.370 R. In the manner previously described by Johns and Yaffe, entrance exposures were calculated for simulated breast tissue, 4.0 cm thick, in which a 0.3 cm lesion had been placed. The calculations assumed complete scatter rejection, unit detector efficiency, breast composition of 50% adipose and 50% glandular tissue and a linear attenuation coefficient of the lesion which is 5% greater than the surrounding breast tissues. An optimized system for breast imaging using monochromatic radiation such as that described here may reduce entrance exposure to the breast by a factor of 9 to 46 times.

As the energy of the x-ray beam produced increases, the techniques described here will be extended to other

areas of the body. keV's of 40-50 should be relatively easy to obtain and will be energetic enough to image any portion of the body with similar results.

Acknowledgments

The authors would like to express their appreciation to Ms. Flo Stiglitz, Alfredo Luccio PhD, A. Bertrand Brill MD, PhD, William Riddle PhD, Mr. Paul Gross, Mr. Frank L. Carroll and Sierra Laser Systems for their excellent secretarial and technical assistance.

This work has been supported in part by grants from The Strategic Defense Initiative Organization, Office of Technology Applications (OSD/SDIO/TTA) Contract #N00014-87-C0146 as of September 1987, Modification #P00003, and the Eastman Kodak Corporation Health Sciences Division, Rochester, New York.

References

1. Brau C. Free electron lasers, *Science* 1988;239:1115-1121.
2. Marshall TC. Free Electron Lasers. New York, NY: Macmillan Publishing Company, 1985.
3. Piestrup MA, Rothbart GE, Fleming RN, Pantell RH. Momentum modulation of a free-electron beam with a laser. *J Appl Phys* 1975;46:132-137.
4. US Pat #4,598,415. Luccio AU, Brill BA. Method and apparatus for producing X-rays. Dated Jul 1, 1986. US Patent Office.
5. Johns PC, Yaffe MJ. X-ray characterization of normal and neoplastic breast tissues. *Phys Med Biol* 1987;32:675-695.

Special Article

Generation of "Soft X-Rays" by Using the Free Electron Laser as a Proposed Means of Diagnosing and Treating Breast Cancer

Frank E. Carroll, MD

Department of Radiology and Radiological Sciences, Vanderbilt University Medical Center, Nashville, Tennessee 37232-2675

The diagnosis and treatment of breast lesions may be markedly enhanced by the use of a unique new source of near-monochromatic x-rays.

Concentric beams of near-monochromatic x-ray photons may be generated by collision of the free electron laser (FEL) electron beam with the optical beam in an interaction zone that delivers the x-rays to a shirtsleeve environment.

The absence of Compton scatter and the photoelectric interaction within tissues improves conspicuity of lesions by two to six times. Increased attenuation of x-rays in malignant vs. normal tissues makes tumors more obvious. K-edge subtraction allows chemical analysis of tumors in vivo—all at radiation doses that are one-tenth to one-fiftieth that delivered by the lowest-dose mammographic x-ray technique available. This allows for an increased sensitivity and specificity and permits prediction of histology, negating necessity for biopsies.

Selective bond-breaking at depth in tissues as well as x-ray-activated photodynamic therapy are also being explored.

Key words: Compton backscatter, monochromatic x-rays, breast lesions

INTRODUCTION

Since Roentgen's initial use of x-rays in 1895, our accuracy in diagnostic radiology has been hampered somewhat by the wide spectrum of radiation emitted by x-ray tubes (Fig. 1). Extremely soft x-rays do not penetrate the skin or other tissues sufficiently to yield detectable information on film or with other imaging devices. (These x-rays only increase the undesirable radiation dose to the patient.) On the other end of the spectrum produced by x-ray tubes, scattered radiation becomes problematic due to off-axis scattering within the part imaged, creating fog (noise) in the imaging chain, which reduces visibility of structures within the tissues. If we were able to produce x-rays at or near the frequency best suited to the particular imaging task at hand, we

could significantly improve the sensitivity and specificity of our diagnostic imaging (Fig. 2).

At the Vanderbilt Medical Free Electron Laser (FEL) Facility, current research is being directed toward the earlier diagnosis and treatment

Accepted for publication September 17, 1990.

Address reprint requests to Frank Carroll, M.D., Department of Radiology and Radiological Sciences, Vanderbilt University Medical Center, Nashville, TN 37232-2675.

This work is supported in part by grants from The Eastman Kodak Corporation—Health Sciences Division, Rochester, NY, and The Strategic Defense Initiative Organization/Office of Technology Applications and Office of Naval Research. Contract #N00014-87-C0146 Mod P00003.

STANDARD X-RAY TUBE SPECTRUM

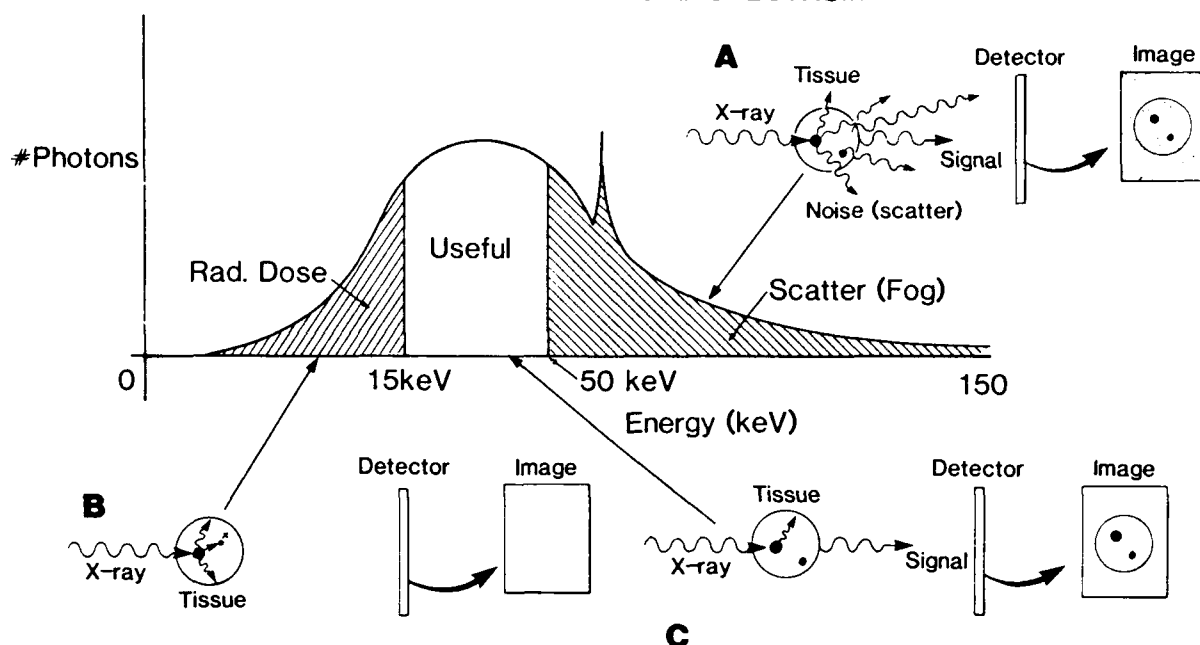


Fig. 1. Standard x-ray tubes emit radiation with a distribution such as that shown. A: At the upper end of the spectrum, Compton scattering contributes significantly to noise by fogging the x-ray film, obscuring detail. B: At the low end of the energy range, the x-rays are so "soft" that they do not penetrate the part being imaged; thus, no image is formed. These

"soft" x-rays impart a marked increase in radiation dose to the patient. C: X-rays from the useful region of the spectrum partially interact with the soft tissues and are absorbed, while the remainder of the beam passes on to the film without any scatter.

of breast cancer without the need for surgical procedures such as biopsy or lumpectomy, through the use of near-monochromatic x-ray beams. This new type of radiation beam has the desirable quality of tunability, high flux rates for imaging, and a pulse structure that mimics that of the FEL.

MATERIALS AND METHODS

The Free Electron Laser

Passage of a near-relativistic electron beam over a magnetic field of alternating north-south polarity stimulates emission of characteristic radiation, which, when bounced between optical cavity end mirrors, interacts with the electron beam in such a way that the light emitted is significantly amplified. The variable pulse structure of the FEL allows emission of exceedingly powerful laser pulses in the picosecond timeframe. Alteration of the periodicity of the magnets, modification of the strength of the magnetic field, or change in the energy of the electron beam permits one to tune the FEL to innumerable frequencies throughout the electromagnetic spectrum. The

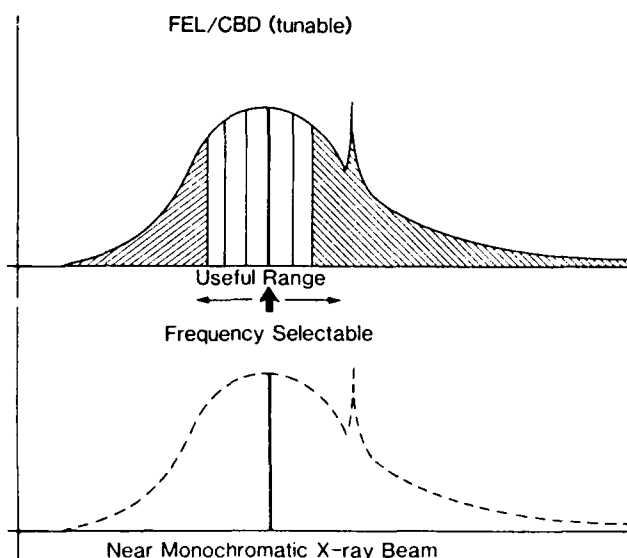


Fig. 2. By tuning the FEL Compton backscatter device to the useful energy range and specifically to the desired narrow frequency, one is better able to image, chemically probe, and treat lesions deep within tissues.

reader is referred to a more comprehensive text for further elucidation of the physics involved in FEL photon production [1].

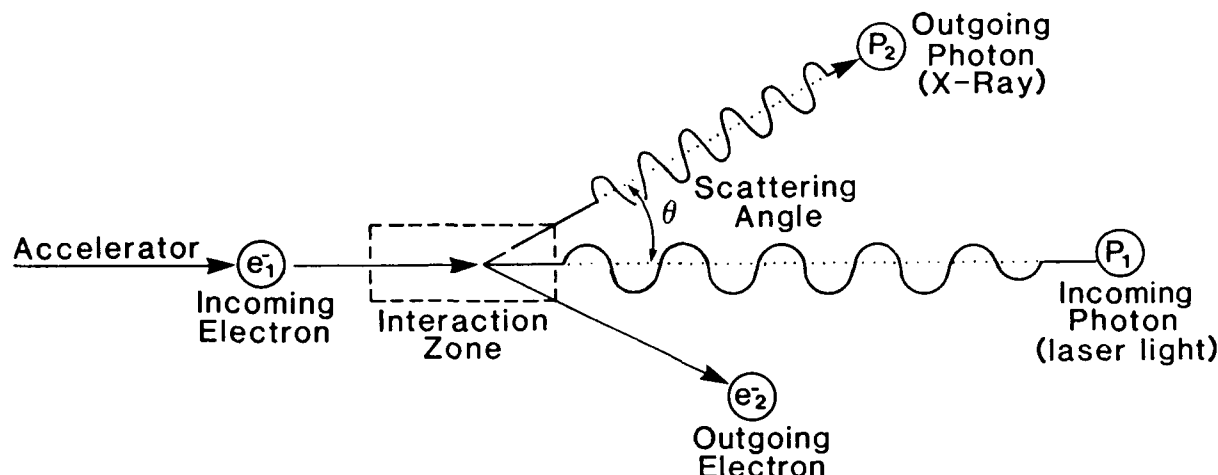


Fig. 3. Head-on collision of an electron beam traveling close to the speed of light with an infrared or light laser photon creates x-ray photons scattered backward along the direction the electrons were traveling. (The angle is exaggerated here for clarity.) Some of the electron's energy is lost to the photon. (From: Carroll FE, Waters JW, Price RR, Brau CA, Roos CF,

Tolk NH, Pickens DR, Stephens WH. Near-monochromatic x-ray beams produced by the free electron laser and Compton backscatter. *Invest Radiol* 1990; 25:465-471. [2] Reprinted with permission of the publisher, JB Lippincott Co., and the author.)

Compton Backscatter Device

Head-on collision of the electron beam normally discarded from the FEL with the intense photon output of the FEL in a specially designed interaction zone [2] produces a near-monochromatic beam of x-rays by a phenomenon long known to high-energy physicists as Compton backscatter (Fig. 3). These near-monochromatic x-rays can be shunted to an imaging laboratory on the floor above the FEL vault at Vanderbilt's facility [3].

Infrared or light photons of different frequencies may be used for these collisions with the electron beam, which itself may be varied by increasing its energy. This allows one to select the most useful frequency for the tissue or part to be studied. The initial configuration of the FEL at Vanderbilt (Fig. 4) will allow the production of 17.9 keV x-rays in a tightly coned beam that diverges very little. The energy spread of the electron beam and the phase differences between the electrons in the beam create concentric circles of near-monochromatic x-rays about the most energetic and intense central beam. An observer gazing directly into the center of the x-ray beam would see concentric circles of different energy (Fig. 5).

DISCUSSION

Radiation Effects in Tissues

X-rays in the 10-30 keV range interact with tissues in two discrete ways. Photoelectric inter-

action predominates from 10 to 20 keV, whereas Compton scattering effects take precedence above 20 keV (Table 1).

The photoelectric interaction is portrayed in Figure 6. An x-ray photon traversing the tissue interacts with electrons in their respective atomic orbits when the energy of the photon is very near the binding energy of one of these electrons. The electron is ejected from the atom, and an electron from an adjacent orbit falls into the void created, releasing characteristic radiation of its own, leaving a positive ion within the tissues. When such an interaction occurs, the incoming photon is essentially extinguished, such that a negative image of the atom or molecule with which it interacted is created in the residual beam that traverses the part imaged to reach the receptor/detector.

At slightly higher energies, x-ray photons scatter off of atoms (with slightly reduced energies) at angles that are off-axis from the central beam, creating a useless fog of radiation that does not impart worthwhile information to most detectors, particularly film.

X-rays are attenuated in soft tissues by differing amounts, depending upon the effective density of the material being traversed, the atomic number of the atoms in the molecules, and the number of electrons per gram of tissue. In breast tissue, measurements have shown that fat has a lower atomic number than glandular tissue, which, in turn, has a lower effective atomic num-

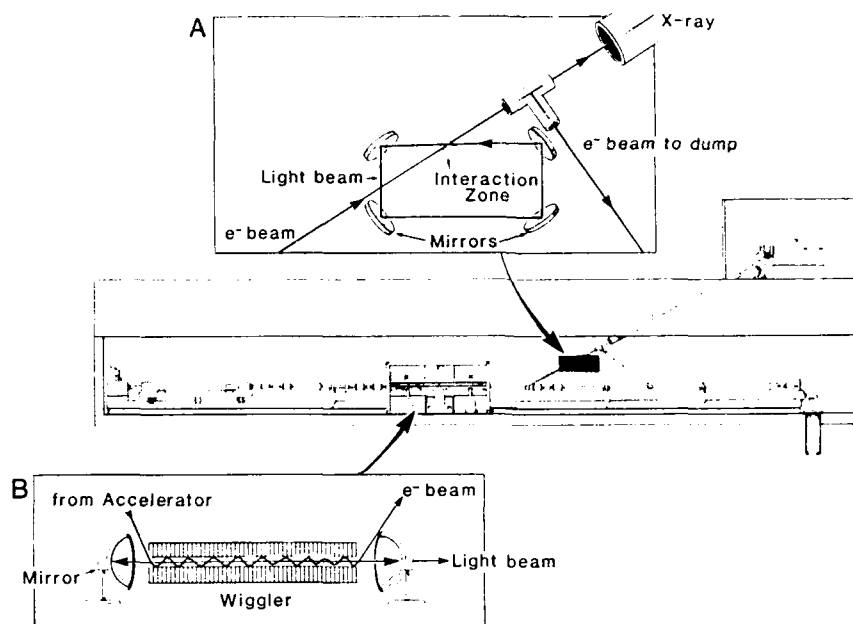


Fig. 4. **A:** The electron beam used for the FEL can be redirected to an interaction zone, where it may collide with the laser beam from the FEL itself or from other conventional lasers. **B:** The FEL consists of an electron source, a linear accelerator to boost the beam to near relativistic energy, and mirrors for the laser cavity, and a series of magnets with alternating north-south orientation (called a "wiggler").

(From: Carroll FE, Waters JW, Price RR, Brau CA, Roos CF, Tolk NH, Pickens DR, Stephens WH. Near-monochromatic x-ray beams produced by the free electron laser and Compton backscatter. *Invest Radiol* 1990; 25:465-471. [2] Reprinted with permission of the publisher, JB Lippincott Co., and the author.)

ber than that of cancer. Johns and Yaffe [4] have shown a distinct difference in the linear attenuation coefficients of fat, normal glandular tissue, and cancers in the energy range from 110 keV to 18 keV, with a noticeably significant and increasing separation of relative attenuation between normal tissues and cancers below 30 keV. This difference becomes even more pronounced below 20 keV. Since the optimal range for the FEL Compton device will be between 15 and 17.9 keV, study of similar breast tissues by our group is presently underway at the Brookhaven National Laboratories at the lower energy range to establish whether or not the widening gap in relative attenuation is a continuum or not. Our earliest data for the energy range from 14.5 to 16.0 keV shows similar characteristic alterations in relative attenuation seen by the Toronto group mentioned above. We will be returning to Brookhaven in the fall of 1990 to complete our work before publication to fill the gap between 16.0 and 18.0 keV.

Had our confirmatory studies underway at Brookhaven yielded negative or equivocal results, we would still have been able to benefit from the

monochromatic beams described here by increasing the effective keV to approximately 20 keV (taking advantage of already proven effects), since we presently plan to explore this energy region anyway, as the device can potentially emit monochromatic x-rays up to 49.0 keV.

Near-Monochromatic X-rays

By eliminating x-ray frequencies that are not in the optimal keV range, radiation dose may be reduced considerably (Table 2). Compared to the lowest dose film-screen mammographic examinations now done in most hospitals, the near-monochromatic study will deliver a radiation dose to the patient that will be from one-tenth to one-fiftieth as much. A patient would be able to receive a mammogram for most of her life and still only receive the same dose now acquired on a single study.

The eradication of scatter also allows any lesions in the breast to be seen two to six times better, due to the reduction of noise/fog on the film.

Use of selected tunable x-ray frequencies such as afforded by the Compton device carries

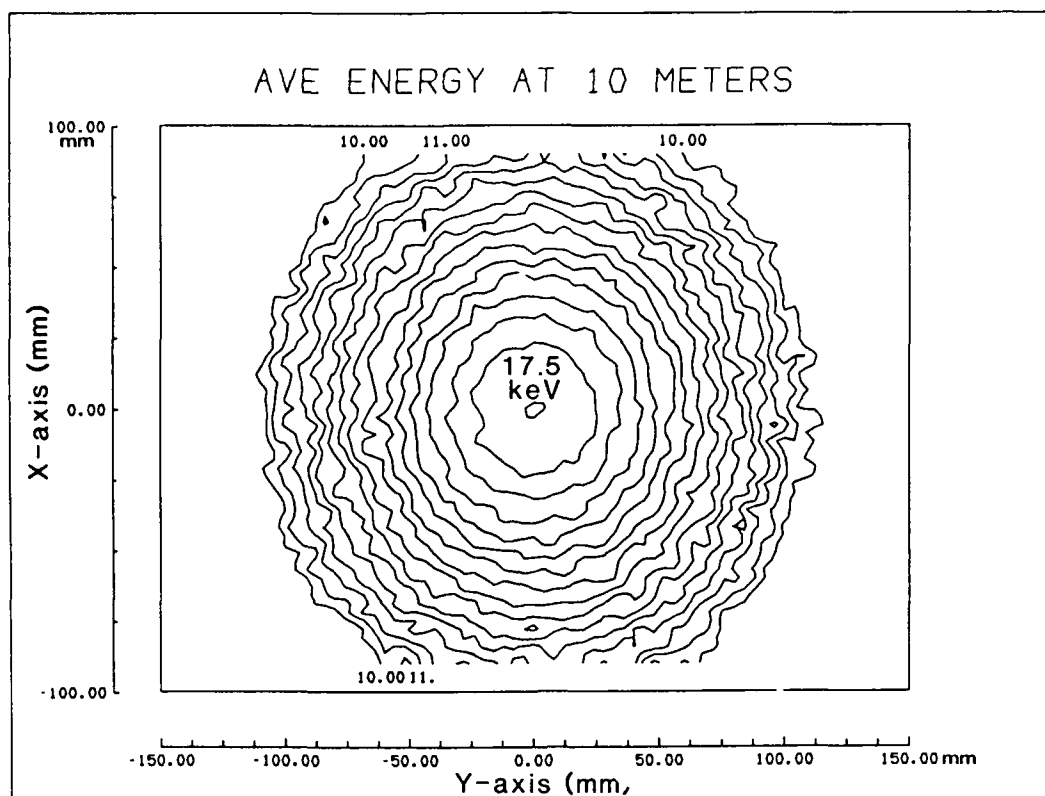


Fig. 5. The x-ray beam created by the Compton backscatter device consists of concentric rings of photons at lower and lower energies as one moves radially outward from the center of the beam. The vast majority of the photons are at the center of the beam—all with the highest energy obtainable for a given set of machine parameters; lower energy rings are of

lower intensity. (From: Carroll FE, Waters JW, Price RR, Brau CA, Roos CF, Tolk NH, Pickens DR, Stephens WH. Near-monochromatic x-ray beams produced by the free electron laser and Compton backscatter. *Invest Radiol* 1990; 25: 465–471. [2] Reprinted with permission of the publisher, JB Lippincott Co., and the author.)

**TABLE 1. X-Ray Interactions With Matter:
% Photoelectric Vs. Compton Scatter**

Photon energy (keV)	Photoelectric interactions as a percent of total (approx.), %
10	95
15	80
20	60
30	30

with it the added benefit of being able to explore K-edge absorption within the tissues, permitting “chemical” analysis of breast tissues without the need for excision. As the x-ray energy reaches the binding energy of the K-shell electron, there is a sudden increase in absorption of the beam (the K-edge), revealing the presence of specific atoms (Fig. 7). Even if the absorption K-edge is lower than the energy selected, some effect can still be seen or observed. As an example, local calcium concentrations are higher in breast lesions. Even

if the K-edge of calcium is too low to image, chromophores that monitor local calcium concentration can be used and imaged.

The exceedingly short pulses delivered by the FEL are also reflected in the monochromatic x-rays produced by the Compton backscatter device. A common thread weaving itself through all of the research being done at the Vanderbilt FEL is an inquiry into the non-thermal/non-linear effects caused in tissues by the unique pulse structure and wavelengths attainable with this exceptional laser. Similarly, we will be searching for frequencies that affect the malignant cells while leaving normal cells and cell processes unchanged. If found (and there are reasons to believe that they will be), this will open the door to a new form of radiotherapy.

Detectors

Traditionally, film-screen combinations have been used for routine mammography. They are not

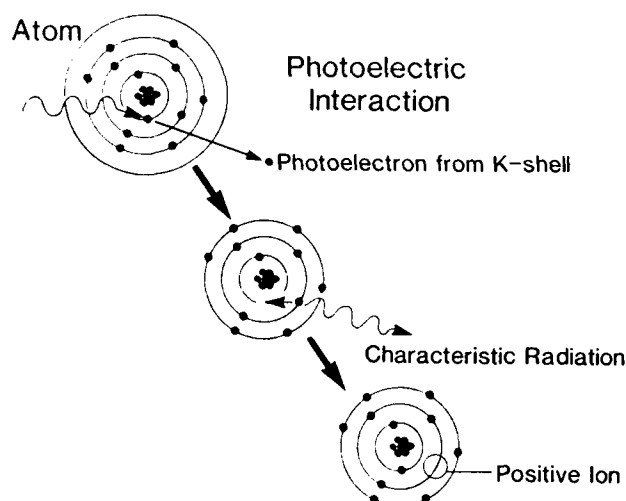


Fig. 6. The photoelectric interaction, dislodgment of a K-shell electron by an x-ray photon, occurs predominantly below 20 keV and can be used to greatest advantage in breast imaging. The characteristic radiation produced when an outer shell electron fills the void left by the photoelectron from the K-shell is of such low energy that it does not leave the soft tissues.

TABLE 2. Radiation Dose Vs. Beam Energy (in keV) in Mammography

Beam energy (keV)	Entrance exposure (R)
10	106.0
15	0.042 (42 mR)
20	0.008 (8 mR)
28 (standard low-dose mammography)	0.370 (370 mR)

always the best or most efficient detectors of x-rays. If only the central portion of our beam is used for imaging, our studies will truly be near-monochromatic. However, the concentric rings of radiation at progressively lower keV can be used not only to impart structural/positional information about a lesion, but also to simultaneously acquire energy information concerning that same lesion. Charge-coupled devices (CCDs) lend themselves to the rapid acquisition of this spatial and energy-dependent data (Fig. 8). By scanning the beam, the patient, or the detection system, one may store information from each pixel into a portion of memory set aside for a particular energy level which could later be formed into a unique energy picture of the part imaged. These several images could stand alone as energy-specific images or be added to or subtracted from one another to synthesize additional, more complex facsimiles of the breast or other part imaged.

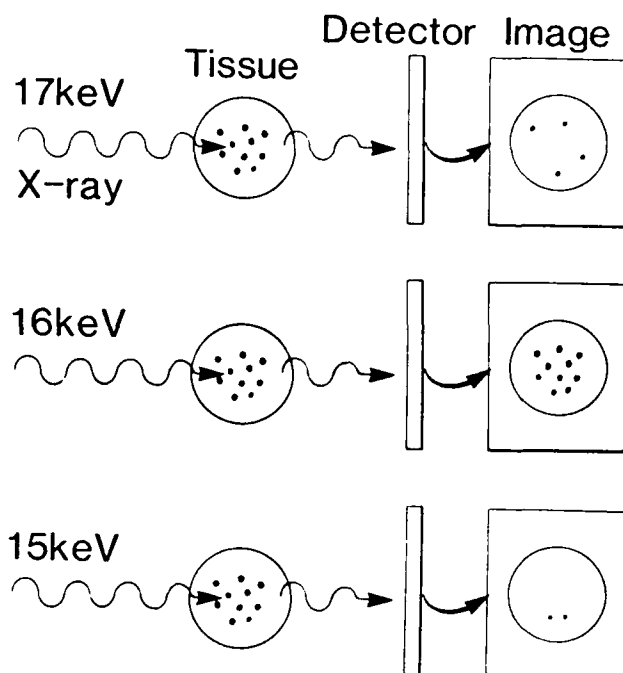


Fig. 7. As progressively higher keV photons are passed through the tissues, a point is reached where the x-ray energy coincides with the binding energy of the K- or L-shell electrons such that the beam is suddenly absorbed to a significantly greater degree, allowing one to detect the presence of specific elements, both with imaging systems and spectral analysis systems.

The characteristics of speed, tunability, power, and versatility permit the FEL to be used to create near-monochromatic x-ray beams that are useful for the earlier diagnosis and treatment of breast malignancies. This technique, however, is not limited to the breast. Breast cancer will be studied first, due to the ideal energy range available on FEL startup, the importance of this illness to an overwhelming portion of our population, and the accessibility and thickness of the part to be imaged. Extension of this procedure to other areas of the body will be pursued in short order as the machine is capable of producing x-rays of up to 49 keV with few adjustments.

ACKNOWLEDGMENTS

The author wishes to express his appreciation to others who continue to contribute to the work on this project on a daily basis: Ron R. Price, Ph.D., James W. Waters, Ph.D., David R. Pickens, Ph.D., Carlton F. Roos, M.D., Charles A. Brau,

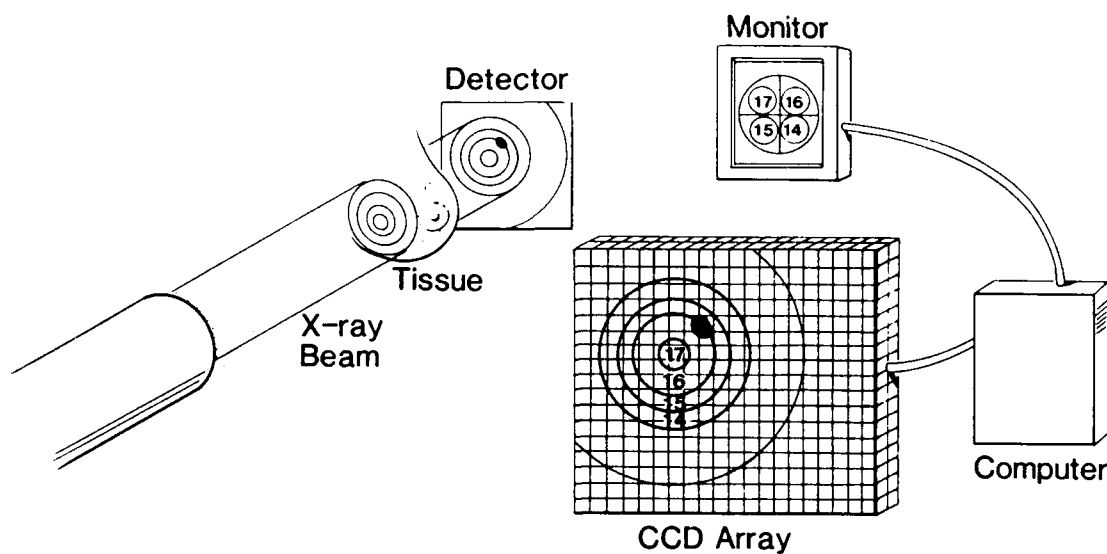


Fig. 8. The concentric rings of distinct x-ray energies in this beam may be coupled with the unique abilities of charge-coupled devices, wherein the spatial and energy information in each picture element (pixel) in the array can be accessed,

stored, and synthesized into images of the part corresponding to its characteristics at any one or some combination of energies in the beam.

Ph.D., Wei W. Dong, M.S., Robert Bain, M.D., Norman H. Tolk, Ph.D., and Paul Wang, M.S. He also expresses his thanks to Tom Ebers for his excellent editorial assistance.

REFERENCES

1. Brau CA. "Free Electron Lasers." Cambridge/Boston: Academic Press, 1990.
2. Carroll FE, Waters JW, Price RR, Brau CA, Roos CF, Tolk NH, Pickens DR, Stephens WH. Near-monochromatic x-ray beams produced by the free electron laser and Compton backscatter. *Invest Radiol* 1990; 25:465-471.
3. Carroll FE, Roos CF, Price RR, Pickens DR, Stephens WH, Waters JW, Brau CA, Tolk NH. Tuneable laser may offer in vivo tissue analysis. *Diagn Imag* 1989; 11:291-296.
4. Johns PC, Yaffe MJ. X-ray characterization of normal and neoplastic breast tissues. *Phys Med Biol* 1987; 32:675-695.

The initial diagnostic application for the free electron laser will probably be in breast screening

Tuneable laser may offer in vivo tissue analysis

While lasers have become common in medicine for cutting, burning and ablation, radiologists have only begun to tap their potential in diagnostic medicine. The use of this unique source of radiation has been limited to patient positioning devices, image printing cameras, and laser angioplasty. Researchers are breaking new ground, however, with work on a "tuneable" laser that could replace surgical biopsies in determining the etiology of breast lesions.

Unlike the typical light bulb, which emits photons across a range of wavelengths, laser light is distinctive in that its photons fall within an extremely narrow bandwidth. Laser photons are emitted in lockstep concordance as a coherent synchronized beam. This coherence, along with the capability of lasers to amplify light to high power densities, has opened the door to such technologies as expanded fiber-optic telecommunications, holography and exceptionally accurate measuring devices.

Standard x-ray tubes are similar to light bulbs in that they emit a broadband spectrum of radiation, including photons with energies from 10 to 150 keV. Much of the output of an x-ray tube is wasted radiation, causing scatter that offers no useful

information but fogs film and is absorbed by the patient. "Softer" x-rays are necessary in modalities like mammography to define contrast differences between the various components of the breast. If the energy of the x-ray beam could be tuned to the most useful frequency for the task at hand, patient dose might be reduced and contrast detail boosted by several orders of magnitude.

X-ray lasers have been devised and operated in brief bursts by emission from excited plasmas pumped by powerful lasers, such as those used in fusion research. A source of narrow-bandwidth x-rays that is tuneable, controllable and of sufficient strength

for imaging has heretofore been unavailable, however.

FREE ELECTRON LASERS

A multidisciplinary research group at Vanderbilt University was awarded a grant in 1987 by the Strategic Defense Initiative Organization and the Office of Naval Research to explore the usefulness of the free electron laser (FEL) in the biomedical and materials areas.¹

The FEL is a unique device that is theoretically capable of being tuned to any frequency across a large portion of the electromagnetic spectrum, from radiowaves to x-rays. This includes the entire visible spectrum. This laser may deliver its radiation in brief bursts lasting picoseconds or femtoseconds, but is also capable of continuous operation. Because of its adjustable pulse structure and tuneability, the FEL can be used to explore the nonlinear and nonthermal

DR. CARROLL is chief of chest radiology at Vanderbilt University, Nashville. Assisting him in the preparation of this article were Carlton F. Roos, M.D., Ron R. Price, Ph.D., David R. Pickens, Ph.D., and W. Hoyt Stephens, all of the department of radiology at Vanderbilt; and James W. Waters, Ph.D., Charles A. Brau, Ph.D., and Norman H. Toik, Ph.D., all of the department of physics and astronomy at the same institution.

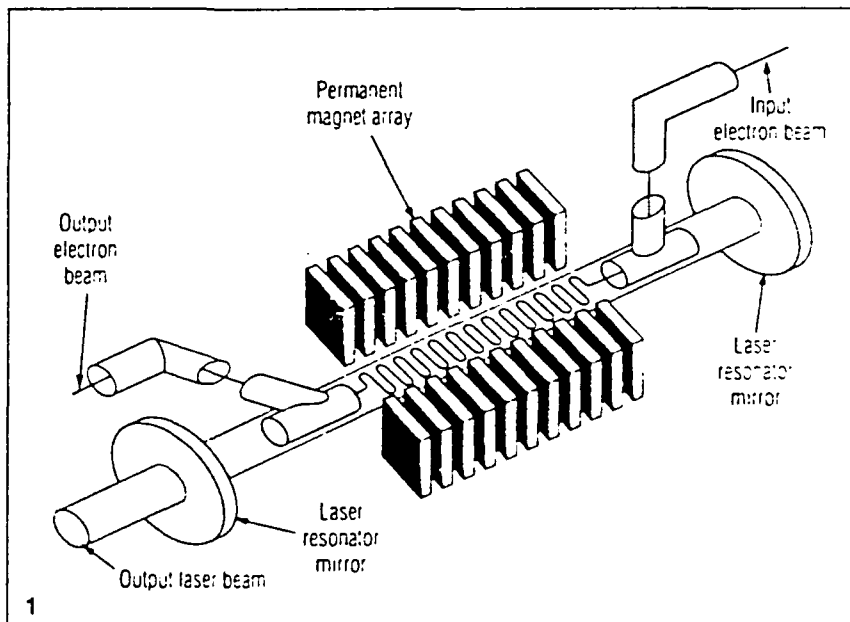


FIGURE 1. Schematic diagram of free electron laser. Electron beam is forced to follow undulating path between magnets with alternating north-south orientation, causing emission of light or infrared photons. As these photons bounce repeatedly between end mirrors of resonator cavity, they interact with electrons, causing extensive amplification.

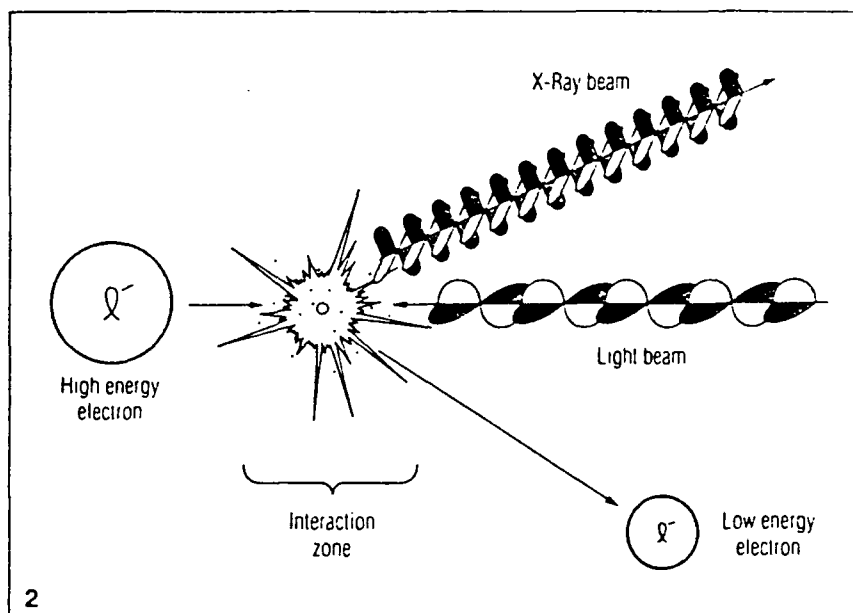


FIGURE 2. Head-on collision of near relativistic electrons and light or infrared photons yields backwardly scattered photons with appreciably shortened wavelengths (x-ray photons). These x-rays are scattered backwards in line that is almost collinear with direction of electron beam. Angle is exaggerated here for clarity.

effects that this type of radiation may have on tissues and other materials.

The FEL consists of an electron source and an accelerating device capable of delivering a beam of high-quality electron bunches at velocities near the speed of light. These electron pulses are directed through an oscillating magnetic field such as is produced by a series of permanent magnets with alternating north-south orientation.

The latter apparatus, called a "wiggler," sits between a pair of mirrors in the laser cavity. As the electron beam traverses the changing magnetic field, it is compelled to wiggle back and forth, emitting characteristic radiation, part of which bounces between the mirrors at the ends of the cavity. As the light repeatedly traverses the wiggler cavity, it too interacts with the electron beam in such a manner that the light is amplified (Figure 1).

By changing the energy of the electron beam, or by altering the periodicity or strength of the wiggler magnets, one may tune the laser to any desired frequency.²³

Conventional lasers produce their

radiation at one or two fixed frequencies (unless their radiation is passed through frequency doubling crystals) or within a small tuneable band. The gaps left in the electromagnetic spectrum can now be filled by the FEL.

This vastly tuneable tool has not yet been driven at x-ray wavelengths directly. It may, in fact, be some time before electron beams of such high quality and energy or wigglers of such design come to pass. However, the Vanderbilt Medical Free Electron Laser group, with grant support from the Eastman Kodak health sciences division,⁴ has devised a method to indirectly force the FEL to produce nearly monochromatic x-ray beams that are tuneable, have a pulse structure identical to the FEL, and have a high enough photon flux to perform both imaging and in vivo tissue analysis.

FEL/COMPTON DEVICE

The electron beam used in the FEL is normally discarded in a "beam dump" after it has excited the wiggler cavity. It may, however, be used in another way. Nuclear physicists have long capitalized on the interaction of

electron beams with other photons to create a type of radiation called Compton backscatter. This is done by colliding laser light into an electron beam. The electrons impart some of their energy to the incoming photons and scatter them backwards in a direction that is almost collinear with the direction of the electron beam. The addition of this energy shortens the photon wavelength appreciably (Figure 2).

If the energy of the electrons and the wavelength of the incoming photons are selected properly, the resultant scattered photons will be shifted into the x-ray energy range of one's choice. Luccio and Brill¹ outlined the procedure in 1986 in their patent application.

The FEL electron beam in the Compton Backscatter Device (CBD) under construction at Vanderbilt will be shunted by bending and focusing magnets to an interaction zone. The infrared or visible light photon output of the FEL itself (or the output of other conventional lasers) will be directed by mirrors to the same interaction area to collide head-on with the electron beam. The x-rays produced in the collision will be directed from the FEL vault (which contains intense gamma and neutron radiation) through the bore of a large PVC pipe that passes obliquely through a 6.5-foot-thick concrete radiation shield situated above the FEL, finally exiting into the imaging laboratory on the floor above the vault (Figure 3).

The energy distribution of the x-rays produced and their angular dispersion are outlined in Figure 4.

An observer looking back along the central axis of the beam produced by this device would see an x-ray beam consisting of concentric rings of different keVs. This spatial separation of near-monochromatic beams can be useful in the simultaneous collection of data from independent loci within tissues at different keVs. While some voxels of tissue are being probed or imaged at 18 keV, others nearby may be examined at 16 or 17 keV, if desired. The complementary spatial

and energy information for each voxel can be compiled and multiple x-ray frequencies explored by scanning the beam over the tissue in question, by moving the sample, or by altering the parameters of the electron beam or light beams in the interaction zone.

The imaging chain will consist of charge-coupled devices, film or scintillation detectors, depending on the characteristics of the tissue under scrutiny.

BREAST IMAGING

Because the x-rays produced by the FEL are nearly monochromatic and spatially defined, they may serve as a probe for the detection of K-edges of various chemical elements. This would allow chemical maps of tissues under study to be made. Because malignant tissues and many benign diseases have clearly defined chemical, physiologic and cellular differences from normal tissues, they may be differentiated by their chemical composition. The tissue in question need not be excised from the body for such discrimination.

The initial use of this device will likely be in breast imaging. Breast biopsy specimens will first be examined. They will be filmed with stan-

dard mammographic techniques, followed by filming with the near-monochromatic beam. The specimens will then be subjected to linear attenuation analysis and K-edge evaluation. The characteristics of a large number of specimens will be used to establish a database from which predictions of histology might be made for future biopsies. Once the sensitivity and specificity of these techniques are known, the experiment will move into the in vivo environment. Nude mice with mammary carcinomas implanted in their backs will be analyzed in a manner similar to the biopsy specimen.

The technique will be used on patients already scheduled for breast biopsies only after its accuracy has been proved. These women will be studied prior to surgery and an attempt will be made to predict the histology of their lesions. The biopsy specimens will also be studied postoperatively and all of the information correlated with pathologic findings.

The entire procedure will eventually be extended in the form of a screening procedure. The entrance radiation dose to the breast has been calculated to be 0.11% to 0.02% of that delivered by conventional screen-

film systems. As this modality is refined, it is meant to replace surgical biopsy in determining the etiology of suspicious lesions.

The last imaging phase of the development project will focus on 3-D x-ray holography of the breast and the extension of its analytic capabilities to other parts of the body. Since relatively low keV photons (under 50 keV) can easily penetrate any body part, this type of radiation may be used to image internal organs and perform chemical analyses in situ. Intravenous angiography becomes more practical and safer at low doses of contrast, as has been shown with synchrotron radiation sources.*

The pulse structure of the FEL x-ray beam is such that radiation pulses may be delivered in picosecond bursts. Such rapid delivery of energy to tissues is useful in another way. The vibrational modes of DNA fall into the picosecond time frame so that energy from one pulse may be delivered to intracellular strands of DNA in a few vibration cycles, breaking certain bonds that are frequency-sensitive.

Instead of the laser energy creating tissue disruption by thermal means, it can enhance or retard cellular func-

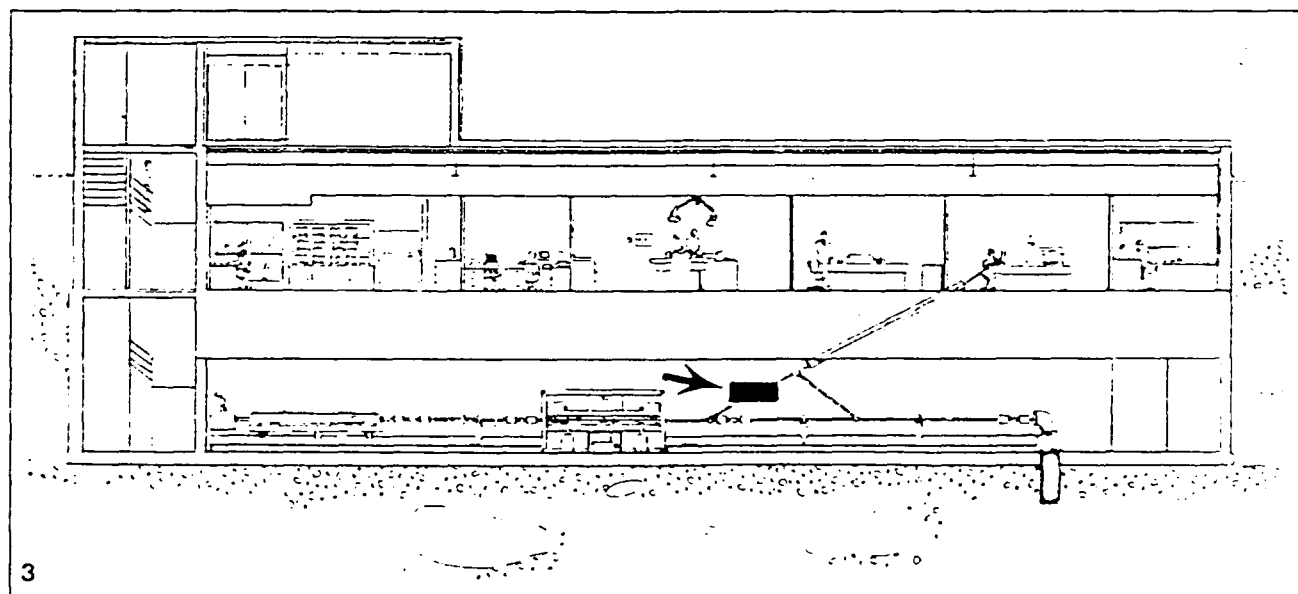


FIGURE 3. Vanderbilt Medical Free Electron Laser building. Shielded vault on lowest level houses FEL. Compton backscatter device is on left leg of triangular addition to electron beam pipe (black box at arrow). X-rays are

delivered to imaging lab through 12-inch PVC pipe that passes through thick concrete shield. Entire building except entrance and HVAC equipment is underground.

tions, such as growth or death by nonthermal action. Such changes have already been demonstrated in cell cultures and intact animals where fibroblast stimulation or retardation has been achieved by exposure to various frequencies and pulse paradigms. These latter effects have been shown at visible and infrared frequencies, but similar effects will be sought at the x-ray frequencies of the FEL/CBD to explore its usefulness as a treatment modality. Potentially, a lesion may be detected, analyzed, identified and treated by a single source of tuneable, near-monochromatic x-irradiation.

SHRINKING LASER

The FEL is an extremely large device that occupies the major portion of a heavily shielded 100-foot-long concrete vault. The laser creates extremely hazardous radiation levels around itself while operating and is an expensive, temperamental apparatus. How practical then are these machines?

The configuration of the Vanderbilt FEL is that of an experimental prototype. It is like a chameleon, flexible enough to act as a surgical tool one day, a spectroscopic probe another day, and a producer of x-rays on a third. It can also service all those needs simultaneously without major changes. When a specific spectral line yields some of its secrets and shows major promise as a surgical tool or as another medical device, a more compact dedicated laser of either the conventional or FEL type may be constructed for further testing or clinical use. The FEL can then be tuned to some other frequency or pulse format of interest for exploration of its usefulness.

Comprehensive research is under way at several national laboratories to devise a more compact FEL. Los Alamos National Laboratories in New Mexico, in particular, has made inroads towards shrinking the electron gun to a device only 18 inches long. Electromagnetic wigglers and newer accelerator technology have advanced to the point of test imple-

mentation. One of the goals of FEL research is to fabricate a laser system that would fit safely into a standard x-ray or operating room.

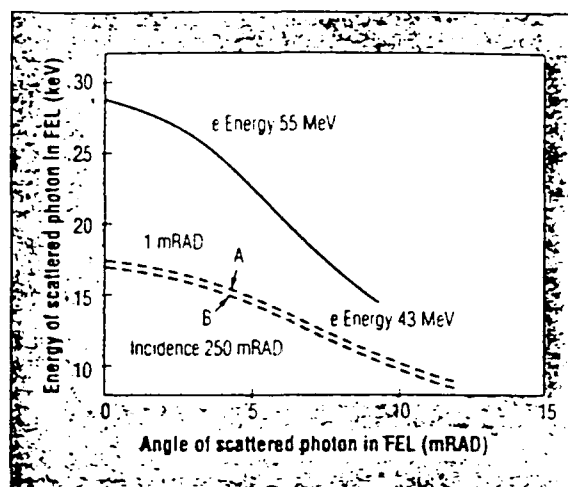
ANGIOPLASTY

Lasers are used in some radiology departments to perform laser angioplasty. This in some respects is a "me too" application, patterned after the preliminary work of surgeons, cardiologists and interventional radiologists. More experimentation is needed before laser angioplasty is accepted as a standard procedure. The reader is directed to a good overview of laser angioplasty for more information.⁷

While the technical success of laser angioplasty is unquestioned, its clinical efficacy remains uncertain. Results of long-term patency studies are still unknown, as are tendencies towards such complications as future aneurysm formation. Research at other frequencies and with new methods of delivering the energy safely to atherosclerotic plaque within intact vessels is needed.

Transillumination of the breast with infrared and visible laser light is also under study. Overlap in the spectroscopic patterns obtained in normal and neoplastic tissues has been a roadblock to higher sensitivity and specificity. The overlap is the result of scattering within the tissues, absorption by blood, and other uncontrollable considerations.

The addition of chromophores (chemicals that give rise to color in molecules) to monoclonal antibodies or other compounds that concentrate in tumors is a possible new way to detect superficial tumors. Hematoporphyrin derivative (HDP), for example, will accumulate in malignant



Distribution of x-ray energies obtained in FEL/BCD using parameters of FEL as delivered (curves A and B) and for system with electron beam energy increased to 55 MeV. Curve B is distribution of x-rays when interaction zone is canted 15° off-axis from photon beam. Little change is seen in number or energy of photons produced. This allows electron and x-ray beams to skirt past end mirrors used to direct photon beam at interaction zone. Were x-ray or electron beam required to pass through mirrors, there would be extensive attenuation of beams and damaging effects to mirror.

tissues in the airways and fluoresce when illuminated with certain frequencies of laser light, thus directing ablative laser surgical beams to their location. HDP or carotenoid beta-carotene can accumulate in atherosclerotic plaques, and may be activated by illumination with less intense laser light. This causes formation of singlet oxygen, which stimulates degeneration of the atherosclerotic plaque or destruction of tumors over longer periods of time.

Medicine needs to look toward such devices as the FEL if it is to reap the benefits of coherent radiation sources. This single laser can be used to explore innumerable wavelengths and pulse formats, without the additional cost of standard lasers.

The FEL can operate at discrete frequencies and set pulse formats until its usefulness has been established. One must keep an open mind about changes at the leading edge of high-technology development, whether it springs de novo from radiology or from research in space exploration or defense technology.

References on page 362

Acknowledgment

The authors wish to express their appreciation to: Ed. S. G. Paul, Paul Gross, Frank L. Carroll, Mark Carroll, and Bert L. Goss Systems for their technical assistance in the preparation of this manuscript.

continued from page 296

PHYSICS

REFERENCES

1. The Strategic Defense Initiative Organization/Office of Technology Applications (OSD/SDIO/TIA), Contract # N00014-87-C0146 Mod. P00003.
2. Meiz H. Applications of the radiation from fast electron Beams. *J Appl Phys* 1951;22:527.
3. Deacor DAG, Elias LR, Madey JM, et al. First operation of a free-electron laser. *Phys Rev Lett* 1977;38:652.
4. The Eastman Kodak Corporation—Health Sciences Division, Rochester, NY.
5. U.S. Patent #4,598,415. Luccio AU, Brill BA. Method and apparatus for producing x-rays. U.S. Patent Office, July 1986.
6. Vinocur B. High-tech physics advance noninvasive angiography. *Diagnostic Imaging* 1985;2:109.
7. Cragg AH, Gardiner GA, Smith TP. Vascular applications of laser. *Radiology* 1985;172:925-935.

DEVELOPMENT OF THE VANDERBILT COMPTON X-RAY FACILITY

Weiwei D. Andrews, MS
Frank E. Carroll, MD*
James W. Waters, PhD
Charles A. Brau, PhD
Ron R. Price, PhD
David R. Pickens, PhD
Perry A. Tompkins, PhD
Carlton F. Roos, MD

VANDERBILT UNIVERSITY

P.O.Box 1807-B
Vanderbilt Univ.
Nashville, TN37235

ABSTRACT

The intense IR photon output of the Vanderbilt FEL is to be made to collide with its own high energy electron beam to create nearly monochromatic Compton Backscattered X-Rays. At Vanderbilt, a sub-project of FEL generated X-Rays is under development parallel to the construction and initial operation of the FEL main project. The electron beamline and IR photon beamline designs are near completion, including design of electron beamline magnets and their layout, design of IR optical beamline elements and their layout, electron and IR optical beam diagnostics and alignment methods.

* Frank E. Carroll, Tel (615) 322-0999, Fax (615) 322-3764

DEVELOPMENT OF THE VANDERBILT COMPTON X-RAY FACILITY

INTRODUCTION

When a photon collides with a free electron, its energy and direction change to conserve energy and momentum. This is called the Compton Effect. When the electron is relativistic, that is $\gamma = E/mc^2 \gg 1$ (where E is the total energy of the electron, m the rest mass, and c the speed of light), and the photon has a low energy, that is $\lambda_L \gg \lambda_C = h / mc = 2.42 \times 10^{-12} \text{ m}$ (where λ_C is the Compton wavelength, h the Planck's constant, λ_L the wavelength of the incident photon), then the wavelength of the scattered photon is given by the formula

$$\lambda_S = \lambda_L (1 + \gamma^2 \theta^2) / 4 \gamma^2 \quad (1)$$

where θ is the angle through which the electron is scattered. For an infrared photon with a $2 \mu\text{m}$ wavelength scattered in the backward direction ($\theta = 180^\circ$) off a 43 MeV electron, the wavelength of the scattered photon is 0.7 \AA , which corresponds to an X-ray with an energy of 17.6 keV, in the X-ray part of the spectrum. Since intense, monochromatic light can conveniently be generated by lasers, and an intense monochromatic electron beam can be generated by conventional accelerators, X-rays produced by Compton scattering can be made quite monochromatic as compared with those generated by conventional X-ray tubes. Such narrow-spectrum X-rays may have important advantages for medical imaging. In particular, the low-energy photons from a conventional X-ray tube are absorbed close to the skin surface in the patient and contribute to the patient's X ray dose, but not to the X-ray image. High energy X-rays, on the other hand, often pass through the patient undergoing scattering which tends to fog the film, and degrade the X-ray image. It is the intermediate X-rays which experience absorption in the body due to photoelectric processes, and form the X-ray image. For mammography, the useful X-rays are those with wavelengths around 0.7 \AA and energies around 18 keV. By using X-rays of this energy and its improved contrast, it is

estimated that the patient dose required to provide the image quality of a standard mammogram can be reduced by a factor of about 50.

In the Vanderbilt Compton X-ray facility, infrared photons at wavelengths around $2\text{ }\mu\text{m}$ are produced by the Vanderbilt free-electron laser, while electrons at energies around 43 MeV are provided by the beam emerging from the free-electron laser. These are collided in a small interaction region, about $40\text{ }\mu\text{m}$ in diameter, to produce X ray photons of the desired wavelength at the rate of about 10^{10} per second. The schematic of this project is shown in Fig.1. These X-rays can be used to explore the use of such photons in medical imaging of breast cancer, and eventually, to perform mammography in clinical trials.

INTERACTION GEOMETRY

Since the expected emittance of the electron beam is smaller than the laser wavelength, the emittance may be ignored in optimizing the interaction geometry. Only the electron pulse length need be considered, so we optimize by setting the Rayleigh range $\approx 1/2$ the electron pulse length ($\approx 1/2$ of the optical wavelength).

The design electron energy of the Vanderbilt FEL is 43 MeV and the infrared optical wavelength is about $2\text{ }\mu\text{m}$. Under these conditions, the X-ray wavelength is $0.7\text{ }\text{\AA}$. For an average laser power of 6 W and an average electron beam current of 200 mA, the optimized X ray photon output is 4.0×10^{12} per second per steradian; the electron beam and the infrared beam are both focused to the same size, $12\text{ }\mu\text{m}$ in radius. Both beams in the interaction zone are shown in Fig.2. For experimental convenience , the beams will be focused to a larger spot, about $20\text{ }\mu\text{m}$ in radius. The number of output photons is then 2.7×10^{12} per second per steradian.

ELECTRON BEAMLINE DESIGN

Since Compton X-rays are generated along the direction of the the electron beamline, and the X-ray laboratory is one floor above the FEL vault, we must either bend the electron beam from its original horizontal direction, into the direction of the laboratory , or generate X-rays along the

original electron direction, and bend the X-rays up to the laboratory. This option, opened up by recent technological developments in X-ray "fiber optics", is discussed later.

The electron beamline design shown in Fig.3 is used to deflect the electron beam up toward the laboratory, so that the X-rays are produced in that direction. After passing through the interaction region, the electrons are directed back to the original beamline and transported to the beam dump.

The beamline design is complicated by the finite emittance and energy spread of the electron beam. A further complication of a practical nature is introduced by the fact that the electron beamline lies in a plane tilted about 47° from the horizontal plane. Because the electron beam has an energy spread of the order of a few percent after emerging from the wiggler, the beam transport system used to focus the beam into the interaction region must be achromatic. Our design is to make four identical bends, each consists of two 20° single bends with a quadrupole in between the two dipoles, together they make an "achromatic bend". Other quadrupoles are needed for focusing and beam-control purposes. A total of eight 20° dipole bending magnets and fifteen quadrupoles are needed for this design. First and second order TRANSPORT and POISSON calculations were used in the design.

Because the emittance of the electron beam is expected to be smaller than the wavelength of the laser, the emittance allows the electron beam to be focused inside the interaction region. However, the emittance affects the monochromatic quality in the following way, within the interaction cone of each electron, the wavelength increases with the angle from the electron direction according to the formula (valid for $\gamma \gg 1$)

$$\lambda = \lambda_0 (1 + \gamma^2 \theta^2), \quad (2)$$

where θ is the angle between the direction of the radiation and the electron motion, λ_0 is the photon wavelength in the forward direction. Thus, if the electrons are not moving parallel to each other, the X-radiation in a given direction will contain a spread of wavelengths. A further spread in the X-ray wavelength is caused by the energy spread of the beam. To minimize this effect, it is

important that the electron beamline not expand the emittance by converting the electron energy spread into emittance growth.

AN ALTERNATIVE ELECTRON BEAMLINE DESIGN

Recently, a new kind of X-ray optics, X-ray "capillary", or X-ray "fiber optics" is under consideration [1]. It uses multiple tiny hollow glass tubes. X-rays undergo myriad glancing incidence total external reflections inside the tubes with only limited loss. With these capillaries we will be able to first collimate, then bend the X-rays up to the X-ray laboratory. The schematic of this design is shown in Fig.4.

With capillary technology, we can avoid having to build a complicated electron beamline with many magnets in order to bend the electrons. This approach will simplify the whole electron beamline design and enable us to use fewer magnets. Another advantage of this design will be to avoid sending the electrons in the direction of the X-ray laboratory where people will be working, thus reducing the potential radiation hazard. The disadvantage of this design is that the capillary technology has not yet been actually used as a scientific research tool, making success uncertain. The cost of a capillary tube bundle device and a few magnets is estimated to be less than the total cost of the magnets needed in the first design .

OPTICAL BEAMLINE DESIGNS

The purpose of the infrared beamline is to transport the FEL infrared optical beam to the interaction region and focus it at the "interaction zone" to a diameter of about 40 μm . When the electron and laser beams are not exactly collinear, the wavelength shifts slightly according to the formula

$$\lambda = \lambda_c / \cos^2 \theta \quad (3)$$

where θ is the angle between the axes of the electron and laser beams, λ_c the wavelength in the collinear case. The angular factor for the produced X-ray beam intensity of the crossing beams is

also $\cos^2 \theta$. This is a small effect for small angles, and it is therefore possible to use geometries in which the beams cross at a small angle. However, if the angle becomes much larger than the convergence angle of the laser beam, the electrons have less time to interact with the laser beam and this reduces the X-ray intensity. Therefore, at the region beyond the interaction zone, all three beams have to overlap geometrically. However, passing the electron beam through any optics transporting the infrared beam is not possible without damaging the optics. Also, the X-ray beam has to be transported through this system to go into the laboratory upstairs. These conditions complicate the infrared beamline design. Four approaches for solving these problems are under consideration:

1) The first approach is to transport the infrared beam collinearly with the electron beam. This is shown in Fig.5, corresponding to the $\theta = 0$ case. The mirror that reflects the infrared beam has a hole at the center, which is also the center of the beamline, large enough to let the electron beam and the accompanying X-rays pass through. The advantage of this method is that it is simple and inexpensive. The disadvantage is loss and distortion of the infrared beam due to the hole in the middle. This causes a loss of the most intense portion of a Gaussian infrared beam. The total loss due to the hole alone is estimated to be 1% of the beam intensity, if we use a 10 mm radius mirror with a 1 mm radius hole placed at 30 cm from the interaction zone. Also, there will be some electrons on the edge of the beam "scraping" the mirror near the hole, which will cause damage to the mirror.

One solution to the intensity loss is to place the hole off center in a region of lower intensity. However, this will make the two beams non-collinear, as shown in Fig.5, for the $\theta \neq 0$ case, and reduce the interaction between the beams. The estimated loss due to the angular factor and the intensity loss is 0.7% of the beam intensity, assuming the hole is mounted to the $1/e$ intensity point of the the infrared beam 30 cm away from the interaction zone.

2) The second approach is an alternative to the first method, replacing the standard mirror for transporting the infrared beam with a beryllium mirror. This mirror can be placed further downstream after the electron beam is directed away. This is (an alternative way for the first

method too) shown in Fig.6. The difference is that this Beryllium mirror is almost transparent to the X-rays and can be coated to reflect infrared photons. Therefore, the use of a Beryllium mirror does not introduce the distortion to the beam because this avoids the need for placing any hole on the mirror.

3) The third approach is to make the infrared beam and the electron beam cross initially with a small angle. This is shown in Fig.7. The reduced X ray output due to the angular factor is estimated to be 0.1%. This is the simplest, most effective and least expensive design of all. It avoids the serious electron damage problem of the first approach.

4) The fourth approach is shown in Fig.8. An axicon pair is used to reshape the infrared beam to a hollow one [2]. The hole necessary for the electrons and X ray photons to pass through can be adjusted to the desired size and placed where the beam itself is hollow. The disadvantage of this approach is the cost and complexity of the axicon pair.

ELECTRON BEAM DIAGNOSTICS AT FOCUS

To optimize the Compton X ray output, the electron beam and the infrared optical beam must be aligned collinearly and focused at a common point of about 20 μm radius. Aligning the system and diagnostics for both beams are necessary. The difficulties for the diagnostics are:

First, at the focus, our electron beam has the luminosity of $4.5 \times 10^7 \text{ W/m}^2$. This is more than enough to melt any screen material in a single macropulse.

Second, both beams have a pulsed structure. Thus not only must both beams be aligned and focused spatially, but also the picosecond micropulses of both beams must meet simultaneously at the focus.

Of these, the first problem is the most difficult one to deal with. The most straightforward and most reliable method for diagnosing an electron beam with a beam size as small as tens of micrometers is to have a screen at the focusing point. To avoid melting diagnostic screens, when diagnosing, we must reduce the electron beam intensity. Beam intensity can be reduced by one of the several ways:

1) The first method is to place a slab with the proper thickness and material, an "attenuator" in the electron beam, at the upstream end of the interaction region so that the multiple scattering processes reduce the number of electrons as shown in Fig.9. Electrons coming out of this attenuator with the "wrong" energy and emittance can be filtered out with a pair of "emittance filters" in each plane and an "energy filter". The latter already exists for the FEL itself. The former can be inserted into the beamline without too much difficulty. Computer simulation with the program EGS4 assures us of the effectiveness of the method and the requirements for the attenuator material.

An alternative method is to place holes in the slab, to form a "pepper pot". The holes allow the desired portion of electrons to go through the attenuator without being disturbed. The emittance filters and the energy filter again filter out the "wrong" electrons scattered by the slab. This is also shown in Fig.9.

2) The second method is to scan the electron beam on the diagnostic screen at the focus with an RF cavity in the horizontal or vertical plane. Instead of having an "image spot" of the electron beam, we get two crossed lines. The width of the horizontal line represents the electron beam size vertically. The width of the vertical line represents the beam size horizontally, as shown in Fig.10. The method is more expensive than the attenuator, even though we can make use of the existing RF source.

3) The third method can be called the "non-interactive" method. It works under the same principle that the Compton X-ray production works. The RF from the same source as the FEL, which has a frequency of 2856 MHz, is guided into the interaction zone where it collides with the electron beam. A light beam of about $3.7 \mu\text{m}$ in wavelength will be generated as a "probe beam", as shown in Fig.11. The probe beam goes through the same optical elements as the infrared beam does so that the alignment of the both beams can be done simultaneously with the same screen.

CONCLUSION

At Vanderbilt, tunable, near monochromatic Compton X-rays will be generated using the FEL residual electrons and the FEL output infrared optical beam. The project is near its construction stage. A few of the possible designs for different parts of beamlines are reported here, including the electron-beam design, the infrared optical-beam design, electron beam diagnostics and a possible X-ray optical design using capillary "fiber optics".

REFERENCES

- [1] V.E.Kovanzev, A.I. Kolomijzev, M.A. Kumakhov et al., Kabardino-Balkarian Univ. Press, Nalchik (1988) 214
- [2] Golub and R. Treblay, Optical Society of America (1990) 1264

ACKNOWLEDGMENT

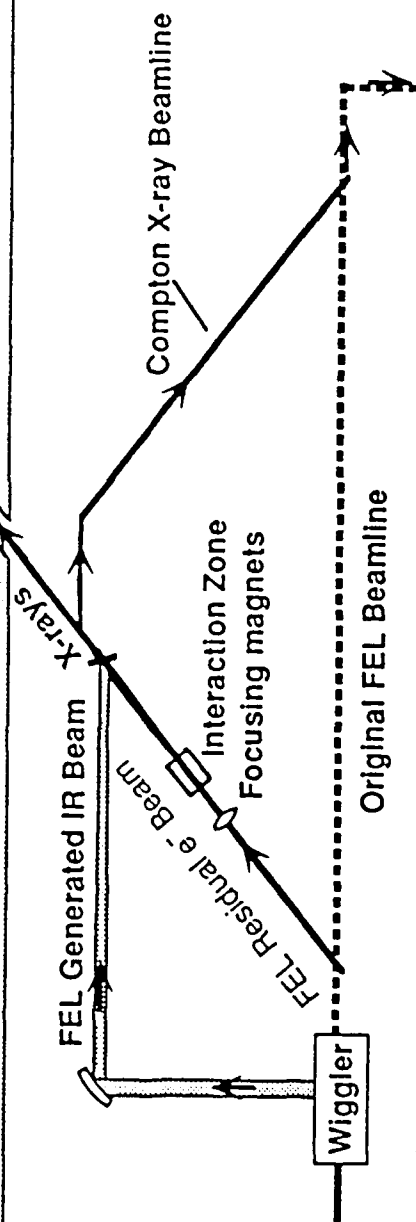
We gratefully acknowledge the support of
the Office of Naval Research, Contract number N000-14-87-C-0146,
Dr Sam Penner of National Institute of Standards and Technology.
and Kodak Cooperation

VANDERBILT MFEL COMPTON X-RAY PROJECT

Near monochromatic X-rays are generated by the backscatter of FEL produced IR photons through head on collision with the FEL residual electrons.

X-ray Lab

concrete floor

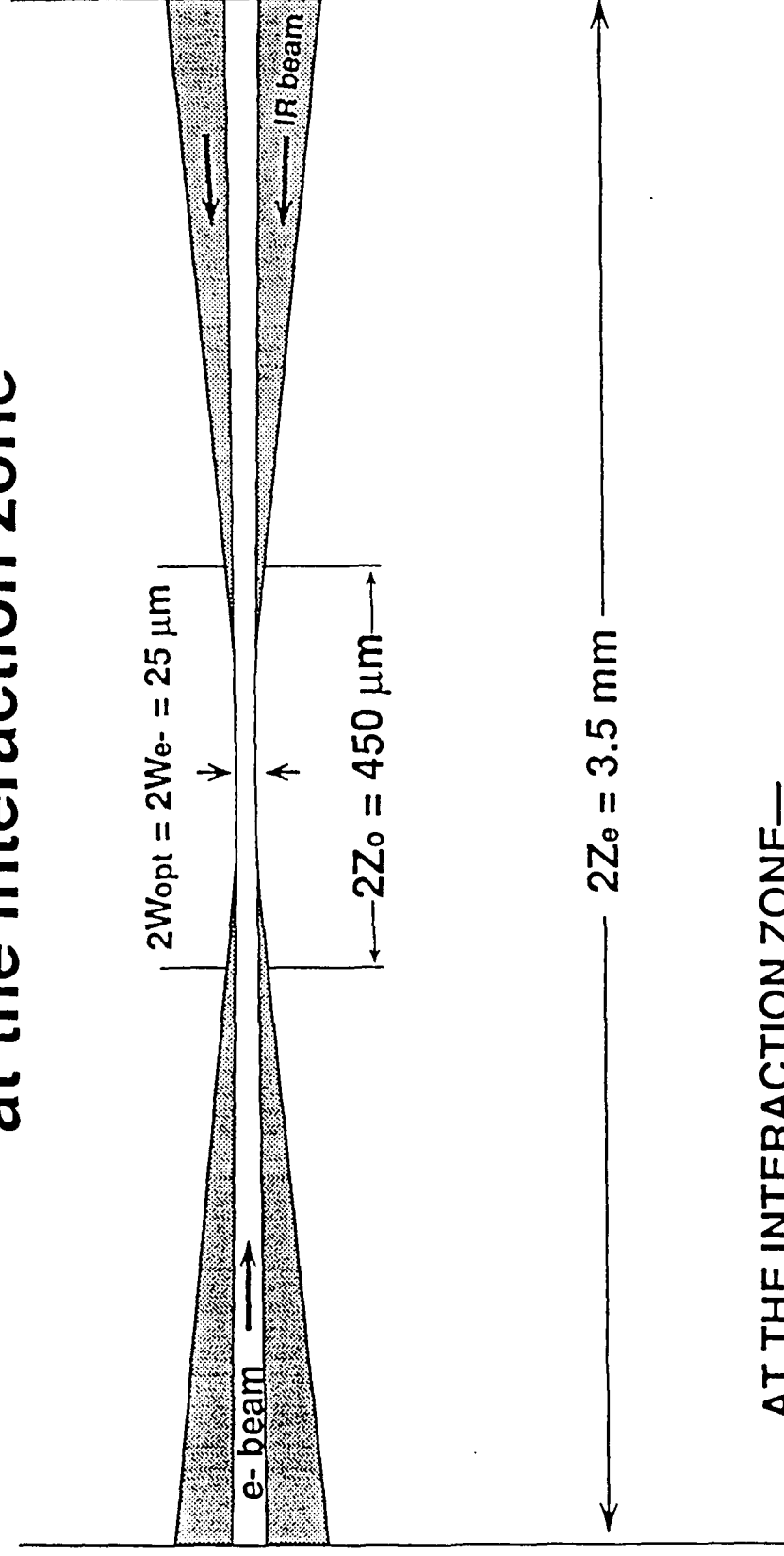


e⁻ Beam Dump

earth

Fig. 1

Optimized e^- beam and IR beam at the interaction zone



AT THE INTERACTION ZONE—

Both the IR beam and the e^- beam need to be focused to a small waist to get optimized x-ray photons.

Fig. 2

e^- BEAMLINE LAYOUT

The e^- beamline bends the e^- beam to the direction of the X-ray lab and to the back to the e^- beam dump.

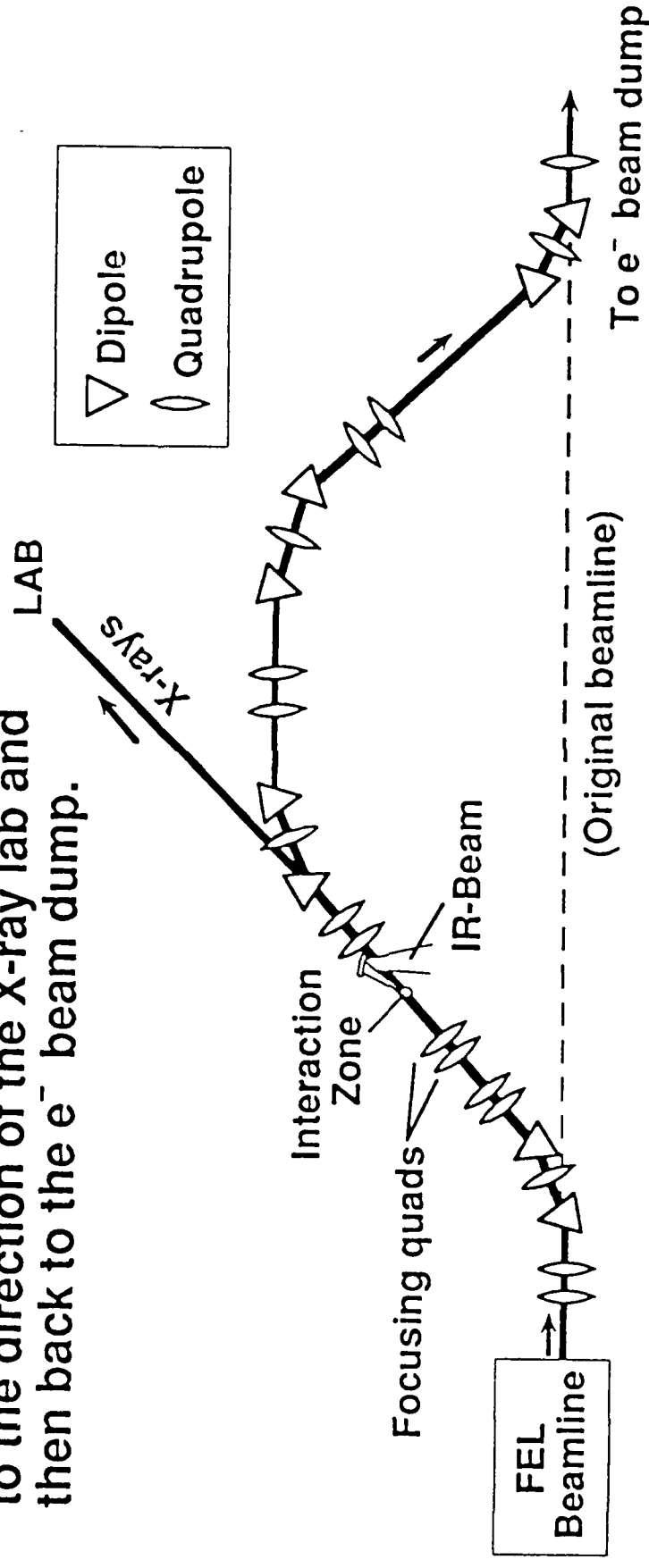


Fig. 3

AN ALTERNATIVE ELECTRON BEAM DESIGN

A new commercial technology makes it possible to bend the x-rays up to the lab using x-ray "fiber optics".

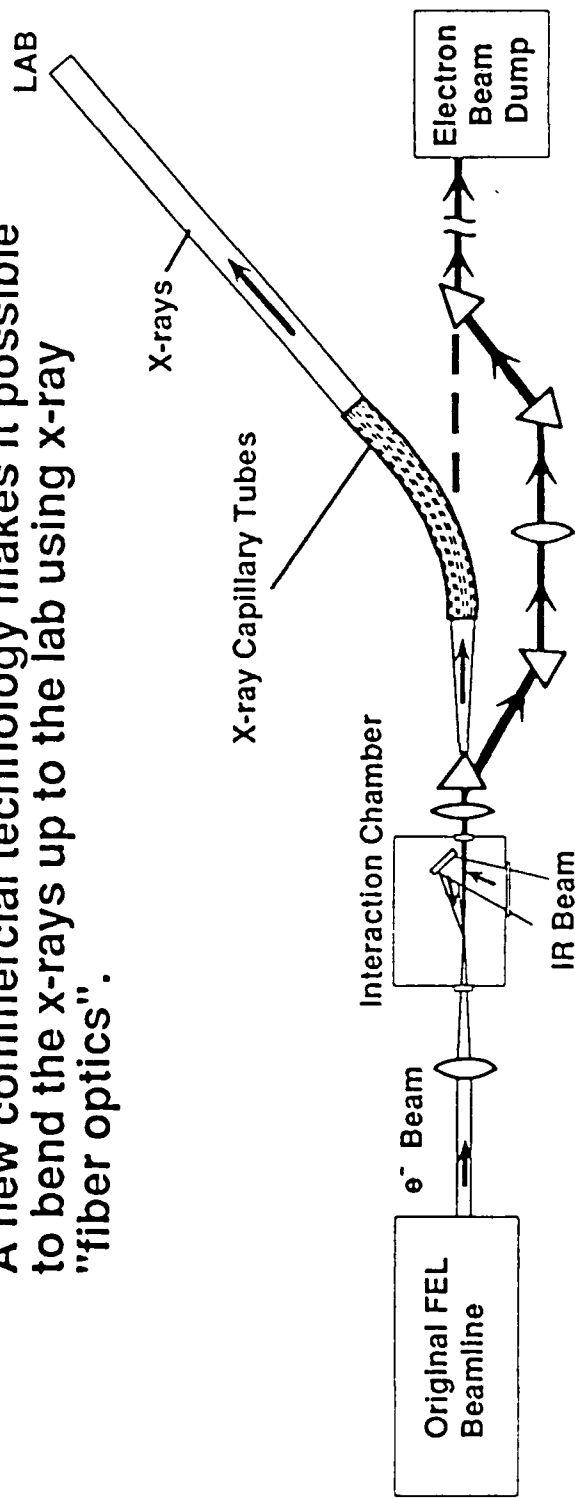


Fig. 4

IR BEAM FOCUSING DESIGNS

Placing a hole in the reflecting mirror reduces the intensity of the IR beam, but this avoids the use of a Be mirror.

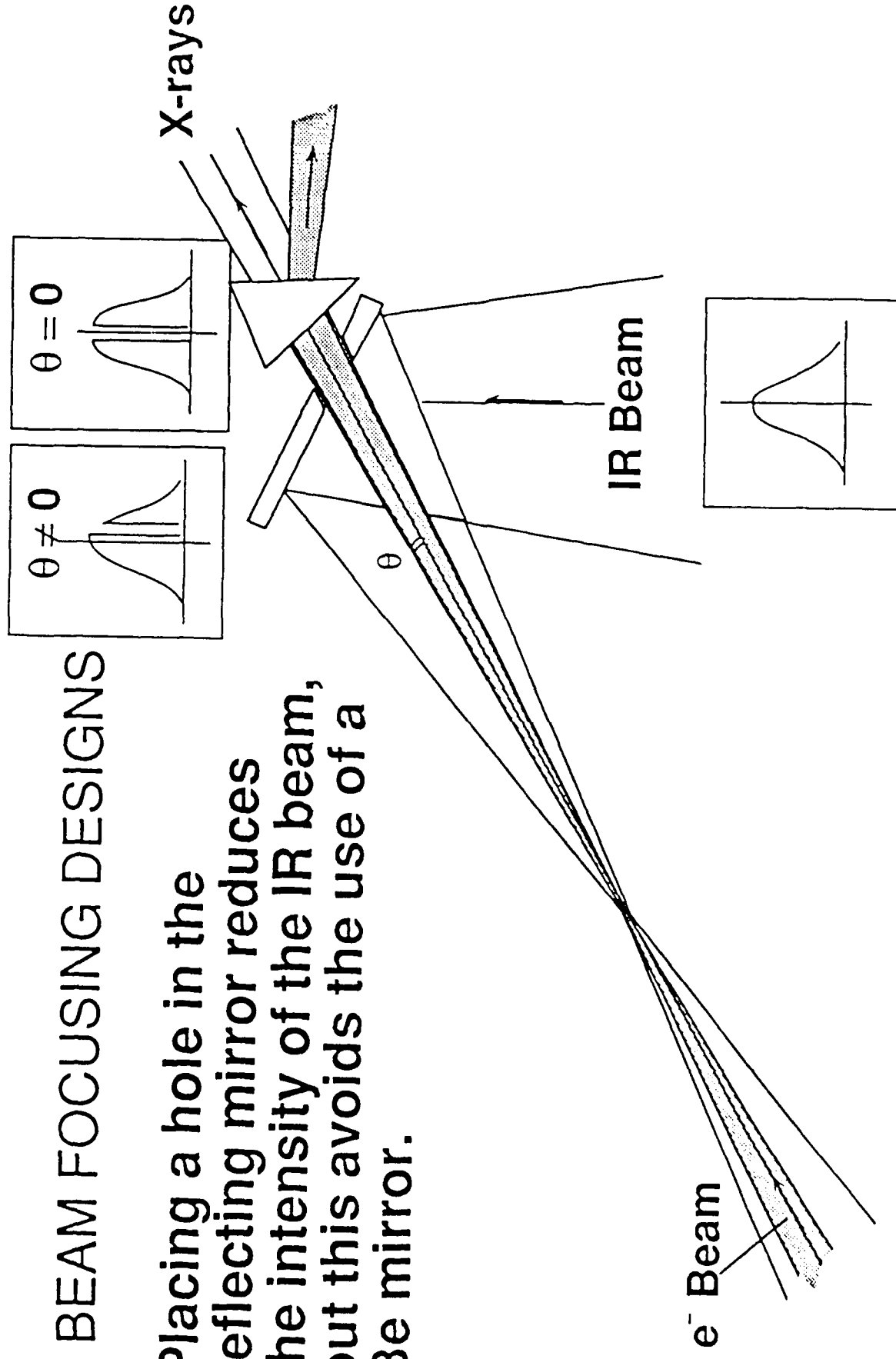


Fig. 5

IR BEAM FOCUSING DESIGNS

The use of a Be mirror allows us to focus the IR beam collinearly with the e^- beam and to let the e^- beam and X-rays go through, but Be mirrors are hard to fabricate.

(Correction: The Be mirror should have been placed beyond the dipole.)

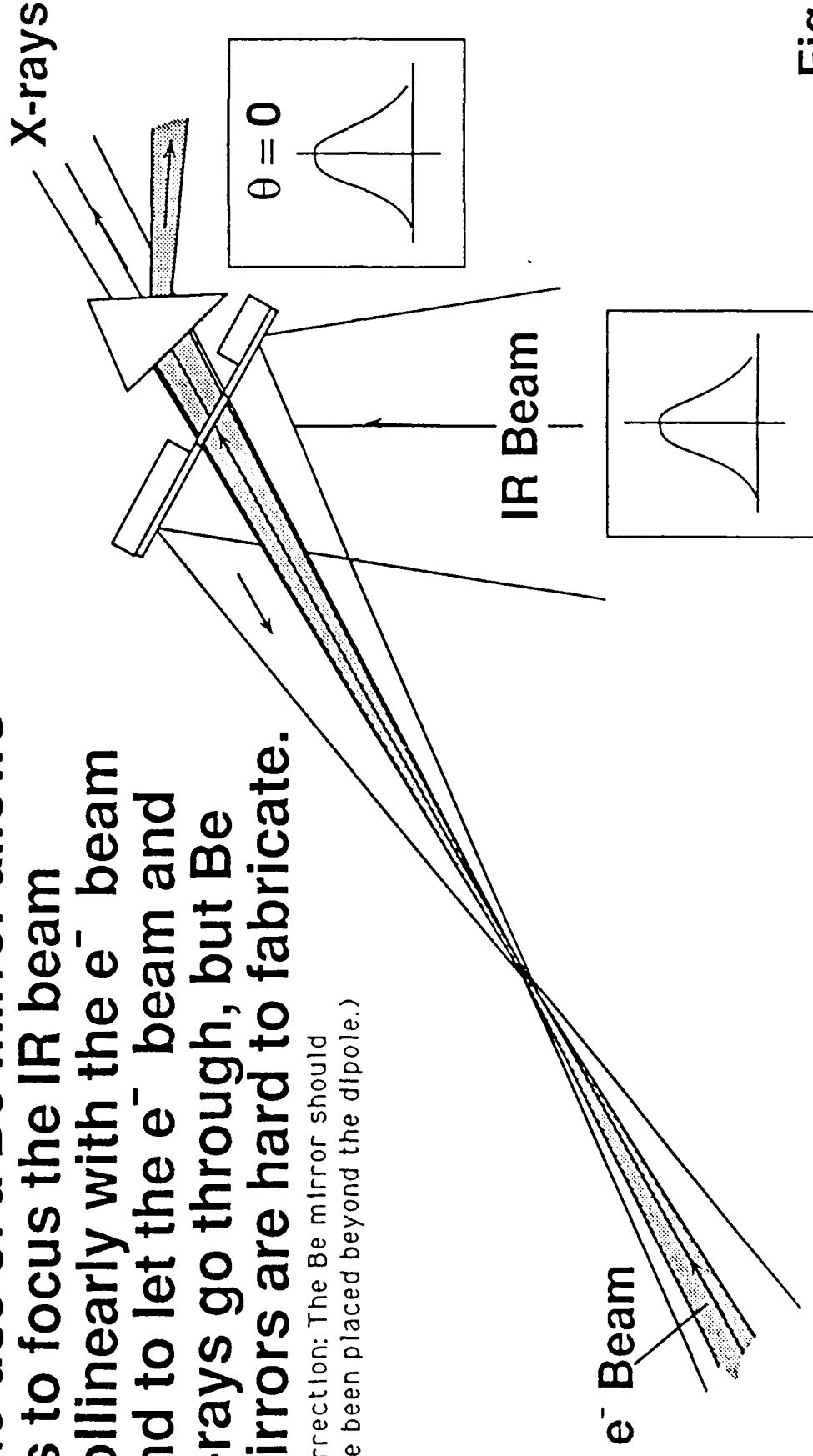


Fig. 6

IR BEAM FOCUSING DESIGNS

Focusing the IR beam non-collinearly with the e^- beam with a single mirror makes the simplest design, keeps the beam intensity, but reduces the interacting length.

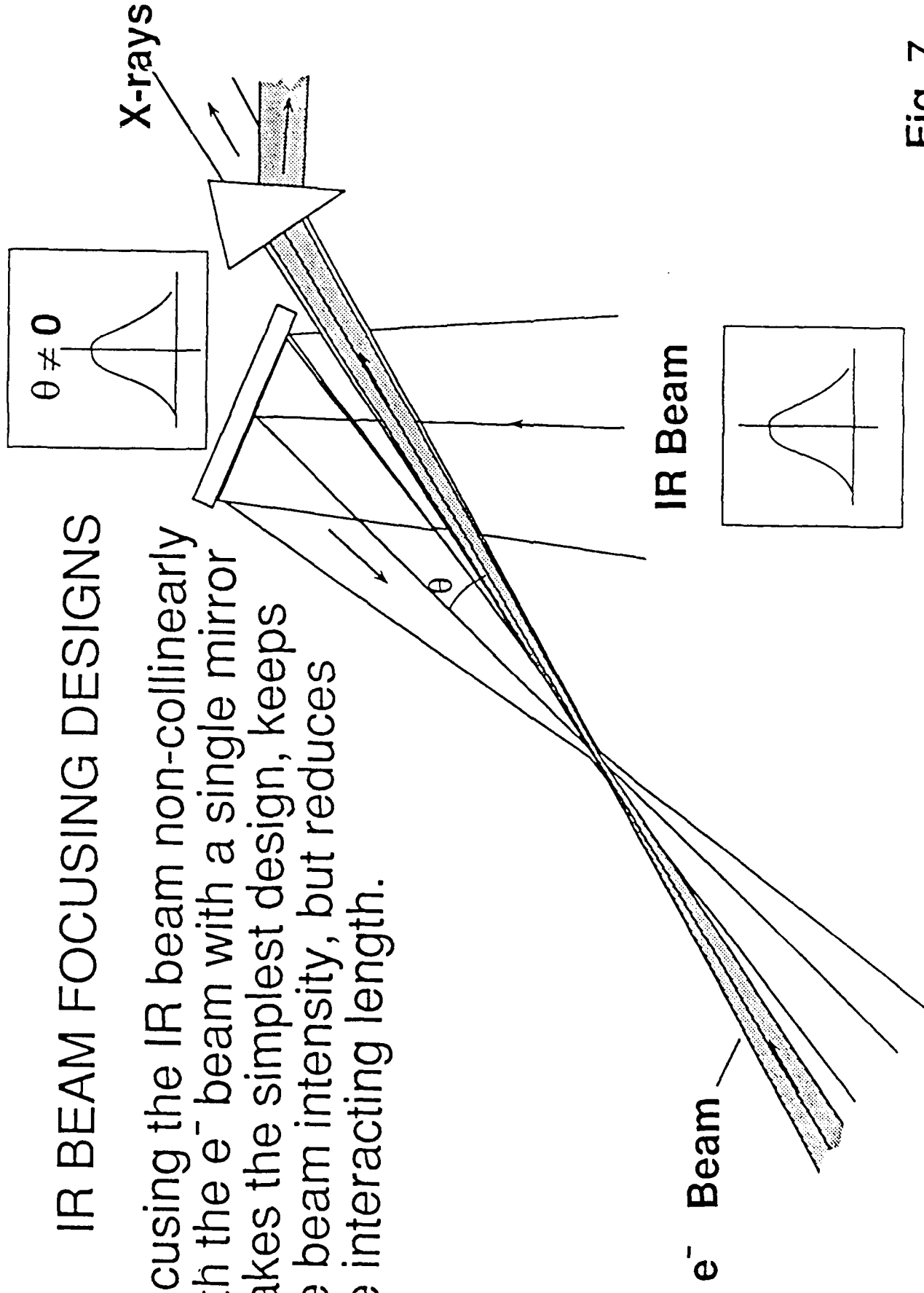


Fig. 7

IR BEAM FOCUSING DESIGNS

An axicon pair makes it possible to have IR beam collinear with the e^- beam and maintain the IR beam intensity. The cost and the possible technical difficulties are the main concerns for this design.

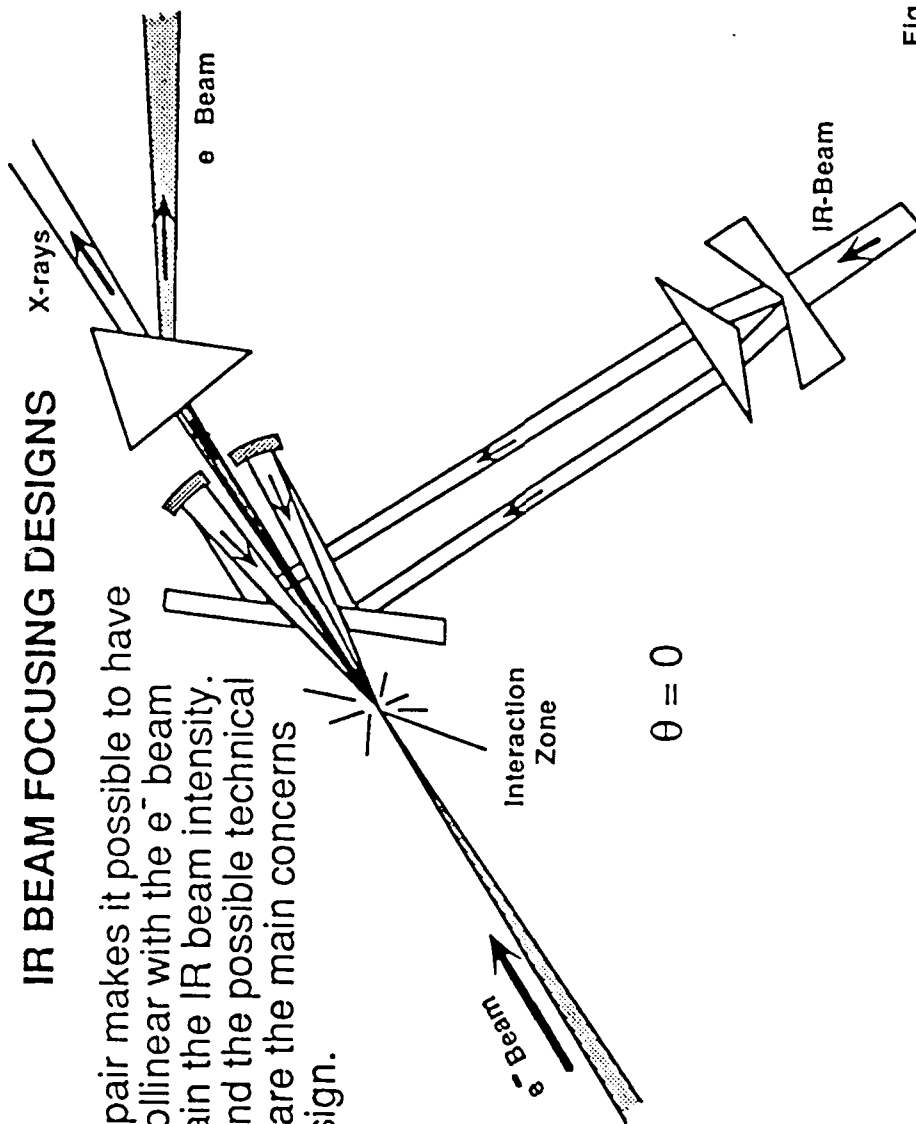


Fig. 8

ELECTRON BEAM DIAGNOSTICS

- (a) A block or a "pepper pot" is used to attenuate the electron number in each micropulse to avoid melting the diagnostic screen at the tightly focused "interaction zone". The "emittance filters" and the "energy filter" are used to keep the beam properties the same with or without the attenuator.

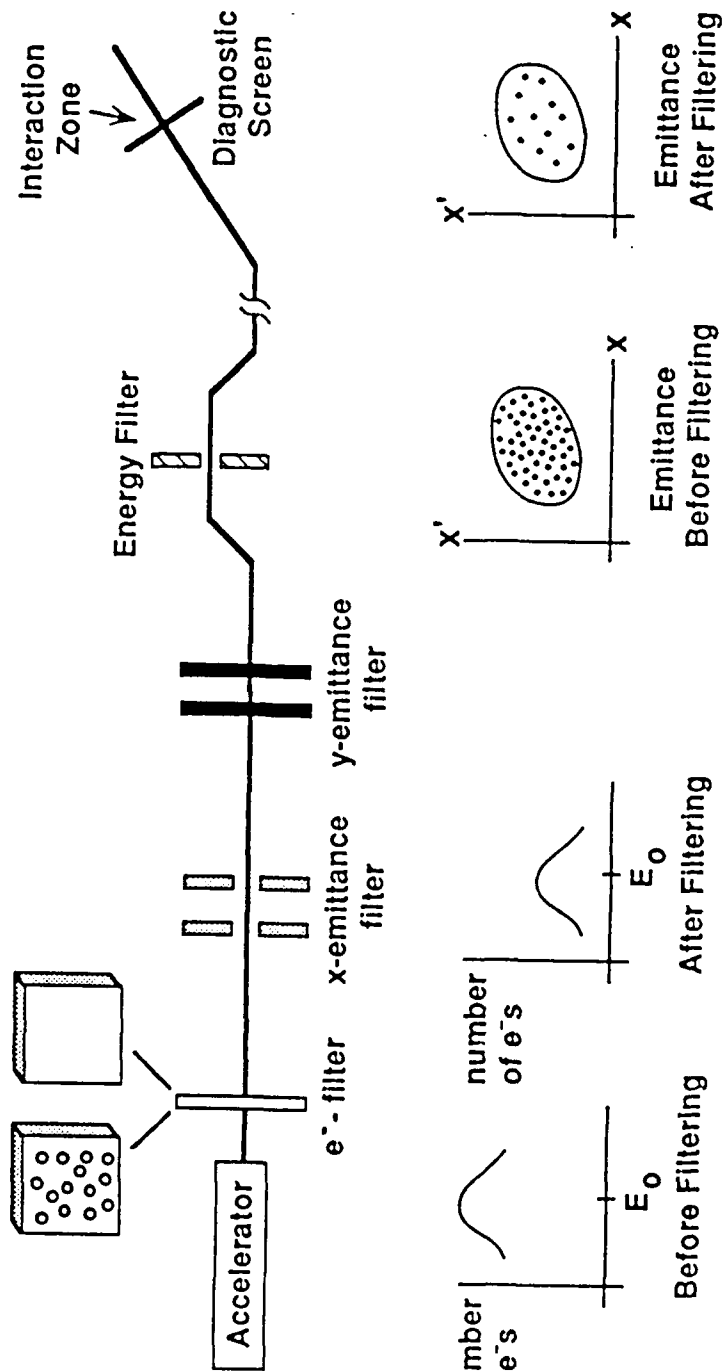


Fig. 9

ELECTRON BEAM DIAGNOSTICS

- (b) "Sweeping" the e^- beam makes it possible to measure the beam dimensions and reduce the number of e^- hitting the diagnostic screen.

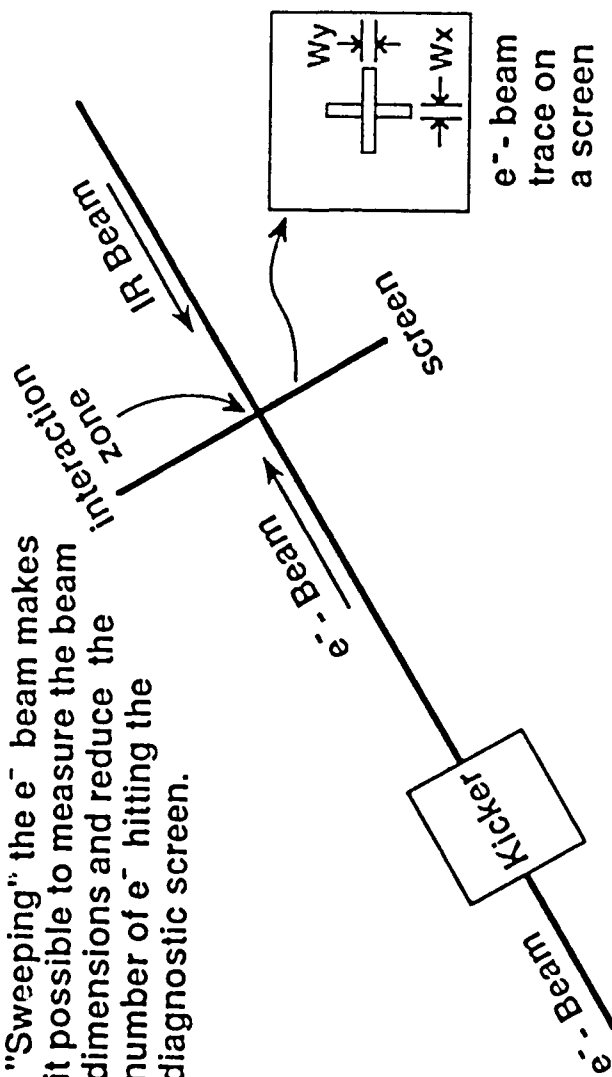


Fig. 10

ELECTRON BEAM DIAGNOSTICS

(c) An RF generated "probe" beam goes through the same optics with the IR beam. This makes it possible to diagnose the alignment of the e^- beam and the IR beam.

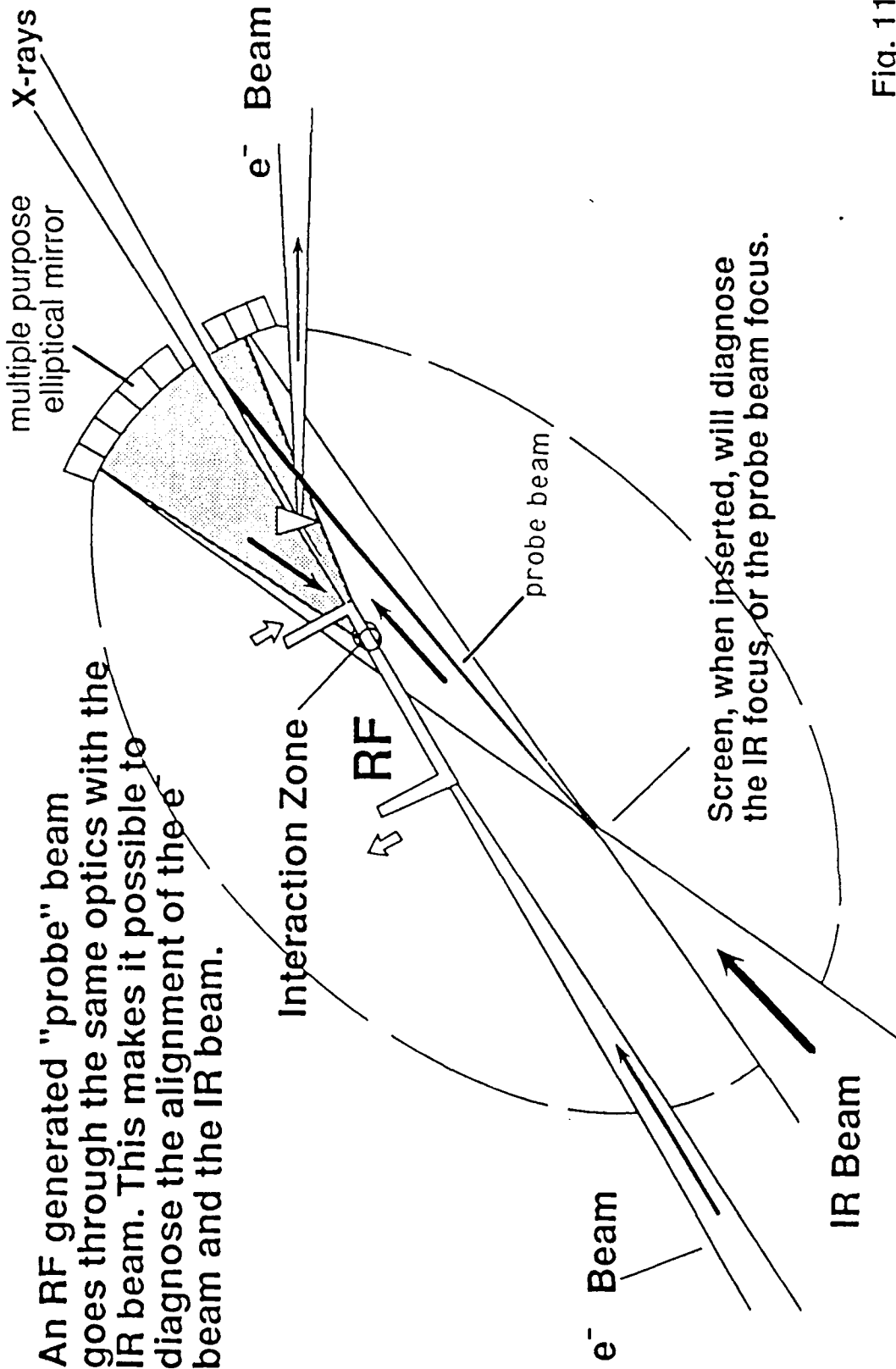


Fig. 11

THE VANDERBILT UNIVERSITY
FREE-ELECTRON LASER CENTER

C. A. Brau
Department of Physics and Astronomy
Vanderbilt University, Nashville, TN 37235

Abstract

Vanderbilt University has established a multidisciplinary Free-Electron Laser Center to exploit the opportunities made possible by the free-electron laser for applications in medicine, biology, materials science, and other fields of research. The free-electron laser, which recently began operation, is tunable over the wavelength range from 2 to 10 μm . The device has demonstrated 400 mJ per pulse at a wavelength of 4.8 μm , in 6- μs pulses, and an average power of 11 W at a repetition rate of 30 Hz. Extensions to the X-ray and far-infrared regions are underway. The Center, which will be used by researchers from within the University and from around the world, has already given birth to a variety of interdisciplinary collaborations among scientists brought together by the unique opportunities provided by the Center.

Please send proofs to Charles A. Brau, Department of Physics, Box 1807 B, Vanderbilt University, Nashville, TN 37027. Phone: (615)322-2559. FAX: (615)322-7263.

1. THE FACILITY

The Vanderbilt University Free-Electron Laser Center is dedicated to exploring the application of free-electron lasers to research in medical and materials sciences. The free-electron laser is located in a new laboratory building located on the University campus adjacent to the Departments of Physics and Chemistry, the School of Engineering, and the School of Medicine. The Department of Molecular Biology is close by. The Center houses not only the free-electron laser, but a variety of experimental laboratories and supporting equipment as well.

A cross-sectional view of the facility is shown in Fig. 1. As indicated there, the free-electron laser is located in a vault in the sub-basement. The control and diagnostic rooms are located on the laboratory level, as indicated in Fig. 2. The control room contains the Sun 386i master control computer as well as the laboratory radiation and laser safety systems. The diagnostic room is used to monitor the performance of the free-electron laser, including the power, the pulse energy, and the spectrum of the laser on a single shot.

The laboratory level provides approximately 600 m² of laboratory space. Five laser target rooms are equipped with general-purpose utilities such as conditioned and isolated power, deionized water, and computer interconnections. An optical-beam transport system designed and built by Optomec Design Company is used to bring the beam from the free-electron laser through the diagnostic room to the various experimental laboratories, as indicated in Fig. 2.

For experiments in surgery, the Center has a complete medical suite. The two operating rooms are built in accordance with American Association for Laboratory Animal Science guidelines and the facility has been approved for animal surgery. The first operating room has been equipped with an operating table and lamp, a complete range of conventional surgical instruments, anesthesia machine, I. V. pump, drill, electrocautery unit, a bank of electrophysiological instruments for assessing laser effects on nerve and brain, and other conventional surgical equipment. In addition, for use with the free-electron laser, the operating room is equipped with an articulated arm, which provides a hand-held optical-beam delivery system to manipulate the free-electron laser beam in surgical procedures, and a Zeiss operating microscope. The second operating room will be equipped later, based on experience with the first operating room. In addition to the operating rooms, the medical suite includes a computer work room for computer-image-guided surgery, lockers for the surgeons, and an approved animal-care facility for the preparation and recovery of the animals used in surgery.

These laboratory facilities are supplemented by a variety of support laboratories in the Center which have special-purpose equipment. A wet lab and a tissue-culture lab are provided to support experiments in biology and medicine. These laboratories are presently equipped with biological and fume hoods, incubators, microscopes, chromatographs, refrigerators, centrifuges, and so on. In addition, an electronics shop is available for the maintenance and development of experimental equipment.

The Center also possesses a combination of instruments which are directly available to the applications experiments. Major items of equipment include a Raman spectrometer, doubled-YAG-pumped dye laser system, excimer laser system with articulated arm and fiber delivery systems, cw modelocked Yag laser, argon laser, fluorescence spectrometer, and FTIR spectrometer. Other facilities and equipment are available through the Departments and Schools of the University which are collaborating in the research at the Center.

2. THE FREE-ELECTRON LASER

The Vanderbilt free-electron laser is a model FEL I built by Sierra Laser Systems. This is a small, infrared free-electron laser similar to the Stanford University Mk. III free-electron laser[1]. The electron beam is produced by a 45-MeV rf accelerator operating at a frequency of 2.856 GHz. The rf pulses are variable in length up to 8 μ s, overall, and the electron-beam pulses last up to 7 μ s. The nominal and measured operating parameters of the laser are summarized in Table I.

The laser pulse length is variable up to about 6 μ s, and the repetition rate is variable up to 60 Hz. Each macropulse consists of a sequence of mode-locked micropulses, each about 2 ps in length, repeated at the accelerator frequency of 2.856 GHz. The wavelength is tunable from 2 to 10 μ m on the fundamental, and down to about 1 μ m on the third harmonic. The power is maximum around 4 μ m, and falls off at longer and shorter wavelengths. Recent experiments have demonstrated pulse energy of 400 mJ in pulses lasting 6 μ s, at a wavelength of 4.8 μ m. A typical macropulse is shown in Fig 3. Operating at a pulse repetition frequency of 30 Hz, a sustained average power of 11 W has been achieved, making the free-electron laser the most powerful in the world.

For maximum flexibility, the FEL 1 is computer controlled by a Sun 386i master computer and three slave computers. For the convenience of the users, it is possible to control the laser from remote computer terminals located in the experimental laboratories.

Although operation as summarized in Table I is well suited to a broad variety of applications, as described in Section 4, other applications demand a variety of other wavelengths and pulse lengths. This will require that the free-electron laser be modified in several ways, with a priority to be established by the demands of the various applications. The following upgrades are in progress, and others may be considered in the future:

Monochromatic (but incoherent) X-rays are important for a variety of applications including hard-X-ray medical imaging and therapy and soft-X-ray microscopy. These X-rays will be produced by Compton backscatter of free-electron laser photons off the electron beam. The electron beam downstream of the wiggler is focused to a 20- μm spot to interact with the focused laser beam. The electron beam may be directed upward toward the laboratory level, as shown in Fig. 3, since the X-rays are produced in this same direction. Alternatively, the X-rays themselves may be directed toward the laboratory by means of X-ray hollow-fiber optics. The X-rays are transmitted to the target room by means of a tube through the concrete radiation shielding. The X-ray facility will initially produce of the order of 10^{10} photons/s in a spot a few centimeters in radius, at wavelengths from 1 nm (1 keV) to 0.06 nm (20 keV).

Far-infrared wavelengths are needed for experiments in biophysics and materials physics. To address these requirements, it is planned to develop a Cerenkov free-electron laser source able to operate in the wavelength region from 50 to 200 μm . A Cerenkov free-electron laser operates by interacting the high-energy electron beam with an electromagnetic wave travelling at the same velocity as the electrons, slightly less than the speed of light, in a dielectric waveguide[2]. The peak power is predicted to be of the order of 10 MW in the micropulses. It will be possible to operate the Cerenkov free-electron laser synchronously with the conventional free-electron laser for pump-probe experiments.

For some experiments, in time-resolved spectroscopy, for instance, it is useful to have shorter macropulses, or even single micropulses. Short macropulses, of the order of 10-ns duration, can be achieved by cavity dumping using a laser-driven silicon output coupler in the optical cavity of the free-electron laser[3]. When the photoelectric injector or pulse chopper is used, single micropulses can be obtained by switching out a single micropulse from the macropulse or by cavity dumping.

Wavelengths shorter than the nominal 2- μm limit of the Sierra Laser Systems FEL I are needed for experiments in materials physics, biophysics, and surgery.

Wavelengths down to about 1 μm , in the near infrared, may be obtained by lasing on the third harmonic of the free-electron laser[4]. Shorter wavelengths, down to the near ultraviolet, may be obtained by conventional nonlinear harmonic generation techniques[5].

For applications in materials physics, molecular dynamics, biophysics, and molecular biology, it is sometimes useful to have micropulses shorter than the nominal 2 ps of the Sierra Laser Systems FEL I. Three techniques will be developed to provide pulses as short as a few optical cycles, tunable throughout the infrared. In the first technique, the electron-beam energy will be chirped within the micropulses to generate chirp in the laser micropulses. This chirp may be used in a dispersive delay line (a grating pair) to compress the optical pulses to a few cycles[6]. In the second technique, the synchrotron instabilities may be used at long wavelengths to compress the pulses within the free-electron laser itself. Finally, at short wavelengths, nonlinear optical fibers may be used to generate a wavelength chirp so the optical pulse may be compressed in a dispersive delay line, as is done with conventional lasers.

3. APPLICATIONS RESEARCH AT THE CENTER

The Center currently supports a broad program of research in medicine and materials science. The experiments in progress are characterized not only by the close relationship between experiments but also by the degree of collaboration between the scientists working on the various projects at the Center. It may be that the most important contribution of Centers such as the one at Vanderbilt will be to bring together investigators from different fields and orientations and cross fertilize projects with ideas which would not have been introduced in the normal course of research. Projects underway at the Center include the linear and nonlinear interaction of laser radiation with optical materials and mammalian tissue, the spectroscopy of species adsorbed on surfaces, the linear and nonlinear spectroscopy of DNA and RNA, the dynamics of proteins in cell membranes, the biomodulation of wound healing by lasers, image-guided stereotactic neurosurgery, and the use of monochromatic X-rays in medical imaging and therapy.

In addition to supporting intramural research, the Center has been established as an international resource to support a broad extramural research program. The selection of programs for the Center and the allocation of the resources of the Center to these programs is the responsibility of the Peer Review Board of the Center.

Applications to use the Center should be directed through the Director of the Center.

Proposals will be accepted in the following categories:

Medical research, including surgery, photodynamic and radiation therapy, medical imaging and diagnostics, and other medical therapy or diagnostics;

Biology, including biophysics, biochemistry, and molecular biology;

Materials science, including optical materials, surface physics and chemistry, laser-materials interactions, condensed-matter physics, radiation damage, and related science and engineering.

To be considered, a proposal must make good use of the Vanderbilt free-electron laser, and must compliment the program underway or planned for the Center.

Although not a requirement, collaboration with other experimenters at the Center is encouraged as this will facilitate the conduct of the experiments and lead to cross-fertilization. Projects meeting these criteria will be prioritized by the Peer Review Board based on generally accepted standards of scientific merit and importance. In 1992 and 1993, the Peer Review Board will also be responsible for funding extramural projects using the Vanderbilt free-electron laser. The procedure for applying for funding under this program is similar to that described above.

Acknowledgement

The author would like to express his appreciation to the scientists at Vanderbilt University who founded the Free-Electron Laser Program and who make it what it is. Their contributions to this review are gratefully acknowledged. This work was supported in part by the Office of Naval Research under contracts N00014-87-C-0146 and N00014-91-C-0109, and by Kodak Corporation, which support is gratefully acknowledged.

--

Table I: Parameters of the Sierra Laser Systems FEL I free-electron laser.

	Nominal	Measured
Accelerator		
Electron energy	20-45 MeV	36-43 MeV
Micropulse peak current	20-40 A	
Macropulse average current	200 mA	250 mA
Energy spread	0.5%	0.5%
Normalized emittance	$4\pi \times 10\pi$ mm-mrad	
Wiggler		
Wiggler length	108 cm	108 cm
Wiggler period	2.3 cm	2.3 cm
Maximum wiggler field (rms)	0.47 T	0.44 T
Laser		
Wavelength	2-10 μm	2.6-5.6 μm
Micropulse duration	0.5-3 ps	
Micropulse repetition rate	2.9 GHz	2.9 GHz
Macropulse duration	0.5-6 μs	6 μs
Macropulse energy	100 mJ	400 mJ
Macropulse repetition rate	0-60 Hz	1-30 Hz
Overall average power	0-6 W	0-11 W

Figure captions:

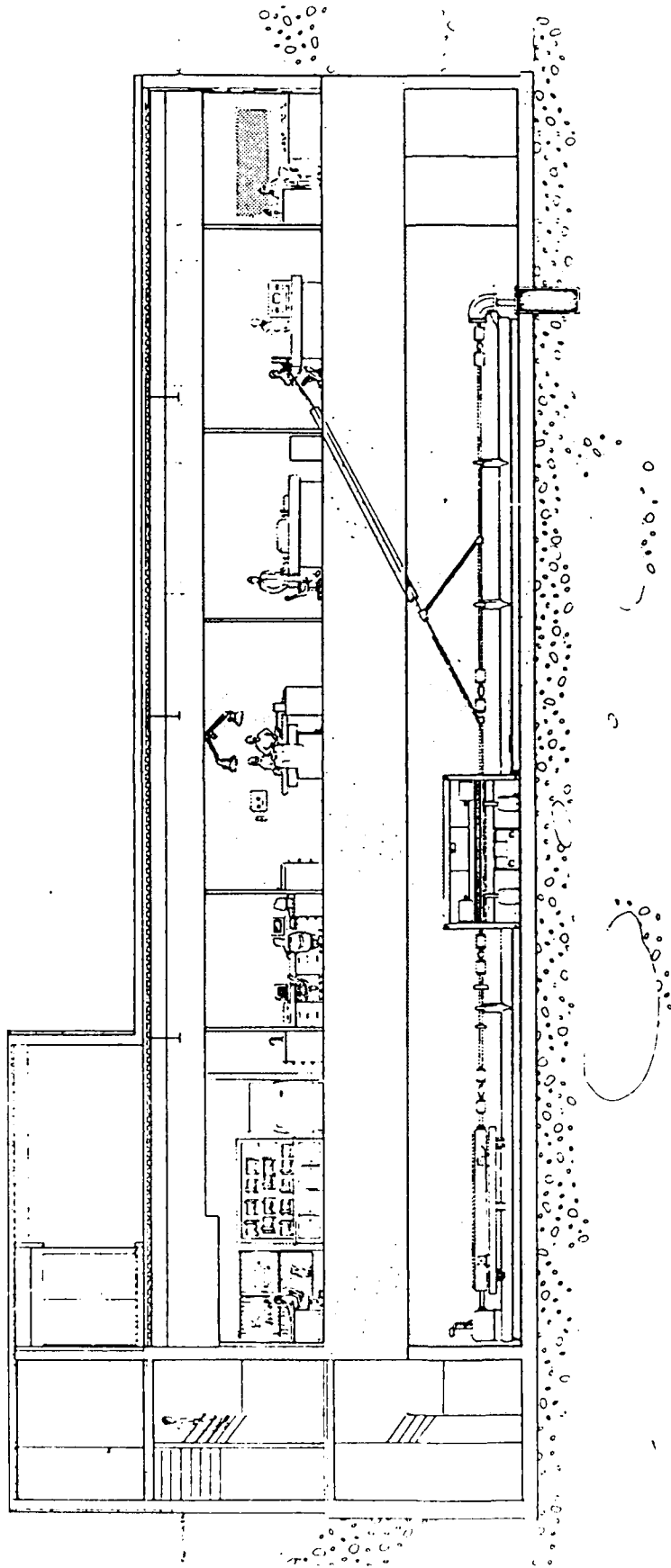
Fig. 1. Cross-sectional view of the Vanderbilt University Free-Electron Laser Center.

Fig. 2. Plan view of the vault level of the Vanderbilt University Free-Electron Laser Center.

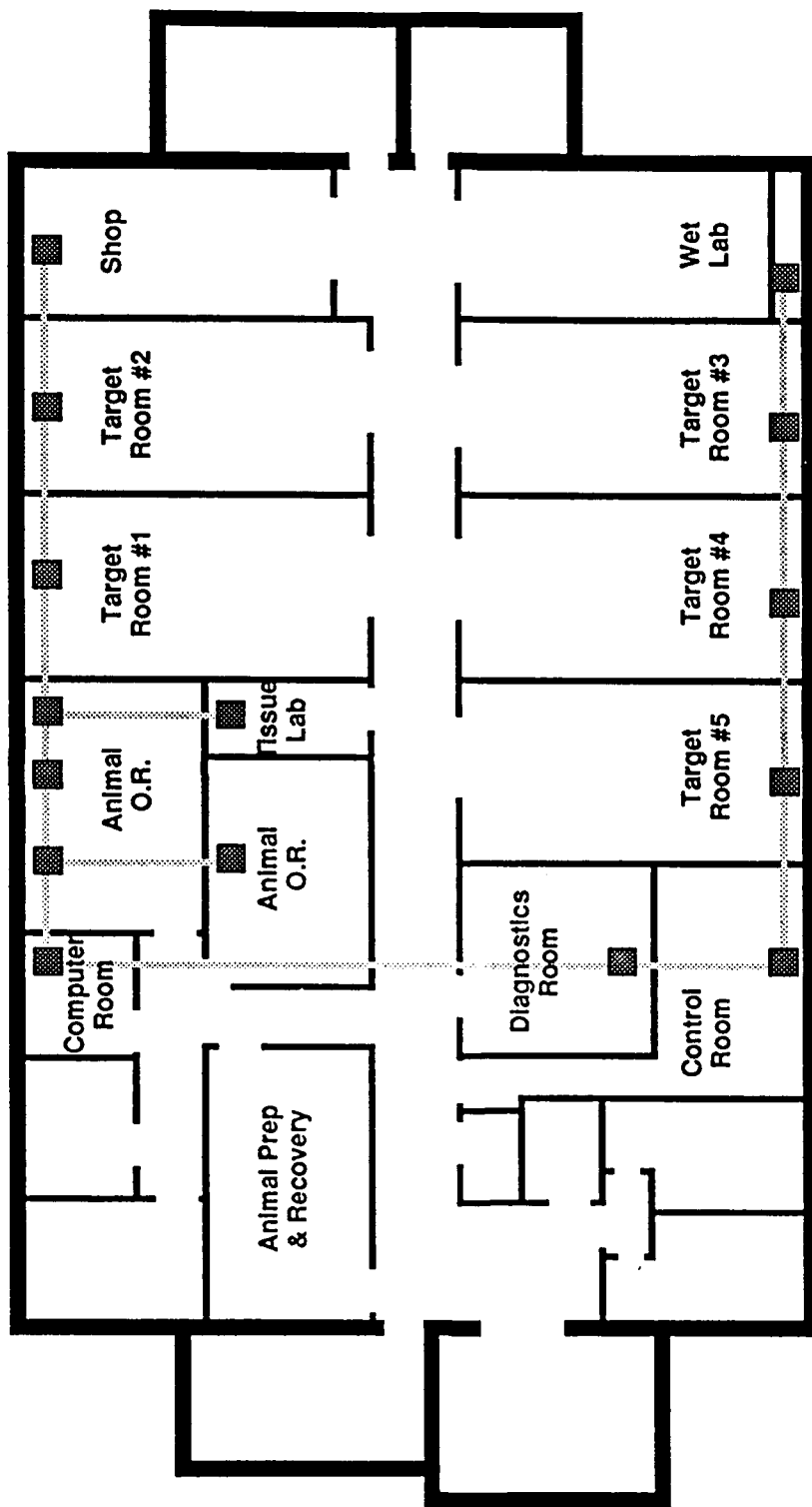
Fig. 3. A typical macropulse from the FEL I laser.

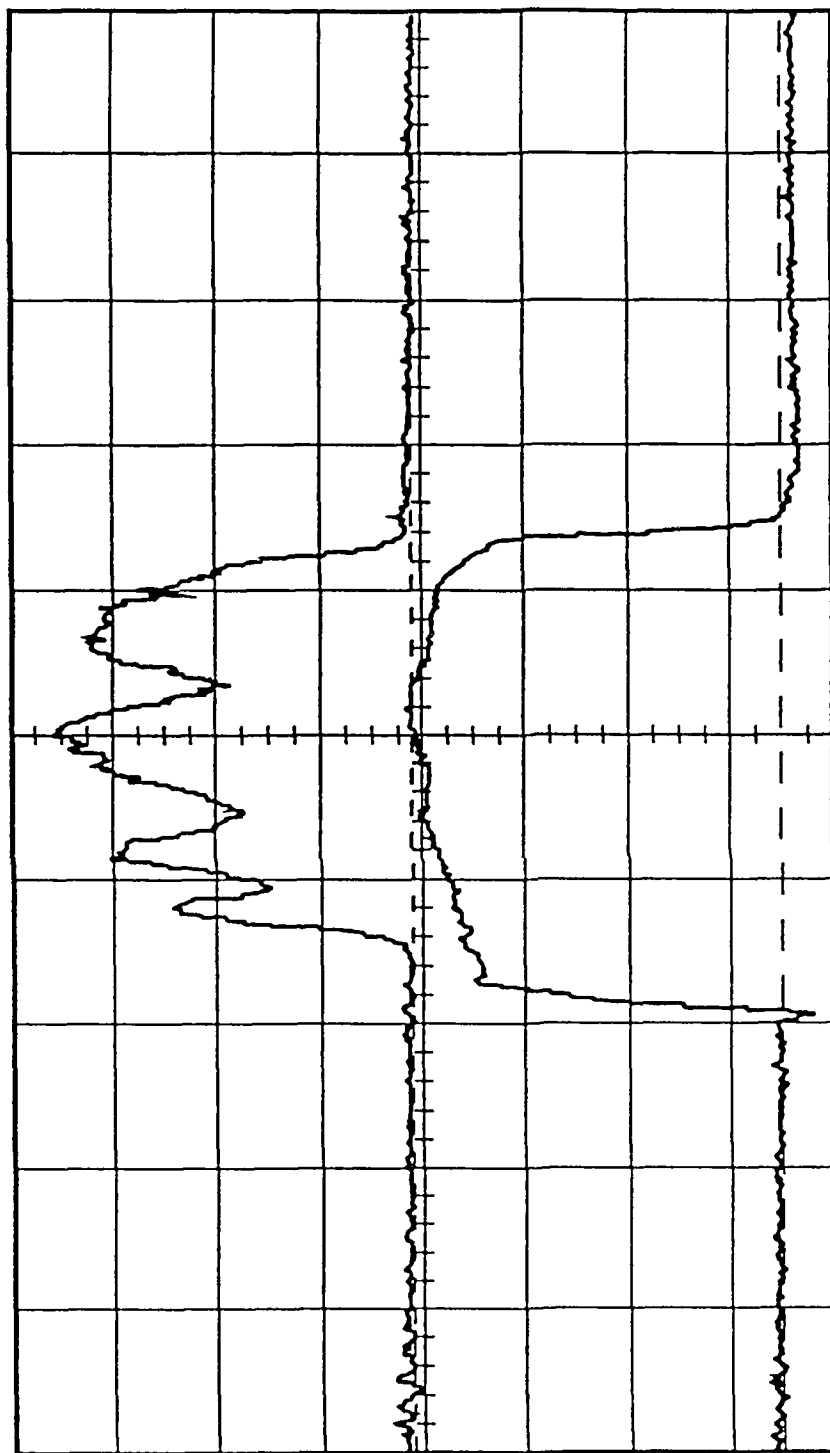
References:

1. S. Benson, *et al.*, J. Laser Applications 1 (July), 49 (1989).
2. J. E. Walsh and J. B. Murphy, IEEE J. Quant. Electron. QE-18, 1259 (1982).
3. S. V. Benson, *et al.*, "A Demonstration of Loss Modulation and Cavity Dumping in a Free-Electron Laser Oscillator," 11th International Conference on Free-Electron Lasers, Naples, FL, 28 August-1 September 1989.
4. R. W. Warren, *et al.*, "Lasing on the Third Harmonic," 11th International Conference on Free-Electron Lasers, Naples, FL, 28 August-1 September 1989.
5. B. A. Hooper, *et al.*, "Applications of Harmonic Generation of Picosecond Pulses from a Free-Electron Laser," 11th International Conference on Free-Electron Lasers, Naples, FL, 28 August-1 September 1989.
6. E. B. Szarmes, *et al.*, "Pulse Compression on the Mark III FEL Using Energy Chirping," 11th International Conference on Free-Electron Lasers, Naples, FL, 28 August-1 September 1989.



VANDERBILT FREE-ELECTRON LASER CENTER BEAM TRANSPORT SYSTEM





Laser
Power ↑

Beam
Current ↑

Time (2μs/div) →

THE VANDERBILT UNIVERSITY
FREE-ELECTRON LASER X-RAY FACILITY

Perry A. Tompkins, Weiwei D. Andrews, Charles A. Brau and James A. Waters
Department of Physics and Astronomy
Vanderbilt University

Frank E. Carroll, David R. Pickens, Ron R. Price and Carlton F. Roos
Department of Radiology and Radiological Sciences
Vanderbilt University Medical Center

We wish to submit this abstract to the conference on
X-Ray Detector Physics and Applications
(Oral).

The Vanderbilt University Free-Electron Laser Program is developing the capability to create near-monochromatic X-Rays for Medical Imaging and other purposes. For this experiment we feed-back the normal infrared FEL light to collide with the electron beam. This causes Compton backscattering of the incident photons which create X-rays. These X-rays cannot feed a X-ray laser, but they have a collimated intensity and tunability which will make them highly suitable for medical imaging. This paper is particularly focussed on the X-Ray beam transport to be used with this experiment. This transport must collimate the X-Ray beam and re-direct it to match a beam chase located in the vault ceiling at a 40 degree angle to the electron beam axis. A brief description of the creation mechanism and X-Ray beam properties are included.

Perry A. Tompkins
Department of Physics and Astronomy
Vanderbilt University
Nashville, TN 37235
(615)343-8505
Bitnet: "tomkipa@vuctrvax"

The Vanderbilt Free-Electron Laser Center for Biomedical and Materials Research

N. H. Tolk, C. A. Brau, G. S. Edwards, G. Margaritondo* and J. T. McKinley

Department of Physics and Astronomy
Vanderbilt University
Nashville, TN 37235

ABSTRACT

The newly commissioned Vanderbilt Free Electron Laser Center for Biomedical and Materials Research is a multidisciplinary users facility intended as an international resource. It provides extremely intense, continuously tunable, pulsed radiation in the mid-infrared (2-10 μm). Projects already underway include the linear and nonlinear interaction of laser radiation with optical materials, semiconductors, and mammalian tissue, the spectroscopy of species adsorbed on surfaces, measurement of vibrational energy transfer in DNA and RNA, the dynamics of proteins in cell membranes, the biomodulation of wound healing by lasers, image-guided stereotactic neurosurgery, and the use of monochromatic X-rays in medical imaging and therapy. The purpose of this article is to introduce the machine to the user community and to describe some of the new experimental opportunities that it makes possible. Details of several research projects are presented.

1. CHARACTERISTICS OF THE FREE-ELECTRON LASER

The Vanderbilt free-electron laser (FEL) is tunable over the 2 to 10 μm wavelength range with high output power. At a wavelength of 4.8 μm , 6- μs pulses with energies of 360 mJ and an average power of 11 W (30 Hz repetition rate) have been reliably demonstrated. This is the highest average power achieved to date by any tunable FEL. Extensions to the X-ray and far-infrared regions are underway. The Vanderbilt machine is a Sierra Laser Systems model FEL I, similar to the Stanford University Mk. III.¹ The electron beam is produced by a 45-MeV rf accelerator operating at a frequency of 2.856 GHz. The laser pulse length is variable up to 6 μs with a repetition rate of up to 60 Hz. Each macropulse consists of a sequence of mode-locked micropulses 2 ps in length and repeated at the accelerator frequency. The wavelength is tunable from 2 to 10 μm on the fundamental, and down to about 1 μm on the third harmonic.

The power is maximum around 4 μm falling off at longer and shorter wavelengths. Pulse power and energy measurements are conducted with Molelectron pyroelectric power detectors; wavelength calibration is done with a MacPherson 0.3-m monochromator fitted with a Spiricon one-dimensional pyroelectric array, allowing the spectrum of a single pulse to be analyzed. Since the FEL is computer controlled, it is possible for users to control the laser from remote computer terminals located in the experimental laboratories. The nominal and measured operating parameters of the laser are summarized in Table I.

* Permanent address of Professor Giorgio Margaritondo: Ecole Polytechnique Federale de Lausanne, Institute de physique appliquee, Departement de Physique, PHB-Ecublens, CH-1015 Lausanne, Switzerland.

Since scientists at Vanderbilt are fundamentally a community of machine users rather than machine builders, demands on the FEL are somewhat different from those laboratories which are specifically concerned with FEL technology development. In particular, the Vanderbilt FEL needs to be highly versatile with regards to a variety of optical output parameters. In the future the operating capabilities of the FEL will be extended to the far-infrared and X-ray regions and a flexible pulse structure (macropulse length and interpulse spacing for both macro- and micro-pulses) will be developed. Some of these future upgrades are described below.

Monochromatic (but incoherent) X-rays are important for a variety of applications including hard-X-ray medical imaging and therapy and soft-X-ray microscopy. There is also interest in studying the interaction of tunable X-rays with model insulator materials in support of the effort to develop this technique for *in-vivo* tissue analysis. In particular, the selectivity mechanisms associated with the creation of inner shell vacancies will be studied by tracing the various reaction channels of the ionizing Auger and radiative decay schemes. The X-rays will be produced by Compton backscatter of free-electron laser photons off the electron beam. The electron beam downstream of the wiggler is focused to a 20- μm spot to interact with the focused laser beam. The electron beam may be directed upward toward the laboratory level, so that the X-rays are produced in this same direction, or the X-rays themselves may be directed toward the laboratory by means of X-ray hollow-fiber optics. The X-rays are transmitted to the target room by means of a tube through the concrete radiation shielding. The X-ray facility will initially produce of the order of 10^{10} photons/s in a spot a few centimeters in radius, at wavelengths from 1 nm (1 keV) to 0.06 nm (20 keV).

Far-infrared wavelengths are needed for experiments in biophysics and materials physics. To address these requirements, it is planned to develop a Cerenkov free-electron laser source able to operate in the wavelength region from 50 to 200 μm . A Cerenkov free-electron laser operates by interacting the high-energy electron beam with an electromagnetic wave travelling at the same velocity as the electrons, slightly less than the speed of light, in a dielectric waveguide.² The peak power is predicted to be of the order of 10 MW in the micropulses. It will be possible to operate the Cerenkov free-electron laser synchronously with the conventional free-electron laser for pump-probe experiments.

For some experiments, in time-resolved spectroscopy, for instance, it is useful to have shorter macropulses, or even single micropulses. Short macropulses, of the order of 10-ns duration, can be achieved by cavity dumping using a laser-driven silicon output coupler in the optical cavity of the free-electron laser.³ When the photoelectric injector or pulse chopper is used, single micropulses can be obtained by switching out a single micropulse from the macropulse or by cavity dumping.

Wavelengths shorter than the nominal 2- μm limit of the Sierra Laser Systems FEL I are needed for experiments in materials physics, biophysics, and surgery. Wavelengths down to about 1 μm , in the near infrared, may be obtained by lasing on the third harmonic of the free-electron laser.⁴ Shorter wavelengths, down to the near ultraviolet, may be obtained by conventional nonlinear harmonic generation techniques.⁵

For applications in material physics, biopolymer dynamics, and molecular biology, it is sometimes useful to have micropulses shorter than the nominal 2 ps of the Sierra Laser Systems FEL I. Three techniques will be developed to provide pulses as short as a few optical cycles, tunable throughout the infrared. In the first technique, the electron-beam energy will be chirped within the micropulses to generate chirp in the laser micropulses. This chirp may be used in a dispersive delay line (a grating pair) to compress the optical pulses to a few cycles.⁶ In the second technique, the synchrotron instabilities may be used at long wavelengths to compress the pulses within the FEL itself. Finally, at short wavelengths, nonlinear optical fibers may be used to

generate a wavelength chirp so the optical pulse may be compressed in a dispersive delay line, as is done with conventional lasers.

2. SUPPORTING FACILITIES

The Center maintains additional core equipment and facilities intended to support the research of both University researchers and those coming from outside of Vanderbilt. These include target rooms and accommodations for both materials and biomedical research programs. The current projects emphasize spectroscopic and laser pump-probe techniques for both fundamental and applied studies of nonthermal energy absorption, localization, and dissipation. For this reason additional apparatus will be available for two-beam experiments, including an ultraviolet fluorometer, a nanosecond-picosecond Nd:YAG-pumped tunable dye laser with frequency doubler, pulsed excimer and CO₂ lasers, and VUV and microwave spectrometers. Other major equipment items include a Raman spectrometer, mode-locked YAG laser, an argon laser, and an FTIR spectrometer.

The facility has five target rooms and two animal operating rooms, one of which is completely equipped for surgery. The surgical room has an articulated arm which allows for a hand held optical-beam delivery system as well as a Zeiss operating microscope. Also provided are an electronics shop, as well as a wet lab and tissue-culture lab equipped with biological and fume hoods, incubators, microscopes, chromatographs, refrigerators, centrifuges, and so on. Five laser target rooms are equipped with general-purpose utilities such as conditioned and isolated power, deionized water, and computer interconnections.

3. ONGOING RESEARCH AT THE CENTER

The Center's users are expected to be a very diverse group. The Center grant funds several interdisciplinary projects involving the Departments of Physics and Astronomy, Molecular Biology, Otolaryngology, Pathology and Neurosurgery. The projects involve picosecond spectroscopy of biopolymers, FEL-based studies of biomembrane dynamics and drug Interactions, non-thermal and selective effects of FEL irradiation of tissue, and FEL applications in neurosurgery. The projects have a common goal of understanding and applying nonthermal mechanisms of radiation interacting with matter. To further assist the interdisciplinary nature of the Center, it has been constructed within a hundred feet of medical, physics, chemistry, and engineering facilities. In the following subsections, a brief description of several of the research projects will be presented. As the Center is meant to be an international resource, inquiries from scientists outside of Vanderbilt University are encouraged and should be sent to the Director of the Center.

3.1. Vibrational relaxation dynamics in materials and biopolymers

The frequency range of the Vanderbilt FEL corresponds to vibrational modes in both biopolymers and more conventional materials. The relaxation processes governing these vibrational modes have been investigated in the past by choosing materials such that the vibrational frequencies, at a given temperature, are coincident with the emission lines of conventional lasers⁷ In the past, this requirement has hindered experimental progress.⁸ The continuously tunable FEL removes this requirement, granting the experimentalist new freedom in choosing systems for investigation.

Using the Vanderbilt FEL, we plan to investigate both intermolecular and intramolecular energy transfer processes of vibrationally excited molecules. Small molecules can be introduced as defects in alkali halide hosts, larger molecular defects can be introduced in rare gas matrices, and biopolymers can be isolated in water/glycerol glasses and in dehydrated films. The Vanderbilt FEL

will be used to vibrationally excite the molecule of interest to a nonequilibrium energy distribution. Intramolecular relaxation to other internal modes of the molecule and intermolecular relaxation to phonon modes of the surrounding material will be monitored using conventional spectroscopic techniques such as Fourier transform infrared and laser-Raman spectroscopies.

With regards to materials science, these studies will improve our understanding of defects in insulators and semiconductor compounds with the aim of extending the lifetimes of semiconductor devices. With regards to biopolymer physics, these studies address the role of vibrational modes in the energetics of nucleic acid-protein interactions. With regards to clinical applications, a number of groups, including the Vanderbilt FEL group, are developing laser protocols that target radiation to selected degrees of freedom in biologic tissue⁹: progress in this clinical research requires experimental determination of mode lifetimes and relaxation rates.

3.2. Selective resonant bond-breaking

Recent evidence^{10,11} has shown that it is possible to selectively break specific chemical bonds within a molecule by choosing the correct photon energy. This has obvious application in chemical engineering for the production of novel molecules. The technique could also result in a gigantic step forward in the medical use of lasers. When conventional fixed-energy lasers are used to cut, burn, or ablate tissue, the laser is simply being used as a convenient tool for delivering power in the form of thermal energy. Selective resonant bond-breaking would allow selective modifications on the molecular level resulting in selective dysfunction without undesirable side effects on the cellular and tissue levels.

Previous photon selectivity experiments have been conducted using conventional lasers and tunable synchrotron radiation (in the vacuum ultraviolet regime). The Vanderbilt FEL will extend the energy range of the experiments into the mid- to near-infrared, visible, and ultraviolet regimes. The research will initially focus on the fundamental dynamics of photon-matter interactions for a variety of model insulator and metal oxide materials, and later with large organic molecules such as DNA. The emphasis will be on the ways in which the energy deposited by the incident photons leads to selective, resonant bond-breaking on surfaces and in the near-surface layers of bulk material. The photon-induced bond-breaking and chemical alterations will be measured by monitoring desorption products, fluorescence, and by using chemical assays. Already, the first resonant photon-energy dependent and temperature-dependent yields of desorbed neutral hydrogen atoms from a surface have been measured.¹¹ In these experiments, incident photons are observed to resonantly and selectively stimulate desorption by a direct, Franck-Condon excitation in the surface alkali hydride to a neutral, antibonding state. Eventually, the measurements will also be extended to layered and bulk systems.

3.3. Intensity-dependent laser-induced emission

The Vanderbilt FEL will be used to extend preliminary research,¹² conducted at the Free University in Berlin, on laser-stimulated emission of electrons, photons, ions, and neutrals from insulators, metal-oxides, and complex organic molecules around the intensity-dependent plasma breakdown threshold. Time-of-flight and mass-spectrographic techniques will be used. In particular, laser-induced desorption from large-band-gap materials is a subject of considerable current interest. The scientific issues in this area involve questions of temporal and spatial localization, energy channeling, the role of surface and bulk defects,¹³ and ultimately the determination of the actual electronic mechanism of single- and multiple-photon-induced desorption. The initial experiments have shown that with increasing intensity, there is a smooth transition from individual particle desorption to massive emission. By using the FEL, the previous experiments can be extended because of the availability of variable wavelength and pulse structure, as well as two-color pump-probe techniques.

3.4. Surface photovoltage effects

The discovery that many photoemission data on the temperature dependence of the Schottky barrier formation have been critically affected by surface photovoltage effects¹⁴ has created a burst of interest in the subject. Surface photovoltage appears when the photojected density of states becomes sufficiently large. Thus, the intense radiation that can be provided by the Vanderbilt FEL will be of crucial importance to the experiment. The FEL-induced surface photovoltage will be measured by looking at the energy shifts of photoelectrons (frequency multiplication and higher-harmonic operation allow the FEL to be used for photoemission). The results will be correlated to conventional Kelvin-probe studies induced by a non-FEL source. The parallel use of these two approaches is dictated by prudence, since the complexity of the phenomenon can produce misleading results with a single approach. The experiments will also take advantage of the FEL's pulsed time-structure. A calibrated retardation between the primary pulse and the (weak) high-energy pulse used to extract the photoelectrons will enable us to follow the time dependence of the effect.

3.5. Resonant two-beam photoemission

The Vanderbilt FEL will also be used in cutting-edge experiments on the electronic structure of semiconductor surfaces, metal-semiconductor interfaces, and semiconductor heterojunction interfaces. The normally unoccupied states near the conduction band minimum are of critical importance for technological applications. These states, however, cannot be studied by ordinary photoemission. Inverse photoemission can be applied, but its energy resolution is much worse.

Recently, a two-photon beam technique has been developed which, in essence, extends the range of applicability of photoemission experiments.^{15,16} It is possible to tune the intense radiation from the Vanderbilt FEL to induce electron transitions from the valence band into a normally unoccupied state in the semiconductor gap or near the conduction band minimum. A second high energy pulse then induces photoemission from the normally unoccupied state. Because the electrons rapidly decay back into the valence band, the high energy pulse must be temporally correlated with the optical pumping pulse. The FEL can produce such a temporally correlated high energy pulse using frequency multiplication. Thus, by scanning the optical pumping energy, photoemission techniques can be extended to the normally unoccupied states in the band gap and near the conduction band minimum. One difficulty is that correlation effects become more complex (two holes are created rather than the single e-h pair created in conventional photoemission). Thus, it is admitted that new theoretical ground will have to be broken in order to fully interpret the results of the experiments. This, however, is also part of the intrigue of the technique.

4. ACKNOWLEDGMENTS

This work was supported in part by the Office of Naval Research under contracts N00014-87-C-0146, N00014-91-C-0109, N00014-91-J-4040 and by Kodak Corporation, which support is gratefully acknowledged.

5. REFERENCES

1. S. Benson, *et al.*, J. Laser Applications **1** (July), 49 (1989).
2. J. E. Walsh and J. B. Murphy, IEEE J. Quant. Electron. **QE-18**, 1259 (1982).
3. S. V. Benson, *et al.*, "A Demonstration of Loss Modulation and Cavity Dumping in a Free-Electron Laser Oscillator," 11th International Conference on Free-Electron Lasers, Naples, FL, 28 August - 1 September 1989.
4. R. W. Warren, *et al.*, "Lasing on the Third Harmonic," 11th International Conference on Free-Electron Lasers, Naples, FL, 28 August - September 1989.
5. B. A. Hooper, *et al.*, "Applications of Harmonic Generation of Picosecond Pulses from a Free-Electron Laser," 11th International Conference on Free-Electron Lasers, Naples, FL, 28 August - September 1989.
6. E. B. Szarmes, *et al.*, "Pulse Compression on the Mark III FEL Using Energy Chirping," 11th International Conference on Free-Electron Lasers, Naples, FL, August 28-September 1, 1989.
7. A.S. Barker and A.J. Sievers, Rev. Mod. Phys. **47**, Suppl. 2, (1975).
8. See, for example, W.E. Moerner (editor), Persistent Spectral Hole-Burning: Science and Applications, Springer-Verlag (1988), Berlin.
9. G.S. Edwards and N. H. Tolk, Nucl. Instr. Meth. Phys. Res. **A272** (1988) 37.
10. C. C. Parks, D. A. Shirley, and G. Loubriel, Phys. Rev. **B 29**, 4709 (1984).
11. L. T. Hudson, J. L. Rose and N. H. Tolk, DIET IV, eds. G. Betz and P. Varga (Springer-Verlag Heidelberg, 1990).
12. H. Cronberg, W. Muydermann, H. B. Nielsen, E. Matthias and N. H. Tolk, DIET IV, eds. G. Betz and P. Varga (Springer-Verlag, 1990).
13. G. M. Loubriel, T. M. Green, P. A. Richards, R. G. Albridge, R. F. Haglund and N. H. Tolk, Phys. Rev. Lett. **53**, 1751 (1986) and Phys. Rev. **B35**, 781 (1987).
14. M. H. Hecht, J. Vac. Sci. Technol. **B 8**, 1018 (1990).
15. R. Haight, J. Boker, J. Stark, R. H. Storz, R. R. Freeman and P. H. Bucksbaum, Phys. Rev. Letters **54**, 1302 (1985).
16. J. M. Moison and M. Bensoussan, Phys. Rev. **B 35**, 914 (1987).

Table I: Parameters of the Vanderbilt Free Electron Laser

	Nominal	Measured
Accelerator		
Electron energy	20-45 MeV	36-43 MeV
Micropulse peak current	20-40 A	
Macropulse average current	200 mA	250 mA
Energy spread	0.5%	0.5%
Normalized emittance	$4\pi \times 10\pi$ mm-mrad	
Wiggler		
Wiggler length	108 cm	108 cm
Wiggler period	2.3 cm	2.3 cm
Maximum wiggler field (rms)	0.47 T	0.44 T
Laser		
Wavelength	2-10 μm	2.7-4.9 μm
Micropulse duration	0.5-3 ps	
Micropulse repetition rate	2.9 GHz	2.9 GHz
Macropulse duration	0.5-6 μs	6 μs
Macropulse energy	100 mJ	360 mJ
Macropulse repetition rate	0-60 Hz	1-30 Hz
Overall average power	0-6 W	0-11 W

VANDERBILT UNIVERSITY FEL CENTER FOR BIOMEDICAL AND MATERIALS RESEARCH *

G.S. EDWARDS and N.H. TOLK

*Department of Physics and Astronomy, Vanderbilt University, Nashville, Tennessee 37235, USA***1. Introduction**

In February of 1987 Vanderbilt University was awarded a contract from the Office of Naval Research to establish an FEL Center for biomedical and materials research. The Center facilitates research in FEL applications and continues the longstanding tradition of interdisciplinary science at Vanderbilt. The project team includes faculty from the College of Arts and Sciences, the School of Medicine, and the School of Engineering unified by an underlying scientific theme of the role of nonthermal processes in physical and biological materials. The Center will be centrally located as the University is constructing a building to house the FEL within a hundred feet of medical, physics, chemistry, and engineering facilities.

The Center grant provides funds for the free electron laser, for additional equipment, and to seed five research projects based on the unique spectral properties of the FEL. In the following we will present the operating parameters for the Vanderbilt FEL, describe the Center in greater detail, and outline the research projects. Applications as represented in several of the research projects will be presented; however, due to the brief nature of this article the interested reader is directed to additional accounts for a more complete description [1-3].

2. Vanderbilt FEL

The scientists at Vanderbilt are fundamentally a community of machine users rather than machine builders. As such our demands on the FEL are somewhat different from those laboratories which are specifically concerned with FEL technology development. In particular, the Vanderbilt FEL needs to be highly versatile with regards to optical output. The scientific program proposed by Vanderbilt to the ONR requires an FEL with a combination of ultrashort micropulses, high average and high peak powers, and tunability from

Table 1
Design parameters of the Vanderbilt FEL

Wavelength [μm]	Technique	Energy per pulse for 60 Hz operation [mJ]
0.25- 0.50	Harmonic generation	Unknown
0.50- 1.00	Harmonic generation	75
1.0 - 2.0	Harmonic generation	300
2.0 - 4.0	Direct FEL-1 light	550
4 - 10	Direct FEL-1 light	300

the ultraviolet to the mid-infrared region of the spectrum. In the future the operating capabilities of the FEL will be extended to the far-infrared and vacuum ultraviolet and a flexible pulse structure (macropulse length and interpulse spacing for both macro- and micropulses) will be developed.

The Vanderbilt FEL is scheduled to operate prior to February 1, 1990. The design parameters for optical output are presented in table 1.

3. The Center

The FEL represents a major research initiative of the College of Arts and Sciences, the School of Medicine, and the School of Engineering. In addition to the original project team, the Vanderbilt FEL community steadily grows as further applications are developed by the faculty. Furthermore, it is fully anticipated that as the facility develops it will serve as a regional, national, and even international resource for biomedical and materials research and there will be non-Vanderbilt users whose research programs will be carried out at the Center.

The design parameters for the FEL have been addressed in the previous section. As a users facility, however, the Vanderbilt Center must support more than just the FEL instrument and thus maintains additional core equipment, target rooms, and accommodations for both materials and biomedical research programs. The current projects emphasize spectroscopic and laser pump-probe techniques for both fundamental and applied studies of nonthermal energy absorption, localiza-

* This project is supported by the Office of Naval Research under Contract no. N00014-87-C-0146.

tion, and dissipation. For this reason additional apparatus will be available for two-beam experiments. This core equipment includes an ultraviolet fluorometer, a nanosecond-picosecond Nd:YAG-pumped tunable dye laser with frequency doubler, a pulsed excimer and CO₂ lasers, and VUV and microwave spectrometers.

The facility has six target rooms, one of which will be completely equipped for surgery. Space is provided for a tissue culture laboratory, a laboratory for molecular biology, a machine shop, an electronics shop, and a sample preparation area for materials science. In addition, there is a suite of rooms for surgical support and control rooms for the FEL. The FEL instrument will be located one level below in a shielded vault.

4. Applications

The Center grant funds five interdisciplinary projects involving faculty from the Departments of Physics and Astronomy, Molecular Biology, Mechanical and Materials Engineering, Otolaryngology, Pathology, and Neurosurgery. The projects are entitled Mechanisms of Photon-Induced Damage in Optical Materials, Picosecond Spectroscopy of Biopolymers, FEL Based Studies of Biomembrane Dynamics and Drug Interactions, Non-thermal and Selective Effects of FEL Irradiation of Tissue, and FEL Applications in Neurosurgery. The projects have a common goal of understanding and applying nonthermal mechanisms of radiation interacting with matter. To this end research will be conducted using existing sources, including FELs at other sites, until the Vanderbilt FEL is operational.

This concludes the general description of the Vanderbilt FEL program. At this point the discussion turns to a more detailed presentation emphasizing a biomedical application.

5. Selective interaction of radiation with tissue

There are several projects in the FEL program that share a common theme of understanding and effecting nonthermal and selective interaction of radiation with biopolymers and tissue. The projects represent research in three different areas of science: the clinical, biochemical, and biophysical areas or levels. This approach has the advantage that progress at any one level will provide the clues to further the other two levels of research.

For comparison purposes consider the vaporization of tissue caused by laser irradiation. It is known that tissue exposed to different irradiation paradigms can respond in markedly different ways. For some paradigms there is vaporization of exposed tissue and additional thermal damage to tissue lateral to the exposed

region. For other exposure paradigms the tissue is "etched" by laser irradiation of specific pulse structure, frequency, and intensity. The latter is an example of spatial selectivity and is clearly of clinical use. In addition, determining the underlying mechanism is physically interesting and these phenomena are being investigated at Vanderbilt. However, such a study is not unique to Vanderbilt and will not be discussed further in this presentation. The program to be discussed involves another type of selectivity.

As a second point for comparison consider the labeling of tissue with chromophores that, for example, specifically bind to membrane receptors. Such chromophores can act as electromagnetic targets. Thus energy can be coupled to a limited number of the degrees of freedom of the system and selectively disrupt tissue. This second example is more relevant to the Vanderbilt project. The distinction is that instead of attaching chromophores onto or inserting chromophores into cells we will take advantage of natural "chromophores" that are indicative of diseased tissue.

The general approach is described in the following. Diseased tissue will be identified in the clinic and presented to biologists for analysis. This analysis will identify unique characteristics, such as excessive chemical or biopolymer content, of the diseased tissue relative to the surrounding healthy tissue. These characteristics represent possible avenues for depositing radiation into diseased tissue with relatively little absorption by healthy tissue. Biophysical consideration will associate mechanisms for coupling radiation through these selective avenues and suggests exposure paradigms that target radiation into selected tissue. The protocols will be investigated at the biological and clinical levels and successive refinement will result from the interplay of research in the three levels.

At this point the three levels of research will be addressed with added emphasis on the biophysical level. As examples of the interplay of the three levels consider first precancerous tissue and then scar tissue. Precancerous tissue can present an excessive amount of calcium relative to healthy tissue and scar tissue contains a large amount of collagen. Spectroscopic studies have demonstrated that clusters of calcium strongly absorb infrared radiation and the biopolymer collagen has many eigenmodes in the spectral region extending from the far-infrared through the visible. These resonant mechanisms present avenues for the deposition of energy into diseased tissue and are currently under investigation. However, tissue is characterized by significant water content resulting in nonselective background absorption; this complication is the next subject of discussion.

It is clear that there are thermal and nonthermal mechanisms that result in the absorption of energy by tissue. In order to achieve selective disruption of diseased tissue the nonthermal mechanisms need to be

optimized relative to the thermal or nonselective mechanisms. Consider a train of pulsed radiation coupling to tissue. During a pulse energy will be absorbed by both selective and nonselective mechanisms. Between pulses the energy will be dissipated to surrounding tissue with a certain rate of dissipation for each mechanism. Absorption mechanisms that have relatively long relaxation times are candidates for mechanisms that optimize selective relative to nonselective deposition of energy into tissue. In other words, such mechanisms suggest exposure paradigms that optimize the targeting of radiation to diseased tissue.

As an example of mechanisms for selective coupling of radiation to biopolymers, a significant component of tissue, consider the resonant modes of DNA. Microwave and far-infrared experiments indicate minimum lifetimes on the order of hundreds of picoseconds [4,5]. A theoretical consideration, however, suggests that the natural lifetime may be several orders of magnitude longer [6]. Experiments are in preparation to determine the natural lifetimes of these modes using pulsed radiation from an FEL tuned to the appropriate eigenfrequencies. To a certain extent the dynamics of DNA generalize to other biopolymers, e.g. collagen or myosin, and therefore biopolymers are the principle candidates for possible targets to effect selective laser-tissue interaction.

6. Concluding remarks

The Vanderbilt University Free Electron Laser Center for Biomedical and Materials Research is a users facility that is developing into a regional, national, and international resource. The Vanderbilt FEL will provide continuously tunable, pulsed radiation from the UV to the IR and will serve as a radiation source for frontier experiments in FEL applications in materials and biomedical sciences. This program carries on the strong tradition of interdisciplinary cooperation at the University and is characterized by the common goals of both understanding nonthermal mechanisms in nature and developing their biomedical and materials applications.

References

- [1] R. Ossoff, J. Duncavage, N. Tolk, G. Edwards and R. Haglund, Proc. 6th Int. Congress on Applications of Lasers and Electro-Optics, San Diego, California (1987) in press.
- [2] G. Edwards, *ibid.*
- [3] N. Tolk, R. Haglund, G. Edwards and R. Ossoff, *ibid.*
- [4] G. Edwards, J. Saffer, M. Swicord and C. Davis, Phys. Rev. Lett. 53 (1984) 1284.
- [5] J. Powell, G. Edwards, L. Genzel, F. Kremer, A. Wittlin, W. Kubasek and W. Petricolas, Phys. Rev. A25 (1987) 3929.
- [6] L. Van Zandt, Phys. Rev. Lett. 57 (1986) 2085.

Vanderbilt University Free-Electron Laser Project
for Biomedical and Materials Research
Contract No. N00014-87-C-0146
October, 1987 - December, 1990

The Vanderbilt University Medical Free-Electron Laser Program

C. A. Brau
Vanderbilt University, Nashville, TN

The Vanderbilt University MFEL program comprises a broad variety of activities ranging from fundamental science to clinical applications. The activities span six departments in three schools of the University, including the Departments of Physics, Molecular Biology, Materials Science, Otolaryngology, Radiology, and Neurosurgery. The compact arrangement of the campus and the anticipation of working together in a single facility have made it possible to establish unique collaborations on innovative experiments.

To support these activities, the University has constructed a \$2.6 million, state-of-the-art laboratory building adjacent to the Medical School, the Physics Department and the Engineering School. A FEL is under construction by Sierra Laser Systems, to produce tunable, high-peak-power, pulsed radiation in the wavelength region from 2 to 10 microns. Construction of the free-electron laser is on schedule, and the machine should be in full operation in the Spring of 1990. Approximately 600 square meters of laboratory space is available on the floor above the vault, including two animal operating rooms. This space is now in use for experiments with conventional lasers, in preparation for the availability of the FEL.

At the present time, the laser applications projects underway include seven separate, but related efforts:

(1) Surface physics: Laser-induced desorption and selective molecular bond-breaking on surfaces, which are important processes in laser-induced damage to optical materials as well as in the nonthermal interaction of lasers with biological materials.

(2) Materials science: Mechanisms of infrared laser-induced damage in glasses and optical fibers, which are of importance to the application of FELs and other infrared lasers in medicine and other fields.

(3) Biophysics: Nonlinear spectroscopy of large biomolecules such as DNA, which is important for biological processes such as the localized melting of DNA during transcription.

(4) Molecular biology: Dynamics of membranes, especially ion transport mechanisms such as the calcium pump protein.

(5) Wound healing: Nonlinear interactions of lasers with tissue, with the objective of understanding the selective, nonthermal effects of short-pulse laser radiation on collagen formation, fibroblast proliferation, and so on.

(6) Neurosurgery: Fundamental studies of the nonlinear interaction of laser radiation with brain tissue, as well as the development of stereotactic imaging for neurosurgical procedures.

(7) X-Ray imaging: Generation and application of monochromatic X-Rays in the region from 5 to 20 kV formed by Compton-backscattering infrared radiation off the electron beam from the FEL.

Production of Near Monochromatic X-rays by
The Vanderbilt Medical Free Electron Laser
Frank Carroll, M.D.
Vanderbilt University Medical Center
Nashville, Tennessee

The creation of a powerful, tuneable, monochromatic X-ray source would herald a new and exceptionally diverse generation of diagnostic medical and material imaging modalities.

The production of 2 micron photons within the Vanderbilt Free Electron Laser by an electron beam of high quality and high peak current, offers an opportunity to use the residual electron beam that is normally "discarded" from the FEL and make it collide with its own generated photons to create tuneable, nearly monochromatic X-rays by Compton backscatter.

Once the electron beam has exited the FEL, it will be transported using bending and focusing magnets to an interaction zone whose axis is aligned with a 12" PVC beam pipe which penetrates the MFEL building structure from the FEL vault to a shirtsleeves environment target room situated on the upper floor of the facility. The electrons will interact with the extremely intense photon flux of the FEL and other conventional lasers. Compton backscattering will generate a cone of intense narrow bandwidth X-rays which will be transported via the PVC beam pipe to a tissue or material sample in the target room.

Monte Carlo algorithms have been used to model the energy and angles of the X-ray beams that will be produced. The initial configuration of this device will generate photons up to 17.9 Kev, although higher energies are easily obtainable through the use of frequency doubling techniques, alterations of electron beam energy, and the utilization of various conventional lasers as well. The photon flux will be sufficient to allow us to perform in vivo and in vitro trace element analysis, near-monochromatic radiography and three-dimensional imaging in a fashion never before possible.

The initial X-ray experiments will include analysis of excised tissues, followed by attempts to detect malignant breast lesions implanted in nude mice. Initial proofs are to be followed by application of this new high contrast/low dose imaging modality to detection, analysis and treatment of breast lesions in humans.

This work has been supported in part by a Grant from the Eastman Kodak Corporation Health Sciences Division.

**THE FREE ELECTRON LASER:
A PHOTON FACTORY FOR SCIENCE AND MEDICINE**

RICHARD F. HAGLUND, Jr.

Department of Physics and Astronomy and
Free-Electron Laser Project in Biomedical and Materials Research
Vanderbilt University, Nashville, TN 37235

The free-electron laser (FEL) is a new kind of coherent light source based on a marriage of laser and high-energy accelerator technology. Vanderbilt's recently-funded FEL Project in Biomedical and Materials Research is an interdisciplinary collaboration between the Schools of Medicine and Engineering and the College of Arts and Science, whose goal is to bring together researchers both from Vanderbilt and other institutions who are interested in studying the electronic interactions of FEL photons with everything from atoms and molecules on surfaces to living tissue.

In this tutorial talk, I shall describe the basic operating principles of free-electron lasers in a qualitative way; summarize the program goals for our FEL project, including collaborative efforts with "outside" users; and finally consider three applications in which Vanderbilt researchers expect to use FEL photons in ways not possible with conventional lasers: studies of laser-induced surface physics and chemistry, especially in beam delivery systems for high-power ultra-short pulse infrared lasers; excitation of the normal modes of DNA and other biologically important macromolecules to study drug action, cross-linking and metabolism; and use of non-thermal laser-tissue interactions to reduce scarring and tissue damage in arthroscopic and other kinds of laser surgery.

New Mechanism for Electron-Stimulated Desorption of Nonthermal Halogen Atoms from Alkali-Halide Surfaces II. A. 1

M. Szymonski, J. Kolodziej, P. Czuba, P. Piatkowski, and A. Poradzisz
Institute of Physics, Jagellonian University, ul. Reymonta 4, 30-059 Krakow, Poland

N. H. Tolk
Department of Physics and Astronomy, Vanderbilt University, Nashville, Tennessee 37235

J. Fine
Surface Science Division, National Institute of Standards and Technology, Gaithersburg, Maryland 20899
 (Received 22 March 1991)

Fully angular-resolved kinetic-energy distributions of alkali and halogen atoms emitted due to electron-stimulated desorption have been measured for (100) and (110) alkali-halide surfaces. An unexpected strong directional emission of nonthermal halogen atoms along the $\langle 100 \rangle$ axis of the investigated crystals has been found which is in contradiction to the predictions of the previously proposed "Pooley model." We propose a new model involving diffusion of hot holes to the surface, and sudden localization of the excited hole at the surface of the crystal.

PACS numbers: 79.20.Kz, 71.35.+z, 78.55.Fv, 82.65.My

Since the early work of Townsend and Kelly [1] and Imberg and Rhodin [2], it is known that electron irradiation of alkali-halide surfaces results in the efficient desorption of alkali and halogen atoms. Several attempts have been made to construct a model of electron-stimulated desorption (ESD) in alkali halides [3-8]. In particular, the "Pooley model" has been applied as an explanation of ESD from alkali halides by Townsend [3,6]. The main idea of this model is that nonradiative decay of a bulk self-trapped exciton followed by a focused recombination sequence along the closely packed $\langle 110 \rangle$ chains of the halogen atoms is responsible for halogen desorption. Thus, this bulk-exciton model predicts strong directional emission of halogen atoms along the $\langle 110 \rangle$ directions of the crystal. Despite a rather wide acceptance of the Pooley model, we believed that a comprehensive experimental test of its predictions had not yet been performed. Early attempts to measure angular dependence of emitted species were done by means of a collector method [3,6,9]. Unfortunately this technique does not provide any information about either mass or charge of different desorbing species that arrive at the collector and stick with various probabilities. In addition, sputtering of the collector deposit by reflected primary electrons, strongly focused along surface crystallographic directions [10], is likely to influence such results.

The first time-of-flight measurements for ESD of alkali halides were performed by Overeijnder *et al.* [11] for compressed powder samples. The only published energy distributions for halogen atoms desorbed from single-crystal material were obtained by Postawa and coworkers [12,13]. In the work we report here, for the first time a direct correlation has been measured among the direction of ejection, the mass and translational energy of desorbed particle, and the crystallographic structure of well-characterized insulator surface. In particular, we

present a direct comparison between angle-resolved energy spectra of bromine atoms taken for (100) and (110) surfaces of KBr. The data demonstrate that independent of the surface orientation the directional ejection of nonthermal halogen atoms takes place along the $\langle 100 \rangle$ axis of the bombarded crystals rather than along the $\langle 110 \rangle$ direction as predicted by the Pooley model. Our data strongly indicate the need for a new theoretical approach to explain the ESD of alkali halides.

The time-of-flight spectrometer used in these experiments was described previously [13,14]. The base pressure in the system was 5×10^{-7} Pa. A 0.7-keV electron gun supplying a beam of 5-10 μ A onto a spot of 3-4 mm was mounted on the same manipulator as the sample holder. Thus, variation of the observation angle during the angular distribution measurements could be achieved with a fixed bombardment angle (45° with respect to the surface normal). In addition, the manipulator allowed independent rotation of the sample in the horizontal plane, so that the angular scans could be made in various, arbitrarily chosen planes of the crystal. Neutral particles leaving the sample within a solid angle of 1.4×10^{-4} sr were ionized in an electron-impact ionizer and mass selected in a quadrupole mass spectrometer. Time-of-flight distributions were measured with a correlation technique [15].

The samples were high-purity (100) and (110) single crystals of KBr and a (100) crystal of KCl, cleaned by heating to 700 K in vacuum for several hours. This procedure is shown to produce well-ordered, single-crystal surfaces of alkali halides as examined by LEED and Auger-electron spectroscopy [10,16]. The composition of the electron-bombarded surface was monitored in this experiment by means of Auger-electron spectroscopy. We found using this technique that the surface composition for KCl and KBr remained stoichiometric for tempera-

tures above 90°C. Consequently, all experimental data were taken above this temperature.

Time-of-flight spectra of Br atoms desorbed from a (100) surface of a KBr crystal for several observation angles are shown in Fig. 1(a). The scans were taken in the (010) plane of the crystal. The spectra were normalized so that the total area under each time-of-flight distribution corresponds to the respective data point of the measured angular dependence of the total Br yield. Two velocity distributions can be distinguished in the time-of-flight spectra in the range of observation angles measured from 0° to 45°. The broad peak with a maximum at 1 ms may be attributed to a Maxwellian distribution of thermal atoms, while the second, sharp peak with a maximum at 0.4 ms and a sharp cutoff below 0.2 ms (1.2 eV),

corresponds to a faster, nonthermal distribution of Br atoms.

Angular-dependent measurements of the thermal and nonthermal distributions show that they have markedly different angular distributions. The thermal particles can be described by a cosinelike function characteristic of isotropic emission; in contrast, the nonthermal bromine atoms have a strikingly more peaked angular dependence as shown in Fig. 2(a). *From the above analysis, it is clear that desorption of nonthermal halogen atoms from a KBr (100) sample is strongly directed along the <100> axis of the crystal.*

Our time-of-flight measurements indicate that for tar-

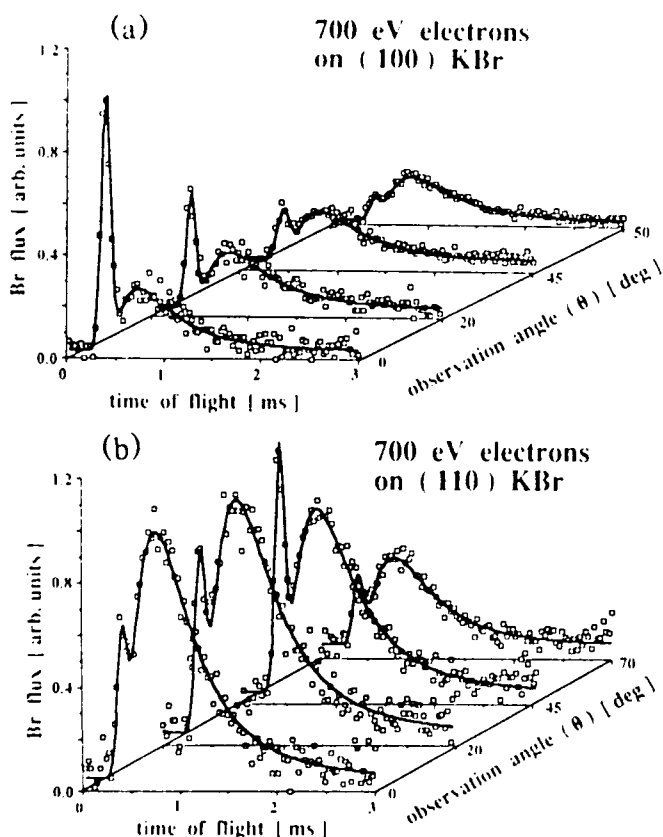


FIG. 1. Time-of-flight spectra of Br atoms desorbed from a KBr crystal at 140°C. The distributions were normalized so that the total area under each distribution corresponds to the respective data point of the measured angular dependence of the total Br yield. The solid lines represent best fits of the superposition of a Maxwellian distribution with temperature $T = 140^\circ\text{C}$ and an arbitrarily chosen Gaussian function. For better visual presentation the time-of-flight distributions were not corrected for varying ionization efficiency of our electron-impact ionizer which is inversely proportional to the velocity of the detected atoms. (a) Distributions measured for four different observation angles in the (010) plane of the (100) KBr crystal. (b) Distributions measured for four different observation angles in the (001) plane of the (110) KBr crystal.

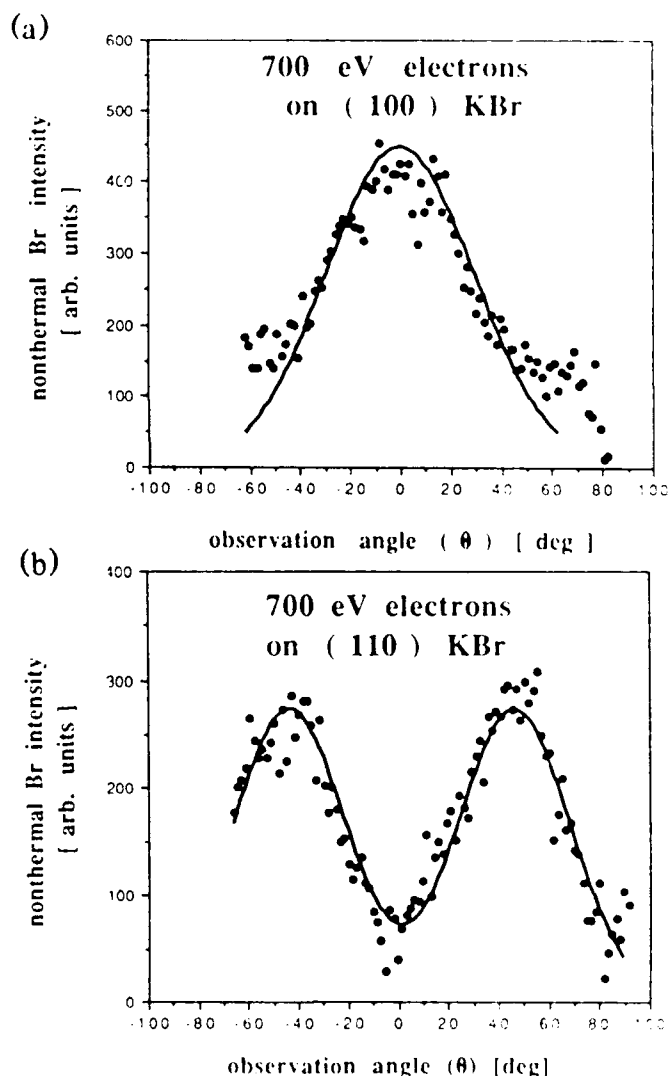


FIG. 2. Angular distributions of the nonthermal Br atoms desorbed from a KBr crystal at 140°C. The data points were obtained by subtracting the cosine angular distribution observed for thermal halogen atoms from the experimentally measured dependence for total Br intensity. The solid curves are drawn to guide the eye. (a) The distribution measured in a (010) plane of the (100) KBr crystal. (b) The distribution measured in a (001) plane of the (110) KBr crystal.

get temperatures below 100°C, practically only nonthermal Br atoms are emitted along the $\langle 100 \rangle$ axis as shown in Fig. 3. The time-of-flight distribution of the nonthermal Br atoms is found to be very narrow (half-width of 0.12 ms); its position and width were observed to be independent of temperature. If the nonthermal atoms would originate in the bulk of the sample, subsequent energy-loss processes, for example, phonon decay occurring during transport to the surface, would result in broadening of the low-velocity side of the time-of-flight spectrum. Such broadening is definitely not observed and this would indicate that the nonthermal halogen atoms are emitted from the surface.

The time-of-flight distributions measured for a $\langle 100 \rangle$ surface of KCl show the same behavior as the ones described for KBr. The ratio of nonthermal-to-thermal halogen yield for KCl, however, for the same observation angle and target temperature, is smaller than that for KBr. For example, at $\Theta = 0^\circ$ and $T = 140^\circ\text{C}$, this ratio equals 0.29 for KCl and 1.88 for KBr.

In order to learn more about the nature of the directional emission of nonthermal halogen atoms, we measured the angle-resolved time-of-flight spectra for a specially polished $\langle 110 \rangle$ surface of KBr. In this case the $\langle 100 \rangle$ axis forms an angle of $\pm 45^\circ$ with the surface normal in the $\langle 001 \rangle$ plane. The time-of-flight spectra for this case are shown in Fig. 1(b). The angular distribution of the nonthermal Br signal, taken in this plane, is shown in Fig. 2(b). In contrast to the distribution from Fig.

2(a), two peaks are seen, centered at $+45^\circ$ and -45° with respect to the surface normal. It has been found, however, that the cosine distribution with respect to the surface normal for the $\langle 110 \rangle$ surface still describes the thermal emission of Br atoms and the total emission of K atoms at all temperatures. Thus, indeed only the nonthermal Br atoms are ejected directionally within the narrow cone around the $\langle 100 \rangle$ axis of the crystal which, in this case, does not coincide with a surface normal.

As we have mentioned above, the Pooley model of ESD of alkali halides predicts that a $\langle 110 \rangle$ direction of the crystal [i.e., $\Theta = \pm 45^\circ$ for the $\langle 100 \rangle$ sample] should be the preferred one for halogen emission. Our experimental results clearly contradict this expectation which was based on bulk exciton decay. In order to explain our results, we propose a new model which invokes a sudden localization of the excited ("hot") hole at the surface of the crystal. Recently, it became evident that hot holes in the valence band and free electrons are created with high probability by ionizing radiation [8,17-20]. The initial kinetic-energy distribution of hot holes could be described by the valence-band density of states [18,21]. It follows from the photoemission measurements that in KBr this energy can be as high as 2.6 eV with the average value of 1.3 eV [22]. Furthermore, due to this high initial energy acquired in primary excitation, hot holes can migrate over considerable distances in alkali halides [17-20], thus providing a necessary transport mechanism for the excitation energy to go from the bulk to the surface. The excited halogen hole X^* arriving nonadiabatically at the surface would likely experience a repulsive potential due to breaking of the bulk symmetry. Simple electrostatic considerations for the ionic, NaCl-type surface indicate that the repulsion would be directed preferentially along the axis between a subsurface alkali ion (M^+) and the surface halogen site occupied by X^* as seen in Fig. 4. Note that the $M^+ - X^*$ axis coincides with the $\langle 100 \rangle$ direction for both $\langle 100 \rangle$ and $\langle 110 \rangle$ surfaces of the NaCl-type crystals; this ejection direction is consistent with our angular-resolved measurements. An alternate possibility of hot-hole localization at the surface would be via a halogen molecular complex $(X_2^{2-})^*$ (in analogy with the bulk decay of a self-trapped exciton), but as pointed out by Williams [8], it would more likely lead to the ejection of a halogen negative ion X^- along $\langle 110 \rangle$.

Although negative ions could not be measured with our time-of-flight spectrometer, significant negative halogen emission has been observed previously [1,9]. Since the collector technique is not able to distinguish between negative-ion and neutral-atom emission, some of the directional $\langle 110 \rangle$ and $\langle 211 \rangle$ spots observed by Townsend *et al.* [3] and by Schmid, Braunlich, and Rol [9], ascribed so far to directional emission of neutrals, could have been due to the negative ions. Note that in the laser experiment of Schmid, Braunlich, and Rol only the lowest excitonic states could be excited with the available photon en-

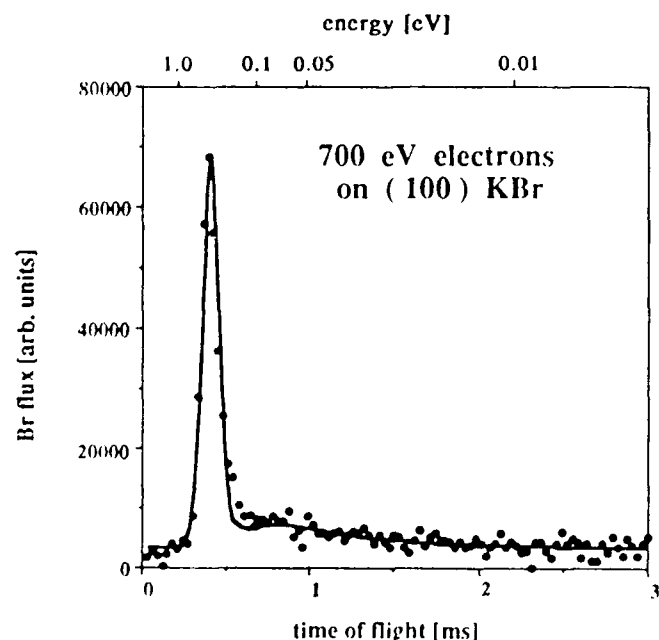


FIG. 3. Time-of-flight distribution of Br atoms desorbed from a $\langle 100 \rangle$ KBr crystal at 95°C . As in Fig. 1 the distribution was not corrected for the velocity-dependent ionization efficiency. The observation angle was 0° . The solid curve is drawn to guide the eye.

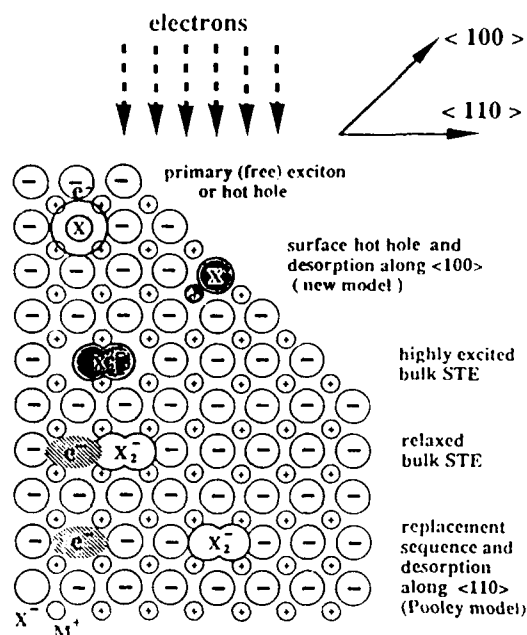


FIG. 4. A schematic view of the lattice excitations in alkali halides leading to desorption via the focused replacement sequence (Pooley model) and repulsion of the hot hole localized at the surface (new model). X denotes a halogen and M an alkali atom.

ergy and the central $\langle 100 \rangle$ spot was not observed. In our experiment, however, as well as in the collector experiment by Townsend *et al.* [3], the energy of primary electrons used for desorption was sufficient to create highly excited holes and indeed the central $\langle 100 \rangle$ emission was observed.

In conclusion, we can distinguish the following steps in the proposed model to explain ESD of nonthermal halogen atoms: (a) creation of highly excited (hot) electron-hole pairs within the penetration range of the primary electrons, (b) fast hot-hole diffusion to the surface within a time range of picoseconds (the mean diffusion range is comparable to the penetration depth of the primary electrons), and (c) hot-hole localization at the surface resulting in directional emission of the nonthermal halogen atoms due to its repulsive interaction with a subsurface alkali ion along the $\langle 100 \rangle$ axis of the crystal.

The authors wish to thank Dr. Hideo Sambe and Dr. David Ramaker for their helpful suggestion concerning the $M^+ - X^0$ complex. Fruitful discussions with Dr. C. S. Ewig are gratefully acknowledged. This work is part of the Joint Collaboration Project No. MEN/NIST-89-6, sponsored by the Polish-American Maria Skłodowska-Curie Fund II and additionally supported by the Polish Ministry of National Education, Grant No. P/04/238.

This project was supported in part by the Office of Naval Research under Contract No. N00014-87-C-0146.

N. H. Tok
Prof. Norman H. Tok, PI

Two of us (N.H.T. and J.F.) express grateful appreciation to the Institute of Physics of the Jagellonian University for its kind hospitality during their stay as visiting scientists.

- [1] P. D. Townsend and J. C. Kelly, *Phys. Lett.* **26A**, 138 (1968).
- [2] P. W. Palmberg and T. N. Rhodin, *J. Phys. Chem. Solids* **29**, 1917 (1968).
- [3] P. D. Townsend, R. Browning, D. J. Garland, J. C. Kelly, A. Mahjoobi, A. J. Michael, and M. Saidoh, *Radiat. Eff.* **30**, 55 (1976).
- [4] N. Itoh, *Nucl. Instrum. Methods* **132**, 201 (1976).
- [5] M. Szymonski, *Radiat. Eff.* **52**, 9 (1980).
- [6] P. D. Townsend, in *Sputtering by Particle Bombardment*, edited by R. Behrish (Springer-Verlag, Berlin, 1983), Vol. 2, p. 147.
- [7] R. F. Haglund, Jr., R. G. Albridge, D. W. Cherry, R. K. Cole, M. H. Mendenhall, W. C. B. Peatman, N. H. Tolk, D. Niles, G. Margaritondo, N. G. Stoffel, and E. Taglauer, *Nucl. Instrum. Methods Phys. Res., Sect. B* **13**, 525 (1986).
- [8] R. T. Williams, *Radiat. Eff. Defects Solids* **109**, 175 (1989).
- [9] A. Schmid, P. Braunlich, and P. K. Rol, *Phys. Rev. Lett.* **35**, 1382 (1975).
- [10] I. Marklund and S. Andersson, *Surf. Sci.* **5**, 197 (1966).
- [11] H. Overeijnder, M. Szymonski, A. Haring, and A. E. de Vries, *Radiat. Eff.* **36**, 63 (1978); **38**, 21 (1978).
- [12] Z. Postawa and M. Szymonski, *Phys. Rev. B* **39**, 12950 (1989).
- [13] Z. Postawa, P. Czuba, A. Poradzisz, and M. Szymonski, *Radiat. Eff. Defects Solids* **109**, 189 (1989).
- [14] M. Szymonski, A. Poradzisz, P. Czuba, J. Kolodziej, P. Piatkowski, and N. H. Tolk, *Nucl. Instrum. Methods Phys. Res., Sect. B* (to be published).
- [15] G. Comsa, R. David, and B. J. Schumacher, *Rev. Sci. Instrum.* **52**, 789 (1981).
- [16] L. S. Cota Araiza and B. D. Powell, *Surf. Sci.* **51**, 504 (1975).
- [17] C. T. Reimann, W. L. Brown, and R. E. Johnson, *Phys. Rev. B* **37**, 1455 (1988).
- [18] V. N. Kadchenko and M. Elango, *Phys. Status Solidi (a)* **46**, 315 (1978).
- [19] M. A. Elango, V. N. Kadchenko, A. M. E. Saar, and A. P. Zharakovski, *J. Lumin.* **14**, 375 (1976).
- [20] T. A. Green, G. M. Loubriel, P. M. Richards, I. T. Hudson, P. M. Savundararaj, R. G. Albridge, A. V. Barnes, and N. H. Tolk, in *Desorption Induced by Electronic Transitions*, edited by G. Beta and P. Varga, Springer Series in Surface Science Vol. 19 (Springer-Verlag, Berlin, 1990), p. 281.
- [21] E. O. Kane, *Phys. Rev.* **159**, 624 (1967).
- [22] S. P. Kowalczyk, F. R. McFeely, L. Ley, R. A. Pollak, and D. A. Shirley, *Phys. Rev. B* **9**, 3573 (1974).

New mechanism for the desorption of excited atoms by photon bombardment of alkali halide crystals

D. Liu, R. G. Albridge, A. V. Barnes, P. H. Bunton^(a), C. S. Ewig, and N. H. Tolk

Department of Physics and Astronomy, and Department of Chemistry

Vanderbilt University

Nashville, Tennessee, USA 37235

M. Szymonski

Institute of Physics, Jagellonian University, ul. Reymonta 4,

30-059 Krakow, Poland

We report measurements of photon-stimulated desorption of excited atoms from LiF and NaCl crystal surfaces. Based on these measurements, we propose a new model of photon-initiated, defect-mediated desorption involving exoergic surface reactions between alkali dimers and halogens. This model consists of two steps: (a) reactants are formed at the surface, directly or by the migration to the surface of holes and defects created in the near surface bulk, due to uv photon bombardment, and (b) excited alkali atoms are emitted following a reaction between the alkali and halogen surface species.

PACS numbers: 82.65Yh, 79.60.-m, 78.60.Ps, 34.20.Mq

In this letter we present a new model for desorption of excited alkali atoms from alkali halide crystal surfaces following photon bombardment. The mechanisms responsible

for the production of excited alkali atoms by photon-stimulated desorption (PSD) and electron-stimulated desorption (ESD) have been the subjects of much controversy. Two models have been invoked most often to account for the production of the excited atoms. One model involves ion neutralization, and is analogous to the Knotek-Feibelman mechanism for ion desorption.^{1,2} According to this mechanism, the interatomic Auger decay of a core hole results in the formation of two valence holes on a single surface anion resulting in ion desorption. Subsequent neutralization of the desorbing ion into an excited state then accounts for the observed excited atom yield. The second model assumes that the excited atoms are produced by secondary-electron excitation of desorbed ground state atoms in the gas phase.³⁻⁶ Recent work⁷ shows that valence excitations alone can lead to excited alkali atom desorption; thus core-hole creation, an essential component of the Knotek-Feibelman mechanism, is not always required for the production of excited alkali atoms. Previous work⁷⁻¹¹ also shows that the excited alkali atom yield of PSD decreases markedly with increasing temperature while both the total electron yield and ground state alkali atom yield increase, in contradiction to the second model involving secondary electron excitation. Thus, both models have been found to exhibit deficiencies when applied to PSD.

The new mechanism we propose is based on one or more exoergic surface reactions between alkali dimers (M_2) and halogens (X or X_2). The most direct possible reaction¹²⁻¹⁹ is $M_2 + X \rightarrow M^* + MX$.²⁰ This reaction was first suggested to explain the observation of sodium D-lines when sodium vapor was mixed with chlorine, bromine, or iodine gas.¹² In general, the reaction occurs with most of the possible combinations of alkali vapors and halogen gases. Subsequently this reaction was studied directly by molecular-beam experiments¹³⁻¹⁷ and its feasibility was demonstrated by semiempirical theoretical calculations.¹⁸ The gas-phase reaction cross section for producing excited alkali atoms was

found by theoretical calculations¹⁹ and by crossed beam studies¹³⁻¹⁷ to be very large, 10 – 100 Å². Figure 1, based on the calculations in Struve's paper,¹⁸ depicts a section of the energy surface of collinear Na₂Cl. The reaction proceeds through a transition state in which an electron from the sodium dimer shifts to the chlorine atom positioning the excited molecular complex, (Na–Na⁺Cl⁻)*, at a point on the potential energy surface corresponding to neutral sodium in a repulsive state. The system may then evolve through this position to form a free sodium atom in its first excited state and an ionically bonded NaCl molecule. The available reaction energy is no greater than 3.50 ± 0.04 eV for Na₂+Cl and 3.30 ± 0.13 eV for Li₂+F.²¹ This limitation rules out the population of those higher excited states that decay in the visible, unless there is a contribution from reagent collision energy. (Polanyi et al.¹⁶ found that, in molecular beam experiments, higher excited states are populated for collision energies in the range 0.2 to 0.5 eV. The first excited state, however, is always populated at least an order of magnitude more than the higher excited states.)

The proposed model depends upon the presence of alkali dimers and halide atoms on the surface. It is well accepted that in PSD or ESD from alkali halide crystals at elevated temperatures the majority desorbing species are ground state halogen atoms and alkali atoms.^{22,23} The desorption of these ground state halogen and alkali atoms is thought to be mediated by self-trapped excitons created either on the surface or in the bulk.²⁴⁻²⁶ The incident photon or electron creates one or more holes in occupied valence bands in the near surface bulk. Energetic "hot" holes may migrate within a picosecond, some further into the bulk and some to the surface, before coming to rest and forming self-trapped excitons.²³ Self-trapped excitons in the bulk may then decay forming an *F*-center/*H*-center pair.^{25,26} Subsequent thermally assisted migration of the *H*-center can produce temperature-

equilibrated halogen at the surface, some of which thermally desorbs leaving excess metal. Nonthermal halogen emission may arise from the decay of surface self-trapped excitons again resulting in excess metal.²⁷ Depending on the degree of metallization, which in turn depends on the irradiation history and temperature, the accumulated neutralized alkali atoms may then form dimers, trimers, and larger clusters on the surface.^{28,29} At some accumulated irradiation dosage, the number of dimers should reach a maximum. Thus during photon or electron bombardment of alkali halide crystals, defect mediated processes create at the surface the necessary reactants for the postulated reaction.

The PSD experiments reported here were performed at the Synchrotron Radiation Center of the University of Wisconsin with the Vanderbilt/SRC 6-meter toroidal-grating monochromator, which provides photons in the energy range of 7 to 180 eV. Excited atoms were detected by monitoring their characteristic optical emission above the surface with a MacPherson 218 monochromator and an EMI S-20 photomultiplier tube. After cleaving, the alkali halide single crystals were exposed to air for less than 30 minutes before the chamber was evacuated. The crystals were then annealed six to eight hours at 350° C.

Shown in figures 2a and 2b are optical spectra of LiF and NaCl crystals under photon bombardment. Sharp peaks superimposed on the continuous bulk luminescence correspond to atomic transitions from the 2p to the 2s state for lithium atoms and the 3p to the 3s state for sodium atoms, respectively. Transitions from higher excited states, such as from the 3p to the 2s state for lithium atoms (323.3 nm) and from the 4p to the 3s state for sodium (330.2 nm) are not seen in our spectra, but will be searched for in future experiments. The absence of the higher states is consistent with the prediction of our surface-reaction model: the reaction energy available is not sufficient to populate higher states provided the reactants on the surface have negligible collision energy.

Figure 3 shows the excited lithium atom yield plotted as a function of irradiation time during 62.2 eV photon bombardment of LiF. The yield was normalized to the photon

flux. The dependence of the yield on the irradiation time, shown in Fig. 3, is consistent with the hypothesis that the yield reflects the instantaneous alkali dimer concentration which in turn depends largely on the degree of metallization of the surface. The nonzero yield at the beginning of the measurement is due to the presence of metal on the surface, even for the annealed samples.²⁸ Initially there are relatively few alkali dimers on the surface; thus even though the halogen yield is large at this stage, the excited atom yield is small. As the metallization increases, there is an optimum stage where many alkali dimers are present while the halogen atom concentration remains large. At this stage the excited alkali atom yield is at a maximum as indicated by the peak in figure 3. With further irradiation the yield decreases because of a decrease in the concentration of dimers due to the formation of larger clusters, and because the metal clusters block halogen atom desorption.

Figures 4a and 4b are plots of the yields of excited Li atoms from LiF and excited Na atoms from NaCl, respectively, as functions of time, showing the effects of transient halogen dosing during uv photon bombardment. To increase the yields, incident zero-order light transmitted through an aluminum filter was used for both of these measurements. Yields were normalized to photon flux. Chlorine gas was introduced into the chamber for a period of 10 seconds resulting typically in an exposure of 86 Langmuirs and causing large enhancements in the excited atom yield for both samples. These observations are consistent with the hypothesis that the enhancements were due to the increase of the concentration of chlorine atoms on the surface. We postulate that chlorine molecules are dissociated on the surface, providing the required chlorine atoms. Note that the enhancement in Li* yield in the LiF case is due to the action of the externally introduced chlorine atoms in contrast to internally generated fluorine atoms. This is a strong evidence that reactions occurring on the surface, as postulated, lead to the emission of the excited metal atoms.

We postulate that our proposed mechanism is also a contributor to *electron-stimulated* desorption of excited alkali atoms. Other likely contributors include excitation of

desorbed ground-state neutral alkalis by primary beam electrons^{4,5} and also to some extent by secondary electrons.³ In support of this postulate, for the case of LiF we have previously measured the temperature-dependent yield of excited lithium atoms during electron bombardment.⁹ The yield was found to be appreciable at room temperature (where desorption of thermal ground-state atoms is low) but increased by two orders of magnitude with temperature up to 400° C (where radiation induced desorption of ground state lithium atoms is increased by *four* orders of magnitude).⁹ In contrast, the yield from photon-stimulated desorption is also appreciable at room temperature but *decreases* markedly with increasing temperature.^{7,8} This indicates that (a) for PSD, there is little contribution from gas-phase excitation by secondary electrons, and (b) for ESD at low temperatures, where gas-phase excitation does not contribute because the desorption yield of ground-state alkalis is low, our proposed mechanism is the principal contributor.

In conclusion, we suggest a new model for the production of excited alkali atoms by PSD. This model is based on experimental measurements of photon-stimulated desorption and the previously known gas-phase chemiluminescent reaction between alkali dimers and halogen atoms. Radiation-induced metallization and halogen atom formation provide the two necessary reactants for the surface reaction. The large enhancement of the excited alkali atom yield due to chlorine dosing, the dependence of the yield on the irradiation time, and the apparent absence of visible emission from other excited electronic states are in strong support of the new model.

The authors wish to thank the staff at the University of Wisconsin's Synchrotron Radiation Center for their excellent support and M. Riehl-Chudoba, T.A. Green, N. Itoh and J. C. Tully for helpful discussions. This work was supported in part by the Air Force Office of Scientific Research under contracts F49620-86-C-0125 and F49620-88-C-0080, grant AFOSR-90-0030, and by the Office of Naval Research under contract N00014-87-C-0146.

References:

(a) Present address: Department of Physics, Austin Peay State University, Clarksville, TN 37044

- ¹ M. L. Knotek and P. J. Feibelman, *Phys. Rev. Lett.* 40, 965 (1978)
- ² P. J. Feibelman and M. L. Knotek, *Phys. Rev. B* 18, 6531 (1978)
- ³ R. E. Walkup, Ph. Avouris, and A. P. Ghosh, *Phys. Rev. Lett.* 57, 2227 (1986)
- ⁴ M. Szymonski, J. Ruthowski, A. Poradzisz, and Z. Postawa, *Desorption Induced by Electronic Transitions, DIET II*, edited by W. Brenig and D. Menzel, Springer Series in Surface Sciences, Vol. 4, Springer-Verlag, Berlin, 1984, 160
- ⁵ J. Ruthowski, A. Poradzisz, Z. Postawa and M. Szymonski, *Nucl. Instr. and Meth.* B34, 27(1988)
- ⁶ Z. Postawa, J. Ruthowski, A. Poradzisz, P. Czuba, and M. Szymonski, *Nucl. Instr. and Meth.* B18, 574 (1987)
- ⁷ P. H. Bunton, R. F. Haglund, Jr., D. Liu, and N. H. Tolk, *Photon-Stimulated Desorption of Excited Alkali Atoms Following Valence Band Excitation of Alkali Halides*, to be submitted to *Phys. Rev. B*
- ⁸ E. Taglauer, N. Tolk, R. Riedel, E. Colavita, G. Margaritondo, N. Gershenfeld, N. Stoffel, J. A. Kelber, G. Loubriel, A. S. Bommanavar, M. Bakshi, and Z. Huric, *Surf. Sci.* 169, 267 (1986)
- ⁹ P. Wurz, E. Wolfrum, W. Husinsky, G. Betz, L. Hudson, and N. Tolk, *Rad. Effects* 109, 203 (1989)
- ¹⁰ W. Husinsky, P. Wurz, K. Mader, E. Wolfrum, B. Strehl, G. Betz, R. F. Haglund Jr., A.V. Barnes, and N. H. Tolk, *Nucl. Instr. and Meth.* B33, 824 (1988)
- ¹¹ R. F. Haglund, Jr., R. G. Albridge, D. W. Cherry, R. K. Cole, M.H. Mendenhall, W. C. B. Peatman, N. H. Tolk, D. Niles, G. Margaritondo, N. G. Stoffel, and E. Taglauer, *Nucl. Instr. and Meth. in Phys. Res.* B13, 525 (1986)

- ¹² Alkali Halide Vapors, Structure, Spectra, and Reaction Dynamics, edited by P. Davidovits and D.L. McFadden, Academic Press, Inc. 1979, Chapter 11, 361
- ¹³ M. C. Moulton and D. R. Herschbach, J. Chem. Phys. 44, 3010 (1966)
- ¹⁴ W. S. Struve, J. R. Krenos, D. L. McFadden, and D. R. Herschbach, J. Chem. Phys. 62, 404 (1975)
- ¹⁵ P. Arrowsmith, S. H. P. Bly, P. E. Charters, P. Chevrier, and J. C. Polanyi, J. Phys. Chem. 93, 4716 (1989)
- ¹⁶ J. C. Polanyi, W. Reiland, C. D. Stanners, D. F. Thomas, and J.-P. Visticot, J. Phys. Chem. 93, 4723 (1989)
- ¹⁷ J. C. Polanyi, D. F. Thomas, and J.-P. Visticot, J. Phys. Chem. 93, 4730 (1989)
- ¹⁸ W. S. Struve, J. Mol. Phys. 25, 777 (1973)
- ¹⁹ J. R. Krenos and J. C. Tully, J. Chem. Phys. 62, 420 (1975)
- ²⁰ Other reactions include the vibrational-to-electronic energy transfer reaction $M_2 + X \rightarrow MX^\dagger + M^0 \rightarrow MX + M^*$, where MX^\dagger stands for a vibrationally excited molecule; and the reaction $M_2 + X_2 \rightarrow M^* + MX + X$. We consider both reactions to be possible contributors to our proposed surface mechanism but less likely based on gas phase studies (see references 12-17).
- ²¹ M. W. Chase, Jr., C. A. Davies, J. R. Downey, Jr., D. J. Frurip, R. A. McDonald, and A. N. Syverud, J. Phys. Chem. Ref. Data, Suppl. No.1, Vol. 14, 1985
- ²² M. Szymonski, Radiat. Eff. 52, 19 (1980)
- ²³ T. A. Green, G. M. Loubriel, P. M. Richards, L. T. Hudson, P. M. Savundararaj, R. G. Albridge, A. V. Barnes, and N. H. Tolk, Desorption Induced by Electronic Transitions, DIET IV, edited by G. Betz and P. Varga, Springer Series in Surface Sciences, Vol. 19, Springer-Verlag Berlin, Heidelberg 1990, 281
- ²⁴ Z. Postawa and M. Szymonski, Phys. Rev. B 39, 12950 (1989)
- ²⁵ N. Itoh, Adv. in Phys. 31, 491 (1982)

- ²⁶ R. T. Williams, K. S. Song, W. L. Faust, and C. H. Leung, Phys. Rev. B 33, 7232 (1986)
- ²⁷ M. Szymonski, J. Kolodziej, P. Czuba, P. Piatkowski, A. Poradziak, and N. H. Tolk, Nucl. Instr. Meth. B, in press
- ²⁸ P. Wurz and C. H. Becker, Surf. Sci. 224, 559 (1989)
- ²⁹ Qun Dou and D. W. Lynch, Surf. Sci. 219, L623 (1989)

Figure Captions

Figure 1: A schematic representation of a section of the semiempirical energy surface for the collinear $\text{Na}_2 + \text{Cl} \rightarrow \text{Na}^* + \text{NaCl}$ reaction based on figure 1 of Struve's paper (ref. 18). The vertical axis represents energy, the R_1 axis the distance between the two sodium atoms, and the R_2 axis the distance between a chlorine atom and the nearer sodium atom of the dimer.

Figures 2a and 2b: Optical fluorescence spectra of LiF and NaCl crystals, respectively, due to photon bombardment.

Figure 3: Effect of irradiation time on the yield of excited lithium atoms. The photon energy was 62.2 eV and the yield is normalized to the Ni mesh current.

Figures 4a and 4b: Effect of chlorine gas dosing on the yields of excited alkali atoms from LiF and NaCl crystals, respectively, under zero-order light bombardment. Dosings started at 0th minute and lasted for 10 seconds.

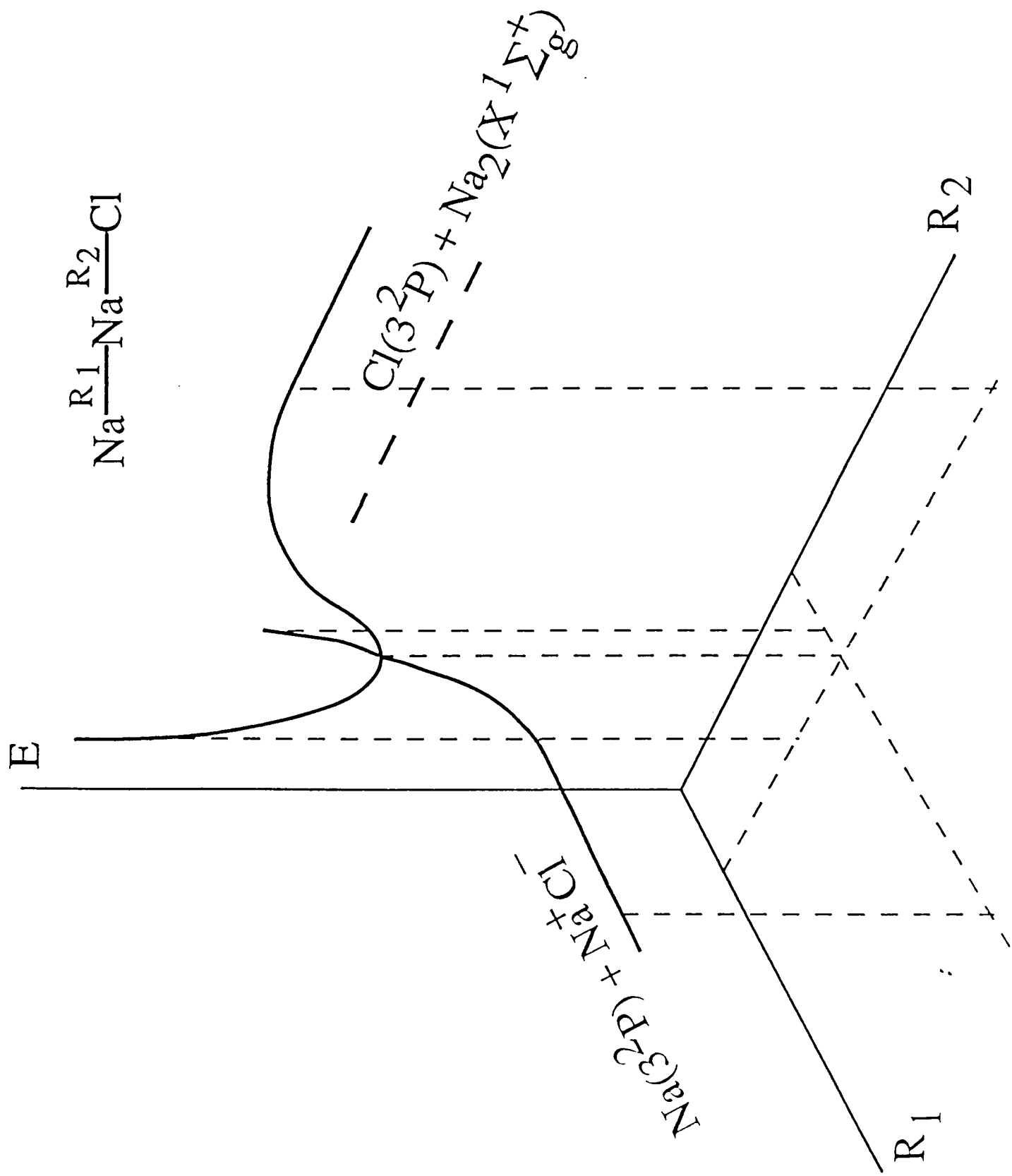


Fig. 1

Fig. 2a

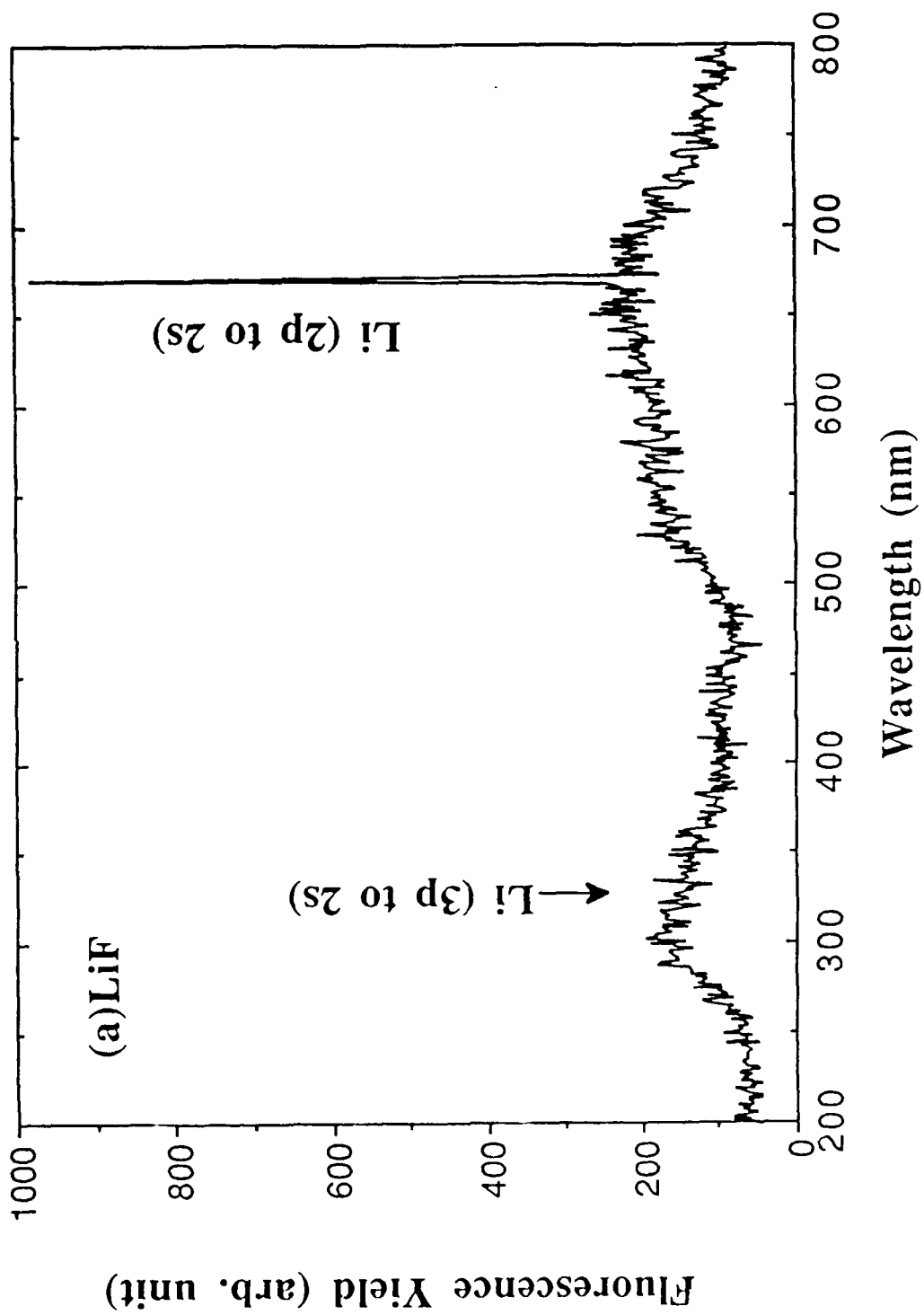


Fig. 2b

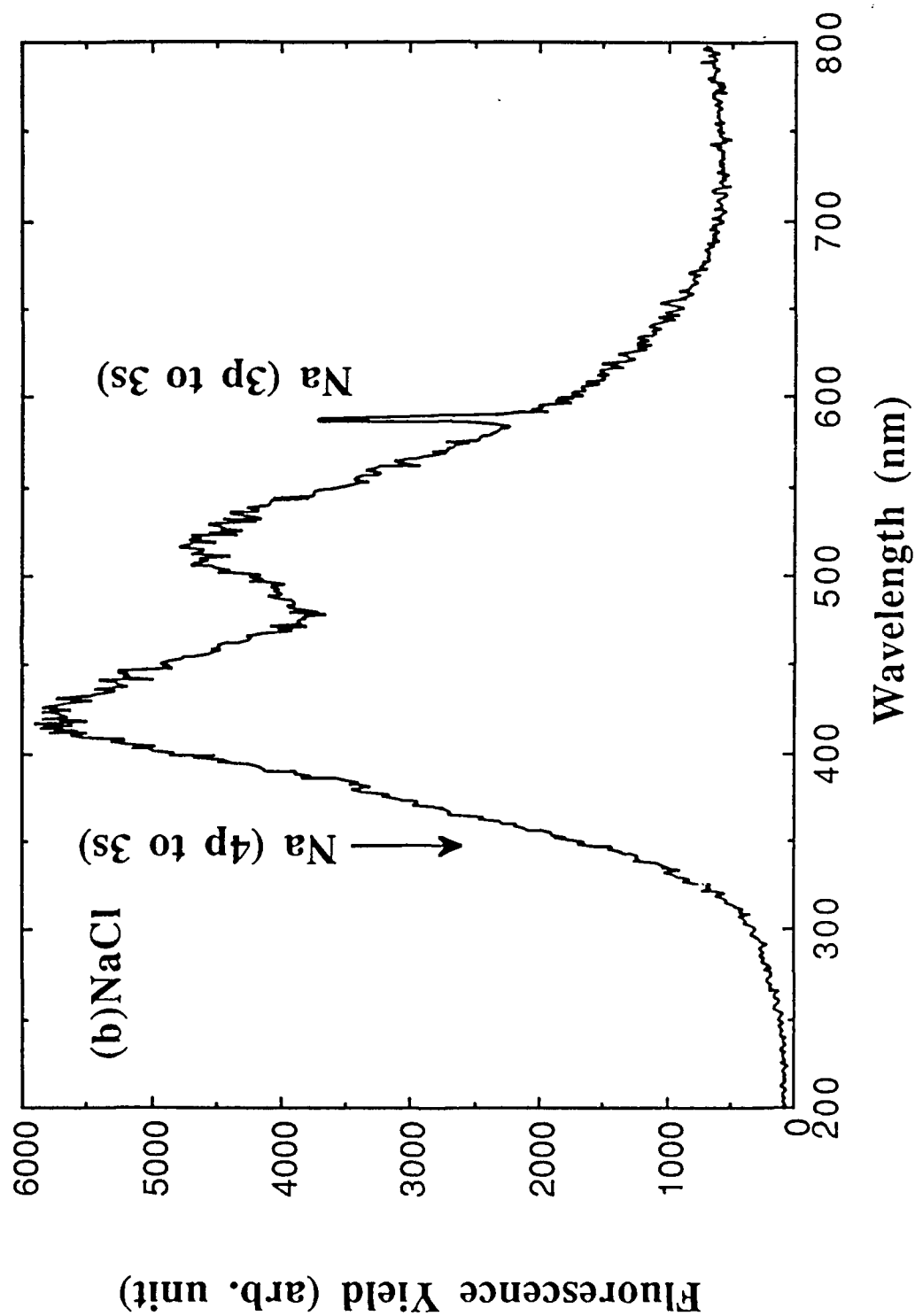


Fig 3

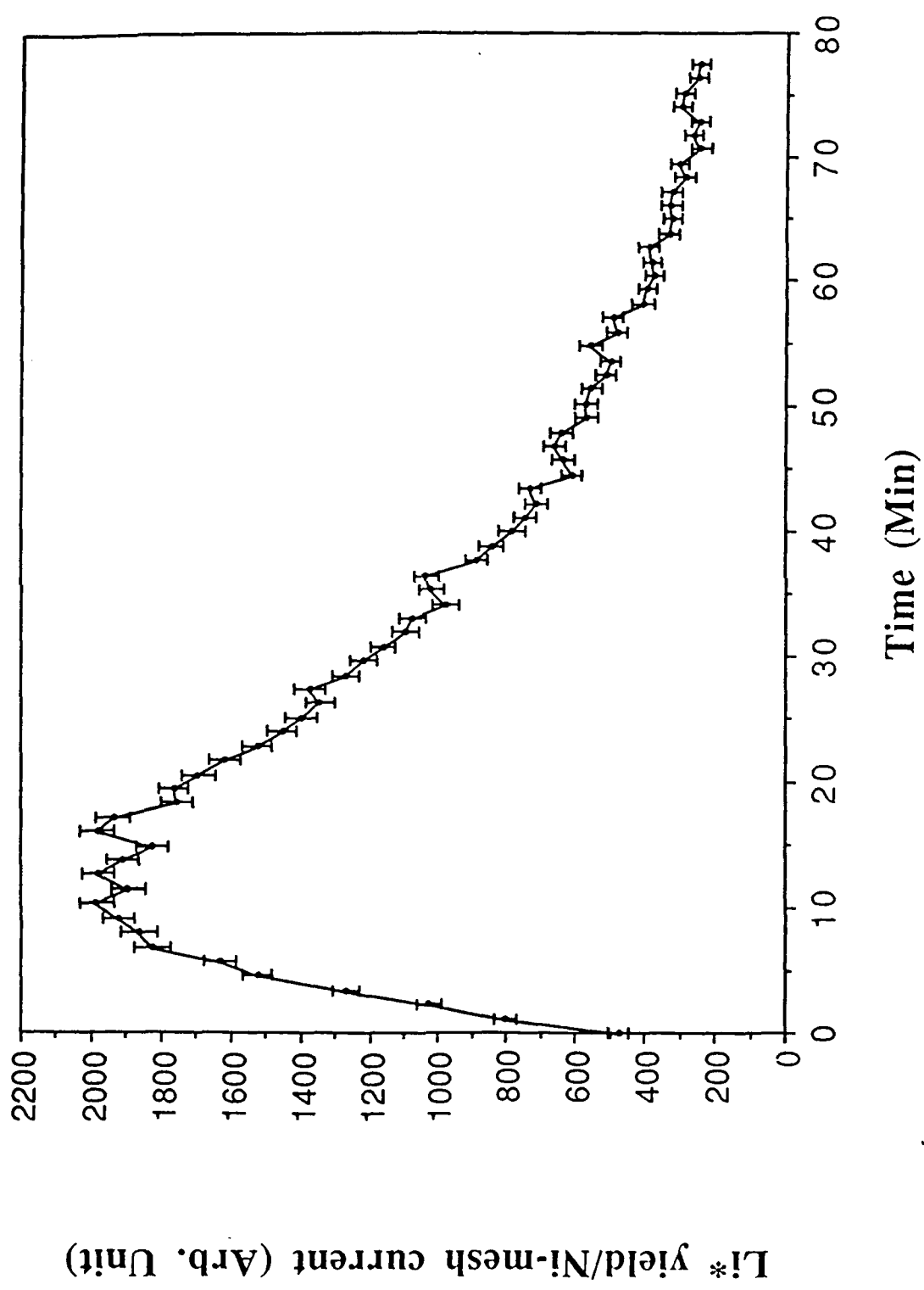


Fig. 4a

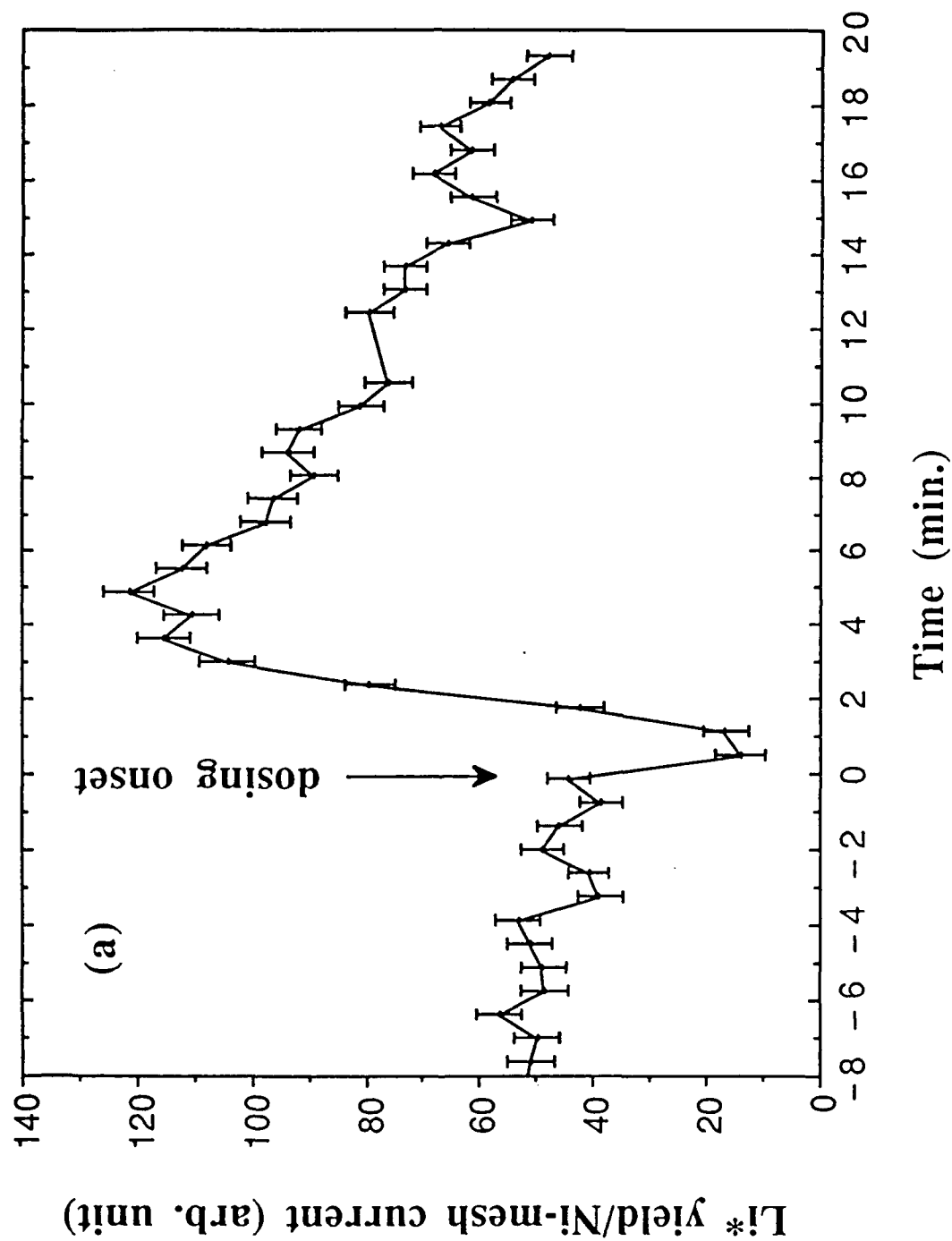
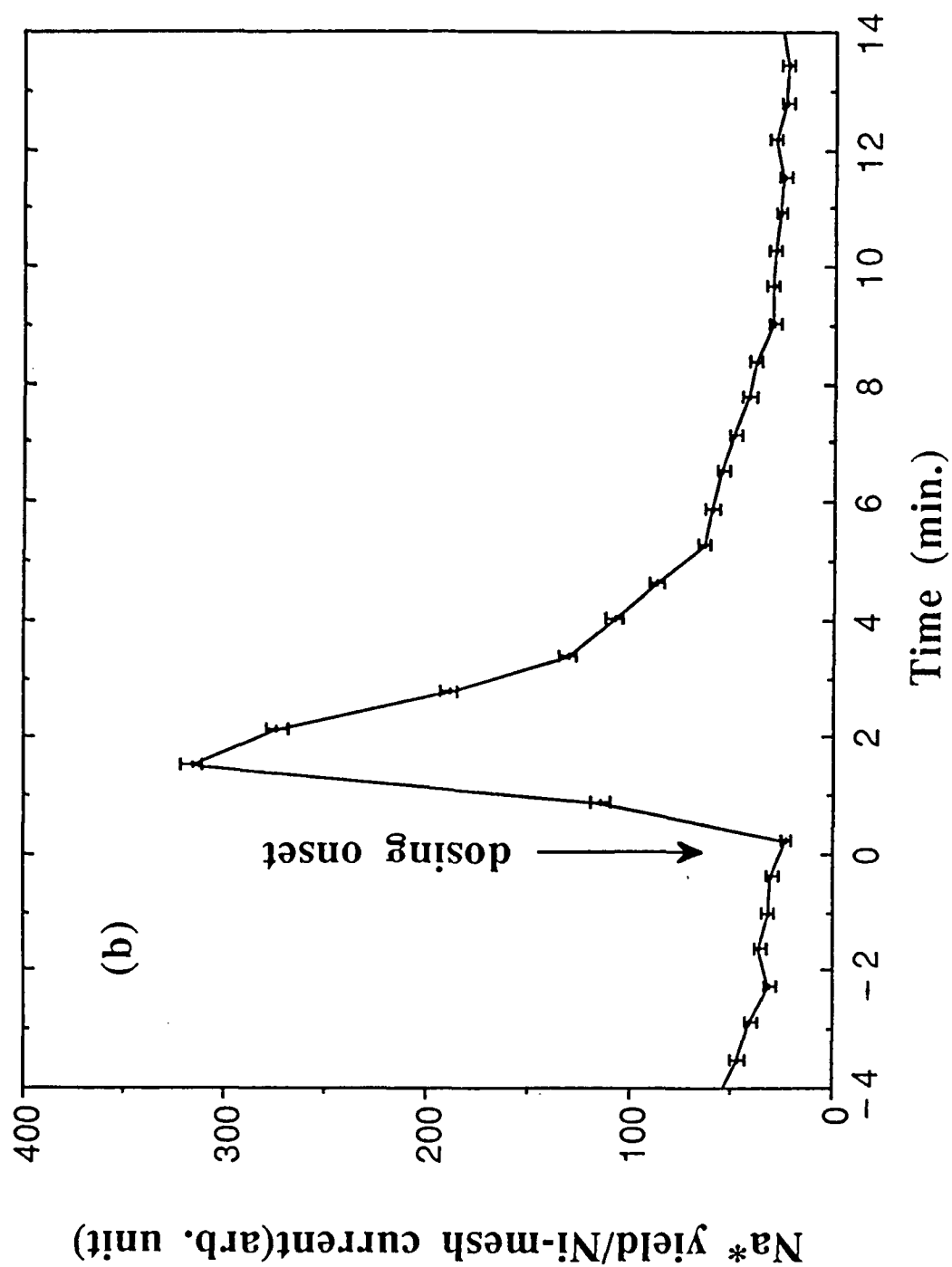


Fig. 4b



Generation of excited CN molecules electronically desorbed from alkali-rich surfaces

Jun Xu¹, Royal Albridge, Alan V. Barnes, Manfred Riehl-Chudoba, Akira Ueda,
Norman Tolk

Center for Molecular and Atomic Studies at Surfaces, Department of Physics and Astronomy, Vanderbilt University, Nashville, TN 37235, USA

Dwight Russell and Paul Wang

The Department of Physics, University of Texas, El Paso, TX 79968-0515, USA

Received 8 July 1991; accepted for publication 12 September 1991

Exposure of alkali-halide crystal surfaces and alkali-metal surfaces to nitrogen- and carbon-containing gases is found to greatly enhance electron- and photon-stimulated desorption (ESD, PSD) of excited CN. The observations that the desorption yield of CN* grows as a function of surface exposure to CO₂ and N₂ gases provide strong insight into the origin of the desorbed CN and the desorption process itself. In addition, the data unambiguously show that pre-irradiation of the alkali-halide surface by electrons or photons is required for this dose-dependent enhancement to occur. The rate of the growth is found to be correlated to the alkali component of the alkali-halide substrate. On the basis of this work we present a new model to explain electronic desorption of excited molecules from alkali-halide surfaces. The model involves three processes: (1) pre-irradiation produces alkali metal-rich surfaces via defect-mediated processes, (2) when the surface is exposed to CO₂ and N₂, surface reactions generate CN molecules bonded to the alkali-rich surface, and (3) electron or photon bombardment induces the desorption of excited CN molecules from the surface by direct bondbreaking.

1. Introduction

Bombardment of alkali-halide surfaces with electrons and with UV synchrotron radiation produces optical emissions which arise from: (a) desorbed excited molecules and atoms, (b) excited bulk-impurities, and/or (c) defect recombination in the bulk material (bulk luminescence). Measurements of these spectra permit one to determine final states of excited neutral desorbates, to interrelate surface and bulk dynamical processes, and thus to elucidate mechanisms responsible for adsorption and desorption phenomena [1].

Atomic or molecular adsorbates on surfaces may originate either by the migration of atoms, molecules, or defects from inside the bulk to the surface or by the adsorption of atoms or molecules from external sources. We utilize the techniques of electron- and photon-stimulated desorption to help distinguish between these two sources of adsorbates. For example, photon-stimulated desorption of H₂ from alkali fluorides has been found to be dependent on photon-activated migration of an intrinsic hydrogen impurity to the surface [2]. For the case of ESD and PSD of Li from LiF surfaces, F-center diffusion was identified as the means by which neutral lithium is supplied to the surface [3]. In contrast, some desorption experiments require that the surface be exposed to gaseous molecules, e.g., NO [4–7],

¹ Present address: Oak Ridge National Laboratory, MS-6142, P.O. Box 2008 Oak Ridge, TN 37831-6142, USA.

CO [8], OH [9] and N₂ [10] desorption from metal surfaces. We note also that ESD and PSD studies are facilitated by knowledge of surface parent molecules.

In a previous paper, we reported first measurements of electron-stimulated desorption of excited CN from alkali halide surfaces [11]; however we did not identify the origin of the atomic components of the desorbed excited CN. As discussed above, it is conceivable that this desorbed species may originate either from migration from the bulk, or from surface dosing, or both. We are aided in this study by the fact that bulk intrinsic impurity CN⁻ centers have been observed from measurements of CN⁻ fluorescence under ion [12] electron and photon [13] bombardment of alkali-halides. From this information one can speculate that a possible source of surface CN adsorbates is the diffusion of these CN⁻ impurities to the surface. However, when Nakagawa and co-workers [14] monitored CN⁻ impurity growth in the near-surface bulk of alkali-halide crystals by observing UV fluorescence while exposing the surfaces to gaseous CO₂ and N₂ under short-wavelength synchrotron undulator light, they showed that surface CN may also migrate *into* the bulk. Although there may be some contribution from the bulk, our present work provides direct evidence that the exposure of alkali-halide surfaces to gaseous CO₂ and N₂ provides the primary source of adsorbates required for electron- and photon-stimulated desorption of excited CN molecules. More specifically, exposure to gaseous molecules followed by dissociation and recombination increases the surface concentration of CN which acts as a source of CN* desorption.

Formation of adsorbates by the dissociation of large molecules or by the recombination of two individually bound atoms or molecules has been investigated in thermal desorption, and reviewed by Zacharias [16]. Modl and co-worker [15] found that NO observed in thermal desorption arises from the decomposition of NO₂ on a Ge(111) surface. On the another hand, H₂ formation was found to be due to the recombination of atomic hydrogen on a Cu(110) surface [17], and the source of CO in thermal desorption to be the recombina-

tion of carbon and oxygen bound to a Pd(100) surface [18]. The present work suggests that the formation of adsorbates which participate in the ESD and PSD of excited CN from alkali-halide crystals and alkali metals proceeds by a reactive mechanism involving both dissociation and recombination processes.

Incident electrons or photons may also stimulate surface processes (adsorption, dissociation, recombination, and desorption) by creating bulk and surface defects, changing surface stoichiometry, modifying the surface structure, and breaking bonds on the surface. Electron-stimulated adsorption (ESA) [19], an enhancement of adsorption initiated by electron irradiation, can be an important step in surface reactions. ESA and its relation to surface reactions have been reviewed by Pantano and Madey [20]. Photon-induced rupture of bonds on surfaces appears to play an important role in photon-stimulated processes involving adsorbates on surfaces. Unfortunately, very little is as yet known, either experimentally [21] or theoretically [22], about photodissociation on solid surfaces. It is therefore of great interest to investigate other radiation-altered surface processes as well as stimulated desorption.

We report below new measurements which for the first time link electron- and photon-stimulated desorption (ESD and PSD) of excited CN molecules from alkali-halide and alkali-metal surfaces to the exposure of these surfaces to gaseous CO₂ and N₂. The results show that the desorption yield grows as a function of the exposure of these surfaces to the gaseous molecules, and that the growth is strongly enhanced by pre-irradiation of the alkali-halide surface. The data indicate that incident electron and UV photon radiation serve two important functions: (1) incident radiation metallizes the alkali-halide surfaces which significantly enhance the surface CN formation process upon subsequent gas exposure, and (2) incident radiation leads to direct scission of the surface-CN bond. These measurements give information on the dynamics of making and breaking of bonds on surfaces and provide insight into related technological applications such as surface catalysis, erosion, surface damage, and lithography.

2. Experimental details

The experimental setup, shown in fig. 1, consists of an ultrahigh vacuum (UHV) system, which operates at a base pressure about 3×10^{-10} Torr. The incident radiation was either electrons or synchrotron radiation. The samples were alkali-halide crystals and alkali metals which could be heated or cooled.

Used was a low-energy, high-brightness electron gun consisting of a diode extraction source and a three-element refocusing lens, similar to the design of Stoffel and Johnson [23]. A heated osmium-coated dispenser cathode emitted electrons with an energy spread of 0.1 to 0.2 eV. The electron beam energy was adjustable in the range of 10 to 1000 eV, with electron current ranging from 20 to 400 μ A. The beam diameter varied from 1.5 to 5 mm.

The photon measurements were carried out at the University of Wisconsin Synchrotron Radiation Center (SRC) using the Vanderbilt/SRC joint beamline. The beamline features a computer controlled 6-meter toroidal grating monochromator delivering dispersed light in the range from 9 to 190 eV. A differential pumping station is located between the beamline and the experimental chamber resulting in a 5 orders of magnitude difference of pressures between the beam

line and the working chamber. At the plane of the sample, the beam spot was 2.7 mm high by 7.4 mm wide. A 93% transparent nickel mesh was mounted in the beamline and used to measure the beam flux.

The alkali-halide crystals were purchased from Harshaw. The crystals were cleaved in air, mounted with their (100) surfaces facing the beam and heated under UHV conditions for cleaning. Alkali-metal surfaces were obtained by evaporation from SAES alkali dosers onto a glass slide. To obtain thick metal layers, we continued the dosing until there was no optical transmission. These evaporated surfaces are referred to hereafter as alkali-metal surfaces. The sample temperature could be varied from 58 to 800 K. An XYZ-adjustable closed-cycle helium cooler was used for low-temperature experiments. A piece of sapphire was mounted between the sample holder and the cold finger, since sapphire has a high heat conductivity at low temperatures (70 K), and is thermally insulating at high temperatures (> 300 K). A chromel–alumel thermocouple, placed in thermal contact with the sample surface, measured temperatures greater than room temperature, and a chromel–gold thermocouple, was used for temperatures lower than room temperature. Dosing gases were admitted to the chamber through two Varian leak valves allowing

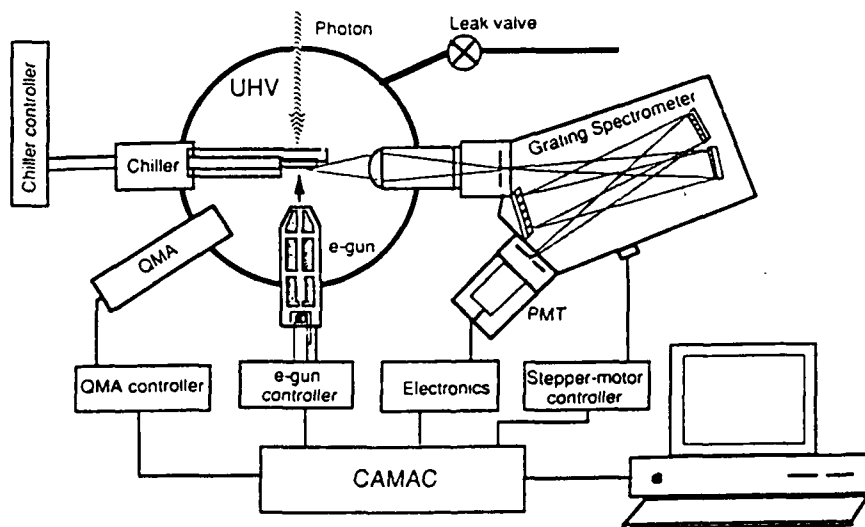


Fig. 1. Experimental configuration used for the CN desorption experiments.

the partial pressures of two gases to be controlled in the range of 1.0×10^{-10} to 1.0×10^{-6} Torr.

Optical emissions from the samples due to electron or photon bombardment were imaged onto the entrance slit of a McPherson 0.3-m monochromator. A 1200 lines/mm grating (5000 Å blaze) was used for fluorescence measurements from 2000 to 8000 Å; and a 2400 lines/mm grating (3000 Å blaze) was used to measure the rotational distribution of the desorbed CN* molecule. Photons were detected by a cooled photomultiplier tube (PMT), operated in a pulse-counting mode. Stepping motor grating controls and photon counting scalars were interfaced through a CAMAC unit to an Apple Macintosh computer. A quadrupole gas analyzer (QMA) was used to detect residual gas, dosing gas, and outgasing due to desorption.

3. Results

3.1. Optical emission due to electron and photon bombardment

Bombardment of alkali-halide surfaces with electron or synchrotron radiation produces optical emissions arising from defect recombination in the bulk, from excited bulk-impurity molecules, and from desorbed excited molecules and atoms. These three features are shown prominently in fig. 2 which is a 2000–8000 Å spectrum from KCl

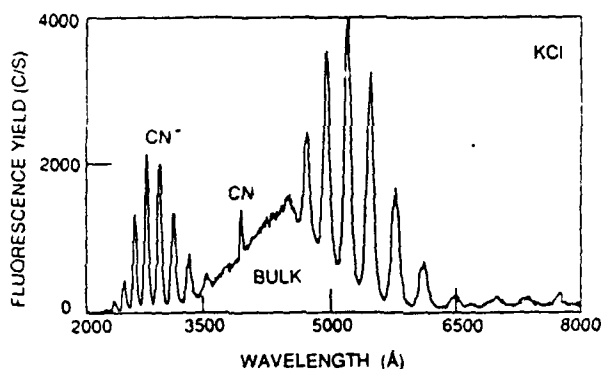


Fig. 2. Typical optical emission spectrum in the range 2000–8000 Å due to zero-order synchrotron light bombardment on a single crystal KCl surface at room temperature. The surface was exposed to gaseous $\text{CO}_2 + \text{N}_2$ (1:1) at 1.0×10^{-7} Torr.

under synchrotron light bombardment at room temperature.

The continuous fluorescence in the range of 3500 to 5500 Å is luminescence accompanying defect recombination [24]. The nine bands between 2000 and 3500 Å (observed here also in second order) is due to optical emission from excited CN^- impurities in the near-surface bulk [25]. By noting the energy of the emitted photons, we have determined that the observed CN^- excited state is at least 5.6 eV above the ground state. If the CN^- molecules were in the gas phase, this energy would be large enough to reach the gas-phase ionization limit of 3.8 eV [26]. Thus the gas-phase CN^- excited state would result in neutralization ($\text{CN} + e$) rather than de-excitation by optical emission as observed. However in alkali-halide lattices, the ionization potential of CN^- is raised to about 10 eV [27]. For this case, the neutralization channel is not available. Instead optical de-excitation provides a readily available relaxation channel for excited CN^- impurities in bulk alkali halides in agreement with experimental results.

The narrow band feature at approximately 3870 Å arises from excited CN desorbed from the KCl surface. This feature was identified in ref. [11] as the $\text{CN } B^2\Sigma^+ \rightarrow X^2\Sigma^+$ transition. This characteristic emission attributed to the decay of a free excited CN^* molecule above the surface has been also observed for LiF, NaF, NaCl, KBr, and CsI crystals, and for lithium-, sodium-, potassium-, and cesium-metal surfaces, under electron bombardment.

Optical radiation arising from above the surface can be distinguished from bulk radiation by measurements of the spatial location of the emission, as shown in fig. 3. This figure is a plot of the intensities of optical emissions from CN^* , from CN^- radiating in the bulk, and from other bulk excitations versus the position of the image of the 300- μm spectrometer slits as the sample is translated along the beam direction. The emission arising from the CN^- impurity and the bulk fluorescence appears along the whole crystal, with an enhancement on the front and rear faces of the sample. The distance between the two peaks matches the thickness of our sample, 2.2 mm. In

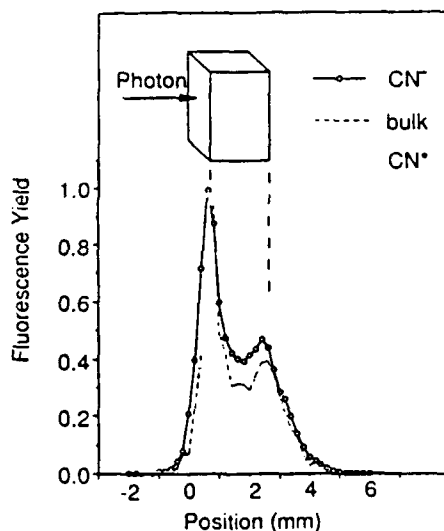


Fig. 3. Position dependence of optical emission arising from CN^* , bulk impurity center CN^{*-} and bulk fluorescence due to zero-order synchrotron light bombardment on a single crystal KCl surface at room temperature. The surface was exposed to gaseous $\text{CO}_2 + \text{N}_2$ (1:1) at 1.0×10^{-7} Torr. The x-axis is the manipulator reading representing the distance between the optics focus region and the front surface of the sample.

contrast, the optical emission from neutral excited CN can be seen only in front of the surface. This confirms that the $\text{CN}^*(\text{B})$ radiation arises from just above the surface.

3.2. Enhancement of CN^* ESD yield due to CO_2 and N_2 exposure

Fig. 4a shows the time-dependent growth of excited CN desorption yield under $110 \mu\text{A}$, 200 eV electron bombardment on KBr(100) surfaces as the surface was exposed to gaseous N_2 at two dosing pressures, 2.0×10^{-8} and 5.7×10^{-8} Torr. The plot is the CN^* emission yield versus the exposure time at a constant N_2 pressure. The surface was irradiated by a beam of 200 eV electrons for four hours prior to gas dosing. Note that the CN^* desorption yield grows with the exposure time and that the growth tends to saturate at a level characteristic of the pressure. The growth of the electron-induced CN^* desorption yield under gaseous N_2 exposure has also been investigated for KCl and LiF surfaces, as shown

in figs. 4b and 4c. The desorption yields for all surfaces show a similar monotonic increase with N_2 gas exposure but differ with regard to the time to reach saturation. The rise times, defined as the time to reach 90% of the saturation yield, are 20 min for KCl, 19 min for KBr and about 40 min for LiF. Note that the time constants for KBr and KCl surfaces are essentially the same, but markedly different from that for the LiF surface. This correlation suggests that the parent bond from which desorbed CN^* arises is the the bond between surface metal and CN where for these measurements, the metal is either lithium or potassium.

In another experiment, a KCl surface, bombarded by 300-eV electrons at a constant current

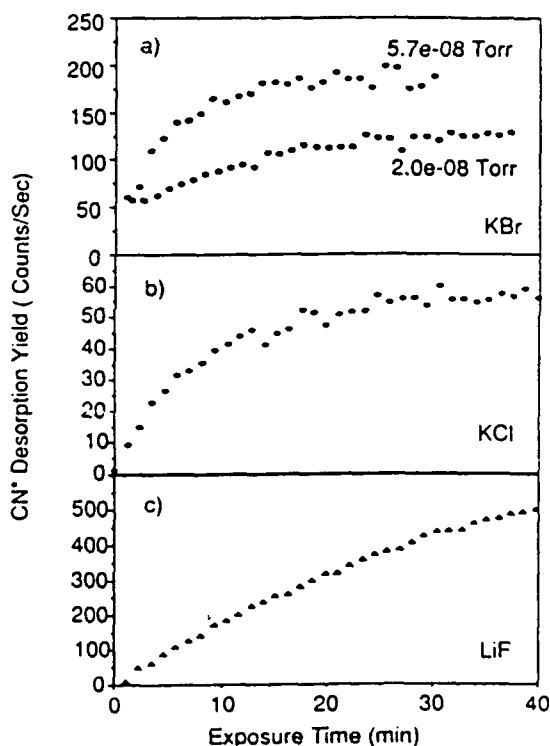


Fig. 4. Growth curves of CN^* desorption yields as a function of time during gas exposure and electron-beam dosing: (a) KBr sample exposed to gaseous N_2 at 2.0×10^{-8} Torr and 5.7×10^{-8} Torr under $110 \mu\text{A}$, 200 eV electron bombardment, (b) KCl sample exposed to gaseous N_2 at 5.0×10^{-8} Torr and (c) LiF sample exposed to gaseous N_2 at 5.3×10^{-8} Torr under $100 \mu\text{A}$, 200 eV electron bombardment. Substrate temperature for these experiments was 60 K.

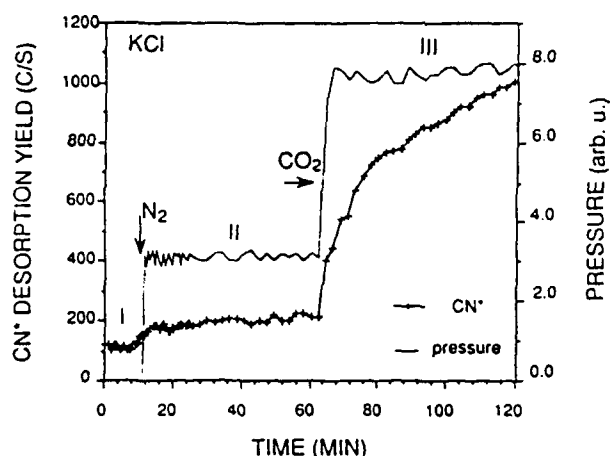


Fig. 5. The CN^* desorption yield measured for a given KCl surface as a function of time under various gas exposure conditions: (I) a clean KCl surface, (II) the same KCl surface exposed to N_2 (1.2×10^{-8} Torr) and (III) the KCl surface additionally exposed to CO_2 (3.2×10^{-8} Torr). The lighter solid line is a plot of total pressure as a function of time. The incident electron beam energy was 300 eV with a constant current of 100 μA . Substrate temperature for this experiment was 60 K.

of 100 μA , was dosed sequentially first by N_2 and then by CO_2 , as shown in fig. 5. This figure is a plot of CN^* emission yield (dark line) and gas pressure (weak line) as a function of time. Initially, there was no external gas introduced into the chamber. Under these circumstances a small, constant CN^* desorption yield was observed. When the surface was exposed to gaseous N_2 at a constant pressure of 1.2×10^{-8} Torr (beginning at the time indicated by the first arrow), the CN^* desorption yield increased toward saturation. Later, the surface was exposed to gaseous CO_2 at a constant pressure, 3.2×10^{-8} Torr, concurrent with N_2 exposure. As shown in the figure, the CN^* desorption yield increased dramatically. The ratio of the saturation yields attributable to the combined CO_2 and N_2 gas exposures is 8.9, which is significantly larger than the ratio of partial pressures of CO_2 and N_2 , which is 1.7. This indicates that simultaneous dosing of CO_2 and N_2 gases results in a significantly higher CN^* desorption yield than N_2 dosing alone. We observe similar effects for KBr and LiF substrates. Thus we find that the CN^* desorption yield markedly increases when alkali-halide surfaces

are exposed to gaseous N_2 and CO_2 under electron or photon irradiation. In addition, we believe that the small yields measured under conditions of no external dosing are due to residual N_2 and CO_2 gases normally in the chamber even under ultrahigh vacuum conditions.

3.3. Enhancement of CN^* PSD yield due to CO_2 and N_2 exposure

Fig. 6 displays optical spectra arising from zero-order synchrotron radiation incident on a glass surface, with and without a thick layer of potassium metal, and with and without $\text{CO}_2 + \text{N}_2$ exposure. Initially the clean glass sample was bombarded by photons *in situ* for 20 min; fig. 6a shows the resulting optical emission. The continuous fluorescence is due to recombination of defects created by photon bombardment in the glass [28]. Next, potassium was evaporated onto

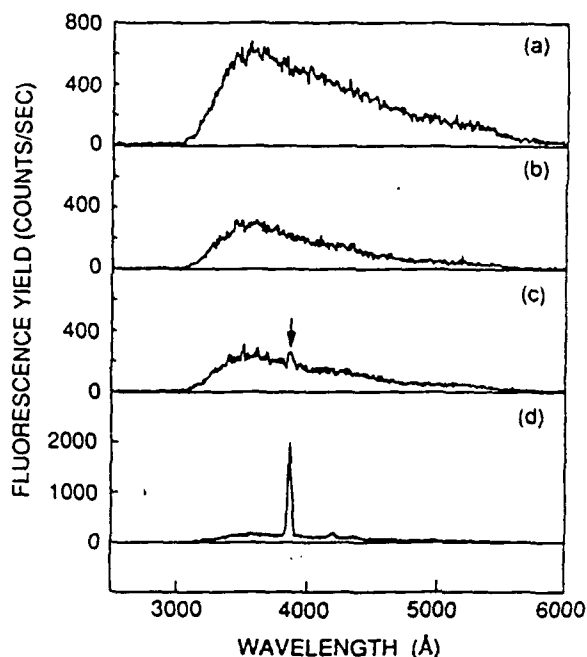


Fig. 6. Optical emission spectra due to zero-order synchrotron light bombardment (a) on a clean piece of glass, (b) on a potassium-covered glass surface, (c) on a potassium-covered surface with exposure of the surface to gaseous $\text{CO}_2 + \text{N}_2$ (1:1) at 1.0×10^{-7} Torr for 2 min, and (d) on a potassium-covered surface following gas exposure ($\text{CO}_2 + \text{N}_2$ (1:1) at 1.0×10^{-7} Torr) for 30 min at room temperature.

the surface. The resulting optical emission spectrum is shown in fig. 6b, where the bulk fluorescence intensity is reduced due to the presence of the potassium layer. Then the potassium-covered surface was exposed for two min to a one-to-one mixture of $\text{CO}_2 + \text{N}_2$ at a pressure of 1.0×10^{-7} Torr. The resulting spectrum, fig. 6c, shows a feature at 3870 \AA which we attribute to the decay of desorbed CN^* . Finally, after 30 min of the $\text{CO}_2 + \text{N}_2$ (1:1) exposure with simultaneous photon irradiation, the intensity of the characteristic line is markedly enhanced as shown in fig. 6(d). We can conclude from these measurements that photon-stimulated CN^* desorption is greatly increased with $\text{CO}_2 + \text{N}_2$ exposure. On a clean glass surface, CN^* desorption was not observed under photon bombardment and simultaneous $\text{CO}_2 + \text{N}_2$ exposure. Similar enhancement of CN^* desorption yields due to $\text{CO}_2 + \text{N}_2$ exposure were observed from KCl, and from sodium- and lithium-covered glass surfaces.

3.4. The role of pre-irradiation in the enhancement of CN^* desorption yield

Three additional experiments were performed which show that the marked increase in the CN^* desorption yield is observed only after the alkali-halide surface is pre-irradiated with electrons or photons.

The first experiment determined the dependence of the CN^* desorption yield on the samples' radiation history. The results are shown in fig. 7, for the case of 300-eV electron bombardment of KCl surface at 60 K. CN^* desorption yield measurements were made for a wide range of pre-radiation doses (defined as the pre-radiation time multiplied by the electron current in units of $\mu\text{A h}$). The CN^* desorption yields, plotted as a function of the exposure time, reach saturation values which are strongly dependent on the pre-radiation dose. The inset in fig. 7 shows that the saturation values plotted as a function of pre-irradiation dose tend toward saturation. For a typical current of $130 \mu\text{A}$, nine hours were required to reach saturation, as shown in fig. 7.

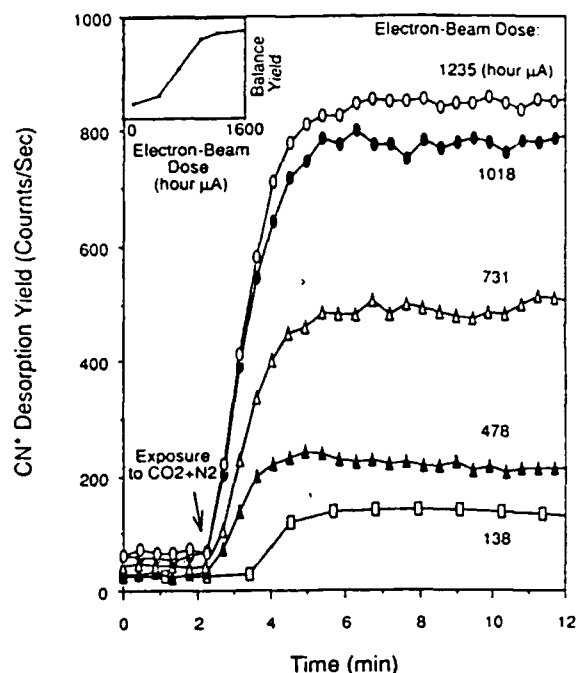


Fig. 7. CN^* desorption yields from a KCl surface at 60 K plotted as a function of time exhibiting the influence of gas exposure, $\text{CO}_2 + \text{N}_2$ (1:1) at 1.0×10^{-7} Torr, for a variety of electron-beam integrated doses.

The second experiment involved a measurement of the difference in the CN^* PSD yield for a KCl surface with and without pre-irradiation. Desorption was measured under zero-order synchrotron light bombardment at 300 K and with exposure to gaseous N_2 and CO_2 . Fig. 8a shows the time-dependent yield after 18 h of pre-irradiation by zero-order synchrotron light prior to the gas exposure. Fig. 8b shows the yield obtained with no pre-irradiation. Except for the radiation history, both experiments were carried out under the same conditions, yet the saturation rise time for the pre-irradiated sample is smaller by a factor of approximately three.

The third experiment involved a measurement of the difference between the CN^* desorption yield for a spot pre-irradiated by 300-eV electrons and the yield for the rest of the sample, which had no radiation history (fig. 9). A KCl sample was cleaved in air and annealed at 450°C in UHV for four h before the surface was cooled to 60 K. A single spot on the surface was pre-

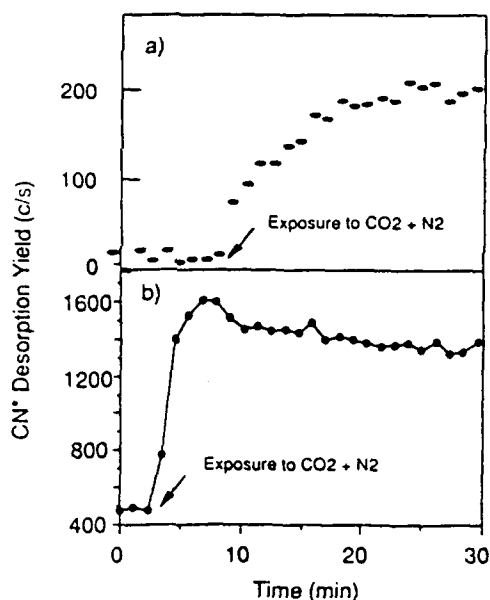


Fig. 8. CN^* desorption yields from KCl surfaces with and without photon pre-radiation at room temperature under zero-order synchrotron light bombardment in the presence of $\text{CO}_2 + \text{N}_2$ (1:1) at 1.0×10^{-7} Torr. (a) CN^* desorption yield for a KCl sample plotted as a function of time for no prior synchrotron light dosing. For this measurement gas exposure commenced at the 9 minute mark. (b) CN^* desorption yield for a KCl sample plotted as a function of time which prior to this measurement had experienced 24 h of synchrotron light dosing. Gas exposure commenced at the 3 min mark.

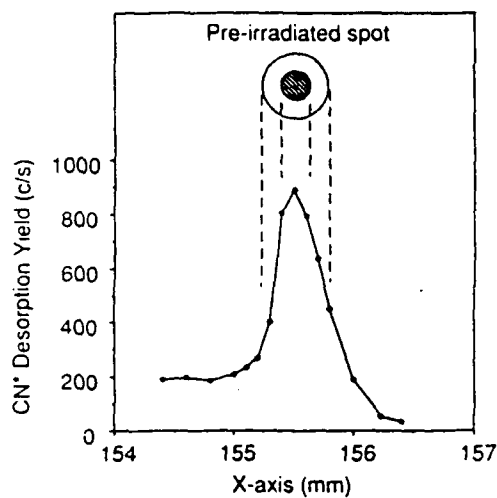


Fig. 9. CN^* desorption yields plotted as a function of distance for a path directed along a KCl sample surface. The path of measurement on the surface intersects a spot pre-irradiated by 300 eV electrons at a current of $80 \mu\text{A}$ for 12 h. The rest of the sample had not previously been irradiated.

irradiated by 300-eV electrons for 12 h; and the surface was then exposed to gaseous CO_2 and N_2 at a combined pressure of 1.0×10^{-7} Torr. The measurements of the position-dependent desorption yields began after the desorption yields reached saturation. The CN^* desorption yield exhibited a maximum at the center of the pre-irradiated spot. Note that the yield greatly lessened as the electron beam moved to regions of the surface of the sample which had little or no previous electron-beam radiation history.

In addition, we have observed that pre-irradiation of a sodium-metal surface by an electron beam does not enhance the CN^* yield, whereas the pre-irradiation of a NaCl surface clearly enhances the CN^* desorption yield. All of these experiments indicates that the pre-irradiation produces alkali-metal-rich surfaces on alkali-halide crystals.

4. Discussion and conclusion

4.1. Surface metallization

Our data strongly suggest that surface metallization is required for CN formation on alkali-halide surfaces. As shown above in figs. 7, 8, and 9, the formation of CN on alkali-halide surfaces requires pre-irradiation by either electrons or photons. Incident electron or UV photon radiation not only serves to stimulate the desorption of excited CN but also plays a role in preconditioning the alkali-halide surfaces for subsequent CN formation. It is extensively documented that electron [29–31] and photon [32] bombardment can induce the accumulation of excess metal on alkali-halide surfaces. Thus, we believe that there is a crucial relationship between the process of radiation-induced metallization of alkali-halide surfaces and the concentration of surface CN leading to CN^* desorption.

Surface metallization is understood in this work as a defect-mediated process. Incident photon or electron bombardment deposits energy in the near surface bulk by hole creation [33]. This deposited energy may generate a Frenkel pair, which consists of a halogen vacancy with an electron (F-

center) and a (halogen) $_2^-$ molecular ion (H-center), either in the near surface bulk or on the surface [34]. Halogen atoms, originating at the surface H-centers, may be emitted from the surface [35]. The F-centers remaining on the surface neutralize excess metal ions left following the halogen emission. Thus, electron or photon bombardment on an alkali-halide surface produces surface metallization.

4.2. CN formation on alkali-rich surfaces

Our data show that the electron- and photon-stimulated CN* desorption yields grow with surface exposure to CO $_2$ or/and N $_2$ gas. The desorption yields are a function of the concentration of the parent adsorbate (this function is complicated since adsorption sites, coadsorbates, defects, and diffusion may all affect the desorption yields). Thus, our experimental results imply that the amount of CN adsorbed on the surface grows with CO $_2$ and N $_2$ exposure. In addition, we have observed a small amount of CN* emission from the surface under ultrahigh vacuum conditions. In fact, CN* emission in the absence of external dosing was observed to increase when residual gas pressure increased. Because of the observed enhancement of CN* desorption yield due to CO $_2$ and N $_2$ dosing, we believe that the CN* desorption from alkali-halide surfaces in the absence of external dosing [11] arises from residual CO $_2$ and/or N $_2$ gases.

Formation of molecular adsorbates can occur either from dissociation of large molecules on surfaces [16] or from the recombination of two individually bound atoms [17,18]. The present work suggests that the CN formation process on alkali-halides involves molecular dissociation on the surface followed by recombination. In the dissociation process, CO $_2$ and N $_2$ molecules decompose on the pre-irradiated surfaces into their constituent atoms. Next is the recombination of these atoms into a new molecule which includes CN as one of its constituent parts.

An important question is what is the identity of the bond present on the pre-irradiated alkali-halide surface prior to CN* desorption. Our data provides evidence that there is a definite correla-

tion between the presence of surface metal and the characteristics of electronically desorbed CN*, which strongly suggests that the parent bond of the desorbing CN* is the ionic bonding between surface alkali and CN molecule. Three important classes of measurements support this conclusion.

The first class of measurements discussed above, relates the rise-time of electronically desorbed CN* (which is related to surface CN concentration) to the alkali component of alkali halide, as shown in fig. 4. Clearly, the halide component is not important.

The second class of experiments described in ref. [36] shows that the rotational distributions of desorbing CN* are systematically correlated to alkali components of alkali-halide and alkali-metal substrates. Alkali metals and alkali-halides with the same alkali component, give rise to the same rotational distribution. The distribution is found to be independent of the halide component of the substrates.

The third class of experimental evidence is that the excitation function of desorbing CN* by photons exhibits resonance structure (16 and 20 eV) for both potassium metal and KCl surfaces, independent of the chloride component of KCl substrate [36].

In all these cases, there exists a strong systematic correlation between the alkali component and the desorbing CN* which suggests that CN is bonded to the surface alkali.

4.3. Mechanism for the desorption of excited CN

As shown above, the presence of alkali-CN on the surface is essential to the desorption phenomena observed. Also, the data suggest that the mechanism responsible for breaking the bond of alkali-CN is desorption induced by electronic transitions (DIET) [37]. Specifically, the parent alkali-CN is excited electronically from its bound state to an anti-bonding state.

An important question is the nature of the anti-bonding state participating in the observed desorption of excited CN in the B state. The B state of neutral CN may be formed directly by the $4\sigma \rightarrow 5\sigma$ excitation of the CN molecule or by the

4σ ionization of ground state CN^- . Our present results cannot determine whether the surface CN is bonded to one or two or possibly more metal atoms (e.g., K_n). However, it is reasonable to assume that the alkali-CN bond is primarily ionic, and hence that the 4σ ionization channel of K_n^+-CN^- system results in a $\text{K}_n^+-\text{CN(B)}$ cationic repulsive state. As discussed in ref. [36], we observed a resonance peak at 16 eV in the photon energy dependent yield of desorbing CN^* from a potassium metal surface, which is close to the calculated value (17 eV) of the 4σ ionization energy for a similar system, CN adsorbed on Ni metal [39]. These considerations suggest that the K_n^+-CN^- system is raised to an antibonding $(\text{K}_n\text{CN})^+$ state by the ionization of the CN^- 4σ state, and the desorption of CN in the B state results.

Another possible channel for surface CN loss in addition to desorption is that CN^- may diffuse from the surface into the near surface bulk. In order to test this hypothesis, we measured the characteristic CN^- UV radiation arising from the near surface bulk, which was observed to increase with exposure to gaseous $\text{CO}_2 + \text{N}_2$ under synchrotron UV photon bombardment. This observation is consistent with Nakagawa and co-worker's earlier observation [14]. Consequently, it is clear that an important source of the CN^- impurity in the near-surface bulk is surface exposure to gaseous $\text{CO}_2 + \text{N}_2$. This indicates that surface CN, probably in the form K_n^+-CN^- , is an important intermediate step in the formation of CN^- impurities in the near surface bulk just as it is an important intermediate step in the desorption process.

In conclusion, the origin of ESD and PSD of excited CN from alkali-metal and pre-irradiated alkali-halide surfaces has been found to be intimately related to exposure of the surfaces to CO_2 and N_2 gases. For alkali-halide surfaces, electron- and photon-induced metallization of alkali-halide surface is required for alkali-CN formation. The data suggest a new desorption model which can be described as a three-step process: (1) pre-irradiation of alkali-halides results in alkali-metal-rich surfaces via a defect-mediated process, (2) a surface reaction produces alkali-CN

molecules on the surface when the alkali-rich surface is exposed to CO_2 and N_2 prior to desorption, and (3) an electron or photon bombardment breaks the $(\text{alkali})^+-\text{CN}^-$ bond and induces electronic desorption of excited CN molecules from the surface.

Acknowledgements

Authors thank Carl S. Ewig and Joel Tellinghuisen in Department of Chemistry, Vanderbilt University for helpful discussions. We also thank the staff of the Synchrotron Radiation Center for their helpful support. This research was sponsored in part by the Air Force Office of Scientific Research (AFOSR) under Contract AFOSR-90-0030, by the Office of Naval Research under Contract N00014-87-C-0146, and by NASA under Contract NAS8-37744.

References

- [1] N.H. Tolk, L.C. Feibelman, J.S. Kraus, R.J. Morries, M.M. Traum and J.C. Tully, *Phys. Rev. Lett.* 49 (1982) 812.
- [2] C.C. Parks, D.A. Shirley and G. Loubriel, *Phys. Rev. B* 29 (1984) 4709.
- [3] T.A. Green, G.M. Loubriel, P.M. Richards, N.H. Tolk and R.F. Haglund, Jr., *Phys. Rev. B* 35 (1987) 781.
- [4] A.R. Burns, *Phys. Rev. Lett.* 55 (1985) 525; A.R. Burns, E.B. Stechel and D. R. Jennison, *Phys. Rev. Lett.* 58 (1987) 250.
- [5] K. Domen and T.J. Chuang, *Phys. Rev. Lett.* 58 (1985) 1484.
- [6] F. Budde, A.V. Hamza, P.M. Ferm, G. Ertal, D. Weide, P. Andresen and H.-J. Freund, *Phys. Rev. Lett.* 60 (1988) 1518.
- [7] D. Burgess, Jr., R.R. Cavanagh and D.S. King, *J. Chem. Phys.* 88 (1988) 6556; S.A. Buntin, L.J. Richter, R.R. Cavanagh and D.S. King, *Phys. Rev. Lett.* 61 (1988) 1321.
- [8] D.R. Sandstrom, M.J. Dresser and W.D. Dong, *Phys. Rev. Lett.* 58 (1987) 250.
- [9] Ph. Avouris, R. Beigang, F. Bozso and R. Walkup, *Chem. Phys. Lett.* 129 (1986) 505.
- [10] Feulner, D. Menzel, H.J. Kreuzer and Z.W. Gortel, *Phys. Rev. Lett.* 53 (1984) 671.
- [11] Jun Xu, Marcus H. Mendenhall and J.S. Tellinghuisen, *J. Chem. Phys.* 93 (1990) 5281.

- [12] A.I. Bazhin, E.O. Rausch and E.W. Thomas, *J. Chem. Phys.* 65 (1976) 3897.
- [13] M.H. Mendenhall, A. Barnes, P. Bunton, R. Haglund, L. Hudson, R. Rosenberg, D. Russell, J. Sarnthein, P. Savundararaj, N. Tolk and J. Tellinghuisen, *Chem. Phys. Lett.* 147 (1988) 59.
- [14] H. Nakagawa, T. Deguchi, H. Matsumoto, T. Miyanaga, M. Fujita, K. Fukui, E. Ishiguro, I.H. Munro, T. Kato and M. Watanabe, *J. Phys. Soc. Jpn.* 58 (1989) 2605.
- [15] A. Modl, H. Robota, J. Seguer, W. Vielhaber, M.C. Lin and G. Ertl, *Surf. Sci.* 169 (1986) L341.
- [16] H. Zacharias, *Appl. Phys. A* 47 (1988) 37.
- [17] G.D. Kubiak, G.O. Sitz and R.N. Zare, *J. Chem. Phys.* 81 (1984) 6397; *J. Chem. Phys.* 83 (1985) 2538.
- [18] M. Kori and B.L. Halpern, *Chem. Phys. Lett.* 98 (1983) 32.
- [19] R.E. Kirby and D. Lichtman, *Surf. Sci.* 41 (1974) 447.
- [20] C.G. Pantano and T.E. Madey, *Appl. Surf. Sci.* 7 (1981) 115.
- [21] P. Avouris and R.E. Walkup, *Annu. Rev. Phys. Chem.* 40 (1989) 173.
- [22] E. Hasselbrink, S. Nettesheim, M. Wolf, A. Cassuto and G. Ertl, *Desorption Induced by Electronic Transitions, DIET IV*, Eds. G. Betz and P. Varga (Springer, New York, 1990) P. 75.
- [23] N.G. Stoffel and P.D. Johnson, *Nucl. Instrum. Methods. Phys. Res. A* 234 (1985) 230.
- [24] A.I. Bazhin, E.O. Rausch and E.W. Thomas, *Phys. Rev. B* 14 (1976) 2583.
- [25] C.S. Ewig and J. Tellinghuisen, *Chem. Phys. Lett.* 153 (1988) 160.
- [26] R. Klein, R.P. McGinnis and S.R. Leone, *Chem. Phys. Lett.* 100 (1983) 475.
- [27] H. Pulm, B. Marquardt, H.-J. Freund, R. Engelhardt, K. Seki, U. Karlsson, E.E. Koch and W. Von Niessen, *Chem. Phys.* 92 (1985) 457.
- [28] K. Tanimura, C. Itoh and N. Itoh, *J. Phys. C: Solid State Phys.* 21 (1988) 1869.
- [29] P. Wurz and C.H. Becher, *Surf. Sci.* 224 (1989) 559.
- [30] G. Roy, G. Singh and T.E. Gallon, *Surf. Sci.* 152/153 (1985) 1042.
- [31] M. Szymonski, J. Ruthowski, A. Poradzisz, Z. Postawa and Jorgensen, *Desorption Induced by Electronic Transitions, DIET II*, Eds. W. Brenig and D. Menzel (Springer, New York, 1985) P. 160.
- [32] K.L. Tsang, C.H. Zhang and T.A. Callcott, *Phys. Rev. B* 35 (1987) 8374.
- [33] Y. Al Jammal, D. Pooley and P.D. Townsend, *J. Phys. C: Solid State Phys.* 6 (1973) 247.
- [34] K. Tanimura and N. Itoh, *Nucl. Instrum. and Methods B* 33 (1988) 815.
- [35] Z. Postawa and M. Szymonski, *Phys. Rev. B* 39 (1989) 12950.
- [36] Jun Xu, Ph D Thesis, Vanderbilt University (1991).
- [37] *Desorption induced by electronic transitions DIET I*, Eds. N.H. Tolk, M.M. Traum, J.C. Tully and T.E. Madey, (Springer, New York, 1983);
Desorption induced by electronic transitions, DIET II, Eds. M. Brenig and D. Menzel (Springer, New York, 1985);
Desorption induced by electronic transitions, DIET III, eds. M.L. Knotek and R.H. Stulen (Springer, New York, 1988);
Desorption induced by electronic transitions, DIET IV, Eds. G. Betz and P. Varga (Springer, New York, 1990).
- [38] T. Torring, J.P. Bekooy, W.L. Meerts, J. Hoefst, E. Tiemann and A. Dymanus, *J. Chem. Phys.* 73 (1980) 4875.
- [39] Zhou Xu-Yan, Shi Dan-Hua and Cao Pei-Lin, *Surf. Sci.* 223 (1989) 393.

Gas-Exposure Enhanced Na* Emission from Na-Rich Surfaces

Jun Xu,^a Royal Albridge, Alan Barnes, Xinxing Yang, and Norman Tolk

Center for Molecular and Atomic Studies at Surfaces

Department of Physics and Astronomy

Vanderbilt University, Nashville, TN 37235

Abstract: The optical emission attributed to electronically desorbed excited sodium atoms from NaCl and Na-evaporated surfaces is shown to be enhanced by exposure of the surface to gaseous CO₂ and N₂. This is the first observation of enhancement of electron-stimulated desorption of *substrate atoms* caused by the exposure of surfaces to gaseous molecules which do not contain the desorbed atoms. The large amount of excited sodium yield at 60 K provides evidence for non-existence of the secondary-electron excitation of thermally desorbed ground sodium.

^a Present Address: Oak Ridge National Laboratory, P. O. Box 2008, Oak Ridge, TN 37831-6142

This work reports the first measurement of the influence of surface impurities on the electron-stimulated desorption of *substrate atoms*. The surface composition can be altered by the migration to the surface of either substrate atoms or bulk defects.¹⁻³ Atomic or molecular adsorbates on surfaces may originate by exposure of the surfaces to gaseous molecules whose atomic constituents are either the same as, or chemically derived from, the dosed molecules.⁴⁻⁶ It is quite understandable that external gas exposure enhances desorption yield of adsorbates since the dosed molecules increase the adsorbate concentration. Recently, the experiments of Johnson and co-workers⁷ and the calculations of Nordlander⁸ show that the probability of hydrogen-atom desorption from metal surfaces can be altered by the presence of impurities on the surfaces. An immediate expectation is that the probability of *substrate-atom* desorption may also be enhanced by the presence of surface impurities. In this paper we show that excited sodium atom emission is dramatically increased when the electron-bombarded sodium surface is exposed to gaseous CO₂ and N₂ molecules. This observation indicates that gas exposure plays an important role in electronic erosion of substrates and is significant to such applications as lithography, surface catalysis, and the analysis of surface damage.

The work was carried out in an UHV system, which operates at a base pressure of 1.0×10^{-10} Torr. Gases were admitted to the chamber through two Varian leak valves allowing the partial pressures of two gases, CO₂ and N₂, to be controlled in the range of 1.0×10^{-10} to 1.0×10^{-6} Torr. Electron gun was operated in the energy range 10 to 400 eV at typical currents of 10-150 μ A. The samples were mounted on a micromanipulator allowing them to be moved relative to the optical detection system. The samples were in thermal contact with both a closed-cycle helium cooler and a heating unit: sample temperatures could be varied from 50 to 800 K. The alkali-halide crystals were cleaved in air, mounted with their (100) surfaces facing the beam and heated under UHV conditions

for cleaning. Thick sodium metal layers were obtained by evaporation from SAES sodium dosers onto a glass slide. Electron bombardment of a surface produces optical emission partially attributed to electronic transitions of desorbed excited species from the surface. Optical emission from the samples was imaged onto the entrance slit of a McPherson 0.3-m monochromator. Photons were detected by a cooled photomultiplier, operated in a pulse-counting mode. The stepping motor for control of the grating and the scaler for photon counting were interfaced through CAMAC and IEEE-488 units to an Apple Macintosh computer.

The results of the experiment are presented in Figures 1-2. Figure 1(a) and (a') compare optical spectra arising from an electron-bombarded NaCl surface without and with gas dosing. Initially without external gas exposure, a freshly cleaved NaCl sample was cooled to 60 K and pre-irradiated by 300-eV electrons for about 12 hours. Figure 1(a) displays a large amount of bulk fluorescence arising from this surface under electron bombardment. There was no observable Na* emission. Later, after the surface was exposed to 30 langmuirs of a 1:1 gaseous mixture of CO₂ and N₂, a large Na* desorption yield appeared, as shown in Figure 1(a'). Figure 1(b) and (b') shows the similar observation for sodium metal surfaces. The difference between the sodium-metal and the NaCl experiments is that, to obtain the above results, electron pre-irradiation was required for the NaCl surfaces but not needed for the sodium-metal surfaces. The data for the both substrates clearly show that gas exposure can influence electron-stimulated desorption of substrate atoms even though the atoms are not chemically related to the dosing molecules. As seen in the figure, we also observe enhancement of the ESD yield of excited CN molecules. The CN enhancement is understood to be due to the increasing concentration of adsorbed CN when the surface is exposed to CO₂ and N₂.⁹

The detailed growth process of the excited sodium desorption yield has been examined for various gas-exposure times. The desorption yield of excited sodium atoms from a Na-metal surface under 110 μA , 300-eV electron bombardment increases as a function of the CO_2 and N_2 exposure time, as shown in Figure 2. The yield for excited sodium increases faster than linearly with the exposure. The yield for excited CN desorption, also shown in Figure 2, increases slower than linearly with the exposure and the growth tends to saturate at large exposures. Although the CO_2 and N_2 exposure enhances both CN^* and Na^* desorption yields, there is an important difference between the enhancements. For CN^* desorption, the exposure is required to increase the concentration of the CN adsorbates on the surface. The saturation yield in the CN growth is understood to be due to a saturation of the surface sites for CN formation and an equilibrium between the formation of surface CN and the CN related desorption.⁹ However for Na^* , there is an abundance of sodium atoms on the surface since these are substrate atoms. The saturation limit observed in CN molecules does not appear for excited sodium desorption in the exposure range investigated here.

Many studies of electron and photon stimulated desorption (ESD and PSD) of excited alkali atoms from alkali-halide surfaces have been carried out.¹⁰⁻¹³ There are long-standing arguments about whether the production of excited alkali atoms come from the secondary electron excitation of *thermally* desorbed ground-state alkali atoms. The some experimental results^{10,11} support this mechanism as follows: 1) the velocity distribution of excited sodium atoms follows a Boltzmann distribution agreeing with the surface temperature, and 2) electronic state populations of excited sodium atoms agree with the populations observed in gas-phase electron-impact excitation cross sections for sodium. On the other hand, some experiments^{12,13} show that excited-alkali production in PSD decreases as the temperature increases while ground-state production of alkali atoms

increases as the temperature. Although the secondary electron excitation mechanism may be important for some high temperature experiments, it cannot explain this difference. Our data show that the yield of excited sodium production at 60 K is very large, even larger than the yield at 300 K. At such a low temperature, it is impossible to produce thermal ground-state sodium desorption followed by secondary electron excitation in such a large amount. A direct desorption induced by excitation to some repulsive electronic state, and/or production due to chemical reactions on the surfaces may be responsible for the production of excited sodium metal.

It is extensively documented that electron^{10, 14, 15} bombardment can induce accumulation of excess metal on alkali halide surfaces. Thus, we believe that the pre-irradiation for NaCl is required to produce metallization of the alkali halide surface. It is generally believed that a metal surface is difficult to produce the metal atom desorption since the initial excitation energy is quickly dissipated to the bulk. This is consistent with our data, which show no excited sodium desorption from sodium metal and Na-rich NaCl surface under electron bombardment.

CO₂ and N₂ exposure to the Na-rich surface produces impurities of the surface. These oxygen, carbon, and nitrogen impurities residing on the sodium surface may form sodium compounds, such as sodium oxide or insulator monolayers/multilayers on the metal surface. Nordlander theoretically predicted⁸ and Johnson and co-workers observed⁷ that probability of excited hydrogen atom desorption is enhanced by coadsorbed impurities on metal surfaces. We postulated that a similar picture may apply to the present result which shows enhancement of substrate atom desorption due to coadsorbed impurities on the sodium surfaces. Formation of the sodium-impurity complex localizes incident energy and consequently enhances the probability of the sodium desorption.

In summary, this is the first observation that electron-stimulated desorption of substrate atoms is enhanced by exposing the surface to gaseous molecules whose atomic constituents differ from the desorbed atoms. This observation indicates that nature of surface bonds plays an important role in electronic erosion. In addition, the large amount of excited sodium desorption at 60 K rules out the second electron excitation mechanism.

Authors thank H. Nielsen, C. Ewig, and D. Liu for helpful discussions. This research was sponsored in part by the Air Force Office of Scientific Research (AFOSR) under Contract AFOSR-90-0030, by the Office of Naval Research under Contract N00014-87-C-0146, and by NASA under Contract NAS8-37744.

References:

- ¹T. A. Green, G. M. Loubriel, P. M. Richards, N. H. Tolk, and R. F. Haglund, Jr., Phys. Rev. **B35**, (1987) 781.
- ²M. Szymonski, J. Kolodziej, T. Czuba, P. Piatkowski, A. Poradzisz, N. Tolk, J. Fine, Phys. Rev. Lett. **67**, 1906 (1991).
- ³C. C. Parks, D. A. Shirley, and G. Loubriel, Phys. Rev. **B29**, 4709 (1984).
- ⁴A. R. Burns, Phys. Rev. Lett. **55**, 525(1985).
- ⁵Ph. Avouris, R. beigang, F. Bozso, and R. Walkup, Chem. Phys. Lett. **129**, 505 (1986).
- ⁶F. Budde, A. V. Hamza, P. M. Ferm, G. Ertal, D. Weide, P. Andresen, and H. -J. Freund, Phys. Rev. Lett. **60**, 1518 (1988).
- ⁷P. D. Johnson, A. J. Viescas, P. Nordlander, and J. C. Tully, Phys. Rev. Lett **64**, 942 (1990).
- ⁸P. Nordlander, in *Desorption Induced by Electronic Transitions*, DIET IV, edited by G. Betz and P. Varga (Springer-Verlag, Berlin, 1990), P. 12.
- ⁹Jun Xu, Royal Albridge, Alan Barnes, Menfred Rield-Choduva, Akira Ueda, Norman Tolk, Dwight Russell, and Paul Wang, submitted to surface science, (1991)
- ¹⁰M. Szymonski, J. Ruthowski, A Poradzise, Z. Postawa, B. Jorgensen, in *Desorption Induced by Electronic Transitions*, DIET II, edited by W. Brenig and D. Menzel (Springer-Verlag, Berlin, 1985), P. 160.
- ¹¹R. E. Walkup, Ph. Avouris, and A. P. Ghosh, Phys. Rev. Lett. **57**, 2227(1986); J. Vac. Sci. Technol. **B5**, 1423 (1987).
- ¹²P. Bunton, R. Hugland, D. Liu, and N. Tolk, Surf. Sci. **243**, 227 (1991).
- ¹³N. H. Tolk, M. M. Traum, J. S. Kraus, T. R. Pian, W. E. Collins, N. G. Stoffel, and G. Margaritondo, Phys. Rev. Lett. **49**, 812 (1982).

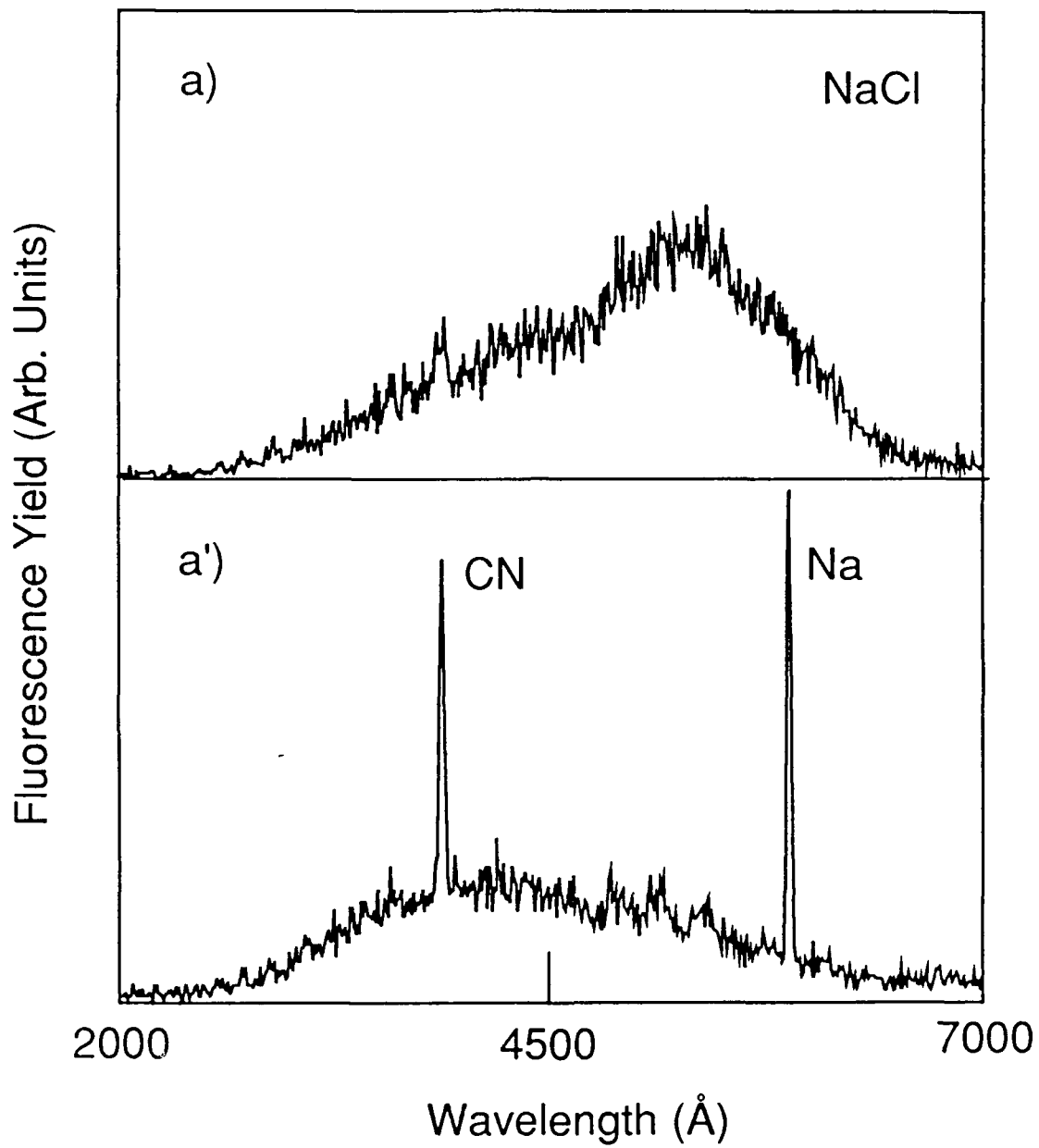
¹⁴P. Wurz and C. H. Becher, Surf. Sci. **224** (1989) 559.

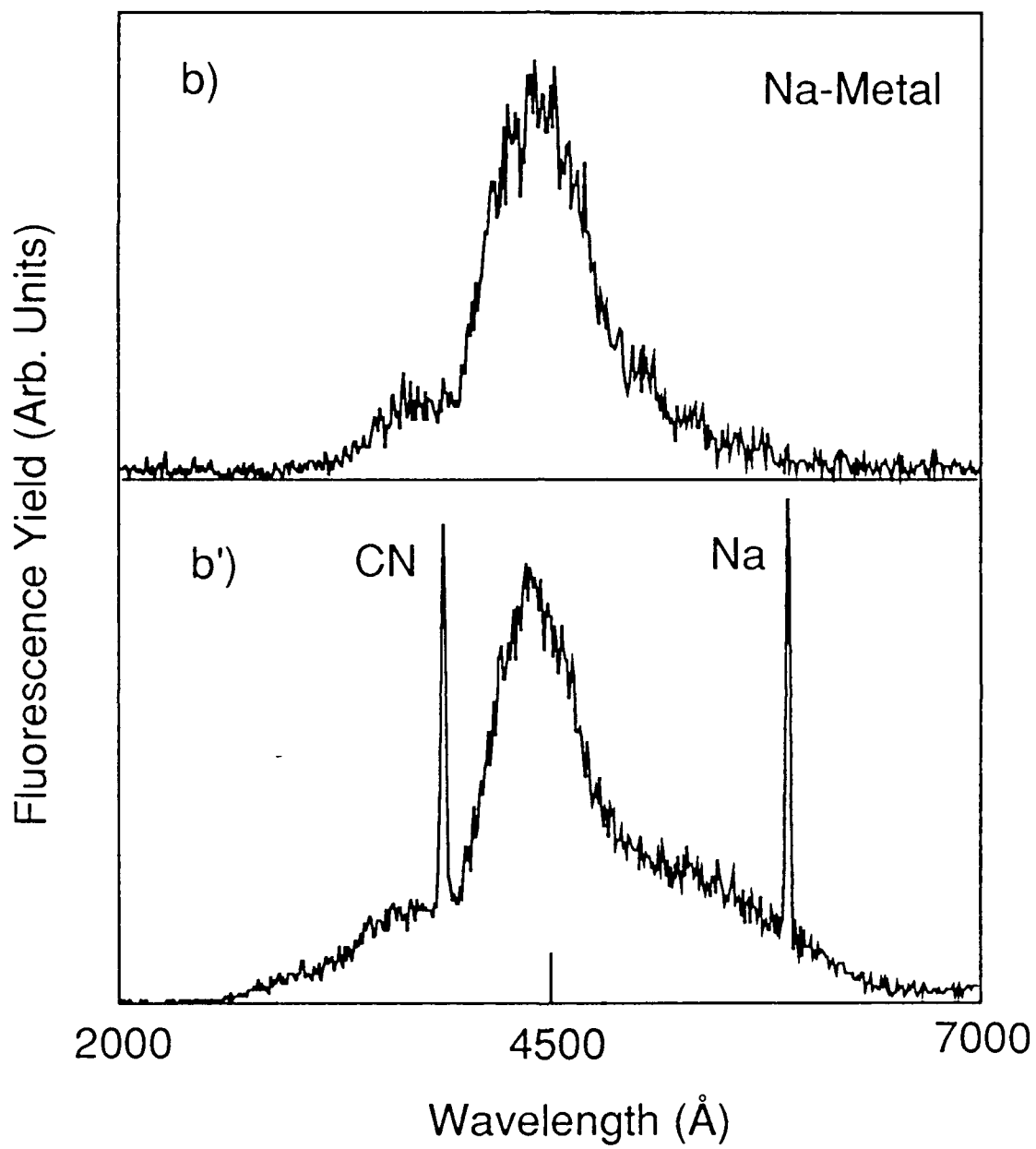
¹⁵G. Roy, G. Singh, and T. E. Gallon, Surf. Sci. **152/153**, 1042(1985).

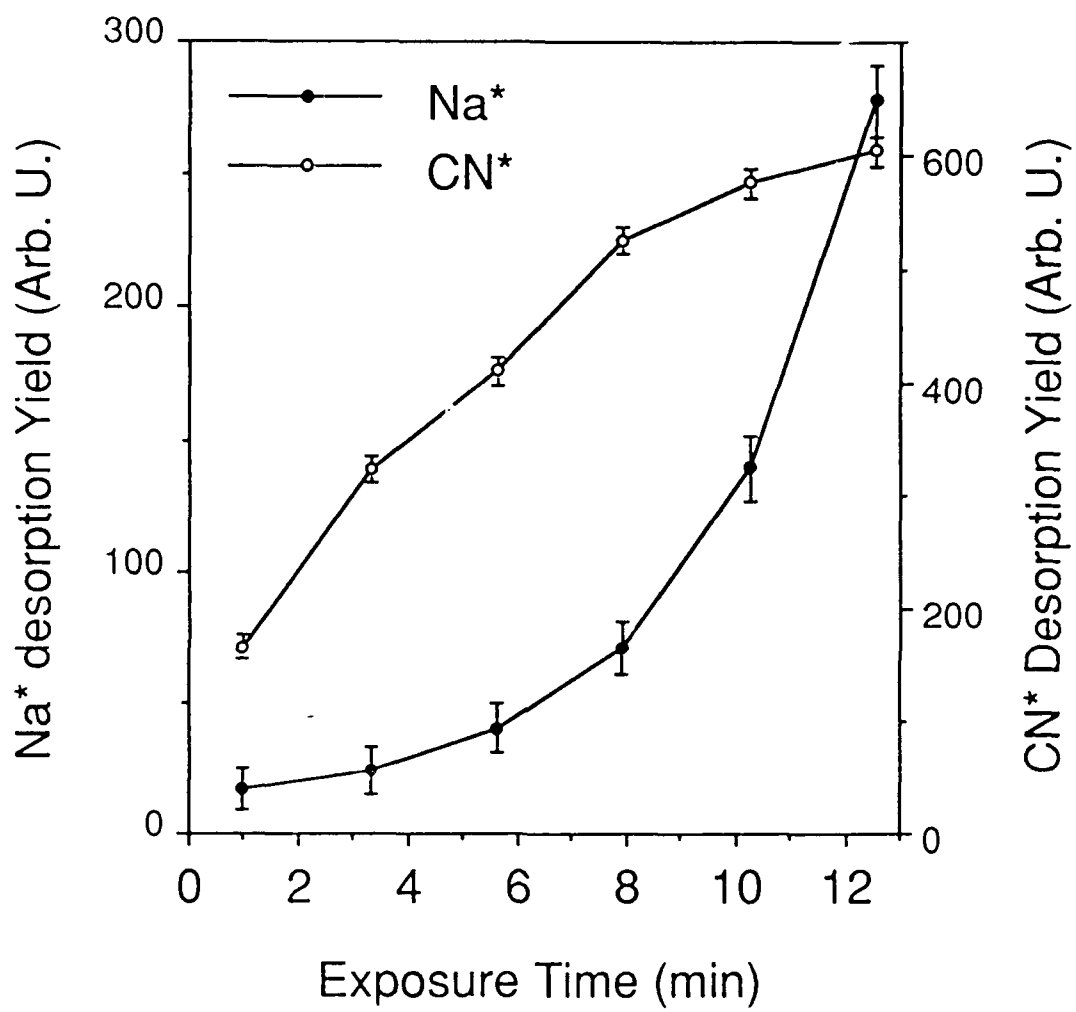
Figure Captions:

Figure 1. Optical emission spectra due to 300-eV electron bombardment (a) on a pre-irradiated NaCl surface at 60 K, (a') on the surface with CO₂+N₂(1:1) exposure at 5.0×10^{-8} Torr, (b) on a sodium metal surface at 60 K, (b') on the surface with CO₂+N₂(1:1) exposure at 5.0×10^{-8} Torr.

Figure 2. Excited sodium and CN desorption yields from a sodium-metal surface at 60 K plotted as a function of time exhibiting the influence of gas exposure, CO₂+N₂(1:1) at 1.0×10^{-7} Torr.







Submitted to Optics Letters, December 1991

**Cu:SILICA NANOCUSTER COMPOSITE MATERIAL WITH
FICOSECOND THIRD-ORDER NONLINEAR OPTICAL RESPONSE**

R. F. HAGLUND, Jr.^(1,3), L. YANG,^(1,3) R. H. MAGRUDER, III⁽²⁾,
K. BECKER,⁽³⁾ J. E. WITTIG⁽²⁾ and R. A. ZUHR⁽⁴⁾

Departments of ⁽¹⁾Physics and Astronomy and of ⁽²⁾Materials Science and Engineering
and ⁽³⁾Free-Electron Laser Center for Biomedical and Materials Research

Vanderbilt University, Nashville, TN 37235

⁽⁴⁾Solid-State Division, Oak Ridge National Laboratory, Oak Ridge, TN 37831

ABSTRACT

We report the creation of a novel composite nonlinear optical material by implanting Cu ions in fused silica. The implanted Cu ions aggregate at room temperature to form nm-size polycrystalline clusters in a high-density thin (~ 150 nm) layer just beneath the surface of the substrate. Measurements of the Kerr-type third-order nonlinear susceptibility $\chi^{(3)}$ of this material shows that it has a response time no longer than 6 ps and a magnitude of order 10^{-8} esu. The nonlinearity is enhanced for laser wavelengths near the surface plasmon resonance of the copper colloids.

The development of practical optical computing and communication devices will require materials with large $\chi^{(3)}$ fabricated by techniques compatible with microelectronics processing technology. Metallic nanoclusters embedded in a dielectric are potentially attractive for these applications, since they exhibit a *nonresonant* ultrafast nonlinear response at the bulk or surface plasmon frequency of the metal. The response time of gold colloids in water has been shown to be less than 5 psec,¹ and the size of $\chi^{(3)}$ and response time of gold colloids both in water² and in Schott (RG6) filter glass³ has been found to depend on colloid shape and size distributions. Enhancements in $\chi^{(3)}$ of several orders of magnitude have been predicted for clusters embedded in dielectrics.⁴ However, metallic colloids have not previously been fabricated in a form compatible with microelectronics technology.

In this paper, we report what to our knowledge is the first observation of picosecond optical nonlinearity in copper clusters produced by ion implantation in silicon dioxide. The Cu clusters have diameters in the 2-28 nm range, as shown by transmission electron microscopy, and are implanted in 150-nm-thick layers. Electron diffraction measurements show that the clusters are polycrystalline, face-centered-cubic structures; the smallest of them could be expected to exhibit quantum size effects. The observed electronic nonlinearity is of the Kerr type, and has a response time no longer than 5.5 ps pulses. The nonlinear index is strongly enhanced at wavelengths near the peak of the surface plasmon resonance in the copper nanoclusters, and has a magnitude of order $10^{-10} \text{ cm}^2 \cdot \text{W}^{-1}$, comparable to the values observed for semiconductor microcrystallites such as $\text{Cd}_x\text{S}_{1-x}$.

Our sample for this experiment was made by implanting a high purity fused silica (Spectrosil®) disk 20 mm in diameter and 1 mm thick with Cu^+ ions at 160 keV energy at room temperature to a total dose of $12 \cdot 10^{16} \text{ ions} \cdot \text{cm}^{-2}$. The ion beam was electrostatically rastered to provide uniform implantation, and the current density was $2.5 \mu\text{A} \cdot \text{cm}^{-2}$, holding the macroscopic

temperature of the substrate below 50 °C. The Cu concentration and depth profiles of the implanted ions were determined by He⁺ ion backscattering (RBS). The total ion dose calculated from RBS was typically 90% of the integrated current measured during implantation, indicating minimal sample charging. The RBS spectra of the implanted layers are bimodal: the larger peak is about twice the size of the smaller and appears nearer the surface. The implanted layer was some 150 nm thick FWHM.

Samples for TEM analysis were prepared by standard grinding, ion-milling and back-thinning techniques, and examined in a Philips CM20/T scanning transmission electron microscope operating at 200 kV. As shown in the bright-field image in Figure 1, the sample clearly contains spherical particles embedded in the silica matrix. This view does not reveal the depth distribution of the nanoclusters; cross-sectional TEM measurements indicate that the larger particles are located closer to the surface in the region of the primary peak in the RBS spectrum; the smaller clusters are beneath this highest-dose region.⁵ Measurements made while tilting the sample revealed that these colloids are spherical in shape with random crystallographic orientation. Electron diffraction measurements, shown in the insert to Fig. 1, display a ring pattern characteristic of face centered cubic (FCC) polycrystalline metallic copper, superimposed on the diffuse diffracted intensity from the amorphous silica matrix.

Particle size distributions were obtained from projected diameters of the clusters from the TEM bright-field images. Regions of the TEM samples were selected which had adequate thickness to represent the overall particle size distribution. By assuming a spherical geometry and a foil thickness equal to the FWHM depth calculated from the RBS profile, these particle-size measurements were used to calculate the areal and volumetric densities listed in Table 1. The computed areal density was in close agreement with that from the RBS measured values. Elsewhere we have reported that such parameters of the nanoclusters as average cluster size, size

distribution and volume fraction are affected and can be controlled both by total dose per side and implantation dose rate. The size distribution of the Cu:SiO₂ sizes is roughly uniform from 5 nm to 25 nm diameter; the total number of clusters is estimated to be $5.1 \cdot 10^4 \mu\text{m}^{-3}$ in the implanted layer. For purposes of comparison, a 5-nm-diameter fcc copper sphere contains some 1800 atoms. For clusters with diameters below 10 nm, quantum size effects are expected.⁷

TABLE I: Characteristics of Implanted Sample

Sample	Nominal Dose (ions·cm ⁻²)	Number of Sides Implanted	RBS Dose (ions·cm ⁻²)	Current Density (μA·cm ⁻²)	Areal Density (ions·cm ⁻²)	Volume Fraction (%)
1	$12 \cdot 10^{16}$	1	$10 \cdot 10^{16}$	2.5	$9.5 \cdot 10^{16}$	7.5

Differential optical absorption measurements on the Cu:silica sample were made over the wavelength range from 650 to 200 nm (1.8 to 6.2 eV) using a Cary 14 dual beam spectrophotometer interfaced to a microcomputer with an unimplanted sample in the reference beam. Absorption measurements were made at three different positions on the sample; scatter in the data from these three points was less than $\pm 5\%$. The absorption spectrum exhibits a peak at 2.2 eV (the solid curve in Fig. 2) which can be attributed to the Cu surface plasmon resonance. The ratio of plasmon peak to background is preparation dependent.⁸ A significant rise (and in some cases, a peak) in absorption near 5 eV is due to ion-beam-induced radiation damage, in particular the formation of the E' and B₂ electronic defects; there is also probably a contribution from plasmon formation.⁹

The nonlinear index of refraction n_2 is defined in terms of the ordinary linear index n_0 and the (complex) third-order nonlinear dielectric susceptibility $\chi^{(3)}$ by:

$$n = n_0 + \gamma \cdot I, \quad \gamma = \frac{4\pi}{3n_0} 10^{-8} \cdot \text{Re}[\chi^{(3)}] \quad (1)$$

where n_0 is the linear index of refraction and I is the laser intensity. The nonlinear index of refraction was measured with the Z-scan method in an optical set-up described by Becker *et al.*¹⁰

The light source was a 5.5 ps, cavity-dumped tunable dye laser with a 3.8 MHz pulse repetition rate and 100 mW average power. Peak irradiance of the dye laser near the top of its tuning curve is $\sim 2 \cdot 10^9$ W·cm⁻². A 1-mm thick sample of CS₂ was used as a reference for calibrating the Z-scan and our sample. The laser intensity in the Cu-implanted layer was varied by translating the sample through the focal plane of a 150-mm lens on a computer-controlled translation stage. The sample acts as a second lens in series, having an intensity-dependent focal length. The transmitted laser intensity was monitored by a power meter located behind a beam-limiting aperture 90 cm from the focal plane, normalized to the signal from a beamsplitter placed before the focusing lens. For a material with a positive nonlinear index of refraction, moving the sample toward, and then away, from the focal plane causes an initial decrease in the normalized far-field intensity, followed by a recovery to unity at the focal plane and a subsequent increase in intensity.

Typical Z-scan plots for our picosecond measurements have been shown elsewhere.⁶ The analysis we use is based on paraxial optical ray-tracing for the equivalent two-lens system, and is described in detail in a forthcoming publication.¹¹ For a thin, highly absorbing layer embedded in a transparent dielectric, the intensity-dependent part of the refractive index $\gamma = \Delta n/I$ is

$$\gamma = \frac{I_{\max} - I_{\min}}{I_{\max} + I_{\min}} \cdot \frac{n_0 r_0^2}{z_0 I_0 L}, \quad z_0 \equiv \frac{\pi r_0^2}{\lambda} \quad (2)$$

where I_{\max} and I_{\min} are the maximum and minimum intensities recorded in the Z-scan; I_0 is the laser peak intensity at the focal spot, r_0 is the radius of the Gaussian beam profile-at the focal plane, L is the thickness of the implanted layer, and z_0 is the diffraction length.

Figure 2 shows the results of Z-scan measurements at several wavelengths between 570 and 600 nm - near the 2.2 eV absorption peak in the spectrum of the samples. The data are values of $\text{Re}[\chi^{(3)}]$ which were extracted from the Z-scan measurements of γ , and are of order of 10^{-8} esu. The fact that $\chi^{(3)}$ exhibits a maximum around 570 nm supports the idea that excitation of the surface plasmon resonance is responsible for the third-order nonlinearity. These values for the nonlinear index are much smaller than the thermo-optic nonlinear susceptibility of $\chi^{(3)} \sim 10^{-6}$ esu reported earlier for 100 ps FWHM laser pulses at 532 nm.¹² This is because at 5.5 ps pulse length, only fast electronic effects of the Kerr type contribute to $\chi^{(3)}$, while at 100 ps pulse length, the high absorption of the sample ($\alpha \sim 10^4 \text{ cm}^{-1}$) leads to thermal self focusing.

Both the magnitude and the enhancement of $\chi^{(3)}$ in Cu:silica resemble the measurements of $\text{Im}[\chi^{(3)}]$ previously carried out on gold colloids in ruby-gold glass and in aqueous solution. The major contribution to this electronic Kerr-type nonlinearity in Au has been shown to arise from photoexcitation of electrons in the conduction band owing to the weak specific heat and consequent ease of raising these electrons to temperatures of many hundreds of degrees.¹ Transient thermorefectance spectroscopy on a 400-nm-thick evaporated Cu film shows that this same hot-electron contribution should be effective in Cu clusters, because several electron-lattice collisions are required to thermalize the incident photon energy in that material also.¹³ In addition, following the analogy with the Au clusters, we expect an *interband* contribution to the nonlinear susceptibility arising from the photoexcitation of electrons from the *d*-band near the *X* point of the Brillouin zone to the *p*-conduction-band states near the Fermi energy. The magnitude of this contribution to $\chi^{(3)}$ in gold is largely imaginary and of order $2 \cdot 10^{-8}$ esu - close to the values of $\text{Re}[\chi^{(3)}]$ measured in our present experiment. It is anticipated that there should be no quantum size effect observed for the broad distribution of relatively large nanoclusters in our sample, since those effects are likely to be seen only for clusters smaller than 2-3 nm in diameter.

The exact relationships between $\chi^{(3)}$ or γ and such materials-preparation parameters as total implantation dose, current density and temperature are currently under investigation. It appears that these parameters determine both the cluster size and cluster size distribution. By controlling the cluster properties, it may be possible to tailor the optical properties for specific applications in optical waveguides and other devices, as well as to enhance the nonlinear optical response. The possibility of controlling the characteristics of nanoclusters through the ion implantation process is particularly intriguing in light of predictions of large enhancements in the third-order nonlinearity for metal-dielectric composite structures created in a nonlinear host matrix.³

In summary, we have shown that it is possible to embed metallic Cu clusters in fused silica using ion-implantation procedures compatible with microelectronics processing techniques to create a novel nonlinear composite material. The ion implanted layers exhibit an electronic nonlinear susceptibility $\chi^{(3)}$ of the Kerr type; the measured nonlinear refractive index is $\gamma \sim 10^{-10} \text{ cm}^2 \cdot \text{W}^{-1}$, comparable to values for II-VI semiconductor nanocrystallites.¹⁴ As we have shown elsewhere, the mean size and size distribution of the clusters can be controlled by varying ion implantation parameters. Thus, using the ion-implantation technique, it should be possible to fabricate metallic nanoclusters in a variety of interesting geometries and at a volumetric density compatible with silica-based optoelectronic device technology.

Acknowledgements

Research at Vanderbilt University was supported in part by the Army Research Office under contract DAAL03-91G-0028 and by the Office of Naval Research through the Free-Electron Laser program for Biomedical and Materials Research. Oak Ridge National Laboratory is partially supported by the Division of Materials Science, U. S. Department of Energy, under contract DE-AC05-84OR21400 with Martin-Marietta Energy Systems, Inc.

REFERENCES

1. F. Hache, D. Ricard, C. Flytzanis and U. Kreibig, *Appl. Phys. A* **47**, 347 (1988).
2. M. J. Bloemer, J. W. Haus and P. R. Ashley, *J. Opt. Soc. Am. B* **7**, 790 (1990).
3. J. W. Haus, N. Kalyaniwalla, R. Inguva, M. Bloemer and C. M. Bowden, *J. Opt. Soc. Am. B* **6**, 797 (1989).
4. J. W. Haus, R. Inguva and C. M. Bowden, *Phys. Rev. A* **40**, 5729 (1989).
5. H. Hosono, private communication and *J. Non-Cryst. Solids*, to be published.
6. R. H. Magruder III, R. F. Haglund, Jr., L. Yang, K. Becker, J. E. Wittig and R. A. Zuhr, *Proc. Mat. Res. Soc.* **244**, to be published (1992).
7. W. P. Halperin, *Rev. Mod. Phys.* **58**, 533 (1986).
8. R.H. Magruder,III, R.A. Zuhr and R.A. Weeks, *Nucl. Instrum. Meth. in Phys. Research B* **59/60**, 1308 (1991)
9. P. D. Townsend, *Rep. Prog. Phys.* **50**, 501(1987).
10. K. Becker, L. Yang, R. F. Haglund, Jr., R. H. Magruder, R. A. Weeks and R. A. Zuhr, *Nucl. Instrum. Meth. in Phys. Research B* **59/60**, 1304 (1991). Detailed descriptions of the Z-scan technique have been given by M. Sheik-Bahae, A. A. Said, T. Wei, D. J. Hagan and E. W. VanStryland, *IEEE J. Quant. Electron.* **26**, 760 (1990).
11. L. Yang, K. Becker and R. F. Haglund, Jr., to be submitted to *J. Opt. Soc. Am. B*.
12. L. Yang, K. Becker, and R. F. Haglund, Jr., *Bull. Am. Phys. Soc.* **35**, 1530 (1990).
13. G. L. Eesley, *Phys. Rev. B* **33**, 2144 (1986).
14. G. I. Stegmann and R. H. Stolen, *J. Opt. Soc. B* **6**, 652 (1989).

FIGURE CAPTIONS

Figure 1. Bright-field TEM image of metallic Cu nanoclusters formed by ion implantation in fused silica. The sample was implanted to a dose of $1.2 \cdot 10^{17}$ ions·cm⁻². **Insert:** Electron diffraction image of the ring pattern characteristic of face-centered cubic copper in the ion-implanted layer.

Figure 2. Measured values of $\chi^{(3)}$ for the sample shown in Figure (1a), superimposed on a section of the absorption spectrum for the sample, shown in units of extinction coefficient per ion.

FIGURE CAPTIONS

Figure 1. Bright-field TEM image of metallic Cu nanoclusters formed by ion implantation in fused silica. The sample was implanted to a dose of $1.2 \cdot 10^{17}$ ions/cm². **Insert:** Electron diffraction image of the ring pattern characteristic of face-centered cubic copper in the ion-implanted layer.

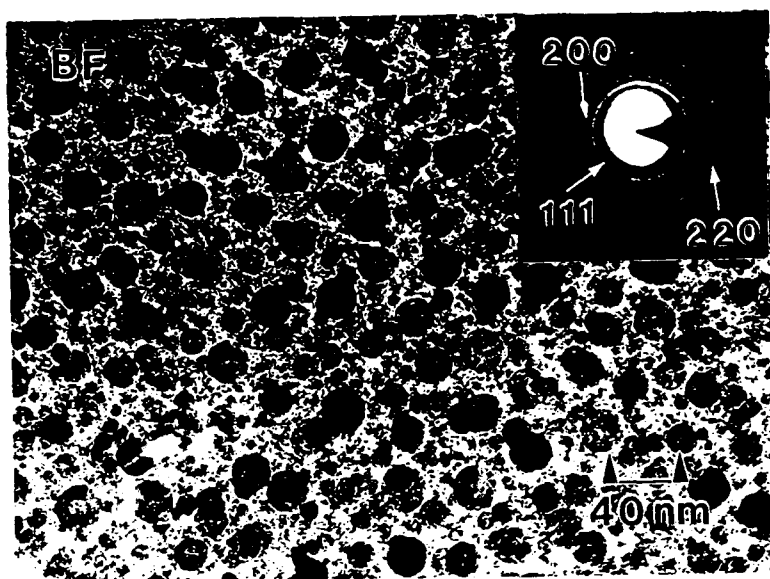
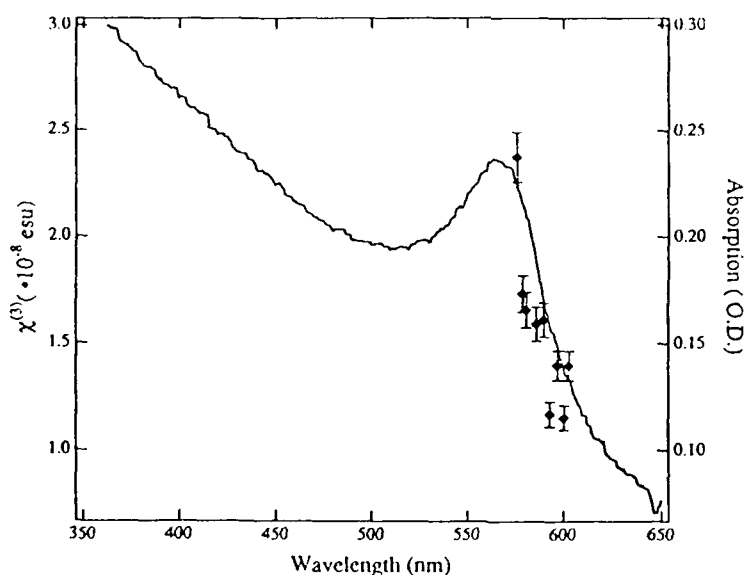


Figure 2. Measured values of $c^{(3)}$ for the sample shown in Figure (1a), superimposed on a section of the absorption spectrum for the sample, shown in units of extinction coefficient per ion.



D4

Ultraviolet laser ablation of halides and oxides *

R.F. Haglund, Jr., M. Affatigato, J.H. Arps and K. Tang

Department of Physics and Astronomy, Vanderbilt University, Nashville, TN 37235, USA

A. Niehof and W. Heiland

Fachbereich Physik, Universität Osnabrück, W-4500 Osnabrück, Germany

We compare and contrast recent measurements of the behavior of ions and excited ions desorbed from samples of alkali halides and oxide ferroelectrics by an excimer laser at 308 nm wavelength. At the intensities used in these experiments, the density of local electronic excitation is low in the halides and high in the ferroelectrics, corresponding to two- and one-photon band-to-band transitions, respectively. The observed desorption yields and changes in the sample surfaces are discussed in terms of the density of electronic excitation, the relative strengths of electron-lattice coupling, and the role of thermal relaxation processes in the two materials.

1. Introduction

Ultraviolet laser ablation is the basis for an increasingly significant area of materials processing technologies, including lithography, patterning, marking, micromachining, and thin-film growth [1]. In many of these applications, laser ablation may be either a competitor for or a complement to traditional ion-beam techniques. However, in spite of the scientific and technological importance of this process, relatively little research has been devoted to microphysical mechanisms of laser-induced desorption and ablation from insulators [2]. The paucity of data on fundamental mechanisms of laser ablation in insulators is partly due to the difficulty of characterizing the state of a dielectric surface before and after ablation, and contrasts starkly with the plethora of work on desorption of molecules adsorbed on metal and semiconductor surfaces [3].

Laser ablation or laser sputtering of surfaces evinces both contrasts with and similarities to collisional sputtering. In laser ablation, energy deposition occurs by electronic excitation, whereas in collisional sputtering, both collision cascades and local electronic excitation absorb the incident ion energy. Nuclear motion leading to particle emission occurs in ion sputtering primarily by momentum transfer, but in laser ablation, by electron-lattice coupling subsequent to the initial elec-

tronic excitation. The dynamics of particle emission varies with local density of electronic excitation and with electron-lattice coupling strength [4].

In this paper, we present recent results on laser ablation of an alkali halide (KCl) and an oxide ferroelectric (KNbO₃). Our motivation is both technological and scientific: In optical technology, halides and other ionic compounds are widely used as optical components, while the oxide ferroelectrics are used as nonlinear optical and photonic materials. Laser-induced material degradation is a major issue in these applications. Because the ferroelectrics are not easily machined or chemically etched, there is also interest in laser-micromachining of these materials [5]. From the perspective of optical physics, on the other hand, halides and oxides fall in the strong and intermediate electron-lattice coupling regimes, respectively. Since the excimer laser with its 4 eV photon energy induces band-to-band excitation by two- and one-photon excitation in the halide and ferroelectric materials, respectively, our experiments also contrast the regimes of low and high absorption and electronic excitation density.

2. Experimental details

Single-crystal targets of KCl were prepared by cleaving bulk material supplied by Harshaw. KCl exhibits the strongest possible electron-lattice coupling, with a Phillips ionicity of 0.95. KCl has a band-gap energy of 8 eV, so band-to-band excitation requires a two-photon transition. Our KNbO₃ targets were grown from a melt and supplied as single crystals with dimen-

* This research was partially supported by the North Atlantic Treaty Organization and by the Office of Naval Research through the Free-Electron Laser Program in Biomedical and Materials Research.

sions of about $10 \times 15 \times 1$ mm³. Some of the KNbO₃ samples used in our experiments were doped with alkali, alkaline earth and transition-metal elements. Potassium niobate has an intermediate electron-lattice coupling, consistent with its somewhat more covalent binding. With a bandgap of 4 eV, electron-hole pairs can be created by single-photon band-to-band transitions in this material.

The laser ablation experiments described here were carried out at room temperature in an ultrahigh vacuum (UHV) chamber with a nominal base pressure of less than 10^{-9} Torr. Samples of KCl and KNbO₃ were mounted on a micromanipulator and placed in the chamber with the surface normal to the beam from the exciting laser.

The ablation laser was a Lumonics Hyper-Ex 460-UB laser oscillator with a nominal pulse width of 15 ns and a maximum pulse energy of 250 mJ for a standard XeCl gas mixture ($\lambda = 308$ nm, $h\nu = 4.02$ eV). The laser was focused gently onto the target with a fused-silica lens of 40 cm focal length located just outside the UHV chamber, to produce a focal spot with an area of some 3–4 mm², as measured by burn patterns. This provided peak intensities in the range of 10^{13} – 3×10^{14} Wm⁻², depending on the discharge voltage selected for the laser oscillator. While the *relative* intensities are well determined in this experiment through the use of a calibrated ultraviolet calorimeter (Sciencetech), the absolute intensity might well be in doubt by as much as a factor of 5, depending on the assumptions one makes about the temporal and spatial profile of the beam.

Fluorescence from ablated excited atoms above the target surface was detected by standard optical tech-

niques. A UV-grade fused silica lens, located inside the UHV chamber approximately 10 cm from the target, at an angle of 45° to the target normal, imaged the fluorescence onto the entrance slit of a Macpherson 218 spectrometer. The fluorescence detector was a photomultiplier operated in pulse-height-analysis mode. The photomultiplier current was summed in a boxcar integrator the output from which was stored in a Macintosh microcomputer for each laser pulse. Ablation yields were computed by integrating over the relevant fluorescence peak and subtracting a linear background.

3. Experimental results

Fig. 1 shows fluorescence spectra of excited atoms desorbed from KCl in the red and blue regions of the spectrum. Unlike photon-stimulated desorption studies on KCl with synchrotron radiation, we observe two excited states of K and one excited state of Cl. The relative yields of these states are strongly dependent on the condition of the surface; once the surface has been damaged by the laser, the yield of the K* atoms is sharply diminished. Hence, the yield of K* is a sensitive diagnostic for the decomposition of the surface by metallization. The Cl* yield, on the other hand, continues essentially without any reduction for as many as several thousand shots [6].

Fig. 2 shows this loss of intensity in the K* yield from the fluorescence doublet at 767 nm as a function of total absorbed photon dose, assuming that a two-photon ~~absorption~~ band-to-band transition is the pri-

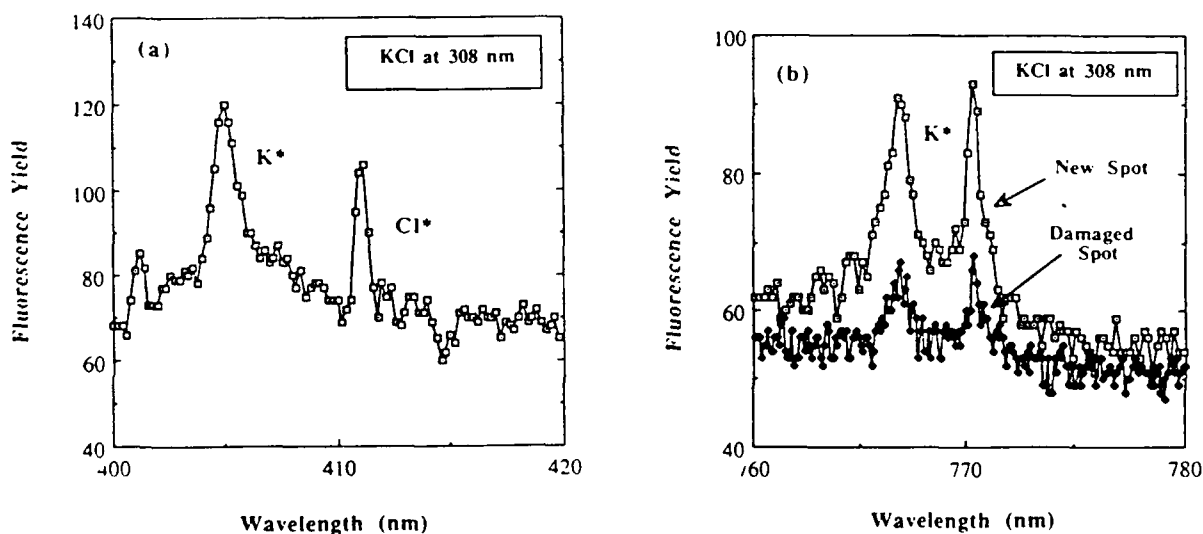


Fig. 1. (a) Fluorescence from excited Cl and K atoms ablated from a KCl target by 4 eV laser irradiation. (b) Doublet fluorescence peaks from excited K atoms ablated from a KCl sample by 4 eV laser irradiation. The laser intensity is of order 3×10^{13} Wm⁻². Adapted from ref. [6].

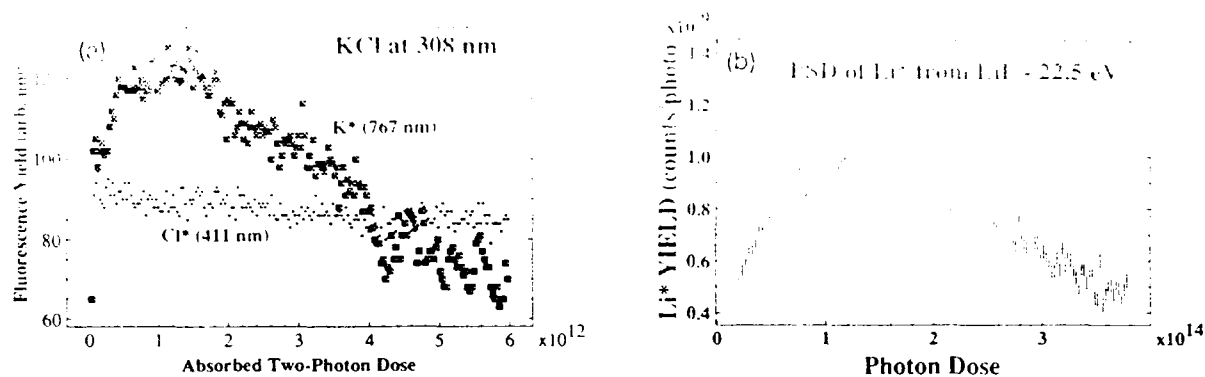


Fig. 2. (a) Fluorescence yields from the 767 nm doublet radiation of K^* and the 411 nm fluorescence from Cl^* ablated from KCl, plotted as a function of laser shot number. (b) Fluorescence yield from Li^* desorbed from a LiF crystal by vacuum ultraviolet synchrotron radiation. Adapted from refs. [6] and [14].

mary mechanism of photon absorption (see the discussion section). The maximum dose for which K^* yield is observed corresponds to some 200 laser shots, at which point one assumes that the surface is completely damaged, i.e. nonstoichiometric. For comparison, we show a yield-dose curve for Li^* desorbed from LiF by vacuum ultraviolet synchrotron radiation with photons of energy 22.5 eV. Note the similar behavior as a function of dose: a rise from a low level to a rather broad maximum, and then a gradual decrease to near background levels.

Fig. 3 shows a fluorescence spectrum of excited Nb and NbO desorbed from Mg:KNbO₃. The vibrational band feature has been tentatively identified as NbO*, highlighting the fact that in these materials ablation of both molecules and atoms occurs. In laser-induced

desorption from LiNbO₃ below the threshold for plasma formation, observed by quadrupole mass spectrometry, several molecular ions and neutrals have also been observed, including the metal monoxide NbO and the LiNbO₃ molecule [7]. In the spectrum of Fig. 3, the resolution is insufficient to allow the extraction of a temperature for the ablated molecules. However, molecular emission appears to be a distinctive feature of laser ablation from oxides, having been observed not only in niobates, but also in the high- T_c perovskite superconductors.

One of the most obvious characteristics of laser ablation in the oxides is the appearance of a well-defined fluence threshold for desorption. A number of examples of particle emission thresholds under different conditions are given elsewhere [8]. A threshold

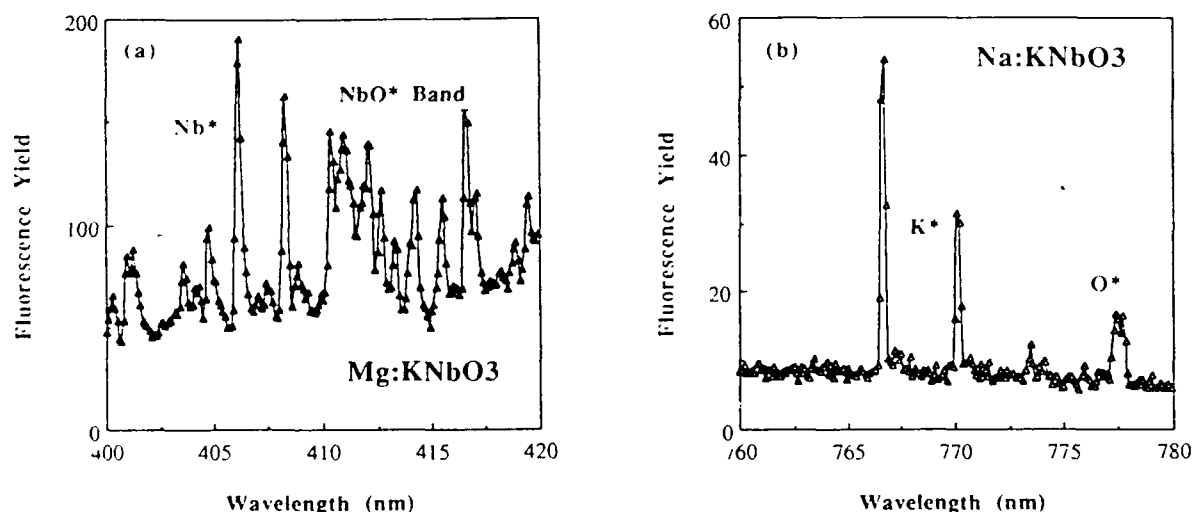


Fig. 3. (a) Fluorescence from Nb^* atoms and NbO^* molecules ablated from Mg-doped KNbO₃ by an XeCl laser. (b) Fluorescence from K^* and O^* ablated from Na-doped KNbO₃ by an XeCl laser. The laser intensity used in obtaining both spectra was of order $6 \times 10^{13} \text{ W m}^{-2}$. Adapted from ref. [8].

measurement for K^* and O^* described from doped and undoped potassium niobate is shown in fig. 4. The laser pulse energy at threshold ~ 30 – 40 mJ – corresponds to fluences of order 1 J cm^{-2} and intensities of order 10^8 W cm^{-2} , which are comparable to the threshold values for lithium niobate [5]. The existence of the threshold clearly indicates that one is not in the regime where the yield scales linearly with the density of electron-hole pairs. This is in sharp contrast to the alkali halides, where the desorption yield at low intensities is proportional to the density of laser-generated electron-hole pairs [9]. It is also noteworthy that the doping by Mg, in this case, seems to have little effect on the ablation thresholds. This is surprising in view of the way in which moderate doping of Mg in LiNbO_3 has been shown to retard photorefractive damage due to prolonged laser irradiation in the visible spectrum [10].

We point out in passing that the apparently similar slopes of the K^* and O^* ablation yield curves – of order ≈ 3 – probably do not reflect a common physical origin or mechanism. The parent state of the observed O^* fluorescence lies some 12 eV above the ground state. This suggests that the O^* is proportional to ground-state oxygen atom yield, the excited state being created by three-photon excitation or by hot-electron impact in the ablation plume above the target.

Still another important contrast between laser ablation of oxides and halides relates to the metallization of the surface. When we measured the decrease in yield of K^* as a function of laser shot number in KNbO_3 , we noted that the excited metal signal gradu-

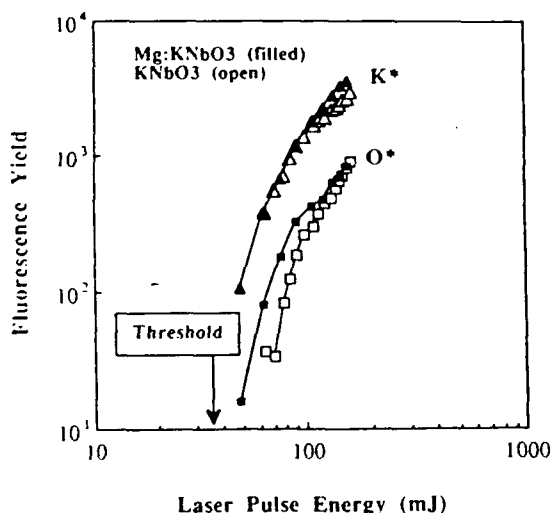


Fig. 4. Threshold behavior of K^* and O^* yields from pure (open plot symbols) and Mg-doped KNbO_3 as a function of laser pulse energy. The laser focal spot was held constant, so that the horizontal axis is proportional to laser intensity. Adapted from ref. [8].

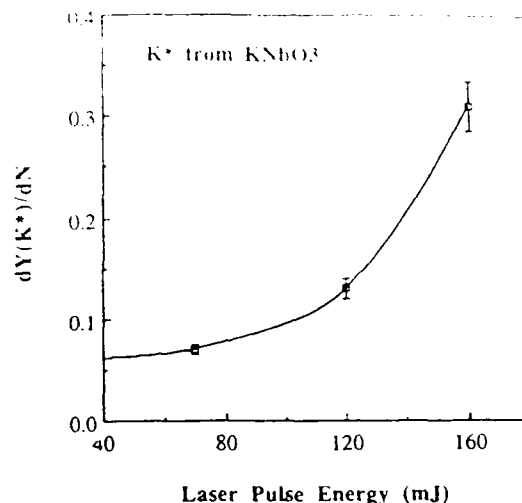


Fig. 5. Rate of decrease of K^* atom yield during laser ablation of a KNbO_3 sample, as a function of laser pulse energy. Each datum represents an average of the slope $-dY(K^*)/dN$ over 3×10^3 laser shots starting with a fresh target under conditions where the focal spot was unchanged while the laser intensity was varied.

ally disappeared as the surface is damaged, consistent with the picture that the surface is metallized and the excited atoms are ionized by resonant charge transfer as the excited atomic level comes in resonance with the Fermi level of metallic clusters on the surface. However, in the oxides, the rate at which this occurs with dose or shot number is strongly dependent on laser intensity.

We sought to quantify this effect by measuring the rate of decrease of K^* yield with laser shot number, $-dY(K^*)/dN$, over some 3×10^3 shots, at different laser pulse energies, beginning each trial at a fresh spot. In Fig. 5 we display $-dY(K^*)/dN$ as a function of laser pulse energy. The strong nonlinear behavior indicates that at higher pulse energies, the surface is metallized at an accelerated rate. Thus, unlike the alkali halides, the nonstoichiometry of the damaged laser surface depends on laser-induced defects as well as on the primary process.

4. Discussion

In order to bring out most clearly the similarities and differences in the laser ablation mechanisms in the halides and oxides, we shall discuss the results in the following order: (1) optical response of halides and oxides; (2) metallization of the surface as the primary electronic effect of laser ablation in halides and in oxides due to expulsion of the halogen and oxygen atoms or ions, respectively; and (3) the correlation

between the strength of the electron-lattice coupling and the characteristics of particle emission. In both cases, we discuss explicitly the role played by density of electronic excitation in the ablation phenomenology; in the case of the oxides, we also point out the effects of thermal relaxation.

In alkali halides, the valence band is formed primarily from the halogen p-states, and the conduction band from the metallic s-states. In the case of KCl, for example, the valence band arises from the Cl(3p) states and the conduction band from the K(4s) states. The fundamental optical response of this material involves a transfer of charge from the halogen to the nearest-neighbor alkali [11]. The same kind of charge transfer occurs in some measure for all ionic materials. Thus, for the perovskite ferroelectric KNbO_3 , the upper valence band comprises the O(2p) orbitals, and the optical response involves primarily charge transfer to the Nb(4d) states [12]. ~~Thus~~ ^{Here} the initial optical response of both halide and oxide materials follows a similar electronic mechanism.

Here, however, the similarities between the laser ablation characteristics of the two materials end. Photon-induced decomposition and desorption in alkali halides have been studied extensively for one-photon band-to-band transitions initiated by synchrotron radiation, and the primary mechanism is widely agreed to be initiated by the decay of the self-trapped exciton (STE) into an F-center-H-center pair. The dissociation of the H-center (an X_2^- molecule) near the surface produces a desorbing X^0 and a bound X^- , while the recombination of an F-center with a surface alkali-metal ion leads to thermal desorption of a neutral alkali atom, usually in the ground state. The exact role of surface metallization in the production of excited alkali atoms is still unclear, but there is no reason to doubt the fundamental correctness of this picture.

One might think that the laser-induced ablation mechanism for the halides would be fundamentally different from that inferred from the low-intensity synchrotron experiments, where the photon flux is only of order 10^{12} photons/s over a larger beam spot. However, for the laser parameters in our experiments with KCl, with peak laser intensities of order 10^{14} W m^{-2} , the local density of electronic excitation is low because creation of the self-trapped exciton whose decay initiates the expulsion of a halogen atom requires a two-photon excitation.

The probability of a two-photon transition may be estimated using a simple physical picture [13]. The intensity I of the laser in a unit cell of material with volume $V = L^3$ for a laser wavelength λ is just

$$I = \frac{\text{energy/photon}}{\text{transit time}} \times \frac{1}{\text{area}} = m \frac{hc/\lambda}{L/(c/n)} \frac{1}{L^2}, \quad (1)$$

where m is the mean photon number and n is the index of refraction. Hence,

$$m = \frac{nIV\lambda}{hc^2}. \quad (2)$$

Assuming that the laser photons obey Poisson statistics, the probability of n photons being simultaneously in a volume of space having an average photon occupation number m is

$$P_n = \frac{m^n}{n!} e^{-m} \approx \frac{m^n}{n!}, \quad m \ll n. \quad (3)$$

where m is given by eq. (2). For KCl and an XeCl laser, band-to-band excitation requires $n = 2$, and, for a laser with the intensity typical of the KCl experiments and a unit cell ~~64~~ ³² Å on a side, [14] we find $P_2 \approx 10^{-7}$. Thus, even at the highest laser intensities used in these experiments, the density of electronic excitation remains low in KCl; to reach high excitation density, say, $P_2 \approx 10^{-3}$, one would have to increase the laser intensity by four or five orders of magnitude!

Therefore, at low excitation density and in solids with strong electron-lattice coupling, we should expect to see only ablation of ions and atoms just as in the case of photon-stimulated desorption initiated by *single-photon* band-to-band transitions [15]. In this work, it was demonstrated that progressive radiation damage eventually extinguishes the K^* emission from excited atoms, probably by resonant ionization at the Fermi level of the metallized surface rises into the insulator band gap. Indeed, as shown in fig. 2, the desorption yield, when scaled as a function of absorbed photon dose required to produce the band-to-band transition, is qualitatively similar for both laser and vacuum-ultraviolet irradiation of alkali halides. The difference in total required dose between the two cases – approximately an order of magnitude when corrected for the finite reflectivity of the surface – may reflect the change in absorption for the laser photons once the surface begins to decompose. Such a change in *single-photon* absorption would signal the onset of a regime in which ablation yield is a strong nonlinear function of laser fluence or intensity.

In the niobates, laser ablation appears to result from a mixture of electronic and thermal effects, possibly changing from electronic to thermal within the same laser pulse. As long as the laser fluence remains below the threshold for plasma ignition, the primary process of particle ejection in the niobates, as in the alkali halides, is the energetic expulsion of the non-metallic component of the compound, in this case oxygen. In LiNbO_3 , for example, measurements of Nb^+ and O^+ yields before and after subthreshold laser irradiation show a depletion of O ions in the ablation pit; scanning electron microscopy confirms that there is melting and refreezing subsequent to laser irradiation,

typical of a partly metallic overlayer [7,8]. At low fluences, below the point at which the process is probably electronic in origin. If one can consider the behavior of LiNbO_3 as a guide, the initial band-to-band excitation transfers electronic charge to the Nb ions, creating Nb^{4+} small polarons [16]. These small polarons cause localized distortions in an ionic lattice which are sufficient to initiate nuclear motion in a lattice as near the edge of stability as a ferroelectric. Once such an Nb-polaron reaches an alkali site, there is little resistance to further motion because of the soft-mode relaxation of the lattice [16]. When this happens near the surface, particle emission begins.

As more and more laser energy is absorbed by band-to-band transitions, the relaxation by electron-lattice coupling heats the crystal, increasing the optical absorption [17] and initiating the nonlinear process of ablation. At these higher fluences, thermal effects dominate the process, and indeed, there is evidence from the shape of yield vs intensity curves for KNbO_3 that melting occurs for laser pulse energies in the range of 80–100 mJ [8]. The changing balance between the thermal and electronic ablation processes can be inferred from the measurements of $-dY(K^*)/dN$ shown in fig. 5. ~~This measurement makes it clear that~~ the nonlinear destruction of the surface is dramatically hastened once the laser fluence exceeds a level of approximately $3\text{--}5\text{ J cm}^{-2}$.

Another contrast between halides and oxides is that in the former, we observe only atomic and ionic emission at these fluences, while in the latter, neutral molecules and molecular ions are also ablated. ~~Although the amount of supporting data available is not overwhelming, one could argue that molecular emission requires the participation of at least the nearest neighbors in the lattice during particle emission, and that this should be a general phenomenon in solids which have moderate-to-weak electron-lattice coupling. For example, one of the few ablation experiments on oxides, emission of vibrationally excited, but translationally cold, AlO was observed in ultraviolet laser ablation of Al_2O_3 [18].~~

5. Conclusions

We have measured the ultraviolet laser ablation yields from KCl and KNbO_3 for a photon energy of 4 eV over a range of intensities up to $3 \times 10^{14}\text{ W m}^{-2}$. The two samples studied represent materials with strong and intermediate electron-lattice coupling, respectively, ~~and exhibit differing physical mechanisms leading to nuclear motion and particle emission. The experimental evidence suggests that the laser ablation mechanism observed in the KCl experiments at low electronic excitation density is, at least in its initial~~ seems to be,

stages, the same as that found in vacuum ultraviolet laser ablation of oxides. In the former, the process is initiated by two-photon Landau band transitions, followed by its decay into F-H-center pairs. Only ions and atoms are observed as ablation products. In the oxide material, on the other hand, the reduced electron-lattice coupling strength leads to molecule emission, while the high local density of electronic excitation produces a nonlinear dependence of the surface metalization rate. Both of these features are evidence for the role of laser-induced electronic defects in the ablation process, even at the highest laser intensities. ~~where thermal effects apparently dominate.~~

Acknowledgements

We thank Dr. H. Hesse (Osnabrück) for the preparation of the KNbO_3 samples and Profs. H. Donnerberg (Osnabrück) and N. Itoh (Nagoya) for illuminating discussions.

References

- [1] For recent examples of many of these applications, see: Proc. spring 1990 meeting of the Europ. Mat. Res. Soc., eds. I.W. Boyd, E. Fogarassy and M. Stuke, Appl. Surf. Sci. 46 (1990).
- [2] For a recent review of laser-induced desorption and ablation of halides and fluoride materials, see: T.A. Green and E. Matthias, Proc. 4th Int. Conf. on Desorption Induced by Electronic Transitions; DIET-IV, eds. G. Betz and P. Varga (Springer, Berlin, 1990) p. 112.
- [3] See, for example, the review by W. Ho, *ibid.*, p. 48.
- [4] Y. Nakai, K. Hattori, A. Okano, N. Itoh and R.F. Haglund, Jr., Nucl. Instr. and Meth. B58 (1991) 452.
- [5] M. Eyett and D. Bäuerle, Appl. Phys. Lett. 51 (1987) 2054.
- [6] R.F. Haglund, Jr., P.H. Bunton, K. Tang and L.J. Wang, Proc. SPIE 1441 (1991) Page?...
- [7] K. Tang, M. Affatigato, R.F. Haglund, Jr. and C.H. Chen, submitted to Appl. Phys. Lett. (1991). ... Please update ...
- [8] R.F. Haglund, Jr., M. Affatigato, J.H. Arps, K. Tang, A. Niehof and W. Heiland, Mater. Res. Soc. Symp. 201 (1991) ... page? 507.
- [9] A. Schmid, P. Bräunlich and P.K. Rol, Phys. Rev. Lett. 35 (1975) 1382.
- [10] J. Wen, L. Wang, Y. Tang and H. Wang, Appl. Phys. Lett. 53 (1988) 261.
- [11] S. Pantelides, Phys. Rev. B11 (1975) 2406.
- [12] H.J. Donnerberg, S.M. Tomlinson and C.R.A. Catlow, J. Phys. Chem. Solids 52 (1991) 201.
- [13] D.L. Andrews, Am. J. Phys. 53 (1985) 1001. year?...
- [14] Charles Kittel, Introduction to Solid-State Physics, 6th ed. (Wiley, New York, 1986) p. 71. We have in fact used a volume which is $16 \times 6.4\text{ Å}$ on a side, on the grounds ~~that the creation of a self-trapped hole in a unit cell can~~ since

-1

-1

-2

Change to CLWD ref.

-1

- ~~created~~ ^{either}
be caused either by creating a hole on a Cl ion in the unit cell or on a Cl ion in the neighboring cell.
[15] P.H. Bunton, R.F. Haglund, Jr., D. Liu and N.H. Tolk, ~~to be published~~ ^{submitted to Phys. Rev. B. Please update?} ●●●
[16] O.F. Schirmer, O. Thiemann and M. Wöhlecke, J. Phys. Chem. Solids 52 (1991) 185.

[17] D. Redfield and W.

4566

[18] R.W. Dreyfus, R. Ket,
Lett. 49 (1986) 1478.

?

PRODUCTION OF MOLECULAR CLUSTERS OF LITHIUM NIOBATE BY ULTRAVIOLET AND VISIBLE LASER ABLATION

II. B. 3

R. F. HAGLUND, Jr.,* K. TANG,* and C. H. CHEN**

*Haglund and Tang Department of Physics and Astronomy, Vanderbilt University,
Nashville, TN 37235

**Chen Chemical Physics Section, Oak Ridge National Laboratory, Oak Ridge, TN 37831

ABSTRACT

We have investigated laser ablation of molecular ions from the ferroelectric LiNbO₃ at 532, 355 and 266 nm, comparing the effects of changing wavelength and intensity. The time-of-flight spectra show great sensitivity to the onset of plasma formation. Just below the plasma formation threshold, production of the monomer, dimer and trimer negative molecular ions were observed. Possible implications for thin-film deposition processing are discussed.

Introduction and Motivation

Laser ablation is the basis for a number of thin-film growth, interconnect and waveguide processing technologies.[1] In many of these applications, laser ablation may be compete with or complement traditional ion-beam techniques such as ion-beam sputtering and rf sputter deposition. However, in spite of the scientific and technological importance of laser-ablation thin-film deposition, relatively little research has been devoted to microscopic physical mechanisms of laser ablation from ferroelectrics, and there exist almost no studies correlating the parameters of laser ablation to quality of film growth.[2]

We have recently shown in studies of uv laser ablation from LiNbO₃ [3] and KNbO₃ [4] that molecules are desorbed intact at low fluences. The ability to deposit molecules or molecular clusters may have important implications for the growth of uniform, dense thin films on appropriate substrates. In this paper, we present studies of laser ablation of molecular ions and clusters from LiNbO₃. Our motivation is both technological and scientific: In thin-film growth, one wants to identify the regime of laser ablation which produces the most uniform possible thin-film deposition of these materials. From the perspective of optical physics, on the other hand, we are interested in the ablation mechanism as changes in laser wavelength and intensity move us from low to high optical absorption and local density of electronic excitation.

Experimental Apparatus and Measurements

The experimental setup is shown schematically in Figure 1. Samples of Y-cut LiNbO₃ crystals from Crystal Technology were mounted in an vacuum chamber with a base pressure of 10⁻⁹ torr provided by a Balzers turbomolecular pump. The ablating laser was a Quanta-Ray Nd:YAG DCR-2A oscillator-amplifier, with an harmonic generator-separator combination producing intense pulses at the second (532 nm), third (355 nm) and fourth (266 nm) harmonics of

the infrared fundamental wavelength (1064 nm). The pulse length varies slightly for the three harmonics, ranging from 6 ns at 532 nm to about 4 ns FWHM at 266 nm. The laser spot was annular with inner and outer diameter of 4.0 and 7.5 mm, respectively; more than 95% of the laser light is concentrated in an area of approximately 0.3 cm². In some cases, the laser light was focused onto the target at normal incidence by a 50-cm focal length lens to form a focal spot which varied according to the distance between lens and target.

Positive and negative ions desorbed from the surface were accelerated to an energy of up to 2.5 keV, traversed an 85-cm field-free drift tube, and were stopped in an aluminum foil. Secondary electrons from the stopped ions were detected in a Johnston multiplier structure. Single-shot spectra were recorded for the most part using a Hewlett-Packard 52401A digitizing oscilloscope. The time-of-flight spectra were precisely calibrated on a Tektronix RTD720 real-time-digitizer using both the Li⁺ ion from lithium niobate (coming 3.7 μ s after the zero-time start signal) and K⁺ from pure KI crystals (8.66 μ s). The mass identification was corroborated by checking the isotope flight times and relative abundances for these two elements.

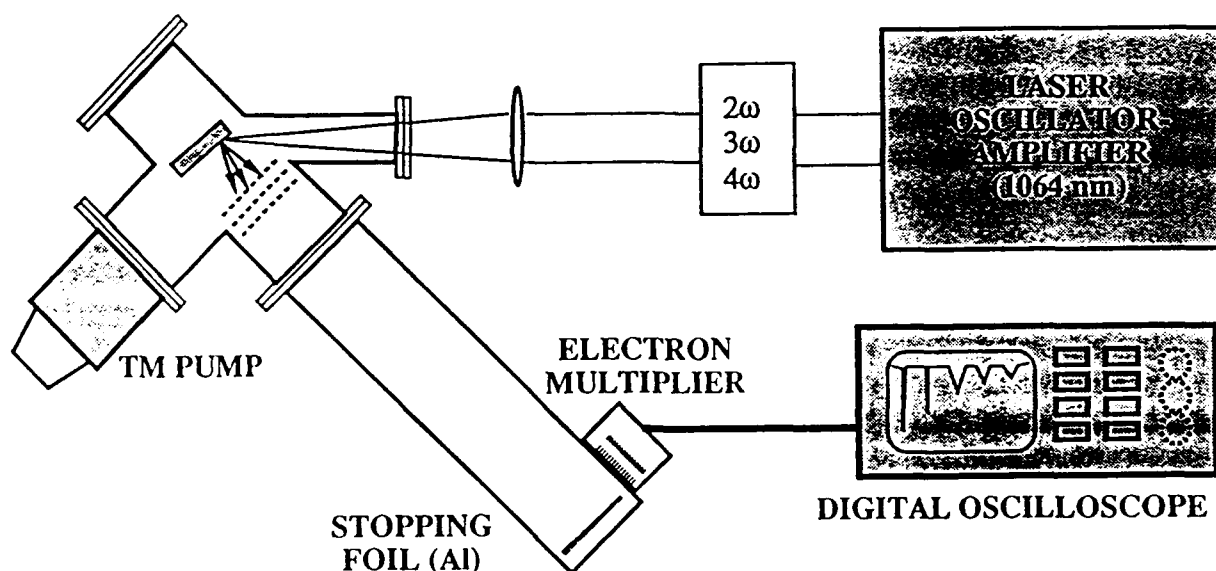


Figure 1. Apparatus for uv laser ablation measurements.

Figures 2 and 3 show typical time-of-flight (ToF) spectra obtained by recording the output of the Johnston multiplier for a single laser pulse. The positive ion spectra frequently showed K⁺ ions, apparently stemming from surface contamination of the sample. The spectral feature with regularly spaced peaks around mass 224 a.m.u. (22 μ s) appears to be due to niobium oxide clusters; the peak corresponds to Nb₂O₅⁺, the maximally valent niobium-oxide compound. The spacing of the peaks corresponds to a mass difference of 16.1 a.m.u. These clusters may also come from oxygen clusters breaking up from a parent cluster in the ToF tube. We observed some differences between the positive-ion spectra taken at different ablation wavelengths. For example, for the third harmonic at λ = 355 nm, the cluster peaks below mass 224 are suppressed and a strong Nb₂O⁺ peak appears at 19.9 μ s.

In the negative-ion spectra, the electrons provide the "zero time" signal, and are also an important indicator of the onset of plasma formation at higher laser intensities. The most notable feature of the negative-ion ToF spectra is the appearance of $(\text{LiNbO}_3)^-$ dimers and trimers, although there is also a strong O^- peak at about 6 μs . This identification of the lithium niobate molecular-ion clusters is confirmed by verifying that the time of arrival goes up as the square root of the mass ratio. Interestingly, the dimer and trimer peaks are most pronounced in the 266 nm ablation, and appear as well-defined peaks only at the lowest fluences for 355 nm ablation.

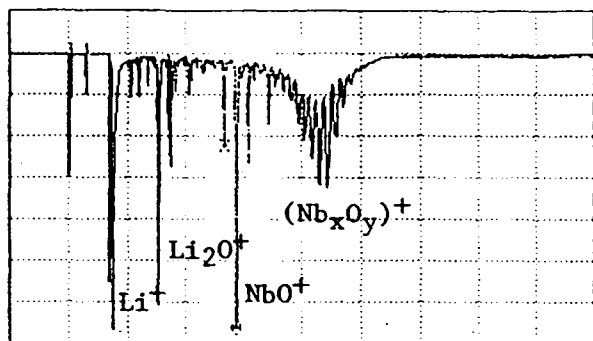


Figure 2. Positive-ion time-of-flight spectrum from 266-nm laser ablation of LiNbO_3 . The vertical scale is 5 mV per division; the horizontal scale is 5 μs per division.

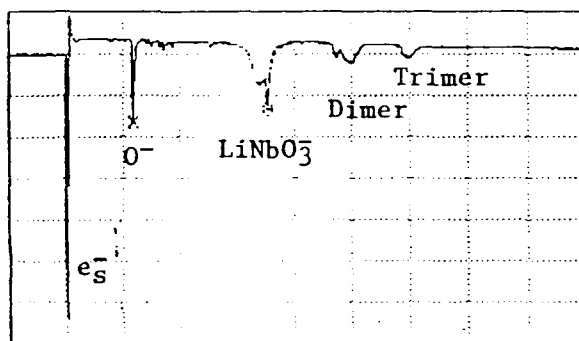


Figure 3. Negative-ion time-of-flight spectrum from 266-nm laser ablation of LiNbO_3 . As in Fig. 2, the vertical scale is 5 mV/division; the horizontal scale is 5 μs /division.

The optical response and the character of the laser ablation can be expected to change based on the relationship between laser wavelength and optical gap. As shown schematically in Figure 4, the bulk conduction-band edge of LiNbO_3 lies almost exactly 4 eV above the bulk valence-band edge; the cross-hatched region below the band edge indicates the energy levels of excitons, impurities and possible surface states. It is clear from this diagram that the 532-nm light induces

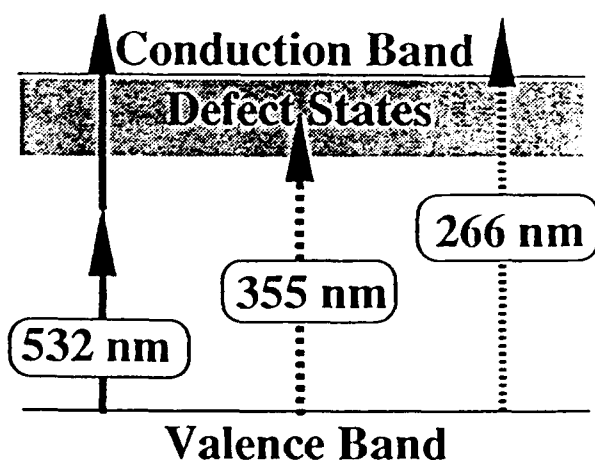


Figure 4. Energy level diagram for laser ablation at the three wavelengths used in these experiments.

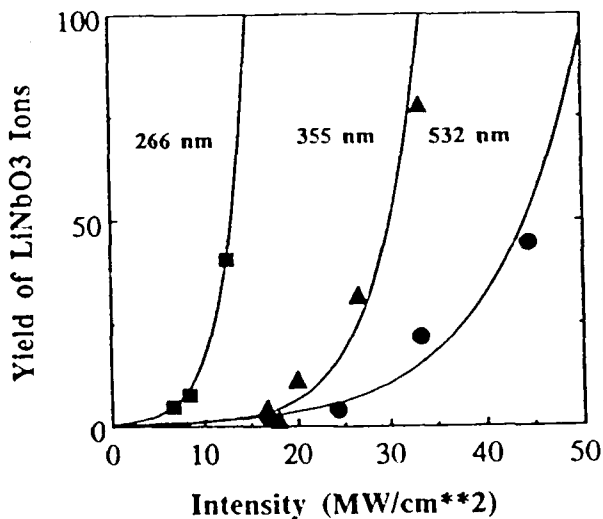


Figure 5. Yield of LiNbO_3^- vs. laser intensity for wavelengths of 266, 355 and 532 nm.

interband transitions only by two-photon excitation, while the 355 nm light may cause electronic transitions leading to ablation by excitation of surface states or defects and the 266 nm light produces interband transitions by a single-photon excitation. This leads us to the expectation, borne out in Figure 5, that the thresholds and intensity dependence of the ablation yields will vary for the three wavelengths. Note in particular the rough correlation between the intensity dependence of the yields for the two-photon-induced laser ablation at 532 nm and the single-photon laser ablation case at 266 nm.

In Figure 6, we compare the time-of-flight spectra for the negative ions recorded at all three laser wavelengths at low, intermediate and high intensities. The broadening of the electron pulse and the other $(\text{LiNbO}_3)_n^-$ peaks is quite pronounced as the intensity increases, indicating the onset of plasma formation. Moreover, above the threshold for plasma formation, the monomer, dimer and trimer peaks all begin to show contributions from both fast- and slow-velocity components. This probably indicates two distinct ablation mechanisms at work at the highest intensities, one related to plasma processes and one arising directly from the laser-surface interaction. The other feature of the negative-ion spectra indicating wavelength-specific electronic effects is the changing behavior of the O^- peak as a function of ablating laser wavelength. No convincing evidence for O_2^- ablation was seen.

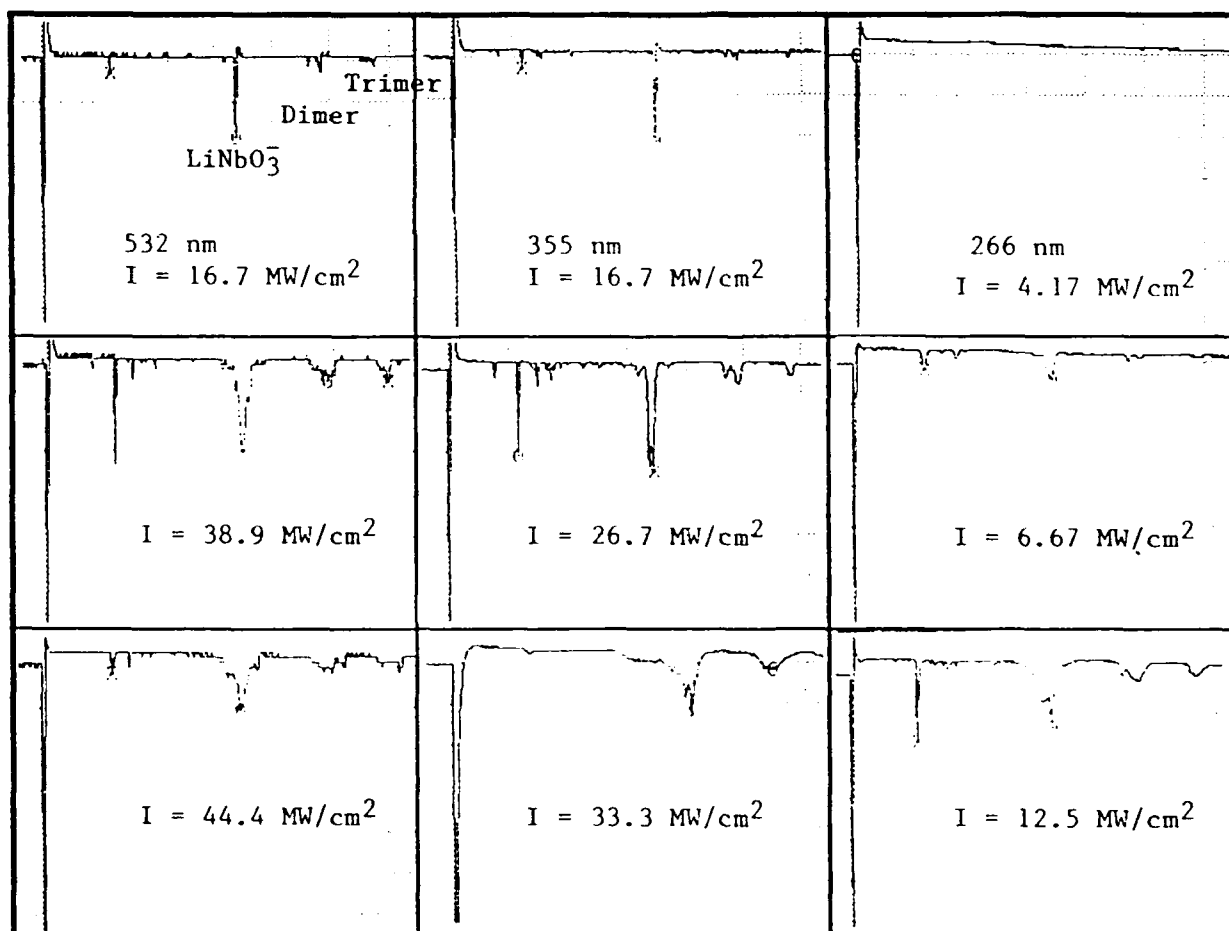


Figure 6. Comparison of negative ion spectra from lithium niobate at laser wavelengths of 532, 355 and 266 nm (left to right) and at low, moderate and high intensities (top to bottom). Vertical and horizontal scales are the same in all the spectra; peaks of interest are identified.

From the negative-ion spectra, the best behavior of LiNbO_3 clusters are those formed for ultraviolet laser ablation (266 nm). There one has significant yield even at low laser fluences, and the complications of other atomic species or the problems of broad velocity groups seem to be the least noticeable.

Discussion: Mechanisms of Ablation

In laser ablation by nanosecond pulses, the energy of the incident photons is deposited by electronic excitation; nuclear motion leading to particle emission occurs by electron-lattice relaxation following the initial excitation. The details of this nuclear motion vary with local density of electronic excitation as well as with the electron-lattice coupling.[5] In ferroelectrics, the previous laser irradiation history of the surface also changes the ablation yield characteristics, probably due to formation of color centers and/or other long-lived electronic defects. It is important to bear in mind that, for nanosecond pulses, both the relaxation processes and the formation of electronic defects can occur before the exciting laser pulses is over.

The characteristic features of laser ablation from specific materials are intimately connected to the relative energies of laser photons and the bulk band-gap energy. Lithium niobate is a ilmenite structure with about one-third metal-ion vacancies.[6] The valence band of LiNbO_3 is formed principally from the 2p orbitals of the oxygen ions; the conduction band is made up primarily of the Li and Nb orbitals. Both the linear and nonlinear optical response of the materials is primarily *interatomic*. [7] Below the threshold for plasma formation, particle emission results indirectly from the creation of holes on the oxygen ions and the consequent transfer of electronic charge to the metal ions. The initial band-to-band excitation transfers electronic charge to the Nb ions, creating creating Nb^{4+} small polarons.[8] These small polarons cause localized distortions in an ionic lattice, distortions which are sufficient to initiate nuclear motion and provide the driving force for the initial ionic motion and, ultimately, particle ejection from the surface.

In our experiments, the local density of electron-hole (e-h) pairs is low for 532-nm irradiation, because the probability for two-photon band-to-band transitions is of order 10^{-8} and only a relatively small fraction of the surface and near-surface ions are affected by laser irradiation, at least in the early stages. The local density of e-h pairs is modest for 355 nm irradiation, since it can only excite surface or defect states; however, the efficiency for desorption may be high in this case precisely because so many of the photoabsorption events occur in the near-surface region. Finally, the local density of e-h pairs is high for 266 nm irradiation, because the probability for e-h pair creation is essentially unity.

As more and more laser energy is absorbed by one- or two-photon band-to-band transitions, relaxation by electron-lattice coupling and absorption by laser-induced defect centers heats the crystal, increasing the optical absorption [9] and initiating the nonlinear process of ablation [10]. At these higher fluences, thermal effects dominate the process and, as we have shown for KNbO_3 , catastrophic destruction of the surface proceeds rapidly. At this point in the laser ablation process, the rubric "thermal" is usually applied and may well be justified.

However, it is essential to realize that, even in this case, significant electronic influences remain from the earliest stages of laser ablation, as shown by the different yield.

With respect to thin-film deposition of lithium niobate, the identification of the ablation characteristics producing a preponderance of molecular clusters is of particular interest. These could, for example, be mass selected to generate a beam of LiNbO_3 clusters for subsequent "cluster assembly" of the thin film, a process which has been shown already to produce superior results in many thin-film fabrication processes. Another possible application is in the area of optical interconnect technology, where one wishes to attach oxide fibers to LiNbO_3 waveguide or other devices. Interconnects "drilled" by laser ablation would be problematical if, as we have shown to be the case at intensities above a few $\text{GW}\cdot\text{cm}^{-2}$, the surface becomes metallized by the preferential ejection of oxygen atoms or ions. On the other hand, ablation of molecular clusters should leave behind a surface which is essentially stoichiometric, permitting direct attachment of fibers without any significant optical losses. Verification that the LiNbO_3 surface indeed remains stoichiometric following ablation is a high priority for future experiments.

Acknowledgements

This research was supported in part by the Office of Naval Research through the Medical Free-Electron Laser Program of the Strategic Defense Initiative Organization and by the SURA/ORAU/ORNL Summer Research Cooperative program. The Oak Ridge National Laboratory is supported in part by the Division of Materials Science, U. S. Department of Energy, under contract DE-AC05-84OR21400 with Martin-Marietta Energy Systems, Inc.

References

1. For recent examples of laser ablation in thin-film deposition, see proceedings of the spring 1990 meeting of the European Materials Research Society, eds. I. W. Boyd, E. Fogarassy and M. Stuke, *Appl. Surf. Sci.* **46** (1990).
2. A brief search of several relevant journals turned up two papers: one describing excimer-laser-ablation assisted deposition of PbTiO_3 , by H. Tabata *et al.*, *Appl. Phys. Lett.* **59** (1991) 2354; and another describing deposition of BaTiO_3 using a pulsed ruby laser, by S. B. Ogale *et al.*, *Ferroelectrics* **102** (1990) 85.
3. R. F. Haglund, Jr., K. Tang, M. Affatigato and C. H. Chen, *Proceedings of the CLEO-QELS 1991*, OSA Technical Digest Series **10** (1991) 258.
4. R. F. Haglund, Jr., M. Affatigato, J. H. Arps, K. Tang, A. Niehof and W. Heiland, *Proc. MRS* **201** (1991) 527.
5. Y. Nakai, K. Hattori, A. Okano, N. Itoh and R. F. Haglund, Jr., *Nucl. Instrum. Methods in Phys. Res. B* **58** (1991).
6. R. S. Weiss and T. K. Gaylord, *Appl. Phys. A* **37** (1985) 191-203.
7. M. E. Lines, *Phys. Rev. B* **41** (1990) 3372-3382.
8. O. F. Schirmer, O. Thiemann and M. Wöhlecke, *J. Phys. Chem. Solids* **52** (1991) 185.
9. D. Redfield and W. J. Burke, *J. Appl. Phys.* **45** (1974) 4566.
10. R. F. Haglund, Jr., J. H. Arps, M. Affatigato, K. Tang, A. Niehof and W. Heiland, *Nucl. Instrum. Meth. in Phys. Research B*, in press.

Characterization of surface defects by means of laser-induced Ga⁰ emission from GaP surfaces

Ken Hattori†, Akiko Okano†, Yasuo Nakai†, Noriaki Itoh† and Richard F Haglund Jr‡

† Department of Physics, Nagoya University, Furo-cho, Nagoya 464-01, Japan

‡ Department of Physics and Astronomy, Vanderbilt University, Nashville, Tennessee 37235, USA

Received 26 February 1991, in final form 10 June 1991

Abstract. We have carried out high-sensitivity measurements of the emission of Ga⁰ neutrals from a clean GaP(110) surface induced by laser pulses of subgap photon energies. We found that, below a sharp threshold laser fluence for evolution of surface damage, the emission yield of Ga⁰ atoms decreases, following two exponential functions, with repeating pulses of the same fluence. These two decays are ascribed to the ejection initiated by defects of two different types. These measurements are shown to be useful for characterizing defects of extremely small concentration.

There is increasing interest in identifying, characterizing and controlling small concentrations of surface defects over a relatively large area in electronic and photonic materials. This capability is important both for technological reasons, as in the fabrication of multiple-quantum-well devices, and for basic scientific studies of surface electronic structure. However, most current techniques for microscopic surface analysis do not have this capability. For example, scanning tunnelling microscopy [1] has an extremely high spatial resolving power but can only evaluate defects quantitatively over a relatively small surface area.

In this paper we report the first demonstration that laser-induced particle emission monitored by resonance ionization mass spectroscopy successfully differentiates between several types of defect in the topmost atomic layer of a GaP specimen. In addition, we show that certain of these defects can be eliminated from the surface by prolonged irradiation of the surface without producing crystallographic damage. Finally, we show that this same technique is able to provide significant clues to the nature of the defects responsible for laser-induced surface damage above a certain fluence threshold.

The specimens used in this experiment were n type (S-doped) GaP single crystals measuring 10 mm × 10 mm × 2 mm. The wide face parallel to the (110) plane was mechanically polished, chemically etched and finally cleaned by Ar⁺ ion bombardment and thermal annealing in ultra-high vacuum (base pressure, less than 2×10^{-8} Pa) [2, 3]. After cleaning, the surface showed a clear (1 × 1) low-energy electron diffraction (LEED) pattern and no Auger signal due to surface contaminations was detected. The surface was bombarded by an excimer-pumped dye laser at a wavelength of 600 nm and a pulse width of 28 ns. The laser beam of this wavelength is capable of exciting the

electrons in the valence band to the unoccupied surface states located 0.3 eV below the conduction band [4] but not of inducing band-to-band transitions. Hence the heating of the surface layer is extremely small [5]. This 'pump' laser beam, which was made as uniform as possible using apertures and lenses, was incident on the specimen at an angle of 45° from the surface normal. The beam spot on the surface was 0.5 mm in diameter.

Emitted neutrals were observed with high sensitivities using the resonance ionization spectroscopy (RIS) technique [6] as reported elsewhere [7]. Frequency-doubled light from a second excimer-pumped dye laser was used to excite the $^2P_{1/2}$ to $^2D_{3/2}$ transition of Ga neutrals, while the fundamental beam from the same laser (at 574.82 nm) ionized excited Ga neutrals. The RIS laser was triggered about 5 μ s after the pump (desorption) laser and passed parallel to the surface at a distance of 2.0 mm. Ga^+ ions were detected with a channeltron, the signals of which were stored in a microcomputer.

We measured the Ga^0 yield from the GaP(110) surface induced by repeated irradiation with laser pulses of a fixed laser fluence on the same spot. Figures 1(a) and 1(b) show typical results for the yield Y of Ga^0 neutrals per pulse as a function of the number n of laser shots at laser fluences of 1.0 J cm^{-2} and 1.2 J cm^{-2} , respectively. A previously unirradiated spot of the sample was bombarded repeatedly by laser beams of each fluence. The fluctuation of the fluence of the laser pulses at each 'fixed' fluence was about 5%. As seen from figure 1(a), Y decreases initially with increasing n , approximately following an exponential relation, and reaches nearly a constant value, which decreases very slowly and lasts over 8000 pulses. The ordinate is given in arbitrary units, of which unity approximately corresponds to the removal of atoms in a 10^{-6} monolayer. We refer to the decreasing component as the A component and the nearly constant component as the S component. The LEED pattern obtained on the laser-focused spot was unchanged after 8000 pulses.

On the other hand, above a fluence of 1.2 J cm^{-2} , a rapid increase in Y with increasing n is seen as shown in figure 1(b). We note a remarkable difference in the Y - n relation by changing the laser fluence by only 20% across a critical fluence I_D of 1.1 J cm^{-2} . Above the critical fluence, each spot of the LEED pattern became weaker after several hundreds of laser shots. Thus we ascribe the increase in Y with increasing n (referred to as the D component) to the evolution of damage on the surface. We note that at the initial stage of evolution the number of atoms emitted by each laser pulse is small, nearly of the order of 10^{-6} monolayer, and that the number of atoms starts to increase if initial damage is produced on the surface. Thus it is clear that the mechanism of initial damage occurs without emitting a large number of atoms and hence is purely electronic.

Since the emission yield of Ga atoms is reduced by repeating laser pulses, even though the surface remains undamaged, the A component in the Y - n relation is undoubtedly due to defect-initiated particle emission. We assign also the S component to defect-initiated particle emission for the following reasons. First no change was observed in the LEED pattern after 8000 shots. Second, no increase in Y was observed even at $n = 8000$, while an increase in Y is seen at $n = 20$ for a fluence larger by only 20%. Suppose that both the S and the D components were due to the evolution of the damage on the surface, then we should see a rapid increase in the probability of destruction of perfect sites as the laser fluence is increased; indeed the yield should follow about the thirtieth power of the laser fluence if Y is a power function of the laser fluence. Since such a high power dependence is unrealistic, we consider that S emission and damage mechanisms are distinct. Thus it is clear that two completely different types of defect can be differentiated by measuring the dependence of the yield on the number of shots.

The number $dN_E(n)/dn$ of atoms emitted by a laser pulse for the A and S components can be fitted to exponential functions $Y_0 \exp(-\alpha n)$, with $Y_0 = 3.0$ (arbitrary units), $\alpha =$

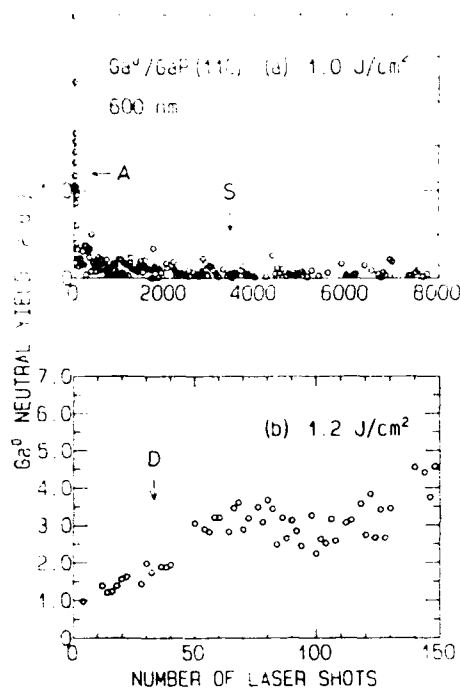


Figure 1. Plots of Ga^0 yield from the GaP(110) surface as a function of the number of laser shots at fluences of (a) 1.0 J cm^{-2} and (b) 1.2 J cm^{-2} . A new spot was exposed to the laser beam at the start of the experimental run for each fluence and the same spot was irradiated repeatedly. Three typical features of the Ga^0 yield as a function of the number of shots, decreasing, constant and increasing, are referred to as A, S and D components, respectively.

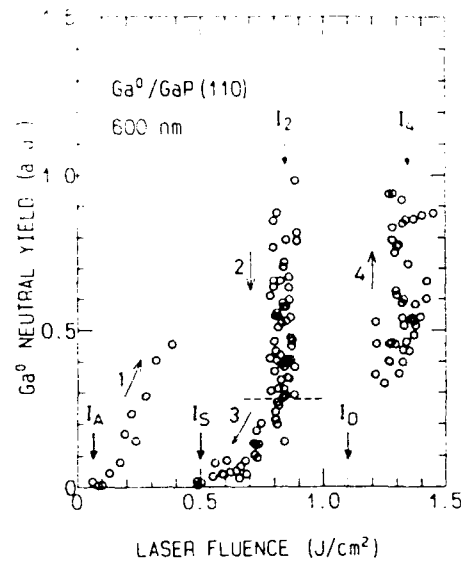


Figure 2. Dependence of Ga^0 yield on the laser fluence for sequential irradiation of the GaP(110) surface: data 1, the laser fluence was increased gradually; data 2, the laser fluence was kept constant at $I_2 = 0.85 \text{ J cm}^{-2}$; data 3, the laser fluence was decreased gradually; data 4 the laser fluence was kept constant at $I_4 = 1.35 \text{ J cm}^{-2}$. The arrows beside the plots show the direction of the change by the sequential irradiation. The threshold laser fluences I_A , I_S and I_D (see text) are indicated by vertical arrows.

1.1×10^{-2} , and $Y_0 = 0.12$ (arbitrary units), $\alpha = 7 \times 10^{-5}$, respectively. If the emission of atoms is initiated by defects, the number of atoms emitted per laser pulse is proportional to the defect concentration on the surface: $dN_E(n)/dn = \eta N_D(n)$, where η is the yield and $N_D(n)$ is the number of defects after the n th shot. It follows that $N_D(0) = Y_0/\eta = (Y_0/\alpha)(\alpha/\eta)$. We obtained the ratio for Y_0/α for the S and A components to be 6.3.

The laser-induced particle emission varies superlinearly with laser fluence [8, 9]. Therefore, one can define an apparent threshold laser fluence above which the particle emission is observed. In order to find the threshold laser fluence for particle emission initiated by each type of defect, we carried out an experiment, for which the results are shown in figure 2. In this experiment we irradiated a new spot on the surface starting from low laser fluences and obtained Y as a function of fluence, as shown by data 1. The threshold laser fluence I_A of 0.07 J cm^{-2} can be ascribed to the A component. Next we repeated irradiation at fluences near $I_2 = 0.85 \text{ J cm}^{-2}$, where Y was decreased as shown by data 2, removing the A component remaining after irradiation at low fluences. When

Y became almost constant, we reached the threshold fluence. Below a threshold laser fluence of $I_0 = 0.5 \text{ J cm}^{-2}$, the yield vanished, as shown by data 3. We consider that this is the threshold fluence for the S component. When the laser fluence was fixed at $I_0 = 1.55 \text{ J cm}^{-2}$ above I_0 , Y was increased with increasing n , as shown by data 4. I_0 can be regarded as the threshold fluence for the D component.

Since the A component is eliminated at the lowest laser fluence, we suggest that it is due to elimination of an adatom-type defect, i.e. a defect which, after the emission of Ga atom, leaves either the perfect configuration or another defect configuration with a higher stability against laser irradiation emerges. In this case, $N_D(0) = Y_0/\alpha$ and hence $\alpha/\eta = 1$. If $\alpha/\eta = 1$ holds for the S component, $N_D(0)$ for the S component is higher than for the A component. Alternatively, if we consider that $\alpha/\eta < 1$ for the S component, the defect concentrations of the S component can be the same and even less than those for the A component. $\alpha/\eta < 1$ may result if particle emission arises from the kink sites of steps; removal of an atom transfers the defect site to the nearest-neighbour site, keeping the structure of defects unchanged until another type of defect emerges. We are tempted to take the latter alternative and refer to the defect that gives rise to the S component as a step-type defect which, after the emission of a Ga atom, leaves a site which has nearly the same stability as before the emission. If the particle emission is initiated from a vacancy cluster, neighbouring sites are destroyed and hence the size of the cluster increases as irradiation proceeds. Therefore the D component can be ascribed to vacancy-initiated particle emission, although the possibility that the D component arises from defect-free sites cannot be excluded.

We did not measure the ejection of P atoms, for which no dye laser for RIS is available at present. No other technique can detect the emission of P atoms with the sensitivity at which Ga atoms are detected. Since the yield continues to decrease, we presume that the stoichiometry is maintained on the surface to a certain degree, and hence that ejection of either Ga or P atoms, whichever is strongly bonded, will be the rate-determining process.† We expect that nearly the same amounts of Ga and P atoms are ejected by a laser pulse and no substantial difference should exist whether measurements of Ga or P atoms are carried out.

Defect-initiated ejection of atoms is induced if the interaction of electrons and holes with defects causes substantial bond weakening or causes asymmetrical lattice relaxation, leading eventually to atomic ejection [9]. Local lattice relaxation around defects by trapping an electron and/or hole in the bulk of solids is well known [10]. Because of the superlinear dependence of the emission yield on the laser fluence, we should assume that at least two excitation events are needed for particle emission. Therefore we suggest that localization of two electron-hole pairs at defect sites causes Ga^0 emission. The occupation of two holes weakens the binding of the emitted atom, and the electronic excitation energy possessed by two electron-hole pairs is converted to the lattice energy needed for the emission of the atom. The process of two-hole localization can be regarded as a negative- U interaction, in which two holes can be localized at a defect site when $(U - E_{\text{LR}}) < 0$, where U is the on-site hole Coulomb repulsion energy and E_{LR} is the lattice relaxation energy [11]. The superlinear relation between emission yield and laser fluence has been explained in terms of the screening of Coulomb repulsion [12] and of the degeneracy of the electron-hole plasma [13]. In each case a larger laser fluence is needed to emit atoms from the defect sites for which the negative- U attractive potential is smaller.

† If the stoichiometry is changed, the yield is considered to increase as is the case above the threshold.

Table 1. A Born-Haber cycle describing the two-hole mechanism of Ga⁰ neutral emission: Pt, perfect lattice; $2E_{\text{gap}} = U = 2E_{\text{el}} = E_{\text{LR}} = E$

Pt $\rightarrow 2e + 2h$	$2E_{\text{gap}}$
Defect + $2h \rightarrow (\text{defect})_2$	$U = 2E_{\text{el}}$
$(\text{Defect})_2 + 2e \rightarrow \text{Ga}^0(\text{vacuum}) + (\text{defect})_{\text{missing Ga}^0}$	$-E_{\text{LR}}$
$\text{Ga}^0(\text{vacuum}) + (\text{defect})_{\text{missing Ga}^0} \rightarrow \text{Pt} + \text{defect}$	$-E_{\text{vap}}$

According to the results in figure 2, larger laser fluences are needed to emit particles initiated by defects in the order of A, S and D types, while we presume that the emitted Ga⁰ atom is bonded more strongly in this order [14]. In order to correlate the threshold laser fluence or E_{LR} with the bonding strength or vaporization energy E_{vap} , we used a Born-Haber cycle shown in table 1. Firstly, two electron-hole pairs are produced from the perfect lattice site on the surface by putting twice the surface gap energy, i.e. $2E_{\text{gap}}$, equal to the energy difference between the occupied and unoccupied surface states. Secondly, two holes are localized at a defect site; U is needed for putting two holes on the same site and twice the trapping energy, i.e. $2E_{\text{el}}$, is emitted. The electron may be loosely bound by two localized holes. Thirdly, the two-hole and two-electron localized state described above relaxes by ejecting Ga⁰, leaving the defect with a missing Ga⁰; here E_{LR} is gained. By putting a Ga⁰ atom back on the defect with the missing Ga⁰, the initial perfect lattice with the defect is gained at a cost of E_{vap} . Since the total energy for the cycle is zero, we obtain

$$U - E_{\text{LR}} = E_{\text{vap}} - 2E_{\text{el}} \quad (1)$$

where $E_{\text{el}} = E_{\text{gap}} - E_{\text{t}}$ is the electronic excitation energy at the defect site. E_{vap} is approximately the difference between zE_{coh} and the relaxation energy after vaporization, where E_{coh} is the cohesive energy per bond and z the number of bonds. Since E_{coh} is about 1.7 eV [15], we expect that the value of $U - E_{\text{LR}}$ can be negative. For most strongly bonded atoms, E_{vap} is larger and hence E_{LR} is smaller. This may explain the experimental results that a higher laser fluence is needed to emit atoms from adatoms, steps and vacancies in increasing order.

In conclusion, we showed that defect-initiated particle emission from the GaP(110) surface is indeed observed for laser pulses of subgap photon energies. The results can give information on extremely low concentrations on the GaP(110) surface. At least two types of defect have been distinguished by observing the variation in Ga⁰ yield as a function of repeating laser pulses of subgap energies: A type or adatom type and S type or step type. We observed also a very sharp threshold laser fluence for damage evolution, which may be ascribed to vacancy-initiated particle emission. The difference in the threshold laser fluence for ejection of defects of each type and the dependence of the yield on the number of shots are shown to be utilized for characterizing surface defects as low as 10^{-5} in concentration.

Acknowledgments

This work has been supported by Grant-in-Aid for specially promoted science of Japanese Ministry of Education, Science and Culture and by US-Japan cooperative research program of the National Science Foundation and the Japanese Society for promotion of

Science. The authors would like to express their gratitude to H Matsuoka for assistance in constructing a part of the experimental apparatus.

References

- [1] Binnig G, Rohrer H, Gerber Ch and Weibel E 1983 *Phys. Rev. Lett.* **50** 120
- [2] Van Bommel A J and Grombeen J E 1980 *Surf. Sci.* **93** 383
- [3] Kumazaki Y, Nakai Y and Itoh N 1987 *Phys. Rev. Lett.* **59** 2883
- [4] Cerrina F 1985 *Phys. Rev. B* **31** 8314
Straub D, Skibowski M and Himpel F J 1985 *J. Vac. Sci. Technol. A* **3** 1484
Straub D, Dose V and Altman W 1983 *Surf. Sci.* **133** 9
- [5] Hattori K, Nakai Y and Itoh N 1990 *Surf. Sci.* **227** L115
- [6] Hurst G S, Payne M G, Kramer S D and Young J P 1979 *Rev. Mod. Phys.* **51** 767
- [7] Yamamoto T, Hattori K, Nakai Y and Itoh N 1989 *Radiat. Eff. Defects Solids* **109** 213
- [8] Nakai Y, Hattori K, Okano A and Itoh N 1991 *Nucl. Instrum. Methods B* at press
- [9] Itoh N 1987 *Nucl. Instrum. Methods B* **27** 155, and references therein
- [10] Williams R T and Song K S 1990 *J. Phys. Chem. Solids* **51** 679
Itoh N and Tanimura K 1990 *J. Phys. Chem. Solids* **51** 717
- [11] Anderson P W 1975 *Phys. Rev. Lett.* **34** 953
- [12] Itoh N and Nakayama T 1982 *Phys. Lett.* **99A** 471
Itoh N, Nakayama T and Tombrello T A 1985 *Phys. Lett.* **108A** 480
Itoh N and Nakayama T 1986 *Nucl. Instrum. Methods B* **13** 550
- [13] Sumi H 1991 *Surf. Sci.* **248** 382
- [14] Haglund R F Jr, Hattori K, Itoh N and Nakai Y 1991 *Proc. 4th Topical Meet. on the Microphysics of Surfaces* at press
- [15] Harrison W A 1989 *Electronic Structure and the Properties of Solids* (New York: Dover)

Surface Science Letters

Effects of oxygen adsorption on laser-induced sputtering from GaP(110) surfaces

J. Kanasaki, H. Yamashita, A. Okano, K. Hattori, Y. Nakai, N. Itoh

Department of Physics, Faculty of Science, Nagoya University, Furocho, Chikuseki, Nagoya 464, Japan

and

R.F. Haglund, Jr.

Department of Physics and Astronomy, Vanderbilt University, Nashville, TN 37235, USA

Received 21 May 1991; accepted for publication 1 August 1991

We have measured the effects of submonolayer oxygen adsorption on laser-induced Ga^0 and Ga^+ emission from GaP(110) surfaces. It is found that oxygen adsorption enhances that component of the Ga^0 emission yield which decays rapidly as irradiation is repeated, but not the Ga^+ emission yield. The results are interpreted in terms of bond weakening due to the interaction of surface defects with adsorbed oxygen.

The interaction of oxygen molecules with III–V compound semiconductor surfaces has been studied extensively by many groups [1–12]. UPS studies on GaAs [1–3] have shown that oxygen molecules chemisorb dissociatively at room temperature on surface defect sites for coverages less than 0.1 ML. At low oxygen coverage, the Ga photoelectron signals are most strongly affected by oxygen. At coverages in excess of 0.1 ML, on the other hand, both As and Ga photoelectron signals are influenced by oxygen. Since the initial oxygen uptake depends on the quality of the cleavage [6], the low-coverage adsorption site has been identified as a Ga-derived surface defect. However, this has not been confirmed because it is difficult to observe photoemission directly from the defect sites on the surface, due to the small concentration of defect sites.

In this Letter, we report the effect of oxygen adsorption on the yield of Ga^0 and Ga^+ emitted from GaP(110) surfaces by repeated laser irradiation. The results show that the laser-induced Ga^0

emission is influenced by oxygen adsorption, and suggest that oxygen atoms weaken the bonding of the surface Ga atoms around defects where the initial oxygen adsorption occurs.

The correlation between the laser-induced emission and defects on surfaces has been shown by recent investigations of laser-induced ejection of Ga^0 and Ga^+ from cleaned GaP(110) surfaces at photon energies below the band gap [13,14]. These investigations have shown that, for laser fluences below 1.0 J/cm^2 , the damage or ablation threshold, the yield of Ga^0 and Ga^+ decreases rapidly from its initial value, and then continues decreasing slowly under repeated pulsed-laser irradiation on the same spot for a fixed laser fluence. Since the (1×1) LEED pattern of the GaP(110) surface does not change even after 8000 shots at this range of laser fluence, the reduction has been ascribed to the defect-initiated emission of Ga^0 and Ga^+ . Experimentally one observes a rapidly decreasing component of the yield (A), and a component (S) which de-

creases only slowly as a function of shot number. The A-component is ascribed to a defect containing a loosely bonded Ga^0 and becomes stable after elimination of a Ga atom; the S-component appears to be related to emission from kink or step sites, the number density of which remains virtually unchanged after removing a Ga atom. Thus, since the change of Ga^0 and Ga^+ emission yields Y as a function of shot number n appears to be sensitive to different types of surface defect sites, this technique may be useful for studies of the initial interaction of oxygen atoms with defect sites on compound semiconductor surfaces. The emission yield for both the A- and S-components varies superlinearly with laser fluence, exhibiting an apparent threshold laser fluence, which can also be used to characterize the defects on surfaces [15].

The pulsed lasers for exciting the surfaces ("pump" laser) and for ionizing the sputtered Ga^0 ("probe" laser) are obtained separately by excimer-laser-pumped dye laser systems, both of which generate laser pulses of 28 ns duration. The pump laser was tuned to a wavelength of 600 nm for selective excitation of electrons of the valence band to an unoccupied surface state, and was focused on a sample surface to a diameter of 0.4 mm. The fluence was varied between several tens and several hundreds of mJ/cm^2 by putting filters on the path of the laser beam. The photon energy of the probe dye laser was tuned to a half of the $^2P_{1/2}-^2D_{3/2}$ energy and the frequency-doubled beam was used for excitation and the fundamental beam for ionization of the excited atoms. Ga^+ emission yield was measured without firing the probe laser. Time-of-flight measurements were made to confirm that Ga^+ is indeed emitted. The probe laser pulse was delayed by 3.0 μs from the pump laser pulse and passed parallel to the surface at a distance of 2.0 mm. The charged particles were detected by an electron multiplier in a shielded box, placed 2.0 cm in front of the sample.

Samples of GaP(110) were etched chemically to remove damage introduced by polishing and then mounted to a Ta sample holder. Following repeated cycles of Ar^+ bombardment (1 keV, 3 $\mu\text{A}/\text{cm}^2$) at 400°C for 30 min, followed by an-

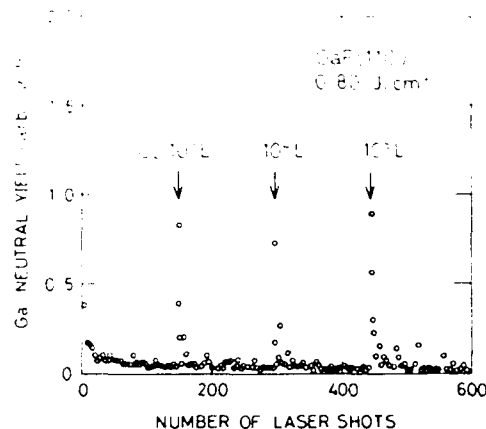


Fig. 1. The 28 ns pulsed laser-induced emission yield of Ga^0 as a function of the number of shots on clean and oxygen-exposed GaP(110) surfaces. The irradiation was started at the clean surface and oxygen was introduced as indicated in the figure at respective exposures. The laser fluence used is 0.8 J/cm^2 (below the damage threshold).

nealing at 600°C for 15 min, a sharp (1×1) LEED pattern was observed and no residual oxygen and carbon on the surface was detected by Auger electron spectroscopy (AES). Oxygen exposures were carried out at room temperature with all heated filaments in the UHV chamber turned off, so as not to produce excited oxygen molecules or atoms. Oxygen coverage was estimated from the intensity ratio of the O(KLL) and P(LMM) AES lines.

The yield versus shot number curve $Y(n)$ for Ga^0 emitted during repeated irradiation on the same spot of GaP(110) surfaces before and after exposures to 10^3 , 10^4 , and 10^5 L O_2 is shown in fig. 1. The laser fluence was 0.8 J/cm^2 , below the threshold for surface damage. Oxygen exposures were begun after the A-component of the desorption yield disappeared, while the S-component still remained. Immediately upon oxygen exposure, a rapidly-decaying component of the Ga^0 emission reappears even though the laser fluence is held constant. The threshold laser fluence above which the Ga^0 emission can be observed after 10^4 L oxygen exposure is 0.38 J/cm^2 , comparable to the threshold fluence of 0.35 J/cm^2 measured for clean, -previously unirradiated surfaces.

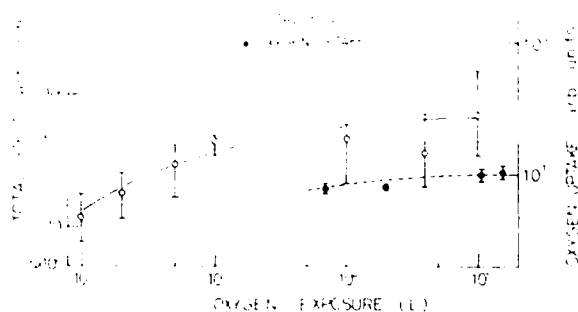


Fig. 2. The integrated Ga⁰ emission yield (open circles) of the rapidly decreasing component from oxygen-adsorbed GaP(110) surfaces as a function of exposure to molecular oxygen. The oxygen coverage determined by Auger analyses is also shown by closed circles. Lines are only guides for the eye.

The total Ga⁰ emission yield of the A-component and the oxygen coverage on the surface are displayed in fig. 2 as a function of total oxygen exposure. Oxygen coverage on the surface is not estimated for total exposures below 10⁴ L, because the coverage is below the AES detection limit. Total emission yield increases gradually with increasing total oxygen exposure, saturating around 10⁵ L. The increase in the A-component emission yield above 10⁴ L is approximately proportional to that for the oxygen coverage. The oxygen coverage at 10 arbitrary units is approximately 10⁻² monolayer.

We compared the decay of the A-component of the Ga⁰ emission yield from the cleaned GaP(110) surface with that for a surface exposed to 10³ L of oxygen under repeated irradiation with a laser fluence of 0.8 J/cm² in fig. 3. We fit the Ga⁰ emission yield curves to an exponential function of the number of shots. The decay constants for the cleaned and the oxygen-exposed surface are estimated to be 0.11 and 0.26, respectively. Although the two curves are normalized at $N = 1$, we found that the absolute area under these curves is nearly equal.

Finally, we measured the change of the emission yield of Ga⁺ induced by repeated irradiation of cleaned and oxidized GaP(110) surfaces. Fig. 4 shows the changes of the Ga⁰ and of Ga⁺ emission yields induced by repeated irradiation with a laser fluence of 0.56 J/cm² of GaP(110) before

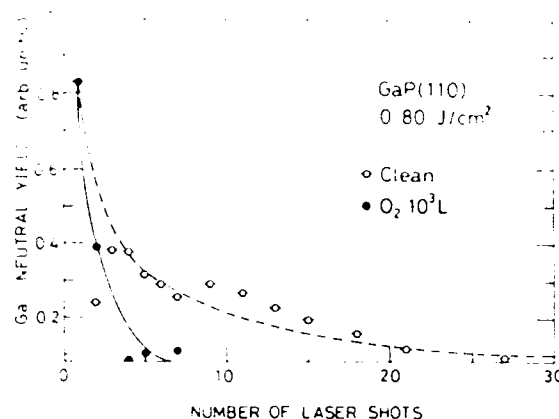


Fig. 3. A comparison of the relations between the Ga⁰ yield and the number of shots for cleaned (open circles) and 10³ L oxygen-exposed (closed circles) GaP(110) surfaces. The irradiation was repeated with a fixed laser fluence of 0.8 J/cm². The solid and dotted lines are exponential functions with decay constants of 0.26 and 0.11, respectively.

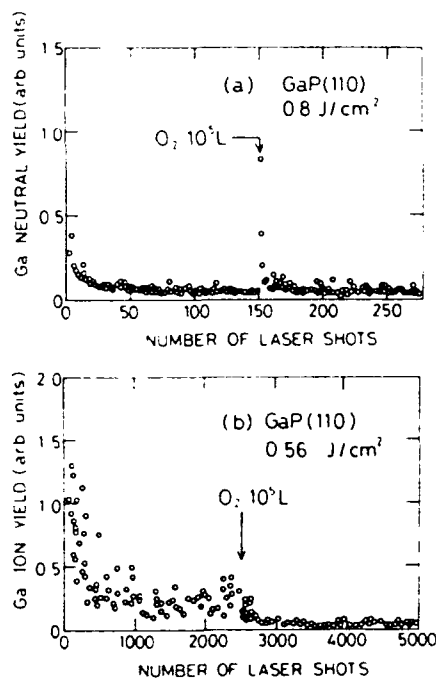


Fig. 4. A comparison between the change of the (a) Ga⁰ and (b) Ga⁺ emission yields before and after oxygen exposure. Each figure shows the relation between the yield and number of laser shots, started from cleaned surfaces and exposed to oxygen indicated. The laser fluences are fixed to 0.8 J/cm² for the Ga⁰ emission and 0.56 J/cm² for the Ga⁺ emission.



the S-component after oxygen exposure. Though the rapid decreasing components of the Ga^0 emission yield were observed before and after the exposure, that for the Ga^+ emission yield is not enhanced significantly by the oxygen exposure. Thus, the ratio of Ga^+/Ga^0 emission yield for the S-component of the cleaned GaP surface is significantly larger than that for the A-component of oxidized surfaces.

As described elsewhere [13] the A-component is initiated by a relatively weakly bonded Ga-rich defect site. The correlation shown in fig. 2 between the integrated yield of the A-component and the oxygen coverage indicates that a weakly bonded Ga atom is produced at each site where oxygen is adsorbed. Furthermore, in view of the saturation as a function of oxygen dose, it has been suggested that the adsorption of oxygen occurs at defect sites [2,3,6]. The present experimental results indicate that adsorption of an oxygen at a defect site, probably on kink sites of steps (S-component), weakens the bonding of a Ga atom.

In view of the UPS [1–3] and EELS [6,7] experiments on GaAs, it is generally believed that oxygen atoms at low coverage are bonded to the Ga atoms; no indication of As–O bonding has been observed. We have no information which would enable us to identify the site of the oxygen bonding on GaP, but it is unlikely that oxygen adsorbed atop a Ga atom would produce a weakened bond in a surface Ga atom. Indeed, according to simple bond-energy arguments [7] it is more likely that the adsorbed oxygen atom bridges the P and Ga on a kink site at the surface. Since the O-adsorption at the bridge site may produce a weakly bonded Ga atom and hence enhance Ga emission, in view of the present results, we consider that the model that an oxygen atom bridges Ga and P atoms [7] is more likely than a bridge between adjacent Ga atoms on the surface [2].

It has been argued that defect sites at which laser-induced particle emission occurs can be partially characterized by three parameters [13]: the threshold laser fluence, the exponent of the yield versus shot number, and the Ga^+/Ga^0 ratio. The threshold laser fluence for emission from the oxygen-adsorbed site is nearly the same as that

for the A-component of the cleaned surface, while the exponential dependence of the $Y(n)$ curve for the former is much smaller than for the latter, indicating that the two types of defect sites are distinctively different.

Two possible scenarios suggest themselves for producing bond weakening. One is that the high electronegativity of an oxygen atom produces a negatively charged surface site [11], making it possible for the oxygen adsorption site to localize two holes and produce desorption, as already suggested for clean GaP surfaces by Itoh and Nakayama [16], and confirmed experimentally by Hattori et al. [14]. Calculations of two-hole laser-induced desorption in the bond-orbital model by Haglund et al. [17] are also consistent with this picture. A second possibility is that the oxidation leads to the formation of a metastable O^- at the defect site, which has been shown in calculations to be metastable and to produce a surface lattice deformation which leaves one Ga more weakly bonded than its neighbors [18]. Both possibilities are consistent with the experimental evidence.

The experimental values of the Ga^+/Ga^0 ratio are also consistent with the picture of Ga^0 emission from an electronegative surface defect site. To describe the correlation, we used a Born–Haber cycle as shown in table 1. First, a Ga^0 on a surface defect is taken out of the surface (from the defect site) by adding the vaporization energy E_{vap} . The vaporization of a Ga^+ requires, in addition, the addition of the ionization energy I of a Ga^0 and the negative of the electron affinity A_d to the defect site with the missing Ga^0 . Thus, we obtain the following relation between the vaporization energy $E_{\text{vap}}(\text{Ga}^0)$ of a Ga atom and the $E_{\text{vap}}(\text{Ga}^+)$ of a Ga ion:

$$E_{\text{vap}}(\text{Ga}^+) = E_{\text{vap}}(\text{Ga}^0) + I - A_d. \quad (1)$$

Table 1
A Born–Haber cycle describing the difference in the energy of emitting Ga^0 and Ga^+ from a GaP surface (see text)

Surface-missing Ga^0 site + Ga^0	+ $E_{\text{vap}}(\text{Ga}^0)$
$\text{Ga}^0 - \text{Ga}^+ + e$	+ I
Missing Ga^0 site + e-missing Ga^+ site	– A_d
Missing Ga^+ site + Ga^+ -surface	– $E_{\text{vap}}(\text{Ga}^+)$
$E_{\text{vap}}(\text{Ga}^+) = E_{\text{vap}}(\text{Ga}^0) + I - A_d$	

From eq. (1), the Ga^+ / Ga^0 ratio should be larger than unity for defects having A_d larger than L . According to the model described above, a defect site with a P-O bond left after Ga emission is not capable of trapping another electron.

In summary, we find that adsorption of an oxygen atom at defect sites on GaP surfaces enhances that component of the laser-induced atom emission which comes from weakly-bonded Ga sites. Although at present no definite conclusion can be drawn about the atomic structure of the adsorption site, our results indicate that the binding of the Ga atoms is strongly altered by oxidation. The bond weakening may be attributed either to the electronegativity of the oxygen or to lattice deformation produced by the formation of O_2 . Our investigation also indicates that laser-induced particle emission is a sensitive and promising probe for investigating small concentrations of electronic defects at surfaces.

This work was supported in part by the Grant-in-Aid for specially Promoted Science of Ministry of Education, Science and Culture of Japan, by the Japan Society for the Promotion of Science and by the National Science Foundation Division of International Programs, Grant Number 89-16097.

References

- [1] D.J. Frankel, J.R. Anderson and G.J. Lapeyre, *J. Vac. Sci. Technol.*, **A 1** (1983) 1043.
- [2] C.Y. Su, T.A. T. Fong, F.W. Chye, P.R. Skeath and W.E. Spicer, *Phys. Rev. Lett.*, **58** (1982) 4045.
- [3] G. Lombardi, K. E. Goh, N. Itoh and R.F. Haglund, Jr., *J. Vac. Sci. Technol. B* **2** (1984) 351.
- [4] P. Pianetta, I. Lindau, C. Garner and W.E. Spicer, *Phys. Rev. Lett.*, **35** (1975) 1356.
- [5] P. Chiaradia, *Solid State Commun.*, **67** (1988) 647.
- [6] F. Bartels and W. Mönch, *Surf. Sci.*, **143** (1984) 315; F. Bartels, L. Surkamp, H.J. Clemens and W. Mönch, *J. Vac. Sci. Technol. B* **1** (1983) 756.
- [7] R. Ludeke, *Solid State Commun.*, **21** (1977) 815.
- [8] W. Ranke and K. Jacobi, *Surf. Sci.*, **63** (1977) 33.
- [9] Y.R. Xing and W. Ranke, *Surf. Sci.*, **167** (1986) L171.
- [10] G. Lucovsky and R.S. Bauer, *Solid State Commun.*, **31** (1979) 931.
- [11] J.A. Stroscio, R.M. Feenstra and A.P. Fein, *Phys. Rev. Lett.*, **58** (1987) 1668.
- [12] J.A. Stroscio and R.M. Feenstra, *J. Vac. Sci. Technol. A* **6** (1988) 577.
- [13] Y. Nakai, K. Hattori, A. Okano, N. Itoh and R.F. Haglund, Jr., *Nucl. Instrum. Methods B*, in press.
- [14] K. Hattori, A. Okano, Y. Nakai, N. Itoh and R.F. Haglund, Jr., *J. Phys. (Condensed Matter)*, to be published.
- [15] K. Hattori, Y. Nakai and N. Itoh, *Surf. Sci. Lett.*, **227** (1990) L115.
- [16] N. Itoh and T. Nakayama, *Phys. Lett. A*, **92** (1982) 471.
- [17] R.F. Haglund, Jr., K. Hattori, Y. Nakai and N. Itoh, *J. Vac. Sci. Technol. B*, to be published.
- [18] G.A. Baraff, E.O. Kane and M. Schluter, *Phys. Rev. B* **25** (1982) 548.

Section IV. Photon- and electron-stimulated desorption

Nonthermal laser sputtering from solid surfaces

Yasuo Nakai, Ken Hattori, Akiko Okano and Noriaki Itoh

Department of Physics, Nagoya University, Furo-cho, Nagoya 464-01, Japan

Richard F. Haglund, Jr.

Department of Physics and Astronomy, Vanderbilt University, Nashville, TN 37235, USA

Current understanding of the phenomena of laser-induced sputtering of nonthermal origin from semiconductors and insulators is reviewed. Experimental observations on laser sputtering of typical insulators and semiconductors are compared, emphasizing laser sputtering by photons having subgap energies. It is pointed out that the sputtering is not induced at low laser intensities in semiconductors, while sputtering in proportion to the density of excitation is observed for alkali halides. The difference is attributed to the absence and presence of self-trapping of excitons in two different types of materials. In high-sensitivity measurements of laser-induced sputtering from GaP surfaces, the change in the sputtering yield as the pulsed-laser irradiation is repeated on the same spot is correlated with the change in the defect concentrations on the surface top layer. Hence, high-sensitivity measurements of nonthermal laser-induced sputtering can be a useful technique for defect and impurity analysis on the top layer of the surface. Theoretical aspects of the laser-induced sputtering, including the nature of excitons, energy localization, bond breaking and dynamics of localisation are discussed. It is suggested that two-hole localisation on surface defect sites is the origin of sputtering in materials in which no self-trapping of excitons is induced.

1. Introduction

Irradiation of solids by pulsed-laser beams induce phenomena which are specific to intense light beams. These phenomena include laser-induced bulk damage, surface damage and sputtering [1]. The latter two phenomena are correlated to each other and form the subject of the present paper. One of the characteristic features of laser-induced sputtering is the superlinear dependence of its yield on the fluence, which often can be regarded as if a threshold laser fluence exists [2]. Such superlinear dependence is often characteristic of thermal sputtering, due to vaporization of the surface by rapid heating during laser irradiation [3]. In this paper we show several examples of laser-induced sputtering of nonthermal origin, which exhibits similar superlinear dependence on the laser fluence.

Experiments on laser-induced sputtering have been carried out using photons both below and above band-gap energies. Because of the large bulk optical absorption coefficients, irradiation with photons above the band-gap energy raises the temperature of the surface layers, and hence may induce thermal evaporation. For photons of subgap energies, however, the bulk optical absorption coefficient is extremely small, less than that

for photons above the band-gap energies often by five orders of magnitude. Thus the temperature rise of the surface layers can be disregarded for subgap excitation. There are three conceivable sources of optical absorption of photons of subgap energies contributing to desorption: multi-photon bulk absorption, single-photon optical absorption by the surface states, and that by defects on surfaces. When photons are absorbed by surface states or surface defects, the thermal energy generated by nonradiative processes will be transferred to the underlayer which is not directly heated. Photons of subgap energies may be absorbed also in a single-photon mode by defects in the bulk but this will not contribute to desorption and hence is disregarded. Since the amount of the energy imparted by each photon-solid interaction is of the order of a few eV, it is improbable that atoms underneath the surface top layer are ejected. In any case sputtering will not be induced unless excitation energy is transported to the surface.

The purpose of the present paper is to review experimental observations of nonthermal laser induced sputtering of halides, oxides and compound semiconductors, and to discuss the various mechanisms of laser-induced desorption in these materials. Theoretical considerations for nonthermal laser sputtering for sub-

gap photon energies are also given, emphasizing the localization of electronic excitation energy and its transformation to the energy for atomic ejection.

2. Survey of experimental results

2.1. Alkali halides and alkaline earth fluorides

A great deal of work has been carried out on sputtering of alkali halides by electrons and ions, and several reviews have been published [4–6]. The mechanism of the sputtering by charged particles is due to both elastic encounters and electronic excitation. The process of sputtering caused by electronic excitation under irradiation with charged particles is essentially the same as for photo-excitation. In this paper, we discuss mainly photo-induced sputtering, but touch upon sputtering induced by charged particles, whenever necessary.

The sputtering yield of halogen atoms from alkali halides by conventional light beams is proportional to the flux [7], as shown in fig. 1, indicating that a single excitation event induces sputtering. The temperature dependence of the sputtering yield at low fluxes has

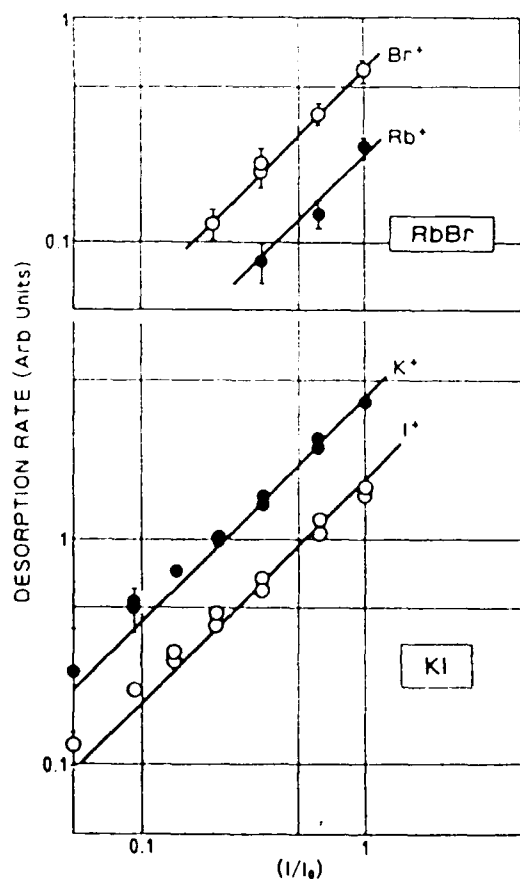


Fig. 1. Photo-induced sputtering rate vs excitation intensity for RbBr and KI. Sputtering rate is proportional to the excitation intensity (After Kanzaki and Mori [7].)

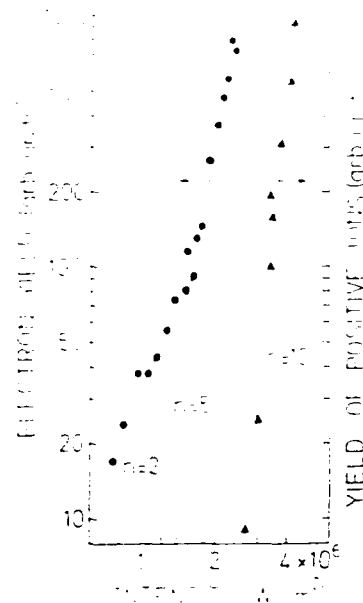


Fig. 2. Emission yields of electrons (dots) and positive ions (triangles) vs laser intensity for $\text{BaF}_2(111)$, for 518 nm laser pulses. The solid lines represent the intensity dependence, of which power is indicated in the figure. (After Reif et al. [14].)

been found to parallel the evaporation rate of alkali metals [8–10]. This result has been interpreted in the following way: the halogen atoms are ejected in the primary event, and deviation from stoichiometry due to loss of halogen reduces the overall sputtering yield. Thus evaporation of alkali deposited on the surface is the rate-limiting process. Not much work on laser-induced sputtering of neutral halogens from alkali halides has been carried out, although laser-induced damage has been studied extensively [11] and it has been shown that the defects at the surface are one of the main factors for producing the laser damage. It has been shown that four-photon band-to-band transition by ruby laser pulses causes desorption [12]; the yield is proportional to the fourth power of the laser fluence, indicating again that a single excitation event results in ejection of a halogen atom.

Extensive work on laser-induced sputtering of cations and electron emission from fluorides has been carried out [13–17]. Fig. 2 shows a typical result of the fluence dependence of the sputtering yield by 518 nm laser pulses [14]. The figure includes also the fluence dependence of the electron emission. A high-power fluence dependence for positive-ion emission from BaF_2 is evident. Spectroscopic studies have shown that the sputtering yield is a maximum at specific wavelengths for all intensity regions, suggesting that resonance (multi-photon) ionisation possibly, of the surface defect states, is responsible for sputtering. Cluster calculations of the BaF_2 surface confirm the plausibility of such an excitation mechanism.

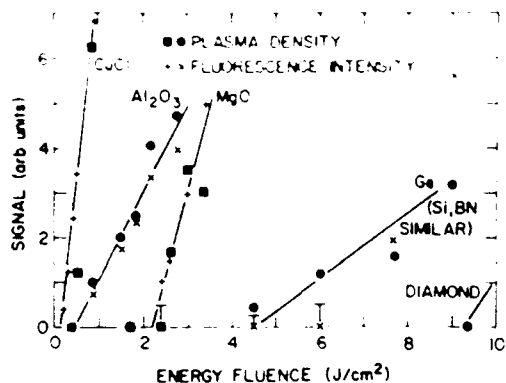


Fig. 3. Effective number of particles emitted for laser pulse from surfaces of CuCl, Al_2O_3 , MgO, Ge and diamond, determined by plasma density and fluorescence measurements, as a function of laser fluence. (After Dreyfus et al. [22].)

2.2. Al_2O_3 and LiNbO_3

There have been a number of recent studies of laser ablation from technologically important oxide materials. Here we mention two cases: Al_2O_3 and the ferroelectric insulator LiNbO_3 .

Sputtering from Al_2O_3 by excimer laser pulses has been studied by direct scanning-microscopic observations of ablation [18–20] and by laser-induced fluorescence (LIF) [21–23] measurements. The photon energy of the excimer laser is well below the band-gap energy of Al_2O_3 , and hence the sputtering in this case is due to subgap excitation. It has been shown that laser ablation occurs for laser fluence only above 0.6 J/cm^2 [21]. The fluence dependence has been shown to be superlinear, as shown in fig. 3. Careful measurements of the energy distribution has been reported both by time-of-flight (TOF) measurements and by measurements of the vibrational and rotational lines of LIF from AlO [21]. Near the threshold laser fluence the TOF energy distribution shows a maximum at 1.2 eV [21], while the energy distribution determined by the vibrational spectra is much lower. A comparison of LIF spectra with calculated spectra shows that the temperature is close to 500 K , which is too small to consider that the sputtering is due to thermal evaporation. The TOF energy distribution is apparently influenced by collisions in the high-density gas layer accumulated above the laser-irradiated surfaces [23], while the energy distribution determined from vibrational frequency is related to the ejection process. The low internal temperature of ejected AlO excludes the thermal evaporation mechanism.

More recently, measurements of excimer-laser-induced ejection of excited atoms and ions from LiNbO_3 have been carried out [24,25]. The laser pulses in this experiment are generated from a XeCl laser, which emits 4 eV photons, very close to the band-gap energy. Threshold behavior similar to that for Al_2O_3 has been

observed. A significant difference has been found between the described behavior of virgin and defect spots or not the irradiated spot had previously received a significant number of shots at fluences insufficient to cause either surface modification observable in an electron microscope, or to generate a visible plasma plume. A representative sample of these data is shown in fig. 4. Interestingly, the Nb^+ threshold behavior is quite similar for the damaged and undamaged surfaces, suggesting that the desorption mechanism is thermal in both cases, while Li^+ emission is considered to be nonthermal. An incubation effect was also observed and found to be different for ejection of Li^+ and Nb^+ .

2.3. Compound semiconductors

Pulsed-laser-induced sputtering of compound semiconductors, such as GaAs [26], GaP [27–35], InP [36] and CdS [37,38] have been studied, for photon energies both above and below the band-gap energies. One of the differences between the sputtering from semicon-

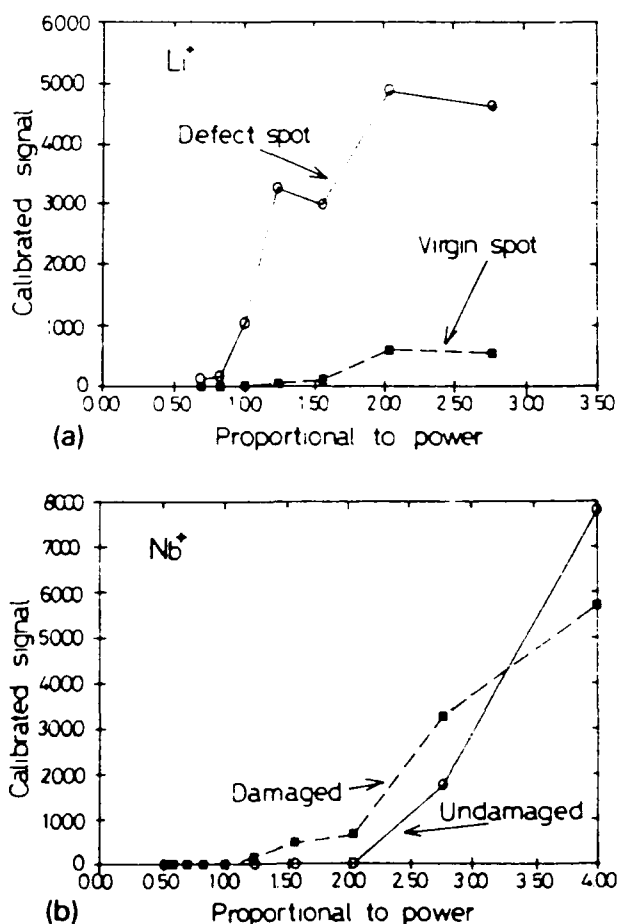


Fig. 4. Nonlinear dependence of the sputtering yields for Li^+ (a) and Nb^+ (b) from LiNbO_3 surfaces on the irradiation power of XeCl laser (308 nm), for damaged and undamaged spots. (After Affatigato et al. [25].)

ductors and from alkali halides is that no desorption is observed for small laser fluences and the sputtering yield increases rapidly with laser fluence in the former as shown in fig. 5 [30]. With alkali halides, on the other hand, the sputtering yield is proportional to the density of excitation (fig. 1). Thus it appears that there is a fundamental difference in the mechanism of desorption between alkali halides and semiconductors. Al_2O_3 and LiNbO_3 show behaviors rather similar to the compound semiconductors.

A large number of sputtering experiments for compound semiconductors have been carried out using photons above the band-gap energies. General characteristics for sputtering by photons above and below the band-gap energies are similar: both show the superlinear dependence on the laser fluence, and even the threshold laser fluences for both cases are within a factor of 3, as seen from fig. 5. Since GaP(110) and $(\bar{1}\bar{1}\bar{1})$ surfaces have surface states located within the band gap [39,40], sputtering by photons below band-gap energies has been ascribed to excitation of the surface states. Measurements of the velocity distribution for photon energies above the band-gap energy have been carried out [26–28,36–38]. The velocity distribution, however, has been shown to be influenced by collisions between sputtered particles [23] and hence does not necessarily reflect the mechanism of sputtering.

In recent work on laser-induced sputtering by the Nagoya group, special care was taken to insure sputtering from cleaned and undamaged surfaces. Two kinds of precaution have been taken in these experiments: (1) the surface was cleaned before the start of sputtering experiments, and (2) highly sensitive detection techniques were used so that irradiation with a pulsed laser beam destroys only a very small fraction of the topmost

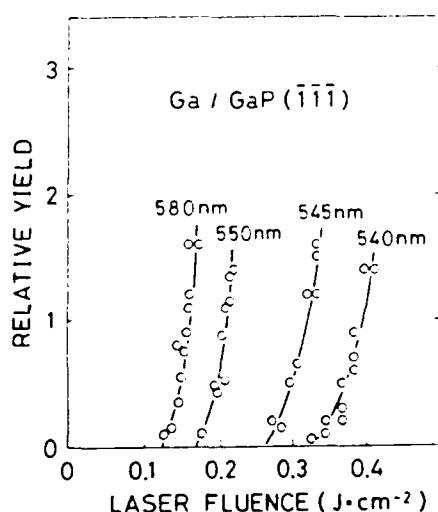


Fig. 5. Dependence of the sputtering yield of Ga^0 neutral atoms on the laser fluence from a $\text{GaP}(\bar{1}\bar{1}\bar{1})$ clean surface for several different wavelengths. (After Hatton et al. [30].)

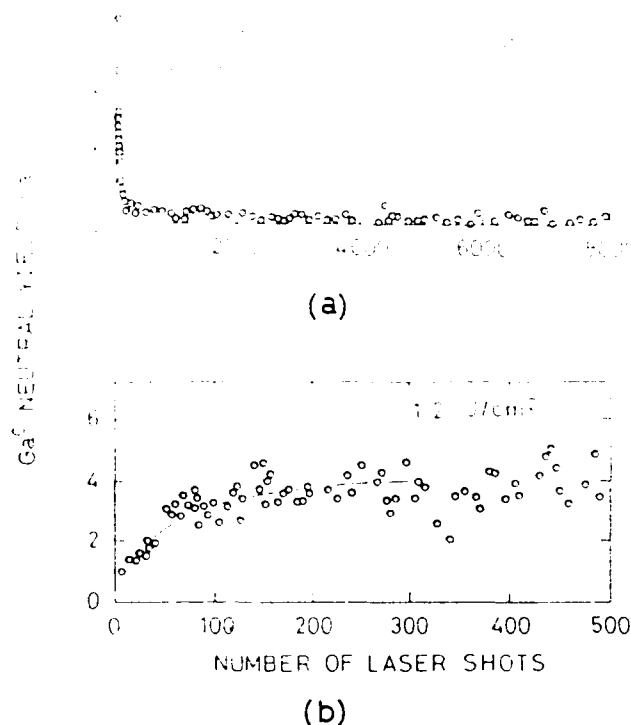


Fig. 6. The change of the sputtering yield of Ga^0 induced by irradiation of $\text{GaP}(110)$ surfaces by 28 ns laser pulses, then irradiation is repeated on the same spot; for different laser fluences (a) 1.0 J/cm^2 and (b) 1.2 J/cm^2 . (After Hatton et al. [33].)

layer. Because of these precautions, it was possible to observe the pulsed-laser-induced sputtering from the same part of the surface repeatedly. Fig. 6 [33] shows a typical example of such experiments. It is clear from fig. 6(a) that the sputtering yield decreases rapidly at the beginning of the irradiation and becomes a constant, if laser fluence is small. We note in particular that the constant sputtering is maintained for 8000 shots (fig. 6(a)) and that if the laser fluence is increased only by 20%, there is an increase in the sputtering yield as pulsed irradiation is repeated (fig. 6(b)). We refer to the threshold laser fluence that produces the increase in the yield as the damage threshold. It has been shown that in the case of a low fluence no change in the LEED pattern was observed, while fading of the LEED spots was seen in the case of a high fluence. Since only atoms on the surface top layer are ejected, the sputtering yield represents the atomic structures of the top layer. Thus the experimental results shown in fig. 6 indicate that the surface is changed as irradiation is repeated and suggest that the surface becomes more perfect if the laser fluence is small and becomes less perfect if the laser fluence is large. From the evaluation of the absolute value of the number of sputtered atoms, it has been shown that each shot gives sputtering of about 10^{-6} monolayer. Since the threshold for collisions between sputtered particles

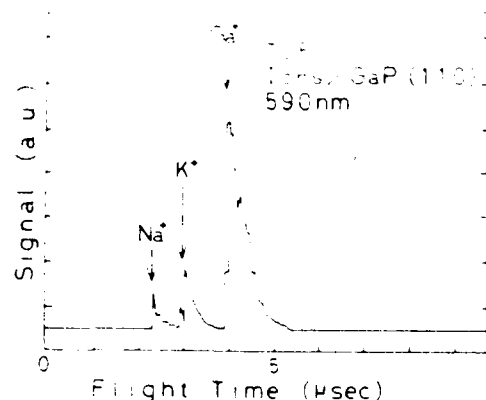


Fig. 7. Time of flight (TOF) mass spectra of ions sputtered from GaP(110) cleaned surfaces by subgap laser photons. (After Nakai et al. [35].)

is about 0.5 monolayer [23,34], such collisions would not be expected.

From the arguments above, it is clear that high-sensitivity measurements of laser-induced neutral emission can serve as a method of high-sensitivity analysis of the surface top layer. It has been shown that ions are also emitted although the number is much smaller. Since ion sensitivity is much higher than the neutral sensitivity, measurements of laser-induced ion emission from the surface is considered to be useful for impurity analysis of the surface top layer. TOF measurements of laser-induced emitted ions has been carried out [35]. In these experiments the high sensitivity was obtained by sacrificing resolution. Fig. 7 shows a typical result. In addition to Ga^+ , emission of K^+ and Na^+ was detected, and it has been found that the intensity of Na^+ and K^+ ions decreases to zero as irradiation is repeated, while that of Ga^+ is decreased also but to a constant value. The yield of Ga^+ is also influenced more significantly than that of Ga^0 , when the surface was annealed [32].

3. Theoretical considerations

3.1. The mechanism of laser-induced desorption, desorption by valence-electron excitation

Laser-induced sputtering of nonthermal origin should involve electronic excitation either in the bulk valence bands or in the surface states or surface defects. If the photon energy exceeds the band-gap energy, electron-hole (e-h) pairs or excitons having three-dimensional extension are produced. If the photon energy is below the band-gap energy but is above the energy of excitation of the surface states, e-h pairs or excitons having two-dimensional extension are produced. There is a variety of two-dimensional e-h pairs or excitons, for example those consisting of electrons in unoccupied

surface states and holes in the valence band. Direct excitation of defects on surfaces may cause emission of atoms from the vicinity of the excited sites and hence sputtering. In solids having a large electron and hole diffusivity, the interaction between the mobile entity and defects will dominate.

Menzel and Gomer [41] and Redhead [42] have suggested that desorption can be induced by valence-electron excitation if an antibonding type adiabatic potential energy surface is formed, which brings an atom out of the surface. The e-h pairs or excitons having three- or two-dimensional extension cannot form an MGR-type adiabatic potential energy surface, unless the energy possessed by the electron-hole pairs or excitons is localized. Thus there are two conditions for desorption to be induced by valence-electron excitation: localization of wave functions and existence of the antibonding or bond-breaking potential surface on the localized site.

In a crystal with a strong electron-lattice coupling, such as alkali halides and alkaline earth fluorides, excitons and holes are localized, producing self-trapped excitons and self-trapped holes, respectively [43]. A self-trapped hole is often converted to a self-trapped exciton by trapping an electron. It is known also that a self-trapped exciton in the bulk possesses structural instability and is converted to a Frenkel pair comprising a vacancy and an interstitial in the halogen sublattice [44]. Desorption of halogen atoms can be ascribed to the instability of self-trapped excitons near the surfaces [45]: an exciton near the surface is eventually decomposed into a halogen vacancy and an emitted halogen atom. Thus self-trapping of excitons provides a site for the localization of the energy possessed by an exciton or electron-hole pair. Furthermore, the energy possessed by localized excitons is converted partly to the kinetic energy of atoms being emitted. It follows that self-trapping of an exciton can satisfy the two conditions for formation of a MGR-type adiabatic potential energy surface at least for the anion sublattice. We suggest that sputtering is induced by formation of self-trapped excitons near the surface and call this process the self-trapped-exciton mechanism of sputtering.^{≡1} When exciton self-trapping is the cause of sputtering, one expects a linear dependence of the sputtering yield on the density of excitation [7] as seen in fig. 1.

In materials with weak electron-lattice coupling in which excitons are not self-trapped, as in semiconduc-

^{≡1} According to Postawa et al. [46] excitation near the surface within a depth of 100 Å results in sputtering. The diffusion of free excitons and e-h pairs to the surface may be involved in the depth described above, while the instability of self-trapped exciton may occur only within a few layers. Neither experimental nor theoretical information is yet available.

Table 1
Grouping of nonmetals according to the location of electronic excitation

Type	Specification	Substance
A	Neither excitons nor holes are self-trapped	Si, Ge, compound semiconductors, Tl-halides, Cu-halides, MgO, CaO
B	Either excitons or holes are self-trapped	alkali halides, alkaline earth fluorides, SiO ₂ , chalcogenides

tors, defects and impurities on the surfaces can also act as localization sites. Almost no information is yet available for defects with localized electrons, holes or excitons on surfaces, although it is known that interaction of bulk defects or impurities with electrons, holes and excitons produces metastable states accompanied by tremendous lattice relaxation [47]. Therefore, it is conceivable that interaction of electrons, holes or excitons with defects on surfaces causes emission of neighboring atoms.

It is convenient to divide nonmetals into two groups: group A, in which neither holes nor excitons are self-trapped [48], and group B, in which either of them is self-trapped. The typical materials belonging to both groups are listed in table 1. We note a substantial difference between the sputtering characteristics for group A and group B nonmetals. In group B nonmetals, desorption is induced even by conventional light beams in proportion to the density of excitation, as in alkali halides. For CaF₂ [49] and SiO₂ [50,51], which belong to group B, the build-up of cation-rich layers by photoexcitation has been observed.

On the other hand, ejection of Ga atoms and ions from the GaP surfaces was not detected with 28 ns laser pulses up to about 0.05 J/cm² (by a sensitivity of approximately 10⁻⁵ monolayer) and desorption which can be definitely ascribed to defect sites arose only when the laser intensity was increased beyond a certain value [30]. It has been suggested that localization of two holes on a lattice site is required to produce sputtering in the group A material (two-hole mechanism [2]).

It is clear that these two cases represent the extreme ends of a spectrum of behaviors. The ferroelectrics, for example, have vacancy-type defects, but it is not known how the soft phonon modes are implicated in the relaxation process preceding defect formation. Hence, it is not yet known whether Al₂O₃ [52] and LiNbO₃ should be assigned to group A or B.

In the following we try to understand the conditions under which the desorption is induced in semiconductors carefully and examine possible mechanisms of de-

sorption. Our emphasis is on the group A nonmetals and description of group B nonmetals is given only when there is relevance.

3.2 Electronic excitation

According to experimental observation of GaP(110) and (111), excitation of surface states induces desorption. Therefore we discuss mainly the effects of excitation of the surface states, assuming that the density of excitation is high and that Auger recombination dominates [53]. The kinetic equation for n_s , the concentration of e-h pairs at the surface, is given by

$$\frac{dn_s}{dt} = \sigma_s \phi N_s + \frac{1}{2} \eta v n_b - C_s n_s^2 - C'_s f(n_s, n_b), \quad (1)$$

where σ_s is the cross section for exciting the surface states, ϕ is the photon flux, N_s is the atomic density at the surface, η the probability that the three-dimensional e-h pairs are converted to two-dimensional e-h pairs, v the average velocity of electrons and holes in the conduction and valence band, n_b is the steady-state bulk concentration of the e-h pairs during irradiation, and C_s and C'_s are Auger recombination rates for surface-surface and surface-bulk processes. The second term is the rate by which the bulk excitons are converted to the surface excitons [54]. The third term is for Auger recombination among surface e-h pairs and the last term is for Auger recombination between surface and bulk electron-hole pairs. The two-hole localisation at defect sites which is considered to cause desorption as described later, is not included in the kinetic equation, since its contribution to n_s is small. In eq. (1), the following relation holds for n_b under dense excitation where the Auger recombination dominates [53,55]:

$$\frac{dn_b}{dt} = \sigma_b \phi N + \sigma_b^{(n)} \phi^n N - C_b n_b^2, \quad (2)$$

where N is the number of atoms per unit volume in the bulk, σ_b is the single photon-excitation cross section for the bulk, $\sigma_b^{(n)}$ is the n -photon bulk absorption cross section and C_b is the Auger recombination rate in the three-dimensional system. Here we presume that the kinetic energies of the holes and electrons are sufficiently low not to cause impact ionization.

A semi-quantitative discussion of eqs. (1) and (2) will reveal which terms dominate. For irradiation with a 1 J/cm² laser pulse of GaP at 620 nm, one-photon optical absorption coefficient is essentially zero [56] and the two-photon absorption cross section is known to be 4×10^{-52} cm⁴ s [57]. With this value for the cross section, it has been shown that the number of e-h pairs generated by a pulse is only 10¹⁷ cm⁻³ [30]. Then the second and fourth term in eq. (1) can be neglected. Using the value of the two-dimensional Auger-recombination rates, 3.2×10^{-17} cm⁴ s⁻¹ estimated on simple dimen-

sional arguments [58], we evaluated the concentration of the surface fractional electron-hole pair concentration to be 0.05. Thus a fractional concentration of this magnitude appears to be sufficient to produce sputtering.

In alkali halides and alkaline earth fluorides, low-density electronic excitation produces sputtering, because of self-trapping. Thus, a small number of multi-photon excitations can cause sputtering and produce defects on surfaces, and the second term in eq. (2) is probably responsible for sputtering. Since defects thus generated can absorb subgap photons, the multi-photon processes associated with defects may also contribute to sputtering, as suggested by Matthias and Green [17].

Irradiation with 310 nm, 1 J/cm^2 laser pulse, above the direct band-gap energy, may produce bulk e-h pairs at a fractional concentration of 0.02, according to eq. (2), in which the experimentally obtained value [59] of C_b was used. Using this value of $n_e = n_h$, we found that the second term of eq. (1) was 300 times larger than the first term if $\eta = 1$. Thus bulk excitation affects the desorption in two opposite ways: by increasing the supply of e-h pairs on the surface and by enhancing the Auger recombination through the fourth term in eq. (1). The fact that these effects oppose each other may explain why the threshold laser fluence for GaP is not changed drastically as the band-gap energy is crossed.

3.3. Desorption and surface damage

Since there is no self-trapping of excitons in group A non-metals, we consider the possibility that localization of electronic excitation energy on surface defect sites results in bond breaking.^{#2} It has been suggested by Wu [60] that defect-related Auger transition is the cause of laser-induced sputtering. We discuss defect-related localisation of electron-hole pairs. First we discuss the consequences of desorption from defect sites on surfaces and secondly we discuss the conditions required for the sputtering to take place.

If an atom near a defect site on the surface is ejected because of the localisation of the exciton or e-h pair energy, the number of defects will be changed. Let N_D be the number of defect sites per unit area responsible for sputtering and let irradiation with dn laser pulses emit dN_E atoms per unit area from the surface. We put

$$dN_E = YN_D dn, \quad (3)$$

where Y is the yield of sputtering per defect during a single laser pulse. Y includes both the cross section of a

defect site for energy localization and the efficiency for the ejection. In eq. (3) N_D implies the number of the defect sites that can act as the localisation sites independently.

There are three typical defect types, each with a distinctive mode of evolution as the laser irradiation proceeds. If the defect is an adatom, desorption from a defect site restores the perfect lattice. It follows that

$$dN_E = -dN_D,$$

and hence

$$N_D = N_D^0 \exp(-Yn), \quad (4)$$

where N_D^0 is the concentration of defects prior to the start of irradiation. In this case the desorption yield is diminished as the laser irradiation is repeated. If adatoms are clustered or form an island, the defect sites responsible for desorption are only at the periphery and the defect sites are not eliminated by sputtering. Suppose that the island is a circle with a large radius r , $dN_E = -\pi d(r^2/a^2)$, while $dN_D = 2\pi d(r/a)$. Thus, in a first-order approximation, we obtain $dN_E = -dN_D^2/4\pi$, and hence $N_D = N_D^0 - \text{const.} \times n$, using eq. (3). Thus, the relation between the number of particles emitted per pulse and the number of shots for cluster-initiated sputtering shows only a slow decrease and can not be distinguished from the step-initiated sputtering. If islands are decomposed into small clusters of adatoms, eq. (4) holds.

For the second type of defect, the step, the defect sites responsible for sputtering are only at the step edges, but not on the terrace. If the sites at the step edge act successively as localization sites for excitation energy and eliminate a row of atoms on the step edge, there is no increase in the number of the defect sites, but only displacement of the step edge. A more realistic picture of this process is that the kink on the step edge acts as the site for localisation until the kink has been traversed from one end to the other. Aside from the details of the microscopic processes of evolution of sputtering from steps, we can consider that ejection of atoms from steps does not influence the number of defect sites responsible for sputtering. Thus, in this case we expect $dn_E \gg dn_D \sim 0$, and hence $n_D = \text{const.}$

If an atom is ejected by localization of excitation energy in a surface vacancy cluster, the size of the cluster increases. If the size of the vacancy cluster is small, we expect that each vacancy site acts as an independent localization center. Then we obtain

$$dN_E = dN_D,$$

and hence

$$N_D = N_D^0 \exp(Yn). \quad (5)$$

If the size of a vacancy cluster increases, the relation between dn_E and dn_D is similar to that for islands.

^{#2} In the previous papers, the possibility that the desorption arises from the localization of two holes at surface perfect sites was invoked [27-31, 61-64]. This possibility cannot yet be excluded, although two-hole localization through defect sites is more favorable as is being discussed.

Then, the number of defect sites becomes constant. When sputtering occurs in the proximity of a vacancy, the vacancies on the top surface start to serve as nucleation sites for evolution of surface vacancy clusters. Simultaneously vacancies at the bottom of the vacancy clusters, namely those in the second layer, can act as nucleation sites for vacancy clusters. Thus under this condition, the damage zone can grow in the direction perpendicular to the surface. If sputtering occurs at perfect sites, due to the self-trapping, the surface damage will also evolve.

The rapidly falling component shown in fig. 6(a) follows eq. (4) and is considered to be due to adatoms. It is followed by a component for which the defect concentration is a constant. We suggest that this component is initiated by steps; they may include large islands as well. The N_D versus n relation above the damage threshold seen in fig. 6(b) follows eq. (5) for small n and becomes constant at larger n , and is considered originated from vacancies. Progressively higher laser fluence is needed to desorb from adatom sites, steps and vacancies. The sputtering from fluorides observed by Matthias and co-workers [13-17] is also considered to arise from defect sites. The high power dependence indicates that the excitation of the defect sites and simultaneous excitation of the valence electrons near the defect sites enhances sputtering.

We have already pointed out that the surfaces are either improved or damaged by laser irradiation, depending on the sputtering source. We should mention that, particularly for subgap photons, the surface optical absorption coefficient increases as the surface damage evolves. Thus once the vacancy-type defects become efficient centers of desorption, an increase in the surface optical absorption coefficient for subgap photons will result and enhance the damage evolution. Therefore, it is conceivable that in a sputtering experiment which uses a relatively large laser fluence, the initial stages of surface damage is the same as that for high-sensitivity measurements described above, but further damage evolution and sputtering in a single pulse is enhanced due to the evolution of the damage at the initial stage. This consideration explains the fact that the 'threshold laser fluence' obtained with less sensitive methods is approximately the same as those obtained with sensitive methods.

3.4 Bond breaking

It has been suggested by Van Vechten et al. [65] that excitation of valence electrons weakens the bonds. They suggest that the bond strength on average is weakened in the presence of many holes having Bloch-type wave functions. The bond weakening simply by producing dense excitation cannot be effective, since each bond in the crystal is weakened by the same fraction as the

fractional contribution of each pair. Indeed, to explain recent results, it is necessary to indicate that the laser plasma itself causes sputtering [67]. On the other hand, if self-trapping of an exciton or e-h pair is localized in a specific lattice site, the effectiveness for bond breaking is enhanced. In many cases the self-trapped excitons in the bulk involve symmetry breaking relaxation [66]. Such an asymmetrical distortion near the surface may result directly in desorption [68]. This is the case for bond-breaking to be induced by localization of a single exciton in type B material.

We point out the role of the Madelung potential in sputtering due to bond weakening by hole localization. Localization of a hole on a cation adatom, for example, increases the positive charge of the cation, increasing the stability. Thus, the bond weakening is compensated by the Madelung force, whose value at the surface does not differ from that in the bulk in ionic crystals [69]. On the contrary, both the Madelung force and the covalent bond weakening favor the ejection of the anions. Thus, we consider that desorption of cations is the rate-limiting process for atomic ejection from compound surfaces, for which stoichiometry should be maintained during desorption.

Turning to type A materials, we find that experimental results for Ga desorption from GaP indicate that the desorption of Ga neutrals does not occur at low laser fluences. Hence one-hole localization on a defect site is not sufficient to induce desorption. The superlinear dependence of the desorption yield on the laser fluence suggests that the desorption is induced only when the density of excitation is high. Itoh and Nakayama [61] suggested that sputtering is induced by the negative- U localization of two holes at surfaces: two holes are localized by the lattice relaxation along the configuration coordinates that eventually lead to ejection of an atom. Here we consider the energetics for desorption by two-hole localization.

The condition for the two-hole localization on defect sites in the bulk of solids has been given by Anderson [70]. Expressing the on-site Coulomb repulsion energy by U and the electron-lattice relaxation energy by E_{LR} , the condition for two-hole localization is $E_{eff} = U - E_{LR} < 0$. The negative- U interaction was first proposed for amorphous materials to explain the absence of paramagnetic impurities or defects. The present suggestion is an extension of this idea to surface defects.

We presume that two electrons in the conduction band are bound at the two-hole localized site; thus the site possesses twice the normal surface excitation energy. The energetics of the desorption from a two-hole localized site can be treated using a Born-Haber cycle. Referring to table 2, two holes produced from the perfect lattice (PL) by ionization are localized by a defect site. To localize two holes the Coulomb repulsion energy U is needed but energy $2E_i$ is gained, where E_i

is the energy depth of the trap site. Suppose that the two-hole localized state relaxes, resulting in emission of a Ga atom by converting the two-hole excitation energy to the lattice relaxation energy causing the emission. In this process, the lattice relaxation energy E_{LR} is gained. By putting a Ga^{II} atom back on the defect site, the perfect lattice is restored at a cost of the vaporization energy E_{vap} . Since the energy for the entire cycle is zero, we obtain

$$U_{eff} = U - E_{LR} = E_{vap} - 2(E_{gap} - E_t), \quad (6)$$

where E_{gap} is the band-gap energy. From eq. (6) it is clear that U_{eff} is negative if the vaporization energy is smaller than twice the energy to create an e-h pair on a defect site. This cycle is represented graphically in fig. 8, where we assume that the reaction coordinate of the lattice relaxation is the one to repel an atom out of the surface.

Using eq. (6), it is clear that the criterion for the negative- U interaction to be effective, i.e., for the bond breaking to take place, depends on the relative magnitude of the energy E_{vap} to take an atom from a defect site and twice the energy $(E_{gap} - E_t)$ to excite an electron on the defect site. E_{vap} is given approximately by the difference between nE_{coh} and the relaxation energy after evaporation, where n is the number of bonds and E_{coh} is the cohesive energy per bond. Since E_{coh} for GaP is 1.78 eV [71] and the indirect band-gap energy is 2.4 eV, it is energetically favorable for two-hole localization at a surface defect site, where atoms are doubly bonded, to eject a Ga atom.

We note the difference in the negative- U type two-hole localization and the two-hole localization arising from core excitation suggested by Feibelman and Knotek [72]. Aside from the difference that the former occurs at defect sites and the latter in perfect sites, the core excitation also produces a localized two-hole state within 1 fs, while the negative- U type localization requires a lattice rearrangement and hence takes about 1 ps. Thus the two-hole localization after core excitation occurs without being preceded by lattice relaxation. Either Coulomb repulsion in ionic crystals or bond-weakening assisted by Coulomb repulsion in less ionic solids can produce desorption [73].

Table 2

A Born-Haber cycle describing the two-hole mechanism of desorption

PL $\rightarrow 2e + 2h$	$2E_{gap}$
Defect $+ 2h \rightarrow (\text{Defect})_{2h}$	$U - 2E_t$
$(\text{Defect})_{2h} + 2e \rightarrow \text{Ga}^0(\text{vacuum}) + (\text{Defect})_{\text{missing Ga}}$	$-E_{LR}$
$\text{Ga}^0(\text{vacuum}) + (\text{Defect})_{\text{missing Ga}} \rightarrow \text{PL}$	$-E_{vap}$
$2E_{gap} + (U - 2E_t) - E_{LR} - E_{vap} = 0$	

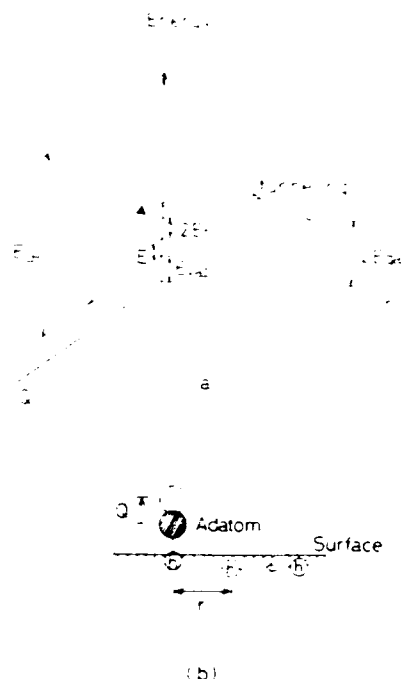


Fig. 8. (a) A schematic adiabatic potential energy surface representing the desorption induced by two-hole localization at a defect site and (b) a schematic diagram describing desorption. The coordinate r is the distance between two holes, one of which is trapped at a defect site and the other in the valence band, and Q the amount of displacement of the desorbed atom. E_{gap} is the band gap energy, $2E_t$ the energy gained by trapping two holes at the defect site and E_{vap} is the energy for vaporization of atoms at the defect site. The screened Coulomb repulsive potential between two holes in a dense electron-hole plasma, can be tunneled by the hole having high kinetic energy because of thermal activation or degeneracy. When energy $E = 2(E_{gap} - E_t) - E_{vap} > 0$, desorption can be induced by two-hole localization.

We consider that the two-hole localization occurs only under dense electronic excitation because of two factors: the reduction of the Coulomb repulsion energy by screening in an e-h plasma [61]; and the enhancement of the hole energy because of the degeneracy [64].

4. Concluding remarks

Only recently has nonthermal laser sputtering from insulators and semiconductors been found, and its general features and mechanism remain unclear. The present paper has reviewed the current status of understanding and pointed out the underlying problems and usefulness of laser sputtering for surface analysis. It appears that there are many problems of scientific and technological interest to be explored. Some of these are summarized below.

(1) In many insulators (type B), in which excitons are self-trapped, sputtering is observed even under con-

ventional light beams which induces band-to-band excitation and in this case the yield is proportional to the photon intensity; single-photon band-to-band excitation can cause sputtering.

(2) Laser sputtering in materials in which excitons are self-trapped (type B) can arise from bulk or surface multi-photon absorption and from cumulative effects of defect generation by multi-photon absorption and sputtering from defects thus generated. The "incubation effect" in LiNbO_3 is one example of this process of cumulative defect generation. For materials in which excitons are not self-trapped (type A), low-density excitation does not induce sputtering, and hence multi-photon absorption cannot make any contribution. In these materials, sputtering is induced when the excitation density exceeds a threshold value. Whether the threshold is real or it is simply apparent because of superlinear dependence is still an open question.

(3) It has been suggested that sputtering in materials in which excitons are not self-trapped is induced by two-hole localization on defect sites. Any microscopic theoretical approach to reveal the problem is of interest. Possibility of two-hole localization on the perfect sites of the surface still has to be examined, but can probably be estimated under reasonable assumptions.

(4) Laser-induced sputtering by photons of subgap energies are indeed observed in GaP, in which subgap surface states exist. The sputtering has been ascribed to two-dimensional excitons or electron-hole plasma at the surface. It is of interest to understand the nature of the two-dimensional electron-hole plasma, particularly phonon-mediated interaction with defects and possible two-hole localization on defect sites. There appears to be no reason why sputtering should not be observed in other materials with the same electronic structure. Indeed, laser desorption may be a sensitive test for the existence of such states.

(5) It is of interest to understand the difference in the laser-induced sputtering by photons having subgap energies and those having energies above the band-gap energies. The problem may be related to the relative contributions of two-dimensional and three-dimensional excitons to lattice relaxation, and/or the transfer from two- to three-dimensional character. It is also of interest to study laser-induced sputtering in other compound semiconductors in which the subgap surface states do not exist.

(6) It is clear that most, though not all, laser-induced sputtering from compound semiconductors involves interaction of excitation with defects. A classification of defects has been made from the dependence of the sputtering yield on the number of laser pulses. It is of great interest to correlate the laser-induced sputtering behavior with the detailed nature of the defects. This might be observed, for example, by means of scanning tunneling microscopy.

(7) Since only atoms on the top surface layer can be ejected in nonthermal laser induced sputtering, the measurements can provide a useful technique of defect and impurity analysis of the surfaces. It is of interest to use the technique for compound semiconductors other than GaP.

References

- [1] See, e.g., P. Kelly, ed., *Laser-induced Material Modification*, in: *Opt. Eng.* 28, 10 (1989).
- [2] N. Itoh, *Nucl. Instr. and Meth.* B27 (1987) 155.
- [3] J.M. Liu, R. Yen, H. Kurz and N. Bloembergen, *Appl. Phys. Lett.* 39 (1981) 755.
- [4] F.D. Townsend, in: *Sputtering by Particle Bombardment II*, ed., R. Behrish (Springer, Berlin, 1990) p. 147.
- [5] M. Szymonski, in: *Desorption Induced by Electronic Transition DIET-IV* (Springer, Berlin, 1990) p. 270.
- [6] N. Itoh, *Nucl. Instr. and Meth.* 132 (1976) 201.
- [7] H. Kanzaki and T. Mori, *Phys. Rev.* B29 (1984) 3573.
- [8] P.D. Townsend and D.J. Elliot, *Phys. Lett.* A28 (1969) 587.
- [9] P.D. Townsend, R. Browing, D.J. Garland, J.C. Kelly, A. Mahjoubi, A.J. Michael and M. Sadoh, *Radiat. Eff.* 30 (1976) 55.
- [10] E. Taglauer, N. Tolk, R. Riedel, E. Colavita, G. Margaritondo, N. Gershenfeld, N. Stoffel, J.A. Kelber and G. Loubriel, *Surf. Sci.* 169 (1986) 267.
- [11] C. Jones, P. Bräunlich, R. Thomas Casper and P. Kelly, *Opt. Eng.* 28 (1989) 1039.
- [12] A. Schmid, P. Bräunlich and P.K. Roj, *Phys. Rev. Lett.* 35 (1975) 1382.
- [13] H.B. Nielsen, J. Reif, E. Matthias, E. Westun and A. Rosen, in: *Desorption Induced by Electronic transitions DIET-III* (Springer, Berlin, 1988) p. 266.
- [14] J. Reif, H. Fallgen, W.E. Cooke and Matthias, *Appl. Phys. Lett.* 49 (1986) 930.
- [15] E. Matthias, H.B. Nielsen, J. Reif, A. Rosen and E. Westun, *J. Vac. Sci. Tech.* B5 (1987) 1415.
- [16] J. Reif, *Opt. Eng.* 28 (1989) 1122.
- [17] E. Matthias and T.A. Green, in: *Desorption Induced by Electronic Transitions DIET-IV* (Springer, Berlin, 1990) p. 112.
- [18] R. Kelly, J.J. Cuomo, P.A. Leary, J.E. Rothenberg, B.E. Braren and C.E. Ahotta, *Nucl. Instr. and Meth.* B9 (1985) 329.
- [19] J.E. Rothenberg and R. Kelly, *Nucl. Instr. and Meth.* B1 (1984) 291.
- [20] R. Kelly and J.E. Rothenberg, *Nucl. Instr. and Meth.* B7-8 (1985) 755.
- [21] R.W. Dreyfus, R. Kelly and R.E. Walkup, *Appl. Phys. Lett.* 49 (1986) 1478.
- [22] R.W. Dreyfus, R.E. Walker and R. Kelly, *Radiat. Eff.* 99 (1986) 199.
- [23] R. Kelly and R.W. Dreyfus, *Nucl. Instr. and Meth.* B32 (1988) 341.
- [24] A. Niehof, K. Becker, R.E. Haglund, Jr., W. Heiland and I.J. Wang, *Nucl. Instr. and Meth.*, to be published.

- [25] M. Attagato, K. Tang and R.F. Haglund, Jr., *Appl. Phys. Lett.*, to be published.
- [26] A. Namiki, T. Kawai, Y. Yasuda and T. Nakamura, *Jpn. J. Appl. Phys.*, 24 (1985) 270.
- [27] T. Nakayama, H. Ichikawa and N. Itoh, *Surf. Sci.* 123 (1982) L693.
- [28] N. Nakayama, *Surf. Sci.* 133 (1983) 101.
- [29] T. Yamamoto, K. Hattori, Y. Nakai, N. Itoh and M. Szymonski, *Radiat. Eff. Defects Sol.* 109 (1989) 213.
- [30] K. Hattori, Y. Nakai and N. Itoh, *Surf. Sci. Lett.* 227 (1990) L115.
- [31] Y. Nakai, K. Hattori and N. Itoh, in: *Desorption Induced by Electronic Transitions DIEL-IV* (Springer, Berlin, 1990) p.143.
- [32] Y. Nakai, K. Hattori and N. Itoh, *Appl. Phys. Lett.* 56 (1990) 1980.
- [33] H. Hattori, A. Okano, Y. Nakai, N. Itoh and R.F. Haglund, Jr., to be published.
- [34] J.P. Cowin, D.J. Auerbach, C. Becker and L. Wharton, *Surf. Sci.* 78 (1978) 545.
- [35] Y. Nakai, T. Taguchi, K. Hattori, A. Okano and N. Itoh, to be published.
- [36] J.M. Moison and M. Bensoussan, *J. Vac. Sci. Tech.* 21 (1982) 315.
- [37] A. Namiki, H. Fukano, T. Kawai, Y. Yasuda and T. Nakamura, *J. Phys. Soc. Jpn.* 54 (1985) 3162;
A. Namiki, K. Watanabe, H. Fukano, S. Nishigaki and T. Noda, *Surf. Sci.* 128 (1983) L247.
- [38] A. Namiki, T. Kawai and K. Ichige, *Surf. Sci.* 166 (1986) 129.
- [39] D. Straub, M. Skibowski and F.J. Himpsel, *J. Vac. Sci. Tech.* A3 (1985) 1484;
D. Straub, V. Dose and W. Altman, *Surf. Sci.* 133 (1983) 9.
- [40] K. Jacobi, *Surf. Sci.* 51 (1975) 29.
- [41] D. Menzel and R. Gomer, *J. Chem. Phys.* 41 (1964) 3311.
- [42] P.E. Redhead, *Can. J. Phys.* 42 (1964) 886.
- [43] M.N. Kabler, in: *Point Defects in Solids*, eds., J.H. Crawford and L.M. Slifkin (Plenum, New York, 1972) p.291.
- [44] Y. Toyozawa, *Physics* (NY) B&C 117/118 (1983) 23.
- [45] N. Itoh and T. Nakayama, *Nucl. Instr. and Meth.* B16 (1986) 550;
N. Itoh, *Nucl. Instr. and Meth.* 132 (1976) 201.
- [46] Z. Postawa, P. Czuba, A. Poradzisz and M. Szymonski, *Radiat. Eff. Defects Sol.* 109 (1989) 189.
- [47] G.D. Watkins, *Mater. Sci. Forum* 37-41 (1989) 39.
- [48] N. Itoh, *Nucl. Instr. and Meth.* B27 (1987) 155.
- [49] R. Souda and M. Aono, in: *The Structure of Surfaces II*, eds., J.F. van der Veen and M.A. van Hove (Springer, Berlin, 1987) p.581.
- [50] C. Eder and R.A.B. Devlin, *Phys. Rev. Lett.* 52 (1984) 2081.
- [51] V.M. Bermudez, *J. Vac. Sci. Tech.* 21 (1982) 81.
- [52] J.A. Valbis and N. Itoh, *Radiat. Eff. Defects Sol.*, to be published.
- [53] W.L. Brown, in: *Laser and Electron-Beam Processing of Materials*, eds., C.W. White and P.S. Peercy (Academic Press, New York, 1980) p.20.
- [54] P.A. Smith, *Semiconductors* (Cambridge Univ. press, Cambridge, 1978).
- [55] E.J. Yoffe, *Phys. Rev.* B21 (1980) 2415.
- [56] J.F. Davey and I. Pankev, *J. Appl. Phys.* 40 (1969) 212.
- [57] V.I. Bredikhin, M.D. Galamin and V.N. Genkin, *Sov. Phys. Usp.* 16 (1973) 299.
- [58] P.T. Landsberg and M.J. Adams, *IEE Proc.* 133 (1986) 118.
- [59] M. Young and D. Wight, *J. Phys.* D7 (1974) 1824.
- [60] Z. Wu, *Phys. Lett.* 131 (1988) 486.
- [61] N. Itoh and T. Nakayama, *Phys. Lett.* A92 (1982) 471.
- [62] Y. Kumazaki, Y. Nakai and N. Itoh, *Phys. Rev. Lett.* 59 (1987) 2883.
- [63] Y. Kumazaki, Y. Nakai and N. Itoh, *Surf. Sci.* 184 (1987) L445.
- [64] H. Sumi, *Surf. Sci.*, to be published.
- [65] J.A. van Vechten, R. Tsu and F.W. Saris, *Phys. Lett.* A74 (1979) 422;
in: *Laser and Electron Beam Processing of Materials*, eds., C.W. White and P.S. Peercy (Academic Press, New York, 1980) p.53.
- [66] Y. Toyozawa, *J. Phys. Soc. Jpn* 44 (1978) 482;
see also A. Shluger and N. Itoh, *J. Phys. Condensed Matter* 2 (1990) 4119.
- [67] W.A. Brown, in: *Laser and Electron-Beam Solid Interactions and Material Processing*, eds., J.F. Gibbons, I.D. Hess and T.W. Sigmon (North-Holland, Amsterdam, 1981) p.1.
- [68] N. Itoh, *Crystal Lattice Defects and Amorphous Materials* 12 (1985) 103.
- [69] J. Magill, J. Bloem and R.W. Ohse, *J. Chem. Phys.* 76 (1982) 6228.
- [70] P.W. Anderson, *Phys. Rev. Lett.* 34 (1975) 953.
- [71] W.A. Harrison, *Electronic Structure and the Properties of Solids: The Physics of Chemical Bond* (Dover, New York, 1989).
- [72] P.J. Feibelman and M.L. Knotek, *Phys. Rev.* B18 (1978) 6531.
- [73] D.F. Ramaker, *J. Vac. Sci. Tech.* A1 (1983) 1137.

UV LASER ABLATION OF FERROELECTRICS

R. L. HAGLUND, Jr.,* J. H. ARPS,* K. TANG,* A. NIEHOF** and W. HEILAND**

*Haglund, Arps and Tang: Department of Physics and Astronomy, Vanderbilt University, Nashville, TN 37235

**Niehof and Heiland: FB Physik, Barbarastrasse 7, Universität Osnabrück, D-4500 Osnabrück, Germany

ABSTRACT

We have investigated laser ablation of excited atoms from the ferroelectrics LiNbO_3 and KNbO_3 at 308 nm. Comparisons of the yields for O^* , K^* and Nb^* from pure and undoped KNbO_3 show the effects of changing intensity, surface condition and irradiation time on the yield of excited atoms. Below about 20 GW/cm^2 , the mechanisms for production of excited atoms differ among the various species; above that intensity, the production of a dense electron-hole plasma appears to impart a collective character to the ablation mechanism.

Introduction and Motivation

Lithium niobate has been for many years the workhorse of nonlinear optics technology, and is currently in wide use for frequency up-conversion, acousto-optic devices [1] and optical switching [2]. More recently, potassium niobate has attracted attention as a ring resonator for frequency doubling diode lasers into the blue region of the spectrum [3]. These applications naturally generate concern for high-intensity laser-induced damage to the surfaces of this material, and for the potential reduction in ablation yield from selective doping. In addition, because these materials are not easily processed by ordinary chemical or mechanical techniques, lasers [4] and ion beams [5] are being considered for micromachining and direct writing in optoelectronic circuits [6] made from these materials. Last but surely not least, the unusual electronic structure of these materials offers intriguing possibilities for creating the localized lattice distortion which is the precursor of laser-induced desorption and ablation.

Experimental Apparatus and Measurements

The experimental setup is shown in Figure 1. Samples of commercial LiNbO_3 and Czochralski-grown KNbO_3 were mounted in an ultrahigh vacuum chamber with a base pressure of 10^{-9} torr. Some of the KNbO_3 samples were doped with Na (~1 %) and Mg (~500 ppm). A Lumonics Hyper-Ex 460 laser with a maximum energy of 180 mJ at 308 nm provided the ablating pulses; the pulse length was of order 12 ns FWHM. Laser light was focused onto the target at normal incidence by a 30-cm focal length lens to form a focal spot approximately $150 \mu\text{m} \times 250 \mu\text{m}$. To avoid artifacts from changes in the focal spot, the laser pulse energy was adjusted over the range from 60 to 180 mJ/pulse by changing the discharge voltage on the laser head; the voltage-vs.-pulse energy curve was calibrated by means of a Scientech ultraviolet calorimeter. These pulse energies, for the measured focal spot, correspond to an intensity range of $13\text{--}36 \text{ GW/cm}^2$, well above the plasma formation threshold. An Apple Macintosh microcomputer controlled the timing of the laser pulse and the entire data acquisition sequence.

Light from excited atoms in the ablation plume was detected at an angle of 45° to the surface normal and focused onto the entrance slit of a Macpherson 218 Czerny-Turner spectrometer with a Thorn EMI photomultiplier tube. Pulses from the photomultiplier were amplified and summed in a Stanford Research gated integrator (SR 245) for an integration time of 300 ns following the start pulse provided by the external trigger signal. The grating spectrometer was scanned by a stepping motor controlled by the microcomputer. Yields were obtained by subtracting a linear background from the Gaussian peak.

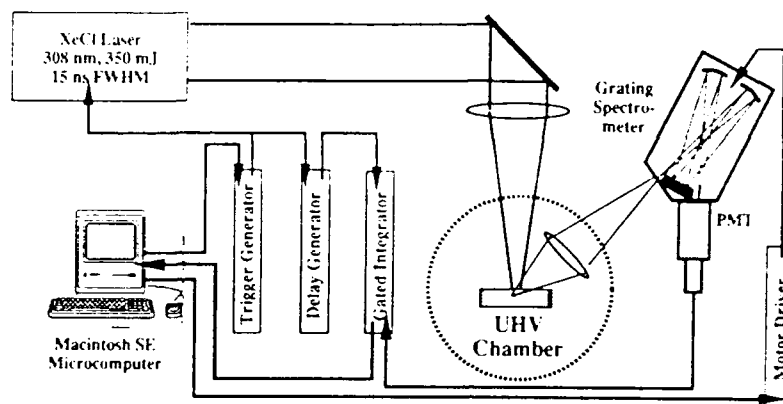


Figure 1. Apparatus for uv laser ablation measurements.

Figures 2 and 3 show typical spectra obtained by scanning the spectrometer with one laser pulse per point. To study the behavior of different species, spectral gates were set and data collected in a range of typically twenty points around each peak. This gave a reasonably rapid data acquisition, and yielded a run-to-run reproducibility of the peak integration of order $\pm 10\%$.

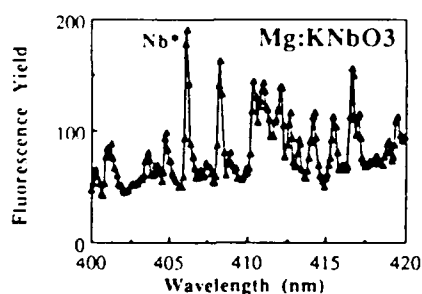


Figure 2. Spectral scan in the range from 400 to 500 nm, showing the Nb^* signal at 406 nm from laser ablation of Mg:KNbO_3 .

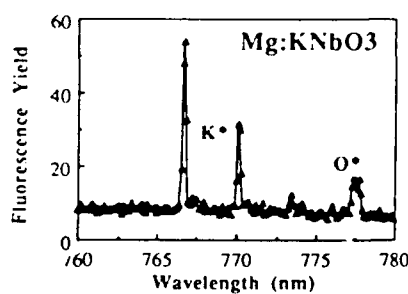


Figure 3. Spectral scan over the range 760-780 nm showing the fluorescence from K^* and O^* atoms ablated by uv laser from Mg:KNbO_3 .

Some clues to the ablation mechanism can be seen from the appearance - or lack thereof - of certain lines in the spectra. The alkali lines are the familiar resonance lines, as one might guess. The O* line - the 777 nm doublet - has a parent state lying close to the ionization limit; however, we do not see cascade transitions we might expect from this state, suggesting selective multiphoton excitation of ground-state oxygen in the laser plume. The table below lists some of the major transitions used to track the ablation process in our experiments.

Atom	λ (nm)	Transition	Level 2 (cm ⁻¹)	Level 1 (cm ⁻¹)	A ₂₁ (10 ⁻⁸ s ⁻¹)	f ₂₁
K	767-770	4s - 4p	13,024	0	0.39	1.02
Nb	406		25,680	1,050		
O	777	2p ³ 3s - 2p ³ 3p	86,629	73,768	0.34	0.92
Na	589	3s - 3p	16,968	0	0.63	0.98

Experimental Measurements

We focus here on three types of measurements on KNbO₃: (1) excited atom yields as a function of laser intensity; (2) relative intensity of impurity vs. intrinsic atoms from the various crystals; and (3) excited atom yield as a function of shot number. We will focus particularly on those features of the data which may reflect the signatures of electronic, rather than thermal, ablation mechanisms. More details of laser ablation experiments on both LiNbO₃ and KNbO₃ are contained in two forthcoming publications [7].

Measurements of the *intensity or fluence dependence* of different excited species furnish important clues to the mechanism of ablation. Figure 4 compares the intensity dependence of Nb* (406 nm), K* (767 nm) and O* (777 nm) over the laser-pulse energy range from 60 to 160 mJ, using the standard log-log plot. While all species show an initial steep rise followed by a saturation behavior with an onset at about 80 mJ, the oxygen and potassium show a pronounced saturation at the highest fluences, going from an initial slope of order 3 to a final slope of order 1 - implying a definite change in the mechanism of ablation. The initial slopes of the K* and Nb* yield curves are approximately 2.3 and 1.3, respectively.

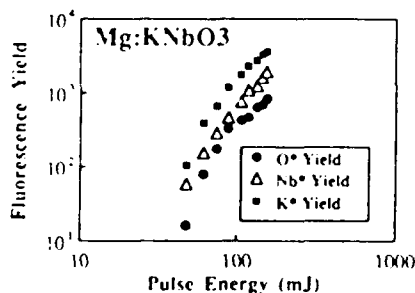


Figure 4. Fluence dependence of the signals from O*, K* and Nb* from Mg-doped KNbO₃. Note the change in slope of the O* curve at about 80 mJ.

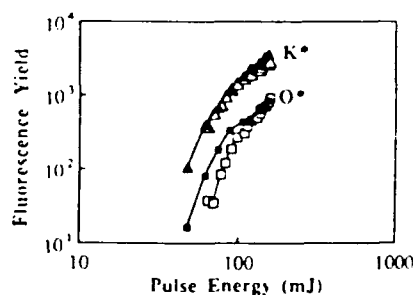


Figure 5. Fluence dependence of the K* and O* signals from pure (open plot symbols) and Mg-doped KNbO₃ (filled symbols).

Figure 5 shows a comparison between K^+ and O^+ from pure $KNbO_3$ and $Mg:KNbO_3$. The horizontal scale is proportional to fluence or intensity. We had expected to see a difference, because experiments on Mg-doped $LiNbO_3$ have shown a lessening of low-intensity photorefractive damage *vis a vis* pure material. Here, however, there is only a slight difference in the intensity dependence of the O^+ yield and threshold for the two materials. Comparison of the K^+ yield from Mg- and Ti-doped $KNbO_3$ also showed very little difference.

Another critical variable for identifying electronic effects in ablation is a change of surface electronic or geometrical structure. In laser ablation, the intensities are so high that if thermal mechanisms are dominant, one would not expect to see any strong dependence on surface condition. With these dielectric materials, the charging of the surface precludes the effective use of many of the standard ultrahigh vacuum surface diagnostics (*e.g.*, low-energy electron diffraction or photoemission). However, we can change the state of the surface by altering the sequence of measurements, in this case comparing intensity-dependent measurements starting at high and low intensities. Since the laser irradiation may create mobile defects, dense electron-hole plasmas, or structural alterations of the surface, a comparison of intensity-dependent measurements made by increasing or decreasing intensity may highlight such electronic effects.

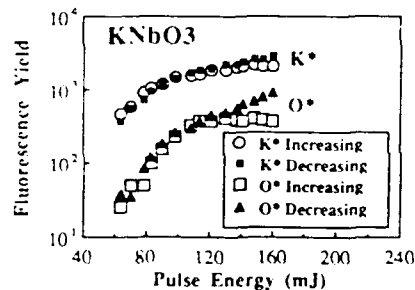


Figure 6. Intensity dependence of the signals from O^+ and K^+ from pure $KNbO_3$, with intensity increasing (open plotting symbols) and decreasing (filled symbols).

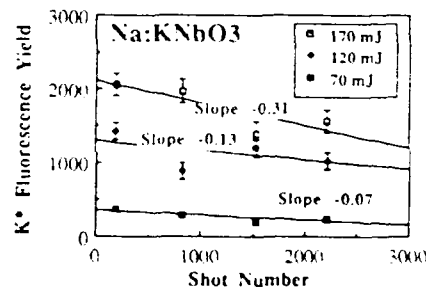


Figure 7. Shot-number dependence of the K^+ atoms from Na-doped $KNbO_3$ at fluences of 170, 120 and 70 mJ. Error bars are the standard deviations of the data (fluorescence yields).

A similar manifestation of the difference created by surface preparation or surface conditioning is shown in Figure 7, where the decrease of fluorescence intensity with shot number is shown at three different fluences. At the maximum pulse energy of 170 mJ/pulse - corresponding to an intensity of some $35 \text{ GW}\cdot\text{cm}^{-2}$ - there is a strong decrease in yield with shot number. In contrast, at 70 mJ/pulse, the slope of yield with shot number is a factor of four smaller. At some smaller fluence, it should be possible to desorb relatively small numbers of excited atoms without any change in yield as a function of shot number. Just this result has been observed in other experiments with $LiNbO_3$, in which desorption yields at low fluence have remained virtually constant for many thousands of shots. Thus there may exist different types of sites - perhaps with identifiable variations in electronic or geometrical structure - which are susceptible to ablation at differing fluence ranges, as recently reported in the semiconductor GaP [8].

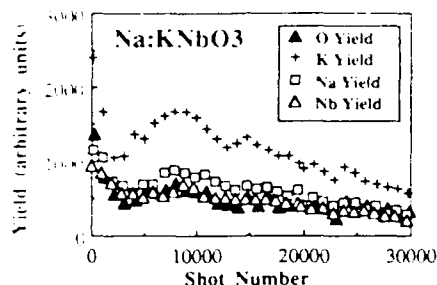


Figure 8. Intensity dependence of the fluorescence signals from K^* , O^* , Na^* and Nb^* from Na-doped $KNbO_3$ as a function of shot number.

Finally, we show in Figure 8 the fluorescence yield of excited atoms from $Na:KNbO_3$ as a function of shot number. Within the standard deviation of the data, there is no difference in the yields of Na^* , O^* and Nb^* ; the K^* shows a significantly higher yield, but also a steeper drop at the beginning of the shot sequence. This suggests that the different species may be ablated from surface sites of correspondingly different geometric or electronic structures. The initial precipitous drop in the yield of excited alkali atoms is in all likelihood caused by metallization of the surface and the subsequent resonant ionization of the excited alkalis.

Discussion: Mechanisms of Ablation

In considering ablation mechanisms, the principal issues are: (1) What is the driving force for the initial motion of ions away from the surface? (2) What is the source of the observed electronically excited atoms? and (3) What are the effects of the electronic or geometric structure of the surface on ablation?

Potassium niobate is an ABO_3 perovskite [9], while lithium niobate is a "perovskite-like" structure with about one-third metal-ion vacancies.[10]. Both materials have bulk band-gap energies slightly less than 4 eV; hence, for the XeCl laser used in these experiments (308 nm = 4 eV) each laser photon excites an electron from the valence band into the conduction band. Both materials are relatively ionic, with the valence band formed principally from the 2p orbitals of the oxygen ions; the conduction band is made up primarily of the K (or Li) and Nb orbitals. Both the linear and nonlinear optical response of the materials is primarily *interatomic* [11]. To the extent that desorption of excited atoms is correlated with the optical response [12], we expect that ablation results from the creation of holes on the oxygen ions and the consequent transfer of electronic charge to the metal ions. This transfer of charge destabilizes the crystal lattice and provides the driving force for the initial ionic motion.

The possible origin of the excited atoms appears to differ from one ablated species to the next. In the case of oxygen, the intensity dependence at low fluences, at least, suggests multiphoton excitation of ground-state neutral oxygen in the ablation plume, because the precursor of the excited state can be excited by a three-photon transition. Excited alkali atoms could be the result of the decay of localized electronic excitations (*e.g.*, excited *F*-centers) at low fluence, or secondary-electron excitation of desorbing ground-state neutrals. Changes in the fluence dependence of the excited-state yield at high fluences may signal a loss of flux from the excited-state channel due to resonant ionization of desorbing excited neutrals. The excited niobium atom yields, on the other hand, show an almost linear intensity or fluence dependence which is not consistent with either of these two pictures, and requires further analysis.

It is tempting to speculate on the significance of the "magic" laser fluence of 80 mJ which divides the yield curves into two distinct intensity regimes. If we assume that the entire flux of incident photons is absorbed in a depth of 2 μm , the volume irradiated by the laser spot is of order $8 \cdot 10^{16} \text{ \AA}^3$, while the number of photons in an 80 mJ laser pulse at 308 nm is of order 10^{17} . At this density, every ion is near an electron-hole pair created by the laser pulse, and the strong interaction between e-h pairs can drastically change the charge-transfer dynamics and Coulomb energy balance on a relatively short time scale. In this limit, we must apply concepts from fluid mechanics or solid-state plasma physics rather than electronic structure in the single-atom or single-ion limit.

We conclude that excited-atom spectroscopy furnishes a variety of important clues to the mechanism of laser ablation of ferroelectrics, because the excited atoms can only be created at the surface or in the plume of the laser-ablated ejecta. The emission spectra can clearly be used as process diagnostics in laser micromachining schemes for the niobates. However, in order to understand the ablation process, it will be necessary to correlate these results with studies of ground-state atom, molecule and cluster ablation, since most of the incident laser energy is generally believed to be channeled into ablation of these species.

Acknowledgements

We appreciate the expert preparation of the KNbO_3 crystals by Dr. H. Hesse, Fachbereich Physik, Universität Osnabrück. This research was supported in part by the Office of Naval Research through the Medical Free-Electron Laser Program of the Strategic Defense Initiative Organization. Travel support for the collaboration between Vanderbilt University and the Universität Osnabrück was provided by the Scientific and Cultural Affairs Office of the North Atlantic Treaty Organization.

References

1. J. Sapriel, *Acousto-Optics* (Chichester: John Wiley, 1979) trans. S. Frances and B. Kelly.
2. Y. Silberberg, *Optics News* **15** (February 1989) 7-12.
3. W. J. Koslovsky, W. Lenth, E. E. Latta, A. Moser and G. L. Bona, *Appl. Phys. Lett.* **56** (1990) 2291-2.
4. M. Eyett and D. Bäuerle, *Appl. Phys. Lett.* **51** (1987) 2054.
5. C. I. H. Ashby, G. W. Arnold and P. J. Brannon, *J. Appl. Phys.* **65** (1989) 93-97.
6. T. Krauss, A. Speth, M. M. Opryski, B. Fan and K. Grebe, *Appl. Phys. Lett.* **53** (1988) 947-949.
7. A. Niehof, K. Becker, R. F. Haglund, Jr., J. Arps, W. Heiland and L.-J. Wang, to be submitted to *Nucl. Instrum. Methods in Phys. Res.*; K. Tang, M. Affatigato and R. F. Haglund, Jr., to be submitted to *Appl. Phys. Lett.*
8. K. Hattori, Y. Nakai, A. Okano, N. Itoh and R. F. Haglund, Jr., submitted to *Phys. Rev. Lett.*
9. M. E. Lines and A. M. Glass, *Principles and Applications of Ferroelectrics and Related Materials* (Oxford: Oxford University Press, 1975).
10. R. S. Weiss and T. K. Gaylord, *Appl. Phys. A* **37** (1985) 191-203.
11. M. E. Lines, *Phys. Rev. B* **41** (1990) 3372-3382.
12. P. H. Bunton, R. F. Haglund, Jr., D. Liu and N. H. Tolk, submitted to *Phys. Rev. B*.

Laser-induced fluorescence and nonlinear optical properties of ion-implanted fused silica

K. Becker, L. Yang and R.H. Haglund, Jr.

Department of Physics and Astronomy, Vanderbilt University, Nashville, TN 37235, USA

R.H. Magruder and R.A. Weeks

Department of Materials Science and Engineering, Vanderbilt University, Nashville, TN 37235, USA

R.A. Zuhr

Solid-State Division, Oak Ridge National Laboratory, Oak Ridge, TN 37831, USA

We report absorption, fluorescence and nonlinear optical properties of fused silica implanted with Ti, Cu and Bi and doses of 1×10^{15} to 6×10^{16} ions/cm² when irradiated with 532 nm laser light. The fluorescence spectrum is a broad band around 640 nm and shows little variation for all ion species. Absorption as a function of implanted dose shows a threshold for Ti between 1×10^{16} and 6×10^{16} ions/cm². The nonlinear optical index is large, $n_2 > 10^{-5}$ esu. All measured quantities show a strong dependence on the implanted ion dose. The source of the nonlinearity, whether electronic or thermal, remains to be more completely determined.

1. Introduction and motivation

Ion implantation has been used to alter electronic, thermal and mechanical properties of substrates. During the last two decades, the growth of optical communications technology has also motivated research on modification of the linear index of refraction of dielectrics in order to make waveguides for optical carrier signals [1]. However, significantly less attention has been paid to other optical properties of ion-implanted dielectrics, even though this technology offers a number of advantages in control of electronic structure and gross optical properties of the implanted region. In this article we present a number of results relevant to the possible use of ion-implanted fused silica in active optical devices and circuits, including intensity-dependent absorption, laser-induced fluorescence and ion-species-dependent nonlinear susceptibility.

2. Sample preparation and characterization

High-purity silica discs, 1 mm thick, 20 mm diameter, were used as substrates for implantation. The manufacturer of the silica (Thermal American, Inc.) lists total cation impurities as < 200 ppm H₂ by weight, all others < 10 ppm. The principal anion impurity is Cl, comprising about 80 ppm by weight. The surfaces of the

discs were polished to optical quality, then cleaned with ethyl alcohol and distilled water and dried in ambient laboratory air prior to implantation. The disks were implanted with 160 keV Ti ions at an average current of $2 \mu\text{A}/\text{cm}^2$. At this current density, the temperature of the substrate remains below 35°C . The concentration of ions as a function of depth in the substrate was measured by Rutherford backscattering. For Ti and Bi it is approximately a Gaussian function with the maximum at 120 nm below the surface and 140 nm full width at half maximum. For Cu and doses $> 3 \times 10^{16}$ ions/cm², the depth profile is bimodal, with peaks at about 90 nm and 170 nm. Some samples were implanted on both sides.

The electronic state of the implanted ions is less well characterized. For doses $> 5 \times 10^{15}$ ions/cm², the fraction of Ti in the $3+$ state, as measured by electron paramagnetic resonance and optical absorption spectroscopy, is $> 10\%$. The fraction decreases with increasing dose [2]. Implanted Cu may be neutral, in the $2+$ state, or aggregated as colloids [3]. The implantation process also produces defects in the implantation zone. In silica the most prominent defects are E' centers, nonbridging oxygen-hole centers and peroxy molecular ions [4]. Concentration of these defects varies with implanted ion species [5,6]. In case of Ti the E' centers have the highest concentration of all defects for doses $> 5 \times 10^{15}$ ions/cm². Since these defects also have a

spectrum of optical transition, it is critical to understand the effect of the ion dose on the absorption spectrum of the implanted silica.

3. Experimental apparatus

The light source was a mode-locked, frequency-doubled Nd:YAG laser (532 nm, 100 ps FWHM pulse width, 76 MHz pulse repetition rate, 1.8 W maximum average power). At this wavelength Bi-, Ti- and Cu-implanted silica absorbs strongly.

Fig. 1a shows schematically the setup for z-scan and absorption measurements. In position (2) power meter D1 measured the total incident power on the sample S. In position (1) it monitored the power reflected from the beamsplitter BS while the sample was irradiated. It was mounted on a self-centering base for accurate repositioning at positions (1) and (2). Power meter D2 measured the transmitted power.

For absorption measurements lens L2 was mounted behind the sample to focus all transmitted light on D2. The laser spot on the sample had about 0.5 mm diameter and the total laser power was varied to measure absorption as function of intensity.

For the z-scan lens L1 with $f = 150$ mm was mounted behind the beamsplitter and the sample was mounted

close to the focal point of the lens, i.e. the sample was placed to the left of the focal point of the lens as shown in Fig. 1a. The distance between the sample and the lens was 800 mm.

Figs. 1b and 1c give a qualitative explanation of the z-scan method. Let the sample be described by $n(r)$ or $v(r)$ (Fig. 1b) or n_2 (Fig. 1c) with the nonlinear index of refraction, n_2 , leads to self-focusing. The incoming plane wave has a Gaussian radial intensity profile, $I(r)$ (r : distance from beam axis). This causes a radial profile for the total index of refraction, $n(r)$, and speed of light, $v(r)$, in the sample (n_0 : linear index of refraction; c : vacuum speed of light; unlike ref. [7] n_2 in this work refers to the nonlinear index independent of units):

$$n(r) = n_0 + \frac{1}{2}n_2I(r), \quad v(r) = c/n(r).$$

The speed profile distorts the plane wave approximately like a lens. Fig. 1c explains how the intensity on detector D2 changes as the self-focussing sample, shown as lens, is moved through the focal point of lens L1. In position (a) the sample increases divergence of the outgoing beam, so the intensity on detector D2 decreases, in (b) it has no effect, in (c) it decreases divergence, so intensity increases. For positions far from the focal point the intensity on the sample itself is so low, that self-focussing can be neglected and the intensity on the detector is the same as in (b).

The laser-induced fluorescence spectra were taken with a double grating spectrometer designed for high rejection of stray light from the laser.

4. Results

4.1. Absorption of Ti-implanted silica

We observed a number of puzzling features in the absorption and reflectivity spectra of the sample. Fig. 2 shows that the absorption of Ti-implanted samples strongly depends on the ion dose. Between 1×10^{16} and 6×10^{16} ions/cm² is a threshold for the dose, where

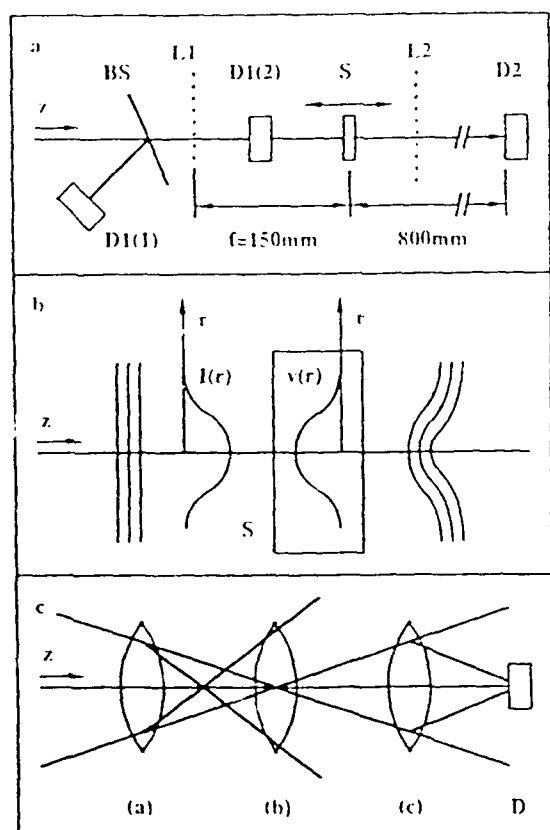


Fig. 1. Experimental apparatus and explanation of z-scan. See text.

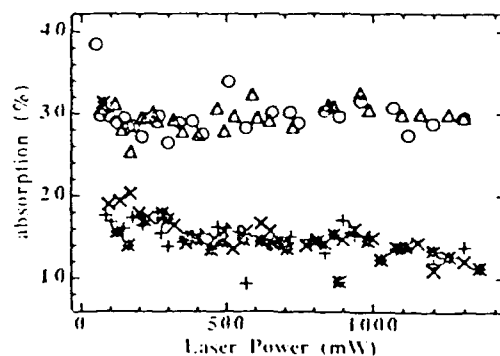


Fig. 2. Absorption of Ti-implanted fused silica. Doses (1×10^{16} ions/cm²): $\circ = 60$, $\Delta = 60$, $+$ = 10, \times = 3, \bullet = 1.

absorption jumps from about 17 to 50%. As shown in Fig. 2, the absorption at 413 nm is independent of the focusing which was observed.

At the power levels used (100 to 150 mW), absorption for the high dose samples is independent of the incident power. The low dose samples show saturation; absorption drops from 17 to 12% as power increases from minimum to maximum. Measurements of reflection, to be published elsewhere, show the onset of saturation more clearly.

4.2. Laser-induced fluorescence (LIF)

A second potentially interesting property of these materials is that the ion-implanted layer exhibits LIF in a broad range, and is thus a *prima facie* candidate for tunable solid-state laser material. In recent years, Ti^{3+} doped crystalline sapphire has been intensely developed as a laser host [8]; it exhibits a broad fluorescence in the near-infrared, a region where laser dyes are either non-existent or have low gains.

We have observed moderately intense LIF for samples implanted with Ti, Bi and Cu. Fig. 3 shows a typical spectrum for Ti. Spectra for Bi- and Cu-implanted samples look nearly identical, with the peak maximum shifted by 10 nm to lower wavelength for Bi and by 30 nm to longer wavelength for Cu. The samples do not show fluorescence over the full implanted area, but only a few spots on each sample of about 1 mm diameter emit light. The mechanism leading to fluorescence is not clear yet. The similarity of the spectra for these different ions indicates that processes independent of the type of ion lead to fluorescence. Currently the role of defects like E' centers is being investigated.

4.3. Nonlinear index of refraction

Among the most striking phenomena observed in these materials is a dose-dependent nonlinear index of refraction. Fig. 4 shows the results for a Ti- and a

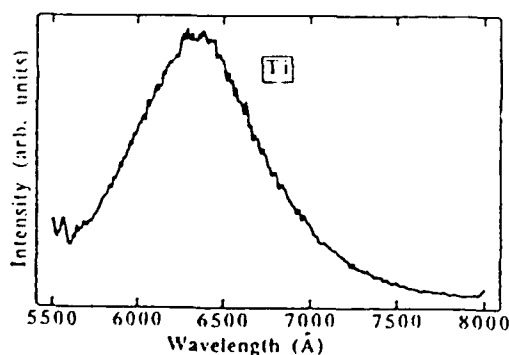


Fig. 3. LIF spectrum of Ti-implanted fused silica. The structures at the ends of the spectrum are from stray light of the laser.

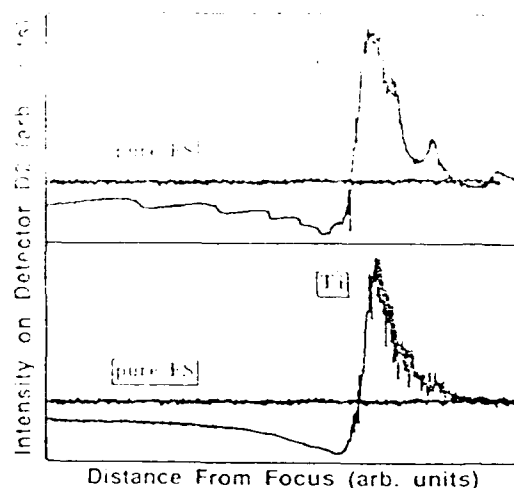


Fig. 4. Results of z -scan for pure, Ti- and Cu-implanted fused silica.

Cu-implanted sample (both 6×10^{16} ions/cm² each side). The intensity on detector D2 first drops, indicating positive self-focussing or positive n_2 , and then rises steeply as the sample crosses the focal point. The absolute value of n_2 can be calculated from the valley to peak ratio [7] and is of the order 10^{-5} esu (or 10^{-11} m²/(W n_0) in mks units) [9].

The curve for the Cu-implanted sample has a significant substructure on the leading and trailing edge. We have two possible explanations for this, none of which can be ruled out without further experiments. One is the formation of colloidal copper: the particles in the colloid have different sizes leading to nonlinear bleaching at different light intensities. The other is constructive and destructive interference between the two implanted layers on the front and back side of the sample, but that leaves the question why the Ti-implanted sample does not show any structure.

5. Conclusions

We have shown that implanted layers exhibit a number of interesting active optical properties in addition to the change in linear index of refraction which accompanies the ion-induced densification of an implanted layer. These properties may well make ion implantation a useful new way to modify silica for light sources and active optical elements. However, the effects of radiation-induced defects must be thoroughly understood before any such applications are possible. Finally, we note that it may also be possible to exploit the nonlinear optical effects to study the interaction between the implanted ion and its environment in ways which are inaccessible to traditional methods of radiation-damage analysis, such as electron paramagnetic resonance.

Acknowledgements

The research at Vanderbilt University was supported in part by the National Science Foundation under contract DMR 88-13731 and by the Office of Naval Research under Contract N00014-87-C-0146. The ion implantation facility and staff at the Oak Ridge National Laboratory are supported in part by the Division of Materials Science, Department of Energy under contract DE-AC05-84OR21400 with Martin-Marietta Energy systems, Inc.

References

- [1] P.D. Townsend, *Rep. Prog. Phys.* **50** (1987) 501.
- [2] R.A. Weeks and G. Whichard, *J. Appl. Phys.* **67** (1990) 7526.

- [3] J. H. Edgar, *Phys. Rev. Lett.* **64**, 1077 (1990).
- [4] J. H. Edgar, *Phys. Rev. Lett.* **64**, 1079 (1990).
- [5] J. H. Edgar and R. A. Weeks, *J. Non-Cryst. Solids* **114**, 115 (1990).
- [6] H. Hosono, *J. Appl. Phys.* **69**, 1250 (1990).
- [7] H. Hosono and R.A. Weeks, submitted to *J. Appl. Phys.*
- [8] M. Sheik-Behae, A.A. Said and E.W. Van Stryland, *Opt. Lett.* **14** (1989) 955.
- [9] P.F. Moulton, *J. Opt. Soc. Am. B5* (1989) 125.
- [10] L. Yang, K. Becker, R.L. Haglund Jr., and R.A. Weeks, *Bull. Am. Phys. Soc.* **35** (1990) 1250.

The Role of Valence-Band Excitation in Laser Ablation of KCl

Richard F. Haglund, Jr., Kai Tang, Patrick H. Bunton* and Ling-Jun Wang**

Department of Physics and Astronomy
Vanderbilt University, Nashville, TN 37235

ABSTRACT

We present recent measurements of excited-atom and ion emission from KCl surfaces illuminated by vacuum-ultraviolet synchrotron radiation ($h\nu = 8\text{--}28\text{ eV}$) and ultraviolet laser light ($h\nu = 4\text{ eV}$). At low intensities characteristic of the synchrotron experiments, excited atoms are desorbed by simple valence-band excitation process involving the metallization of the KCl surface. At the higher intensities typical of laser desorption and ablation, we observe a strong decrease in K^+ emission as a function of the number of laser shots, but an essentially constant yield of Cl^+ . K^+ and Cl^+ emission at high intensities show similar behavior. The energetics of these desorption phenomena can be treated in a bond-orbital model which shows that creation of a single valence hole is sufficient to excite an ion to an anti-bonding state.

1. INTRODUCTION AND MOTIVATION

The need to improve the laser damage resistance of optical materials, and the growing interest in the use of high-intensity lasers for processing electronic and photonic devices, are the primary drivers for fundamental studies of laser-surface interactions. Laser-induced surface¹ and bulk² damage in KCl have been studied for many years, perhaps because KCl is the simplest of all the wide-bandgap ionic solids from the standpoint of electronic structure. We have recently begun a systematic study of ultraviolet photon-stimulated desorption (PSD) of excited atoms and ions from the surface of KCl, which has led to new understanding of the mechanisms of desorption following both valence-band³ and core-level⁴ excitation. These experiments also illustrate the specific sensitivity of ion- and excited-atom desorption spectroscopy to details of the surface before and after particle emission.

In this paper, we briefly summarize the status of these experiments and propose a unified view for the mechanisms of PSD and laser-induced desorption (LID) and ablation of excited atoms in KCl, a view which probably applies generically to materials which have self-trapped excitons and/or permanent, mobile electronic defects, such as SiO_2 and the alkaline-earth halides. In the VUV experiments, the yield of desorbed excited atoms follows the excitonic optical response of these crystals at photon energies near the bulk band gap. Secondary electron measurements, taken simultaneously, implicate the formation of excess metal in PSD of excited alkalis, and suggest some clues to the time dependence of the M^+ yields. At the higher intensities characteristic of LID and laser ablation, a common mechanism of desorption due to valence-hole creation, as well as charge exchange mediated by surface metallization, is at work.

The energetics governing desorption may be interpreted within the framework of a detailed mechanistic picture of laser-induced desorption and ablation, based on the bond-orbital model of electronic structure. In this model, ion motion is caused by localized deformation of the lattice and bond-breaking near the site where the photon is absorbed. Neutralization of the moving ion into an excited atomic state, on the other hand, is a manifestation of the local electronic structure near the desorption site, at least in the low-intensity limit. Both desorption and excitation may arise from the same mechanism. For example, desorption following valence-band excitation may be described as the decay of an excited quasi-molecular-state of the crystal; in KCl, the desorption of K^+ could be initiated by relaxation of an excited F -center.

* Now at Department of Physics, Box 4608, Austin Peay State University, Clarksville, TN 37044

** Now at Department of Physics and Astronomy, University of Tennessee, Chattanooga, TN 37403

2. APPARATUS AND MEASUREMENTS

The following discussion of the role of valence-band excitations in laser-induced desorption from KCl is based on two distinct sets of measurements: photon-stimulated desorption (PSD) measurements using ultraviolet radiation, and laser-induced desorption (LID) using an excimer laser. The photon source for the PSD experiments was the Aladdin facility of the Synchrotron Radiation Center (SRC) at the University of Wisconsin. Bending-magnet radiation from the 800-MeV electron storage ring was dispersed by a Seya-Namioka (SN) normal-incidence monochromator and focused onto a sample at normal incidence. Useable photon flux is available in the approximate range of 8 eV to 28 eV. The light source for the LID measurements was an XeCl excimer laser operating at a wavelength of 308 nm, likewise incident along the surface normal.

Single-crystal targets of KCl, typically measuring 5x12 mm and cleaved from bulk material prepared by Harshaw were mounted on a micromanipulator in high or ultrahigh vacuum (UHV). In the UHV measurements, the target holder was equipped with a Varian button heater capable of heating targets to approximately 450° C. The target could be rotated about a vertical axis perpendicular to the plane of the incident photon beam.

Two generic measurement schemes were used in the experiments described in this paper. Fluorescence from desorbed excited alkali atoms was detected with an 0.3 meter monochromator and a photomultiplier (PMT) operated in pulse counting mode for the PSD measurements, and in pulse-height analysis mode, using a gated integrator, for the LID measurements. Amplified PMT pulses which exceeded the threshold of a discriminator were counted and stored in an Apple microcomputer. Secondary electrons were collected by a biased stainless-steel collector positioned close to the target; the current was monitored by a picoammeter connected to an analog-to-digital converter channel of a Hewlett-Packard 7090A plotter; these data were then likewise stored in the computer. All of the PSD experiments and most of the LID measurements were carried out in an ultra-high vacuum chamber with a base pressure generally in the range of $\sim 10^{-10}$ Torr.

In other LID experiments, the optical detection system shown in Fig. 1 was replaced by a quadrupole mass spectrometer which could be operated to collect either positive or negative ions. A mass scan was performed to ascertain that the peak corresponding to a particular mass was stable and well above background. Then an electronic gate was set to capture the peak signal after each laser shot. These peak height data were stored on-line in an IBM microcomputer for subsequent retrieval and analysis.

In the PSD experiments, single KCl crystals were cleaved in air and inserted immediately into the UHV chamber; they were typically under vacuum within an hour after cleaving. The UHV system was then baked at 200°C for several hours following insertion of the target; samples were then cleaned by heating a few hours at 300 to 400° C. Numerous studies, cited in Reference [4], have shown that this procedure yields a stable and reproducible surface. For the LID experiments, the samples were cleaved in air using the same precautions (use of rubber gloves, methanol cleaning of all cleaving and handling tools)

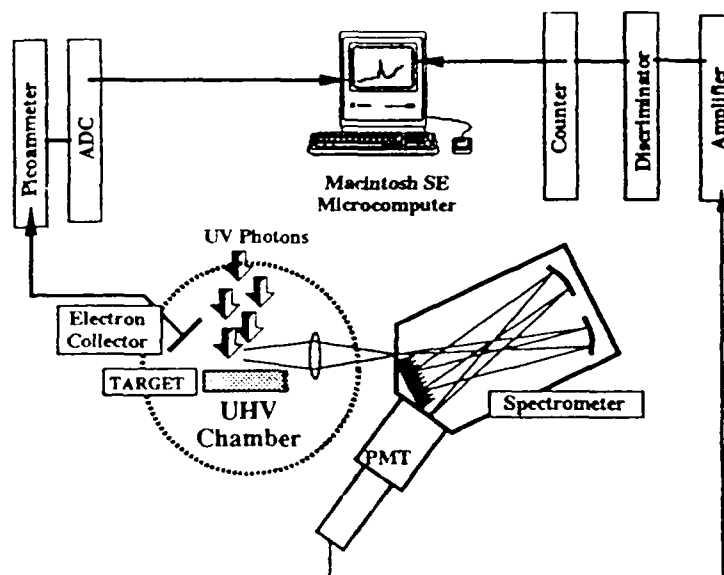


Figure 1. Schematic diagram of apparatus for simultaneous measurements of excited-atom yield and secondary-electron current in photon-stimulated desorption experiments.

taken in preparing UHV samples. However, the samples were not baked, and indeed were not always in ultrahigh vacuum. We assume that the surface is well cleaned due to sputtering by the high intensity laser pulses. Thus these laser desorption and ablation experiments must be viewed as having been carried out under reproducible conditions, but not necessarily on well-characterized surfaces.

3. PHOTON-STIMULATED DESORPTION IN THE VACUUM ULTRAVIOLET

Ultraviolet photon-stimulated desorption has been studied in the alkali halides for many years. Only recently, however, has it been demonstrated that PSD of excited atoms can be caused by valence-band, in contrast to core-level, excitation. Because these measurements have an important impact on our understanding of the mechanisms of laser-induced desorption, we summarize briefly the results of these recent experiments on both KCl and LiF. Details may be found in Reference [4].

Figure 2 shows an excitation function for desorbed excited potassium under photon irradiation of KCl near the surface exciton peak at 9.5 eV. The bulk bandgap of KCl is 8.4 eV. The monochromator flux was too low to search for structure in the desorption curve at lower energies. Shown for comparison in Figure 3 is the optical absorption spectrum of KCl measured by Eby, Teegarden and Dutton.⁵ Structure in the excitation function for desorbed K^* corresponding to the valence exciton at approximately 9.5 eV is evidence that desorption due to valence excitation in KCl is occurring, and that excited-atom desorption may be related to identifiable electronic excitations of the surface.

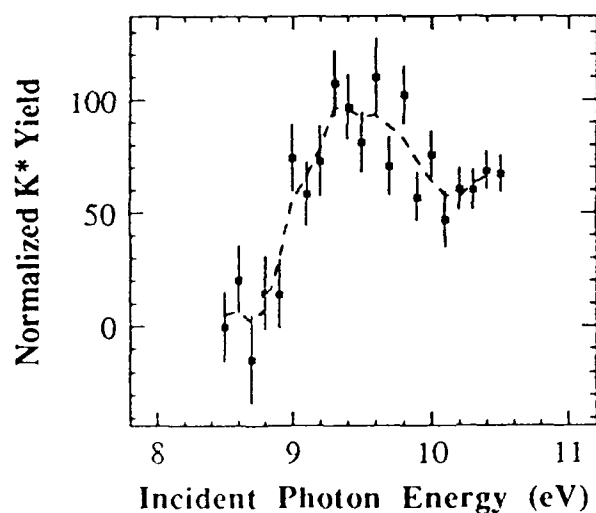


Figure 2. Excitation function for K^* atoms desorbed from a KCl surface by VUV light with valence-band energies. From Reference [4].

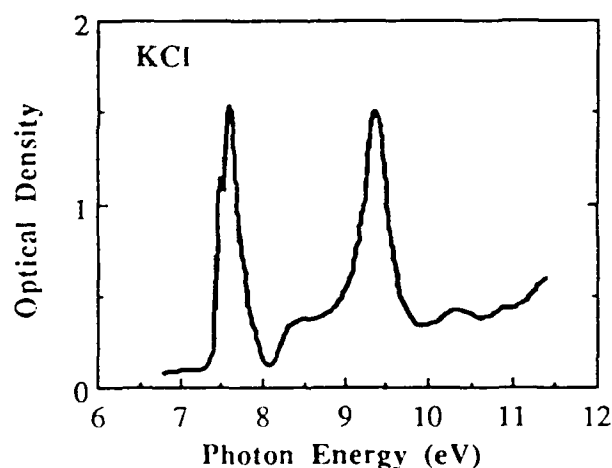


Figure 3. Optical absorption spectrum from KCl in the vacuum ultraviolet region. Figure is from Reference [5].

Studies of the variation in excited-atom and total electron yield, described in detail in Reference [4], clearly implicate the formation of excess metal on the surface in the desorption process. Those experimental results are consistent with the following picture: As a pristine spot on the surface is irradiated, metallization begins due to two separate processes. One is the loss of halogen because of the preferential ejection of ions from the halogen sublattice; the other is the creation of mobile defects (*e.g.*, *F*-centers) in the near-surface bulk and their subsequent diffusion to the surface, where they neutralize the positive metal ions. The experimental evidence for this is primarily the rapid decrease in secondary electron yield from the high values which characterize the insulating surface as cleaved to the lower values (an order of magnitude or more for most of the alkali halides) characteristic of the alkali metal.⁶

This progressive metallization can be stopped by heating the surface to the point at which the excess metal will evaporate thermally, leaving a stoichiometric surface. These thermally desorbing atoms constitute the bulk of the total desorption yield of the metal atoms, in the ground electronic state.⁷ The metallization also affects the yield of excited atoms, because as the metal agglomerates, its work function changes. When the metallic patches are small, the work function of the surface is rather large, and there are no metallic electrons which can be donated to fill the electronic state of a desorbing alkali ion. As metallization progresses, the work function decreases, and when the Fermi level is nearly resonant with the atomic excited state, neutralization of the ion into that excited state is probable. As the surface becomes more strongly metallized, the Fermi level of the metal patches rises *above* the first excited electronic state, and resonant charge exchange into the ground state becomes the dominant process. Thus, below the temperatures at which the metal evaporates, excited state desorption will first increase and then decrease as the Fermi level rises above the first excited state of potassium.

4. LASER-INDUCED DESORPTION AND ABLATION FROM KCl

The description of laser-induced particle emission is as problematical as the phenomenon itself is complex. In the following discussion, we shall refer to particle emission at low laser intensities as laser-induced desorption (LID); we mean to imply by this the absence of plasma and collective effects, and that the particle emission is, in this case, essentially a localized event resulting in the removal of an isolated atom or ion from an (at least hypothetically) identifiable surface site. By laser ablation we refer to the high-intensity limit, in which rapid damage to surface may involve collective effects and the generation of a plasma plume; in laser ablation, the characterization of the surface site is probably not possible.

We have carried out a series of experiments to study the change in the surface of KCl by monitoring the yields of excited atoms and ions from the surface, including K^* , Cl^* , K^+ and Cl^- . We have studied the change in K^* and Cl^* yields as a function of number of shots on the sample, and as a function of intensity. In addition, we have carried out simple measurements of the time dependence for the emission of positive and negative ions from the surface. These measurements are consistent with the PSD picture, but show in addition that laser-induced desorption (LID) proceeds through the same mechanism independent of the condition of the surface. Hence, LID from perfect lattice sites and defect sites appears to result from the same kind of valence-band excitation as observed in PSD, but with slightly different consequences because of the high density of local electronic excitation.

4.1 Laser-Induced Desorption of Excited Atoms

Optical spectra taken during laser ablation experiments generally show a relatively broad fluorescence background on which are superimposed atomic emission lines from excited atoms, radiating as they move away from the surface. In contrast to PSD experiments, we observe not only the first resonance line of the metallic atom, but lines originating in other excited states and the atomic emission lines of chlorine atoms and ions. Of particular interest is the appearance of excited-state emission whose parent states lie very near the ionization limits of the atoms in question; the mechanism for the creation of these highly excited states is not clear, although multiphoton excitation of ground-state atoms in the laser-produced plasma is probably the most likely possibility. Properties of the observed lines are shown in Table I.⁸

The calculated oscillator strengths shown in Table I are not always reflected in the relative spectral yields of the lines in question. This seems to be particularly true for the Cl^* states observed. We assume that this is indicative of highly nonequilibrium conditions which are likely to prevail both in the laser-produced plasma and at the surface. Also, the centroids of the lines as shown in the accompanying figures disagree slightly with those shown in the Table. Part of this discrepancy, typically 4 Å, is the result of calibration error in the spectrometer drive; the magnitude of the error was checked using a He-Ne laser at 6328 Å. In addition, since the excited atoms are emitted with non-zero velocity and since the spectrometer line-of-sight is not parallel to the surface plane, the lines will be Doppler shifted. This shift can, in principle, be calculated from a knowledge of the geometry of the desorption experiment.

TABLE I: Spectral Characteristics of Observed Atomic Transitions

Atomic Species	Wavelength (Å)	Atomic Transition	Upper Level (cm ⁻¹)	Lower Level (cm ⁻¹)	Oscillator Strength	Transition Rate (10 ⁸ s ⁻¹)
K	7676	4p → 4s	24,714	0	0.68	0.385
K	7699	4p → 4s	13,024	0	0.34	0.382
K	4045	5p → 4s	24,714	0	0.0091	0.0124
Cl	4105	3p ⁴ 5P → 3p ⁴ 4S	96,309	71,954	3.4·10 ⁻⁴	0.002
Cl	4601	3p ⁴ 5P → 3p ⁴ 4S	96,590	74,861	0.012	0.039
Cl	4624	3p ⁴ 5P → 3p ⁴ 4S	96,482	74,861	0.0029	0.0045
Cl	4654	3p ⁴ 5P → 3p ⁴ 4S	95,702	74,221	0.0016	0.0049
Cl	4661	3p ⁴ 5P → 3p ⁴ 4S	96,309	74,861	0.0065	0.01

Figure 4 shows the spectrum of excited potassium atoms near the first resonance lines at 7668 Å, observed at laser intensities on the order of 1 GW·cm⁻². Each point on the spectrum represents a single laser shot; there are two hundred points in each spectral scan from 7600 to 7800 Å. Thus some 140 shots intervene between the upper spectrum and the lower. The decrease in the K* yield with absorbed photon dose is evident. This phenomenon is well known from PSD studies, in which progressive ultraviolet irradiation of the alkali halides results in a steady decrease of the excited-state atomic emission.⁹ This

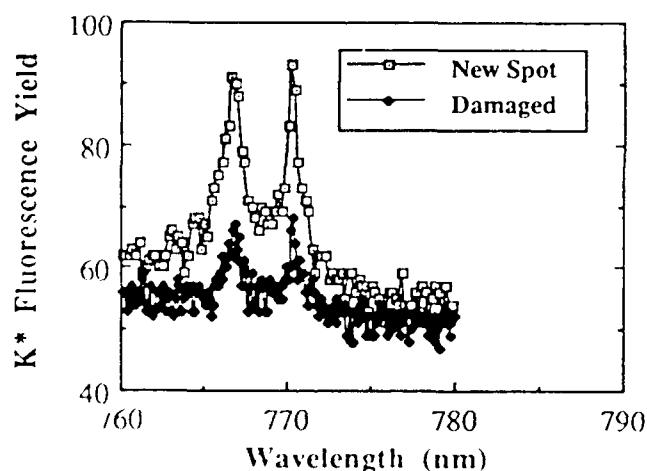


Figure 4. Spectrum of K* atoms desorbed from KCl at an intensity of 1 GW·cm⁻² on two successive scans, starting from a pristine spot on the surface. The atomic transition is 4p → 4s.

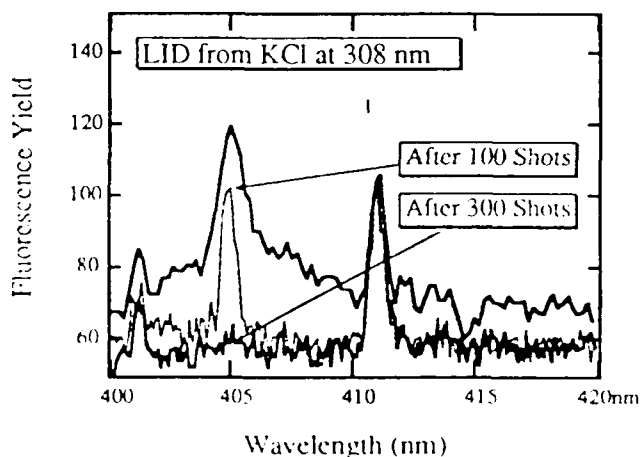


Figure 5. Optical spectrum of K* (405 nm) and Cl* (411 nm) atoms in the ablation plume from a KCl crystal surface at a laser intensity of order 1 GW·cm⁻², as a function of shot number.

behavior is consistent with a surface accumulation of excess metal leading to resonant ionization of desorbing K* atoms, thus reducing the total excited-state signal. Shown for comparison in Figure 5 are the relative yields of K* (from the 5p → 4s transition) and of Cl* emission originating from transitions in the (3p⁴5P → 3p⁴4S) manifold. The K* emission in this state also decreases after a few hundred shots, consistent with the resonant ionization picture. The Cl* emission, on the other hand, is virtually constant in amplitude as a function of total absorbed dose, indicating that the Cl* production is not affected by surface conditions, such as metallization. Given the high excitation required to produce the parent states of these emission lines (nearly 12 eV, as shown in Table I), we suggest that multiphoton excitation of ground-state Cl in the laser-produced plasma is producing these signals. Accurate measurements of the Cl* yields as a function of intensity should reflect this difference in origin.

In these experiments, a region of the optical spectrum containing lines from K^* and/or Cl^* was scanned by the spectrometer, and the optical signal at each wavelength from a single laser pulse was counted. The excited K was only observed when there was a visible plasma. This could indicate that the surface is so rapidly metallized that one can only produce desorption following ablation of the metal, which should be strongly heated and vaporized at these intensities. Most notable is the contrast between the persistence of the Cl^* yield and the relatively rapid disappearance of any K^* signal.

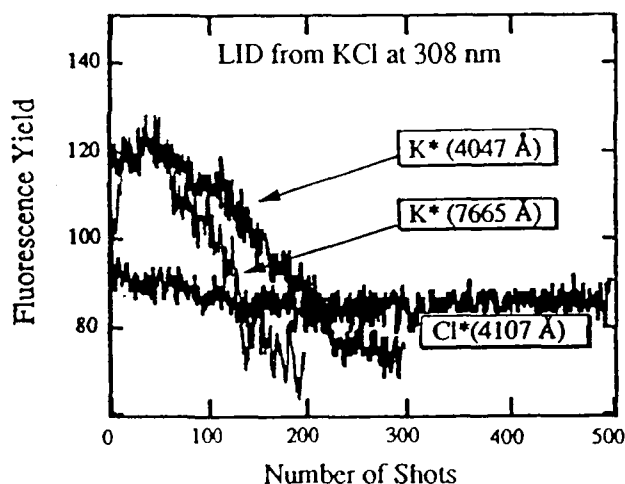


Figure 6. Spectrum of excited K atoms desorbed from KCl at an intensity of 1 GW-cm^{-2} starting from a pristine spot on the surface.

Figure 6 shows the yield of excited atoms desorbed from KCl at a laser wavelength of 308 nm and an intensity of about 4 GW-cm^{-2} , as a function of the number of laser shots on a particular spot. The measurements begin, in each case, from a previously undamaged spot. The transitions identified in the Figure are the 7668 Å line of K^* , the 4052 Å line of K^* , and the 4112 Å line of Cl^* . The variation in the behavior of the three species of excited atoms is: The K^* yields in both cases rise rapidly from the first laser shot, peak near the same value, and then drop off, but the K^* (7668 Å) yield goes to its background value after about 200 shots, whereas the K^* (4052 Å) yield does not decrease to background level for some 300 shots. The Cl^* yield, on the other hand, is essentially unchanged through the entire sequence. This behavior is consistent with the idea that excited K atoms are created in a different process than the excited Cl atoms.

If, indeed, resonant ionization of desorbing excited metal atoms is the mechanism, these data are consistent with the idea of progressive metallization of the surface with dose, since the Fermi level of the metal clusters would rise through the $4p \rightarrow 4s$ transition energy before the $5p \rightarrow 4s$, taking flux out of the former K^* channel prior to the latter.

4.3 Intensity Dependence of Positive and Negative Ion Yields

Yields of positive and negative ions were measured as a function of intensity using a quadrupole mass spectrometer in the geometry of Figure 1. In general, at laser intensities below 100 MW-cm^{-2} , stable ion signals were measured which showed that ion yield increased with roughly the second power of intensity. This is consistent with valence-band excitation. However, above this intensity the ion signals rapidly became unstable, and showed an initial high yield followed by a rapid drop in intensity. This phenomenon was observed for both K^+ and Cl^- ions, as shown in Figures 7 and 8.

After the ion yields dropped to their minimum values and the visible plasma indicating desorption of excited atoms disappeared, it was observed that bright fluorescence from color centers was being excited by the laser beam. No other signs of damage to the surface - cratering or etching - were observable by eye. As soon as the laser beam was directed to a fresh spot on the surface, the strong ion signal was once again observed. This suggests that the disappearance of the Cl^- signal and the diminution of the K^+ signals are both tied to the creation of defects in the near-surface region of the bulk. The initial high yields in both ion species apparently comes from defect sites, while K^+ originates, at a low level, in the perfect sites. The Cl^- ions, on the other hand, are apparently only ablated from defect sites, and once the surface becomes stoichiometric, the negative ion signal disappears too. Cl neutral atoms, of course, continue to be produced, as shown above and in the neutral Cl laser-desorption measurements of Reference [1].

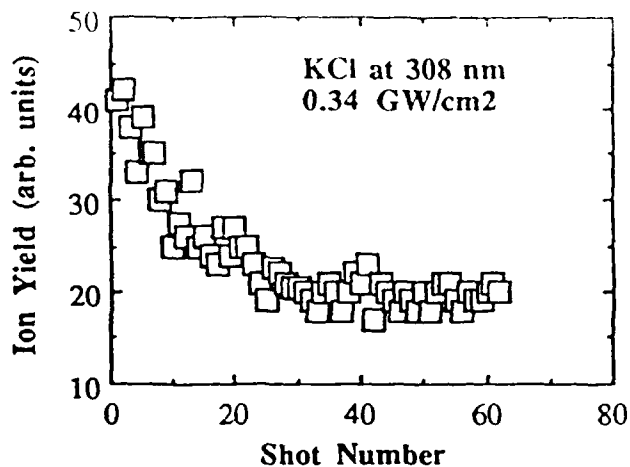


Figure 7. Intensity dependence of K^+ desorbed from KCl by an excimer laser (XeCl) at a wavelength of 308 nm. Intensity in the focal spot was $0.34 \text{ GW}\cdot\text{cm}^{-2}$.

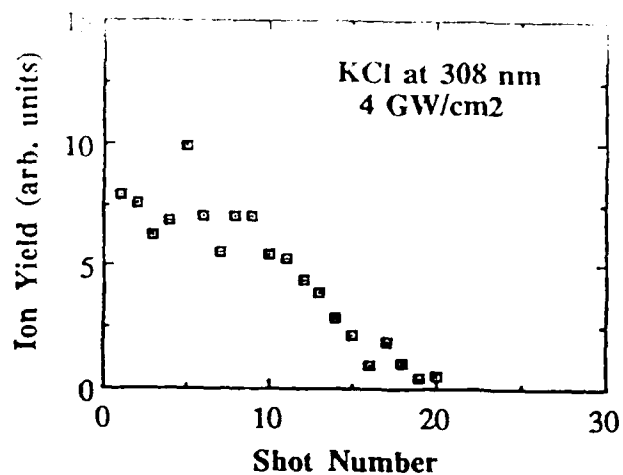


Figure 8. Intensity dependence of K^+ desorbed from KCl by an excimer laser (XeCl) at a wavelength of 308 nm. Intensity in the focal spot was about $4 \text{ GW}\cdot\text{cm}^{-2}$.

4.4 Time Dependence of Ion Yields

We have measured the time dependence of positive and negative ion yields from KCl by placing a biased stainless steel probe in the UHV chamber approximately 4 cm from the surface of the target and at an angle of 45° to the target normal. By switching the polarity of the probe from +67 V to -67 V, it was possible to collect both the positive and negative charges. For that voltage, the time of flight for a typical alkali ion is of order $4 \mu\text{s}$ and that for fast electrons is about 16 ns. Ion current was recorded on a synchronized single-shot basis by a 100 MHz transient waveform recorder interfaced to a microcomputer.

Figure 9 shows the transient signals of both positive and negative ions desorbing from the KCl crystal surface. The positive ion signal has an apparent decay time of some 25-30 μs , much longer than that measured for NaCl, and is initiated well after the negative ion fast signal has already begun to decay. The current of negative ions has both a fast and slow component. The slow component can be strongly suppressed by applying a magnetic field, and is thus assumed to consist primarily of slow electrons. The decay

time of the fast negative ion signal is much less than that of the K^+ signal, indicating that the Cl^- ion is desorbed by a different mechanism than the positive ions. This is consistent with earlier results from electron-stimulated desorption studies which show that neutral halogens are ejected from the surface before sodium atoms, and that the halogen is ejected in a non-thermal process on a time scale much less than 100

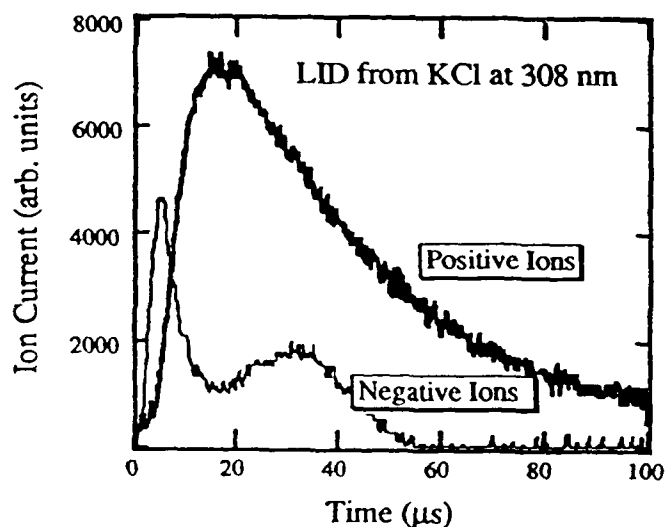
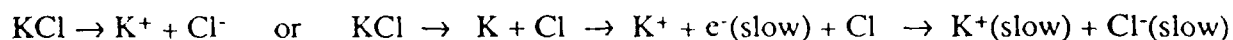


Figure 9. Time dependence of positive and negative ion signals following desorption from KCl by an excimer laser (XeCl) at a wavelength of 308 nm. Intensity in the focal spot was of order $1 \text{ GW}\cdot\text{cm}^{-2}$.

μs.¹⁰ The slow emission of electrons is particularly noteworthy: it may signal the diffusion out of the laser-produced plasma plume.

The differences in the behavior of the positive and negative ions suggests that there are mainly two processes involved: One is the direct desorption of the positive and negative ions, producing both the fast negative ion peak and the initial rise in the positive ion peaks. The second process proceeds through desorption of neutral atoms followed by ionization. These two processes are, schematically:



Since we do not yet have an accurate determination of how much of the slow negative-ion peak is actually electrons and how much is Cl^- , we can not yet rule out either of the two final states of the neutral-atom channel. Indeed, there is no reason to think that the late negative-ion peak might not include both components.

5. MECHANISM OF PHOTON-STIMULATED DESORPTION IN ALKALI HALIDES

Any proposed mechanism for LID or laser ablation of excited atoms or ions must answer two fundamental questions: (1) How is the absorbed photon energy localized to produce ion motion? and (2) What is the origin of the excited electronic state observed in the case of excited atoms or ions? We propose to discuss the first of these questions by referring to the bond-orbital model - a localized picture of electronic structure in solids within the framework of which bond-breaking has a particularly intuitive formulation. The question of the origin of the excited electronic state is particularly intriguing, and we show one example - applicable to KCl but not necessarily to alkali halides - of how such a state might be created by the decay of a highly localized excitonic state of the solid.

5.1 Energetics of Desorption Induced by Electron-Hole-Pair Creation

It is now generally accepted that laser induced desorption is related to the generation of a localized instability in the unperturbed crystal lattice.¹¹ Prior to the instant of desorption, the ion is in a band state with quantum numbers characteristic of the unperturbed lattice; following desorption, the ion (or atom) is a single-particle state with quantum numbers characteristic of its internal configuration, which may, of course, have been modified during the desorption process. The transition to the surface with a defect and a desorbing atom is the result of excitation from a bonding to an anti-bonding state, as described in the Menzel-Gomer-Redhead model.¹² This model, by itself, contains no specific information which would permit the computation of the details of the bonding and anti-bonding potentials; these details must be supplied from a model of the specific desorbing species and its surface environment.¹³

The initial event in this sequence is photon absorption and the creation of electron-hole pairs, which will depend on both the optical properties of the material and the laser wavelength. The absorbed photon, if it creates an electron-hole pair by valence-band excitation, breaks or weakens a bond. If the electron is in the conduction band - which would be typical of valence-band single-photon excitation or two-photon laser excitation in KCl - we are left with an electron in the conduction band and a much less mobile, usually self-trapped, hole. This electron can lose energy in one of two ways: by *delocalizing* in a band state, or by *self-trapping* through creation of a localized [metastable] lattice distortion. In the alkali halides, that metastable lattice distortion is called a self-trapped exciton. If the decay of that trapped exciton produces an atom on a repulsive potential energy surface, desorption will occur.

Thus the energetics of the desorption process are governed by the three parameters W (bandwidth), E_{ST} (the energy gained by self-trapping) and E_{DES} (the energy available from "rolling down" the repulsive potential energy surface of the anti-bonding state). Desorption occurs if $W < E_{ST}$ and if $E_{DES} > E_{ST}$.

2.4. Desorption Energetics in the Bond-Orbital Model

One of the primary obstacles to making quantitative predictions about desorption lies in our inability to compute the energies W , E_{ST} and E_{DES} in a reliable and relatively simple way. We have calculated the initial effects of electron-hole pair formation following the bond-orbital theory of Harrison.¹⁴ In spirit, it is closely related to the bond-charge model of Phillips,¹⁵ although the details of the parametrization differ. In this model, the energy per bond in the perfect crystal is computed from the second and fourth moments of the density of states function using linear combinations of atomic orbitals, and is given by¹⁶

$$E_{\text{pair}} = -n \left[M_2 - \frac{M_4(\vartheta) - M_2^2}{4 \cdot M_2} \right]^{1/2} + n \cdot V_o + E_{\text{pro}}$$

where n is the coordination number; M_2 and $M_4(\vartheta)$ are, respectively, the second and fourth moments of the electronic density of states (EDOS); ϑ is the angle between neighboring bonds; V_o is the repulsive screening potential; and E_{pro} represents the energy required to create the hybridized sp^3 bonds for the LCAO model of the solid. The fourth moment is a function of the bond angle ϑ , and will, in covalent solids, be influenced strongly by the dangling bonds and back-bonding required by surface reconstruction in those materials.¹⁷ In ionic materials, of course, we can expect much less dependence on the bond angle and more on the coordination number. The repulsive screening potential can be adjusted to fit the experimentally determined equilibrium inter-ionic spacing and the bulk modulus of the solid.

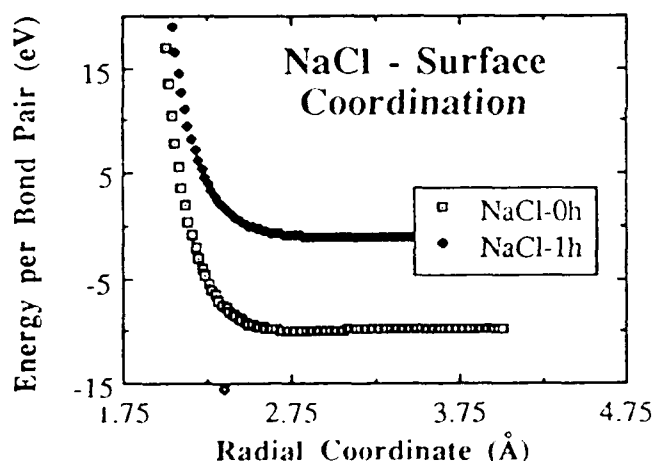


Figure 10. Bond-orbital calculation of the potential energy curves for a surface (five-fold) coordinated site in NaCl and for the same site with a one-hole excitation in a bond. The one-hole potential curve goes slightly negative at large radii.

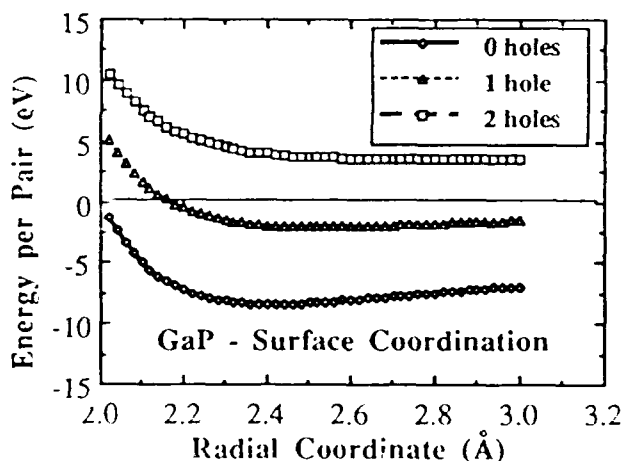


Figure 11. Bond-orbital calculation of the potential energy curves for a surface (three-fold) coordinated site in the compound semiconductor GaP and for the same site with one-hole and two-hole excitations. The one-hole potential curve is still characteristic of a weakly bound state.

We have used this expression for the energy per pair to model bond-breaking at a surface site in an ionic insulator. Because of their availability, we have used self-consistent Hartree-Fock matrix elements for NaCl taken from Reference [18] to calculate the moments M_2 and M_4 ; the same behavior can be expected from KCl. As an illustration of the technique, we show in Figure 10 the potential function that results when we begin with a five-fold (nearest-neighbor only) coordinated surface atom and create a hole in a single bond. One sees that the energy gained by creation of a single hole is already sufficient to put

the ion on a repulsive energy surface. However, the potential curve for the one-hole state goes slightly negative at large distances. This is probably a result of the fact that the bond-orbital model in this form assumes *sp*-hybridized bonds, whereas we know that the bonding orbitals in alkali halides are almost entirely of *p* character.

Thus, although it is qualitatively correct, this model still has some difficulties. Most notable is the fact that it does not yet properly account for the next-nearest neighbor interactions which are indispensable (and intractable!) in the alkali halides. Nevertheless, one sees by contrast with Figure 11 that the bond-orbital model at least shows a difference between the alkali halides - in which a single hole already puts the system on a repulsive energy surface - and the compound semiconductor GaP for which two holes are required to achieve the same end even though the binding energies are similar.

5.3 Source of the Excited Electronic State in Desorbing K Atoms

The origin of the electronic excitation which produces desorbing excited atoms is a separate but not unrelated question from the problem of ion motion we considered in Section 5.2. One possibility is that an excited *F*-center is the source of the excited atom desorption following valence excitation. Certainly valence excitation can form *F*-centers. It is conceivable that some of them may be excited, perhaps from scattering of secondary electrons, fluorescence, or, in the case of laser-induced desorption, by the high local density of electronic excitation. The strong coupling of an excited *F*-center to the lattice could both initiate ion motion and simultaneously provide the electron needed for neutralization of a departing ion. Such a mechanism would explain the observed decrease of the excited atom yield as a function of temperature in PSD measurements, since the lifetime of the excited *F*-center would decrease with increasing temperature. Alkali desorption (without reference to the electronic state of the atom) has been observed from RbBr containing *F*-centers during irradiation with *F*-band light.¹⁸

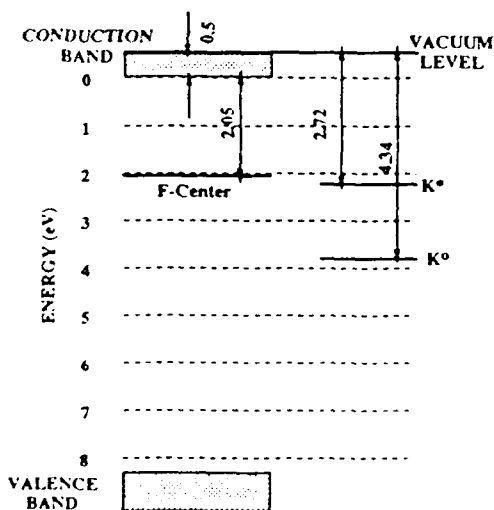


Figure 12. Energies of the 4*p* electronic state in the K atom and the relevant *F*-center energies in KCl. All energies are given in eV.

A simple consideration of the energetics will show that an excited *F*-center in KCl has about the right energy to neutralize a potassium ion into the first excited state of the neutral. Figure 12 shows an approximate band diagram for KCl including an *F*-center. Notice that the ground state *F*-center is almost resonant with an excited neutral alkali atom, so the excited state will clearly have sufficient energy to do so. The thermal ionization energy of the *F*-center¹⁹ was used to position the *F*-center below the conduction band. The ionization limit of the atom was made coincident with the vacuum level of KCl. These methods are approximate, since both the lattice distortion and the surface of itself will alter the band structure; indeed, the lattice relaxation - an essential feature in the dynamics of desorption - will almost certainly modify the relative energies of the various levels shown here.

Localized vibrational excitations of the charged lattice could also produce electronic excitation in a desorbing ground-state atom via electric dipole interactions. Calculations by Bickham and Sievers²⁰ show that excitation of a crystal with an anharmonic lattice potential can lead to the formation of localized vibrational modes of a solid. The energy required is typically that required for creation of an excited *F*-center. However, in the alkali halides, these modes are only formed for the two-dimensional lattice - consistent with the idea that this might be a purely surface phenomenon. That, of course, would fit the case either of PSD or laser desorption/ablation.

6. CONCLUSIONS

We have observed desorption and ablation of excited atoms and ions from the surface of KCl as a function both of dose and, in the case of ions, as a function of time following the arrival of the laser pulse. These experiments demonstrate the sensitivity of the excited-atom yields to the conditions of the surface, even at intensities characteristic of laser ablation; moreover, the excited atoms show evidence for a different dynamical origin than the ions, thus making them interesting objects of study.

Experimental results for laser-induced desorption and ablation are consistent with the low-intensity results of valence-band-induced desorption by synchrotron radiation. However, at high powers, there is evidence for desorption not only from perfect lattice sites but from defects created by the laser radiation. The final states of the desorbing atoms and ions appear to be strongly influenced by the metallization of the surface - a metallization arising from the preferential ejection of atoms and ions from the halogen sublattice of KCl. The defect sites which play a prominent role in the or shot-number dependence of the ion and excited atom yields at high intensities are energetically more susceptible to desorption than perfect lattice sites. Therefore, even though multiphoton excitation may be required initially to create the lattice defects, desorption can occur even for sub-bandgap photon energies characteristic of lasers because the electronic structure of the defects places them closer to the conduction band than the bulk bandgap energy.

The origin of the excited electronic state observed in desorbing atoms remains something of a mystery. While it is clear that the metallization of the surface plays a role in the initial creation of this state and in its temporal evolution with absorbed photon dose, we presently have no knowledge of the temporal evolution of either the ground-state or the excited state yields following irradiation by a laser pulse.

7. ACKNOWLEDGEMENTS

We are grateful to: the staff of the Synchrotron Radiation Center (SRC) for their expert handling of the Aladdin storage ring; Dr. Winston Chen of the Oak Ridge National Laboratory for the use of his laboratory in some of the laser ablation measurements; Mario Affatigato for his help with the ion ablation experiments; Dengfa Liu for assisting in the synchrotron radiation experiments; and Dr. Russell Dreyfus for illuminating discussions. This research was sponsored in part by the University Research Initiative of the Air Force Office of Scientific Research, by the SURA/ORAU/ORNL Summer Cooperative Program, and by the Medical Free-Electron Laser program managed by the Office of Naval Research for the Strategic Defense Initiative Organization. The SRC is supported by the National Science Foundation. Patrick H. Bunton was supported by a National Aeronautics and Space Agency training grant.

8. REFERENCES

1. A. Schmid, P. Bräunlich and P. K. Rol, "Multiphoton-induced directional emission of halogen atoms from alkali halides," *Phys. Rev. Lett.* **35** (1975) 1382.
2. Reviewed in S. C. Jones, P. Braunlich, R. T. Casper, X.-A. Shen and P. Kelly, "Recent progress on laser-induced modifications and intrinsic bulk damage of wide-gap optical materials," *Opt. Eng.* **28** (1989) 1039-1068.
3. P. H. Bunton, R. F. Haglund, Jr., D. Liu and N. H. Tolk, "Photon-stimulated desorption of excited alkali atoms following valence-band excitation of alkali halides," to be submitted to *Phys. Rev. B*.
4. P. H. Bunton, R. F. Haglund, Jr., D. Liu and N. H. Tolk, "Photon-stimulated desorption of excited alkali atoms from alkali halides following core level excitation," in press, *Surf. Sci.*

5. J. E. Eby, K. J. Teegarden, and D. B. Dutton, "Ultraviolet Absorption of Alkali Halides," *Phys. Rev.* **116**, 1099 (1959).
6. Secondary electron yields are tabulated with references in the *CRC Handbook of Chemistry and Physics*, R. C. Weast, ed., (Boca Raton, Florida: CRC Press, Inc., 1988), p. E-376.
7. N. G. Stoffel, Riedel, E. Colavita, G. Margaritondo, R. F. Haglund, E. Taglauer and N. H. Tolk, "Photon-stimulated desorption of neutral sodium from alkali halides observed by laser-induced fluorescence," *Phys. Rev. B* **32** (1985) 6805.
8. W. L. Wiese, M. W. Smith and B. M. Miles, *Atomic Transition Probabilities II: Sodium through Calcium*, NSRDS-NBS 22 (1965).
9. R. F. Haglund, Jr., M. H. Mendenhall, N. H. Tolk, G. Betz and W. Husinsky, "Surface and Near-Surface Radiation Effects in Photon-Stimulated Desorption," *Nucl. Instrum. Meth. in Phys. Res.* **B32** (1988) 321.
10. H. Overeijnder, K. R. Tol and A. E. DeVries, "Delay times in the sputtering of atoms from alkali crystals during low-energy electron bombardment," *Surf. Sci.* **90** (1979) 265.
11. K. Tanimura and N. Itoh, "Generation of Lattice Defects by Exciton Interaction in RbI: Lattice Instability under Dense Electronic Excitation," *Phys. Rev. Lett.* **60** (1988) 2753-2756.
12. D. Menzel and R. Gomer, "Desorption from metal surfaces by low-energy electrons," *J. Chem. Phys.* **41** (1964) 3311. P. A. Redhead, "Interaction of slow electrons with chemisorbed oxygen," *Can. J. Phys.* **42** (1964) 886.
13. Y. Nakai, K. Hattori, A. Okano, N. Itoh and R. F. Haglund, Jr., "Non-Thermal Laser Sputtering from Solid Surfaces," *Nucl. Instrum. Methods in Phys. Res. B*, to be published (1991).
14. W. A. Harrison, *Electronic Structure and the Properties of Solids* (New York: Dover, 1989).
15. J. C. Phillips, *Bonds and Bands in Semiconductors* (New York: Academic Press, 1973)
16. W. A. Harrison, "Interatomic interactions in covalent and ionic solids," *Physical Review B* **41** (1990) 6008-6019.
17. R. F. Haglund, Jr., K. Hattori and N. Itoh, "Bond-Orbital Model of Two-Hole Laser-Induced Desorption from Semiconductors," to be published.
18. H. Kanzaki and T. Mori, "Photon-stimulated desorption of neutrals from silver and alkali halides," *Phys. Rev. B* **29**, 3573 (1984).
19. N. Itoh, A. M. Stoneham, and A. H. Harker, "A theoretical study of desorption induced by electronic transitions in alkali halides," *Surf. Sci.* **217** (1989) 573; J. J. Markham, *F - Centers in Alkali Halides* (Academic Press, NY, 1966), p. 123.
20. S. R. Bickham and A. J. Sievers, "Intrinsic localized modes in a monatomic lattice with weakly anharmonic nearest neighbor force constants," submitted to *Phys. Rev. B*. We thank Professor Sievers for sharing this work with us prior to publication.

Section VI. Sputtering and desorption

ELECTRONIC TRANSITIONS IN SURFACE AND NEAR-SURFACE RADIATION EFFECTS *

R.F. HAGLUND Jr., M.H. MENDENHALL and N.H. TOLK

*Department of Physics and Astronomy and Center for Atomic and Molecular Physics at Surfaces, Vanderbilt University,
Nashville, TN 37235 USA*

G. BETZ and W. HUSINSKY

Institut für Allgemeine Physik, Technische Universität, A-1040 Vienna, Austria

Studies of surface effects arising from ion, heavy particle or photon irradiation of dielectric surfaces are increasingly focusing on the electronic interactions by which the incident energy is absorbed, localized, and transformed or transferred prior to the ultimate dissipation of the incident energy — through, for example, ejection of atoms or molecules from the dielectric. Recent experiments in our laboratories illustrate the varied roles played by electronic transitions in determining the flow of electronic energy during the bombardment of dielectric surfaces by photons, electrons and heavy particles. Specific examples include: the effects of surface overlayers and adsorbed hydrogen in retarding substrate desorption; substrate-temperature- and energy-resolved studies of photon-stimulated desorption from alkali halides; and electronic level-hybridization effects in the sputtering of metal oxides by argon ions. These simple model systems are a critical testing ground for studying the mechanisms of surface radiation damage in more complex materials because of the wealth of information available about their electronic and geometric structure, and because the character and modes of formation of their permanent electronic defects are well understood.

*Reprinted from NUCLEAR INSTRUMENTS AND METHODS
IN PHYSICS RESEARCH B*

ELECTRONIC TRANSITIONS IN SURFACE AND NEAR-SURFACE RADIATION EFFECTS *

R.F. HAGLUND Jr., M.H. MENDENHALL and N.H. TOIK

Department of Physics and Astronomy and Center for Atomic and Molecular Physics at Surfaces, Vanderbilt University, Nashville, TN 37235 USA

G. BETZ and W. HUSINSKY

Institut für Allgemeine Physik, Technische Universität, A-1040 Vienna, Austria

Studies of surface effects arising from electron, heavy particle or photon irradiation of dielectric surfaces are increasingly focusing on the electronic interactions by which energy is absorbed, localized, and transformed or transferred prior to the ultimate dissipation of the incident energy - through, for example, ejection of atoms or molecules from the dielectric. Recent experiments in our laboratories illustrate the varied roles played by electronic transitions in determining the flow of electronic energy during the bombardment of dielectric surfaces by photons, electrons and heavy particles. Specific examples include the effects of surface overlayers and adsorbed hydrogen in retarding substrate desorption; substrate-temperature- and energy-resolved studies of photon-stimulated desorption from alkali halides; and electronic level-hybridization effects in the sputtering of metal oxides by argon ions. These simple model systems are a critical testing ground for studying the mechanisms of surface radiation damage in more complex materials because of the wealth of information available about their electronic and geometric structure, and because the character and modes of formation of their permanent electronic defects are well understood.

1. Introduction

The phenomenology of radiation effects at dielectric surfaces exhibits a remarkable richness and complexity, ranging from luminescence to desorption of individual atoms or molecules, and on to rapid, efficient etching of large surface areas and macroscopic track formation. Scientifically, surface radiation effects in dielectrics are interesting because the large band-gap of these materials creates many channels through which incident energy can be absorbed, localized and transformed into the kinetic energy necessary to break a bond in a solid lattice or network. In technology, dielectric surface damage plays a critical role in such diverse areas as microelectronics fabrication and reliability, damage to high-power laser optical elements, and the development of optical elements for high-power tunable ultraviolet and X-ray light sources.

Studies of desorption, ablation, erosion and etching induced by energetic photons, electrons and heavy particles are increasingly emphasizing the microscopic de-

tails of the *electronic* mechanisms responsible for these phenomena. This concern for electronic rather than thermal mechanisms is particularly appropriate for dielectrics, because electronic features play significant roles in virtually all radiation effects, including those accompanying low-energy sputtered particles moving adiabatically with respect to electronic velocities in the solid; low-energy (primary or secondary) electrons or ultraviolet photons which are absorbed in thin layers near the surface; and laser photons for which the broken spatial symmetry at the surface allows nonlinear or resonant interactions which are forbidden in the bulk. Moreover, in many instances - as in intracavity optical damage in gas lasers or reactive ion etching - simultaneous irradiation by photons and/or electrons and/or heavy particles produces synergistic effects which cannot be explained as a linear superposition of individual processes. Hence, a detailed understanding of the available electronic channels through which energy can be absorbed, localized, transformed and dissipated is a *sine qua non* for understanding the immense variety of radiation effects.

Conversely, the need for identifying the specific material characteristics that play the decisive roles in enhancing or inhibiting damage is pushing us beyond older models of desorption (or sputtering), particularly at low energies, because it is becoming increasingly apparent that energy is often *not* shared in a statistical (thermal or collisional) way among all the atoms in the

* Supported in part by the Office of Naval Research (Contract Number N00014-86-K-0735), the Air Force Office of Scientific Research (Contract Numbers 86-0150 and F49-620-86-C-0125), Sandia National Laboratories (Contracts 65-2377 and 53-6681), Acurex Corporation (Contract RC-6334), and the National Science Foundation (Grant Number INT-8512674).

the development of a detailed understanding of the processes behind pictures of competition between direct and indirect desorption [1]. The picture is a sophisticated picture in which the flow of energy into and out of the surface is tracked within the framework of models which are faithful both to the fundamental interaction physics of particles or photons with the surface, and to the electronic properties of those materials.

In particle-, electron- and photon-induced radiation damage, electronic mechanisms are manifested in several generically distinct ways, including: excitation of electrons into the conduction band and excitation of atomic and molecular species on and near the surface; creation of bound electron-hole pairs, possibly with subsequent relaxation into permanent electronic defects and atomic/molecular excitations in surface overlayers; competition between “direct” desorption and desorption following diffusion of radiation-induced defects to the surface; and effects of the energy-level structure of a particle-surface system on the internal quantum status of desorbed particles. In this review, we shall illustrate these general considerations with several examples:

- optical radiation from electron- and photon-irradiated surface overlayers;
- photon-stimulated desorption of alkali metals from alkali halides; and
- velocity distributions of excited metal atoms sputtered from a metal and its oxide.

The emphasis in the experiments is on measurements of quantum states of desorbed particles, including their temporal evolution, with the ultimate goal of inferring the details of the potentials which give rise to the observed states.

2. Experimental apparatus and procedure

The key insight underlying the dynamical studies presented here is that desorption from dielectric surfaces is overwhelmingly dominated by the emission of neutral ground-state and excited-state atoms and molecules. Therefore, the techniques of gas-phase atomic and molecular optical spectroscopy are the critical tools, rather than the charged-particle spectroscopies typical of surface analysis experiments. Details of the experimental method have been presented elsewhere [1,2], so that only the essential features of our neutral desorption spectroscopy apparatus and techniques will be highlighted here.

The experimental layout of the ESD/PSD experiments is shown schematically in fig. 1. The sample – typically a cleaved, single-crystal alkali halide – is mounted on a heated micromanipulator in an ultrahigh vacuum (UHV) system, at a nominal base pressure of a few times 10^{-10} Torr. Radiation incident on the target

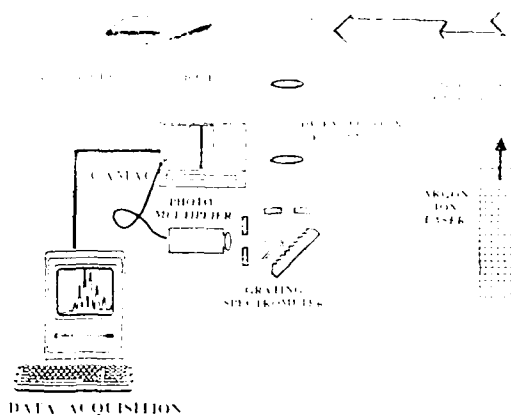


Fig. 1. Schematic of experimental apparatus for measuring the properties of neutral atoms and molecules desorbed from solid surfaces by electron, ion or photon impact. Radiation from the desorbed particles is detected in a spectrometer arranged to view them in flight from the surface; the tunable laser is used to induce fluorescence in selected ground-state species.

produces desorbed species emerging toward the irradiation source, which in our experiments was either a low-energy, high-current electron gun or the beam from the Aladdin synchrotron storage ring at the University of Wisconsin. De-excitation radiation from neutral atoms leaving the surface of the target material was detected by an optical system arranged to view a small volume (about $5 \times 10^{-5} \text{ cm}^3$) out in front of the target. Radiation emitted from this volume along a line orthogonal to the irradiating source beam and parallel to the exposed face of the sample was imaged by a lens system onto the entrance slit of a spectrometer-photomultiplier combination. The optimum observation volume was selected by manipulating the target to minimize background from the bulk luminescence of the sample.

In this experimental geometry, desorbing ground-state neutral alkali atoms are illuminated from the rear of the sample by the TEM₀₀ (fundamental Gaussian) mode from a single-frequency, actively-stabilized tunable dye laser. Alkali atoms leaving the surface undergo resonant absorption at the Doppler-shifted frequency appropriate to their rest frame and radiate at the characteristic first resonance transition (3p to 2s) as they fly away from the sample surface. This radiation is detected by the spectrometer-photomultiplier combination and the results are stored in a computer for off-line analysis. Excited-state neutral alkalis, on the other hand, are detected from their characteristic de-excitation fluorescences lines when the tunable laser is turned off. Desorbing halogen species are not observed in the present experimental setup, because their resonance lines are in the ultraviolet. However, excited desorbing halogens should, in principle, be observable with a uv spec-

resonant multiphoton ionization – capable of inducing

permits the measurement of relative yields for different particle species, desorption velocity distributions, and changes in emission characteristics as a function of sample temperature, orientation and surface preparation. Accurate yield measurements for a particular desorbing species, on the other hand, can be made in a Doppler-free geometry, in which the laser is injected perpendicular both to the incident electron or photon beam and to the spectrometer line-of-sight. Desorbed ions and electrons can also be measured by inserting, close to the point of electron or photon impact, an electrostatic analyzer with an exit-plane Channeltron detector. In this way, it is possible to measure essentially all the desorption products relevant to the dynamics.

In the sputtering experiments described in section 5, the geometry is similar, but the spectrometer views the desorbing particles at an angle to the surface normal in order to measure their velocity distribution. Connecting the observed laser-induced fluorescence with the velocity distribution requires the choice of a model for the sputtering process, in order to deconvolute the contributions of excited-state radiation from atoms traveling in different directions; in this case, we assume the validity of the collision cascade and calculate the velocity distribution for a given spectrometer angle using the Thompson formula. That this is a reasonable choice has been shown in a great many experiments, provided the direct knock-on contribution remains insignificant – which requires using the incident sputtering beam at near-normal incidence.

3. Experiments: luminescence and desorption from surface overlayers

Surface overlayers play a critical role in understanding desorption phenomena at surfaces, whether they are artifacts of surface preparation, are deliberately introduced, or are created by diffusion from the sub-surface bulk. These overlayers can saturate dangling bonds, influence surface composition and chemistry, modify surface geometry or electronic structure, and provide a nonvacuum interface which getters defects and impurities from the bulk. In the experiments described below, we shall discuss results suggesting that surface overlayers may also inhibit desorption, thus acting as an energy reservoir, or even a protective medium, for the substrate.

Experimentally, it is found that low-energy electrons, heavy particles (atoms or ions) and photons incident on

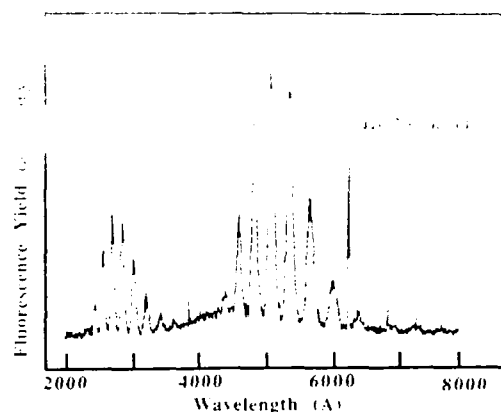


Fig. 2. Broadband luminescence in the form of molecular vibrational bands observed during photon bombardment of a single crystal of KCl in ultrahigh vacuum; the source is the first-order light from the Aladdin synchrotron light source. The ultraviolet light spectrum in the region between 230 and 300 nm is the fundamental; the visible bands come from the second order of the diffraction grating in the spectrometer. Note the He-Ne laser line used for wavelength calibration at 632.8 nm.

dielectric surfaces produce two readily distinguishable optical signals: a broad-band bulk luminescence, and line radiation from excited atomic and molecular species originating both in the nominal substrate surface and in the overlayer. The bulk luminescence, which is frequently considered as a superposition of separately identifiable bands tens of nanometers wide, arises from the decay of electrons excited into the conduction band to lower-lying defect states ("trap states") whose energies lie within the bulk band gap. The bulk luminescence is relatively structureless, and varies only a little from one material to another. Its amplitude is, however, a strong function of the sample preparation; it can be considerably reduced, for instance, by heating.

One feature of the spectrum which does change from material to material is a molecular band system in the ultraviolet, shown in fig. 2. This striking radiation signature has been observed in a number of experiments with electron, ion, and photon bombardment of alkali halides [4–7], including excitation by the white-light spectrum of the Aladdin synchrotron light source [5]. The spacing of the bands in this system is approximately 0.25 eV, which is characteristic of the most strongly bound diatomic molecules and molecular ions, such as H_2^+ , CO, CN^- and NO^+ .

The most frequently nominated candidate for the source of the radiation has been CN^- , because it is a pseudo-halide [5,6], has a size consistent with the Cl^- ion in a normal alkali halide lattice, and because the bands match expectations for the $A(^3\Pi) - X(^1\Sigma)$ transition in CN^- . (The long lifetime of the transition

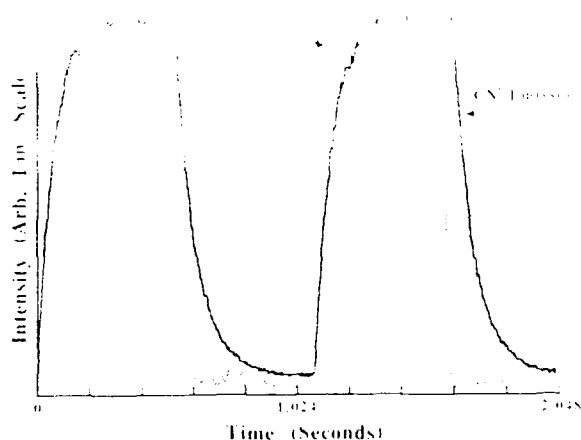


Fig. 3. Comparison of the time dependence of the radiation from the vibrational bands of CN^- (measured lifetime 80 ms) and from the bulk luminescence created by electron bombardment of KCl ("instantaneous" decay on this time scale). The long lifetime of the CN^- radiation is characteristic of a triplet-singlet transition.

argues in favor of its being emission from the lowest triplet state to a singlet ground-state; however, arguments can be adduced in favor of either a $^3\Pi$ or a $^3\Sigma$ initial state in this case. A definitive identification of the upper level would require determination of the symmetry of the excited state.) However, some experimental observations – notably, the growth in intensity of the bands as the sample is dosed with water vapor [6] – are not consistent with a simple picture of CN^- substitutional impurities. Moreover, it remains unclear

where the CN^- ions are localized; previously, there has been speculation that the CN^- might be bound at the surface as a hindered rotor. Also, the threshold energy required to create the radiation is exceptionally low: synchrotron radiation experiments show that the CN^- radiation can be excited with 8.5 eV ultraviolet photons. These issues are a matter of continuing investigation [7].

Time-resolved measurements of this radiation have revealed a number of interesting properties relating to the role of the molecular luminescence in the dynamics of desorption from the underlying substrate. This is illustrated in fig. 3, where the behavior of the bulk fluorescence is contrasted with that of the CN^- . The KCl sample was irradiated with a pulsed electron beam at low energy (200 eV), while the output of the spectrometer detecting the radiation was fed into a multichannel analyzer. The bulk fluorescence turns on and off synchronously with the electron pulse (to within the 10- μs time resolution of the multichannel analyzer), while the CN^- radiation is astonishingly long-lived, with a lifetime of ~ 80 ms. This means that the incident electronic energy is "stored" as it strikes the surface, then released for a long period of time after the radiation source is turned off, probably because it arises from a forbidden triplet-singlet transition.

There is evidence that the presence of these bands is correlated with the absence of excited-state radiation from substrate atoms – thus showing that the CN^- radiation acts as a kind of reservoir for the incident electronic energy, competing with excited-state desorption for the available energy. Whether or not this indi-

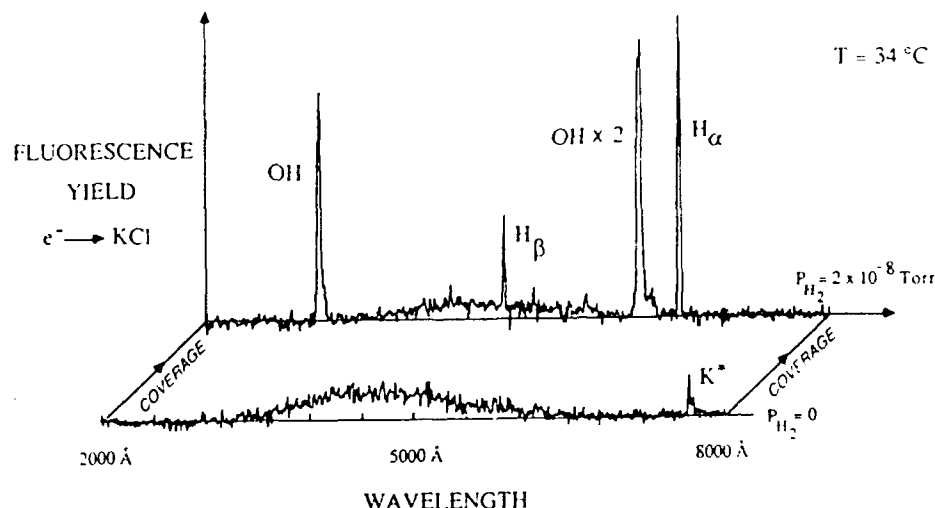


Fig. 4. Optical emission spectra of excited atoms emitted from the surface of clean KCl and from KCl in a low ambient pressure of hydrogen gas, under low-energy electron bombardment. Note the disappearance of the excited potassium line when the hydrogen is admitted to the ultrahigh vacuum chamber. The KCl sample was at room temperature, so the hydrogen is presumed to be weakly physisorbed.

dates the presence of a "protective barrier" against macroscopic erosion, which has not yet been established.

However, the notion of a surface reservoir of electronic states which preferentially absorb the incident energy is clearly an interesting one, for both scientific and technological reasons. We have found that the physisorption of hydrogen on KCl is correlated with the disappearance of excited-state potassium atoms desorbed from the clean KCl surface at room temperature, as shown in fig. 4; the potassium doublet at 776-770 nm disappears from the spectrum with the addition of a partial pressure of H_2 amounting to only 2×10^{-8} Torr. This shows that hydrogen has inhibited the otherwise efficient electron-stimulated desorption of excited potassium atoms from the substrate, and thus effectively closed a particular electronic mechanism for energy absorption, transformation and dissipation, presumably through the alteration of the surface electronic structure. Whether or not the hydrogen might be functioning as a kind of "protective barrier" against macroscopic erosion can only be conjectured for now, since simultaneous measurements of the desorbing ground-state potassium atoms – which should be by far the more numerous species – have not yet been undertaken. In any case, other measurements made with hydrogen on KCl indicate that the physisorbed hydrogen dissociates to form strong surface bonds, and this "chemical" interaction has a strong effect on the electronic channels available for electron-induced desorption.

Both of these examples illustrate the importance of surface overlayers not only in influencing surface chemistry, but also in controlling the flow of energy deposited by electrons, ions and photons in the surface and near-surface bulk regions of dielectrics. The CN^- radiation, for example, appears to be a result of a mechanism for storing incident energy for long periods of time and then releasing it through nondesorptive channels. In contrast to the bulk luminescence, the incoming energy appears to be localized on a particular molecular species, and to be exceedingly long-lived (on the time scale of typical molecular excitation lifetimes) – but the initial excitation does not give rise to the localized distortion of the surface lattice that could produce desorption.

4. Experiments: surface effects in photon-stimulated desorption

A large number of experiments conducted over some two decades [8,9] has shown that the electron- and photon-stimulated desorption (ESD/PSD) of halogen atoms from alkali halides is a result of the formation of mobile H centers (the so-called "crowdion", neutral

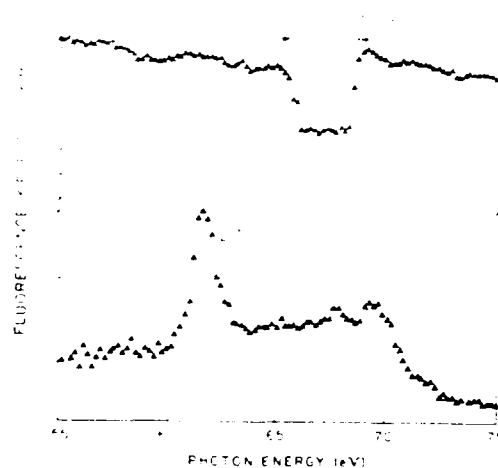


Fig. 5. Comparison of ground-state with excited-state lithium atom yield from the photon-irradiated surface of LiF, measured as a function of bombarding photon energy. The "off-resonance" points were taken by shifting the tunable dye laser (see fig. 1) off the first resonance line of the lithium atoms at 670.7 nm.

halogen atoms compressed into interstices along the $\langle 110 \rangle$ crystal directions). Systematic studies of alkali metal atoms desorbed by photon irradiation of sodium halides showed that the velocity distributions of the ground-state alkalis were Maxwellian with a temperature equal to that of the surface [10], leading to the conclusion that the desorption of the alkalis was essentially a thermal process. However, more recent ESD studies [11] of Li^0 desorbed from LiF have shown that at high temperatures, the rate-limiting time scale in the ESD process is that of F-center diffusion from the near-surface bulk to the surface.

Experiments in both the electron- and photon-stimulated desorption of excited and ground-state neutral alkalis from alkali halides showed that, where the ground state neutral alkalis are desorbed thermally, following the diffusion of radiation-induced F-center to the surface, the excited states exhibited a more complex behavior [12,13]. In recent experiments using synchrotron radiation, we have measured the behavior of the desorbed excited-state lithium atoms in the vicinity of the 1s core exciton. In fig. 5, yields of both the desorbed ground-state (Li^0) and excited-state (Li^*) atoms are shown as a function of incident photon energy. The clear signature of an electronic excitation mechanism is the large resonant yield of Li^* shown. Such a large yield could, of course, be evidence of the excitation of *gas-phase* Li^0 already desorbed from the surface but not yet outside the collection solid angle of the spectrometer (see fig. 1), as has already been proposed as a mechanism for creating Na^* by electron bombardment

VI. SPUTTERING/DESORPTION

of NaCl [14]. However, recent measurements in which Li^0 , Li^+ , Li^* and secondary electron yields were measured simultaneously as a function of photon energy in this region show no corresponding rise in secondary-electron production in the vicinity of the core exciton, and the secondary electron spectrum is too soft in energy to account for the observed increase in fluorescence yield [15]. The virtually instantaneous desorption of the Li^* compared to the slow, diffusion-dominated desorption of Li^0 indicates that a specific electronic mechanism – a core-hole excitation, in this case – is directly correlated with the desorption phenomenon.

A further indication that the yield of excited alkalis is, to a significant degree, influenced by electronic excitation mechanisms and surface electronic structure rather than thermally-driven processes, such as diffusion, comes from studies of excited atom yields as a function of temperature. In an earlier experiment, photon-stimulated desorption of Na^* was measured as a function of temperature [16], and there were indications that the yield of Na^* decreased with temperature, while the yield of Na^0 increased. Corresponding measurements in electron-stimulated desorption of Li^* from LiF showed that Li^* emission yields remained essentially constant throughout a temperature range in which the yield of Li^0 increased from zero to its saturation value [12].

However, the opposite trend as a function of sub-

strate temperature has been measured as well. In fig. 6, we show a series of the yield of Li^* as a function of temperature under white-light irradiation from the Aladdin storage ring University of Wisconsin Synchrotron Radiation Center. These data were obtained at incident flux levels significantly (perhaps a factor of 100) in excess of those available for the measurements of ref. [14]. They indicate an increase of yield with temperature, although the rate of increase appears to be less than that observed for the ground-state yield.

The resolution of this apparently contradictory behavior may lie, perhaps, in the foremost spectrum in fig. 6, which shows that the yield returns to its former value when a new spot is irradiated. Since the near-surface bulk luminescence retains its general shape and yield for all the spectra, we can infer that the absorption of the incident energy in the near-surface bulk is not much affected by surface radiation damage. But the Li^* yield is evidently extremely sensitive to surface conditions, and it is difficult to imaging a thermally activated process with that degree of sensitivity unless it involves the interaction of thermally-driven defects with the surface. The measurements of ref. [14] were taken using the Tantalus storage ring as the ultraviolet photon source, while those shown above were measured on Aladdin – a source with both significantly higher brightness and a higher endpoint energy than the photon flux from Tantalus.

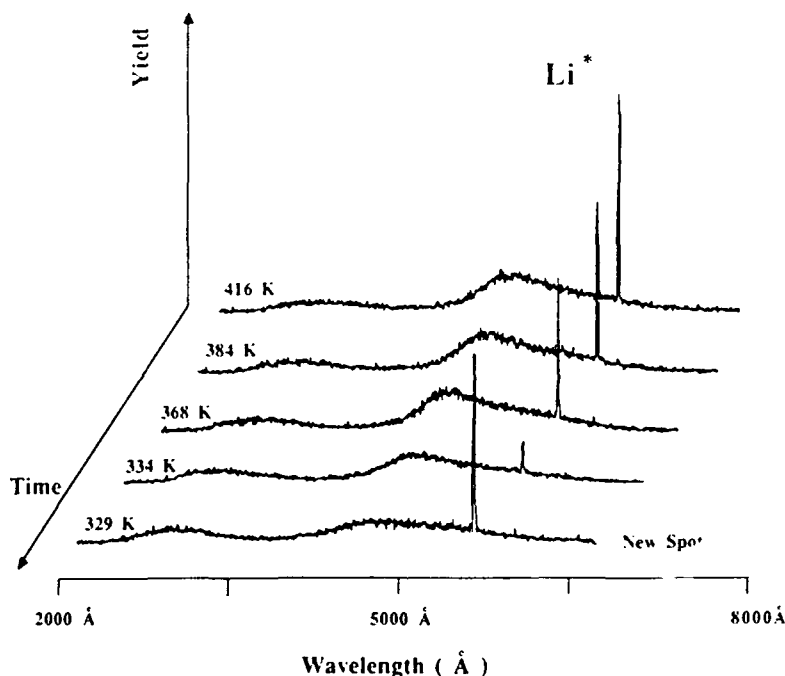


Fig. 6. Temperature dependence of the radiation from excited-state lithium atoms desorbed from the surface of LiF under ultraviolet photon irradiation. Note that the final (foremost) spectrum is taken with the photon beam striking a previously unirradiated spot on the crystal surface, but is taken at virtually the same temperature as the spectrum just preceding it.

It is clear that quite opposite trends in sputtering yields can be observed in experiments differing only in the state of the surface suggest that excited-neutral species desorption may be a sensitive probe of surface composition and electronic structure. Since the mechanisms of desorption are well understood

5. Experiment: final-state particle-surface interactions in sputtering

The collision-cascade theory of sputtering [17] has been applied with significant success to the prediction of yields and energy distributions of substrate atoms desorbed by energetic ions from both metals and insulators [18]. However, the study of more detailed dynamical characteristics of desorbed excited atoms – such as their velocity distributions – has remained an active and even controversial field of inquiry, because the statistical distributions of excited states predicted by the cascade model fail to agree with experimental data. Resonant tunneling models [19] by themselves also apparently do not give a complete picture. We have found in recent experiments that the electronic properties of the sputtered solid can have significant effects on velocity distributions, and may hold the key to a more complete understanding of internal quantum states of desorbed excited atoms. Indeed, these recent results suggest that neither the simple resonant tunneling model nor the static bulk band theory is adequate to explain

the observed energy distributions of sputtered atoms from either metals or oxides.

The final states of atoms sputtered from a solid surface may be determined in several different ways: (1) through the formation of excited final-state quantum states created in the interaction of (internal) collision products with the surface; (2) through charge-exchange processes (such as Auger decay and tunneling) in the final (external) interaction with the surface; (3) from the inflight decay of molecules created in pre-dissociative states via collisions with surface atoms; and (4) through secondary electron impact on desorbed ground-state atoms and molecules. In all of these processes, it is assumed that the relevant quantum numbers are to be found from an examination of the band structure of the sputtered solid (modified as appropriate at the surface) and the electronic structure of the desorbed atom. However, both the band structure and the atomic structure are modified spatially and temporally in a dynamical way by the interaction, and it is necessary to consider those modifications to the static picture if we are to understand the sputtering process.

The model we have in mind is sketched in fig. 7: to simplify matters, we deal only with the first resonance level of the desorbing atom. For an atom desorbed from the surface, we are dealing with a bond-breaking process made possible by collisional processes, and we assume in general that the desorbing particle exists as an ion inside the solid. As is well known, the atoms escaping from the surface have energies which are typi-

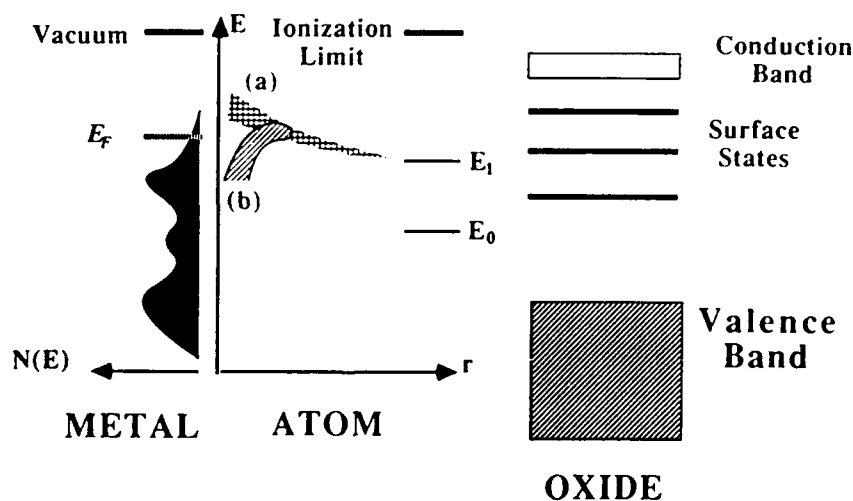


Fig. 7. Schematic energy-level diagram showing the relative positions of (from left) the density of states in a metal; the spectrum of a two-level atom as a function of distance from the metal; and the spectrum of bands and surface states in a metal oxide. Note the shifting and broadening of the atomic levels very close to the metal surface, which may have the effect either of raising the excited level E_1 above the Fermi surface (case (a), typical of transition metals) or of lowering it below the Fermi level (case (b), as calculations show to be the situation for the 4s level of Al, for example). The existence and the spectrum of the surface states for the oxide is extremely sensitive to the type of material and the condition of the surface.

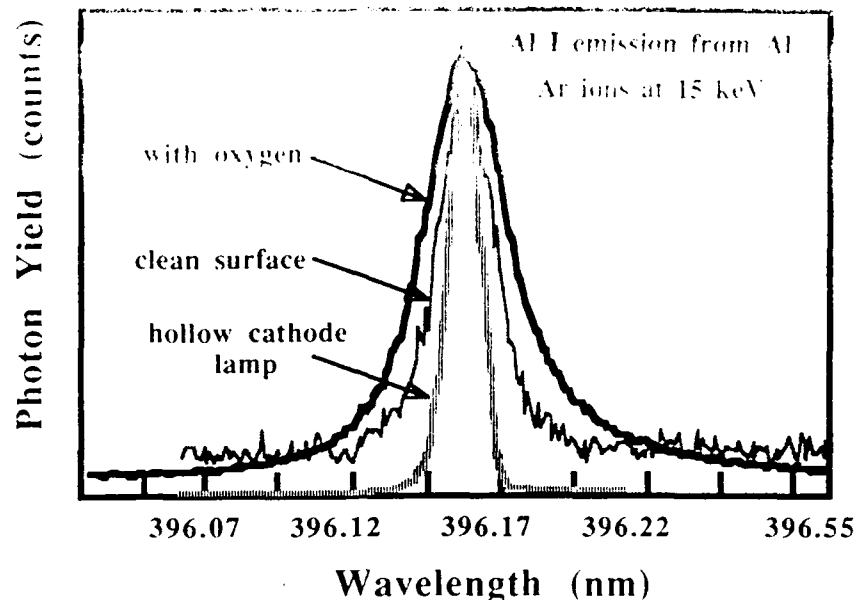


Fig. 8. Measured Doppler-shifted laser-induced emission spectra for excited Al atoms sputtered from the surfaces of clean Al and aluminum oxide, as indicated. The emission line shown is the first resonance line. The hollow-cathode lamp spectrum gives a calibration for thermal velocity atoms. Velocity distributions are inferred by convoluting the emission spectra with the Thompson form of the sputtered atom energy distribution.

cally much less than the Bohr velocity (corresponding to an energy of a few electron volts), so we can assume that the adiabatic condition is satisfied. In our experiments, where the velocity distributions of only the excited atoms are observed, the changes in velocity distribution from metal to oxide can only be interpreted as arising from loss of flux in the excited-atom exit channel; since we have no information about other desorbing species, we can only guess at the most likely mechanism(s).

Now two separate kinds of experimental observations need to be reconciled: First, the yield of sputtered excited neutral atoms always appears to increase in comparing desorption (sputtering) from a metal to desorption from its corresponding oxide; in the present work, changes of factors of two to ten in the total intensity of the observed atomic emission line were observed. Second, the velocities and the velocity distribution of the desorbing particle appears to be strongly influenced by the ability to lose excitation through resonant tunneling. That is, the flux of excited *slow* atoms can be reduced by tunneling deexcitation (or resonant neutralization), thus preferentially preserving the fast excited neutrals. As we shall show, even a consistent, qualitative treatment of this process requires an understanding of the dynamical relationships between atomic or ion levels and the solid state electronic structure.

It has been known for a long time that the flux of excited sputtered atoms increases from a metal to its corresponding oxide. The classic picture of resonance tunneling [20] used to explain this effect assumed that, if the excited atomic level were in the unoccupied region of states above the metal Fermi level, resonance ionization would occur due to tunneling into an unoccupied metallic electron state – thus preferentially removing an electron from slow-moving atoms near the surface. In the case of the oxide, on the other hand, it was assumed that no such tunneling would be possible since the excited atomic state would lie in the forbidden band gap of the oxide, permitting the excited atoms to survive long enough to escape from the surface. Such a picture would support both a broadening of the velocity distribution of excited atoms sputtered from a metal, and the increased yield in excited states for sputtering from the corresponding oxide.

Our recent experiments on Al and Al_2O_3 , however, show precisely the opposite result: the yield of Al^* is higher from the oxide, but the velocity distribution for the oxide is *broader* than that observed for Al^* desorbed from the metal surface, indicating a *preferential* destruction of slower moving excited Al atoms for the oxide, rather than for the metal where resonant tunneling should be easier. This suggests that the simple resonant-tunneling model, which explains both the change in yield and the change in velocity distribution

as manifestations of the same mechanism, is inadequate. We suggest that, in fact, the higher excited states of oxides may reflect nothing more complicated than the fact that sputtering from insulators and from metals takes place on a time scale of a vibrational period, 10^{-13} – 10^{-12} s. On this time scale, there are some 10^7 electronic fluctuations in the neighborhood of a given atom desorbing from a metal, giving many possible deexcitation interactions for the excited desorbing atom. For an atom desorbed from an insulator, on the other hand, the desorption lifetime is comparable with the significantly slower hopping rate for electrons in an insulator, and hence the possibility of deexcitation for any given atom is less.

If electronic tunneling is a significant contributor to the differences in desorption between metals and oxides, however, the measured velocity distributions will also be very sensitive not only to the velocity with which the excited atoms leave the surface, but also to the relative positions of the excited atomic level and the Fermi surface. If there are surface states in the band gap of the oxide – well-known to be the case in aluminum oxide – those states represent available channels for the excited electron to tunnel into; if, in addition, the excited atomic level is depressed with respect to the Fermi surface of the metal, the number of accessible tunneling states will also be reduced. Thus, the velocity distribution of sputtered excited atoms will be sensitive not simply to the perpendicular velocity of escape from the surface [19] – which is determined by the properties of the collision cascade in the cases we have studied – but also the relative positions of the excited level vis à vis the Fermi surface of the metal and any band-gap states in the oxide. We are continuing the investigation of these phenomena by comparing a variety of metals and their oxides in order to determine how differing band structures and the presence or absence of surface states affects the velocity distributions.

6. Conclusions

Both the material surface and the near-surface bulk play significant roles, particularly in low-energy radiation effects in dielectrics. The surface, with its exposed network of bonds, respects the fragile, reactive interface which acts to influence the transfer of energy from external sources and the rates at which substrate atoms and molecules can be ejected, as well as providing the final-state interactions determining the asymptotic quantum states of the ejecta. The properties of this "nominal" surface can be strongly influenced by (deliberately or unintentionally) adsorbed layers, even to the point of retarding desorption from the nominal surface. The subsurface atomic layers contribute as well, by generating the band structure of the material and

thus determining the channels through which electronic excitations and deexcitations can occur. Also, radiation-induced changes in surface composition can influence on desorption dynamics, overcoming even the effects of radiation-induced defects migrating from the near-surface bulk. In the long run, understanding the mechanisms of surface and near-surface radiation damage will require a more or less complete description of all of these effects.

From the point of view of surface dynamics, the problem of desorption and other radiation effects in insulators may be characterized as a series of differentiated steps, each one of which has a more or less well-known microscopic (i.e., atomic scale) character. There is an *initial state* of the system, consisting of the probing particles or photons in known energy, momentum and internal quantum states, and a well-characterized surface with a given set of energy bands and constituents. The radiation effects begin with an *interaction* phase, described by the microscopic physics of the probe-surface interaction; this interaction may be a photon-electron interaction, creating excited states of atoms or molecules, or electron-hole pairs; for incident heavy particles, it may be a collision cascade, producing a shower of particles internal to the solid, jarred loose by the momentum transferred by an energetic ion. In any case, this interaction is likely to be much better known and understood than the phase of localization, transformation, and dissipation, during which the initial electronic energy deposited by the probes is converted into electronic energy of desorbing particles, localized electronic defects and restructured surface and sub-surface bonds. The final state is once again composed of desorbing particles and a well-characterized surface, either of both of which may be different states than the initial state of the system. The challenge to the experimenter consists in elucidating the localization, transformation and dissipation mechanisms in such a way as to account for the observed yields and, one hopes, to provide information on the microscopic potentials responsible for the observed interaction products.

In recent years, methods of atomic and molecular spectroscopy – such as laser-induced fluorescence and other optical technique – have been employed with increasing success to determine the quantum states of desorbing or sputtered particles. However, these particles are only part of the final state of the system, of course; thus, the next stage in fully characterizing the dynamical processes involved in radiation effects is perhaps dependent more on an enhanced understanding of the initial and final states of the insulator surface than any other single experimental variable. For example, understanding the structural and compositional evolution of an alkali halide surface undergoing ultraviolet photon bombardment is vital to resolving the

sorption, because whether the surface is stoichiometric or metal-enriched determines the kinds of surface excitations or surface states which may be present, as well as the nature of the solid lattice or network whose distortion results in the ejection of a particle.

This knowledge of the composition and structure of the surface is not easily obtained for insulators, since typical surface analytic tools – such as low-energy electron diffraction and secondary ion mass spectroscopy – work well for metals and even semiconductors, but are known to cause radiation damage in dielectrics. However, studies of desorption dynamics are themselves hinting at ways in which desorption provides spectroscopic clues about the state of the surface. In addition, a continuing focus on the *electronic* mechanisms of particle-, electron- and photon-surface interactions will make it possible to use the specific clues available from solid-state physics about the initial and final states of the surface and near-surface regions of differing materials. As long as one treats the irradiated material as an undifferentiated aggregation of particles characterized by thermal or collisional properties, it is not possible to use the more differentiated electronic characteristics – such as band structure – to help solve the dynamical problem by selectively emphasized certain reaction pathways. Experiments emphasizing the electronic mechanisms involved in desorption and other radiation effects in insulators are thus both part of the problem and, very likely, a key ingredient in the solution.

It is a pleasure to acknowledge our debt to colleagues who participated in many of the experiments reported here, including: Royal G. Albridge, Alan V. Barnes and Dwight P. Russell of Vanderbilt, and Richard A. Rosenberg of the Synchrotron Radiation Center of the University of Wisconsin. We also thank Joel Tellinghuisen, of the Vanderbilt University Department of Chemistry, for sharing his spectroscopic insights about the CN^- vibrational bands and for a thoughtful reading of the manuscript.

References

- [1] N.H. Tolk, R.F. Haglund, Jr., M.H. Mendenhall and E. Taglauer, *Desorption Induced by Electronic Transitions (DIET-II)*, eds. W. Brenig and D. Menzel (Springer, Heidelberg, 1985) pp. 152–159.
- [2] M.L. Yu, D. Guschowski and A.C. Balant, *Phys. Rev. Lett.* **48** (1982) 472.
- [3] A.I. Baglan, F.O. Raabe and F.W. Thomas, *J. Chem. Phys.* **65** (1976) 3897.
- [4] W.A. Metz and E.W. Thomas, *Nucl. Instr. and Meth.* **194** (1982) 505.
- [5] E. von der Heyden and E. Fischer, *Phys. Status Solidi* **69** (1975) 63.
- [6] N.H. Tolk, L.C. Feldman, J.S. Kraus, R.J. Morris, M.M. Traum and J.C. Tully, *Phys. Rev. Lett.* **46** (1981) 134.
- [7] D. Cherry et al., *Nucl. Instr. and Meth.* **B13** (1986) 533.
- [8] T.-K. Ha and G. Zumofen, *Molec. Phys.* **40** (1980) 445.
- [9] J. Berkowitz, W.A. Chupka and T.A. Walter, *J. Chem. Phys.* **50** (1969) 1497.
- [10] J. Tellinghuisen, A.V. Barnes, R.F. Haglund, Jr., L.T. Hudson, M.H. Mendenhall, D.P. Russell and N.H. Tolk, submitted to *Chem. Phys. Lett.*
- [11] Some important references for electron-stimulated desorption of halogens are in: P.D. Townsend, R. Browning, D.J. Garland, J.C. Kelly, A. Mahjoobi, A.M. Michael and M. Saidoh, *Radiat. Eff.* **30** (1976) 55.
- [12] F. Agullo-Lopez and P.D. Townsend, *Phys. Status Solidi* **B97** (1980) 9.
- [13] H. Overijnder, R.R. Tol and A.E. DeVries, *Surf. Sci.* **90** (1979) 265.
- [14] M. Syzmonski, *Radiat. Eff.* **52** (1980) 9.
- [15] Multiphoton laser-induced desorption of chlorine from NaCl has been treated by A. Schmid, P. Bränlich and P.K. Rol, *Phys. Rev. Lett.* **35** (1975) 1382. See also N.L. Boling, P. Bränlich, A. Schmid and P. Kelly, *Appl. Phys. Lett.* **27** (1975) 191.
- [16] N.G. Stoffel, R. Riedel, E. Colavita, G. Margaritondo, R.F. Haglund, E. Taglauer and N.H. Tolk, *Phys. Rev.* **B32** (1985) 6805.
- [17] G.M. Loubriel et al., *Phys. Rev. Lett.* **57** (1986) 1781.
- [18] T.A. Green, G.M. Loubriel, P.M. Richards, N.H. Tolk and R.F. Haglund, Jr., *Phys. Rev.* **B35** (1987) 781.
- [19] R.F. Haglund, Jr. et al., *Nucl. Instr. and Meth.* **B13** (1986) 525.
- [20] R.F. Haglund, Jr. and N.H. Tolk, *Proc. SPIE* **690** (1986) 9.
- [21] P. Avouris, R.V. Walkup and A. Ghosh, *Phys. Rev. Lett.* **57** (1986) 2227.
- [22] R.F. Haglund, Jr., A.V. Barnes, M.H. Mendenhall, and N.H. Tolk, submitted to *Phys. Rev. Lett.*
- [23] E. Taglauer, et al., *Surf. Sci.* **169** (1986) 267.
- [24] P. Sigmund, *Phys. Rev.* **184** (1969) 383.
- [25] T.A. Tombrello, *Nucl. Instr. and Meth.* **B2** (1984) 555.
- [26] M.L. Yu and N.D. Lang, *Phys. Rev. Lett.* **50** (1983) 127.
- [27] C.W. White, N.H. Tolk and D.L. Simms, *Characterization of Solid Surfaces*, eds. P.F. Kane and G.B. Larrabee (Plenum, New York, 1974) p. 641.

PHYSICS OF FREE-ELECTRON-LASER APPLICATIONS

Physics of Free-Electron-Laser Applications in the Visible and Infrared

Introduction		972
Two-color free-electron laser driven by a radio-frequency linear accelerator	H. A. Schwettman, T. I. Smith	973
Application of a two-color free-electron laser to condensed-matter molecular dynamics	Dana D. Dlott, Michael D. Fayer	977
Infrared free-electron laser as a probe of vibrational dynamics on surfaces	N. J. Tro, D. A. Arthur, S. M. George	995
Excitation spectroscopy of thin-film amorphous semiconductors using a free-electron laser	N. J. Ristein, B. Hooper, P. C. Taylor	1003
Effects of introducing a gas into the free-electron laser	R. H. Pantell, A. S. Fisher, J. Feinstein, A. H. Ho, M. Özcan, H. D. Dulman, M. B. Reid	1008
Optical spectroscopic diagnosis of cancer and normal breast tissues	R. R. Alfano, Asima Pradhan, G. C. Tang, S. J. Wahl	1015
Ultrafast carrier relaxation in hydrogenated amorphous silicon	P. M. Fauchet, D. Hulin	1024
Far-infrared photo-Hall experiments on GaAs:Si	J. Kaminski, J. Spector, C. T. Foxon, T. O. Klaassen, W. Th. Wenckebach	1030
Material applications of the far-infrared free-electron laser	John D. Simon, John E. Crowell, John H. Weare, David R. Miller	1035
Applications of far-infrared free-electron lasers to condensed-matter physics	W. M. Dennis	1045
Enhancement of ligand binding to myoglobin by far-infrared excitation from a free-electron laser	Bernard Gerstman, Mark Roberson, Robert Austin	1050
Proposal for the direct electromagnetic generation of coherent terahertz acoustic phonons in semiconductor superlattices at the University of California, Santa Barbara far-infrared free-electron-laser facility	T. E. Wilson	1058

Physics of Free-Electron-Laser Applications in the Vacuum Ultraviolet-Extreme Ultraviolet

Introduction		1061
Fluorescence spectroscopy as a probe of the electronic structure and the dynamics of rare-gas clusters	T. Möller, G. Zimmerer	1062
Prospects for photoionization studies of weakly bound molecular complexes using free-electron-laser vacuum-ultraviolet radiation	E. A. Walters, J. R. Grover	1072
Precision spectroscopy on stored, highly charged ions using free-electron-laser radiation	D. A. Church, S. D. Kravis	1075
Free-electron lasers in ultraviolet photobiology	Thomas P. Coohill, John C. Sutherland	1079
Testing the photon-photon sector of quantum electrodynamics with free-electron lasers	W. Becker, J. K. McIver, R. R. Schlicher	1083

Physics of Free-Electron-Laser Applications in the Visible and Infrared

INTRODUCTION

It is now eighteen years since John Madey published a paper pointing out that a high-brightness relativistic electron beam traversing a spatially periodic magnetic field could stimulate the emission of photons over a broad range of wavelengths, indeed, from the far infrared to the ultraviolet. In a way, the free-electron laser was the ultimate homage paid by the laser, viewed as an optical device, to its antecedents in radar and electron-beam science and technology dating back into the 1940's.

In the intervening years, successful infrared and visible free-electron-laser (FEL) experiments, for example, at Stanford, Orsay, Santa Barbara, and Los Alamos, have shown significant promise for applications based on the unique optical characteristics of the FEL. A variety of accelerators can provide the high-brightness electron beams necessary for the FEL: room-temperature pulsed linear accelerators, superconducting accelerators, storage rings, and Van de Graaff generators have all been successfully used so far for this purpose. The existence of this variegated collection of pumps for the stimulated emission generated in the FEL implies a correspondingly broad range of temporal pulse shapes, interpulse spacings, pulse-repetition frequencies, output powers, and spectral ranges for users.

With the increasing maturity of the free-electron laser comes a new phase of scientific opportunity for those who are primarily laser users rather than laser physicists. During the past two years, FEL users' facilities at Stanford University and the University of California at Santa Barbara began to provide significant quantities of time to photon users, particularly in surface and materials science and biomedical studies. In the coming year, new FEL users' facilities devoted to biomedical and materials research as well as to FEL development will begin to operate at Vanderbilt and Duke; plans for additional facilities of this type are already far advanced.

Free-electron lasers now support significant experimental activities in a wide range of scientific and technological applications, including biomedical research. The spectrum of wavelengths now demonstrated in FEL's ranges from 0.25 to 800 μm , the region that includes atomic and molecular transitions as well as many elementary excitations in solids. While at least some parts of this spectral region can be covered by conventional lasers, the FEL has at least two major benefits compared with conventional lasers:

- The variety of FEL accelerator types offers the potential for decoupling the laser temporal-pulse structure and power output from the constraints of discharge or laser-pumping schemes and
- Beyond a wavelength of approximately 10 μm , the FEL has significantly greater tunability and higher power than any currently available lasers.

In addition, the fact that the interpulse spacing can be set much shorter than that available from mode-locked pulse trains (the Mark III FEL at Stanford and slated for installation at Vanderbilt, for example, has a rf accelerator frequency of 2.865 GHz, so that its pulses are 330 psec apart) makes it possible to carry out experiments in which the laser pulses follow one another on a time scale comparable with many relaxation times of physical, chemical, and biological interest.

In this special issue of *Journal of the Optical Society of America B*, we have collected a round dozen papers describing the physics of FEL applications in the visible and infrared. First, the companion papers on two-color FEL technology and applications suggest new opportunities in fundamental science that can be attained with the unique technology of the free-electron laser. In the near infrared, additional condensed-matter studies and surface science—particularly vibrational spectroscopy—have become possible with existing free-electron lasers. The gas-loaded free-electron laser can shift infrared FEL output into the visible, where work done with existing tabletop lasers can suggest ways in which the FEL, with its unique temporal pulse characteristics, might enhance our understanding of laser-induced processes both in materials science and in biomedical research. Finally, the far-infrared region was pinpointed early on as a place where exciting studies could be carried out in condensed-matter physics and biological physics. The papers submitted for this issue covering both recent research applications and new possibilities for direct excitation of far-infrared vibrational modes in solids suggest that this promise of the FEL is already being realized.

However, as with any new photon source, much of the challenge in developing new science will revolve around "thinking the unthinkable," or at least thinking the heretofore unthought. Thus the material ranges from reports of experimental results to inform speculations on possible future directions in FEL applications based on the unique properties of the FEL. Even though the *Journal of the Optical Society of America B* is an archival journal with a retrospective point of view, we hope that the speculation will stimulate as yet unthought, forward-looking applications of the FEL in the larger optical-science community.

Richard F. Haglund, Jr.
Howard Schlossberg
Feature Editors

*Physics of Free-Electron-Laser Applications
in the Visible and Infrared*

1.

Rf
a tr
wel
wh
che
pu
par
des
bot
ove
ma
ed:
J
ove
wig
of e
sig
mu
the
onc
plis
lin:
syn
ent
A
Fay
the
(SC
Sta
ogy
oth
wig
the
ins
a ri
int.
anc
ber

The Role of Valence-Band Excitation in Laser-Induced Desorption

Richard F. Haglund, Jr., Kai Tang, Patrick H. Burton* and Ling Jun Wang
Department of Physics and Astronomy
Vanderbilt University, Nashville, TN 37235

ABSTRACT

We present recent measurements of excited-atom and ion emission from KCl surfaces illuminated by vacuum-ultraviolet synchrotron radiation ($h\nu = 8\text{--}28\text{ eV}$) and ultraviolet laser light ($h\nu = 4\text{ eV}$). At low intensities characteristic of the synchrotron experiments, excited atoms are desorbed by simple valence-band excitation process involving the metallization of the KCl surface. At the higher intensities typical of laser desorption and ablation, we observe a strong decrease in K^* emission as a function of the number of laser shots, but an essentially constant yield of Cl^* . K^+ and Cl^+ emission at high intensities show similar behavior. The energetics of these desorption phenomena can be treated in a bond-orbital model which shows that creation of a single valence hole is sufficient to excite an ion to an anti-bonding state.

1. INTRODUCTION AND MOTIVATION

The need to improve the laser damage resistance of optical materials, and the growing interest in the use of high-intensity lasers for processing electronic and photonic devices, are the primary drivers for fundamental studies of laser-surface interactions. Laser-induced surface¹ and bulk² damage in KCl have been studied for many years, perhaps because KCl is the simplest of all the wide-bandgap ionic solids from the standpoint of electronic structure. We have recently begun a systematic study of ultraviolet photon-stimulated desorption (PSD) of excited atoms and ions from the surface of KCl, which has led to new understanding of the mechanisms of desorption following both valence-band³ and core-level⁴ excitation. These experiments also illustrate the specific sensitivity of ion- and excited-atom desorption spectroscopy to details of the surface before and after particle emission.

In this paper, we briefly summarize the status of these experiments and propose a unified view for the mechanisms of PSD and laser-induced desorption (LID) and ablation of excited atoms in KCl, a view which probably applies generically to materials which have self-trapped excitons and/or permanent, mobile electronic defects, such as SiO_2 and the alkaline-earth halides. In the VUV experiments, the yield of desorbed excited atoms follows the excitonic optical response of these crystals at photon energies near the bulk band gap. Secondary electron measurements, taken simultaneously, implicate the formation of excess metal in PSD of excited alkalis, and suggest some clues to the time dependence of the M^* yields. At the higher intensities characteristic of LID and laser ablation, a common mechanism of desorption due to valence-hole creation, as well as charge exchange mediated by surface metallization, is at work.

The energetics governing desorption may be interpreted within the framework of a detailed mechanistic picture of laser-induced desorption and ablation, based on the bond-orbital model of electronic structure. In this model, ion motion is caused by localized deformation of the lattice and bond-breaking near the site where the photon is absorbed. Neutralization of the moving ion into an excited atomic state, on the other hand, is a manifestation of the local electronic structure near the desorption site, at least in the low-intensity limit. Both desorption and excitation may arise from the same mechanism. For example, desorption following valence-band excitation may be described as the decay of an excited quasi-molecular-state of the crystal; in KCl, the desorption of K^* could be initiated by relaxation of an excited F -center.

* Now at Department of Physics, Box 4608, Austin Peay State University, Clarksville, TN 37044

** Now at Department of Physics and Astronomy, University of Tennessee, Chattanooga, TN 37403

The following discussion of the role of valence-band excitations in laser-induced desorption from KCl is based on two distinct sets of measurements: photon-stimulated desorption (PSD) measurements using ultraviolet radiation, and laser-induced desorption (LID) using an excimer laser. The photon source for the PSD experiments was the Aladdin facility of the Synchrotron Radiation Center (SRC) at the University of Wisconsin. Bending-magnet radiation from the 800-MeV electron storage ring was dispersed by a Seya-Namioka (SN) normal-incidence monochromator and focused onto a sample at normal incidence. Useable photon flux is available in the approximate range of 8 eV to 28 eV. The light source for the LID measurements was an XeCl excimer laser operating at a wavelength of 308 nm, likewise incident along the surface normal.

Single-crystal targets of KCl, typically measuring 5x12 mm and cleaved from bulk material prepared by Harshaw were mounted on a micromanipulator in high or ultrahigh vacuum (UHV). In the UHV measurements, the target holder was equipped with a Varian button heater capable of heating targets to approximately 450° C. The target could be rotated about a vertical axis perpendicular to the plane of the incident photon beam.

Two generic measurement schemes were used in the experiments described in this paper. Fluorescence from desorbed excited alkali atoms was detected with an 0.3 meter monochromator and a photomultiplier (PMT) operated in pulse counting mode for the PSD measurements, and in pulse-height analysis mode, using a gated integrator, for the LID measurements. Amplified PMT pulses which exceeded the threshold of a discriminator were counted and stored in an Apple microcomputer. Secondary electrons were collected by a biased stainless-steel collector positioned close to the target; the current was monitored by a picoammeter connected to an analog-to-digital converter channel of a Hewlett-Packard 7090A plotter; these data were then likewise stored in the computer. All of the PSD experiments and most of the LID measurements were carried out in an ultra-high vacuum chamber with a base pressure generally in the range of $\sim 10^{-10}$ Torr.

In other LID experiments, the optical detection system shown in Fig. 1 was replaced by a quadrupole mass spectrometer which could be operated to collect either positive or negative ions. A mass scan was performed to ascertain that the peak corresponding to a particular mass was stable and well above background. Then an electronic gate was set to capture the peak signal after each laser shot. These peak height data were stored on-line in an IBM microcomputer for subsequent retrieval and analysis.

In the PSD experiments, single KCl crystals were cleaved in air and inserted immediately into the UHV chamber; they were typically under vacuum within an hour after cleaving. The UHV system was then baked at 200°C for several hours following insertion of the target; samples were then cleaned by heating a few hours at 300 to 400° C. Numerous studies, cited in Reference [4], have shown that this procedure yields a stable and reproducible surface. For the LID experiments, the samples were cleaved in air using the same precautions (use of rubber gloves, methanol cleaning of all cleaving and handling tools)

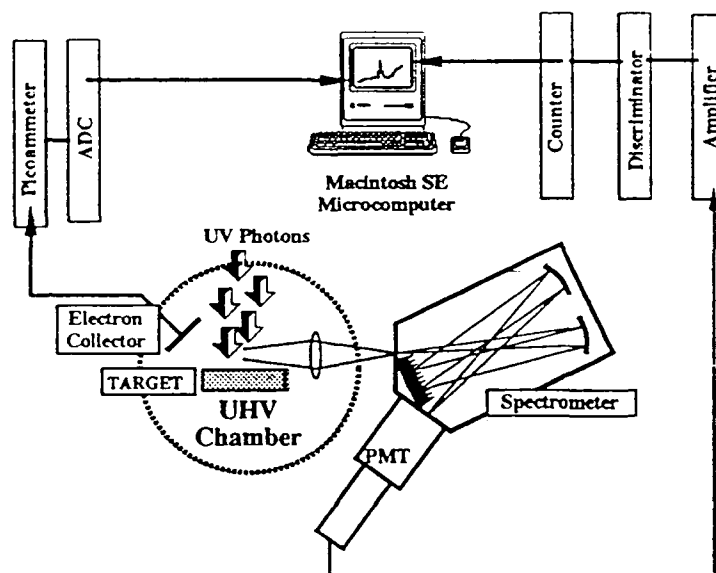


Figure 1. Schematic diagram of apparatus for simultaneous measurements of excited-atom yield and secondary-electron current in photon-stimulated desorption experiments.

ultrahigh vacuum. We assume that the surface is well cleaned due to sputtering by the high-intensity laser pulses. Thus these laser desorption and ablation experiments must be viewed as having been carried out under reproducible conditions, but not necessarily on well-characterized surfaces.

3. PHOTON-STIMULATED DESORPTION IN THE VACUUM ULTRAVIOLET

Ultraviolet photon-stimulated desorption has been studied in the alkali halides for many years. Only recently, however, has it been demonstrated that PSD of excited atoms can be caused by valence-band, in contrast to core-level, excitation. Because these measurements have an important impact on our understanding of the mechanisms of laser-induced desorption, we summarize briefly the results of these recent experiments on both KCl and LiF. Details may be found in Reference [4].

Figure 2 shows an excitation function for desorbed excited potassium under photon irradiation of KCl near the surface exciton peak at 9.5 eV. The bulk bandgap of KCl is 8.4 eV. The monochromator flux was too low to search for structure in the desorption curve at lower energies. Shown for comparison in Figure 3 is the optical absorption spectrum of KCl measured by Eby, Teegarden and Dutton.⁵ Structure in the excitation function for desorbed K^* corresponding to the valence exciton at approximately 9.5 eV is evidence that desorption due to valence excitation in KCl is occurring, and that excited-atom desorption may be related to identifiable electronic excitations of the surface.

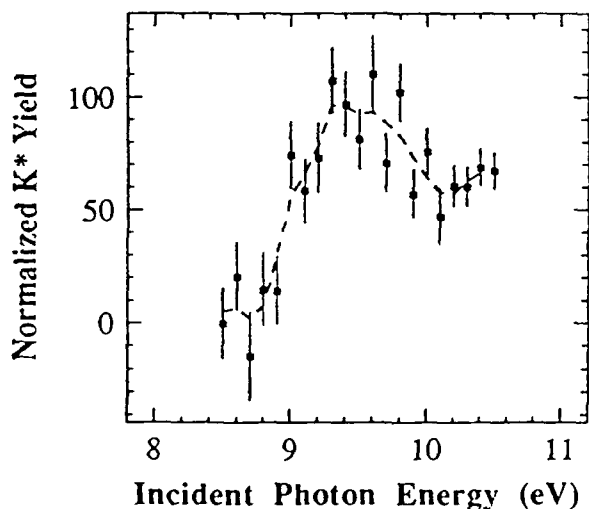


Figure 2. Excitation function for K^* atoms desorbed from a KCl surface by VUV light with valence-band energies. From Reference [4].

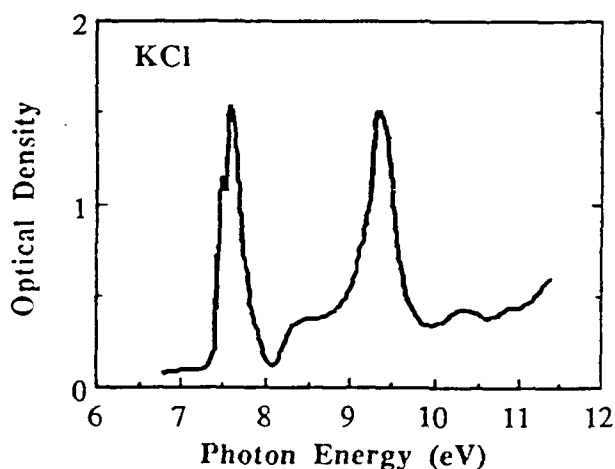


Figure 3. Optical absorption spectrum from KCl in the vacuum ultraviolet region. Figure is from Reference [5].

Studies of the variation in excited-atom and total electron yield, described in detail in Reference [4], clearly implicate the formation of excess metal on the surface in the desorption process. Those experimental results are consistent with the following picture: As a pristine spot on the surface is irradiated, metallization begins due to two separate processes. One is the loss of halogen because of the preferential ejection of ions from the halogen sublattice; the other is the creation of mobile defects (e.g., F -centers) in the near-surface bulk and their subsequent diffusion to the surface, where they neutralize the positive metal ions. The experimental evidence for this is primarily the rapid decrease in secondary electron yield from the high values which characterize the insulating surface as cleaved to the lower values (an order of magnitude or more for most of the alkali halides) characteristic of the alkali metal.⁶

metal will evaporate thermally, leaving a stoichiometric surface, which is primarily desorbing alkali ions; thus, the bulk of the total desorption yield of the metal atoms is in the ground electronic state.⁷ The metallization also affects the yield of excited atoms, because as the metal agglomerates, its work function changes. When the metallic patches are small, the work function of the surface is rather large, and there are no metallic electrons which can be donated to fill the electronic state of a desorbing alkali ion. As metallization progresses, the work function decreases, and when the Fermi level is nearly resonant with the atomic excited state, neutralization of the ion into that excited state is probable. As the surface becomes more strongly metallized, the Fermi level of the metal patches rises *above* the first excited electronic state, and resonant charge exchange into the ground state becomes the dominant process. Thus, below the temperatures at which the metal evaporates, excited state desorption will first increase and then decrease as the Fermi level rises above the first excited state of potassium.

4. LASER-INDUCED DESORPTION AND ABLATION FROM KCl

The description of laser-induced particle emission is as problematical as the phenomenon itself is complex. In the following discussion, we shall refer to particle emission at low laser intensities as laser-induced desorption (LID); we mean to imply by this the absence of plasma and collective effects, and that the particle emission is, in this case, essentially a localized event resulting in the removal of an isolated atom or ion from an (at least hypothetically) identifiable surface site. By laser ablation we refer to the high-intensity limit, in which rapid damage to surface may involve collective effects and the generation of a plasma plume; in laser ablation, the characterization of the surface site is probably not possible.

We have carried out a series of experiments to study the change in the surface of KCl by monitoring the yields of excited atoms and ions from the surface, including K^* , Cl^* , K^+ and Cl^- . We have studied the change in K^* and Cl^* yields as a function of number of shots on the sample, and as a function of intensity. In addition, we have carried out simple measurements of the time dependence for the emission of positive and negative ions from the surface. These measurements are consistent with the PSD picture, but show in addition that laser-induced desorption (LID) proceeds through the same mechanism independent of the condition of the surface. Hence, LID from perfect lattice sites and defect sites appears to result from the same kind of valence-band excitation as observed in PSD, but with slightly different consequences because of the high density of local electronic excitation.

4.1 Laser-Induced Desorption of Excited Atoms

Optical spectra taken during laser ablation experiments generally show a relatively broad fluorescence background on which are superimposed atomic emission lines from excited atoms, radiating as they move away from the surface. In contrast to PSD experiments, we observe not only the first resonance line of the metallic atom, but lines originating in other excited states and the atomic emission lines of chlorine atoms and ions. Of particular interest is the appearance of excited-state emission whose parent states lie very near the ionization limits of the atoms in question; the mechanism for the creation of these highly excited states is not clear, although multiphoton excitation of ground-state atoms in the laser-produced plasma is probably the most likely possibility. Properties of the observed lines are shown in Table I.⁸

The calculated oscillator strengths shown in Table I are not always reflected in the relative spectral yields of the lines in question. This seems to be particularly true for the Cl^* states observed. We assume that this is indicative of highly nonequilibrium conditions which are likely to prevail both in the laser-produced plasma and at the surface. Also, the centroids of the lines as shown in the accompanying figures disagree slightly with those shown in the Table. Part of this discrepancy, typically 4 Å, is the result of calibration error in the spectrometer drive; the magnitude of the error was checked using a He-Ne laser at 6328 Å. In addition, since the excited atoms are emitted with non-zero velocity and since the spectrometer line-of-sight is not parallel to the surface plane, the lines will be Doppler shifted. This shift can, in principle, be calculated from a knowledge of the geometry of the desorption experiment.

Species	Wavelength (Å)	Atomic Transition	Upper Level (cm ⁻¹)	Lower Level (cm ⁻¹)	Oscillator Strength	Transition Rate (10 ⁸ s ⁻¹)
K	7676	4p → 4s	24,714	0	0.68	0.385
K	7699	4p → 4s	13,024	0	0.34	0.382
K	4045	5p → 4s	24,714	0	0.0091	0.0124
Cl	4105	3p ⁴ 5P → 3p ⁴ 4S	96,309	71,954	3.4·10 ⁻⁴	0.002
Cl	4601	3p ⁴ 5P → 3p ⁴ 4S	96,590	74,861	0.012	0.039
Cl	4624	3p ⁴ 5P → 3p ⁴ 4S	96,482	74,861	0.0029	0.0045
Cl	4654	3p ⁴ 5P → 3p ⁴ 4S	95,702	74,221	0.0016	0.0049
Cl	4661	3p ⁴ 5P → 3p ⁴ 4S	96,309	74,861	0.0065	0.01

Figure 4 shows the spectrum of excited potassium atoms near the first resonance lines at 7668 Å, observed at laser intensities on the order of 1 GW·cm⁻². Each point on the spectrum represents a single laser shot; there are two hundred points in each spectral scan from 7600 to 7800 Å. Thus some 140 shots intervene between the upper spectrum and the lower. The decrease in the K* yield with absorbed photon dose is evident. This phenomenon is well known from PSD studies, in which progressive ultraviolet irradiation of the alkali halides results in a steady decrease of the excited-state atomic emission.⁹ This

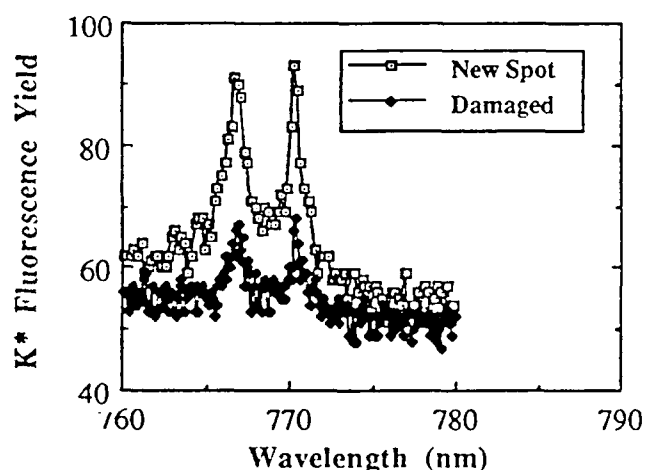


Figure 4. Spectrum of K* atoms desorbed from KCl at an intensity of 1 GW·cm⁻² on two successive scans, starting from a pristine spot on the surface. The atomic transition is 4p → 4s.

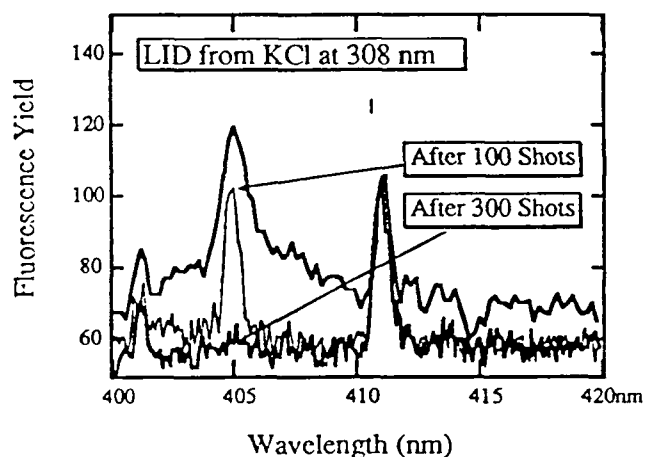


Figure 5. Optical spectrum of K* (405 nm) and Cl* (411 nm) atoms in the ablation plume from a KCl crystal surface at a laser intensity of order 1 GW·cm⁻², as a function of shot number.

behavior is consistent with a surface accumulation of excess metal leading to resonant ionization of desorbing K* atoms, thus reducing the total excited-state signal. Shown for comparison in Figure 5 are the relative yields of K* (from the 5p → 4s transition) and of Cl* emission originating from transitions in the (3p⁴5P → 3p⁴4S) manifold. The K* emission in this state also decreases after a few hundred shots, consistent with the resonant ionization picture. The Cl* emission, on the other hand, is virtually constant in amplitude as a function of total absorbed dose, indicating that the Cl* production is not affected by surface conditions, such as metallization. Given the high excitation required to produce the parent states of these emission lines (nearly 12 eV, as shown in Table I), we suggest that multiphoton excitation of ground-state Cl in the laser-produced plasma is producing these signals. Accurate measurements of the Cl* yields as a function of intensity should reflect this difference in origin.

In these experiments, a region of the surface was scanned by the spectrometer, and the optical signal at each wavelength from a single laser pulse was counted. The excited K was only observed when there was a visible plasma. This could indicate that the surface is so rapidly metallized that one can only produce desorption following ablation of the metal, which is then being heated and vaporized at close proximity. Most notable is the contrast between the persistence of the Cl^* yield and the relatively rapid disappearance of any K^* signal.

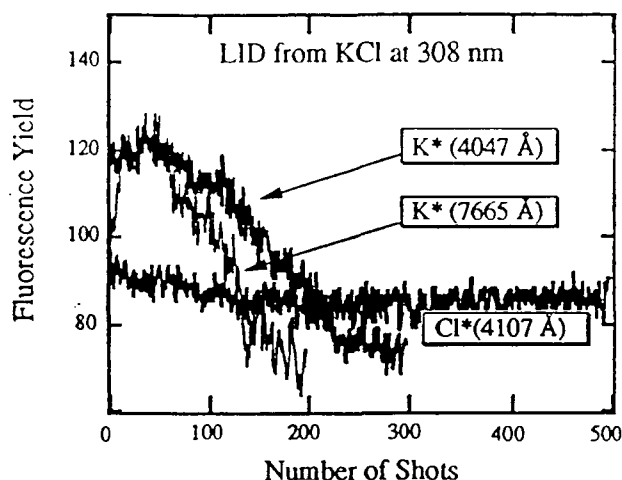


Figure 6. Spectrum of excited K atoms desorbed from KCl at an intensity of $1 \text{ GW}\cdot\text{cm}^{-2}$ starting from a pristine spot on the surface.

Figure 6 shows the yield of excited atoms desorbed from KCl at a laser wavelength of 308 nm and an intensity of about $4 \text{ GW}\cdot\text{cm}^{-2}$, as a function of the number of laser shots on a particular spot. The measurements begin, in each case, from a previously undamaged spot. The transitions identified in the Figure are the 7668 Å line of K^* , the 4052 Å line of K^* , and the 4112 Å line of Cl^* . The variation in the behavior of the three species of excited atoms is: The K^* yields in both cases rise rapidly from the first laser shot, peak near the same value, and then drop off, but the $\text{K}^*(7668 \text{ Å})$ yield goes to its background value after about 200 shots, where the $\text{K}^*(4052 \text{ Å})$ yield does not decrease to background level for some 300 shots. The Cl^* yield, on the other hand, is essentially unchanged through the entire sequence. This behavior is consistent with the idea that excited K atoms are created in a different process than the excited Cl atoms.

If, indeed, resonant ionization of desorbing excited metal atoms is the mechanism, these data are consistent with the idea of progressive metallization of the surface with dose, since the Fermi level of the metal clusters would rise through the $4p \rightarrow 4s$ transition energy before the $5p \rightarrow 4s$, taking flux out of the former K^* channel prior to the latter.

4.3 Intensity Dependence of Positive and Negative Ion Yields

Yields of positive and negative ions were measured as a function of intensity using a quadrupole mass spectrometer in the geometry of Figure 1. In general, at laser intensities below $100 \text{ MW}\cdot\text{cm}^{-2}$, stable ion signals were measured which showed that ion yield increased with roughly the second power of intensity. This is consistent with valence-band excitation. However, above this intensity the ion signals rapidly became unstable, and showed an initial high yield followed by a rapid drop in intensity. This phenomenon was observed for both K^+ and Cl^- ions, as shown in Figures 7 and 8.

After the ion yields dropped to their minimum values and the visible plasma indicating desorption of excited atoms disappeared, it was observed that bright fluorescence from color centers was being excited by the laser beam. No other signs of damage to the surface - cratering or etching - were observable by eye. As soon as the laser beam was directed to a fresh spot on the surface, the strong ion signal was once again observed. This suggests that the disappearance of the Cl^- signal and the diminution of the K^+ signals are both tied to the creation of defects in the near-surface region of the bulk. The initial high yields in both ion species apparently comes from defect sites, while K^+ originates, at a low level, in the perfect sites. The Cl^- ions, on the other hand, are apparently only ablated from defect sites, and once the surface becomes stoichiometric, the negative ion signal disappears too. Cl neutral atoms, of course, continue to be produced, as shown above and in the neutral Cl laser-desorption measurements of Reference [1].

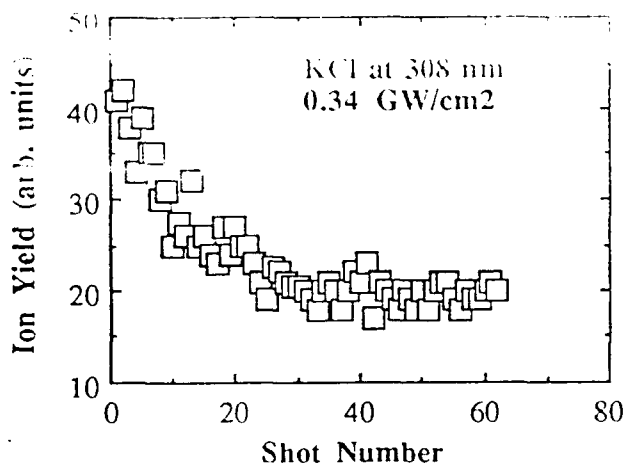


Figure 7. Intensity dependence of K^+ desorbed from KCl by an excimer laser (XeCl) at a wavelength of 308 nm. Intensity in the focal spot was $0.34 \text{ GW}\cdot\text{cm}^{-2}$.

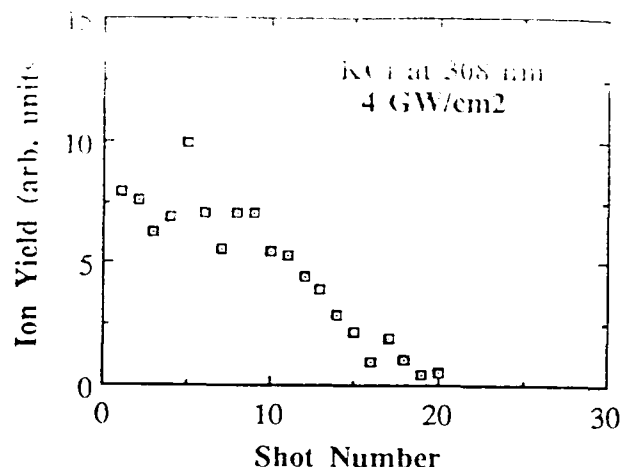


Figure 8. Intensity dependence of K^+ desorbed from KCl by an excimer laser (XeCl) at a wavelength of 308 nm. Intensity in the focal spot was about $4 \text{ GW}\cdot\text{cm}^{-2}$.

4.4 Time Dependence of Ion Yields

We have measured the time dependence of positive and negative ion yields from KCl by placing a biased stainless steel probe in the UHV chamber approximately 4 cm from the surface of the target and at an angle of 45° to the target normal. By switching the polarity of the probe from +67 V to -67 V, it was possible to collect both the positive and negative charges. For that voltage, the time of flight for a typical alkali ion is of order $4 \mu\text{s}$ and that for fast electrons is about 16 ns. Ion current was recorded on a synchronized single-shot basis by a 100 MHz transient waveform recorder interfaced to a microcomputer.

Figure 9 shows the transient signals of both positive and negative ions desorbing from the KCl crystal surface. The positive ion signal has an apparent decay time of some $25\text{--}30 \mu\text{s}$, much longer than that measured for NaCl, and is initiated well after the negative ion fast signal has already begun to decay. The current of negative ions has both a fast and slow component. The slow component can be strongly suppressed by applying a magnetic field, and is thus assumed to consist primarily of slow electrons. The decay

time of the fast negative ion signal is much less than that of the K^+ signal, indicating that the Cl^- ion is desorbed by a different mechanism than the positive ions. This is consistent with earlier results from electron-stimulated desorption studies which show that neutral halogens are ejected from the surface before sodium atoms, and that the halogen is ejected in a non-thermal process on a time scale much less than 100

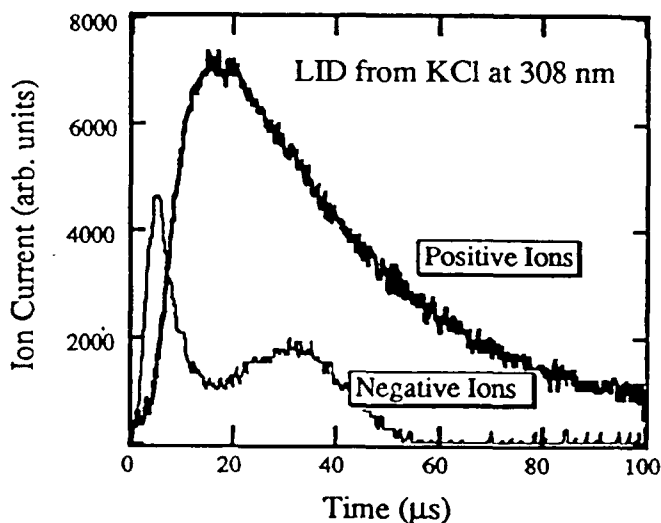
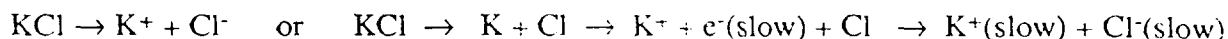


Figure 9. Time dependence of positive and negative ion signals following desorption from KCl by an excimer laser (XeCl) at a wavelength of 308 nm. Intensity in the focal spot was of order $1 \text{ GW}\cdot\text{cm}^{-2}$.

The differences in the behavior of the positive and negative ions suggests that there are mainly two processes involved: One is the direct desorption of the positive and negative ions, producing both the fast negative-ion peak and the initial rise in the positive ion peaks. The second process proceeds through desorption of neutral atoms followed by ionization. These two processes are, schematically:



Since we do not yet have an accurate determination of how much of the slow negative-ion peak is actually electrons and how much is Cl^- , we can not yet rule out either of the two final states of the neutral-atom channel. Indeed, there is no reason to think that the late negative-ion peak might not include both components.

5. MECHANISM OF PHOTON-STIMULATED DESORPTION IN ALKALI HALIDES

Any proposed mechanism for LID or laser ablation of excited atoms or ions must answer two fundamental questions: (1) How is the absorbed photon energy localized to produce ion motion? and (2) What is the origin of the excited electronic state observed in the case of excited atoms or ions? We propose to discuss the first of these questions by referring to the bond-orbital model - a localized picture of electronic structure in solids within the framework of which bond-breaking has a particularly intuitive formulation. The question of the origin of the excited electronic state is particularly intriguing, and we show one example - applicable to KCl but not necessarily to alkali halides - of how such a state might be created by the decay of a highly localized excitonic state of the solid.

5.1 Energetics of Desorption Induced by Electron-Hole-Pair Creation

It is now generally accepted that laser induced desorption is related to the generation of a localized instability in the unperturbed crystal lattice.¹¹ Prior to the instant of desorption, the ion is in a band state with quantum numbers characteristic of the unperturbed lattice; following desorption, the ion (or atom) is a single-particle state with quantum numbers characteristic of its internal configuration, which may, of course, have been modified during the desorption process. The transition to the surface with a defect and a desorbing atom is the result of excitation from a bonding to an anti-bonding state, as described in the Menzel-Gomer-Redhead model.¹² This model, by itself, contains no specific information which would permit the computation of the details of the bonding and anti-bonding potentials; these details must be supplied from a model of the specific desorbing species and its surface environment.¹³

The initial event in this sequence is photon absorption and the creation of electron-hole pairs, which will depend on both the optical properties of the material and the laser wavelength. The absorbed photon, if it creates an electron-hole pair by valence-band excitation, breaks or weakens a bond. If the electron is in the conduction band - which would be typical of valence-band single-photon excitation or two-photon laser excitation in KCl - we are left with an electron in the conduction band and a much less mobile, usually self-trapped, hole. This electron can lose energy in one of two ways: by *delocalizing* in a band state, or by *self-trapping* through creation of a localized [metastable] lattice distortion. In the alkali halides, that metastable lattice distortion is called a self-trapped exciton. If the decay of that trapped exciton produces an atom on a repulsive potential energy surface, desorption will occur.

Thus the energetics of the desorption process are governed by the three parameters W (bandwidth), E_{ST} (the energy gained by self-trapping) and E_{DES} (the energy available from "rolling down" the repulsive potential energy surface of the anti-bonding state). Desorption occurs if $W < E_{ST}$ and if $E_{DES} > E_{ST}$.

One of the major obstacles to making quantitative calculations of the energy per pair to compute the energies E_{ESI} and E_{PPS} in a relatively simple way, has been calculating the initial effects of electron-hole pair formation following the bond-orbital theory of Harrison.¹⁴ In spirit, it is closely related to the bond-charge model of Phillips,¹⁵ although the details of the parametrization differ. In this model, the energy per bond in the perfect crystal is computed from the second and fourth moments of the density of states function using linear combinations of atomic orbitals, and is given by¹⁶

$$E_{\text{pair}} = -n \left[M_2 - \frac{M_4(\vartheta) - M_2^2}{4 \cdot M_2} \right]^{1/2} + n \cdot V_0 + E_{\text{pro}}$$

where n is the coordination number; M_2 and $M_4(\vartheta)$ are, respectively, the second and fourth moments of the electronic density of states (EDOS); ϑ is the angle between neighboring bonds; V_0 is the repulsive screening potential; and E_{pro} represents the energy required to create the hybridized sp^3 bonds for the LCAO model of the solid. The fourth moment is a function of the bond angle ϑ , and will, in covalent solids, be influenced strongly by the dangling bonds and back-bonding required by surface reconstruction in those materials.¹⁷ In ionic materials, of course, we can expect much less dependence on the bond angle and more on the coordination number. The repulsive screening potential can be adjusted to fit the experimentally determined equilibrium inter-ionic spacing and the bulk modulus of the solid.

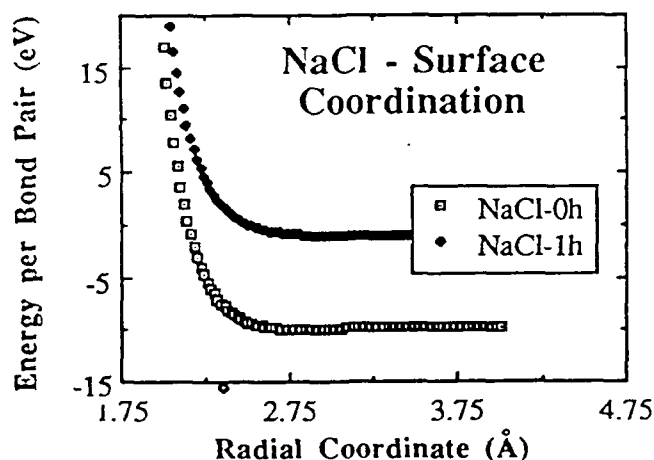


Figure 10. Bond-orbital calculation of the potential energy curves for a surface (five-fold) coordinated site in NaCl and for the same site with a one-hole excitation in a bond. The one-hole potential curve goes slightly negative at large radii.

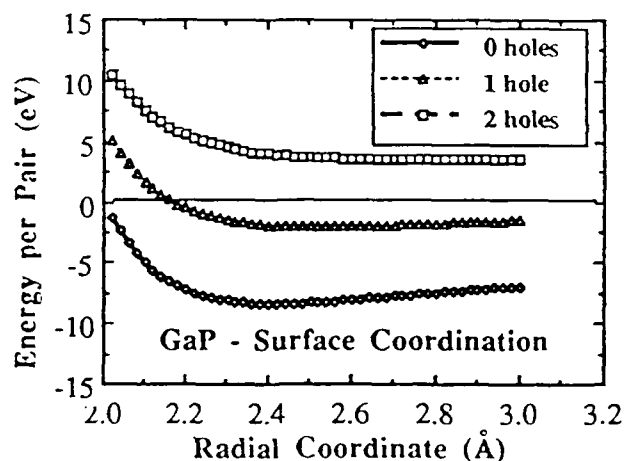


Figure 11. Bond-orbital calculation of the potential energy curves for a surface (three-fold) coordinated site in the compound semiconductor GaP and for the same site with one-hole and two-hole excitations. The one-hole potential curve is still characteristic of a weakly bound state.

We have used this expression for the energy per pair to model bond-breaking at a surface site in an ionic insulator. Because of their availability, we have used self-consistent Hartree-Fock matrix elements for NaCl taken from Reference [18] to calculate the moments M_2 and M_4 ; the same behavior can be expected from KCl. As an illustration of the technique, we show in Figure 10 the potential function that results when we begin with a five-fold (nearest-neighbor only) coordinated surface atom and create a hole in a single bond. One sees that the energy gained by creation of a single hole is already sufficient to put

negative at large distance. The $4p$ electronic state of the alkali atom is therefore entirely of p character.

Thus, although it is qualitatively correct, this model still has some difficulties. Most notable is the fact that it does not yet properly account for the next nearest neighbor interactions which are indispensable (and intractable!) in the alkali halides. Nevertheless, one sees by contrast with Figure 11 that the bond-orbital model at least shows a difference between the alkali halides - in which a single hole already puts the system on a repulsive energy surface - and the compound semiconductor GaP for which two holes are required to achieve the same end even though the binding energies are similar.

5.3 Source of the Excited Electronic State in Desorbing K Atoms

The origin of the electronic excitation which produces desorbing excited atoms is a separate but not unrelated question from the problem of ion motion we considered in Section 5.2. One possibility is that an excited F -center is the source of the excited atom desorption following valence excitation. Certainly valence excitation can form F -centers. It is conceivable that some of them may be excited, perhaps from scattering of secondary electrons, fluorescence, or, in the case of laser-induced desorption, by the high local density of electronic excitation. The strong coupling of an excited F -center to the lattice could both initiate ion motion and simultaneously provide the electron needed for neutralization of a departing ion. Such a mechanism would explain the observed decrease of the excited atom yield as a function of temperature in PSD measurements, since the lifetime of the excited F -center would decrease with increasing temperature. Alkali desorption (without reference to the electronic state of the atom) has been observed from RbBr containing F -centers during irradiation with F -band light.¹⁸

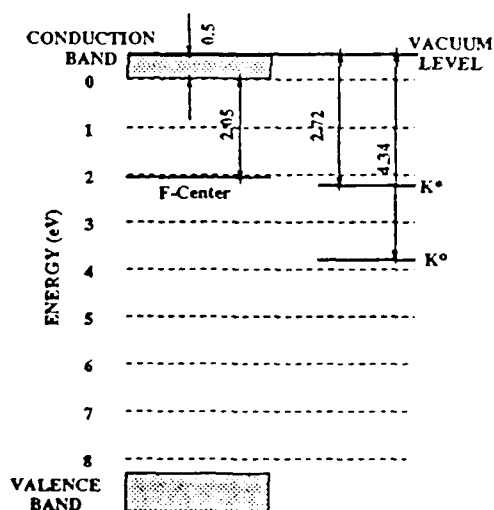


Figure 12. Energies of the $4p$ electronic state in the K atom and the relevant F -center energies in KCl. All energies are given in eV.

A simple consideration of the energetics will show that an excited F -center in KCl has about the right energy to neutralize a potassium ion into the first excited state of the neutral. Figure 12 shows an approximate band diagram for KCl including an F -center. Notice that the ground state F -center is almost resonant with an excited neutral alkali atom, so the excited state will clearly have sufficient energy to do so. The thermal ionization energy of the F -center¹⁹ was used to position the F -center below the conduction band. The ionization limit of the atom was made coincident with the vacuum level of KCl. These methods are approximate, since both the lattice distortion and the surface of itself will alter the band structure; indeed, the lattice relaxation - an essential feature in the dynamics of desorption - will almost certainly modify the relative energies of the various levels shown here.

Localized vibrational excitations of the charged lattice could also produce electronic excitation in a desorbing ground-state atom via electric dipole interactions. Calculations by Bickham and Sievers²⁰ show that excitation of a crystal with an anharmonic lattice potential can lead to the formation of localized vibrational modes of a solid. The energy required is typically that required for creation of an excited F -center. However, in the alkali halides, these modes are only formed for the two-dimensional lattice - consistent with the idea that this might be a purely surface phenomenon. That, of course, would fit the case either of PSD or laser desorption/ablation.

We have observed desorption and ablation of excited atoms and ions from the surface of KCl as a function both of dose and, in the case of ions, as a function of time following the arrival of the laser pulse. These experiments demonstrate the sensitivity of the excited-atom yields to the conditions of the surface, even at intensities characteristic of laser ablation; moreover, the excited atoms show evidence for a different dynamical origin than the ions, thus making them interesting objects of study.

Experimental results for laser-induced desorption and ablation are consistent with the low-intensity results of valence-band-induced desorption by synchrotron radiation. However, at high powers, there is evidence for desorption not only from perfect lattice sites but from defects created by the laser radiation. The final states of the desorbing atoms and ions appear to be strongly influenced by the metallization of the surface - a metallization arising from the preferential ejection of atoms and ions from the halogen sublattice of KCl. The defect sites which play a prominent role in the or shot-number dependence of the ion and excited atom yields at high intensities are energetically more susceptible to desorption than perfect lattice sites. Therefore, even though multiphoton excitation may be required initially to create the lattice defects, desorption can occur even for sub-bandgap photon energies characteristic of lasers because the electronic structure of the defects places them closer to the conduction band than the bulk bandgap energy.

The origin of the excited electronic state observed in desorbing atoms remains something of a mystery. While it is clear that the metallization of the surface plays a role in the initial creation of this state and in its temporal evolution with absorbed photon dose, we presently have no knowledge of the temporal evolution of either the ground-state or the excited state yields following irradiation by a laser pulse.

7. ACKNOWLEDGEMENTS

We are grateful to: the staff of the Synchrotron Radiation Center (SRC) for their expert handling of the Aladdin storage ring; Dr. Winston Chen of the Oak Ridge National Laboratory for the use of his laboratory in some of the laser ablation measurements; Mario Affatigato for his help with the ion ablation experiments; Dengfa Liu for assisting in the synchrotron radiation experiments; and Dr. Russell Dreyfus for illuminating discussions. This research was sponsored in part by the University Research Initiative of the Air Force Office of Scientific Research, by the SURA/ORAU/ORNL Summer Cooperative Program, and by the Medical Free-Electron Laser program managed by the Office of Naval Research for the Strategic Defense Initiative Organization. The SRC is supported by the National Science Foundation. Patrick H. Bunton was supported by a National Aeronautics and Space Agency training grant.

8. REFERENCES

1. A. Schmid, P. Bräunlich and P. K. Rol, "Multiphoton-induced directional emission of halogen atoms from alkali halides," *Phys. Rev. Lett.* **35** (1975) 1382.
2. Reviewed in S. C. Jones, P. Braunlich, R. T. Casper, X.-A. Shen and P. Kelly, "Recent progress on laser-induced modifications and intrinsic bulk damage of wide-gap optical materials," *Opt. Eng.* **28** (1989) 1039-1068.
3. P. H. Bunton, R. F. Haglund, Jr., D. Liu and N. H. Tolk, "Photon-stimulated desorption of excited alkali atoms following valence-band excitation of alkali halides," to be submitted to *Phys. Rev. B*.
4. P. H. Bunton, R. F. Haglund, Jr., D. Liu and N. H. Tolk, "Photon-stimulated desorption of excited alkali atoms from alkali halides following core level excitation," in press, *Surf. Sci.*

5. J. H. Eby, K. J. Tee garden, and D. B. Dutton, "Ultraviolet Absorption of Alkali Halides," *Phys. Rev.* **116**, 1099 (1959).
6. Secondary electron yields are tabulated with references in the *CRC Handbook of Chemistry and Physics*, R. C. Weast, ed., (Boca Raton, Florida: CRC Press, Inc., 1988), p. E-376.
7. N. G. Stoffel, Riedel, E. Colavita, G. Margaritondo, R. F. Haglund, E. Taglauer and N. H. Tolk, "Photon-stimulated desorption of neutral sodium from alkali halides observed by laser-induced fluorescence," *Phys. Rev. B* **32** (1985) 6805.
8. W. L. Wiese, M. W. Smith and B. M. Miles, *Atomic Transition Probabilities II: Sodium through Calcium*, NSRDS-NBS **22** (1965).
9. R. F. Haglund, Jr., M. H. Mendenhall, N. H. Tolk, G. Betz and W. Husinsky, "Surface and Near-Surface Radiation Effects in Photon-Stimulated Desorption," *Nucl. Instrum. Meth. in Phys. Res. B* **32** (1988) 321.
10. H. Overeijnder, R. R. Tol and A. E. DeVries, "Delay times in the sputtering of atoms from alkali crystals during low-energy electron bombardment," *Surf. Sci.* **90** (1979) 265.
11. K. Tanimura and N. Itoh, "Generation of Lattice Defects by Exciton Interaction in RbI: Lattice Instability under Dense Electronic Excitation," *Phys. Rev. Lett.* **60** (1988) 2753-2756.
12. D. Menzel and R. Gomer, "Desorption from metal surfaces by low-energy electrons," *J. Chem. Phys.* **41** (1964) 3311. P. A. Redhead, "Interaction of slow electrons with chemisorbed oxygen," *Can. J. Phys.* **42** (1964) 886.
13. Y. Nakai, K. Hattori, A. Okano, N. Itoh and R. F. Haglund, Jr., "Non-Thermal Laser Sputtering from Solid Surfaces," *Nucl. Instrum. Methods in Phys. Res. B*, to be published (1991).
14. W. A. Harrison, *Electronic Structure and the Properties of Solids* (New York: Dover, 1989).
15. J. C. Phillips, *Bonds and Bands in Semiconductors* (New York: Academic Press, 1973)
16. W. A. Harrison, "Interatomic interactions in covalent and ionic solids," *Physical Review B* **41** (1990) 6008-6019.
17. R. F. Haglund, Jr., K. Hattori and N. Itoh, "Bond-Orbital Model of Two-Hole Laser-Induced Desorption from Semiconductors," to be published.
18. H. Kanzaki and T. Mori, "Photon-stimulated desorption of neutrals from silver and alkali halides," *Phys. Rev. B* **29**, 3573 (1984).
19. N. Itoh, A. M. Stoneham, and A. H. Harker, "A theoretical study of desorption induced by electronic transitions in alkali halides," *Surf. Sci.* **217** (1989) 573; J. J. Markham, *F - Centers in Alkali Halides* (Academic Press, NY, 1966), p. 123.
20. S. R. Bickham and A. J. Sievers, "Intrinsic localized modes in a monatomic lattice with weakly anharmonic nearest neighbor force constants," submitted to *Phys. Rev. B*. We thank Professor Sievers for sharing this work with us prior to publication.

24-5 13

FOREIGN TRIP REPORT TO THE OFFICE OF NAVAL RESEARCH

Atlantic Research Conference on

the Application of Lasers in Surface Science

*International Centre for Theoretical Physics, Trieste, Italy
August 23-27, 1988*

Richard F. Haglund, Jr.

Department of Physics and Astronomy and
Free-Electron Laser Project for Biomedical and Materials Research
Vanderbilt University, Nashville, TN 37235
(615) 322-2828

Contract Number N00014-87-C-0146

This conference, the first on this topic to be held under the auspices of the International Centre for Theoretical Physics, brought together some eighty participants primarily from the United States and Germany. There were participants from other countries, including two from the Soviet Union, at least one from the People's Republic of China, and some occasional visitors from developing countries visiting the Centre for other workshops.

Conference co-chairs were Ward Plummer (University of Pennsylvania), Hans-Joachim Freund (Bochum), and Peter Andresen (Göttingen). Vanderbilt sent two speakers: me and Peter Nordlander (whose trip was supported in part by the National Science Foundation.) The conferees included an amazingly good representation of major laser-surface science groups, certainly a tribute to the organizing committee. The level of enthusiasm of the participants was also high, as indicated by the fact that over half the participants came to the last session on Saturday

morning! A copy of the program is attached, listing the speakers and their titles.

The major scientific themes of the conference included techniques for state-selective detection of desorbing atoms and molecules; laser-induced (both resonant and nonresonant) desorption; two-photon photoemission; studies of gas-surface interactions using various laser spectroscopies; laser-induced chemical and structural modifications on and of surfaces; molecular spectroscopy at surfaces; nonlinear and ultrafast time-resolved surface spectroscopies; and theoretical developments in surface dynamics of atoms and molecules and in surface spectroscopies. Unusually, it seemed to me, there was a significant and interesting selection of non-ultra-high-vacuum surface studies, including studies of interfaces, electrodes, and metal overlayers.

The following paragraphs give a random sampling of highlights from the thirty or so sheets of notes I took during the week.

Laser-Induced Desorption

This continues to be an area drawing much experimental activity and lively theoretical discussion, with the weight of effort (at this meeting, anyway) shifting either toward non-thermal mechanisms of laser-induced desorption (LID) or toward understanding where thermal phenomena end and nonthermal begin.

Everybody's favorite object of study - NO on a well-characterized metal surface - has shown unusual features, including a nonthermal desorption component attributed by Richter, Cavanaugh and King (NBS) to laser-excited hot electrons interacting with the adsorbed molecules prior to desorption via a negative-ion resonance; translational and rotational energy distributions which do not represent the same temperatures, as observed by Alan Burns (Sandia) and many others; and "fast" and "slow" molecular distributions in the NO molecules desorbed from thin NO films grown at low temperatures, as well as some evidence for exciton-mediated desorption at high film thickness, as measured by Steve Sibener (Chicago). The studies of surface coverage effects on the competition between photofragmentation and charge transfer in uv photolysis by Jim Cowins (UC Santa Barbara). All of these represent, in my mind, a continuing evolution and application of familiar concepts of "state-to-state" chemistry to surfaces.

More generally, as pointed out by Dietrich Menzel (TU-Munich), photon-stimulated desorption must be treated with an eye toward localization mechanisms, and he pressed for a molecular dissociation point of view as a way of gaining theoretical insight; certainly in the case of insulators and semiconductors this seems to be necessary. However, in the case of metals, where dynamical screening effects are operating, some way of taking into account charge transfer on the femtosecond time scale as well as the slower (essentially vibrational?) desorption pro-

cess needs more development, as discussed by Phaedon Avouris (IBM).

Laser-Induced Surface Chemistry/Physics

A growing arsenal of sophisticated diagnostics - such as two-photon photoemission, surface second-harmonic generation, ultrafast laser-induced fluorescence, and sum-frequency infrared vibrational spectroscopy, for example - is making possible studies of molecules *on* surfaces with good spatial resolution and hitherto undreamed-of temporal resolution. A sampler from the numerous studies given at the Conference would include: hole-burning experiments in diffusion, including the use of a free-electron laser (Steven George, Stanford); observation of extremely slow work-function "diffusion" on adsorbate-covered surfaces where a hole has been burned with a laser (G. Ertl, Berlin); evidence for an ultrafast (150 fs) disordering process caused by direct electronic excitation preceding the liquification or melting phase in Si (Harry Tom, AT&T Bell Labs) showing ; studies of electrode chemistry by using second harmonic generation to probe stepwise deposition of submonolayer quantities of metal atoms onto metal substrates (Gerry Richmond, Oregon); and observation of layer-by-layer laser-induced damage to a BaF₂ surface undergoing pulsed laser irradiation - a new view of the classic (and still unsolved) problem of laser-induced damage (Jürgen Reif, Berlin, as discussed by Arnie Rosén, Chalmers, Sweden).

Rick Osgood (Columbia) pointed out that a critical unresolved problem in laser-induced surface chemistry is light-enhanced oxidation, which has a major impact on laser processing of materials for microelectronics. Indeed, oxidation reactions came up in several other contexts during the conference. Another interesting dimension in laser-induced surface chemistry came from Wilson Ho (Cornell) who has combined thermal desorption (TDS) and electron-energy-loss (EELS) spectro-

scopies to give information on the effects of both adsorbed species and substrate excitation.

An unusual mixture of what would normally be considered surface physics and chemistry was presented by Ian Harrison (Berkeley), who described photoacoustic excitation of F centers at 222 nm, as observed in experiments where the surface characteristics were used to control spacing and orientation of adsorbed molecules for photofragmentation studies.

Laser-Semiconductor Experiments

Several papers dealt with electron-hole pair excitation by lasers in electronic materials. Jeff Bokor (AT&T) gave a review paper on two-photon photoemission describing the use of this technique to look at relaxation processes in Si and GaAs. Naomi Halas (AT&T) described time resolved studies of surface recombination of bulk laser-excited electrons which, in combination with theoretical studies, have provided a detailed picture of surface electron-hole recombination in silicon.

Rich Haight (IBM) added to this picture by showing direct observations of electronic intervalley scattering between states at a semiconductor surface, with time resolutions on the order of 1-2 ps. Jim Long (NRL) presented results of laser-induced surface photovoltage from Si(111) surfaces modified in ultrahigh vacuum, to determine the surface recombination velocities and bulk carrier lifetimes. The interesting combination of laser techniques applied in synchrotron radiation studies suggests a number of significant studies which could be carried out if lasers were more readily available at synchrotron light sources.

A number of papers also covered areas of laser-surface studies relevant to the characterization and processing of semiconductor materials and semiconductor-insu-

lator interfaces. Tony Heinz (IBM) used three-wave mixing spectroscopy to study an epitaxially-grown $\text{CaF}_2/\text{Si}(111)$ interface; Wilson Ho (mentioned elsewhere in the report) is studying a variety of desorption processes applicable to organic and metallorganic adsorbates on GaAs and Si substrates.

Laser Studies of Metal-Surface Physics

In many studies of laser-surface interactions, it has been assumed that the metal acts as a sink for the incident photon energy, with the deposited energy leaking at essentially infinite speed into the Fermi sea of delocalized electrons. However, new spectroscopic tools, including ultrafast time-resolved and surface-second-harmonic generation spectroscopies, are showing that the metal-adsorbate interactions are in fact a good deal more complex and more interesting.

There was considerable discussion of the detailed dynamics of electron-hole screening at metal surfaces. K. J. Song (Penn) showed evidence from surface second-harmonic generation of Friedel oscillations generated by dynamical screening of the longitudinal field at the surface. Eli Burstein (also University of Pennsylvania) discussed the contributions of the third-order, symmetry-breaking properties of surface fields to polarization of electron-hole pairs. Robert Schoenlein (MIT) presented recent work on measurements of two-dimensional image-state lifetimes at metal surfaces; the lifetimes are (to me) surprisingly long, in the range of 15-35 fs.

Theoretical Studies

The primary emphasis at the Conference was clearly on experiment and experimental techniques, but there were several intriguing papers on surface theory.

Tom George (SUNY-Buffalo) surveyed the various competing (and, to some extent, complementary) approaches to the study of energy transfer in solids. Bill Gadzuk (NBS) gave a brief survey of possible applications of nonlinear dynamics (and chaos) to surface physics. Peter Nordlander (Vanderbilt) has developed, along with John Tully at AT&T, an application of complex scaling techniques to studies of atomic lifetimes near surfaces which should make possible microscopic calculations that can be checked by experiment. John Harris (KFA-Jülich) touched off what may have been one of the liveliest debates on a theoretical question with his review of the allowed molecular trajectories on the potential energy surface in the desorption of H_2 and D_2 from Cu(100).

In addition, there were invited theoretical treatments of second harmonic generation at metal surfaces by Ansgar Liebsch (KFA Jülich) currently a problem of great experimental significance; a group-theoretical treatment of sum- and difference-frequency generation using spherical tensor formalism by Bernhard Dick (Göttingen); and a reprise of work on surface-enhanced Raman scattering from metals by Prof. A. Otto (Düsseldorf), a hot topic in former years which has cooled somewhat in recent years due to lack of reproducible data.

FEL Applications in Surface Science

Of special interest in light of the FEL research program at Vanderbilt was the interest expressed by members of this part of the surface-science community in the possibilities for the use of the free-electron lasers (FEL). The two major FEL applications discussed at the meeting were vibrational spectroscopy of adsorbates in the mid-infrared, say, from 10 to 100 microns, and time-resolved spectroscopy of molecular and atomic hydrogen in the vacuum ultraviolet. Steve George (Stanford) sparked much of the discus-

sion with his report on vibrational spectroscopy studies at John Madey's Mark III infrared FEL. It seemed to be agreed by many of those present -- some of whom have on other occasions been quite skeptical about the potential for the FEL -- that conventional laser sources have so many limitations in these regions of the spectrum that the mid- to far-infrared free-electron laser may well represent the best option for pushing back the frontier in this region of the spectrum.

Since it appears that the region beyond 10 microns is accessible with relative ease for Mark III-type machines, it seems that this is an area worth examining and exploiting in the near future. This area of science is relevant not only to surface physics and chemistry, but also to the biomedical community, since vibrational spectroscopy at interfaces is a major problem in the biochemistry and molecular biology underlying more sophisticated medical laser applications.

Of course, the presently available pulse structure from the Mark III type FELs would need to be modified to allow single-pulse excitations; however, such issues are already being addressed in a number of ways -- as in the cavity-dumping experiment under way in John Madey's laboratory -- and it is likely that the modification of FEL temporal pulse structure to fit into standard pump-probe spectroscopic techniques will soon be a "solved" problem.

Of course, the ultraviolet FEL is another question, involving either accelerators with much higher energy than the Mark III, electron storage rings, or the introduction of radically new wiggler technologies. On the other hand, however, the problem of hydrogen at surfaces is so fundamental that it might be significant, if partial, justification for a concerted development effort on VUV-XUV free-electron laser projects.

DESIGN TRAVEL REQUEST FORM (Rev. 5-72) (FORM NO. NAVJAG 3603)

READ INSTRUCTIONS ON REVERSE SIDE OF FORM. THIS FORM IS TO BE FILLED OUT BY THE TRAVELER AND SUBMITTED TO THE CHIEF OF NAVAL RESEARCH (Code 1141/MS) FOR APPROVAL.

1. Chief of Naval Research (Code 1141/MS)

ONR ATLANTA

7/5/88

TRAVELER Richard F. Haglund, Jr.

CONTRACT NUMBER

FORM NUMBER

MAILING ADDRESS Dept of Physics & Astronomy
Vanderbilt University
Nashville, TN 37235
HOME ADDRESS 1797 Harpeth River Drive
Brentwood, TN 37027

N00014-87-C-0148

CONTRACTOR (Name, address, telephone no.)

Vanderbilt University
Office of Sponsored Research

STATUS (CONTRACTOR EMPLOYEE
CONSULTANT, ETC.)

TRAVELER'S SSAN

PRINCIPAL INVESTIGATOR AND TELEPHONE NO.

Contractor Emp.

481-50-3112

Self

PURPOSE

PARTICIPATE IN MEETINGS



FIELD WORK SPECIFIED
IN CONTRACT



VISIT RESEARCH CENTERS



OTHER (SPECIFY)

JUSTIFICATION FOR VISIT

Meetings and discussions related to FEL technology and FEL Photo-matter interactions
FIELD OF INTEREST AND SCOPE OF MATERIAL TO BE COVERED (BE SPECIFIC)

Laser-surface science and technology, FEL technology development

13. ITINERARY

DATE TRAVEL TO BEGIN

A. VISIT DATES	B. CITY AND COUNTRY	C. INSTITUTION/GOVT. AGENCY	D. PERSON TO BE CONTACTED
August 21-25	Trieskte, Italy	Int. Center for Theoretical Physics-Ward Plummer	
August 26-28	Frascari, Italy	CEU-Frascati (FEL Proj.)	F. Tazzioli
August 30-Sept. 1	Vienna, Austria	Technical University	W. Husinsky

TRANSPORTATION (GOVT. FACILITIES)

CAT. Z &



SHIP

MAC (SPECIFY PREP. DATES)



OTHER
(SPECIFY)

1.
2.
3.

15 ONR FINANCIAL SUPPORT

A. PER DIEM 10 DAYS \$ 80
B. COMMERCIAL AIR (NOT CAT Z) 900
C. MISCELLANEOUS 400
D. EXCESS BAGGAGE ALLOWANCE
E. TOTAL \$2100

16. OTHER SUPPORT

SOURCE University
Workshop Stipend
AMOUNT \$ 500

ESTIMATED TIME OF ARRIVAL

18. ESTIMATED TIME OF DEPARTURE

19. LOCAL SUPPORT REQUESTED

1 August 88

2 Sept. 88

none

20. CITIZENSHIP

IF NATURALIZED GIVE

U.S.A. CERT. NO.

ISSUED

(PLACE)

(DATE)

☐ REGISTERED
ALIEN

REGISTRATION NO.

ISSUED

(PLACE)

(DATE)

☐ OTHER
(specify)

BIRTH DATE

21. BIRTH PLACE

1/7/42

Washington, D. C.

23. PASSPORT (Number, date and place issued)

080291611

Issued April 7, 1986- New Orleans

24. SECURITY CLEARANCE DATA

HIGHEST NOW HELD

25. LEVEL REQUIRED FOR THIS TRIP

Q (DOE Consultant)

None

DISCLOSURE FOR CLASSIFIED TRAVEL (GIVE UNCLASSIFIED STATEMENT OF PROPOSED SUBJECTS TO BE DISCUSSED, WITH WHOM AND
(c. Append agenda if available)

N/A

COMMENTS

Estimates are considered reasonable.
Inds. are available

THOMAS A. BRYANT

Administrative Contracting Officer

APPROVED

BRUCE B. ROBINSON

SEZ

ASSISTANT CHIEF FOR RESEARCH
DIRECTOR, CONTRACT RESEARCH PROGRAM

27. COMMENTS

The trip just to Trieskte, Italy is approved
with a reduced cost of \$1860.00

APPROVED

MICHAEL T. MARRON

SCIENTIFIC OFFICER
APPROVED

DEPUTY AND ASSISTANT CHIEF OF NAVAL RESEARCH

*Contributed discussion paper for the
Adriatico Research Conference on Applications of Lasers in Surface Science
August 23-26, 1988, Trieste, Italy*

**Differentiating Primary and Secondary Processes in Electron- and Photon-
Stimulated Desorption using Laser Detection of Desorbed Neutral Atoms**

Richard F. Haglund, Jr.*

Department of Physics and Astronomy and
Free-Electron Laser Project in Biomedical and Materials Research
Vanderbilt University, Nashville, TN 37235

Recent experiments by several groups on electron- and photon-stimulated desorption (ESD/PSD) of ground-state and excited-state neutral atoms from dielectrics suggest that a variety of competing mechanisms contribute to the observed desorption yields. I shall describe recent experiments in which we have tried to differentiate primary processes (such as ion- and excited-atom production at the surface) from secondary mechanisms (such as ground-state neutral production from defect diffusion and excited-state atom production from secondary electron emission) in ESD/PSD studies of alkali halides. The implications for future experimental directions, especially for the use of time-resolved laser spectroscopies, will also be discussed.

* In collaboration with Alan Barnes, Naomi Halas, Marcus Mendenhall and Norman Tolk. This work is supported in part by the Office of Naval Research and the Air Force Office of Scientific Research.

TUESDAY
AUG. 23, 1988

Morning Session: General Overview

Chairperson: H.-J. Freund

8.15-8.45	Registration
8.45-9.00	Opening and Introduction
9.00-9.45	G. Ertl, General Overview of the Applications of Lasers in Surface Science.
9.45-10.00	Discussion
10.00-10.45	T. George, General Perspective of the Theoretical Advances and Challenges of the Applications of Lasers in Surface Science.
10.45-11.00	Discussion
11.00-11.30	Coffee Break
11.30-12.00	Contributed Session a of General Nature
W. Gadzuk (1)*	Chaos in Surface Physics
P. Nordlander (2)*	Lifetimes of Excited Adsorbate Levels at Metal Surfaces
12.00-12.45	A. Champion, Lasers in Surface Spectroscopy
12.45-13.00	Discussion
13.00	Lunch Break

* Poster Number

**Scientific and Technological Applications of Free-Electron Lasers
in Ultraviolet Photon-Stimulated-Desorption Spectroscopy**

R. F. Haglund, Jr.

Department of Physics and Astronomy and
Free-Electron Laser Center for Biomedical and Materials Research
Vanderbilt University, Nashville, TN 37235 USA

(615) 322-7964

ABSTRACT

Recent synchrotron light sources suggest that VUV and XUV free-electron lasers could provide new spectroscopic tools for studying photon-surface interactions and simultaneously drive needed developments in ultraviolet optics technology.

Scientific and Technological Applications of Free-Electron Lasers
in Ultraviolet Photon-Stimulated Desorption Spectroscopy

R. F. Haglund, Jr.

Department of Physics and Astronomy and
Free-Electron Laser Center for Biomedical and Materials Research
Vanderbilt University, Nashville, TN 37235 USA

(615) 322-7964

Discussions of photon-surface interactions have traditionally been cast in terms of the collective properties (*e.g.*, the heat capacity or the optical susceptibility) of the irradiated material. However, the development of lasers and synchrotron light sources, coupled with innovative applications of both mass and optical spectroscopy, is making it possible to study photon-surface interactions at an atomic scale by determining the quantum states of atoms and molecules at and near material surfaces. Short-wavelength free-electron lasers operating in the XUV and VUV regions of the spectrum offer some exciting prospects for novel photon-matter interaction experiments which take advantage of the FEL's intrinsic properties of narrow bandwidth, high intensity, short temporal pulse length and coherence. In this review, we examine some of the ways in which free-electron lasers in the VUV and XUV can lead both to new tools for studying photon-surface interactions through uv-photon-stimulated-desorption (PSD) spectroscopy, and to new developments in optical technology which might help solve certain pressing technological needs of XUV FELs.

Much of the interest in PSD spectroscopy in the last decade has been focussed on the specific electronic mechanisms through which incident electronic energy is absorbed, localized and ultimately transformed or dissipated into luminescence, creation of electron hole pairs, and, in some cases, into kinetic energy of desorbing atoms or molecules. The early work of Knotek and Feibelman [1] showed, for example, that the desorption of oxygen ions from titania surfaces was made possible by a specific core-level excitation which led to the creation of stable hole pairs on individual ions, with the subsequent Coulomb deformation of the lattice

providing the energy needed to expel the oxygen ion. A key element in elucidating that particular mechanism was the identification of the specific core levels which were excited -- an identification made possible by the availability of tunable synchrotron light.

The energy of a specific atomic core level is relatively easy to pinpoint in an excitation spectrum, even with the relatively coarse wavelength tunability provided by a synchrotron light source. However, in dealing with molecular desorption processes of interest in surface chemistry and catalysis, where energy may be shared among many competing levels, is much more difficult. Synchrotron sources do not presently provide the intensity needed for many important experiments, and the bandwidth of the synchrotron light is often too large to resolve molecular levels. However, an XUV or even VUV free-electron laser, with its high intensity and much narrower bandwidth, would make it possible to provide similarly detailed information about the flow of energy in molecular desorption. A particularly tantalizing example of the possibilities here has been furnished by recent work in our laboratory on electron-stimulated desorption of OH from surfaces [2]. The rotational distribution of the excited OH is distinctly non-Maxwellian, suggesting an electronic rather than a thermal origin for the desorption. However, the electron-induced excitation is not state-specific enough to allow the identification of the entrance-channel states of the excited OH molecules. The use of a tunable VUV FEL would allow identification of the precise entrance channels leading to the formation of excited OH, and remove much of the guesswork from attempts to ferret out the desorption mechanism. In addition, the spectrum of light emitted by excited OH should show entrance-channel polarization effects because of the symmetry imposed on the single hole in the OH electronic shell structure by the presence of the surface; here again, the ultraviolet FEL could provide detailed state selection in the entrance channel which would help to pinpoint the dynamics of the desorption process.

Matrix isolation spectroscopy furnishes another intriguing example of the possibilities for an ultraviolet FEL, this time because of the FEL's ability to generate tunable, narrowband

radiation in a region of the spectrum where synchrotron sources are not particularly efficient. In synchrotron radiation experiments on KCl crystals, we have identified a characteristic band of vibrational transitions of the CN^- radical from a metastable excited state in the ultraviolet [3]. The CN^- , well known as a pseudo-halide and substitutional impurity in bulk alkali halide studies, appears in this case to be bound to the surface as if it were a gas of non-interacting molecules. In carrying out an excitation function measurement, we found a sharp peak at 7 eV and significant fine structure superimposed on a broader peak at synchrotron photon energies above 12 eV. The 7 eV peak is a barely resolved doublet, and matches the position of a transition known from molecular computations. However, the transition cannot be studied in gas phase, because it is above the autoionization limit; it is also impossible to see the transition in the bulk, because coupling to the crystal lattice quenches the excitation before radiation occurs. Thus it is apparently possible to have a kind of two-dimensional matrix isolation spectroscopy for many important molecules, in which the binding to the surface is just sufficient to depress certain high-lying excited states below the conduction band. While synchrotron radiation is a relatively imprecise probe for studying molecular transitions in the matrix-isolated species, the XUV or VUV free-electron laser, once again because of its narrow linewidth and tunability, would be an ideal tool.

In addition to these novel spectroscopic applications of the proposed ultraviolet free-electron lasers, photon-stimulated desorption spectroscopy with XUV-VUV FELs could also contribute directly to the solution of a pressing problem in FEL optical technology: the identification of the fundamental mechanisms for damage to XUV and VUV optics. We have argued elsewhere [4] that laser-surface interactions are generically related to the process of desorption induced by electronic transitions (DIET), a phenomenon triggered in exemplary fashion by both photons and electrons. At the atomic or molecular scale, an understanding both of the desorption rates and of the effects of desorption on surface composition and electronic structure, would help immeasurably in identifying the underlying physics of the laser

damage mechanisms. Recent work with synchrotron radiation has shown, for instance, that under certain circumstances, hydrogen appears to inhibit DIET of excited-state atoms; apparently the weak physisorption of hydrogen is still sufficient to change the electronic structure of alkali halide surfaces in a way which prevents the formation of excited, energetic alkali atoms. However, whether the hydrogen inhibits desorption of ground-state alkali atoms, which are by far the most numerous desorption products [5], or of the halogen atoms, remains to be seen. Free-electron lasers operating in the vacuum or extreme ultraviolet could provide a new tool for studying this phenomenon because of their ultrashort pulse structure and their ability to tune through specific entrance-channel excitations leading to the formation of self-trapped excitons, permanent mobile defects, and ultimately to desorption. In this case, then, the FEL provides a state-specific, impulse excitation whose relaxation through many different channels could be followed in both time- and spectrally-resolved fashion. While the vigorous efforts now going on to develop damage resistant ultraviolet optics will certainly bring significant improvements in performance, "state-to-state" measurements of this type will be required to make significant breakthroughs in fabricating damage-resistant uv optics.

The synchrotron light source has brought significant new scientific and technological developments from a deeper understanding of photon-surface interactions. The prospect of free-electron lasers operating in the VUV and XUV -- with the tunability of synchrotron sources and the additional advantages of high intensity, coherence, and narrow bandwidth -- are likewise certain to create novel and exciting classes of photon-surface studies.

REFERENCES

1. M. L. Knotek and P. J. Feibelman, Phys. Rev. Lett. **40**, 964 (1979).
2. M. J. Mendenhall *et al.*, submitted to Nucl. Instrum. Meth. in Phys. Research B.
3. J. Tellinghuisen *et al.*, submitted to Chem. Phys. Letters.
4. R. F. Haglund and N. H. Tolk, Proc. SPIE **690**, 9 (1986)
5. R. F. Haglund, Jr. *et al.*, Nucl. Instrum. Meth. in Phys. Research B **13**, 525 (1986).

Lecture Notes in Physics

Edited by H. Araki, Kyoto, J. Ehlers, München, K. Hepp, Zürich
R. L. Jaffe, Cambridge, MA, R. Kippenhahn, Göttingen, D. Ruelle, Bures-sur-Yvette
H. A. Weidenmüller, Heidelberg, J. Wess, Karlsruhe and J. Zittartz, Köln
Managing Editor: W. Beiglböck

389

J.C. Miller R.F. Haglund, Jr. (Eds.)

Laser Ablation Mechanisms and Applications

Proceedings of a Workshop
Held in Oak Ridge, Tennessee, USA
8–10 April 1991



Springer-Verlag
Berlin Heidelberg New York London Paris
Tokyo Hong Kong Barcelona Budapest

II-B 15

In KCl, with a bandgap of approximately 8 eV, two photons are required to generate electron-hole pairs by valence-band excitation. Desorption occurs via the decay of the self-trapped exciton and the subsequent relaxation of *F*-center-*H*-center pairs near the surface. For example, diffusion of *F*-centers to the surface from the near-surface bulk neutralizes alkali ions on the surface which then desorb thermally, with a significant fraction in excited states [1]. Figure 2 shows the fluorescence spectrum of excited potassium atoms near the first resonance lines at 7668 Å, at laser intensities on the order of $1 \text{ GW}\cdot\text{cm}^{-2}$. Each point on the spectrum is from a single laser shot; there are two hundred points in each spectral scan from 7600 to 7800 Å. Thus some 140 shots intervene between the upper spectrum and the lower. The decrease in K^* yield with increasing photon dose

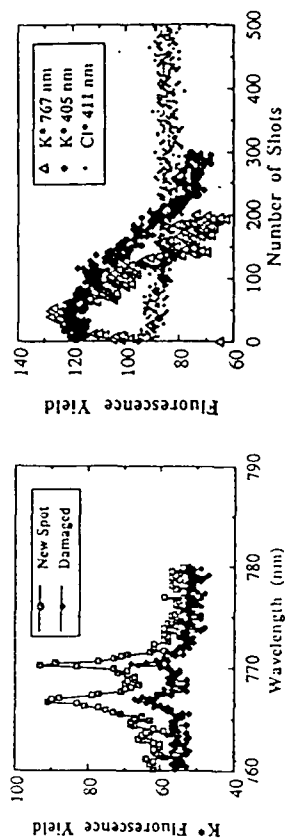


Figure 2. Spectrum of K^* atoms desorbed from KCl at an intensity of $1 \text{ GW}\cdot\text{cm}^{-2}$ on successive scans, starting from a pristine spot. The atomic transition is $4p \rightarrow 4s$.

is well known from PSD studies of alkali halides where valence-band ultraviolet irradiation leads to a steady decrease of excited-atom fluorescence due to metallization of the surface [2]. This excess metal allows resonant ionization of desorbing K^* atoms, thus reducing the total excited-state yield. Figure 3 shows a comparison of relative yields of K^* (from the $5p \rightarrow 4s$ and $4p \rightarrow 4s$ transitions) and of Cl^* emission originating from transitions in the ($3p5p \rightarrow 3p4s$) manifold. Again, the K^* emission vanishes after a few hundred shots, while the Cl^* yield is virtually constant as a function of total dose. Note that the 767 nm K^* transition vanishes before the 405 nm transition, consistent with the picture of the Fermi level rising into the insulator bandgap to ionize the excited atoms. The parent states of the Cl emission line are 12 eV above the ground state, suggesting that the Cl⁺ arises from multiphoton excitation of ablated ground-state Cl in the laser-produced plasma. This is consistent with the generally accepted picture that ground-state Cl emission is the primary ablative process, and results from the decay of the *H*-centers [3].

UV LASER ABLATION FROM IONIC SOLIDS

Richard F. Huglund, Jr., Mario Affatigato, James Arps and Kai Tang
Department of Physics and Astronomy
Vanderbilt University, Nashville, TN 37235

Abstract. We compare ultraviolet laser ablation at a wavelength of 308 nm from ionic solids with the photon energy is much less than (KCl), or approximately equal to (LiNbO_3), the bulk band gap energy. The results are interpreted in the framework of simple charge-transfer models.

Ultraviolet laser ablation products from KCl and LiNbO_3 surfaces subjected to ultraviolet laser irradiation indicate that relative yields of different species depend both on laser intensity and on the wavelength of the irradiated spot. This suggests that the ablation process involves laser-induced charge transfer as well as the electronic structure of the perfect lattice sites.

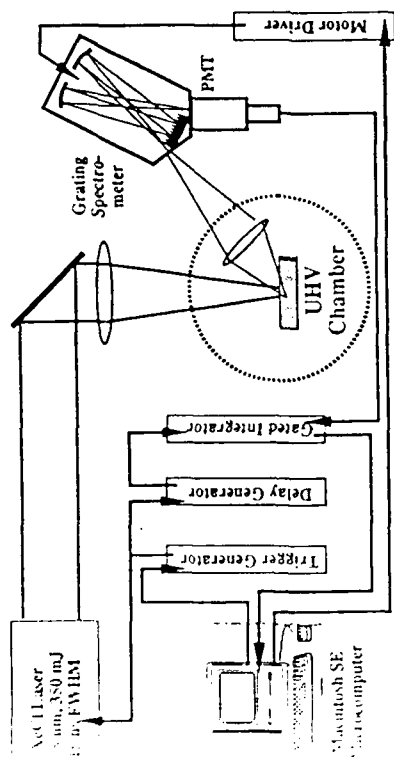


Figure 1. Apparatus for measurements of laser-ablated excited atoms from KCl.

In these experiments, single-crystal targets of either single-crystal KCl cleaved from bulk material or of optically polished, Y-cut LiNbO_3 were mounted on a manipulator in high or low vacuum, as required. Visible fluorescence from ablated K^* atoms was detected by an 0.3 meter spectrograph and a photomultiplier operated in pulse-height analysis mode; spectra were stored on a Macintosh microcomputer. In the LiNbO_3 experiments, neutrals and ions were detected by a channeltron detector (QMS) with a channeltron detector; peak height data for each ionized species were stored on-line in an IBM microcomputer for subsequent analysis.

Laser ablation of lithium niobate is currently of interest partly because LiNbO_3 is not easily processed by chemical or mechanical means, so that lasers are being used for micromachining [4] and direct writing in optoelectronic circuits [5]. Laser-ablation-assisted deposition is also being used to fabricate ferroelectric thin films for optoelectronic applications.

Samples used in our experiments were polished Y-cut LiNbO_3 crystal wafers from Crystal Technology, Inc., with a nominal bandgap energy of 4.0 eV. A Lumonics XeCl laser with 15 ns pulse width and maximum energy in a 15 ns pulse was focused on the targets in a vacuum chamber with a base pressure of 1×10^{-6} torr. The beam was focused on the target at angles of incidence between 45° and 60° with a 175-mm focal length lens and a focal spot area of 0.2 to 7.5 mm^2 . These parameters yield a range of laser intensities spanning the plasma formation threshold, varying from 10^7 to as much as $6.7 \times 10^8 \text{ W/cm}^2$.

We observed a number of ablated atomic, ionic and molecular species by means of quadrupole mass spectrometry, including Li^+ , O^+ , Nb and Nb^+ , NbO and NbO^+ , NbO_2 and LiNbO_3 . The threshold for the LiNbO_3 molecular desorption was below the threshold for all other species of interest discussed elsewhere [6]. The intensity dependence of the yields of the NbO and NbO_2 molecules are shown in Figure 4. We suggest that the observed saturation of the NbO_2 yield arises as this species reaches an equilibrium population in the ablation plume due to ionization by hot electrons. As shown in Figure 5, a comparison of Li^+ and Nb^+ yields for undamaged and damaged surface in both cases and evidence for saturation at nearly the same intensity level.

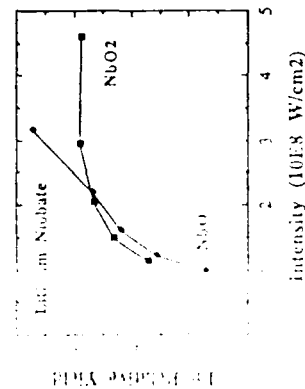


Figure 4. Relative ablation yield of NbO_2 and NbO molecules as a function of uv laser intensity. The surface was damaged at low intensities (several hundred ablation spots).

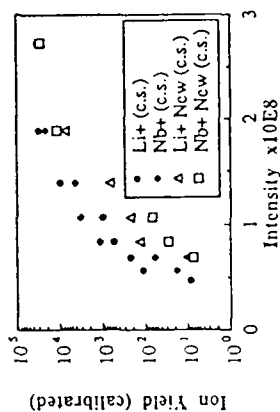


Figure 5. Comparison of the intensity dependence of Li^+ and Nb^+ ion yields as a function of laser intensity for damaged and undamaged spots.

In both the alkali halides and the ferroelectrics, the initial response of the material to photons is the creation of an electron-hole pair by a band-to-band transition: by two-photon absorption in KCl and by one-photon absorption in LiNbO_3 . Also, in both materials, the valence band is formed primarily from the non-metallic ion: the $3p$ Cl orbital in the case of KCl, and the $O 2p$ orbital in LiNbO_3 . The optical response in these ionic insulators is primarily an inter-atomic charge transfer arising from ineffective screening of the valence-band hole. The inter-atomic charge transfer upsets the balance of Coulomb forces in the ionic crystal, initiating ion motion and desorption as in the Klotek-Feibelman mechanism. Further irradiation produces mobile holes in a dense electron-hole plasma which can be localized at the defects created during the latent phase of the damage.

However, whereas in alkali halides the decay of permanent electronic defects formed from the decay of the self-trapped excitation produces the characteristic features of the desorption yield, such as surface metallization. In the ferroelectric oxides, however, it appears that excitation of pre-existing defects and molecular emission may be involved significantly in the desorption process. The super-linear intensity dependence of the ablation yield in the oxides may reflect the exponential variation of the screening potential for charge trapping at defect sites as a function of the electron-hole plasma density.

Acknowledgements

We thank Prof. W. Heiland of the University of Osnabrück for supplying the LiNbO_3 samples, and Dr. C. H. Chen of Oak Ridge National Laboratory for the use of his laboratory for portions of this work. Our research was partially supported by the Office of Naval Research through the Vanderbilt University Free-Electron Laser Center, and by the SURVORNL/ORAU Summer Cooperative Research Program. One of us (MA) gratefully acknowledges a scholarship from the Society for Photo-Optical Instrumentation Engineering.

References

1. P. H. Bunton, R. F. Haglund, Jr., D. Liu and N. H. Tolk, submitted to Phys. Rev. B.
2. P. H. Bunton, R. F. Haglund, Jr., D. Liu and N. H. Tolk, Surf. Sci. 243, 227 (1991).
3. R. F. Haglund, Jr., K. Tang, L.-J. Wang and P. H. Bunton, SPIE Proc. 1441 (1991).
4. M. Eyett and D. Bäuerle, Appl. Phys. Lett. 51, 2054 (1987).
5. T. Krauss, A. Speh, M. M. Opryski, B. Fan and K. Grebe, Appl. Phys. Lett. 53, 947 (1988).
6. K. Tang, M. Afraugato, R. F. Haglund, Jr. and C. H. Chen, submitted to Appl. Phys. Lett.

DEFECT FORMATION IN FUSED SILICAS DUE TO PHOTON IRRADIATION AT 5 AND 50 eV

P.W. Wang(a)(b), G. Escher(c), R.F. Haglund, Jr.(b),

D.L. Kinser(a), N.H. Tolk(b), and R.A. Weeks(a)

(a) Department of Materials Science and Engineering,
Vanderbilt University, Nashville, TN 37235

(b) Department of Physics and Astronomy,
Vanderbilt University, Nashville, TN 37235

(c) Sematech, Austin, Texas 78741

Abstract

We have compared the paramagnetic defect formation in two types of pure fused silica glass irradiated with intense photon fluxes at 5 eV (KrF laser) and 50 eV (undulator beam from Aladdin Synchrotron Light Source), using electron paramagnetic resonance spectroscopy with a frequency of 9.7 GHz and sample temperatures of 110 and 300K. The 5 eV photons produce approximately 10^{-14} paramagnetic defects per photon and the 50 eV photons produce approximately 10^{-5} defects per photon. The ratio of E' centers to oxygen related centers is ~10 times greater for 5 eV photons than for 50 eV photons in type III silica.

Introduction

Intrinsic defects in silicas have drawn considerable attention since Weeks initially identified and characterized the E' center in 1956.¹ This attention results from increased understanding of the scientific and technological importance of defects in a wide variety of materials. Many questions about defects in SiO₂ have not been resolved. Defects affect several important applications of silicas. These include optical fibers, both core and cladding regions, and VLSI's (Very Large Scale Integrated Circuits) in which SiO₂ functions as an insulator or passivating layer.

Many interesting phenomena have been discovered with improvements of brightness, pulse duration and the wavelength-tunability of light sources. Stathis and Kastner² reported that different defects are created in silicas by 5.0, 6.4, and 7.9 eV photons from excimer lasers whose energies are all smaller than the bandgap energy of silica, which is almost 10 eV.^{3,4} They found that 5.0 eV photons are the most efficient in producing E' centers.⁵ They also observed that 7.9 eV photons introduced different defects in dry and wet silicas.

The purpose of this work was to determine the relative and absolute efficiency of 5 and 50 eV photons in producing intrinsic defects in silicas. Five eV photons were produced by a KrF excimer laser and the 50 eV photons were produced by the undulator beamline of Synchrotron Radiation Center at Madison, Wisconsin.

Experimental Procedure

The silica samples consisted of Type III and IV⁵ high-purity synthetic silicas, specifically Suprasil W1 (dry), which contains about 5 ppm OH by weight, and Suprasil I (wet), which contains 1200 ppm OH. Total metallic impurities were of the order of 1 ppm.

Samples were cut from a 30 mm diameter and 1 mm thick disk to the dimensions 5 mm x 18 mm x 1 mm. The samples were cleaned, mounted on a sample holder attached to a manipulator, and inserted into an UHV (Ultra High Vacuum) chamber for the 50 eV irradiations. Several samples were mounted on the same holder. The same optical geometry for each sample was achieved by changing the height of the sample holder inside the UHV chamber. The experimental setup is shown in Fig. 1. The vacuum was kept at 10⁻⁹ torr during the 50 eV exposure at room temperature. For the 5 eV exposure, 50 mJ/cm² unfocused KrF excimer laser beam was used to expose the sample in air at room temperature. The total number of shots was 10¹⁰.

The types and concentrations of paramagnetic defects produced by 5 and 50 eV light were measured by electron paramagnetic resonance spectroscopy (Bruker ESR 200 at 9.7 GHz). The E' centers (singly charged oxygen vacancies) and oxygen-related centers were monitored at room temperature and 110K, respectively. The number of defects in silica was determined by comparison with a standard sample (a Bruker strong pitch secondary standard) whose paramagnetic state concentration was known. The error in the relative numbers of paramagnetic defects was $\pm 10\%$. The absolute numbers of paramagnetic centers has an error estimated at $\pm 100\%$.

The flux of 5 eV photons incident on a sample was determined through calculations based on measurements of power density and total number of pulses. The total number of 50 eV photons was also calculated from the exposure time and the photon flux. The photon flux was calculated from measurements of current produced in a calibrated gold diode and the photoelectric yield on gold.⁶ The flux of 50 eV photon was $(1.1 \pm 0.1) \times 10^{18}$ photons per 1mm diameter spot per minute.

The irradiated volume was calculated from the 1/e penetration depth of 50 eV photons in silica and the beam diameter. The 1/e penetration depth was assumed to be 3.2 μm ⁷ and the beam diameter was 1 mm. Seven to fourteen spots were irradiated on each sample. We estimate the uncertainty of the diameter of the beam size as $\pm 30\%$ when the distribution of photons across the beam is taken into account. The photon energy is lower than the bandgap energy in the case of the 5 eV photons; hence, the irradiation volume is the entire sample.

Results

Paramagnetic resonance spectra of E' centers and oxygen related (OR) centers, including peroxy radicals⁸ and non-bridging oxygen hole centers⁹ were detected in both 5 and 50 eV irradiated silicas. The concentrations of defects of each type in each sample were calculated from measurements of the number of defects and the irradiated volume. The defect formation rate per photon was obtained by dividing the total number of defects by the total number of photons.

The concentrations of defects, the defect formation per photon, the ratio of E' center to OR centers, and the total number of photons used in exposure are all listed in Table I and II.

The 50 eV light created about 10^{15} E' centers per cm^3 and about 10^{13} OR centers per cm^3 in both dry and wet silicas. The formation rate of E' and OR centers are 10^{-4} and 10^{-5} per photon respectively. The ratio of E' center to OR center is three times higher in wet silica than dry silica.

The 5 eV photons introduced about 10^{16} E' centers in both samples. These photons induced approximately 30 times higher concentration of OR centers in dry silica (6.0×10^{14}) than in wet silica (1.7×10^{13}). The formation rate of E' center is about 10^{-12} per photon in both silicas, and 6×10^{-13} and 1.6×10^{-15} OR center per photon in Suprasil W1 and Suprasil 1, respectively. The E'/OR Center ratio is 50 times higher in wet silica than dry silica and has the same trend as in 50 eV irradiated silicas.

Discussion

A flux of 10^{18} 50 eV photons create the same order of magnitude of E' and OR centers as 10^{26} 5 eV photons. The absorption coefficient for the 5 eV photons in silica is about $7 \times 10^{-3} \text{ cm}^{-1}$,¹⁰ while all the 50 eV light is absorbed. Taking this difference in absorptivity into account, the 50 eV light produces $\sim 10^5$ to 10^6 more defects than the 5 eV light.

Three possible reasons may explain this difference in defect formation per photon between the 5 and 50 eV photons. First, E' center formation by 5 eV photons may be due to a two photon process.¹¹ If this is the case, the low absorptivity for a two photon process, which is $2 \times 10^{-3} \text{ cm}^{-1}$,^{1,12} would result in an absorptivity of $\sim 10^{-5} \text{ cm}^{-1}$. Thus, the ratio absorptivities for 5 eV and 50 eV photons is approximately 10^{-10} . The ratio of paramagnetic states produced by 5 eV to 50 eV photons is $\sim 10^{-12}$. Thus, the 50 eV photons produced ~ 100 times more paramagnetic defects than did the 5 eV photons. Second, Arai et al.¹¹ suggested that the E' center induced by 5 and 6.4 eV light is through hole capture at precursor sites. At a flux of 10^{21} 6.4 eV photons cm^{-2} the onset of saturation of E' centers was observed. This saturation effect may also occur for 10^{26} 5 eV photons cm^{-2} . In addition, the 50 eV photons may produce new E' and OR centers by Si--O bond breaking. The threshold energy for Si--O bond breaking is about 8.5 eV;¹³ hence, in case of 50 eV photons we assume that their energy is sufficient to break Si--O bonds. Bond breaking process may well explain why 50 eV light produces 2 or 3 orders more defects in silica than 5 eV light.

Acknowledgement

This work was supported by the Naval Research Laboratory under contract number N00014-86-C2546 and partially supported by the University Research Initiative of the Air Force Office of Scientific Research under contract No. F49620-86-C0125DEF and in part by Office of Naval Research/SDIO contract No. N0014-87-C-0146. We thank the technical staff of the Synchrotron Radiation Center, University of Wisconsin, for the diligent application of their expertise on our behalf. The Synchrotron Radiation Center is supported in part by the National Science Foundation.

Table I Silicas Irradiated by 50 eV Light from Synchrotron

Silicas	$E'(\text{cm}^{-3})$	$\text{ORC}(\text{cm}^{-3})$	E'/Photon	ORC/Photon	E'/ORC	Total Photons
Sup W1	1.1×10^{15}	6.4×10^{13}	3.0×10^{-4}	1.8×10^{-5}	17	3.7×10^{18}
Sup I	3.3×10^{15}	6.7×10^{13}	4.5×10^{-4}	0.9×10^{-5}	49	7.4×10^{18}
Error	($\pm 40\%$)	($\pm 40\%$)	($\pm 50\%$)	($\pm 50\%$)	($\pm 20\%$)	($\pm 10\%$)

5.3×10^{17} photons per 5 mins per 1 mm dia. beam size

The penetration depth for 50 eV photon in silica is $3.2 \mu\text{m}$

Table II 5 eV (248 nm) KrF Excimer Laser Irradiated Silicas

Silicas	$E'(\text{cm}^{-3})$	$\text{ORC}(\text{cm}^{-3})$	E'/Photon	ORC/Photon	E'/ORC	Total Photons
Sup W1	6.8×10^{15}	6.0×10^{14}	6.0×10^{-13}	6.0×10^{-14}	10	7.8×10^{26}
Sup I	8.5×10^{15}	1.7×10^{13}	8.0×10^{-13}	1.6×10^{-15}	500	7.8×10^{26}
Error	($\pm 40\%$)	($\pm 40\%$)	($\pm 50\%$)	($\pm 50\%$)	($\pm 20\%$)	($\pm 10\%$)

50mJ per cm^2 per shot, total shots 10^{10} , total photons on $.5 \times .5 \times .3 \text{ cm}^3 = 7.8 \times 10^{26}$

The absorption coefficient of 5 eV photon in silica is about $7.0 \times 10^{-3} \text{ cm}^{-1}$

Oxygen Related Centers (ORC) include Peroxy Radicals (POR) and Non-Bridging Oxygen Hole Centers (NBOHC)

References

1. R.A. Weeks, J. App. Phy. 27, 1376 (1956)
2. J.H. Stathis and M.A. Kastner, Phys. Rev. B 29, 7079 (1984).
3. T.H. DiStefano and D.E. Eastman, Solid State Commun. 9, 2259 (1971).
4. R. Evrard and A.N. Trukhin, Phys. Rev. B 25, 4101 (1982).
5. G. Hetherington, J. British Ceram. Soc. 3, 595 (1966).
6. P.W. Wang, R.F. Haglund, Jr., L. Hudson, D.L. Kinser, N.H. Tolk, and R.A. Weeks, in SPIE Symposium on Optoelectronic Applied Science and Engineering, Aug. 14-19, 1988, San Diego, CA, USA
7. J. Barth, E. Tegeler, M. Krisch, and R. Wolf in Soft X-ray Optics and Technology Conf., Dec. 1986, Berlin, Proceedings of SPIE, Vol. 733.
8. A.H. Edwards and W.B. Fowler, Phys. Rev. B26, 6649 (1982).
9. M. Stapelbroek, D.L. Griscom, E.J. Friebele, and G.H. Sigel, Jr., J. Non-Cryst. Solids, 32, 313 (1979).
10. Ryoichi Tohmon, Yoshiya Yamasaka, Kaya Nagasawa, Yoshimichi Ohki, and Yoshimasa Hama, J. Non-Cryst. Solids, 95 & 96, 671 (1987)
11. K. Arai, H. Imai, H. Hosono, Y. Abe and H. Imagawa, App. Phys. Lett., 1891 (1988).
12. R.A.B. Devine, Phys. Rev. Lett. 62, 340 (1989).
13. A.R. Silin, L.N. Skuja, and A.N. Trukhin, J. Non-Crys. Solids, 38 & 39, 195 (1980).

Sequence dependence of low-frequency Raman-active modes in nucleic acids

Glenn Edwards and Changle Liu

Department of Physics and Astronomy, University of California, Santa Barbara, California 93106

(Received 11 December 1990)

We have measured the low-frequency ($< 200\text{ cm}^{-1}$) Raman activity of dehydrated fibers and films of polynucleotides and random-sequenced nucleic acids. The spectra exhibit a pronounced, unresolved band in the range $10\text{--}150\text{ cm}^{-1}$. A nonlinear least-squares algorithm optimally fits the spectra from all samples with three low-frequency modes in the range $25\text{--}100\text{ cm}^{-1}$ and a fourth mode near 200 cm^{-1} . A mode near 25 cm^{-1} is sequence independent, but does shift to marginally higher frequency in RNA. The mode frequencies and oscillator strengths of two modes in the range $35\text{--}100\text{ cm}^{-1}$ exhibit sequence dependence.

INTRODUCTION

Vibrational modes of nucleic acids with frequencies less than about 300 cm^{-1} are characterized by in-phase motion extending over many nucleotides. These phonons are commonly referred to as long-wavelength or low-frequency modes of nucleic acids. Recent infrared [1], Raman [2–4], and neutron-scattering [5] experiments have provided complementary data contributing to an improved understanding [6,7] of the long-wavelength dynamics of nucleic acids. It has been proposed that these modes mediate structural or conformational variability [8–10] in nucleic acids and play a role in the dynamics of nucleic-acid-protein interactions [11]. In addition, nucleic acids serve as a useful system for investigating polymer dynamics in general.

A number of theoretical models [1,9,12,13] have given a general accounting of the low-frequency experimental results. Detailed dynamical models predict a large number of spectral features which, to some extent, scale with the model parameters. In some cases it is not obvious how to correlate the relatively large number of predicted eigenfrequencies with the limited number of spectral features. While substantial progress has been made, our understanding of the low-frequency dynamics of nucleic acids remains incomplete. Additional experimental results are necessary to fix model parameters and to allow for a more complete assignment of modes with improved eigenvector information.

Nucleic acids assume a series of *conformations* depending on base sequence and the local environment [10]. The effect of base sequence and local environment on the *low-frequency dynamics* has been the subject of a number of recent and ongoing experimental efforts. For example, Powell *et al.* have measured the infrared activity of a number of vacuum-dried polynucleotides as a function of counterions, crystallinity, and temperature, demonstrating four particularly sharp bands near 63, 83, 100, and 110 cm^{-1} in vacuum-dried films of poly(dA)-poly(dT) at cryogenic temperatures [1]. These features were modeled as intrahelical modes. It should be pointed out that dehydrated fibers and films of nucleic acids yield poor x-ray-diffraction patterns and therefore have come to be

viewed as having a “disordered” conformation [10]. Liu *et al.* have made low-frequency measurements of films of poly(dA)-poly(dT) prepared with the same protocol, demonstrating a pronounced Raman spectrum with bands near 60, 75–100, and $125\text{--}140\text{ cm}^{-1}$ [3]. They propose that in dried fibers and films the low-frequency modes are subject to inhomogeneous broadening. Thomas *et al.* have recently measured the low-frequency Raman spectra of films of calf thymus DNA and fibers of poly(rI)-poly(rC) as a function of water content and counterion species and in crystallites of two oligomers [4]. They propose that a minimum of five low-frequency modes are required where a mode in the range $12\text{--}31\text{ cm}^{-1}$ is interhelical in character and modes in the ranges $34\text{--}45$, $68\text{--}77$, $92\text{--}105$, and $113\text{--}117\text{ cm}^{-1}$ are “mostly internal.” Wet DNA films have been investigated as a function of temperature by Tominaga *et al.* monitoring the Raman activity of a mode near 30 cm^{-1} [2], and by Tao, Lindsay, and Rupprecht using Brillouin scattering [14]. Both groups account for their data in terms of a coupled-mode model of the low-frequency vibrational modes and relaxational modes of the surrounding solvent. Thomas and Lindsay have investigated the low-frequency dynamics of concentrated solutions of a number of polynucleotides with controlled sequence, conformation, and strand number [15]. They do not observe a mode near 25 cm^{-1} and in this investigation B-DNA exhibits modes near 32, 63, and 95 cm^{-1} and A-DNA and RNA exhibit modes near 31, 70, and 117 cm^{-1} .

An important characteristic of the experimental evidence summarized in the above paragraph is that measurements of minimal-salt dehydrated fibers and films yield some of the highest-resolution spectra of low-frequency modes of nucleic acids. This is at least in part due to experimental complications associated with water, sample crystallinity, and the distribution of salts in the fibers or films. Recognizing this, we have undertaken an investigation of the effect of base sequence on the low-frequency modes of nucleic acids cast in dehydrated films. In this paper we report on room-temperature measurements of the Raman activity of dehydrated, oriented fibers of random-sequenced Na-DNA and Li-DNA, random-sequenced Na-RNA, and the sodium

poly(dA)-poly(dT), poly(dA)-poly(dC), poly(dA)-poly(dG), poly(dA)-poly(dC)-poly(dG-dC), and poly(rA)-poly(rU), where the sugar is deoxyribose for DNA or ribose for RNA and the bases are adenine (A), thymine (T), guanine (G), cytosine (C), uracil (U), or inosine (I).

METHODS

Oriented fibers of nucleic acids were pulled, films were cast, and ions were exchanged in our laboratory as described previously [1]; excess salt was removed after the film was cast or the fiber was pulled by bathing in ethanol-water solutions for approximately 10 h. All of the nucleic acids were purchased from Sigma Chemical Company. The sodium salt of random-sequenced DNA was isolated from calf thymus and purified by the vendor. Further purification in our laboratory did not affect the spectroscopic results. The sodium salt of random-sequenced DNA was studied both as fibers and as films. The sodium salts of poly(dA)-poly(dT), poly(dA)-poly(dT)-poly(dA-dT), poly(dG-dC)-poly(dG-dC), and poly(rA)-poly(rU) were pulled into fibers without further purification. The sodium salt of random-sequenced RNA was isolated from *E. coli* and purified in our laboratory. The samples were generally stored in a 0%-humidity environment. During measurements the fibers and films were exposed to ambient conditions, typically 40% humidity and 70°F. The water content of the fibers and films was not directly monitored.

Raman spectra were taken with a Jobin-Yvon U-1000 double monochromator in a photon-counting configuration. The exciting line was either the 488- or 514-nm line of a Spectra Physics Model 2016 4-W argon-ion laser, and the power at the sample was less than approximately 40 mW. The scattering geometry was 90°.

The unresolved bands of the Raman spectra were analyzed using a nonlinear least-squares routine based on the Levenberg-Marquardt method [16]. We have modified a commercial code (LAB CALC, Galactic Industries) to account for a shuttered Rayleigh line; we are unaware of an equivalent code and therefore describe the fitting routine in greater detail in the Appendix. The data reduction was carried out on a 33-MHz, Intel 80386-based personal computer.

RESULTS

Low-frequency Raman spectra are presented in Fig. 1. There are eight frames corresponding to the eight nucleic acids investigated. In each frame raw spectra are presented with the exception that residual plasma lines have been removed in some spectra. The asymmetry of the spectra is to be expected, as can be seen from the equation

$$\frac{I_{AS}}{I_S} = \left[\frac{\nu_0 + \nu}{\nu_0 - \nu} \right]^4 \frac{e^{-h\nu/kT}}{1 - e^{-h\nu/kT}},$$

where I_S and I_{AS} are the intensities of the Stokes and anti-Stokes lines, respectively, ν_0 is the frequency of the

Rayleigh line, and ν is the frequency of the Raman-active mode. The experimental data and the experimental results of the nonlinear least-squares fitting routine (see Appendix) are also presented in Fig. 1. The fitting routine consists of a central feature, a linear background representing fluorescence and instrumental response, and an even number of spectral modes: the sum of these curves is the smooth curve drawn through the data. The fitting routine treats each mode independently, i.e., the parameters of the Stokes and anti-Stokes modes are not restricted in any way during the convergence of the fitting algorithm. It became clear during the analysis that the data certainly did not warrant consideration of more than six pairs of modes. The best fit for each spectrum, as determined by comparing the minimized χ^2 value for each trial solution, uniformly corresponds to a four-phonon-mode model. For clarity of presentation, the central feature and the linear background have been suppressed in Fig. 1.

Multiple spectra of samples were taken; the fits for different spectra of the same nucleic acid with the same salting yield equivalent parameter sets. Table I presents the fitting parameters for the spectra presented in Fig. 1. For each sample the oscillator strengths are relative to the dominant mode in the spectrum. Four modes are evident for all eight samples; one broad mode near 200 cm^{-1} and three modes with the eigenfrequencies less than 100 cm^{-1} . Our consideration of the mode near 200 cm^{-1} , however, will be limited, since a significant portion of this feature lies outside of the experimental frequency range.

Table II presents the average eigenfrequencies, relative oscillator strengths, and relative polarizability derivatives for the three lowest-lying modes, where the polarizability derivative $(\partial\alpha_{ij}/\partial Q_i)_0$ is related to the intensity by the expression

$$I_S \propto \frac{(\nu_0 - \nu)^4}{\nu} \frac{g_i \left| \frac{\partial\alpha_{ij}}{\partial Q_i} \right|_0^2}{1 - e^{-h\nu/kT}},$$

where g_i is the degeneracy factor. Figure 2 presents bar graphs of both the relative oscillator strengths and the relative polarizability derivatives for the three lowest-lying modes.

DISCUSSION

The analysis described above indicates that three modes lying at frequencies less than 100 cm^{-1} , and one additional mode near 200 cm^{-1} , are required to account for the experimental data presented in Fig. 1. Averaging over the eight spectra, the modes lie near 25, 50, and 85 cm^{-1} . Although the fitting of the central feature is approximate, the analysis does not indicate the need for Raman-active modes at frequencies less than 25 cm^{-1} . This may, however, be attributable to limitations of the experimental apparatus.

Naturally it is possible that additional modes may contribute to the unresolved band. Indeed, a previous fitting of complementary data has attributed additional modes

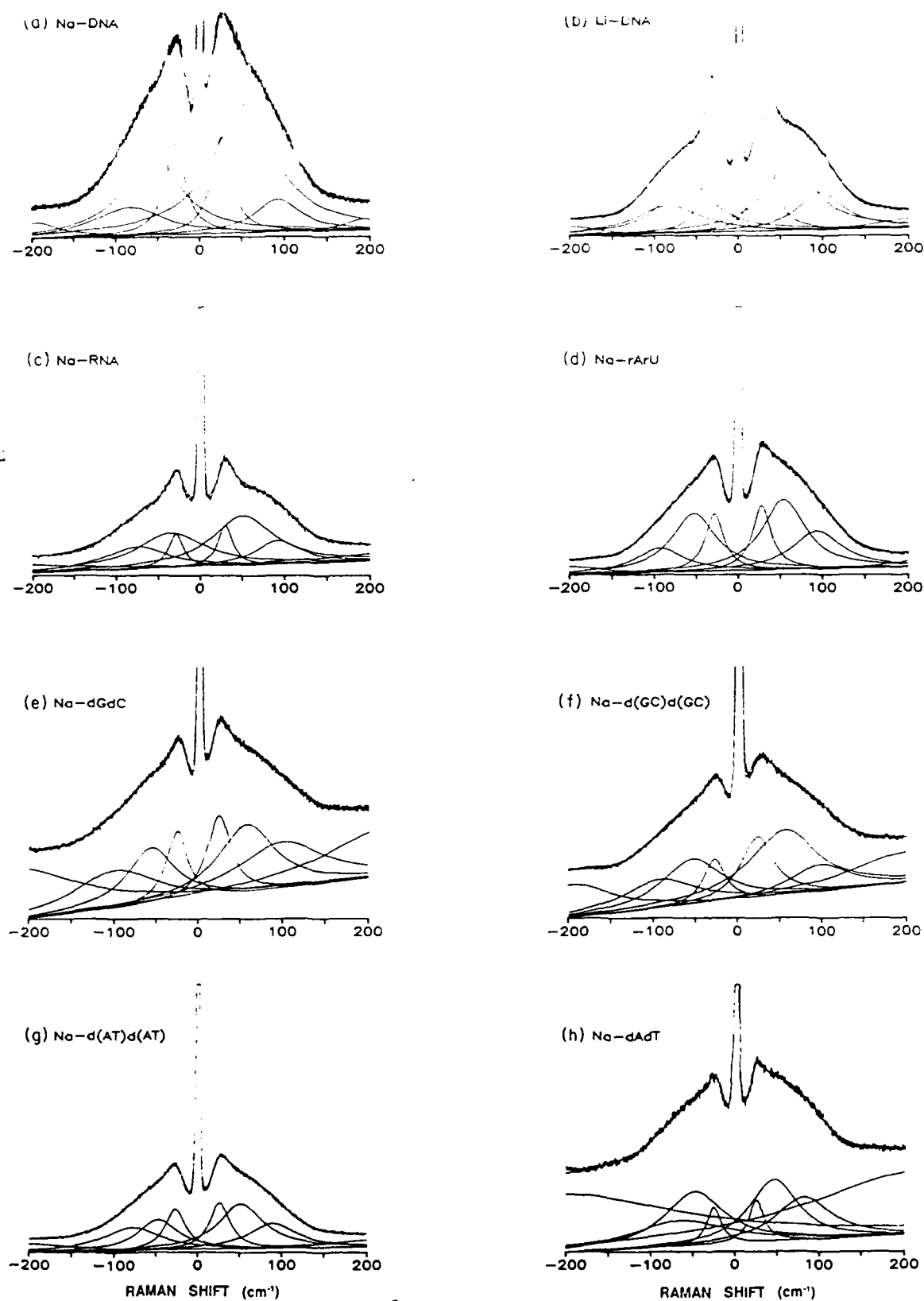


FIG. 1. Low-frequency Raman spectra for eight nucleic acids. The frequency axes have the units of wave numbers (cm^{-1}). Each spectrum has been fit (see text) with nine modes corresponding to a central feature and four Stokes-anti-Stokes pairs of phonon modes. A linear background was included to approximate fluorescence and instrumental response. The sum of the nine modes and linear background is the smooth curve drawn through the data. For clarity of presentation the central feature and the linear background have been suppressed, the latter being evident from the presentation of the phonon modes. Plasma lines have been removed from some spectra, but otherwise the figure presents raw data.

TABLE I. Frequencies and Oscillator Strengths of the Normal Modes of the Nucleic Acids. The frequency indicates the eigenfrequency of the modes. The oscillator strength is normalized for each spectrum.

Nucleic acid	Frequency (cm ⁻¹)	Relative oscillator strength	Full width at half height (cm ⁻¹)
Na-DNA			
	25.8	0.27	28.1
	-28.7	0.26	28.5
	52.2	1	88.5
	-56.6	0.59	79.6
	92.3	0.19	65.1
	-83.8	0.24	97.4
	192.9	0.03	52.3
	-194.8	0.06	64.5
Li-DNA			
	31.6	0.58	22.7
	-31.5	0.52	22.8
	61.7	1	71.1
	-60.7	0.77	71.1
	97.5	0.49	64.0
	-95.4	0.34	67.0
	195.9	0.07	72.6
	-199.8	0.07	71.8
Na-RNA			
	29.1	0.21	21.5
	-29.4	0.18	21.7
	50.3	1	88.1
	-35.3	0.79	99.9
	91.3	0.36	65.3
	-76.6	0.46	91.2
	264.3	0.31	237.6
	-277.7	0.35	206.2
Na-poly(rA)·poly(rU)			
	28.3	0.42	26.7
	-28.1	0.38	26.7
	54.3	1	62.7
	-52.6	0.85	64.3
	94.0	0.59	70.1
	-93.5	0.38	70.7
	206.3	0.05	74.0
	-204.5	0.08	91.9
Na-poly(dG)·poly(dC)			
	24.5	0.55	35.0
	-25.3	0.43	30.9
	57.2	1	81.8
	-55.9	0.73	70.5
	99.1	0.93	127.0
	-98.1	0.72	117.1
	219.7	0.63	171.4
	-220.3	0.73	184.5
Na-poly(dG-dC)·poly(dG-dC)			
	22.9	0.49	46.1
	-27.4	0.24	31.5
	54.2	1	97.9
	-53.5	0.63	85.8
	97.8	0.36	83.4
	-92.0	0.47	108.4
	197.0	0.40	153.6
	-196.0	0.34	116.8

TABLE I. *Continued*

Nucleic acid	Frequency (cm ⁻¹)	Relative oscillator strength	Full width at half height cm
Na-poly(dA-dT)·poly(dA-dT)	26.7	0.50	29.0
	26.5	0.47	30.2
	52.2	1	62.5
	47.5	0.63	60.6
	88.8	0.59	70.7
	79.5	0.63	82.1
	205.1	0.15	138.4
	203.3	0.18	130.8
Na-poly(dA)·poly(dT)	25.4	0.12	20.9
	25.1	0.10	21.6
	45.6	0.52	71.1
	47.9	0.53	86.7
	81.2	0.41	84.4
	65.4	0.40	144.9
	213.9	0.94	313.9
	214.1	1	373.6

TABLE II. Average eigenfrequencies, relative oscillator strengths, and relative polarizability derivatives for the three lowest-lying modes.

Nucleic acid	Frequency (cm ⁻¹)	Relative oscillator strength	Relative polarizability derivative
Na-DNA	27	0.33	0.29
	54	1	1
	88	0.27	0.82
Li-DNA	32	0.62	0.39
	61	1	0.95
	97	0.47	1
Na-RNA	29	0.22	0.25
	43	1	0.78
	84	0.46	1
Na-poly(rA)·poly(rU)	28	0.21	0.29
	47	1	0.81
	73	0.77	1
Na-poly(dG)·poly(dC)	25	0.57	0.21
	57	1	0.61
	99	0.96	1
Na-poly(dG-dC)·poly(dG-dC)	25	0.45	0.27
	54	1	0.83
	95	0.50	1
Na-poly(dA-dT)·poly(dA-dT)	27	0.58	0.29
	50	1	0.71
	84	0.74	1
Na-poly(dA)·poly(dT)	25	0.57	0.19
	47	1	0.74
	73	0.77	1

to the unresolved band at 84; however, this may be a consequence of differences in salt content or hydration, or of restricting the parameters of the functions in fitting the data. In this regard, the Raman-active modes near 75 and 85 cm^{-1} can be compared with the observation of infrared-active modes near 60 and 85 cm^{-1} in dehydrated samples of Na-poly-dA-poly-dT_{1/2} measured at room temperature [1]. At low temperatures the infrared data

could satisfactorily split the bands into more than two modes as the approximately 50- and 82- cm^{-1} modes observed here; however, the low-temperature infrared measurements did not resolve the features near 60 cm^{-1} into more than two modes.

As can be seen in Table II and Fig. 2, the mode frequencies depend on the base sequence and salting conditions. Furthermore, while the Raman spectra do not

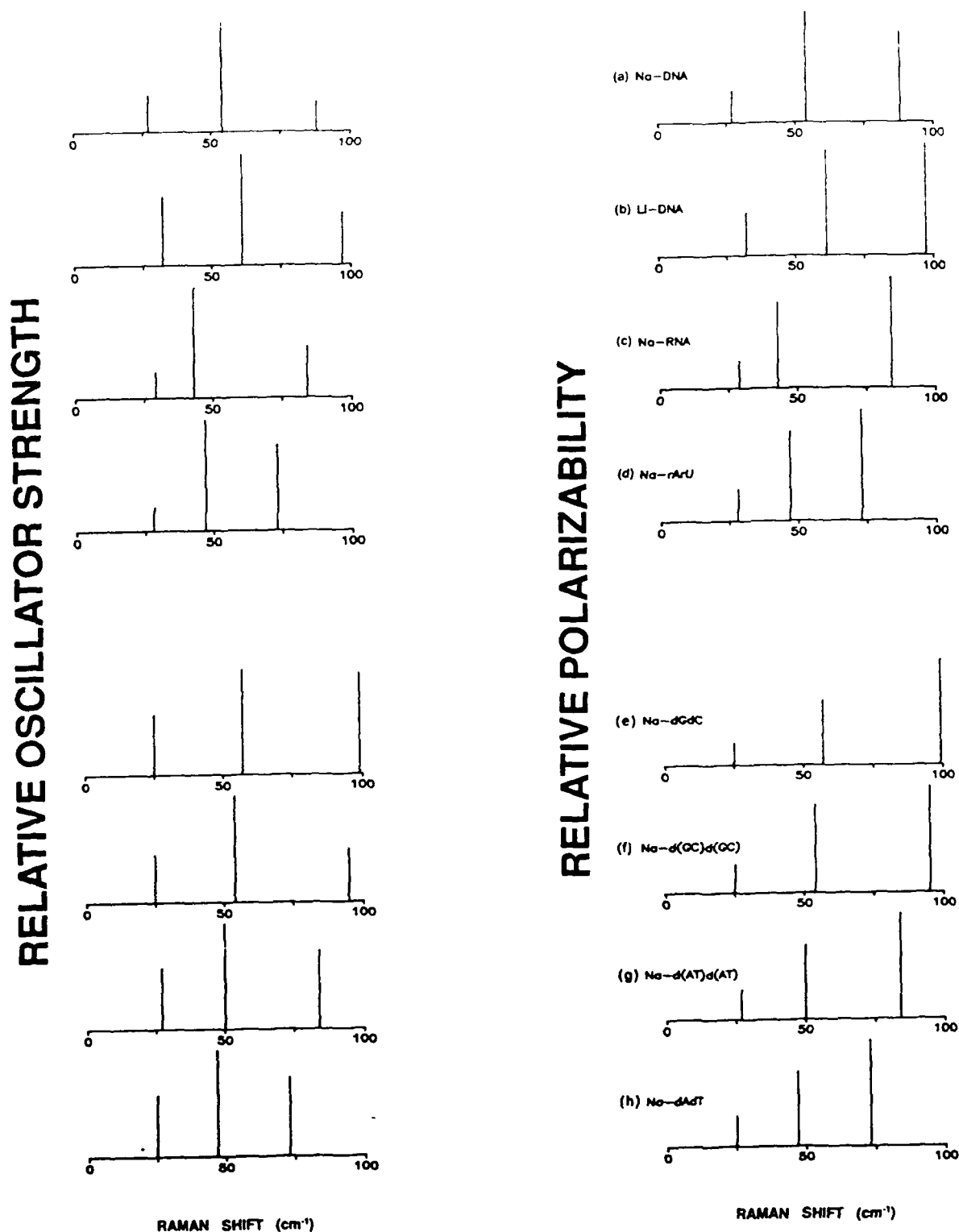


FIG. 2. Relative oscillator strengths (left column) and relative polarizability derivatives (right column) for the eight nucleic acids as listed in Table II. The frequency axes have the units of wave numbers.

relative oscillator strengths.

or polarizability derivatives, they do provide relative information within a given spectrum. The distribution of relative oscillator strengths of the Raman-active modes on base sequence and salting conditions.

It has become common practice to refer to a spectral feature observed near 25 cm^{-1} in Raman spectra of nucleic acids as the " 25-cm^{-1} mode." Depending on the sequence and salting conditions, a mode in the $25\text{--}32\text{-cm}^{-1}$ range is evident in the spectra shown in Fig. 1. As discussed in the Appendix, the fitting parameters listed in Tables I and II are at best a statistical estimate. It should be pointed out, however, that the parameters for the 25-cm^{-1} mode are the most reliable of the parameter sets and are generally repeatable to within less than one wave number. Urabe and Tominaga have reported that the 25-cm^{-1} mode softens with hydration, [17], and Linday, Weidlich, and Rupprecht [18] have reported that the mode frequency depends on counterion species. The results shown in Fig. 2 suggest that the 25-cm^{-1} mode shifts to higher frequency for RNA as compared to DNA, but otherwise is essentially independent of base sequence. The observation of the 32-cm^{-1} feature in Li-DNA is in agreement with the previously observed dependence on counterion species [4].

In addition to the 25-cm^{-1} mode, the analysis of each of the eight spectra shown in Fig. 1 indicates a minimum of three additional spectral features that are candidates for long-wavelength modes. However, unlike the 25-cm^{-1} mode, the frequency and intensity of two of these spectral features show a strong sequence dependence and a dependence on counterion species. The fitting parameters listed in Table I indicate that one feature lies in the $35\text{--}61\text{-cm}^{-1}$ range and the other in the $65\text{--}99\text{-cm}^{-1}$ range. Both frequency ranges are significantly larger than the uncertainty in the fitting parameters. While it is unclear, for example, how the 47-cm^{-1} "mode" in Na-poly(dA)-poly(dT) may correlate with the 61-cm^{-1} "mode" in Li-DNA, the analysis of the data indicates that the low-frequency Raman spectra of different nucleic acids exhibit correspondingly different mode frequencies and relative oscillator strengths.

The fitting of all the spectra uniformly indicate a fourth mode at frequencies near or greater than 200 cm^{-1} . A number of complementary infrared active modes have previously been seen in the $200\text{--}250\text{-cm}^{-1}$ range, with the prediction that Raman-active modes should occur in the same frequency range [1].

The analysis of the spectra yields three long-wavelength, Raman-active modes lying below 100 cm^{-1} that divide into two classes. The 25-cm^{-1} mode forms one class that is insensitive to base sequence and in this sense does not contradict the suggestion that this mode is predominantly interhelical in nature [4]. This mode does shift to higher frequency in spectra of RNA samples: this may indicate that the additional furanose hydroxyl group contributes to the interhelical force constant. It may be premature, however, to rule out the possibility of a 25-cm^{-1} intrahelical mode that both softens with hydration and is insensitive to base sequence. The full width at half maximum of the 25-cm^{-1} mode averages 28 cm^{-1} .

second class of mode characterized by a strong dependence on base sequence, counterion species.

is predominantly intrahelical in nature as suggested previously [4]. The full width at half maximum of these two modes is about three times that of the 25-cm^{-1} mode.

These results, and their interpretation, are based on the modeling of a partially resolved spectral band with known functions. The fitting parameters are a valid statistical estimate and provide useful information regarding low-frequency, Raman-active modes in nucleic acids. The measurements and analysis described in this paper require a minimum of three long-wavelength, Raman-active modes to account for the data. This result for dehydrated fibers and films should be compared with the results of previous investigations of fibers and films as a function of humidity [4] and of concentrated solutions of polynucleotides [15] that require a minimum number of five and three modes, respectively. These findings suggest a possible influence of water content on the number of observable low-frequency, Raman-active modes of nucleic acids; however, it may also indicate the limitations of nonlinear fitting routines and the caution with which these results should be taken. With regard to future experiments, however, these considerations emphasize the need for low-temperature Raman measurements of polynucleotides, analogous to the low-temperature measurements of infrared-active modes discussed above [1], to attempt to experimentally resolve this band.

CONCLUDING REMARKS

We have measured the Raman activity of dehydrated films of nucleic acids as a function of base sequence and, to a lesser extent, counterion species. The spectra have been modeled with a nonlinear fitting routine, and the data reduction indicates that each spectrum is optimally fit with four modes. Three of the modes lie in the $25\text{--}100\text{-cm}^{-1}$ range and an additional mode near 200 cm^{-1} is indicated.

The 25-cm^{-1} mode is essentially independent of base sequence, but does depend on counterion species and shifts to higher frequency in RNA samples relative to DNA samples. A minimum of two additional modes in the $35\text{--}61\text{-cm}^{-1}$ and $65\text{--}99\text{-cm}^{-1}$ ranges are required to account for the spectra. The value of the mode frequencies and the distribution of relative oscillator strengths vary with base sequence. A fourth mode or set of modes near 200 cm^{-1} is consistent with previous measurements [1]. These results indicate that the long-wavelength dynamics of nucleic acids can be sequence dependent. This observation has intriguing implications for the investigation of nucleic-acid-protein interactions.

ACKNOWLEDGMENTS

We thank J. P. Wikswo for his comments concerning nonlinear modeling of data. This research has been supported by the University Research Council and Natural Science Committee at Vanderbilt University and by the Office of Naval Research through Contract No. ONR N00014-87-C-0146.

APPENDIX

The Raman spectra shown in Fig. 1 exhibit unresolved bands of phonon modes, a fluorescence background, and the wings of a shattered central feature, all of which are convoluted with an instrumental response function. In each spectrum, however, the low-frequency edge of an approximately 25-cm⁻¹ mode is partially resolved. This fact encouraged us to attempt to fit the spectra with sets of Lorentzian and/or Gaussian line shapes. In this Appendix we will first summarize nonlinear modeling of data, and then outline the modifications to standard algorithms that are necessary for consideration of the spectra presented in Fig. 1.

Fitting spectral data with a set of Lorentzian functions, Gaussian functions, or functions that are a linear combination of the two, is a special case of nonlinear modeling and is based on iterative techniques. The general approach for modeling the data is to minimize a χ^2 function by varying the parameters of the known functions. The Levenberg-Marquardt method has become the standard routine for nonlinear least-squares fitting of data [16]. Initially, a trial function is chosen, in our case a combination of $2n+1$ Lorentzian and/or Gaussian functions, where n is the number of phonon modes and one function represents the central feature. Each mode is characterized by three parameters: an eigenfrequency, a width or damping coefficient, and an intensity or oscillator strength. In addition, for this application a linear background is included to partially account for fluorescence and instrumental response; this adds two additional parameters.

The Levenberg-Marquardt method iteratively searches for improved solutions by calculating the gradient of the χ^2 function, i.e., all experimental frequencies are considered, with respect to the fitting parameters. At each iteration the parameters are incrementally adjusted, where the increment is determined by a constant times the partial derivative of the χ^2 function. Initially, the constant alternates between a large and small value, i.e., ideally allowing the algorithm to escape local minima and to converge to the global minimum in parameter space. After the algorithm locates a robust, and hopefully global, minimum, the constant is set to the small value to complete the convergence. This algorithm "works very well in practice," although it must be emphasized that the solution "is at best only a statistical estimate of the parameters" [16].

The choice of standard codes to implement the Levenberg-Marquardt method. In our version of the algorithm the shuttered region is considered a constant, i.e., the shuttered region does not influence refinements of the parameter set. It should be noted that the goodness of fit is determined by χ^2 , which is dominated by the fitting of the wings of the central feature. With regard to curve fitting, the shuttered central feature is the most challenging spectral feature in the spectrum.

In the ideal case the known functions would correspond to experimentally measured line shapes. To keep the calculation tractable, however, we determined the optimal approximate line shape by considering linear combinations of Gaussian and Lorentzian functions, i.e., adding one more parameter per function. These linear combinations approximate Voigt line shapes, where the Voigt function is the convolution of a Gaussian and a Lorentzian. In all cases the central feature converged to 100% Gaussian functions and the phonon modes converged to 100% Lorentzian functions.

While the phonon modes appear as Stokes-anti-Stokes pairs, we have not restricted the fitting routine to reflect this, preferring to treat the pairs independently. This provides some measure of the reliability of the fit. In addition, while the frequency of the Stokes and anti-Stokes shifts are identical for a harmonic oscillator, the frequencies will differ according to anharmonicity and the energy level (temperature). For these reasons we have chosen not to symmetrize the data, preferring to avoid filtering the data whenever possible. The fitting did not clearly indicate anharmonic effects.

To determine the optimal fit for each spectrum we have considered trial functions with up to six pairs of phonon modes, where we have chosen the term "pair" to stress that a phonon mode contributes both Stokes and anti-Stokes spectral features. For each trial function of n pairs the algorithm converged to a parameter set that minimizes χ^2 . n is then incrementally adjusted, i.e., another phonon mode is considered in the trial function, the procedure is repeated, and the χ^2 values are compared. Eventually an increase in n does not improve the fitting; in fact, in some cases the algorithm substantially broadened the additional modes, rendering the additional modes as small contributions to the linear background. For each of the eight spectrum shown in Fig. 1, the optimal fit corresponds to four phonon modes.

- [1] J. W. Powell, G. S. Edwards, L. Genzel, F. Kremer, A. Wittlin, W. Kubasek, and W. Peticolas, *Phys. Rev. A* **35**, 3929 (1987).
- [2] For example, see Y. Tominaga, M. Shida, K. Kubota, H. Urabe, Y. Nishimura, and M. Tsuboi, *J. Chem. Phys.* **83**, 5972 (1985).
- [3] C. Liu, G. S. Edwards, S. Morgan, and E. Silberman, *Phys. Rev. A* **40**, 7394 (1989).
- [4] For example, see T. Weidlich, S. M. Lindsay, Q. Rui, A. Rupprecht, W. L. Peticolas, and G. A. Thomas, *J. Biomol. Struct. Dynam.* **8**, 139 (1990).
- [5] H. Grimm, H. Stiller, C. F. Majkrzak, A. Rupprecht, and U. Dahlborg, *Phys. Rev. Lett.* **59**, 1780 (1987).
- [6] For example, see L. Young, V. V. Prabhu, E. W. Prohofsky, and G. S. Edwards, *Phys. Rev. A* **41**, 7020 (1990).
- [7] For example, see V. K. Saxena, L. L. Van Zandt, and W. K. Schroll, *Phys. Rev. A* **39**, 1474 (1989).
- [8] J. M. Eyster and E. W. Prohofsky, *Phys. Rev. Lett.* **38**, 371 (1977).
- [9] A. Garcia and D. M. Soumpasis, *Proc. Natl. Acad. Sci. USA* **86**, 3160 (1989).
- [10] W. Saenger, *Principles of Nucleic Acid Structure*

Springer-Verlag, Berlin, 1981.

- [11] For example, see L. W. Flomolsky, *Phys. Rev. A* **30**, 1111 (1988).
- [12] J. M. Lyster and F. W. P. Gray, *Phys. Rev. A* **10**, 2227 (1974).
- [13] V. K. Saxena, L. L. Van Zandt and W. K. Schroll, *Chem. Phys. Lett.* **164**, 82 (1989).
- [14] N. J. Tao, S. M. Lindsay, and A. Rupprecht, *Biopolymers* **27**, 1655 (1988).
- [15] J. W. Gray, S. M. Lindsay, and A. Rupprecht, *Phys. Rev. Lett.* **62**, 1156 (1989).
- [16] W. H. Press, B. P. Flannery, S. A. Teukolsky, and W. T. Vetterling, *Numerical Recipes in C: The Art of Scientific Computing*, Cambridge University, Cambridge, 1989, Sec. 14.4.
- [17] H. Urabe and Y. Tominaga, *Biopolymers* **23**, 1185 (1984).
- [18] T. Weidlich, S. M. Lindsay, and A. Rupprecht, *Phys. Rev. Lett.* **61**, 1674 (1988).

L. Yu. I. N. V. P. P. and L. W. P. P. P.
Department of Physics, Purdue University, West Lafayette, Indiana 47907

G. S. Edwards
Department of Physics and Astronomy, Vanderbilt University, Nashville, Tennessee 37235
(Received 3 April 1989; revised manuscript received 12 December 1989)

In solving the secular equation of a one-dimensional infinite lattice model of poly(dA)-poly(dT), we obtain dispersion relations. [The notation poly(dA)-poly(dT) means that one strand contains only adenine (A) bases, and the other only thymine (T) bases.] We solve the equation for consecutive refinements of the nonbonded force constants based on Raman, Brillouin, and neutron scattering and Fourier-transform infrared experiments in both polynucleotides and random sequence DNA. When these eigenvectors are examined for base roll and propeller twist, such characteristics are found to be dominant in modes around 50 cm^{-1} .

I. INTRODUCTION

The polymer poly(dA)-poly(dT) is a one-dimensional infinite lattice with the nucleotide pair adenine (A)-thymine (T) for a unit cell. Both bases are planar ringed structures. The orientation of these planar structures is described in terms of two parameters.¹ One is the angle between the bases in a pair, referred to as the propeller twist. The other is the base roll which describes the rotation of the base pair as a whole. We calculate the absolute base roll which is the change of angle the base pair, rolling as one unit, makes with the mean base pair plane. Structural investigations by the Klug² and Rich³ groups of single crystals of DNA dodecamers have identified a "propeller twist" conformation for regions containing a homopolymeric run of A-T base pairs. Austin has suggested that propeller twist and base pair roll are temperature dependent in solutions of poly(dA)-poly(dT).⁴ Liu *et al.*⁵ suggest that the onset of these departures from a more regular structure could be soft mode mediated. To explore this possibility we examine the eigenvectors of our dynamical matrix for dominant base roll and propeller twist.

Forty-one atoms comprise the unit cell, the masses and charges of the hydrogen atoms being included in the heavy atoms to which they are attached. The resulting 123 modes range in frequency from 0.0 to 1700 cm^{-1} . The eigenvectors are from five different calculations, based on consecutive refinements of the nonbonded force constants⁶⁻⁸ and also on two different coordinate refinements.^{9,10} On average, for these calculations at zone center, 12.4% of the modes lie in the $0-100\text{-cm}^{-1}$ range, 6.7% in the $100-200\text{-cm}^{-1}$ range, 5.5% in the $200-300\text{-cm}^{-1}$ range, 8.3% in the $300-400\text{-cm}^{-1}$ range, and 67.1% above 400 cm^{-1} . The first refinement of the nonbonded force constants by Devi-Prasad and Prohofsky⁶ is in agreement with the acoustic velocity of the compressional mode obtained by Brillouin scattering on

randomly sequenced DNA.¹¹ The second nonbonded force-constant refinement, in addition, uses parameters from a calculation of the vibrational modes of the copolymer *B*-poly(dA-dC)-poly(dG-dT) (Ref. 7) which is fitted to neutron scattering on randomly sequenced DNA.¹² The final and most recent refinement⁸ fits the van der Waals term to data from a Fourier-transform infrared experiment on a sample of poly(dA)-poly(dT) (Ref. 13). In all of our present homopolymer calculations,^{8,13,14} we use this latest refinement, as it gives the most extensive agreement with experimental results. However, since we have available dispersion data from previous refinements and for the two different coordinate refinements, we should also like to record the effects of these changes on our results.

II. CALCULATION

The eigenvectors for these calculations are found as follows. The equation of motion¹⁵ of the polymer is given by

$$(\underline{B}^T \underline{F} \underline{B}) \mathbf{q} = \omega^2 \mathbf{q} . \quad (1)$$

\mathbf{q} are the eigenvectors, ω the eigenfrequencies, \underline{F} the matrix of force constants of the internal coordinates of the lattice, and \underline{B} the transformation matrix from internal coordinates to Cartesian coordinates. The force-constant matrix \underline{F} can be considered as

$$\underline{F} = \underline{F}_V + \underline{F}_{NB} . \quad (2)$$

\underline{F}_V is the matrix of valence force constants refined from spectral data above 400 cm^{-1} .¹⁶ In seeking to compare dispersion relations, that is, relationships between frequency and wavelength of the normal modes in the lattice, to experiment, we find that to the valence force constants \underline{F}_V must be added nonbonded interactions \underline{F}_{NB} between a unit cell and its neighbors. The nonbonded in-

interaction consists of a Coulombic term and a van der Waals term, the specific form of which affects modes below 200 cm⁻¹.

A. Nonbonded interaction

Our present refinement of the nonbonded or long-range force constants is based on Brillouin and Fourier-transform infrared experiments as well as a copolymer model refined to fit neutron scattering data on random sequence DNA. We shall describe the three successive refinements of the nonbonded or long-range forces specified below as LRF1, LRF2, and LRF3. The specific form of both the Coulombic and van der Waals force needed for such correlation is also affected by the model assumed for both charges on the atoms and their position coordinates. Thus, in Table I, CR1 and CR2 refer to two different coordinate refinements from Arnott *et al.*^{9,10} We use charges from Miller¹⁷ in the first, second, fourth, and fifth columns of Table I and charges from Renugopalkrishnan *et al.*¹⁸ in the third column. The Miller charges are reduced by 2.31 by comparison to experimentally determined charges.¹⁹ In Eqs. (3), (4), and (5), e_i refers to the charge on atom i , r_{ij} to the distance between atoms i and j , and ϵ the dielectric constant. Two dielectric constants are required as some atoms affect each other through water and some through bases. Our earlier nonbonded or long-range force model LFF1 has

$$F_{ij} = \frac{\alpha |e_i e_j|}{(\epsilon_i \epsilon_j)^{1/2} r_{ij}^3}, \quad (3)$$

with a fitting parameter $\alpha = 1.8$, the dielectric constant of water taken as 81.0, and the dielectric between bases be-

ing 6.0.¹⁷ This reproduces the acoustic velocity of the compressional mode obtained by Brillouin scattering.² The third column of Table I is labeled LRF1a, since, as mentioned previously, different charges are used.

The nonbonded model LRF2 has

$$F_{ij} = \frac{2\eta |e_i e_j|}{(\epsilon_i \epsilon_j)^{1/2} r_{ij}^3} + \left[-\frac{42.0 A}{r_{ij}^8} + BC^2 e^{-Cr_{ij}} \right]. \quad (4)$$

Since Lee *et al.*²⁰ have indicated that the water dipole orientation time near the DNA polymer varies with frequency, we have improved our model of nonbonded interaction, by using a value of 9.0 for the dielectric constant of water. For the dielectric between the bases, we continue to use 6.0. $\eta = 0.43$ which accounts for the scaling of the charges and a conversion factor to give the force constants in units of mdyne/A, for charges given in units of electronic charge and coordinates given in angstroms. The constants for the van der Waals term come from Eyster and Prohofsky,¹⁵

$$A = 1.85;$$

$$B = 209.2;$$

$$C = 3.7.$$

This model is used by Prabhu *et al.*⁷ for the DNA copolymer poly(dA-dC)-poly(dG-dT) in fitting the acoustic compressional mode to that observed in inelastic neutron scattering.¹²

Our third model LRF3 has

$$F_{ij} = \frac{2\eta |e_i e_j|}{(\epsilon_i \epsilon_j)^{1/2} r_{ij}^3} + \left[\frac{42 A}{r_{ij}^8} \right]. \quad (5)$$

TABLE I. Frequency ranges (cm⁻¹) for base roll and propeller twist.

Calc.	CR1 ^a -LRF3 ^b		CR1-LRF3a ^c		CR1-LRF1a ^d		CR2 ^e -LRF2 ^f		CR2-LRF1 ^g	
	Freq.	t_i^2	Freq.	t_i^2	Freq.	t_i^2	Freq.	t_i^2	Freq.	t_i^2
Twist	51.9	0.76	49.4	0.74	43.3	0.45				
Twist-adenine			47.6	0.69			43.4	0.51	43.5	0.55
	49.9	0.70	49.4	0.75					46.3	0.40
	51.9	0.76			52.0	0.73	53.4	0.61	65.1	0.61
Twist-thymine			47.6	0.89	43.3	0.88	43.4	0.77	43.5	0.46
	49.9	0.86	49.4	0.84					46.3	0.48
	51.9	0.81			52.0	0.46				
Roll	49.9	0.79	47.6	0.79	43.3	0.58	43.4	0.69		

^aCR1 refers to the coordinate refinement of Ref. 9.

^bLRF3 refers to Eq. (5) with $A = 0.12$.

^cLRF3a refers to Eq. (5) with $A = -0.048$.

^dLRF1 refers to Eq. (1) with charges from Ref. 19. (Except for this column, all charges are from Ref. 18.)

^eCR2 refers to the coordinate refinement of Ref. 10.

^fLRF2 refers to Eq. (4).

^gLRF1 refers to Eq. (1).

Here a constant displacement $d = 0.35$ Å is used with the distance r measured between atoms separated by a separation of 2 Å. The water dielectric rises to 81.0 at a distance of 10 Å, and the base dielectric rises to $\epsilon = 2$, $\eta = 0.45$ as in LRF2. However, the van der Waals term has been simplified for fitting to data in the far-infrared region ($50\text{--}115\text{ cm}^{-1}$) measured by Fourier-transform infrared methods (Fig. 5 of Powell *et al.*).²² Thus $A = 0.12$. This latest model is the best fit to experimental data for poly(dA)-poly(dT). Initially, we had used a value $A = -0.048$ which we label LRF3a in the second column of Table I.

Because of the variation of water dipole orientation time with frequency, the dielectric constant is frequency dependent as well. For this reason, a value of 81.0 is used for the dielectric constant of water in reproducing the Brillouin scattering results (5–20-GHz range), and a value of 9.0 is used in reproducing inelastic neutron scattering data (THz region). Using the appropriate nonbonded force-constant matrix, E_{NB} , we diagonalize $B^T E B$ in Eq. (1) and obtain normalized eigenvectors and eigenvalues of the lattice. Depending on the nonbonded interaction used, the lowest-lying optical mode varies between 6 and 9 cm^{-1} . The next highest optical mode varies between 11 and 18 cm^{-1} . The lowest observed optical mode in Raman scattering is at 12 cm^{-1} .²³

B. Absolute base roll and propeller twist

The components of an eigenvector interpret as the relative amplitudes of motion of all the atoms in the unit cell. These amplitudes are calculated in mass-weighted, Cartesian displacement coordinates. By convention the axis of roll or twist for the bases is through the pyrimidine C(6) atom and the purine C(8) atom. We construct a test vector with no displacement in the sugar phosphate (backbone) atoms but a roll or twist about the above-mentioned axis in the two bases. We mass weight this vector in the same way the eigenvectors are mass weighted, and then take the dot product of this test vector with all eigenvectors of the dynamical matrix (that is, an orthogonal and normalized set). If the dot product with the i th eigenvector is t'_i ,

$$\sum_i (t'_i)^2 = 1. \quad (6)$$

Those eigenvectors of the dynamical matrix, whose square of the inner product with the test vector is greater than 0.5, are interpreted as possessing in character the roll or twist of the test eigenvector.

III. RESULTS

We employed four kinds of test vectors.

1. A test vector with unit angular propeller twist between the two bases about the C(6)-C(8) axis. The results are displayed in the first row of Table I.

2. A test vector with unit angular displacement of adenine about the C(6)-C(8) axis with all other atoms at rest. The results are displayed in the second row of Table I.

3. A test vector with unit angular displacement of adenine about the C(6)-C(8) axis with all other atoms at rest. The results are displayed in the third row of Table I.

4. A test vector with unit base roll about the C(6)-C(8) axis with all atoms in the sugar phosphate backbone at rest. The results are displayed in the fourth row of Table I.

In each column of Table I, we specify first the modes which have the value of the square of inner product $t_i'^2$ greater than 0.5 and then the value of $t_i'^2$ itself. However, we must note one point. In order to detect the tendency of the bases to twist or roll, even when the backbone atoms have a large-amplitude motion, we keep only the part of the eigenvector representing the amplitude of the base atoms and normalize this new set. In this process, we lose the orthogonality of our set of eigenvectors and thus the relation in Eq. (6). For this reason, we denote the inner product of test vector with the new i th eigenvector as t_i instead of t'_i . (This change is not a problem for our study, since we are not interested in the actual amplitude of motion of the atoms so much as the tendency of the bases to twist.)

We notice that in all the models employed for the nonbonded forces, the dominant response of base roll or propeller twist is in the range 43–53 cm^{-1} . In each column

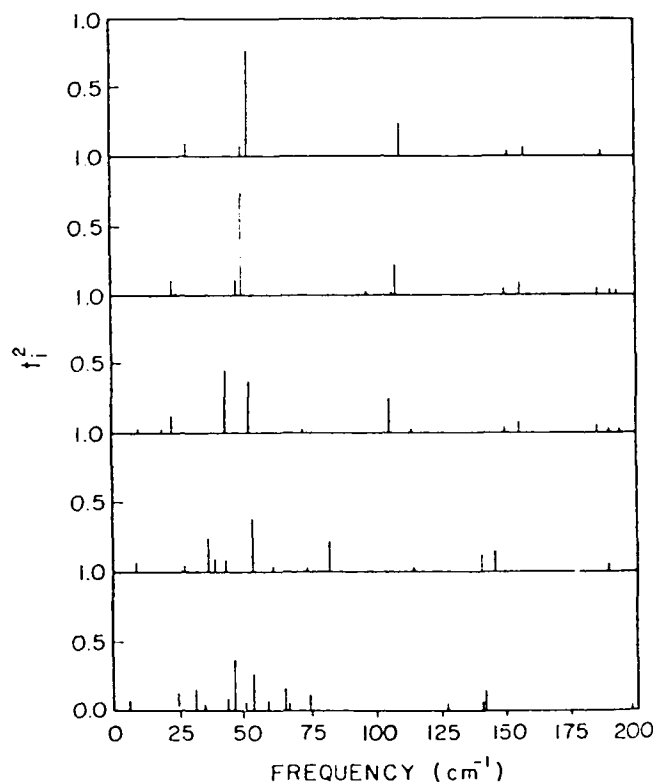


FIG. 1. Distribution of propeller twist modes in the 0–200- cm^{-1} range for each column of the first row in Table I. (Note: first row, the fourth and fifth columns of Table I are blank, since the square inner products for those calculations are less than 0.5 as seen here.)

of Table I, we see that either the adenine or the thymine base shows a tendency to rotate about the C6-C8 axis. These details show the contribution of the separate motion of each base unit to the propeller twist and base roll. For example, in the first and second columns, we see that the thymine base contributes more to the propeller twist and base roll than the adenine base. That is, the propeller twist and base roll have larger projections onto the thymine-only twist.

In Fig. 1, we show the distribution of the propeller twist modes in the 0–200-cm⁻¹ range. This figure corresponds to the first row of Table I; that is, starting from the top of Fig. 1, and counting downward, the first plot corresponds to propeller twist for CR1-LRF3. The second plot is for propeller twist, CR1-LRF3a; the third plot, for propeller twist, CR1-LRF1a; the fourth, for propeller twist, CR2-LRF2; and the fifth, for CR2-LRF1. The total number of modes in the 0–200-cm⁻¹ region is 24 for the first three plots and 20 and 25 for the fourth and fifth plots, respectively. In those cases in which one mode has most of the propeller twist character, the other modes will have very small or zero t_i^2 and thus will not appear in the figure. Values for propeller twist are not given in the fourth and fifth columns of Table I, since the t_i^2 for these calculations is less than 0.5. However, we note that even for these calculations, the highest values of the t_i^2 are centered around 50 cm⁻¹ (Fig. 1).

In comparing the first and second columns of Table I (also the upper two plots in Fig. 1), we see that the effect of adjusting Δ in Eq. (5) is a slight decrease in the frequencies of the modes in the 50-cm⁻¹ range. In the other long-range force models (Fig. 1), the propeller twist character is less distinct for a particular mode. Instead, it appears to be shared over two or three modes.

In measuring the low-frequency Raman spectra of oriented fibers of poly(dA)-poly(dT), Liu *et al.*⁵ report bands near 60 and 130 cm⁻¹ which appear to "melt out" with prolonged laser exposure. One explanation⁵ proposed is that the bands are associated with a temperature-dependent soft mode for the transition to a propeller twist conformation, and thus the bands disappear as the temperature of the sample rises with increased photon counts. The implication of the present calculation is that a mode in the 43–53-cm⁻¹ range should be a candidate for this soft mode. This calculation also suggests a correlation between the experimentally observed mode near 135 cm⁻¹ and the calculated modes in the 105–110-cm⁻¹ range (Fig. 1).

ACKNOWLEDGMENTS

This project has been supported in part by U.S. Office of Naval Research Contract No. N00014-86-K-0252 and National Institutes of Health Grant No. GM24443.

¹W. Saenger, *Principles of Nucleic Acid Structure* (Springer-Verlag, New York, 1984), p. 26.

²H. C. M. Nelson, J. T. Finch, B. F. Luisi, and A. Klug, *Nature* (London) **330**, 221 (1987).

³M. Coll, C. A. Frederick, A. H. J. Wang, and A. Rich, *Proc. Natl. Acad. Sci. USA* **84**, 8385 (1987).

⁴R. Austin (private communication).

⁵C. Liu, G. S. Edwards, S. Morgan, and E. Silberman, *Phys. Rev. A* **40**, 7394 (1989).

⁶K. V. Devi-Prasad and E. W. Prohofsky, *Biopolymers* **23**, 1795 (1984).

⁷V. V. Prabhu, W. K. Schroll, L. L. Van Zandt, and E. W. Prohofsky, *Phys. Rev. Lett.* **60**, 1587 (1988).

⁸L. Young, V. V. Prabhu, and E. W. Prohofsky, *Phys. Rev. A* **39**, 3173 (1989).

⁹S. Arnott, P. J. Campbell Smith, and R. Chandrasekaran, in *Handbook of Biochemistry and Molecular Biology*, 3rd ed., edited by G. D. Fasman (Chemical Rubber, Cleveland, 1975), Vol. 2, p. 411.

¹⁰R. Chandrasekaran and S. Arnott, in *Landolt-Börnstein Numerical Data and Functional Relationships in Science and Technology*, Vol. VII/1b of *Landolt-Börnstein*, edited by W. Saenger (Springer-Verlag, Berlin, 1989).

¹¹S. M. Lindsay and J. Powell, in *Structure and Dynamics—Nucleic Acids and Proteins*, edited by E. Clementi and R. H. Sarma (Adenine, New York, 1983), p. 241.

¹²H. Grimm, H. Stiller, C. F. Majkrzak, A. Rupprecht, and U. Dahlborg, *Phys. Rev. Lett.* **59**, 1780 (1987).

¹³L. Young, V. V. Prabhu, and E. W. Prohofsky, *Phys. Rev. A* **40**, 5451 (1989).

¹⁴K. M. Awati and E. W. Prohofsky, *Phys. Rev. A* **40**, 497 (1989).

¹⁵J. M. Eyser and E. W. Prohofsky, *Biopolymers* **13**, 2505 (1974).

¹⁶K. C. Lu, E. W. Prohofsky, and L. L. Van Zandt, *Biopolymers* **16**, 2491 (1977).

¹⁷K. J. Miller, *Biopolymers* **18**, 959 (1979).

¹⁸V. Renukopalakrishnan, A. V. Lakshminarayanan, and V. Sashisekaran, *Biopolymers* **10**, 1159 (1971).

¹⁹D. A. Pearlman and S. H. Kim, *Biopolymers* **24**, 327 (1985).

²⁰S. A. Lee *et al.*, *Biopolymers* **26**, 1637 (1987).

²¹A. J. Hopfinger, *Conformational Properties of Macromolecules* (Academic, New York, 1973), Chap. 2.

²²J. W. Powell *et al.*, *Phys. Rev. A* **35**, 3929 (1987).

²³Y. Tominaga *et al.*, *J. Chem. Phys.* **83**, 5972 (1985).

Low-frequency Raman active vibrational modes in dehydrated, oriented

C. L. Ed and G. S. Edwards

Department of Physics and Astronomy, Vanderbilt University, Nashville, Tennessee 37235

S. Morgan and F. Silberman

Department of Physics, Fisk University, Nashville, Tennessee 37208

(Received 21 July 1989)

The Raman activity of low-frequency ($20\text{--}300\text{ cm}^{-1}$) vibrational modes of dehydrated, oriented fibers of the sodium salts of poly(dA)·poly(dT) and random sequenced DNA have been measured. Distinct bands near 60 , $75\text{--}100$, and $125\text{--}140\text{ cm}^{-1}$ are resolved in poly(dA)·poly(dT). The Raman activity of the two lowest bands correlate with the previously observed infrared activity of poly(dA)·poly(dT). The apparent reduction in spectral line broadening for poly(dA)·poly(dT), as demonstrated by this and previous measurements of a number of different polynucleotides, is considered as possible evidence for inhomogeneous line broadening.

In 1987 Genzel and co-workers¹ published results of a far-infrared ($40\text{--}500\text{ cm}^{-1}$) investigation of long-wavelength vibrational models in polynucleotides. Measurements of vacuum-dried, free-standing, unoriented films of poly(dA)·poly(dT), poly(dA·dT)·poly(dA·dT), poly(dG)·poly(dC), and poly(rA)·poly(rU) under various temperature and salting conditions were reported. The spectra of poly(dA)·poly(dT) were unique in that, for the appropriate salting conditions, three sharp bands at 62 , 80 , and 95 cm^{-1} were resolved in room-temperature spectra and, in addition, a detailed spectrum of "outer" modes from 125 to 250 cm^{-1} were observed. These experimental results were described in terms of a lattice-dynamical model that predicts Davydov pairs of vibrational modes that are split by a few wave numbers. One mode of the pair will be principally infrared active and the other principally Raman active. The purpose of this Brief Report is to present the results of low-frequency ($20\text{--}300\text{ cm}^{-1}$) Raman measurements of poly(dA)·poly(dT) and random sequenced DNA. Before describing these results, however, a brief summary of related research is presented.

Prior to the far-infrared measurements, Urabe and Tominaga published low-frequency Raman measurements² of nucleic acids including the observation of a broad feature near 85 cm^{-1} . Together with co-workers they also observed modes at frequencies below 50 cm^{-1} ,³ as have Lindsay and co-workers.⁴ Since the appearance of the far-infrared measurements several complementary investigations have been reported. Prohofsky and co-workers⁵ have presented a lattice-dynamical calculation that addresses the temperature dependence of these modes. In addition, during the preparation of this manuscript Weidlich and Lindsay⁶ reported measurements of polynucleotide gels ($70\text{--}150\text{ g/l}$) which revealed features in difference spectra where a water background has been subtracted from the gel spectra.

For this investigation the nucleic acid samples were prepared as follows. Single fibers of the sodium salts of

poly(dA)·poly(dT) (Sigma Chemical Company, lots 127F03421 and 127F03431) and of calf thymus DNA (Sigma Chemical Company, lot 17F-9610) were pulled yielding DNA molecules that are essentially oriented along the fiber direction.⁷ The fibers were then dialyzed in a 73% (by volume) ethanol and 27% (by volume) distilled water solution to remove excess salt and then dried in a desiccated environment as done previously.¹ The spectra were obtained using a Spex Model 1403 double monochromator and a Coherent Inova 90 argon-ion laser. The laser was operated at 488 nm with a power at the fiber of 10 mW . Spectra were obtained in a 90° geometry and polarization occurred along the fiber axis. Scattered light was detected by an RCA C3103M GaAs photomultiplier tube. Liquid-nitrogen-temperature spectra were taken under vacuum with a cold-finger bath cryostat. For some spectra the plasma emission lines have been partially filtered. Experimental spectra present raw data; no averaging was used and there has not been subtraction of any type of background. Collection times of many hours were required to achieve acceptable signal-to-noise ratios. The performance of the spectrometer has been confirmed with more conventional solid-state samples and multiple fibers were investigated to ensure that the features are reproducible.

Figure 1(a) presents a room-temperature spectrum of poly(dA)·poly(dT) showing a distinct band in the 75 to 100 cm^{-1} region. Figure 1(b) presents a lower resolution, room-temperature spectrum of poly(dA)·poly(dT); for reduced photon counts additional bands near 60 cm^{-1} and $125\text{--}140\text{ cm}^{-1}$ are observed. For comparison, in Fig. 1(c) the room-temperature spectrum from a fiber of calf thymus DNA is presented demonstrating a broad feature near 85 cm^{-1} ; changes of scale do not reveal any additional structure. For these purposes calf thymus DNA may be viewed as having a random sequence.

In an attempt to resolve the 75 to 100 cm^{-1} band in poly(dA)·poly(dT) we have paralleled the far-infrared experiments by making low-temperature measurements as

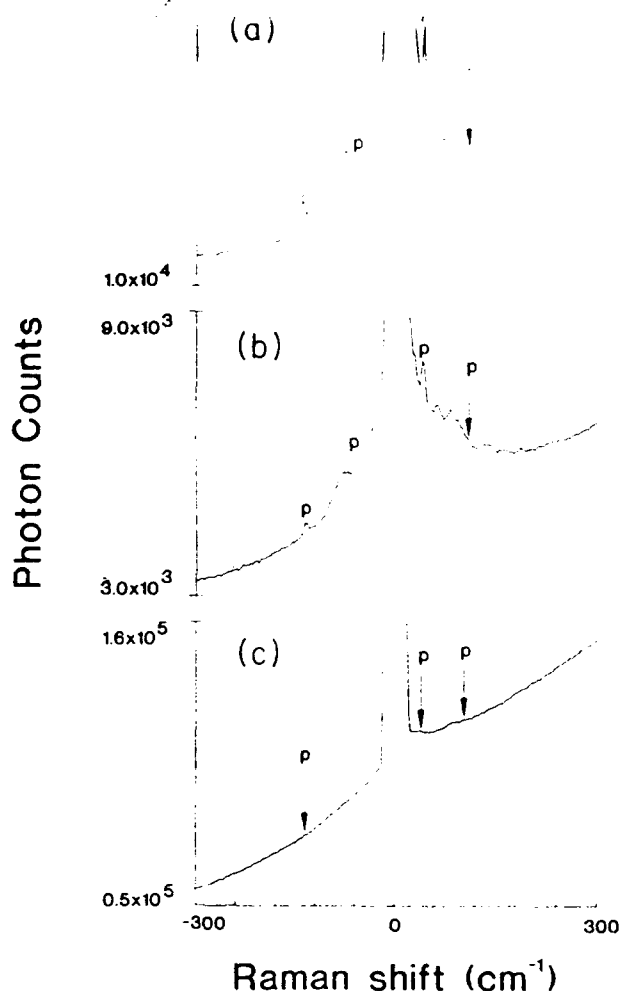


FIG. 1. Low-frequency Raman spectra of DNA at room temperature: (a) poly(dA)·poly(dT), approximately 10^4 counts; (b) poly(dA)·poly(dT), approximately 10^3 counts; (c) random sequenced DNA. Plasma emission lines of the argon-ion laser are indicated by p.

ated with the use of the cryostat led to a decrease in the signal-to-noise ratio. In addition, the signal-to-noise ratio improved upon heating of the fiber. It should be noted that our low-temperature spectra show indications of a band near 25 cm^{-1} as previously observed.²

To determine the parameters of the spectra, the spectra have been modeled as a sum of oscillators.¹ A spectrum was first symmetrized to remove the fluorescence background and plasma lines. The symmetrized spectrum was then modeled as a sum of Lorentzian curves; the spirit of this process is to fit a spectrum with as few oscillators as is reasonable. As an example, the multioscillator fit to the spectrum shown in Fig. 1(a) is presented in Fig. 3. Multioscillator fits of the data in Figs. 1(a) and 1(b) clearly assign modes at 78 and 92 cm^{-1} and 58 , 78 , 94 , and 134 cm^{-1} , respectively; although additional oscillators were required to achieve reasonable fits, these modes are not obvious in the original spectra. These "weak" modes include 52 , 60 , and 84 cm^{-1} modes in Fig. 1(a). In addition, both spectra required a mode near 35 to 40 cm^{-1} ; the intensity of this mode was particularly sensitive to the fitting of the central feature. The spectral features of poly(dA)·poly(dT) are summarized in Table I and are compared with previous observations of infrared- and Raman-active modes. It may be interesting to point out that far-infrared measurements of polyethylene and other polyethylenelike polymers demonstrate a mode at 73 cm^{-1} for room temperature and a weak 108 cm^{-1} mode for low temperature.¹⁰

There are several aspects of these data to be discussed. First, Raman-active modes lie at 58 – 60 , 78 , and 92 – 94 cm^{-1} in definite correlation to the infrared-active modes observed at 62 , 80 , and 95 cm^{-1} by previous room-temperature measurements.¹ Although Landau splitting predicts the Raman-active modes to lie at higher frequency, the splittings are small and, given the resolution of the respective measurements and limitations in comparing Fourier transform infrared (FTIR) and Raman spectra, these differences are not significant.

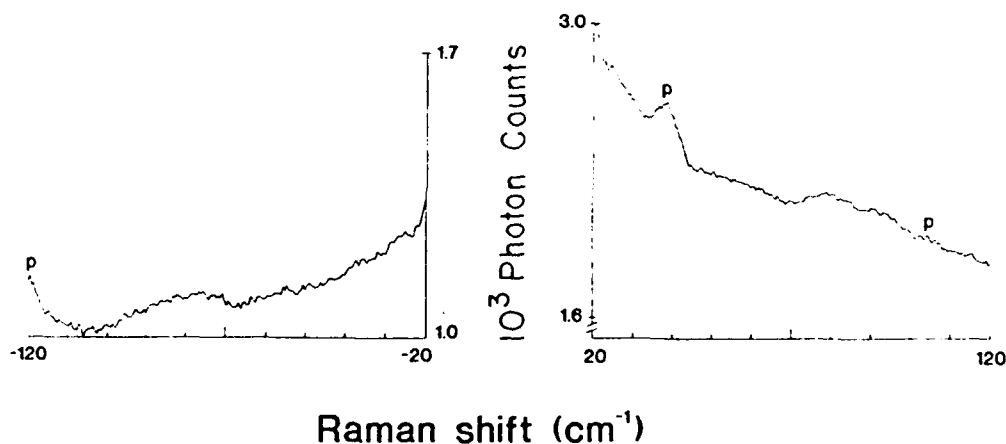


FIG. 2. Liquid-nitrogen-temperature spectra of poly(dA)·poly(dT). Plasma emission lines of the argon-ion laser are indicated by p.

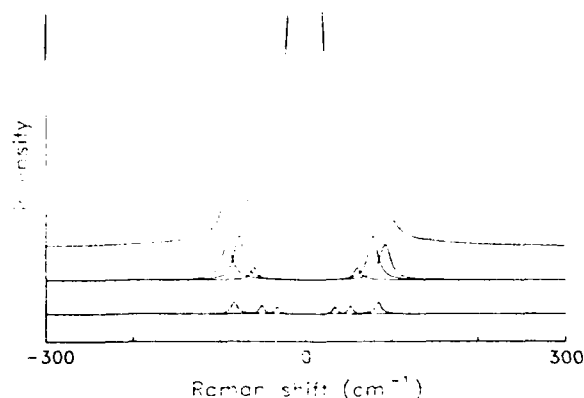


FIG. 3. Multioscillator fit to the spectrum presented in Fig. 1(a). The top curve represents the sum of Lorentzian curves (plus one Lorentzian to model the central feature) and the points represent the symmetrized data (see text). The lower six curves represent the six oscillators used in the model; an offset was introduced for clarity.

It is clear from these results and from the results of previous measurements as summarized above that the low-lying spectral features of poly(dA)·poly(dT), as seen in dehydrated fibers and films and in gels, are sharper than comparable measurements of other nucleic acids. What causes this apparent reduction in spectral line broadening? Of the known line-broadening mechanisms,¹¹ most relevant to these studies is inhomogeneous

broadening due to variations in the local strain. The length of the DNA polymers used for these experiments is on the order of 1000 to 10000 base pairs. These results suggest that poly(dA)·poly(dT), relative to other sequences, may exhibit enhanced base-pair to base-pair structural uniformity. For long-wavelength vibrational modes, lack of structural uniformity along a DNA polymer is equivalent to a distribution of defects in a one-dimensional lattice, i.e., a source of spectral line broadening. This may explain the experimental requirement of dialyzing samples to eliminate randomly distributed salt crystals: measurements of infrared activity in films (1) and Raman activity in fibers (data not shown), in the presence of excess salt, fail to resolve these low-lying features.

It is well known that poly(dA)·poly(dT) has many unique structural and physical properties. Two recent structural determinations¹² of *A* tracts in DNA dodecamers have reported that tracts of dAdT assume an unusual *B*-type structure whose characteristics include an extreme propeller twist, maximized base stacking, a system of bifurcated hydrogen bonds, and a narrowing of the minor groove. It has been proposed¹³ that a spine of hydration in the minor groove stabilizes this structure. Poly(dA)·poly(dT) does not exhibit the *A* to *B* conformational transition as a function of salt and hydration; however, Austin and co-workers¹⁴ have pointed out that for physiological conditions poly(dA)·poly(dT) does exhibit conformational flexibility as a function of temperature. A candidate for a temperature-mediated soft mode associated with this transition is evident in a lattice-dynamical model.¹⁵

Another aspect of these data is evident from comparison of Figs. 1(a) and 1(b). In the first spectrum the feature near 60 cm⁻¹ is not as well resolved as the 75–100 cm⁻¹ band. In the second spectrum, however, bands near 60 and 125–140 cm⁻¹ are apparent. In our measurements the 60 and 125–140 cm⁻¹ bands are resolved in early scans of a fiber but appear to “melt out” as photon counts mount during later scans. One possible explanation is that these modes may be interhelical and the order necessary to support such modes is thermally disrupted. A second possible explanation is that these modes are associated with a temperature-dependent soft mode as discussed in the preceding paragraph. These issues are of particular interest since two lattice-dynamical models^{5,16} differ in their ability to account for the 60-cm⁻¹ mode as an intrahelical mode.

In conclusion, we have made measurements of dehydrated, oriented fibers of poly(dA)·poly(dT) with improved resolution of several low lying, Raman-active bands. A multioscillator fit of the spectra assigns modes at 58–60, 78, and 92–94 cm⁻¹ that correlate with those observed in far-infrared measurements.¹ These features have a high *Q* relative to comparable measurements of other DNA sequences and are well described by lattice dynamics. These results suggest that further experiments be done to address whether these modes are indeed inhomogeneously broadened. With regards to the modes near 58–60 and 134 cm⁻¹, their dynamical behavior appears to differ from those modes in the 75 to 100 cm⁻¹ band.

TABLE I. Observed low-frequency modes in room-temperature spectra of Na-poly(dA)·poly(dT). Column one summarizes the results of this investigation; *w* indicates relatively weak modes (see text). The three modes reported in Ref. 6 are presented in the second column; these modes formed an unresolved band and eigenfrequencies were determined in a method similar to that discussed in the text. In the third column the modes as reported in Ref. 1 are presented. Frequencies are in wave numbers.

Figures 1 and 2	Raman activity		ir activity Reference 1
	Reference 6		
22–25 <i>w</i>			
35–40 <i>w</i>	32		
52 <i>w</i>			
58–60			62
	71		
78			80
84 <i>w</i>			
92–94	95		95
			106
			122
134			136
			170
			214
			238

ACKNOWLEDGMENTS

We thank J. W. Powell and S. M. Lindsay for insightful comments and R. H. Austin for providing us with a copy of Ref. 14 prior to publication. This research has

been supported by the University Research Council and Natural Science Committee at Vanderbilt University and by Contract Nos. BRSG 2-S07-RR07201-08, Office of Naval Research (ONR) (N00014-87-C-0140), and National Science Foundation (NSF) Grant No. RII-8604131.

¹J. W. Powell *et al.*, Phys. Rev. A **35**, 3929 (1987).

²See, for example, H. Urabe and Y. Tominaga, J. Phys. Soc. Jpn. **50**, 3534 (1981).

³Y. Tominaga *et al.*, J. Chem. Phys. **83**, 5972 (1986).

⁴See, for example, S. M. Lindsay *et al.*, Phys. Rev. Lett. **53**, 1853 (1984).

⁵L. Young *et al.*, Phys. Rev. A **39**, 3173 (1989).

⁶T. Weidlich and S. M. Lindsay, J. Phys. Chem. **92**, 6479 (1988).

⁷W. Fuller *et al.*, J. Mol. Biol. **27**, 507 (1967).

⁸C. Demarco *et al.*, Biopolymers **24**, 2035 (1985).

⁹C. Liq and G. S. Edwards (unpublished).

¹⁰H. W. Siesler and K. Holland-Moritz, *Infrared and Raman*

Spectroscopy of Polymers (Marcel Dekker, New York, 1980).

¹¹R. Loudon, *The Quantum Theory of Light* (Clarendon, Oxford, 1983).

¹²H. C. M. Nelson *et al.*, Nature **330**, 221 (1987); and M. Coll *et al.*, Proc. Natl. Acad. Sci. U.S.A. **84**, 8385 (1987).

¹³A. A. Lipanov and V. P. Chuprina, Nucl. Acids. Res. **15**, 5833 (1987).

¹⁴S. Chan *et al.* (unpublished).

¹⁵L. Young *et al.* (unpublished).

¹⁶L. L. Van Zandt and V. K. Saxena, Phys. Rev. A **39**, 2672 (1989).

Applications of free-electron lasers to measurements of energy transfer in biopolymers and materials

Glenn Edwards, Bruce Johnson, John Kozub,
Jerri Tribble, and Katrina Wagner

Vanderbilt University, Department of Physics and Astronomy
Nashville, Tennessee 37235

ABSTRACT

Free-electron lasers (FELs) provide tunable, pulsed radiation in the infrared. Using the FEL as a pump beam, we are investigating the mechanisms for energy transfer between localized vibrational modes and between vibrational modes and lattice or phonon modes. Either a laser-Raman system or a Fourier transform infrared (FTIR) spectrometer will serve as the probe beam, with the attribute of placing the burden of detection on two conventional spectroscopic techniques that circumvent the limited response of infrared detectors. More specifically, the Raman effect inelastically shifts an exciting laser line, typically a visible frequency, by the energy of the vibrational mode; however, the shifted Raman lines also lie in the visible, allowing for detection with highly efficient visible detectors. With regards to FTIR spectroscopy, the multiplex advantage yields a distinct benefit for infrared detector response.

Our group is investigating intramolecular and intermolecular energy transfer processes in both biopolymers and more traditional materials. For example, alkali halides contain a number of defect types that effectively transfer energy in an intermolecular process. Similarly, the functioning of biopolymers depends on efficient intramolecular energy transfer. Understanding these mechanisms will enhance our ability to modify biopolymers and materials with applications to biology, medicine, and materials science.

1. INTRODUCTION

Vanderbilt University has recently constructed a multidisciplinary research center to investigate the applications of FELs to medical and materials research.¹ The FEL was commissioned during the summer of 1991 and now serves as a national facility offering unique opportunities for scientific research. In the past, scientists working with FELs have been specifically concerned with FEL technology development;² after all, a stable and reliable radiation source is required for applications research. FELs are on the verge of achieving both stability and reliability³ and many scientists working with FELs are now concerned with applications of these tunable, pulsed infrared sources with high output power.

In the following we outline the operating characteristics of the Sierra Laser Systems model FEL I and briefly describe the Vanderbilt FEL Center. The FEL is then assessed as a pulsed infrared radiation source for spectroscopic research, two specific FEL applications are described and then discussed as novel spectroscopic techniques for materials and biopolymer research. We conclude with a brief description of future FEL applications currently planned for development at Vanderbilt.

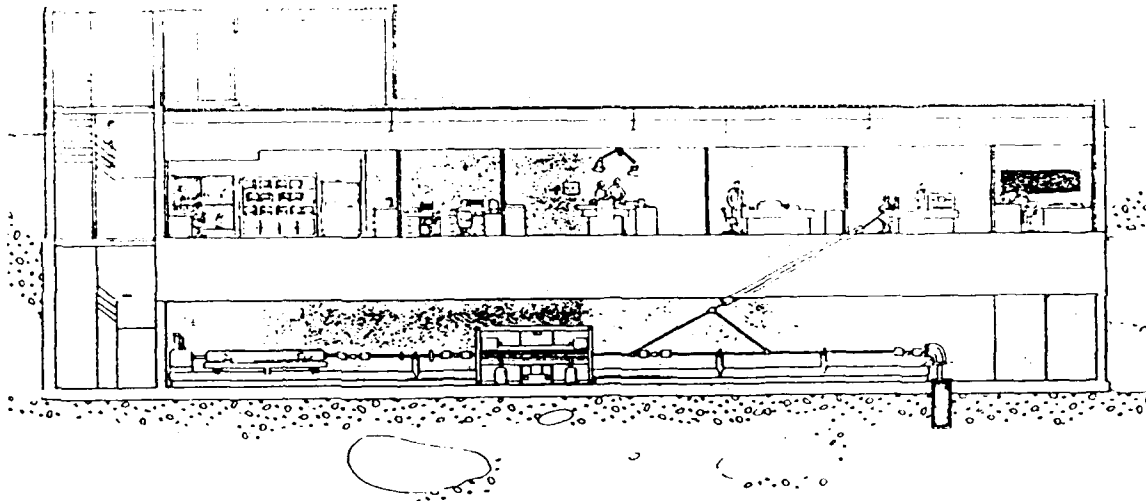


Figure One: Side-View of FEL Facility

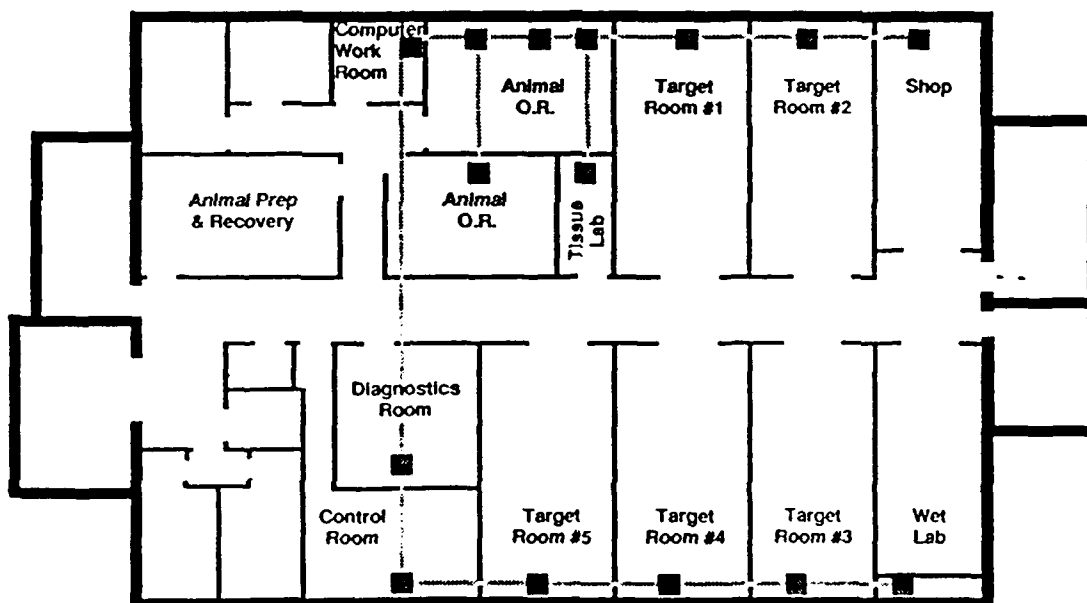


Figure Two: Laboratory Level

Table I: Parameters of the Vanderbilt Free Electron Laser

	Nominal	Measured
Accelerator		
Electron energy	20-45 MeV	36-43 MeV
Micropulse peak current	20-40 A	
Macropulse average current	200 mA	250 mA
Energy spread	0.5%	0.5%
Normalized emittance	4πx10π mm-mrad	
Wiggler		
Wiggler length	108 cm	108 cm
Wiggler period	2.3 cm	2.3 cm
Maximum wiggler field (rms)	0.47 T	0.44 T
Laser		
Wavelength	2-10 μm	2.7-4.9 μm
Micropulse duration	0.5-3 ps	
Micropulse repetition rate	2.9 GHz	2.9 Ghz
Macropulse duration	0.5-6 μs	6 μs
Macropulse energy	100 mJ	360 mJ
Macropulse repetition rate	0-60 Hz	1-30 Hz
Overall average power	0-6 W	0-11 W

2. VANDERBILT UNIVERSITY FREE-ELECTRON LASER CENTER

The FEL Center is an operational, state-of-the-art research facility offering a stimulating and diverse environment for scientific research. Figures one and two have been included to give the reader a sense of the scale of the FEL facility. As shown in these figures, the FEL is housed in a vault located below the laboratory level. The FEL control and diagnostics rooms and approximately 6000 square feet of laboratory space, including five target rooms, are located on the laboratory level, as shown in figure two. The FEL Center is located on the main campus, very close to the School of Medicine, the Departments of Physics and Astronomy, Chemistry, and Molecular Biology, and the School of Engineering. The Vanderbilt FEL is a Sierra Laser Systems model FEL I, similar in design to the Stanford Mark III FEL,⁴ providing continuously tunable, pulsed radiation from 2 to 10 microns with both high average and high peak power. The operating parameters are summarized in Table I.

The Vanderbilt Center is the first FEL facility dedicated to applications research. Applications programs in surface physics, materials science, biological physics, molecular biology and biochemistry, biomedical engineering, neurosurgery, head and neck surgery, and radiology have been active since 1987. A large amount of equipment is available for applications research, including ultra-high vacuum chambers, nanosecond and picosecond pulsed-lasers, a laser-Raman system, a Fourier Transform Infrared (FTIR) spectrometer, and a frequency-domain fluorometer. In addition, the Center has well-equipped supporting laboratories for preparing samples for materials and biophysical research and for preparing specimens for biological and medical investigations.

3. APPLICATIONS FOR MATERIALS AND BIOPOLYMERS

During the past several years we have been planning the initial phase of FEL application experiments. One of the first stages in the planning exercise was an assessment, outlined in subsection 3.1, of the infrared FEL as a spectroscopic tool. This assessment indicated that a prudent scientific approach is based on two-color experiments, described in subsection 3.2, using the FEL as the pump beam with more proven spectroscopic techniques serving as the probe beam. We conclude this section with an outline of the scientific issues in materials science (subsection 3.3) and biological physics (subsection 3.4) to be investigated with these techniques.

3.1. Initial considerations for FEL applications research

What non-trivial investigations are appropriate for the initial phase of FEL-application experiments? This question needs to be considered from several points of view. One point of view recognizes the FEL as a novel source of infrared radiation offering continuous tunability over a wide frequency range and delivering pulsed radiation with both high-peak and high-average power. A class of spectroscopic experiments that were impossible a decade ago can now be undertaken: this implies a wealth of experimental opportunity. Another point of view draws the unavoidable comparison to the field of visible spectroscopy, which has enjoyed considerable scientific progress in part due to both the high-Q of visible lasers and to the sensitivity of visible detectors. The performance of infrared detectors does not match that of visible detectors; this wavelength dependence is a fundamental limitation.⁵ Similarly, the power density depends on the ability to focus the laser beam; with regards to infrared investigations of certain non-linear effects an infrared beam does not compare favorably with a visible beam. A third

point of view recognizes the FEL as new technology and at this time it must be regarded as an unproven spectroscopic tool.

After considering the attributes, limitations, and cautionary notes listed in the preceding paragraph, we feel the most prudent phase-one FEL applications should utilize the unique capabilities of the FEL, place the burden of detection on proven spectroscopic techniques, and not place excessive demands on the reliability and stability of the FEL. Two-color experiments meet these guidelines and two examples are described in the following subsections.

3.2. Two-color FEL applications

Recognizing the considerations presented in subsection 3.1, we have configured the FEL as a "pump" beam and two proven, conventional spectroscopic techniques as possible "probe" beams. The fundamental limitation of infrared detectors has been circumvented; the pump-probe schemes to be outlined below can be viewed as replacing the infrared detector with either a Raman or FTIR spectrometer. Our experiments both take advantage of the unique tunability of the infrared FEL beam and the experimental design is such that it does not place heavy demands on FEL performance.

Using two-color techniques, we are investigating the vibrational dynamics of materials and biopolymers with three experimental designs: hole burning measurements using both laser-Raman and FTIR spectrometers as probes to set experimental limits on the lifetime and anharmonicity of vibrational modes and anti-Stokes Raman experiments to measure intermolecular and intramolecular energy transfer.

3.2.1. Applications based on laser-Raman spectroscopy

The first class of two-color experiments uses a laser-Raman spectroscopic system as the probe beam. The Raman effect is due to inelastic scattering of light where the Stokes and anti-Stokes features correspond to phonon creation and annihilation, respectively. If the ratio of transition energy over thermal energy is sufficiently large, the "oscillator" will be in the ground state, phonons will not exist to be annihilated, and thus there will be no thermal contribution to the anti-Stokes spectrum. More specifically, the ratio of the anti-Stokes to Stokes scattering intensity is given by:

$$\frac{I_{AS}}{I_S} = \left[\frac{\nu_o + \nu}{\nu_o - \nu} \right] \frac{e^{-h\nu/kT}}{1 - e^{-h\nu/kT}}$$

where ν_o is the transition frequency and ν is the excitation frequency of the probe laser. For example, at room temperature a vibrational transition at 1000 cm⁻¹ probed with a visible excitation frequency of 514 nm has an anti-Stokes to Stokes intensity ratio of 0.01. Thus under appropriate conditions anti-Stokes Raman spectroscopy can serve as a probe for nonequilibrium contributions to vibrational energy levels.

For our experimental setup the FEL is tuned to and "pumps" an infrared-active mode of the system. This results in a non-equilibrium energy distribution, i.e. a "hot" mode that in general couples to other modes with varying efficiencies rendering a distribution of athermally populated modes. A second, visible beam from a conventional laser scatters from this excited system and the scattered light is

collected and focused on the input slit of a double monochromator, effectively probing the occupation numbers of Raman-active vibrational modes. With regards to choice of conventional lasers, experiments using a cw laser identify pathways for energy transfer; experiments using a picosecond pulsed laser will establish rates of energy transfer.

Laser-Raman spectroscopy has added advantages for biological physics. The chronic problem of strongly absorbing water bands in the infrared is avoided since water is relatively transparent in the visible range. Furthermore, in many cases sensitive visible array detectors can be used avoiding the tediously long measurements typical of the photon counting mode. To keep experimental run times manageable, however, somewhat concentrated samples may still be required.

3.2.2 Applications based on FTIR spectroscopy

The second class of two-color experiments uses an FTIR spectrometer system as the probe beam. FTIR spectroscopy is based on the Michelson effect and benefits from the multiplex advantage, i.e. frequencies throughout a broad spectral range are measured simultaneously: for sufficient integrated intensity the impact of the relatively poor performance of infrared detectors is significantly reduced. In this class of experiments the FEL is used as the pump beam to "burn holes" in spectral lineshapes. Hole burning is an experimental technique that modifies a normally smooth inhomogeneously broadened absorption line to elucidate approximate homogeneous lineshapes and lifetimes.⁶ Condensed matter is subject to strains, impurities, and other imperfections that effect a distribution of local environments and thus can result in inhomogeneous broadening of spectral lines. The FEL will be used to burn a homogenous line within the inhomogeneous envelope; the homogeneous line corresponds to a subpopulation of absorbers that experience similar local environments. In some cases the hole can be "persistent," i.e. it remains evident after the pump beam is turned off. The resulting hole renders information concerning mode lifetimes and is the basis for models of energy relaxation. Similarly, for modes that share infrared and Raman activity, the FEL can be used to hole burn modes that are probed with a laser-Raman system.

3.3. Investigations in materials science

Our research group is primarily interested in biopolymer physics. It has usually been our experience that the condensed matter literature contains experimental and theoretical accounts that have served as both guidance for our experimental protocols and as points of comparison to our biophysical results. However, in the past experimental investigations at infrared frequencies have been limited by the lack of a tunable infrared source. The continued development of the FEL is removing this limitation; consequently, we now find ourselves with experimental capabilities for which there is a lack of comparable results from more traditional condensed materials. Naturally we view this development as a great scientific opportunity and in response have expanded our research program to include more traditional materials with the goals of providing both fundamental results in condensed matter physics and leading to a more complete understanding of vibrational dynamics in biopolymer systems.

As a general example of an FEL application investigating more conventional condensed materials we outline collaborative projects with Norman Tolk of Vanderbilt University and Enrigue Silberman and Don Henderson from Fisk University. Energy transfer and energy relaxation processes for molecular species isolated in crystals and low-temperature matrices have received significant experimental and

theoretical attention. The vibrational dynamics of impurities isolated in alkali halides have been previously investigated indicating both a fast relaxation between vibrational modes⁷ and the occurrence of persistent holes in inhomogeneously broadened spectral lines.⁸ In addition, more complicated systems have been investigated. For example, matrix isolated 1,2-difluoroethane exhibits persistent holes;⁹ to account for this effect it has been proposed that pumping the system at low power leads to a molecular reorientation within the matrix cage. In the past, experimental progress has been hindered by the requirement that the spectral lines be coincident with existing infrared sources. Using the two-color techniques described above we will take advantage of the tunability of the FEL to further elucidate the mechanisms for energy transfer and relaxation.

3.4. Investigations in biopolymer physics

Nucleic acids and proteins exhibit a number of vibrational modes in the infrared,^{10,11} as listed in Table II. A subset of these modes are known to be sensitive to conformation and have served as structural markers.¹² In addition, specific base sequences alter the local structure in nucleic acids, as do specific amino acid sequences in proteins, possibly serving as a mechanism for nucleic acid-protein recognition.¹³ The consensus picture is that biopolymers are conformationally flexible and under certain conditions exhibit a range of local conformations and local environments. This structural variability suggests the possibility of inhomogeneous broadening of spectral lines.^{6,14} In fact, FTIR measurements have identified an anomalous spectral feature associated with the sugar ring in nucleic acids. It is well known that A-DNA and B-DNA have structurally distinct sugar ring conformations; we have identified this apparently broadened spectral feature as a candidate mode for hole burning experiments and this serves as a first example of a specific FEL application in biopolymer physics.

Any biological relevance for vibrational modes in biopolymers will be crucially dependent on the mode lifetimes.¹⁵ While picosecond CARS measurements have set limits on the low-temperature vibrational lifetimes (picoseconds to 5 nanoseconds) of amino acids and peptides,¹⁶ this technique is insensitive to a set of closely spaced vibrational lines.¹⁷ The FEL provides the opportunity to carry out hole burning experiments with the aim of both establishing improved limits on mode lifetimes and determining the mechanisms for energy relaxation. This serves as a second example of an FEL application in biopolymer physics.

Energy transfer of excited **electronic** states in biopolymers has been the subject of intense research with a number of experimental and theoretical techniques;¹⁸ however, the limitations of conventional infrared lasers has complicated the investigation of **vibrational** energy transfer. The FEL overcomes these limitations of conventional infrared sources and as a third example we will consider the role of anti-Stokes Raman spectroscopy for two-color FEL applications. The FEL will pump a specific vibrational mode of the biopolymers into a non-equilibrium energy distribution and the laser-Raman spectroscopic system will probe the transfer of energy to other modes of the system. Probing with a cw laser will identify pathways for energy transfer; probing with a pulsed picosecond laser will establish rates of energy transfer for a given energy cascade.

Table II: Frequency Range of Vibrational Modes in Biopolymers

Band	Frequency Range		Assignment
	(cm-1)	(microns)	
PROTEINS			
Amide A	3300	3.0	N-H
Amide B	3100	3.3	N-H (Fermi resonance)
Amide I	1650	6.1	C=O, N-H, C-N
Amide II	1560	6.4	C-N, N-H
Amide III	1300	7.7	C-N, N-H
Amide IV	625	16.6	O=C-N
Amide V	725	13.8	N-H
Amide VI	600	16.7	C=O
Amide VII	200	50.0	C-N
NUCLEIC ACIDS			
Base	3300-3600	2.8-3.0	N-H
Sugar	3300-3600	2.8-3.0	O-H
Base	3000-3100	3.2-3.3	C-H
Sugar	2800-3000	3.3-3.6	C-H
Base	1600-1750	5.7-6.2	C-O
Base	1550-1650	6.1-6.5	N-H
Base	1450-1550	6.5-6.9	ring
Base	1300-1460	6.8-7.7	C-H
Sugar	1300-1460	6.8-7.7	C-H
Base	1250-1450	6.9-8.0	ring
Phosphate	1225	8.2	PO2
Phosphate	1080-1100	9.1-9.3	PO2
Sugar	850-1100	9.1-11.8	C-O, C-C
Phosphate	780-820	12.2-12.8	PO2
Sugar	780-820	12.2-12.8	C-O, C-C
Base	650-800	12.5-15.4	ring
Base and Sugar	300-650	15.4-33.3	skeletal
polymer	12-200	50.0-833	long wavelength

4. FUTURE APPLICATIONS OF THE VANDERBILT FEL

Now that we are moving into an FEL era that emphasizes applications research, FEL facilities will need to respond to the somewhat diversified demands of the users community. The staff of the Vanderbilt FEL Center are striving to achieve a highly versatile spectroscopic laboratory for infrared physics with broad applications including physical, chemical, engineering, clinical, and biomedical research. Charles Brau, the Director of the Vanderbilt FEL Center, is pursuing ongoing and planned developments for the FEL which have recently been described in detail;³ for completeness, however, we include a summary of these developments. Vanderbilt has an active developmental program to Compton backscatter FEL laser photons off the FEL's electron beam to achieve tunable X-rays with significant applications for radiology. The Center also plans to develop a tunable far-infrared source, known as a Cerenkov FEL, which will be operated synchronously with the conventional infrared FEL allowing novel two-color FEL applications. For time-resolved spectroscopy and other FEL applications shorter macropulses or even single micropulses may be required. Cavity dumping can produce macropulses of the order of 10 nanosecond duration; single micropulses can be produced when a photoelectric injector or pulse chopper is used in conjunction with cavity dumping. Lasing on the third harmonic of the FEL provides photons with wavelengths to about 1 micron and photons down to the near ultraviolet can be obtained with conventional nonlinear harmonic generation techniques. Three techniques have been identified to produce micropulses with durations less than 2 ps: chirping the electron-beam energy, utilizing the synchrotron instabilities, and implementing nonlinear optical fibers and a dispersive delay line will provide compressed optical pulses throughout the wavelength range provided by the Vanderbilt FEL. The reader should not consider this listing to be all inclusive; novel demands from users will challenge the ingenuity of the of the Vanderbilt FEL community.

5. CONCLUDING REMARKS

We are developing FEL applications to investigate hole burning and energy transfer processes in materials and to apply these experimental techniques and results to characterize similar relaxation processes in biopolymers. It should be emphasized that these materials and biopolymers are not disparate systems linked together by a common need for equipment. Clearly biopolymers have many more internal modes and in nature reside in a more complex "host matrix." However, excited vibrational levels of both biopolymers and materials relax via intermolecular and intramolecular processes for energy transfer: while the detailed mechanisms may be system specific, the systematic investigation of energy transfer is not.

The research program described in this paper is also significant from an instrumental point of view. Both materials and biopolymers exhibit a large number of vibrational modes in the infrared. In the past it has been difficult to achieve coincidence between vibrational eigenfrequencies and the lines of conventional lasers, complicating and to an extent limiting the investigation of hole burning and energy transfer in materials. Current FEL technology overcomes this limitation. We will use the FEL as a tunable pump in the infrared and are interfacing conventional instrumentation, the FTIR and laser-Raman systems, as "probe beams." The FEL will be used to burn infrared-active modes to be probed with FTIR spectroscopy and modes that have mixed infrared and Raman activity to be probed with laser-Raman spectroscopy. Energy transfer will be measured using anti-Stokes Raman spectroscopy. These two-color techniques extend the applications of FEL laser technology in a manner that allows for the utilization of the unique capabilities of the FEL, place the burden of detection on proven

spectroscopic techniques that circumvent the limitations of infrared detectors, and do not place excessive demands on the reliability and stability of the FEL.

6. ACKNOWLEDGMENTS

This work has been supported by the Office of Naval Research under contract NOOO14-87-C-0146 and by the College of Arts and Science, Vanderbilt University.

7. REFERENCES

1. G.S. Edwards and N.H. Tolk, "Vanderbilt University FEL Center for Biomedical and Materials Research," Nucl. Instr. Meth. Phys. Res. A272, 37-39 (1988).
2. C.A. Brau, "Free-Electron Lasers," Science 239, 1115-1121 (1988).
3. N.H. Tolk, et al., "The Vanderbilt Free-Electron Laser Center for Biomedical and Materials Research," SPIE 1552, 7-13 (1991).
4. S. Benson, et al, "A Demonstration of Loss Modulation and Cavity Dumping on a Free-Electron Laser," Nucl. Instr. Meth. Phys. Res. A296, 762-768 (1990).
5. J.H. Moore, C.C. Davis, and M.A. Coplan, Building Scientific Apparatus, section 4.8, Addison-Wesley, Don Mills, Ontario (1983).
6. W.E. Moerner (editor), Persistent Spectral Hole-Burning: Science and Applications, Springer Verlag, New York (1988).
7. D.M. Kammen, et al., "Vibrational Relaxation Dynamics of Matrix-Isolated BH_2D_2^- ," J. Chem. Phys. 87, 4371-4375 (1987).
8. A.J. Sievers and W.E. Moerner, "Persistent Infrared Spectral Hole-Burning," Chapter 6 in reference 6.
9. M. Dubs and H.H. Gunthard, "IR Hole-Burning and Line Shape of Matrix Isolated 1,2-Difluoroethane with Tunable Diode-Lasers," Chem. Phys. Lett. 64, 105-197 (1979); M. Dubs and H. Gunthard, "IR Hole-Burning and Line-Shape of Matrix-Isolated 1,2-Difluoroethane with Tunable Diode-Lasers.2," J. Mol. Struct. 60 311-316 (1980); M. Dubs, L. Ermanni and H.H. Gunthard, "Infrared Hole Burning in Matrix Isolated 1,2-Difluoroethane with a Tunable Diode-Laser," J. Mol. Struct. 91, 458-491 (1982).
10. C.P. Beetz and G. Ascarelli, "Far-infrared Absorption of Nucleotides and Poly(I).Poly(C) RNA," Biopolymers 21, 1569-1586 (1982); Y. Tominaga, et al., "Coupled Dynamics Between DNA Double Helix and Hydrated Water by Low Frequency Raman Spectroscopy," J. Chem. Phys. 83, 5972-5975 (1986); S.M. Lindsay, et al., "Observation of Low-Lying Raman Bands in DNA by Tandem Interferometry," Phys. Rev. Lett. 53, 1853 (1984).
11. E.G. Brame, Jr. and J.G. Grasselli, Infrared and Raman Spectroscopy, Volume 1, Part C, Marcel Dekker, New York (1977).
12. E. Taillandier, et al, "Infrared and Raman Studies Show That Poly(dA).Poly(dT) and d(AAAAATTTTT)2 Exhibit a Heteronomous Conformation in Films at 75 Percent Relative Humidity and a B-type Conformation at High Humidities and in Solution," Biochemistry 26, 3361-3368 (1987).
13. W. Saenger, Principles of Nucleic Acid Structure, Springer-Verlag, New York (1984).
14. R. Loudon, The Quantum Theory of Light, 2nd Edition, Oxford Science Publications, Oxford (1985).
15. G. Edwards, G. Ying, and J. Tribble, "Role of Counterions in the Gigahertz Relaxation of DNA," submitted to Phys. Rev. A.
16. T.J. Koscic, et al., "Picosecond Coherent Raman Investigation of the Relaxation of Low Frequency Vibrational-Modes in Amino Acids and Peptides," J. Chem. Phys 81(11), 4932-4949 (1984).
17. D. Dlott, personal communication.
18. A.D. Abbate and C.B. Moore, "Intramolecular Vibrational Relaxation of a Polyatomic in the Solid State," J. Chem. Phys. 82, 1263-1270 (1985).

**Role of Immersion Refractometry for
Investigating Laser Induced Effects in Cells**

Jerri Tribble, M.S., John Kozub, B.S., Al Ali, M.D.,
Robert Ossoff, M.D., and Glenn Edwards, Ph.D.

Department of Otolaryngology (JT,AA,RO) and
Department of Physics and Astronomy (JT,JK,GE)
Vanderbilt University
Nashville, Tennessee

ACKNOWLEDGMENTS

E. coli Cla was a gift from J.M. Davidson, Vanderbilt University. This research has been supported by the University Research Council and Natural Science Committee at Vanderbilt University and by the Office of Naval Research through Contract Number ONR N00014-87-C-0146.

KEYWORDS

Bacteriostasis, phototherapy, porphyrin complexes, Soret Band, tunable-dye laser

ABSTRACT

The broad background of scattered light observed in spectra of cell suspensions is reduced by factors of up to twenty by immersion refractometry allowing for improved spectroscopic determination of the absorption properties of cells in the 325 to 820 nm range. Refractive-index matched spectra of E.coli C1a exhibit a set of resonant features near 422, 561, and 582 nm. Exposure wavelengths are chosen based on this spectrum and cell viability is investigated in E.coli suspensions exposed to 350, 400, 422, 440, and 700 nm radiation delivered in nanosecond pulses with total doses from 500 millijoules to 60 Joules. We observe a loss in cell viability for doses greater than 1 Joule at 422 nm and for all doses at other wavelengths; exposures of less than 1 Joule at 422 nm enhance growth. Excluding exposures at wavelengths within the resonant feature, longer wavelengths are less effective at reducing the viability of E.coli C1a. This indicates the occurrence of at least two absorption processes.

INTRODUCTION

Recent advances in laser technology have resulted in broadly tunable radiation sources in the ultraviolet, visible, and infrared wavelength ranges with pulsed or continuous wave operation (1,2). These sources provide a wide range of wavelengths and pulse lengths for investigating laser induced effects in biological systems. The choice of wavelength is often strongly influenced by the absorption characteristics of cells, tissues, or their components, which in principle can be measured

with standard spectroscopic techniques (3). In many cases, however, the spectroscopic measurements are dominated by scattered light, obscuring the absorption spectra.

In general terms, the mechanisms for the absorption of light can be described as photochemical or photothermal in nature and, in some cases, result in significant biological effects (4,5). In the past, most biomedical applications of lasers have been attributed to photothermal mechanisms (6,7). The biomedical applications of broadly tunable and pulsed lasers are currently under investigation with the aim of developing more selective effects based on photothermal or possibly photochemical mechanisms. A systematic investigation of the effects of laser light on a given biological system will be based on knowledge of the absorption characteristics throughout the accessible wavelength range. It must be recognized, however, that while spectroscopic analysis identifies mechanisms for depositing energy into a biological system, it is not necessarily the case that these mechanisms will result in biomedical effects.

Relative to x rays, which generally induce major damage in molecular structure, UV wavelengths can be quite selective in their interactions with biological molecules. It has become common practice to view the 300 nm wavelength as the demarcation between far-UV (<300 nm) and near-UV (300-380 nm) radiation (4). The far-UV is characterized by a strong absorption by nucleic acids centered near 260 nm and a weaker, but still significant, absorption by proteins centered near 280 nm. Investigations of

the viability of E.coli irradiated with near-UV to visible (<550 nm) radiation suggest additional absorption bands in this wavelength range (8).

In this study we develop a protocol for investigating the effect of laser light on the viability of cells. To reduce light scattering in absorption measurements we implement the technique of immersion refractometry which is based on matching the refractive index of the suspending solution to that of the cell membrane (9). Guided by the absorption spectra we select a set of wavelengths for laser irradiation. Cells suspended in Luria broth are exposed to increasing doses of nanosecond pulses of near ultraviolet and visible laser light. The subsequent viability of the cells is monitored by two techniques, plate counting and absorption measurements of cell cultures. We have chosen E.coli as the initial system for investigation.

MATERIALS AND METHODS

Spectroscopy

Measurements of the optical properties of cell suspensions are typically obscured by a dominant background of scattered light. Biological applications of immersion refractometry reduce light scattering by suspending the cells in a protein solution that matches the refractive index of the cell membrane (9). By varying the protein content of the suspending solution, one can minimize the scatter and thus optimize the determination of the absorption spectra. Bovine serum albumin (BSA) was purchased

from Sigma Chemical Company and initially prepared as a stock solution of 45% weight/volume in distilled water. The solution was manually stirred and then clarified by centrifuging at 1000g for 30 minutes and had a refractive index of greater than 1.42. Refractive indices were measured with a Bausch & Lomb Abbe-3L refractometer.

E.coli Cla to be used in the immersion refractometry measurements were grown overnight in Luria broth and centrifuged for five minutes at 10,000g. The pellets of wet packed cells (wpc) were resuspended to a concentration of 100 mg-wpc/ml. The cell suspension was diluted 1:9 with BSA solution yielding a concentration of 10^8 cells/ml. Absorbance was measured with a Milton Roy Spectronic 601 spectrophotometer.

Spectra of optimally index-matched cells were taken with a Hewlett Packard 8452 multidiode array spectrometer with 2 nm resolution. Some of the spectra reveal artifactual lines due to the deuterium source (10); these lines lie near, with decreasing intensity, 656, 486, and 580 nm. The residual background of scattered light was modeled with the function:

$$A = \frac{C}{\lambda^p}$$

where A is the absorbance, λ is the wavelength of light, and C and p are parameters to be fit with a linear least squares algorithm. The scattering background was subtracted and the remaining resonant features were modeled with Gaussian lineshapes.

Laser Irradiation

Laser light was produced by a Quantel 571C Nd:YAG pumped TDL50 dye laser system with doubling crystals. Pulses of 6-8 ns duration at 10 Hz repetition rate had an energy per pulse of approximately 3 mJ/pulse as determined with an Ophir 30 AP calorimeter. Bacteria were kept on ice prior to and after exposure, but during exposure were at room temperature in 20 microliter aliquots in a microcentrifuge tube. The laser beam is approximately 5 mm in diameter and the sample was centered in the beam.

Bacteriology

E.coli Cla was grown to the stationary phase in Luria broth at 37 C and put on ice for laser irradiation. After irradiation the viability of the exposed and control cells was assayed by two techniques. In one technique growth was monitored by measuring the absorbance at 600 nm at 20 minute intervals. The log phase of the growth curve was fit with an exponential function in the standard way (11), the ratio of the concentration of the exposed cells relative to the control cells was extrapolated to the time of exposure to yield a relative initial concentration. The absorbance method is susceptible to a laser induced growth delay being misinterpreted as laser induced bacteriostasis, i.e. a significant growth delay will be interpreted as an erroneously large reduction in the number of viable cells.

The other technique determines cell viability by counting colonies on agar plates. Although this technique is less precise

than absorption measurements, it has the attribute of being less sensitive to variations in growth delay.

RESULTS

Absorption spectra for E.coli in the 325 to 820 nm range are presented in Figure 1. Figure 1a refers to E.coli suspended in saline and exhibits a broad shoulder near 350 nm and domination of the spectrum by scattered light. Figure 1b presents the absorption spectrum for E.coli suspended in the BSA solution that optimally matches the refractive index, as shown in figure 2. Note that in comparing figures 1a and 1b, the index matching reduces the light scattering background by a factor of 20 at 350 nm.

The results of the curve fitting are presented in figure 3. The residual light scattering as shown in figure 1b is modeled in figure 3a and a resonant feature centered near 422 nm is evident. The p value for fitting the spectrum shown in figure 1a is 2.11, in agreement with earlier work (12). For the index matched solution, the p value reduces to 1.67.

In light of these spectroscopic results, we selected 350, 400, 422, 440, and 700 nm as wavelengths for further investigation. tRNA (13), flavins (14,15), cytochrome (16), and NADH (17) contribute to the broad absorption near 350 nm. In addition, absorption measurements of water (18) indicate a broad, intense band centered at terahertz frequencies that also contributes to the absorption at 350 nm. Absorption measurements of Luria broth

(data not shown) reveal no resonant features in this frequency range. The intensity pattern of the 422, 582 and 561 nm features are reminiscent of the Soret, α , and β bands, respectively, observed in porphyrin complexes (16,19); 422 nm was chosen since it corresponds to the dominant resonant feature. 400 and 440 nm were chosen to demarcate the resonant feature. 700 nm was chosen as a nonresonant wavelength in the red. Figure 4 presents the percentage kill for E.coli exposed to increasing doses of radiation at these wavelengths. Figure 5 presents the percentage kill at a dose of approximately 4 J as a function of wavelength. With the exception of exposures to 350 nm, there were no significant differences between plate counting and absorption measurements for determining cell viability. Exposures to 350 nm indicate a radiation induced growth delay (5). Cells exposed to 422 nm radiation did repeatably indicate a growth enhancement for doses of less than 1 joule. There have been previous reports of stimulatory effects (20).

DISCUSSION

As shown in figures 1 and 2, immersion refractometry successfully reduces light scattering and significantly improves spectroscopic measurements of the absorption properties of E.coli suspensions. We have recently extended these studies to other cell lines with similar success.

With regards to biological effects of laser irradiation of E.coli, the cell viability studies summarized in figures 4 and 5 indicate the occurrence of at least two absorption processes.

More specifically, one process is indicated by the growth enhancement due to low doses of 422 nm radiation. A second process is indicated at larger doses where increasing dose corresponds to increasing lethality and, excluding the 422 nm data, cell viability is less effectively reduced with longer wavelength radiation. This second process is in line with conclusions drawn from previously observed action spectra of *E. coli* where nucleic acids have been assigned as the principle chromophore (4,5,8). At lower doses and for wavelengths near 422 nm, however, the first process is apparent and the net effect on cell viability is opposite to that of the second mechanism. Furthermore, in our studies with the nanosecond pulsed laser, lethality is achieved at significantly lower doses than previously reported (4,5). While this is a promising observation for future biomedical investigations, the results discussed above indicate that competing processes occur for irradiation near 422 nm at relatively low doses. This consideration suggests that caution be used with regards to biomedical investigations using wavelengths near the Soret band of porphyrin complexes.

In conclusion, we have reported a systematic investigation of the wavelength dependence of near ultraviolet and visible radiation, delivered in nanosecond pulses, on the growth of *E. coli* suspensions. Exposure wavelengths were chosen based on improved spectroscopic measurements of the absorption characteristics of cell suspensions where the technique of immersion refractometry has resulted in a significant reduction in the background of scattered light revealing resonant features at 422,

582 and 561 nm. We observe a definite wavelength dependence for the effect of pulsed laser light on the viability of cells that can be reasonably accounted for by spectral assignments and suggests at least two absorption processes. This experimental approach should be of general utility for future investigations of the effects of laser light on cellular systems.

REFERENCES

1. Young M, "Optics and Lasers." (Springer-Verlag, Berlin, 1984).
2. Brau CA, Free-Electron Lasers, Science 1988; 239:1115-1121.
3. Cantor CR, Schimmel PR. "Biophysical Chemistry Part II." (W.H. Freeman and Company, New York, 1980).
4. Jagger J in Wang, SY (ed): "Photochemistry and Photobiology of Nucleic Acids, Volume II: Biology." (Academic Press, New York, 1976) Chapter 4.
5. Jagger J. Near-UV radiation effects on microorganisms. Photochem Photobiol 1981; 34:761-768.
6. Anderson RR, Parrish JA. Selective photothermolysis: precise microsurgery by selective absorption of pulsed radiation. Science 1983; 220:524-527.
7. Hillenkamp F, Pratesi R, Sacchi CA (eds): "Lasers in Biology and Medicine." (Plenum, New York, 1980).
8. Webb RB and Brown SB, Sensitivity of Strains of Escherichia Coli Differing in Repair Capability to Far UV, Near UV and Visible Radiations. Photochem Photobiol 1976; 24:425-432. See Figure 7.
9. Bateman JB, Wagman J, Carstensen EL, Refraction and absorption of light in bacterial suspensions. Kolloid-Zeit 1966; 208:44-58.
10. Moore JH, Davis CC, Coplan MA: "Building Scientific Apparatus." (Addison-Wesley, Don Mills, Ontario 1983) See figure 4.78.

11. Willett HP. Physiology of Bacterial Growth. In Joklik WK, Willett HP, Amos DB (eds): "Zinsser Microbiology." 17th ed. (Appleton-Century-Crofts, New York, 1980) pages 86-90.
12. Koch AL. Some Calculations on the turbidity of mitochondrial and bacterial suspensions. Biochem Biophys Acta 1961; 51:429-441.
13. Favre A, Michelson AM, Yaniv M. Photochemistry of 4-thiouridine in Escherichia coli transfer RNA(val). J Mol Biol 1971; 58:367-379.
14. Iwatsuki N, Joe CO, Werbin H. Evidence that deoxyribonucleic acid photolyase from bakers yeast is a flavoprotein. Biochemistry 1980; 19(6):1172-1176.
15. Metzler DE. "Biochemistry: the Reactions of Living Cells." (Academic Press, 1977, New York) pages 594, 478.
16. ibid, p.568.
17. ibid, p.478.
18. Jackson JD: "Classical Electrodynamics." 2nd ed. (John-Wiley and Sons, New York, 1975). p. 291.
19. Lemberg R, Barrett J: "Cytochromes." (Academic Press, New York, 1973).
20. Tiphlova O, Karu T. Stimulation of Escherichia coli division by low intensity monochromatic visible light. Photochem Photobiol 1988; 48(4):467-471.

FIGURE LEGENDS

Figure 1. Absorption spectra of E.coli Cla: a) suspended in saline solution exhibiting a shoulder near 350 nm and a broad scattering background, b) suspended in the BSA solution that optimally matches the refractive index of the cell membranes. Resonant features near 422, 582, and 561 nm are revealed due to the reduction in scattered light. Instrumental features occur near 488, 580, and 656 nm (see text); however, the observed intensity of the spectral feature at 582 nm cannot be completely accounted for as an instrumental line.

Figure 2. Optimization of refractive index of suspending solution. Absorption of cell suspensions measured at 589 nm as a function of refractive index of suspending solution. Refractive index varies with BSA concentration. Minimum absorption corresponds to optimally matching the refractive index of the suspending solution to that of the cell membrane.

Figure 3. Curve fitting of absorption spectra. Spectrum shown in figure 1b is fit with a scattering background and resonant feature: a) determination of power law of scattering background, b) Gaussian fit of resonant feature centered at 422 nm.

Figure 4. Wavelength and dose dependence on percentage kill of E.coli: a) exposures to 350, 400, 422, and 700 nm radiation indicating relative effectiveness at reducing cell viability as determined by absorbance measurements of the growth kinetics (see text), b) exposures at 400, 422, and 440 nm indicating growth enhancement for 500 millijoule dose of 422 nm radiation and reduction in cell viability for larger doses. The error in determining percentage kill is approximately 11%.

Figure 5. Percentage kill at a dose of approximately 4 J as a function of irradiation wavelength. The error in determining percentage kill is approximately 11%.

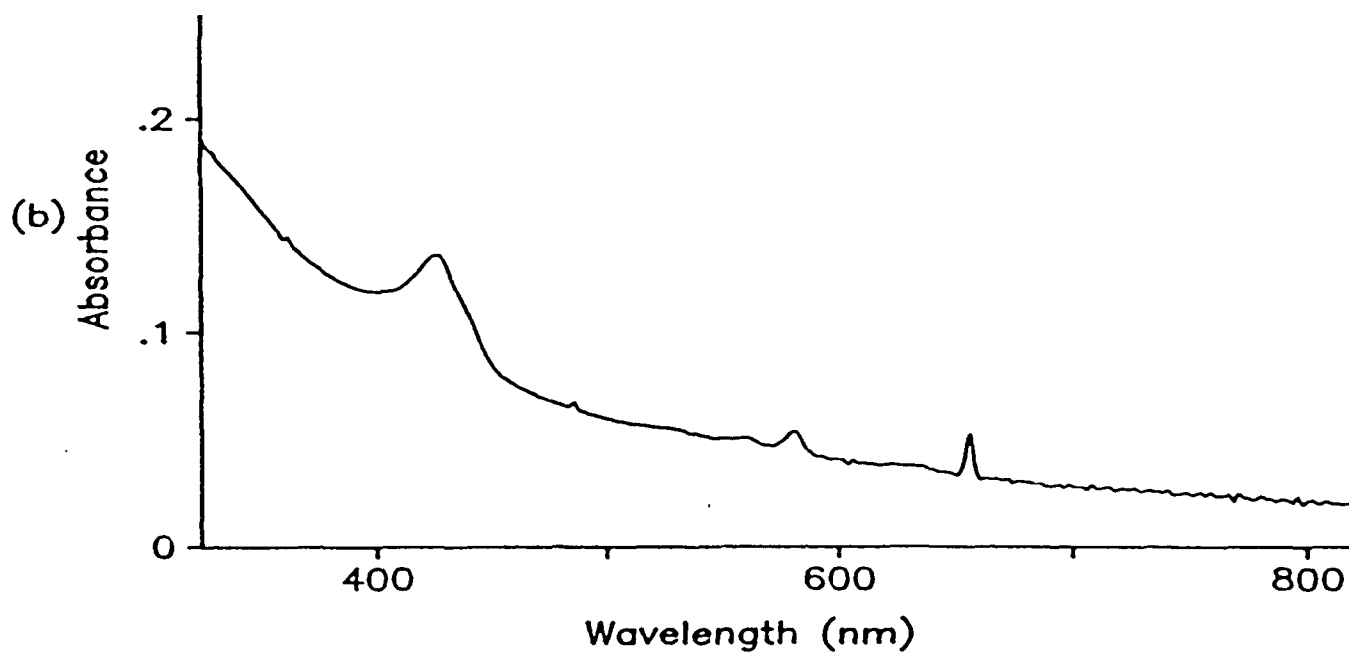
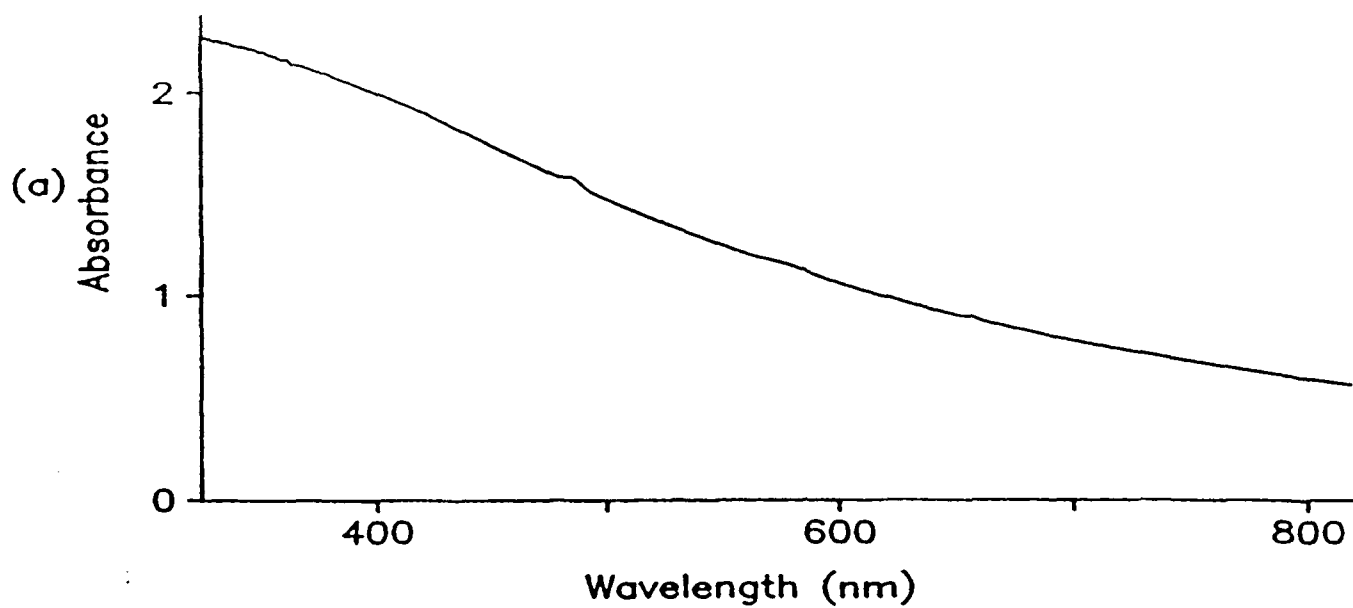


Figure 1

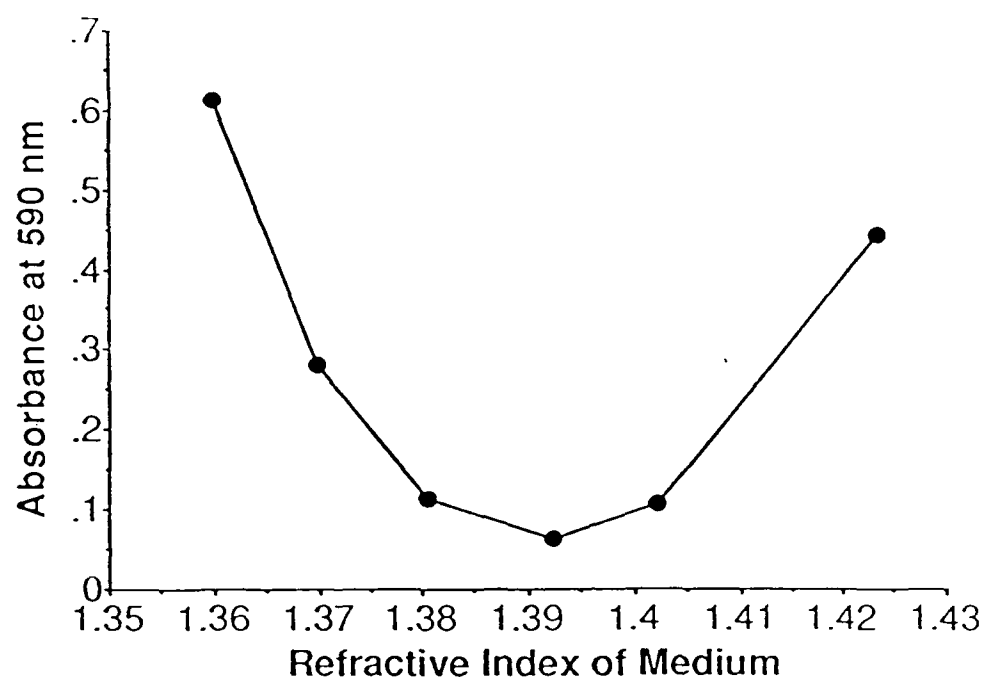


Figure 2

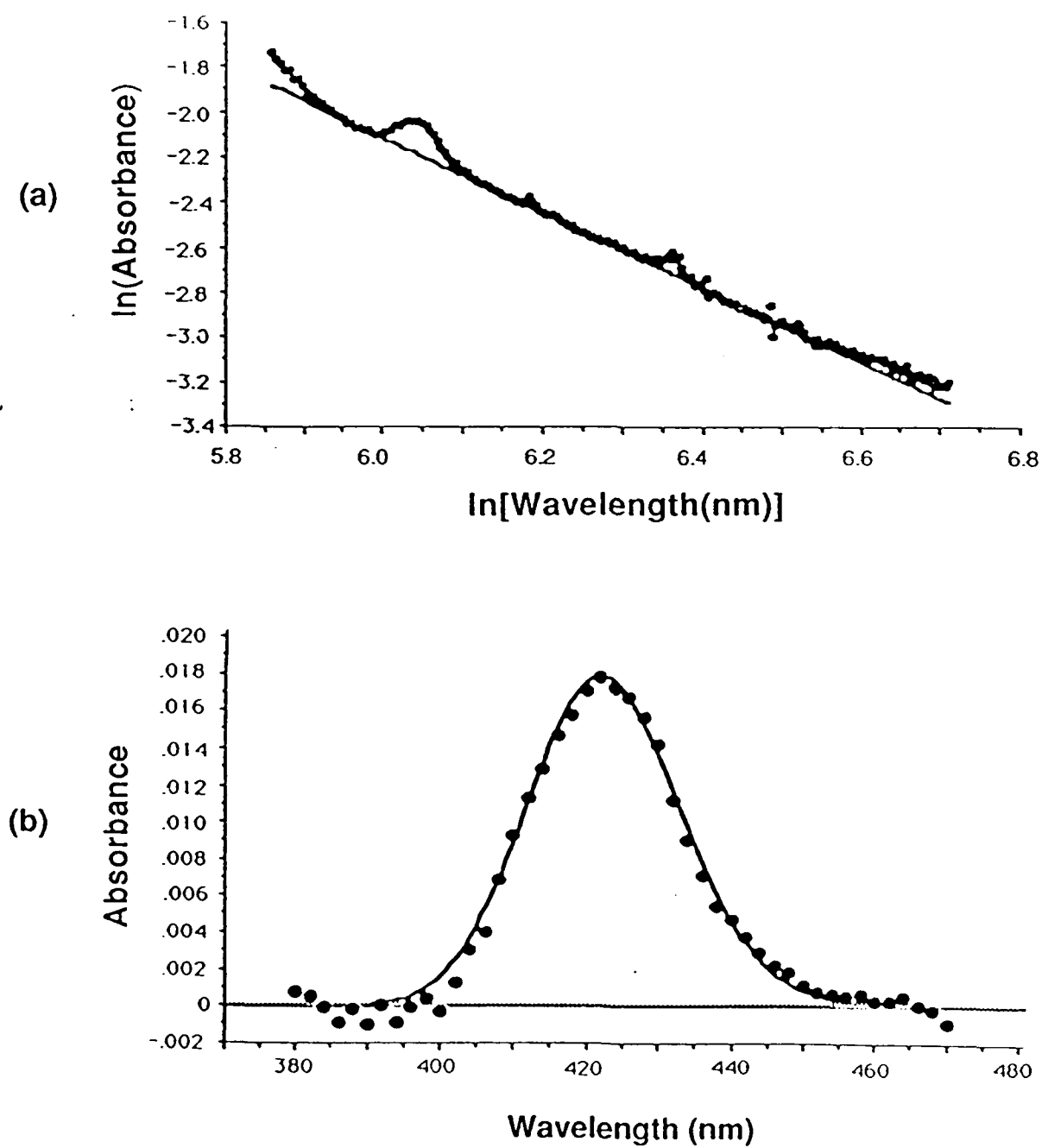


Figure 3

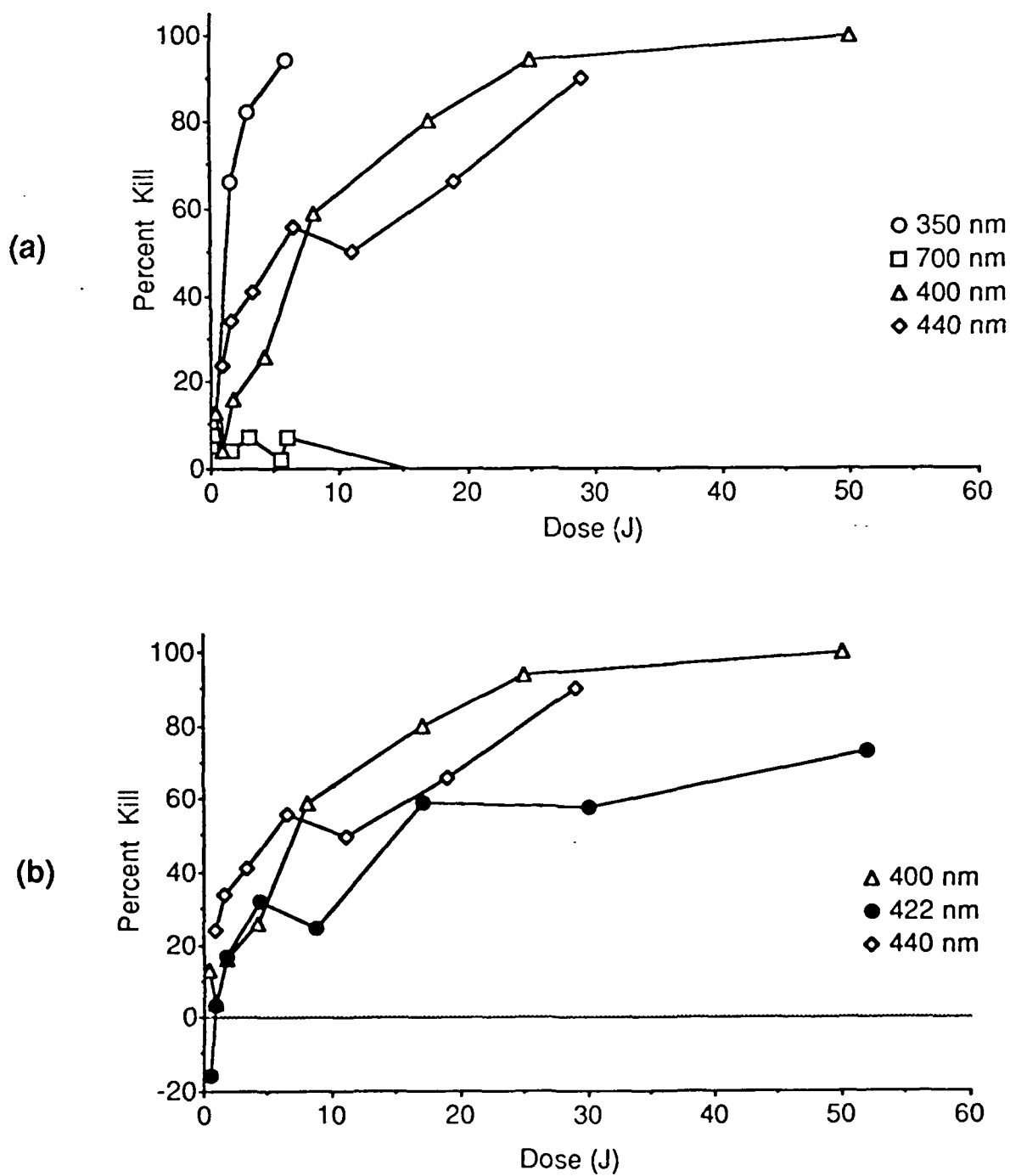


Figure 4

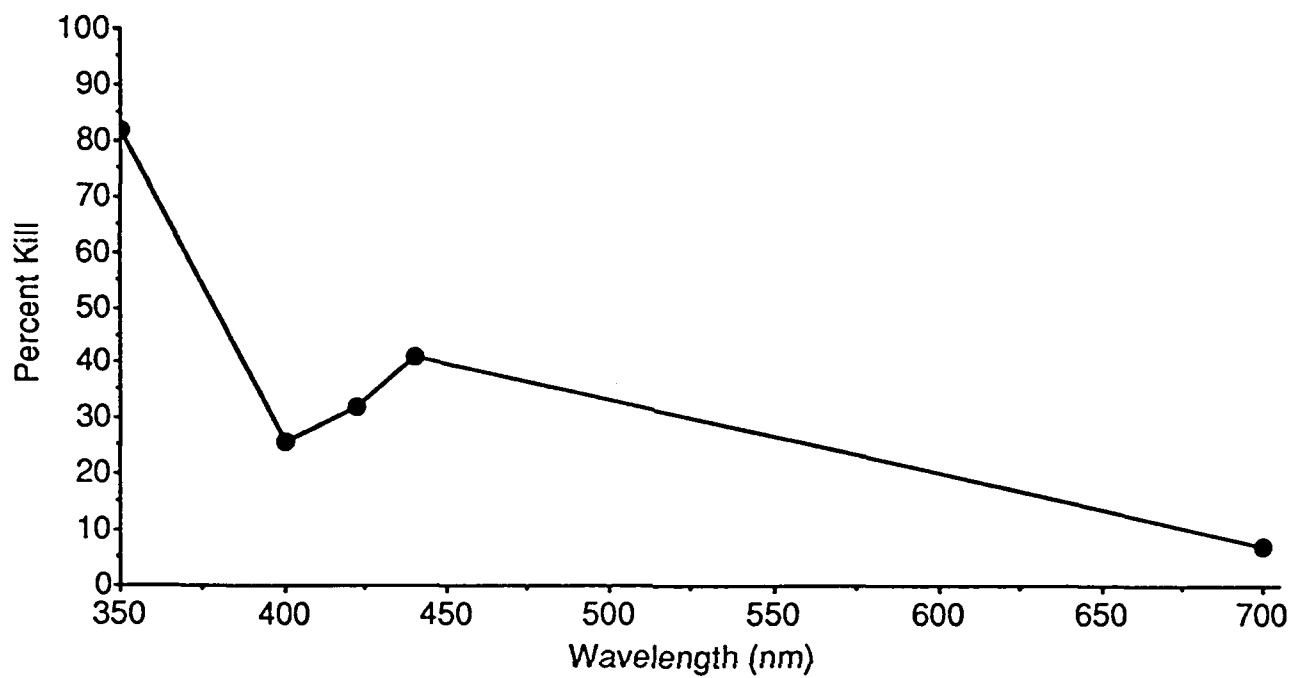


Figure 5

Role of Counterions in the Gigahertz Relaxation of Wet DNA

Glenn Edwards, Guangtao Ying, and Jerri Tribble
Department of Physics and Astronomy
Vanderbilt University
Nashville, Tennessee 37235

ABSTRACT

We have measured the dielectric properties of concentrated solutions and gels (≤ 30 mg/ml) of random-sequenced DNA from E.coli in the 400 MHz to 26 GHz range. Two Debye-type relaxations are evident, one with a relaxation time near 9 ps and attributable to the classical Debye relaxation of water. More noteworthy is a second relaxation process with a characteristic time in the 20 to 200 ps range, i.e. a relaxation frequency in the 0.8 to 8 GHz range, depending upon the species of the counterions and the temperature. The slower relaxation process has an enthalpy of 3.3 kcal/mol and is accounted for by a counter-ion-based relaxation process. These experimental results are considered in terms of two models from polyelectrolyte theory, one by Oosawa and Wyllie and the other by Manning, and we propose that different ion-based relaxation mechanisms dominate in different hydration regimes.

PACS Numbers: 87.15-v, 77.40, 36.20

There is considerable experimental evidence (1-8) indicating the occurrence of far-infrared (~ 200 cm⁻¹) vibrational modes in nucleic acids. These vibrational or phonon modes are characterized by in-phase motion extending over many nucleotides and it is believed that these modes mediate structural transitions and may serve as an avenue for energy transport. Any biological relevance crucially depends on the lifetimes of these modes. Theoretical models (9-12) give a general description of the low-frequency dynamics of nucleic acids; however, a detailed understanding of the damping mechanism(s) governing the solvent-biopolymer interface is lacking. Previous experimental investigations have, however, made progress in this regard. Coupled-mode theory has been implemented to account for Raman and Brillouin investigations of DNA gels as a function of temperature (3) and hydration (4) where the damping mechanism was attributed to a nucleic-acid-water relaxation. The coupled-mode theory produced relaxation times in the gigahertz frequency range, indicating that dielectric techniques may be used to directly probe the relaxation process(es). Here we report on our experimental investigation of the dielectric properties of DNA.

Vector dielectric measurements were carried out with a Hewlett Packard 8510 Network Analyzer where a coaxial line (13) is terminated at the surface of several milliliters of either calibration or sample solutions. Accurate determination of the permittivity of the solutions requires a calibration model (14) to remove the effect of internal reflections inherent to the apparatus. We have found that the optimum calibration procedure

for the open-ended-coaxial-line technique is based on the measurements of an open circuit and two known solutions with well characterized salinity and temperature (15); the dielectric properties of the two calibration solutions should bracket the dielectric properties of the sample. To analyze the permittivity data we have modified a commercial software package (LAB CALC, Galactic Industries) based on the Levenberg-Marquardt method (16,8) to fit the permittivity as a sum of Debye relaxation processes and a conductivity term (17):

$$\epsilon' = \sum_i \frac{\Delta_i}{1 + \omega^2 \tau_i^2} + \epsilon_\infty$$

$$\epsilon'' = \sum_i \frac{\Delta_i \omega \tau_i}{1 + \omega^2 \tau_i^2} + \frac{\sigma}{\epsilon_0 \omega}$$

where ϵ' and ϵ'' are the real and imaginary parts of the permittivity, τ_i and Δ_i are the relaxation time and the dielectric increment of the i^{th} relaxation process, ϵ_∞ is the infinite frequency dielectric constant, σ is the conductivity, ϵ_0 is the permittivity of free space and ω is the angular frequency. To demonstrate the capabilities of both the experimental technique and the data analysis, figure one presents both measurements of a known saline solution and the results of fitting the data with a single Debye relaxation process. The Debye model works remarkably well in this frequency regime.

NaDNA from calf thymus, with a wide distribution of lengths, was purchased from Sigma Chemical Company (lot 109F9540). The salting of the sample solutions was established in a multi-step process. First, the lyophilized NaDNA was dissolved in 100 mM NaCl, LiCl, KCl, CsCl, MgCl₂, or CaCl₂ solutions. Two-and-one-

half volumes of ethanol were added and the DNA was precipitated at -20 Celsius. The resulting pellet was redissolved in the appropriate solution and this process was repeated to complete the salt exchange. The final pellet was dried under vacuum and then placed in a solution ranging from 10 to 100 mM salt and with DNA concentrations ranging from 1 mg/ml to 30 mg/ml, resulting in solutions at the lower concentrations and concentrated gels at the higher concentrations.

Measurements were initially made in the 400 MHz to 26 GHz range. It soon became clear, however, that no new information was provided at the higher and relatively noisier frequencies and thus the experimental frequency range was limited to 400 MHz to 10 GHz, as displayed in figures one and two. Figure two presents measurements and curve fitting results for CaDNA at room temperature: this data is optimally fit with two Debye relaxations. Table one summarizes the results of the CaDNA measurement and of similar measurements of CsDNA, KDNA, LiDNA, MgDNA, and NaDNA, which uniformly require two Debye relaxation processes to fit these data. In general terms, these measurements of concentrated DNA gels exhibit a dominant relaxation process with a relaxation time near 9 ps, characteristic of bulk water (18), and a less prominent relaxation process with a relaxation time in the 20 to 200 ps range depending on the species of counterions and the temperature. This range of relaxation times corresponds to a relaxation frequency range of 0.8 to 8 GHz. Figure three

presents an Arrhenius plot of KDNA yielding an enthalpy of 3.3 kcal/mol.

The most remarkable feature of these data is the occurrence of a counterion-dependent relaxation process with a relaxation time in the 20 to 200 ps range. With regards to this gigahertz relaxation process, the LiDNA and MgDNA data are fit with the shortest relaxation times, CsDNA and KDNA data the longest, and the CaDNA and NaDNA data exhibit intermediate relaxation times (see table one).

We have considered these experimental results in terms of both the theory of dielectrics and polyelectrolyte theory. Frohlich (19) has shown that the Debye equations follow from an exponential decay function and has considered several models for which these equations hold. For an ion-based mechanism the relevant model is essentially a double-well potential where the height of the potential barrier is given by the enthalpy. Dielectric theory, however, does not provide a detailed description of the interaction of the ions with their local environment. There are two models from polyelectrolyte theory that address the local environment and are particularly relevant to these results. In an earlier theory, Oosawa (20) and Wyllie (21) modelled the dielectric dispersion in linear polyelectrolytes by considering the thermal fluctuations of bound counterions. The polyion was modelled as a uniformly charged rod, the counterions were modelled as a dilute solution, and the motion was confined to one dimension. The theory relates the

relaxation time τ to the fluctuation length b , the counterion mobility u , and the temperature T :

$$\tau = b^2 / (\pi^2 u k T)$$

where k is Boltzmann's constant. Oro and Grigera (22) have observed a 1 ns relaxation process corresponding to a fluctuation length of 11 angstroms and attribute this feature to "counterion fluctuations on short sections, probably in a direction transverse to the macromolecular axis." Within the counterion-fluctuation model, the 20-200 ps relaxation times observed here correspond to fluctuation lengths in the 1 to 5 angstrom range. It is somewhat intriguing that such a continuum theory yields a length scale suggestive of a multiwell potential with minima centered on the phosphate groups.

Alternatively, this data may be considered in light of Manning condensation theory (23,24). This theory distinguishes between counterions in direct contact with phosphate groups, termed "site bound" ions, and counterions, termed "territorial bound" ions, which form a Debye screening atmosphere in a delocalized cloud near the polyelectrolyte. Manning cites extensive experimental evidence that DNA in solution is dominated by territorial bound ions and proposes that the counterions condense in a concentrated cloud of counterions forming a thin cylindrical shell about DNA. Manning calculates that the shell has a counterion concentration of 1.2 M and the outer surface of the shell is 17 angstroms from the symmetry axis. Furthermore, DNA is stabilized by the formation of this condensed cloud and the enthalpy change

associated with an ion moving between free solvent and the condensed cloud is calculated to be 3.2 kcal/mol, in favorable agreement with the experimental value of 3.3 kcal/mol. These considerations suggest a relaxation process pictured as a double well potential where one well characterizes free ions and the other condensed ions. This dielectric relaxation is spatially localized about the outer surface of Manning's cylindrical shell.

As pointed out in the introductory paragraph, coupled-mode analyses of Raman and Brillouin measurements (3,4) indicate the occurrence of gigahertz relaxations in DNA films at known relative humidities. The dielectric relaxations have been attributed to a nucleic-acid-water relaxation, where the two observed relaxation times near 40 and 2 picoseconds correlate to the primary and secondary hydration shells, respectively. Can these relaxations be attributed to a nucleic-acid-ion mechanism? Light scattering measurements determine an enthalpy of about 5 kcal/mol which compares favorably with previous measurements of the enthalpy of ATP solutions (25). ATP serves as a model system for nucleic acids and the enthalpy of the ATP solutions has been accounted for in terms of a phosphate-ion interaction as summarized by Phillips (26). Such an ion-based mechanism may serve as an alternative explanation of the relaxation process indicated by the coupled-mode-based model of the light scattering data.

The experimental results and theoretical considerations discussed above suggest the possibility that different relaxation

mechanisms dominate in different hydration regimes. We propose that at high water content a condensed cloud forms and the dielectric relaxation is dominated by ions near the outer surface of the cloud while at lower water content the ions associate more intimately with DNA and the dielectric relaxation is dominated by a phosphate-counterion-based mechanism.

In conclusion, we have observed two Debye-type relaxations in dielectric measurements of concentrated DNA gels in the 400 MHz to 26 GHz range. Of most interest is the low-frequency process with relaxation times in the 20 to 200 ps range, time scales accessible to computational models of DNA-solvent interactions. This process is dependent on counterion species and concentration, indicating that a counterion-dependent relaxation process occurs at gigahertz frequencies. Comparison with other experimental results suggest the occurrence of two relaxation mechanisms, one due to site-bound ions and dominating the low-hydration regime and the other involving territorial-bound ions and dominating the highly hydrated regime. These results highlight the role of counterions in the damping mechanisms governing the DNA-solvent interface.

ACKNOWLEDGMENTS

This research has been supported by the University Research Council and Natural Science Committee at Vanderbilt University and by the Office of Naval Research through Contract No. ONR N00014-87-C-0146.

REFERENCES

1. G. Maret, R. Oldenbourg, G. Winterling, K. Dransfeld, and A. Rupprecht, Colloid and Polymer Science 257, 1017 (1979); H.B. Hakim, S.M.Lindsay, and J. Powell, Biopolymers 23, 1185 (1984).
2. M.L. Swicord and C.C. Davis, Biopolymers 21, 2453 (1982).
3. Y. Tominaga, M. Shida, K.Kubota, H. Urabe, Y. Nishimura, and M. Tsuboi, J. Chem. Phys. 83, 5972 (1986).
4. N.J. Tao, S.M. Lindsay, and A. Rupprecht, Biopolymers 26, 171 (1987); Biopolymers 27, 1655 (1988); and Biopolymers 28, 1019 (1989).
5. J.W. Powell, G.S. Edwards, L. Genzel, F. Kremer, A. Wittlin, W. Kubasek, and W. Peticolas, Phys. Rev. A 35, 3929 (1987).
6. H. Grimm, H. Stiller, C.F. Majkrzak, A. Rupprecht, and U. Dahlborg, Phys. Rev. Lett. 59, 1780 (1987).
7. T. Weidlich, S.M. Lindsay, and A. Rupprecht, Phys. Rev. Lett. 61, 1674 (1988).
8. G. Edwards and C. Liu, Phys. Rev. A 44, 2709 (1991).
9. J.M. Eyster and E.W. Prohovsky, Phys. Rev. Lett 38, 371 (1977).
10. V. K. Saxena and L.L. Van Zandt, Phys. Rev. A (accepted for publication).
11. A. Garcia and D.M. Soumpasis, Proc. Natl. Acad. Sci. USA 86, 3160 (1989).
12. L. Young, V.V. Prabhu, E.W. Prohovsky, and G.S. Edwards, Phys. Rev. A 41, 7020 (1990).

13. T.W. Athey, M.A. Stuchly, and S.S. Stuchly, IEEE Trans. MTT-30, 82 (1982).
14. J.E. Dalley, IEEE Trans. MTT-17, 572 (1969).
15. G. Ying, G. Edwards, and J. Tribble, unpublished results.
16. W. H. Press, B.P. Flannery, S.A. Teukolsky, and W.T. Vetterling, Numerical Recipes: The Art Scientific Computing (Cambridge University, Cambridge, 1989), Sec. 14.4.
17. E.H. Grant, R.J. Sheppard, and G.P. South, Dielectric Behaviour of Biological Molecules in Solution (Clarendon Press, Oxford, 1978), Sec. 2.3.3.
18. ibid, Sec. 5.1.
19. H. Frohlich, Theory of Dielectrics, (Clarendon Press, Oxford, 1958).
20. F. Oosawa, Biopolymers 9, 677 (1970).
21. G. Wyllie, Dielectric and Related Molecular Processes, Vol. 1, M. Davies, Editor, (The Chemical Society, 1972), Chapter 2.
22. J.R. de Xammar Oro and J.R. Grigera, Biopolymers 23, 1457 (1984).
23. G.S. Manning, Q. Rev. Biophy. 11, 179 (1978).
24. G.S. Manning, Acc. Chem. Res. 12, 443 (1979).
25. W. Saenger, Principles of Nucleic Acid Structure (Springer-Verlag, Berlin, 1984), Secs. 8.4 and 7.6.
26. R. Phillips, Chem Rev 66(5), 501 (1966).

TABLE I. Relaxation times for concentrated DNA gels (near 25 mg/ml) at room temperature as determined by the nonlinear least-squares fitting of the permittivity data (see text).

<u>Nucleic Acid</u>	<u>τ_w (ps)</u>	<u>τ (ps)</u>
CaDNA	8.9	117
CsDNA	9.0	151
KDNA	8.9	170
LiDNA	9.2	103
MgDNA	8.9	96
NaDNA	8.6	134

Figure 1. Permittivity measurements of and curvefitting results for 100 mM NaCl at room temperature. The real (ϵ') and imaginary (ϵ'') parts of the permittivity as measured by the vector network analyzer are presented. These data are fit with a single Debye relaxation process and a conductivity term. For ϵ' the data and fitted curves are both plotted and are nearly coincident, exhibiting a minor mismatch at the lowest frequencies. For ϵ'' both the Debye relaxation of water and the conductivity curves are shown, and the sum of the two (plotted) is coincident with the data curve (also plotted).

Figure 2. Measurement of the imaginary part of the permittivity and curvefitting results for 25 g/l CaDNA at room temperature. The conductivity, Debye relaxation of water, and DNA-counterion relaxation are shown, and the sum of the three (plotted) is nearly coincident with the data curve (plotted).

Figure 3. Arrhenius plot of 30 g/l KDNA.

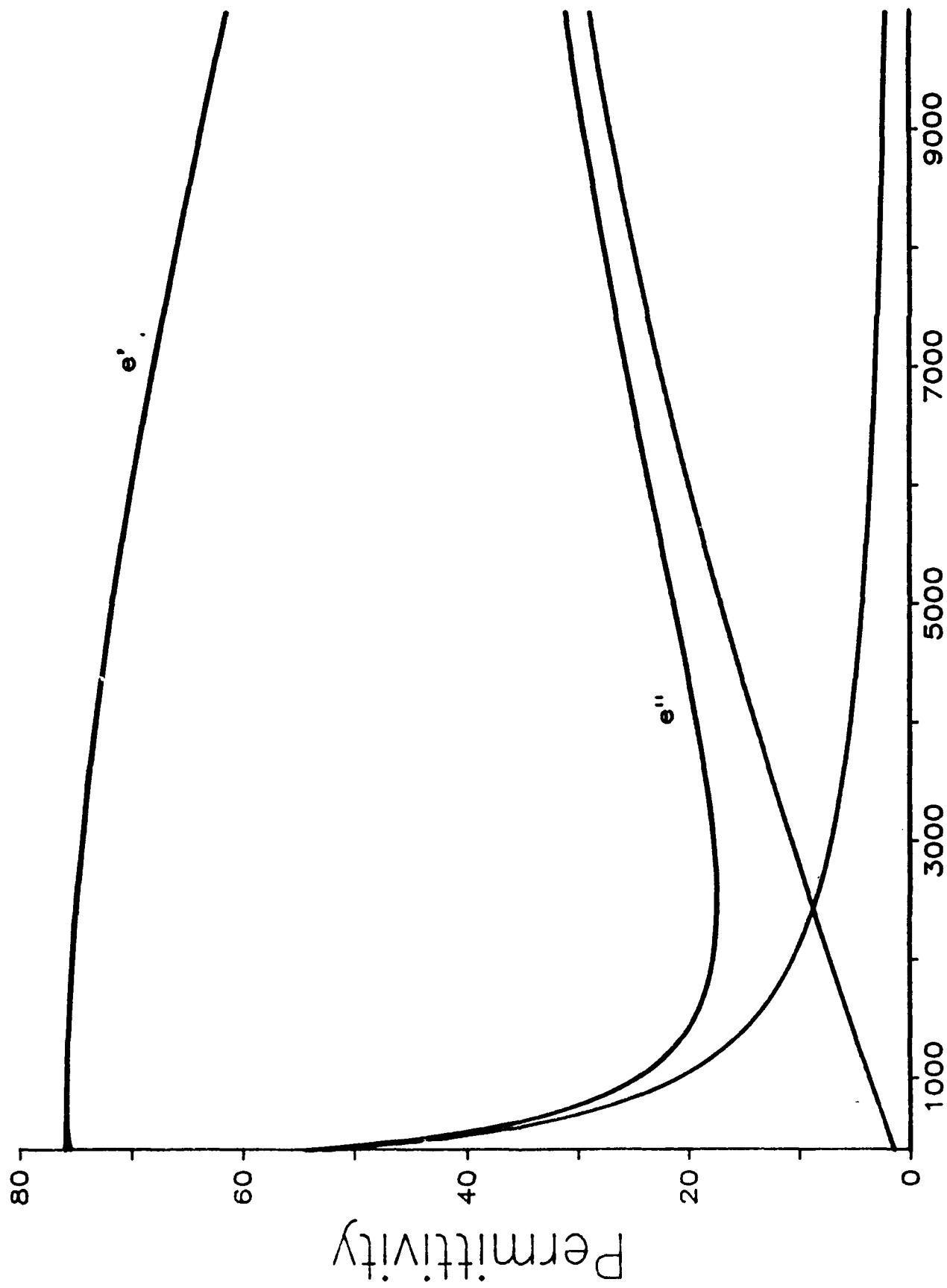


Figure One

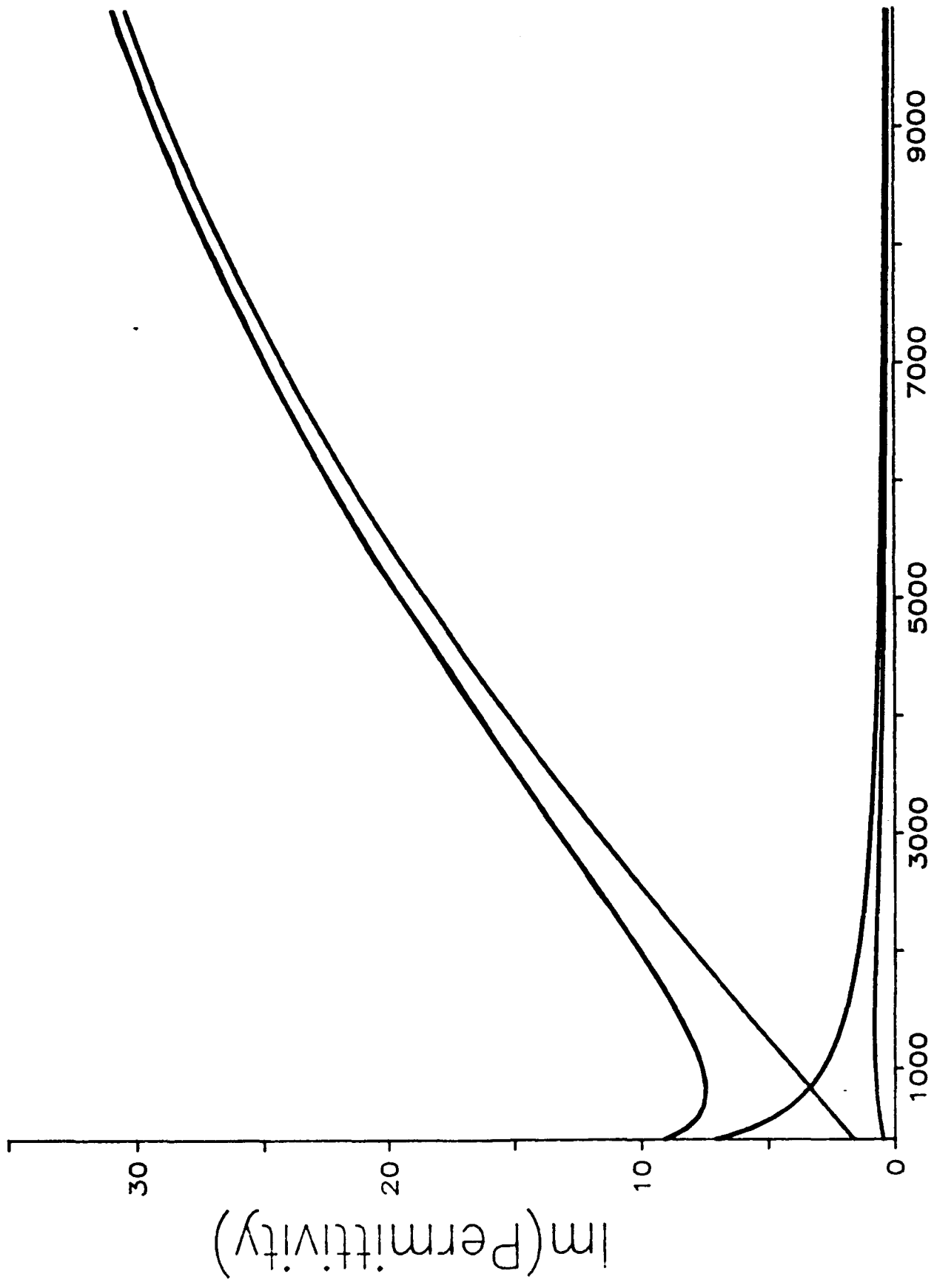


Figure Two

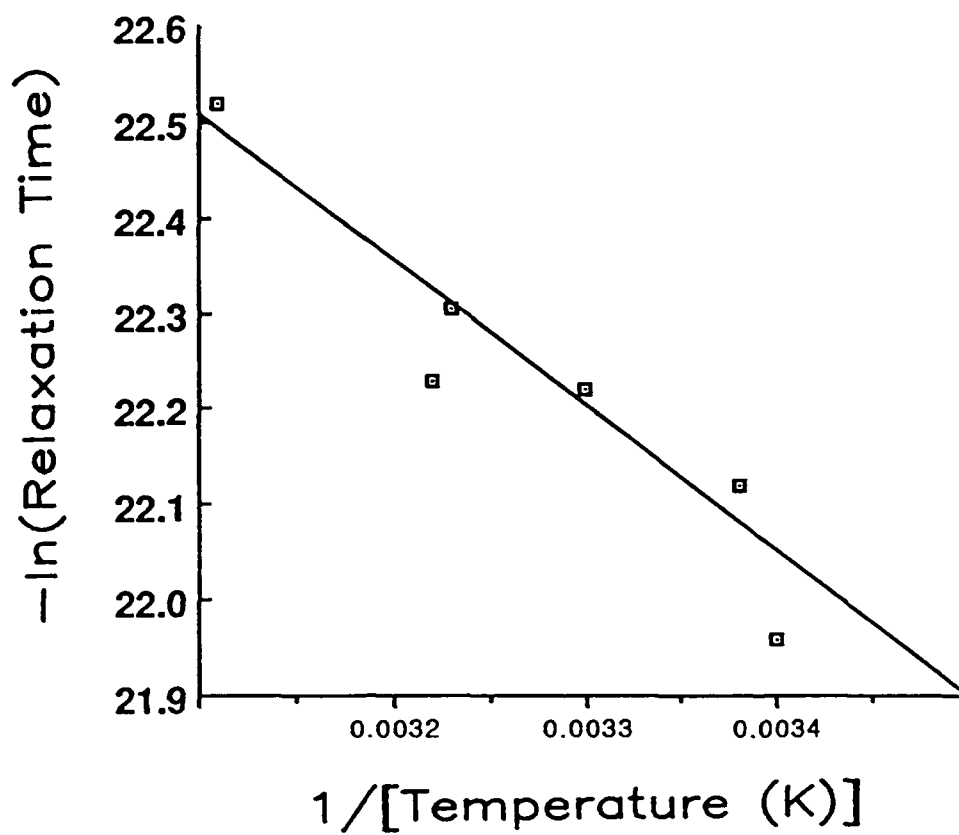


Figure Three

III. G.

Vanderbilt University Free-Electron Laser Project
for Biomedical and Materials Research
Contract No. NO0014-87-C-0146

Far-Infrared Vibrational Modes of DNA

C. Liu and G.S. Edwards
Department of Physics and Astronomy
Vanderbilt University

and

S. Morgan and E. Silberman
Department of Physics
Fisk University

Nashville, Tennessee

Raman and infrared activity of low-frequency (20 to 300 cm^{-1}) vibrational modes of naturally occurring nucleic acids and polynucleotides have been measured (1,2). Distinct bands are clearly resolved in poly(dA).poly(dT) but are only weakly seen in other sequences of both DNA and RNA. These results are discussed in terms of inhomogeneous line broadening of vibrational modes. These experimental results are well described by lattice dynamics (3,4). Temperature dependent experiments (1) indicate that these modes are nonlinear and calculations imply that they may play an important role in the localized "melting" of DNA that is required for transcription and translation.

The Vanderbilt FEL Center has recently installed a Raman laser system with enhanced stray-light rejection and throughput that promises improved resolution of the observed bands and a more thorough investigation of the line broadening process is underway. In addition to the investigation of Raman activity, both line broadening and non-linear processes may be probed directly by intense, far-infrared sources such as the UC-Santa Barbara FEL; preliminary experiments have been performed at this facility.

1. J.W. Powell, G.S. Edwards, L. Genzel, F. Kremer, A. Wittlin, W. Kubasek, and W. Peticolas, Physical Review A 35, 3929 (1987).
2. C. Liu, G.S. Edwards, S. Morgan, and E. Silberman, submitted.
3. Y. Kim and E.W. Prohofsky, Physical Review B 36, 3449 (1987).
4. L. Young, V.V. Prabhu, E.W. Prohofsky, and G.S. Edwards, submitted.

Vanderbilt University Free-Electron Laser Project
for Biomedical and Materials Research
Contract No. N00014-87-C-0146

Pulsed-UV Induced Photochemistry of
RNA-Protein Complexes

J. Kozub and G.S. Edwards
Department of Physics and Astronomy

and

S. Northington and W. LeStourgeon
Department of Molecular Biology

Vanderbilt University
Nashville, Tennessee

It has recently been shown by Von Hippel and coworkers that nanosecond pulses of UV radiation can crosslink nucleic acids to proteins in a selective and wavelength dependent manner. In addition, it is well known that uv radiation can cause pyrimidine dimers. We have used a nanosecond Nd:YAG pumped dye-laser system with doubling and mixing crystals to generate 8 ns pulses of 263 nm radiation to investigate dimer formation in RNA and RNA-protein crosslinking in hnRNP, the RNA-protein complex that may play a role in post-transcriptional processing. We conclude that i) the energy required for uv damage to RNA is the same energy required to crosslink the C proteins of hnRNP. The events can be detected at 7 millijoules of UV irradiation. ii) C proteins specifically crosslink to RNA through uridine; and iii) UV light-induced site-specific termination of reverse transcription is due to uridine damage especially at sites with the potential to form pyrimidine dimers, i.e. UU > UC > C.

These studies imply that the mechanism of UV-induced protein-nucleic acid crosslinking is largely dependent on the photochemistry of specific nucleotides and on the nature of the protein-RNA interaction. Currently we are studying the effect of wavelength on the selectivity of induced crosslink and have evidence that suggests at least two crosslinking mechanisms are available. We plan to extend these results to investigate the possibility that different mechanisms will be optimized for picosecond pulses as available from the FEL being installed at Vanderbilt University.

Vanderbilt University Free Electron Laser Project for Biomedical and Material Research. Contract NOO14-87-C-0146. October 1987 to December 1990.

Nonthermal and selective effects of Free Electron Laser irradiation of tissue. Robert Ossoff, M.D., David L. Zealear, Ph.D., Debra Gonzalez, M.D. and Jerri Tribble, M.S. Department of Otolaryngology, Vanderbilt University Med Center, Nashville, TN.

Our ongoing and planned research efforts encompass several diverse projects. These come together under a common theme: an investigation of the laser's potential to affect biological tissue in selective and nonthermal ways.

Investigations into the area of laser tissue interactions have focused primarily on the problem of wound healing. We have used, and continue to use, a tri-level approach which involves experimentation on the whole animal (macroscopic), cellular (microscopic), and molecular levels. We have been active in defining the effect of laser wavelength, power and pulse structure on various aspects of the wound healing process. With this approach, we hope to refine the laser as an ablative and biostimulating instrument.

Our approach to the study of selective laser effects has begun with an investigation of the spectral properties of whole cells, subcellular organelles and macromolecules, and the extracellular matrix. Spectrophotometric analysis has allowed us to identify particular tissue chromophores with characteristic absorption peak profiles. The transfer of laser energy can be largely restricted to a particular chromophore, if the laser is tuned to match a distinguishing peak within the chromophore's spectral fingerprint. For example, in a study of laser bacteriostasis, enhanced kill of *E. coli* was demonstrated if the laser (Nanosecond Nd-YAG pumped tunable dye) was tuned to one of the two distinguishing absorption peaks for *E. coli*. The broad and continuously tunable features of the FEL will provide greater flexibility in targetting specific chromophores, in particular those possessing absorption peaks outside the range of conventional lasers.

Our interest in laser tissue ablation extends to deriving methods for the clean dissection and removal of diseased tissue while eliminating lateral thermal damage to healthy tissues. In theory, this may be achieved by using laser energy of the appropriate wavelength with minimal pulse duration for the diffusion of thermal energy. The effect of various irradiation paradigms on the degree of tissue ablation and wound healing over time is being investigated using conventional as well as short pulsed lasers (eg., excimer and tunable dye lasers capable of delivering nano or picosecond pulses). In a study of pulsed versus continuous carbon dioxide laser irradiation of tissue, crater profiles (e.g. depth, width) varied in a manner consistent with less nonspecific thermal damage resulting from pulsed irradiation. Laser paradigms found to minimize thermal tissue damage with these conventional lasers will guide our search for purely nonthermal tissue interactions with the FEL, clearly the best technology available for achieving this type of interaction.

Within the last ten years there have been numerous reports of the biostimulating effects of laser irradiation. Biostimulating effects are defined as nondestructive interactions which alter the structure and function of cells or extracellular matrix. Our own work has focused on the effect of sublethal laser irradiation on aspects of the wound healing process. These include: collagen synthesis, elastin synthesis, overall protein synthesis, fibroblast proliferation and wound tensile strength. Studies have been conducted at all three levels of investigation in our laboratory. At the macroscopic level, rat wounds withstood greater breaking tensions when exposed to sublethal laser irradiation. One possible explanation was increased collagen deposition in wounds as a result of laser biostimulation of protein synthesis by fibroblast cells. This biostimulating effect on fibroblasts has been demonstrated in our laboratory at the microscopic level (i.e. tissue culture) as revealed by polyacrylamide gel electrophoretic patterns. Preliminary studies at the molecular level in our laboratory have suggested that laser induced cross linking of ribosomal RNA may be the mechanism underlying the biostimulating effect. Using sublethal FEL doses at the appropriate wavelength we hope to develop the technology to change the behavior of cells in ways that would be clinically relevant and beneficial.

13 May 1988

MECHANISMS OF LASER-TISSUE INTERACTION AND CLINICAL APPLICATIONS

Glenn Edwards, Robert Ossoff, Al Ali, John Kozub, and Changle Liu
Progress Report, May 1988

As stated in the original proposal "the theme of this project is the targeting of electromagnetic energy into diseased tissue, with an emphasis on selective laser-tissue interactions matched to cellular characteristics that are unique to the diseased tissue. In order to establish selective methods of interaction, the first goal of the project is to characterize the frequency specific mechanisms of absorption by DNA, proteins, and lipids as a function of intensity and pulse duration. The second goal is to determine the lifetimes of the various excited states; this information will suggest parameters for ultrafast pulses that will maximize the nonthermal relative to the thermal effect. The third goal of this project is to refine these pulse parameters to optimize selective tissue interaction and thus produce the desired clinical effect."

During the past year we have undertaken a number of steps to initiate this research effort: the steps include assembling qualified personnel, developing a number of spectroscopic systems for pre-FEL and dual-beam FEL experiments, initiating pre-FEL experiments at Vanderbilt, and performing experiments at existing FEL centers. Progress for each of these steps will be addressed below.

1

Personnel. This research effort calls for interdisciplinary expertise and cooperation. Towards this end we have added a number of collaborators to the original investigators. Two graduate students in the Department of Physics and Astronomy are supported as research assistants by the contract and are working with Professor Edwards on problems that will evolve into their dissertation topics. Both of these students came to Vanderbilt to work in this research area. John Kozub has just finished his first year and is investigating the manner in which electromagnetic radiation interrupts the natural interaction of biopolymer systems. It is worthwhile to point out that John has been quite successful during his first year and has recently been nominated by the Graduate Program Committee to receive Vanderbilt's Lagemann Award presented to "the most promising entering or first-year graduate student in the Department of Physics and Astronomy." The other student is Changle Liu, an advanced graduate student, who left Purdue University to take advantage of Vanderbilt's graduate program in experimental biophysics. Changle joined the department only four months ago and is investigating the effect of pulsed radiation on biopolymer systems. In addition to these physics graduate students, Al Ali is a medical doctor working for Dr. Ossoff and in close collaboration with the physicists in developing protocols for laser-tissue interaction.

Equipment. During the past year we have exerted a significant effort to develop two different spectroscopic systems. One of these systems is the Hewlett Packard 8510

Network Analyzer. We have modified this spectrometer to allow an alternative calibration scheme that greatly enhances reproducibility and yields high precision measurements of biological solutions and tissue. This project required significant software/hardware development. For the past three months we have been measuring biopolymer solutions and cellular suspensions with good preliminary results. The second radiation source is a Quantel Nd:YAG pumped dye laser system that is to be used as a nanosecond or picosecond laser for both pre-FEL and dual-beam FEL experiments. Currently this laser is being integrated into a complete spectroscopic system for biophysical research. The laser arrived only a month ago and is currently operating at specification and is being modified for lasing in an extended wavelength regime.

In order to produce and characterize biopolymer samples we have developed a nearly complete laboratory of molecular biology in the first floor of the Department of Physics and Astronomy. Since early this spring we have been producing large quantities of purified DNA samples for spectroscopic investigation.

Pre-FEL Experiments. As mentioned above we have performed a number of preliminary experiments investigating the fundamental mechanisms of laser-tissue interaction. We have measured the infrared absorption properties of DNA which is an essential step in the series of experiments that will determine the lifetime of the various excitations. In addition, we have measured the ultraviolet scattering and absorption properties of cell suspensions with intriguing results in laser induced cell death.

During the summer we will extend these measurements beyond the preliminary stages.

During the summer we will begin a series of experiments investigating the effect of pulsed radiation of DNA protein interactions. We will monitor the effect of radiation induced changes on the cell and related clinical applications.

FEL Experiments. During the past year we have been planning a series of experiments for the far-infrared FEL at the University of California, Santa Barbara. The pulsed nature of the UCSB FEL, as enhanced by switching techniques, will be used to measure the homogenous and inhomogeneous nature of the broadening of DNA features in the infrared. This will allow us to determine the lifetime of these modes. Although a minimum lifetime has been determined by cw experiments, a more accurate estimate of the lifetime is necessary in order to design an exposure protocol that will optimize the resonant effect.

Publication

Vanderbilt University FEL Center for Biomedical and Materials Research, G.S. Edwards and N.H. Tolk, Ninth International FEL Conference, Williamsburg 1987. Proceedings to appear in Nuclear Instruments and Methods in Physics Research.

**Role of Immersion Refractometry for
Investigating Laser Induced Effects in Cells**

Jerri Tribble, M.S., John Kozub, B.S., Al Ali, M.D.,
Robert Ossoff, M.D., and Glenn Edwards, Ph.D.

Department of Otolaryngology (JT,AA,RO) and
Department of Physics and Astronomy (JT,JK,GE)
Vanderbilt University
Nashville, Tennessee

ACKNOWLEDGMENTS

E. coli Cla was a gift from J.M. Davidson, Vanderbilt University. This research has been supported by the University Research Council and Natural Science Committee at Vanderbilt University and by the Office of Naval Research through Contract Number ONR N00014-87-C-0146.

KEYWORDS

Bacteriostasis, phototherapy, porphyrin complexes, Soret Band, tunable-dye laser

ABSTRACT

The broad background of scattered light observed in spectra of cell suspensions is reduced by factors of up to twenty by immersion refractometry allowing for improved spectroscopic determination of the absorption properties of cells in the 325 to 820 nm range. Refractive-index matched spectra of E.coli Cla exhibit a set of resonant features near 422, 561, and 582 nm. Exposure wavelengths are chosen based on this spectrum and cell viability is investigated in E.coli suspensions exposed to 350, 400, 422, 440, and 700 nm radiation delivered in nanosecond pulses with total doses from 500 millijoules to 60 Joules. We observe a loss in cell viability for doses greater than 1 Joule at 422 nm and for all doses at other wavelengths; exposures of less than 1 Joule at 422 nm enhance growth. Excluding exposures at wavelengths within the resonant feature, longer wavelengths are less effective at reducing the viability of E.coli Cla. This indicates the occurrence of at least two absorption processes.

INTRODUCTION

Recent advances in laser technology have resulted in broadly tunable radiation sources in the ultraviolet, visible, and infrared wavelength ranges with pulsed or continuous wave operation (1,2). These sources provide a wide range of wavelengths and pulse lengths for investigating laser induced effects in biological systems. The choice of wavelength is often strongly influenced by the absorption characteristic of cells, tissues, or their components, which in principle can be measured

with standard spectroscopic techniques (3). In many cases, however, the spectroscopic measurements are dominated by scattered light, obscuring the absorption spectra.

In general terms, the mechanisms for the absorption of light can be described as photochemical or photothermal in nature and, in some cases, result in significant biological effects (4,5). In the past, most biomedical applications of lasers have been attributed to photothermal mechanisms (6,7). The biomedical applications of broadly tunable and pulsed lasers are currently under investigation with the aim of developing more selective effects based on photothermal or possibly photochemical mechanisms. A systematic investigation of the effects of laser light on a given biological system will be based on knowledge of the absorption characteristics throughout the accessible wavelength range. It must be recognized, however, that while spectroscopic analysis identifies mechanisms for depositing energy into a biological system, it is not necessarily the case that these mechanisms will result in biomedical effects.

Relative to x rays, which generally induce major damage in molecular structure, UV wavelengths can be quite selective in their interactions with biological molecules. It has become common practice to view the 300 nm wavelength as the demarcation between far-UV (<300 nm) and near-UV (300-380 nm) radiation (4). The far-UV is characterized by a strong absorption by nucleic acids centered near 260 nm and a weaker, but still significant, absorption by proteins centered near 280 nm. Investigations of

the viability of E.coli irradiated with near-UV to visible (<550 nm) radiation suggest additional absorption bands in this wavelength range (8).

In this study we develop a protocol for investigating the effect of laser light on the viability of cells. To reduce light scattering in absorption measurements we implement the technique of immersion refractometry which is based on matching the refractive index of the suspending solution to that of the cell membrane (9). Guided by the absorption spectra we select a set of wavelengths for laser irradiation. Cells suspended in Luria broth are exposed to increasing doses of nanosecond pulses of near ultraviolet and visible laser light. The subsequent viability of the cells is monitored by two techniques, plate counting and absorption measurements of cell cultures. We have chosen E.coli as the initial system for investigation.

MATERIALS AND METHODS

Spectroscopy

Measurements of the optical properties of cell suspensions are typically obscured by a dominant background of scattered light. Biological applications of immersion refractometry reduce light scattering by suspending the cells in a protein solution that matches the refractive index of the cell membrane (9). By varying the protein content of the suspending solution, one can minimize the scatter and thus optimize the determination of the absorption spectra. Bovine serum albumin (BSA) was purchased

from Sigma Chemical Company and initially prepared as a stock solution of 45% weight/volume in distilled water. The solution was manually stirred and then clarified by centrifuging at 1000g for 30 minutes and had a refractive index of greater than 1.42. Refractive indices were measured with a Bausch & Lomb Abbe-3L refractometer.

E.coli Cla to be used in the immersion refractometry measurements were grown overnight in Luria broth and centrifuged for five minutes at 10,000g. The pellets of wet packed cells (wpc) were resuspended to a concentration of 100 mg-wpc/ml. The cell suspension was diluted 1:9 with BSA solution yielding a concentration of 10^8 cells/ml. Absorbance was measured with a Milton Roy Spectronic 601 spectrophotometer.

Spectra of optimally index-matched cells were taken with a Hewlett Packard 8452 multidiode array spectrometer with 2 nm resolution. Some of the spectra reveal artifactual lines due to the deuterium source (10); these lines lie near, with decreasing intensity, 656, 486, and 580 nm. The residual background of scattered light was modeled with the function:

$$A = \frac{C}{\lambda^p}$$

where A is the absorbance, λ is the wavelength of light, and C and p are parameters to be fit with a linear least squares algorithm. The scattering background was subtracted and the remaining resonant features were modeled with Gaussian lineshapes.

Laser Irradiation

Laser light was produced by a Quantel 571C Nd:YAG pumped TDL50 dye laser system with doubling crystals. Pulses of 6-8 ns duration at 10 Hz repetition rate had an energy per pulse of approximately 3 mJ/pulse as determined with an Ophir 30 AP calorimeter. Bacteria were kept on ice prior to and after exposure, but during exposure were at room temperature in 20 microliter aliquots in a microcentrifuge tube. The laser beam is approximately 5 mm in diameter and the sample was centered in the beam.

Bacteriology

E.coli Cla was grown to the stationary phase in Luria broth at 37 C and put on ice for laser irradiation. After irradiation the viability of the exposed and control cells was assayed by two techniques. In one technique growth was monitored by measuring the absorbance at 600 nm at 20 minute intervals. The log phase of the growth curve was fit with an exponential function in the standard way (11), the ratio of the concentration of the exposed cells relative to the control cells was extrapolated to the time of exposure to yield a relative initial concentration. The absorbance method is susceptible to a laser induced growth delay being misinterpreted as laser induced bacteriostasis, i.e. a significant growth delay will be interpreted as an erroneously large reduction in the number of viable cells.

The other technique determines cell viability by counting colonies on agar plates. Although this technique is less precise

than absorption measurements, it has the attribute of being less sensitive to variations in growth delay.

RESULTS

Absorption spectra for E.coli in the 325 to 820 nm range are presented in Figure 1. Figure 1a refers to E.coli suspended in saline and exhibits a broad shoulder near 350 nm and domination of the spectrum by scattered light. Figure 1b presents the absorption spectrum for E.coli suspended in the BSA solution that optimally matches the refractive index, as shown in figure 2. Note that in comparing figures 1a and 1b, the index matching reduces the light scattering background by a factor of 20 at 350 nm.

The results of the curve fitting are presented in figure 3. The residual light scattering as shown in figure 1b is modeled in figure 3a and a resonant feature centered near 422 nm is evident. The p value for fitting the spectrum shown in figure 1a is 2.11, in agreement with earlier work (12). For the index matched solution, the p value reduces to 1.67.

In light of these spectroscopic results, we selected 350, 400, 422, 440, and 700 nm as wavelengths for further investigation. tRNA (13), flavins (14,15), cytochrome (16), and NADH (17) contribute to the broad absorption near 350 nm. In addition, absorption measurements of water (18) indicate a broad, intense band centered at terahertz frequencies that also contributes to the absorption at 350 nm. Absorption measurements of Luria broth

(data not shown) reveal no resonant features in this frequency range. The intensity pattern of the 422, 582 and 561 nm features are reminiscent of the Soret, α , and β bands, respectively, observed in porphyrin complexes (16,19); 422 nm was chosen since it corresponds to the dominant resonant feature. 400 and 440 nm were chosen to demarcate the resonant feature. 700 nm was chosen as a nonresonant wavelength in the red. Figure 4 presents the percentage kill for E.coli exposed to increasing doses of radiation at these wavelengths. Figure 5 presents the percentage kill at a dose of approximately 4 J as a function of wavelength. With the exception of exposures to 350 nm, there were no significant differences between plate counting and absorption measurements for determining cell viability. Exposures to 350 nm indicate a radiation induced growth delay (5). Cells exposed to 422 nm radiation did repeatably indicate a growth enhancement for doses of less than 1 joule. There have been previous reports of stimulatory effects (20).

DISCUSSION

As shown in figures 1. and 2, immersion refractometry successfully reduces light scattering and significantly improves spectroscopic measurements of the absorption properties of E.coli suspensions. We have recently extended these studies to other cell lines with similar success.

With regards to biological effects of laser irradiation of E.coli, the cell viability studies summarized in figures 4 and 5 indicate the occurrence of at least two absorption processes.

More specifically, one process is indicated by the growth enhancement due to low doses of 422 nm radiation. A second process is indicated at larger doses where increasing dose corresponds to increasing lethality and, excluding the 422 nm data, cell viability is less effectively reduced with longer wavelength radiation. This second process is in line with conclusions drawn from previously observed action spectra of *E. coli* where nucleic acids have been assigned as the principle chromophore (4,5,8). At lower doses and for wavelengths near 422 nm, however, the first process is apparent and the net effect on cell viability is opposite to that of the second mechanism. Furthermore, in our studies with the nanosecond pulsed laser, lethality is achieved at significantly lower doses than previously reported (4,5). While this is a promising observation for future biomedical investigations, the results discussed above indicate that competing processes occur for irradiation near 422 nm at relatively low doses. This consideration suggests that caution be used with regards to biomedical investigations using wavelengths near the Soret band of porphyrin complexes.

In conclusion, we have reported a systematic investigation of the wavelength dependence of near ultraviolet and visible radiation, delivered in nanosecond pulses, on the growth of *E. coli* suspensions. Exposure wavelengths were chosen based on improved spectroscopic measurements of the absorption characteristics of cell suspensions where the technique of immersion refractometry has resulted in a significant reduction in the background of scattered light revealing resonant features at 422,

582 and 561 nm. We observe a definite wavelength dependence for the effect of pulsed laser light on the viability of cells that can be reasonably accounted for by spectral assignments and suggests at least two absorption processes. This experimental approach should be of general utility for future investigations of the effects of laser light on cellular systems.

REFERENCES

1. Young M, "Optics and Lasers." (Springer-Verlag, Berlin, 1984).
2. Brau CA, Free-Electron Lasers, Science 1988; 239:1115-1121.
3. Cantor CR, Schimmel PR. "Biophysical Chemistry Part II." (W.H. Freeman and Company, New York, 1980).
4. Jagger J in Wang, SY (ed): "Photochemistry and Photobiology of Nucleic Acids, Volume II: Biology." (Academic Press, New York, 1976) Chapter 4.
5. Jagger J. Near-UV radiation effects on microorganisms. Photochem Photobiol 1981; 34:761-768.
6. Anderson RR, Parrish JA. Selective photothermolysis: precise microsurgery by selective absorption of pulsed radiation. Science 1983; 220:524-527.
7. Hillenkamp F, Pratesi R, Sacchi CA (eds): "Lasers in Biology and Medicine." (Plenum, New York, 1980).
8. Webb RB and Brown SB, Sensitivity of Strains of Escherichia Coli Differing in Repair Capability to Far UV, Near UV and Visible Radiations. Photochem Photobiol 1976; 24:425-432. See Figure 7.
9. Bateman JB, Wagman J, Carstensen EL, Refraction and absorption of light in bacterial suspensions. Kolloid-Zeit 1966; 208:44-58.
10. Moore JH, Davis CC, Coplan MA: "Building Scientific Apparatus." (Addison-Wesley, Don Mills, Ontario 1983) See figure 4.78.

11. Willett HP. Physiology of Bacterial Growth. In Joklik WK, Willett HP, Amos DB (eds): "Zinsser Microbiology." 17th ed. (Appleton-Century-Crofts, New York, 1980) pages 86-90.
12. Koch AL. Some Calculations on the turbidity of mitochondrial and bacterial suspensions. Biochem Biophys Acta 1961; 51:429-441.
13. Favre A, Michelson AM, Yaniv M. Photochemistry of 4-thiouridine in Escherichia coli transfer RNA(val). J Mol Biol 1971; 58:367-379.
14. Iwatsuki N, Joe CO, Werbin H. Evidence that deoxyribonucleic acid photolyase from bakers yeast is a flavoprotein. Biochemistry 1980; 19(6):1172-1176.
15. Metzler DE. "Biochemistry: the Reactions of Living Cells." (Academic Press, 1977, New York) pages 594, 478.
16. ibid, p.568.
17. ibid, p.478.
18. Jackson JD: "Classical Electrodynamics." 2nd ed. (John-Wiley and Sons, New York, 1975). p. 291.
19. Lemberg R, Barrett J: "Cytochromes." (Academic Press, New York, 1973).
20. Tiphlova O, Karu T. Stimulation of Escherichia coli division by low intensity monochromatic visible light. Photochem Photobiol 1988; 48(4):467-471.

FIGURE LEGENDS

Figure 1. Absorption spectra of E.coli Cla: a) suspended in saline solution exhibiting a shoulder near 350 nm and a broad scattering background, b) suspended in the BSA solution that optimally matches the refractive index of the cell membranes. Resonant features near 422, 582, and 561 nm are revealed due to the reduction in scattered light. Instrumental features occur near 488, 580, and 656 nm (see text); however, the observed intensity of the spectral feature at 582 nm cannot be completely accounted for as an instrumental line.

Figure 2. Optimization of refractive index of suspending solution. Absorption of cell suspensions measured at 589 nm as a function of refractive index of suspending solution. Refractive index varies with BSA concentration. Minimum absorption corresponds to optimally matching the refractive index of the suspending solution to that of the cell membrane.

Figure 3. Curve fitting of absorption spectra. Spectrum shown in figure 1b is fit with a scattering background and resonant feature: a) determination of power law of scattering background, b) Gaussian fit of resonant feature centered at 422 nm.

Figure 4. Wavelength and dose dependence on percentage kill of E.coli: a) exposures to 350, 400, 422, and 700 nm radiation indicating relative effectiveness at reducing cell viability as determined by absorbance measurements of the growth kinetics (see text), b) exposures at 400, 422, and 440 nm indicating growth enhancement for 500 millijoule dose of 422 nm radiation and reduction in cell viability for larger doses. The error in determining percentage kill is approximately 11%.

Figure 5. Percentage kill at a dose of approximately 4 J as a function of irradiation wavelength. The error in determining percentage kill is approximately 11%.

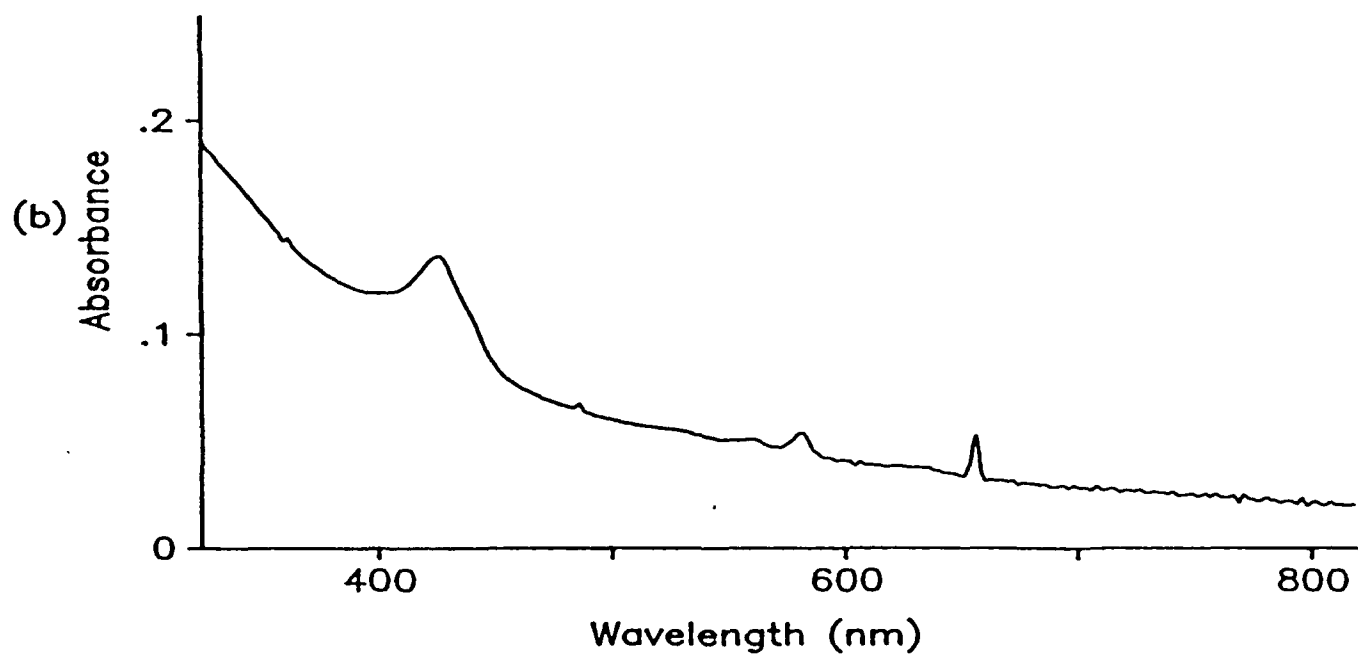
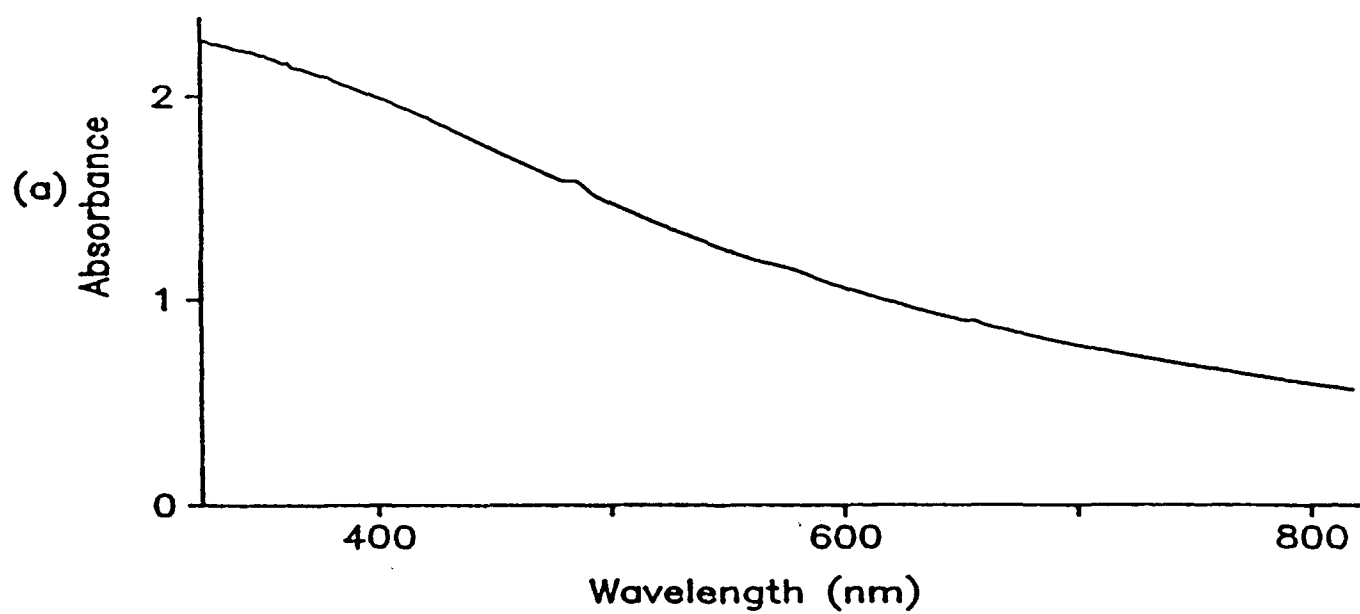


Figure 1

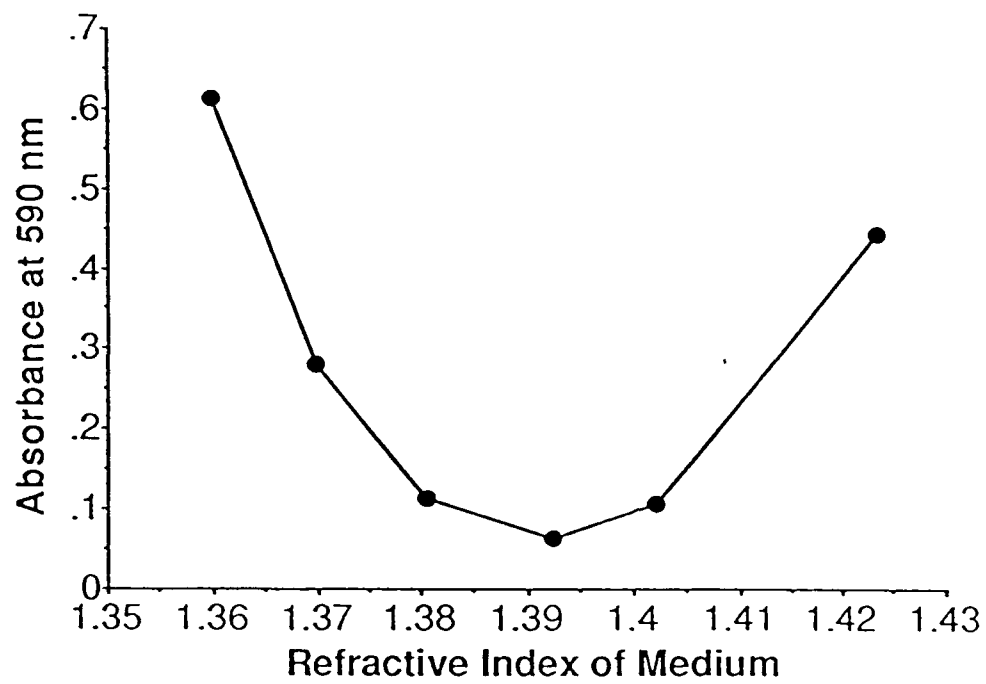


Figure 2

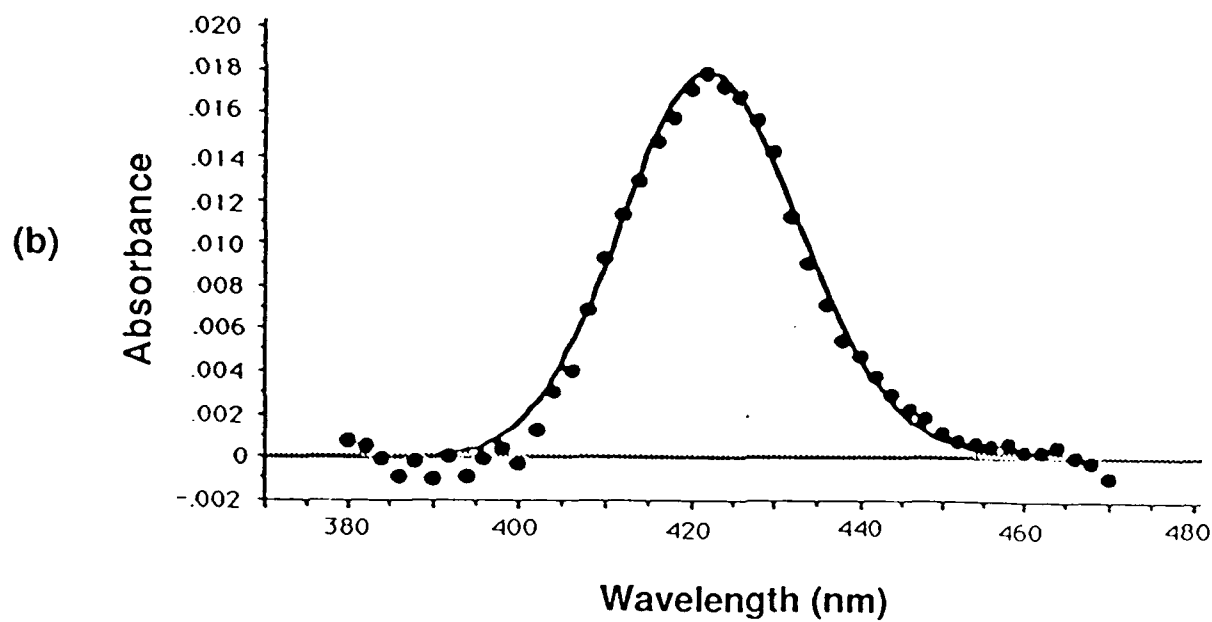
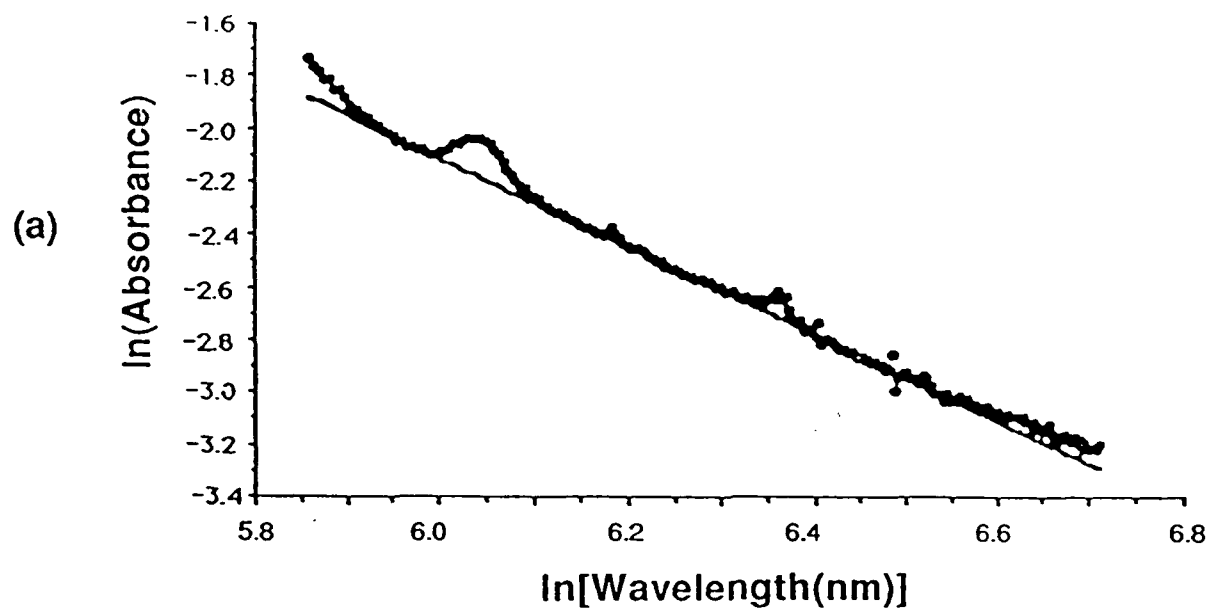


Figure 3

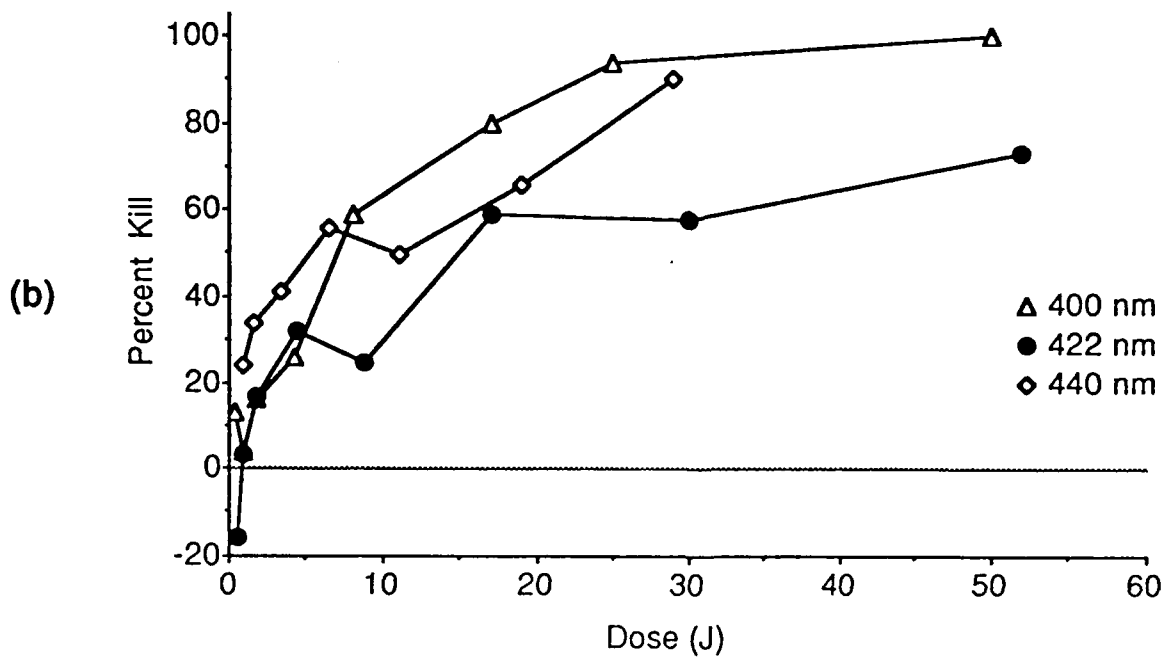
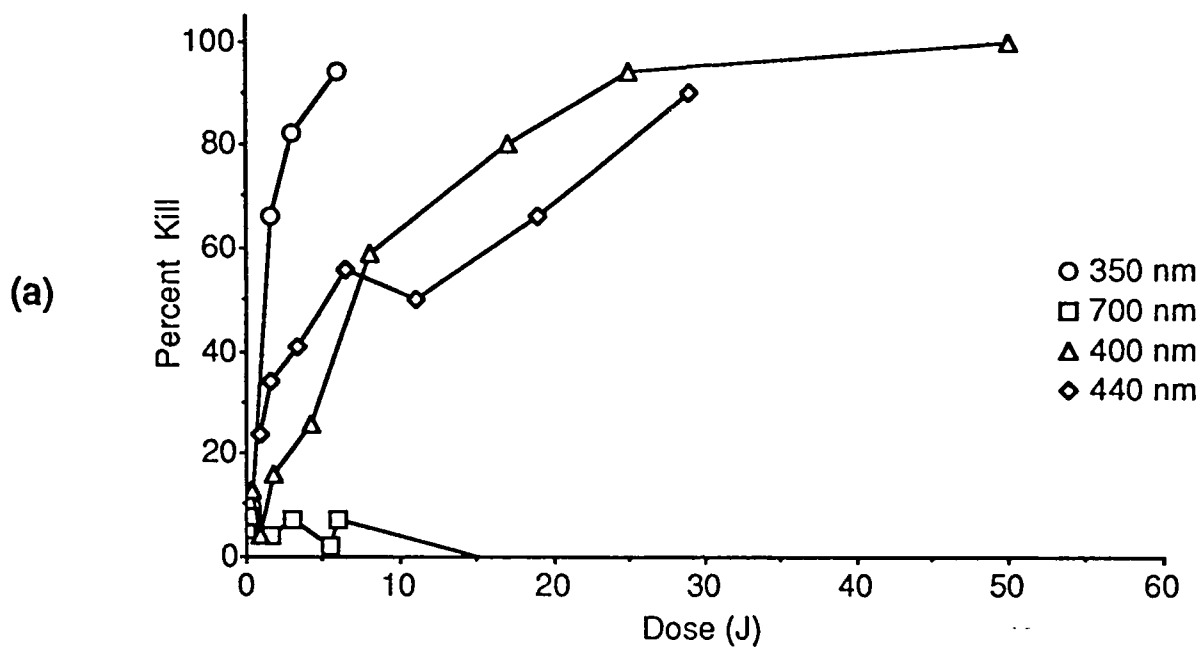


Figure 4

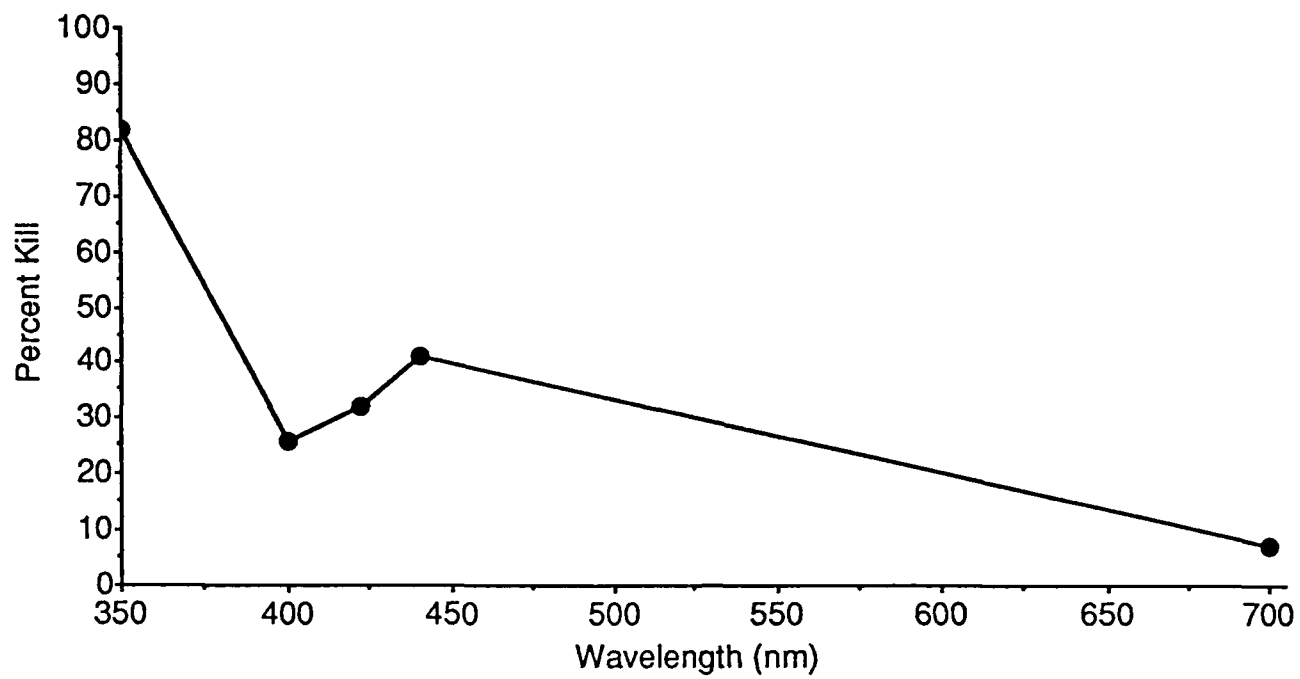


Figure 5

To be submitted as Laboratory Investigation, January 1992. ^{IV-D}
This is an introductory paper as a series on vocal fold fibroblasts
in culture which will include the effects of laser irradiation
on this cell type. This work was supported in part from
a grant from ONR.

Title: Canine Vocal Fold Fibroblasts in Culture: Expression of α -Smooth Muscle
Actin and Modulation of Elastin Synthesis.

Authors: Caroline Broadley[†], Debra A. Gonzalez[†], Rhada Nair* and Jeffrey M.
Davidson*. [†]Department of Otolaryngology, Vanderbilt University, Nashville, TN.
*Department of Pathology, Vanderbilt University, Nashville, TN.

Address for Correspondence: Caroline Broadley, Department of Otolaryngology,
S2100 MCN, Vanderbilt University, Nashville, TN, 37232

Running Title: Vocal Fold Fibroblasts

Abstract

Fibroblasts from canine vocal fold tissue have been isolated and maintained in culture. These cells express vimentin and α -smooth muscle actin, the characteristic marker of myofibroblast differentiation. Elastin production by vocal fold fibroblasts was compared to that of skin fibroblasts. The effects of transforming growth factor- β and hydrocortisone on elastin production were examined. Vocal fold fibroblasts in culture have a high elastogenic capacity compared to skin fibroblasts, and their elastin production can be enhanced by hydrocortisone (1.3 μ M) and TGF- β (10ng/ml). We conclude that the cells within the vocal fold are myofibroblastic in nature, and have high elastogenic potential *in vitro*. We suggest that connective tissue remodelling may be a continuous process in the vocal fold.

Key words: vocal fold, myofibroblast, α -smooth muscle actin, elastin, TGF- β

Introduction

Impaired voice quality, due to trauma, surgery, or advancing age, is a serious problem for many individuals. The inability to communicate effectively can interfere with an individual's career, and can lead to serious psychological problems. The human vocal fold, viewed in cross-section, consists of an epithelial layer, three layers of connective tissue comprising the lamina propria, and the vocalis muscle (14). The connective tissue composition of the lamina propria determines the biomechanical properties of the vocal fold, and thus the range sounds which can be produced.

Alterations in voice quality, including changes in pitch and increased hoarseness, which occur with age (16), are known to be associated with structural changes. These changes occur mostly within the lamina propria and include decreased elastin content in the intermediate layer, and increased collagen content in the deep layer (12,16). Similar changes in collagen:elastin ratio have been observed in other tissues in response to various types of injury (3,18). Most elastin synthesis occurs during development (4), so elastin is not normally replaced after injury.

Vocal fold tissue is required to have higher elasticity than many other tissues in order to perform its normal function. Histological studies of vocal folds from a variety of mammals have shown that this tissue is rich in elastic fibers. This is particularly true for vocal folds in both human and dog which are highly vocalizing mammals (14). Clearly, replacement of the elastic tissue with collagen following injury will severely affect voice quality. As the vocal fold is a highly dynamic tissue and is in constant use, it might be reasonable to expect cells from within this tissue, in particular the fibroblasts within the lamina propria to be specialized in some way. Subclasses of fibroblasts, which are believed to be functionally differentiated, have been identified recently in both injured and normal lung (1).

This paper describes the isolation, culture and characterization of the vocal fold fibroblast. These studies demonstrate that vocal fold fibroblasts in culture express α -smooth muscle actin, which is characteristic of myofibroblasts. The results also show that these cells in culture have high elastogenic potential, and that their elastin synthesis can be increased by both transforming growth factor-beta (TGF- β) and hydrocortisone. The culture of fibroblasts from the vocal fold provides a model system in which to study the normal physiology and pathological changes leading to decreased voice quality which are currently poorly understood.

Experimental Design

Canine vocal fold explants were cultured using standard techniques. Primary cultures and cultures up to passage four were examined for the presence of the cytoskeletal components vimentin, α -smooth muscle actin and desmin, in order to establish the phenotype of the vocal fold fibroblast. The production of elastin by vocal fold fibroblasts was measured by an indirect enzyme-linked immunosorbent assay, and was compared to elastin production by skin fibroblasts from the same species. The effects of TGF- β and hydrocortisone on elastin production were examined.

Results

Histology

The vocal fold is lined with stratified squamous epithelium, which is suitable for withstanding frictional stress. Nuclei of fibroblasts can be observed within the vocal fold mucosa, specifically within the loose connective tissue of the lamina propria (Figure 1a). There is an abundance of elastin within the vocal fold mucosa (Figure 1b) with both elastin and collagen dispersed throughout the canine vocal fold lamina propria (Figure 1c). The vocalis muscle is a striated muscle (Figure 1d).

Cultured Cells from the Vocal Fold Mucosa and Vocalis Muscle.

Cells from the vocal fold mucosa and vocalis muscle were isolated using standard explant culture techniques as described below. The small pieces of tissue were placed in a minimal amount of growth medium to encourage attachment to the petri dish. After 24 hours, the tissue was attached firmly enough so as to allow the gentle addition of growth medium to the cultures. The explants can be left in a small amount of growth medium for up to 72 hours before requiring additional medium.

Within two to four days, cells were observed migrating from the vocal fold mucosa explant. The first cells to migrate from the explant were epithelial-like cells as suggested by their cobblestone appearance (Figure 2). These cells migrate as a flat sheet of closely apposed cells, which do not overlap one another. One to two days later, fibroblasts begin to appear as single cells. These cells were recognized by their elongated appearance (Figure 3), and their migration out from the explant over the epithelial cells. The fibroblasts continued to migrate and eventually made up the bulk of the cell population in the culture dish. On very rare occasions, single fibroblast-like cells were observed migrating from the explants prior to the emergence of the epithelial layer. Subculture of the cells resulted in a pure population of fibroblasts as the epithelial cells remained attached to the culture dish following trypsinization. Although within the vocal fold mucosa these are small vessels which are composed of smooth muscle and endothelial cells, these were not evident in culture probably due to their low numbers compared to the abundance of fibroblasts.

Within 3-4 days muscle-like cells had migrated from the vocalis muscle explants (Figure 4). No epithelial monolayer was observed migrating from these explants.

Immunocytochemical Characterization.

Vocal fold fibroblasts which had migrated from explants and subcultured up to passage 4 expressed α -smooth muscle cell actin (Figure 5a). However, between passage 1 and passage 4, the percentage of cells which stained positively for this cytoskeletal protein decreased from approximately 90% in passage 1 cultures, to around 50% in cultures at passage 4. These cells also stained positively for vimentin (Figure 5b). Epithelial-like cells from the explant were negative both for α -smooth muscle cell actin and vimentin. Neither fibroblasts nor epithelial cells expressed desmin. Fibroblasts isolated from dog skin expressed vimentin but not α -smooth muscle actin.

Elastin Production.

Elastin production from canine vocal fold fibroblasts was compared to that of canine skin fibroblasts. Vocal fold fibroblasts produced approximately twice that of skin fibroblasts (Figure 6). Furthermore, elastin production by canine vocal fold fibroblasts was stimulated by both TGF- β (10ng/ml) and hydrocortisone (1.3 μ M) (Figure 7).

Discussion

The vocal fold is a unique mammalian tissue which exists in a highly dynamic environment. The human vocal fold differs structurally from that of the dog in that the lamina propria in humans is divided into three layers, while the dog has only two layers and, therefore, has no structure equivalent to the vocal ligament. In the human, the layers are clearly defined with most of the elastin present in the superficial and intermediate layers, while the deep layer consists mostly of collagen fibers. In contrast, the superficial layer of the canine lamina propria is dense with both collagen and elastin, while the deep layer is loose in fibrous components as observed by Hirano and Kurita (14) and confirmed in this study. However, owing to

the overall abundance of elastin within the tissue from both species, we considered the canine vocal fold to be a suitable model. In addition, the macroscopic structure of the canine larynx is very similar to that of the human larynx (14).

The abundance of elastin within vocal fold suggests that this tissue is specialized. Vocal fold fibroblasts can be obtained from the canine vocal fold and maintained in culture for several months without any difficulty. In this study we used fibroblast cultures no older than passage four (maximum of four weeks old) so as to keep as close to the normal phenotype as possible.

The phenotype of the vocal fold fibroblasts was determined by immunocytochemical analysis of the cytoskeletal components. Fibroblasts from the vocal fold express both vimentin and α -smooth muscle actin, but not desmin. Vimentin is expressed equally by cells from primary explants and passage four cultures. However, α -smooth muscle actin expression appears to diminish between passage one and passage four.

The expression of α -smooth muscle actin in fibroblasts was initially described as a characteristic of the "injury" phenotype, and was observed in a population of cells which appeared transiently in experimental wound repair (5,8,26). Fibroblasts expressing α -smooth muscle actin have since been described in both injured and normal tissue (1,27). The population of cells sharing both fibroblast and smooth muscle properties are known as myofibroblasts. Several subclasses of myofibroblasts have now been identified and are distinguished by the pattern of staining for cytoskeletal components (27). The appearance of myofibroblasts in injury is thought to be central to the mechanisms of connective tissue remodelling and wound contraction (7), and may be important where structural integrity of the tissue is crucial for normal function.

Routine culture of fibroblasts on plastic and glass is reported to cause these cells to assume a phenotype closer to myofibroblasts (7). However, the fibroblasts

which migrated from the vocal fold explant expressed α -smooth muscle actin when examined after only six days in culture, and the expression of this cytoskeletal component appeared to diminish with time.

Vocal fold fibroblasts appear to be a myofibroblast-like cell expressing vimentin and α -smooth muscle actin. It is possible that the expression of α -smooth muscle actin in vocal fold fibroblasts reflects their normal function. Connective tissue remodelling may be a continuous process in the vocal fold. Changes in voice quality with age may be associated with loss of contractile properties and decreased elastin synthesis by vocal fold fibroblasts.

Early studies from our laboratory indicated that vocal fold-derived fibroblasts had a greater elastogenic capacity compared to skin-derived fibroblasts (11). The present study confirms that vocal fold fibroblasts produce approximately twice the elastin of skin fibroblasts *in vitro*. Vocal fold fibroblasts grown in culture appear to exhibit levels of elastogenesis which might represent their elastogenic potential *in vivo*. This might be useful for increasing elastin production in cells within the vocal fold which have undergone some kind of injury. Treatment with factors which stimulate elastin synthesis could restore elasticity to the tissue and thereby accelerate voice recovery after injury.

Candidates for stimulating elastin synthesis include glucocorticoids and TGF- β . The effects of glucocorticoids on connective tissue synthesis are usually inhibitory and include decreased synthesis of both collagen (22) and glycosaminoglycan (25). However, elastin synthesis in bovine nuchal ligament cells is increased by glucocorticoids (21). TGF- β is a known modulator of elastin synthesis and has been shown to upregulate elastin production in cultured porcine aortic smooth muscle cells (19) and granulation tissue fibroblasts (23). Our results show that treatment with TGF- β or hydrocortisone increased elastin production by vocal fold fibroblasts.

Mechanical deformation has been shown to increase elastin (24) and collagen synthesis (28) by aortic smooth muscle cells. Preliminary findings from our laboratory suggest that mechanical deformation of vocal fold fibroblasts stimulates elastin production (10). This could be useful in indicating whether light vocal fold exercise would be beneficial for voice recovery instead of complete voice rest which is now indicated after injury or surgery. The effects of mechanical deformation on elastin production by vocal fold fibroblasts will be the subject of a further study.

In summary, the vocal fold fibroblast appears to be a myofibroblast-like cell which has high elastogenic potential. The vocal fold may be a highly specialized tissue which, due to constant use, is in a continuous process of repair or remodelling in order to maintain normal function. Elastin production by the vocal fold fibroblast can be enhanced by TGF- β and hydrocortisone. This could be important in the treatment of injured or aged vocal folds for recovery of normal voice quality.

Methods

Histology. A whole larynx was obtained from a euthanized dog and was fixed in 10% formalin for 72 hours at 4°C. The vocal fold was removed and embedded in paraffin from which 4µm tissue sections were cut. The tissue was then stained with Masson's trichrome with Azan (M&A), Elastic van Gieson (EvG) or Hematoxylin and Eosin (H&E) using standard procedures.

Isolation and Culture of Vocal Fold Cells. Laryngeal tissue was obtained from dogs which had been euthanized by intravenous injection of a lethal dose of sodium pentobarbital. The tissue was collected in Hank's balanced salts solution buffered with 10mM HEPES (buffered-HBSS), containing penicillin (50U/ml), streptomycin (50µg/ml) and amphotericin B (12ng/ml). The tissue was rinsed twice with buffered-HBSS containing antibiotics, and placed in a petri dish where the larynx was cut open to expose the vocal folds. The vocal fold mucosa was elevated and a small strip of mucosa containing the epithelium and lamina propria, was removed using forceps and small scissors, and placed into a 15ml centrifuge tube. A small part of the vocalis muscle from deeper in the vocal fold was removed and placed into another 15ml centrifuge tube. The tubes were filled with buffered-HBSS containing antibiotics and the tissue washed and collected by centrifugation. Each tissue was then placed into a Petri dish and teased into small pieces (~1mm³) using forceps and a scalpel. The pieces were collected and washed in buffered-HBSS by centrifugation, then resuspended in a small amount (3-5ml) of culture medium consisting of Dulbecco's Modified Eagle's Medium supplemented with 10% Fetal Bovine Serum, penicillin (50 U/ml), streptomycin (50µg/ml) and amphotericin B (12ng/ml) (DMEM+10%FCS). The suspension was poured into a 100 mm diameter petri dish (Falcon Labware) and the medium swirled so as to cover as much of the plate as possible. In some cases the explants were plated into Labtek™ 8-well slides (Nunc) for immunocytochemistry. The dishes were placed in an incubator (5% CO₂/95%

O₂) at 37°C. After 24 hours 10ml growth medium was added gently to the cultures. All tissue culture reagents were obtained from Gibco Biotechnologies, Grand Island, N.Y.

Isolation and Culture of Skin Fibroblasts. Skin tissue was obtained from the dorsal pelt of euthanized dogs and collected in buffered-HBSS containing antibiotics. The tissue was washed twice in buffered-HBSS then placed into a petri dish. The fascia was removed and small pieces of skin dissected from the pelt. The skin was teased into small (~1mm³) pieces and cultured in the same manner as described for vocal fold tissue. All cell types were subcultured using standard trypsinization procedures.

Immunocytochemical characterization. Cells were subcultured onto Labtek™ 8-well slides and grown in DMEM+10%FCS. When the cells were 80-90% confluent, they were washed twice in buffered-HBSS then fixed in 10% formalin for 30 minutes and stored in Dulbecco's phosphate buffered saline (PBS) (Gibco) at 4°C in a humidified atmosphere. Prior to staining, the cells were permeabilized in acetone for 5 minutes at -20°C. The slides were placed in PBS for 2 minutes then the primary antibody was added in PBS +1% bovine serum albumin (BSA) at 1:50, 1:100 and 1:200 dilutions, and incubated for 2 hours. Antibodies used were monoclonal anti- α -smooth muscle actin antibody, monoclonal anti-desmin antibody and monoclonal anti-vimentin antibody. The slides were washed 3 times in PBS, then incubated with TRITC-conjugated goat anti mouse IgG for 1 hour. The slides were then washed 3 times in PBS, rinsed once in water, and mounted in glycerol:water (1:1). Photographs were taken using a Nikon Optiphot photomicroscope equipped with epiillumination and specific filters for rhodamine, and a plan apochromate X40/0.75 objective and Ektachrome 400 ASA color slide film (Eastman Kodak Co., Rochester, NY). All antibodies were obtained from Sigma Chemical Co., St. Louis, MO.

Elastin Synthesis Measurements. Measurements of elastin synthesis were obtained from canine vocal fold fibroblasts between passages 2 and 4, at the late log phase of

growth. Cells were subcultured onto 24-multi-well dishes (Costar, Cambridge, MA) and grown to confluence. The medium was then replaced with 1ml DMEM+10% Newborn calf serum (NBCS). This medium was used in order to maximize differences in elastin production in response to the treatments described, as elastin production by cells cultured in FCS is very high (unpublished observation). This medium was then collected at given time intervals and elastin production measured by an indirect enzyme-linked immunosorbent assay (9). Briefly, microtiter plates were coated with dog α -elastin (25ng) in Voller's buffer (30) and incubated at 4°C overnight. Competition plates containing standard antigen (bovine tropoelastin, Elastin Products Company, Owensville, MO) or samples and polyclonal rabbit anti-pig α -elastin (1:3000) (9) were incubated at 4°C overnight. The following day, the contents of the competition plate were transferred to the coated plate and allowed to react. The reaction was visualized using horseradish peroxidase-conjugated goat anti rabbit IgG (1:2000) (Kirkegaard and Perry Laboratories). The plates were read in a Thermomax plate reader (Molecular Devices Corporation) at OD490nm and the results extrapolated from a 4-parameter, non-linear regression analysis of the standard curve (24) using SOFTmax software (Molecular Devices). Results are expressed as molecular equivalents of soluble elastin normalized to cell number. Cell number was determined by DNA content as described previously (15).

Treatment with TGF- β and Hydrocortisone. TGF- β (provided by Dr. Rik Derynck, Genentech, Inc.) or hydrocortisone (Sigma Chem. Co.) at the given concentrations were added to late log phase cultures of vocal fold fibroblasts in DMEM + 10% NBCS for times indicated in the figures.

References

1. Adler KB, Low RB, Leslie KO, Mitchel J, Evans JN: Biology of disease. Contractile cells in normal and fibrotic lung. *Lab Invest* 60:473-, 1989
2. Border WA, Okuda S, Nakamura T: Extracellular matrix and glomerular disease. *Sem Nephrol* 9:307, 1989
3. Clark JG, Overton JE, Marino BA, Uitto J, Stracher BC: Collagen biosynthesis in bleomycin-induced pulmonary fibrosis in hamsters. *J Lab Clin Med* 96:943, 1980
4. Davidson JM, Giro MG : Regulation of elastin production. In *Biology of the extracellular matrix*, edited by Mecham RP. Vol 1 p177 Academic Press NY, 1986
5. Gabbiani G, Chaponnier C, Huttner I: Cytoplasmic filaments and gap junctions in epithelial cells and myofibroblasts during wound healing. *J Cell Biol* 76:561, 1978
6. Gabbiani G: The myofibroblast: A key cell for wounding healing and fibrocontractive diseases. *Connective Tissue Research: Chemistry, Biology and Physiology*, p183, Alan R Liss Inc, New York, 1981
7. Gabbiani(aquisition of α -actin in culture)
8. Garrels JI, Gibson W: Identification and characterization of multiple forms of actin. *Cell* 9:793, 1976
9. Giro GM, Hill KE, Sandberg LB, Davidson JM: Quantitation of elastin production in cultured vascular smooth muscle cells by a sensitive and specific enzyme-linked immunoassay. *Collagen Rel Res* 15:108, 1981
10. Gonzalez DA, Nair RR, Ossoff, R.H: Vocal cord fibroblast elastin production in tissue culture. *Association for Research in Otolaryngology* p203 (abstr), 1990
11. Gonzalez DA, Zeale DL, Davidson JM, Ossoff RH: A comparison of vocal fold and skin fibroblast elastin production in tissue culture. *Otolaryngology-Head and Neck surgery*. 103:192 (abstr), 1990

12. Hirano M, Kurita S, Nakashima T: Growth, development and aging of human voice folds. In Vocal Fold Physiology, edited by Bless DM, Abbs JH p22. College Hill Press San Diego, CA, 1983
14. Hirano M, Kurita S: Vocal Fold Histopathology. p17 JA Kirchner, College Hill Press, San Diego, CA. 1986
15. Johnson-Witt B, Hollis S: A rapid in situ deoxyribonucleic acid assay for determining cell number in culture and tissue. Anal Biochem 122:338, 1982
16. Kahane JC: Connective tissue changes in the larynx and their effects on voice. J Voice 1:27, 1987
17. Leslie KO, Taatjes DJ, Schwarz J, vonTurkovich M, Low RB: Cardiac myofibroblasts express alpha smooth muscle actin during right ventricular pressure overload in the rabbit. Am J Path 139:207, 1991
18. Low RB, Strewalt WS, Hultgren P, Loe EP, Starcher B: Changes in collagen and elastin in rabbit right ventricular overload. Biochem J 263:709, 1989.
19. Lui J, Davidson JM: The elastogenic effect of recombinant transforming growth factor- β on porcine aortic smooth muscle cells. Biochem Biophys Res Commun 154:895, 19.....
20. Majno G: The story of the myofibroblasts. Am J Surg Pathol 3:535,1979
21. Mecham RP, Morris SL, Levy BD, Wrenn DS: Glucocorticoids stimulate elastin production in differentiated bovine ligament fibroblasts but do not induce synthesis in undifferentiated cells. J Biol Chem 259:12414, 1984
22. Ockarinen J, Ryhanen, L:Biochem J 198:519, 1981
23. Quaglini D, Nanney LB, Kennedy R, Davidson JM: Transforming growth factor- β stimulates wound healing and modulates extracellular matrix gene expression in pig skin. Lab Invest 63:307,1990

24. Rodbard D: Statistical aspects of radioimmunoassay in competitive binding assays. p158, edited by Daughaday WA, Odell WA, Lippincott PA 1977
25. Sarnstrand B, Bratts R, Malmstrom A:J Invest Dermatol 79:412-417, 1982
26. Skalli O, Schurch W, Seemayer T, Legace R, Pittet B, Montadon D, Gabbiani G: Actin isoform and intermediate filament composition of myofibroblasts from diverse settings and from experimental wound healing. J Cell Biol 107:685 (abstr), 1988
27. Skalli O, Schurch W, Seemayer T, Lagace R, Montadon D: Myofibroblasts from diverse pathologic settings are heterogeneous in their content of actin isoforms and intermediate filament proteins. Lab Invest 60:275, 1989
28. Sumpio BE, Banes AJ, Johnson G: Cyclic stretching of aortic smooth muscle cells stimulates collagen synthesis. Proc 14th New Eng Soc Vasc Surg, 1987
29. Sutcliffe MC, Davidson JM: Effect of static stretching on elastin production of porcine aortic smooth muscle cells. Matrix 10:148, 1990
30. Voller A, Birdwell DE, Bartlett A: In Manual of Clinical Immunology, edited by Rose N, Fishman H. p506, Washington DC, Amer Soc for Microbiology

Figure Legends

Figure 1(a). H&E stained canine vocal fold showing stratified squamous epithelial lining and nuclei of fibroblasts within the lamina propria (Xxx mag.)

Figure 1(b). Elastic van Gieson stained canine vocal fold showing distribution of elastin within the lamina propria (X200 mag.)

Figure 1(c). Masson's trichrome stained canine vocal fold showing distribution of collagen (X200 mag.)

Figure 1(d). H&E stained canine vocal fold showing striated vocalis muscle (X200 mag.)

Figure 2. Canine vocal fold explant 4 days in culture showing epithelial monolayer (X250 mag.)

Figure 3. Canine vocal fold explant 6 days in culture showing fibroblasts (X250 mag.)

Figure 4. Canine vocalis muscle explant 4 days in culture showing muscle cells (X250 mag.)

Figure 5(a). Vocal fold fibroblasts stained with antibody to α -smooth muscle actin (X300 mag.)

Figure 5(b). Vocal fold fibroblasts stained with antibody to vimentin (X300 mag.)

Figure 6. Elastin production by canine skin vs canine vocal fold fibroblasts. Each point represents the mean \pm s.e. of two experiments performed in duplicate. $p < 0.05$ using Student's paired t-test.

Figure 7. Effect of hydrocortisone and TGF- β on elastin production. Each point represents the mean \pm s.e. of three experiments performed in duplicate. $p < 0.05$ compared to control at each time point using Student's paired t-test.

Figure 1(a)

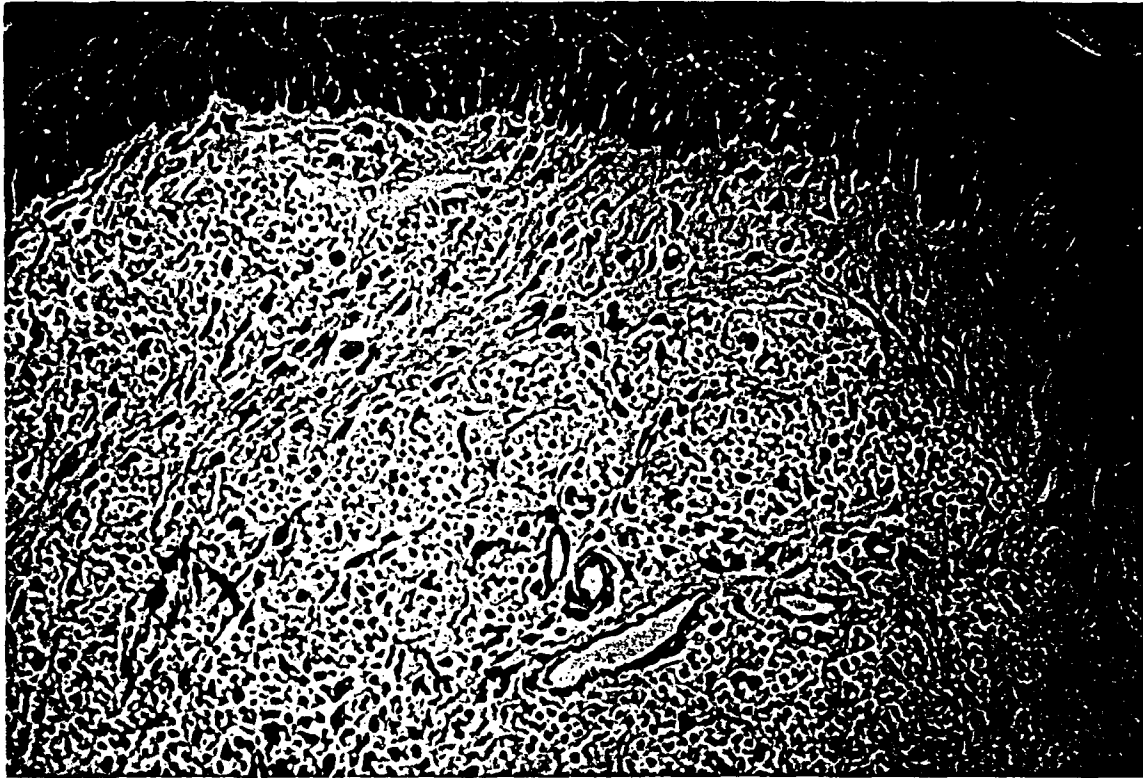


Figure 1(b)

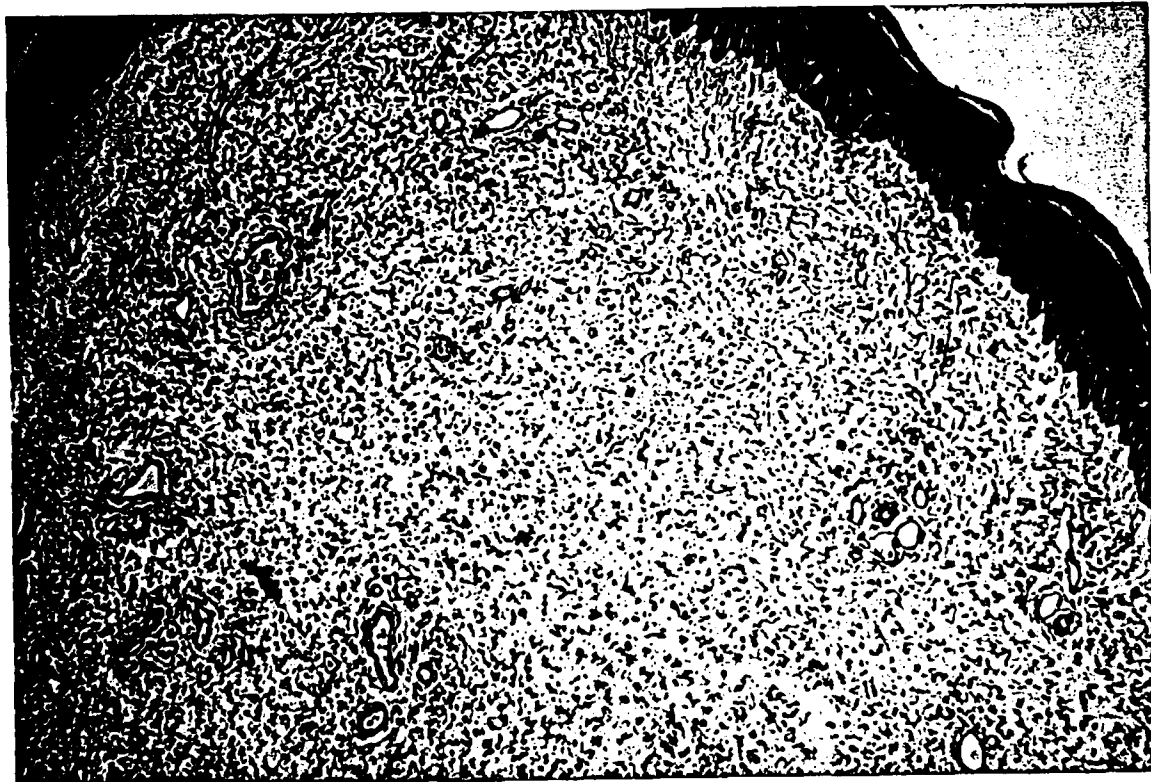


Figure 1(c)



Figure 1(d)

Figure 2

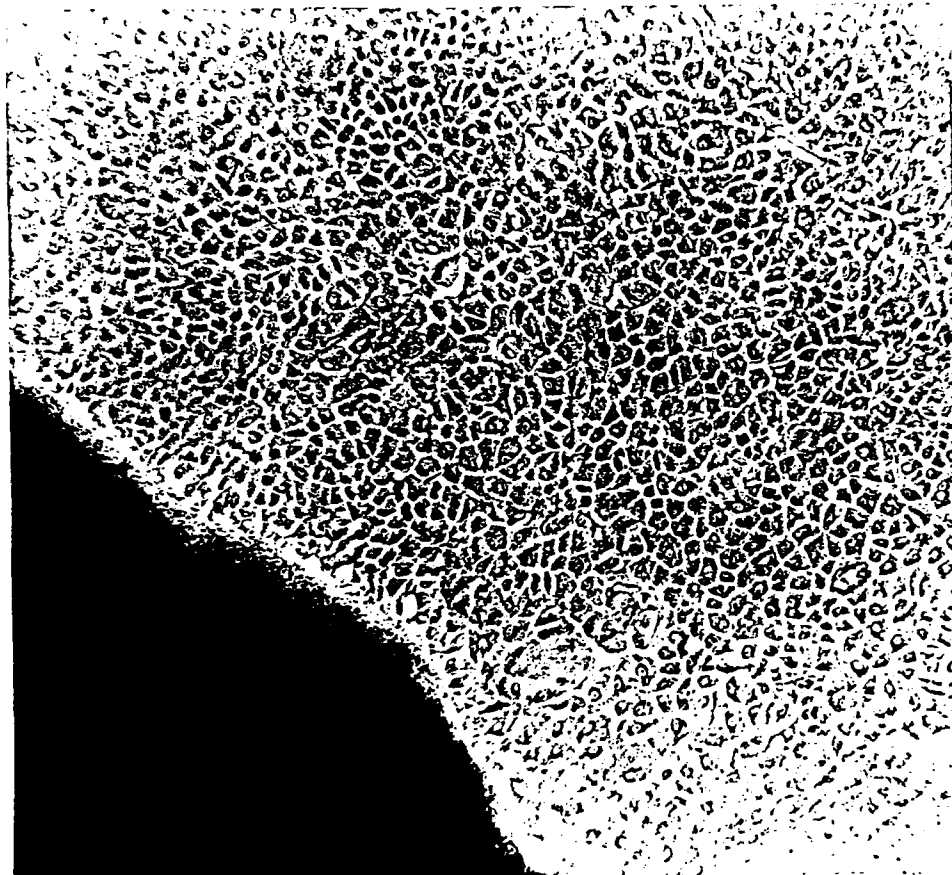


Figure 3

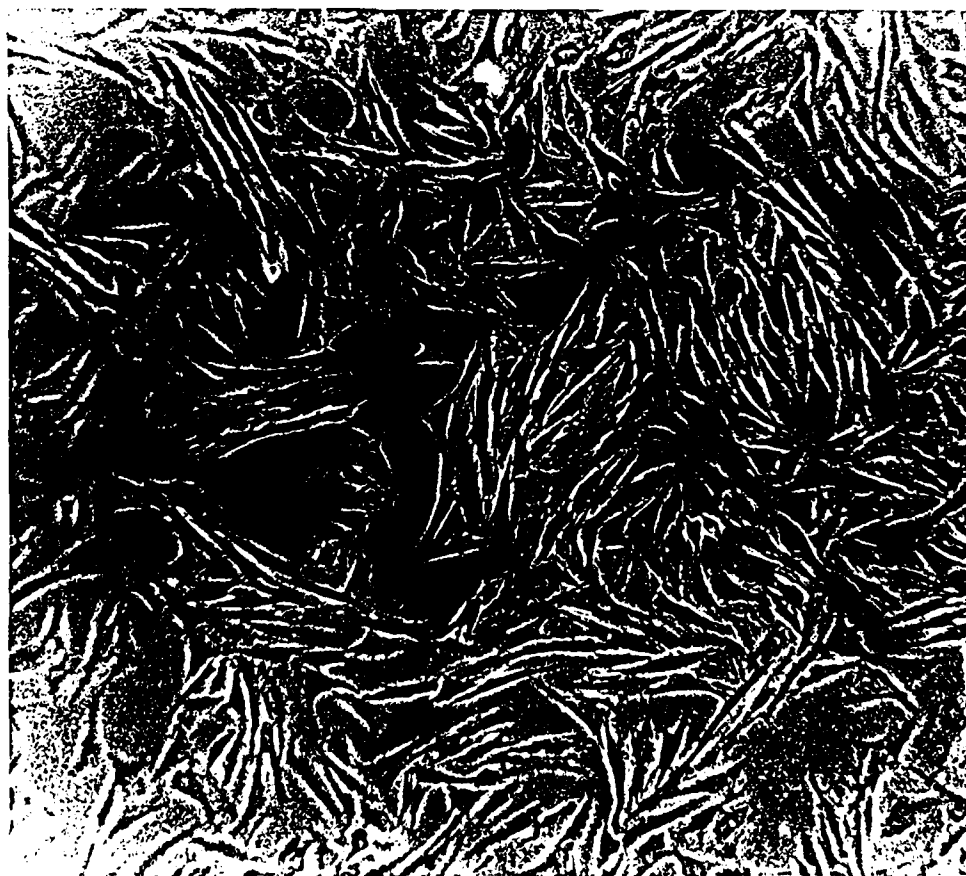


Figure 4

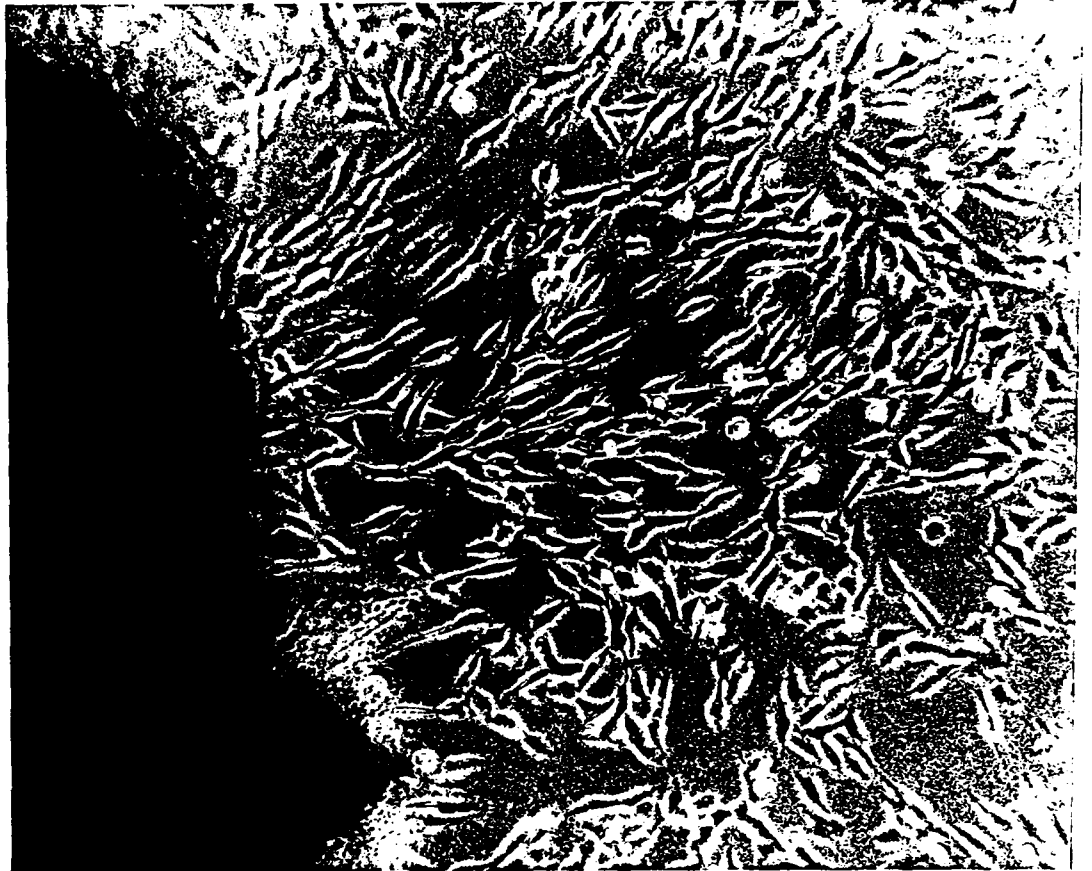


Figure 5



Figure 6

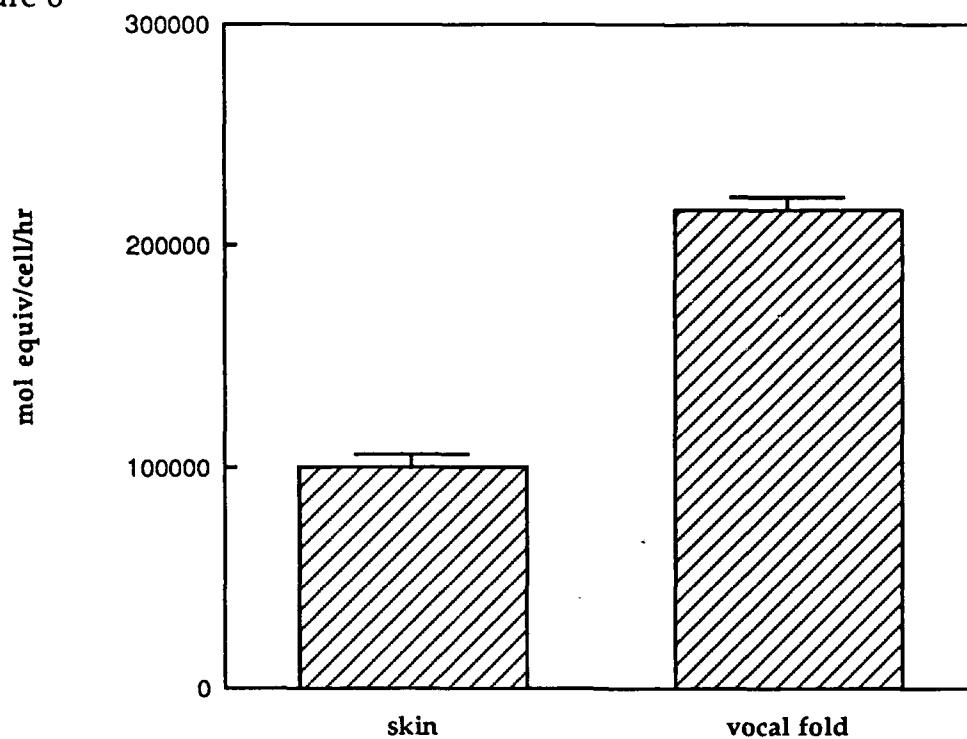
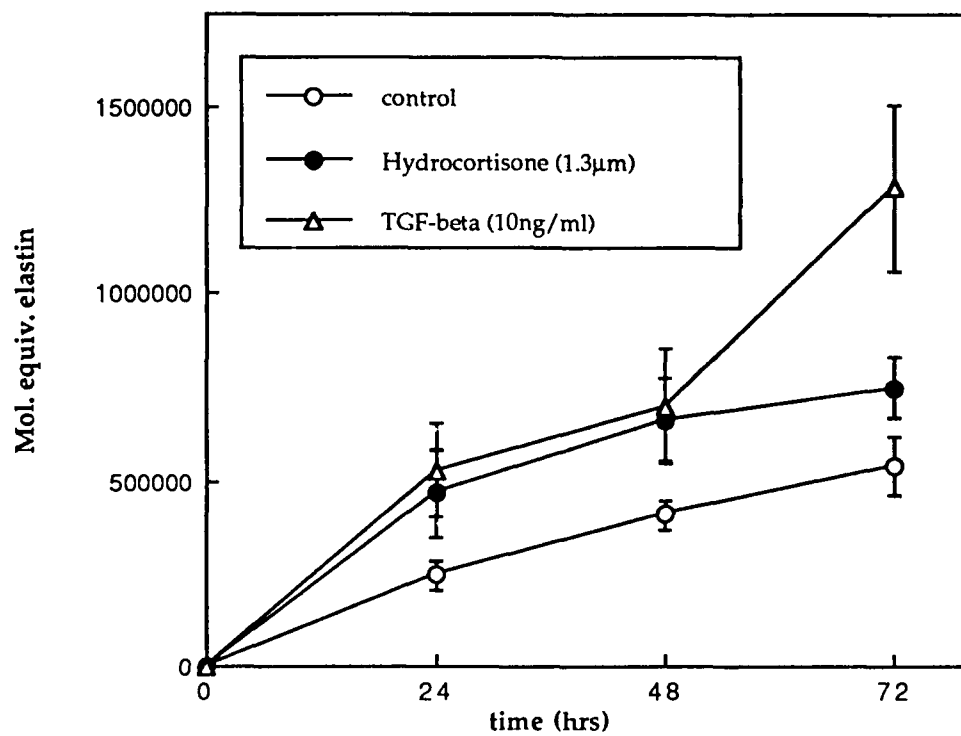


Figure 7



Submitted 18 Lasers in Surgery and Medicine

IV-E.

1

KTP LASER-INDUCED BIOMODULATION OF THE WOUND-HEALING PROCESS

Michael D. Kyzer, M.D.; Al S. Aly, M.D.; Robert H. Ossoff, D.M.D., M.D.

Department of Otolaryngology, Vanderbilt University Medical Center (M.D.K,
A.S.A, and R.H.O.), Nashville, Tennessee, 37232.

Partially funded by the A. Ward Ford Memorial Grant and by a summer research
stipend from the American Society for Lasers in Medicine and Surgery

Address Correspondence to:

Michael D. Kyzer, M.D.

Research Associate

Department of Otolaryngology

S-2100, MCN

Vanderbilt University Medical Center

Nashville, TN 37232

Phone: (615) 322-7267

FAX: (615) 343-7604

KEY WORDS

Biostimulation, KTP laser, laser tissue interaction, low-energy laser, tensiometry, wound healing

ABSTRACT

The KTP laser (wavelength, 532 nm) was used in a subablative format to determine whether low energy density irradiation would affect the normal healing by primary intention of scalpel skin incisions in rats. Two longitudinal lased strips were created by a 1 cm diameter defocused beam on the shaved, cleaned dorsal epidermis of 32 Sprague-Dawley rats; one strip was produced with a 2.0 W beam (54 J, or 18 J/cm² total dose), and the other with a 3.5 W beam (94.5 J, or 31.5 J/cm², total dose). Scalpel incisions were made longitudinally within the irradiated zones, using contralateral scalpel incisions on unirradiated skin as controls. Tensiometric analysis of wound strength was performed at 3, 7, 14, and 23 days following surgery. The data from fresh tissue tensiometry indicate that KTP laser irradiation of skin incisions results in a triphasic tensile strength response for the 54 J (2.0 W) exposure, but not for the 94.5 J (3.5 W) exposure. For the 54 J irradiated incisions, the fresh tensile strength is greater than control at days 3 and 23, but less than control at the intermediate days 7 and 14. The 94.5 J irradiated incisions are consistently weaker than controls. These effects may be explained by the interplay of localized transient cellular injury effected by the low energy density laser and a concomitant biomodulatory response.

INTRODUCTION

Medical lasers have traditionally been used for tissue ablation since laser energy can cause intense localized heating sufficient to vaporize both extra- and intracellular water, producing a coagulative necrosis.¹⁻³ The carbon-dioxide (CO₂) laser is often the laser of choice when laser incision and tissue ablation are desired, but the hemostatic effects are suboptimal.^{3,4} Other lasers, such as the KTP and argon (wavelengths of 532 nm and 488 nm, respectively), are much more effective at hemostasis since their frequencies of emission lie near the absorption maximum of hemoglobin. Any of these lasers, especially the CO₂, may be expected to produce thermal tissue damage lateral to the site of irradiation when used in the ablative energy range.⁵ This lateral damage may be responsible for the well-known delay in the healing of laser incisions.^{1,6}

More recent literature has begun to focus on the non-thermal, or photochemical, property of the laser and its use in the biomodulation of physiologic processes.^{5,7-12} Both the helium-neon and argon lasers, when operated in a subablative format, have been shown to augment the rate of collagen synthesis and the total collagen deposition in skin wounds,⁷ but an attenuated rate of wound reepithelialization was documented when using the CO₂ laser.⁵ Unfortunately, however, the degree to which photochemical and thermal processes contribute to the biomodulation is not easily delineated, although it is predicted that photochemical processes are favored at lower

irradiences. We investigated the effect of low energy density KTP irradiation on the normal wound healing process of skin incisions in rats, and our results suggest that the KTP laser can be utilized as a biomodulatory tool.

MATERIALS AND METHODS

Male Sprague-Dawley rats, weighing 275-300g initially, were anesthetized intraperitoneally with Ketaset (ketamine hydrochloride, 22.0 mg/kg body weight; Aveco, Co., Inc., Fort Dodge, IA) and Rompun (xylazine, 2.2 mg/kg body weight; Haver, Mobay Corp., Shawnee, KS). With the onset of analgesia, the dorsal pelt of each animal was clipped (Model #5-01, Head #80, size 10; Oster, Inc., Allegheny International Co., Professional Products Department, Milwaukee, WI), shaved, and the exposed dorsal epidermis was treated with a depilatory (Magic Depilatory Cream, Carson Products Co., Savannah, GA) to remove any residual stubble which would interfere with absorption of the laser. Each rat was mounted on a 20.4 cm X 20.4 cm plexiglass translation stage. The stage was propelled horizontally at a constant rate of 0.11 cm/sec via its attachment to both pistons of a Harvard pump, and the translation stage was positioned immediately beneath the vertical KTP beam (KTP/532 Laser, Serial #1605246, Laserscope, Santa Clara, CA). The Laserscope KTP is a quasi-continuous wave laser whose pulse regime consists of a 25 kHz pulse repetition rate with a 1 μ sec pulse width; the beam profile, as determined by another member of our department (see Acknowledgments), was shown to be near Gaussian.

The KTP beam was defocused to a diameter of 1 cm through the use of a Microbeam 1 (Laserscope, Santa Clara, CA) attachment on a Storz (Model US-1, M1061-50/50, Storz Urban, Urban Engineering, Inc., Burbank, CA) operating

microscope, the vertical distance from the beam orifice to the rat's dorsum being 18 cm. Each rat was translated under a 2.0 W KTP beam for a duration of 27 sec (54 J, or 18 J/cm², total dose) to produce a 3 cm longitudinal strip 1.5 cm to the left of the spinal column. A second 3 cm lased longitudinal strip was created ipsilateral and 2 cm posterior to the first strip by using a 94.5 J (3.5 W, 31.5 J/cm) KTP beam. The total doses delivered were 18.0 J/cm² for the 2.0 W exposure and 31.5 J/cm² for the 3.5 W exposure. These two doses were chosen empirically as a result of a pilot study involving one rat which was exposed to a range of power settings (0.5 W to 15 W) at the corresponding doses of 1.9 J/cm² to 57.3 J/cm²: the observations lead us to select two levels of irradiance, one of which (54 J) produced no evidence of erythema or induration and the other of which (94.5 J) was just sufficient to produce visible erythema and induration. These irradiances were termed maximally sublethal and minimally lethal, respectively, although these terms were chosen only for descriptive purposes.

Immediately subsequent to the irradiation procedure, 3 cm longitudinal scalpel incisions were created with a No. 20 blade (SteriSharps, Seamless Hospital Products Co., Wallingford, CT) in the midline of each of the lased strips. Control scalpel incisions were created contralaterally at identical vertebral levels. All scalpel incisions extended down to the panniculus carnosus, and each incision was closed with four skin staples following careful apposition of the skin flaps. The rats were then housed in individual cages without wood shavings (to keep the wounds as clean as possible), with water and chow (Wayne Feeds, Precision Milling, Chicago, IL) *ad libitum*, and on a 12 h light / 12 h dark cycle *per diem*. After excluding one rat which was sacrificed acutely for histology, each of the

remaining rats was randomly allocated to one of four recovery groups: the groups were terminated at 3, 7, 14, and 23 days postoperatively.

On the designated days the rats were sacrificed by a lethal dose of inhaled halothane (containing 0.01% Thymol, Halocarbon Laboratories, Inc., Hackensack, NJ), and a 2.5 to 3.5 cm X 2.0 to 3.0 cm skin patch containing the wound was excised using a No. 20 scalpel blade. A 1 cm X 2 to 3 cm block was removed from one end of the initial patch to be processed for routine light microscopy. The remaining patch (1.5 to 2.5 cm X 2.0 to 3.0 cm) was placed in PBS buffer [8.1 mM Na_2HPO_4 , 0.5 mM MgCl_2 (all obtained from Fisher Scientific, Fair Lawn, NJ) in sterile saline (0.9% NaCl, Travenol Laboratories, Inc., Deerfield, IL)] and chilled on ice until fresh-tissue tensiometry was performed, which was within 1.5 hours in all cases. All of the wounds were excised in the above manner, and extreme care was taken to avoid exerting any stress on the wound prior to its tensiometric measurements. In an effort to aid in this respect, the skin staples were not removed until immediately prior to placing the skin patches in PBS buffer.

Each of the skin patches was positioned in the jaws of the tensiometer (Instron, Model 1130, Instron, Inc., Canton, MA) which was equipped with a 5000g head; the patch was oriented with the scalpel incision parallel to the edge of the tensiometer's jaw. In the event that the skin patch was dislodged from the jaws during tensiometry, the measurement was aborted. Peak breaking forces were measured, and the forces were converted to strain values (g force/incision length) based on the length of the incision.

Statistical Method

The tensiometric data were transferred manually from tensiograms to an IBM Turbo AT computer operating with the statistical software SYSTAT (SYSTAT, Inc., Evanston, IL). This software package was then utilized to analyze the data and calculate confidence intervals based on the Wilcoxon signed-rank test.

RESULTS

Tensiometry

All wounds showed a time-dependent increase in tensile strength over the 23 day period (refer to Table I). However, the wounds which had been irradiated with 54 J (2.0 W beam) showed a triphasic tensile strength response. Figure 1 illustrates that at postoperative day 3, the irradiated incisions were **stronger** than control incisions by 59% ($p \leq 0.05$). However, for postoperative days 7 and 14, the irradiated incisions were weaker by 44% and 19%, respectively ($p \leq 0.01$ for both days). Then by postoperative day 23, the strength of the irradiated incisions has again superceded that of controls by 29% at the 90% confidence limit. The incisions which were irradiated with 94.5 J (3.5 W beam) were consistently weaker than those of controls, as depicted in Figure 2, although only the point at day 14 is statistically significant within the 95% confidence interval. The points at days 7 and 23 are, however, suggestive of reduced tensile strength in the 94.5 J (3.5 W) irradiated incisions.

Histology

Analysis of the tissue sections revealed several remarkable findings. In the animal which was acutely sacrificed, the 54 J (2.0 W) irradiated wound showed no destruction of the epidermis or subjacent dermal stroma, no evidence of tissue edema, and was identical to control (refer to Figures 3 and 4). The 94.5 J (3.5 W) irradiated wound, however, showed a zone of thermal disruption of the dermal collagenous

stroma to a depth of 0.6 mm, leaving the reticular dermis unaffected; substantial tissue edema was noted (refer to Figure 5). On postoperative day 3, an augmented coagulum was seen in the 54 J (2.0 W) irradiated wound as compared to control, accompanied by a substantial inflammatory cell infiltrate throughout the dermis (refer to Figures 6 and 7). Furthermore, the epithelial bridging of the incision appeared to be attenuated. The sections for the remaining days of the study were unremarkable except that reepithelialization was retarded for both 54 J and 94.5 J irradiations until day 14. Dermal collagen content and organization appeared to be similar in irradiated and control wounds for all days surveyed, but visual quantitation is highly subjective and unreliable.

DISCUSSION

Recent literature in the field of medical application of laser irradiation suggests that some of the currently used medical lasers may be utilized for purposes other than mere tissue ablation.^{7-14,17,18} Laser-mediated biomodulation of tissue, either *in vitro* or *in vivo*, is a new field of investigation in which the laser is operated at energy densities which are insufficient to effect tissue vaporization, but which appear to be sufficient to cause both biostimulation and bioinhibition. Both types of modulation appear to have some energy density and wavelength specificity.^{9,12,15,17}

In this study we investigated the potential use of the KTP laser (532 nm wavelength) as a biomodulatory tool when operated in a subablative format. Our tensiometric data indicate that the KTP laser can be used to alter the normal healing by primary intention of skin wounds. The distinctly different results obtained from the 54 J (2.0 W, 18 J/cm²) and 94.5 J (3.5 W, 31.5 J/cm²) irradiations show that the tissue response is indeed energy density dependent. The 54 J irradiation produced a triphasic tensile strength response as evinced by an initial increase in tensile strength over control at day 3, followed by a decreased tensile strength as compared to control, and concluded by another increase in tensile strength by postoperative day 23. Indeed, the initial increase in tensile strength at postoperative day 3 for the 54 J irradiation could be explained by local vascular injury resulting in increased vascular permeability with a resultant increase in fibrin exudation; this hypothesis is supported by the presence of

an increased coagulum in the 54 J wound at day 3. The reduction in tensile strength of the 54 J irradiated wounds on days 7 and 14 is probably best explained by a transient cellular injury causing the release of proteases which may delay the reparative process, and by the attenuated reepithelialization of the irradiated incisions (refer to Histology Results). However, under this schema the eventual rise in tensile strength over control by day 23 is enigmatic unless one also posits a concomitant biostimulatory effect of the laser. In contrast, the 94.5 J (3.5 W, 31.5 J/cm²) irradiation did not produce a triphasic response. Instead, these irradiated wounds were consistently weaker than their matched controls, even after 23 days of recuperation, perhaps as a result of irreparable cellular and/or microvascular damage.

Other investigators have reported that the helium-neon laser has biostimulatory effects on collagen synthesis in wound healing as early as 3 to 4 days postoperatively.^{13,14} As we have demonstrated, however, the response to 54 J (2.0 W) KTP radiation can not be explained mechanistically in such simple terms. If the observed response is due to laser biostimulation of collagen synthesis in the wound, such a stimulation would then necessarily be followed by either a resultant increase in collagenase activity or a decrease in collagen synthetic activity, or both: this scenario would be in agreement with our observations, but upregulation of collagen synthesis is not expected as early as three days postoperatively. Alternatively, the 54 J (2.0 W) irradiation may cause the local transient release of various tissue trophic factors such as epidermal growth factor (EGF) or transforming growth factor-*beta* (TGF- β) or various mediators of the inflammatory response such as interleukin-1 (IL-1) and other chemoattractants; such a local release may be explained by local microvascular changes, especially with regard to the endothelium, which are mediated by intense hemoglobin

absorption of the KTP beam. While these various tissue factors may be released early after laser exposure, their biomodulatory effects may be initially masked by protease release from transiently injured cells, only to be manifested once these cells have resumed their normal metabolism. The consistently weaker wounds for the 94.5 J (3.5 W) irradiation could be explained by irreparable microvascular and cellular damage to the area, causing a paucity of nutrients, growth factors, and inflammatory cells necessary to promulgate expedient healing.

We have shown that the KTP laser can be used in a subablative format to effect alterations in normal wound-healing physiology. The changes which were noted on routine light microscopy include thermal disruption of the dermal collagenous stroma in 94.5 J (3.5 W) irradiated wounds, increased wound coagula through day 7 for the 54 J (2.0 W) irradiated wounds, and attenuated reepithelialization through day 14 for both irradiances. The precise molecular mechanisms accounting for the observed histologic and tensiometric changes remain obscure. In order to elucidate these mechanisms, one must employ molecular probing techniques for biomolecules such as messenger RNAs (ribonucleic acids) for collagen, IL-1, EGF, and TGF- β , which are known to have pivotal roles in wound healing. Such probing techniques afford the localization and quantitation of these molecules within the tissue. Future studies of this sort are planned in an effort to characterize more precisely the biologic response to the KTP laser.

REFERENCES

1. Hall RR. The healing of tissues incised by carbon-dioxide laser. *Br J Surg* 1971; 58:222-225.
2. Fleischer D. Lasers and gastroenterology, a review. *Am J Gastroenterology* 1984; 79:406-415.
3. Cochrane JPS, Beacon JP, Creasey GH, Russel CG. Wound healing after laser surgery: An experimental study. *Br J Surg* 1980; 67:740-743.
4. Bellina JJ, Hemmings R, Voros JJ, Ross LF. Carbon-dioxide laser and electrosurgical wound study with an animal model: A comparison of tissue damage and healing patterns in peritoneal tissue. *Am J Obstet Gynecol* 1984; 148:327-334.
5. Hambley R, Hebda PA, Abell E, Cohen BA, Jegasothy BV. Wound healing of skin incisions produced by ultrasonically vibrating knife, scalpel, electrosurgery, and carbon-dioxide laser. *J Dermatol Surg Oncol* 1988; 14(11):1213-1217.
6. Fox JL. The use of laser radiation as a surgical "light knife." *J Surg Res* 1969; 9:199-205.
7. Kana JS, Hutschenreiter G, Haina D, Waidelich W. Effect of low-power density laser radiation on healing of open skin wounds in rats.

- Arch Surg* 1981; 116:293-296.
8. Mester E, Nagylucskay S, Waidelich W, Tisza S, Greguss P, Haina D, Mester A. The effect of laser radiation on the phagocytic activity of leukocytes. *Arch Dermatol Res* 1978; 263(3):241-245.
 9. Hug DH. The activation of enzymes with light. In: Smith KC, ed. *Photochem Photobio Rev* 1978; 3:1-33.
 10. Kollias N, Melander WR. Laser induced stimulation of chymotrypsin activity. *Phys Lett A* 1976; 57:102-104.
 11. Takeda Y. Irradiation effect of low-energy laser on alveolar bone after tooth extraction. Experimental study in rats. *Int J Oral Maxillofac Surg* 1988; 17:388-391.
 12. Marchesini R, Dasdia T, Melloni E, Rocca E. Effect of low-energy laser irradiation on colony formation capability in different human tumor cells in vitro. *Lasers Surg Med* 1989; 9:59-62.
 13. Auerbach MM. Effect of helium-neon laser on the healing of aseptic experimental wounds. *Eksp Khir Anesteziol* 1976; 3:56-59.
 14. Urazalin ZB, Antipova ZP. Effect of monochromatic red light on mandibular fracture healing. *Stomatologiia* 1978; 57(5):5-9.
 15. Puolakkainen P, Brackett K, Sankar MY, Joffe S, Schroder T. Effects of electrocautery, CO₂ laser, and contact Nd:YAG laser scalpel on the healing of intestinal incision. *Lasers Surg Med* 1987; 7:507-511.
 16. Gaster RN, Berns M, Coalwell K, Binder PS, McCord RC, Burstein NL. Corneal surface ablation by 193 nm Excimer laser and wound healing in rabbits. *Invest Ophthalmol Vis Sci* 1989;30:90-98.

17. Braverman B, McCarthy RJ, Ivankovich AD, Forde DE. Effect of helium-neon and infrared laser irradiation on wound healing in rabbits.
Lasers Surg Med 1989; 9:50-58.
18. Anneroth G, Hall G, Ryden H, Zetterqvist L. The effect of low-energy infrared Laser radiation on wound healing in rats. *Br J Oral Maxillo Surg* 1988; 26:12-17.
19. Buell BR, Schuller DE. Comparison of tensile strength in CO₂ laser and scalpel skin incisions. *Arch Otolaryngol* 1983; 109:465-467.
20. Ben-Baruch G, Fidler JP, Wessler T, Bendick P, Schellhas HF. Comparison of wound healing between chopped mode-superpulse mode CO₂ laser and steel knife incision. *Lasers Surg Med* 1988; 8: 596-599.
21. Zachariae H. Delayed wound healing and keloid formation following argon laser treatment or dermabrasion during isotretinoin treatment.
Br J Derm 1988; 118:703-706.
22. Pensel J, Sommer K, Thomas S, Lieck P, Baretton G. Functional and histological restitution in the urinary tract after Nd:YAG laser coagulation. *Lasers Surg Med* 1988; 8:371-376.

ACKNOWLEDGMENTS

The authors wish to thank Nick Houchin in the Department of Otolaryngology for his patience and diligence in the design of the translation stage and in the preparation and handling of the animals. We are also grateful to Sarah Holly, Editorial Assistant, Department of Otolaryngology, for her expert technical advise during the preparation of the manuscript. In addition we wish to express our indebtedness to Jeff Davidson, Ph.D., Professor of Pathology, Vanderbilt University Medical Center, for stimulating conversation and unbiased perspectives, and to Jerri Tribble, M.S., for establishing a beam profile for the KTP laser. Furthermore, the authors wish to express our gratitude for partial funding of this effort by the A. Ward Ford Memorial Grant and to the American Society for Lasers in Medicine and Surgery for providing a summer medical student stipend to M.D.K during the initial phase of this research. Finally, the authors appreciate the many useful comments provided by David Zealea, Ph. D., Assistant Professor and Director of Research, and Caroline Broadley, Ph. D., Assistant Professor, both in the Department of Otolaryngology, Vanderbilt University Medical Center.

Table 1. Tensiometric data for laser irradiated incisions and their respective controls.

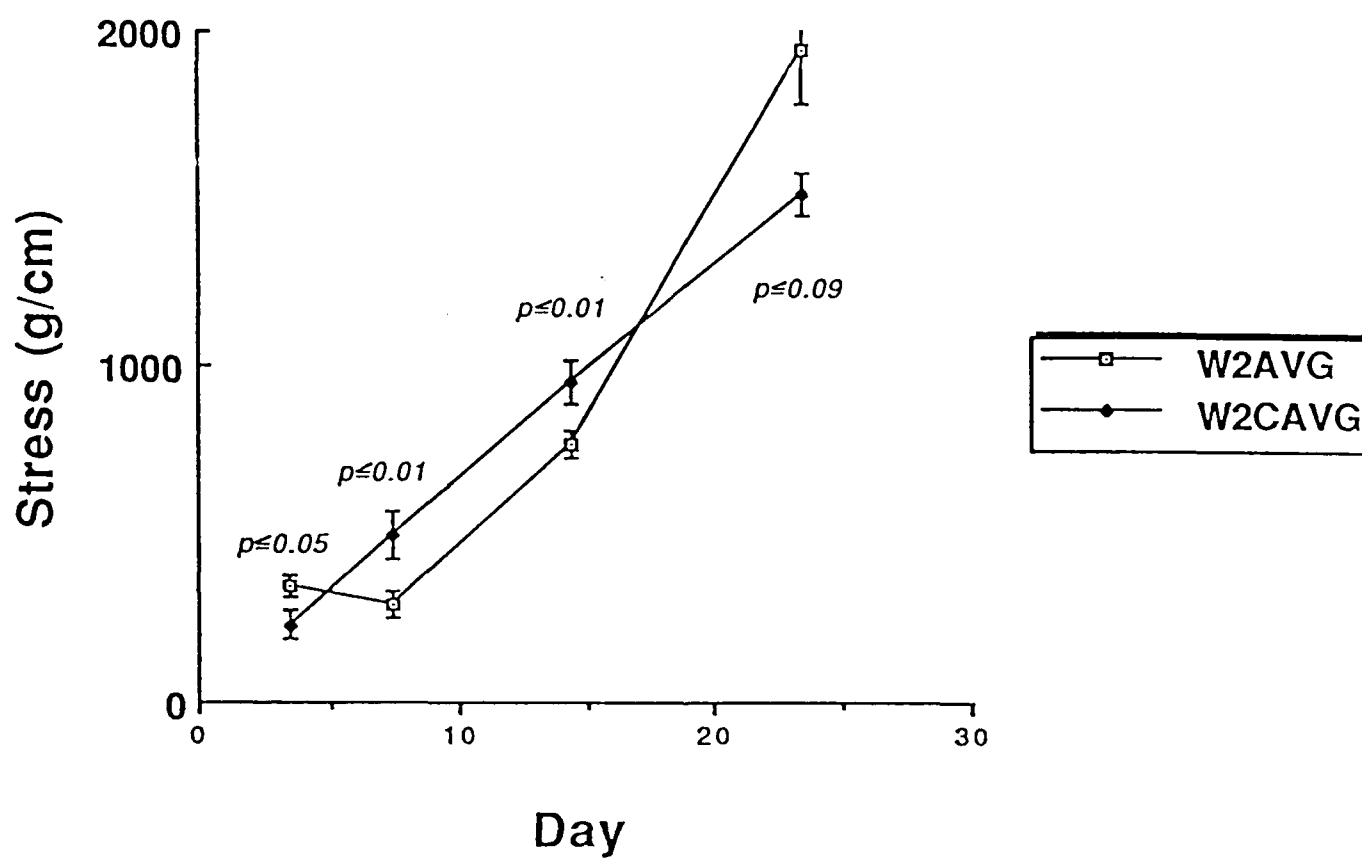
Postoperative Day	2.0W Irradiation	2.0W Control	3.5W Irradiation	3.5W Control
3	317.7 \pm 34.0 (n=7)	200.2 \pm 44.2 (n=9)	241.9 \pm 18.2 (n=7)	262.2 \pm 15.5 (n=9)
7	263.9 \pm 39.5 (n=8)	470.2 \pm 69.1 (n=8)	276.8 \pm 38.4 (n=8)	472.2 \pm 53.1 (n=8)
14	743.9 \pm 40.3 (n=8)	921.1 \pm 63.4 (n=7)	655.1 \pm 41.9 (n=8)	854.9 \pm 68.1 (n=8)
23	1909 \pm 154 (n=8)	1480 \pm 63.3 (n=5)	1689 \pm 207 (n=8)	2145 \pm 194 (n=7)

LEGEND FOR TABLE 1

The values represent average breaking strain (g force per cm incision length) for the indicated incisions. The numbers in parentheses represent the number of animals used per trial, and the tolerance values are standard errors of the means. Controls are unirradiated scalpel incisions on the contralateral side of the animal.

Figure 1

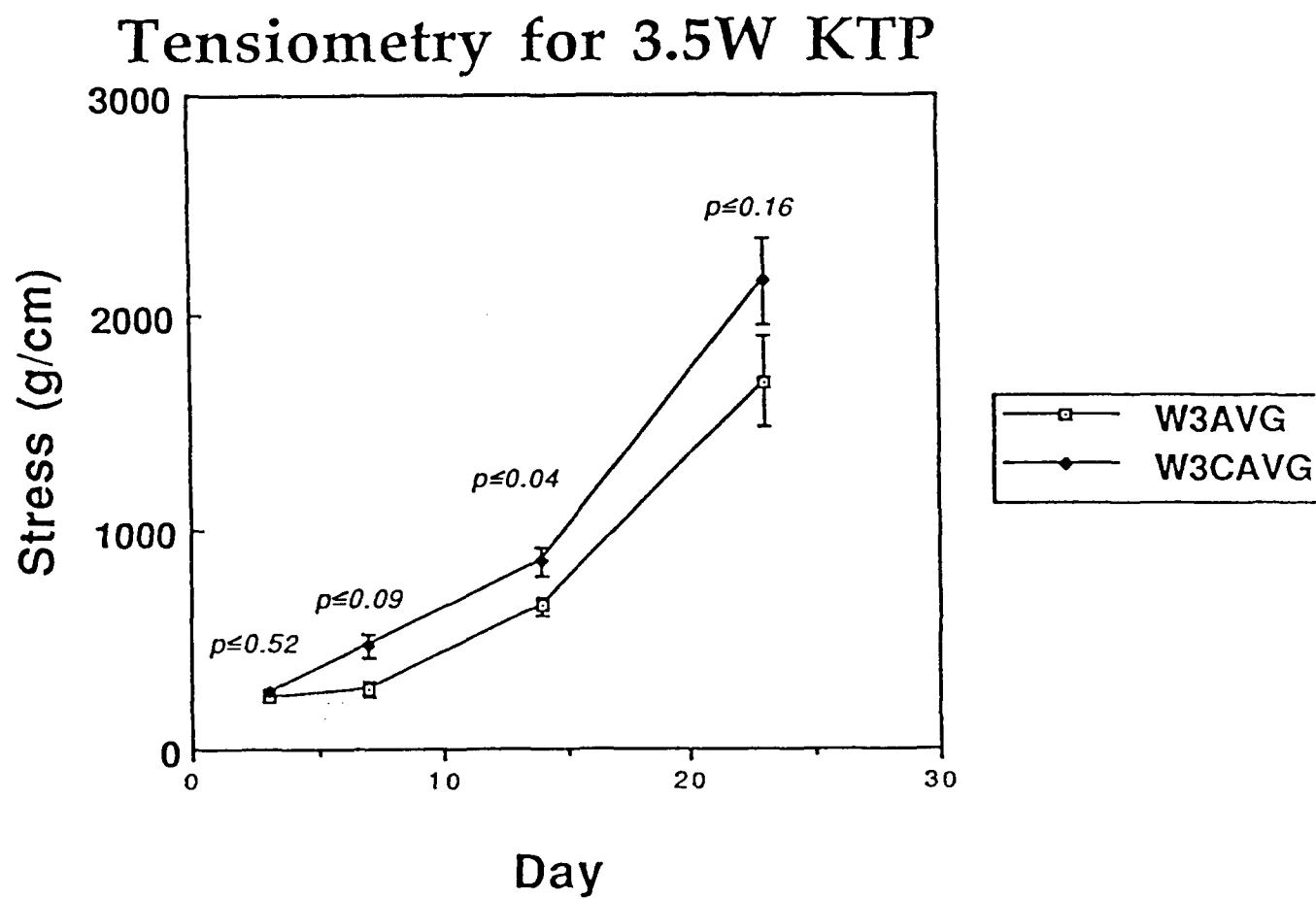
Tensiometry for 2.0W KTP



LEGEND FOR FIGURE 1

Graph illustrates temporal profile of tensiometric data for two watt irradiated incisions and their matched controls. The open boxes (W2AVG) represent mean stress values for the two watt irradiated incisions on the given days, and the solid boxes (W2CAVG) represent mean values for the two watt matched control incisions. Error bars represent standard errors of the mean. The p values were calculated using the Wilcoxon signed-rank test.

Figure 2

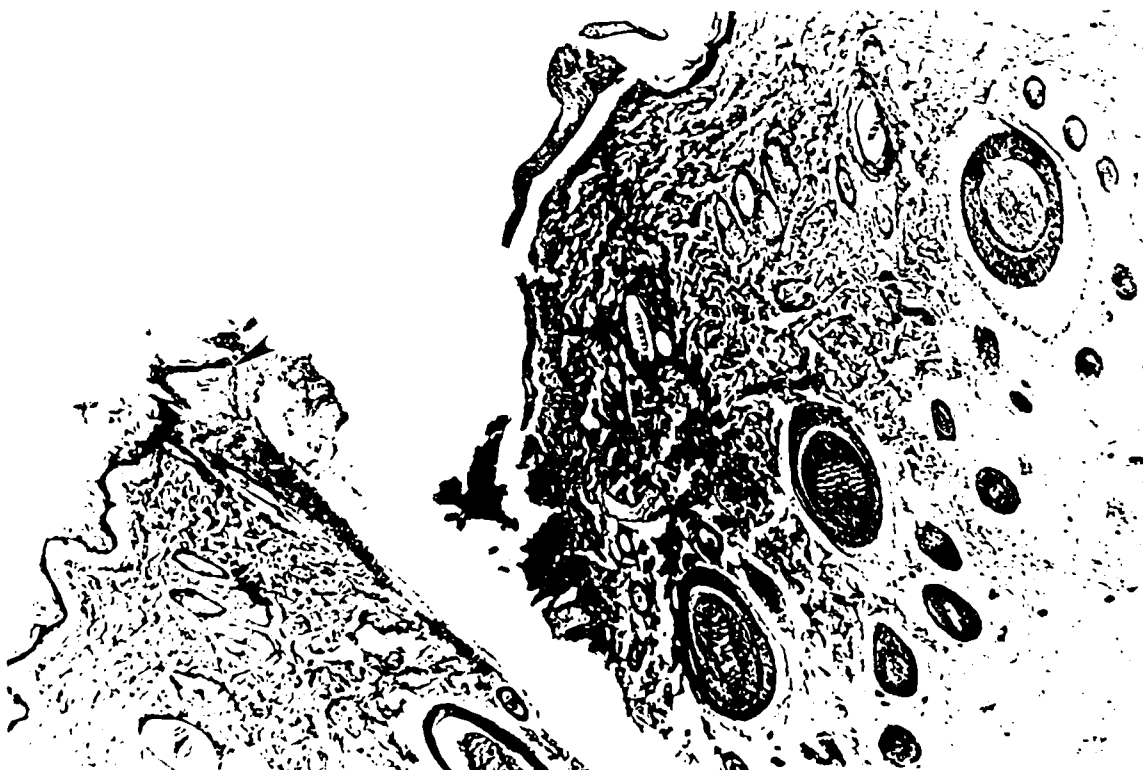


LEGEND FOR FIGURE 2

Graph illustrates temporal profile of tensiometric data for 3.5 watt irradiated incisions and their matched controls. The open boxes (W3AVG) represent mean stress values for the 3.5 watt irradiated incisions on the given days, and the solid boxes (W3CAVG) represent mean values for the 3.5 watt matched control incisions. Error bars represent standard errors of the mean. The p values were calculated using the Wilcoxon signed-rank test.

Legend for Figure 3

Figure 3: Photomicrograph of an unirradiated (control) incision harvested from an animal which was acutely sacrificed. Note the normal appearing epithelial layer (arrowhead) and subjacent dermal stroma without tissue edema. A small amount of coagulum is seen in the incisional space. Original magnification 160 X. Verhoeff's elastin stain.



Legend for Figure 4

Figure 4: Photomicrograph of a 54J (2.0W) irradiated incision from an acutely sacrificed animal. Note again the normal appearing epithelial layer (arrowhead) adjacent to the incision, the intact dermal stroma, and the absence of tissue edema. Original magnification 160 X. Verhoeff's elastin stain.



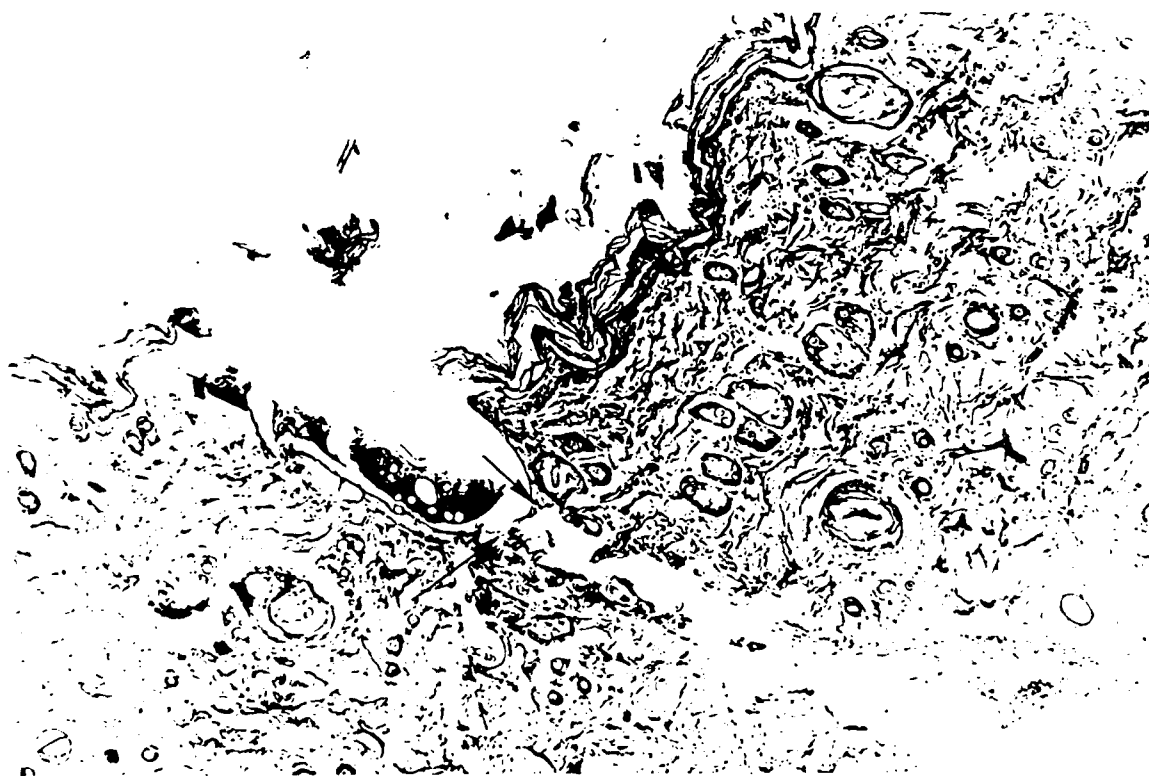
Legend for Figure 5

Figure 5: Photomicrograph of a 94.5J (3.5W) irradiated incision from an acutely sacrificed animal. Note now that although the epithelial layer remains intact (arrowhead), the superficial edge of the incision appears dark with slight eschar, and a zone of disorganized dermal collagen is seen to a depth of 0.6 mm with significant accompanying edema. Original magnification 160 X. Verhoeff's elastin stain.



Legend for Figure 6

Figure 6: Photomicrograph of an unirradiated incision at 3 days following surgery. Note that the borders of the regenerating epithelial bridge (arrows) are nearly apposed, that there are few inflammatory cells present, and that there is no apparent tissue edema. A small amount of coagulum is seen in the incision. Original magnification 160 X. Verhoeff's elastin stain.



Legend for Figure 7

Figure 7: Photomicrograph of a 54J (2.0W) irradiated incision at postoperative day 3.

In comparison to postoperative day 3 control (Figure 6), note the attenuated reepithelialization (arrows indicate epithelial borders), the dense population of inflammatory cells within the dermis (arrowhead), and the augmented coagulum in the incision. Original magnification 160 X. Verhoeff's elastin stain.



Legend for Figure 7

Figure 7: Photomicrograph of a 54J (2.0W) irradiated incision at postoperative day 3. In comparison to postoperative day 3 control (Figure 6), note the attenuated reepithelialization (arrows indicate epithelial borders), the dense population of inflammatory cells within the dermis (arrowhead), and the augmented coagulum in the incision. Original magnification 160 X. Verhoeff's elastin stain.



CO₂ LASER MICROMANIPULATOR PARALLAX ERROR RESOLVED

Jay A. Werkhaven, M.D.¹,
Jerri A. Tribble, M.S.², Robert H. Ossoff, D.M.D., M.D.³

1 Assistant Professor, Department of Otolaryngology - Head and Neck Surgery, Vanderbilt University Medical Center, Nashville, TN

2 Ph.D. Candidate in the Department of Physics, Vanderbilt University, Nashville, TN and former Research Assistant in the Department of Otolaryngology

3 Chairman and Guy M. Maness Professor, Department of Otolaryngology - Head and Neck Surgery, Vanderbilt University Medical Center, Nashville, TN

Presented as a poster to the American Academy of Otolaryngology - Head and Neck Surgery 95th Annual meeting, September 22-26, 1991, Kansas City, Missouri.

Address for correspondence:

Jay A. Werkhaven, M.D.
Department of Otolaryngology
S-2100 MCN
Vanderbilt University
Nashville, TN 37232-2559
Telephone: 615/322-7267

ABSTRACT

Most current CO₂ laser micromanipulators for microlaryngoscopy experience the parallax aiming problem. This occurs when the beam mirror is offset below the optical path for the microscope, making use of the laser difficult through small laryngoscopes or in pediatric patients. The newer "hot mirror technology" micromanipulators that are now available overcome this problem.

In addition to providing a laser beam coincident with the optical path, the newer units offer much smaller spot sizes (250-micron diameter at 400-mm focal length), but all partially absorb some of the light available for illumination. To quantitate this, optical absorption spectra were determined for five "hot mirrors". Clinical experience with more than 100 cases has demonstrated the advantages of these new mirrors to minimize mucosal thermal damage and give improved exposure for subglottic and pediatric laryngoscopy.

Key Words: CO₂ laser, micromanipulator, parallax

INTRODUCTION

The carbon dioxide laser has been used for endolaryngeal procedures since the early 1970's when Jako demonstrated the safety and effectiveness of this tool on dogs¹. The micromanipulators for these early lasers had a much larger minimum spot size compared with the standard microscope micromanipulator that is currently available. Originally, the minimum spot size was approximately 1 mm in diameter. The second generation micromanipulators used with carbon dioxide lasers had a spot size of approximately 800 microns, and the newest generation of which this report is concerned, have minimum spot sizes on the order of 250 microns.

As a consequence of engineering limitations involved with the diameter of the raw beam from the laser, the beam path of these early micromanipulators was offset below the optical path line in the microscope. This resulted in frequent instances where the CO₂ beam impacted on the rim of the laryngoscope or, worse yet, on the lip of the patient, as the beam originated from below the optical path and traveled upward to meet the optical path at a distance of 400 mm. The mirror was offset in order to provide a large enough reflecting surface for the CO₂

beam without impeding on the medial field of view through the microscope.

The newest generation of micromanipulators employ a "hot mirror" that allows the carbon dioxide beam to be directed coincident with the optical path, eliminating this problem. It has been noted that each of these hot mirrors subjectively degraded the optical spectrum and altered the color balance of the target tissues.

In order to more fully evaluate the problems with the early micromanipulators this study was undertaken to measure the extreme of the parallax problem in representative early micromanipulators and to characterize the optical characteristics of these "hot mirrors".

THE PARALLAX PROBLEM

Carbon dioxide laser micromanipulators without a "hot mirror" use a front surfaced mirror to redirect the carbon dioxide and aiming beams down the laryngoscope. This front surfaced mirror is reflective for both the carbon dioxide wavelength as well as the 632 mm wavelength of the helium neon aiming beam. The diameter of the raw beam emerging from the lens assembly on the micromanipulator is of a size that would require the front surfaced mirror to be larger than would be allowed to fit between the independent optical paths for each eye (at the objective lens

level of the microscope). If the mirror were situated in this position, a significant limitation to the nasal field of view would be encountered for each eye. To overcome this limitation, the front surfaced mirrors are mounted below the optical path length (Figure 1). In some laser micromanipulators the front surface mirror is mounted as much as 1 cm or more below the optical path length (Sharplan 719 M).

Difficulties arise when using pediatric laryngoscopes, or when using laryngoscopes or subglottiscopes with limited vertical opening heights. The proximal opening available on pediatric laryngoscopes and some subglottiscopes often is as small as 1 cm in vertical height, due to anatomic limitations.

A situation then results where the surgeon may be able to see the target at a distance of 400 mm from the objective lens, but the carbon dioxide laser beam directed up from below the optical path length then impacts on the rim of the laryngoscope (Arrow, Figure 1). Anecdotal cases have been related to the two senior authors (RHO and JW) where inadvertent burns of the patient's upper lip have occurred when this problem has not been recognized.

This parallax error (the variation between the optical path and the laser beam path) has limited the potential applications of the carbon dioxide laser for some pediatric and subglottic applications. This parallax

error problem was resolved by the development of the "hot mirror technology", which employs a lens placed in the optical path itself. Through the development of proprietary dichroic coatings these lenses are capable of reflecting the carbon dioxide laser beam (and in some cases the helium neon beam as well) coincident with the optical path down the laryngoscope (Figure 2). This results in the surgeon visualizing the target directly and may be described as "if you can see it you can hit it" which was not the case with the early micromanipulators.

Coherent Medical (Palo Alto, California) was one of the first companies to employ this hot mirror technology in a standard micromanipulator. This micromanipulator still had a spot size of 800 microns at 400 mm focal length but was the first parallax free micromanipulator available. Since the development of this micromanipulator, advances in engineering and technology have allowed the development of other hot mirror micromanipulators with much smaller spot sizes (i.e. the new generation microspot micromanipulators). These newer hot mirror micromanipulators are capable of producing spot sizes of 300 to 250 microns in diameter at 400 mm focal length. It has been noted by most surgeons operating with hot mirrors that there is a subjective decrease in the available light that is reflected back to the surgeon through these lenses and that there is also a subtle subjective

alteration in color balance. This is due to the dichroic coatings that are employed on the hot mirrors. To quantitate this optical degradation, the optical characteristics of each of the hot mirrors commercially available was performed.

MATERIALS AND METHODS

The hot mirror lens assemblies from four different manufacturers were obtained for testing. A prototype hot mirror as well as a production hot mirror was obtained from Sharplan Lasers, Inc. (Allendale, New Jersey). Hot mirrors were also tested from Coherent Medical (Palo Alto, California), Heraeus LaserSonics, Inc. (Milpitas, California), and I.L. Med, Inc. (Walpole, Massachusetts).

A Hewlett Packard 8452A diode array UV-visible spectrophotometer was used for all testing. The hot mirrors were compared to an air reference standard. Optical spectra were obtained between 400 nm wavelength (near UV) to 700 nm wavelength (near infrared).

RESULTS

The optical spectra for each of the five hot mirrors tested is represented in figure 3. Absorbance is defined as the logarithmic ratio of incident light to transmitted light. From the graphs it can be seen that all

hot mirrors reduce the available light by a smaller factor in the middle of the spectrum than at either extremes. Also, since the optical spectrum is not flat, this implies that the subjective color balance that the surgeon would view when looking through the hot mirrors would not be identical to normal vision.

The prototype Sharplan hot mirror demonstrated a significant absorption when compared to the production version of the mirror. The Coherent and I.L. Med hot mirrors have identical spectra with fairly low optical absorbance. All of the mirrors partially absorb some of the available light.

DISCUSSION

There are some subtle differences between the hot mirrors from each corporation. The Heraeus hot mirror assembly was the first on the market and does not use a helium neon aiming beam. Instead, the Heraeus unit uses a virtual image aiming dot that is provided by a light emitting diode that must be aligned with the CO₂ beam in a test firing procedure prior to use on the patient^{2,3}. The Sharplan hot mirror assembly uses a unique coating which not only reflects the carbon dioxide wavelengths but also reflects the 632 wavelength of the helium neon aiming beam as well⁴. The Coherent and I.L. Med units both utilize a very small mirror in

the center of the optical assembly to reflect the helium neon beam while the remainder of the assembly contains the coating for the carbon dioxide beam.

The Heraeus hot mirror assembly is capable of producing microspot sizes on the order of 300 microns in diameter while the others have produced spot sizes of 250 microns in diameter²⁻⁴. These small spot sizes are not the result of the hot mirror assembly alone, in fact the hot mirror assembly does not contain any focusing apparatus as such. Rather, the lens assemblies that are mounted above the hot mirror focus the carbon dioxide beam which is merely reflected off the mirror assembly to its final small spot size. It should be noted that the I.L. Med unit uses a unique approach to achieving its small spot size by mounting the laser itself within close proximity to the lenses and mirror. This is in contrast to each of the other units in which an articulated arm assembly is used to redirect the beam from the laser to the micromanipulator.

Prototype or working models of the microspot micromanipulators with the hot mirror assemblies have been used at our institution for over 2 years. To date, over 100 cases have been completed using these micro spot micromanipulators. While in the past it was difficult and frequently impossible to obtain adequate exposure for laser applications in the subglottis, or to perform pediatric microlaryngoscopy with the CO₂ laser,

it is now a routine part of our practice. The absence of the parallax problem encountered with previous micromanipulators combined with the small spot sizes has enabled the carbon dioxide laser to be applied to smaller patients and more limited surgical exposures. Pediatric and adult subglottic stenoses have been treated with sequential micro-trapdoor flaps, and the necessity of an open laryngotracheoplasty has been avoided⁴. We believe this technology to be the new standard of care for most of our microlaryngeal carbon dioxide laser applications.

CONCLUSION

Previous micromanipulators had unfortunate problems with alignment that allowed the CO₂ beam to impact on the rim of the laryngoscope or on the patient due to beam offset from the optical path. The new generation of micro spot micromanipulators with hot mirror technology has solved the parallax problem of exposure to the distal subglottis in adults, and for the larynx in pediatric patients. The newer micromanipulators have been in use now for over 2 years and in greater than 100 patients and have been found to be an absolute necessity for the performance of certain procedures. We believe these new units to be the new standard of instrumentation for use in endoscopic microlaryngeal cases.

This research was funded entirely within the Department of Otolaryngology and no outside funding was used. The authors wish to acknowledge that no one involved has any financial interest in any of the companies whose products are described herein. Dr. Ossoff served as a consultant to Sharplan Lasers, Inc. for the development of their microspot micromanipulator.

REFERENCES

1. Jako GJ: Laser Surgery of the vocal cords. Laryngoscope 1972;82:2204-2216.
2. Shapshay SM, Wallace RA, Kveton JF, Hybels RL, Setzer SE: New microspot micromanipulator for CO₂ laser applications in otolaryngology-head and neck surgery. Otolaryngol Head Neck Surg 1988;98:179-181.
3. Shapshay SM, Wallace RA, Kveton JF, Hybels RL, Bohigian RK, Setzer SE: New microspot micromanipulator for carbon dioxide laser surgery in otolaryngology. Arch Otolaryngol Head Neck Surg 1988;114:1012-1015.
4. Ossoff RH, Werkhaven JA, Rafe J, Abraham M: Advanced microspot microslad for the CO₂ laser. Otolaryngol Head Neck Surg 1991;105:411-414.

LEGENDS

Figure 1. Micromanipulator with parallax error. Laser beam is offset below the optical path. Note potential impact of laser beam with rim of laryngoscope or patient's lip (arrow).

Figure 2. Micromanipulator with "hot mirror" lens. Laser beam path is coincident with optical path.

Figure 3. UV-visible absorbance spectra for the prototype (S₁) and production (S₂) Sharplan, Coherent ,I.L. Med and Heraeus mirrors.

In Press Book Chapter

H.L. Meyerhoff, D.H. Rice, Editors, Otolaryngology -
Head & Neck Surgery H.B. Saunders, Co.

IV-G

LASERS

Jay A. Werkhaven, M.D.
Robert H. Ossoff, D.M.D., M.D.
David Harris, M.D.

INTRODUCTION

The optical laser was first developed in 1960. Among the first medical applications for lasers was the dermatologic application of this Ruby laser in 1964. Since that time, the application of lasers in medical and surgical uses has grown quite extensively. Within the field of otolaryngology, Jako began his pioneering work in 1967 with the use of the Carbon Dioxide laser for laryngeal applications. Also in 1967, Sataloff reported the first applications of Neodymium and Ruby lasers for otosclerosis. The acceptance of lasers within the field of otolaryngology has progressed to the point now, that the American Board of Otolaryngology recommends that each residency program provide residents with experience and instruction in safety and use of, at a minimum, the Carbon Dioxide laser. The list of types of lasers in routine use within the field of Otolaryngology-Head and Neck Surgery is growing daily with a partial list that includes the Carbon Dioxide, Argon, ND:YAG, KTP and Flash Lamp or Argon Pumped Dye Lasers. Experimental lasers which have not yet received FDA approval for otolaryngology applications, but which may hold potential for the future include the Excimer lasers and other near and mid infrared laser such as the Erbium YAG and Holmium YAG. One of the future lasers under development as an off-shoot of the strategic defense initiative is the Tunable Free Electron Laser. This laser, although still experimental, eventually has the potential for being tunable from X-ray wavelengths to far infrared, and provide

power levels ranging from milliwatts to megawatts. This laser may eventually be the ultimate answer to the question of (Which laser, When and Why?)

Vital to understanding the current and future laser instruments and applications is an understanding of three principle parameters of laser energy: wavelength, power density, and timing. In addition, its also necessary to have an understanding of the interaction of these three parameters with biological tissue to fully appreciate the range of biological effects that result.

This chapter is a brief introduction to laser biophysics. This will include the generation of the laser beam, the transmission of the laser beam to the tissue, and the understanding of some of the limitations. In addition, this chapter will introduce the concept of optical biophysics i.e. an introduction to the interaction of light with tissue and the resulting biological effects.

HISTORY

The ideological basis for the concept of the laser was proposed in the late 19th Century with atomic Quantum Theory. Einstein in 1917 predicted the existence of a phenomenon known as the stimulated emission of energy from atoms. This was only a theory until Schawloss and Towns in 1958 developed the first working maser (microwave application by stimulated emission of radiation). They were awarded the Nobel Prize for this. (Chester

Gould) The maser operating in the microwave length was invisible. The first visible laser (Light Application by Stimulated emission of Radiation) was invented in 1960 by Maiman. Advances came quickly with the development of the gas laser in 1961 by Javan, the Neodymium Glass Pulse laser by Johnson in 1961 and the CO₂ laser by Patel in 1964. The Ruby laser invented by Maymen in 1960 was first applied for medical applications by Leon Goldman in the field of dermatology for the treatment of port-wine stains with moderate success. Sataloff in 1967 reported the effects of Neodymium Glass lasers and Ruby lasers used for stapedotomy and otosclerosis with some success. Since that time, the introduction of the Argon laser, Neodymium YAG laser, KTP laser, Argon Pump Dye and Flash Lamp Pump Dye have all been shown to have unique and beneficial applications within the field of medicine and surgery.

The future history of laser development applications looks very bright. In the near future, head and neck applications of the Excimer (near ultraviolet) and newer infrared lasers such as the Erbium YAG (2.9 micron wavelength) and Holmium YAG (2.12) show great promise.

Within the field of otology, the CO₂ laser, KTP and Argon laser have been the lasers most studied and used. Each laser has some distinct advantages based on understanding of their wavelength/tissue effects and each in turn has several distinct disadvantages which will be covered more in depth in the section on laser tissue interaction.

BASIC LASER PHYSICS

In this section, we will explain the generation of the laser beam itself, and include some description of the various laser systems relating to the types of lasers and the delivery systems that are unique for each laser.

GENERATION OF A LASER BEAM

The basic phenomenon of lasing takes place usually at the atomic level, although certain lasers such as the Argon laser use ions, and the Carbon Dioxide laser uses molecules. For purposes of the initial discussion here, we will discuss the generation of a laser beam from a single atom. The atom is generally represented as a core of neutrons and protons surrounded by a cloud of electrons located in discrete orbitals. Those orbitals that are more distant from the nucleus contain electrons of higher energies. These energies are directly related to the distance from the nucleus. In the early 19th Century, the atomic Quantum Theory proposed that each of these discrete orbitals are separate and independent. This implied that there was not a continuous gradation of energies between orbitals and that a unique energy was necessary to change the electron from one orbital to another orbital. The most stable configuration of an atom is called the ground state. This state represents the lowest possible energy present within that particular atom.

When atoms absorb energy, these electrons are elevated to

higher energy levels. An excited electron may spontaneously release this energy and decay back to a lower orbit (lower energy state). This energy released must correspond by the laws of conservation of energy to the energy that was originally placed into the system to excite this electron to a higher energy level in the first place. This energy may be released as a photon (as light) and/or as heat, (as kinetic energy). This release of energy may occur in several transitions or in one large transition. The spontaneous release of energy if it is omitted as light, is called spontaneous emission. Molecular lasing differs somewhat from atomic lasing in that molecules are much more complex structures. Not only do molecules have unique electron orbitals as earlier stated, but they also have rotational and vibrational modes that may also represent higher energy states. As molecules increase in size or the number of atoms, the potential number of energy levels increases. Large organic molecules that form the substrate for lasing in an Argon Pumped Dye laser thus can be responsible for a broad range of output wavelengths.

Stimulated emission of energy was proposed by Einstein in 1917, as was predicted from Quantum Theory. Energy transitions must be initiated by input of energy of the appropriate discrete amounts. A photon entering the system of appropriate energy level may trigger the decay of an excited electron. This decay transition again may occur in one or in several steps and may result in the emission of a photon. Stimulated emission may

occur only when the incident photon has the same energy as the photon that is released. This triggers a chain reaction with the result that one photon results in the release of two, and these two photons may stimulate the release of four photons. Thus, the final result is an increase in the photons of identical energy and in a simultaneous and in-parallel vector. Additionally, the photon that is released is temporally locked to the oscillations of the first photon. The final result is that the incident of photon and the emitted photon are coherent, monodramatic and spatially and temporally aligned. If all of the atoms in a lasing medium exist in an excited state, then the incident photon can initiate a cascade very similar to a nuclear fusion reaction. One photon can yield two, two photons can yield four and so on, on a chain reaction. This can only occur provided that all of the atoms in the lasing medium are at a higher energy state than the ground state. When more than half of the atoms in such a system are in the excited state, the system is said to be in population envision. Lasing can only continue when the atoms are kept in a population aversion. Should for instance, a lasing medium be brought up into an excited state, and then stimulated, this would result in one very brief, very intense pulse, and this is the mechanism of functioning for certain of the lasers which will be discussed later. If one wished to maintain a continuous wave output from a laser, then energy must be continuously applied to the system to keep the atoms in such a population inversion.

The direct emission of photons from such a stimulated system may be random. Photons may exit the system from the side walls, but some of the photons eventually are going to start traveling parallel to the long path of the lasing cavity. A laser is composed of lasing cavity with mirrors on either end to reflect these photons back into the system. These photons, traveling back and forth between the two mirrors, are able to continue this photon chain reaction occurring in a longitudinal axis and reinforce the laser beam by this method. Photons that are randomly scattered from the system and exiting from another direction other than long axis of the lasing medium, are then lost to the system and often converted to heat. This is the reason that many of these lasers need quite extensive cooling systems (either air cooled or water cooled systems). This is also the reason that most lasers have a very low operating efficiency. For example, for an efficient carbon dioxide laser has an operating efficiency of only 15% or less.

The two mirrors of this system may either be 100% reflective mirrors in which case the laser would continue to build up in energy within the tube until eventually the mirror was destroyed, or partially reflecting allowing a continuous beam. Another system uses a mirror in a shutter, and when the light to be released in one very strong pulse. This system which allows for a build-up of a very powerful pulse is employed in some of the Nd:YAG Q switch lasers and will be discussed later. Most often, one of the mirrors is totally reflecting while the other allows a

portion of the light to escape. This produces a continuous wave beam (providing of course energy is continuously applied to the system to keep the atoms in a population of inversion). There is a precise relationship between the wavelength output and the distance between the mirrors. The mirrors must be an integral wavelength distance separate from one another. Otherwise, standing waves within the system would serve to decrease the output efficiency of the laser cavity.

The relationship between the energy and wavelength of a photon is expressed via the constant in the following equation $E = h\nu$ where E is energy, ν is the frequency and h is Planck's constant (6.626×10^{-34} Joule seconds). From this equation, it can be seen that the energy in a photon is directly proportional to the frequency. From the relationship $\lambda\nu = c$ where λ is the wavelength, ν is the frequency and c is the speed of light, it can be seen that the frequency is inversely proportional to wavelength. The implications here are that short wavelength ultraviolet and blue light have higher energy than longer wavelength red or infrared light.

The relationship between energy and wavelength is very important. When considering both the absorption and emission of light by an atom or molecular species, if the transition from the ground state to the excited state requires an amount of energy that is equal to the energy in an incident photon, then that photon is easily absorbed. Conversely, the energy decay back to a ground state is accompanied by the emission of a photon of

specific wavelength based on the energy and the transition. The implications from this are that different species of atoms have different absorption spectra and thus the emission spectra, (or laser output wavelength). Specific atomic and molecular species are unique and possess discrete energy characteristics for each electron orbital.

Characteristics of Laser Light

From the previous discussion, it can be seen that the mechanics of generating a laser beam results in the generation of light that is unique from normal light. Normal light such as that from the sun or from a light bulb is composed of multiple wavelengths traveling in various directions at different time frames. Laser light has three basic characteristics that are unique. One, laser light is monochromatic. Since the photons are emitted from a homogeneous population of atoms or molecules, all must come from the same energy transitions. These photons are all of identical wavelength. This monochromaticity is unique to lasers and enables tunable lasers to target specific biomolecules having absorption at that characteristic wavelength. Two, laser light is coherent. All of the photons in a laser beam, because they are stimulated by the same initial photon, oscillate together in phase. This coherence of the output of photons permits focusing the beam into a very small spot to create extremely high power densities. Three, laser light is collimated. Because of the design of the laser cavity, the output energy is concentrated into a narrow minimally divergent

beam. For example, in a surgical CO₂ laser, the beam can be directed down the center of a long articulated arm to be focussed at the end by lens and hand piece or a micromanipulator. Because there is minimal diversions of the beam, there is very little energy lost in this transmission within the articulated arm.

Timing of the Laser Beam

The laser beam can either be continuous (i.e. on all the time) or may be intermittent or pulsed. Laser pulses can be generated from the femtosecond (10^{-15} second) all the way up to multiple seconds of pulses by several different means. These mechanisms of pulsing a laser beam range from physical pulsing by means of a shutter, to pulsing the energy input into a laser medium, to using a optical shutter within the cavity to release all of the energy at a short-time duration.

Nanosecond pulses are generated within an Nd:YAG laser through a mechanism called Q-switching. This is most commonly used in the ophthalmologic lasers. The flash lamp within an Nd:YAG laser stimulates the YAG crystal to generate the laser pulse. At either end of the YAG crystal is a 100% reflective mirror. In the simplest of Q-switching cases, one of these mirrors is rotating very fast and constrains the laser output within the cavity. As the mirror rotates, a open window eventually crosses across the cavity and releases the laser energy. This releases all of the stored energy in one burst of power. Another method of generating Q-switching is to put an optical shutter within the cavity that reflects light until a

higher enough energy level is obtained. At this point, the chemical shutter undergoes a phased transition which allows the energy to escape. The result of each of these methods is that very high powers are generated with very short pulse durations. Such high levels of energy directed into very small volumes can disrupt the structure of materials and cause damage via electromechanical or acoustic shock. The practical application of this is for capsulotomy after cataract surgery.

Some pulsed lasers get their timing parameters from the timing of the pump source. The original flash light pump Ruby laser invented in the 1960's produced its laser output beam in this manner. For every flash of the flash lamp the chromium atoms within the Ruby laser are pumped into an excited state and spontaneous decay triggered the stimulated emission resulting in a brief flash of laser light. Repetitive pulses can be generated at the rate determined by the cycle time of the flash lamp.

Most gas laser which can function in the continuous mode use a mechanical shutter to modulate the beam. This is a impervious metal plate that fits across the beam path and is opened only when the actuating foot switch is engaged. This system is the most common system in use in the Argon and CO₂ lasers and is fail safe feature also found in most medical laser systems as a safety switch. Shutters are usually accurate down to 50 milliseconds, although some are capable of functioning much faster than this in experimental lasers. A unique phenomenon with the CO₂ laser is the super pulse mode. Pulses on the order

of microseconds are generated by pumping the laser cavity either with radio frequency energy or high peak power electric current. The energy is not stored within the cavity but is released at the time of generation and the repetition rate is determined by the cycle time of the energy input source. Powers on Medical CO₂ lasers as high as 1 kilowatt may be generated at intervals. The repetition rate of the pulse generation may vary from two pulses per second to as high as 5,000 pulses per second on some lasers. The total energy delivered to the tissue is a function of the pulse duration and the repetition rate. In general, the more pulses delivered to the tissue, the higher the average power applied to the tissue. Further discussion of super pulse is covered in the section on (laser tissue interaction).

Types of Lasers

Given enough energy input, almost any material can be made to undergo stimulated emission. Newer medical lasers are now being designed from the application standpoint initially, as opposed to early laser design. Early laser design was on the order of "generate the laser beam and let's see what it does with tissue." Now, however, surgeons are able to request a wavelength and the physicists are able to build a laser with that specific output. Unfortunately, sometimes the efficiency of energy conversion is not very good and the output energies are sometimes too low to be medically useful, but do provide some interesting data within a laboratory setting. Lasers are generally identified by the nature of the laser medium. This laser medium

can exist in a solid state as in the Nd:YAG laser, within a liquid state as within the Argon pumped dye laser, within a gaseous state as in the CO₂ laser or as an ion in the Argon laser. In addition, two lasers which are just beginning to have medical application, are the Excimer laser in which a chemical reaction generates the laser beam and the Free Electron Laser in which the lasing medium is actually excited electrons. A partial listing of some of the lasers that have been tested for medical applications is included in Table X. For brevity, we will discuss only those lasers in most common use in Otolaryngology-Head and Neck Surgery at the present time, and make note of some of the potentials of the newer lasers.

Carbon Dioxide Gas Laser

The carbon dioxide laser actually uses a mixture of nitrogen, carbon dioxide and helium gasses in its cavity. Energy can be applied to the carbon dioxide laser either by radio frequency or direct current. Direct current can be applied either longitudinally down the cavity or transversely across the cavity. While transversely excited carbon dioxide lasers are capable of generating very high peak powers on the order of kilowatts, these lasers are generally reserved for commercial applications as they require careful alignment and maintenance. Most CO₂ lasers today now use radio frequency and sealed tube systems, some of the earlier lasers were flowing gas systems which required constant replenishment of the laser mixture, because with continued applied energy some of the carbon dioxide

atoms are eventually broken down into component atoms. Energy applied to a carbon dioxide laser cavity is initially absorbed by the nitrogen molecule. The decay of energy from the nitrogen molecule then allows transfer of energy to the carbon dioxide molecule. Specifically, the output energy of 10.6 microns represents one of the bending frequencies of the CO₂ molecule. Helium gas helps to dissipate the heat from the laser cavity. Because the carbon dioxide lasing medium is a molecule, there is the capability for these lasers to produce a wide range of possible energy level transitions and therefore wavelength output. The wavelength of 10.6 is the most efficient output for the CO₂ laser and efficiencies on the order of 20% are possible. It is fortuitous that the CO₂ laser invented in 1964 is absorbed well by water and since tissue is composed of between 70 and 85% water, this laser has now become the workhorse laser in medicine. The specific reactions of the CO₂ laser with tissue are covered more fully under the section (Laser Tissue Interaction).

Argon Ion Laser

This laser uses charged argon ions as the lasing medium. Because argon ions have such a diffuse range of energy levels available, this laser gives rise to a composite laser output with several visible wavelength created simultaneously. The strongest emissions are at 488 nanometers and 514 nanometers, although there are several other output wavelengths that are easily identified on spectroscopy. Each wavelength may be

selectively filtered out to give a monochromatic beam if desired and the green wavelength is commonly used by ophthalmologists for retinal photocoagulation. Argon lasers are generally much less efficient than CO₂ lasers because much of the energy input into the system must be used to generate the argon ion, and then further energy must be applied to stimulate the ion to a state of population inversion. Inherent in all of this energy input is high heat generated, and most argon lasers need to be cooled by flowing water. Medical argon lasers are now capable of producing on the order of 20 watts and their beams are capable of being transmitted to via quartz fibers.

Dye Laser

There are two dye lasers in common use within medicine currently. One is the Argon Pumped Dye Laser, and the other is the Flash Lamp Excited Dye Laser (FEDL). In the Argon pumped dye laser, an argon laser is used as the input energy source to initiate the stimulation of the dye molecules. In the Flash Lamp Excited Dye Laser, a flash lamp performs the same function. Within the laser, the dye is constrained within a cavity and energy placed into the dye results in a population inversion and generation of the laser beam. Because the dye is a complex macromolecule, the potential exists for multiple wavelength output. In practice, once the dye is energized it often lases at multiple output frequencies simultaneously. The output from a dye laser is then directed across a diffraction grating which allows the selection and tuning of one particular wavelength

(usually accurate within 1/2 to 2 nanometers). Because of the design of the cavity, dyes can be changed to allow a wide range of tunability for output wavelengths and the selection of dyes that are efficient in the particular wavelength under consideration.

Nd:YAG Solid State Laser

The Nd:YAG laser is a solid state laser using the rare earth element neodymium in a crystal composed of yttrium and aluminum in a garnet arrangement. This laser is stimulated using a flash lamp and, although the output appears continuous, in reality it is a quasi-continuous laser. Quasi-continuous lasers function with repetition rates so fast as to appear to be continuous for all intents and purposes. The output of the Nd:YAG laser is in the near infrared at 1.064 microns, but because of the arrangement of the crystal other outputs are possible from this same laser. It should also be noted that the neodymium glass laser was invented first and has an output of 1.060 microns. This output demonstrates an important point in the physics of lasers in that the environment surrounding the lasing material may alter the output wavelength by placing constraints on the energy level transitions available. Most YAG lasers initially were water cooled because of the high heat generated, but most recently several medical YAG lasers have come on the market which are air cooled with power capabilities in the 100 watt range.

Frequency Doubled YAG

Several years ago when argon lasers were not capable of

producing power outputs in the deep coagulation and vaporization range (i.e. above 8 watts) a technological variation of the Nd:YAG laser was produced. This unit was known as the KTP 532 system. In this unit, a YAG output wavelength of 1.064 microns was directed through a potassium (K) titanium (T), Phosphorus (P) non linear crystal. This crystal has the unique property of doubling the frequency of the laser beam (thereby cutting the wavelength in half). This laser was capable of generating out approximately 17 watts of power from a 100 watt YAG input power. Its output is therefore in the green wavelength and falls intermediate between two of the major absorption bands for hemoglobin. There are other crystals which exist which can triple the Nd:YAG frequency and produce wavelengths in the near ultraviolet region at 354 nanometers, but these have not seen extensive medical use yet.

Excimer

The term excimer is a contraction of the words "excited dimer". Molecular dimers such as argon fluoride or xenon chloride are used to produce the laser beam. Outputs are ultra short pulses in the near ultraviolet range at wavelengths from 157 to 351 nanometers (please see table). Due to the extreme short pulse duration and the high energy of ultraviolet wavelengths, the effect of the excimer laser is photoablative. Photoablative effects can work by physically disrupting the molecular bonds within tissue. This will be covered further in the section on laser tissue interaction.

Equipment Requirements

Each laser will have unique power, water and maintenance requirements which should be carefully considered before purchase and installation in the operating room. Many times, medical lasers require modifications to the operating room that need to be in place before a laser can be used, and this may unnecessarily delay the start up of the medical laser. Certain lasers require specific water and electrical modifications to specific operating rooms. In addition, certain lasers are too large to be easily transported between rooms, therefore one operating room should be dedicated as a laser operating room. Some carbon dioxide lasers are low power (generally less than 40 watts and usually less than 40 to 60 pounds using 110 volt 28 amp power). These lasers are self contained and most often air cooled. The higher power CO₂ lasers have self contained water cooling systems and do not require external cooling, although some of the higher power CO₂ lasers use two 110 volt, 20 to 30 amp circuits: one for the cooling system and one for the laser. Most carbon dioxide lasers on the market at the present time are sealed systems which means that no external tanks need to be attached to the CO₂ system to generate the laser beam, although some of these lasers do require an external nitrogen purge gas system to be attached. Sealed tube systems have a fairly long life-time in the current lasers and, because of the stability and ease of use, most manufactures have switched to this type of system.

Nd:YAG lasers due to their inefficiency usually require 220 volt AC 40 to 60 amp power, although some newer units on the market are now powered with 115 volt circuitry. Older Nd:YAG units often needed an external water source for cooling, but the newer units that are available up to 100 watts of power are now available with internal cooling systems. These older high powered YAG lasers, the KTP laser and the Argon laser all require a source of cool water to operate the system. Flow rates of several liters per minute are often required. In addition, a separate consideration in the south is that tap water may not be cool enough and built-in interlocks within the lasers will shut the system down. Often, an inter-cooler needs to be installed so that the tap water can be run through an air conditioning unit to make it cool enough to allow the lasers to be used. All these requirements should be considered before purchasing a laser and before having a laser shipped, so that the operating room and related facilities are ready for laser use.

Laser Delivery Systems

The beam emitted from a laser tube is a collimated monochromatic coherent beam of light traveling in a straight direction. Some mechanical system must be employed to re-direct the beam in a useful fashion so that it can be used for medical applications (the alternative is to move the patient underneath the beam itself).

Hand Held Laser

Helium neon laser pointers, gallium arsenide diode lasers

and one brand of a low output (less than 20 watt CO₂ laser) can be held in the hand like a pencil. The beam is directed to the tissue without any delivery device except for a focussing lens. Diode array lasers are now capable of providing power up into the watt range and experimental systems using diode lasers through non-linear crystals can provide a variety of wavelengths with powers around 1 watt.

Articulated Arms

Mid and far infrared lasers such as the carbon monoxide and carbon dioxide lasers use an articulated arm system to deliver the beam. This is because there are no FDA approved optical fibers at the present time capable of transmitting in this wavelength. The laser beam is directed down the center of a series of hollow tubes with mirrors positioned at the ends to reflect the beam at 90° angles. Mirrors are mounted in a gimble joint to allow free rotation in three dimensions. The articulated arm then can be attached to a hand piece, microscope or bronchoscope adapter, or the newer CO₂ wave guides (please see below). Some of the hand pieces provide a variable spot size and obviate the need for moving the hand piece away from the tissue to de-focus the beam. The accessories attached to the end of an articulate arm often need the accessory nitrogen gas purge system to keep the laser plume from fouling the reflective mirror or lenses. The articulated arm is able to maintain both monochromaticity and coherence of the laser beam unlike fibers or wave guides.

Optical Fibers

Most lasers from the near ultraviolet up through the near infrared (including the visible spectrum) are capable of being transmitted through small diameter flexible fibers. The advantage to these fibers is that they may be inserted through endoscopes to deliver energy deep into the body. This has been one of the major advances in the use of lasers, and smaller and smaller fibers are now permitting the use of lasers to re-canalize blocked coronary arteries and peripheral veins. Some of these fibers while being only 2mm in diameter, also employ a visualization system as well as the laser delivery system.

Quartz silica fibers transmit light energy from ultraviolet to near infrared wave lengths, and thus this material is useful for delivering energy of Excimer, Argon, KTP, dye and YAG lasers, but unfortunately are not capable of delivering the output from a carbon dioxide laser. Fibers that are capable of transmitting the carbon dioxide wavelength are in the developmental stage and several are on clinical trials right now. Materials include tellurium bromide and silver iodide, but these materials are very fragile and tellurium specifically is toxic to the body and thus a bio-compatible cladding which protects the body from this material has to be developed. These fibers have a very complex crystal matrix and have a limited bend radius before cracking, but still are capable of maintaining a tighter bend radius than the hollow wave guides that have currently been developed for the CO₂ laser (please see below).

These quartz fibers alter the characteristics of the laser beam. The beam is reflected multiple times within the fiber due to the difference between the optical coefficient between the fiber itself and the cladding. Because of the multiple reflections within the fiber, although the beam remains monochromatic, it loses its coherence. Most fibers do not employ a focussing lens at their terminal end, and therefore the beam diverges fairly quickly once it leaves the fiber. This divergence is a function of the optical material and the size of the fiber and can range from 8° of divergence to as high as a 30° divergence. The implications for this range of divergence are that the fiber must be held closer to the tissue to maintain high enough power density to be able to perform vaporization and or coagulation. For most endoscopic applications, the end of the fiber is cleaved smooth to provide an even distribution of light output, so that there is no hot spot generated. Another point should be made about using the fibers with endoscopes is that because of the divergence of the beam as soon as it leaves the fiber, if the fiber is accidentally withdrawn within the endoscope, the rapid divergence of the laser beam can be responsible for melting the tip of the bronchoscope (a very expensive mistake). Thus, when using a laser endoscopically, it is imperative that one can see the fiber and the point to be vaporized or coagulated at the same time to avoid this mistake.

Contact Tips

The development of a tapered lens made of silicone or

synthetic sapphire allows the re-focusing of the laser beam from the end of the optical fiber. This advantage of returning a lens system to the optical fiber actually can allow one to concentrate the laser beam into a smaller diameter than that carried through the optical fiber itself. These optical fibers are available in various shapes and lengths and use silica lenses for Argon applications and generally synthetic sapphire for Nd:YAG applications. These contact tips come in several shapes and sizes and the shape determines the concentration of the light energy. A very long tapering point brings the laser energy into a very concentrated point for cutting and with this lens in contact with the tissue, this serves to cut through tissue "like butter". If the tip is not held in contact with the tissue however, the laser energy has limited methods for dispersement and can actually vaporize the tip of the lens, effectively ruining it. These contact tips can be very expensive running from \$150 to \$600 dollars apiece for specialized shapes. Other shapes that are available include a chisel tip that allows one to shave layers off a tissue from a obstructing tumor, and frosted tips which are capable of dispersing light at all angles which are especially effective at coagulation.

Wave Guides

Several manufactures have recently introduced hollow wave guides which can be used to transmit the 10.6 nanometer light from the carbon dioxide laser. These wave guides range from 3mm in diameter down to 2.7mm in diameter and have some limited

flexibility, although the size and capability for bend radius limits their applications to generally free hand work. They are not capable of being placed down a flexible endoscope.

Gynecologist were among the first to explore the capabilities of these CO₂ wave guides inter-abdominally and newer advances in these wave guides have seen their adoption by orthopedic surgeons for arthroscopy and potentially by otolaryngologist for intranasal work.

Microscope and Bronchoscope Adapters

The near ultraviolet, visible and near infrared wavelengths can be transmitted through fibers and therefore can be passed down the side channel on ventilating bronchoscopes or down the operating channel in flexible bronchoscopes. For laryngoscopy work and for otologic work hand, held probes composed of these fibers may be used. The KTP laser also has a microscope adapter which functions by bringing the laser beam into the adapter via a fiber and then this is reflected off a mirror and redirected into the operating field. A necessary modification for each of these units is an eye piece filter to protect the surgeons eyes while these lasers are being used.

The carbon dioxide laser beam because it cannot be passed through a flexible fiber is often directed down the center of a rigid ventilating bronchoscope either as a collimated beam or through a rigid wave guide. When the laser beam is directed as a collimated beam, the articulated arm is connected to a bronchoscope adapter, but employs a beam splitter to redirect,

laser beam and allow visualization of the target simultaneously. The aiming beam is also re-directed to allow the surgeon to plan the laser impacts. The nitrogen gas purge system is used to remove laser plume and smoke from the operating channel of the bronchoscope. The microscope adapters (also called micromanipulator) allow lasers to be used for laryngeal, otologic or precise microscopic control of laser beam. The micromanipulator has a gimble controlled mirror assembly that is attached in front of the objective lens of a microscope. As mentioned before, the KTP laser delivers the beam to the micromanipulator by means of a flexible fiber and the CO₂ laser directs the beam to the micromanipulator by means of the articulating arm. Either the mirror itself or another lens with a micromanipulator is used to focus the laser beam. Microscopic focal lengths from 200 to 400mm may be selected allowing use from the standard otologic operating distance all the way out to the standard laryngeal operating distance. Because of the variation in focal length, the spot size of the laser also varies. In the traditional micromanipulator (prior to those developed about 1989) the smallest spot size capable at 400mm focal length was approximately 750 microns while the spot size at 200 microns was approximately 350 microns in diameter. This spot size is a function of both the focal length and the wavelength of the laser beam itself. In general, the shorter the wavelength of the laser the tighter focus can be obtained. The newer micromanipulator recently developed for use with the carbon dioxide laser are now

known as "microspots". These microspots are capable of yielding a focused beam of 250 micron diameter at 400mm and 125 microns at 200mm when properly focused. This has implications for the amount of power that is necessary to be used and will be covered later under the section on laser tissue interactions. A potential difficulty with some of the older micromanipulator for use with the carbon dioxide laser is a concept known as parallax. The carbon dioxide laser beam as it emerges from the lasing tube is broad, and a larger mirror than that used for a fiber is used to redirect the beam. The size of this mirror is limited to the inter-pupillary distance on the microscope and oftentimes this is not big enough to redirect the entire CO₂ beam. If the mirror was large enough and placed inter pupillary, it would then interfere with the nasal field of view for both eyes. Many of the micromanipulator in use bypass the mirror size limit by off setting the mirror below the plane of vision by almost to 1 to 1 1/2cm. This allows them to use a large enough mirror to redirect the beam. The difficulty with this engineering design however, is that when used in tight areas such as laryngoscopy in children when using a subglottiscope with limited vertical height, this discrepancy between the plane of view and the path of laser beam may lead to inadvertent burns to the patient near the lip of the laryngoscope (Figure X). The newer microspots and the some of the newer micromanipulator from some of the companies employ a different optical system using a "hot mirror" assembly. This hot mirror is specially coated lens

which is able to reflect the far infrared wave length of the CO₂ laser while also allowing visible wavelength radiation to pass through. Therefore, the object to be hit with the laser beam can be visualized through this lens assembly while the CO₂ beam is reflected off of this assembly allowing coincidence of optical path and laser path. This allows the laser to be used in much tighter areas such as through an otologic speculum or a neonatal subglottiscope.

Aiming Beam

The Argon, KTP, helium neon, gold vapor and visible dye wavelengths all by nature work in the visible wavelength range of the spectrum and an attenuated version of their output beam can serve as their own aiming beam. Lasers in the ultraviolet and infrared regions such as the Excimer and the Nd:YAG and CO₂ laser emit invisible radiation and therefore need an aiming beam to allow the surgeon to select the impact site. The Nd:YAG often uses an attenuated output from the Krypton or xenon arc lamp which appears as a very bright spot when aiming this unit. Alternatively, some manufactures have added a helium neon laser to be used as a guide beam for the Nd:YAG laser. In the CO₂ laser oftentimes a helium neon red laser is used for the aiming spot. This is often a 5 to 10 milliwatt small Class IV laser unit. When using either system, it is important that prior to patient application, test spots should be fired to assure that the burn created by the operative beam coincide with that from the aiming beam and are of known size. Because the helium neon

beam is generally of shorter wavelength than the YAG or the CO₂ beam, the aiming beam is much smaller than the resultant impact.

Potential difficulty arises here with the use of the red helium neon laser as an aiming spot in a bloody field. The helium neon beam is often very difficult to pick up against a red background. Manufacturers have tried to overcome this by including more powerful helium neon lasers as part of the aiming package, but potential difficulty is reached when the power for the helium neon is bright enough that the glare is potentially painful to the surgeons eyes. One system to overcome this aiming problem would utilize an aiming spot in the green or yellow wavelengths, and although these systems are currently being testing and on the production drawing board, there are no medical systems available yet which use a green or yellow laser aiming spot.

Basic Laser Tissue Effects

Beam Profile

The measurement of the energy output in a cross section across the beam from most medical laser systems would reveal a gaussian or bell shaped distribution of power. This beam profile has the highest power concentration at the center and drops off exponentially as one moves further away from the center of the beam. For practical purposes, the radius of the spot for a gaussian distribution beam is to find the distance from the center to the point where the power has decreased to $1/e^2$ peak power. In fact, this defines the portion of the gaussian curve

that contains 87% of the total power and is defined as the spot size. This holds true for most medical lasers when viewing the beam as it is emitted from the laser cavity. However, once a beam has been transmitted through a fiber, or reflected off mirrors, the spot can change to a non-gaussian distribution beam profile. In addition, certain lasers produce beams in non-gaussian profiles directly from the cavity. These spots have a much steeper rise to a peak with a flattened top similar to a "top hat". When defining the tissue effects it is most appropriate and meaningful to define the spot size in terms of square centimeters or radius. This would allow one to directly calculate power densities and energy density.

Beam profiles are also specified by their transverse electromagnetic mode (TEM). A TEM_{00} is considered the fundamental mode and is a gaussian distribution. Higher modes (TEM_{01} and TEM_{10}) produce a power distribution that can be described as a doughnut with a relatively low powered section in the center. A TEM_{11} has an essentially rectangular distribution and can be represented as a "top hat" profile. The smallest spot sizes are achieved with a gaussian distribution (TEM_{00}). As (TEM) mode increases, spot size also increases, therefore decreasing power density (see below).

Power Density

Due to the nature of laser light being coherent and collimated, the laser beam can be focussed into extremely small spot sizes with the possibility of creating very large power

densities. The laser can be focussed into a spot of less than one micron in diameter (depending upon the wavelength and focal length of the lens) and thus is capable of generating the power densities that are equivalent to the energy available at the surface of the sun. Power density is defined as the power (or watts) over area in square centimeters (see Figure 3). For a constant power output, from the equation it can be seen that the smaller beam spot size i.e. the smaller the area, the greater the concentration of power. This follows the inverse square law. The area increases as the square of the diameter increases. The following table illustrates the relationships among spot area and power. Notice that a lens system that is capable of delivering a 50 micron spot can produce power densities of one million watts per centimeter squared with only a 20 watt power input. Another relationship which can be visualized from the table is that achieved by focussing or de-focussing the hand piece. If the spot diameter is increased, then the power density decreases by an exponential factor. For example, if the spot diameter is doubled, then the power density will decrease by a factor of 2^2 or 4. If the spot diameter decreases by half, then the power density would increase by 4. When the beam is de-focussed, the spot diameter increases and this decreases the power density geometrically. Because of this relationship between power and spot to produce a power density, it is important to communicate the spot size and the input power when describing tissue effects.

All laser delivery systems have an optimum focal distance responsible for the smallest spot size. In general, this is the usual working distance for the hand piece or for the micromanipulator. However, there exist situations in which it is necessary to have a broader beam, as for coagulation or with higher powers for vaporization of a larger surface area. This is accomplished by defocusing the beam or prefocusing the beam. When using a hand piece, defocusing is done by simply pulling the hand piece further away from the tissue, therefore removing the focal spot away from the tissue and broadening the beam. On micromanipulators and on bronchoscopes, there is a defocusing lens which is used to accomplish the same purpose. Defocusing, as can be seen from the table above, results in a lower power density and therefore is more effective for coagulation given the same input power. The focal spot from a hand piece can also be enlarged by bringing it closer to the tissue, called prefocusing. This results in the focal point being projected beneath the surface of the tissue and may cause uncontrolled damage deep in the tissue. The effect is that the overlying tissue is vaporized fairly slower because of the lower power density and as this tissue is ablated and it comes closer to the focal spot itself, the power density increases and the rate of vaporization also increases, making control of this technique very difficult.

Understanding the concept of power density is sufficient for working with the CO₂ laser and other lasers which have immediate tissue effects, but tissue effects generated by some lasers are

not always immediately apparent. For example, the extent of deep thermal necrosis from the Neodymium:YAG laser is a function of laser power and the time the laser is in contact with the tissue. Some of these effects only become visible 24 to 48 hours after laser impact. This is not to say that laser tissue interactions are totally unpredictable. As a matter of fact, the amount of necrosis can be predicted but only if the total light dose delivered to the tissue is known. The inter-relationship of laser power spot size and duration of effect on duration of exposure to tissue is represented in the following figure. The output power from the laser is measured in watts. The amount of energy applied over time is energy (Joules = watts x seconds). Energy density (Joules per square centimeters) is a composite measurement of the power duration of exposure to tissue and spot size. Within medicine, energy density is referred to as light dose by the clinician, and physicists refer to it as fluence.

Tissue Optics

An overview of the effects of light interacting with tissue is represented in Figure 4. For this initial discussion of basic tissue optics the effect of wavelength and the rate of energy delivery to the tissue will be postponed until later.

Progressing from the surface of the tissue inward, we will discuss reflection scattering transmission and absorption, and the various interactions that can occur between and among these properties. Light incident upon tissue can be reflected from the surface of the tissue. The minimum amount of reflectance

occurs when the incident light is directed orthogonal to the tissue. As the angle of the light incident to the tissue decreases, more and more light may be reflected from the surface. In clinical application, this is important because most surgeons have a tendency to hold a laser hand piece at an angle to a tissue like a pencil. There can be significant reflection and therefore decreased power delivery to the tissue but also, the spot will form an oval instead of the smallest focal spot (circle). Awareness of the concept of reflection is also important when a laser is used in a lumen such as in the trachea or bronchi. The beam in this instance may achieve a very low angle of incidence with the wall and the energy may be reflected to a remote site and damage may occur to normal tissue. This effect is clinically more commonly seen with the Nd:YAG than with the CO₂ laser.

Light may also be reflected from internal components of the tissue, including atoms, molecules, and macromolecular structures. Multiple reflections within tissue is termed scattering. At any point, light may be reflected back out of the tissue and this results in what is called diffuse reflectance. Clinical application of this principle is in reflective pulse oximetry. Here, a diode directs light into tissue and the reflective light is measured for spectral absorption or changes, giving a relative measure of the oxygenated hemoglobin to the de-oxygenated hemoglobin ratio, since these two forms of hemoglobin have different absorption characteristics.

Light may also pass completely through tissue without any interaction with any of the tissue material. This is very uncommon and in fact the only wavelengths that can commonly pass through the body are cosmic rays. Visible light and all medical laser wavelengths are eventually reflected or absorbed within tissue, although some wavelengths are able to penetrate deeper before this effect occurs. The concept of light passing through tissue without an interaction is called direct transmission and for most medical lasers is limited to a millimeter or so within tissue, but may extend to as deep as 3 or 4mm for the Nd:YAG laser. The most common form of transmission of light through tissue is called diffuse transmission. This results from light that is scattered or multi-reflected within tissue that may be eventually transmitted deep within the tissue. The total of the through transmission and diffuse transmission is simply the transmission of light through tissue. A clinical example of this effect is trans illumination of a sinus with a very bright light. The diffuse red glow is the transmittance. Another example is the transmission of light through a finger. If the light is bright enough, the bone can actually be seen and this concept is now being developed for detection of breast masses and is known as diaphanography. In this technique, the breast tissue is supported as in a mammogram and then the intense light is transmitted through the tissue. There is no radiation in the basic procedure, but unfortunately at the present time, the sensitivity and specificity is not high enough. Another clinical

destruction when illuminated at one wavelength, but when illuminated at another wavelength, undergoes a fluorescence. This property of fluorescence is being investigated for the possible detection of metastases within tissue. Another potential application is the illumination of tissue, blood or serum looking for the fluorescence of specific target macromolecules. The concept here is that if one were able to identify a specific protein antigen such as carcinoembryonic antigen and were able to identify a specific fluorescence spectrum present in serum, this would afford a very quick screening test for this tumor marker.

Wavelength Dependence of Tissue Interaction

In general, light must be absorbed by a molecule or tissue component to have an effect. As demonstrated in the section on tissue optics, this absorption can cause effects of heat, or fluorescence, or optical breakdown of that particular compound. These compounds are also known as chromophores. The major tissue chromophores are water, melanin and hemoglobin. Each of these chromophores exhibits a complex absorption spectra as represented in Figure X. Melanin shows a gradually decreasing absorption as one increases in wavelength. Water demonstrates a relative window or lack of absorption in the visible wave ranges and hemoglobin is more strongly absorbed in the blue-green region. It can also be seen that the strongest absorbing chromophore is water, and the most efficient peak for absorption occurs around 3 nanometers. The absorption of the CO₂ laser energy at 10.6

microns is accounted for in the molecular transition and vibration modes of water. Since water is one of the most efficient absorber of energies, and given the fact that the tissue is largely water, this means that laser energy is absorbed very efficiently and penetrates very little in the 10.6 nanometer wavelength. The energy from a CO₂ beam is absorbed in a very shallow distance at the surface of the tissue, vaporizing the surface water and then proceeding to be absorbed by the next layer down and so on. The interaction of laser through the thermal interaction with tissue then can be thought of as a sequential process where the laser vaporizes the superficial tissue proceeding deeper into the structure. Because of the high heat diffusion capability of tissue due to the water content, the thermal spread ground the CO₂ laser impact area is limited somewhat. The thermal affect has been estimated to range from 50 to 250 microns surrounding the point of impact of the CO₂ beam. Better absorption of water occurs at round 3 nanometers, and several lasers are being tested to take advantage of this very high absorption. The Erbium YAG laser at 2.94 microns is one of these, and because of the higher absorption of energy, and therefore the relative lack of penetration, the thermal damage surrounding the zone of vaporization is even less for the Erbium: YAG laser (as small as 2 microns for the thermal effect _____ for the Erbium YAG compared to 11 microns for the CO₂. Bone is composed of less water and, therefore, reacts less to a CO₂ beam. However, the Erbium YAG laser in particular has

been shown to be somewhat effective for cutting through bone. The CO₂ laser creates a ring of black char where the temperatures can reach several hundreds of degrees surrounding the zone of laser vaporization. This is not seen with the Erbium:YAG lasers.

There are several medical laser in the visible wavelengths, including the argon, KTP and Flash Lamp-Pump Dye lasers which all take advantage of absorption by hemoglobin and melanin. These lasers effective pass through the superficial lasers that are transparent to these wavelengths because of their high water content and are preferentially absorbed by hemoglobin and melanin in the connective tissue layers. Because of the absorption of energy by blood, these lasers can be used to effect coagulation within the vasculature. Hemostasis with these lasers is excellent. The Pulsed Yellow Dye Laser is more highly selective in targeting hemoglobin to the exclusion of other skin chromophores (melanin) and has found widespread application in photocoagulating port wine stains. The KTP and argon lasers due to some of their absorption with melanin are less specific for these applications.

An "optical window" exists in tissue from approximately 600 to 1800 nanometers, due to the relative drop-off in absorption for melanin, hemoglobin and lack of absorption for water. In this region there is no major tissue chromophore and light will pass deep into the tissue and scatter widely. The Nd:YAG laser wavelength of 1.064 nanometers occurs within this window and as a

result, this laser penetrates very deeply and scatters widely. The clinical effect is that this laser can raise the temperature of a large volume of tissue effecting coagulation and tissue thermal effects as deep as 4 to 5 millimeters under proper conditions. Thus the Nd:YAG laser is good as a coagulator, but is not as efficient at vaporizing tissue unless the power densities are increased into a very high level such as can be accomplished by focusing the Nd:YAG to the tip of a contact fiber. The red wavelengths of light used for photodynamic therapy (630 nanometers) and for laser biostimulation with the Helium Neon laser (632.8 nanometers) are also within this region of relatively deeper tissue penetration.

Tissue Response to Light

The response of tissue to light is dependent upon several factors. The first factor is wavelength, but in addition, the power or total energy applied, and the rate of time over which is energy is applied, and the duration of light application are also vitally important in characterizing the response of light with tissue. Total light doses of between 1 and 10,000 Joules per centimeter squared are most commonly used for biological effect. It should be apparent that the same light dose may be delivered by very high intensity brief flashes or by low intensity illumination over a very long period of time. Each of these results in very different tissue responses. Very low levels of light energies applied over long periods of time have the

potential to drive photochemical reactions such as photosynthesis. On the other hand, focusing laser energy into very small spots creating very high power densities and applying this energy over a very short time can result in extreme thermal effects within the tissue. Sometimes these thermal effects are so high as to generate plasmas within a tissue. The interaction of light with tissue can be broken down into four basic types of reactions. Photochemical, thermal, photoablative and electromechanical reactions.

Photochemistry

Low levels of light energy applied to tissue over long durations of time can result in photochemical reactions. Photosynthesis is a common example of this. In photosynthesis, photons are absorbed by chlorophyll molecules and plant chloroplasts and eventually converted into a photon concentration gradient driving the synthesis of adenosinetriphosphate.

The experimental treatment for cancer, photodynamic therapy (PDT) is an example of clinically useful interaction of light with tissue on a low energy level. In PDT, a light absorbing chromophore such as the drug Hematoporphyrin Derivative, (HpD), is the compound responsible for light absorption. HpD is preferentially localized in malignant and embryonic tissue following systemic injection. Once the drug has localized within the tumor, the tissue is illuminated with light on to one of the absorption peaks of hematoporphyrin derivative.

Fortunately, HpD has a moderately good absorption peak at 630 nanometers (red light) which allows moderately deep penetration of light into the tissue. Please see Figure X. The reaction in photodynamic therapy depends upon the presence of the molecule of HpD, light of the proper wavelength, and molecular oxygen. The interaction of these three initiates a photochemical reaction. The photon of light stimulates HpD to a high energy level and through a series of electron tranferances singlet oxygen is produced. Localized tumor necrosis is a result of oxidation of the host tissue by this singlet oxygen. In this reaction, the light that is applied to the tumor is given in such a low rate of fluence that there is no thermal effect resulting from the use of the laser. Areas of normal tissue that do not contain metaporpharine derivative are spared. However, most tissue does retain some HpD to a slight extent for up to six weeks after application, and the major side effect of is photosensitivity to sunlight.

The concept of laser biostimulation was originally advanced in Europe and in Asia and is being currently investigated with applications in wound healing, chronic pain and arthritis. The mechanism of action of low level light interaction with tissue to bring these changes about has not been well worked out yet, but may be related to a similar mechanism as is found in acupuncture. The effects on wound healing (i.e. faster wound healing) and on arthritis (decreased inflammation and increased joint motion) potentially may be mediated by a reaction with mitochondria. It

has been suggested that absorption of light by respiratory enzymes in mitochondria can be converted into chemical energy such as ATP. The rationale for this being that mitochondria probably started as a purple algae, and retain the ability to undergo a basic form of photosynthesis. As stated before, the mechanism has not yet been completely worked out.

Non-thermal Laser Tissue Effects

Photoplasmolysis

At the upper end of the power density time continuum is photoplasmolysis. In this application, very high energies of light are applied to a tissue and focused into very small areas over a very short duration. The extremely high energy levels results in a plasma formation within tissue with the electrons being stripped away from component atoms generating the plasma. This field of plasma then expands throughout the tissue generating an acoustic or mechanical shock wave thereby disrupting the tissue. This mechanism has also sometimes been called photoacoustic, acoustic mechanical, or electromechanical disruption. The most common medical procedure employing this type of tissue effect is posterior capsulotomy to remove the fibrous capsule that sometimes forms secondary to artificial lens implantation for ophthalmology. A Q switch Nd:YAG laser generated peak powers in mega watt range delivered in ultrashort nano second or pica second pulses. The plasma shock wave literally "blows apart" the fibrous capsule. More recently,

exploration in the use of plasmolysis for the disruption of ureteral stones or biliary stones has been investigated with Pulse Dye laser. Pulses of intense light are transmitted through a fiber and directed at calculi through a endoscope. The acousto-mechanical disruption of these calculi yields smaller particles which can be easily excreted. This procedure has been found to yield promising results in treatment for ureteral calculi and biliary calculi.

Photoablation

The process of photoablation is thought to occur through direct breakage of intramolecular bonds. The ultraviolet light is preferentially absorbed by proteins, RNA, and DNA and the wavelength is short enough to allow disruption of these bonds within tissue. The very short pulses also minimize any potential thermal effects and may contribute to the non-thermal cutting. These lasers are known as Excimer lasers and are used in the UvA,B and C wavelengths. Also, because of their very short wavelength, they can be focused into a very small spot size and their depth of penetration is very shallow. Since scattering also is minimized, there is very little effect adjacent to the area of photoablation. Unfortunately, one disadvantage to the use of short wavelengths for photoablation is the possibility of ultraviolet induced mutagenesis.

Thermal Tissue Effects

Hyperthermia

At one step up from photochemistry, and several degrees down from more intense light interaction with tissue is a concept known as hyperthermia. Everyone has felt the warmth of the sun during the summer, and knows the potential of light for heating tissue. If light energy is controlled in its application to tissue in a very slow manner it is possible to heat tissue very gently without causing irreversible damage. The CO₂ laser is difficult to use for this because of its very limited optical penetration depth within tissue. However, the Nd:YAG laser due to its deeper optical penetration depth, may have a heating effect than can be transmitted several millimeters. An experimental treatment of cancer known as hyperthermia takes advantage of the discovery that malignant cells do not tolerate temperatures above 42.5⁰ centigrade as well as normal tissues. Therefore, the laser may be used in a low power output to raise tissue temperature within a sphere of tissue significantly enough to effect malignant cell death. The combination of photodynamic therapy with hyperthermia has also been found especially promising. The application of hyperthermia for cancer treatment is not exclusively a domain of lasers, however. Other systems for the generation of heat within tissue include microwaves and magnetic field induction heating which have also been used with similar success to lasers.

Denaturation (welding)

When the tissue temperature is raised above 45 degrees

centigrade, protein de-naturalization may occur. In some cells and tissues this process may be irreversible, but often time results in a slow cell death, and necrosis may not be clinically evident for some time.

Above 60 degrees centigrade, collagen is uncoiled and at higher temperatures is eventually coagulated. Collagen, a triple helix, under mild heating may uncoil and exhibit characteristics of "flowing". Once this has cooled, it may spontaneously re-coil into a helix regaining its basic form. In theory, this de-naturalization/re-naturalization underlies the technique of laser tissue welding. Argon, Nd:YAG and CO₂ lasers have been used in a very small focus, 200 microns, and power densities of 50 to 250 watts per centimeter to weld together skin, nerves, arteries, veins, vas deferens, and bowel. This is accomplished by heating the tissue to a high enough temperature to allow the collagen to flow into itself and then allowing it to cool, thereby binding one edge of the tissue to the other edge. While the tensile strength is low, there is no foreign body reaction involved as there would be if sutures were used, and healing appears to progress in a unimpeded manner.

Coagulation

Between 65 and 70 degrees centigrade, collagen is irreversibly coagulated and cell death is obvious. On microscopic examination with hemotoxin eosin the coagulated zone appears deeply stained with loss of cellulase architecture.

There is a uniformity in appearance across the area of coagulation. Coagulation is the principle means of effecting hemostasis with the laser and the depth or extent of coagulation is directly related to the penetration depth of the laser that is being used. Greatest hemostasis is seen with the Nd:YAG laser and the least hemostasis seen with the Excimer and Erbium:YAG lasers. The potential for hemostasis with the Nd:YAG laser allows the potential for coagulating vessels up to 2 mm in diameter while the CO₂ laser may effectively seal vessels up to 0.5 mm in diameter.

Vaporization

Vaporization of tissue occurs when the water in the tissue is heated above 100 degrees centigrade. At this point, water is converted to vapor and in the conversion to steam ejected from the tissue. Other tissue constituents may also be atomized and injected along with the steam. Ejection velocities of 2 to 3 meters per second have been observed. While the water is vaporized due to the osmotic gradient, fluid is drawn from surrounding tissue and may cause desiccation. This can be seen on the skin where contracture around the impact site may be visualized as ripples or irregularity in the skin surface.

The CO₂ laser since it is absorbed primarily by water is the most efficient at vaporizing tissue, but any laser capable of raising tissue temperature adequately may be used for

vaporization. The total energy applied however, depends upon the ability of tissue to absorb that particular wavelength. For example, while CO_2 is usually absorbed by water, more energy needs to be applied for an Argon or KTP laser to cause tissue vaporization and yet quite a bit more is needed to accomplish the same effect with the Nd:YAG laser.

Tightly focussing a laser beam and drawing it across tissue effectively vaporizes a line of tissue and thus the laser may be used for cutting. If the laser beam is defocused and the power density maintained the same as that for cutting, as the laser is swept over the tissue, ablation of the tissue occurs. This technique is very useful for rapid debulking of large masses.

Carbonization

Biomolecules and constituents of tissue which are not vaporized or removed with the laser plume may remain in the zone of laser impact. If this material is not effectively heated above its boiling point, it may be reduced to component carbon and remain within the area as a char. Continual application of laser energy to this char may increase the temperature quite beyond 100 degrees centigrade. The potential for reaching temperatures of several thousand degrees centigrade is significant and this mechanism may account for some of the deep thermal effects that are seen around some laser vaporization craters, especially with the carbon dioxide laser. In certain lasers such as the Nd:YAG laser, the char is used as a

chromophore and heat sink. The thermal effect resulting from the absorption of the Nd:YAG laser by this char is actually used to effect tissue thermal coagulation. For CO₂ laser applications especially within the larynx, it is advisable to remove the char during the procedure to minimize the thermal effect deep within the tissue.

Timing of the Laser Pulse

The duration that the laser pulse is in contact with the tissue has important applications for the ultimate tissue effect. As seen from the previous section, long exposures of low power lasers result in photochemical effects, whereas very short exposures of very high powers can result in the formation of a plasma. Between these two extremes, modification of the timing parameters of specific lasers can effect the depth of the thermal effect within tissue. The two most obvious areas that timing plays a critical role is in the use of the Flash Lamp-Excited Dye laser for port wine stains and in the use of CO₂ laser in the suprapulse mode.

The use of the Flash Lamp- Excited Dye laser for decolorization of port wine stains takes advantage of the fact that the wavelength of 577 nanometers is absorbed by hemoglobin very well, resulting in coagulation of the vasculature. However, if the pulse of laser energy is supplied to the tissue for too long, the thermal effect would not only effect the vasculature, but would also have deleterious effects on the tissue surrounding

the vasculature, thus leading to scarring. The Flash Lamp-Excited Eye laser takes advantage of the concepts of thermal diffusion and thermal relaxation time of tissue. Thermal diffusion is the time required for heat to be conducted from the site of energy absorption to an adjacent area, this amount of time is both tissue and area dependent. Thermal relaxation is the time necessary for the tissue to dissipate ($1/e$ of the accumulated heat by re-radiation. This value is independent of area, but is specific for each tissue type. Thermal diffusion times are shorter for highly vascularized tissue, and much longer for bone. The Flash Lamp-Excited Dye laser takes advantage of the vasculature within the port wine stains using a pulse duration of 450 microseconds and an off-time that allows diffusion of the heat away from this area before a second pulse is applied to the tissue. The end result is coagulation only at the vasculature and not the surrounding tissue.

The concept of suprapulse on a CO_2 laser was advanced by Hill in 1967 and given clinical application by Terry Fuller, et al. in 1982. The impact of a CO_2 laser beam on a homogeneous tissue composed of approximately 80% water can be visualized, to a first order approximation, as the impact of CO_2 on water. The thermal diffusion for water is $0.001 \text{ cm}^2/\text{sec}$ and the thermal relaxation time is 0.001 seconds. If the laser pulse is much shorter than the thermal diffusion time, then the heat will not spread beyond the optical penetration depth for that tissue (optical penetration depth is the depth in which light will

penetrate into the tissue with an attenuation of $1/e$). If the pulse is then terminated, and a period of time longer than the thermal relaxation time for that tissue is allowed to elapse, the tissue will again return to a steady state base line temperature, thus heat will not accumulate and the thermal effect surrounding the zone of laser vaporization will be minimal. Potential applications include the larynx, where one would wish to limit possible coagulation on the vocalis muscle. The potential for scarring to the underlying vocalis ligament and the associated vibratory mass change for the vocal cord is something one would wish to avoid. Another potential application is in acoustic neuroma dissection close to the 11th nerve where one would wish to limit the thermal spread surrounding the removal of the tumor.

Another method for limiting the duration of the tissue exposure can be accomplished by adjusting the speed of movement the of laser beam across the surface of the tissue. Often, the novice laser surgeon tends to use low power and moves slowly and cautiously which results in longer exposure of the energy to the tissue and deeper thermal coagulation. More experienced surgeons use higher powers with rapid movement. Although total energy delivered is the same in both instances, the expert achieves thermal precision and limited coagulation deep within the tissue.

Clinical Consequences of Tissue Effects

Previous sections have concentrated on demonstrating the initial tissue effects at the cellular level. The clinical consequences of tissue effects may be examined at the tissue and organ system. These include the effects of hemostasis, antisepsis, analgesia, necrosis and the influence on healing.

Hemostasis

The degree of hemostasis available varies between types of lasers and is predictable from the optical penetration depth as discussed earlier. The Neodymium Yag laser which has the deepest optical penetration depth (of 25mm) has the deepest coagulation and can seal blood vessels up to 2mm in diameter with proper application of power parameters. At the other extreme, the CO₂ laser is only able to seal vessels up to 0.5mm in diameter. Even with the carbon dioxide limitations for hemostasis it provides a more bloodless field than a comparable scalpel incision. Several surgeons have elected to use the CO₂ laser for skin incisions. The resultant scar from CO₂ incision at 6 months is almost indistinguishable from a scalpel incision although the early appearance is somewhat disconcerting. CO₂ laser has also been used for mastectomy markedly reducing the blood loss and rate of transfusion for this procedure.

Antisepsis

The thermal effect of laser incision and ablation also and antiseptic property. By raising the tissue temperatures above 100 degrees centigrade. The superficial surface is often sterilized. Bacterial counts of the surface after ablation or

removal of burn wound eschar with the CO₂ laser have shown marked reduction in bacterial load. In addition, postoperative infection rates have been less following mastectomy performed with the carbon dioxide laser than with scalpel incision.

Analgesia

Several papers have claimed that by use of laser excision or laser incision, the postoperative pain is minimized. The theory behind this is that as the laser cuts or ablates tissue it seals or welds nerve endings closed. This reduces leakage of axoplasm around the end of the cut nerve with decrease in spontaneous depolarization of the nerve. Several studies have claimed this effect, but to date no good prospective controlled studies have been designed to conclusively demonstrate this fact.

Necrosis and Influence on Healing

The depth of necrosis is directly related to the optical penetration depth and thus the coagulation. When tissue temperatures are raised over approximately 45° centigrade, irreversible cell death occurs. Therefore, the magnitude of tissue destruction is greater for those lasers which have deeper optical penetration depth (Nd:YAG is much deeper than CO₂).

The rate of healing depends upon the ability of the body to remove this necrotic tissue. Therefore the rates of healing generally can be expressed linearly going from faster rates of healing for the shallower thermal effect from CO₂ laser to longer rates of healing for KTP and Nd:YAG laser. The scalpel incisions having much less tissue damage on either side of the cut would

heal faster than any of the laser incisions, however when wound tinsel strength is compared at six weeks, there is not difference between scalpel incision and most laser incisions.

Lasers in Otology

Three of the most common medical lasers have all been used at one time or another for various procedures within the ear. The first report of laser use for otology was by Sateloff in using the ruby laser in 1967. This laser was soon abandoned because of poor results. In 1980, Perkins (ref. 1 on Silverstein's paper) reported on laser stapedotomy for otosclerosis using the Argon laser. Since that time, the Argon, KTP and CO₂ lasers have all been used for stapedotomy. In addition, these lasers have been used for tissue welding for tympanoplasty and for vaporization for removal of granulation tissue within the mastoid cavity and middle ear space. It is of note that most people have recognized that the thermal effect from the Nd:YAG laser is too great and have not attempted to apply the Nd:YAG laser for middle ear work or stapedotomies. However, the Nd:YAG has been investigated for heating of the horizontal semi-circular canal in an attempt to control positional vertigo.

Lasers for Tympanoplasty

The three medical lasers have all been used for tympanoplasty. Each laser has been used to try and weld the tympanic membrane into place with moderate success. Most surgeons have not embraced this technique whole-heartedly as the laser

parameters necessary to accomplish the weld are very precise and control is somewhat lacking. However, the use of lasers for removal of granulation tissue in the middle ear space has found application with the use of lasers. Lasers are very effective at tissue vaporization and in this instance, the CO₂ laser is probably the safest laser to use due to its limited thermal penetration depth. One study has looked at the thermal effect of CO₂ laser use over the fallopian canal and concluded that direct application of electromagnetic energy in this region can cause facial paralysis in laboratory animals. The cavity must be extended there for that any radiation or heating over the fallopian canal can be accompanied by facial paralysis and should be avoided.

Lasers for Mastoidectomy

The most common medical lasers have not been used for mastoidectomy except for the removal of granulation tissue encountered within the mastoid. There is not commercially available laser at the present time which is very efficient at removal of bone. The CO₂, KTP and Argon lasers all are done by a similar method. This method involves heating the bone until a char is formed and then picking away at the char. Often times, this char can be removed with minimal effort once the bone has been heated. Concern exists however about the spread of thermal effect around this area of this char. In discussing laser tissue effects, it was noted that when laser energy was continual applied to a char temperatures in excess of 2,000 degrees have

been recorded. Temperatures of this order obviously must be avoided within the ear space.

Lasers Stapedotomy

Many surgeons have promoted the use of the lasers for stapedotomy. Various proponents have claimed advantages for the CO₂, Argon and the KTP, each for laser stapedotomies. Reported advantages to the use of the laser include a "non-contact technique", bloodless field, and 3 ease of surgery.

The "non-contact" claim is somewhat misleading however. While the laser is used in a non-contact technique to vaporize the stapes tendon and eventually char the crura and the foot plate, a straight pic must be used to manually remove the char. This involves less pressure than maybe involved with drilling out the foot plate with a rotating burr or a buckingham hand drill but is not a true "non-contact technique".

Each laser has unique advantages and disadvantages in regard to stapedotomy. The Argon and KTP lasers are not absorbed by white bone and therefore, much of the energy is reflected from the surface of the foot plate until the heat has caused a char formation then the laser is absorbed quite adequately at the foot plate site. Potential difficulties with both the use of the Argon and by extension, the KTP laser include energy transmission through an intact foot plate. Several authors have demonstrated temperature rises within the vestibule after application of Argon and KTP laser to an intact stapes foot plate. In addition, Boraf in studying stapedotomies performed with an Argon laser on cats

noted damage to the sacculi on 3 of 8 cats. This damage was due to the beam transmitting across the clear fluid and impacting on the sacculi directly opposite the stapedotomy site. While this has not been documented with KTP laser, the visible wavelength of KTP being so close to that of Argon this possibility must be considered as well. The CO₂ laser does not vaporize bone per say. It also works by creating a char on the foot plate which must be then picked away using a straight pic. The CO₂ laser having a small thermal damage radius and very high absorption by water is then rapidly absorbed by the surface of the perilymph. While some surgeons have cautioned about the possibility of boiling the surface of the perilymph Lesinski has shown that the temperature rise with the perilymph is limited to 1 degrees centigrade or less and can be modified by appropriate selection of pulse parameters with the CO₂ laser.

Overall results for the use of the laser to perform stapedotomies have delivered results comparable and in some cases slightly superior to results obtained by conventional techniques using rotating burr or buckingham hand drill. Silverstein's most recent reporting better overall hearing results when compared to conventional techniques also noted an increase incidence in postop vertigo with the use of the KTP laser. He stated that all vertigo had responded within 3 weeks however.

Conclusion

The use of lasers for otologic surgery has been performed safely through judicious use of pulse parameters to limit thermal

effect. Overall, results are comparable to conventional techniques and in some hands may actually be superior. The extensive thermal effect from use of Argon and KTP lasers must be considered and the anatomy fully appreciated before application of energy from these two units is employed. The CO₂ laser while having less thermal effect is still not without draw-backs. The ultimate answer of which laser to use and when in ear surgery has not yet been determined.

References

1. Marhic M: The free-electron laser: A powerful source of broadly tunable coherent radiation. Bio-Laser News 1985; 1-3.
2. Einstein A: Zur quantentheorie der strahlung. Physik Zeitschr 1917; 17:121-128.
3. Apfelberg DB: Biophysics, advantages, and installation of laser systems, in Apfelberg DB (ed): Evaluation and Installation of Surgical Laser Systems. New York, Springer-Verlag, 1987, pp 1-17.
4. Fuller TA: Fundamentals of lasers in surgery and medicine, in Dixon JA (ed): Surgical Applications of Lasers. Chicago, New Book Medical Publishers, Inc, 1983, pp 11-28.
5. Goldman L: Comparison of the biomedical effects of the exposure of human tissues to low and high energy lasers. Ann NY Acad Sci 1965; 122:802-813.
6. Jako GJ: Laser surgery of the vocal cords. Laryngoscope 1972; 82:2204-2216.
7. Sataloff J: Experimental use of laser in otosclerotic stapes. Arch Otolaryngol 1967; 85:58-60.
8. Council on Scientific Affairs: Lasers in medicine and surgery. JAMA 1986; 256:900-907.
9. Fuller TA: The physics of surgical lasers. Lasers Surg Med 1980; 1:5-14.

10. Polanyi TG: Physics of surgery with lasers. Clin Chest Med 1985; 6:179-202.
11. Stein BS: Laser physics and tissue interaction. Urol Clin North Am 1986; 13:365-380.
12. Fuller TA: Fundamentals of laser surgery, in Fuller TA (ed): Surgical Lasers. New York, Macmillan Publishing Co, Inc, 1987, pp 1-17.
13. Stamp JM: An introduction to medical lasers. Clin Phys Physiol Meas 1983; 4:267-290.
14. Boulnois JL: Photophysical processes in recent medical laser developments: A review. Lasers Med Sci 1986; 1:47-66.
15. Mainster, MA: Finding your way in the photoforest: Laser effects for clinicians. Ophthalmology 1984; 91:886-888.
16. Sliney DH: Laser-tissue interactions. Clin Chest Med 1985; 6:203-208.
17. Haldorsson T, Langerhold J: Thermodynamic analysis of laser irradiation of biological tissue. Appl Optics 1978; 17:3948-3958.
18. Polanyi TG, Bredemeir HC, Davis TW: A CO₂ laser for surgical research. Med Biol Eng 1970; 8:541-548.
19. Deckelbaum LI, Isner JM, Donaldson RF, et al: Reduction of laser-induced pathologic tissue injury using pulsed energy delivery. Am J Cardiol 1985; 56:662-667.
20. Hill AJ: Multijoule pulses from CO₂ lasers. Appl Phys Lett 1968; 12:324-327.

21. Walsh JT, Flotte TJ, Anderson RR, et al: Pulsed CO₂ laser tissue ablation: Effect of tissue type and pulse duration on thermal damage. *Lasers Surg Med* 1988; 8:108-118.
22. Hobbs ER, Baililn PP, Wheeland RG, et al: Superpulsed lasers: Minimizing thermal damage with short duration, high irradiance pulses. *J Dermatol Surg Oncol* 1987; 13:955-964.
23. Rattner WH, Rosemberg SK, Fuller T: Difference between continous wave and superpulse carbon dioxide laser in bladder surgery. *Urology* 1979; 13:264-266.
24. Lanzafame RJ, Naim JO, Rodgers DW, et al: Comparison of continuous-wave, chop-wave, and super pulse laser wounds. *Lasers Surg Med* 1988; 8:119-124.
25. McKenzie AL, Carruth JAS: Lasers in surgery and medicine. *Phys Med Biol* 1984; 29:619-641.
26. Ossoff RH, Duncavage JA: Past, present, and future usage of lasers in otolaryngology-head and neck surgery, in Aptelberg DB (ed): *Evaluation and Installation of Surgical Laser Systems*. New York, Springer-Verlag NY, 1987; pp 127-149.
27. Norris CW, Mullarky MB: Experimental skin incision made with the carbon dioxide laser. *Laryngoscope* 1982; 92:416-419.
28. DiBartolomeo JR: The argon and CO₂ lasers in otolaryngology: Which one, when and why? *Laryngoscope* 1981; 91: 1-16.

29. Report of Panel on Lasers in Medicine and Surgery, Part I. Conn Med 1986; 50:406-409.
30. Morelli JG, Tan OT, Garden J, et al: Tunable dye laser (577 nm) treatment of port wine stains. Lasers Surg Med 1986; 6:94-99.
31. Report of Panel on Laser in Medicine and Surgery, Part II. Conn Med 1986; 50:466-470.
32. Isner JM, Donaldson RJ, Decklebaum LI, et al: The excimer laser: Gross, light microscopic and ultrastructural analysis of potential advantages for use in laser therapy of cardiovascular disease. J Am Coll Cardiol 1985; 6:1102-1109.
33. Medical application of the excimer laser. Lancet 1986; 2:82-83.
34. Fuller TA, Nadkarni VJ, Pavlov IK, et al: Carbon dioxide laser fiber optics. Bio-Laser News 1985; April: 1-6.
35. Fuller TA: Mid-infrared fiber optics. Lasers Surg Med 1986; 6:399-403.
36. Weiss R: Advances in infrared fibers. Laser Optonics 1988; 7:29-37.
37. Stone J, Earl HE, Derosier RM: Measurement set for optical fiber loss spectra., Rev Sci Instrum 1982; 53:197-201.
38. Mehta AC, Livingston DR, Golish JA: Artificial sapphire contact endoprobe with Nd-YAG laser in the treatment of subglottic stenosis. Chest 1987; 91:473-474.

39. Shapshay SM: Laser application in the trachea and bronchi: A comparative study of the soft tissue effects using contact and non-contact delivery systems. *Laryngoscope* 1987; 97(suppl 41):1-26.
40. Baggish MS, ElBakry MM: A flexible CO₂ laser fiber for operative laparoscopy. *Fertil Steril* 1986; 46:16-20.
41. Beckman H, Fuller TA: Carbon dioxide laser fiber optics in endoscopy, in Atsumi K (ed): *New Frontiers in Laser Medicine and Surgery*. Amsterdam, Excerpta Medica 1983, pp 76-80.
42. Ossoff RH: Bronchoscopic laser surgery: Which laser when and why. *Otolaryngol Head Neck Surg* 1986; 94:378-381.
43. Fried MP: Complications of CO₂ laser surgery of the larynx. *Laryngoscope* 1983; 93:275-278.
44. Fava G, Emanuelli H, Cascinelli N, et al: CO₂ lasers: Beam patterns in relation to surgical use. *Lasers Surg Med* 1983; 2:331-341.
45. Bodecker V, Buchholz J, Drake KH, et al: Influence of thermal effects on the width of necrotic zones during cutting and coagulating with laser beams. Presented at the Second International Symposium on Laser Surgery. Dallas, October 23-26, 1977, pp 101-108.
46. Burke L, Rovin RA, Cerullo LJ, et al: Thermal effects of the Nd:YAG and carbon dioxide lasers on the central nervous system. *Lasers Surg Med* 1985; 5:67-71.

47. Anderson RR, Hu J, Parrish JA: Optical radiation transfer in the human skin and application in vivo remittance spectroscopy, in Marks R, Payne PA (eds): Bioengineering and the Skin. Lancaster, England, MTP Press Limited, 1979, pp 253-265.
48. Anderson RR, Parrish JA: The optics of human skin, *J Invest Dermatol* 1981; 77:13-19.
49. Bruls WAG, van der Leun JC: Forward scattering properties of human epidermal layers. *Photochem Photobiol* 1984; 40:231-242.
50. Solon LR, Sims SD: Fundamental physiological optics of laser beams. *Med Res Eng* 1970; 9:10-25.
51. Evans LR, Sims SD: Fundamental physiological optics of laser beams in biomedical studies. *Phy Med Biol* 1969; 14:205-212.
52. Kolari PJ: Penetration of unfocused laser light into the skin. *Arch Dermatol Res* 1985; 277:342-344.
53. Pratesi R, Ronchi L, Cecchi G, et al: Skin optics and phototherapy of jaundice. *Photochem Photobiol* 1984; 40:77-83.
54. Wan S, Parrish JA, Anderson RR, et al: Transmittance of nonionizing radiation in human tissues. *Photochem Photobiol* 1981; 34:679-681.
55. Ertefai S, Profilio AE: Spectral transmittance and contrast in breast diaphanography. *Med Phys* 1985; 12:393-400.

56. Profio AE, Doiron DR: Dosimetry considerations in phototherapy. *Med Phys* 1981; 8:190-196.
57. Werkhaven JA, Harris DM, Krol G, et al: Light dosimetry in animal models, application to photodynamic therapy in otolaryngology. *Laryngoscope* 1986; 96:1058-1061.
58. Harris DM, Hill JH, Werkhaven JA, et al: Prophyrin flourescence and photosensitization in head and neck cancer. *Arch Otolaryngol Head and Neck Surg* 1986; 112:1194-1199.
59. Harris DM, Werkhaven JA: Endogenous porphyrin flourescence in tumors. *Lasers Surg Med* 1987; 7:467-472.
60. Bayly JG, Kartha VB, Stevens WH: The absorption spectra of liquid phase H₂O and D₂O from .7 mm to 10 mm. *Infrared Phys* 1963; 3:211-222.
61. Wolbarsht ML: Laser Surgery: CO₂ or HF. *IEEE J Quantum Electronics* 1984;20:1427-1432.
62. Smith T, Apfelberg DB, Maser MR, et al: 532-nanometer green laser beam treatment of superficial varicosities of the lower extremities. *Laser Surg Med* 1988; 8:130-134.
63. Apfelberg DB, Maser MR, Lash H, et al: The role of the argonlaser inteh management of hemangiomas. In *J Dermatol* 1982; 21:579-589.
64. Apfelberg DB, Bailin P, Rosenberg H: Preliminary investigation of KTP/532 laser light in the treatment of hemangiomas and tattoos. *Laser Surg Med* 1986; 6:38-42.

65. Lahaye CTW, Van Gemert MJC: Optimal laser parameters for port wine stain therapy: A theoretical approach. *Phys Med Biol* 1985; 30:573-576.
66. Greenwald J, Rosen S, Anderson RR, et al: Comparative histological studies of the tunable dye (at 577 nm) laser and argon laser: The specific vascular effects of the dye laser. *J Invest Dermatol* 1981; 77:305-310.
67. Hulsbergen JP, Van Gemert MJC: Port wine stain coagulation experiments with a 540 nm continuous wave dye-laser. *Lasers Surg Med* 1983; 2:205-210.
68. Landthaler M, Haina D, Brunner R, et al: Effects of argon, dye and Nd:YAG lasers on epidermis, dermis, and venous vessels. *Lasers Surg Med* 1986; 6:87-93.
69. Dougherty TJ, Kaufman JE, Goldfarb A, et al: Photoradiation therapy for the treatment of malignant tumors. *Cancer Res* 1978; 38:2628-2635.
70. Karu TI: Photobiological fundamentals of low-power laser therapy. *IEEE J Quantum Electronics* 1987; 23:1703-1717.
71. Gomer CJ, Dougherty TJ: Determination of [³H]- and [¹⁴C] hematoporphyrin derivative distribution in malignant and normal tissue. *Cancer Res* 1979; 39:146-151.
72. Kessel D: Determinants of hematoporphyrin-catalyzed photosensitization. *Photochem Photobiol* 1982; 36:99-101.
73. Weishaupt KR, Gomer CJ, Dougherty TJ: Identification of singlet oxygen as the cytotoxic agent in photo-inactivation of a murine tumor. *Cancer Res* 1976; 36:2326-2329.

74. McCaughjan JS, Guy JT, Hawley P, et al: Hematoporphyrin-derivative and photoradiation therapy of malignant tumors. *Lasers Surg Med* 1983; 3:199-209.
75. Moan J: Porphyrin-sensitized photodynamic inactivation of cells: A review. *Lasers Med Sci* 1986; 1:5-12.
76. Wile AG, Novotny J, Mason GR, et al: Photoradiation therapy of head and neck cancer. *Am J Clin Oncol* 1984; 6:39-43.
77. Harris DM: Establishing the scientific basis of laser biostimulation. *LIA Laser Top* 1988; 10:9-14.
78. Dretler SP: Review: Laser lithotripsy. A review of 20 years of research and clinical applications. *Lasers Surg Med* 1989; 8:341-356.
79. Medical application of the excimer laser. *Lancet* 1986; 2:82-83.
80. Parrish JA: Ultraviolet-laser ablation. *Arch Dermatol* 1985; 121:599-600.
81. Svaasand LO, Boerslid T, Oeveraasen M: Thermal and optical properties of living tissue: Application to laser-induced hyperthermia. *Lasers Surg Med* 1985; 12:455-461.
82. Svaasand LO: Photodynamic and photohyperthermic response of malignant tumors. *Med Phys* 1985; 12:455-461.
83. Daikuzono N, Suzuki S, Tajiri H, et al: Laserthermia: A new computer-controlled contact Nd:YAG system for interstitial local hyperthermia. *Lasers Surg Med* 1988; 8:254-461.

84. Quigley MR, Bailes JE, Kwaan HC, et al: Microvascular anastomosis using the milliwatt CO₂ laser. Lasers Surg Med 1985; 12:455-461.
85. Ulrich R, Durselen R, Schober R: Long-term investigations of laser-assisted microvascular anastomoses with the 1.318-mm ND:YAG laser. Lasers Surg Med 1988; 8:104-107.
86. Ashworth EM, Dalsing MC, Olson JF, et al: Large artery welding with a miliwatt carbon dioxide laser. Arch Surg 1987; 122:673-677.
87. Garden JM, Robinson JK, Taute PM, et al: The low-output carbon dioxide laser for cutaneous wound closure of scalpel incisions: Comparative tensile strength studies of the laser to the suture and staple for wound closure. Lasers Surg Med 1986; 6:67-71.
88. White RA, Abergel RP, Klein SR, et al: Laser welding of venotomies. Arch Surg 1986; 121:905-907.
89. Anderson RR, Jaenicke KF, Parrish JA: Mechanisms of selective vascular changes caused by dye lasers. Lasers Surg Med 1983; 3:211-215.
90. Mihashi S, Jako GJ, Incze J, et al: Laser surgery in otolaryngology: Interaction of CO₂ laser and soft tissue. Ann NY Acad Sci 1976; 267:263-293.
91. Komisar A, Ruben RJ: Use of the carbon dioxide laser in pediatric otolaryngologic disease. NY State J Med 1981; 81:1761-1764.

92. Meyers AD, Kuzela DC: Dose-response characteristics of the human larynx with carbon dioxide laser radiation. *Am J Otolaryngol* 1980; 1:136-140.
93. Werkhaven JA, Harris DM: Superpulse CO₂ laser tissue effects. Presented at the Second International Laser Surgery Congress, Nashville, Tenn, June 22-24, 1988.
94. Bellina JH, Meandzija MP, Shillt V, et al: Analysis of electronically pulsed versus quasi-continuous wave carbon dioxide lasers in an animal model. *Am J Obstet Gynecol* 1984; 150: 934-940.
95. Baggish MS, ElBakry MM: Comparison of electronically superpulsed and continuous-wave CO₂ laser on the rat uterine horn. *Fertil Steril* 1986; 45:120-127.
96. Sinofsky E: Comparative thermal modeling of Er:YAG, Ho:YAG, and CO₂ laser pulses for tissue vaporization. *Proceedings of SPIE. Laser Med* 1986; 712:188-192.
97. Armon E, Laufer G: Asymptotic and dimensionless analysis of the response of living tissue to surgical pulsed CO₂ lasers. *Biomechanical Engineering* 1986; 108:368-371.
98. Apfelberg DB, Maser MR, Lash H, et al: Benefits of the CO₂ laser in oral hemangioma excision. *Plast Reconstr Surg* 1985; 75:46-50.
99. Apfelberg DB, Maser MR, Lash H: Review of usage of argon and carbon dioxide lasers for pediatric hemangiomas. *Ann Plast Surg* 1985; 75:46-50.

100. Carruth JAS, Shakespeare P: Toward the ideal treatment for the port wine stain with the argon laser: Better prediction and "optimal" technique. *Lasers Surg Med* 1986; 6:2-4.
101. Hobby LW: Argon laser treatment of superficial vascular lesions in children. *Lasers Surg Med* 1986; 6:16-19.
102. Hulsbergen JP, Van Gemert MJC, Lahaye CTW: Clinical and histological evaluation of port wine stain treatment with a microsecond-pulsed dye-laser at 577nm. *Lasers Surg Med* 1984; 4:375-380.
103. Levine NS, Salisbury RE, Peterson HD, et al: Clinical evaluation of the carbon dioxide laser for burn wound excisions: A comparison of the laser scalpel, and electrocautery. *J Trauma* 1975; 15:800-807.
104. Lanzafame RJ, Rodgers DW, Naim JO, et al: The effect of the CO₂ laser excision on local tumor recurrence. *Lasers Surg Med* 1986; 6:103-105.
105. Madden JE, Edlich RF, Custer JR, et al: Studies in the management of the contaminated wound, IV. Resistance to infection of surgical wounds made by knife, electrosurgery, and laser. *Am J Surg* 1970; 119:222-224.
106. Allan SN, Spitz L, Van Noort R, et al: A comparative study of scalpel and electrosurgical incision on subsequent wound healing. *J Pediatr Surg* 1982; 17:52-54.

107. Bellina JH, Hemmings R, Voros JI, et al: Carbon dioxide laser and electrosurgical wound study with an animal model: A comparison of tissue damage and healing patterns in peritoneal tissue. Am J Obstet Gynecol 1984; 148:327-334.
108. Buell BR, Schuller DE: Comparison of tensile strength in CO₂ laser and scalpel skin incisions. Arch Otolaryngol 1983; 109:465-467.
109. Schroder T, Joffe N: Will lasers replace electrocautery in surgery? Ann Chir Gynaecol 1986; 75:3-4.
110. Lesinski GS, Palmer A: Lasers for Otosclerosis: CO₂ vs. Argon and KTP-532. Laryngoscope; 1989, 99:1-12.
111. Lesinski SK, Stein JA: Stapedectomy Revision with the CO₂ Laser. Laryngoscope, 1989, 99:(Suppl. 46):13-24.
112. Lesinski SG, Palmer A: CO₂ laser for otosclerosis: Safe energy parameters. Laryngoscope, 1989, 99:9-12.
113. Lensinski SG, Stein JA: CO₂ laser stapedectomy. Laryngoscope, 1989, 99:20-24.
114. Silverstein H, Rosenberg S, Jones R: Small fenestra stapedotomies with and without KTP laser: A comparison. Laryngoscope, 1989 99:485-488.
115. Perkins RC: Laser stapedectomy for Otosclerosis. Laryngoscope, 1980, 90:228-241.
116. Gantz BJ, Jenkins HA, Kishimoto S., et al: Argon laser stapedectomy. Ann Otol, 1982, 92:25-26.

117. Vollrath V, Schreiner M: Influence of argon laser stapedectomy on cochlear potentials. *Acta Otolaryngol*, (Stockh), Suppl, 1982, 385:1-32.
118. Vollrath M, Schreiner M: The effects of the argon laser on temperature within the cochlea. *Acta Otolaryngol* (Stockh), 1982, 93:341-348.
119. Ricci T, Mazzoni M: Experimental investigation of temperature gradients in the inner ear following argon laser exposure. *J Laryngol Otol*, 1985, 99:359-362.
120. McGee TM: The argon laser in surgery for chronic ear disease and otosclerosis. *Laryngoscope*, 1983, 93:1177-1182.
121. DiBartolomeo JR, Ellis M: The argon laser in otology. *Laryngoscope*, 1980, 90:1786-1796.
122. Vollrath M, Schreiner C: The effects of the argon laser on temperature within the cochlea. *Acta Otolaryngol*, 1981, 93:341-348.
123. Ator GA, Coker NJ, Jenkins HA: Thermal injury to the infratemporal facial nerve following CO₂ laser application. *Am J of Otolaryngol*, 1985, 437-442.
124. Thomas J, Unger V, Kastenbauer E: Temperature-und Druckmessungen im Innenohr bei der Anwendung des Argon-Laser. *Laryngol Rhinol*, 1981, 60:587-590.
125. Sataloff J: Experimental use of laser in otosclerosis stapes. *Arch Otolaryngol*, 1967, 85:58-60.
126. McGhee TM: The argon laser in surgery for chronic ear disease and otosclerosis. *Laryngoscope*, 1983, 93:1177-1181.

127. Myer CM, Miller GW, Keith RW: Use of the neodymium/yttrium aluminum garnet laser in middle ear surgery: A preliminary report. Am J of Otolaryngol, 1986, 7:38-40.
128. Coker NJ, Ator GA, Jenkins HA, Neblett CR, Morris JR: Carbon dioxide laser stapedectomy. Arch Otolaryngol, 1985, 3:601-605.
129. Coker NJ, Ator GA, Jenkins HA, Neblett CR: Carbon Dioxide laser stapedotomy: A histopathologic study. Am Jour of Otolaryngol, 1986, 7:253-257.
130. Epley JM: Tympanic membrane debridement with the CO₂ laser. Otolaryngol Head Neck Surg, 1981, 89:898-902.
131. Escudero LH, Castro AO, Drumond M, Porto S, Bozinis DG, Penna FS, Gallego-Liuesma E: Argon Laser in Human Tympanoplasty. Arch Otolaryngol, 1979, 105:252-253.
132. Garner G, Robertson JH, Tomoda K, Clark WC: CO₂ Laser stapedectomy: Is it practical?, Am J Otolaryngol, 1984, 5:108-117.
133. Goode RL: CO₂ laser myringotomy. Laryngoscope, 1982, 92:420-423.

- Supplement 3, 1991

IV-H.

AMERICAN SOCIETY FOR LASER MEDICINE AND SURGERY ELEVENTH ANNUAL MEETING SAN DIEGO, CALIFORNIA ABSTRACTS

BASIC SCIENCES AND SAFETY

1

THE EFFECTS OF THERMAL DAMAGE AND DEHYDRATION ON THE OPTICAL PROPERTIES OF TISSUES

Inci Cilcisz, A.J. Welch

The University of Texas, Austin, TX

Previous studies on laser-tissue interaction have shown that the appearance of tissues changes considerably during photothermal processes. Either exposure to air or protein coagulation alters the optical properties of biological media. Thus dosimetry considerations have to be reviewed if repetitive laser irradiation is required or long irradiation times are used.

To observe the influence of dehydration and thermal damage, two groups of experiments were carried out on fresh aorta samples from human cadavers within 24 hours post mortem. A VARIAN 2300 UV-Vis-NIR spectrophotometer was used. Measurements of total transmission and diffuse reflection were taken from 300-1800 nm using a reflectance accessory. Data were analyzed in a one dimensional inverse delta Eddington diffusion model to calculate absorption and reduced scattering coefficients.

To determine the effects of hydration levels, samples were subjected to slow and relatively uniform dehydration in a cold environment. The reflectance was lower than the reflectance of the control samples; whereas the transmittance of the dehydrated samples were higher. However an overall increase in the absorption coefficient was observed except for an anticipated decrease in the water absorption band around 1350 nm. Reduced scattering coefficient changed little in most cases.

To simulate thermal damage, samples were cooked in constant temperature saline bath at temperatures varying from 60-100°C for 300 seconds. The optical behavior of the samples cooked at 60-70°C were very inconsistent; whereas the reduced scattering coefficient of samples cooked at 100°C almost doubled control values. Relative changes in the optical properties supported published values at a number of discrete wavelengths in the visible spectrum.

2

OPTICAL DETECTION OF HEAT DAMAGE IN FRESH CANINE MYOCARDIUM.

J. Bosman¹, S. L. Thomsen², I. S. Saidi², S. L. Jacques²,¹Academic Medical Centre in Amsterdam, The Netherlands,²University of Texas M. D. Anderson Cancer Center, Houston, Texas, USA

Measured optical property changes were correlated to birefringence loss as a quantifiable histologic marker of

thermal damage in myocardial slices heated *in vitro*. Thin slices (300-600 μm) of fresh canine myocardium were wrapped in water-tight aluminum foil packets and heated in a water bath at different temperatures for 1000 s. Light reflection and transmission were measured with an integrating sphere spectrophotometer in the wavelength range of 590-750 nm at intervals of 10 nm. The absorption coefficient, μ_a , and the reduced scattering coefficient, $\mu_s(1-g)$, were calculated by the adding-doubling method. Light microscopic paraffin sections (5- μm thick) stained with hematoxylin and eosin were examined by transmission polarization microscopy for thermally induced partial and total loss of birefringence. Birefringence was measured as total image intensity, I , using the microscope photometer. The room temperature controls and the completely denatured samples defined the 100% scale for birefringence ($100\% = I_{\text{native}} - I_{\text{completely denatured}}$). Thermally induced coagulation resulted in an increase in tissue scattering that was temperature dependent. Tissue scattering increased about 2-fold at 50°C and 10 to 15-fold at 80°C for all wavelengths. Intermediate temperatures yielded intermediate increases in scattering. Such results suggest that more than one type of denaturation event occurs during heating of myocardium. We hypothesize (1) a distribution of macromolecular structures within the tissue, and (2) each structure has a different rate process for denaturation that leads to increased scattering.

Loss of birefringence began at 45°C (loss of about 30% of total native birefringence) and progressively increased with temperature to reach a plateau of about 88% loss at 65-75°C. Complete loss of birefringence (the remaining 12%) occurred at 78-90°C. We hypothesize that (1) the 88% fraction corresponds to the form birefringence secondary to the regular array of the actin-myosin molecules in the sarcomere, and (2) the 12% fraction corresponds to the intrinsic molecular birefringence associated with the α -helical structure of actin and myosin.

3

MULTIPHOTON NUCLEIC ACID CROSSLINKING DEVELOPMENT OF A QUANTITATIVE APPROACH J.A. Tribble, M.S., W. Smithwick, B.S., M.D. Kyzer, B.S., G.S. Edwards, Ph.D., R.H. Ossoff, M.D., D.M.D.

Nucleic acid photo-crosslinking has for some time been a useful tool to the molecular biologist seeking to freeze biologically important, dynamic structures. Applicants however, have been limited both by a lack of selectivity and low damage thresholds. Theoretical arguments and limited qualitative evidence¹ exists that multiphoton processes may push back both of these limits considerably. We have undertaken a quantitative comparison of single-photon and two-

photon singlet excitation leading to the formation of a covalent intramolecular crosslink in a tRNA system whose photochemistry is otherwise well understood. One unit (A260) of Valine specific tRNA (SIGMA R-8258, <1% other amino acid acceptor activity) was exposed in 10 μ l of buffer (1xTBE and .01 M MgCl₂) in a .5mm path length quartz cell. Using 5 minute exposures the power density from an Nd:YAG pumped tunable dye laser (Quantel) was varied through a range .017 to 1.2 mJ per 8ns pulse (at 10 Hz, measured continuously using a pyroelectric detector) with a spot diameter of 5mm. Product yield quantitated by the reduction assay described by Favre and Yaniv² spanned the entire range of linear to non-linear response to the power density. Further evidence for extent and nature of the crosslink yield was obtained by studies of electrophoretic mobility using a gel system of Quarless and Cantor³, modified to resolve the 5 base loop formed by the specific intramolecular crosslink induced by 335nm light. The same methods have been applied to the study of the rate of forming this product with a two-photon mechanism using 670nm light. At presnet, powers up to 1.6×10^8 W/cm² (28 mJ per 8 ns pulse) have not induced measurable yield but efforts to increase this power density are ongoing. The spectroscopy of this tRNA system also provides an excellent example for the discussion of ways in which multiphoton processes can be applied to biological systems.

- (1) see e.g., P.P. Calmette M.W. Berns, PNAS, 80(23):7197-9 1983
- (2) A. Favre, M. Yaniv, FEBS Lett, 17(2):236-240 (1971)
- (3) S.A. Quarless, C.R. Cantor, Anal. Biochem. 147:296-300 (1985).

4

PULSED LASER GENERATION AND OPTICAL FIBRE DETECTION OF THERMOELASTIC WAVES IN ARTERIAL TISSUES

TN Mills, SML Andrew and M Essenpreis

Department of Medical Physics and Bioengineering, University College, London, UK.

Perforation of the arterial wall due to poor guidance of the optical fibre and incorrect targeting of the laser energy remains the principal drawback of laser angioplasty. In an attempt to overcome this problem, we are developing a laser light delivery system which incorporates a device for sensing the vessel environment, and identifying and delineating areas of atheromatous plaque. The system employs a multimode optical fibre for transmission to the target tissue of low energy 10ns Q switched Nd:YAG laser pulses and 100 μ s fixed Q Nd:YAG laser pulses. The 10ns pulses generate thermoelastic waves in the target tissue, while the 100 μ s pulses are used to ablate the plaque. The temporal profile of the thermoelastic waves is dependant upon the light attenuating properties of the target tissue at the wavelength of the optical pulse. A frequency doubler and Raman cell shift the output of the Q switched laser to a region of the spectrum where the thermoelastic waves generated in plaque differ from those generated in healthy arterial tissues. To sense the thermoelastic waves and their reflections from subsurface tissue boundaries, a wide bandwidth pressure sensor comprising a Fabry-Perot interferometer, transparent to the laser pulses, is bonded to the distal end of the optical fibre. The thermoelastic waves modulate the length of the interferometer, and hence, the power of a coherent light source reflected back through the optical fibre. Once an area of plaque has been positively identified following demodulation of the intensity of the fringes of the interferometer, treatment using the 100 μ s pulses can proceed immediately. The system is being developed for use with not only the pulsed Nd:YAG laser, but the Ho:YAG, Er:YAG and excimer lasers as well.

5

THERMAL RESPONSE DURING TISSUE COAGULATION BY SUCCESSIVE LASER EXPOSURES

G. Yoon¹, P. S. Sriram², R. C. Straight¹, A. J. Welch²

1. Utah Laser Institute, University of Utah, Salt Lake City

2. Electrical Engineering, University of Texas at Austin

Tissue properties change during laser irradiation. Depending on power density and exposure time, varying degrees of physical change occur. In this work, temperature response caused by laser coagulation was studied. Laser irradiation with the same power density and exposure time was repeated on the same spot to measure each temperature response as the tissue was being coagulated. The time interval between the exposures was set so that the tissue temperature returned to the initial temperature. Energy was limited to avoid ablative processes. A Nd:YAG (1.06 μ m) laser was used and a thermal camera measured surface temperature. Samples of human aorta and chicken breast were used. Coagulation was observed to increase both absorption and scattering. This change was observed in the temperature response. When the tissue was coagulated, the temperature increase became higher for subsequent power density exposures, which did not produce visual damage. Computer simulations based on the light diffusion and bio-heat conduction equations were applied to analyze the experimental data.

6

SOFT TISSUE EFFECT OF PULSED AND CONTINUOUS WAVE 1.32 AND 1.06 μ m WAVELENGTHS OF THE Nd:YAG LASER

Elie E. Rebeiz, Stanley M. Shapshay, Michail M. Pankratov, Femke Van Overbeek, Lahey Clinic, Burlington, MA. The Nd:YAG laser is widely used clinically for vaporization, coagulation and ablation of soft tissue tumors. It is however poorly absorbed by water due to its conventional wavelength of 1.06 μ m. Previous investigations have shown good clinical potential for the use of the 1.32 μ m wavelength Nd:YAG laser because of its better soft tissue absorption than the 1.06 μ m wavelength Nd:YAG laser. The absorption coefficient in water of the 1.32 μ m wavelength Nd:YAG laser is 10 times higher than the 1.06 μ m wavelength Nd:YAG laser. A comparative *vivo* study of laser soft tissue effects was performed using the 1.32 μ m wavelength and 1.06 μ m wavelength Nd:YAG lasers in a pulsed wave (PW) mode and continuous wave (CW) mode using a noncontact delivery system. A standard 5 mm skin lesion was made in rat using a hand held, 600 μ m fiber, at a power of 15 to 36 Watts, and 0.5 second exposure time PW. Soft tissue effects were examined by light microscopy, acutely, 1 week, and 2 weeks after operation, and a comparison was made between the different laser modalities relative to acute damage and to healing. To create a 0.5 cm lesion, higher energy was required when using the 1.06 μ m wavelength Nd:YAG laser. Soft tissue injury was greater with the 1.06 μ m wavelength in CW mode. Soft tissue healing after 1 and 2 weeks was better with the 1.32 μ m wavelength laser. In comparison, the CO₂ laser and the contact Nd:YAG laser proved to be more precise cutting tools than the 1.32 μ m wavelength or the 1.06 μ m wavelength Nd:YAG lasers. Both Nd:YAG laser wavelengths were useful for coagulation and vaporization of tissues and blood vessels. More studies are needed to determine the effect of the new 1.32 μ m wavelengths, and the possibility of combining a cutting and coagulating Nd:YAG laser wavelengths, to be used simultaneously.

IV-I

Poster 10

An Investigation of Laser-Induced Protein Synthesis by Cultured Fibroblasts

DEBRA A. GONZALEZ, MD, JEFFREY M. DAVIDSON, PhD,
DAVID L. ZEAL, PhD, and ROBERT H. OSSOFF, DMD, MD,
Nashville, Tenn.

While lasers have been conventionally used in medicine as ablative or photocoagulating instruments, there is growing evidence in the literature that laser energy may also be used in subtle ways to modulate cellular metabolic activity and wound repair. The purpose of this investigation was twofold: (1) to determine whether sublethal laser irradiation can alter the pattern of overall protein synthesis by cells in culture and (2) whether the observed changes in protein synthesis are caused by nonspecific thermal mechanisms or to specific photochemical events related to the spectral characteristics of the irradiation.

Cultured human skin fibroblasts were exposed to either sublethal Nd:YAG laser irradiation or heat shock at 42° C. Laser power densities and heat intensities used were determined to be sublethal by a dye exclusion-viability assay. After laser irradiation or heat shock, cells were incubated in media containing ³⁵S-methionine and time allowed for the incorporation of radioactivity during protein synthesis. Radiolabelled proteins were separated from unincorporated amino acids in the cell lysates and incubation media by TCA precipitation. Equal numbers of precipitable counts per minute were loaded onto SDS-polyacrylamide gels. After electrophoresis, autoradiography was performed in order to detect bands of newly synthesized radioactive proteins. The media were processed separately from the cell lysates in order to analyze the pattern of secretory proteins in isolation. These represented the extracellular matrix proteins that participate in wound healing. Proteins within the cell lysates represented cytoplasmic proteins, whose synthesis has been shown to be induced by heat shock and other stresses.

Preliminary results indicated that sublethal Nd:YAG irradiation, delivered continuously at power densities ranging from 500 to 1750 Joules/cm², was capable of inducing changes in the type and quantity of synthesized proteins by fibroblasts. Autoradiography of the cell lysates revealed at least one new protein induced by either laser irradiation or heat shock. This protein band had a molecular weight of 85 to 89 kilodaltons. Within the media fractions, increased synthesis of a 60-kilodalton molecular weight protein was observed after laser irradiation, but not after heat shock at 42° C.

These observations suggest that both thermal and spectral components may play a role in the alteration of protein synthesis by cultured fibroblasts. However, laser photochemical effects may more readily influence synthesis of those proteins secreted by cells during wound healing.

(Supported by the SDIO Office of Naval Research)

Poster 11

Intraoperative Photodynamic Therapy for the Eradication of Aggressive and Invasive Tumors

RANDY L. JENSEN, R. KIM DAVIS, MD, and
RICHARD C. STRAIGHT, PhD, Salt Lake City, Utah

This study involves the use of intraoperative photodynamic therapy (PDT) for the treatment of aggressive and invasive carcinomas. C1300 mouse neuroblastoma was surgically resected from the flank of AJ/CR mice and PDT of the operative bed was used to destroy remaining tumor cells. Others have shown this to be an effective modality for tumor removal (75% cure rate with 514 nm light and 50% with 628 nm light) when using high light doses (127 mW/sq cm) and long (10-minute) exposure times.

Our goal was to use a low light dose and short exposure time (41 mW/sq cm, 2-minute exposure) to develop a more clinically useful model for adjuvant surgical PDT. Standard PDT treatments, comparable to those used in the intraoperative study, showed no cure of tumor, but growth was lagged for 3 days. Animals receiving surgical resection only had a 12% cure rate. Intraoperative PDT with 628 nm light showed a 32% cure rate, and 514 nm laser light provided a 41% cure rate. Therefore, we believe that intraoperative PDT, even with low light doses and short exposure time, can substantially decrease the recurrence of tumor after surgical resection.

Poster 12

The Detection and Treatment of Post-Thyroidectomy Hypocalcemia

HUGH E. HETHERINGTON, MD, DON B. BLAKESLEE, MD,
NEWTON O. DUNCAN, MD, JAMES C. ROCKWELL, MD, and
STANLEY C. HARRIS, MD, Tacoma, Wash.

Hypocalcemia following thyroid surgery is not uncommon, but in most cases is transient in nature. Close monitoring, however, is necessary to avoid complications if significant hypocalcemia occurs. Various authors have reported hypocalcemia requiring treatment in 13% to 28% of cases post-thyroidectomy, with an incidence of permanent hypocalcemia in 2% to 4% of patients.

Records of 112 patients who underwent partial or total thyroidectomy at Madigan Army Medical Center over the past 5 years were retrospectively reviewed. Significant postoperative hypocalcemia, defined by serum <8.0 mg/dl, occurred in 24 (21.4%) patients. Fifteen (13.4%) of these were treated for hypocalcemia, whereas 12 (10.7%) had transient, self-limited hypocalcemia not requiring therapy. Hypocalcemia occurred in 31.9% of patients undergoing thyroidectomy for malignant disease and in 18.5% with benign thyroid disease. Treatment for hypocalcemia was required in 21.3% of malignant thyroid cases, compared to 7.7% of benign thyroid pathology. Therapy for hypocalcemia was not required in patients simply undergoing hemithyroidectomy.

From this experience, we describe in detail and advocate a rational protocol for the detection and treatment of hypocalcemia post-thyroidectomy. This protocol represents a safe, practical approach to management of post-thyroidectomy hypocalcemia and is of particular value in a teaching institution.

August 1990

IV-J.

9:00 A.M.

A Comparison of Vocal Fold and Skin Fibroblast Elastin Production in Tissue CultureDEBRA A. GONZALEZ, MD, DAVID L. ZEALEAR, PhD,
J.M. DAVIDSON, PhD, and ROBERT H. OSSOFF, MD, DMD,
Nashville, Tenn.

The biomechanical properties of the vocal cord allow for its vibration, lengthening, and shape change during voice production. Histologic studies have shown that the vocal fold mucosa is primarily a connective tissue, and that elastin is prominent within the lamina propria. Because the only known function of elastin is to provide elastic recoil to tissues, we suspect vocal fold elastin is a necessary feature for normal voice production. Experiments were performed in order to determine if a structure requiring high elasticity for normal function—such as the vocal fold—contains fibroblast cells distinguished in their elastogenic capacity.

Vocal cord and skin fibroblasts were explanted and maintained in tissue culture. An enzyme-linked immunoassay was used to quantify the soluble tropoelastin (TE) secreted by early passage cells into the tissue culture media. Comparison of dog vocal fold and pig skin elastin production revealed that the vocal fold cells produced 150,000 molecules TE/cell/hour, which was 2 to 4 times greater than skin fibroblast TE production. TE production by both cell types was up-regulated by treatment with 1.6 μ M hydrocortisone (increased 120% by skin cells and 53% vocal fold cells). These models were initially chosen because they closely resemble human tissues: vocal cords of dogs and human beings have similar histologic features, whereas the skin of pigs and human beings is noted to be biochemically similar. Despite the attempt to individualize each assay by using competing antigen (alpha elastin) purified from the same species, we were concerned about the accuracy of an inter-species comparison. Comparing elastin production by fibroblasts taken from vocal cord and skin of the dog, vocal fold cells produced twice as much TE as skin cells.

In order to assess the functional significance of cells exhibiting high elastogenic activity, fibroblast elastin synthesis was compared in two species differing in their vocalization behavior. Dog vocal fold cells produced 5 times more TE (>100,000 molecules/cell/hour) than pig vocal fold cells.

Vocal fold fibroblast cell cultures represent a valuable tool for the study of vocal fold connective tissues. The finding that dog vocal fold cells produce significantly more elastin than skin cells supports the idea that elastin is an important component within the vocal fold mucosa. The finding that dog vocal fold cells produce significantly more TE than pig vocal fold cells correlates well with published comparative histology showing less elastin within pig vocal fold mucosa, and suggests that vocal fold fibroblasts grown in culture exhibit levels of elastogenesis that are representative of their physiologic activity in vivo.

(Supported in part by the Veterans Administration, Genentech, Inc., and NIH grants AG 06528 and GM 37387 [J.M.D.] and the SDIO Office of Naval Research [R.H.O.])

9:15 to 10:15 A.M.

Posters (Session C)

See pages 195 to 210

10:15 A.M.

Effect of Superior Laryngeal Nerve on Vocal Fold Function: An In Vivo Canine ModelDAVID H. SLAVIT, MD, and THOMAS V. McCAFFREY, MD, PhD,
Rochester, Minn.

Assessment of laryngeal framework surgery requires an awareness of the effect of vocal fold mass, stiffness, and position on voice production. The vibratory pattern of the vocal folds during phonation depends on the transglottic pressure plus the mass and stiffness of the folds. To assess the effect on phonation of variations in vocal fold tension with contraction of the cricothyroid muscle, eight mongrel dogs were studied using an in vivo canine model. Photoglottography, electroglottography and subglottic pressure were simultaneously recorded as airflow rate and superior laryngeal nerve (SLN) stimulation were varied. Stimulation of the SLN was modified by varying the frequency and voltage of the stimulating electrical signal.

Multiple regression analysis of the data revealed a direct relationship between the voltage of SLN stimulation and frequency of vibration ($p < 0.001$). Increases in the stimulating voltage to the SLN also led to an increase in open quotient ($p < 0.001$), but no statistically significant change in speed quotient, subglottic pressure, or sound intensity. Changing the frequency of SLN stimulation had only a modest change in frequency of vibration.

These results for the in vivo canine model are consistent with the reported findings of an increase in frequency and open quotient with increased tension in an in vitro canine model. The clinical implications of these results will be discussed, with emphasis on the changes in vibratory pattern of the vocal folds produced by changes in their stiffness and tension with laryngeal framework procedures.

10:30 A.M.

Study of Phonation in the Excised Canine LarynxERICO YANAGI, MD, and THOMAS V. McCAFFREY, MD, PhD,
Rochester, Minn.

The excised canine larynx has been a useful research model for the analysis of the mechanical factors affecting vocal fold vibration. With the vocal folds in the maximally abducted position, previous studies have demonstrated that the laryngeal muscles responsible for pitch variation and vocal efficiency are the cricothyroid muscles affecting longitudinal tension of the vocal folds and the thyroarytenoid muscle controlling the lateral stiffness of the vocal folds.

Longitudinal tension in the vocal fold is easily simulated in the excised canine larynx. The effect of the thyroarytenoid muscle, however, has not been adequately analyzed. To simulate the effect of the thyroarytenoid muscle in producing lateral stiffness of the vocal fold, small balloons were placed

August 1991
IV-K

21

Late Esophageal Rupture as a Complication of Anterior Cervical Spine SurgeryMONTE S. KEEN, MD, and DEBORAH SEELIG, MD,
New York City, N.Y.

Esophageal rupture as a complication of anterior neck surgery is a rare and life-threatening entity that usually manifests early in the postoperative course. Early diagnosis and aggressive management are necessary in order to avert a mortality. It is almost unheard of for a surgically related esophageal perforation to occur 3 weeks postoperatively.

We report a case of late esophageal perforation induced by a stripped screw used to plate the anterior cervical spine. The management of this interesting and highly unusual case will be presented along with a review of the literature.

22

Inverted Papilloma of the Temporal Bone With Neoplastic DegenerationDIANE G. HEATLEY, MD, ASHLEY G. ANDERSON, Jr., MD, and
DOUGLAS M. ENGLAND, MD, Madison, Wis.

Inverted papilloma of the sinonasal tract is a well-described pathologic entity, although its cause remains obscure. It is known to be locally aggressive and often recurrent after surgical excision. Inverted papilloma has been associated with squamous cell carcinoma in a significant number of patients.

We present the case of one patient, treated over a 9-year period for nasal inverted papilloma, in whom ipsilateral involvement of the middle ear and mastoid developed. The mastoid papilloma degenerated into squamous cell carcinoma and invaded the posterior cranial fossa. The tumor eventually extended into the temporal lobe, despite surgical excision and radiotherapy. Inverted papilloma in the temporal bone has not been previously documented in the literature. Inverted papilloma, its association with malignancy and metastasis, and the possible role of human papilloma virus are discussed.

23

Distribution of Human Mast Cell Subsets in Nasal TissueKEITH M. DOCKERY, MD, ARISTIDES SISMANIS, MD,
ANNE-MARIE IRANI, MD, and E. SPOCK, MD, Atlanta, Ga.,
Richmond, Va., and Durham, N.C.

The distribution of two types of human mast cells was determined in nasal biopsies from normal individuals ($n = 12$) and subjects with allergic rhinitis ($n = 13$), as well as in nasal polyps of subjects with allergic rhinitis ($n = 6$), aspirin sensitivity ($n = 6$), chronic sinusitis ($n = 9$), and cystic fibrosis ($n = 16$).

A double immunohistochemical staining technique was used to differentiate between mast cells containing tryptase but not chymase (MC_T cells) and mast cells containing tryptase as well as chymase (MC_{TC} cells). MC_T cells were the predominant type of mast cell present in the epithelium, whereas MC_{TC} cells predominated in the subepithelium. No significant differences in distribution of MC_T and MC_{TC} cells were seen between the various groups. Thus, the distribution of MC_T and MC_{TC} cells does not appear to be altered in diseased nasal tissue as compared to normal.

24

CO₂ Laser Micromanipulator Parallax Error ResolvedJAY A. WERKHAVEN, MD, JERRI TRIBBLE, and
ROBERT H. OSSOFF, MD, DMD, Nashville, Tenn.

Most current CO₂ laser micromanipulators for microlaryngoscopy experience the parallax aiming problem. This occurs when the beam mirror is offset below the optical path for the microscope, making use of the laser difficult, through small laryngoscopes or in pediatric patients. The newer "hot mirror technology" micromanipulators that are now available overcome this problem.

In addition to providing a laser beam coincident with the optical path, most offer much smaller spot sizes (250-micron diameter at 400-mm focal length), but all partially block some of the light available for illumination. To quantitate this, optical absorption spectra were determined for six hot mirrors. Clinical experience with more than 100 cases has demonstrated the advantages of these new mirrors to minimize mucosal thermal damage and give improved exposure for subglottic and pediatric laryngoscopy.

IV - L.

10:30 A. M. to 12:10 P.M.
Room 215, KCCC

● **BIOTECHNOLOGY IN OTOLARYNGOLOGY**

G. RICHARD HOLT, MD, MSE,
San Antonio, Texas (moderator)

10:30 A.M.

**Introduction of a New Device, the "Scope Scrubber",
For Endoscopic Sinus Surgery**

ELIE E. REBEIZ, MD, STANLEY M. SHAPSHAY, MD,
DAVID W. KENNEDY, MD, and MICHAEL M. PANKRATOV, MS,
Burlington, Mass., and Philadelphia, Pa.

Since its introduction, the instrumentation for nasal endoscopic surgery has continued to evolve. However, deposition of debris and blood on the lens remains a major problem. The necessity to clean the lens delays the surgery significantly, and calls for frequent removal of the telescopes. The currently available suction irrigators are too bulky for atraumatic use.

In order to overcome this problem, a new instrument, the "scope scrubber", was designed to allow self-cleaning of the telescope lens. It consists of a thin metallic sleeve that fits around 0° and 30° sinus telescopes and is connected to a suction-irrigation machine, operated by a foot control.

This instrument was easy to use in the laboratory on a live canine model and on 37 patients undergoing endoscopic sinus surgery. The volume of fluid delivered per stroke was 0.1 ml, and the average volume of irrigation fluid was 45 cc during a standard procedure. The telescope was removed only occasionally, even when bleeding was moderate-to-severe.

The "scope scrubber" is a major addition to the endoscopic sinus surgery instrumentation. It makes the procedure significantly easier, improves visualization, and shortens operating time. The device can be modified to fit bronchoscopic telescopes, as it may be very useful in laser bronchoscopy.

10:36 A.M.

**Improved Endoscope Technique For Establishment of
Tracheoesophageal Puncture For Speech Restoration**

ISAAC ELIACHAR, MD, FRCS, Cleveland, Ohio

A new endoscopic method to safely and readily establish a tracheoesophageal puncture for accommodation of voice prostheses after total laryngectomy is presented. This technique uses a newly designed, double-tubed esophagoscope that incorporates a distal aperture through which the tracheal esophageal puncture may be executed while the risk of misplacement, false passage, mediastinal trauma, or infection is minimized. A special clamp ensures introduction of the catheter/stent into the esophagus, simultaneously guiding it caudally through the lumen in one single motion. The introducer can then be retracted, leaving the catheter in its desired position.

The design of the endoscope permits its removal without disturbing the catheter. This method requires minimal training and should be safe and fool-proof. Its clinical advantages will be reviewed.

10:42 A.M.

**A New Endotracheal Tube for CO₂ and KTP/532 Laser
Surgery of the Upper Aerodigestive Tract**

ROBERT H. OSSOFF, MD, DMD, AL ALY, MD,
NICK HOUGHIN, AAS, and DEBRA GONZALEZ, MD,
Nashville, Tenn., and Burlington, Vt.

A new endotracheal (ET) tube has been developed for laser surgery of the upper aerodigestive tract with the carbon dioxide (CO₂) and potassium titanyl phosphate/532 (KTP/532) lasers. The tube itself is made of silicone, which is wrapped circumferentially with reflective, metallic tape by a special process that uses no adhesive backing. Teflon tape is wrapped over the reflective, metallic tape to prevent any mucosal injury during either intubation or extubation. This Teflon tape retracts out of the way during impact with either laser.

Because methylene blue crystals are present within the ET tube cuff insufflation line, inflating the cuff with saline will yield methylene blue-colored saline in the cuff. The tube is shipped sterile and ready for intubation; neurosurgical cottonoids are included in the package.

This tube has been tested extensively in our laboratory with the CO₂ laser, including microspot and the KTP-532 laser, and has been found to resist penetration and combustion with both wavelengths under normal operating conditions.

10:48 A.M.

Self-Monitoring Tracheotomy Tube

ROBERT K. EINHORN, MD, STEVE I. SZOKE, MS, and
YOSEF P. KRESPI, MD, New York and Brooklyn, N.Y.

This electronic safety device attaches to tracheotomy tube for maintaining and monitoring airway patency in a tracheotomized patient. The apparatus is comprised of two independent sensing devices. This device is designed to (1) warn when there is absence of air flow and (2) send an alarm when the tube becomes obstructed, because of a plug or mucus buildup. The first sensor includes thermocouple sensors, disposed in such a way that the movement of the air in the tracheotomy tube is identified. The second sensor includes a capacitor disposed in the tracheotomy tube to detect the percent of occlusion. Both sensing signals are electronically connected with an alarm and display system, the systems being (1) a patient unit and (2) a remote radio nursing station unit.

SCIENTIFIC
SESSIONS

1. Fluorescence detection and identification in the management of acute otitis media.

Collaborators: Jay Werkhaven, M.D.
The Nemours Children's Clinic
Jacksonville, Florida

Jerri Tribble
Dept. of Physics
Vanderbilt University

Fluorescence Spectroscopy of Bacteria in Otitis Media, J.A. Tribble, J. Werkhaven and L. Reinisch, Applied Spectroscopy (in preparation).

Abstract

The management of otitis media in children continues to be hampered by two fundamental problems: The prevalence of bactericidal resistant species is increasing (frequent misdiagnosis lead only to enhancement of the growth conditions for resistant species); The identification of resistant species is time consuming, expensive and requires drainage of the middle ear. The fluorescence spectra of four strains of bacteria, commonly found in otitis media: *P. aeruginosa*, *S. aureus*, *B. catarrhalis* and *H. influenzae* has been measured. The excitation wavelength has been varied from 280 to 500 nm and the emission spectra measured. The fluorescence spectra are presented at two dimensional fluorescence finger prints. These fingerprints will ultimately be used to identify the bacteria remotely, and non invasively from otitis media.

Future Research Support:

(i) An Innovative Technology Research Grant to the National Institutes of Health is being prepared and will be submitted February 1, 1992.

(ii) The Deafness Research Foundation has been contacted. A proposal will be submitted before their annual due date in June, 1992.

(iii) We are in the initial stage of contacting the Whitaker Foundation for support.

2. Measurement of the membrane dynamics of the activated purple membrane.

Collaborator: J. Czégé
Uniformed Services University of the
Health Sciences
Bethesda, Maryland

The Effect of Triton X-100 on Purple Membrane as Measured by Changes in the Dynamics. J. Czégé and L. Reinisch, Photochem. and Photobiol (submitted, 1992).

Abstract

We have observed the light scattering transients arising from changes in the curvature of purple membrane fragments upon photoexcitation at pH 8.05 and 4.1 with and without treatment of Triton X-100. The low ionic strength room temperature suspensions are excited with 532 nm light pulses from a Nd:YAG laser (20 ns). The scattering of 320 nm light is monitored from 3 μ s to 1 s at scattering angles from 15° to 60°. We simultaneously measure the transient transmission changes at 320 nm. The transient light scattering signals change significantly with the addition of 0.02% Triton X-100 at pH 8.05 and 0.006% Triton X-1000 at pH 4.1. At these concentrations of Triton we observed maximal amplitudes in the transient changes of the scattered light intensity. At higher concentrations, the Triton solubilizes the protein and the scattering signals are completely attenuated. The transient transmission changes become severely distorted by the scattering changes in the Triton treated samples. We can explain these changes using our bent membrane model and assuming a greater initial curvature and an increased transient curvature change in the membrane fragments after the Triton X-100 is added. The amplitudes of the scattering changes as a function of the scattering angle from 15° to 60° agree with model calculations of the scattering amplitudes.

Future Research Support:

- (i) A R01 grant proposal has been submitted to the National Institutes of Health, 1 November, 1991.

AN INVESTIGATION OF THE POTENTIAL FOR LASER NERVE WELDING

MARJORIE KORFF, M.D.; STEPHEN W. BENT, B.S.;
MICHAEL T. HAVIG, B.S., MITCHEL K. SCHWABER, M.D.
ROBERT H. OSSOFF, M.D.; DAVID L. ZEALEAR, PH.D.

VANDERBILT UNIVERSITY, NASHVILLE, TENNESSEE 37232

Direct Correspondence To:

David L. Zealear, Ph.D.

Department of Otolaryngology-Head & Neck Surgery

Medical Center North S2100

Vanderbilt University Medical Center

Nashville, TN 37232

615-322-7267

Presented at the Research Forum of the Annual Meeting of the American Academy of Otolaryngology-Head & Neck Surgery, Washington D.C., September 27, 1988.

Supported by Office of Navy Research, Contract #NOO14-87-0146

ABSTRACT

Suture repair of a severed peripheral nerve is cumbersome, presents a focus for infection and neuroma formation, and does not always produce adequate stump alignment. An alternative form of repair is laser nerve welding which is attractive because it does not introduce foreign material into the anastomotic site, it forms a circumferential seal, and it can be performed in difficult to reach areas. Laser repair has not been widely accepted both because the effect of laser irradiation on intact nerves is not well documented, and the anastomotic strength of the weld has been inferior to suture repair. In the first part of the present study, rat sciatic nerves were exposed and irradiated with increasing intensities from a Sharplan CO₂ and a KTP laser to document nerve damage as recorded by decreases in the peak compound action potential (CAP). A new technique of laser repair (S-Q weld) was then developed which involved harvesting subcutaneous tissue from the adjacent dermis, wrapping it around the two opposed nerve stumps, and lasering it to the epineurium to effect a weld. The strength of the S-Q weld (6.1 grams) was considerably greater than that produced by laser welding alone. The third phase of the study compared regeneration at two months in severed rat sciatic nerves repaired by either microsuture or S-Q weld. Analysis of the CAP values indicated that the number of regenerating fibers following laser repair was greater than that following suture repair, although a significant difference could not

be demonstrated. The rate of nerve dehiscence in the laser repair was unacceptably high, but the observed advantages of the technique indicate a need for further investigation.

INTRODUCTION:

Microsuture repair is the most commonly used method for anastomosis of severed peripheral nerves. However, functional recovery following this type of repair is often inadequate even though the peripheral nervous system has a remarkable ability to regenerate adequate sizes and numbers of axons. The most significant problems with microsuture repair are inherent in the technique: 1) Surgery traumatizes the nerve by repeated introduction of a needle. 2) Suture material at the anastomotic site presents a focus for scar and neuroma formation which may impede the growth of regenerating axons from the proximal segment into the proper distal segment endoneurial tubes and, ultimately, the neuromuscular junction. 3) Microsurgical repair inevitably leaves small gaps which allow entry of fibroblasts and other scar tissue forming cells, permit regenerating axons to escape into an improper extraneural space, and promote loss of neurotrophic hormones that may be secreted locally to aid in the conduction of regenerating axons to their proper target. 4) Microsurgery is time consuming and may be difficult to perform in restricted areas (e.g. intraoral repair of lingual and mandibular nerves), particularly when supportive epineurial material is scarce (1).

Laser repair of severed peripheral nerves has been investigated by several authors, since it offers a significant theoretical improvement to the problems noted above. The mechanism of laser repair involves protein denaturation and subsequent fusion of the collagenous portion of the proximal and distal segment epineurium

by low level thermal coagulation (1). Laser application has been shown to cause a change in collagen substructure with interdigitation of altered fibrils (2). This mechanism of repair avoids the trauma imposed by needles, and it does not introduce foreign material into the anastomotic site. Furthermore, the seal formed by the laser repair is circumferential and therefore discourages entry of fibroblasts or exit of regenerating axons and neurotrophic hormones. Lastly, several authors have noted that laser welding takes significantly less time than microsuture repair, and it can be performed in difficult to reach areas (3, 4).

The advantages of laser nerve welding indicate that it has potential for clinical application. However, there are two major problems that prevent the widespread acceptance of this technique. First, the effect of laser radiation on intact nerves has not been well documented. Second, the anastomotic strength of the laser weld has been found consistently inferior to that of microsuture repair for at least the first four days following surgery (5). The weak initial weld has caused unacceptable rates of dehiscence and prompted the use of stay sutures in many of the animal models (1,3,4,6,7).

The present study attempted to improve upon the laser weld technique by first examining the effect of laser radiation on the compound action potential of intact rat sciatic nerves. In the second phase of the study, a new technique to improve anastomotic strength was developed (S-Q weld) which involved harvesting a sheet of subcutaneous tissue from the experimental animal, wrapping it around the cut nerve ends, and lasering it to the epineurium. The

final part of the study examined the long term effectiveness of the technique as compared to microsuture repair in the rat sciatic nerve model.

MATERIALS AND METHODS:

Study 1: The Effect of Laser Irradiation on Intact Nerve Function:

In this initial study, the effect of KTP, nd:YAG, and CO₂ laser irradiation on the compound action potential (CAP) of intact sciatic nerves was investigated. All animals used in these experiments were cared for in compliance with "The Principles of Laboratory Animal Care" formulated by the National Society for Medical Research. Twenty-one Sprague Dawley rats were anesthetized with an intraperitoneal injection of 0.13 cc sodium pentobarbital mixed with 0.87 cc ketamine (per Kg). The sciatic nerve of each rat was exposed and a pair of differential recording electrodes positioned just proximal to the nerve trifurcation. A pair of stimulating electrodes was then placed 3 centimeters proximal to the recording electrodes and the nerve suspended in air to improve recording isolation. Single square-wave pulses were applied to the nerve using a Grass S88 stimulator. The stimulus intensity was increased until a CAP of maximum peak to peak amplitude (P-P CAP) was recorded. The nerve was then irradiated midpoint between the electrodes using increasing laser intensities as listed in Table I. CAP recordings were obtained following the laser treatment at each intensity. Each treatment involved irradiation with 30 pulses, 0.05

seconds in duration at a spot size of 0.36 mm. A Sharplan 1060 CO₂ laser and a Laserscope KTP laser were used in these experiments. The effect of laser irradiation on nerve function at each wattage was then determined by expressing post-irradiation P-P CAP values as a percentage of pre-irradiation P-P CAP value, indicating the percent of viable fibers still remaining in the nerve.

Study 2: Tensile Strength of Repaired Nerves

a. Surgical Technique:

Twenty-five Sprague Dawley rats were anesthetized using the mixture as described previously. Employing sterile technique, the sciatic nerves were exposed bilaterally and transected 3 centimeters proximal to the trifurcation with a steel scalpel. On the left side, the nerve stumps were realigned and repaired using 2 epineural sutures of 10-0 nylon placed 180 degrees apart. On the right side, the nerve stumps were reanastomosed using the subcutaneous tissue weld technique (S-Q weld). A small piece of translucent subcutaneous tissue was harvested and stretched over a 1 cm² piece of aluminum foil. The foil was placed under the transected nerve ends. The nerve ends were reapproximated and the S-Q tissue was wrapped around the nerve and spot welded to the epineurium using a Sharplan 1060 CO₂ laser. The energy paradigm of 1.00 Watt, 0.05 sec single pulses, 0.36 mm spot size was chosen, since this appeared to represent the nominal power level for bonding subcutaneous tissue to nerve epineurium. Multiple pulses were applied to the S-Q sheath a few millimeters from the anastomotic site around a circumference of 180 degrees to allow for adequate

stump alignment with room for nerve swelling. (The S-Q sheath completely encircled the anastomotic site). All surgeries were performed by the same surgeon (M.K.) until the sheath appeared tightly bound.

In ten of the rats, the laser and suture repaired nerves were harvested immediately for tensile strength measurements. In the remaining fifteen, wounds were closed and the animals were placed in their cages with no restriction of movement for two months.

b. Measurement of Tensile Strength:

Suture, laser repaired, and intact nerves were evaluated for tensile strength. Approximately 4 cm of sciatic nerve was excised. 4-0 silk ligature was tied from one end of each nerve to a calibrated force transducer (Grass Instruments, Quincy Mass) whose output was amplified and visualized on an oscilloscope. The opposite nerve end was attached with 4-0 silk ligature to a platform mounted on a variable speed infusion pump (Harvard apparatus) which generated slow, steady tension. Tension was applied until the nerve separated, and breaking force was recorded.

Study 3: Electrophysiological and Histological Evaluation of Regeneration in Repaired Nerves.

After allowing two months for regeneration, the sciatic nerves were removed from 15 rats for CAP transmission studies and histological examination. Nerves were harvested, placed in an isolation chamber, and bathed in Ringer's solution. Bipolar stimulating electrodes were placed proximal and recording electrodes positioned distal to the anastomotic site. The P-P CAP

from the laser repaired nerve was recorded and expressed as a percentage of the P-P CAP of the suture repaired nerve in each rat. All recordings were taken with nerves suspended in air. Each nerve was then fixed in 4% paraformaldehyde buffered by .1 M phosphate (pH 7.4), post-fixed in osmium tetroxide, alcohol dehydrated, imbedded in epon, and thin sectioned for histological and E.M. analysis.

Results:

The effects of laser irradiation on compound action potential transmission are presented in Table I. The nd:YAG laser was dropped from the study because it caused significant endoneurial damage at nominal intensities, as evidenced by CAP depression. As can be seen from the table, both the CO₂ and the KTP lasers produced almost no decrease in P-P CAP transmission at 0.5 watts. However, this level of irradiation did not provide adequate bonding of subcutaneous tissue to nerve epineurium during S-Q welding in the later two studies. In these studies, a higher power of 1.0 watt was used, since it produced adequate bonding with minimal anticipated increase in damage to endoneurial axons and support structures. It was estimated that considerably less than 40% of the radiation penetrated the endoneurium in these studies, corresponding to 60% remaining axon function in Table 1, since some of the radiation was absorbed by the subcutaneous tissue wrap. Intensities as high as 2.5 watts were often sufficient to cut a nerve in half as indicated in the table. In such instances, the P-P CAP value was recorded as zero.

The results of the tensile strength study are presented in Figure I. Intact nerves (n=11) showed a breaking force of 218.6 gms \pm 14.6. Suture repaired nerves (n=10) showed a breaking force of 47 gms \pm 10.8, which represented 21.5% of the intact nerve strength. The S-Q Weld technique (n=10) had a breaking force of 6.1 gms \pm 5.0, which represented 2.8% of the intact nerve strength.

At two months post surgery, 6 of 15 rats had intact laser anastomosis while 14 of 15 had intact suture anastomosis. The P-P CAP value from each laser repaired nerve was recorded and expressed as a percentage of the P-P CAP of the suture repaired nerve. The average ratio for all animals measured was 1.05 ± 0.18 , indicating that the number of regenerating fibers following laser repair was greater than that following suture repair, although a significant difference could not be demonstrated. Histological examination of nerve segments distal to the laser or suture repair sites demonstrated no significant differences in the numbers of axons or their population diameters (Figure II).

Discussion:

There is a wide range of reported energy paradigms for laser welding of severed peripheral nerves in animal models. Fischer et. al. used the CO₂ laser on the rat sciatic nerve at a power of 5 watts (0.6 mm spot size, 0.5 sec pulses (4), while Maragh et. al. used a power of 90-95 mW (0.2 mm spot size, 2 msec pulses (5). Our initial study was undertaken to determine an energy paradigm that would create a strong anastomosis without inflicting excessive damage upon the regenerative elements of a severed peripheral

nerve. This study assumes that irradiation which reduces the CAP of an intact nerve would also damage the endoneurial tubes in a traumatized or severed nerve. The endoneurial tubes serve as conduits to regenerating nerve fibers and are necessary in the reestablishment of appropriate target connections. A power setting of 1.0 watt was chosen, since this wattage could produce adequate welds with minimal endoneurial damage.

Inadequate tensile strength of laser anastomosis has been a problem in most of the experimental trials that have been reported. Benke et. al. reported that the tensile strength of rat sciatic nerves repaired using only the CO₂ laser was less than , as strong as normal nerves immediately following the repair. They concluded that the CO₂ laser weld alone does not provide enough tensile strength to be practical, and they employed the use of two stay sutures for laser anastomosis (7). Fischer et. al. used one stay suture for repair of rat sciatic nerves with the CO₂ laser, and then removed the suture after laser welding unless they felt removal would compromise the repair. They observed a dehiscence rate of 13% (4 of 31 rats) in laser repaired nerves 60 days postoperatively (4). Maragh et. al. used no stay sutures in laser repair of rat sciatic nerves, but observed a 12% dehiscence rate (2 of 17 rats) at 2 months postoperatively (5).

Other researchers have used the rabbit facial nerve model (1), the rabbit peroneal nerve model (6), and the Rhesus monkey peroneal nerve model (3). All used either stay sutures for support of laser welds or nerve grafts to reduce tension at the anastomotic site, or they observed nerve dehiscence following laser repair. These

adaptations to increase bonding strength compromise nerve regeneration. As stated earlier, suture material presents a focus for scar and neuroma formation, and nerve grafts add the additional complication of two anastomotic sites.

The S-Q weld technique employs host tissue, which is allographic, biocompatible, and readily available to provide an instrument for sealing and binding severed nerve stumps. Using this approach, the laser energy is focused on the subcutaneous wrap at sites removed from the actual nerve juncture where scarring and neuroma formation should be avoided. The tensile strength of the S-Q weld immediately following repair was far greater than the tensile strength without the subcutaneous sheath. Indeed, nerves repaired without a sheath separated before measurements could be taken. The only other study of acute tensile strength of laser repaired rat sciatic nerves reported a breaking strength of less than 10% of intact nerves (7). The strength of S-Q welded nerves was also inferior to the tensile strength of the acute suture repair, but the improvement over CO₂ laser weld alone was substantial and would encourage further refinement of this procedure. As reported by Maragh et. al. in the rat sciatic nerve model, there was no significant difference in tensile strength of the laser repaired nerves and the suture repaired nerves at 8 days postoperatively (5). The critical period is clearly the first week before host connective tissue elements add the necessary stability. In order to make laser repair an attractive alternative to suture repair, we feel that the tensile strength of the laser repaired nerve must be improved further without the use of stay sutures or grafts, which may impair

the healing process.

The rate of dehiscence for laser repair at two months postoperatively was disappointing. The nerve separation may have been due to an inordinate amount of movement of the rats in the cages. However, it is significant to note that when the anastomosis remained intact, the quality of nerve regeneration may have been superior to that following suture repair, as demonstrated by the CAP transmission studies.

We conclude that laser nerve repair employing the S-Q weld technique has several theoretical advantages over suture repair. The observed improvement in initial anastomotic strength over laser repair alone warrants the need for further investigation with different laser energies and other improvements in technique.

REFERENCES:

1. Eppley BL, Kalendarian E, Winkelmann T, Delfino JJ. Suture versus laser-assisted anastomosis. *Int. J. Oral Maxillofac. Surg.* 1989; 18: 50-54.
2. Schober R, Ulrich F, Sander T, Durselen H, Hessel S, Laser-induced alteration of collagen substructure allows microsurgical tissue welding. *Science* 1986, 232: 1421-1422.
3. Bailes JE, Cozzens JW, Hudson AR, Kline DG, Ciric I, Gianaris P, Bernstein LP, Hunter RT. Laser-assisted nerve repair in primates. *J. Neurosurg* 1989; 71:266-272.
4. Fischer DW, Beggs JL, Kenshalo DL, Shetter AG. Comparative study of microepineurial anastomoses with the use of CO₂ laser and suture techniques in rat sciatic nerves. Part 1, Surgical technique, nerve action potentials, and morphological studies. *Neurosurgery* 1985; 17:300-308.
5. Maragh H, Hawn RS, Gould JD, Tezis JK. Is laser nerve repair comparable to microsuture coaptation? *Journal of Reconstructive Microsurgery* 1988; 71:266-272.
6. Champion ER, Bynum DK, Powers SK. Repair of Peripheral Nerves with the Argon Laser. *J. Bone and Joint Surgery* 1990; 72-A:715-723.
7. Benke TA, Clark JW, Wisoff PJ, Schneider S, Balasubramaiam C, Hawkins HK, Laurent J, Perling L, Shehab A. Comparative study of suture and laser-assisted anastomoses in rat sciatic nerves. *Lasers in Surgery and Medicine* 1989; 9:602-615.
8. Beggs JL, Fischer DW, Shetter AG. Comparative study of microepineurial anastomoses with the use of CO₂ laser and suture

techniques in rat sciatic nerves. Part 2, A morphometric analysis of myelinated nerve fibers. Neurosurgery 1986; 18:266-269.

9. Almquist EE, Nachemson A, Auth D, Almquist B, Hall S. Evaluation of the use of the argon laser in repairing rat and primate nerves.

The Journal of Hand Surgery 1984; 9A:792-9.

FIGURE LEGENDS:

Figure I: Breaking force of normal, suture, and laser repaired nerves immediately following repair.

Table I: Percent function of nerves following laser irradiation is expressed as the ratio between post laser P-P CAP and pre laser P-P CAP. Increasing wattages were applied to the same nerve after a one minute interval.

Figure II: Brightfield micrographs of cross sections taken from the distal segment of an S-Q weld repaired nerve (A) and a suture repaired nerve (B). There was no significant difference in the number of axons in the two preparations.

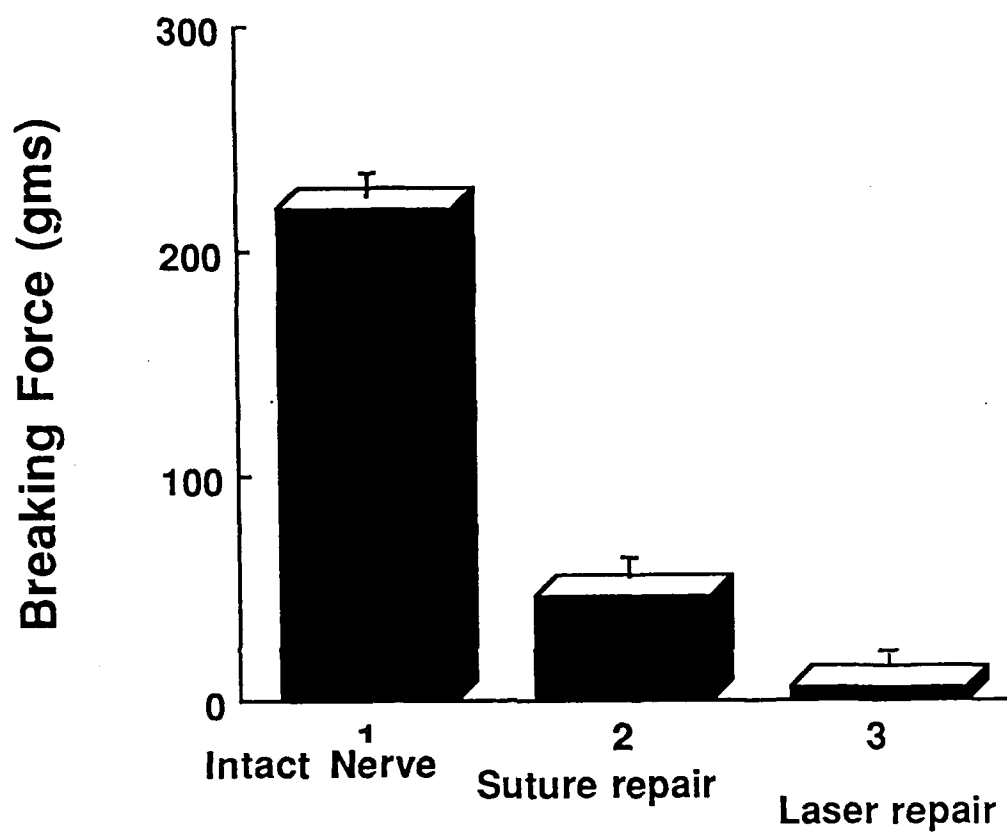


Fig. 1

TABLE 1: THE EFFECTS OF LASER IRRADIATION ON NERVE FUNCTION

<u>KTP:</u>	<u>0.5 WATTS</u>	<u>1.0 WATTS</u>	<u>1.6 WATTS</u>	<u>2.5 WATTS</u>
# Trials	8	10	10	8
% Function	0.91	0.62	0.45	0.31
St. Dev.	0.08	0.26	0.20	0.26
 <u>CO₂:</u>	 <u>0.5 WATTS</u>	 <u>1.0 WATTS</u>	 <u>1.6 WATTS</u>	 <u>2.5 WATTS</u>
# Trials	13	13	13	10
% Function	0.91	0.59	0.57	0.09
St. Dev.	0.16	0.19	0.24	0.20



Fig 2A

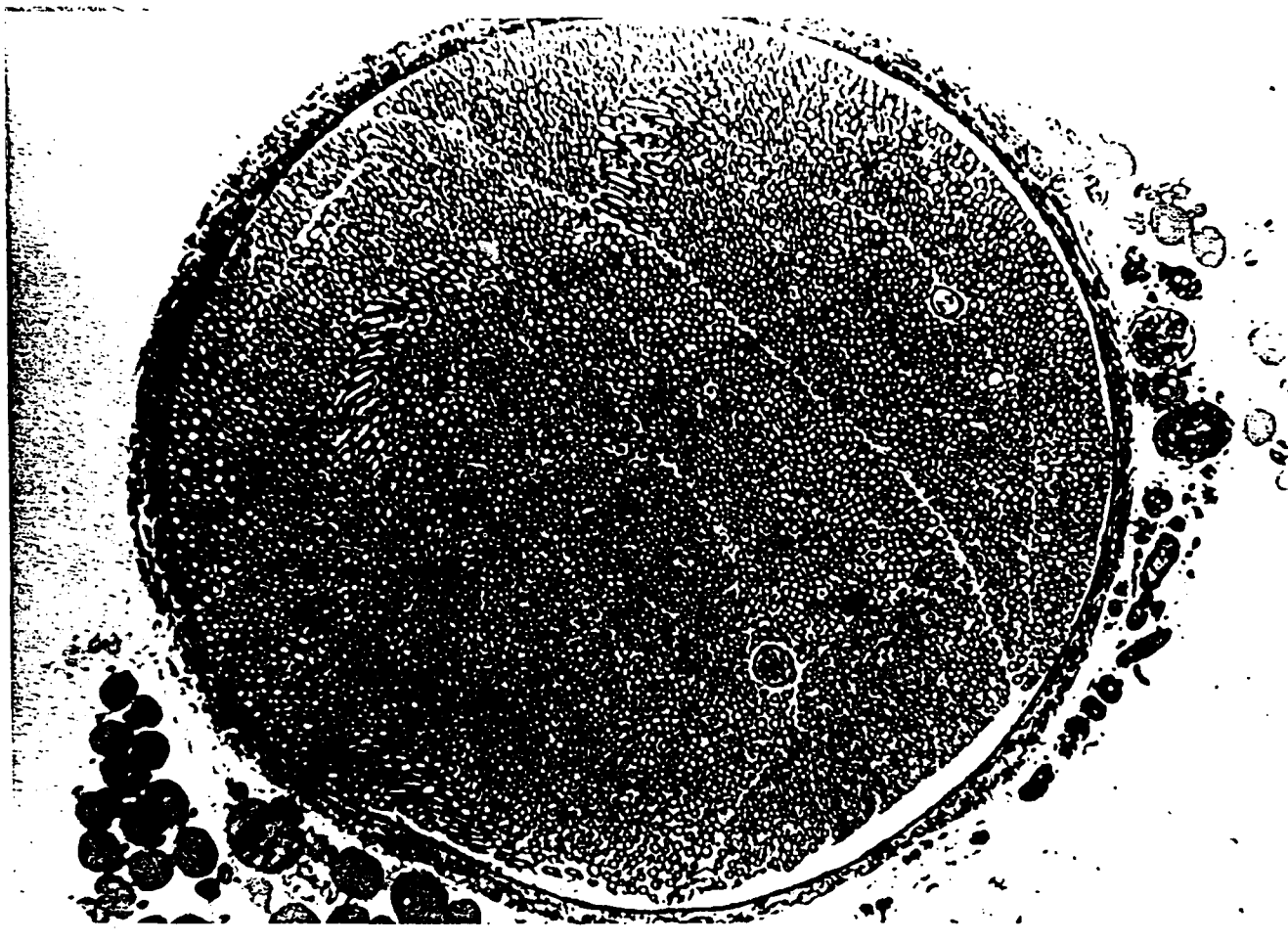


Fig 2B

Submitted: Photochemistry and Photobiology
January, 1992

**The Effect of Triton X-100 on Purple Membrane
as Measured by Changes in the Dynamics**

József Czégé⁽¹⁾ and Lou Reinisch⁽²⁾

*(1)The Department of Radiology, Uniformed Services University,
4301 Jones Bridge Road, Bethesda, MD 20814, and*

*(2)The Department of Otolaryngology, Vanderbilt University Medical Center,
Nashville, TN 37232*

Running Title: The Effect of Triton on Dynamics

Key Words: Bacteriorhodopsin, Purple Membrane, Photocycle, Light Scattering, Membrane Dynamics, Triton X-100, Dynamics

List of Abbreviations: bR (bacteriorhodopsin)
pm (purple membrane)
Nd:YAG (neodymium doped yttrium aluminum garnet)
cw. (continuous wave)

Send Correspondence to: Lou Reinisch
Department of Otolaryngology
Vanderbilt University
S-2100 Medical Center North
Nashville, TN 37232

Abstract:

We have observed the light scattering transients arising from changes in the curvature of purple membrane fragments upon photoexcitation at pH 8.05 and 4.1 with and without treatment of Triton X-100. The low ionic strength room temperature suspensions are excited with 532 nm light pulses from a Nd:YAG laser (20 ns). The scattering of 320 nm light is monitored from 3 μ s to 1 s at scattering angles from 15° to 60°. We simultaneously measure the transient transmission changes at 320 nm. The transient light scattering signals change significantly with the addition of 0.02% Triton X-100 at pH 8.05 and 0.006% Triton X-100 at pH 4.1. At these concentrations of Triton we observe maximal amplitudes in the transient changes of the scattered light intensity. At higher concentrations, the Triton solubilizes the protein and the scattering signals are completely attenuated. The transient transmission changes become severely distorted by the scattering changes in the Triton treated samples. We can explain these changes using our bent membrane model and assuming a greater initial curvature and an increased transient curvature change in the membrane fragments after the Triton X-100 is added. The amplitudes of the scattering changes as a function of the scattering angle from 15° to 60° agree with model calculations of the scattering amplitudes.

I. Introduction

Bacteriorhodopsin (bR) is the well studied photo-activated proton pump found in the purple membrane (pm) patches of the bacteria *Halobacterium halobium* (Stoeckenius and Rowen, 1967; Oesterhelt and Stoeckenius, 1971; Stoeckenius *et al.*, 1979). After the absorption of a photon, the protein progresses through a

sequence of intermediate states during a photocycle. These states are evidenced by changes in the optical absorption spectrum (Stoeckenius and Lozier, 1974). There have been attempts to link these absorption changes with significant rearrangements of the protein conformation. Many studies, on the contrary, measure little or no significant movement of the retinal chromophore during the photocycle (Razi Naqvi, *et al.*, 1973; Cherry, *et al.*, 1977a; Cherry, *et al.*, 1977b; Sherman and Caplan, 1977; Korenstein and Hess, 1978). Also, investigations of the protein side chains show no evidence for motion during the photocycle (Czégé, *et al.*, 1982). Time resolved x-ray diffraction also shows only a small amount of bR structure change 1 ms after illumination (Frankel and Forsyth, 1985). A one to two degree tilt of the 3 or 4 transmembrane alpha helices during the photocycle has been measured with neutron diffraction (Dencher, *et al.*, 1989). Some motion is probably involved in the photocycle since it can be influenced by the viscosity of the surrounding medium (Beece, *et al.*, 1981). When the membrane fragments are suspended in the higher viscosity medium of glycerol/water, the photocycle is slowed. The motion of the proton moving across the membrane during the photocycle strongly suggests some protein motion. The proton motion has been directly measured by the protein electric response signal (PERS) method (Keszthelyi and Ormos, 1980; Keszthelyi, 1984).

The bR is found as trimers in the pm patches (Oesterhelt and Stoeckenius, 1973; Henderson and Unwin, 1975; Stoeckenius *et al.*, 1979). The trimers are regularly arranged in a two dimensional crystal lattice (Blaurock and Stoeckenius, 1971). The protein accounts for about 77% of the membrane by dry weight (Kushwaha, *et al.*, 1975; Stoeckenius and Bogomolni, 1982; Lozier and Parodi, 1984).

This translates to roughly 10 lipid molecules per bR molecule.

The chromophore of the protein is a retinal attached to the lysine 216 residue of the protein with a protonated Schiff base (Heyn, *et al.*, 1988). The angle of the visible absorbance dipole of the chromophore has been determined to be about 70° with respect to the membrane normal (Heyn, *et al.*, 1977; Lin and Mathies, 1989). In the light adapted state, bR has a broad absorption band centered at 568 nm ($\epsilon = 63,000 \text{ cm}^{-1}\text{M}^{-1}$) (Becher, *et al.*, 1978).

The pm fragments are thin sheets. Measurements have determined that they are slightly less than or approximately 0.6 μm in diameter (Barabás *et al.*, 1983; Arrio *et al.*, 1986) and approximately 4 to 5 nm thick (Blaurock, 1975; Tristram-Nagle *et al.*, 1986). Our recent work has shown that the membrane fragments change their curvature, or “flap” during the photocycle (Czégé, 1987a,b; 1988; Czégé and Reinisch, 1990; 1991a-c). The surface of the pm fragment is asymmetrically charged (Keszthelyi, 1980; Renthall and Chung, 1984; Ehrenberg and Berezin, 1984). Since the most energetically favorable configuration for a flexible membrane with an asymmetric charge distribution is curved, it is reasonable to assume that the pm fragment is curved. The charge asymmetry is pH dependent and changes sign near pH 5 (Barabás *et al.*, 1983). From the change in sign of the asymmetric charge distribution it follows that the initial curvature is reversed near pH 5.

We observe transient changes in the scattering cross section at 320 nm of the pm fragments during the photocycle. We use 320 nm because of the large scattering cross section for this wavelength. The 320 nm light does not photodestroy the bR. Also, the absorption and the transient absorption changes are minimal at 320 nm. We interpret these scattering changes to be due to changes in the curvature of the

membrane fragment.

Here, we investigate the transient scattering changes from suspensions of pm before and after treatment with Triton X-100. We use small concentrations of Triton, which do not solubilize the bR.

The detergent is expected to interact with hydrophobic parts of the protein structure. This should change the physical characteristics of the membrane sheet. Since the light scattering kinetics are sensitive to the changes in curvature, we expect to see significant changes.

Materials and Methods

Purple membrane fragments are isolated from the strain S9 of *Halobacterium halobium* according to the procedure of Oesterhelt and Stoebenius, 1974. The samples are graciously provided by Dr. J.K. Lanyi and Dr. György Váró. The samples are suspended in 10 mM sodium acetate buffer for the pH 4.1 and in 10 mM potassium dihydrogen phosphate at pH 8.05. The samples are stable and show no signs of aggregation with the low salt ion concentration. No settling of the pm fragments is observed during the course of the experiments. The Triton X-100 (Rohm and Haas, Philadelphia, PA) is used as is. The percentages of Triton are measured as a volume to volume ratio.

The measuring system is described in detail in previous publications (Czégé and Reinisch, 1990, 1991a-c). The scattering is measured as function of the scattering angle from 15° to 60° in 5° increments. The transmission changes along the optical axis are measured simultaneously for the same wavelength range. The transient

scattering signals are normalized with the transient transmission signals. We make the normalization to correct for any changes in the exciting laser intensity when the polarization is changed. Typically, the correction is less than 10%.

In the centrifugation experiments, we used a Microfuge II (Beckman Instruments, Inc., Fullerton, CA) table top centrifuge at the highest speed.

The transient scattering signals are slightly distorted by the transient changes in the transmission of the sample at 320 nm. We have previously corrected this distortion by making measurements as a function of the bR concentration (Czégé and Reinisch, 1990). We have also used a first order approximation to correct the scattering signals (Czégé and Reinisch, 1991b,c). This first order approximation is not necessarily valid in the measurements made here. So, we correct the scattering signals by subtracting 70% of the measured transmission change. The 70% is estimated from measurements on aggregated and gel samples.

The measured scattering transients are described with 25 exponential curves, equally spaced on the $\log(\text{time})$ axis (Czégé and Reinisch, 1991c). The choice of exponentials is justified by the exponential nature of the steps in the bR photocycle. This mathematical description causes some smoothing of the data and allows us to make the surface plots using Mathematica (Wolfram Research, Champaign, IL). The curves are then normalized and corrected for transient absorption changes distorting the transient scattering changes. The scattering at each time point as a function of the scattering angle is described with a fourth order polynomial. Again, this allows us to interpolate and make the appropriate contour surface plots with Mathematica.

III. Results

We show contour curves of the intensity of scattered light as a function of time on a logarithmic axis from μs to s and scattering angle from 15° to 60° at pH 4.1. At the top left of Fig. 1 the pm suspension is excited with vertically polarized light (polarized perpendicularly to the scattering plane) at 532 nm. This plot is marked with a “vertical” double arrow. Right at the top of Fig. 1 the pm suspension is excited with horizontally polarized light (polarized parallel to the scattering plane). This plot is marked with a “horizontal” double arrow. The scattering shown in these two plots can be compared to earlier publications where the scattering angle was fixed at 30° (Czégé and Reinisch, 1990; 1991a-c). With the horizontal excitation, a fast initial decrease in the scattering amplitude is observed, followed by a slower increase in the scattering amplitude. The sign of the scattering transients reverses for vertical excitation.

In the bottom half of Fig. 1 we show similar contour curves of the scattering transient amplitudes from pm suspension at pH 4.1 treated with 0.006% Triton X-100. Note that the amplitude of the scattering transients as function of the scattering angle has much more structure after the addition of Triton.

In the top half of Fig. 2 we show contour curves of the scattering transient amplitudes from pm suspensions at pH 8.05. We show both vertically and horizontally polarized excitation light as a function of the $\log(\text{time})$ and the scattering angle from 15° to 60° . Again, the scattering at 30° agrees with the transients reported in earlier publications (Czégé and Reinisch, 1991b,c). In the bottom half of Fig. 2 we show the contour curves of the scattering transient amplitudes from the same pm suspensions treated with 0.02% Triton.

We centrifuge the pH 8 pm suspension for 5 minutes. Then we mix the precipitated membranes with the same supernatant and the large scattering transients are attenuated. This procedure can be repeated on the suspension and additional attenuation is observed. In Fig. 3 there are shown the transient scattering and transmissions changes before and after a series of 5 centrifugations. The Triton treatment and the centrifugation procedure stop the transient changes in the membrane curvature. However, the transient absorption changes remain. We did not fully investigate, at this point, how the centrifugation stops the curvature changes. It is shown in Fig. 3 that not only are the scattering kinetics attenuated with centrifugation, but the apparent transmission kinetics have also changed. In Fig. 3 we also compare the normalized differences for both the scattering and absorption transients before and after the centrifugation series. We find that they are the same, within the experimental errors. The noise in the data increases at shorter times due to the nature of the logarithmic averaging.

IV. Discussion

After the Triton treatment, there are significant changes in the pattern of the scattering kinetics. One is that "vertical" and "horizontal" (vertically and horizontally polarized exciting light) scattering kinetics are no longer opposite relative to the transmission transients. They have significantly increased amplitudes (especially at pH 8.05), and they are unidirectional with respect to the excitation polarization over a range of the scattering angle. The other main difference is the oscillation of the scattering components as a function of the scattering angle. The changes in the scattering cross section of the pm fragments during the photocycle

of the bR can be explained by transient changes in the curvature of the membrane fragments (Czégé 1987a,b, 1988; Czégé and Reinisch 1990, 1991b,c). Using this theory of curvature changes, the angular dependence of the scattering kinetics of the Triton treated samples can be understood. We recall that, in a monodisperse sample (theoretically) an oscillation can be observed in the amplitude of the scattering transients as a function of the scattering angle (Czégé 1987b). The oscillations arise from the interference nature of the scattering. The "frequency" of the oscillations depend upon the particle size.

For a constant radius of curvature, the bending angle of the pm depends upon the fragment size. The larger fragments have a greater bending, because the apparent diameter is nonlinear with the bending. It follows that the pm fragments will have a more uniform apparent diameter when the initial curvature increases. We therefore make the plausible assumption that the observed changes in the scattering after the Triton treatment are the result of an increased initial (and transient) bending of the Triton weakened membrane fragments. The idea of the increased initial bending is also in accordance with the scattering transient being independent of the polarization of the exciting light in the Triton treated pm.

Simply note, that the different signs of the scattering transients in the untreated samples are from the photoselection of the polarized exciting flash and that, with the increased bending of the membranes, the photoselection greatly decreases.

To support theoretically the increased bending idea, in Fig.4, we show the calculated amplitudes of the scattered light as a function of the scattering angle for both polarizations of the exciting light. We first consider the pH 8.05 results. The triangular points show the calculated angular dependence of the maximum

scattering amplitude for a small initial curvature. The square points show the calculated angular dependence of the maximum scattering amplitude for a large initial curvature of the pm fragments. The dashed line connects the points for a simulated vertically polarized excitation and the solid line connects the points for a simulated horizontally polarized excitation. The calculations take into account a log normal distribution of membrane fragment sizes with an average diameter of $0.6\ \mu\text{m}$ and a random orientation. The initial curvature is given as $100^\circ/\mu\text{m}$ for the triangular points and $230^\circ/\mu\text{m}$ for the square points.

The slowest process at pH 8.05 has been shown to be a decrease in the curvature of the membrane (Czégé and Reinisch, 1991b,c). We therefore calculated the scattering transients for a *reduction* of $80^\circ/\mu\text{m}/\text{excitation factor}$.^{*} The amount of curvature change depends, of course, on the fraction of bR molecules excited in a membrane fragment. Because of the polarized exciting light and the photoselection, the excitation factor is typically less than 0.4.

The triangular points do, indeed, follow the trends of the slowest scattering process as shown in the top half of Fig. 2. The horizontally polarized excitation leads to a decrease in scattering for the slowest process. This decrease in scattering is small for the small scattering angles and remains negative across the entire range. The vertically polarized excitation shows a slow process with a modest, negative scattering amplitude for the smallest scattering angle. At larger scattering angles, the scattering amplitude becomes positive and increases in size. The calculated

* The excitation factor takes into account the fraction of chromophores properly oriented to absorb an excitation photon. This is not an absolute number. However, the product of the curvature change, the size the excitation factor is an absolute factor. In this case, if the excitation factor is 0.4 for a $0.6\ \mu\text{m}$ membrane fragment, then the curvature reduces 19.2° .

amplitudes vary slightly from the measured amplitudes. This is expected. We used simple square membrane sheets with a uniform cylindrical radius of curvature. The actual situation is probably much more complicated. The close agreement with the sign of the scattering process and the trends in the size of the scattering is remarkably close.

The squares were calculated with an *increase* of curvature of $80^\circ/\mu\text{m}/\text{excitation}$ factor. The change from a decrease to an increase of curvature for the transient process was needed to achieve an agreement between the sign of the measured and calculated scattering amplitudes. The squares agree with slowest process measured in the Triton treated samples at pH 8.05. From the bottom half of Fig. 2, it is clear that the slowest process is positive for small and large scattering angles, and negative for the $30\text{--}40^\circ$ scattering angle range. Also, the vertically polarized excitation gives a larger negative scattering amplitude in this mid range. However, the calculated scattering amplitudes are smaller than the measured scattering amplitudes.

If we increase the transient increase of curvature to $150^\circ/\mu\text{m}/\text{excitation}$ factor (and keep the $230^\circ/\mu\text{m}$ initial curvature), we calculate scattering amplitudes that are shown as circles on Fig. 4. The amplitudes of the scattering kinetics are increase, but the angular dependence remains. The agreement between the calculations and the measurements is impressive.

A similar analysis of the pH 4.1 is possible. One needs to start with an increase in curvature for the sample without the Triton treatment. The calculated scattering amplitudes are then very nearly the negative of the triangles shown on Fig. 4. After the Triton treatment the curvature still increased, but it is hard to say if the

amount of transient increase changes.

We do not have an explanation why the Triton changes the direction of bending for the pH 8.05 sample. We can assume that only process B is enhanced by the Triton treatment. The altered membranes may not have the possibility to complete process C (Czégé and Reinisch, 1991b,c). We do note that the bending processes also change in time after Triton is added. The analysis is complicated because the Triton not only changes the physical mechanics of the membrane, but also affects the release of non proton ions (see below).

As for the Triton concentrations, at both pH's we use the concentrations at which the scattering changes are maximal. At these concentrations the protein is still not solubilized (cf. centrifugation experiment above). The difference of the necessary concentrations for pH 4.1 and 8.05 indicates that the properties of the membrane changes significantly with the pH. If we follow the effect of adding more Triton at pH 8.05 we find that the scattering changes soon disappear together with the initial scattering intensity. Yet, several hours later, the initial scattering of the solubilized sample is restored. However, the suspension still does not show any transient scattering changes during the photocycle.

It is interesting to note that at pH 8.05 the 0.02% is the same Triton concentration where enhanced nonproton ion movements can be observed during the photocycle (Marinetti and Mauzerall, 1986). We do not have the possibility to measure the transient conductivity of our samples. However, measuring the transient conductivity together with the centrifugation experiment could teach us a lot about the connection of the transient membrane bending and the nonproton ion release.

The distortion of the transient absorption (transmission) changes as shown in Fig. 3 (compare before and after centrifugations) more than likely is due to the effect of the scattering changes. Because of the decreased photoselection, the integrated scattering changes become greatly enhanced which results in a severely distorted transient transmittance of the sample. Even without Triton, the transient scattering changes may significantly distort the transient absorption changes. This is obviously an effect that must be considered in a careful analysis of the absorbance kinetics.

The membrane bending is significant in the study of bR. Measurement of the bending before and after treatment with Triton X-100 shows significant changes in the angular dependence of the scattering transients. Calculations using our model of a bent membrane fragment changing curvature during the photocycle describe the changes well. They suggest that Triton weakens the membrane, leading to an increase in the initial bending angle and an increase in the amount of transient bending also supports our model. We have shown in earlier papers that two of the fundamental bending processes have been associated with the protein conformational changes during the proton pumping process (Czégé and Reinisch, 1990). A third fundamental bending processes has been circumstantially linked to a change of the ion concentrations near the membrane (Czégé and Reinisch, 1991c). Also, the transient scattering amplitude is very sensitive to low levels of photodestruction (Czégé and Reinisch, 1991a). Thus, the transient scattering is sensitive to critical aspects of bR, where the absorbance measurements do not show such sensitivity. In addition, changes in the scattering cross section can and will influence the changes in absorption of the pm observed during the photocycle. Understanding

the changes in the scattering is important in the understanding of the mechanism of the proton pump.

Acknowledgements

We thank J.K. Lanyi and György Váró for the generous supply of pm used in these experiments. This work has been supported in part by grants from the Office of Naval Research, Grant N00014- WR-24020 and the Strategic Defense Initiative Organization under the Medical Free Electron Laser program. The opinions and assertions contained in this paper are the private views of the authors and are not to be construed as reflecting the views of the Uniformed Services University of the Health Sciences or the Department of Defense.

References

Arrio, B., G. Johannin, P. Volfin, M. Lefort-Tran, L. Packer, A.E. Robinson, and E. Hrabeta. 1986. Aggregation and proton release of purple and white membranes following cleavage of the carboxyl-terminal tail of bacteriorhodopsin. *Arch. Biochem. Biophys.* 246:185-191.

Barabás, K., A. Dér, Zs. Dancsházy, P. Ormos, M. Marden and L. Keszthelyi. 1983. Electro-optical measurements on aqueous suspension of purple membrane from *Halobacterium halobium*. *Biophys. J.* 43:5-11.

Becher, B., F. Tokunaga, and T.G. Ebrey. 1978. Ultraviolet and visible absorption spectra of purple membrane protein and photocycle intermediates. *Bio-*

chemistry. 17:4923-4926.

Beece, D., S.F. Bowne, J. Czégé, L. Eisenstein, H. Frauenfelder, D. Good, M.C. Marden, J. Marque, P. Ormos, L. Reinisch, and K.T. Yue. 1981. The effect of viscosity on the photocycle of bacteriorhodopsin. *Photochem. Photobiol.* 33:517-522.

Blaurock, A.E., and W. Stoeckenius. 1971. Structure of the purple membrane. *Nature new Biol.* 233:152-155.

Blaurock, A.E. 1975. Bacteriorhodopsin: a trans-membrane pump containing α -helix. *J. Mol. Biol.* 93:139-158.

Cherry, R.J., M.P. Heyn, and D. Oesterhelt. 1977a. Rotational diffusion and exciton coupling of bacteriorhodopsin in the cell membrane. *FEBS (Fed. Eur. Biochem. Soc.) Lett.* 78:25-30.

Cherry, R.J., U. Müller, and G. Schneider. 1977b. Rotational diffusion of bacteriorhodopsin in lipid membranes. *FEBS (Fed. Eur. Biochem. Soc.) Lett.* 80:465-469.

Czégé, J., A. Dér, L. Zimányi, and L. Keszthelyi. 1982. Restriction of motion of protein side chains during the photocycle of bacteriorhodopsin. *Proc. Natl. Acad. Sci. USA.* 79:7273-7277.

Czégé, J. 1987a. Light scattering changes during the photocycle of bacteriorhodopsin. *Acta Biochim. Biophys. Hung.* 22:463-478.

Czégé, J. 1987b. Bent membrane model of the purple membrane. Theoretical details and further experimental data. *Acta Biochim. Biophys. Hung.* 22:479-489.

Czégé, J. 1988. Light scattering changes and protein distortion in the bacteriorhodopsin during the photocycle. *FEBS (Fed. Eur. Biochem. Soc.) Lett.* 242:89-93.

Czégé, J. and L. Reinisch. 1990. Cross-correlated photon scattering during the photocycle of bacteriorhodopsin. *Biophys. J.* 58:721-729.

Czégé, J. and L. Reinisch. 1991a. Photodestruction of bacteriorhodopsin. *Photochem. Photobiol.* 53:659-666.

Czégé, J. and L. Reinisch. 1991b. The pH dependence of transient changes in the curvature of the purple membrane. *Photochem. Photobiol.* 00:0000-0000.

Czégé, J. and L. Reinisch, 1991c. The pH dependence of transient changes in the curvature of the purple membrane with visible and ultraviolet excitation. *Biophys. J.* (submitted).

Dencher, N.A., D. Dresselhaus, G. Zaccai and G. Buldt. 1989. Structural changes in bacteriorhodopsin during proton translocation revealed by neutron diffraction. *Proc. Natl. Acad. Sci. USA.* 86:7876-7879.

Ehrenberg, B., and Y. Berezin. 1984. Surface potential on purple membranes and its sidedness studied by a resonance Raman probe. *Biophys. J.* 45:663-670.

Frankel, R.D., and J.M. Forsyth. 1985. Time-resolved x-ray diffraction study of photostimulated purple membrane. *Biophys. J.* 47:387-393.

Henderson, R., and P.N.T. Unwin. 1975. Three-dimensional model of purple membrane obtained by electron microscopy. *Nature (Lond.).* 257:28-32.

Heyn, M.P., R.J. Cherry, and U. Müller. 1977. Transient and linear dichroism

studies on bacteriorhodopsin: determination of the orientation of the 568 nm all-trans retinal chromophore. *J. Mol. Biol.* 117:607-620.

Heyn, M.P., J. Westerhausen, I. Wallat, and F. Seiff. 1988. High-sensitivity neutron diffraction of membranes: Location of the Schiff base end of the chromophore in bacteriorhodopsin. *Proc. Natl. Acad. Sci. USA.* 85:2146-2150.

Keszthelyi, L. 1980. Orientation of membrane fragments by electric field. *Biochem. Biophys. Acta.* 598:429-436.

Keszthelyi, L. and P. Ormos. 1980. Electric signals associated with the photocycle of bacteriorhodopsin. *FEBS (Fed. Eur. Biochem. Soc.) Lett.* 109:189-193.

Keszthelyi, L. 1984. Intramolecular charge shifts during the photoreaction cycle of bacteriorhodopsin, *in*, Information and Energy Transduction in Biological Membranes. C.L. Bilis, E.J.M. Helmreich and H. Passow, editors. Alan R. Liss Inc., N.Y. 51-72.

Korenstein, R., and B. Hess. 1978. Immobilization of bacteriorhodopsin and orientation of its transition moment in purple membrane. *FEBS (Fed. Eur. Biochem. Soc.) Lett.* 89:15-20.

Kushwaha, S.C., M. Kates, and W.G. Martin. 1975. Characterization and composition of the purple and red membrane. *Can. J. Biochem.* 53:284-292.

Lin, S.W., and R.A. Mathies. 1989. Orientation of the protonated retinal Schiff base group in bacteriorhodopsin from absorption linear dichroism. *Biophys. J.* 56:653-660.

Lozier, R.H. and L.A. Parodi. 1984. Bacteriorhodopsin: Photocycle and stoichiometry *In* Information and Energy Transduction in Biological Membranes. C.L.

Bolis, E.J.M. Helmreich and H. Passow, editors. Alan R. Liss Inc., NY 39-50.

Marinetti, T., and D. Mauzerall 1986. Large transient nonproton ion movements in purple membrane suspensions are abolished by solubilization in Triton X-100. *Biophys. J.* 50:405-415.

Oesterhelt, D., and W. Stoeckenius. 1971. Rhodopsin-like protein from the purple membrane of *Halobacterium halobium*. *Nature New Biol.* 233:149-152.

Oesterhelt, D., and W. Stoeckenius. 1973. Functions of a new photoreceptor. *Proc. Natl. Acad. Sci. USA.* 70:2853-2857.

Oesterhelt, D., and W. Stoeckenius. 1974. Isolation of the cell membrane of *Halobacterium halobium* and its fractionation into red and purple membrane. *Methods Enzymol.* 31:667-678.

Razi Naqvi, K., J. Gonzalez-Rodrigues, R.J. Cherry, and D. Chapman. 1973. Spectroscopic technique for studying protein rotation in membranes. *Nat. New Biol.* 255:249-251.

Renthal, R., and Chung H-C. 1984. Charge Asymmetry of the purple membrane measured by uranyl quenching of dansyl fluorescence. *Biophys. J.* 45:1001-1006.

Sherman, W.V., and S.R. Caplan. 1977. Chromophore mobility in bacteriorhodopsin. *Nature (Lond.)*. 265:273-274.

Stoeckenius, W., and R. Rowen. 1967. A morphological study of *Halobacterium halobium* and its lysis in media of low salt concentration. *J. Cell Biol.* 34:365-393.

Stoeckenius, W., and R.A. Bogomolni. 1982. Bacteriorhodopsin and related pigments of halobacteria. *Annu. Rev. Biochem.* 52:587-615.

Stoeckenius, W. and R.H. Lozier. 1974. Light energy conversion in *Halobacterium halobium*. *J. Supramol. Struc.* 2:769-774.

Stoeckenius, W., R.H. Lozier and R.A. Bogomolni. 1979. Bacteriorhodopsin and the purple membrane of halobacteria. *Biochim. Biophys. Acta.* 505:215-278.

Tristram-Nagle, S., C.-P. Yang, and J.F. Nagle. 1986. Thermodynamic studies of purple membrane. *Biochim. Biophys. Acta.* 854:58-66.

Figure Captions

Figure 1: Contour plots of the scattering of light at 320 nm from suspensions of pm during the photocycle. The suspensions are approximately 5 μ M bR and at pH 4.1. The exciting light is at 532 nm (20 ns laser flash). The horizontal axis is the logarithmic time during the photocycle from μ s to s. The vertical axis is the scattering angle, linear from 15° to 60°. Each contour line is a 0.3% change in the intensity of the scattered light. The shading shows the sign of the scattering transients. Lightly shaded regions have positive changes (increases) in scattering and dark regions have negative changes (decreases) in scattering. The shading near 1 s represents a zero percent change in scattering. The data was described with 25 exponential curves, and the absorption changes have been subtracted from the data shown as explained in the text. The top half of the figure is from pm not treated with Triton. The vertical double arrow designates the data from vertically polarized excitation. The horizontal double arrow designates the data from horizontally polarized excitation. The bottom half of the figure is from pm treated with 0.006% Triton X-100. In the bottom half of the figure each contour line is a 0.1% change in the intensity of the scattered light.

Figure 2: The same as Fig. 1, except the sample is at pH 8.05. In the top half of the figure, without the Triton treatment, each contour line is a 0.1% change in the intensity of the scattered light. In the bottom half of the figure, the Triton treatment is 0.02%, and each contour line is a 0.3% change in the intensity of the scattered light.

Figure 3: The scattering change. The percent change in scattering near 320 nm from a suspension of pm, pH 8.05, treated with 0.02 % Triton on a loga-

rhythmic time scale. The 5 μm suspension of bR is excited with 20 ns pulse at 532 nm. The dashed line is from the Triton treated sample. The solid line is from the same sample centrifuged five times and resuspended, as explained in the text. The scattering angle is 20° .

The transmission change. The percent changes in transmission near 320 nm from the same bR suspension. These data were measured simultaneously with the scattering changes. Again, the dashed line is from the Triton treated sample. The solid line is after the same sample was centrifuged and resuspended five times.

The normalized differences. The normalized differences in the scattering and transmission transients before and after the centrifugation. The dashed line is the difference in the scattering transients. The solid line is the difference in the transmission transients.

Figure 4: The calculated amplitudes for the scattering transients at 320 as a function of the scattering angle. The details of the calculation are given in the text. The triangular points are from a $100^\circ/\mu\text{m}$ initial curvature and a *decrease* in curvature of $80^\circ/\mu\text{m}/\text{excitation factor}$. The square points are from a $230^\circ/\mu\text{m}$ initial curvature and an *increase* in curvature of $80^\circ/\mu\text{m}/\text{excitation factor}$. The circles are from a $230^\circ/\mu\text{m}$ initial curvature and an *increase* in curvature of $150^\circ/\mu\text{m}/\text{excitation factor}$.

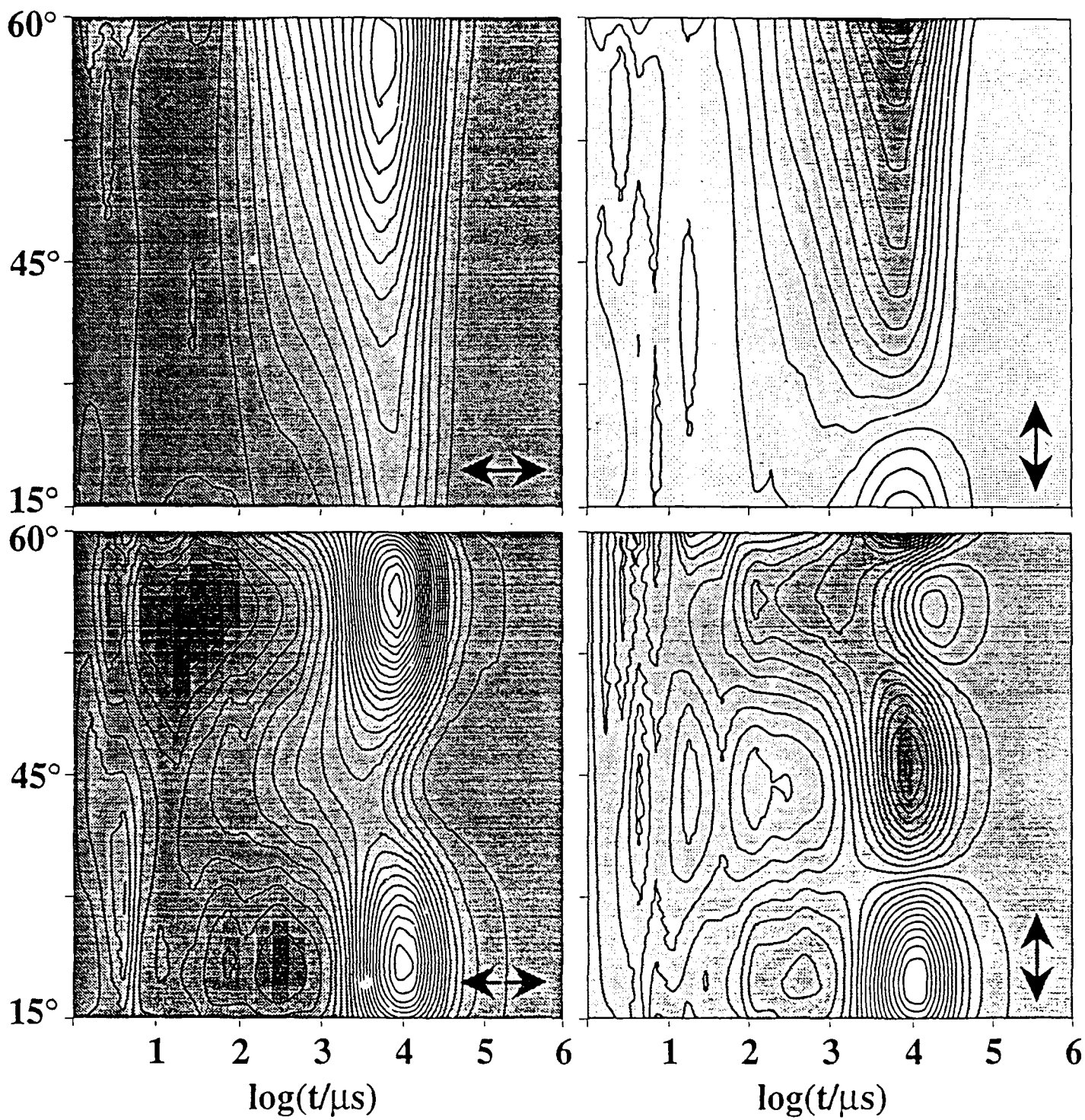


Figure 1

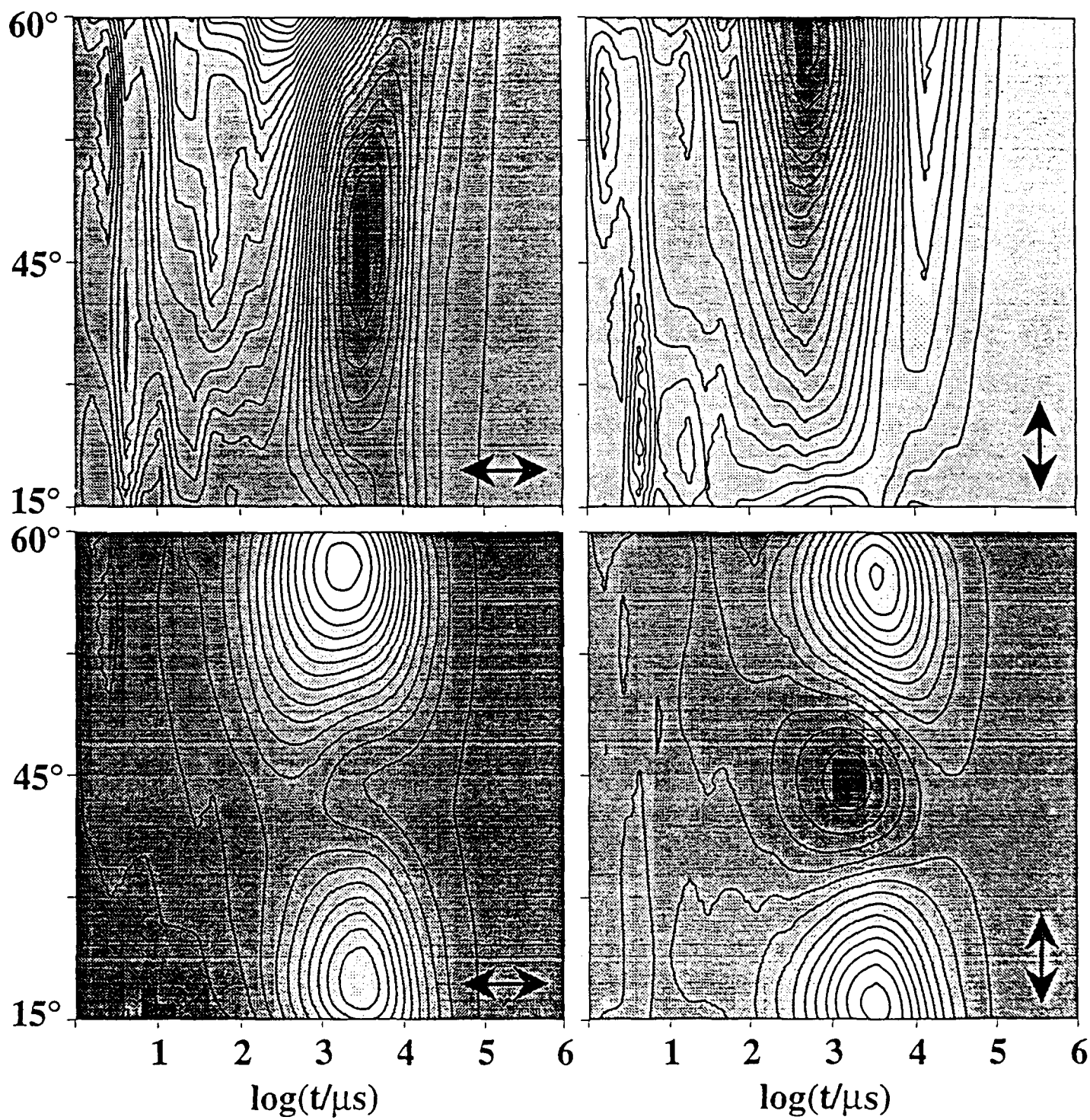


Figure 2

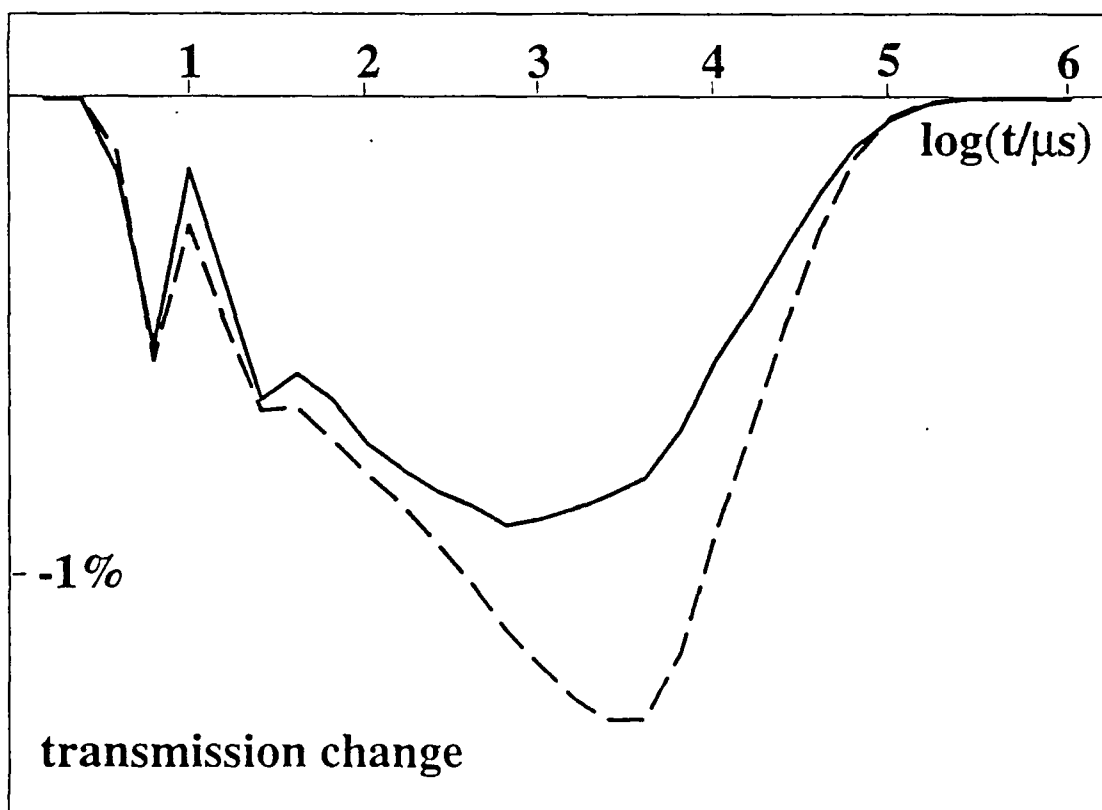
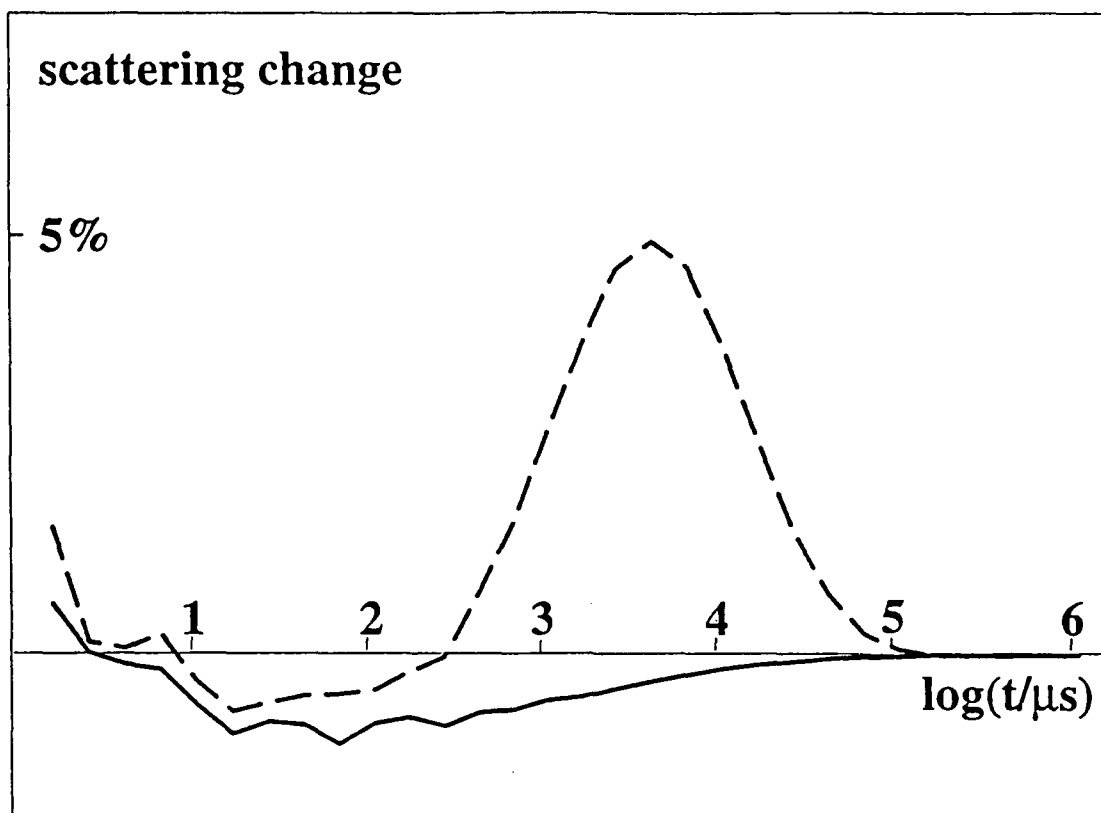


Figure 3 (page 1 of 2)

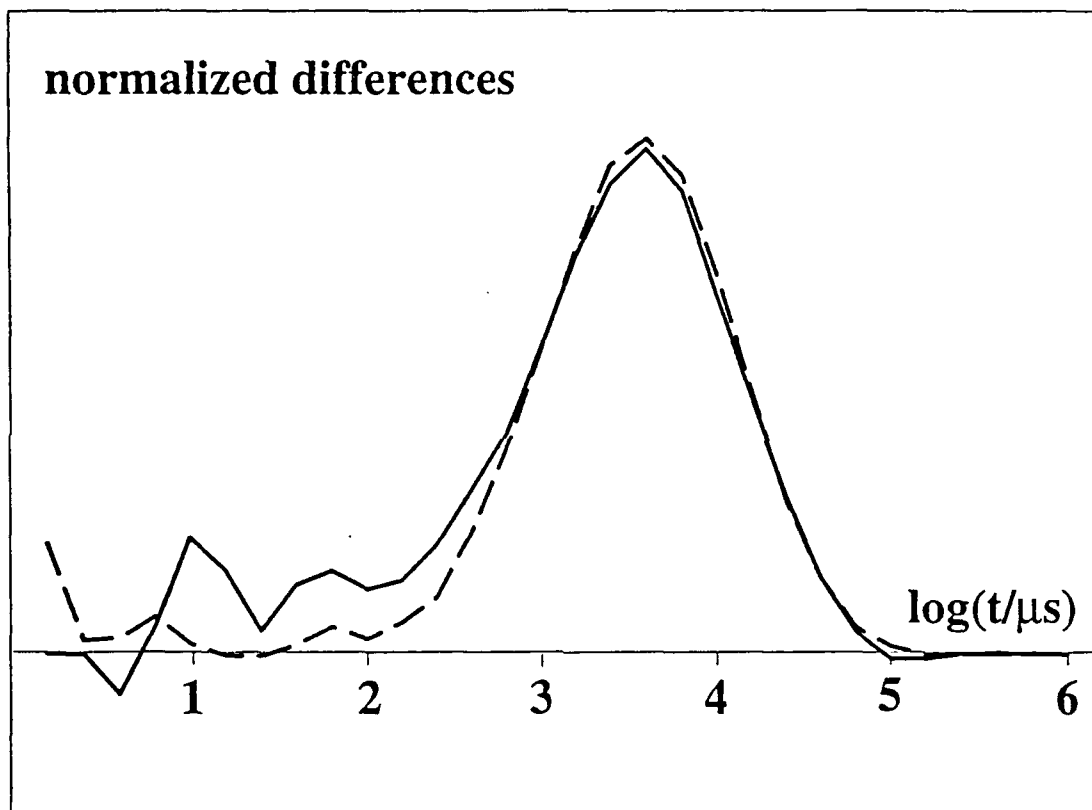


Figure 3 (page 2 of 2)

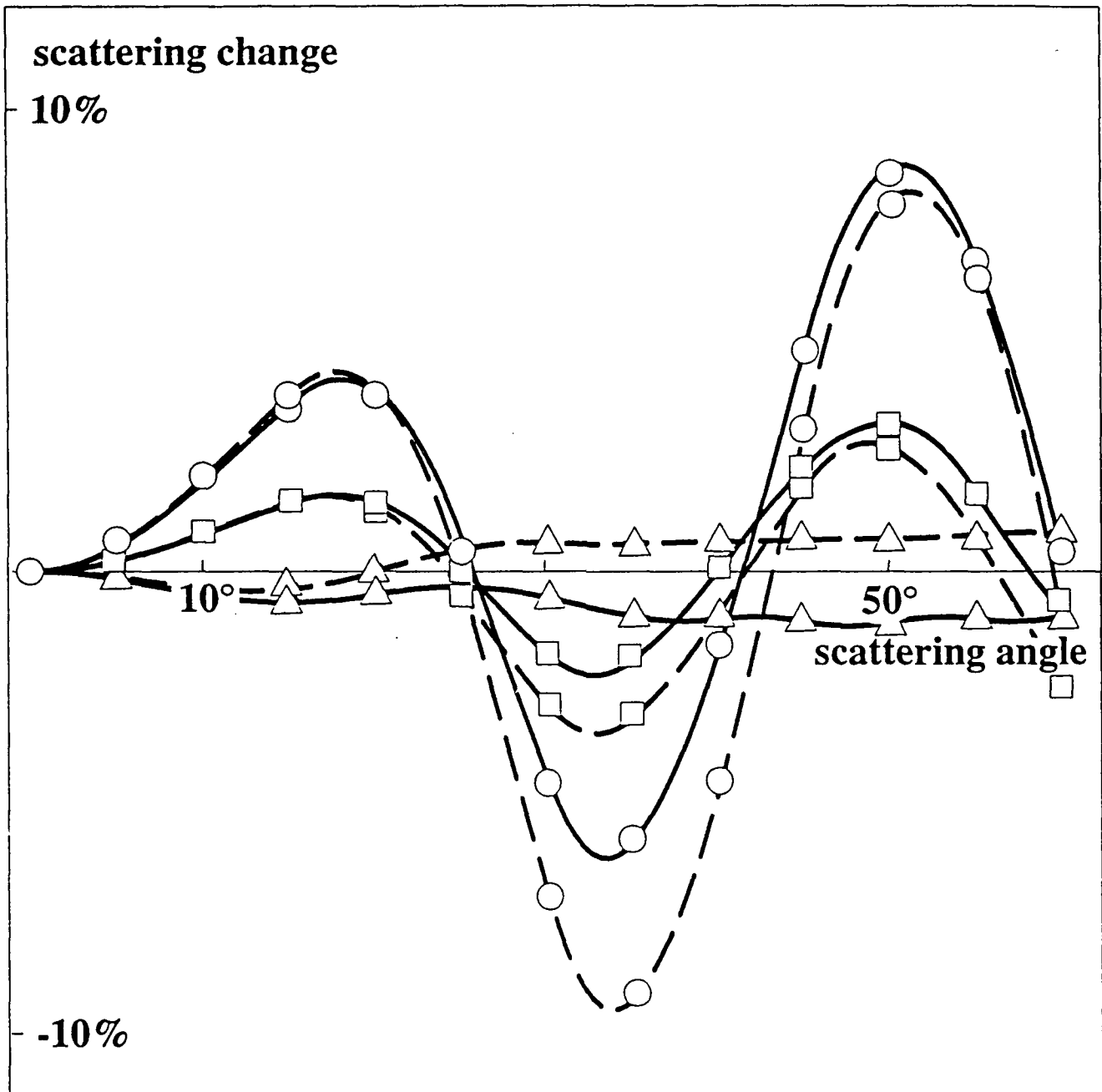


Figure 4

Research supported by Vanderbilt FEL from L Reinisch

10 January, 1992

1. Fluorescence detection and identification in the management of acute otitis media.

Collaborators: Jay Werkhaven, M.D.
The Nemours Children's Clinic
Jacksonville, Florida

Jerri Tribble
Dept. of Physics
Vanderbilt University

Fluorescence Spectroscopy of Bacteria in Otitis Media, J.A. Tribble, J. Werkhaven and L. Reinisch, Applied Spectroscopy (in preparation).

Abstract

The management of otitis media in children continues to be hampered by two fundamental problems: The prevalence of bactericidal resistant species is increasing (frequent misdiagnosis lead only to enhancement of the growth conditions for resistant species); The identification of resistant species is time consuming, expensive and requires drainage of the middle ear. The fluorescence spectra of four strains of bacteria, commonly found in otitis media: *P. aeruginosa*, *S. aureus*, *B. catarrhalis* and *H. influenzae* has been measured. The excitation wavelength has been varied from 280 to 500 nm and the emission spectra measured. The fluorescence spectra are presented at two dimensional fluorescence finger prints. These fingerprints will ultimately be used to identify the bacteria remotely, and non invasively from otitis media.

Future Research Support:

- (i) An Innovative Technology Research Grant to the National Institutes of Health is being prepared and will be submitted February 1, 1992.
- (ii) The Deafness Research Foundation has been contacted. A proposal will be submitted before their annual due date in June, 1992.
- (iii) We are in the initial stage of contacting the Whitaker Foundation for support.

2. Measurement of the membrane dynamics of the activated purple membrane.

Collaborator: J. Czégé
Uniformed Services University of the
Health Sciences
Bethesda, Maryland

The Effect of Triton X-100 on Purple Membrane as Measured by Changes in the Dynamics. J. Czégé and L. Reinisch, Photochem. and Photobiol (submitted, 1992).

Textbooks and Book Chapters Published

4. R.H. Ossoff and L. Reinisch, "Laser Surgery in Otolaryngology: Basic Principles and Safety Considerations" in *Otolaryngology--Head and Neck Surgery, Second Edition.*, C. Cummings, ed. (C.V. Mosby, St. Louis, Missouri), (in press).

**LASER SURGERY IN OTOLARYNGOLOGY:
BASIC PRINCIPLES AND SAFETY CONSIDERATIONS**

Robert H. Ossoff, D.M.D., M.D., F.A.C.S.

Lou Reinisch, Ph.D.

From the Department of Otolaryngology, Vanderbilt University Medical Center
Nashville, Tennessee

Address communication to: Robert H. Ossoff, D.M.D., M.D., F.A.C.S.
Department of Otolaryngology
Vanderbilt University Medical Center
S-2100 Medical Center North
Nashville, TN 37232-2559

INTRODUCTION

Laser light is the brightest monochromatic (single color) light existing today. Besides being a standard tool of the research lab, the laser is currently used in communications, surveying, manufacturing, diagnostic medicine and surgery. Supermarket bar code scanners and the compact disk player have even moved lasers into everyday life. The addition of lasers and the development of new lasers to the surgical armamentarium in otolaryngology--head and neck surgery offers new and exciting possibilities to improve conventional techniques and to expand the scope of this specialty.

The purpose of this chapter is to review the principles, applications, and safety considerations associated with the use of lasers in the upper aerodigestive tract. It is hoped that the material presented here will provide a foundation upon which the otolaryngologist--head and neck surgeon can begin to apply this exciting technology in his daily practice.

LASER BIOPHYSICS

Laser is an acronym for *light amplification by the stimulated emission of radiation*. Albert Einstein postulated the theoretical foundation of laser action, stimulated emission of radiation, in 1917. In his now classic publication, "*Zur Quantum Theorie der Strahlung*" ("The Quantum Theory of Radiation") he discussed the interaction of atoms, ions, and molecules with electromagnetic radiation (Einstein, 1917). He specifically addressed absorption and spontaneous emission of energy and proposed a third process of interaction: stimulated emission. Einstein postulated that the spontaneous emission of electromagnetic radiation from an atomic transition has an enhanced rate in the presence of similar electromagnetic radiation. This "negative absorption" is the basis of laser energy.

Many attempts were made in the following years to produce stimulated emission of electromagnetic energy, but it was not until 1954 that this was successfully accomplished. In that year, Dr. Charles Townes and two of his students discussed their experiences with stimulated emission of radiation in the microwave range of the electromagnetic spectrum. This represented the first *maser* (*microwave amplification by the stimulated emission of radiation*) and paved the way for the development of the first laser.

In 1958, Dr. Townes and another physicist, Dr. Arthur Schawlow published "Infrared and Optical Masers" (Schawlow and Townes, 1958), in which they discussed stimulated emission in the microwave range of the spectrum and described the desirability and principles of extending stimulated emission techniques to the infrared and optical ranges of the spectrum. Dr. Theodore Maiman expanded on their theoretical writings and built the first laser in 1960 (Maiman, 1960). Using synthetic ruby crystals, this laser produced electromagnetic radiation at a wavelength of $0.69\ \mu\text{m}$ in the visible range of the spectrum. Although the laser energy produced by Maiman's ruby laser lasted less than a millisecond, it paved the way for explosive development and widespread application of this technology.

A laser is an electrooptical device that emits organized light (rather than random-pattern light emitted from a light bulb) in a very narrow, intense beam by a process of optical feedback and amplification. Since the explanation for this organization involves stimulated emission, a brief review of quantum physics is necessary.

In the semi-classical picture of the atom, each proton is balanced by an electron that orbits the nucleus of the atom in one of several discrete shells or orbits. A shell corresponds to a specific energy level and these energy levels are characteristic of each different atom or molecule. The smaller shells, where the electron is closer to the nucleus,

have a lower energy than the larger shells, where the electron is farther away from the nucleus. Electrons of a particular atom can only orbit the nucleus at these levels, or "floors." Radiation of energy does not occur while the electrons remain in any of these shells.

Electrons can change their orbits or energy levels, thereby changing the energy state of the atom. During excitation, an electron can make the transition from a low energy level to a higher energy state. If the excitation comes from the electron interacting with a discrete packet of light (a photon), this is termed absorption. The atom always seeks its lowest energy level, the ground state. Therefore, the electron will spontaneously drop from the high energy shell back to the lowest energy shell in a very short time (typically 10^{-8} s). As the electron spontaneously drops from the higher energy shell to the lower energy shell, the atom must give up the energy difference. The atom emits the extra energy as a photon of light in a process termed the spontaneous emission of radiation (Fig. 1).

Einstein postulated that an atom in a high energy state would be induced to make the transition to a lower energy state even faster than the spontaneous process if it interacted with an existing photon of the same energy. One might imagine a photon colliding with an excited atom and the collision results in two identical photons (one incident and one produced by the decay) leaving the collision. The two photons have the same frequency, have the same energy and are travelling in the same direction in spatial and temporal phase (Einstein, 1917). This process, which Einstein called *stimulated emission of radiation*, is the underlying principle of laser physics (Fig. 1).

All laser devices have an optical resonating chamber (cavity) with two mirrors; the space between these mirrors is filled with a lasing medium such as argon, neodymium:yttrium aluminum garnet (Nd:YAG) or carbon dioxide (CO_2). An external

energy source such as an electric current excites the lasing medium within the optical cavity. This pumping causes many atoms of the lasing medium to be raised to a higher energy state. When more than half the atoms in the resonating chamber have reached a particular excited state, a population inversion has occurred. Spontaneous emission is taking place in all directions; light (photons) emitted in the direction of the long axis of the laser is retained within the optical cavity by multiple reflections off the precisely aligned mirrors. One mirror is completely reflective and the other partially transmissive (Fig. 2). Stimulated emission occurs when a photon interacts with an excited atom in the optical cavity, yielding pairs of identical photons that are of equal wavelength, frequency and energy and are in phase with each other. This process takes place at an increasing rate with each passage of the photons through the lasing medium; the mirrors serve as a positive feedback mechanism for the stimulated emission of radiation by reflecting the photons back and forth. The partially transmissive mirror emits some of the radiant energy as laser light. The radiation leaving the optical cavity through the partially transmissive mirror quickly reaches an equilibrium with the pumping mechanism's rate of replenishing the population of high energy state atoms.¹

The radiant energy emitted from the optical cavity is of the same wavelength (monochromatic), is extremely intense and unidirectional (collimated), and is coherent both temporally and spatially. *Temporal coherence* refers the waves of light oscillating in phase over a given time interval, Δt . Whereas *spatial coherence* means that the photons are equal

¹We have used the term atom in the preceeding discussion when referring to the lasing material. In reality, the lasing material can be molecules, ions, atoms, semi conductors and even free electrons in an accelerator. In these other systems, it does not have to be the bound electron that is excited. It can be many different excitations, including molecular vibrational excitation or the kinetic energy of an accelerated electron.

and parallel across the wave front. These properties of monochromaticity, intensity, collimation and coherence distinguish the organized radiant energy of a laser light source from the disorganized radiant energy of a light bulb or other light source (Ossoff and Karlan, 1985). (see Fig. 3)

After the laser energy exits the optical cavity through the partially transmissive mirror, the radiant energy typically passes through a lens that focuses the laser beam to a very small beam diameter, or spot size, ranging from 0.1 to 2.0 mm. When necessary, the lens system is constructed to allow the visible helium-neon aiming laser beam and the invisible CO₂ or Nd:YAG laser beam to be focused coplanar. The optical properties of each focusing lens determine the focal length or distance from the lens to the intended target tissue for focused use.

CONTROL OF THE SURGICAL LASER

With most surgical lasers, the physician can control three variables: (1) power (measured in watts), (2) spot size (measured in millimeters), and (3) exposure time (measured in seconds). Of these three variables, power is the least useful as a parameter and may be kept constant with widely varying effects, depending on the spot size and the duration of exposure. For example, the relationship between power and depth of tissue injury becomes logarithmic when the power and exposure time are kept constant and the spot size is varied (Ossoff and Karlan, 1985).

Power density (PD) is a more useful measure of the intensity of the beam at the focal spot than power because it takes into account the surface area of the focal spot. Specifically, power density or power per unit area of the beam, expressed in watts per

square centimeter, is a measure of the power output of the laser in watts divided by the cross-sectional area of the focal spot in square centimeters.

$$PD = \frac{\text{power in the focal spot}}{\text{area of the focal spot}}$$

Power and spot diameter are considered together and a combination is selected to produce the appropriate power density. If the time of exposure is kept constant, the relationship between power density and depth of injury is linear as the spot size is varied. Power density is the most important operating parameter of a surgical laser at a given wavelength.

Therefore, surgeons should calculate the appropriate power density for each procedure to be performed; these calculations would allow the surgeon to control in a predictable manner the tissue effects when changing from one focal length to another (400 mm for microlaryngeal surgery to 125 mm for handheld surgery) or when using surgical lasers with different transverse electromagnetic modes (TEM_{00} vs TEM_{01}). Power density varies directly with power and inversely with surface area (A). This relationship of surface area to beam diameter is an important when evaluating the power density. The larger the surface area, the lower the power density; conversely, the smaller the surface area, the higher the power density. Surface area is expressed as:

$$A = \pi r^2$$

where r is the beam radius. Since the radius is one-half of the beam diameter (d/2), surface area also can be expressed as:

$$A = \pi d^2/2^2 \text{ or } A = \pi d^2/4$$

Surface area, then, varies as the square of the beam diameter; doubling the beam diameter will increase the surface area by four times, while halving the beam diameter will yield only one-quarter the area. Therefore, power density varies inversely with the square of the diameter. For example, doubling the beam diameter (from d to $2d$) reduces the power density to one-fourth (PD to $PD/4$) and halving the spot diameter (d to $d/2$) increases power density by a factor of 4 (Ossoff and Karlan, 1985).

Newer CO₂ lasers emit radiant energy with a characteristic beam intensity pattern different from that produced by older-model lasers. Because this beam pattern ultimately determines the depth of tissue injury and vaporization pattern across the focal spot, the surgeon must be aware of the characteristic beam pattern of the laser. *Transverse electromagnetic mode* (TEM) refers to the distribution of energy across the focal spot and determines the shape of the laser's spot. The most fundamental transverse electromagnetic mode is TEM₀₀, appearing circular when cut in cross section; the power density of the beam follows a gaussian distribution, with its greatest amount of energy at the center of the beam, then diminishing progressively toward the periphery. TEM₀₁ and TEM₁₁ modes are less fundamental modes that have a more complex distribution of energy across their focal spot, causing predictable variations in tissue vaporization depth. Additionally, their beams cannot be focused down to as small a spot size at the same working distance as TEM₀₀ lasers (Fuller, 1980).

Although simple ray diagrams normally show parallel light to be focussed to a point, the actual situation a bit more complicated. A lens will focus a gaussian beam to a *beam waist* or a finite size. This beam waist is the minimum spot diameter, d , and can be written as

$$d \sim \frac{2 f \lambda}{D}$$

where f is the focal length of the lens, λ is the wavelength of light and D is the diameter of the laser beam incident on the lens (Fig. 4). The beam waist occurs not at one distance from the lens, but over a range of distances. This range is termed the *depth of focus* and can be written as

$$\text{depth of focus} \sim \frac{\pi d^2}{2 \lambda}$$

We realize the depth of focus every time we focus a camera. With a camera, a range of objects is in focus, and we can set the focus without carefully measuring the distance between the object and the lens. Notice from the above equations that a long focal length lens (a large f) leads to a large beam waist. A large beam waist also translates as a large depth of focus.

The size of the laser beam on the tissue (spot size) can therefore be varied in two ways. Because the minimum beam diameter of the focal spot increases directly with increasing the focal length of the laser focusing lens, the surgeon can change the focal length of the lens to obtain a particular beam diameter. As the focal length becomes smaller, there is a corresponding decrease in the size of the focal spot; also, the smaller the spot size is for any given power output, the greater the corresponding power density. The second way the surgeon can vary the spot size is by working either in or out of focus. The minimum beam diameter and highest power concentration occur at the focal plane, where

much of the precise cutting and vaporization is carried out (Fig. 5a). As the distance from the focal plane increases, the laser beam diverges or becomes defocused (Fig. 5b). Here, the cross sectional area of the spot grows larger and thus lowers the power density for a given output. As one can readily see the size of the focal spot depends on both the focal length of the laser lens and whether the surgeon is working in or out of focus. Fig. 6 demonstrates these concepts using arbitrary ratios accurate for a current model TEM₀₀ CO₂ laser. The laser lens setting (focal length) and working distance (focus/defocus) combinations shown here determine the size of the focal spot. The height of the various cylinders represents the amount of tissue (depth and width) vaporized after a 1-second exposure at the three focal lengths.

Varying the exposure time represents the third way in which the surgeon can vary the amount of energy delivered to the target tissue. *Radiant exposure* (RE) refers to the amount of time (measured in seconds) that a laser beam irradiates a unit area of tissue at a constant power density. Radiant exposure is a measure, then, of the total amount of laser energy per unit area of exposed target tissue and is expressed as joules per square centimeter:

$$RE = \text{Power Density} \times \text{Time}$$

The radiant exposure varies directly with the length of the exposure time. The exposure time can be varied by working in either the pulsed mode, with durations ranging from 0.05 to 0.5 seconds, or in the continuous mode.

In summary, the surgeon can control the CO₂ laser to incise, coagulate, or vaporize tissue by varying the power output, spot size or exposure time of the laser unit.

TISSUE EFFECTS

When electromagnetic energy (incident radiation) interacts with tissue, the tissue reflects part, the tissue absorbs part, and the tissue transmits and scatters part of the light. The surgical interaction of this radiant energy with tissue is caused only by that portion of the light that is absorbed (that is, the incident radiation minus the sum of the reflected and transmitted portions) (Polanyi, 1983).

The actual tissue effects produced by the radiant energy of a laser vary with the specific wavelength of the laser used. Each type of laser exhibits characteristic and different biological effects on tissue and is therefore useful for different applications. Yet, certain similarities exist regarding the nature of interaction of all laser light with biological tissue. The lasers used in medicine and surgery, today, can be ultraviolet where the interactions are a complex mixture of heating and photodissociation of chemical bonds. The more commonly used lasers emit light in the visible or the infrared region of the electromagnetic spectrum, and their primary form of interaction with biological tissue leads to heating. Therefore if the radiant energy of a laser is to exert its effect upon the target tissue, it must be absorbed by the target tissue and converted to heat (Fig. 7). Scattering tends to spread the laser energy over a larger surface area of tissue, but limits the penetration depth (Fig. 8). The shorter the wavelength of light, the more it is scattered by the tissue. If the radiant energy is reflected from (Fig. 9) or transmitted through (Fig. 10) the tissue, no effect will occur. To select the most appropriate laser system for a particular application, the surgeon must have a thorough understanding of these four characteristics regarding the interaction of laser light with biologic tissue (Fuller, 1984).

The CO₂ laser creates a characteristic wound (Fig. 11). When the target absorbs a specific amount of radiant energy to raise its temperature to 60° to 65° C, protein denaturation occurs. Blanching of the tissue surface is readily visible and the deep structural integrity of the tissue is disturbed. When the absorbed laser light heats the tissue to approximately 100° C vaporization of intracellular water occurs. This causes vacuole formation, cratering and tissue shrinkage. Carbonization, disintegration, smoke and gas generation with destruction of the laser radiated tissue occurs at several hundred degrees centigrade. In the center of the wound is an area of tissue vaporization; here just a few flakes of carbon debris are noted. Immediately adjacent to this area is a zone of thermal necrosis measuring approximately 100 μ m wide. Next is an area of thermal conductivity and repair, usually 300 to 500 μ m wide. Small vessels, nerves, and lymphatics are sealed in the zone of thermal necrosis; the minimal operative trauma combined with the vascular seal probably account for the notable absence of postoperative edema characteristic of laser wounds (Mihashi et al., 1976).

Comparison studies have been performed with experimental animals on the histological properties of healing and the tensile strength of the healing wound following laser and scalpel produced incisions. Hall (1971) noted that the tensile strength in a CO₂ laser induced incision was less up to the twentieth day post-injury; by the fortieth day, however, it equaled that of the scalpel produced incision. Norris and Mullarry (1982) studied the healing properties of laser induced incisions on hogs and concluded that scalpel induced incisions exhibited better wound healing characteristics histologically up to the thirtieth day, after which time, both incisions exhibited similar results. Buell and Schuller (1983) compared the rate of tissue repair after CO₂ laser and scalpel incisions on hogs. In this study the tensile strength of the laser incisions was less than similar scalpel incisions

during the first 3 weeks after surgery; after that time rapid increases in the tensile strength of both wounds occurred at similar rates.

LASER TYPES AND APPLICATIONS

Six types of lasers are commonly in use in otolaryngology--head and neck surgery and many more are in various stages of development. These include the argon laser, the argon pumped tunable dye laser, Nd:YAG laser, KTP laser, flash lamp pumped dye laser, and CO₂ laser. The potential clinical applications of each of these surgical lasers are determined by their wavelength and specific tissue absorptive characteristics. Therefore, the surgeon should consider the properties of each wavelength when choosing a particular laser. This will facilitate the achievement of his surgical objective with minimal morbidity and maximal efficiency.

Argon laser

Argon lasers produce blue-green light in the visible range of the electromagnetic spectrum with primary wavelengths of .488 and .514 μm . The radiant energy of an argon laser may be strongly absorbed, scattered, or reflected, depending upon the specific biological tissues with which it interacts. Its extinction length in pure water is about 80 m (*extinction length* refers to the thickness of water necessary to absorb 90% of the incident radiation). Therefore the radiant energy from an argon laser is readily transmitted through clear aqueous tissues such as cornea, lens, and vitreous humor, and is absorbed and reflected to varying degrees by tissues white in color such as skin, fat, and bone. Light from an argon laser is absorbed by hemoglobin and pigmented tissues; a localized thermal

reaction takes place within the target tissue, causing protein coagulation. The clinician uses this selective absorption of the light from an argon laser to photocoagulate pigmented lesions such as port-wine stains, hemangiomas and telangiectasias (Apfelberg et al., 1981; Parkin and Dixon, 1981). Gradual blanching of the laser-photocoagulated tissue takes place over several months.

When the beam of the argon laser is focused to a small focal spot, its power density increases sufficiently to cause vaporization of the target tissue. This characteristic has allowed otologists to use this laser for the performance of stapedotomy procedures in patients with otosclerosis (Perkins, 1980). Bone, being a white tissue, reflects most of the incident radiation from an argon laser. Therefore, when performing an argon laser stapedotomy, it is necessary to place a drop of blood on the stapes to initiate absorption. Other applications of this laser in the middle ear include lysis of middle ear adhesions (DiBartolomeo and Ellis, 1980) and spot welding of grafts in tympanoplasty surgery (Escudero et al., 1979).

Argon tunable dye laser system

The argon tunable dye laser system works on the principle of the argon laser making a high intensity beam that is focused on dye that is continuously circulating in a second laser optically coupled with the argon laser. The argon laser beam energizes the dye, causing it to emit laser energy at a longer wavelength than the pump beam. By varying the type of dye and using a tuning system, different wavelengths can be obtained. The laser energy from this dye laser can then be transmitted through flexible fiberoptics and delivered through endoscopic systems or inserted directly into tumors. The major clinical use of this laser is with selective photodynamic therapy of malignant tumors following the intravenous

injection of the photosensitizer, hematoporphyrin derivative (Dougherty et al., 1975).

After the intravenous injection, the hematoporphyrin derivative disseminates to all the cells of the body, rapidly moving out of normal tissue, but remaining longer in neoplastic tissue. After a few days a differential in concentration exists between the tumor cells and the normal cells. When the tumor is exposed to red light (630 nm), the dye absorbs the light; the absorption of this red light causes a photochemical reaction to occur. Toxic oxygen radicals such as singlet oxygen are produced within the exposed cells causing selective tissue destruction and cellular death. Since there is less photosensitizer in the normal tissues, a much less severe or no reaction occurs. The main technical problem is getting enough light to the target area. Here, the argon tunable dye laser system has helped to solve this problem (Hayata et al. 1982). Additional research to increase the laser intensity and simplify the sometimes cumbersome setup is being conducted with gold vapor lasers and argon pumped titanium sapphire lasers (Petrucco et al., 1990).

Results obtained by many investigators in this country demonstrate that the premise of treating selected neoplasms with hematoporphyrin derivative followed by activation with red light is valid (Dougherty et al., 1978; Cortese and Kinsey, 1982; Wile et al., 1984a,b). The overall potential and exact place of maximum value of this form of treatment remain to be established. Areas that appear to be very promising include carcinoma of the urinary bladder (Tsuchiya et al., 1983), endobronchial lesions of the lung (Hayata et al., 1984), selected carcinomas of the upper aerodigestive tract (Wile et al., 1984a), skin cancers (McCaughan et al., 1983), and metastatic dermal breast cancers (Dougherty et al., 1979). Trials are now being conducted in certain specialties on intraoperative photodynamic therapy in conjunction with conventional surgery and on photodynamic therapy as the sole modality for the treatment of selected superficial mucosal carcinomas (Balchum et al.,

1984). The potential for this compound to serve as a tumor marker in sites where multicentric tumors are common, such as the mucosal surfaces lining the upper aerodigestive tract, has been recently discussed (Ossoff et al., 1984b). The use of a krypton laser with an image intensifier system to facilitate endoscopic detection of hematoporphyrin derivative fluorescence looks promising in the tracheobronchial tree (Dorion et al., 1984).

Nd:YAG laser

Nd:YAG lasers produce light with a wavelength of $1.064\ \mu\text{m}$ in the near infrared (invisible) range of the electromagnetic spectrum. Pure water weakly absorbs the radiant energy of the Nd:YAG laser. The extinction length is about 40 mm. Therefore its radiant energy can be transmitted through clear liquids facilitating its use in the eye or other water filled cavities such as the urinary bladder. The absorption of light from this laser is slightly color dependent, with increased absorption in darkly pigmented tissues and carbonaceous debris. In biological tissue, strong scattering, both forward and backward, determines the effective extinction length, which is usually 2 to 4 mm. Back scattering can account for up to 40% of the total amount of scattering. The zone of damage produced by the incident beam of a Nd:YAG laser produces a homogeneous zone of thermal coagulation and necrosis that may extend up to 4 mm deep and lateral from the surface, making precise control impossible.

This laser is an excellent surgical instrument with which to perform tissue coagulation; vaporization and incision also can be performed with this wavelength. When used for these two functions, however, precision is lacking and tissue damage is wide spread.

The radiant energy from the Nd:YAG laser can be transmitted through flexible

fiberoptic delivery systems, allowing its use with flexible endoscopes. When used in the management of patients with obstructing neoplasms of the tracheobronchial tree, it is considered safer to use a rigid, ventilating bronchoscope, rather than a flexible fiberoptic bronchoscope (Dumon et al., 1984). With this approach, the laser fiber is passed down the lumen of the rigid bronchoscope with a rod lens telescope and suction catheter (Dumon et al., 1982). Otolaryngologists may begin to use this laser with the CO₂ laser when performing bronchoscopic laser surgery. The effective coagulating properties of the Nd:YAG laser should augment the predictable vaporizing properties of the CO₂ laser when treating patients with obstructive tracheal and proximal endobronchial cancers, especially when faced with an ulcerative or actively bleeding tumor (Ossoff, 1986).

CO₂ laser

CO₂ lasers produce light with a wavelength of 10.6 μ m in the infrared (invisible) range of the electromagnetic spectrum. A second, built-in, coaxial helium neon laser is necessary to indicate with its red color the site where the invisible CO₂ laser beam will impact the target tissue. This laser, then, acts as an aiming beam for the invisible CO₂ laser beam. The radiant energy produced by the CO₂ laser is strongly absorbed by pure, homogeneous water and by all biological tissues high in water content. The extinction length of this wavelength is about 0.03 mm in water and in soft tissue; reflection and scattering are negligible. Because absorption of the radiant energy produced by the CO₂ laser is independent of tissue color, and because the thermal effects produced by this wavelength on adjacent nontarget tissues are minimal, the CO₂ laser has become extremely versatile for use in otolaryngology--head and neck surgery.

With current technology, light from this laser cannot be transmitted through existing flexible fiberoptic endoscopes, although research and development of a suitable flexible fiber for transmission of this wavelength is being carried out on an international level. Presently, the radiant energy of this laser is transmitted from the optical resonating chamber to the target tissue via a series of mirrors through an articulating arm to the target tissue (Ossoff and Karlan, 1985). This laser can be used free-hand for macroscopic surgery, attached to the operating microscope for microscopic surgery, and adapted to an endoscopic coupler for bronchoscopic surgery (Ossoff and Karlan, 1982); in this application, rigid, nonfiberoptic bronchoscopes must be used (Ossoff and Karlan, 1983b).

The CO₂ laser has become indispensable for the practice of laryngology, bronchology, neurotology, and pediatric otolaryngology. Many procedures in the upper aerodigestive tract that previously required prolonged hospitalization and tracheotomy can now be performed without the need for tracheotomy (Holinger, 1982), and often as an outpatient procedure. Within the field of neurotology and neurosurgery, recent reports have shown that the length of stay and perioperative morbidity associated with laser removal of acoustic neuromas is reduced when compared to conventional techniques (Cerullo and Mkrdichian, 1987).

In the oral cavity, benign tumors can be excised with the laser (McDonald and Simpson, 1983). A one-stage tongue release can be performed for patients requiring rehabilitation of speech following composite resection with tongue flap reconstruction (Liston and Giordano, 1981). Multiple areas of leukoplakia can be precisely excised; often, a graft is not necessary to resurface the operative field. Selected superficial carcinomas can be precisely excised with the use of the laser, and large recurrent or inoperable tumors can be debulked for palliation (Strong et al., 1979).

The laser has also been used in the management of nasal and paranasal sinus disease; choanal atresia (Healy et al., 1978), hypertrophic inferior turbinates (Mittelman, 1982), squamous papilloma and hereditary hemorrhagic telangiectasia have been treated with the CO₂ laser (Simpson et al., 1982). Yet, the argon laser is a more efficacious instrument for the treatment of hereditary hemorrhagic telangiectasia.

Facial plastic surgical applications where the CO₂ laser has shown promise include the excision of rhinophyma (Shapshay et al., 1980), the excision of benign and malignant skin tumors (Kirschner, 1984), and the vaporization and excision of nevi and tattoos (Levine and Balin, 1982).

The CO₂ laser has found its greatest use in otolaryngology--head and neck surgery in the microscopic surgical management of benign and malignant diseases of the larynx. Surgery for recurrent respiratory papillomatosis has advanced with the use of the laser. The increased ability to preserve normal laryngeal structures while maintaining the translaryngeal airway more than offsets the initial disappointment associated with the laser's inability to cure the disease (Simpson and Strong, 1983). In the pediatric patient population, surgery for webs, subglottic stenosis, capillary hemangiomas and other space occupying airway lesions has been significantly improved by the precision, preservation of normal tissue, and predictable minimal amount of postoperative edema associated with the judicious use of the CO₂ laser (McGill et al., 1983).

In adults, surgery for polyps, nodules, leukoplakia, papilloma, cysts, granulomas, and other benign laryngeal conditions can be performed effectively with the laser (Vaughan, 1983). A new era of conservation surgery or phonosurgery for benign laryngeal disease has been created by the laser. In the past, microlaryngeal surgery for benign disease has been mucosal stripping with healing by remucosalization. Now, normal mucosal tissue can

be preserved by elevating and advancing mucosal flaps with new endoscopic laser techniques (Karlson and Ossoff, 1984). The addition of the microspot micromanipulator has furthered these techniques (Shapshay et al., 1988; Ossoff et al., 1991).

The addition of the CO₂ laser to endoscopic arytenoidectomy allows the surgeon to precisely vaporize the mucosa and underlying arytenoid cartilage layer by layer in a dry field (Ossoff et al., 1984a). The precision associated with the use of the laser facilitates performance of this operation even by surgeons who had difficulty mastering the conventional techniques of endoscopic arytenoidectomy (Thornell, 1984).

The transoral management of squamous cell carcinoma of the larynx using the CO₂ laser is an obvious extension of the application of this surgical instrument. The advantages of precision, increased hemostasis, and decreased intraoperative edema allow the surgeon to perform exquisitely accurate and relatively bloodless endoscopic surgery of the larynx. Recent reports have shown that determinate cure rates with this method of management are equivalent to radiotherapy (Blakeslee et al., 1984; Koufman, 1986).

Bronchoscopic indications for CO₂ laser surgery include management of recurrent respiratory papillomatosis or granulation tissue within the tracheobronchial tree, excision of selected subglottic or tracheal strictures, excision of bronchial adenomas and reestablishment of the airway in patients with obstructing tracheal or endobronchial cancers. In this latter instance, palliation or reduction of the patient's symptoms of airway obstruction or hemoptysis is the desired goal (Ossoff et al., 1986).

KTP laser

The potassium titanyl phosphate (KTP) laser has been recently introduced for surgery. It lases at 532 nm, and therefore compares with the argon laser. The scattering

and absorption by skin pigments are nearly the same as the argon laser. Yet, the KTP laser light is more strongly absorbed by hemoglobin. The KTP laser has shown success with stapedotomies (Bartels, 1990). Thedinger (1990) has promoted the KTP for chronic ear surgery. He specifically identifies the removal of hyperplastic infected mucosa, disarticulating mobile stapes suprastructure in a complete cholesteatoma removal and the removal of previously inserted middle ear implants. The KTP crystal actually frequency doubles (halves the wavelength) of a Nd:YAG laser. Therefore, this laser usually allows one to switch the output between the 532 nm KTP light and the 1064 nm Nd:YAG light.

Flash lamp pumped dye laser

The treatment of hemangiomas and port wine stains with lasers has benefitted from the application of the flash lamp pumped dye laser. The dye was initially selected for maximum absorption by the oxyhemoglobin at 577 nm. A study by Tan et al., (1990a) showed that at 585 nm there is maximal hemoglobin absorption with a minimum of scattering and minimal absorption by melanin and other pigments. The light pulse is about 400 μ sec long to minimize thermal diffusion in the tissue. Although dark Negroid skin types show little or no selective vascular photothermolysis with the laser, the results with lighter skin are significant. At a threshold dose, specific vascular injury is observed without the disruption of the adjacent tissue in lightly pigmented skin (Tan, et al., 1990b).

Other lasers

In an effort to have a more controlled laser effect with less damage to adjacent tissue, several lasers in the near to mid infrared region have been investigated. These include the

erbium:YAG (Er:YAG) and the holmium:YAG (Ho:YAG). The Er:YAG lases at the infrared peak of water absorption at $2.94\ \mu\text{m}$. Here the extinction length in water is less than $2\ \mu\text{m}$. The laser produces very clean incisions with a minimal amount of thermal damage to the adjacent tissue. There are two negative aspects to this laser: The wavelength is too long to be transmitted through normal optical fibers. This gives a distinct advantage to lasers that produce light that can be transmitted through fibers. More importantly, the thermal propagation is so short there is practically no tissue coagulation and no hemostasis. This laser is therefore unsuitable of use in highly vascular tissue.

The Ho:YAG laser operates at $2.1\ \mu\text{m}$. This wavelength can be effectively transmitted through fibers. The extinction length in water is about $0.4\ \text{mm}$, which suggests that this laser light should interact with tissue very similar to the CO_2 laser. The Ho:YAG has been combined with fiberoptic endoscope for sinus surgery (Schlenk et al., 1990). The hemostasis is good and the soft bone ablation is readily controlled. Adjacent thermal damage zones varied from 130 to $220\ \mu\text{m}$ in a study by Stein et al., (1990).

There is also work with other materials that lase in the near infrared region of the spectrum, such as the cobalt:magnesium fluoride laser (tunable from 1.8 to $2.14\ \mu\text{m}$). Alexandrite lasers ($750\ \text{nm}$) and titanium sapphire lasers (tunable from 0.6 to $1.0\ \mu\text{m}$) have also been considered. Ultimately, many parameters such as cost, reliability and size, in addition to the tissue response, will influence choice of lasers in medicine.

PULSE STRUCTURE

In the section on the **Control of the Surgical Laser** it was pointed out that the surgeon has three parameters to select when using a particular laser. The intensity of the

laser is the least useful. The exposure time is important in that it controls the total amount of light incident on the tissue, the Radiant Exposure. The pulse structure of the laser light within the given exposure time is also crucial. The pulse structure is a characteristic of the lasing medium and the cavity configuration. It is often fixed and the surgeon cannot change or modify it.

Many lasers operate in a continuous wave (cw) mode. In this mode, the laser is always on. The instantaneous intensity and the average laser intensity are essentially the same. A shutter, external to the laser cavity, usually controls the exposure time. This allows the laser to operate independent of the exposure time or the frequency of exposures. This gives the most stable operation. A surgical CO₂ or Nd:YAG laser will operate cw at intensities of a few watts to more than 50 W.

Certain lasers operate in a pulsed mode. Flash lamp pumped lasers can pulse from about 0.5 μ s to several 100 ms. The first Ruby laser operated in a pulsed mode. The flashlamp used to pump the ruby crystal had about a 1 msec pulse duration. It was clear that the laser output of this first laser was irregular and unstable. Observing the output with a fast detector and oscilloscope, the output intensity was not a millisecond long laser pulse, but it observed to be a series of irregular spikes. Each spike was a few microseconds long and there were several microseconds between the spikes. The stimulated emission in the ruby is so efficient, that it quickly depletes the population inversion, and the lasing stops. After the lasing stops the flashlamp can reestablish the population inversion. The lasing can then resume. The process repeats until the flash lamp stops. Most of the long pulsed lasers operate in a spiking mode.

The spiking of the laser output can be controlled to produce a single very short laser pulse, much shorter than the flashlamp lifetime. One technique to produce the short pulses

is *Q-switching*. Here, the laser pumping process (usually a flash lamp) builds up a large population inversion inside the laser cavity. The laser is prevented from lasing by blocking or removing one of the mirrors. After a large population inversion has developed the feedback is restored, and a short intense burst of laser light depletes the accumulated population inversion in typically 10 to 50 ns. Q-switching can be accomplished by several different methods. The most direct and earliest method used was rotating the end mirror so that lasing could take place during the short interval when the mirror was correctly aligned. Waring blender motors were often used as a fast, stable motors. However, uncertain timing, lack of reliability and vibration (not to mention the noise) lead to many problems, particularly with the alignment. Electrooptic polarization rotators and acoustooptic beam deflectors are now commonly used for Q-switching.

Cavity dumping produces slightly shorter pulses of light. In this technique, the laser is pumped and allowed to lase between completely reflecting mirrors. The light energy is trapped in the cavity until it reaches a maximum. Then one of the mirrors is "removed" from the cavity and allows all the light to leave the cavity. The laser pulse has a physical length of twice the cavity length. The time duration of the laser pulse is then $2l/c$ where l is the length of cavity and c is the speed of light ($c \sim 3 \times 10^{10}$ cm/s or $c \sim 1$ ft/ns).

Mode locking produces pulses of light as short as a few ps. A Q-switched laser operates in several longitudinal modes (or slightly shifted frequencies). A fast saturable dye brings all these modes into phase. The nanosecond macro pulse of light is actually a train of micro pulses. Each micro pulse in the train is several picoseconds long and repeats at about 100 MHz. These pulses can be further compressed by various compression techniques. The shortest laser light pulses achieved in the laboratory are less than 4 wave oscillations long (~ 6 fs).

The pulsed laser dramatically changes the interactions of the light with tissue. The intensity of the laser during the pulse is extremely high (approaching 10^9W). The high intensity and short pulse duration enables the laser light efficiently to ablate tissue before the thermal energy spreads by thermal diffusion. The pulse needs to be significantly shorter than the thermal diffusion times to prevent thermal diffusion from spreading damage. Typically, a tissue under laser irradiation reaches thermal equilibrium within a few milliseconds. The heat will spread over several micrometers in less than $10\text{ }\mu\text{sec}$ (Reinisch, 1989). Also, the transverse mode structure of the laser beam must be preserved in the short pulses to yield the small focal spot size.

SAFETY CONSIDERATIONS

Education

The laser is a precise but potentially dangerous surgical instrument that must be used with caution. While certain distinct advantages are associated with the use of this relatively new technology in the management of certain benign and malignant diseases of the upper aerodigestive tract, these advantages must be weighed against the possible risks of complications associated with laser surgery. Because of these risks, the surgeon must first determine if the use of the laser affords an advantage over conventional surgical techniques. For the surgeon to exercise this required good judgement in the selection and use of lasers in his practice, prior experience in laser surgery is necessary. Therefore exposure to some type of formal laser education program has to be a prerequisite to the use of this technology. The surgeon who has not received training in laser surgery as a resident should attend one of the many excellent hands-on training courses in laser surgery given in this country. Such a course should include laser biophysics, tissue interactions, safety

precautions, and supervised hands-on training with laboratory animals. Following completion of such a course, the surgeon should practice laser surgery on cadaver or animal specimens before progressing to the more simple procedures on patients.

Each hospital performing laser surgery should appoint a laser safety officer and set up a laser safety committee consisting of the laser safety officer, two or three physicians using the laser, one or two nursing representatives from the operating room, a hospital administrator, and a biomedical engineer. The purpose of this committee is to develop policies and procedures for the safe use of lasers within the hospital. As such, the safety protocols that will be established by this committee will vary with each specialty and use of the laser. In addition, the laser safety committee should make recommendations regarding the appropriate credential-certifying mechanisms required for physicians and nurses to become involved with each laser. Educational policies for surgeons, anesthesiologists, and nurses working with the laser should be developed. Other responsibilities of this important committee include the accumulation of laser patient data in cases where an investigational device was used and a periodic review of all laser related complications.

Suggested minimal educational requirements for surgeons to use lasers are discussed above. Because the anesthesiologist is also concerned with the airway and because potent oxidizing gases pass through the airway in close approximation to the path of the laser beam, it is necessary to develop a team approach to the anesthetic management of the patient undergoing laser surgery of the upper aerodigestive tract. Therefore, it is highly recommended that the anesthesiologists involved with laser surgery cases attend a didactic session devoted to that subject. Finally, the operating room staff must receive some education with regard to laser surgery. Attendance at an in-service workshop with exposure to clinical laser biophysics and the basic workings of the laser as well as hands-on

orientation should be the minimal requirement for nursing participation in laser surgery cases (Spilman, 1983).

Safety protocol

Development of an effective laser safety protocol that stresses compliance and meticulous attention to detail by the surgeon, anesthesiologist, and operating room nurse (laser surgery team) is probably the single most important reason this potentially dangerous surgical instrument can be used so safely in treating patients with diseases of the upper aerodigestive tract (Ossoff, 1989). Such a laser safety protocol is usually general enough to list all the major and most minor precautions necessary when laser surgery is being performed in the specialty of otolaryngology--head and neck surgery. General considerations concern the provision for protection of the eyes and skin of patients and operating room personnel, as well as the provision for adequate laser plume (smoke) evacuation from the operative field. Additional precautions concern the choice of anesthetic technique, the choice and protection of endotracheal tubes, and the selection of proper instruments, including bronchoscopes.

Eye protection

Depending on the wavelength, corneal or retinal burns, or both, are possible from acute exposure to the laser beam. The possibility for corneal or lenticular opacities (cataracts) or retinal injury exists following chronic exposure to excessive levels of laser radiation. Several different structures of the eye are at risk; the area of injury usually depends upon which structure absorbs the most radiant energy per volume of tissue. Retinal effects occur when the laser emission wavelength occurs in the visible and

near-infrared range of the electromagnetic spectrum (0.4 to 1.4 μm). When viewed either directly or secondary to reflection from a specular (mirror-like) instrument surface, laser radiation within this wavelength range would be focused to an extremely small spot on the retina, causing serious injury. This occurs because of the focusing effects of the cornea and lens. Laser radiation in the ultraviolet (less than 0.4 micrometers) or in the infrared range of the spectrum (greater than 1.4 micrometers) produce effects primarily at the cornea, although certain wavelengths also may reach the lens ("American National Standard," 1981).

To reduce the risk of ocular damage during cases involving the laser, certain precautions should be followed. Protection of the eyes of the patient surgeon and other operating room personnel must be addressed; the actual protective device will vary according to the wavelength of the laser used. A sign should be placed outside the operating room door warning all persons entering the room to wear protective glasses because the laser is in use. In addition, extra glasses for the specific wavelength in use at the time should be placed on a table immediately outside the room. The doors to the operating room should remain closed during laser surgery with the CO₂ laser, and locked when working with the Nd:YAG or argon laser.

For patients undergoing CO₂ laser surgery of the upper aerodigestive tract, a double layer of saline moistened eye pads should be placed over the eyes. All operating room personnel should wear protective glasses with side protectors. Regular eyeglasses or contact lenses protect only the areas covered by the lens and do not provide protection from possible entry of the laser beam from the side. When working with the operating microscope and the CO₂ laser, the surgeon need not wear protective glasses; here the optics of the microscope provide the necessary protection (Ossoff et al., 1983a).

When working with the Nd:YAG laser, all operating room personnel must wear wavelength specific protective glasses that are usually of a blue/green color. The patient's eyes also should be protected with a pair of these glasses. Though it may appear that the beam direction and point of impact are confined within the endoscope, inadvertent deflection of the beam may occur due to a faulty contact, a break in the fiber, or accidental disconnection between the fiber and endoscope. Special wavelength-specific filters are available for flexible and rigid bronchoscopes; when these filters are in place, the surgeon need not wear protective glasses ("Guide," 1984).

When working with the argon, KTP, or dye lasers, all personnel in the operating room, including the patient, should again wear wavelength specific protective glasses, which are usually of an amber color. When performing photocoagulation procedures for selected cutaneous vascular lesions of the face, protective metal eye shields rather than protective glasses are usually used on the patient (DiBartolomeo, 1981). Similar precautions are necessary for the newer visible and near infrared wavelength lasers. The major difference is the type of eye protection that is worn.

Skin protection

All exposed skin and mucous membranes of the patient outside the surgical field should be protected by a double layer of saline saturated surgical towels, surgical sponges, or lap pads. When microlaryngeal laser surgery is being performed, the possibility exists that the beam might partially reflect off the proximal rim of the laryngoscope, rather than go down it. So, saline saturated surgical towels completely drape the patient's face; only the proximal lumen of the laryngoscope is exposed. Great care must be exercised to keep the wet draping from drying out; it should be moistened from time to time during the case.

Teeth in the operative field also need to be protected; saline saturated telfa, surgical sponges, or specially constructed metal dental impression trays can be used. Meticulous attention is paid to the protective draping procedures at the beginning of the surgery; the same compulsion should be displayed for the continued protection of the skin and teeth during the surgical procedure (Ossoff et al., 1983a).

Smoke evacuation

Two separate suction setups should be available for all laser cases in the upper aerodigestive tract; one provides for adequate smoke and steam evacuation from the operative field, while the second is connected to the surgical suction tip for the aspiration of blood and mucous from the operative wound (Spilman, 1983). When performing laser surgery with a closed anesthetic system, constant suctioning should be used to remove laser-induced smoke from the operating room; this helps to prevent inhalation by the patient, surgeon or operating room personnel. When the anesthetic system used is an open one or with jet ventilation systems, suctioning should be limited to an intermittent basis to maintain the forced inspiratory oxygen (FIO₂) at a safe level. Laryngoscopes, bronchoscopes, operating platforms, mirrors, and anterior commissure and ventricle retractors with built-in smoke evacuating channels facilitate the easy evacuation of smoke from the operative field (Ossoff and Karlan, 1983a). A recent report has suggested that the smoke created by the interaction of the CO₂ laser with tissue is probably mutagenic (Tomita et al., 1981). Filters in the suction lines should be used to prevent clogging by the black carbonaceous smoke debris created by the laser (Mohr et al., 1984).

Anesthetic considerations

Optimal anesthetic management of the patient undergoing laser surgery of the upper aerodigestive tract must include attention to the safety of the patient, the requirements of the surgeon, and the hazards of the equipment. Because of the length of time required to expose the larynx and suspend the laryngoscope, manipulate the operating microscope into position, and accurately align the laser beam down the center of the long axis of the laryngoscope, most patients require general anesthesia for this type of surgery. Any nonflammable general anesthetic is suitable; halothane and enflurane are most often used. Because of the risk of fire associated with general endotracheal anesthesia, the inspired concentration of oxygen, a potent oxidizing gas, is important. Mixtures of helium, nitrogen, or air plus oxygen are commonly used to maintain the FIO_2 around but not above 40% and insure that the patient is adequately oxygenated. Nitrous oxide is also a potent oxidizing gas; and should not be used in the anesthetic mixture to cut the oxygen concentration. When performing laser surgery in the tracheobronchial tree through the rigid, ventilating bronchoscope, 100% oxygen may be used. In either case, intravenous supplementation with small doses of narcotics and/or tranquilizers is often used to shorten the emergence period following anesthesia. Muscle relaxation is required to prevent movement of the vocal cords when working in the larynx. Jet ventilation techniques during laser surgery work well for selected patients (Edelist and Alberti, 1982); the present unavailability of a satisfactory method of total intravenous anesthesia has limited its widespread use in complicated cases, or those requiring multiple frozen-section examinations.

At the present time a nonflammable, universally accepted endotracheal tube for laser surgery of the upper aerodigestive tract does not exist. The polyvinyl endotracheal tube should not be used, either wrapped or unwrapped. It offers the least resistance to penetration by the laser beam of all the endotracheal that have been tested, and

fire-breakdown products and tissue destruction associated with combustion of this tube are the most severe. The Rusch red rubber tube offers some resistance to penetration by the laser beam and causes mild to moderate damage to the tracheobronchial tree should a fire occur. The silicone tube offers more resistance to penetration than the red rubber tube; however, silica ash can be seen in the airway after fires with these tubes and raises the possibility of future problems with silicosis (Ossoff et al., 1983b). Although the Norton metal tube (Norton and DeVos, 1978) is nonflammable, problems with rigidity, inner-to-outer diameter ratios, gas leakage, and lack of a cuff have prevented it from becoming the universally accepted tube of choice for CO₂ laser surgery. Newer endotracheal tubes for laser surgery (wavelength specific) are now available from several manufacturers.

Protection of the endotracheal tube from either direct or reflected laser beam irradiation is of primary importance. Should the laser beam strike an unprotected endotracheal tube carrying oxygen, ignition of the tube could result in a catastrophic, intraluminal, blow-torch type endotracheal tube fire (Schramm et al., 1981). Red rubber endotracheal tubes wrapped circumferentially from the cuff to the top with reflective metallic tape reduces the risk of intraluminal fire when a special laser protective endotracheal tube cannot be used. Metallic tape covered with merocel™ is another acceptable alternative. Mylar tape offers no protection from the laser and should not be used (Ossoff and Karlan, 1984b).

Protection also needs to be provided for the cuff of the endotracheal tube. Methylene blue-colored saline should be used to inflate the cuff (Ossoff et al., 1983a). Saline-saturated neurosurgical cottonoids are then placed above the cuff in the subglottic larynx to further protect the cuff. These cottonoids require frequent moistening during the procedure. Should the cuff become deflated from an errant hit by the laser beam, the

already-saturated cottonoids would turn blue to warn the surgeon of impending danger. The tube should then be removed and replaced with a new one. Use of the operating platform is strongly recommended as a further insulation against potential danger. Inserted into the subglottic larynx above the level of the packed cottonoids, this unique instrument serves as a catcher's mitt to protect the cottonoids, endotracheal tube and cuff from any direct or reflected laser beam irradiation (Ossoff and Karlan, 1984a).

The Nd:YAG laser has a different interaction with endotracheal tubes than the CO₂ laser. *In vitro* testing of various endotracheal tubes with the Nd:YAG laser has demonstrated that the safest tube to use is a colorless or white polyvinyl endotracheal tube or silicone endotracheal tube without any black or dark colored lettering on the tube itself. Also, the tube should not have any lead-lined marking. The Rusch red rubber tube with or without metallic tape did not protect against ignition with the Nd:YAG laser (Shapshay, no date).

Instrument selection

The surface characteristics of instruments used in laser surgery should provide for low specular or direct reflectance and large diffuse or scattered reflectance of the laser beam, should the beam inadvertently strike the instrument. Plastic instruments should be avoided since they can melt with the laser irradiation. Use of instruments with these surface characteristics will contribute to minimizing tissue injury or endotracheal tube ignition from direct or reflected laser beam irradiation.

Rigid instrumentation is the preferred method of laser bronchoscopy with either the CO₂ or Nd:YAG laser; should active bleeding occur during a case, it would be extremely difficult or impossible successfully to control the airway and evacuate the blood using

flexible instrumentation. Additionally, rigid instrumentation allows the surgeon to pass one, two, or three suction cannulas through the bronchoscope to facilitate blood evacuation and airway control. This point must be emphasized because of the recent proliferation of the Nd:YAG laser surgery and the ability of this laser light to be delivered through flexible fiberoptic endoscopes as well as rigid endoscopes.

Bronchoscopic couplers for CO₂ laser surgery must have an optical system that allows the visible helium-neon aiming laser beam to be passed coaxially with the invisible CO₂ laser beam. In addition, the surgeon should be able to center the beam within the lumen of the bronchoscope to avoid the hazards of the beam reflecting off the inside wall of the bronchoscope, with subsequent loss of power and possible heating of the bronchoscope itself. Burns of the trachea, larynx, pharynx, and oral cavity have occurred as a direct result of such an event (Ossoff and Karlan, 1983b).

Effectiveness of a safety protocol

Strong and Jako (1972) and later Snow et al. (1976) warned of the possible complications associated with laser surgery of the upper aerodigestive tract including the risks of endotracheal tube fires and tissue damage from reflection of the laser beam. Following these early warnings, several reports of complications uniquely attributable to use of the CO₂ laser appeared in the literature (Alberti, 1981; Burgess and Lejeune, 1979; Cozine et al., 1981; Meyers, 1981). In a survey of laser-related complications reported by Fried (1984), 49 of 152 otolaryngologists who used the laser reported 81 complications that included 28 separate incidents of endotracheal tube fires. A recent analysis of complications unique to the use of the laser that occurred under a rigid safety protocol at Northwestern University Medical School and affiliated hospitals revealed a 1.7% incidence

of complications; no fires were reported in this group (Ossoff et al., 1983). Healy et al. (1984) published a 0.2% complication rate in 4416 cases of CO₂ laser surgery in the upper aerodigestive tract. Ossoff (1989) published an extensive review of laser-related complications experienced by 218 past registrants of hands-on laser surgery training courses that he directed. Seven surgeons experienced 8 complications and no endotracheal tube fires. The complication rate was 0.1% in over 7200 laser surgical procedures. The conclusions of these papers are similar. First, certain precautions are necessary when performing laser surgery of the upper aerodigestive tract. Second, adherence to a rigid safety protocol allows laser surgery of the airway to be performed safely and with an extremely small risk of serious complications.

REFERENCES

- Alberti, P.W.: The complications of CO₂ laser surgery in otolaryngology. *Acta Otolaryngol*, 91:375-381, 1981.
- American national standard for the safe use of lasers, Z136.1. American National Standards Institute, Inc., New York, New York, 1981.
- Apfelberg, D.B., Maser, M.R., Lash, H., et al: The argon laser for cutaneous lesions. *JAMA*, 245:2073-2075, 1981.
- Balchum, O.J., Dorion, D.R., and Huth, G.C.: Photoradiation therapy of endobronchial lung cancers employing the photodynamic action of hematoporphyrin derivative. *Lasers Surg Med*, 4:13-30, 1984.
- Bartels, L.J.: KTP laser stapedotomy: is it safe?. *Otolaryngol Head Neck Surg*, 103:685-692, 1990.
- Blakeslee, D., Vaughan, C.W., Shapshay, S.M., Simpson, G.T., and Strong, M.S.: Excisional biopsy in the selective management of T1 glottic cancer: a three-year follow-up study. *Laryngoscope*, 94:488-494, 1984.
- Buell, B.R., Schuller, D.E.: Comparison of tensile strength in CO₂ laser and scalpel skin incisions. *Arch Otolaryngol*, 109:465-467, 1983.
- Burgess, G.E., and LeJeune, F.E.: Endotracheal tube ignition during laser surgery of the larynx. *Arch Otolaryngol*, 105:561-562, 1979.
- Cerullo, L.J., and Mkrdichian, E.: Acoustic nerve tumor surgery before and since the laser: comparison of results. *Lasers Surg Med*, 7:224-228, 1987.

- Cortese, D.A., Kinsey, J.H.: Hematoporphyrin-derivative phototherapy for local treatment of cancer of the tracheobronchial tree. *Ann Otol Rhinol Laryngol*, 91:652-655, 1982.
- Cozine, K., Rosenbaum, L.M., Askanzi, J., et al: Laser-induced endotracheal tube fire. *Anesthesiology*, 55:583-585, 1981.
- DiBartolomeo, J.R.: The argon and CO₂ lasers in otolaryngology: which one, when and why? *Laryngoscope*, 91:Supplement 26, 1981.
- DiBartolomeo, J.R., and Ellis, M.: The argon laser in otology. *Laryngoscope*, 90:1786-1796, 1980.
- Dorion, D.R., Profio, E., Vincent, R.G., and Dougherty, T.J.: Fluorescence bronchoscopy for detection of lung cancer. *Chest*, 76:27-32, 1984.
- Dougherty, T.J., Grindley, G.B., Fiel, R., Weishaupt, K.R., and Boyle, D.G.: Photoradiation therapy II. cure of animal tumors with hematoporphyrin and light. *J Natl Cancer Inst*, 55:115-121, 1975.
- Dougherty, T.J., Kaufman, J.E., Goldfarb, A., Weishaupt, K.R., Boyle, D., and Mittleman, A.: Photoradiation therapy for the treatment of malignant tumors. *Cancer Res*, 38:2628-2635, 1978.
- Dougherty, T.J., Lawrence, G., Kaufman, J.H., Boyle, D., Weishaupt, K.R., and Goldfarb, A.: Photoradiation in the treatment of recurrent breast carcinoma. *J Natl Cancer Inst*, 62:231-237, 1979.
- Dumon, J.F., Reboud, E., Garbe, L., Aucomte, F., Meric, B.: Treatment of tracheobronchial lesions by laser photoresection. *Chest*, 81:278-284, 1982.

- Dumon, J.F., Shapshay, S., Bourcereau, J., Cavaliere, S., Meric, B., Garbi, N., and Beamis, J.: Principles for safety in application of Neodymium-YAG laser in bronchology. *Chest*, 86:163-168, 1984.
- Edelist, G., and Alberti, P.W.: Anesthesia for CO₂ laser surgery of the larynx. *J Otolaryngol*, 11:107-110, 1982.
- Einstein, A.: Zur Quanten Theorie der Strahlung. *Phys Zeit*, 18:121-128, 1917.
- Escudero, L., Castro, A.O., Drumond, M., et al.: Argon laser in human tympanoplasty. *Arch Otolaryngol*, 105:252-259, 1979.
- Fried, M.P.: A survey of the complications of laser laryngoscopy. *Arch Otolaryngol*, 110:31-34, 1984.
- Fuller, T.A.: The physics of surgical lasers. *Lasers Surg Med*, 1:5-14, 1980.
- Fuller, T.A.: The characteristics of operation of surgical lasers. *Surg Clin North Am*, 64:843-849, 1984.
- Guide for the selection of laser eye protection. Laser Institute of America, Toledo, Ohio, 1984.
- Hall, R.R.: The healing of tissues incised by carbon dioxide laser. *Br J Surg*, 58:222-225, 1971.
- Hayata, Y., Kato, H., Konaka, C., Ono, J., and Takizawa, N.: Hematoporphyrin derivative and laser photoradiation in the treatment of lung cancer. *Chest*, 81:269-277, 1982.
- Hayata, Y., Kato, H., Konaka, C., Amemiya, R., Ono, J., Ogawa, I., Kinoshita, K., Sakai, H., and Takahashi, H.: Photoradiation therapy with hematoporphyrin derivative in early

- and stage 1 lung cancer. *Chest*, 86:169-177, 1984.
- Healy, G.B., McGill T., Jako, G.J., Strong, M.S., Vaughan, C.W.: Management of choanal atresia with the carbon dioxide laser. *Ann Otol Rhinol Laryngol*, 87:658-662, 1978.
- Healy, G.B., Strong, M.S., Shapshay, S.M., Vaughan, C.W., and Jako, G.J.: Complications of CO₂ laser surgery of the aerodigestive tract: experience of 4416 cases. *Otolaryngol Head Neck Surg*, 92:13-18, 1984.
- Holinger, L.D.: Treatment of severe subglottic stenosis without tracheotomy: a preliminary report. *Annals of Otology Rhinology & Laryngology*, 91:407-412, 1982.
- Karlan, M.S., and Ossoff, R.H.: Laser surgery for benign laryngeal disease: Conservation and ergonomics. *Surg Clin North Am*, 64:981-994, 1984.
- Kirschner, R.A.: Cutaneous plastic surgery with the CO₂ laser. *Surg Clin North Am*, 64:871-883, 1984.
- Koufman, J.A.: The endoscopic management of early squamous carcinoma of the vocal cord with the carbon dioxide surgical laser: clinical experience and a proposed subclassification. *Otolaryngol Head Neck Surg*, 95:531-537, 1986.
- Levine, H., and Balin, P.: Carbon dioxide laser treatment of cutaneous hemangiomas and tattoos. *Arch Otolaryngol*, 108:236-238, 1982.
- Liston, S.L., and Giordano, A.: tongue release using the CO₂ laser. *Laryngoscope*, 91:1010-1011, 1981.
- Maiman, T.H.: Stimulated optical radiation in ruby. *Nature*, 187:493-494, 1960.
- McCaughan, J.S., Guy, J.T., Hawley, P., Hicks, W., Inglis, W., Laufman, L., May, E., Nims,

- T.A., and Sherman, R.: Hematoporphyrin-derivative and photoradiation therapy of malignant tumors. *Lasers Surg Med*, 3:199-209, 1983.
- McDonald, G.A., and Simpson, G.T.: Transoral resection of lesions of the oral cavity with the carbon dioxide laser. *Otolaryngol Clin North Am*, 16:839-847, 1983.
- McGill, T.J.I., Friedman, E.M., and Healy, G.B.: Laser surgery in the pediatric airway. *Otolaryngol Clin North Am*, 16:865-870, 1983.
- Meyers, A.: Complications of CO₂ laser surgery of the larynx. *Ann Otol Rhinol Laryngol*, 90:132-134, 1981.
- Mihashi, S., Jako, G.J., Incze, J., Strong, M.S., and Vaughan, C.W.: Laser surgery in otolaryngology: interaction of the CO₂ laser in soft tissue. *Ann NY Acad Sci*, 267:263-293, 1976.
- Mittleman, H.: CO₂ laser turbinectomies for chronic obstructive rhinitis. *Lasers Surg Med*, 2:29-36, 1982.
- Mohr, R.M., McDonnell, B.C., Unger, M., and Mauer, T.P.: Safety considerations and safety protocol for laser surgery. *Surg Clin North Am*, 64:851-859, 1984.
- Norris, C.W., and Mullarby, M.B.: Experimental skin incision made with the carbon dioxide laser. *Laryngoscope*, 92:416-419, 1982.
- Norton, M.L., DeVos, P.: New endotracheal tube for laser surgery of the larynx. *Ann Otol Rhinol Laryngol*, 87: 554-557, 1978.
- Ossoff, R.H.: Laser Safety in Otolaryngology-Head and Neck Surgery: Anesthetic and educational considerations for laryngeal surgery. *Laryngoscope*, 99:1-26, 1989.

- Ossoff, R.H.: Bronchoscopic laser surgery: which laser when and why. *Otolaryngol Head Neck Surg*, 94:378-381, 1986.
- Ossoff, R.H., and Karlan, M.S.: Universal endoscopic coupler for carbon dioxide laser surgery. *Ann Otol Rhinol Laryngol*, 91:608-609, 1982.
- Ossoff, R.H., and Karlan, M.S.: Instrumentation for micro-laryngeal laser surgery. *Otolaryngol Head Neck Surg*, 91:456-460, 1983a.
- Ossoff, R.H., and Karlan, M.S.: A set of bronchoscopes for carbon dioxide laser surgery. *Otolaryngol Head Neck Surg*, 91:336-337, 1983b.
- Ossoff, R.H., and Karlan, M.S.: Instrumentation for CO₂ laser surgery of the larynx and tracheobronchial tree. *Surg Clin North Am*, 64:973-980, 1984a.
- Ossoff, R.H., and Karlan, M.S.: Safe instrumentation in laser surgery. *Otolaryngol Head Neck Surg*, 92:664, 1984b.
- Ossoff, R.H., and Karlan, M.S.: Laser Surgery in Otolaryngology. In Ballenger, J.J. (ed.): *Diseases of the Nose, Throat, Ear, Head and Neck*, Philadelphia, Lea & Febiger, 1985.
- Ossoff, R.H., Hotaling, A., Karlan, M.S., Sisson, G.A.: The CO₂ laser in otolaryngology--head and neck surgery: a retrospective analysis of complications. *Laryngoscope*, 93:1287-1289, 1983a.
- Ossoff, R.H., Duncavage, J.A., Eisenman, T.E., and Karlan, M.S.: Comparison of tracheal damage from laser-ignited endotracheal tube fires. *Ann Otol Rhinol Laryngol*, 92:333-336, 1983b.

- Ossoff, R.H., Sisson, G.A., Duncavage, J.A., Mosell, H.I., Andrews, P.E., and McMillan, W.G.: Endoscopic laser arytenoidectomy for the treatment of bilateral vocal cord paralysis. *Laryngoscope*, 94:1293-1297, 1984a.
- Ossoff, R.H., Pelzer, H.J., Atiyah, R.A., Berkold, R.E., and Sisson, G.A.: Potential applications of photoradiation therapy in head and neck surgery. *Arch Otolaryngol*, 110:728-730, 1984b.
- Ossoff, R.H., Karlan, M.S., Duncavage, J.A., Toohill, R.J., Gluckman, J.L., Keane, W.M., Adkins, J.P., Norris, C.W., and Tucker, J.A.: The universal endoscopic coupler for bronchoscopic carbon dioxide laser surgery: a multi-institutional clinical trial. *Otolaryngol Head Neck Surg*, 93:824-830, 1985.
- Ossoff, R.H., Werkhaven, J.A., Raif, J., and Abraham, M.: Advanced microspot microslad for the CO₂ laser. *Otolaryngol Head Neck Surg*, 105:411-414, 1991.
- Parkin, J.L., and Dixon, J.A.: Laser phototherapy in hereditary hemorrhagic telangiectasia. *Otolaryngol Head Neck Surg*, 89:204-208, 1981.
- Perkins, R.C.: Laser stapedotomy for otosclerosis. *Laryngoscope*, 90:228-240, 1980.
- Petrucchio, O.M., Sathanandan, M., Petrucchio, M.F., Knowles, S., McKenzie, L., Forbes, I.J., Cowled P A., and Keye, W E.: Ablation of endometriotic implants in rabbits by hematoporphyrin derivative photoradiation therapy using the gold vapor laser. *Lasers Surg Med*, 10:344-348, 1990.
- Polanyi, T.G.: Laser physics. *Otolaryngol Clin North Am*, 16:753-774, 1983.
- Reinisch, L.: Laser induced heating and thermal propagation: a model of tissue interaction with light. *Proc. Conf. on Lasers and Elect. Optics* 11:TuR4, 1989.

- Schawlow, A.L., and Townes, C.H.: Infrared and optical masers. *Phys Rev*, 112:1940, 1958.
- Schlenk, E., Profeta, G., Nelson, J.S., Andrews, J.J., and Berns M.W.: Laser assisted fixation of ear prostheses after stapedectomy. *Lasers Surg Med*, 10:444-447, 1990.
- Schramm, V.L., Mattox, D.E., and Stool, S.E.: Acute management of laser-ignited intratracheal explosion. *Laryngoscope*, 91:1417-1426, 1981.
- Shapshay, S.M., personal communication.
- Shapshay, S.M., Strong, M.S., Anastasi, G.W., et al: Removal of rhinophyma with the carbon dioxide laser. *Arch Otolaryngol*, 106:257-259, 1980.
- Shapshay, S.M., Wallace, R.A., Kveton, J.F., Hybels, R.L., Bohigian, R.K., Setzer, S.E.: New microspot micromanipulator for carbon dioxide laser surgery in otolaryngology. *Arch Otolaryngol Head Neck Surg*. 114:1012-1015, 1988.
- Simpson, G.T., Shapshay, S.M., Vaughan, C.W., and Strong, M.S.: Rhinologic surgery with the carbon dioxide laser. *Laryngoscope*, 92:412-415, 1982.
- Simpson, G.T., and Strong, M.S.: Recurrent respiratory papillomatosis; the role of the carbon dioxide laser. *Otolaryngol Clin North Am*, 16:887-894, 1983.
- Snow, J.C., Norton, M.L., Saluja, T.S.: Fire hazard during CO₂ laser micorsurgery on the larynx and trachea. *Anesth Analg*, 55:146-147, 1976.
- Spilman, L.S.: Nursing precautions for CO₂ laser surgery. *Symposium Proceedings, The Laser Institute of America*, 37:63-64, 1983.
- Stein, E., Sedlacek, T., Fabian, R.L., Nishioka, N.S.: Acute and chronic effects of bone

ablation with a pulsed holmium laser. *Lasers Surg Med*, 10:384-388, 1990.

Strong, M.S., and Jako, G.J.: Laser surgery in the larynx. *Ann Otol Rhinol Larynol*, 81:791-798, 1972.

Strong, M.S., Vaughan, C.W., Jako, G.J., and Polanyi, T.: Transoral resection of cancer of the oral cavity: the role of the CO₂ laser. *Otolaryngol Clin North Am*, 12:207-218, 1979.

Tan, O.T., Stafford, T.J., Murray, S., and Kurban, A.K.: Histologic comparison of the pulsed dye laser and copper vapor laser effects on pig skin. *Lasers Surg Med*, 10:551-558, 1990.

Thedinger, B.S.: Applications of the KTP laser in chronic ear surgery. *Am J Otol*, 11:79-84, 1990.

Thornell, W.C.: Intralaryngeal approach for arytenoidectomy in bilateral abductor vocal cord paralysis. *Arch Otolaryngol*, 47:505-508, 1984.

Tomita, Y., Mihashi, S., and Nagata, K.: Mutagenicity of smoke condensates induced by CO₂ laser irradiation and electrocauterization. *Mutat Res*, 89:145-149, 1981.

Tsuchiya, A., Obara, N., Miwa, M., Ohi, T., Kato, H., and Hayata, Y.: Hematoporphyrin derivative and laser photoradiation in the diagnosis and treatment of bladder cancer. *J Urol*, 130:79-82, 1983.

Vaughan, C.W.: Use of the carbon dioxide laser in the endoscopic management of organic laryngeal disease. *Otolaryngol Clin North Am*, 16:849-864, 1983.

Wile, A.G., Novotny, J., Mason, G.R.: Photoradiation therapy of head and neck cancer.

Am J Clin Oncol, 6:39-43, 1984a.

Wile, A.G., Coffey J., Nahabedian, M.Y., Baghdassarian, R., Mason, G.R., Berns, M.W.:

Laser photoradiation therapy of cancer: an update of the experience at the

University of California, Irvine. Lasers Surg Med, 4:5-12, 1984b.

FIGURE LEGENDS

Figure 1: The interaction of light (a photon) with an atom. Three processes are shown: the absorption of a photon by an atom in a low energy state, the spontaneous emission of a photon from an atom in an excited state, and the stimulated emission of a photon by a second photon of the same wavelength from an excited state atom.

Figure 2: The optical resonating chamber of a CO₂ laser. The gas molecules are excited by an electric current. The gas is cooled by a water jacket. The two mirrors provide the optical feedback for the amplification. The emitted light is coherent, monochromatic and collimated. The light can be focussed to a small point with an external lens.

Figure 3: (a) Laser-tissue interaction when the tissue is the focal distance away from the lens. Note the minimum beam diameter in the focal plane. (b) Laser-tissue interaction when the tissue is not in the focal plane of the lens. The laser covers a much larger area on the tissue surface.

Figure 4: (a) Light emitted from a conventional lamp. The light travels in all directions, is composed of many wavelengths and the light is not coherent. (b) Light emitted from a laser. The light all travels in the same direction, it is a single wavelength and all of the waves are in phase (the light is coherent).

Figure 5: The beam waist of parallel light focussed by a lens. The focal length of the lens

is f , the incident beam is TEM_{00} and has a diameter incident on the lens of D . The beam waist has a diameter of d .

Figure 6: Schematic graph of power density vs. spot size. The ratios are arbitrary for a current model CO_2 laser. The cylinder height represents the amount of tissue vaporized after a one second exposure at the three designated focal lengths.

Figure 7: Schematic illustration of absorption.

Figure 8: Schematic illustration of scattering.

Figure 9: Schematic illustration of reflection.

Figure 10: Schematic illustration of transmission.

Figure 11: Schematic illustration of the wound created by the carbon dioxide laser, showing the representative zones of injury.

OUTLINE

I. INTRODUCTION

II. LASER BIOPHYSICS

III. CONTROL OF THE SURGICAL LASER

IV. TISSUE EFFECTS

V. LASER TYPES AND APPLICATIONS

- A. Argon laser
- B. Argon tunable dye laser system
- C. Nd:YAG laser
- D. CO₂ laser
- E. KTP laser
- F. Flash lamp pumped dye laser
- G. Other lasers

VI. PULSE STRUCTURE

VII. SAFETY CONSIDERATIONS

- A. Education
- B. Safety protocol
- C. Eye protection
- D. Skin protection
- E. Smoke evacuation
- F. Anesthetic considerations
- G. Instrument selection
- H. Effectiveness of a safety protocol

VIII. REFERENCES

FIGURE SUMMARY SHEETS

LASER SURGERY: OSSOFF AND REINISCH

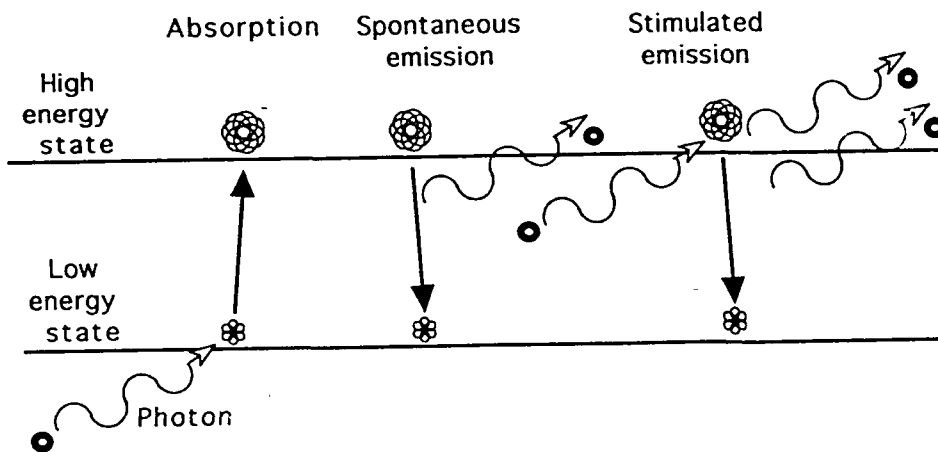


FIGURE 1

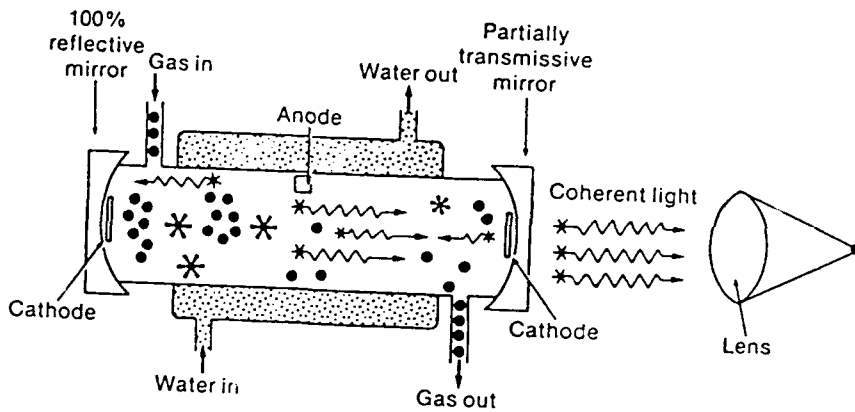


FIGURE 2

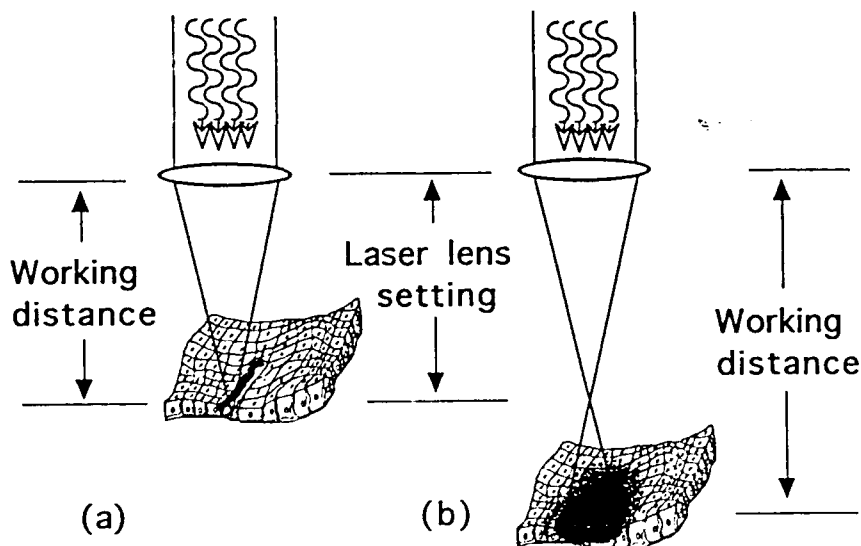
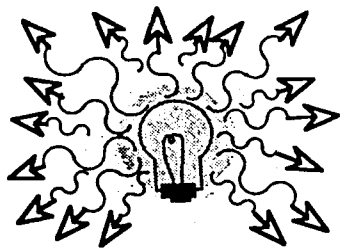
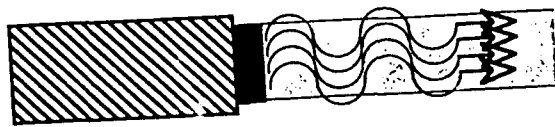


FIGURE 3



(a)



(b)

FIGURE 4

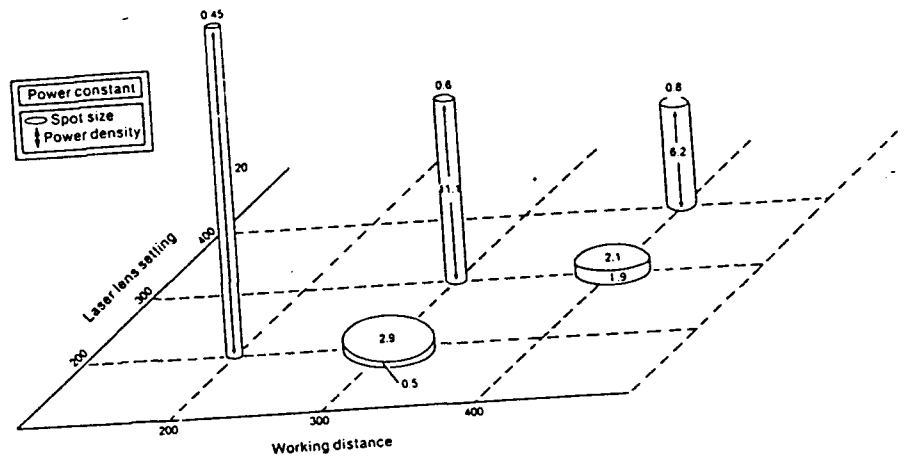
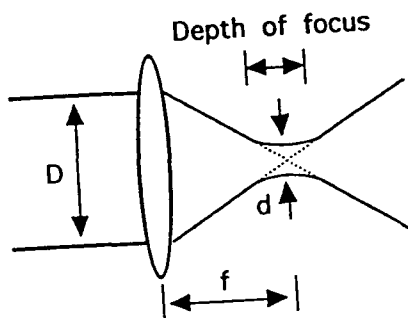


FIGURE 5

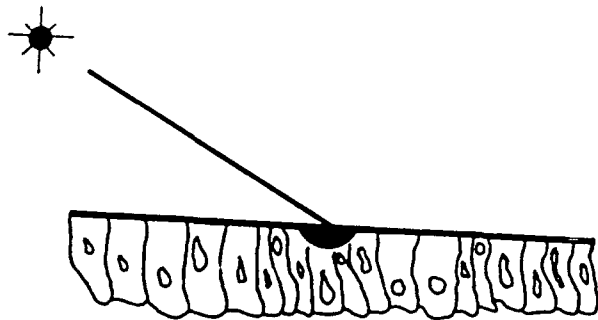


FIGURE 6

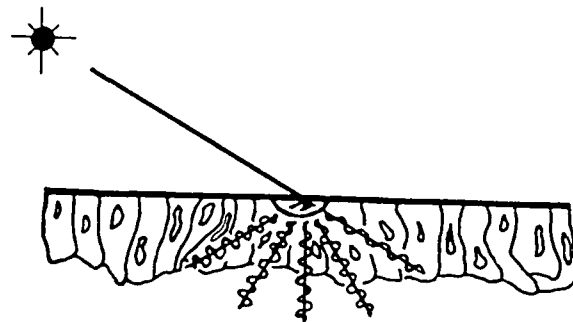


FIGURE 7

FIGURE 8

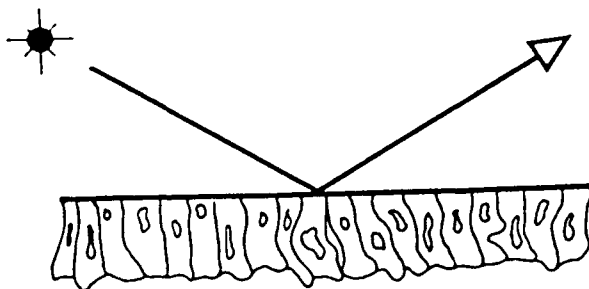


FIGURE 9

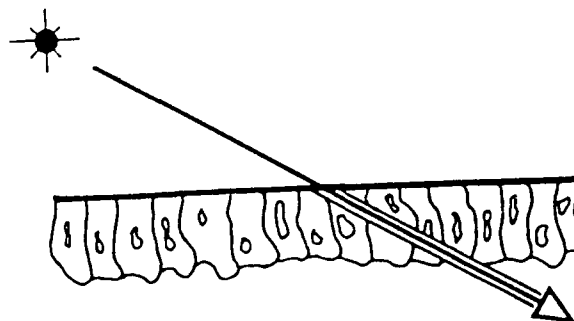


FIGURE 10

OSSOFF AND REINISCH

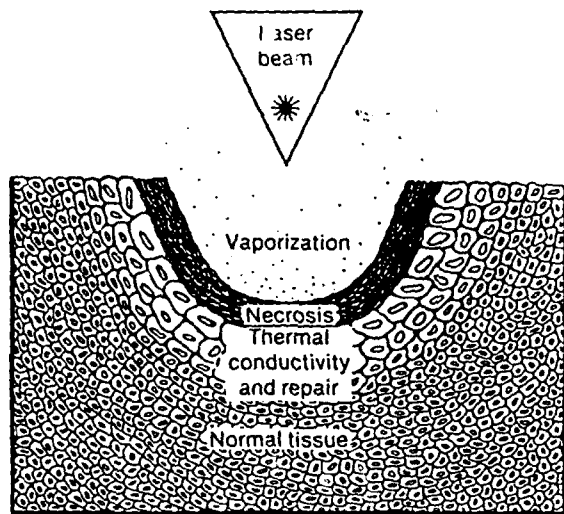


Figure 11

significant. The zone of coagulation for skin ranged from 126 ± 13 (SD) μ to 437 ± 73 (SD) μ . Optimum incision of skin was observed with blade diameters ≤ 0.6 mm. The zone of coagulation for liver ranged from 279 ± 63 (SD) μ to 447 ± 57 (SD) μ . Optimum cutting and hemostasis was observed with blades ≥ 0.6 mm diameter. Frosting did not improve blade function. It is concluded that sapphire tips from all manufacturers are similar. Frosting appears to be superfluous as does the wide variety of sizes available. The clinician and hospital should choose blade sizes judiciously, based on durability and longevity characteristics for their institution.

28

MOLECULAR SURGERY OF THE BASEMENT MEMBRANE: DOSE EFFECTS OF THE ARGON LASER. T. Helmsworth, C. Wright, S. Scheffter*, and S. Keller*. The Jewish Hospital of Cincinnati, Goldman Laser Institute, *Department of Biological Science, University of Cincinnati.

The current theories to explain vascular welding are based on electronmicrographs. The purpose of this study is to determine if there is a measurable biochemical effect on basement membrane related to the dose of laser energy. Murine basement membrane, EHS (Engelbreth, Holm, Swarm) 50 u1 was aliquoted into micro-centrifuge tubes and allowed to gel at room temperature. It was then exposed to an argon laser beam at energy fluences of 0, 100, 500, 750, 1000, and 1500 joules/cm². The exposures were carried out with the sample in a circulating water bath to prevent thermal build up. The gels were then solubilized in SDS electrophoresis running buffer. The basement membrane proteins were separated by electrophoresis through acrylamide gradient gels (3 to 22%) under denaturing and reducing conditions. No differences in the polypeptide composition were noted between irradiated and control samples using either coomassie or silver staining techniques. This suggests that the laser irradiation did not result in the breakdown in any of the basement membrane polypeptides. The irradiated and control samples of gelled basement membrane were then analyzed on 1.5% agarose gels in 10mM Tris, pH8 containing 0.1 SDS. The preparations produced a single coomassie positive band, but the control migrated at 0.5 and the laser irradiated samples and increasing distance up to 0.7 for the 1500 joules/cm². Thus, the argon laser appears not only to have altered the relationship between the basement membrane polypeptides but this change is dose dependent. The addition of 5mM beta-mercaptoethanol eliminated these differences, so that the argon laser appears to target cysteines and disulfid groups associated with basement membrane proteins. The laser energy changes the solubility of the fibers, allowing them to move and the bonds to reform with the adjacent tissue being welded. In sum, the argon laser's effect of formed basement membrane may provide for the development of new reagents and allow for a systematic search for the best conditions for vascular welding.

29

PHOTOINDUCED RIBONUCLEIC ACID CROSSLINKING USING VISIBLE AND INFRARED WAVELENGTHS. Michael D. Kyzer, Jerri A. Tribble, Walter-G Wrobel, Robert H. Ossoff. Vanderbilt University Medical Center, Department of Otolaryngology, Nashville, TN.

Efforts to study the effect of high intensity, short duration laser radiation on cell metabolism have yielded preliminary evidence of RNA crosslinking induced by radiation of visible (532nm) and infrared (1064nm) wavelengths. This is interesting both from a photochemical mechanistic and from a clinical point of view. Cytoplasmic RNA was exposed to 35 picosecond pulses (at 10Hz) from a Q-switched, mode locked Nd:YAG laser at power densities from 2.3×10^{13} to 7.5×10^{13} at 532nm and from 1.1×10^{13} to 5.4×10^{13} Watts/m² at 1064nm, at a constant total dose of 10 J. Irradiated and control samples were eluted through agarose gels under non-denaturing and denaturing conditions. No difference was observed between the control and irradiated samples on the non-denaturing gel, giving

evidence that fragmentation and intermolecular crosslinking was minimal. On the denaturing gel, however, samples irradiated at both wavelengths showed distinctly similar mobility shifts suggesting a possible multiphoton mechanism. Further investigations are underway to study the power and wavelength dependence of RNA crosslinking induced by this spectral region.

30

193nm EXCIMER LASER RADIATION: MOLECULAR RESPONSES OF CULTURED HUMAN CELLS. Donata Rimoldi, Alexandra C. Miller, Elaine Young and Dvorit Samir. Uniformed Services University of the Health Sciences, and Armed Forces Radiobiology Research Institute, Bethesda, MD. The Wilmer Eye Institute, The Johns Hopkins School of Medicine, Baltimore, MD.

The effect of sublethal doses of 193nm laser radiation on cellular DNA and gene expression has been examined in cultured human skin fibroblasts. Northern blot analysis of mRNA from irradiated cells revealed a dose-dependent increase in the levels of the c-fos proto-oncogene, interstitial collagenase, and metallothionein transcripts. While the biological significance is not clear at this time, it should be noted that similar changes in gene expression have been previously observed in cells treated with different carcinogens, including classical UV light (254nm) and phorbol esters. Preliminary studies with cultured human corneal epithelium also showed induction of collagenase in irradiated cells. In contrast to the conventional UV light or laser radiation at 248nm, the 193nm radiation did not cause significant pyrimidine dimer formation in the skin cells, as determined by measurements of unscheduled DNA synthesis (UDS). However, both 193nm and 248nm radiation induced micronuclei formation, indicative of chromosome breakage. These data suggest that exposure of actively replicating human skin fibroblasts to sublethal doses of 193nm laser radiation may result in molecular changes associated with carcinogenesis. Studies aimed to further evaluate the potential carcinogenic risk involved in 193nm laser treatment of the skin and cornea will be presented. We thank W.P. Vandemerwe and M. Smith for help with the laser. Supported by MAALT and NIH Grant R03-EY0822001.

31

EFFECT OF He-Ne LASER IRRADIATION ON CHEMICAL INTERMEDIARIES OF INFLAMMATION "IN VITRO". J. Palma, H. Juri, J. Lillo, S. Yung, R. Lapin. Córdoba Laser Center. National University of Córdoba - Argentina.

The known increment of Plasma Fibrinogen Level (P.F.L.) after surgical injury, is produced by the interaction of Prostaglandins, (PGE) Bradykinin (B) and Histamine (H).

It has been demonstrated that He-Ne laser irradiation "in vivo" at the injury site or at the injection site of the "Inflammatory Hormones", blocks the mentioned increment of P.F.L.

With the intention to understand better the intrinsic mechanism of action we studied the P.F.L. in rats injected with PGE₁, B, and H, previously irradiated with He-Ne laser "in vitro" (31 total energy to the combined drugs).

Results: the P.F.L. measured in mg per one hundred ml of plasma increased significantly in animals injected with non-irradiated PGE₁ + B + H (356.6 ± 13.6); PGE₁ + B (345.0 ± 19.4); PGE₁ + H (363.0 ± 15.3) compared with normal non-injected animals (221.2 ± 9.1).

On the contrary, with previously irradiated drugs ("in vitro"), showed not significant modification of P.F.L. in animals injected with PGE₁ + B + H (220.5 ± 16.9) and PGE₁ + B (209.6 ± 13.6) but showed the usual increment after injection of PGE₁ + H (365 ± 12.9).

Considering the mentioned results it is concluded that the He-Ne laser effect on P.F.L. is produced at the inter-

time to 90 min caused a further increase in the number of labeled neurons (2366 labeled on day 9). To maximally increase the rate of nerve regeneration, laser irradiation must occur daily. When laser stimulation was done on alternating days, the number of labeled neurons dropped to 291 on day 9 which was still 3 times greater than the controls. When the rats were treated daily for the first 4 days only, the number of labeled neurons on day 9 also decreased but was still 10-fold greater than that of non-irradiated facial nerves.

37

THE EFFECTS OF LOW LEVEL LASER THERAPY ON THE PROLIFERATION OF KERATINOCYTES *IN VITRO*.

C.W.B. Steinlechner and M. Dyson, Tissue Repair Unit, United Medical and Dental Schools of Guy's and St. Thomas's Hospitals (Guy's Hospital Campus), London, England.

The effects of coherent red (632.8 nm) and infrared light (904 nm) on the proliferation of keratinocytes *in vitro* have been investigated. The light was delivered by means of a Space Mix-5 mid-laser at energy densities ranging from 0.25 - 4.0 J/cm². The laser system used produces coherent visible red light in continuous mode, and coherent infrared light in 200 ns pulses. These pulses were delivered at either 1205 or 3125 pulses per second. The equipment was modified so that either red or infrared light could be produced independently. Keratinocytes from both subconfluent and confluent cultures were irradiated. They were subsequently grown in culture medium containing either 5% or 1% fetal calf serum, proliferation being slower in the latter. The results obtained indicate that (1) exposure to either coherent continuous visible red or pulsed infrared light can stimulate keratinocyte proliferation, variation in pulsing being insignificant when the energy density is maintained constant, (2) the delay in onset of proliferation normally observed in keratinocytes obtained from confluent cultures can be reduced by exposure to laser irradiation, and (3) a greater response can be obtained in keratinocytes whose growth rate has been reduced by maintenance in medium containing 1% fetal calf serum than in those grown in medium containing 5% fetal calf serum. In a second series of experiments the proliferation of keratinocytes exposed to supernatants obtained from irradiated macrophages was examined. As with direct irradiation, it was found that although the lower energy densities were stimulatory, exposure to 4 J/cm² was inhibitory.

38

CORRELATIVE ULTRASTRUCTURAL AND BIOMECHANICAL CHANGES INDUCED IN REGENERATING TENDONS EXPOSED TO LASER PHOTOSTIMULATION

Chukuka S., Enwemeka, Oscar Rodriguez, Norman G. Gall, Nicholas E. Walsh, Veterans Administration Medical Centers at San Antonio & Miami, University of Texas Health Science Center at San Antonio and the University of Miami School of Medicine, Miami, FL.

The purpose of this study was to determine the ultrastructural and biomechanical effects of laser photostimulation on healing tendons. Under anaesthesia, the right calcaneal tendons of 71 rabbits were tenotomized, repaired and immobilized. After random assignment to six groups, the tenotomized tendons of five groups of rabbits were stimulated daily with He-Ne laser of 632.8 nm wavelength. Each group received the same energy density of laser therapy, thus, five dose levels, namely, 1, 2, 3, 4, and 5 mJ/cm² were utilized. The remaining group of rabbits served as non-treated controls. On the 21st post-operative day, each tendon was excised and either processed for electron microscopy or frozen at -70°C in 0.09% NaCl until they were biomechanically tested on an Instron device. The modulating effect of laser therapy was evident in the tendency of treated tendons to shrink to sizes that were akin to those of intact non-tenotomized tendons. Treated

tendons were consistently smaller in size than controls ($P < .001$). *Ipso facto*, tendons treated at each dose level developed nearly twice the tensile stress of control tendons ($P < .001$). Ultimate tensile strength, energy absorption capacity and strain did not differ between treated and control tendons ($P > .10$) and no dose dependent effects were observed in the biomechanical characteristics of treated tendons. Electron microscopy revealed that unlike control tendons, the fibroblasts and collagen fibrils of laser treated tendons were mostly aligned in their longitudinal axis. These findings demonstrate for the first time that laser biostimulation modulates the ultrastructure and biomechanics of healing tendons.

39

A STUDY OF DE-NOVO PROTEIN SYNTHESIS BY LASER IRRADIATED HUMAN NEUTROPHILS. D.A. Gonzalez¹, J. Hurig¹, J.M. Davidson², C.K. Broadley², R.L. Hoover², R.H. Ossoff¹.

¹ Dept. of Otolaryngology and ² Dept. of Pathology, Vanderbilt University Medical Center, Nashville, TN

There is growing interest in the biostimulating effects of laser irradiation. With the advent of laser angioplasty and the introduction of techniques for laser purification of banked blood, we are interested in the effects of sublethal laser energy on blood cells, particularly those involved in inflammation. The purpose of this investigation was: 1) to determine whether sublethal Nd:YAG laser irradiation can alter the pattern of protein synthesis by human neutrophils in short-term culture and 2) whether the observed changes in protein synthesis are due to nonspecific thermal mechanisms or to specific photochemical events.

Human neutrophils were isolated from whole blood, maintained in short-term culture and exposed to either heat (42°C 60 min) or to sublethal continuous Nd:YAG irradiation. Sublethal dose, defined using a dye exclusion viability assay, ranged from 500-2000 joules/cm². After laser irradiation or heat shock, newly synthesized proteins were labelled *in vitro* with ³⁵S-methionine. TCA precipitation of proteins, polyacrylamide gel electrophoresis and autoradiography were performed in order to detect bands of newly synthesized proteins.

Autoradiography revealed a new protein band with a molecular weight of 40 kilodaltons that was induced by laser irradiation but not by heat shock. Increased synthesis of 21 and 26 kilodalton proteins was also noted following laser irradiation but not following heat shock. These data suggest that neutrophil protein synthesis can be altered by sublethal Nd:YAG irradiation in a non-thermal way. Similar experiments using picosecond pulsed Nd:YAG irradiation are under way.

Supported in part by the SDIO Office of Naval Research (RHO), by the Veterans Administration, Genentech, Inc., and NIH grants AG 06528 and GM 37387 (JMD) and NIH grant HL-36526 (RLH)

40

EVALUATION OF PULSATILE LASER, NON-PULSATILE LASER AND RADIOFREQUENCY GENERATED THERMOPLASTY FOR PERCUTANEOUS TRANSPLEURAL CERVICODORSAL SYMPATHECTOMY.

Malek Massad, Joseph LoCicero III, Jun Matano and Rodney Greene, Northwestern University, Chicago, IL.

We describe a new technique for percutaneous denervation of the cervicodorsal sympathetic chain to relieve pain due to several disease processes including Raynaud's syndrome, Buerger's disease, palmar hyperhidrosis, frostbite and sympathetic dystrophy. The technique involves transpleural ablation with laser under thorascopic guidance through the second intercostal space-anterior axillary line. We compared four different modes of denervation: excimer laser, CO₂ and Nd:YAG laser and radiofrequency generated thermoplasty (RF, Advanced International Systems Inc., Irvine, CA) using 12 mongrel dogs (3 animals each). Criteria analyzed included duration of exposure, power and total energy input, volume and morphology of destroyed neuronal tissue, and intra-operative hemorrhage. Total ablation of the inferior segment of the stellate ganglion and the first two thoracic dorsal nerve roots by excimer laser required a total energy input of 6.3 Joules for a cumulative exposure of 180 seconds (repetition rate 20 pulses/sec). In contrast, ablation of the same volume of tissue by RF required more than one hundred fold that amount of energy (810 Joules) and a cumulative exposure

each larynx was studied under 50 different conditions. The G.C.I. and true vocal efficiency were then calculated for each combination of airflow rate, width and tension. Linear regression analysis of data obtained from ten larynges proved G.C.I. to have a highly statistically significant linear relationships with vocal efficiency ($p < 0.001$, $R^2 = .95$). When sound intensity was expressed in dB rather than Watts/cm², the competence index did have a statistically significant relationship with vocal efficiency. These results confirm that G.C.I. (expressed in Watts/cm² ÷ cc/sec) is a simple clinical measure for assessing vocal efficiency of the larynx.

234 VOCAL CORD FIBROBLAST ELASTIN PRODUCTION IN TISSUE CULTURE. *D.A. Gonzalez¹, R.R.Nair³, R.H. Ossoff¹, J.M. Davidson^{2,3}, Depts. of ¹Otolaryngology and ²Pathology, Vanderbilt Univ. Medical Ctr., Nashville, TN; ³V.A. Medical Ctr., Nashville, TN 37232

The biomechanical and anatomical properties of the vocal fold, an elastic tissue, are thought to influence voice production in man; however, there is little information in the literature concerning the biochemistry of connective tissues within the vocal cord. A series of experiments was performed to detect and quantify vocal cord fibroblast elastin production. The effect of mechanical and chemical stimuli were also investigated in order to identify potential changes in elastogenesis.

Cultures of adult canine vocal cord fibroblasts were established by explanting, and an enzyme linked immunosorbent assay was used to quantify the soluble tropoelastin (TE) secreted by 2nd-3rd passage cells into the culture medium. Control cell populations were found to synthesize large quantities of elastin precursor, greater than 115,000 molecules TE/cell/hr. Treatment with ascorbic acid suppressed TE synthesis whereas treatment with hydrocortisone (1.3 uM) and transforming growth factor-B (TGF-B, 10ng/ml) led to significant increases in TE production by 28% and 91% respectively. Cells were subjected to mechanical stretch in order to simulate the stimulus of vocal fold movement during phonation. When cells were stretched (5%, 0.5 Hz, Flexercell[®]) for a period of 48 hours they synthesized 23% more TE than the stationary controls. Stretched cells pretreated with either hydrocortisone or TGF-B also demonstrated further significant increases in TE production (37% and 29% respectively) noted after 24 hrs of stretching when compared to similarly treated stationary controls.

This study demonstrates the successful isolation and culture of a vocal cord fibroblast cell strain, and will provide a tool for further study of the extracellular matrix components that may be responsible for the biomechanical properties and functional correlates of this unique structure. We report the discovery that vocal cord fibroblasts synthesize significant amounts of elastin. The finding that these cells respond to hormonal and mechanical stimuli by increasing elastin production may have clinical implications for minimizing loss of vocal cord elasticity in the injured or aging larynx.

Supported in part by the Veterans Administration, Genentech, Inc., and NIH grants AG 06528 and GM 37387 (JMD) and the SDIO Office of Naval Research (RHO).

If these differences in PCA function exist, they can be used to design more efficient surgical therapies for bilateral vocal cord paralysis. Further research will be required to investigate the regional histochemical differences of the human PCA, as well as record the EMG signal in different regions of the muscle during various laryngeal movements.

9:15 A.M.

Excitation Thresholds for Nerve-muscle Pedicles: A Preliminary Report

MICHAEL BRONIATOWSKI, MD,
SHARON GRUNDFEST-BRONIATOWSKI, MD,
CHARLES R. DAVIES, BSE, JERALD C. KASICK,
GORDON B. JACOBS, MSEE, YUKIHIKO NOSÉ, MD, PhD,
and HARVEY M. TUCKER, MD, Cleveland, Ohio

Ongoing interest in the rehabilitation of paralyzed musculature in the head and neck has focused on the electronic stimulation of nerve-muscle pedicles (NMP) that have been reimplanted into the incapacitated effector(s). Despite visual and histochemical evidence of reinnervation, it is still not known whether the excitability of an NMP is as good as or better than reinnervated or normal muscle. Such information is necessary for the eventual construction of an implantable stimulator.

Six rabbits were anesthetized with intramuscular xylazine and ketamine, and the ansa hypoglossi was cut on one side. A crossover nerve-muscle pedicle was brought in from the opposite sternothyroid muscle to the sternohyoid. After a minimum neurotization period of 3 months, the animals were re-explored. An electrical stimulator, capable of delivering square wave pulses of variable amplitude and pulse width, was used to determine the threshold of contraction of the NMP, an intact motor nerve of similar size, the reinnervated strap, and another normal muscle. In this manner, strength duration curves were established (Lapicque L, and M. Recherches sur la loi d'excitation électrique. *J Physiol Path Gen* 1903;5:843-58).

The data indicate that (1) thresholds for NMP fall between that of normal nerve and muscle, and (2) reinnervated muscle was sometimes hyperexcitable, with a threshold below that of a normal nerve.

(Supported by RPC grant 2010 from the Cleveland Clinic Foundation)

9:30 to 10:15 A.M.

Posters (Session C)

See pages 157 to 163

10:15 A.M.

Soft Tissue Effects of the Holmium-YSGG Laser in the Canine Trachea

S.M. SHAPSHAY, MD, S.E. SETZER, BS, J.G. MANNI, MS, and
H.T. ARETZ, MD, Burlington and Concord, Mass.

Difficulties with fiber transmission and excessive tissue trauma associated with both CO₂ and Nd-YAG laser wave-

lengths, respectively, has prompted investigation of the Holmium-YSGG laser for tracheobronchial endoscopy. The Holmium-YSGG laser is a pulsed, flash lamp-generated crystalline laser with a 2.1 micron wavelength in the near infrared spectrum transmissible through flexible quartz fibers. Using a live canine tracheobronchial model for precise tissue ablation, the acute 1- and 2-week healing effects were studied using light microscopy (hematoxylin and eosin stain) and scanning electron microscopy. Laser parameters were 400 mJ and 600 mJ at 2 Hz using an unfocused 300 micron quartz fiber. Better control of laser ablation with no cartilaginous damage or perforation was noted, as compared to both continuous wave CO₂ and Nd-YAG laser.

Healing was somewhat slower than with the CO₂ laser; however, there was less granulation and fibrinous debris. Further studies are planned to determine ideal laser dosimetry for tissue ablation and healing prior to clinical applications.

10:30 A.M.

Comparison of Wound Healing with CO₂ "Superpulse" and Erbium-YAG Lasers

C.W. PARHAM, BS, S.M. SHAPSHAY, MD, G. PERETTI, MD,
H.T. ARETZ, MD, and S.E. SETZER, BS, Burlington, Mass.

Continuous wave CO₂ laser (10.6 microns) created wounds have been somewhat slower to heal than scalpel incisions caused by associated thermal effects. In an attempt to improve precision and diminish soft tissue trauma, a pulsed Erbium-YAG laser was compared to a "Superpulsed" CO₂ laser in a series of 16 rats to ablate and incise skin. The Erbium-YAG laser is a pulsed flash lamp-generated crystalline laser with a 2.9 micron wavelength with greater water absorption than the CO₂ laser, theoretically making it more precise for tissue incision and ablation. Laser parameters were 250 mW at 4 Hz for the Erbium-YAG and 4.5 W at 90 to 110 Hz for the CO₂ laser. Acute, 48-hour, 1-, 2-, and 3-week specimens were evaluated with light and scanning electron microscopy. Less tissue trauma (50 to 75 microns) without debris or necrosis and better healing was associated with the Erbium-YAG laser.

10:45 A.M.

An Investigation of the Potential for Laser Nerve Welding

M. KORFF, MD, D.L. ZELEAR, PhD, M. SCHWABER, MD, and
R.H. OSSOFF, DMD, MD, Nashville, Tenn.

Suture repair of a severed nerve is cumbersome, presents a focus for infection and neuroma formation, and does not always produce adequate stump alignment. An alternative method of nerve repair involves the use of the laser to effect epineurial welding. In the present study, two factors were investigated to elucidate the potential of the laser in nerve anastomosis: first, the initial strength of the bond created, and second, the long-term damage inflicted on the nerve by the laser.

Experiments were performed to determine the appropriate laser energy using the Laserscope KTP/532 and Sharplan

Korff et al

1060 CO₂ lasers on intact rat sciatic nerves. Significant damage was detected with both lasers at 1.6 watts, as shown by decreases in the nerve compound action potential (CAP). Thirty pulses of 0.05-second duration were used to approximate the type of exposure required for effective epineural welding. At energies less than or equal to 1 watt, acute damage was minimal. However, significant CAP decreases were observed 1 week postoperatively in these animals. This effect was most likely caused by nerve entrapment, since epineural shrinkage was noted during the initial laser irradiation. In subsequent studies, this problem was alleviated by limiting circumferential exposure to 180 degrees. The axonal damage and epineural effects created by the KTP/532 laser were more variable than those observed with the CO₂ laser, making the CO₂ a safer laser for nerve welding.

The low breaking force generated by the laser anastomosis using 1-watt pulses indicated that a larger surface area of adhesion was necessary. A layer of subcutaneous tissue was wrapped around the apposed sciatic nerve ends and laser welded to the epineurium a few millimeters back from the anastomotic site using the CO₂ laser. This produced a higher breaking strength than with epineural welding alone. The laser irradiation was performed around 180° to maintain adequate stump alignment while allowing for nerve swelling. Chronic studies are under way to determine the quality of regeneration of subcutaneous tissue wrapped and laser anastomosed nerves as compared to suture anastomosed nerves.

11:00 A.M.

Effects of Cyclosporin A on Axonal Regeneration Through Frozen Peripheral Nerve Allografts

RICHARD P. WIKHOLM, MD, YASUHIRO TORIGOE, PhD, THANH HO, BS, ALISHA WHITE, BS, and ROBERT H.I. BLANKS, PhD, Irvine, Calif.

A rat sciatic nerve model incorporating both functional and anatomic evaluation techniques was used to evaluate the effects of the immunosuppressant cyclosporin A (CYA) on nerve regeneration through frozen peripheral nerve allografts. Three groups of animals were evaluated: (1) those with fresh isografts (controls); (2) those with frozen allografts without CYA; and (3) those with frozen allografts with CYA.

Female Brown Norway (BW) and Lewis (LE) rats, which differ in both their major and minor histocompatibility antigens, were used as donors or host in a random fashion. Donor, 4-cm sciatic nerve grafts were frozen for 2 weeks at -7° C in a solution of 87.5% Dulbecco's Modified Eagles medium, 10% heat-inactivated horse serum, and 2.5% chicken embryo extract. Grafting was performed in all animals with a conventional epineural suture technique and the animals were maintained on daily intraperitoneal injections of CYA (8 mg/kg/day) postoperatively until they were killed. Functional recovery was evaluated quantitatively using a method based on measures of the rats' walking tracks. One hundred days after grafting, three levels (proximal and middle parts of the graft; a part distal to the graft) of the nerves were fixed, stained for myelin with osmium tetroxide, sectioned,

and counterstained. Axonal diameters and counts were performed at the above three levels.

The results of functional testing failed to reveal any statistical differences between any of the three groups. Our anatomic results show that there is axonal regeneration through frozen peripheral nerve allografts in all groups. The use of CYA more than doubles the number of axons crossing the graft, and allows the total number of regenerating axons to approach that seen in fresh isografts. The axon diameters were significantly decreased when compared to normal control sciatic nerves. Further work investigating the effects of discontinuing CYA, frozen allografts in higher animals, and neurotropic effects of the distal nerve is planned before the use of allografts in the clinical setting.

11:15 A.M.

The Application of Finite Element Methods to the Study of Airflow in the Anterior Nasal Cavity

M. TARABICHI, MD, and N. FANOUS, MD, Montreal, Canada
(2nd Place—Resident Clinical Science Award)

The management of anterior nasal obstruction and collapse is one of the most challenging problems in nasal surgery. The complexity of the segment's anatomy and a poorly understood pattern of airflow have resulted in ill-conceived surgical approaches. Finite element analysis of airflow has long been used in aeronautics to study flow patterns. We digitized the outline of the nasal cavity from images obtained after applying contrast material to the nasal cavity in two volunteers and by reviewing CTs of six patients. A computer-aided simulation of flow was undertaken in the sagittal plane in the anterior nasal cavity. A critical review of previous work on the nasal valve was undertaken because of the wide controversy in the literature. Our results showed that the nasal valve is an oblique structure bound laterally by the anterior end of the upper lateral cartilage, medially by the septum, and inferiorly by the rim of the piriform aperture. We found that this rim projecting from the floor of the nose produces an uneven distribution of airflow through the valve, with most of the flow occurring in the distal segment. We also found that removal of this rim would result in a better distribution of flow across the valve, producing a 20 to 25 percentile increase in flow.

11:30 A.M.

Effect of *Klebsiella Ozenae* on Ciliary Activity In Vitro: Implications in the Pathogenesis of Atrophic Rhinitis

JONATHAN L. FERGUSON, MD,
THOMAS V. McCAFFREY, MD, PhD, EUGENE B. KEPN, MD, and
WILLIAM J. MARTIN II, MD, Rochester, Minn.
(1st Place—Resident Clinical Science Award)

Klebsiella ozenae is a gram-negative rod that has been isolated with relative frequency from patients with atrophic rhinitis (AR). The relationship of this bacterium to the pathogenesis of AR is not understood, and whether it is simply an opportunistic colonizer of the injured nose or the etiologic

IV - U

11:00 A.M.

Investigation of the Wavelength Dependence of Laser Induced Bacteriostasis

JERRI A. TRIBBLE, MS, JOHN A. KOZUB, BS,
GLENN S. EDWARDS, PhD, AL ALY, MD, and
ROBERT H. OSSOFF, MD, Nashville, Tenn.

The wealth of literature recently addressing the question of which medical lasers are best for affecting particular biologic responses has prompted us to develop a method to study wavelength dependence of laser-induced biologic effects. The first step in this investigation was to measure the absorption spectra of living cells. By suspending the cells in a medium that matched their refractive index, the dominant scattering background was significantly reduced. Limiting this background revealed underlying absorption peaks that were characteristic of this cell type, providing a spectral window to which a laser could be tuned for optimal effect. Our model bacteria, *Escherichia coli* Cla, was observed to have a strong absorption peak near 268 nm, and weaker maxima near 350 nm and 426 nm. We found that maximal laser-induced cell death occurred when the laser was tuned to wavelengths corresponding to peaks within the bacteria's spectral fingerprint. The laser used for this study was an Nd:Yag pumped tunable dye laser delivering nanosecond pulses, tunable over the UV-visible range.

This two-phase study has since been extended to another Enterobacteriaceae, *Serratia marcescens* Nima, which has shown strong absorption peaks at 268 nm and 538 nm, with weaker absorption features near 390 nm and 510 nm, in agreement with the literature. Laser experiments with this bacteria are underway. While this investigation represents a model study of correlations between absorption characteristics of living cells and wavelength-dependent laser-induced biologic effects, it also has significant clinical implications for a novel approach to bacteriostasis.

(Supported by the Strategic Defense Initiative Organization program for free electron laser research)

11:15 A.M.

Correlation Between Histology and Nerve Excitability After Reinnervation of Paralyzed Trapezius Muscles in the Rabbit

MICHAEL BRONIATOWSKI, MD,
SHARON GRUNDFEST-BRONIATOWSKI, MD,
SAMUEL M. CHOU, MD, YUKIHIKO NOSÉ, MD, PhD, and
HARVEY M. TUCKER, MD, Cleveland, Ohio

The authors have recently shown that the mean muscle chronaxie for nerve pedicle implanted into denervated rabbit trapezius muscles is comparable to that of normal nerve. This study correlates excitability with histologic characteristics of muscles reinnervated via nerve-muscle pedicles (NMP) and direct nerve implants (DNI).

Strength duration curves were measured in 13 rabbits 3.5 to 5 months after reinnervation by NMP (N = 6) and DNI (N = 7). Following this, control (N = 5) and reinnervated trapezius muscles were harvested immediately before the

animals were killed and frozen in liquid nitrogen. The material was submitted for hematoxylin and eosin for general morphology, myofibrillar ATPase for fiber typing, esterase for determination of denervated fibers, and trichrome stains for cytoplasmic inclusions.

In all of the animals that had low chronaxie, satisfactory type grouping was noted (N = 10). By contrast, the three animals in which chronaxie was abnormally elevated demonstrated fibrosis, infection, and an absence of or poor type grouping.

This suggests that type grouping is necessary for excitability after reinnervation of paralyzed striated muscles.

(Supported by Cleveland Clinic RPC grant no. 2010)

11:30 A.M.

Baseline Motility of the Free Jejunal Graft in a New Canine Model

NATAN SCHER, MD, JAIME R. GARZA, MD, DDS,
BRUCE H. HAUGHEY, MB, and MICHAEL L. WIEDERHOLD, PhD,
San Antonio Texas, and St. Louis, Mo.

Reconstruction of pharyngoesophageal defects with free jejunal grafts has become an accepted technique of reconstruction. Ideally, the jejunal graft should allow a smooth, rapid, and unimpeded passage of a bolus of food.

However, functional problems are associated with the jejunal graft. Uncoordinated motility in these grafts often impedes the patient's swallowing function. This seems to be because of a continued unmodulated peristalsis initiated and propagated by intrinsic intramural neuroplexi, independent of extrinsic innervation. The ability to study the grafted jejunum and characterize qualitatively and quantitatively its intrinsic motility as described by various authors has proved to be difficult.

We developed a canine model that allows us easy access to perform various studies on grafted jejunum, including video-fluoroscopy and pressure manometry to determine baseline function, excluding the effect of gravity on bolus transport. Using microvascular technique, free jejunal grafts 10 to 30 cm in length were implanted in 11 mongrel dogs. The jejunal segments were implanted subcutaneously and exteriorized proximally and distally.

The grafted dogs underwent video-fluoroscopic studies using barium paste. These studies revealed three different types of jejunal graft contractions, all of variable intensity: (1) unifocal circumferential contractions, (2) multifocal circumferential contractions, and (3) to-and-fro longitudinal contractions. These contractions resulted in four patterns of barium movement: (1) fast isoperistaltic propulsion; (2) slow isoperistaltic propulsion; (3) no propulsion, in spite of circumferential or longitudinal contraction; and (4) retrograde propulsion.

The video-fluoroscopic studies were then repeated on five dogs after an intravenous injection of metoclopramide (Reglan), which caused significant short-term enhancement of intensity of the basic jejunal contractions and barium propulsion.

Advanced microspot microslida for the CO₂ laser

Robert H. Ossoff, MD, DMD, and Robert H. Ossoff, MD, DMD
Nashville, Tennessee, and Allendale, New Jersey

New advances in instrumentation have facilitated the development of a second generation carbon dioxide (CO₂) laser microspot micromanipulator. The 710 Acuspot has unique advantages over the previous generation of microspots. The compact design is easier to handle and has attachment points for sterile draping. The unit produces a spot size of 250 microns at a 400-mm focal length and 160 microns at 250 mm; the maximum de-focus is 3.2 mm at all focal lengths. An innovative dichroic mirror allows use of the laser unit's own HeNe laser as the aiming beam, eliminating possible aiming error introduced with a virtual image-aiming system. The dichroic mirror also allows better light transmission, resulting in a brighter field of view. As with first generation microspots, the laser beam path is coincident with the microscope optical path, eliminating parallax; this feature has been especially advantageous in pediatric and otologic cases. Having used this unit for 6 months on more than 50 patients, we now consider the use of a microspot to be our delivery system of choice for most micro-laryngeal laser surgical applications. (OTOLARYNGOL HEAD NECK SURG 1991;105:23-31)

The number of potential surgical applications for the carbon dioxide laser is increasing daily. Since Jako's first report¹ of the use of the carbon dioxide laser for endoscopic laryngeal microsurgery in 1970, indications for the use of the CO₂ laser have expanded to the point that it is now the surgical instrument of choice for several varied microlaryngeal operative procedures. In addition, use of the carbon dioxide laser has also been found to be beneficial for cutaneous and otologic applications.

The early CO₂ micromanipulators had a minimum spot size of approximately 800 microns, which was adequate for most laser surgical procedures. As technology and the thermal effects of laser applications have become better understood, the desirability of using a smaller spot size for laser tissue interaction has become evident. Shapshay et al.^{2,3} presented the first generation microspot micromanipulator in 1987 and reported clinical results in 1988. This micromanipulator was the first

to provide an approximately 300-micron spot size at 400-mm focal length, and greatly expanded the applications of endoscopic laser surgery.

Newer advances in instrumentation and optics have allowed the development of the second generation CO₂ laser microspot micromanipulator. The design and capabilities of this microspot manipulator are presented, as well as clinical examples of its use.

METHODS AND MATERIAL

The 710 Acuspot (Sharplan Lasers, Inc., Allendale, N.J.) is a second generation CO₂ microspot micromanipulator, designed to couple to existing Sharplan articulated arms and to fit standard operating microscopes. It uses the standard joystick hand control and hand rest (Fig. 1).

The technologic advances in the development of this microspot are related to its compact design and its ability to deliver a very small spot size—250 microns at 400-mm focal length and 160 microns at a focal length of 250 mm. This is one-third the spot size available from the older generation micromanipulators and an approximately 20% improvement over the first generation microspot micromanipulators (300 microns spot size).²

Similar to most microspot micromanipulators, use of this unit allows direct visualization of the surgical target. The parallax problem previously encountered when the CO₂ mirror was offset mounted from the optical beam path has been eliminated by use of a see-through ("hot") steering mirror, which uses a dichroic coating to allow reflection of the CO₂ beam while permitting

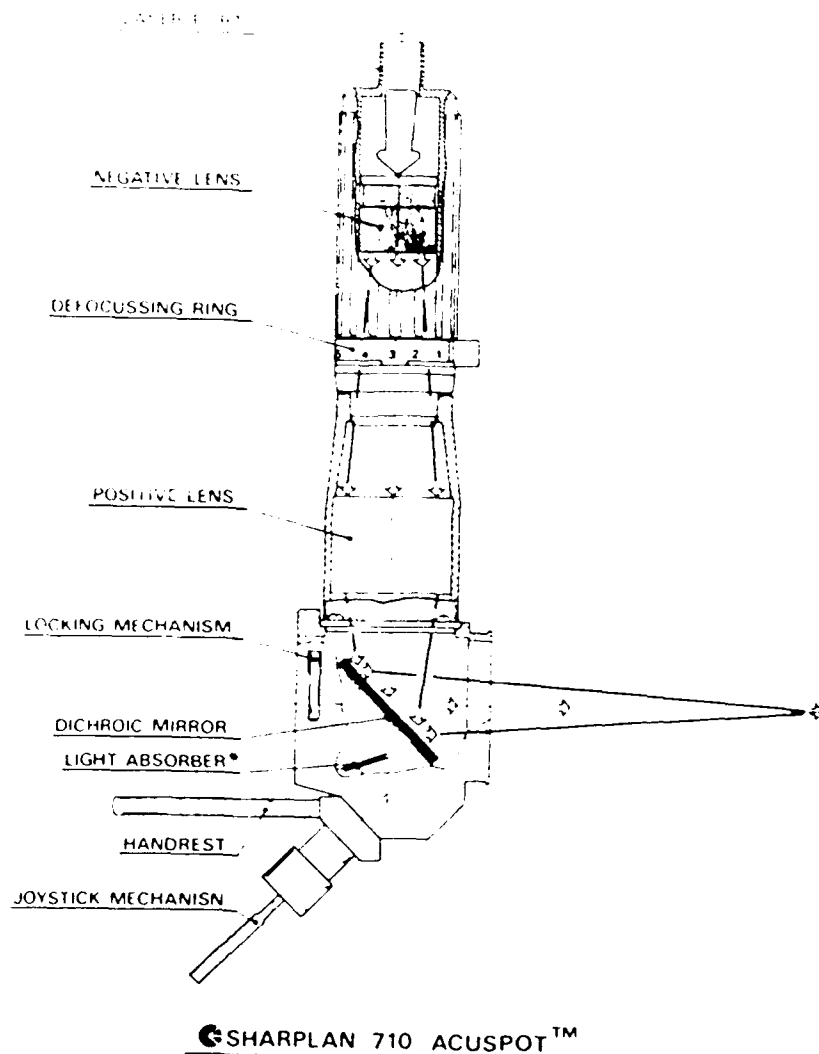
From the Department of Otolaryngology (Drs. Ossoff and Werkhaven), Vanderbilt University Medical Center, and Sharplan Lasers, Inc. (Mr. Rait and Mr. Abraham).

Presented at the Annual Meeting of the American Academy of Otolaryngology-Head and Neck Surgery, San Diego, Calif., Sept. 9-13, 1990.

Received for publication Sept. 11, 1990; revision received March 4, 1991; accepted March 11, 1991.

Reprint requests: Robert H. Ossoff, MD, DMD, Department of Otolaryngology, Vanderbilt University Medical Center, S-2100 Medical Center North, Nashville, TN 37232-2559.

23/1/29649



SHARPLAN 710 ACUSPOT™

• PATENTED

Fig. 1. Cutaway diagram of Sharplan 710 microspot laser.

passage of visible wavelengths. Light transmission of the visible region of the optical spectrum is approximately 75%. This dichroic coating on the steering mirror facilitates use of the laser's helium-neon-aiming beam, instead of using a virtual image-aiming system; this design keeps the aiming beam coincident with the laser beam at all times. Potential problems with virtual image-aiming systems were frequently encountered when the arm assembly was manipulated during the procedure; if the arm assembly was not optically perfect, misalignment of the CO₂ beam from the previously aligned virtual image-aiming system occurred.

In addition, the microspot micromanipulator uses a continuously variable defocus ring that allows the beam to be defocused to a maximum diameter of 3.2 mm from all focal lengths, in an infinite range of steps.

An external locking ring on the front of this micromanipulator allows the placement of sterile drapes for use in otologic surgery. With previous units, it has been difficult to maintain sterility within the operative field.

CLINICAL APPLICATIONS AND EXAMPLES

We have used this unit for approximately 6 months on more than 50 patients with laryngeal pathology, in-



Fig. 2. Photograph of Acuspot micromanipulator attached to microscope in clinical applications.

cluding recurrent respiratory papillomatosis, subglottic stenosis (both neonatal and adult), anterior and posterior glottic webbing, vocal cord polypoidosis, vocal cord cysts, carcinoma in situ, and T₁ vocal cord carcinoma localized to the midcordal region of the vocal fold. In addition, we have found this unit to be especially helpful in applications in neonates, when a very small spot size is desirable and a laser beam that is coincident with the optical path is absolutely necessary to facilitate laser exposure through a small laryngoscope and/or neonatal or pediatric microsubglottoscope (Fig. 2).

Laryngeal Papillomatosis

Twelve patients with recurrent respiratory papillomatosis requiring repeated endoscopic excisions at 4- to 12-week intervals have been managed using this new micromanipulator. The microspot is used in the defocused mode to debulk papilloma. Then, the focused 250-micron spot size is used to excise papilloma from anatomically sensitive areas, such as the anterior and/or posterior commissure, both of which are susceptible to web formation. In addition, the microspot, when used with a subglottoscope, has facilitated good exposure of the subglottis for removal of papilloma in this region.

Subglottic Stenosis

Both adult and neonatal subglottic stenoses have been managed with the microspot using microtrapdoor flap

techniques^{4,5} and/or radial incision and dilation.⁶ The limited thermal effect on soft tissue produced by the small spot size has facilitated our ability to develop improved, more precise microtrapdoor flaps with preservation of overlying mucosa. Several patients with subglottic stenosis have been managed using this technique without needing to undergo a tracheotomy; the predictable diminished thermal effect and reduced edema associated with the use of this small spot size has helped minimize the risk of airway obstruction.

We also have used the microspot for vaporization/ablation of subglottic hemangioma. Here, we use the microspot in a slightly defocused mode, however, that more nearly approximates the 800-micron spot size of standard micromanipulators. Our technique for hemangioma uses a slightly longer pulse structure (on the order of 0.2 to 0.5 seconds) to allow thermal diffusion and coagulation into tissue before vaporization is performed.

Anterior and Posterior Glottic Webbing

Both anterior and posterior glottic webbing have been managed by use of the microspot micromanipulator in a number of patients. This procedure is performed using a microtrapdoor flap. In posterior glottic webbing, a vertically oriented flap of mucosa is developed while the scar tissue deep to the mucosa is vaporized. Again, the small spot size has proved to be advantageous in permitting the development of very thin flaps. In pa-

crease the edges of the web to meet along the axis of one vocal fold and then retracted superiorly. The scar on the undersurface of the web is then excised and the mucosa covered by linear tissue to the underlying tissue. This effectively covers the exposed phonating surface on one true fold and minimizes the re-development of a recurrent anterior glottic web, which is often seen after laser excision or vaporization of the web.

Vocal Cord Polypsis

Vocal cord polypsis has traditionally been treated by either vocal cord stripping, Hirano's incision and enucleation technique, or a modification of Hirano's technique using the CO₂ laser for incision and ablation of the polypoid stroma.⁹ While previous studies have shown that Hirano's method demonstrated more rapid return of functional voice use, the microspot technique has the advantage of better hemostasis, allowing better and more complete visualization of the polypoid stroma before enucleation.⁹ We have used this microspot on several adult patients and have been gratified by the clinical results obtained in these cases.

Vocal Cord Cysts

Vocal cord cysts are often diagnosed on videostroboscopy, but sometimes are encountered during direct laryngoscopy for diagnosis of vocal dysfunction. A knife incision on the superior-lateral surface of the vocal cord usually gives good exposure for enucleation of the cysts. Standard micromanipulators have a spot size too large to allow a precise incision, but we have found the microspot set to its small focused spot size to be adequate for incision of the superior surface of the vocal fold with excellent hemostasis, allowing good visualization of the underlying vocal fold cysts. The precision associated with use of the focused beam (250 microns) of the microspot, along with the accompanying increase in hemostasis, greatly facilitates the performance of this procedure, compared to using conventional microlaryngeal instruments.^{10,11}

Carcinoma In Situ and T₁ Squamous Cell Carcinoma

Both carcinoma in situ and small midcordal T₁ lesions of the true vocal cord have been excised using the microspot. The minimal thermal effect surrounding the incision makes histologic interpretation of the margins

possible. The microspot has been used to excise the vocal cord lesions and the vocal cord surface has been covered by linear tissue to the underlying tissue.

CONCLUSIONS

In summary, we have found the second generation microspot, with the smaller spot sizes of 250 microns at 400 mm and 160 microns at 250 mm, to be a significant clinical advantage in the treatment of many benign and malignant laryngeal diseases. The combined advantages of a smaller spot size with the associated limited thermal effects on tissue and a laser beam path coincident with the optical beam path represent significant advance in the field of operative microlaryngoscopy, making the CO₂ laser microspot manipulator our delivery system of choice for endoscopic laryngeal surgery.

REFERENCES

1. Jako GJ. Laser Surgery of the vocal cords. *Laryngoscope* 1972;82:2204-16.
2. Shapshay SM, Wallace RA, Kveton JE, Hybels RL, Setzer SE. New microspot micromanipulator for CO₂ laser application in otolaryngology, head and neck surgery. *Otolaryngol Head Neck Surg* 1988;98:179-81.
3. Shapshay SM, Wallace RA, Kveton JE, Hybels RL, Boligian RK, Setzer SE. New microspot micromanipulator for carbon dioxide laser surgery in otolaryngology. *Arch Otolaryngol Head Neck Surg* 1988;114:1012-5.
4. Dedo HH, Sooy CD. Endoscopic laser repair of posterior glottic subglottic and tracheal stenosis by division of microtrapdoor flap. *Laryngoscope* 1984;94:445-50.
5. Duncan JA, Piazza LS, Ossott RH, Toohill RL. The microtrapdoor technique for the management of laryngeal stenosis. *Laryngoscope* 1987;97:825-8.
6. Shapshay SM, Hybels RL, Beamis JJ, Boligian RK. Endoscopic treatment of subglottic and tracheal stenosis by radial laser incision and dilatation. *Ann Otol Rhinol Laryngol* 1987;96:661-4.
7. Lumpkin SMM, Bishop SG, Bennett S. Comparison of surgical techniques in the treatment of laryngeal polypoid degeneration. *Ann Otol Rhinol Laryngol* 1987;96:254-7.
8. Yates A, Dedo HH. Carbon dioxide laser enucleation of polypoid vocal cords. *Laryngoscope* 1984;94:731-6.
9. Bennett S, Bishop SG, Lumpkin SMM. Phonatory characteristics following surgical treatment of severe polypoid degeneration. *Laryngoscope* 1989;99:525-32.
10. Karlan MS, Ossott RH. Laser surgery for benign laryngeal surgery disease. *Surg Clin North Am* 1984;64:981-94.
11. Bouchayer M, Cornut G, Loue R, Witzig E, Roch JB. Epidermoid cysts, sulci, and mucosal bridges of the true vocal cord: a report of 157 cases. *Laryngoscope* 1985;95:1087-94.

112-W

The Use of the Laser in Head and Neck Surgery

Robert H. Ossoff, D.M.D., M.D.

Professor and Chairman, Department of Otolaryngology, Vanderbilt University
Medical Center, Nashville, Tennessee

Dean M. Toriumi, M.D.

Department of Otolaryngology, Northwestern University School of Medicine,
Chicago, Illinois

James A. Duncavage, M.D.

Associate Professor, Department of Otolaryngology, Vanderbilt University Medical
Center, Nashville, Tennessee

In 1960, Maiman¹ introduced the principle of the laser (light amplification by stimulated emission of radiation). Lasers are actually devices that emit electromagnetic radiation. Laser-emitted light is unique in that it is coherent, collimated, monochromatic light that allows one to intensely concentrate energy over a relatively small area. The concentration of electromagnetic energy produced by the parallel bundles of light of the laser cannot be reached with a nonlaser light source.

The carbon dioxide laser, neodymium-yttrium aluminum garnet (Nd:YAG), argon, and argon dye are the lasers presently being used in otolaryngology-head and neck surgery. The difference between these lasers is their wavelength and their effect on tissues. The relationship between the wavelength of the laser and the tissue effect determines the applications of each laser as a tool in otolaryngology-head and neck surgery.

Carbon Dioxide Laser

The carbon dioxide (CO₂) laser has a wavelength of 10.6 μ , which is in the mid infrared spectrum. The beam is invisible to the human eye and is coupled with a coincident helium-neon laser so the beam can be visualized. The majority of the CO₂ laser energy is absorbed by biologic tissues, with some being reflected. Upon contact with tissue, an initial tissue temperature elevation occurs followed by tissue vaporization and crater formation (Fig 1).²⁻⁴ The laser energy is principally absorbed by water. There

decreased postoperative edema, and pain. They also aid in cavity drainage. The early use of the laser is important on selective accurate tissue examination. The ability to remove those areas of the oral mucosa that appear abnormal on a direct microscopic examination represents a significant advance in the treatment of the oral cavity.

Patients with clinical leukoplakia, erythroplakia, and small intraepithelial lesions can be treated with the carbon dioxide laser.¹⁵ The excision is done in the operating room with either a regional anesthetic or in the patient under general anesthesia, depending on the location and patient tolerance. The laser is coupled to an endotracheal tube and the patient is placed in a supine position with the head tilted back. All cutaneous surfaces of the face are covered with moist towels and the eyes of the patient are covered with moist towels. The patient is protected with moistened telfa strips. The infiltration of anesthetic is avoided because of the tissue distortion and fluid content. All lesions are stained with a supravital dye.¹⁶ The suspicious area is excised with the carbon dioxide laser. The specimen is placed on a saline saturated specimen tray and hand carried to the pathologist.

Small excisions of the oral cavity are gently wiped with a saline-soaked sponge to remove the charred carbonaceous debris. This debris is then removed by body giant cell reaction.¹⁷

Excisions of oral cavity tumors using the CO₂ laser can be of great value to the otolaryngologist-head and neck surgeon. Careful patient selection and on-specific criteria will determine the success of this treatment.

The laser can be used to perform a one stage tongue release to patients who underwent composite resection with tongue-flap anastomosis. In most cases, speech can be improved with limited immobilization. The laser is used in the repeat mode at approximately 0.5 sec/cm. Anteromedial traction of the tongue is used to free the tongue and the attachment is carefully vaporized.

Applications in Skin Surgery

The laser can be used to remove cutaneous lesions such as small basaloid cysts, giant skin lesions, rhinophyma,¹⁸ and superficial scars.¹⁹ The laser can also be used for tattoo removal and photothermal ablation of the argon laser in cutaneous skin surgery are used in conjunction with argon laser surgery.

Applications in Diseases of the Larynx

The laser is well suited for management of benign and malignant laryngeal lesions. The ability to perform "hands off" surgery on the

airway decreases the risk of airway obstruction after microlaryngeal surgery. The precision and decreased edema of CO₂ laser surgery are ideal for microlaryngeal surgery.

General anesthetic considerations are crucial to safe microlaryngeal laser surgery. The anesthesiologist, otolaryngologist, and nursing staff must work together to guarantee safety for the patient, as well as for the surgical team. Either general endotracheal intubation, venturi-jet ventilation, high-frequency ventilation, or the apneic technique can be used by the anesthesiologist. A red rubber or Silastic tube wrapped with reflective aluminum tape should be used for endotracheal intubation. The cuff should be filled with saline colored with methylene blue and then covered with several counted saline-soaked cottonoids placed in the subglottic region. Special nonflammable, nonreflective instruments should be used. Two separate suction setups should be available for all microlaryngeal cases. One provides for adequate evacuation of smoke and steam from the operative field, while the second is connected to the surgical suction tip for the aspiration of blood and mucus from the operative site. An operating platform can be used to protect the subglottic airway while laser energy is being applied to the glottis. The surgical field is exposed by using a wide-bore microlaryngoscope and operating microscope. Initial identification of the extent of disease is very important and will determine the mode of therapy. Other diagnostic tests such as computed tomography (CT), tomograms, and pulmonary function tests may be necessary to determine the type and extent of treatment.

Technique in Microlaryngeal Surgery

The power density and radiant energy are crucial to achieving good results with microlaryngeal laser surgery. The surgeon should use the lowest power density (1,200 to 2,000 W/sq cm) and the shortest time exposure to achieve the desired tissue effect. A supraglottic test spot should be used to check alignment and power settings of the beam prior to starting the procedure. Cord rolling and gentle palpation can be used to help evaluate the size and depth of laryngeal lesions. The skipping technique of moving the laser beam from one area to the other should be used to prevent adjacent tissue damage. The delivery of laser energy in the continuous mode is seldom necessary. Traction of the lesion facilitates excision of the specimen. The buildup of carbonaceous char should be avoided, and gentle debridement should be performed.

Postoperative care should include humidified oxygen, steroids, and antibiotics, as needed. Absolute voice rest is not necessary, but limited use of the voice is suggested. Postoperative voice therapy is very important and may help prevent recurrent disease.

Benign Laryngeal Disease

The CO₂ laser has proved to be very useful in the treatment of congenital and acquired subglottic stenosis,^{22,23} laryngeal webs, capillary heman-

quiescent, and other lesions of the airway.⁴⁰ Advantages of the laser in the pediatric airway include precision, preservation of tissue, and predictable minimal postoperative edema.

When applied to an operating microscope offers a precise method and soft tissue stenosis of the larynx.^{36, 41, 42} However, the tissue remains a problem. The choice of when to use the laser in the form of periodic dilations, intralesion injections of topically placed stents, or microtrapdoor flaps appears to be less.⁴³ The open repair and reconstructive procedures need if the right combination of endoscopic techniques

the stenosis may be of importance in the therapeutic approach. In other reports in the literature, four of five patients with anterior commissure webs improved after vaporization of the webs in the early utilization of the voice may be helpful in preventing the web at the raw anterior commissure surfaces. The laser also appear ideal for excision with the CO₂ laser.

At the posterior commissure, subglottic larynx, or both the laser surgery because of their extensive vertical medial nature, loss of cartilaginous support, and fibrotic fixations.⁴⁴ Only three of these lesions in ten of our patients were cured. It is believed that periodic dilations and intralesional microtrapdoor flaps may improve results if used as a laser vaporization.⁴¹

The stenosis and the presence of a tracheostomy appear to be on the therapeutic results. The supraglottic soft tissue lesions quite favorably, much as one would expect benign polyps at tissue lesions to respond.⁴² The number of excisions related to lack of response from previous procedures. If two or more do not improve the airway or result in recurrent stenosis, tracheostomy probably will also fail.

Applications in Recurrent Respiratory Papillomatosis

The recurrent respiratory papillomatosis has advanced with the use of the laser.⁴⁵ Although it cannot cure the disease, its effectiveness in clearing the larynx of structures and in maintaining the translaryngeal patency made it the instrument of choice for treatment of this disease. The papilloma should be done prior to each laser ablation. Work at a lower power density, 1,200 to 2,400 W/sq cm, and a mode with 100 msec time duration. These settings will avoid normal heat damage, thereby preserving normal anatomical papillomas over the vocal cords are vaporized to the ligament. Working with the operating microscope on 10-

power magnification, the underlying laryngeal muscles should be preserved. A first treatment should remove as many papillomas from one vocal fold and spare the opposite anterior cord 2 to 3 mm up to the anterior commissure. It must be remembered that the larynx will heal by secondary intention after the laser vaporization of the papilloma. If too much lining is removed, the chance for scarring is increased. It should be planned for the patient to have a repeat treatment in four to six weeks. If there has been no regrowth, then the remaining papillomas can be removed. If regrowth of the papilloma has occurred, the goals then should be the maintenance of an airway and voice. The frequency of laser treatment will be determined by the regrowth of the papilloma. No special voice instructions or medications have been necessary in the postoperative period.

Applications in Polypoid Degeneration

Patients with polypoid degeneration of the true vocal cords require both preoperative and postoperative voice therapy. Prior to surgery, they should be informed that they may have a weak, breathy, rough voice for six to eight weeks postoperatively. The laser technique involves elevation of a laryngeal microflap (Fig 2). The polypoid mass is pulled medially and an incision in the superior surface of the vocal cord is made, just medial to the laryngeal ventricle. The laser should be set at repeat mode (0.1 sec-

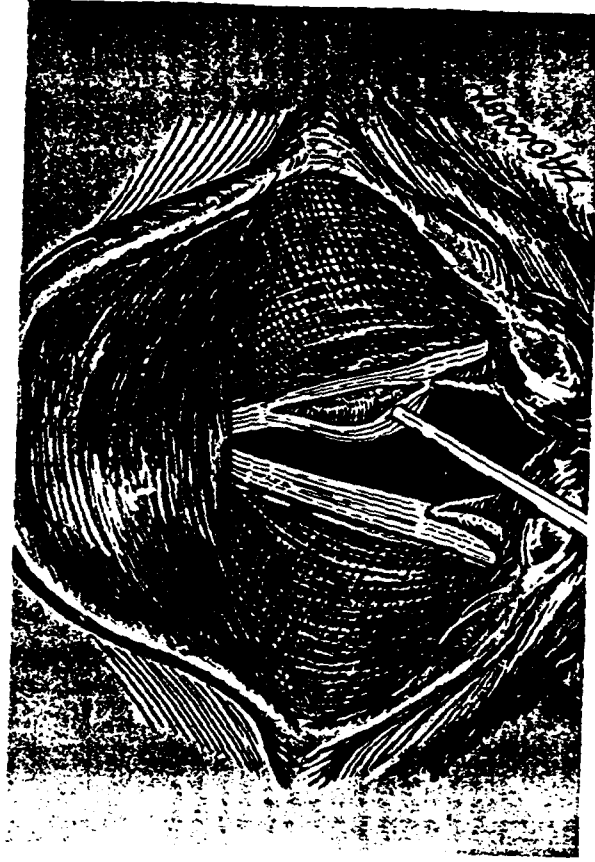


FIG 2. Elevation of laryngeal microflap.

ond) at 2,000 W sq cm. A flap of mucosa is raised from lateral to medial while the underlying mucoid material is vaporized. The microflap is repositioned after any redundant mucosa is excised. The flap is welded into position with the laser at 200 W sq cm with a slightly defocused beam. This maneuver essentially resurfaces the vocal cord. The effect of this flap on long-term voice quality is still being determined.

Applications in Treating Granulomas

The most effective way to treat vocal cord granulomas is to correct the source of chronic irritation. Conservative treatment includes voice therapy and treatment of gastric reflux. When there is no response to conservative management, surgical intervention may be considered. The surgeon can attain superior exposure with a posterior commissure laryngoscope.¹³ The lesion is visualized and the major portion is excised with the laser on repeat (0.1 second) at 2,000 W sq cm. The remaining portion of the granuloma is vaporized until the matrix is encountered. Care is taken not to expose the vocal process. The carbonaceous debris should be removed carefully. Benjamin and Croxson¹⁴ showed that there was no significant difference in recurrence rates between granulomas treated with the CO₂ laser versus those treated conventionally.

Applications in Treating Nodules

Patients with vocal cord nodules must have their condition evaluated by a speech pathologist. Surgery may be needed for fibrotic nodules in those patients who do not respond to voice therapy. When using the CO₂ laser, the surgeon should use the lowest power density that will vaporize the nodules. The technique of using only half the laser beam to vaporize the nodule and allowing the medial half of the beam to impact on the opening platform is called shaving. Care must be taken not to violate Reinke's space.

Applications in Vocal Cord Paralysis

Airway insufficiency due to bilateral vocal cord paralysis has been successfully treated by endoscopic laser arytenoidectomy.¹⁵ The procedure is performed through a posterior commissure laryngoscope. With sufficient exposure, the mucoperichondrium is vaporized, exposing the cartilage (Fig 3). The laser should be set on repeat mode (0.1 second) at 2,000 W sq cm. The corniculate cartilage is vaporized to expose the apex of the arytenoid cartilage. The mucoperichondrium of the superior portion of the arytenoid cartilage is vaporized; this is followed by vaporization of the cartilage itself (Fig 4). The lateral ligament is transected and the cricoid cartilage is exposed after the entire arytenoid cartilage is vaporized (Fig 5). Then the mucoperichondrium over the vocal process and most of the muscular process are vaporized, exposing the vocal and muscular processes.

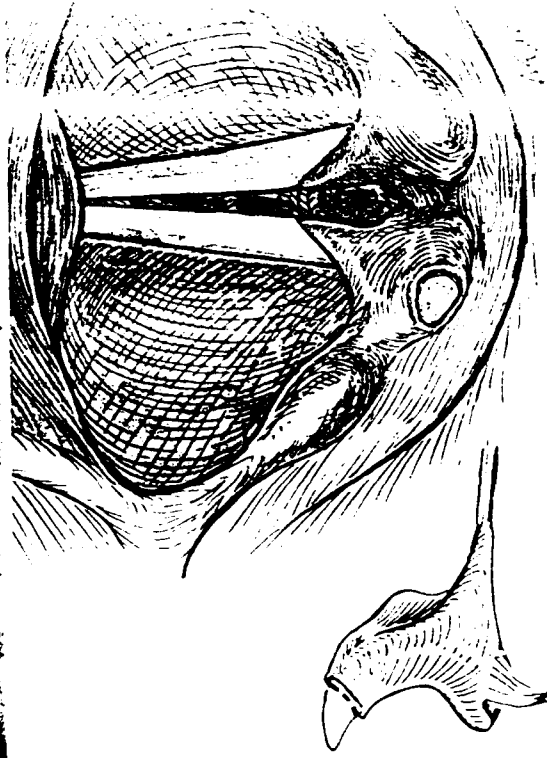


FIG 3 (top).

Outline of area to be vaporized on arytenoid cartilage.

FIG 4 (bottom).

The apex of the arytenoid cartilage is exposed.



FIG 5.
The cricoid cartilage is exposed.

(Fig 6). The vocal process, with adjacent vocalis muscle and the muscular process, up to but not including the attachment of the arytenoid muscle, is vaporized (Fig 7). Care is taken not to vaporize the mucosa of the interarytenoid cleft. An area lateral to the vocalis muscle is vaporized to allow the vocal cord to lateralize during the healing process (Fig 8). In their series, Ossoff et al.³⁶ noted one complication of a posterior laryngeal web, likely due to submucosal thermal injury of the interarytenoid cleft. Care must be taken when using the continuous mode to prevent buildup of carbonaceous debris and spread of thermal injury. In this series, 10 of 11 patients had successful stabilization of their airway and were decannulated.³⁶ Patient selection for this procedure is crucial to its long term success.

Applications in Malignant Laryngeal Disease

The treatment options for patients with early T₁ glottic carcinoma include external beam irradiation, laryngofissure and cordectomy, and endoscopic excision utilizing the CO₂ laser or conventional instruments.³⁷ Laryngofissure and cordectomy have been used for patients with large or bulky tumors on mobile cords. This procedure offers control rates similar to those of radiation therapy but permanently alters the voice.³⁸

For patients with early (T₁) glottic cancer, radiation therapy remains the most commonly prescribed treatment modality. Patients usually receive

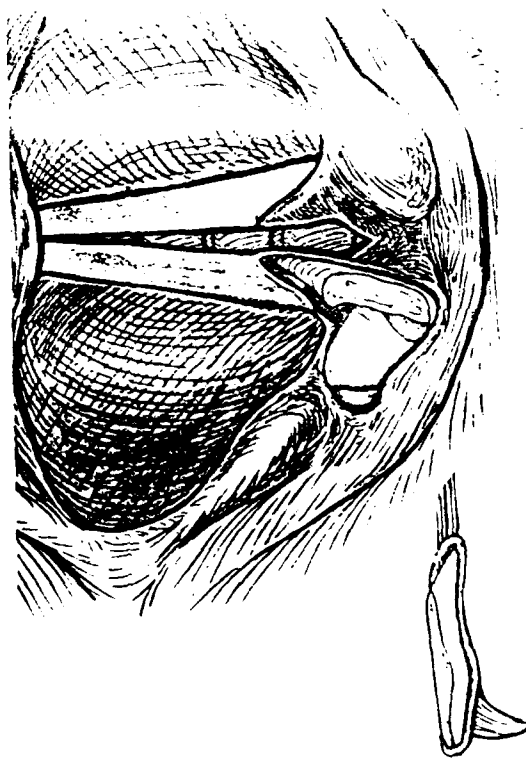


FIG 6 (top).
Vocal and muscular process is exposed.

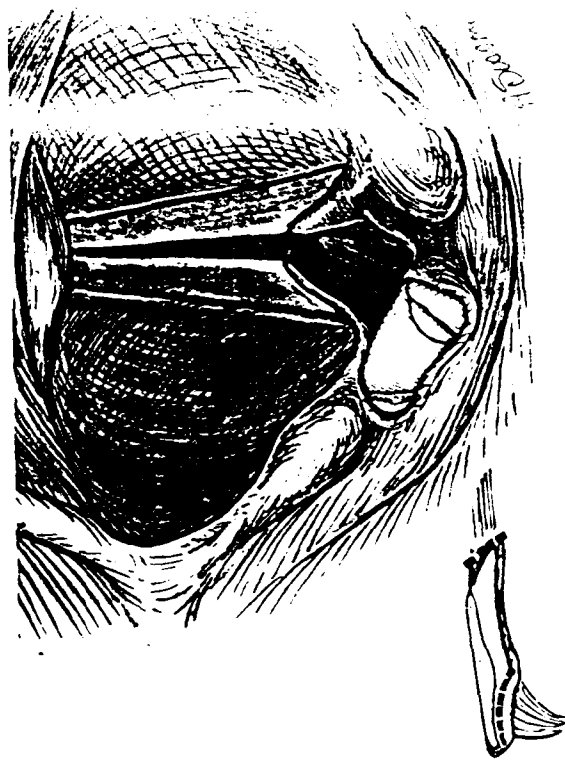


FIG 7 (bottom).
Vocal process is vaporized.



FIG 8. Area lateral to vocalis muscle is vaporized to aid in vocal cord lateralization.

doses in the range of 5,600 to 6,500 rads over 5½ to 6½ weeks. Local control rates have been reported in the range of 90%.³⁹

In 1920, Lynch⁴⁰ reported 9 of an eventual 39 cases of glottic cancer managed by endoscopic excision. Then, in 1941, New and Dorton⁴¹ reported 10 of 11 cases managed by endoscopic excision of early glottic cancer. Nine of their patients were cured of their disease. In 1971, Stutman and McGavran⁴² studied serial sections of specimens from patients with T₁-glottic cancer treated by laryngofissure and cordectomy. They found that 11 specimens had no tumor in the cordectomy sections and concluded that the biopsy alone had effectively treated the cancer. The present concept of endoscopic excisional biopsy evolved from the realization of the potential for overtreatment of early midcordal glottic cancers.⁴³ In 1972, Strong and Jako⁴⁴ endoscopically using a CO₂ laser managed a case of bilateral glottic carcinoma in situ. They stressed the need for prolonged follow-up to assess this technique. In 1973, Lillie and DeSanto⁴⁵ reported cases of 57 patients with early glottic cancer who were treated endoscopically by excision and diathermy. None of the patients died of their disease, but five patients had a recurrence or a second primary tumor develop.

In 1975, Strong⁴⁶ treated 11 patients with T₁-glottic cancer using the CO₂ laser and reported on recurrences. Then, in 1983, Blakeslee et al.⁴⁷ identified patients who needed further treatments based on positive deep

margins on the endoscopic excisional biopsy. Of the 88 patients treated primarily by endoscopic excision with the CO₂ laser, 60 patients, 88% had an absolute three-year survival rate. Thirty-two underwent endoscopic excision alone, with successful management (89%). Thirty-four patients had endoscopic excision and postoperative radiation therapy, with successful management in 29 (85%). Forty-one underwent endoscopic excision followed by partial laryngectomy with a 100% success rate.

Ossoff et al.⁴⁸ managed cases of selected patients with T₁-glottic carcinoma by endoscopic excisional biopsy using the CO₂ laser. These patients with early, midcordal squamous cell carcinomas of the larynx treated by endoscopic excisional biopsy and followed up for a period of three years.

Patients were followed up closely, with repeat microendoscopic examinations being performed when suspicious areas were on office examination. Ossoff et al. reported 24 of 25 patients free of disease with a follow-up period of three years or more (96%). One patient died of both local and regional recurrence two years after a partial laryngectomy. There were no operative complications of the patients requiring a tracheotomy.

Excisional biopsy is performed by applying medial traction on the vocalis muscle with cup forceps and using the laser in the repeat mode (0.1 sec, 2,000 W/sq cm) to dissect the lesion. The cancer is dissected off the underlying vocalis muscle. A 2- to 3-mm strip of muscle is included in the specimen. Care is taken not to lose the spatial orientation of the specimen which is labeled and oriented prior to frozen section examination. Biopsies may be taken from the deep margin and sent for frozen section. If the margins are clear, then no further treatment is necessary. If the margins cannot be obtained due to extension to the posterior aspect of the thyroid cartilage, further treatment is necessary.

Precision, hemostasis, and decreased postoperative edema are advantages of the CO₂ laser in the endoscopic management of early glottic carcinoma. The cure rates of endoscopic excisional biopsy are equivalent to those of early, midcordal glottic carcinoma are equal to those of both radiation therapy and laryngofissure with cordectomy. The advantage of this mode of therapy is the ability to differentiate between "early midcordal" T₁-glottic cancers from those that are more advanced. These invasive cancers will require further treatment to prevent extension and metastasis. Excisional biopsy can be performed with precision and will not interfere with further treatment when necessary.

Applications in Otolologic Disease

The use of the CO₂ laser in otologic disorders has been reported. The treatment of tumors of the cerebellopontine angle. Several investigators have used the CO₂ laser to treat acoustic neuromas, meningiomas,

used to perform myringotomies.⁵² The CO₂ milliwatt laser has recently been used for the treatment of otosclerosis by Lesinski with promising results.⁵³

Bronchoscopic Applications

In 1973, Strong et al.⁵⁴ utilized the CO₂ laser with a ventilating bronchoscope to allow hands-off endoscopic surgery of the intrathoracic airway. This system provided precise, hemostatic manipulation, with decreased perioperative edema and scarring. In 1982, Ossoff and Karlan⁵⁵ introduced a universal endoscopic coupler for bronchoscopic CO₂ laser surgery with a helium-neon aiming beam to permit precise application of laser energy. In 1985, applications and results with this new instrument were reported by Ossoff et al.⁵⁶

The applications of bronchoscopic CO₂ laser surgery include treatment of tracheal stenosis, recurrent respiratory papillomatosis, granulation tissue, tracheal webs, and proximal endobronchial neoplasms.⁵⁶ In some cases, the CO₂ laser can be used for palliative treatment of patients with obstructing tracheal and proximal endobronchial malignancies. Contraindications are extraluminal compression and loss of cartilaginous support of the trachea and bronchi. The disadvantages of the CO₂ laser in bronchoscopic surgery include hemostasis limited to vessels smaller than 0.5 mm in diameter. If a vascular tumor is encountered, bleeding can be difficult to control with the CO₂ laser. In some cases, the surgeon can topically apply pledgets saturated with epinephrine (adrenaline) or use the bipolar bronchoscopic suction cautery. The lack of a fiberoptic delivery system limits the use of the CO₂ laser in bronchoscopic surgery. The Nd:YAG laser has proved to be more practical in bronchoscopic laser surgery due to its improved hemostatic properties and the ability of the laser energy to be passed through a flexible fiberoptic delivery system. The development of a fiberoptic delivery for the CO₂ laser will surely enhance the applicability of the CO₂ laser in bronchoscopic surgery.

Neodymium-YAG Laser

The neodymium-yttrium-aluminum-garnet (Nd:YAG) laser has a wavelength of 1.06 μ in the infrared spectrum.⁵⁷ This is a continuous wave laser, and its medium is a solution of neodymium ions in a crystal of yttrium-aluminum-garnet (YAG).⁵⁸ The maximum power output is 100 W. The laser energy can be carried through a flexible fiberoptic delivery system and does require an aiming beam (helium-neon).

The tissue effect of the Nd:YAG laser is due to the high degree of scattering of the laser energy.⁵ Heat energy is produced by the scattering of the laser energy, resulting in a coagulation effect and superficial vaporization of cells. A significant amount of carbonization can result if blood is allowed to collect along the laser-tissue interface. The depth of penetration

of the Nd:YAG laser energy can result in transmural injuries when in certain regions of the body (such as the trachea, bronchus, esophagus, GI tract). If the Nd:YAG laser is used in short, repeated bursts, then penetration can be minimized. The main advantage of the Nd:YAG laser is its ability to coagulate large volumes of tissue.

Applications

The primary applications of the Nd:YAG laser in head and neck include photocoagulation of vascular lesions⁵⁹ and the palliation of obstructing tracheobronchial^{60,61} and esophageal⁶² lesions. Perhaps one of the most common and life-threatening complications of laser bronchoscopy. The ability of the Nd:YAG laser to penetrate deeper and scatter makes it a much more effective instrument for control of bleeding. The Nd:YAG laser energy can be passed through a flexible fiberoptic delivery system coupled to a rigid bronchoscope. Both of these factors make the Nd:YAG laser very effective in laser bronchoscopy.

Disadvantages of the Nd:YAG laser include less predictable effects. The laser is set at 40 to 50 W, for 0.5- to 1.0-second pulses. Laser energy should be applied parallel to the long axis of the trachea or proximal bronchi to avoid transmural damage. Patient selection is most important. In the tracheobronchial tree, lesions should be proximal, endotracheal or endobronchial. Tumors that are primarily peripheral are compressing the airway should not be treated by this procedure. They result in transmural damage and collapse of the airway. Computerized tomography scans or tomograms should be obtained preoperatively to assess such criteria.

Argon Laser

The argon laser is a continuous wave laser, operating at 0.48 μ in the blue-violet region of the visible spectrum.⁶³ The medium consists of highly ionized argon gas at a low pressure. Pumping is achieved by high current discharges. The argon laser energy is strongly absorbed by water and other pigmented tissues.⁶⁴ The argon laser energy is theoretically transmitted through skin and fat but reflected by bone. The argon laser energy is absorbed by transparent media, such as water or glass. The spot size of the laser can be as small as 0.15 mm. The argon laser can be carried through a fiberoptic delivery system.

Tissue Effects

The tissue effects of the argon laser are characterized by a coagulation followed by raising of the tissue, and, finally, vesicle formation. With increased laser energy, the vesicle ruptures, revealing the actual laser defect. There is minimal char formation and a relatively smooth surface.

surrounding thermal damage. As wound healing occurs and the edema dissipates, the actual margin of the defect begins to demarcate. The final demarcated defect is about 30% larger than the initial defect. The primary advantage of the argon laser is its high absorption coefficient for hemoglobin, small spot size, and the ability to transmit the laser energy through a fiberoptic delivery system.

Applications in Skin Surgery

The argon laser is preferentially absorbed by hemoglobin and other pigmented tissues.⁶⁶ For this reason, the argon laser has proved to be very useful in the ablation of vascular cutaneous lesions and other pigmented skin lesions.

Port-wine stains are congenital hemangiomas that consist of an overabundance of mature capillaries in the superficial dermis. Goldman^{67,68} was one of the first investigators to use the argon laser for treating port-wine stains. Several authors feel that the older the patient, the better the result.⁶⁹⁻⁷³ Dolsky does not treat patients under 18 years of age due to increased scarring and poor results.⁶⁶

There are presently two different techniques for treating port-wine stains. Parkin and Dixon⁷⁴ describe a technique using the optimal power setting of the argon laser that produces a blanch of the vascular lesion and then using a continuous time setting to cause coagulation of the vascular lesion. Keller and associates⁷⁵ describe a technique in which a power setting on the argon laser is used that is sufficient to cause blanching of the vascular lesion, but then a time setting of 0.1 to 0.2 second is used, rather than a continuous time setting. The argon laser energy is delivered with a 1-mm spot size to the vascular lesion in a beading pattern. Keller has called this technique "minimal treatment/retreatment methods."⁷⁵

Misconceptions about the effects of the argon laser on skin are prevalent. Although a large part of the argon laser energy is absorbed by the target vascular lesion, the heat produced causes destruction of the epidermis, upper dermis, and melanin and carotene skin pigment.

Tatoos can be made less noticeable and lightened to a variable degree with the use of the argon laser. Treatment is only effective if the tattoo was professionally applied, with dye limited to the dermis. Any dye located below the dermis would require a full-thickness burn to remove the dye. The argon laser is used to vaporize the tissue, lifting the epidermis off the dermis. Argon laser energy is applied at 4 to 4.5 W with repeated applications; eventual vaporization of the epidermis results so the dye can be rubbed off the dermis. Not all the dye can be removed. The dermis is rubbed daily by the patient until an eschar forms and peels away with most of the dye after two to three weeks. Then reepithelialization occurs several weeks later. There is never complete tattoo removal, but frequently only a light outline of the tattoo persists.

Telangiectasias of the head and neck can be effectively treated with the

argon laser. Telangiectasias can result from autoimmune disease, congenital condition, trauma, solar exposure, etc. Etiology does not have any on the treatment result. Local anesthetic agents should not be used in a manner that produces direct pressure on the lesion. Otherwise, the may collapse and decrease the amount of pigment in the vessel, which can be iced prior to treatment. The surgeon should use a 1.0 mm spot size at 1.1 to 1.6 W. Lesions frequently recur because of the underlying disease. Lesions of the face and nose are usually treated with a 0.6 mm spot size.

Applications in Otolologic Surgery

The argon laser has specific characteristics that make it a valuable tool in otologic surgery. The laser's small spot size, transmission through fluids, and simultaneous hemostasis make the argon laser a good choice for otologic surgery.⁷⁷ The argon laser has been used for vaporization of scar tissue in chronic ear disease, pigmented cholesteatomas, granulation and mucosal bands. For vaporization in such cases, the surgeon uses a spot size of 1 to 2 mm, with an output of 1.8 to 2 W for 0.1 to 0.2 second. When removing tissue from the round or oval windows, a spot size of 120 μ at 1.5 W for no longer than 0.1 second should be used. When revising or cleaning mastoid cavities, the output can be increased to 3 W in the continuous mode. To stop microbleeding in the middle ear, a spot size of 120 μ at 1.4 W for 0.1 second can be used.

The use of the laser for otosclerosis on an experimental basis was reported to 1967 by Sataloff⁷⁸ and to 1972 by Stahle and associates.⁷⁹ Sataloff and DiBartolomeo^{81,82} reported their results using the argon laser for otosclerosis in 1980 and 1982. Both authors reported good results without, if any, adverse effects.

In 1983, McGee⁸³ compared patients treated with the argon laser for otosclerosis with those treated by conventional means. The procedure was performed with the patient under local anesthesia, with the laser set at 1 W, 0.1 second, and a spot size of 120 μ . The stapedotomy was performed in the usual manner except that the argon laser was utilized. A piston to eight laser impulses were grouped in a rosette pattern and used to create a fenestra slightly greater than 0.6 mm in diameter. The 1-mm piston was inserted in the fenestra and secured to the incus with the incus. There was no statistically significant difference between the otologic results of the two groups at six months and one year. In only 3 of 100 patients treated by laser stapedotomy were there any vertigo during surgery and those brief episodes were due to the instrumentation. There was no vertigo noted during laser application. 75% of the patients were discharged the morning following surgery. There were no cases of persistent postoperative vertigo or disequilibrium. The long-term results of laser stapedotomy are still being studied.

termine if the amount of reduction of surgical trauma will significantly preserve the patient's auditory acuity and discrimination. Other middle ear applications of the argon laser include spot welding of grafts in tympanoplasty, ossicular sculpturing, and lysis of middle ear adhesions.^{84, 85}

Argon-Pumped Tunable Dye Laser

The argon-pumped tunable dye laser consists of an argon laser that is focused on dye circulating in a second laser that is optically coupled to the argon laser. The argon laser energy excites the dye, resulting in emission of laser energy. The dye can be varied, allowing different wavelengths to be produced. This variable wavelength laser energy can be used in selective photodynamic therapy of cancer, following injection of a hematoporphyrin derivative that acts as a photosensitizer.⁸⁶ The photosensitizer moves to all cells of the body, then is rapidly cleared from normal tissue. The hematoporphyrin derivative remains in neoplastic tissue for an extended period. A few days later, there is a significant concentration gradient between normal and neoplastic cells. The neoplastic tissue is then exposed to the red light of the dye laser (630 nm) and the hematoporphyrin derivative absorbs the light, resulting in a photochemical reaction. Toxic oxygen radicals, such as singlet oxygen, are produced in the exposed cells, resulting in selective tissue destruction. The normal cells have much less hematoporphyrin present, so there is less tissue damage. The wavelength of 630 nm is used because it offers the greatest skin penetration, approximately 1 cm.⁸⁷

Present reports with this treatment modality are promising, but the overall clinical application remains to be established.⁸⁸ Ossoff et al.⁸⁹ proposed the use of hematoporphyrin derivative to act as a tumor marker to identify multicentric disease in regions where panmucosal disease is common. Photodynamic therapy is presently being evaluated clinically in a phase III study as the single mode of therapy in selected, superficial, mucosal carcinomas of the upper aerodigestive tract.

Safety Precautions

Educating and qualifying physicians to use the laser is crucial to the safety of the patient and all personnel involved. Laser safety criteria should be outlined and monitored by a safety committee. Preventive and emergency procedures should be familiar to all personnel working with the laser.^{90, 91}

The laser safety committee should delegate officials to organize safety guidelines and mandate credentialing requirements. Attendance at a hands-on laser training course should be required. The courses should be 16 to 20 hours, with about 50% of the time devoted to practicing handson skills in the lab.⁹² As the scope of laser applications expands in otolar-

ynology-head and neck surgery, the depth of these courses will increase. Not only the surgeon, but the anesthesiologist and nursing personnel should be educated in laser safety. The laser safety committee should keep records of all surgeons credentialed in laser surgery as a record and review all laser cases.

Specific precautions include periodic maintenance and testing of the laser system. The operating room should be prepared to manage electrical, and fume hazards. All endotracheal tubes, instruments, anesthetic mixtures should be used with special consideration of laser. All personnel should have protective eye-wear for the wavelength of laser energy being used.

To protect the eyes of the patient when CO₂ laser is used, a layer of saline moistened eye pads should be placed over the eyes. Exposed skin and mucous membranes not in the surgical field should be covered with saline-soaked surgical towels, lap pads, or sponges. For microlaryngeal surgery, the patient's face is completely covered with saline-soaked towels to protect the skin from stray laser energy. Teeth also be protected in a similar fashion with saline-soaked gauze sponges. The protective draping must be kept wet by moistening the drapes periodically.

Two separate suctions are needed to keep the field clear of smoke, steam, and blood. Smoke or steam buildup retards visibility and is inhaled by the surgeon or other personnel. Blood and mucous secretions are important. With the jet-ventilation system, care must be taken to suction continuously; otherwise the FiO₂ may decrease. Many bronchoscopes and bronchoscopes have their own built-in suction channels.

Anesthetic management of the patient undergoing laser surgery of head and neck involves a team approach. Use of the CO₂ laser in nasopharynx, oral cavity, larynx, or tracheobronchial tree requires use of a red rubber or silicone tube wrapped with reflective material. The cuff should be inflated with methylene-blue colored saline and protected with saline-soaked neurologic cottonoids. The operating platform should be used to avoid aberrant laser energy from striking the tube. The cuff is struck and deflated, then a new wrapped tube should be placed. The safest tube to use with the Nd-YAG laser is a colorless or white polyvinyl or silicone) endotracheal tube that does not have any black or lettering. The tube should not have any lead lined marking along the

Future Directions

Research and development of new wavelengths of laser energy and delivery systems will surely continue to extend the applicability of the laser in otolaryngology-head and neck surgery. The development of a fiberoptic delivery system for the CO₂ laser will permit its use in the

nasal sinuses and nasopharynx. Intranasal endoscopic sinus surgery will become even a greater therapeutic instrument with the use of the CO₂ laser as a cutting, vaporizing, and coagulating instrument. Contact Nd:YAG laser surgery of the mucosal lining of the upper aerodigestive tract may permit practical laser tonsillectomies. There are investigators studying the use of multiple wavelengths in laser surgery to explore the advantages of each different type of laser energy.

The initial trials of photodynamic therapy are promising and the possible applications are endless. The effective treatment of cancer with photodynamic therapy awaits further clinical trials and improvement in the photosensitizing drug and the laser delivery systems. The cure rates of cancer may be altered dramatically by the coming of this new mode of cancer therapy.

The laser has resulted in great advances in the surgical specialties. Widespread use of laser energy in the operative field has permitted the precise extension of the surgeon's hand.

References

1. Maiman TH: Stimulated optical radiation in ruby. *Nature* 1960; 187:493-494.
2. Andrews AH, Polanyi TG (eds): *Microscopic and Endoscopic Surgery with the CO₂ Laser*. Littleton, Mass, John Wright PSG Inc Publishers, 1982.
3. Mihashi S, Jako GJ, Incze J, et al: Laser surgery in otolaryngology: Interaction of the CO₂ laser in soft tissue. *Ann NY Acad Sci* 1976; 267:263-293.
4. Stern LS, Abramson AL, Grimes GW: Quantitative and morphometric evaluation of vocal cord lesions produced by the carbon dioxide laser. *Laryngoscope* 1980; 90:792-808.
5. Gillis TM, Strong MS: Surgical lasers and soft tissue interaction. *Otolaryngol Clin North Am* 1983; 16:775-784.
6. Hall RR: The healing of tissues incised by carbon dioxide laser. *Br J Surg* 1971; 58:222-225.
7. Simpson GT, Shapshay SM, Vaughan CW: Rhinologic laser surgery. *Otolaryngol Clin North Am* 1983; 829-837.
8. Healy GB, et al: Management of choanal atresia with the CO₂ laser. *Ann Otol Rhinol Laryngol* 1978; 87:658-662.
9. Mittleman H: CO₂ laser turbinectomies for refractory obstructive allergic rhinitis, abstract. *Otolaryngol Head Neck Surg* 1980; 88:154.
10. Selkin SG: Laser turbinectomy as an adjunct to rhinoseptoplasty. *Arch Otolaryngol* 1985; 111:446-449.
11. King GD: Transoral resection of cancer of the oral cavity. *Otolaryngol Clin North Am* 1972; 5:321-325.
12. Strong MS, Vaughan CW, Healy GB, et al: Transoral management of localized carcinoma of the oral cavity using the CO₂ laser. *Laryngoscope* 1979; 89:897-905.
13. Strong MS, Vaughan CW, Jako GJ, et al: Transoral resection of cancer of the oral cavity: The role of the CO₂ laser. *Otolaryngol Clin North Am* 1979; 12:207-218.
14. McDonald GA, Simpson GT: Transoral resection of lesions of the oral cavity with the carbon dioxide laser. *Otolaryngol Clin North Am* 1983; 16:829-839.
15. Carruth JAS: Resection of the tongue with the dioxide laser. *J Laryngol* 1982; 96:529-543.
16. Vaughan CW: Supravital staining for early diagnosis of carcinoma. *Otolaryngol Clin North Am* 1972; 5:301-302.
17. Durkin GE, Duncavage JA, Toothill RJ, et al: Wound healing of tongue and squamous epithelium following CO₂ laser ablation and cupping of tongue. *Otolaryngol Head Neck Surg* 1986; 95:273-277.
18. Shapshay SM, Strong MS, Anastasi GW, et al: Removal of a large tongue tumor with the carbon dioxide laser. *Arch Otolaryngol* 1980; 106:257-259.
19. Kirschner RA: Cutaneous plastic surgery with the CO₂ laser. *J Am Coll Surg* 1984; 64:871-883.
20. Levine H, Balin P: Carbon dioxide laser treatment of cutaneous lesions and tattoos. *Arch Otolaryngol* 1982; 108:236-238.
21. Reid R, Muller S: Tattoo removal by CO₂ dermatoblaston. *Plast Reconstr Surg* 1980; 65:717-728.
22. McGill TJ, Friedman EM, Healy GB: Laser surgery in the pediatric head and neck. *Otolaryngol Clin North Am* 1983; 16:865-870.
23. Holinger LD: Treatment of severe subglottic stenosis without tracheotomy: preliminary report. *Ann Otol Rhinol Laryngol* 1982; 91:407-412.
24. Healy GB, McGill TJ, Friedman EM: Carbon dioxide laser in subglottic stenosis. *Ann Otol Rhinol Laryngol* 1984; 93:370-373.
25. Karlan MS, Ossoff RH: Laser surgery for benign laryngeal disorders. *Classification and ergonomics. Otolaryngol Clin North Am* 1984; 64:983-994.
26. Duncavage JA, Ossoff RH, Toothill RJ: Carbon dioxide laser in benign laryngeal stenosis. *Ann Otol Rhinol Laryngol* 1985; 95:565-569.
27. Kaufman JA, Thompson JN, Kohut RI: Endoscopic management of glottic stenosis with the CO₂ laser surgical laser. *Otolaryngol Head Neck Surg* 1989; 215-220.
28. Healy GB: An experimental model for the endoscopic treatment of glottic stenosis with clinical applications. *Laryngoscope* 1982; 92:1160-1163.
29. Dedo HH, Sorey CD: Endoscopic laser repair of postinfectious glottic stenosis: tracheal stenosis by division of microthrips or flap. *Laryngoscope* 1984; 94:445-450.
30. Simpson GT, Strong MS, Healy GB, et al: Postinfectious glottic stenosis: failure in the endoscopic management of laryngeal and tracheal stenosis. *Otol Rhinol Laryngol* 1982; 91:384-388.
31. Campbell RH, Dennison BF, Durkin GE, et al: Laser and laser ablation acquired subglottic stenosis. *Otolaryngol Head Neck Surg* 1980; 88:150-153.
32. Shugar JMA, Biller HF: Evaluation of the carbon dioxide laser in the treatment of traumatic laryngeal stenosis. *Laryngoscope* 1982; 92:23-26.
33. Strong MS, Vaughan CW, Healy GB, et al: Recurrent respiratory papillomatosis: Management with the CO₂ laser. *Ann Otol Rhinol Laryngol* 1985; 94:508.
34. Ossoff RH, Karlan MS, Sisson GA: Posttraumatic commissure lesions treated with carbon dioxide laser surgery. *Ann Otol Rhinol Laryngol* 1983; 92:304-307.
35. Benjamin B, Croxson G: Vocal cord granulomas. *Ann Otol Rhinol Laryngol* 1985; 92:538-541.
36. Ossoff TH, Sisson GA, Duncavage JA, et al: Endoscopic laser treatment of

- for the treatment of bilateral vocal cord paralysis. *Laryngoscope* 1984; 94:1293-1297.
37. DeSanto LW: Options in early laryngeal cancer. *N Engl J Med* 1982; 306:910-912.
38. Neel HB III, Devine KD, DeSanto LW: Laryngofissure and cordectomy for early cordal carcinoma: Outcome in 182 patients. *Otolaryngol Head Neck Surg* 1980; 88:79-84.
39. Millon RR, Cassisi NJ: Larynx, in Millon RR, Cassisi NJ (eds): *Management of Head and Neck Cancer: A Multidisciplinary Approach*. Philadelphia, JB Lippincott Co, 1984; pp 315-364.
40. Lynch RC: Intrinsic cancer of the larynx with a second report of the cases operated on by suspension and dissection. *Trans Am Laryngol Assoc* 1971; 80:507-512.
41. New GB, Dorton HE: Suspension laryngoscopy in the treatment of malignant disease of the hypopharynx and larynx. *Mayo Clin Proc* 1941; 16:411-416.
42. Stutsman AC, McGavran MH: Ultraconservative management of superficially invasive epidermoid carcinoma of the true vocal cord. *Ann Otol Rhinol Laryngol* 1971; 80:507-512.
43. DeSanto LW: Selection of treatment for in situ and early invasive carcinoma of the glottis. *Can J Otolaryngol* 1974; 3:552-556.
44. Strong MS, Jako GJ: Laser surgery in the larynx: Early clinical experience with continuous CO₂ laser. *Ann Otol Rhinol Laryngol* 1972; 81:791-798.
45. Lillie JC, DeSanto LW: Transoral surgery of early cordal carcinoma. *Trans Am Acad Ophthalmol Otolaryngol* 1973; 77:92-96.
46. Strong MS: Laser excision of carcinoma of the larynx. *Laryngoscope* 1975; 85:1286-1289.
47. Blakeslee D, Vaughan CW, Shapshay SM, et al: Excisional biopsy in the selective management of T₁ subglottic cancer: A three-year follow-up study. *Laryngoscope* 1984; 94:483-494.
48. Ossoff RH, Sisson GA, Shapshay SM: Endoscopic management of selected early vocal cord carcinoma. *Ann Otol Rhinol Laryngol* 1985; 94:560-564.
49. Gardner G, Robertson JH, Clark WC, et al: Acoustic tumor management: Combined approach surgery with CO₂ laser. *Am J Otol* 1983; 5:87-108.
50. Cerullo LJ, Burke LP: Use of the laser in neurosurgery. *Otolaryngol Clin North Am* 1984; 64:995-1000.
51. Smith MFW, Lagger RL: Hearing conservation in acoustic neuromatoma surgery via the retrosigmoid approach. *Otolaryngol Head Neck Surg* 1984; 92:168-175.
52. Goode RL: CO₂ laser myringotomy. *Laryngoscope* 1981; 92:420-424.
53. Lesirski SG: CO₂ laser surgery for otosclerosis. Presented at the Trilogic, Middle section, Chicago, January 24-26, 1986.
54. Strong MS, Vaughan CW, Polanyi T, et al: Bronchoscopic carbon dioxide laser surgery. *Ann Otol Rhinol Laryngol* 1974; 83:769-776.
55. Ossoff RH, Karlan MS: Universal endoscopic coupler for carbon dioxide laser surgery. *Ann Otol Rhinol Laryngol* 1982; 91:608-609.
56. Ossoff RH, Karlan MS, Duncanage JA, et al: The universal endoscopic coupler for bronchoscopic carbon dioxide laser surgery: A multi-institutional clinical trial. *Otolaryngol Head Neck Surg* 1985; 93:824-830.
57. Polanyi TG: Laser physics. *Otolaryngol Clin North Am* 1983; 16:753-774.
58. Fuller TA: The physics of lasers. *Lasers Surg Med* 1980; 1:5-14.
59. Shapshay SM, Oliver P: Treatment of hereditary hemorrhagic telangiectasia with Nd:YAG laser photocoagulation. *Laryngoscope* 1984; 94:1554-1556.
60. Toly A, Personne C, Célèche A, et al: Bronchoscopic management of lesions using the Nd:YAG laser. *Thorax* 1981; 36:175-178.
61. Dumon JF, Reboulet E, Garbe L, et al: Treatment of tracheal aneurysms by laser photoresection. *Chest* 1982; 81:278-284.
62. Shapshay SM, Simpson GT: Lasers in bronchoscopy. *Otolaryngol Clin North Am* 1983; 16:879-886.
63. McDougall JC, Cortese DA: Neodymium YAG laser therapy of mediastinal obstruction. *Mayo Clin Proc* 1983; 58:35-39.
64. Breams JF Jr, Shapshay SM: Nd:YAG laser therapy for laryngeal cancer orders. *Head Neck Surg* 1984; 75:173-180.
65. Fleischer D: Endoscopic laser therapy of gastrointestinal neoplasms. *Cancer Clin North Am* 1984; 64:947-953.
66. Delisky RL: Argon laser skin surgery. *Surg Clin North Am* 1984; 64:561-564.
67. Goldman L: Effects of new laser systems on the skin. *Arch Dermatol* 1983; 119:385-390.
68. Goldman L, Drexler R, Rockwell JR, et al: Treatment of head and neck cancer with argon laser. *J Dermatol Surg* 1976; 2:385-388.
69. Apfelberg DB, Maser MR, Lash H: Argon laser treatment of cutaneous lar abnormalities: Progress report. *Ann Plast Surg* 1978; 1:14-18.
70. Apfelberg DB, Maser MR, Lash H, et al: The argon laser for treatment of cutaneous lesions. *JAMA* 1981; 245:2073-2075.
71. Cosman B: Experience in argon laser therapy for port-wine stains. *J Reconstr Surg* 1980; 65:119-129.
72. Noe J: Laser use in dermatology plastic surgery. in Dixon JA (ed): *Application of Lasers*. Chicago, Year Book Medical Publishers Inc, 1980; 1:1-10.
73. Noe JM, Barsky SH, Geer DE, et al: Port wine stains and the use of the argon laser therapy: Successful therapy and the predictive value of biopsy and biopsy. *Plast Reconstr Surg* 1980; 65:130-136.
74. Parkin J, Dixon J: Argon laser treatment of head and neck vascular lesions. *Otolaryngol Head Neck Surg* 1985; 93:211-216.
75. Keller GS, Doiron D, Weingarten C: Advances in laser skin surgery: Cutaneous lesions. *Arch Otolaryngol* 1985; 111:437-440.
76. Cosman B: Role of retreatment in minimal power argon laser therapy for port-wine stains. *Lasers Surg Med* 1981; 1:263-276.
77. McGee TM: The argon laser in surgery for chronic ear disease and otitis media. *Laryngoscope* 1983; 93:1177-1182.
78. Sataloff J: Experimental use of the laser in otosclerotic stapes. *Arch Otolaryngol* 1967; 85:58-60.
79. Stahle J, Hoegberg L, Engstrom B: The laser as a tool in inner ear surgery. *Acta Otolaryngol (Stockh)* 1972; 73:27-37.
80. Perkins RC: Laser stapedotomy for otosclerosis. *Laryngoscope* 1980; 90:240-249.
81. DiBartolomeo JR: The argon laser in otology. *Laryngoscope* 1980; 90:1796-1796.
82. DiBartolomeo JR: A versatile argon microvascular laser. *Otolaryngol Neck Surg* 1982; 90:139-141.
83. McGee TM: Comparison of small fenestra and total stapedectomy. *Rhinol Laryngol* 1981; 90:633-636.

84. EdBartolomeo JK: The argon and CO₂ laser in otolaryngology: Which one, when and why? *Laryngoscope* 1981, 91(suppl 26):1-16.
85. Escudero L, Castro AO, Drummond M, et al: Argon laser in human tympanoplasty. *Arch Otolaryngol* 1979; 105:252-259.
86. Dougherty TJ, Grindley GB, Fiel R, et al: Photoradiation therapy. II. Cure of animal tumors with hematoporphyrin and light. *J Natl Cancer Inst* 1975; 55:115-121.
87. Hayata Y, Kato H, Konako C, et al: Hematoporphyrin derivative and laser photoradiation in the treatment of lung cancer. *Chest* 1982; 81:269-277.
88. Wile AG, Coffey J, Nahabedian MY, et al: Laser photoradiation therapy of cancer: An update of the experience at the University of California, Irvine. *Lasers Surg Med* 1984; 4:5-12.
89. Ossoff RH, Pelzer HJ, Atiyah RA, et al: Potential applications of photoradiation therapy in head and neck surgery. *Arch Otolaryngol* 1984; 110:728-730.
90. Schramm VL, Mattox DE, Spaul SE: Acute management of laser-ignited intratracheal explosion. *Laryngoscope* 1981; 91:1417-1425.
91. Davis RK, Simpson GT: Safety with the carbon dioxide laser. *Otolaryngol Clin North Am* 1983; 16:801-813.
92. Ossoff RH, Karlan MS: Safe instrumentation in laser surgery. *Otolaryngol Head Neck Surg* 1984; 92:644.

ADULT SUBGLOTTISCOPE FOR LASER SURGERY

ROBERT H. OSSOFF, DMD, MD

JAMES A. DUNCAN, MD

NASHVILLE, TENNESSEE

A subglottiscope for use in adult men and women has been developed for microlaryngeal laser operations in the subglottic region of the larynx. The tip has been designed to facilitate exposure of the subglottis and upper trachea in both short-necked and long-necked individuals. A smoke evacuation channel has been included, as has a nonreflective finish. Finally, a port for jet ventilation has been added to facilitate use of this anesthetic technique when indicated. The authors have used the prototypes of these subglottiscopes on six patients, four women and two men, and have found the exposure of subglottic and upper tracheal lesions to be improved over that obtained with existing microlaryngoscopes.

KEY WORDS — laser surgery, subglottiscope.

An adult subglottiscope for laser surgery has been developed to facilitate endoscopic exposure of the entire subglottic larynx and upper trachea to the level of the second ring in patients of both sexes with strictures and benign and malignant neoplasms located in these two anatomic sites. Limitations of the presently available endoscopic armamentarium (including microlaryngoscopes and tracheoscopes) for exposure to perform laser operations of the subglottic space in adults, combined with many favorable experiences with use of the Healy subglottiscope¹ in pediatric patients, prompted our development of this instrument.

The tip is small enough to pass through the vocal cords, facilitating exposure of the subglottic larynx and upper trachea. The tube of this subglottiscope

has been lengthened to facilitate its use in both short- and long-necked individuals (Fig 1A). The stainless steel tubing from which this instrument has been manufactured has been treated to render it low in specular or direct reflectance and high in diffuse or scattered reflectance when irradiated with mid-infrared laser energy.² A smoke evacuation channel has been added and a jet ventilation port has been included to facilitate use of this anesthetic technique when indicated (Fig 1B).

An example of the exposure of the subglottic space with this instrument is shown in a patient with an obstructing subglottic granuloma (Fig 2A) that measured 8 mm in diameter at the time of resection (Fig 2B). Following excision of this lesion, the patency of the airway was reestablished, allow-

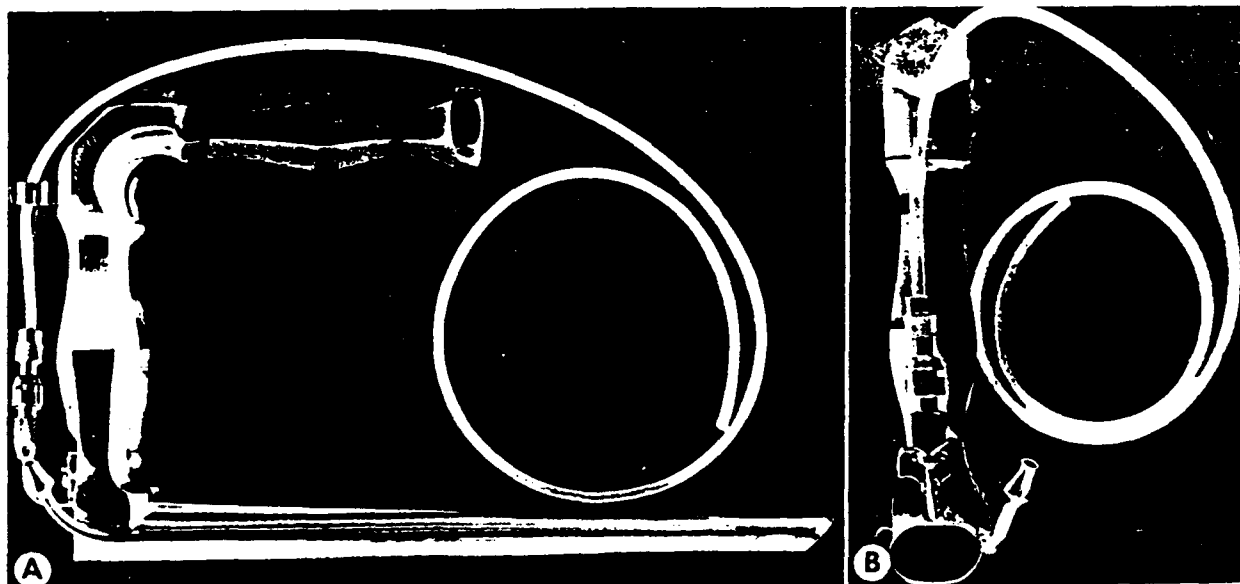


Fig 1. Subglottiscope. A) Side view showing distal tip and elongated tube. B) Proximal view showing jet ventilation and smoke evacuation ports.

From the Department of Otolaryngology, Vanderbilt University School of Medicine, Nashville, Tennessee.

Presented at the meeting of the American Broncho-Esophagological Association, Palm Beach, Florida, April 25-26, 1986.

REPRINTS — Robert H. Ossoff, DMD, MD, Dept of Otolaryngology, Vanderbilt University Medical Center, Medical Center North S-6441, Nashville, TN 37232.

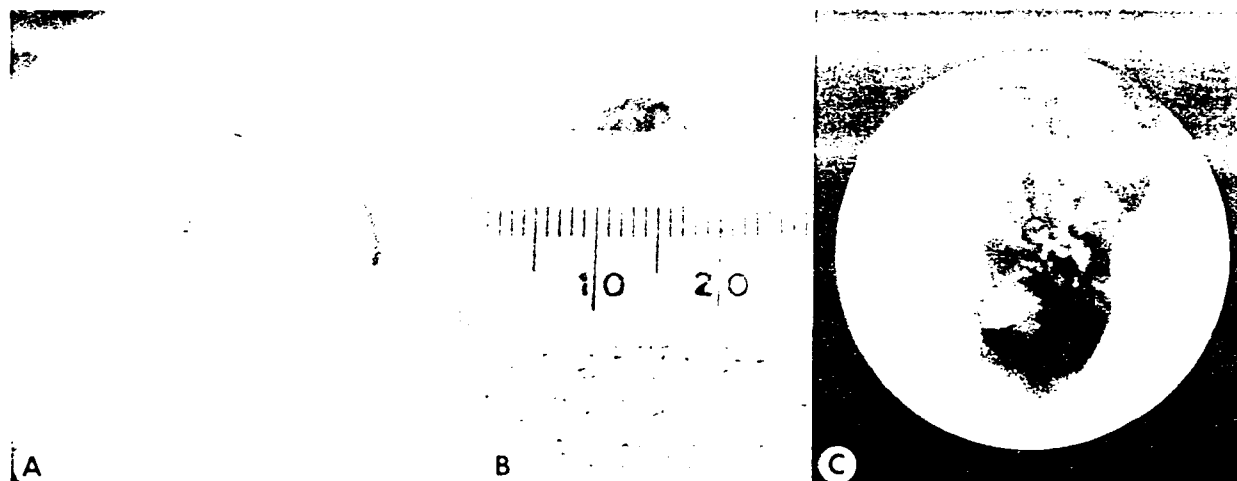


Fig 2. Removal of obstructing subglottic granuloma. A: Endoscopic view of granuloma exposed by subglottiscope and visualized through operating microscope. B: High-magnification granuloma following endoscopic laser resection. C: Endoscopic view of patent subglottic airway following resection.

ing the patient to be decannulated (Fig 2C). The Table summarizes the authors' experience with this instrument in treating six patients, three with subglottic lesions and three with upper tracheal lesions.

Potential applications for the use of this subglottiscope in the upper trachea and subglottic larynx include subglottic stenosis excision with or without the micro-trap door flap,^{1,4} excision of granulomas and other benign lesions, and excision or ablation of malignant neoplasms with either the carbon dioxide or potassium-titanyl phosphate laser. Advantages include the capability of simultaneously grasping, retracting, and or suctioning the lesion during laser resection and the ability to use either joystick or fiber laser delivery systems. A disadvantage is the need to purchase a new set of microlaryngeal instruments with longer shafts than those ordinarily used for microlaryngeal surgery through the tradi-

tional-length microlaryngoscopes. We have not experienced any limitations with these subglottiscopes to date.

USE OF ADULT SUBGLOTTISCOPE IN SIX PATIENTS

Patient No.	Sex	Diagnosis	Treatment and Outcome
1	F	Subglottic granuloma	Successful excision; patient decannulated
2	F	Suprastomal granuloma	Successful excision; patient decannulated
3	M	Suprastomal granuloma	Successful excision; patient decannulated
4	F	Subglottic stenosis	Radial incisions and dilation; patient decannulated
5	F	Subglottic stenosis	Radial incisions and dilation; patient plugged, but not decannulated
6	M	Tracheal stenosis at previous tracheostomy site	Radial incision and dilation twice; successful outcome with 9-month follow-up

REFERENCES

1. Healy GB. Subglottiscope. *Trans Am Broncho-Esophagol Assoc* 1987;130.
2. Ossoff RH, Karlan MS. Safe instrumentation in laser surgery. *Otolaryngol Head Neck Surg* 1984;92:644-8.
3. Dedo HH, Sow CD. Endoscopic laser repair of posterior glottic, subglottic, and tracheal stenosis by division of micro-trap door flap. *Laryngoscope* 1984;94:445-50.
4. Duncavage JA, Piazza LS, Ossoff RH, Toohill RJ. The microtrapdoor technique for the management of laryngeal stenosis. *Laryngoscope* 1987;97:825-8.

PRINTED IN THE U.S.A.

FOUNDED IN 1896

IV - Y.

Laser Safety in Otolaryngology— Head and Neck Surgery: Anesthetic and Educational Considerations for Laryngeal Surgery

Robert H. Ossoff, DMD, MD

SUPPLEMENT NO. 48

Laser Safety in Otolaryngology—Head and Neck Surgery: Anesthetic and Educational Considerations for Laryngeal Surgery

Robert H. Ossoff, DMD, MD

Two investigations concerning anesthetic and educational considerations for laser safety in microlaryngeal carbon dioxide laser surgery have been performed. The first study demonstrated that attendance at a "hands-on" laser surgery course that stressed safety precautions was associated with a reduced rate of laser-related complications in the selected group of otolaryngologists who participated in the course, when compared to another selected group of otolaryngologists who were members of a senior otolaryngology society, and surveyed solely on the basis of their society membership.

The second series of studies compared the incendiary characteristics of three endotracheal tubes in various mixtures of oxygen, diluted with either helium or nitrogen. It was determined that the polyvinyl chloride tube should not be used for laser surgery, even when wrapped with reflective, metallic tape. The safest anesthetic gas mixture was found to be 30% oxygen in helium; the addition of 2% halothane did not have an adverse effect, as had been previously reported. Both the Xomed Laser-Shield® and Rusch® red rubber endotracheal tubes were found to be safe, when used with the laser in the pulsed mode in an atmosphere of 100% oxygen. When the laser was used in the continuous mode, both tubes ignited in an atmosphere of 30% oxygen in helium. These findings challenged the previously reported levels of safety associated with the use of an unwrapped Xomed tube. Based on the results of this investigation, it has been concluded that both the Rusch red rubber tube and the Xomed Laser-Shield tube should be wrapped with reflective, metallic tape, when used for cases of microlaryngeal surgery with the carbon dioxide laser.

INTRODUCTION

Laser is an acronym for Light Amplification by the Stimulated Emission of Radiation. In 1919, Albert Einstein published his now classic treatise, "Zur Quantum Theorie der Strahlung" ("The Quantum Theory of Radiation") in which he postulated

the theoretic foundation of laser action, stimulated emission of radiation.¹ Einstein discussed the interaction of atoms, ions, and molecules with electromagnetic radiation and specifically addressed absorption with spontaneous emission of radiation, and proposed a third process of atomic interaction: stimulated emission. Einstein postulated that electromagnetic radiation could be produced by this atomic interaction which is the basis of laser energy.

The development and subsequent addition of laser technology to existing surgical techniques offered new and exciting possibilities for improving traditional endoscopic operations and expanding the scope of the specialty of otolaryngology—head and neck surgery. Lasers were found to be precise, but potentially dangerous, surgical instruments whose use was associated with certain distinct and unprecedented advantages, but also with many unique and potentially serious, and sometimes catastrophic, complications. Reports about many of these unique, laser-related complications, complete with conflicting discussions detailing how to avoid these laser-related accidents, appeared to increase in frequency as the use of the technology proliferated. The lack of a definitive, fail-safe solution to prevent a laser-ignited endotracheal tube fire from occurring stimulated this investigation.

The purpose of this research was twofold. The first goal was to determine if attendance at a small "hands-on" laser surgery course that stressed safety precautions and complications for specialists in otolaryngology—head and neck surgery might lead to a reduced rate of laser-related complications in this selected group of otolaryngologists when compared to another selected group of otolaryngologists, members of a senior otolaryngology society, previously surveyed by Fried² solely on the basis of their society membership. The second objective was to compare the incendiary characteristics of three endotracheal tubes in various mixtures of oxygen

Presented as a Candidate's Thesis to the American Laryngological, Rhinological and Otolological Society, Inc., 1988.

From the Department of Otolaryngology, Vanderbilt University Medical Center, Nashville, Tenn.

Send Reprint Requests to Robert H. Ossoff, MD, Department of Otolaryngology, S-6441, Medical Center North, Vanderbilt University Medical Center, Nashville, TN 37232-2559.

learned from the first part of the study would help to convince otolaryngologists, head and neck surgeons that they should attend a "hand-on" laser course prior to use of this technology in their clinical practice. The findings of the second part of this study should provide help to the otolaryngologist—head and neck surgeon who after the course when they are faced with the problem of choosing an endotracheal tube and gas mixture for a patient about to undergo microlaryngeal carbon dioxide laser surgery.

REVIEW OF THE LITERATURE

Early Laser Development

In 1958, thirty-nine years following Einstein's classic publication, Charles Townes and Arthur Schawlow³ published "Infrared and Optical Masers" in which they discussed stimulated emission in the microwave range of the electromagnetic spectrum (maser) and described the desirability and principles of extending the techniques of stimulated emission to the infrared and optical ranges of the electromagnetic spectrum (laser). Theodore Maiman⁴ expanded on the writings of Schawlow and Townes and built the first laser, a synthetic ruby laser, in 1960. This laser produced pulsed electromagnetic radiation at a wavelength of $0.69\ \mu\text{m}$ in the visible range of the spectrum and lasted only 1 msec or less; however, it stimulated much interest in the scientific and medical fields and paved the way for the future development and widespread application of lasers in industry and medicine. The output power of the ruby laser was soon increased to levels that allowed it to pierce a stack of steel razor blades. Snitzer (1961)⁵ developed the Nd-in-glass laser, which also operated in the pulsed mode at a wavelength of 1.06 micrometers; its output power greatly exceeded that of the ruby laser.

The development of these two lasers stimulated interest in the field of medical research regarding the possible application of laser energy to destroy cancer. Scientists began to apply energy from both of these lasers to various tumor lines implanted in experimental animals. Conflicting results were reported from the several laboratories performing this pioneering research. It was quickly determined that the entire tumor had to be destroyed to achieve a cure—a difficult task with either of the lasers because of the low absorption of the wavelengths 0.69 and $1.06\ \mu\text{m}$ in nonpigmented biologic tissue. Researchers began to use higher and higher power densities to facilitate tumor destruction when using either of the two lasers. This, in turn, caused mechanical tissue disruption with viable cancer cells being disseminated to distant areas in the experimental animal, as well as into the laboratory environment.⁶ From the results of these early investigations, scientists learned the principle of differential absorption of electromagnetic radiation by biologic

tissue. The first continuous-wave, molecular-gas laser, the carbon dioxide (CO_2) laser, which emitted radiation in the infrared range of the electromagnetic spectrum. The major characteristics of this laser that made it potentially interesting for medical applications were its high-power, continuous output and its infrared wavelength of $10.6\ \mu\text{m}$, which was almost completely absorbed by most biologic tissues. This high degree of absorption, high-output power, continuous mode of operation, and ability to focus the beam to a very small spot size permitted early investigators working with this laser to destroy a localized volume of tissue by burning and vaporizing it. The tissue interaction characteristic of the CO_2 laser, therefore, was found to be a localized, precise, thermal injury that offered potential in surgical research.

Yahr and Strully⁷ soon discovered that they could make a fine incision in skin and perform a partial liver resection with minimal blood loss using a laboratory model carbon dioxide laser. Encouraged by the results of Yahr and Strully, Polanyi, *et al.*⁸ developed a CO_2 laser system for surgical research. This permitted multiple investigators to study the potential applications of carbon dioxide lasers in medicine and surgery.¹⁰⁻¹³

Early Research with the Carbon Dioxide Laser in Otolaryngology

Jako¹⁴ performed the first carbon dioxide laser surgery experiments on a cadaver larynx in 1967, and produced discrete, localized lesions using the laser's focusing handpiece. Encouraged by his results, Jako stimulated Bredemeier¹⁵ to develop an endoscopic delivery system which allowed Jako to perform the first in vivo experiments on canines. He was able to produce discrete lesions in the canine larynx; the operative field was found to be bloodless and the postoperative healing was excellent. Further encouraged by these results, Jako quickly realized that the development of an attachment to allow the use of the laser with the operating microscope and fiberoptic laryngoscope was necessary. Bredemeier¹⁶ produced an attachment that coupled the laser's arm to the Zeiss operating microscope and termed it a "stereoendoscope" and later a "micromanipulator." Using this attachment, Jako was able to develop and study laser surgical techniques on the canine vocal fold. These experiments were completed in 1970 and submitted by Jako as a candidate's thesis to the American Laryngological, Rhinological and Otological Society, Inc. In his discussion, Jako cited the possibility of reflecting laser energy off metal instruments to remote areas in the airway and also mentioned that the surgeon's eyes would be protected by the oculars of the Zeiss operating microscope. He concluded that the instrumentation used for his experiments could be used for human application "without any further modification."¹⁴

Early Clinical Experience with the Carbon

Dioxide Laser in Surgery, Otolaryngology, 1972, 1:19.

Strong and Jako¹⁷ presented their initial clinical report on the use of the carbon dioxide laser in otolaryngology at the 1972 Annual Meeting of the American Broncho-Esophagological Association where its use was described in 11 procedures involving 12 patients with laryngeal pathology. Certain potential dangers were raised by the authors regarding the use of the laser in microlaryngeal surgery. First, the possibility of beam reflection off a shiny metal instrument was discussed, and the authors strongly suggested that personnel in the operating room wear glasses as a means of protection from this risk. The potential for corneal injury by the carbon dioxide laser had been previously described by Leibowitz and Peacock.¹⁸ Second, they emphasized the need to avoid injury to the cuff of the endotracheal tube; here, Strong and Jako suggested that the cuff either be advanced "down the trachea out of sight" or protected by a piece of moist "selvage gauze." Third, and most importantly, the authors warned that the endotracheal tube, in the presence of a high oxygen flow rate, could be made to burn. They concluded that use of the carbon dioxide laser was "practical for incision or excision of tissue," and that the use of the micro-manipulator with the operating microscope allowed "laser surgery of the vocal cords to be carried out with exquisite precision." Their final conclusion predicted that further applications of laser surgery in otolaryngology would "be forthcoming as experience and expertise accumulates."¹⁷

The potential impact of Strong and Jako's initial carbon dioxide laser presentation was highlighted by Ward (1972)¹⁹ when he described the use of the laser in microlaryngeal surgery as the "singular outstanding new development" in otolaryngology during his "What's New in Surgery" presentation at the Clinical Congress of the American College of Surgeons. Earlier that same year, the American Medical Association awarded Strong, Jako and their collaborators, Polanyi and Bredemeier, from the American Optical Research Laboratories, the Hektoen Gold Medal for their exhibit "Laser Surgery of the Larynx" which was displayed at the Annual Convention of the American Medical Association. News of this award was featured in the Medical News section of the *Journal of the American Medical Association*.²⁰

Strong and Jako²¹ presented their experience with the use of the CO₂ laser in the management of 75 patients requiring 142 procedures at the 1973 First Joint Meeting of the Society of Head and Neck Surgeons and the American Society for Head and Neck Surgery. Once again, they cautioned the reader about the possibility of damage to either the rubber or plastic endotracheal tube when performing laser

surgery. For the first time, they suggested protective measures for the endotracheal tube, such as applying the tube with a piece of moist gauze and covering the cuff with aluminum tape.

Andrews began working with the carbon dioxide laser in 1972 and published two papers on the subject in 1974, one in the general surgery literature²² and the other in *Annals of Otolaryngology, Rhinology and Laryngology*²³ based on his presentation at the Annual Meeting of the American Laryngological Association. He emphasized safety in both publications and suggested that, in addition to all personnel in the operating room wearing glasses, the eyes of the patient should be taped closed and covered. Protection of the patient's lips with moist gauze was suggested to guard against any possible vertical or horizontal maladjustment of the microscope with the laryngoscope.

The greatest focus of Andrews' safety concerns involved the anesthetic management of the airway when performing microlaryngeal laser surgery. He exposed endotracheal tubes to laser energy in the laboratory and recognized the potential for a catastrophic airway fire, should the laser beam hit an endotracheal tube in the presence of high oxygen concentration. He also determined that plastic endotracheal tubes were more easily penetrated than red rubber tubes and that these same plastic tubes ignited far more easily in the presence of oxygen than did the red rubber tubes. Andrews further noted that the red rubber tubes would only burn on the outside and would not be penetrated, when exposed to greater than 15 seconds of 20 W (maximum power) at 0.1 second in the presence of oxygen. He concluded, therefore, that only red rubber tubes should be used for microlaryngeal laser surgery and that these tubes should be protected with aluminum foil tape as previously described by Strong and Jako. Additional safety precautions included limiting the concentration of oxygen in the anesthetic gas to 30%, protecting the cuff of the endotracheal tube with saline-saturated neurosurgical gauze pads and counting these gauze pads in the same manner as a sponge count, and limiting the duration of the laser exposure to the shortest time possible to help minimize the risk of endotracheal tube cuff perforation.

These reports stimulated the specialty of anesthesiology to write prolifically about the safe anesthetic management of patients undergoing this relatively new form of surgery. Several anesthetic techniques, endotracheal tubes, methods of protecting endotracheal tubes, and methods of administering jet ventilation were published in the anesthesiology literature beginning in 1973.

Birch²⁴ was the first in his specialty of anesthesiology to publish on anesthetic considerations for laser surgery; however, he focused on the subject in general, and did not discuss any specific airway considerations.

During the same year, Konchigeri and Shaker²⁶ published their experiences providing anesthesia for Andrews. These investigators raised the question about the risk of laser-ignited fire or explosion in the presence of different concentrations of oxygen or anesthetic gases.

During the same year, Konchigeri and Shaker²⁶ published their experiences providing anesthesia for Andrews. These investigators raised the question about the risk of laser-ignited fire or explosion in the presence of different concentrations of oxygen or anesthetic gases.

In 1975, Snow and Norton²⁷ reviewed and published their experiences managing 250 consecutive patients who underwent 700 microlaryngeal or bronchoscopic laser procedures over a 42-month period. Wrapped red rubber endotracheal tubes were used in most cases, although Venturi or jet ventilation was employed in several of the pediatric cases. No morbidity or mortality occurred according to these investigators, although four fire accidents were reported in their publication. Snow and Norton discussed two of the fires: one that occurred in an unwrapped tube and another that occurred in a reflective tape-wrapped tube. No serious injury was mentioned from any of the four fires.

Strong and his colleagues (1976)²⁸ presented their experiences in treating 110 patients with recurrent respiratory papillomatosis using the carbon dioxide laser. General anesthesia was administered in all patients using a small-sized endotracheal tube protected with aluminum tape. In some patients, especially children, the tube was removed during the case to facilitate exposure of the posterior commissure; in these cases, the patient was ventilated with a Venturi system. The only laser-related complication cited in this paper was that of an acquired anterior glottic web that occurred in seven patients treated early in the series; this most probably resulted from simultaneous excision of papillomas from the anterior commissure of both vocal cords. Strong and his colleagues did not realize this possibility when performing the microlaryngeal laser surgery in the very early cases of recurrent respiratory papillomatosis.

Later that same year, Strong, *et al.*²⁹ updated the members of the American Academy of Otolaryngology by presenting a progress report on laser surgery at the Annual Meeting of the Academy. Precautions for laser surgery were highlighted and complications were discussed. For the first time, Strong, *et al.* cautioned against using the polyvinyl chloride endotracheal tube and, once again, recommended using an aluminum tape-wrapped red rubber tube. They cited two episodes of extraluminal endotra-

cheal tube fistulas that occurred prior to their article.

During that same year, Shaker, *et al.*³⁰ retrospectively reviewed 71 laser procedures performed on 51 patients for various intralaryngeal pathological conditions. Anesthesia was maintained with halothane or enflurane in a mixture of oxygen in nitrous oxide (30:70). There were no complications in this series.

Snow and his colleagues (1976)³¹ published a paper describing the fire hazard during microlaryngeal laser surgery. They presented four cases of laser-ignited tube fires (same cases as reference 27) that healed uneventfully. This was the first publication in the anesthesiology literature to state that the red rubber endotracheal tube had to be wrapped with reflective aluminum tape if it was situated within the operative field (microlaryngeal surgery). A similar warning had been issued by Strong, *et al.*²¹ in the otolaryngological literature in 1973.

Norton and his associates (1976)³² reviewed their experiences using the combined technique of endotracheal intubation and Venturi (jet) ventilation for the anesthetic management of 100 patients requiring microlaryngeal laser surgery. In their series, the distal orifice of the jet ventilation needle was located above the level of the true vocal cords. They found that the primary advantage of this anesthetic technique was that it provided the surgeon with total access to the larynx and trachea, without visual or mechanical obstruction by an endotracheal tube. Additionally, the risk of a laser-ignited airway fire was eliminated, since no combustible materials, such as an endotracheal tube or cottonoids, were present in the airway. Certain disadvantages were noted by Norton and his colleagues that included: 1. risk of pneumomediastinum or pneumothorax; 2. risk of gastric distention and regurgitation; 3. trap-door obstruction; 4. vocal cord motion; 5. mucosal dehydration; 6. lower respiratory tract involvement; 7. inadequate ventilation; 8. hypocarbia; and 9. hypercarbia. These investigators did not look at Venturi ventilation as a substitute for endotracheal intubation, but rather, as an adjunct to their instrumentation for the expressed goal of "meeting the otolaryngologist's needs for unobstructed access to his surgical field."

Vaughan³³ wrote his candidate's thesis for the American Laryngological, Rhinological and Otolaryngological Society, Inc. in 1976 in which he discussed "Transoral Laryngeal Surgery Using the CO₂ Laser: Laboratory Experiments and Clinical Experience." Four problem areas associated with laser surgery were identified: 1. smoke and vapor; 2. hemostasis; 3. endotracheal tube; and 4. lack of experience with the CO₂ laser. Of the four problem areas, Vaughan cited the last-named as "the most significant and unique problem." He also performed tests of the combustibility of red rubber endotracheal tubes and noted that the laser beam, on full power, would burn

tube into a new technique in 1961. Oxygen was then reported through the tube at the time of laser beam penetration.

Hicks, *et al.* (1978)³⁴ discussed the use of the carbon dioxide laser in surgery of the larynx. They noted that this technology was most suited for laryngeal surgery and that recurrent respiratory papillomatosis in children was the most common indication for its use.

Norton and DeVos (1978)³⁵ developed and presented a new, nonreflective, metal endotracheal tube for carbon dioxide laser surgery of the larynx. At the time of their presentation to the American Broncho-Esophagological Association, they had used the tube in 77 patients, both adult and pediatric, and had worked out what they believed to be the early problems with their tube. They concluded their presentation by stating that they had "presented here in the solution to the last major problem involved in the use of the CO₂ laser for microsurgery of the larynx."

Publications describing complications associated with Venturi jet ventilation began to appear in the literature in 1978. Chang, *et al.*³⁶ described a case of severe abdominal distention in a 44-year-old man following jet ventilation for microlaryngeal surgery. The next year, Oliverio and his associates³⁷ published a case of pneumothorax accompanied by a pneumomediastinum and subcutaneous emphysema following jet ventilation for a carbon dioxide laser operation on a patient with recurrent respiratory papillomatosis of the larynx. The needle jet orifice was located below the vocal cords in this case.

Healy and his colleagues³⁸ published their experiences with the use of the carbon dioxide laser in the pediatric airway in 1979. Two precautions were discussed: protection of the patient's eyes with moist gauze pads and intubation with an aluminum tape-wrapped endotracheal tube. Healy noted that a fire would develop if the laser beam accidentally impacted a polyvinyl chloride endotracheal tube, and further stated that wrapping the tube with the aluminum covering would cause the beam to "be reflected harmlessly from the tube." He and his colleagues cited a complete lack of complications associated with the use of the laser at their institution.³⁹

In 1979, Andrews⁴⁰ recommended that the string attached to the neurosurgical cottonoids, used to protect the endotracheal tube cuff, be replaced with fine, nickel-plated jewelry chain. This suggestion followed the realization that the string would often be severed by the laser beam, which sometimes made removal of the cottonoids with microlaryngeal forceps difficult.

In the same year, DiBartolomeo⁴¹ published an extensive review of laser surgery in otolaryngology and recommended that Portex endotracheal tubes

be used for laser surgery.

Also in 1979, Benjamin and Gronow⁴² introduced a new catheter for Venturi ventilation for microlaryngeal surgery. The "Benjamin jet tube" or "Benjet tube" was made of fairly rigid plastic and came in both adult and pediatric sizes. Four soft plastic "petals" located at the distal end centered the tube in the trachea and prevented the tube from moving. After using this tube successfully in over 200 patients (pediatric and adult) for both conventional and laser microlaryngeal surgery, Benjamin and Gronow felt that it did not need to be protected with aluminum tape for laser surgery. Brown⁴³ utilized the "Benjet" tube to provide anesthesia for a patient undergoing microlaryngeal laser surgery for recurrent respiratory papillomatosis; during this procedure, the tip of the tube ignited and separated from the main body of the catheter. It was retrieved during bronchoscopy, which was immediately undertaken to assess the extent of the mucosal damage. Fortunately, the patient made an uneventful recovery.

Patil and his associates⁴⁴ published "A Modified Endotracheal Tube for Laser Microsurgery" in 1979. They wrapped commercially available muslin in a spiral manner around a red rubber or PVC endotracheal tube; the proximal end was secured with a heavy silk tie. Prior to intubation, the tube was soaked in a basin of saline and it was periodically saturated with saline during the procedure. After exposing this tube to multiple, short bursts of laser energy at the same site, they failed to cause an ignition or even a char to form at the site of impact.

Vourc'h and his co-workers⁴⁵ reviewed their experience in 257 patients undergoing microlaryngeal laser surgery in 1979. One fire occurred in a pediatric patient with a red rubber tracheostomy tube which had not been protected prior to beginning the procedure. The endotracheal tube was perforated by the laser beam in two patients without incident. In a third patient, a cottonoid which was left in the larynx caused respiratory obstruction upon extubation. The cottonoid was quickly removed and the respiratory distress reversed. Although they did not specify which tube they were using, Vourc'h and his associates did stress the importance of protecting the tube with aluminum foil tape. This group of physicians noted that "both oxygen and nitrous oxide support combustion and that it may be better to mix oxygen with air to reduce the risk of endotracheal tube fire." Later that year, Vourc'h, *et al.*⁴⁶ published a case report of a patient in whom they had experienced an endotracheal tube fire. At some point during the operation, the surgeon noted that "the cuff was burst and upon application of the next laser impact, the tube caught fire and flames erupted from the patient's mouth." The surgeon immediately pulled the tube (PVC) out and noted that it was

charred, even beneath the aluminum tape. The patient recovered without serious sequelae. Vourek's commented "that should the cuff become deflated during a procedure, then the tube must be removed, and the patient reintubated." He also cautioned against taping the tube too firmly to the patient, and emphasized the need for immediate removal of the tube, should a fire occur.

Burgess and LeJeune⁴⁷ published a case report of an endotracheal tube fire that occurred in a 6-year-old girl in 1979. They were ventilating through a reflective tape-wrapped PVC tube in the presence of 100% oxygen and believed that the ignition occurred because the unprotected extreme distal portion of the tube was hit by the laser. They mentioned that the ideal inspired-oxygen concentration should have been between 30% and 50%; however, because of this patient's history of intraoperative cardiac problems they chose to ventilate with 100% oxygen.

Later that same year, Kaeder and Hirshman⁴⁸ reported a case of acute airway obstruction during microlaryngeal and bronchoscopic carbon dioxide laser surgery in a patient with recurrent respiratory papillomatosis of the larynx and trachea. In this instance, passing the rigid bronchoscope during the procedure apparently dislodged some of the aluminum tape from the endotracheal tube, causing intraoperative airway obstruction when the bronchoscope was removed. The patient was subsequently extubated and reintubated with an unwrapped tube of the same size. Because the ventilation remained very difficult, Kaeder and Hirshman inspected the wrapped tube, which had been removed, and noted several areas of missing tape. Immediate endoscopic removal of the aluminum tape foreign bodies reversed the airway obstruction. Based on their experience with this case, Kaeder and Hirshman concluded that the tube should be checked at extubation "to make certain that all the tape is still present on the tube."

In 1980, Pratt⁴⁹ reviewed his experience with the carbon dioxide laser and noted that burning plastic tubes gave off toxic fumes not produced by burning red rubber tubes.

Carruth and his colleagues (1980)⁵⁰ reviewed the safety aspects of carbon dioxide laser surgery in their practice and recommended the appointment of a "Laser Safety Officer" and the establishment of a "Safety Code for the use of the laser in the Operating Theatre." Additionally, they cited two main dangers associated with the use of the laser: remote tissue damage to the patient or a member of the operating room team from either direct or reflected laser energy, and ignition of the endotracheal tube. Carruth and his associates recommended that all personnel in the operating room wear protective glasses and that the patient's eyes be protected by saline-saturated eye pads. Plastic or rubber endo-

tracheal tubes had to be protected with red aluminum tape. They suggested that the otolaryngologist work as a team with an anesthesiologist thoroughly familiar with the problems and techniques of laser surgery of the upper airway.

During the same year, Hirshman and Smith⁵¹ described the risk of "Indirect Ignition of the Endotracheal Tube During Carbon Dioxide Laser Surgery." This new contribution to the literature stressed the need to develop nonflammable endotracheal tubes for laser surgery. Because the inner walls of the endotracheal tube could not be protected with aluminum tape or some other reflective material, the possibility of flaming tissue causing ignition of the tube by being either drawn through the tube on exhalation or by being merely in close proximity to the distal end of the tube was a real risk. The fire that Hirshman and Smith experienced was postulated to have occurred in this way. These investigators⁵² also performed studies to determine if there was any combination of anesthetic gases that would be less flammable than the oxygen-nitrous oxide mixtures commonly used. They noted that tubes did not burn in room air, but did ignite in 100% oxygen, 100% nitrous oxide, or in any combination of the two. They also concluded that the red rubber tubes burned more easily than did the polyvinyl chloride tubes. Strong⁵³ commented on Hirshman and Smith's publication through an editorial immediately following their article. He corroborated their findings and also stated that "the CO₂ laser is a truly remarkable instrument, but it is up to us as surgeons to be careful with its use so that we can bring its benefits to our patients with an absolute minimum risk."

Hirshman and her co-workers⁵⁴ also presented a new endotracheal tube for carbon dioxide laser surgery of the airway in 1980. This tube was designed for use with the technique of Venturi jet ventilation and was constructed of metal.

Torres and Reynolds⁵⁵ introduced a modified, longer than normal, 4-mm I.D. cuffed PVC endotracheal tube later that same year. These authors strongly recommended that it be wrapped with aluminum tape when used for laser surgery. Kalhan and Regan (1980)⁵⁶ introduced a further modification to the tube of Patil, *et al.*⁴⁴ by including an epidural catheter alongside the endotracheal tube, prior to wrapping it in muslin. The infusion of saline into the catheter kept the muslin saturated and, thus, reduced the risk of ignition.

Rontal, *et al.*⁵⁷ reviewed their experience with jet ventilation for microlaryngeal surgery in 1980. These investigators demonstrated the safety of this technique; however, they recommended that the catheter be wrapped in aluminum tape, prior to performing laser surgery. No complications were cited in their review. During the same year, Chang and his

surgery.⁵⁸

Clinical Experience with the Carbon Dioxide Laser in Microlaryngeal Surgery: The Age of Proliferation, Increased Complications, and Testing (1981-1986)

In 1981, reports of complications associated with performing microlaryngeal carbon dioxide laser surgery began to appear in the otolaryngology-head and neck surgery literature. Many of these reports discussed the individual author's experiences with endotracheal tube fires, and included data from testing the numerous endotracheal tubes available for use at the time of the reports, in an attempt to determine which tube was the safest for microlaryngeal laser surgery.

Meyers⁵⁹ reported a case of an endotracheal tube fire (aluminum tape-wrapped polyvinyl chloride tube) that occurred while using the laser to treat a 28-year-old male with recurrent respiratory papillomatosis of the larynx. During the procedure, the cuff of the tube was inadvertently deflated and additional cottonoids were placed into the subglottic larynx in an attempt to assure an adequate seal and protect the tube. Shortly thereafter, the endotracheal tube ignited and was quickly removed from the airway. The patient was immediately reintubated and intravenous Decadron[®] and ampicillin were administered. Rigid bronchoscopy was performed and a neurosurgical cottonoid foreign body was discovered approximately 1 cm above the carina. The foreign body was removed and the patient recovered uneventfully.

Meyers tested polyvinyl chloride and red rubber endotracheal tubes to determine their resistance to penetration and fire, when laser energies comparable to those used in surgery were applied to these tubes in the presence of 50% and 100% oxygen. His results indicated that the red rubber tubes were less flammable and, therefore, safer to use in conjunction with carbon dioxide laser surgery. He further noted that the cuff of each was equally vulnerable to penetration by the laser and that "a new endotracheal tube equipped with a balloon capable of withstanding usual doses of laser irradiation is needed." Other conclusions drawn by Meyers included the need to extubate and reintubate if the cuff was deflated by the laser, the frequent need to remoisten both cottonoids and their strings during the procedure, placement of the endotracheal tube cuff far below the undersurface of the vocal cords, use of adhesive tape-wrapped red rubber tubes, and the absolute need for the surgeon to be prepared ahead of time to handle an endotracheal tube fire, should it occur.

Alberti (1981)⁶⁰ published an extensive review of the literature, as it dealt with laser-related complications. Although no new complications were pre-

dications in otolaryngology-head and neck surgery, he stated that the literature by 1981 included the need to use instruments with nonreflective matt finish surfaces, to reduce the potential for personnel and/or tissue injury from beam reflection, the requirement that the staff be well-trained in laser surgery, the use of a moist stockinette covering for the endotracheal tube, and the provision for adequate smoke evacuation from the operative site.

Schramm, *et al.* (1981)⁶¹ published "Acute Management of Laser-Ignited Intratracheal Explosion" in which they presented their observations and recommendations, based on two cases, of airway management following laser-ignited endotracheal tube fires. Several important factors emerged from their paper, including comments about the incendiary characteristics of both red rubber and polyvinyl chloride tubes, the use of water or saline as a heat sink, and the need to keep the concentration of oxygen in the anesthetic gas mixture below 40%. Schramm, *et al.* described, in detail, the pathophysiology of an airway burn and differentiated it from the intratracheal explosion burn characteristic of the laser type of injury. They stated that "the degree of burn depends on the duration of heat exposure" and emphasized that the first step in the management of this type of accident is the simultaneous removal of the burning tube and shutting off the anesthetic gases. They also pointed out that the hydrochloride gases associated with burning polyvinyl chloride tubes were toxic to the airway and could be associated with severe pneumonitis.

Schramm, *et al.* stressed the absolute requirement that the surgeon and operating room team have "prior training and rehearsal" to avoid even a momentary delay in the management of the emergency. Rigid bronchoscopy followed by flexible bronchoscopy were cited as the initial steps in the damage evaluation following reintubation and stabilization of the patient. If foreign bodies were encountered, they should be removed; attempts should be made to wash away any black carbonaceous debris that may have been deposited secondary to the fire. This publication included a table that outlined, in step-by-step fashion, the management of an airway explosion.

During the same year, Fried⁶² reviewed laser-related complications cited in the literature. He found four reported cases of direct endotracheal tube ignitions, none of which resulted in serious sequelae. It was his impression that the "phase of development and application had passed" and that it was now time to "assess possible complications of widespread use of this remarkable device."

Treyve, *et al.* (1981)⁶³ studied the incendiary characteristics of four different types of endotracheal

They also reported that their purpose was to define safe laser and oxygen concentration parameters, to preclude the possible ignition of an endotracheal tube. They utilized the Cavitron[®] laser, which had a 2-mm spot size when used for microlaryngeal laser surgery, and found that the polyvinyl chloride (PVC) tube, without an impregnated line, was the safest tube of the four that they tested (American Hospital Supply PVC tube, Portex tube, polyvinyl chloride tube, and red rubber tube). They also found that the impregnated line, common to many of the endotracheal tubes, exploded violently and represented a more vulnerable area on the American Hospital and Portex tubes than the shaft itself. Treyve, *et al.* noted that their findings differed from those of Meyers and others who had concluded that the red rubber tubes were safer than the PVC tubes. The discussion of these findings by Treyve, *et al.* was noteworthy because it drew attention to the possible existence of both laser and tube variables.

In 1982, Yarrington and Thompson⁶⁴ published a supplemental report to their 1981 study in which they studied a new silicone tube. Although they stated that the previous experimental studies using this new tube were duplicated, the oxygen concentration reference they cited was 20% rather than the 30% cited in their 1981 study. These authors were unable to achieve combustion with this new tube and concluded that such tubes, in oxygen levels of 20%, "might offer a reasonably safe route for anesthesia when using the carbon dioxide laser."

In 1981, Ruder, *et al.*⁶⁵ retrospectively reviewed 253 cases of microlaryngeal laser surgery performed using jet ventilation. In this presentation, the authors discussed Abramson's modification to the Dedo laryngoscope, to which four ports were added to facilitate placement of the jet ventilation needle. The orifice of the needle was situated below the vocal cords in all cases in this report. Two complications occurred in their series—both related to barotrauma. The distally located (below the vocal cords) jet ventilation needle used by this group of investigators may have increased the potential for a barotrauma-type injury to occur in their patient population. These authors concluded that jet ventilation was superior to traditional techniques of anesthesia for laser surgery because "the endotracheal tube was eliminated, thus improving the surgical field and reducing burn hazards owing to ignition of the tube." They cited three contraindications to the use of jet ventilation: 1. obesity; 2. large obstructing laryngeal lesions; and 3. poor chest wall or lung compliance.

Kumar and Frost (1981)⁶⁶ described another endotracheal tube modification for laser surgery. Here, the authors applied dental acrylic to the outside of the endotracheal tube to protect it from the heat and

avoided all the above contribution, as well as on previous contributions to the literature by Hirshman, *et al.*⁶⁷ Vourel, *et al.*⁶⁸ and Kaeder and Hirshman.⁶⁹ He suggested that a nonflammable endotracheal tube would solve the problem and, until such a tube became available, jet ventilation should be strongly considered as the anesthetic technique of choice for patients requiring microlaryngeal laser surgery.

Wainwright, *et al.*⁶⁸ reviewed their anesthetic experience for microlaryngeal laser surgery in 1981 and included a lengthy description of the disadvantages of wrapping tubes. They also pointed out, once again, that nitrous oxide supported combustion as efficiently as oxygen; therefore, reducing the oxygen concentration in nitrous oxide would do nothing to reduce the risk of laser-ignited endotracheal tube fires.

Kalhan and Cascorbi⁶⁹ reviewed the literature and published their experiences with laser surgery in 1981. They noted six problems for the anesthesiologist that the use of lasers in otolaryngology had created: 1. shared airway; 2. possibility of airway fire; 3. perforation of tube cuff; 4. drying of muslin or cottonoids; 5. possibility of ocular injury; and 6. need for paralysis. Their preferred technique employed small endotracheal tubes, wrapped either in muslin with the epidural catheter or in aluminum tape.

During the same year, Cozine and her co-workers⁷⁰ reported the first serious laser-ignited endotracheal tube fire. The accident occurred during laser surgery with a wrapped, cuffed PVC tube where saline-saturated cottonoids had been placed to protect the cuff. The authors concluded that the laser beam had either come in contact with the unprotected distal portion of the tube or that the cottonoids had dried out immediately prior to the fire. Unlike previously reported cases of endotracheal tube fires following laser surgery of the larynx in which the patient recovered without incident, the injury suffered by the patient in this instance was extensive to both the airway and the parenchyma of the lung.

Patel and Hicks (1981)⁷¹ published an endotracheal tube study in which they compared the incendiary properties of the Rusch red rubber tube and the Portex PVC tube in an *in vitro* experiment. Mixtures of 25% oxygen and 60% oxygen in nitrous oxide were passed through the tubes in a controlled environment while the laser power settings were at either 15 or 30 W, and the time settings increased from 15 to 500 msec. The results of their study demonstrated that the PVC tubes were more easily penetrated and ignited more readily than did the red rubber tubes. Based on these results, the authors concluded that "Rusch red rubber tubes should be used in preference to PVC Portex tubes." They also concluded that the tubes had to be protected with

25% in nitrous oxide.

LeJeune and his colleagues⁷ presented a major contribution towards solving the endotracheal tube cuff problem at the 1982 Annual Meeting of the American Broncho-Esophagological Association. By filling the endotracheal tube cuff with saline rather than the commonly utilized air, LeJeune, *et al.* were able to defuse the cuff as a potential kindling site for a laser-ignited endotracheal tube fire. Their solution to the cuff problem worked because the saline would either act as a heat sink, helping to prevent perforation of the cuff, or in case the cuff became perforated by the laser beam, the saline-filled cuff would act as a fire hose, spraying the area with saline that would cool and extinguish any potential combustion.

Healy and his colleagues⁷³ reviewed their unique, laser-related complications associated with performing 4,416 cases of surgery of the aerodigestive tract requiring the use of the carbon dioxide laser in 1982. They identified nine complications in this group of 4,416 cases, for an overall complication rate of 0.2%. Four of these complications were associated with endotracheal tube fires, all of which occurred early in their experience, prior to protecting the tubes with reflective metallic tape. A fifth fire occurred while Healy and his colleagues were performing rigid bronchoscopic carbon dioxide laser surgery; here, the latex cuff around the bronchoscope ignited. The sixth fire in their series occurred when a surgical sponge used to occlude a tracheostoma during bronchoscopic laser surgery suddenly ignited. None of the fires resulted in serious injury. The other complications in their series included a facial burn from an imperfectly aligned laser beam heating a bronchoscope that was in contact with the skin of the face, and two cases of bleeding while resecting obstructing tracheobronchial carcinoma.

Several important issues related to safety were discussed by Healy, *et al.* First, they believed that anesthetic delivery systems presented the single greatest risk of complications associated with laser surgery. Second, they supported LeJeune's contribution of filling the cuff with saline. Third, they warned against vaporizing tissue located distal to the tip of the endotracheal tube to prevent indirect ignition; this important, potential hazard was previously discussed by Hirshman and Smith.⁵¹ Fourth, they suggested cleaning the red rubber tubes with acetone and spraying them with benzoin prior to wrapping with the reflective metallic tape. Their description of tube wrapping was the most complete, to date, in the literature. Fifth, Healy, *et al.* made recommendations about the anesthetic management of patients with tracheotomies, and suggested using either metal tubes or reflective tape-wrapped red rubber tubes. Finally, Healy and his colleagues cautioned against using mylar tape, which looked like the reflective metallic tape, but

During the course of the review of the literature, in which a laser-induced endotracheal tube fire occurred following endotracheal intubation. In this report, the authors discovered a tear in the anterior tracheal wall following a microlaryngeal laser procedure performed using a Norton tube. It was concluded that the tracheal injury was most probably induced by a portion of the beam passing between the vocal cords and continually striking and burning through the anterior tracheal wall. The patient recovered uneventfully.

In 1983, Ossoff and Karlan⁷⁵ presented a set of instruments that they developed for microlaryngeal carbon dioxide laser surgery. Their rationale for these new, modified instruments included both safety and ease of use. The operating platform was "the most significant instrument in the set" and served as a "catcher's mitt to protect the cottonoids, endotracheal tube and cuff, and tissues of the subglottic larynx from any direct or reflected laser beam irradiation. Thus the risk of ignition of the endotracheal tube is markedly reduced." They stated that the surfaces of the instruments in their set had been treated to "provide for maximum dispersion of any reflected laser energy."

Also in 1983, Ossoff, *et al.*⁷⁶ reviewed their experiences with 204 cases and 12 laser-related complications at their institution over a 2-year period. One extraluminal endotracheal tube fire that occurred early in their work with the carbon dioxide laser prompted a departmental review and "formulation and implementation of a laser safety protocol." All cases included in this paper were operated upon under the provisions of this safety protocol that included, in addition to many of the previously referenced precautions, a few new items. First, Ossoff, *et al.* inflated the endotracheal tube cuff with methylene-blue-colored saline to facilitate the surgeon differentiating saline-saturated cottonoids (normal cuff) from saline-saturated cottonoids (perforated cuff). In the latter instance, the cottonoids would turn blue. Second, use of the "operating platform" was recommended as an added layer of protection for the endotracheal tube cuff, subglottic larynx, and saline-saturated cottonoids. Third, the entire face and neck of the patient were protected with saline-saturated surgical towels to prevent any possibility of reflected laser burn. In the past, only the lips had been protected with saline-saturated gauze sponges. Fourth, Ossoff and his colleagues mandated that all personnel in contact with the laser in the operating room environment have some "exposure to laser education." Attendance at a laser education program became the primary requirement for certification for use of the laser. Attending surgeons were required to take a "hands-on" laser course prior to receiving permission to use the laser: "attendance at a one-day didactic session was not considered adequate."

service on anesthetic techniques and precautions, and operating room personnel had to attend an in-service conducted by the department of nursing. Of the 12 complications cited in this publication, 2 were finger burns suffered by the surgeon and 10 were minor patient-related accidents. No instances of endotracheal tube fires were recorded by Ossoff, *et al.* while working under the aforementioned safety protocol.

Ossoff, *et al.*⁷⁷ studied the tracheal damage secondary to laser-ignited endotracheal tube fires in 1983. After a 5-second exposure to a planned, laser-ignited endotracheal tube fire using either red rubber, polyvinyl chloride, or silicone tubes in a 30% oxygen, 70% nitrous oxide anesthetic gas mixture, the experimental animal was killed and sections of the trachea were submitted for histologic evaluation. Polyvinyl chloride tubes caused the most damage, both grossly and histologically, and this group of investigators stated that they should not be used for laser surgery. Because silica ash was found throughout the tracheobronchial tree after the fires using the silicone tube, Ossoff, *et al.* cautioned against its use until the effects of this ash could be determined. The least gross and histological damage was noted following the fires using the red rubber tubes, and the authors concluded that these tubes, when wrapped with reflective tape, probably were the safest to use for carbon dioxide laser surgery.

Later that same year, Ossoff and Karlan⁷⁸ presented "Safe Instrumentation in Laser Surgery" in which they discussed three general areas of concern: 1. nonflammable instrumentation; 2. nonreflective instrument-surface preparation; and 3. provision for adequate smoke evacuation. A detailed description of the anesthetic management of the airway in patients undergoing microlaryngeal laser surgery was included in this paper. Specifically, the authors noted that, at the time of their publication, a "universally accepted endotracheal tube for carbon dioxide laser surgery of the upper aerodigestive tract" did not exist. They advocated using the Rusch red rubber tube wrapped with reflective tape.

Fried (1983)⁷ presented the results of "A Survey of the Complications of Laser Laryngoscopy" that he had sent out to 229 members of a senior otolaryngology society. His results were based upon receiving responses from 210 of the 229 polled otolaryngologists (91.7% response rate). Fifty-seven respondents did not use the laser (27.2%) and another 103 surgeons used the laser without any complications (49%). The remaining 49 otolaryngologists (23.3%) had all experienced at least one complication while using the laser. Fried commented that he thought the laser-associated complication rate was higher than that suggested by the literature; this hypothesis was proven by his survey, which identified 28 instances of endotracheal explosion, 9 facial burns, 3 endotracheal tube cuff ignitions and 2 cot-

ted in his presentation. The 33 documented ignitions (tube, cuff, and cottonoid) among 49 senior otolaryngologists was both striking and alarming. Fried postulated that perhaps there was no direct correlation between "increased experience leading to fewer complications" with respect to laser surgery. He concluded that both the otolaryngologist and anesthesiologist "should have adequate knowledge and training" before using the laser clinically in their practice.

During the same year, Woo and Vaughan⁷⁹ introduced the idea of using Norton's metal tube as a conduit for jet ventilation. They cited several advantages of this all-metal system: the most obvious being the elimination of all potentially flammable materials from the airway.

Chilcoat, *et al.* (1983)⁸⁰ published a short message in the anesthesiology literature discussing "The Hazard of Nitrous Oxide During Laser Endoscopic Surgery." Once again, it was stressed that the reduction in oxygen concentration by dilution with nitrous oxide did not provide any additional safety when performing laryngeal laser surgery. Chilcoat went on to recommend the use of either nitrogen, air, or helium, when it was desired to reduce the oxygen concentration in the anesthetic gas mixture to levels of 30% or less for laser surgery.

Hermens, *et al.*⁸¹ published an extensive review of the literature as it related to anesthesia for laryngeal laser surgery in 1983. They reemphasized that nitrous oxide supported combustion almost as well as oxygen. Other important observations included their suggestion that, since both red rubber and PVC tubes have been demonstrated to burn, adequate protection in the form of reflective tape and saline-saturated cottonoids should be used with each, to minimize the risk of combustion. These authors were the first to use copper metallic tape as an alternative to aluminum tape for tube wrapping. Additionally, they calculated the reported incidence of endotracheal tube ignition to be between 0.4% and 1.5%, based on reported cases in the literature.

Brightwell (1983)⁸² published a case report in which he described a severe case of epistaxis requiring posterior packing and transfusion for management, following nasotracheal intubation with a reflective tape-wrapped endotracheal tube for laser surgery. He labeled this case as a complication of laser surgery.

Norton (1983)⁸³ published a review of anesthetic techniques for laryngeal laser surgery. He cited four hazards unique to the use of the laser: 1. fire hazards; 2. improper focusing of the incident beam; 3. perforation of tissues; and 4. beam reflection. This article contained an excellent review of the principles of Venturi ventilation. Norton also included a

was no longer considered experimental. He referenced the courses in laser surgery conducted at Boston University and stated that "failure to obtain proper instruction places the burden on the physician and hospital to demonstrate adequate preparation for this deceptively simple therapeutic modality."

Andrews⁸⁴ reviewed his 10-year experience with 304 patients and 734 surgeries using the carbon dioxide laser in 1984. No accidents occurred that were directly related to the use of the laser. In all cases, a red rubber tube wrapped with aluminum tape was used, and the concentration of oxygen in the anesthetic gas mixture was maintained below 50%.

In 1984, Johans and Reichert⁸⁵ published a modification of the Andrews anterior-commissure retractor for use as a delivery device for jet ventilation, in cases where the pathology occurred in the subglottic larynx. Benjamin⁸⁶ reviewed anesthetic techniques for laryngoscopy and presented a new laryngoscope with a jet ventilation adapter during the same year. He described his new pediatric laryngoscope with insufflation channel as being particularly useful for laser surgery.

During the same year, Silver and his co-workers⁸⁷ reported a new prototype airway system for laser surgery. This involved the use of a "parachute cuff" mounted on a Norton endotracheal tube.

Hayes, *et al.*⁸⁸ presented results from their investigation of the incendiary characteristics of a new "laser-resistant" endotracheal tube in 1984. They compared the new tube with a polyvinyl chloride tube and a red rubber tube in both varying oxygen/nitrous oxide/nitrogen concentrations, as well as varying laser power settings. Hayes, *et al.* did not wrap any of these tubes because they wanted to study the tube itself, and not any artificial protection administered to the tube. They found the new "laser-resistant" silicone tube most resistant to laser energy; in fact, it only ignited when exposed to continuous laser irradiation for between 2 to 6 seconds at laser power settings higher than would normally be used in performing microlaryngeal laser surgery. It would not ignite when exposed to single laser pulses of up to 25 W for 1 second. Increasing the oxygen concentration made the "laser-resistant" tube, as well as the PVC and red rubber tubes, more susceptible to combustion. Hayes, *et al.* suggested using the lowest oxygen concentration (less than 30%) "consistent with safe patient management." They stated that the risk of endotracheal tube ignition substantially increased when oxygen concentrations greater than 30% were used.

In 1985, Ohashi and his colleagues⁸⁹ studied the hazard to endotracheal tubes posed by the carbon dioxide laser. They irradiated polyvinyl chloride and silicone tubes in different oxygen concentrations

and found that ignition may occur when the laser was set above 30 W in the presence of 100% oxygen. They also determined that four layers of saline-saturated cottonoids were required to protect the cuff from penetration by the laser beam.

In 1985, O'Sullivan and Healy⁹⁰ published an excellent and extensive review of the complications of jet ventilation during microlaryngeal laser surgery. They found seven reported complications, including one death, in the literature and added an eighth complication—a case of bilateral pneumothorax in an 11-week-old infant.

Also in 1985, Pashayan and Gravenstein⁹¹ published a manuscript entitled, "Helium Retards Endotracheal Tube Fires from Carbon Dioxide Lasers." Because both oxygen and nitrous oxide have been previously shown to support combustion of endotracheal tubes near laser energy, the authors investigated two inert gases—helium and nitrogen—to determine if the addition of one of these gases to oxygen could delay ignition of endotracheal tubes, when exposed to a carbon dioxide laser beam. Their study was well designed and analyzed in an appropriate manner. They concluded that helium, but not nitrogen, significantly retarded endotracheal tube ignition (PVC tubes) when it was present in a concentration of 60% or more, and the laser was set to 10 W or less of energy bursts of 10 seconds or less. The addition of 2% halothane to the gas mixture slightly reduced the beneficial effects of helium. The radiopaque barium sulfate stripe on the endotracheal tube was also tested and was found to be far more flammable than the PVC tube. For this reason, these investigators have suggested that the tube be turned so that this stripe would lie outside of the laser's range, or better, that tubes without these stripes be used for laser surgery. Pashayan and Gravenstein did not recommend wrapping the PVC tubes with any protective tape or using saline-saturated cottonoids to protect the cuff.

Lim and Kenney (1986)⁹² reviewed 3,500 otolaryngologic procedures in which they had used the carbon dioxide laser. The authors reported a 0.17% complication rate with 6 instances of laser-related patient complications in the 3,500 cases; 1 of these complications was a laser-ignited endotracheal tube fire that occurred in a patient intubated with a Rusch red rubber tube.

Review of the literature to this point has demonstrated that the true state of the art with respect to the safe anesthetic management of the airway of the patient undergoing carbon dioxide laser surgery of the larynx has not yet been adequately defined. Specifically, a well-read otolaryngologist—head and neck surgeon or anesthesiologist would have found that there had not been uniform agreement in the literature regarding the choice of anesthetic tech-

endotracheal tube and cuff, and choice of gas to dilute the concentration of oxygen in the anesthetic gas mixture. Furthermore, the well-read otolaryngologist would have also questioned whether attendance at a laser course, as recommended by Norton,¹ would have helped to reduce the risk of laser-ignited tube fires and other complications associated with the use of this technology.

Fried's publication² discussing the results of the survey he conducted on laser-related complications experienced by members of a senior otolaryngology society certainly reinforced Norton's recommendation. Until the time of Fried's presentation at the 1983 Annual Meeting of the American Society for Head and Neck Surgery, there had been a significant number of publications in both the anesthesiology and otolaryngology—head and neck surgery literature that specifically warned the reader of the risk of an endotracheal tube fire when performing microlaryngeal surgery with the carbon dioxide laser. His presentation, detailing 28 endotracheal tube fires, 3 endotracheal tube cuff ignitions, and 2 cottonoid ignitions among a total of 81 complications reported by 47 of the 210 respondents to his survey, certainly raised doubts about the adequacy of the literature as a method of transferring vital information concerning laser safety to the practicing otolaryngologist—head and neck surgeon.

MATERIALS AND METHODS

The discussion of the materials and methods used in this study is divided into two sections. The first part deals exclusively with the "hands-on" laser surgery course and the questionnaire on laser-related complications mailed to all past registrants of the workshop. The second part describes the materials and methods used to perform the tests on the incendiary characteristics of the endotracheal tubes used in this study.

Survey of Laser-Related Complications

In an attempt to determine if attendance at a "hands-on" laser surgery course might lead to a reduced rate of laser-related complications experienced by otolaryngologists who attended the course when compared to a selected group of otolaryngologists who were members of a senior otolaryngology society previously surveyed by Fried (1984)³ solely on the basis of their society membership, a similar questionnaire to that published by Fried was developed (Table I). This questionnaire was mailed to 337 otolaryngologist—head and neck surgeons in attendance at a "hands-on" laser surgery course between August 1981 and December 1985. The didactic portion of the course stressed laser biophysics, tissue interactions, applications in the larynx, oral cavity, and tracheobronchial tree, anesthetic techniques and precautions, and laser safety (Table II). During the didactic section of this course, a laser safety protocol was discussed in detail; as changes in the state of the art with respect to laser safety evolved, this protocol was updated (Table III). All complications either experienced by the faculty of the course, published in the literature, or presented at a national or regional meeting were discussed and examined to emphasize for the registrants what could go wrong, why it went wrong, and how to avoid it. Videotapes demonstrating the exercises to be performed in an introductory lab, a microlaryngeal lab, a macroscopic lab, and a bronchoscopic lab were shown before course participants were allowed to perform these exercises under the supervision of the

Laser Workshop Questionnaire

1. Did you use the laser prior to attending the "hands-on" workshop?
YES _____ NO _____
 2. Were you using this laser prior to attending the "hands-on" workshop?
YES _____ NO _____
 3. If not, how long have you used it since the workshop?

 4. Was the course instrumental in your decision to use the laser clinically?
YES _____ NO _____
 5. Do you think you would/could have begun to use the laser clinically without a "hands-on" course?
YES _____ NO _____
 6. Did you use the laser in a lab or on cadaver material upon your return from taking the course prior to using it clinically?
YES _____ NO _____
 7. Have you performed any basic scientific investigations in your lab or hospital using the laser, i.e., histological studies, etc.?
YES _____ NO _____
If you answered yes, please describe the study.
 8. How long, approximately, did it take you to become comfortable using the laser clinically?

 9. In what percentage of your microlaryngoscopy cases do you use the laser?

 10. In what percentage of your bronchoscopy cases do you use the laser?

 11. In what type of endoscopic cases do you find the laser most useful?

 12. In what type of endoscopic cases do you find the laser least useful?

 13. Are there any endoscopic cases in which you find the laser absolutely indicated, i.e., you would not do them without the laser? If so, which cases?
YES _____ NO _____
 14. Approximately how many endoscopic laser cases have you performed? Approximately how many endoscopic cases do you perform each month?

 15. Have you found the safety protocol taught during the "hands-on" workshop that you attended to be efficacious?
YES _____ NO _____
If no, please elaborate.
 16. Have you had any complication(s) using the carbon dioxide laser?
YES _____ NO _____
If yes, how many complication(s) have you had?
Did the complication(s) occur before or after taking the course?
BEFORE _____ AFTER _____
 17. If you have had complication(s), please list them and the eventual outcome. Use the back of this sheet if necessary.
Surgical Procedure _____ Complication _____ Outcome _____
 18. Do you have any specific ideas on how laser education could be improved?
YES _____ NO _____
If yes, please elaborate.
- Thank you for taking the time to fill out this questionnaire.

faculty. An endotracheal tube fire was demonstrated at each course at the end of the first day's microlaryngeal laboratory. A second microlaryngeal laboratory was conducted on day 2; this served to reinforce the skills required to perform microlaryngeal laser surgery using the unique delivery system (micromanipulator and joy stick) required for laryngeal laser surgery. A syllabus was distributed that contained outlines of the laboratory exercises with suggested power density settings, reprints of important laser-related publications including those on safety and complications, abstracts of each lecture given during the course, and a list of up-to-date references on the use of the carbon dioxide laser in otolaryngology—head and neck surgery.

Tests on the Incendiary Characteristics of Endotracheal Tubes

Experiments on the incendiary characteristics of the endotracheal tubes used in this study were divided into three parts. First, the tubes were tested in the presence of varying oxygen concentrations diluted in either helium or nitrogen using the laser in the shuttered (pulsed) mode with 0.1-second exposures. After completion of this first part of this experiment, the tubes were then tested using the same protocol with one exception—

Didactic Portion:

1. Laser Physics and Tissue Interaction.
2. Laser Surgery for Benign Laryngeal Disease.
3. Laser Surgery of the Oral Cavity.
4. Endoscopic Management of Selected Early Glottic Carcinomas.
5. Anesthetic Techniques and Precautions.

Laboratory Exercises:

1. Introductory Laser Laboratory.
2. Laryngeal Applications Laboratory I.
3. Demonstration: Endotracheal Tube Fire.

Day 2

Didactic Portion:

1. Advantages, Precautions, and Complications.
2. Bronchoscopic Laser Surgery.

Laboratory Exercises:

1. Laryngeal Applications Laboratory II.
2. Bronchoscopic Laser Laboratory.
3. Oral Cavity/Oropharyngeal Laser Laboratory.
4. Final Discussion.

the laser was now used in the continuous mode. The third part of this experiment studied the thermal absorptive qualities of each tube, using a thermocouple.

Gases were delivered through the circuit of a Vernitrol® Vaporizing System laboratory anesthesia unit (Ohmeda Products, Division of the BOC Group, Inc.) at a rate of 2.5 or 3 liters per minute. These flow rates simulated standard anesthesia conditions in the adult; the reduced flow rate of 2.5 liters per minute was used in the 2% halothane experiments to facilitate reading the concentrations of halothane in oxygen when using the Vernitrol Vaporizing System. The final oxygen concentration was measured using an Instrumentation Laboratory Sensor Labs Division oxygen analyzer. The endotracheal tube was suspended from a ringstand (Fig. 1); a flame-retardant shield was placed beneath the tube to protect the laboratory counter top from ignition, and a Geraci-Miller gas evacuator was used to collect the anesthetic gases exiting from the distal end of the tube (Fig. 2). A Kelly clamp was positioned on the gas hose leading from the anesthesia machine to the tube to facilitate clamping the hose when a fire occurred, thus shutting off the supply of oxygen flowing to the tube which in turn would help to extinguish the experimental laser-ignited tube fire. Once the fire was extinguished, the burned portion of the tube was discarded and the remainder of the tube was allowed to cool for 90 seconds before the next trial.

A Sharplan® model 733 carbon dioxide laser with a maximum power output of 40 W was used. The laser was coupled to a Zeiss operating microscope using the Sharplan microslad coupler (Fig. 3). The microscope objective lens and laser focusing lens used for these studies had a focal length of 400 mm which produced a surgical spot size of 0.8 mm. Laser calibrations were performed prior to beginning these experiments, using a Coherent® power meter. The laser was used at powers of 10 (1,992 W/cm²), 15 (2,988 W/cm²), and 20 (3,984 W/cm²) W in the shuttered mode for a maximum of 60 pulses (each pulse lasting for 0.1 second in 1-second intervals) and in the continuous mode for a maximum of 180 seconds. The repeat pulse mode was not used in this study. The number of pulses or time in seconds required by the laser to ignite the tube was recorded. The angle of incidence was 90°. Each gas mixture was tested at each power setting for a minimum of 13 times in the pulsed mode and eight times in the continuous mode.

Using the above-referenced protocol, National Catheter 6.0-mm I.D. polyvinyl chloride endotracheal tubes, Rusch® red rubber

I. Eye protection

A. Patient

1. Tape patient's eyes shut
2. Double layer of saline-saturated eye pads placed over the patient's eyes

B. Operating room personnel

1. Wear protective glasses with side protectors
2. Surgeon does not require protective glasses when working with the operating microscope

C. Warning signs

1. Placed outside of all entrances into the operating room where the laser is used
2. Caution persons entering the room that the laser is in use and that protective glasses are required

D. Limited access

1. Limit traffic into the operating room when the laser is in use
2. Keep doors to the operating room closed when laser is in use

II. Skin protection

- A. Use a double layer of saline-saturated surgical towels, surgical sponges, or lap pads to cover all exposed skin and mucous membranes of the patient outside of the surgical field

1. Keep this protective layer wet during the case

2. Do not forget to protect the teeth, when exposed

- B. When microlaryngeal surgery is performed, the patient's face is completely draped with saline-saturated towels

III. Smoke evacuation

- A. Aspirate laser-induced smoke from the operative field

- B. Have two separate suction setups available in the operating room

1. One suction for laser-induced smoke and steam

2. One suction for blood and mucous

- C. Use filters in the suction lines for the laser-induced smoke and steam

IV. Anesthetic considerations

- A. Use of nonflammable general anesthetic

- B. Limit oxygen concentration to maximum of 40%

1. Mix oxygen with helium, nitrogen, or air—do not use nitrous oxide

2. Mix oxygen with helium

- C. Use Rusch red rubber endotracheal tube wrapped with reflective metallic tape

- D. Protection of the endotracheal tube cuff

1. Use saline-saturated cottonoids to protect the endotracheal tube cuff

- a. Keep the cottonoids moist

- b. Count the cottonoids

2. Inflate the cuff with saline

3. Use methylene blue colored saline to inflate cuff

4. Use the operating platform

V. Instrument selection

- A. Use of wide-bore microlaryngoscope

- B. Choose instruments with a nonreflective surface

6.0-mm I.D. endotracheal tubes, and Xomed Laser-Shield® 6.0-mm I.D. endotracheal tubes were tested with 100% oxygen using the laser in the shuttered mode. Because the laser burned through the PVC tube before it ignited, a sheet of white paper was placed under the tube, thereby allowing the number of pulses required to burn through the tube to be recorded. Following the experiments using 100% oxygen, similar studies were run using 30%, 40%, and 50% oxygen in nitrogen and 30%, 40%, and 50% oxygen in helium. The oxygen or oxygen gas mixture was delivered at 3 liters per minute. Following this part of the study, PVC tubes wrapped in either 3-M #425 or Radio Shack #44-1155 aluminum tape were tested with 100% oxygen, using the above-referenced laser parameters.

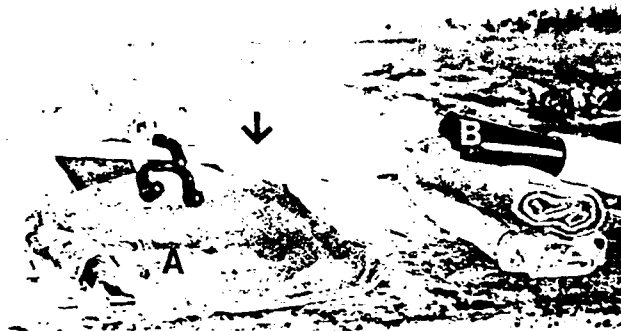


Fig. 1. Rusch red rubber endotracheal tube suspended from a ring-stand (arrow). Note the flame-retardant shield beneath the tube (A) and the distal end of the Geraci-Miller gas evacuator in the field (B).

In the second part of this experiment, National Catheter PVC, Rusch red rubber, and Xomed Laser-Shield endotracheal tubes were tested using the laser in the continuous mode; here, 30%, 40%, and 50% oxygen in both nitrogen and helium (3 liters per minute) were tested, as in the first part of this study described previously. Following completion of this part of the experiment, the effects of adding 2% halothane to the oxygen gas mixtures was studied.

The endpoint of each trial was determined by one of the following: 1. onset of an intraluminal fire that continued to burn between laser pulses; 2. delivery of a total of 60 laser pulses without the onset of an intraluminal fire (first set of experiments); or 3. delivery of 180 seconds of continuous laser energy without the onset of an intraluminal fire (second set of experiments). When a surface (extraluminal) fire occurred during a trial (this occurred in the Rusch red rubber tubes only), the time was recorded and the gas evacuator was moved close to the tube to control the fire, allowing the trial to be continued until one of the endpoints was reached.

Upon completion of this aspect of the research project, the PVC, red rubber, and Laser Shield tubes were wrapped in both 3-M® #425 and Radio Shack® #44-1155 metallic tape and tested with the laser in the continuous mode at 10, 15, and 20 W respectively, in 100% oxygen flowing at 3 liters per minute. Each tube was irradiated until either a fire occurred or 180 seconds elapsed.

In the third part of this study, the heat absorptive qualities of each tube were measured using a Hewlett-Packard® model 347B digital multimeter thermocouple with Chromel-Alumel type thermocouple wire. An ice bath at 0°C was used as the reference



Fig. 2. Geraci-Miller gas evacuator (A) next to Zeiss operating microscope (B). The Vermitrol laboratory anesthesia unit (C) and Sharplan carbon dioxide laser (D) are in the foreground.

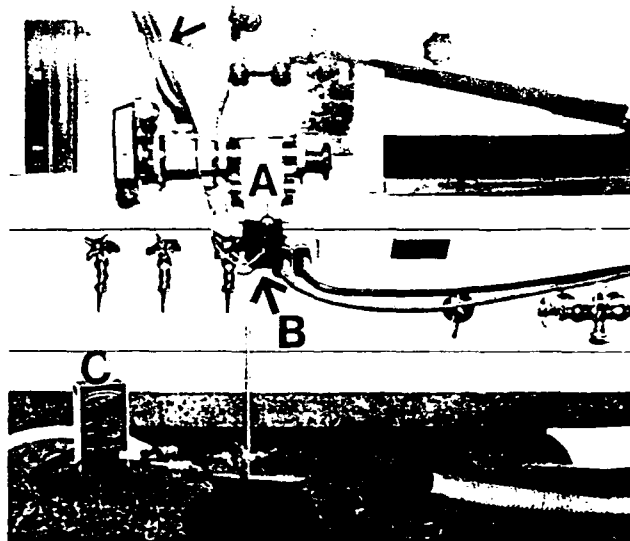


Fig. 3. Articulated arm of the Sharplan laser (arrow) coupled to the Zeiss operating microscope (A) using the Sharplan microslad coupler (B). Note the thermocouple (C) on the laboratory counter top.

junction, and the measuring end of the wire was placed against the upper wall of the interior of the tube with the end of the wire immediately distal to the laser impact site. Measurements were made at 5-second intervals, with an accuracy range of 5°C. The tube was irradiated, using the laser at 20 W in the continuous mode, until either the tube was penetrated or until 180 seconds elapsed. These studies were conducted in room air without any gas mixtures passing through the tube.

The data generated by these experiments were analyzed using computer software produced by Systat Inc. The following statistical tests were run using Systat: 1. two-way analysis of variance; 2. Student's *t*-test; 3. Wilcoxon rank (Fisher) test; and 4. rank-sum test. The two-way analysis of variance could be used only when all three trials ignited at all three powers. The Student's *t*-test was used to compare two sample populations in the study when all trials in both sample populations ignited. When some tubes in a trial in one or both sample populations failed to ignite, the Student's *t*-test could not be applied; in these instances, the Wilcoxon rank test (Fisher test) and/or rank-sum test were used to analyze the data.

RESULTS

Survey of Laser-Related Complications

Of the 337 questionnaires sent out to participants in the "hands-on" laser surgery course, 23 were returned by the post office for lack of a forwarding address and 253 were returned completed; this represented a 75% response rate. Thirty-five respondents (13.8%) did not use the laser in their practice. Thirty-eight former registrants in the course (15%) had used the laser prior to attending the course, and an additional 180 respondents (71.1%) used the laser after attending the course. Of those respondents who had not used the laser prior to attending the course, 146 (81%) felt that attendance at the course was instrumental in their decision to use the laser clinically. Of this same group, 164 physicians (91%) felt that they would not have/could not have begun to use the laser clinically without a "hands-on"

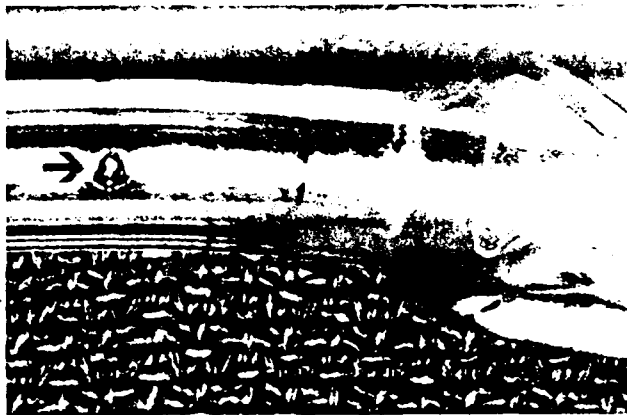


Fig. 4. Penetration (arrow) of the polyvinyl chloride (PVC) tube after irradiation with the carbon dioxide laser.

course. Thirty-two (14.6%) of the total number of respondents using the laser practiced in the lab or on cadavers prior to beginning to use it clinically and only six (2.7%) of this same group had performed any scientific investigations in either the lab or hospital using the laser.

The responses to question 8 (Table I) were expressed in months by 68 respondents (3.5 months average), cases by 54 respondents (5 cases average), time, *i.e.*, very quickly by 67 respondents (1 week average) and still not comfortable (12.3%). This question should have been written more specifically to elicit responses using one common measure. The average number of endoscopic cases performed by the past participants who had used the laser prior to attending the course was 100 (6.4 cases/month), while the average number of cases performed by those who used the laser for the first time after attending the course was 40 (5 cases/month). All but one of the laser-using respondents (99.5%) found the safety protocol taught during the course to be efficacious. Eleven physicians (5.0%) reported a total of 12 laser-related complications (Table XVII). Four of these complications, including two endotracheal tube fires, had occurred before the responding otolaryngologists attended the "hands-on" course. No endotracheal tube fires were reported by any of the respondents following completion of the course. Of



Fig. 5. PVC tube demonstrating an intraluminal, laser-ignited fire.

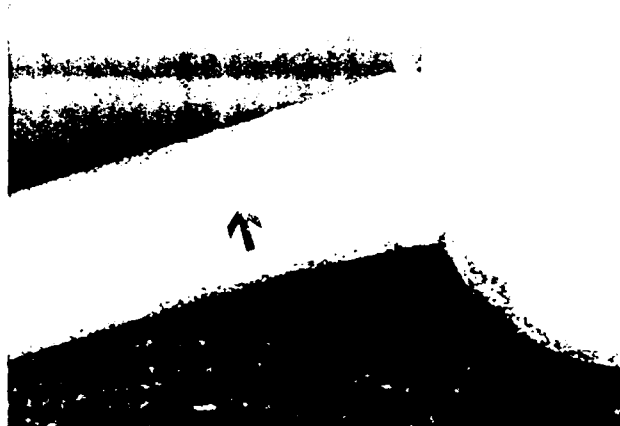


Fig. 6. Xomed Laser-Shield tube demonstrating the formation of white ash (arrow) at the laser-impact site.

the other reported complications, 4 involved lip burns (patient), 4 involved skin burns (patient), 1 involved ignition of a plastic tooth protector (patient), and 1 involved a finger burn (surgeon). All complications reportedly healed uneventfully.

Tests on the Incendiary Characteristics of Endotracheal Tubes

The three types of endotracheal tubes examined in this study demonstrated a wide range of incendiary characteristics. When struck by the laser beam, the National Catheter PVC tube was quickly vaporized; the laser would burn completely through the tube within 1 second when using the continuous mode or after 10 pulses (0.1-second each), even at 10 W, when using the shuttered mode. After the laser penetrated the tube, most of its energy passed straight through the tube and was absorbed by the heat shield underneath (Fig. 4). The tube usually ignited when the polyvinyl chloride around the laser-penetration site melted and flowed into the beam,

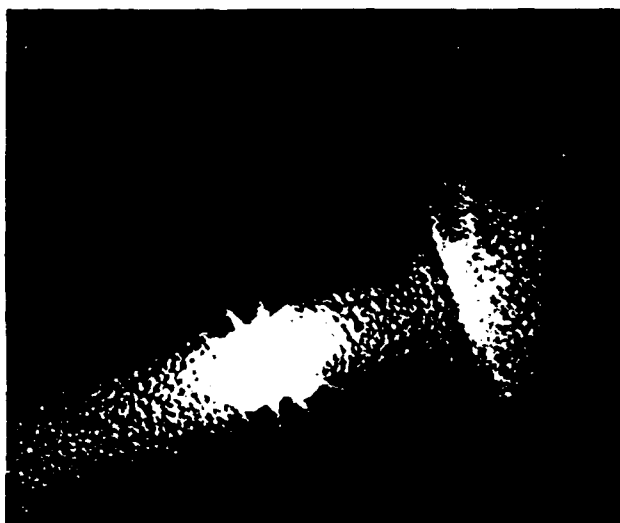


Fig. 7. Bright glow of the Xomed Laser-Shield tube during impact with the carbon dioxide laser.



Fig. 8. Laser-ignited fire using the Xomed Laser-Shield tube.

causing the tube to be heated by the laser. At that point, the plastic tube would glow brightly, resulting in either a fire or further vaporization of the tube (Fig. 5).

When the Xomed Laser-Shield tube was hit by the laser beam, a white ash formed at the impact site (Fig. 6). The laser then had to burn through this ash in addition to the wall of the tube. During impact from the carbon dioxide laser beam, the tube would glow brightly (Fig. 7). A fire started when the laser heated the inner wall of the tube beyond the temperature of ignition (Fig. 8). The Xomed Laser-Shield tube absorbed the laser energy quickly; it remained warm for a short time after laser impact. Following the occurrence of a laser-ignited fire, this tube had to be allowed to cool down before gas flow was restarted; otherwise the tube would reignite spontaneously.

A layer of ash also formed when the laser struck the Rusch red rubber tube; however, in this case it was black, carbonaceous debris that was formed (Fig. 9). In addition, some of the rubber of the outer wall was momentarily vaporized and then recon-

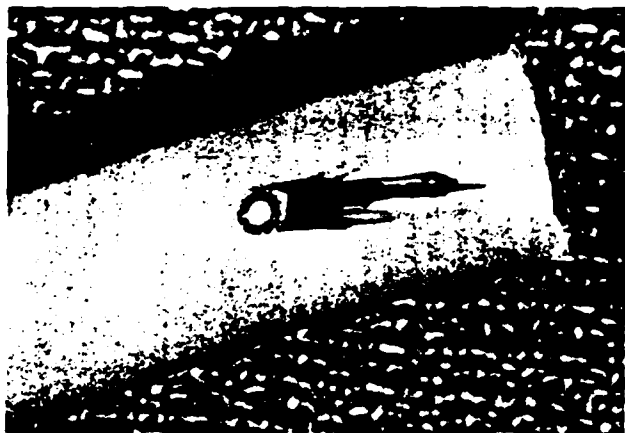


Fig. 9. Rusch red rubber tube demonstrating the formation of black carbonaceous ash at the laser impact site.

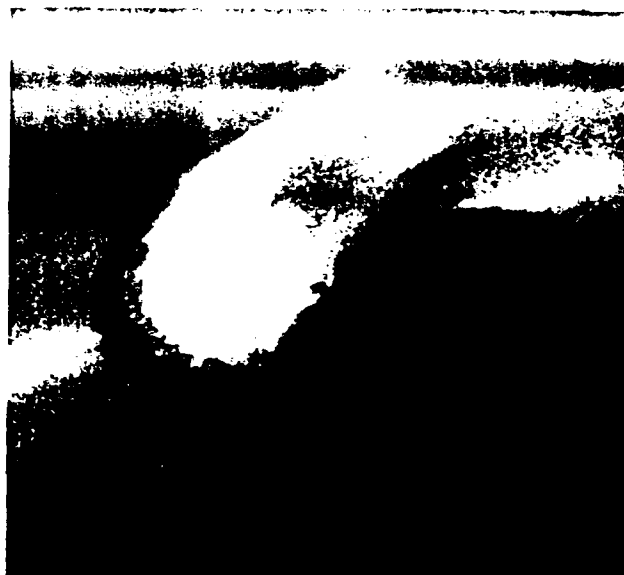


Fig. 10. Rusch red rubber tube demonstrating an extraluminal (surface) fire.

densed in the air, forming thin, black strands. The Rusch red rubber tube produced a large amount of black smoke, due to the occurrence of a surface (extraluminal) fire (Fig. 10). The laser energy produced a larger hole in the red rubber tube than in either the PVC tube or Xomed tube. A fire started when the laser penetrated through the tube and heated up the inside of the tube in a similar fashion to that which occurred in the Xomed tube (Fig. 11).

Analysis of the data obtained from the first part of the experiment clearly showed the polyvinyl chloride tube to be inferior to the Rusch red rubber or Xomed Laser-Shield tubes. In the presence of 100% oxygen, the PVC tube ignited after 14, 9.46, and 6.62 pulses of 0.1-second duration when exposed to laser radiation of 10, 15, and 20 W, respectively (Table IV). The PVC tube also ignited in 40% oxygen in nitrogen at 15 and 20 W, in 50% oxygen in nitrogen at all three power settings, and in 50% oxygen in helium at 15 and 20 W. The Rusch red rub-



Fig. 11. Intraluminal fire (arrow) in the Rusch red rubber tube caused by the extraluminal surface fire burning through the tube.

Tube Type	Laser Power		
	10 W	15 W	20 W
PVC	14.00 ± 2.22	9.46 ± 1.40	6.62 ± 1.11
Red rubber	>60	>60	>60
Xomed	>60	>60	>60

ber and Xomed Laser-Shield tubes failed to ignite in 100% oxygen and all other gas mixtures at all laser settings during the shuttered (pulsed) mode experiments (Table V). The cuffs of all three tubes were easily penetrated and deflated after 1 to 2 pulses of the laser set at 10 W. The PVC tubes wrapped with the 3-M #425 and Radio Shack #44-1155 metallic tape were tested in 100% oxygen at 10, 15, and 20 W power for 60 pulses of 0.1 second each. None of the metallic tape-wrapped tubes ignited.

Because some of the PVC and Xomed tubes in several of the trials did not ignite during exposure to the laser in the continuous mode, analysis of the data obtained from the second part of this experiment required the use of both parametric and non-parametric statistics. All three tubes ignited in eight out of eight trials when tested at 10, 15 and 20 W, continuous mode in 100% oxygen (Fig. 12 and Table VI). At 10 W, the mean time to ignition (MTI) for the PVC tube was 3.06 seconds, while the MTI for the red rubber and Xomed tubes were 33 and 17.85 seconds, respectively. At these parameters, the Rusch red rubber tubes were significantly ($p < .01$) more resistant to ignition than either the PVC or Xomed tubes. The Rusch tube ignited 8 of 8 times in all trials except 30% oxygen in 58% helium and 2% halothane; here, it ignited only 4 of 8 times. In all red rubber tube trials, a surface fire was noted be-

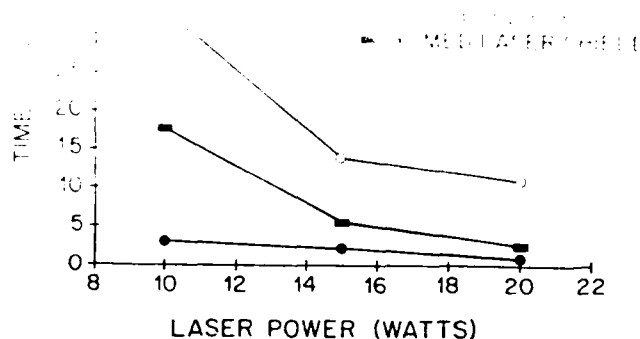


Fig. 12. Ignition times of three endotracheal tubes in 100% oxygen with the CO₂ laser in the continuous mode.

fore the endpoint was recorded (Tables VII through XII). The shortest mean time to ignition in the red rubber tube trials was 16.99 seconds, which occurred in 50% oxygen in 50% nitrogen at 20 W continuous mode. It took only 4.96 seconds for the PVC tube to ignite at these same settings. Because of a limited supply of the Xomed tubes, they were tested only in the trials in which halothane was included in the gas mix. In the trials run in 50% oxygen in 48% nitrogen and 2% halothane, 23.45 seconds were required for the red rubber tube to ignite at 20 W continuous mode. At these same gas concentrations and laser settings, it took only 7.57 seconds for the PVC tube and 4.36 seconds for the Xomed tube to ignite (Table IX).

When analyzing the data in this part of the study, four questions were examined: 1. is there a difference between the Rusch and Xomed tubes at oxygen concentrations other than 100%; 2. is there a difference between helium and nitrogen; 3. is there a difference between oxygen concentrations in helium; and 4. what is the effect of halothane when added to the gas mixture? Statistical analysis of the data obtained from the PVC trials was not compared with the Rusch and Xomed tubes at all the gas mixtures in the continuous mode because the PVC tube was the only tube to ignite in the shuttered (pulsed) mode experiments and the MTI for this tube was so short (3.06 seconds) in the 100% oxygen continuous mode trial. When the Rusch red rubber tube was compared to the Xomed Laser-Shield tube in the continuous mode trials, statistically significant differences ($p < .01$) were noted in the MTI at 15 and 20 W in 30%, 40%, and 50% oxygen in nitrogen, at 20 W in 30% oxygen in helium, at 10, 15, and 20 W in 40% oxygen in helium, and at 15 and 20 W in 50% oxygen in helium (Table XIII).

TABLE V. Mean Number of Pulses (0.1 Second) to Ignition in Varying Gas Mixtures.				
Gas Mixture at 2.5 Liters per Minute	Type of Tube	Laser Power		
		10 W	15 W	20 W
<u>O₂ in N₂</u>				
30%	PVC	>60	>60	>60
	Red rubber	>60	>60	>60
	Xomed	>60	>60	>60
40%	PVC	>60	2/13 N/A	11/13 32.82
	PVC	9/13 41	11/13 28	12/13 26
50%	Red rubber	>60	>60	>60
	Xomed	>60	>60	>60
	<u>O₂ in Helium</u>			
30%	PVC	>60	>60	>60
	Red rubber	>60	>60	>60
	Xomed	>60	>60	>60
40%	PVC	>60	>60	>60
	PVC	>60	1/13 N/A	4/13 N/A
50%	Red rubber	>60	>60	>60
	Xomed	>60	>60	>60

TABLE VI. Mean Time to Ignition (Seconds) in 100% Oxygen.			
Type of Tube	Laser Power		
	10 W	15 W	20 W
PVC	3.06 ± 0.79	2.38 ± 0.63	0.95 ± 0.37
Red rubber	33 ± 1.01	14.04 ± 0.90	10.99 ± 0.61
Xomed	17.85 ± 1.74	5.62 ± 0.75	2.66 ± 0.25

		10 W		15 W		20 W	
		W	W/O	W	W/O	W	W/O
PVC	No. of ignitions	5/8	6/8	8/8	8/8	6/8	7/8
	MTI (sec.)	28.88	34.88	15.14	31.56	11.17	13.88
	Penetration time (sec.)	—	0.79	—	0.68	—	0.59
Red Rubber	No. of ignitions	8/8	8/8	8/8	8/8	8/8	8/8
	MTI (sec.)	77.11	51.65	69.88	37.12	51.71	21.65
	Surface fire time (sec.)	23.51	23.39	19.76	14.74	8.16	2.78
Xomed	No. of ignitions	7/8	—	8/8	—	8/8	—
	MTI (sec.)	37.09	—	8.14	—	6.33	—

When the data were analyzed to determine if any differences existed between helium and nitrogen, the following results were calculated: 1. 30% oxygen in helium was significantly better in retarding ignition than 30% oxygen in nitrogen in the Rusch tube at 10 W ($p < .01$) and in the Xomed tube at 10 and 15 W ($p < .01$); 2. 40% oxygen in helium was significantly better in delaying ignition than 40% oxygen in nitrogen in the Rusch tube at 15 W ($p < .01$); and 50% oxygen in helium was significantly better than 50% oxygen in nitrogen at 10 W ($p < .01$). Because these findings revealed that helium was superior to nitrogen at the previously mentioned gas concentrations and laser settings (Table XIV), the data analysis concerning the significance, if any, of varying oxygen concentrations was calculated using oxygen in helium. These calculations revealed statistically significant differences ($p < .01$) in the Rusch tube when 30% oxygen in helium was compared to both 40% and 50% oxygen in helium at all three power settings. Comparison of 40% oxygen in helium with 50% oxygen in helium in the Rusch tube was significantly different ($p < .01$) only at 15 W, continuous mode. When these same comparisons were made in the Xomed tube, statistically significant differences occurred in 30% oxygen versus 40% oxygen at 10, 15, and 20 W ($p < .01$) and in 30% oxygen versus 50% oxygen at 10 and 15 W ($p < .01$). When 40% oxygen in helium was compared to 50% oxygen in helium in the Xomed tube, significant difference ($p < .01$) occurred only at 15 W (Table XV).

TABLE VIII.
Forty Percent Oxygen in Nitrogen (2% Halothane).

		10 W		15 W		20 W	
		W	W/O	W	W/O	W	W/O
PVC	No. of ignitions	8/10	8/8	8/8	8/8	8/8	8/8
	MTI (sec.)	25.65	13.44	21.81	18.81	13.29	13.44
	Penetration time (sec.)	1.46	0.86	0.93	0.64	0.61	0.47
Red Rubber	No. of ignitions	8/8	8/8	8/8	8/8	8/8	8/8
	MTI (sec.)	76.54	40.92	52.47	24.64	27.10	17.07
	Surface fire time (sec.)	13.34	15.76	8.03	5.35	1.22	2.41
Xomed	No. of ignitions	1/8	6/8	8/8	8/8	8/8	8/8
	MTI (sec.)	N/A	27.15	8.48	9.15	7.42	5.43

TABLE IX.
Thirty Percent Oxygen in Nitrogen (2% Halothane).

		10 W		15 W		20 W	
		W	W/O	W	W/O	W	W/O
PVC	No. of ignitions	8/8	8/8	8/8	8/8	8/8	8/8
	MTI (sec.)	11.97	11.14	8.74	7.04	7.57	4.96
	Penetration time (sec.)	—	0.77	—	0.54	—	0.51
Red Rubber	No. of ignitions	8/8	8/8	8/8	8/8	8/8	8/8
	MTI (sec.)	43.09	41.48	32.86	21.35	23.45	16.99
	Surface fire time (sec.)	26.67	23.48	18.26	2.99	3.63	1.94
Xomed	No. of ignitions	5/8	—	8/8	—	8/8	—
	MTI (sec.)	17.97	—	5.57	—	4.36	—

The effect of adding 2% halothane to the gas mixture was analyzed by using the Student's *t*-test. These results revealed that the addition of 2% halothane to the gas mixture significantly retarded ignition ($p < .01$) only with the Rusch tube when tested with: 1. 30% oxygen in helium at 15 and 20 W; 2. 40% oxygen in helium at 15 and 20 W; and 3. 50% oxygen in helium at 10, 15, and 20 W (Table XVI).

All three tubes were wrapped in 3-M #425 and Radio Shack #44-1155 reflective, metal tape and exposed to the laser beam until ignition, or for 180 seconds, at 10, 15, and 20 W, continuous mode. None of the reflective tape-wrapped tubes in this part of the study ignited.

Analysis of the data from the third part of this study, using the thermocouple, revealed that the Xomed Laser-Shield tube absorbed laser energy, in the form of heat, in an unproductive fashion, retaining this absorbed energy over a longer interval of time than either the PVC or red rubber tubes. The surface of the Xomed tube should have been designed to be reflective rather than absorptive; this characteristic would have allowed this tube to handle exposure to the laser energy in a more efficient and safer manner. The Rusch tube, in comparison, had a high and fast peak in temperature, but unlike the Xomed tube, it dispersed the heat much more efficiently and rapidly. The PVC tube retained only a minimal amount of energy as heat (Fig. 13).

TABLE X.
Thirty Percent Oxygen in Helium (2% Halothane).

		10 W		15 W		20 W	
		W	W/O	W	W/O	W	W/O
PVC	No. of ignitions	3/8	1/8	4/8	3/8	4/8	2/8
	MTI (sec.)	N/A	N/A	24.38	N/A	17.45	N/A
	Penetration time (sec.)	0.90	0.77	0.67	0.59	0.59	0.45
Red Rubber	No. of ignitions	4/8	8/8	8/8	8/8	8/8	8/8
	MTI (sec.)	118.97	47.31	73.78	34.99	46.67	25.09
	Surface fire time (sec.)	15.30	15.58	11.32	7.26	1.61	1.58
Xomed	No. of ignitions	0	—	2/8	—	8/8	—
	MTI (sec.)	N/A	—	N/A	—	17.73	—

		Laser Power Settings					
		0 W	5 W	10 W	15 W	20 W	25 W
PVC	No. of ignitions	0	5/8	6/8	6/8	7/8	7/8
	MTI (sec.)	N/A	25.18	16.54	25.11	15.69	22.57
	Penetration time (sec.)	0.79	0.50	0.40	0.60	0.78	0.81
Red Rubber	No. of ignitions	8/8	8/8	8/8	8/8	8/8	8/8
	MTI (sec.)	67.58	55.52	41.94	33.46	29.60	19.75
	Surface fire time (sec.)	8.66	10.348	5.02	4.98	1.34	1.46
Xomed	No. of ignitions	0	—	8/8	—	8/8	—
	MTI (sec.)	N/A	—	9.35	—	6.94	—

DISCUSSION

The purpose of this study was to determine if attendance at a "hands-on" laser surgery course for specialists in otolaryngology—head and neck surgery might lead to a reduced rate of laser-related complications in this selected group when compared to another selected group of otolaryngologists (members of a senior otolaryngology society) previously surveyed by Fried¹ on the basis of their society membership, and to compare the incendiary characteristics of three endotracheal tubes in various mixtures of oxygen diluted with either helium or nitrogen with and without 2% halothane. Initial discussion focuses on the results of the questionnaire mailed to 337 otolaryngologist—head and neck surgeons who had attended a "hands-on" laser surgery course between August 1981 and December 1985.

Survey of Laser-Related Complications

Although questionnaires are often considered to be an annoyance, especially by the busy otolaryngologist—head and neck surgeon, examination of the information included within a well-designed questionnaire can help to establish the opinion of a selected group about a certain topic. The favorable response rate of 75% to the questionnaire mailed to past registrants of the "hands-on" carbon dioxide laser surgery course has facilitated and substan-

		Laser Power Settings					
		0 W	5 W	10 W	15 W	20 W	25 W
PVC	No. of ignitions	6/8	6/8	8/8	7/8	6/8	6/8
	MTI (sec.)	25.42	23.89	17.57	18.15	12.91	17.06
	Penetration time (sec.)	0.79	0.50	0.40	0.60	0.78	0.81
Red Rubber	No. of ignitions	8/8	8/8	8/8	8/8	8/8	8/8
	MTI (sec.)	59.11	34.47	40.19	22.65	28.36	17.43
	Surface fire time (sec.)	14.40	7.64	6.39	2.51	2.04	1.91
Xomed	No. of ignitions	4/8	—	8/8	—	8/8	—
	MTI (sec.)	30.69	—	6.11	—	5.88	—

tiated analysis of the data contained within the aforementioned survey. Additionally, the large number of physicians (81%) who answered that attendance at the course was instrumental in their decision to use the laser clinically would seem to validate the claim that participation in a "hands-on" workshop was a valuable means of preparing a physician for the clinical use of the laser.

The necessity of attending a "hands-on" laser workshop prior to clinical use was suggested by the large number of physicians (91%) who responded that they would not have and could not have used the laser clinically without this type of course. The responses to this question indicated both a strong desire on behalf of the registrants for formal laser training prior to using this technology in clinical practice and a need to document that formal laser training had indeed taken place. Many of the hospitals where the course participants practiced required that all surgeons attend "hands-on" training courses in laser surgery prior to using the laser clinically. The small number of participants (14.6%) who practiced in the lab or on cadavers prior to clinical use of the laser indicated that this desirable step was not always possible and perhaps not always necessary.

The true value of a "hands-on" course in laser surgery in otolaryngology—head and neck surgery was measured best by the very favorable response (99.5%) rate to the safety protocol taught during the course and by the very small number of physicians using the laser who reported having any laser-related complications (3.6%) following their atten-

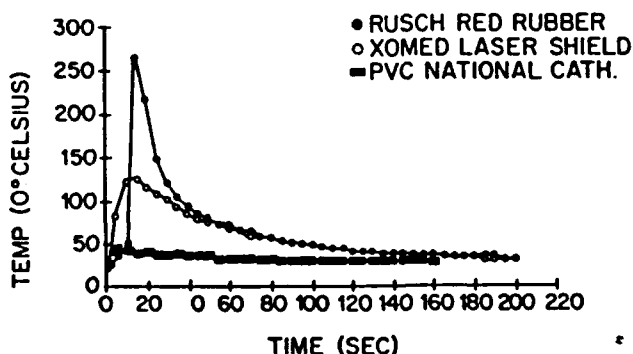


Fig. 13. Thermal absorptive characteristics in room air of three endotracheal tubes during exposure to the CO₂ laser in the continuous mode.

TABLE XIII.
Statistical Analysis:
Rusch Red Rubber Tube vs. Xomed Laser-Shield Tube.

	Laser Power Settings		
	10 W	15 W	20 W
30% oxygen in nitrogen	—	$p < .01$	$p < .01$
40% oxygen in nitrogen	—	$p < .01$	$p < .01$
50% oxygen in nitrogen	—	$p < .01$	$p < .01$
30% oxygen in helium	—	—	$p < .01$
40% oxygen in helium	$p < .01$	$p < .01$	$p < .01$
50% oxygen in helium	—	$p < .01$	$p < .01$

TABLE XV

	Laser Power Settings		
	10 W	15 W	20 W
Rusch Red Rubber Tube			
30% oxygen in helium vs. nitrogen	$p < .01$	—	—
40% oxygen in helium vs. nitrogen	—	$p < .01$	—
50% oxygen in helium vs. nitrogen	$p < .01$	—	—
Xomed Laser-Shield Tube			
30% oxygen in helium vs. nitrogen	$p < .01$	$p < .01$	—
40% oxygen in helium vs. nitrogen	—	—	—
50% oxygen in helium vs. nitrogen	—	—	—

dance at this course. Analysis of the 12 complications (Table XVII) experienced by 11 past course registrants revealed that 4 of these complications, including 2 endotracheal tube fires, occurred prior to the physician's attending the course. None of the past registrants reported experiencing an endotracheal tube fire following their attendance at this "hands-on" workshop. Perhaps the endotracheal tube fire demonstration at each course served to reinforce the safety protocol. Of the eight complications that were reported following attendance at the workshop, all were stated to be minor, with an uneventful outcome. Lip burns occurred most frequently (4), followed by skin burns (2), ignition of a tooth protector (1), and a finger burn suffered by one of the surgeons (1).

The most important observation to emerge from the discussion of the results of this survey was that the complication rate experienced by the otolaryngologists who attended the workshop was significantly different from the unacceptably high complication rate discovered by Fried when he polled the membership of a senior otolaryngology society about their experience with laser-related accidents. One obvious shortcoming of the Fried study was that he did not investigate, through his questionnaire, whether the surveyed otolaryngologists had taken any formal or informal laser training courses. For purposes of discussion, it was assumed that the majority of those experiencing laser-related complications in the Fried study had not taken any formal laser surgery courses prior to using the laser clinically. This assumption was justified because any sort of formal laser training would have taken place with one of the pioneers (Strong and his colleagues or Andrews) who would have included a strong warning about the possibility of an endotracheal tube fire. Beginning in 1973, Strong and his colleagues²¹ presented and published a paper on the use of reflective aluminum tape to protect the tube and moist selva gauze to protect the cuff.

Andrews²² performed a series of experimental, laser-induced, endotracheal tube fire studies in 1974

	Laser Power Settings		
	10 W	15 W	20 W
Rusch Red Rubber Tube			
30% oxygen vs. 40% oxygen in helium	$p < .01$	$p < .01$	$p < .01$
30% oxygen vs. 50% oxygen in helium	$p < .01$	$p < .01$	$p < .01$
40% oxygen vs. 50% oxygen in helium	—	$p < .01$	—
Xomed Laser-Shield Tube			
30% oxygen vs. 40% oxygen in helium	$p < .01$	$p < .01$	$p < .01$
30% oxygen vs. 50% oxygen in helium	$p < .01$	$p < .01$	—
40% oxygen vs. 50% oxygen in helium	—	$p < .01$	—

and advocated the use of the Rusch red rubber tube wrapped in reflective, metallic tape in an anesthetic gas mixture limited to 30% oxygen in nitrous oxide, as well as the use of saline-saturated cottonoids to protect the cuff and saline-saturated gauze to protect the patient's lips. Although we have since learned from Vourc'h, *et al.*,⁴⁶ Hirshman, *et al.*,⁵¹ Chilcoat, *et al.*,⁵⁰ and others that there was no significant difference "between an atmosphere of pure oxygen, an atmosphere of pure nitrous oxide containing no oxygen, or any combination of the two," Andrews was headed in the proper direction in 1974 by emphasizing the use of a 30% concentration of oxygen. Based on the early emphasis on safety, which was presented and published by both the Strong group and the Andrews group, it was difficult to conceive that an otolaryngologist would have received formal laser training in the 1970s without some meaningful exposure to laser safety. Therefore, the statement questioning the adequacy of the literature as a method of transferring vital information concerning laser safety to the practicing otolaryngologist—head and neck surgeon might seem justified.

During the 3-year period 1980 to 1982, many manuscripts were published concerning laser-related complications, including endotracheal tube fires. It has already been pointed out that the literature was confusing during those 3 years regarding which tube to use for laryngeal laser surgery. This confusion created a critical mass of publications, in both the anesthesiology and otolaryngology literature, that should have served as a warning that the risk of fire was always there. The fact that so many laser-ignited endotracheal tube fires occurred in the midst of all these publications, either warning of the possibility (1972-1980) or reporting the occurrence (1976-1983) of laser-ignited airway fires, strengthens the contention that the literature might not have been the best vehicle for transferring this vital information to the practicing anesthesiologist and otolaryngologist. The fact that none of the participants in the "hands-on" laser surgery course experienced an endotracheal tube fire following their participation

TABLE VI
Oxygen, 2% Halothane and Helium vs. Oxygen in Helium
Time to Ignition (seconds)

	10 W	15 W	20 W
Rusch Red Rubber Tube			
30% oxygen in 2% halothane and helium vs. 30% oxygen in helium	—	$p < .01$	$p < .01$
40% oxygen in 2% halothane and helium vs. 40% oxygen in helium	—	$p < .01$	$p < .01$
50% oxygen in 2% halothane and helium vs. 50% oxygen in helium	$p < .01$	$p < .01$	$p < .01$

at the workshop demonstrates the superiority of this method of transfer of important information.

This study has demonstrated the efficacy of attending a "hands-on" laser surgery course, and all otolaryngologist—head and neck surgeons contemplating the use of this technology in their practice should be encouraged to participate in any one of the many excellent courses available today throughout the country.

Tests on the Incendiary Characteristics of Endotracheal Tubes

The experimental methods employed in this study measured the time to ignition (intraluminal fire) or the designated endpoint of 60 pulses, 0.1 second each, in part 1 and 180 seconds continuous exposure in part 2. The time it took to either penetrate the tube or burn through the tube in the absence of an intraluminal fire was noted, but did not constitute an endpoint that was analyzed statistically. This experimental methodology proved to be significant in the case of the polyvinyl chloride tube trials. Most often, the laser would burn completely through one of the PVC tubes during a trial, leaving a hole in the tube that allowed additional laser energy to pass through it without starting a fire. Consequently, many of the trials with the PVC tube did not ignite; this, in turn, could cause the casual reader of this manuscript to falsely interpret the data reflected by the PVC experiments and to conclude that this tube was safer than it actually was. Similarly, although the time of occurrence of an extraluminal, surface fire in the red rubber tube trials was recorded, the endpoint in these trials was either the occurrence of an intraluminal fire, 60 pulses at 0.1 second each, or 180 seconds of continuous laser irradiation. This methodology probably accounted for the prolonged ignition times for the red rubber tubes in this study. It was felt that the mean time to ignition would best characterize the incendiary properties of each tube; this, in turn, would help the clinician to interpret the data with respect to a known endpoint—an intraluminal fire. The frequent occurrence of an extraluminal, surface fire in the red rubber tube trials should be looked at as a positive characteristic of this tube because these fires should warn the sur-

Tube	Result	Before or After
1. Tube fire	Uneventful	Before
2. Tube fire	Uneventful	Before
3. Lip burn	Uneventful	After
4. Lip burn	Uneventful	After
5. Lip burn	Uneventful	After
6. Lip burn	Uneventful	After
7. Skin burn (face)	Uneventful	After
8. Skin burn	Uneventful	Before
9. Skin burn	Uneventful	Before
10. Skin burn	Uneventful	After
11. Ignition of tooth protector	Uneventful	After
12. Finger burn	Uneventful	After

geon that serious trouble in the form of an intraluminal fire is threatening. Unless such a fire occurred distal to the cuff, within 1 cm of the distal end of the tube, it took at least 14.66 seconds for an extraluminal fire to transform into an intraluminal blaze (Tables VI-XII).

Both types of reflective aluminum tape, 3-M #425 and Radio Shack #44-1155, protected the polyvinyl chloride tubes from igniting in 100% oxygen when exposed to 60 pulses (0.1 second) at 10, 15, and 20 W, respectively in the first part of this experiment and when exposed to 180 seconds of continuous mode laser energy at 10, 15, and 20 W in the second part of this experiment. The use of the reflective aluminum tape, however, has been associated with certain problems, including acute airway obstruction secondary to the tape becoming dislodged from the tube as reported by Kaeder and Hirshman.⁴⁸ Wrapping the tube should be performed with great care, starting just above the cuff and working towards the proximal end of the tube in a circumferential, overlapping fashion. The tube should be inspected before intubation, and again after extubation, to make certain that all the tape that was on the tube at intubation is still present at extubation. When missing tape is noted, the oral cavity, oropharynx, hypopharynx, larynx, and trachea must be thoroughly inspected. Rigid bronchoscopy must be performed if the tape cannot be located using a laryngoscope.

The cuff of all three types of endotracheal tubes was easily penetrated after one to three pulses (0.1 second) at all three powers and in less than 1 second using the continuous mode. Without doubt, the unprotected cuff has been shown to be the weakest part of the endotracheal tube with respect to laser penetration. However, the safety precautions that have been proposed by Strong, *et al.*,¹⁷ LeJeune, *et al.*,⁷² and Ossoff, *et al.*,^{75,76} have served to adequately protect the cuff. Strong and his colleagues had introduced the use of moist selvage gauze to protect the cuff as early as 1972. LeJeune, *et al.* introduced their solution to the tube-cuff problem by inflating the

cuff with saline, which caused the cuff to act as a heat sink. The cuff, when filled with saline, when perforated by the laser beam. Ossoff, *et al.* suggested adding methylene blue to the saline in the cuff; by coloring the saline blue, a leak in the cuff would turn the previously moistened cottonoids blue, making it easier for the surgeon to recognize the problem. The development of the operating platform by Ossoff and Karlan in 1983 completed the commonly utilized protocol for cuff safety. The operating platform served as a "catcher's mitt" to protect the cottonoids, cuff, and tissues of the subglottic larynx from any direct or reflected laser beam irradiation.

The findings from the first part of this experiment revealed that the PVC tube was the only tube to ignite when exposed to 0.1-second pulses of carbon dioxide laser radiation in the presence of 100% oxygen. The fact that the laser-ignited fires in the PVC tubes occurred after only 14 pulses or less (Table IV) indicated the relative lack of resistance of this tube to the laser beam. This conclusion was confirmed in the second part of this study using the continuous mode in 100% oxygen (Table VI). The mean time to ignition of the PVC tube was 3.06 seconds, compared to 17.85 seconds for the Xomed tube and 33 seconds for the red rubber tube. Although the PVC tube did not ignite in all trials of oxygen in either nitrogen or helium, the penetration time of the tube was 1.46 seconds or less (Tables VI-XII), a clear indication that this tube was less resistant to perforation by the laser beam than either of the other two tubes. Therefore, the risk of a fire with this tube was always present and, as previously stated, the tube was found to be far more dangerous than a casual perusal of Tables VI through XII would indicate.

The findings of this study contradict the previous investigations of Treyve, *et al.*⁶³ and Hirshman, *et al.*⁵¹ who found the PVC tube to be superior to the red rubber tube. Andrews, *et al.*,²² Strong, *et al.*,²⁹ Vaughan,³³ DiBartolomeo,⁴¹ Meyers,⁵⁹ and others^{25,71} found that the PVC tube was both more easily penetrated and more readily ignited than the red rubber tube. Furthermore, the first reported, serious laser-ignited endotracheal tube fire occurred when the patient was intubated with a PVC tube,⁷⁰ and Schramm, *et al.*⁴⁴ have shown that the gases associated with burning PVC tubes were toxic to the airway and could be associated with severe pneumonitis. Ossoff, *et al.*⁷⁷ demonstrated that the PVC tube caused the most mucosal damage, both grossly and histologically, after a 5-second exposure to a planned, laser-ignited endotracheal tube fire. They recommended against using the PVC tube, either wrapped or unwrapped, for laryngeal laser surgery.

Pashayan and Gravenstein (1985)⁹¹ determined that helium, but not nitrogen, significantly retarded endotracheal tube ignition when it was present in a 60% or greater concentration with oxygen and the laser was set at 10 W or less of energy for bursts of

10 seconds or less. This utilized PVC tubes, and they did not have to be wrapped with reflective tape. Furthermore, they did not recommend using fully saturated cottonoids to protect the cuff. The use of helium instead of nitrous oxide to dilute the concentration of oxygen in the inspired gas mix represented a major breakthrough in laser safety, because it prevented an oxidizing atmosphere in the anesthetic gas mixture. The protective effect of helium was probably caused by its high thermal diffusivity, which prevented a rise in temperature around the site of laser exposure and, thus, prevented the laser-irradiated endotracheal tube from reaching its temperature of spontaneous ignition. As great a contribution as the use of helium was, however, Pashayan and Gravenstein's advocacy of the use of the PVC tube was dangerous and served to create an atmosphere of controversy over which endotracheal tube to choose: PVC or red rubber.

It had already been shown that PVC tube fires produced gases that were toxic to the airway, tissue injury that was more severe than that seen with fires from either the red rubber or silicone tubes, and an outcome in patients that was far more damaging than that seen from fires with red rubber tubes. Because there was always the possibility that the laser power meter could be inaccurate, the anesthesia mixing valve might be incorrect, the oxygen analyzer might be read improperly or malfunction, or the surgeon use too high a power setting or too long an exposure time, the risk of occurrence of a laser-ignited endotracheal tube fire associated the tight parameters (60% helium, 10 W, and maximum of 10 seconds exposure) advocated by Pashayan and Gravenstein, was too great. Should such a fire occur, the likely outcome would be the most damaging to the patient, because of the extreme severity of the tissue injury caused by a burning polyvinyl chloride tube. These same risks would be associated with using the PVC tube, when wrapped with reflective metallic tape. In this case, the tape could be dislodged from the tube, exposing a vulnerable area of unprotected endotracheal tube. Should the laser beam hit such an unprotected spot, a catastrophic intraluminal fire could occur. Therefore, the polyvinyl chloride tube should not be used for laser surgery, either wrapped or unwrapped.

The findings of the second part of this study revealed several important conclusions. First, the red rubber tube was significantly better ($p < .01$) at preventing ignition than the Laser-Shield tube at the three laser power settings in varying concentrations of helium and nitrogen (Table XIII). Second, helium in oxygen was significantly better than nitrogen ($p < .01$) at retarding endotracheal tube ignition in both the red rubber and Laser-Shield tubes (Table XIV). These results were only noted at 10 and 15 W in varying oxygen concentrations. Third, the use of 30% oxygen in helium was significantly better

gas (O₂) that the addition of 2% halothane appeared to significantly retard ignition (p < 0.01) at the three laser power settings in varying concentrations of oxygen and helium.

These conclusions differed considerably from the findings of Hayes, *et al.*²⁸ and Fontenot, *et al.*²⁹ who found the Xomed Laser-Shield tube to be more resistant to laser-ignition than the Rusch red rubber tube. Possible reasons for the findings of this study differing from the previously published results of Hayes, *et al.* and Fontenot, *et al.* included differences in experimental design, instrument variation (anesthesia unit and laser), and tube-batch variability. Because the Xomed Laser-Shield tube was molded from a polymer (silicone), it was possible that batch variability could have existed. However, it was difficult to conceive that the variability could be as significant as was demonstrated by these findings, when compared to the two previously referenced studies. Laser variability and anesthesia unit variability most probably did not account for the differences noted here. The most likely reason for the above-mentioned differences, then, had to be within the category of experimental design. The trials performed in the second part of this study utilized the entire endotracheal tube; the distal portion was ignited, allowed to cool and cut off. The next trial irradiated an area of the tube adjacent to that which had been previously burned and cut off. It was possible that the heating-cooling-heating cycle introduced into the experimental design could have caused a change in the incendiary characteristics of the silicone polymer of the Xomed tube.

Both Hayes, *et al.* and Fontenot, *et al.* characterized an ignition as any form of combustion (continuous fire or burst of flame) that occurred during irradiation with the laser. In this study, ignition was considered to occur only when an intraluminal fire was noted. Specifically, extraluminal fires did not count as an ignition. Although unintended, this experimental design favored the Rusch red rubber tube. Comparison of the surface fire time of the Rusch tube with the mean time to ignition of the Xomed tube would yield different conclusions (Tables VII-XII). When compared in this way, the Xomed tube would be more resistant than the Rusch tube and parallel the findings of Hayes, *et al.* and Fontenot, *et al.*, with one exception. This study demonstrated ignition of the Xomed tube in 10 W and 15 W of laser power, while the aforementioned studies did not. Because it was felt that the extraluminal fire served as a helpful warning to alert the surgeon that his safety precautions were not working, and that the intraluminal fire, rather than the extraluminal fire, represented the significant risk of airway injury to the patient, this study was designed to use the presence of an intraluminal fire as its endpoint.

The most important observation to emerge from

the study was that the Xomed Laser-Shield tube ignited during these tests. In the first part of this study, neither tube burned when exposed to the three laser power settings in 100% oxygen. The use of the continuous mode of laser energy in 100% oxygen significantly demonstrated the ignition tolerance limits of both of these tubes. Varying the oxygen in helium or nitrogen concentrations from 30% to 50% (Tables VII-XII) also revealed the incendiary characteristics of these tubes in an atmosphere similar to that found in the operating room. The finding that the Xomed tube ignited at 10 W in 30% oxygen in nitrogen, and at 15 W in 30% oxygen in helium, was not observed by either Hayes, *et al.* or Fontenot, *et al.* This finding was significant because these power settings and oxygen concentration mixtures represented commonly used choices by many otolaryngologists who performed microlaryngeal laser surgery. Also, the power densities of these power settings were not in excess of 3,900 W/cm²—the maximum power density that Xomed advised to use with this tube. Xomed also cautioned that care had to be exercised when using the Laser-Shield tube in high oxygen concentrations (above 25%).³⁴ Endotracheal tubes designed for use in laryngeal laser surgery must allow the anesthesiologist certain flexibility with respect to the maximum safe oxygen concentration limit; this threshold should allow for an oxygen concentration of 40% to be used, to provide the anesthesiologist with the necessary flexibility for the safe management of the patient. There has been at least one operating room accident involving a laser-ignited Xomed Laser-Shield tube (J.V. McCormack, personal communication, 1987).

The finding that helium was more protective than nitrogen in retarding laser-ignited endotracheal tube fires supported the conclusions of Pashayan, *et al.* Oxygen diluted in helium should be used in all cases of laryngeal laser surgery requiring general endotracheal anesthesia.

Analysis of the experimental results also revealed that 30% oxygen was superior to either 40% or 50% oxygen in terms of preventing tube ignition. Andrews (1974)²² recommended limiting the oxygen concentration to 30%. Based on the results of this study, his recommendation was correct.

The finding that 2% halothane added to the gas mixture impaired ignition did not agree with results of Pashayan, *et al.* In 1966, Brown, *et al.*³⁵ studied the ignition risk of oxygen and nitrous oxide with halothane and concluded that halothane did not contribute to the risk of ignition "provided the concentrations of halothane recommended for use" were not greatly exceeded. Based on the conclusions of Brown, *et al.*, it would appear that the addition of 2% halothane to the anesthetic gas mixture should not alter the incendiary characteristics of an endotracheal tube. Therefore, the results of this part of the study were confusing. Two possible explana-

source of thermal energy in this study and the cautery and electrocautery knife which were used as the source of thermal energy by Brown, *et al.* and 2. differences in experimental design.

The findings from the third part of this study using the thermocouple revealed that the Xomed tube retained heat over a longer interval of time than either of the other two tubes. This might have accounted for the spontaneous reignition phenomenon noted in the continuous trials with this tube.

Although the results of this study strongly demonstrated that the red rubber tube was significantly more resistant to ignition than the Xomed tube, these findings should not be considered an endorsement of one tube over the other. In studies such as this, statistics have to be interpreted practically. All the data have to be analyzed and pieced together before any conclusions should be reached. For example, in this study, both tubes were found to be inferior because they both ignited when exposed to the laser in the continuous mode. However, most otolaryngologist—head and neck surgeons use the carbon dioxide laser in the shuttered (pulsed) mode for laryngeal surgery. Neither tube ignited in the pulsed mode trials in 100% oxygen. On occasion, the laser must be used in the continuous mode to control bleeding or to facilitate an endoscopic resection. The results of this study demonstrated the lack of safety of both tubes, when used unwrapped, in the continuous mode. Since present-generation carbon dioxide lasers cannot be programmed to eliminate the continuous mode option from their console, there is always the possibility that the laser nurse could depress the continuous button instead of the pulse button, jeopardizing an unwrapped endotracheal tube. Therefore, the Rusch red rubber tube and Xomed Laser-Shield tube should only be used for laryngeal laser surgery when they have wrapped with reflective, metallic tape.

Possible criticisms of this research project include the lack of individual trials on individual endotracheal tubes. This limitation was cited in the discussion about differences in experimental design, and raises certain questions about the Xomed Laser-Shield tube data. The choice of mean time to ignition endpoints is subject to criticism; if the surface fire time had been used as the endpoint instead of the intraluminal fire time, the Xomed tube would have been found to be the more resistant tube.

CONCLUSIONS

Many questions concerning laser safety in laryngeal surgery have been addressed by this research project. The laser-related complication rate in a selected group of otolaryngologists who attended a "hands-on" course that stressed safety precautions

was significantly lower than the complication rate in a group of otolaryngologists who had not attended such a course. All the participants in the study were members of a senior society. This study revealed a statistically significant complication rate in the group who had taken the "hands-on" workshop. Attendance at a "hands-on" laser course should be mandatory for all otolaryngologist—head and neck surgeons contemplating the use of this technology in their clinical practice, if they have not been adequately trained in laser surgery during their residency.

The knowledge gained from the tests on the incendiary characteristics of endotracheal tubes has raised some doubts about the level of safety associated with the use of the unwrapped Xomed Laser-Shield tube. Specifically, this tube was found to ignite at power densities lower than that suggested by the manufacturer in an atmosphere of 30% oxygen in helium. The polyvinyl chloride tube was the only tube to ignite during the shuttered mode trials and was considered unsafe for use in microlaryngeal laser surgery, even when wrapped with reflective, metallic tape. Both the Xomed Laser-Shield and Rusch red rubber tubes ignited during the continuous mode trials. Therefore, they should be wrapped with reflective, metallic tape if they are to be used in cases of laryngeal laser surgery. The safest anesthetic gas mixture for laryngeal laser surgery was found to be 30% oxygen in helium. Safety associated with the addition of 2% halothane to the anesthetic gas mixture was substantiated.

Based on the findings of this study, use of a reflective, metallic tape-wrapped Rusch red rubber endotracheal tube, or a Xomed Laser-Shield tube wrapped with reflective, metallic tape, should be considered the current standard of care when performing microlaryngeal surgery with the carbon dioxide laser in an intubated patient. The laser should be used in the shuttered mode, except when controlling bleeding or performing certain types of endoscopic resections. The anesthesiologist should ventilate the patient with 30% oxygen in helium and may use 2% halothane without any extra risks.

Additionally, the tube cuff should be protected by inflation with methylene blue-colored saline, neurosurgical cottonoids should be saturated with saline, and the operating platform should be utilized.

The development of a nonflammable endotracheal tube and cuff, for use in cases where microlaryngeal surgery is performed with the carbon dioxide laser, is still as necessary today as it was when Hirshman and Smith first stressed this need in 1980.

BIBLIOGRAPHY

1. Einstein, A.: Zur Quanten Theorie der Strahlung. *Phys. Zeit.*, 18:121, 1917.
2. Fried, M.P.: A Survey of the Complications of Laser Laryngoscopy. *Arch. Otolaryngol.*, 110:31-34, 1984.

3. Schawlow, A.L. and Townes, C.H.: Infrared and Optical Lasers. *Nature*, 187:393, 1960.
4. Schawlow, A.L. and Townes, C.H.: Atomic Frequency in the Crown Glass. *Phys. Rev. Lett.*, 7:444, 1961.
5. Ketcham, A.S., Hoyer, R.C. and Riggle, G.C.: A Surgeon's Appraisal of the Laser. *Surg. Clin. North Am.*, 47:1249-1263, 1967.
6. Patel, C.K.N.: Interpretation of CO₂ Optical Laser Experiments. *Phys. Rev. Lett.*, 12:588-590, 1964.
7. Yahr, W.Z. and Strully, K.J.: Blood Vessel Anastomosis and Other Biomedical Applications. *J. Assoc. Adv. Med. Inst.*, 1:28-31, 1966.
8. Polanyi, T.G., Bredemeier, H.C. and Davis, T.W., Jr.: A CO₂ Laser for Surgical Research. *Med. Biol. Eng.*, 8:541-548, 1970.
9. Gonzales, R., Edlich, R.F. and Bredemeier, H.C.: Rapid Control of Massive Hepatic Hemorrhages by Laser Radiation. *Surg. Gynecol. Obstet.*, 131:198-200, 1970.
10. Goodale, R.L., Okada, A., Gonzales, R., et al.: Rapid Endoscopic Control of Bleeding Gastric Erosions by Laser Radiation. *Arch. Surg.*, 101: 211-214, 1970.
11. Hall, R.R.: The Healing of Tissues Incised by a Carbon Dioxide Laser. *Br. J. Surg.*, 58:222-225, 1971.
12. Stellar, S.: The Carbon Dioxide Laser in Experimental and Clinical Surgery for Neoplasms. *Panminerva Med.*, 16: 32-36, 1974.
13. Jako, G.J.: Laser Surgery of the Vocal Cords. An Experimental Study with Carbon Dioxide Lasers on Dogs. *LARYNGOSCOPE*, 82:2204-2216, 1972.
14. Bredemeier, H.C.: 1969, *Laser Accessory for Surgical Applications*. U.S. Patent. 3, 659, 613, issued 1972.
15. Bredemeier, H.C.: 1973, *Stereo Laser Endoscopes*. U.S. Patent, 3, 796, 220, issued 1974.
16. Strong, M.S. and Jako, G.J.: Laser Surgery in the Larynx. *Ann. Otol. Rhinol. Laryngol.*, 81:791-798, 1972.
17. Leibowitz, H.M. and Peacock, G.R.: Corneal Injury Produced by Carbon Dioxide Laser Radiation. *Arch. Ophthalmol.*, 81:713-721, 1969.
18. Ward, P.H.: Otorhinolaryngology. *Surg. Gynecol. Obstet.*, 136:206-207, 1973.
19. Medical News: CO₂ Laser Used to Remove Lesions from Vocal Cords. *JAMA*, 221:451-453, 1972.
20. Strong, M.S., Jako, G.J., Polanyi, T., et al.: Laser Surgery in the Aerodigestive Tract. *Am. J. Surg.*, 126:533, 1973.
21. Andrews, A.H., Jr., Goldenberg, R.A., Moss, H.W., et al.: Carbon Dioxide Laser for Laryngeal Surgery. *Surg. Ann.*, 6:459-476, 1974.
22. Andrews, A.H., Jr. and Moss, H.W.: Experiences with the Carbon Dioxide Laser in the Larynx. *Ann. Otol. Rhinol. Laryngol.*, 83:162-170, 1974.
23. Birch, A.A.: Anesthetic Considerations During Laser Surgery. *Anesth. Analg.*, 52:53-58, 1973.
24. Snow, J.C., Kripke, B.J., Strong, M.S., et al.: Anesthesia for Carbon Dioxide Laser Microsurgery on the Larynx and Trachea. *Anesth. Analg.*, 53:507-512, 1974.
25. Konchigeri, H.N., Shaker, M.H.: Anaesthesia for Intralaryngeal Laser Surgery. *Can. Anaesth. Soc. J.*, 21:343-349, 1974.
26. Snow, J.C. and Norton, M.L.: Lasers and Anesthesia. *J. Am. Assoc. Nurs. Anesth.*, 43:464-469, 1975.
27. Strong, M.S., Vaughan, C.W., Healy, G.B., et al.: Recurrent Respiratory Papillomatosis. *Ann. Otol. Rhinol. Laryngol.*, 85:508-516, 1976.
28. Strong, M.S., Jako, G.J., Vaughan, C.W., et al.: The Use of the CO₂ Laser in Otolaryngology: A Progress Report. *Trans. Am. Acad. Ophthal. Otol.*, 82:595-602, 1976.
29. Shaker, M.H., Konchigeri, H.N., Andrews, A.H. Jr., et al.: Anesthetic Management for Carbon Dioxide Laser Surgery of the Larynx. *LARYNGOSCOPE*, 86:857-861, 1976.
30. Snow, J.C., Norton, M.L., Saluja, T.S., et al.: Fire Hazards During CO₂ Laser Microsurgery on the Larynx and Trachea. *Anesth. Analg.*, 55:146-147, 1976.
31. Norton, M.L., Strong, M.S., et al.: The Use of the CO₂ Laser in Otolaryngology. *LARYNGOSCOPE*, 86:656-663, 1976.
32. Vaughan, C.W.: Intraoperative Control of the CO₂ Laser: Laboratory Experiments and Clinical Experience. *LARYNGOSCOPE*, 88:1399-1420, 1978.
33. Hicks, J.J., Hicks, J.N., White, B.J., et al.: The Carbon Dioxide Laser in Surgery of the Larynx. *J. Med. Assoc. Ala.*, 29-30, May, 1978.
34. Norton, M.L. and de Vos, P.D.: New Endotracheal Tube for Laser Surgery of the Larynx. *Ann. Otol. Rhinol. Laryngol.*, 87:554-557, 1978.
35. Chang, J.L., Meeuwis, H., Bleyaert, A., et al.: Severe Abdominal Distention Following Jet Ventilation During General Anesthesia. *Anesthesiology*, 49:216, 1978.
36. Oliverio, R., Jr., Ruder, C.B., Fermon, C., et al.: Pneumothorax Secondary to Ball-Valve Obstruction During Jet Ventilation. *Anesthesiology*, 51:255-256, 1979.
37. Healy, G.B., McGill, T., Simpson, G.T., et al.: The Use of the Carbon Dioxide Laser in the Pediatric Airway. *J. Pediatr. Surg.*, 14:735-739, 1979.
38. Simpson, G.T., Healy, G.B., McGill, T., et al.: Benign Tumors and Lesions of the Larynx in Children. *Ann. Otol. Rhinol. Laryngol.*, 88:479-485, 1979.
39. Andrews, A.H.: Jewelry Chain on Cottonoids for CO₂ Laser Surgery. *Ann. Otol. Rhinol. Laryngol.*, 88:827, 1979.
40. DiBartolomeo, J.R.: Lasers in Modern Otolaryngology. *Trans. Pacific Coast Oto-Ophthal. Soc.*, 60:65-83, 1979.
41. Benjamin, B. and Gronow, D.: A New Tube for Microlaryngeal Surgery. *Anaesth. Intens. Care*, 7:258-263, 1979.
42. Brown, T.C.K.: Laser and the "Benjet" Tube. *Anaesth. Intens. Care*, 7:387, 1979.
43. Patil, V., Stehling, L.C. and Zauder, H.L.: A Modified Endotracheal Tube for Laser Microsurgery. *Anesthesiology*, 51:571, 1979.
44. Vourc'h, G., Tannieres, M.L. and Freche, G.: Anaesthesia for Microsurgery of the Larynx Using a Carbon Dioxide Laser. *Anaesthesia*, 34:53-57, 1979.
45. Vourc'h, G., Tannieres, M. and Freche, G.: Ignition of a Tracheal Tube During Laryngeal Laser Surgery. *Anaesthesia*, 34:685, 1979.
46. Burgess, G.E., III and LeJeune, F.E., Jr.: Endotracheal Tube Ignition During Laser Surgery of the Larynx. *Arch. Otolaryngol.*, 105:561-562, 1979.
47. Kaeder, C.S. and Hirshman, C.A.: Acute Airway Obstruction: A Complication of Aluminum Tape Wrapping of Tracheal Tubes in Laser Surgery. *Can. Anaesth. Soc. J.*, 26: 138-139, 1979.
48. Pratt, L.W.: The CO₂ Laser in Otolaryngology. *J. Maine Med. Assoc.*, 71:39-40, 45, 1980.
49. Carruth, J.A.S., McKenzie, A.L. and Wainwright, A.C.: The Carbon Dioxide Laser: Safety Aspects. *J. Laryngol. Otol.*, 94:411-417, 1980.
50. Hirshman, C.A. and Smith, J.: Indirect Ignition of the Endotracheal Tube During Carbon Dioxide Laser Surgery. *Arch. Otolaryngol.*, 106:639-641, 1980.
51. Hirshman, C.A. and Leon, D.: Ignition of an Endotracheal Tube During Laser Microsurgery. *Anesthesiology*, 53: 177, 1980.
52. Strong, M.S.: Editorial Comment. *Arch. Otolaryngol.*, 106: 641, 1980.
53. Hirshman, C.A., Leon, D., Porch, D., et al.: Improved Metal Endotracheal Tube for Laser Surgery of the Airway. *Anesth. Analg.*, 59:789-791, 1980.
54. Torres, L.E. and Reynolds, R.C.: Experiences with a New Endotracheal Tube for Microlaryngeal Surgery. *Anesthesiology*, 52:357-359, 1980.
55. Kalhan, S. and Regan, A.G.: A Further Modification of Endotracheal Tubes for Laser Microsurgery. *Anesthesiology*, 53:81, 1980.
56. Rontal, M., Rontal, E. and Wenokur, M.: Jet Insufflation Anesthesia for Endolaryngeal Surgery. *LARYNGOSCOPE*, 90:1162-1168, 1980.

58. Chang, J.L., Bleyaert, A. and Bedger, R.: Unilateral Pneumothorax Following Jet Ventilation During General Anesthesia. *Anesthesiology*, 53:244-246, 1980.
59. Meyers, A.: Complications of CO₂ Laser Surgery of the Larynx. *Ann. Otol. Rhinol. Laryngol.*, 90:132-134, 1981.
60. Alberti, P.W.: The Complications of CO₂ Laser Surgery in Otolaryngology. *Acta Otol.*, 91:375-381, 1981.
61. Schramm, V.L., Jr., Mattox, D.W. and Stool, S.E.: Acute Management of Laser-Ignited Intratracheal Explosion. *LARYNGOSCOPE*, 91:1417-1426, 1981.
62. Fried, M.P.: Complications of CO₂ Laser Surgery of the Larynx. *LARYNGOSCOPE*, 93:275-278, 1983.
63. Treyve, E., Yarrington, C.T., Jr. and Thompson, G.E.: Incendiary Characteristics of Endotracheal Tubes with the Carbon Dioxide Laser. *Ann. Otol. Rhinol. Laryngol.*, 90:328-330, 1981.
64. Yarrington, C.T., Jr. and Thompson, G.E.: Incendiary Characteristics of Endotracheal Tubes with the Carbon Dioxide Laser. *Ann. Otol. Rhinol. Laryngol.*, 91:605, 1982.
65. Ruder, C.B., Rapheal, N.L., Abramson, A.L., et al.: Anesthesia for Carbon Dioxide Laser Microsurgery of the Larynx. *Otolaryngol. Head Neck Surg.*, 89:732-737, 1981.
66. Kumar, A., Frost, E.: Prevention of Fire Hazard During Laser Microsurgery. *Anesthesiology*, 54:350, 1981.
67. Palas, T.A.: The Risk of Endotracheal Intubation for Carbon Dioxide Laser Microsurgery of the Larynx. *Anesthesiology*, 55:718-719, 1981.
68. Wainwright, A.C., Moody, R.A. and Carruth, J.A.S.: Anaesthetic Safety with the Carbon Dioxide Laser. *Anesthesia*, 36:411-415, 1981.
69. Kalhan, S.B. and Cascorbi, H.F.: Anesthetic Management of Laser Microlaryngeal Surgery. *Anesth. Rev.*, 8:23-27, 1981.
70. Cozine, K., Rosenbaum, L.M., Askanazi, J., et al.: Laser-Induced Endotracheal Tube Fire. *Anesthesiology*, 55:583-585, 1981.
71. Patel, K.F. and Hicks, J.N.: Prevention of Fire Hazards Associated with Use of Carbon Dioxide Lasers. *Anesth. Analg.*, 60:885-888, 1981.
72. LeJeune, F.E., Jr., LeTard, F., Guice, C., et al.: Heat Sink Protection Against Lasering Endotracheal Cuffs. *Ann. Otol. Rhinol. Laryngol.*, 91:606-607, 1982.
73. Healy, G.B., Strong, M.S., Shapshay, S., et al.: Complications of CO₂ Laser Surgery of the Aerodigestive Tract: Experience of 4416 Cases. *Otolaryngol. Head Neck Surg.*, 92:13-16, 1984.
74. Ganfield, R.A. and Chapin, J.W.: Pneumothorax with Upper Airway Laser Surgery. *Anesthesiology*, 56:398-399, 1982.
75. Ossoff, R.H., Karlan, M.S.: Instrumentation for Microlaryngeal Laser Surgery. *Otolaryngol. Head Neck Surg.*, 91:456-460, 1983.
76. Ossoff, R.H., Hotaling, A.J., Karlan, M.S., et al.: CO₂ Laser in Otolaryngology-Head and Neck Surgery: A Retrospective Analysis of Complications. *LARYNGOSCOPE*, 93:1287-1289, 1983.
77. Ossoff, R.H., Eisenman, T.S., Duncavage, J.A., et al.: Complications of Tracheal Damage from Laser-Ignited Endotracheal Tube Fires. *Ann. Otol. Rhinol. Laryngol.*, 92:333-336, 1983.
78. Ossoff, R.H. and Karlan, M.S.: Safe Instrumentation in Laser Surgery. *Otolaryngol. Head Neck Surg.*, 92:644-648, 1983.
79. Woo, P. and Vaughan, C.W.: A Safe, Nonflammable, All-Metal, Cuffless Endotracheal Venturi Ventilation System for Use in Laser Surgery. *Otolaryngol. Head Neck Surg.*, 91:497-501, 1983.
80. Chilcoat, R.T., Byles, P.H. and Kellman, R.M.: The Hazard of Nitrous Oxide During Laser Endoscopic Surgery. *Anesthesiology*, 59:258, 1983.
81. Hermens, J.M., Bennett, M.J. and Hirshman, C.A.: Anesthesia for Laser Surgery. *Anesth. Analg.*, 62:218-229, 1983.
82. Brightwell, A.P.: A Complication of the Use of the Laser in ENT Surgery. *J. Laryngol. Otol.*, 97:671-672, 1983.
83. Norton, M.L.: Anesthesia for Laser Surgery in Laryngobronchoesophagology. *Otolaryngol. Clin. North Am.*, 16:785-791, 1983.
84. Andrews, A.H.: The Use of the CO₂ Laser in Otolaryngology: Ten Years of Experience. *Lasers Surg. Med.*, 4:305-310, 1984.
85. Johans, T.G. and Reichert, T.J.: An Insufflation Device for Anesthesia During Subglottic Carbon Dioxide Laser Microsurgery in Children. *Anesth. Analg.*, 63:368-370, 1984.
86. Benjamin, B.: Anesthesia for Laryngoscopy. *Ann. Otol. Rhinol. Laryngol.*, 93:338-342, 1984.
87. Silver, C.E., Schneider, K.L., Merav, A.D., et al.: Prototype Airway Management System for Use During Laser Surgery. *LARYNGOSCOPE*, 94:1511-1512, 1984.
88. Hayes, D.M., Gaba, D.M. and Goode, R.L.: Incendiary Characteristics of a New Laser-Resistant Endotracheal Tube. *Otolaryngol. Head Neck Surg.*, 95:37-40, 1986.
89. Ohashi, N., Asai, M., Ueda, S., et al.: Hazard to Endotracheal Tubes by CO₂ Laser Beam. *ORL J. Otorhinolaryngol. Relat. Spec.*, 47:22-25, 1985.
90. O'Sullivan, T.J. and Healy, G.B.: Complications of Venturi Jet Ventilation During Microlaryngeal Surgery. *Arch. Otolaryngol.*, 111:127-131, 1985.
91. Pashayan, A.G. and Gravenstein, J.S.: Helium Retards Endotracheal Tube Fires from Carbon Dioxide Lasers. *Anesthesiology*, 62:274-277, 1985.
92. Lim, R.Y. and Kenney, C.L.: Precaution and Safety in Carbon Dioxide Laser Surgery. *Otolaryngol. Head Neck Surg.*, 95:239-242, 1986.
93. Fontenot, R., Jr., Bailey, B.J., Stiernberg, C.M., et al.: Endotracheal Tube Safety During Laser Surgery. *LARYNGOSCOPE*, 97:919-921, 1987.
94. *Product Information Insert: Laser-Shield Endotracheal Tube, Cuffed* Xomed, Inc., Jacksonville, Fla.
95. Brown, T.A. and Morris, G.: The Ignition Risk with Mixtures of Oxygen and Nitrous Oxide with Halothane. *Br. J. Anaesth.*, 38:164-173, 1966.

with bone samples placed at the focal point. The efficiency of bone tissue ablation is expressed as time needed to remove a certain ablation length at a standard bone thickness. The experimental results indicated that using an Er:YAG laser with single pulse energy ranging from 46.5 to 344 mJ, repetition rate of 1-5 Hz, the mastoid bone was removed at the ablation speeds varying from 0.022 to 0.208 mm/s, dependant upon the given laser output settings. At repetition rates of 4 Hz or 5 Hz, the ablated line was wider. These preliminary tests showed the single pulse energy ranging from 46.5 to 200 mJ with 2 a Hz repetition rate might be the optimal condition for the mastoid bone removal with minimal damage in surrounding tissue.

207

PHOTOTHERAPY OF EXPERIMENTAL BRAIN TUMORS WITH CHALCOGENAPYRYLIUM DYES

Selenapyrylium and tellurapyrylium dyes act as effective photosensitizers *in vitro* by targeting to the mitochondria of transformed cells. Radiation of mitochondrial suspensions treated with these dyes causes inhibition of the function of cytochrome c oxidase via the production of singlet oxygen. Electronmicrographs of U-251 glioma cells treated for 15 minutes with 10 μ M of a telluro-selenapyrylium compound and then exposed to 100 mW/cm² of 775 \pm 15 nm light for 15 minutes produced by an argon-pumped dye laser show swelling of the mitochondria with disruption of the mitochondrial inner membrane. Furthermore, these cationic lipophilic dyes are capable of passing the blood brain barrier and are concentrated in tumor tissue relative to normal brain tissue (selectivity ratio equal to 5.3 or greater). Preliminary *in vivo* studies show delayed cellular necrosis following intravenous injection of these compounds and irradiation of the tumor by laser light. Thus, these compounds appear to have a tremendous potential for *in vivo* management of neoplastic disease. We are currently investigating the function of other mitochondrial enzymes upon treatment with the chalcogenapyrylium dyes as well as investigating the presence of these dyes in other subcellular sites.

208

STATE OF THE ART, LASERS IN NEUROSURGERY
P.W.Ascher

Over 1300 procedures on the central and peripheral nervous system have been done with the CO₂ and the Nd:YAG lasers since their introduction at the Department of Neurosurgery at the University of Graz. The biophysical fundamentals of laser surgery were evaluated experimentally at our hospital and have been described in detail. The theoretical considerations that led to the laser's use have been confirmed. The CO₂ laser, with a wavelength of 10.6 μ m, is a superior instrument for cutting and vaporization. Its penetration depth is under precise control, making the CO₂ laser predesigned for use on the brainstem (92 patients) and in the spinal cord (18 patients). The 1.06 μ m Nd:YAG laser's deep penetration is a result of scatterin, and prohibits its use in these areas. Its advantages lie in its ability as an excellent coagulator, and to denature tissue in depth. With the available fiber optic systems, the Nd:YAG lasers is also well suited for endoscopic procedures as well as for operations on highly vascular tumors such as meningiomas. Since October 1986 we are studying the applicability of the 1.32 μ m Nd:YAG laser. The cutting ability of this laser approaches that of the CO₂ laser, its penetration is significantly less than that of the original 1.06 μ m Nd:YAG laser. We have experimentally tested the argon laser for the obliteration of plaque and thrombus in carotid artery disease. The results were not encouraging. Thus today we use both the 1.06 μ m and the 1.32 Nd:YAG laser for endoscopic recanalization of central and peripheral arteries. We are also studying the Nd:YAG lasers for the vaporization of

the nucleus pulposus in patients with intervertebral disc disease (appropriate fiber optics for the CO₂ laser are not available). Preliminary results are encouraging here, as in the preganglionic stellatum denervation on patients with hyperhidrosis. The 1.06 μ m Nd:YAG laser has proven an excellent tool in over 100 endoscopic procedures. With the introduction of nuclear magnetic resonance imaging, we are studying the stereotactic use of the Nd:YAG laser for interstitial heat denaturation of semibenign central astrocytomas.

Otolaryngology/Pulmonary

209

CONTACT YAG LASER FOR TONSILLECTOMY

Deniz F. Bastug, MD; Romeo Y. Lim, MD, FACS, West Virginia University Health Sciences Center, Charleston Division
The advent of the laser ushered in a new era of surgical versatility and precision. This paper reports the use of the contact Nd:YAG laser for tonsillectomy in 100 consecutive patients. When compared to the conventional and electrocoagulation technique the Nd:YAG laser method had distinct benefits of less blood loss, less postoperative tissue reaction and granulation tissue formation, subjectively less postoperative pain, and less postoperative bleeding. Because of decreased morbidity, 90% of these patients were discharged on the same day of surgery.

210

KTP LASER-INDUCED MODULATION OF THE WOUND HEALING PROCESS

Michael D. Kyzer, Al S. Aly, and Robert M. Ossoff, Vanderbilt University Medical Center, Nashville, TN 37232
Castro, et. al., have reported the Nd:YAG mediated alteration of fibroblast collagen synthesis *in vitro* without concomitant cellular damage. This project investigates a similar process in an *in vivo* rat system using the KTP laser (532 nm). Sprague-Dawley rats were anesthetized with ketamine and pentobarbital (intraperitoneally), and subsequently their dorsal epidermis was shaved. The exposed epidermis was then cleaned with a moist cloth to remove residual melanin pigment which possesses a significant extinction coefficient at 532 nm. The rats were then mounted on a plexiglass translation stage whose rate of horizontal movement was fixed at 0.11 cm/s; the defocused KTP beam (dia. 1 cm) was directed at the rats' dorsum, and the translation was of sufficient duration to produce two discrete 3.0 cm ipsilateral strips. One of these strips was produced with a 2W beam and the other with a 3.5W beam. A scalpel was then used to create an incision down the center of each lased strip; matched control incisions of identical length were made on the contralateral side. The incisions were each closed with four skin staples, and the tensile strength of the wounds was measured acutely, and on days 3, 7, 14, and 23 postoperatively. The results show that the KTP laser effected the alteration of normal wound healing biology in such a manner as to accelerate the initial formation of wounds having supranormal tensile strength. Indeed, preliminary data indicate that these hypertensile wounds supercede the strength of their matched controls by 32% at day 3 (n=5 for each time point), presumably secondary to augmented fibroblast collagen deposition at the wound site. The rate of collagen synthesis in the irradiated tissue will be determined by a ³H-hydroxyproline assay specific for collagen production. Furthermore, the distribution of fibroblast activity will be investigated by an *in situ* immunohistochemical localization technique which utilizes a radioactive probe specific for collagen messenger RNA. The present results already suggest the potential role of the laser in modulating the process of scar formation.

211

ENDOSC

Romeo Y

Various

lead to

arytenoi

preserve

facility

airway

laser ar

212

CO₂ LA

Romeo Y

Introduc

laryngea

in otol

aciatric

transora

dioxide

various

are: p

and avc

213

CO₂ LA

Romeo Y

The CO

for pa

prepara

98% of

is an

predict

214

ENDOS

BARE

Medic

Cente

laser

tip c

flow

tissi

cerar

be he

exper

both

diff

fibe

bronc

keep

This

nece

tips

expe

tips

watt

have

manu

cann

of t

que.

fibe

can

tech

char

core

the

necr

beco

be s

two.

Technical Solutions Using Q-switched Nd:YAG Lasers
for Laser Induced Shockwave Lithotripsy

F. Frank¹, F. Wondrazek¹, J. Pensel², N. Schmeller²

¹ HBB-Medizintechnik GmbH, Applikationsforschung, München

² Urologische Klinik und Poliklinik der Medizinischen
Universität zu Lübeck, Lübeck

With high power lasers electrical field strengths of light above the threshold of optical breakdown can be generated. The amplitudes of the emitted shockwaves are high enough to fracture all kinds of stones deposited in the human body. Via a special device light pulses of 70 mJ and 20 ns generated by a Q-switched Nd:YAG laser are coupled into a flexible optical fiber. The parameters of the laser system are optimized for the beam transmission in thin quartz-glass fibers of down to 0,6 mm in diameter. In the vicinity of the concrement the electromagnetic energy of the light pulse is converted into acoustic shockwave energy by means of special optical devices or opto-acoustic couplers. These systems are combined with miniaturized acoustic reflectors which direct the shockwaves towards the calculus. An essential feature of these devices is their endoscopic application.

137

The pulsed dye laser versus the Q-switched Nd:YAG laser in laser induced shock wave lithotripsy -
Physical and technical aspects

S. Thomas, J. Pensel, W. Meyer, R. Engelhardt, M. Köster
Medical Laser Center Lübeck and Dept. for Urology,
Medical University Lübeck

Two laser systems for laser induced shock wave lithotripsy are available as of today, the pulsed dye laser and the Q-switched Nd:YAG laser. The two systems differ in such essential parameters as wavelength, pulselength, and fiber input and output characteristics.

For clinical application the following demands must be met:

- high stone selectivity
- easy maintenance
- high effectiveness
- easy applicability
- high flexibility
- pain-free treatment

A critical evaluation of advantages and disadvantages of both systems as to the demands mentioned above is given. Special stress is laid on the wavelength dependent effects of calculus destruction and the main side effect of tissue injury.

138

Laser induced shock wave lithotripsy -
The Q-switched Nd:YAG Laser in clinical practice

S. Thomas, J. Pensel, A.G. Hofstetter
Medical Laser Center Lübeck and Dept. for Urology,
Medical University Lübeck

The development of an opto-mechanical coupler for Q-switched Nd:YAG laser lithotripsy enables ureteral application either endoscopically or non-visual application under fluoroscopic control.

The Q-switched Nd:YAG laser system employing the opto-mechanical coupler has decisive advantages in urologic applications over the dye laser:

- 1) the laser induced breakdown is created independent of stone or surrounding medium
- 2) the plasma bubble is shielded against the tissue
- 3) direct contact or defined distance to the stone is not necessary
- 4) tissue damage is minimal even if direct irradiation is maintained over a prolonged period.

Clinical assessment of endoscopic and blind application is currently being performed at the Urologic department of the

Medical University Lübeck.

Results: During the technical development of an endoscopically applicable system 2 patients were treated percutaneously and 16 patients by transurethral approach. In 11 patients stone desintegration was performed solely by LSL. In two cases the impacted ureteral stone was mobilized and pushed into the renal pelvis where following ESWL could be performed. Technical defects necessitated the adjuvant use of conventional sonotrodes.

A state up of all patients treated until April 1, 1988 will be given.

Biostimulation

139

ARE MAST CELLS IMPLICATED IN THE INTERACTION OF LOW-POWER-LASER AND TISSUE?

M.A.Trelles, M.D.*. E.Mayayo, M.D.Ph.Dr.**. L.Miro, M.D.Ph.Dr., Dr.Phys.***
J.Rigau, M.D.*, G.Baudin, M.D.***

Summary

We have examined the tongue of the swiss mouse, (rich in these cells) after 2,4 j/cm² He-Ne 632 nm laser irradiation on alternate days (5 sessions) to confirm the possible non-selective action of low power laser in the degranulation of mast cells (MC). Results after irradiation with two different out-put lasers, but applying the same energy density, were quantitatively and morphometrically evaluated by using optomicroscopy and electromicroscopy examination. At the same time, by means of Radio Immunity Assay (RIA), the tongue, which was previously pulverized, was analyzed quantitatively and statistically in their Histamine component, observing that its level changed at the end of the experiment compared with the normal level of Histamine of the non-irradiated tongues.

On the other hand, Histamine contained in MC granules which may pass into the blood stream of the animal on account of the tongue laser irradiation was also gauged, noting that practically in all cases, the level vary after laser irradiation and that just one laser irradiation, of the above mentioned characteristics, was capable of producing histological changes on the tissue as for example vasodilation and active releasing of MC granules to the interstitial cell-medium.

The observations of this study may serve as one of the possible explanations regarding the biostimulatory mechanisms of low-power-laser-radiation, a process not yet fully understood and which has been presented as an effective therapeutic procedure.

* The Medical Institute of Vilafortuny, Cambrils/Tarragona -E

** Histology Dept. of the Medical School of Reus/University of Barcelona -E

*** Central Service of Nuclear Medicine, Medical Biophysics and Radioimmunology/Regional University Hospital of Nimes -F

IV-AA

140

A PRELIMINARY STUDY OF THE EFFECT OF CO₂ LASER RADIATION ON CULTURED ENDOTHELIUM AND ON THE ADHESION OF NEUTROPHILS TO THESE IRRADIATED CELLS. ALALY, Caroline Kerr, Richard Hoover, Robert H. Ossoff. Vanderbilt University, Nashville Tennessee.

Polymorphonuclear leukocytes (neutrophils) and vascular endothelial cells interact with each other for a variety of physiologic and pathologic reasons. The initial step in an inflammatory response is increased neutrophil adhesion to the endothelium. The purpose of this study is to determine whether CO₂ laser radiation affects neutrophil-endothelial cell adhesion and thus modify the inflammatory response. Initially the effect of irradiation on endothelium integrity was determined, using a ⁵¹Cr release assay. Endothelial cells (from bovine lung microvasculature) were grown to

Aly et al

confluence in 6.4 mm diameter wells and labelled with ^{51}Cr . The cells were irradiated with CO_2 laser energy in the range 0.34 - 10.00 watts/cm². The amount of ^{51}Cr released from the cells, as an indicator of cell injury, was measured 1, 24, 48 and 72 hours after irradiation. Power densities of 2.31 watts/cm² and above, when delivered to the cells, caused a significantly greater amount of ^{51}Cr release compared to that from non-lased, control cells ($p < 0.01$; Student's t-test). ^{51}Cr release, as a result of power densities of 1.44 watts/cm² or below, was no different from that of controls.

Using the same laser energies as above, the effect of CO_2 radiation on neutrophil-endothelial adhesion was measured. Endothelial cells were grown to confluence in 11 mm diameter wells and irradiated. ^{51}Cr -labelled neutrophils were then added to the cultures 1 and 6 hours after irradiation. The ^{51}Cr -neutrophils were left to attach for 45 minutes, excess neutrophils removed and the remaining ^{51}Cr measured and used as an index of neutrophil attachment. Preliminary results indicate that adhesion of neutrophils to endothelial cells is not affected up to 6 hours after lasing. Further study will determine whether adhesion is altered up to 24 hours post radiation.

141

EFFECTS OF WEAK LASER LIGHT AND OXYGEN ACTIVATION IN OPEN BIOLOGICAL SYSTEMS. H. Klima, Atomic Institute of the Austrian Universities, Vienna, Austria

Our knowledge of open systems has been extensively improved during the last decade. It was found that open systems can create new structures, which can be compared with essential states of living systems. One specific feature of these new structures is their weak stability and their ability to change from one structure into another one, even by weak stimuli.

From a biophysical point of view, the main interaction in living systems is the electromagnetic interaction. Therefore, weak electromagnetic stimuli, e.g. appropriate laser light, are able to influence macroscopic changes of biological patterns (cell division, tissue growth, etc.). Such phenomena have been studied in vitro and in vivo in photomedicine and photobiology as well as in photobiophysics.

Normally, living systems like human beings are able to produce such an active biological light spontaneously. This photon emission can be measured by sensitive photon counting devices. As for immune reactions, one of the main sources of these photons seems to be activated oxygen. Oxygen molecules in activated singlet states are produced by oxidases located in the membranes of phagocytes.

It is well known that activated singlet oxygen can be produced by ionized oxygen under certain conditions in a spontaneous reaction called dismutation. Immunological effects of activated or ionized oxygen are known in oxygen therapies. Therefore, one can assume that there are the same fundamental photobiophysical processes in laser therapy and activated oxygen therapy.

142

LASER WOUND HEALING CAN BE EXPLAINED BY THE PHOTODISSOCIATION OF OXYHEMOGLOBIN. Irving Itzkan, Stephen Tang, Donna Bourgelais. Medical Laser R&D Corporation, Woburn, MA.

Abstract. A proposed physiological explanation for some observed biostimulation effects, in particular laser enhanced wound healing, may be the photodissociation of oxyhemoglobin. The use of hyperbaric oxygen is known to be efficacious in accelerating wound healing. Published in vitro measurements of photodissociation quantum efficiency support the conclusion that metabolically significant O_2 can also be provided by the topical application of light, enhancing the delivery of O_2 from the blood at the irradiated site. Proposed mechanisms for the O_2 effects include stimulating the activity of leukocytes and other high metabolic rate cells and direct action on anaerobic bacteria. Appropriate fluences, wavelength range, and treatment schedules may be estimated from previously published results.

143

MECHANISMS OF LASER-TISSUE INTERACTION IN HIGH AND LOW POWER LASER APPLICATIONS

Dr. S. K. Davi, Director of Clinical Investigations, Medical Lasers, Inc., Rockville, Maryland 20852

Laser-tissue interaction in tissues that result in observed effects of tissue ablation, vaporization and biostimulation is thought to be mediated through processes that include,

- 1) Direct photon induced ablation,
- 2) Ultrafast thermal events, as in photon/phonon interaction,
- 3) Remote effects due to a. fluorescence and scattering, b. resonance induced as a result of pulse repetition, c. acoustic recoil, d. shock waves due to supersonic expansion related to energy deposition during ultrashort pulses,
- 4) Photo dissociation.

The postulated molecular mechanisms of some of these processes are briefly reviewed.

144

LOW-ENERGY HE-NE + I.R. LASER EFFECTS ON WOUND HEALING IN ANIMALS AND HUMAN BODY. Z. Simunovic and A.D. Ivankovich, Department of Anaesthesiology, District Hospital "La Carità", Locarno, Switzerland and Department of Anaesthesiology, University of Illinois, Chicago, Illinois.

In this study, we have examined evaluation on wound healing by a full skin thickness incision on rabbits randomly divided into four equal groups.

Photographs of the wounds were taken on different days and wound areas were analysed by ANOVA. After three weeks the animals were sacrificed and tissue samples through the wound site were taken for histology and tensile strength determination.

The ways of application of the laser therapy in human body are analogous to those of similar pathological contests in other tissues.

The main difference consists in the fact that, while for the affections of the locomotor and cutaneous systems the rays are applied on tissues covered by more or less integral skin, in this case when you irradiate a mucous membrane i.e. a subtle tissue without corneus stratum, the mucous area is able to absorb better the laser rays, and for this reason the total energy-rate of rays is lower.

In conclusion we observed that He-Ne + I.R. laser irradiation accelerated speed of the cicatrization with significant effects on tissue tensile strength, epidermal growth, rate of wound contracture, collagen formation and lymphocyte concentration rushing regression of post-operative oedema with pain relieve.

145

THE INFLUENCE OF LASER ON THE LYMPHATIC SYSTEM

P.C. LIEVENS, University of Brussels, Belgium

Two indications where laser therapy is often prescribed are edema and wound healing.

Clinically it is observed that there is a better drainage of the edema after laser treatment. We examined the vasomotricity of the lymphatic system in order to find a reason of these spectacular results. We found that only in cases where edema was evident, we were able to activate the lymphvessels with laser. When no edema was present no action was observed. As Mester stated it, wounds have the tendency to heal

coefficient, μ_a , is $\approx 17,900 \text{ cm}^{-1}$, which is higher than previously thought.

(2) Expt (2): the rate of surface disruption, $-dT/dt$, is slow (10^3 - 10^4 s^{-1} , or 0.1-1 ms) when the laser-induced energy density produces temperatures of 100-635°C. Above 635°C the disruption rate increases ≈ 3000 -fold (10^7 - 10^8 s^{-1} , or 10-100 ns). This temperature corresponds to the 2570 J/cc enthalpic energy required for complete phase change of the irradiated water.

(3) Expt (3): the photographic records directly support the above results, and illustrate explosive vaporization of the ablation site irradiated by the central region of the Gaussian laser beam that attains 635°C, and slight surface disruption in a surrounding ring that reaches 100-635°C.

The results for the Q-switched Ho-YAG indicate that explosive vaporization can occur if the laser-induced temperature exceeds only 100°C. The deep penetration of the Ho-YAG laser heats a thicker tissue layer and defeats thermal diffusion. A great deal of liquid water is subsequently ejected on the ms timescale, apparently due to the low-pressure that trails the initially ejected mass.

In contrast, the Er-YAG laser heats only a surface layer ($<1\text{-}\mu\text{m}$ thick), and thermal diffusion can cool the heated layer. Unless the temperatures achieve 635°C, the surface layer cools rapidly by diffusion, and rapid evaporation rather than explosive phase change occurs.

24

A HISTOLOGIC COMPARISON OF SUPERPULSE CO₂ AND CHOPPED CONTINUOUS WAVE CO₂ LASER TISSUE EFFECTS

Jay Weckhaver, Vanderbilt University, Nashville, TN.

Bruce R. Maddern, Nemours Clinic, Jacksonville, Fla.

David Kardatzke, University of Pittsburgh, Pittsburgh, Pa.

David M. Harris, Wensku Laser Center, Chicago, Ill.

Superpulsing a carbon dioxide laser beam is an option on many medical lasers. The observation of less charring at the impact site is observed clinically but no quantitative study has been done to examine the range of effects of the various parameters of superpulse (i.e. pulse duration [PD] and repetition rate [RR]).

Quantitative histologic measurements on an animal model (depilated rat skin) were performed using a Coherent XL-55 CO₂ laser. The available range of superpulse parameters were a pulse duration of 100 - 900 microseconds and repetition rate from 100 - 900 Hz (RR dependent upon PD). Nineteen sets of superpulse variables were paired with chopped continuous wave pulses of the same average power to tissue. The zone of thermal coagulation for each impact was measured.

Eighteen of nineteen superpulse parameters demonstrated less thermal coagulation than the continuous wave impact. Most were significant at the $p < 0.05$ level (controlling for the comparison-wise error rate).

The advantage of less charring and less thermal coagulation suggests superpulse is clinically useful, especially in areas such as the glottis where minimal thermal effect is desired.

Supported by a grant from The Children's Hospital of Pittsburgh and Coherent Medical Lasers, Palo Alto, Ca.

25

PRIMARY LABORATORY RESEARCH FOR CUTTING & WELDING OF SKIN SOFT TISSUE LIVER AND SPLEEN OF THE ANIMALS WITH LOW POWER YAG-CO₂ JOINED LASERS

Fu-Shou Yang, Zi-Fang Qiu, Zeng-Ji Xu, Dong-Mei Yuan, et al.

Dept. of Laser Medicine, Shanghai Seamen's Hospital, Shanghai 200080, China.

In this research, the operation was made by low power: 10.6 μm (0-3w) CO₂ laser and 1.06 μm (0-1w) YAG laser. As a scalpel, the focal spot diameter $< 0.5 \text{ mm}$ of CO₂ laser was used to cutting the skin of abdomen wall, and internal organs of small rats. We welded the tissues, closed the blood vessels with the terminal power $\leq 1\text{w}$ of YAG laser fiber. The manual operation of the cutting and welding by lasers was made under the magnifying lens.

20 pure race, small and male rats were used in the research, the weight of each was about of 20 grams. They were divided into liver group and spleen group. Each group contained 10 rats. After laser operation, the survival rate was separately 70 % (liver group) and 56 % (spleen group). One week after the operation, the activity of these

rats recovered to normal conditions. After one month's following inspection, the rats were then anatomized.

Through histological observation, we found the appearance of an evident laser biological effect in the welding area of operation.

26

EFFECT OF WAVELENGTH ON THE SAFETY AND EFFICACY OF LASER LITHOTRIPSY, Krishna M. Bhatta, Thomas Flotte, Norman S.

Nishioka, Wellman Laboratories of Photomedicine,

Massachusetts General Hospital, Boston, Massachusetts

The pulsed dye laser has been used for laser lithotripsy since 1985. The wavelength for laser lithotripsy (504 nm) was chosen based on stone fragmentation efficiency data. However, we recently demonstrated that in the presence of blood, the clinically used dye laser system can perforate a rabbit bladder in 2 pulses. This has raised concerns about the feasibility of developing a safe technique for performing lithotripsy without the benefit of direct visualization. Because the absorption coefficient of blood decreases at longer wavelengths, we wondered whether using longer wavelength laser pulses might yield a greater margin of safety. Therefore, we compared the fragmentation thresholds, fragmentation rates and tissue effects produced by dye lasers operating at 504, 630 and 695 nm. All laser pulses were transmitted through a 0.2 mm core-diameter quartz fiber. Fragmentation threshold and fragmentation rate increased with increasing wavelength. The magnitude of this increase was strongly influenced by stone composition, with the lighter colored stones having the greatest increase. Satisfactory fragmentation was achieved with 60 mJ/pulse at 504 nm, 65 mJ/pulse at 630 nm, and 90 mJ/pulse at 695 nm. Using these pulse energies, *in vivo* experiments in rabbits demonstrated that in the absence of blood, more than 100 pulses were required to perforate a rabbit bladder, regardless of wavelength. However, in presence of a submucosal blood vessel or overlying blood, perforation of the bladder was produced by 2 pulses at 504 nm, 20 pulses at 630 nm, and more than 100 pulses at 695 nm. Thus, our results suggest that using a longer wavelength laser increases the margin of safety for laser lithotripsy. These findings may be useful to investigators developing laser lithotripsy applications that dispense with direct visualization.

27

COMPARISON OF SAPPHIRE CONTACT SCALPERS FOR SURGERY

RJ Lanzafame, T Brien, DW Rogers, J Blackman, JR Hinshaw, Rochester General Hospital Laser Center, Rochester, NY

Controversy remains as regards the mechanism for the observed tissue effects of sapphire tips as well as what is the optimum use of the myriad of tips available. This study investigated the ability of sapphire scalpels to incise, achieve hemostasis and the speed of incision. Sapphire contact scalpels were obtained from Heraeus Lasersonics (Santa Clara, CA), Sharplan (Allendale, NJ) and Surgical Laser Technology (SLT, Malvern, PA). Frosted and unfrosted versions were tested. All blades were tested at 15W continuous wave output on skin and liver in anesthetized New Zealand white rabbits. Histologic evaluation of the zone of coagulation was performed on coded samples by an observer who was unaware of the code. The duration of each incisional procedure was timed with a chronograph and recorded on videotape. The following observations were made: speed of warm up (virgin blade) SLT > Sharplan > Heraeus, subcutaneous hemostasis after skin incision - Sharplan > Heraeus > SLT, speed of incision after warm up SLT > Sharplan > Heraeus. In general, there was no significant difference between the manufacturers as regards the width of the zone of coagulation, nor were any major differences observed when clear and frosted versions were tested. Some Sharplan prototype tips (specially coated) had a faster warm up and slightly faster incisional speed than commercial production tips. However, this was not statistically

Interaction of Radiation with Cells and Cell Components

J. Tribble, J. Kozub, G. Edwards, K. Lane, A. Aly, and R. Ossoff,
Vanderbilt University

The first step of this study involved reducing the scattered light from a suspension of living cells in order to reveal their UV-Vis absorption characteristics. Low power optical density was measured for suspensions of different cell types as a function of refractive index of the suspending protein solution. The protein concentration yielding minimum optical density was found and UV-Vis absorbance spectra of the "clarified" suspension and of cells in normal saline were recorded. Based on these results, we are investigating wavelength dependent effects of pulsed radiation from an Nd:YAG pumped tunable dye laser. The first series of laser experiments, to determine bacteriostasis as a function of laser power and wavelength, correlate with absorption spectra.

IV.- DD

THE EFFECT OF CO₂ LASER ON FIBROBLAST CULTURES

John F. Laurenzo

Al S. Aly, M.D.

Jeffrey Davidson, Ph.D.

Robert M. Ossiff D.M.D., M.D.

Achilles A. Demetrio M.D., Ph.D.

Surgeons, particularly in the field of otolaryngology/head and neck surgery, have been developing and refining applications for the carbon dioxide (CO_2) laser for the past 10 to 15 years. During this time, many studies of CO_2 laser wound healing have appeared, most comparing healing of laser and standard scalpel incisions. These reports consistently described delays in CO_2 laser wound healing when compared to healing of scalpel incisions. Several studies involving skin wound tensile strength comparisons between scalpel and laser incisions in rats (6) and pigs (2,5) have shown that healing laser wounds are significantly weaker for several weeks post-incision. In a histologic comparison of laser and scalpel incisions in pigs, Norris and Mullarky (10) noted delayed collagen formation in laser incisions as compared to scalpel incisions. Using laser- and scalpel-cut explants taken from pig skin, Moreno et al (9) found that while epithelialization proceeded at the same rate from both types of explant, the onset of epithelialization from laser-cut explants was delayed. Despite this accumulation of information on CO_2 laser wound healing, a good understanding of this topic as well as the effects of CO_2 laser on cell growth and metabolism has not yet been achieved. Our study investigated the CO_2 laser wound healing process by examining laser effects on fibroblasts, perhaps the most important cells involved in the wound healing process. Specifically, we studied the effect of noncytotoxic, defocused CO_2 laser energy, similar to that experienced by cells adjacent to a surgical laser wound, on proliferation of human dermal fibroblasts in culture.

Materials and Methods

The basic method used in this experiment is based on that used by Castro et al (4) in a previous Nd/YAG laser experiment.

Preparation of cell cultures

Frozen samples of human dermal fibroblasts were thawed and plated in culture flasks containing a growth medium composed of Dulbecco's modified Eagle's medium (DMEM) with 20% fetal bovine serum, 100 U/ml penicillin, 100 ug/ml streptomycin, and .025 ug/ml amphotericin. Cells were then removed by trypsinization and suspended for inoculation into 96-well tissue culture plates (Gibco, diameter of single well = .64 cm). Prior to inoculation, the suspension was counted by hemacytometer and the volume then adjusted to allow inoculation of 5×10^3 cells in .2 ml medium per well. Pilot experiments demonstrated that cells reached confluence at approximately 1×10^5 fibroblasts per well as determined by Coulter counter, following trypsinization. Since fibroblasts typically divide every 12 to 24 hrs. until reaching confluence and subsequent growth inhibition, inoculation of cells at less than 10% of confluence assured that cells would be in the logarithmic growth phase throughout the experiment. Cells were allowed 24 hrs. to attach prior to laser treatment. Immediately prior to irradiation, the medium was removed to minimize energy absorption by the growth medium, thereby limiting possible thermal effects due to laser heating of the growth medium. After laser treatment, culture wells received .2 ml of fresh medium and were then returned to incubation at 37° C. Culture medium was changed every 2 days.

Laser properties

The laser used in this experiment was a Sharplan 1040 surgical CO₂ laser with milliwatt capabilities (100 mW and up). Culture irradiation was performed using continuous wave mode. We adjusted beam diameter using the continuously variable defocus dial (CVD) on the Sharplan 719 micromanipulator attachment. Using a 400 mm focal length lens, adjustment of the CVD allowed us to produce a .616 cm diameter spot. This spot diameter allowed coverage of 92.6% of the culture surface, thereby producing extensive coverage of

the culture yet allowing room to avoid interference of the beam by the sides of the well.

Selection of Beam Intensities

Information on laser-tissue interactions published by Sliney (12) suggested that the maximal noncytotoxic CO₂ beam intensity was in the range of 10 W/cm² and less (precise CO₂ laser dose-response curves using fibroblast cultures are presently being established in our laboratory). We therefore chose to irradiate cultures using power levels from 0.1 to 3.0 W., holding spot diameter constant at .616 cm (Table 1). Exposure duration was held constant at .5 seconds.

Determination of cell viability and proliferation

At 1, 12, 24, 48, and 72 hrs. post-irradiation, cells from 4 wells per each power setting along with 4 control wells were examined for viability and proliferation using the trypan blue exclusion test and hemacytometer counting. Preparation of each well for the trypan blue exclusion test involved removal of growth medium, followed by a single wash using .2 ml of phosphate buffered saline (PBS) warmed to 37° C. Cells were then trypsinized for 3 minutes using .1 ml of .25% trypsin in Hank's salts with EDTA. A .1 ml aliquot of growth medium warmed to 37°C was then added to the well, raising the volume of cell suspension to .2 ml. In a separate vial, a .1 ml sample of cell suspension was added to .2 ml of growth medium, followed by the addition of .025 ml trypan blue, to produce the final sample used for viability examination and hemacytometer counting. For all wells, the number of viable cells at a particular time point was calculated from the average of 4 wells.

Statistical Method:

Data were analyzed statistically using one way analysis of variance.

Results

The actual data are shown in Table 2. Each cell count shown represents a mean of 4 sample wells per energy and time point. Note first that all cells appear to remain in the lag phase of growth until some time after 48 hrs. post-inoculation. The normal lag phase for most cells lasts approximately 24 hrs. post-inoculation. Therefore, a separate experiment was performed to study the effect. Cultures from the same stock and cell line as those used in this experiment were grown under identical conditions (with the exception of being radiated), and their normal growth behavior observed. Indeed this particular line of fibroblasts consistently showed a 48 hr. lag phase post-inoculation, demonstrating this to be a normal variation for this individual cell line.

Figure 1 summarizes the data. Compared to sham-treated controls, cells treated with 3.0 W (intensity = 10.1 W/cm^2) demonstrated a significant (P 0.01) decrease in rate of cell growth when compared to the control, non-irradiated group 0.1 W (intensity = $.336 \text{ W/cm}^2$) had significantly (P 0.02) accelerated growth rate. Cells treated with 0.6, 1.2, 1.8 and 2.4 W had growth rates statistically similar to control cells.

Discussion

The purpose of this experiment was to study fibroblast response to noncytotoxic CO_2 laser energies. In particular, we were interested in responses to energy levels experienced by viable fibroblasts adjacent to laser wounds. These would presumably be the fibroblasts involved in wound repair.

Our results demonstrate that CO_2 laser energy delivered at intensities in the range of 10 W/cm^2 has an inhibitory effect on fibroblast proliferation.

This suggests that the well-characterized delay seen in CO₂ laser wound healing is due, at least in part, to inhibited fibroblast proliferation. Several explanations for this effect are possible. A thermal effect caused by heating of intracellular water may have caused a generalized disruption in cell metabolism. The laser could also be exerting specific inhibitory effects on individual processes associated with cell division, one example being DNA synthesis. Further studies examining the effect of these CO₂ beam intensities on fibroblast DNA synthesis and collagen production are now underway and will hopefully clarify the nature of the effect demonstrated in this experiment.

This ability to inhibit fibroblast proliferation within the range of maximum noncytotoxic laser intensities suggests that the CO₂ laser would be quite useful in situations where minimal postoperative scarring is desired. One such instance in which a CO₂ laser is already often used as the method of choice is in treatment of vocal chord lesions. Postoperative vocal chord fibrosis with residual impairment in chord function is a complication that could potentially be eliminated by optimal use of the CO₂ laser. Pending the development of flexible fiberoptic endoscopes capable of transmitting the CO₂ wavelength, CO₂ laser vaporization could become an ideal method for treatment of esophageal strictures with a minimal rate of stricture recurrence.

In contrast to the growth inhibiting effect discussed above, CO₂ laser irradiation at an intensity of .336 W/cm² produced an increased rate of fibroblast proliferation compared to sham-treated controls. Potential explanations could include a proliferation-enhancing thermal effect or perhaps specific effects on processes involved in cell division.

Possible enhancement of wound healing and cell metabolism using low dose laser radiation has been studied by a number of investigators using lasers other than CO₂ (1,3,7,8,11). The results of our experiment suggest

that low dose CO₂ laser irradiation could potentially be used to accelerate the wound healing process. In this manner, the CO₂ laser could be used to enhance wound healing in patients with impaired wound healing ability, including elderly, nutritionally deficient, diabetic, and steroid-dependent patients.

While the results of this experiment are interesting, further studies regarding the nature of CO₂ laser effects on fibroblasts are needed before this information can be considered for practical use. In currently ongoing experiments, we plan to measure the effect of CO₂ laser energies on fibroblast collagen synthesis in tissue culture. Indeed future developments within the broader field of laser-cellular interactions will certainly present many new, therapeutically beneficial options involving the use of lasers.

REFERENCES

1. Abergel RP, Lyons RF, Castel JC. Biostimulation of wound healing by lasers: experimental approaches in animal models and in fibroblast cultures. J Dermatol Surg Oncol 13:127-133, 1987.
2. Buell BR, Schuller DE. Comparison of tensile strength in CO₂ laser and scalpel incisions. Arch Otolaryngol 109:465-467, 1983.
3. Castro DJ, Abergel RP, Johnston KJ, et al. Wound healing: biological effects of Nd:YAG laser on collagen metabolism in pig skin in comparison to thermal burn. Ann Plast Surg 11:131-140, 1983.
4. Castro DJ, Abergel RP, Meeker C, et al. Effects of the Nd:YAG laser on DNA synthesis and collagen production in human skin fibroblast cultures. Ann Plast Surg 11:214-222, 1983.
5. Cochrane JPS, Beacon JP, Creasey GH, et al. Wound healing after laser surgery: an experimental study. Br J Surg 67:740-743, 1980.
6. Hall RR. The healing of tissues incised by a carbon dioxide laser. Br J Surg 58:222-225, 1971.
7. Hunter J, Leonard L, Wilson R, et al. Effects of low energy laser on wound healing in a porcine model. Lasers Surg Med 3:285-290, 1984.
8. McCaughan JS, Bethel BH, Johnston T, et al. Effect of low-dose argon irradiation on rate of wound closure. Lasers Surg Med 5:607-614, 1985.
9. Moreno RA, Hebda PA, Zitelli JA, et al. Epidermal cell outgrowth from CO₂ laser- and scalpel-cut explants: implications for wound healing. J Dermatol Surg Oncol 10:863-868, 1984.

10. Norris CW, Mullarky MB. Experimental skin incision made with CO₂ laser. Laryngoscope 92:416-419, 1982.
11. Saperia D, Glassberg E, Lyons RF, et al. Demonstration of elevated type I and type III procollagen mRNA levels in cutaneous wounds treated with helium-neon laser. Biochemical and Biophysical Research Communications 138:1123-1128, 1986.
12. Sliney DH. Laser-tissue interactions. Clinics in Chest Medicine 6:203-208, 1985.

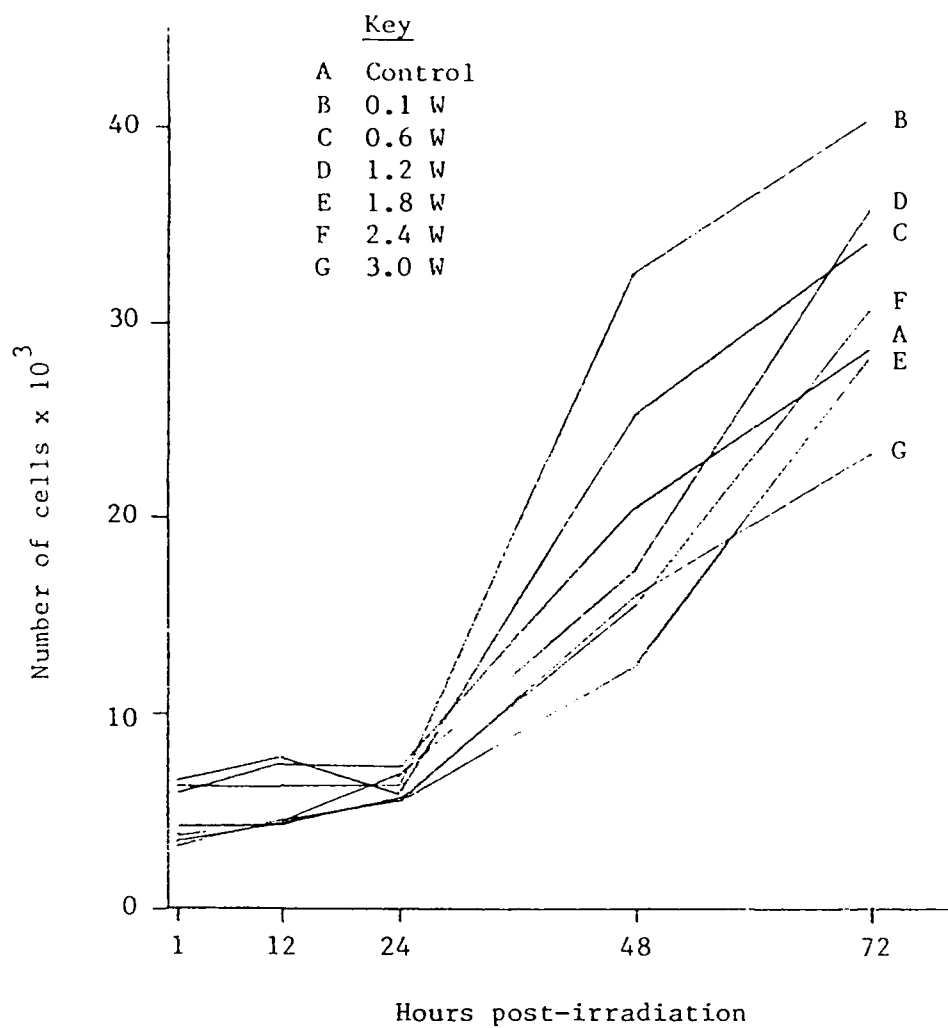


Figure 1. Effect of CO₂ laser irradiation on human dermal fibroblast proliferation

TABLE 1. Intensity and Energy Density Delivered to Fibroblasts at Six Different Power Settings

<u>Power Setting (W)</u>	<u>Intensity (W/cm²)</u>	<u>Incident Energy Density (Joules/cm²)</u>
.1	.336	.168
.6	2.01	1.01
1.2	4.03	2.01
1.8	6.04	3.02
2.4	8.05	4.03
3.0	10.1	5.03

* spot diameter .616 cm

* exposure duration .5 sec

TABLE 2: Effect of CO₂ Laser Irradiation on Human Dermal Fibroblast Proliferation (cells/well)

Power Setting (W)	Intensity (Wcm ²)	1	Hours Post-irradiation			
			12	24	48	72
0	CONTROL	5938 ± 51	7500 ± 62	7188 ± 60	20469 ± 190	28594 ± 130
0.1	.336	6250 ± 58	6250 ± 59	6563 ± 60	32500 ± 141	40313 ± 146
0.6	2.01	6563 ± 45	7813 ± 48	5938 ± 50	25313 ± 137	34063 ± 150
1.2	4.03	3750 ± 37	4688 ± 35	6875 ± 52	17188 ± 125	35938 ± 138
1.8	6.04	3125 ± 29	4688 ± 30	5625 ± 45	12188 ± 128	28438 ± 133
2.4	8.05	3438 ± 38	4375 ± 35	5313 ± 51	15313 ± 133	30625 ± 139
3.0	10.1	4063 ± 38	4063 ± 31	5625 ± 55	15938 ± 131	23125 ± 132

N00014-87-C-0146

October 1987 - December 1990

**Dynamic Characteristics of Biomembranes and
Membrane Proteins**J. Oliver McIntyre, and Sidney Fleischer
Vanderbilt University
Nashville, Tennessee

Our long-range research interest is to understand how the cell works in terms of its component organelles and membranes. We are studying cell function at several levels of organization, from the intact cell, to organelles, to membranes and to molecular components. The focus of our biophysical studies is on two **membrane proteins**. The first is the **calcium pump protein (CPP)** of skeletal muscle sarcoplasmic reticulum, which is one of the extensively studied examples of a membrane ion pump due to its importance in cell and muscle physiology as well as being a model for understanding biological pumps generally. The second, **3-hydroxybutyrate dehydrogenase (BDH)**, is the best-studied example of a lipid-requiring enzyme. BDH has an absolute and specific requirement for the phospholipid phosphatidylcholine (PC) for enzymic activity.

Our pre-FEL research includes studies to characterize the **rotational motion** of membrane proteins as well as to measure **distances** between unique sites on membrane proteins with respect to one another and with respect to defined positions in the phospholipid bilayer. The biophysical methods employed are fluorescence lifetime and time-dependent anisotropy.

Preliminary studies have been carried out with the calcium pump protein, a transmembrane ion pump. The pump protein has been labeled at unique sites with either IAEDANS or FITC or EOSIN fluorescent probes and fluorescence lifetime and time-dependent anisotropy studies are in process. We have also begun studies to characterize the dynamic properties of BDH reconstituted into phospholipid vesicles both in the presence and absence of activating phospholipid, i.e., PC. Initial studies are carried out using the fluorometry facilities at the Laboratory for Fluorescence Dynamics of the University of Illinois at Urbana together with Enrico Gratton, our collaborator. Studies are now in progress with equipment recently installed in the FEL facility at Vanderbilt. Multifrequency phase and modulation fluorometry, with excitation from a sync-pumped, mode-locked cavity-dumped dye laser system, was used to obtain fluorescence lifetime and time-dependent anisotropy data for both the intrinsic fluorescence (tryptophan) of BDH as well as for BDH covalently derivatized with IAEDANS.

Lifetime data were analyzed independently (two or three component analyses) as well as with a model-dependent global analysis. The data indicate that the tryptophan fluorescence of BDH exhibits three lifetime components, which are similar in the presence versus absence of PC, suggesting the environment and motional characteristics of the tryptophan of BDH are not modulated by PC. For the IAEDANS-BDH, three lifetime components were also detected in the presence of PC. With this probe, time-dependent anisotropy data for BDH in presence of PC yielded rotational correlation times of 2.2×10^{-7} sec and 4.7×10^{-9} sec. Studies are in progress to relate dynamic processes with functional state of BDH in the membrane. We are in the process of modifying the fluorometry facility in the FEL Center so as to enable both broad multifrequency detection and quantitation of more rapid dynamic processes as required for correlation of structure with function.

Strategic Defense Initiative Organization

Fourth Annual

Contractors' Meeting

on

Medical Free Electron Lasers

ABSTRACTS

September 22-24, 1989

Dallas, Texas

Lipid-dependent membrane enzymes. Kinetic modelling of the activation of protein kinase C by phosphatidylserine

Heinrich Sandermann, Jr.¹ and Thomas M. Duncan²

¹ Institut für Biochemische Pflanzenpathologie, GSF München, Neuherberg (Germany) and ² Department of Molecular Biology, Vanderbilt University, Nashville, TN (U.S.A.)

(Received 13 May 1991)

Key words: Protein kinase C; Lipid regulation; Phosphatidylserine; Activation; Kinetic model; Hill coefficient; Ligand trapping

A previously developed kinetic theory for lipid-dependent membrane enzymes (Sandermann, H. (1982) Eur. J. Biochem. 127, 123–128) is used to examine the activation of protein kinase C by phosphatidylserine. Hill-coefficients ranging up to 11 have been reported for activation in mixed micelles with Triton X-100. On the basis of this uniquely high degree of cooperativity, protein kinase C has been postulated to represent a new class of lipid-dependent membrane enzymes (Newton, A. and Koshland, D.E., Jr. (1989) J. Biol. Chem. 264, 14909–14915). In contrast, activation in the absence of Triton X-100 has led to Hill-coefficients of only ≤ 2.6 . In order to resolve the apparent discrepancy, activation is now considered to involve binding of PS monomers to interacting sites on the enzyme, a non-activating PS trapping process also occurring in the presence of Triton X-100. Estimates for trapping are made for several sets of published data for micellar activation. The kinetic model developed here successfully fits each data set using a Hill-coefficient of only 3.0. An influence of Ca^{2+} ions or of a two-step mechanism of lipid-protein interaction are considered as possible molecular explanations. It is concluded (i) that lipid activation of protein kinase C may proceed without unique cooperativity and (ii) that ligand trapping could provide another means for 'threshold-type' kinetic regulation of membrane enzyme and receptor systems.

Introduction

The activity of membrane-bound enzymes is in most cases dependent on, or modulated by, the membrane lipid phase [1]. Lipid activation curves are as a rule sigmoidal and thus possess positive kinetic cooperativity [2,3]. In the special case of diacylglycerol kinase from *Escherichia coli*, a lipid-dependent enzyme has even been shown to be capable of autocatalytic self-activation [4].

The molecular basis for lipid regulation is as yet ill understood. Lipid/protein binding equilibria are at present accessible by two major approaches that have

not yet merged. ESR-spectroscopy considers a 1:1 exchange of bound versus free lipid and leads to dimensionless binding exchange constants [5,6] which are, however, not useful for biochemical kinetics [3].

The second approach is based on multiple binding site kinetics [2,3]. Kinetic cooperativity is attributed to either allosteric interactions between lipid binding sites or to a non-allosteric mechanism resulting from the lipid solvation of the membrane protein. A kinetic theory for both allosteric and non-allosteric cooperativity of lipid activation has been developed [7]. However, there is still a paucity of experimental systems where the theoretical models can be tested, and support by biophysical data is lacking. Na^+/K^+ -ATPase [8,9] and β -hydroxybutyrate dehydrogenase [10,11] probably represent the best-defined systems.

Kinetic studies on membrane enzymes are generally difficult because the usual kinetic formalism refers to non-aggregated homogeneous solutions. The recognition and elimination of kinetic artifacts caused by micellar or liposomal aggregation processes is therefore of great importance in the study of membrane enzymes [3]. This type of kinetic analysis is presented here for

Abbreviations: v , actual enzyme velocity, V , maximal enzyme velocity; n_H , Hill coefficient; PC, phosphatidylcholine; PE, phosphatidylethanolamine; PG, phosphatidylglycerol; PS, phosphatidylserine; $[\text{PS}]_t$, concentration of total PS; $[\text{PS}]_c$, concentration of complexed PS; $[\text{PS}]_{10}$, $[\text{PS}]_{50}$, $[\text{PS}]_{90}$, total phosphatidylserine concentrations required to reach 10%, 50% and 90%, of V , respectively.

Correspondence: H. Sandermann, GSF München, BIOP, Ingolstädter Landstrasse 1, D-8042 Neuherberg, Germany.

the activation of protein kinase C by phosphatidylserine (PS). The lipid-dependence of this membrane enzyme has been reviewed [12,13]. Protein kinase C is of particular interest since it acts as a receptor for phorbol diesters, and plays a central role in tumor promotion and numerous other important physiological events [14,15].

Bell and co-workers [16,17] have developed a mixed micellar system (using Triton X-100) to allow systematic studies of the interactions of protein kinase C with its most effective phospholipid activator, phosphatidylserine (PS), as well as with other activators and inhibitors. The detergent was reported to provide a kinetically inert matrix and to solubilize protein kinase C in monomeric form [16,17]. Curves for the PS-dependence of histone phosphorylation in micelles were highly sigmoidal, with Hill-coefficients (n_H) of up to 11 [16-23]. In contrast, previous activation curves for PS determined in liposomes had failed to display a pronounced sigmoidal shape [24,25]. Activation in Triton X-100 mixed micelles also gave high n_H values for the PS-dependent binding of phorbol-diester and for the autophosphorylation of the enzyme.

Hill-coefficients approaching 11 are unique and have not been previously reported for any other enzyme. Newton and Koshland [23] have therefore concluded that protein kinase C represents a new group of lipid-dependent enzymes, that interacts specifically and cooperatively with ≥ 12 phospholipid activator molecules. This far-reaching conclusion may, however, be based on a kinetic artifact, as indicated by the present kinetic analysis. When the phenomenon of ligand trapping is taken into account, the published data sets reduce to a fairly common Hill-coefficient, $n_H = 3$. At the same time, ligand trapping is identified as a possible mechanism for 'threshold-type' kinetic regulation.

Results

Hill coefficients for PS activation

Many data sets for activation of protein kinase C by phosphatidylserine have been published. As shown in Table I, activation in mixed micelles with Triton X-100 has led to Hill-coefficients in the range of 4.7-11, whereas activation in the absence of Triton X-100 has led to Hill coefficients in the range of 0.7-2.6. Table I contains data from three separate laboratories where reconstitution in the presence or absence of Triton X-100 was studied under similar experimental conditions.

Basic kinetic models

PS is proposed to bind cooperatively to protein kinase C, with a stoichiometry of 4 [30] or of ≥ 12 [23] lipid monomers per enzyme monomer, with the additional participation of Ca^{2+} and a diacylglycerol or

TABLE I

Hill coefficients (n_H) for the PS dependence of histone phosphorylation by protein kinase C

In the cases tested autophosphorylation of protein kinase C as well as phorbol-diester binding had similar Hill coefficients.

Amount of Triton X-100 used (% w/v)	Ca^{2+} concn. (mM)	n_H	Ref.
0.3	0.1	4.8	16
0.3	0.1	≤ 8.8	17-22
0.3	0.1	4.67	26
0.3	0.1	5.4 ^a	27 (Fig. 1B)
0.1	1.3	≤ 11	23
0	0.01	0.8 ^a	26 (Fig. 2A)
0	1.3	≤ 2.6 ^a	28 (Fig. 1)
0	0.6	≤ 1.02	29
0	0.2	0.7 ^a	27 (Fig. 7)

^a n_H estimated by linear regression (Hill plot) from the published data points between $[\text{PS}]_{10}$ and $[\text{PS}]_{90}$. The figures used are indicated together with the reference numbers. The correlation coefficient was > 0.98 in all cases.

phorbol-diester activator molecule. As previously discussed, a number of mechanisms can lead to kinetic cooperativity in the absence of true cooperative interactions [3]. In the present communication, a specific alternative kinetic model is considered. This model involves activation by binding of PS monomers at distinct interacting sites on protein kinase C. In addition, a PS complexation process induced by Triton X-100 is considered to occur as a non-activating trapping event. This trapping phenomenon is similar to substrate depletion by complexation which is known to convert hyperbolic velocity curves to sigmoidal curves with $n_H > 1$ [31].

Rate equation for ligand trapping

In the alternative kinetic model, PS in mixed micelles with Triton X-100 may undergo two types of interaction. Firstly, PS molecules are withdrawn by some as yet undefined binding reaction that does not occur in liposomal systems. The second possible interaction involves binding of PS monomers to activator sites on the enzyme. A simplified kinetic model is based on the following assumptions:

(1) Trapping proceeds with such high affinity that all initial PS is consumed until the total possible concentration of complexed PS, $[\text{PS}]_c$, is reached.

(2) The concentration of excess free PS, available for enzyme activation, is given by the difference between total and complexed PS concentrations, $([\text{PS}]_t - [\text{PS}]_c)$.

The degree of kinetic cooperativity can be described

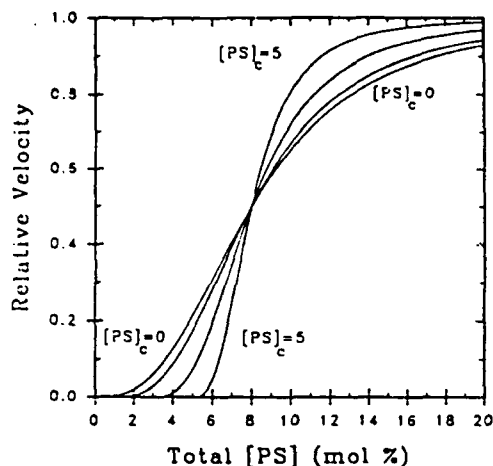


Fig. 1. Effects of activator trapping on activation curves. Eqn. 1 of the text was used, with arbitrary values $n_H = 2.8$, $[PS]_{50} = 8$ mol%, to calculate separate curves for $[PS]_c = 0, 1, 3$, and 5 mol%. The curves for $[PS]_c = 0$ and $[PS]_c = 5$ mol% are labeled; the curves for $[PS]_c = 1$ and 3 mol% occupy the intermediate positions.

by a modified form of the nonlinear Hill-type equation (cf. Ref. 7):

$$v = \frac{([PS]_t - [PS]_c)^{n_H}}{([PS]_t - [PS]_c)^{n_H} + ([PS]_{50} - [PS]_c)^{n_H}} \quad (1)$$

Here, v is actual velocity. V is maximal velocity, $[PS]_{50}$ is the total PS concentration required for half-maximal activation, and n_H is the Hill coefficient. Remember that the value of n_H is less than n , the number of PS binding sites, but will approach n if the strength of cooperativity between the sites is high.

Specific features of the trapping model

According to Eqn. 1, activator trapping should significantly influence overall apparent kinetic cooperativity and Hill coefficients. Two types of calculated data are used to illustrate this point.

First, in Fig. 1 activation curves calculated with Eqn. 1 become significantly steeper with increased trapping of PS. Eqn. 1 predicts that at various amounts of trapping, 50% relative activity will always occur at the same value of $[PS]_{50}$. To achieve 50% activity at the same value of $[PS]_t$ means that, in the presence of trapping, the overall cooperative affinity of the sites for PS must be correspondingly higher than if no trapping occurred.

Each curve of Fig. 1 was analyzed with the standard linearized Hill equation between $[PS]_{10}$ and $[PS]_{90}$, not correcting for trapping. The apparent Hill-coefficients obtained are 2.8 (for $[PS]_c = 0$), 3.2 (for $[PS]_c = 1$), 4.4 (for $[PS]_c = 3$), and 7.0 (for $[PS]_c = 5$). Another index of cooperativity, the ratio $[PS]_{90}/[PS]_{10}$, progressively decreases from 4.7 (for $[PS]_c = 0$) to 3.9 (for $[PS]_c = 1$),

2.6 (for $[PS]_c = 3$) and finally to 1.8 (for $[PS]_c = 5$). Non-cooperative, hyperbolic kinetics would have a value of 81. This example shows that, if trapping did occur in an enzyme-activator system but was not accounted for in the analysis of the behavior, kinetic cooperativity versus the activator (and thus n_H) would appear larger.

Second, a complementary treatment was developed as follows. Three sets of activation data, (v/V) versus $[PS]_t$, were calculated from Eqn. 1 assuming no trapping ($[PS]_c = 0$) and fixed values of $[PS]_{50} = 8$ mol%, and $n_H = 2.8, 4$ or 8 . Then the data set for each fixed n_H value was fitted with Eqn. 1, now invoking increasing PS trapping. As summarized in Table II, the apparent value for n_H decreases when an increased trapping term (larger $[PS]_c$) is inserted into the fitting equation. Thus, in the presence of activator trapping, a smaller number of cooperative binding sites on the enzyme would be sufficient to explain an apparently high degree of kinetic cooperativity.

Application of trapping model to published data

In order to apply the present kinetic model to protein kinase C, three published data sets have been analyzed. In the original publications, the data were fit to the standard Hill equation (Fig. 2, dashed curves), and yielded the published n_H values of 4.8 (Fig. 2A) and 8 ± 2 (Fig. 2B) for histone phosphorylation and of 8.7 ± 0.9 (Fig. 2C) for autophosphorylation.

With values of PS trapping estimated from the data (see legend of Fig. 2), Eqn. 1 leads to calculated activation curves with a uniform value of $n_H = 3.0$ (Fig. 2; solid lines). Thus the various published high values for n_H are considerably lowered. The present and the previous treatments result in the solid and the dashed

TABLE II

Fitting activation data with Eqn. 1. Increased trapping yields lower n_H values

Three data sets of (v/V) versus $[PS]_t$ were calculated using Eqn. 1 of the text, using fixed values of $[PS]_c = 0$ (e.g., no trapping) and of $[PS]_{50} = 8$ mol% in each case. Each data set was calculated with a different fixed n_H value: $n_H = 2.8$ (set 1), $n_H = 4.0$ (set 2), and $n_H = 8.0$ (set 3). Each data set was generated for $[PS]_t$ ranging from 0 to 20 mol%, in 0.1 mol% increments. The data sets were then fit (by nonlinear regression) to Eqn. 1, assuming increasing values for $[PS]_c$. Each column lists apparent n_H values (near half-maximal velocity) that were obtained for the different assumed value of $[PS]_c$.

$[PS]_c$	Fitted Hill-coefficients		
	set 1	set 2	set 3
0	2.8	4.0	8.0
1	2.5	3.5	7.0
2	2.1	3.0	6.0
3	1.8	2.5	5.0
4	1.4	2.0	4.0
5	1.1	1.5	3.0

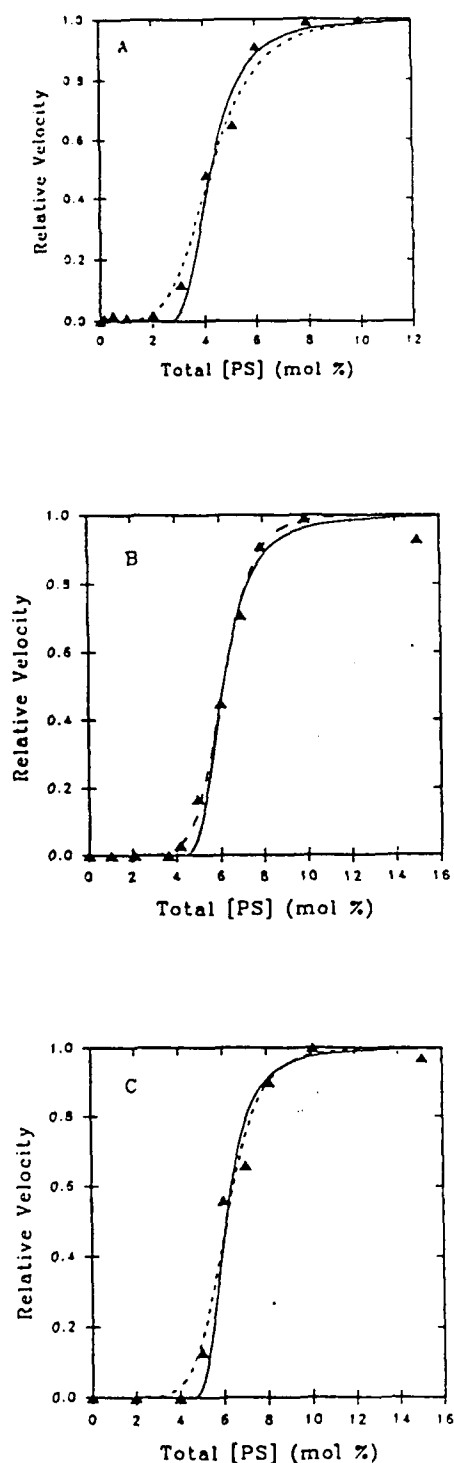


Fig. 2. Analysis of published PS-activation data with the trapping model. Data points and the values for $[PS]_{50}$ and for V were taken from the following sources: Fig. 3 of Ref. 16; Fig. 2A of Ref. 23; Fig. 1A of Ref. 23, data obtained with 7.5 mol% dioleoylglycerol. The dashed curves correspond to the previously published Hill-coefficients and were calculated with Eqn. 1 using $[PS]_c = 0$. The theoretical curves for the trapping model (solid lines) were obtained using Eqn. 1 of the text with a value of $n_H = 3.0$ and the following values for $[PS]_c$: (A), 2.48 mol%; (B) 4.2 mol%; (C), 4.5 mol%; each value for $[PS]_c$ was determined graphically as the x-intercept of a line drawn tangent to the mid-range of the published curve.

theoretical curves of Fig. 2. These curves have a comparable fit to the experimental data points. No decision between models is therefore possible on the base of mathematical arguments. However, the present uniform Hill coefficient of 3.0 is in a range also found for other lipid-dependent enzymes [3], so that protein kinase C may not be unique.

Discussion

Triton X-100 has been reported to act as an inert matrix in the activation of protein kinase C [16,17]. The data summarized in Table I show, however, that Triton X-100 has a drastic effect on apparent cooperativity. The reports on the micellar reconstitution method [16–22] ignored the lack of an apparent threshold in PS activation curves for liposomal systems (see, for example, Refs. 24 and 25). It should be noted that most bilayer titrations were carried out by increasing the ratio of total lipid to enzyme, at constant PS mole fraction. For a ligand such as PS in a bilayer, it is more appropriate to vary the mole fraction for the activator, PS, at constant total phospholipid; it has been shown for β -hydroxybutyrate dehydrogenase, for its activator PC in a bilayer 'background', that varying the PC mole fraction yields a higher Hill coefficient ($n_H \approx 2.4$) than titration at constant PC mole fraction ($n_H = 1.8$) [11,32]. However, it is clear that the unique degree of cooperativity observed for activation of protein kinase C by PS in the Triton X-100 detergent system has not been observed in bilayer systems.

There has been a tendency to accept the uniquely high Hill coefficients in Triton X-100 as a fact. The earlier model postulating a geometrically defined complex involving four PS molecules [30] has recently been replaced by a geometrically undefined complex with six PS molecules [22]. Protein kinase C is thus thought to interact in a highly cooperative fashion with 6 [22] or ≥ 12 PS molecules [23,28]. In contrast to these reports, all other previously investigated lipid-dependent enzymes had much lower degrees of kinetic cooperativity [3,7]. Three of the most highly cooperative lipid-activated enzymes known are Na^+/K^+ -ATPase (n_H up to 2.7; [8]), pyruvate oxidase (n_H up to 3.6; [33]) and β -hydroxybutyrate dehydrogenase (n_H up to 2.4; [11]). A Hill-coefficient in the same range (3.0) was obtained here for protein kinase C after taking ligand trapping into account. However, it became clear from Fig. 2 that the published data points were too imprecise to distinguish between the high cooperativity models and the present ligand trapping model. There is thus a need for better kinetic data and for direct PS binding data in order to decide between models. In view of the great physiological importance of protein kinase C, a more detailed discussion seems of interest.

Possible influence of Ca^{2+} ions

A complex phase equilibrium between PS, diacylglycerol, detergent, substrate and enzyme proteins, Ca^{2+} and Mg^{2+} , ATP and buffer components exists in the kinase assay mixture used [16-23]. The complex and non-physiological conditions employed make reliable conclusions difficult. Interactions between histones and PS are well known [22,27,29], but are perhaps not critical for the present kinetic analysis. Autophosphorylation and phorbol-diester binding had the same high Hill coefficients as histone phosphorylation, although each of these processes had a different PS dependence.

[34] A possible role of Ca^{2+} -ions in the mixed micellar assay with Triton X-100 may result from the known strong interaction of Ca^{2+} with phosphatidylserine and the phosphatidylserine polar group alone [35]. The concentration of Ca^{2+} used in the micellar assays ($\geq 100 \mu\text{M}$) was much above the physiological range ($\leq 10 \mu\text{M}$) which was used in some of the liposomal activation studies [12,13,24,25]. When 0.3% w/v Triton X-100 was used in the complete absence of Ca^{2+} , a Hill coefficient of ≈ 2.5 was obtained for PS activation of the Ca^{2+} -independent isoenzyme and of protein kinase C [36]. This Hill coefficient (estimated from Fig. 2A of Ref. 36) approximates the Hill coefficient of 3.0 found here for the Ca^{2+} -dependent isoenzymes of protein kinase C after correcting for PS trapping. Isoenzyme ϵ lacks one of the sequence domains that are involved in the binding of Ca^{2+} , but also in binding of diacylglycerol and PS [15]. On the other hand, when Ca^{2+} concentration was lowered in the standard micellar assay, no obvious decrease in the initial threshold became apparent [17]. The available data therefore allow no firm conclusion as to a role of Ca^{2+} or Ca^{2+} /Triton X-100 in PS trapping.

Two-step mechanism of lipid-protein interaction

Protein kinase C exists as a monomer in Triton X-100, and the monomer has been proposed to be the active species [16,17]. However, the enzyme may need oligomerization [37] or a bulk binding step to the micelle prior to the specific activation step. Oligomerization or bulk binding of protein may occur much more easily in liposomal than in micellar systems, and may initially consume PS in micelles. Other acidic phospholipids could conceivably replace PS in oligomerization or bulk binding, but not in the specific activation step. It has indeed been observed that equimolar phosphatidic acid significantly reduced the threshold for PS and also reduced the Hill coefficient for PS from 9.6 to 4.8 [23]. Other phospholipids (PC, PE, PG) also caused a significant though less pronounced decrease of the Hill coefficient for activation by PS [23]. Kinetic anomalies were also indicated by the described strong variation of Hill coefficients for

PS activation when phorbol diester [18], diacylglycerol [17] or sphingosine [19] were included in the assay mixture. The idea of ≥ 12 PS molecules being the activating species [23] may furthermore be difficult to reconcile with the stereospecificity for an L-serine moiety in PS [38]. However, stereospecificity was not absolute, and the published data [38] did not clarify whether all or only part of the added PS had to contain L-serine.

Conclusion

In summary, it now appears that the published interpretations for the PS activation of protein kinase C may have been inconclusive because experimental artifacts may have occurred in the mixed micellar assay using the detergent Triton X-100. Although other alternative mechanisms may apply, the present analysis indicates that protein kinase C may be regulated not through the lipid activator concentration per se, but through the effective lipid activator concentration remaining after physical and chemical sequestering processes. Such processes may occur as artifacts, but they could also occur physiologically and provide another general mechanism for 'threshold-type' regulation of membrane enzyme and receptor systems.

Acknowledgements

We thank Prof. Sidney Fleischer and Dr. J. Oliver McIntyre of the Department of Molecular Biology, Vanderbilt University, for valuable suggestions. This work has been supported by a grant from the Deutsche Forschungsgemeinschaft (Sa 180/18-2) and by the Fonds der Chemischen Industrie; T.M.D. was supported by the FEL grant to Vanderbilt University from the Office of Naval Research.

References

- 1 Sandermann, H. (1978) *Biochim. Biophys. Acta* 515, 209-237.
- 2 Sandermann, H. (1983) *Trends Biochem. Sci.* 8, 408-411.
- 3 Sandermann, H. (1986) in *Progress in Protein-Lipid Interactions* (Watts, A. and De Pont, J.J.H.M., eds.), Vol. 2, pp. 197-220, Elsevier, Amsterdam.
- 4 Russ, E., Kaiser, U. and Sandermann, H. (1988) *Eur. J. Biochem.* 171, 335-342.
- 5 Griffith, O.H., Brotherus, J.R. and Jost, P.C. (1982) in *Lipid-Protein Interactions* (Jost, P.C. and Griffith, O.H., eds.), Vol. 2 pp. 225-237, J. Wiley, New York.
- 6 Marsh, D. (1985) in *Progress in Protein-Lipid Interactions* (Watts, A. and De Pont, J.J.H.M., eds.), Vol. 1, pp. 143-172, Elsevier, Amsterdam.
- 7 Sandermann, H. (1982) *Eur. J. Biochem.* 127, 123-128.
- 8 Ottolenghi, P. (1979) *Eur. J. Biochem.* 99, 113-131.
- 9 Sandermann, H. and Gottwald, B.A. (1983) *Biochim. Biophys. Acta* 732, 332-335.
- 10 Fleischer, S. and McIntyre, J.O. (1985) in *Achievements and Perspectives of Mitochondrial Research* (Quagliariello, E., Slater,

- E.C., Palmieri, F., Saccone, C. and Kroon, A.M., eds.), Vol. 1, pp. 347-356, Elsevier, Amsterdam.
- 11 Sandermann, H., McIntyre, J.O. and Fleischer, S. (1986) *J. Biol. Chem.* 261, 6201-6208.
- 12 Ashendel, C.L. (1985) *Biochim. Biophys. Acta* 822, 219-242.
- 13 Rando, R.R. (1988) *FASEB J.* 2, 2348-2355.
- 14 Nishizuka, Y. (1986) *Science* 233, 305-312.
- 15 Nishizuka, Y. (1988) *Nature* 334, 661-665.
- 16 Hannun, Y.A., Loomis, C.R. and Bell, R.M. (1985) *J. Biol. Chem.* 260, 10039-10043.
- 17 Hannun, Y.A., Loomis, C.R. and Bell, R.M. (1986) *J. Biol. Chem.* 261, 7184-7190.
- 18 Hannun, Y.A. and Bell, R.M. (1986) *J. Biol. Chem.* 261, 9341-9347.
- 19 Hannun, Y.A., Loomis, C.R., Merrill, A.H. and Bell, R.M. (1986) *J. Biol. Chem.* 261, 12604-12609.
- 20 Hannun, Y.A. and Bell, R.M. (1988) *J. Biol. Chem.* 263, 5124-5131.
- 21 Hannun, Y.A., Foglesong, R.J. and Bell, R.M. (1989) *J. Biol. Chem.* 264, 9960-9966.
- 22 Hannun, Y.A. and Bell, R.M. (1990) *J. Biol. Chem.* 265, 2962-2972.
- 23 Newton, A.C. and Koshland, D.E., Jr. (1989) *J. Biol. Chem.* 264, 14909-14915.
- 24 Kaibuchi, K., Tabai, Y. and Nishizuka, Y. (1981) *J. Biol. Chem.* 256, 7146-7149.
- 25 Boni, L.T. and Rando, R.R. (1985) *J. Biol. Chem.* 260, 10819-10825.
- 26 Orellana, A., Hidalgo, P.C., Morales, M.N., Mezzano, P. and Bronfman, M. (1990) *Eur. J. Biochem.* 190, 57-61.
- 27 Bazzi, M.D. and Nelsestuen, G.L. (1987) *Biochemistry* 26, 5002-5008.
- 28 Newton, A.C. and Koshland, D.E., Jr. (1990) *Biochemistry* 29, 6656-6661.
- 29 Bazzi, M.D. and Nelsestuen, G.L. (1987) *Biochemistry* 26, 115-122.
- 30 Ganong, B.R., Loomis, C.R., Hannun, Y.A. and Bell, R.M. (1986) *Proc. Natl. Acad. Sci. USA* 83, 1184-1188.
- 31 Segel, I.H. (1975) *Enzyme Kinetics, Behavior and Analysis of Rapid Equilibrium and Steady-State Enzyme Systems*, pp. 203-206, J. Wiley & Sons, New York.
- 32 Sandermann, H. (1984) *FEBS Lett.* 168, 271-274.
- 33 Blake, R. II, Hager, L.P. and Gennis, R.B. (1978) *J. Biol. Chem.* 253, 1963-1971.
- 34 Cullis, P.R., Hope, M.J., De Kruijff, B., Verkleij, A.J. and Tilcock, C.P.S. (1985) in *Phospholipids and Cellular Regulation*, Vol. I (Kuo, J.F., ed.), pp. 1-59, CRC Press, Boca Raton.
- 35 Schumacher, G. and Sandermann, H. (1976) *Biochim. Biophys. Acta* 448, 642-644.
- 36 Schaap, D. and Parker, H.J. (1990) *J. Biol. Chem.* 265, 7301-7307.
- 37 Mochly-Rosen, D. and Koshland, D.E., Jr. (1987) *J. Biol. Chem.* 262, 2291-2297.
- 38 Lee, M.-H. and Bell, R.M. (1989) *J. Biol. Chem.* 264, 14797-14805.

Vanderbilt University Free Electron Laser Center
for Biomedical and Materials Research
N00014-87-C-0146

V. C.

October 1987 - December 1990
Becca Fleischer, Sidney Fleischer, and J. Oliver McIntyre
Vanderbilt University
Nashville, TN

DYNAMIC CHARACTERISTICS OF BIOMEMBRANES AND MEMBRANE PROTEINS

J. Oliver McIntyre and Sidney Fleischer

Our long-range research interest is to understand how the cell works in terms of its component organelles and membranes. We are studying cell function at several levels of organization, from the intact cell, to organelles, to membranes and to molecular components. The focus of our biophysical studies is on two **membrane proteins**. The first is the **calcium pump protein (CPP)** of skeletal muscle sarcoplasmic reticulum which is one of the extensively studied examples of a membrane ion pump due to its importance in cell and muscle physiology as well as being a model for understanding biological pumps generally. The second, **3-hydroxybutyrate dehydrogenase (BDH)**, is the best-studied example of a lipid-requiring enzyme. BDH has an absolute and specific requirement for the phospholipid phosphatidylcholine (PC) for enzymic activity.

Our pre-FEL research includes studies to characterize the **rotational motion** of membrane proteins as well as to measure **distances** between unique sites on membrane proteins with respect to one another and with respect to defined positions in the phospholipid bilayer. The biophysical methods employed are fluorescence lifetime and time-dependent anisotropy.

Preliminary studies have been carried out with the calcium pump protein, a transmembrane ion pump. The pump protein has been labeled at unique sites with either IAEDANS or FITC or EOSIN fluorescent probes and fluorescence lifetime and time-dependent anisotropy studies are in progress. We have also begun studies to characterize the dynamic properties of BDH reconstituted into phospholipid vesicles both in the presence and absence of activating phospholipid, i.e., PC. Initial studies were carried out using the fluorometry facilities at the Laboratory for Fluorescence Dynamics of the University of Illinois at Urbana together with Enrico Gratton, our collaborator. Studies are now in progress with equipment recently installed in the FEL facility at Vanderbilt. Multifrequency phase and modulation fluorometry, with excitation from a sync-pumped, mode-locked, cavity-dumped dye laser system, was used to obtain fluorescence lifetime and time-dependent anisotropy data for both the intrinsic fluorescence (tryptophan) of BDH as well as for BDH covalently derivatized with IAEDANS. Lifetime data were analyzed independently (two or three component analyses) as well as with a model-dependent global analysis. The data indicate that the tryptophan fluorescence of BDH exhibits three lifetime components which are similar in the presence versus absence of PC, suggesting that the environment and motional characteristics of the tryptophan of BDH are not modulated by PC. For the IAEDANS-BDH, three lifetime components were also detected in the presence of PC. With this probe, time-dependent anisotropy data for BDH in presence of PC yielded rotational correlation times of 2.2×10^{-7} sec and 4.7×10^{-9} sec. Studies are in progress to relate dynamic processes with functional state of BDH in the membrane. We are in the process of modifying the fluorometry facility in the FEL Center so as to enable both broad multifrequency detection and quantitation of more rapid dynamic processes as required for correlation of structure with function.

We anticipate that the broad tunability of the FEL especially in the UV and IR will enable studies including specific crosslinking of ligands to membrane components and detection of new resonances for study of lipid-protein interaction in biomembranes.

700010001
VI-A

EFFECTS OF WAVELENGTH, PULSE DURATION AND PULSE
REPETITION FREQUENCY OF THE INTERACTIONS
AND DESORPTION OF BRAIN TISSUE

M. AFFATIGATO,⁽¹⁾ B.A., R.J. MACIUNAS,⁽²⁾ M.D., R.F. HAGLUND Jr.,⁽¹⁾ Ph.D.,
and R. CARVER,⁽²⁾ B.S.

*(1) Dept. of Physics and Astronomy
Vanderbilt University
Nashville, TN 37235*

*(2) Dept. of Neurosurgery
Vanderbilt University Medical Center
Nashville, TN 37235*

ACKNOWLEDGEMENTS:

This research was supported in part by the Office of Naval Research under the auspices of the Vanderbilt Medical Free Electron Laser Project.

ADDRESS ALL CORRESPONDENCE TO:

Prof. Richard F. Haglund, Jr.
Department of Physics and Astronomy
Vanderbilt University
Nashville, Tn 37235 U.S.A.

PHONE: (615) 322 7964 FAX: (615) 343-7263

ABSTRACT

We report a phenomenological study of the effects of 532 and 308 nm laser light at nanosecond and picosecond pulse durations and at two different repetition rates on a rat-brain model. The quality and morphology of each ablation well and of its relationship with the laser parameters were made. Special attention was paid to unusual shapes of the cavity, such as "keyholes," and the effect of focussing on cavity shape was investigated.

INTRODUCTION: Neurosurgical applications of laser-tissue interactions have been directed to (1) singlet oxygen-mediated tumoricidal photodynamic therapy via excitation of various fluorescing compounds by fiber-delivered monochromatic light, and (2) precision tissue ablation, predominantly using the CO₂, Nd:YAG and KTP-532 lasers via microslade-directed intramicroscopic systems. While the successful application of photodynamic therapy techniques to central nervous system tissue requires fabrication of an efficient but relatively nontoxic agent with excitatory wavelengths suitable for maximal light penetration through brain parenchyma, precision ablation of central nervous system tissue requires the experimental identification of combinations of laser light wavelengths, pulse and power characteristics that are optimized for clinical use. This in turn requires a fundamental understanding of the processes leading to the laser irradiation-induced desorption of brain tissue.

In this paper we report observations of the effects of laser wavelength, pulse repetition frequency, pulse duration and fluence on the ablation of brain tissue. In this investigation, the influence of these parameters on the quality, morphology and depth of the ablation well was qualitatively described, and related to observed physical characteristics of rat brain. The consequences of shifting the focal spot deeper than the surface were considered along with other possible causes of the "keyhole effect," previously noted in the literature. We also noted the effect of the saline solution as a control for tissue hydration. The application of results from such an inquiry would allow the development of clinically optimal paradigms for laser wavelength,

pulse and related characteristics to guide appropriate selections for laser-induced ablation of neural tissue.

MATERIALS AND METHODS: Freshly excised, intact rat brains were prepared and placed in a normal saline solution (0.86 %). The brains were then taken to the laser site and irradiated in air, noting whether they were wet (saline solution on the surface), or dry (no liquid evident). An average of five spots per brain were exposed to the laser light, to facilitate histological analysis.. The brain was affixed to a microscope glass slide mounted on a translation stage. The laser beam was reflected from a mirror and passed vertically downward through a focussing lens to strike the surface of the brain, located near the focal plane of the lens.

The size of the laser spot was noted before the lens and at the surface of the brain, and used to estimate the fluence. The translation stage was used to move the brain and locate each new area of irradiation. Care was taken to allow for the curvature of the brain and the consequent shift in the placement of the focal spot above or below the surface. Lenses of different focal lengths and diameters were used, and the power levels of the laser were monitored several times during the experiment to insure the constancy of the experimental conditions.

After exposure, the rat brains were fixed in 10 % buffered neutral Formalin overnight. Graded alcohols and Xylene were allowed to infiltrate the tissue, and the whole brain was then embedded in paraffin. Sections were cut at 5 micron intervals and stained with Harris Hematoxylin and Eosin (HxE). The slices were then placed on microscope slides and microphotographs prepared, at two different magnifications (60 times, 26 times).to generate relative comparisons of ablation well depth and thermal damage zones.

The laser used varied in wavelength λ , power, pulse repetition frequency (PRF), and pulse durations. as shown in Table I.

Laser Type	λ (nm)	Pulse Duration	PPF (Hz)	P (W)	E (mJ)	I (MW·cm ⁻²)
Nd:YAG, CW, mode-locked	532	100 ps	76 · 10 ⁶	1		0.03-0.08

Nd:YAG, Q-switched, mode-locked	532	35 ps	10		15	636
Nd:YAG, Q-switched	532	11 ns	10		400	46
Excimer (XeCl)	308	15 ns	10		230	1.7

RESULTS:

Figure 1 shows a comparison of the effects of two different wavelengths on ablation. The first dry sample (on the left), irradiated at 532 nm and magnified 60 times, shows less ablation and a greater zone of thermal damage. Yet the peak fluence of this irradiation was about 30 times that of the 308 nm exposure. Irradiation at 308 nm (on the right), also magnified 60 times, shows deeper ablation, and the thermal damage seems rather limited. The ultraviolet light is more attuned to the vibrational modes of the proteins and nucleic acids present in the components of gray matter, but this of course ignores the *in vivo* effect due to the presence of blood.

The heating of tissue by a continuous 1064-nm laser light has already been studied¹, and it has been shown that this wavelength of light heats the blood very quickly to 90 % of its maximum temperature within 3 s, and the thermal damage to the brain is still relatively severe. The thermal damage from 532-nm light follows the same pattern, although it is diminished.

Figure 2 illustrates the effects of high and low pulse repetition frequencies. The sample on the left was dry and irradiated with 532 nm light at 76 MHz and with picosecond pulses. Notice the greater thermal damage and immediate carbonization at the surface. The fast repetition rate does not allow for significant diffusion of the pulse energy. The sample on the right, dry and also exposed to 532 nm light with picosecond pulses but at 10 Hz shows an entirely different morphology. A keyhole effect now appears, and the surface damage is more contained. Both areas received the same approximate amount of total energy (≈ 35 J), and were photographed at 60 times magnification.

The dry sample on the left of Figure 3 was exposed to picosecond pulses of 532 nm light. The incision created ragged, deeper damage, with a relatively small zone of thermal damage. The same amount of total energy was deposited on each site, but the pulse energy is more

localized in time, and thus does not have sufficient time to diffuse. The sample on the right was irradiated with nanosecond pulses. Greater thermal damage and a shallower ablation well are apparent. The effect of pulse length becomes obvious if one considers the peak intensities involved: 636 MW/cm^2 for the picosecond pulses vs. 45.8 MW/cm^2 for the nanosecond ones.

The analysis of all the previous effects was done in the absence of blood flow. The *in vivo* case would of course require knowledge of the absorption bands due to oxyhemoglobin and other blood components, and of the interactions between light and liquid. Figure 4 shows the different absorption bands of heparinized rat blood (1:100 concentration in a saline solution): note the the absorbances at 308 nm and 532 nm are not too dissimilar. Also note the significant drop in absorbance near 290 nm, suggesting the utility of future study of the interactions of 248 nm excimer laser light with blood-irrigated brain tissue.

As a first order model, we considered the effect of the presence of the saline solution (0.86 % salt content). Although this solution contains none of the absorption bands of blood, it does provide a zeroth-order model of the light-liquid interaction. Figure 5 compares the ablation wells caused by 532 nm light (picosecond pulses) at 76 MHz on dry and wet samples. Dry samples had no solution apparent on the surface at the time of irradiation; the wet samples has a visible liquid layer on the surface. The exposed areas were on different hemispheres of the same rat brain.

The wet sample shows a ragged incision, characteristic of a "boiling away" of material. The dry sample, albeit smoother, shows a greater degree of carbonization. Thermal damage seems to be limited in both areas.

The "keyhole" effect appeared when the brain was irradiated with 532 nm light picosecond pulses at 10 Hz. Note that this exposure has the highest peak power used, about 636 MW/cm^2 . This strange shape seemed to be related to the depth of the placement of the focal spot, appearing only when the spot was underneath the surface, but within the penetration depth of gray matter ($\approx 0.6 \text{ mm}$). This suggests that the keyhole effect is simply a focussing problem, with the following explanation: the first (conical) part of the well is due to the continued convergence within the

brain; the second part, a spherical cavity, occurs when the reduced area causes the power to pass a threshold value, on the order of 1 GW. This causes an explosion of ablation centered around the focal point, due perhaps to thermal lensing.

DISCUSSION:

The presence of a liquid is also important in another respect. Figure 6 is a photograph of a side slice of an ablation cavity. Being near the edge of the well, it is completely covered by tissue. Thus, the morphology of the cavity is more like a sub-surface "bubble", with a small centrally located hole through which the laser light penetrates. Hillenkamp has suggested that the bubble is caused by the vaporization of liquid within the tissue, and the cover remains because the liquid present is able to evaporate from the surface, thus dissipating the energy. For the 76 MHz, 532 nm picosecond laser irradiation, an audible "pop" was heard after 4 or 5 seconds of exposure. It is assumed that this is the sound of the bubble bursting due to the superheated vapor inside: the heated vapor cannot leave through the central hole faster than the rate of energy being deposited. The following simple calculation seems to support the hypothesis.

The penetration depth² of 532 nm light in gray matter is ≈ 0.6 mm. If we assume a cylindrical volume, with the upper and lower circular areas equal to the area of the focal spot, and the height of the cylinder to be the penetration depth, we then have:

$$\Delta Q = m c_p \Delta T + m L$$

The mass is given by the volume and the density of water, so $m = 1.2$ mg, and $\Delta T = 78$ C. If we assume the mass of the tissue to be 80 % water, then $m = 0.965$ mg. Thus, $\Delta Q = 2.26$ J. We now use the average power of the laser, 1.25 W, after noting that the absorbance of gray matter is 42 % at 532 nm. So the time it takes to boil the water contained in the cylindrical volume is approximately 4.3 s, well in agreement with the observed results for brain tissue with no water on the surface. In the case of the collimated (unfocussed) beam, the radius was approximately 2.2 times the focussed beam waist, so $m = 5.8$ mg, and $\Delta Q = 10.86$ J, leading to an evaporation time of 21 s. The actual time, as determined by the audible "pop", was 25-26 sec. The differences might be attributed to the heating of the vapor to the point of tissue explosion. Sa'ar³ *et al.* have shown that cavitation facilitates the transmission of laser light in liquids, but in this case the liquid is trapped within the tissue, allowing for localized dessication of the material and explosive liberation of the heated steam, and this was observed in 1064-nm light incident on brain tissue.¹ The clinical importance of understanding such explosive ablation processes is obvious and well documented.⁴

The quick rise in the depth of penetration for the focussed beam occurs around 5 s, due to the explosion of the vapor bubble and the consequent rapid increase in yield. For the unfocussed, collimated beam, the rate of removal also increases dramatically after approximately 20 s, again due to the vapor bubble explosion. It is also worthy of note that the depth of penetration for the focussed beam is expected to saturate after some time, due to the divergence of the beam waist, which leads to a decrease in the fluence and in the removal of new tissue. This is not observed, however, even after 2 min of exposure. The collimated beam diverges only slightly, and it could penetrate the entire brain if the irradiation lasted long enough. This might suggest the use of lenses with short focal lengths, which might lead to lesser damage in the tissue underneath the irradiated area due to their greater divergence with respect to depth and consequent decrease in the fluence of the beam after it passes its focal point.

CONCLUSIONS:

First order observations of the effects of wavelength, pulse length and pulse repetition frequency were reported. Ultraviolet light (308 nm), attuned to the vibrational modes of the gray matter components (such as proteins and the bases of the nucleic acids), showed better ablation profiles, causing deeper etch wells and lesser thermal damage than the 532 nm light. Picosecond pulses (35 ps) created deep, ragged ablation wells, whereas nanosecond pulses (11 ns) made smoother but shallower impressions and caused greater thermal damage. The optimal length ought to be between these two extremes, perhaps around 1 ns. A weaker dependence on the pulse repetition frequency was observed, in which light at 76 MHz inflicted more surface damage, but did not etch any deeper than light at 10 Hz. The "keyhole" effect was also studied, and an explanation was suggested according to which the morphology is due to the continued convergence of high peak-power laser light within the penetration depth of gray matter. Other factors were also considered in the creation of the ablation well, such as the saline solution and the influence due to the absence of blood flow.

ACKNOWLEDGEMENT

Thank go to Ms. Deborah Hefner for her extraordinary work in the preparation of the slices, and to Dr. Glenn Edwards for the use of the Quantel nano-picosecond laser.

FIGURE CAPTIONS

Figure 1: Comparison of the effect of irradiation with 532 nm light (on the left), and 308 nm ultraviolet light (on the right) on the ablation well morphology.

Figure 2: Comparison of two different pulse repetition frequencies on the desorption of gray matter. The sample on the left was shot at 76 MHz, while the one on the right at 10 Hz (the wavelength was kept constant at 532 nm).

Figure 3: Picosecond-duration pulses of 532 nm light were used to irradiate the sample on the left, whereas nanosecond pulses were used on the sample on the right.

Figure 4: Absorption bands of heparinized rat blood, in a 1:100 saline solution.

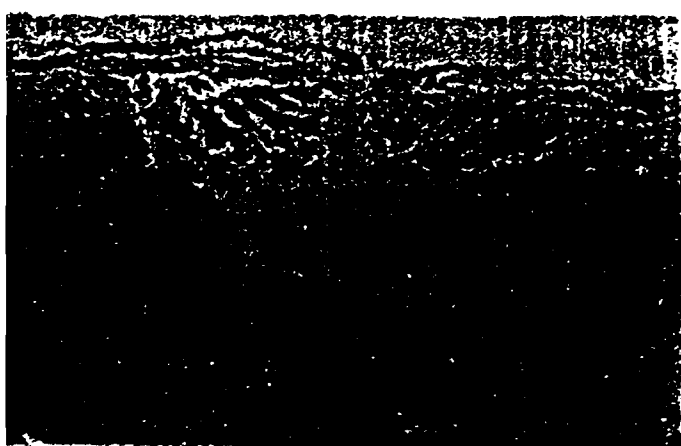
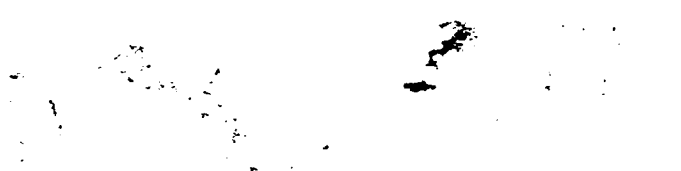
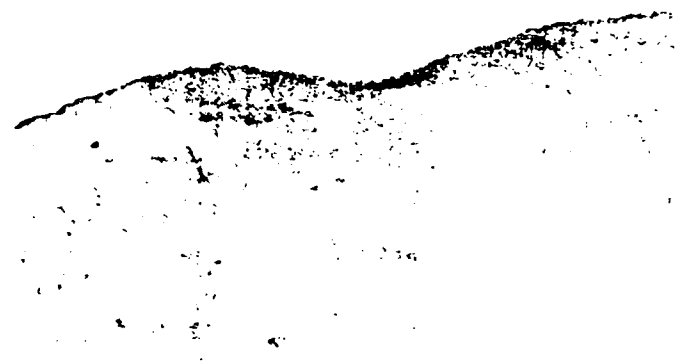
Figure 5: Effect of the presence of water on the tissue. The sample on the left was wet and irradiated with 532 nm light at 76 MHz; the one on the right was dry.

Figure 6: Sub-surface bubble in gray matter, near the edge of the ablation well.

Figure 7: Penetration depth of 532 nm light in gray matter, approx. 0.6 mm.

Figure 8: Illustration of the keyhole effect, created with 532 nm, 10 Hz, light with nanosecond-length pulses.

-
- ¹ Wharen, R.E. et al. "The Nd:YAG lser in neurosurgery; Part 1". J. Neurosurg. 60, March 1984, pgs. 531-539.
 - ² Eggert, H.R. and Blazek, V., Neurosurgery, Vol. 21, No. 4, 1987.
 - ³ Sa'ar, A. et al. "Transmission of pulsed laser beams through "opaque" liquids by a cavitation effect". Appl. Phys. Lett. 50 (22), 1 June 1987, pgs. 1556-1558.
 - ⁴ Jain, K.K. "Complications of the Use of the Nd:YAG Laser in Neurosurgery", Neurosurgery, Vol. 16, No. 6, June 1985, pgs. 759-762.



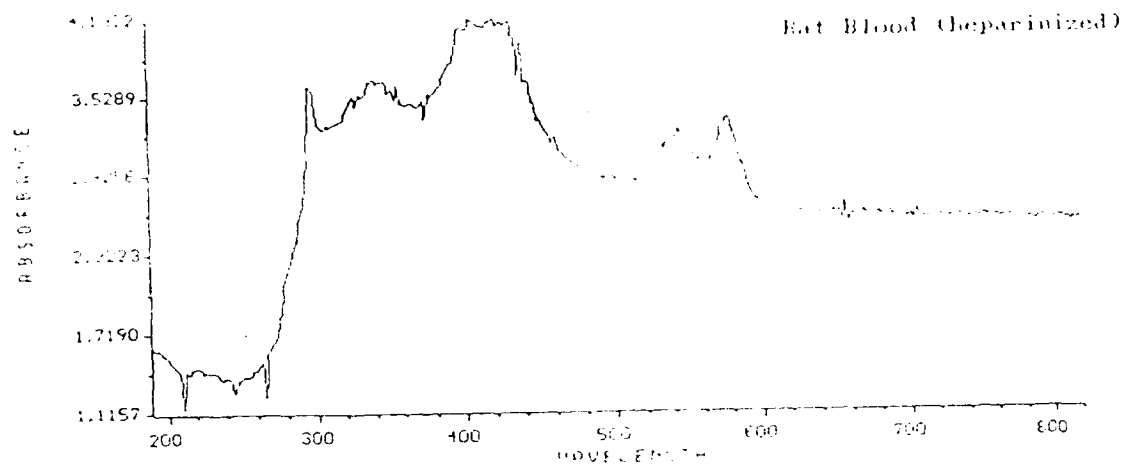
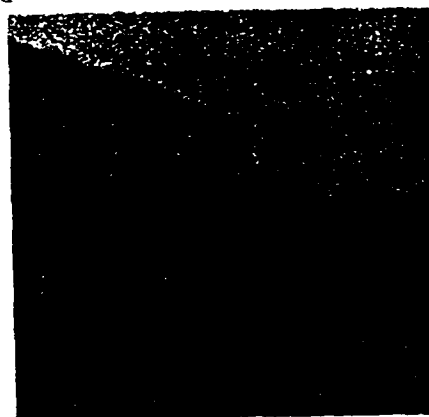


Figure 4. The absorption of heparinized rat blood.



WET



DRY

Figure 5. Comparison of ablation wells from wet and dry sites



Figure 6. Sub-surface vapor bubble.

Galloway Jr.^{1,2}, Charles A. Edwards II², Judith G. Thomas²,
Steven Schreiner², Robert J. Maciunas¹

1. Department of Neurological Surgery 2. Department of Biomedical Engineering
Vanderbilt University, Nashville, Tn. 37232

ABSTRACT

Stereotactic neurosurgery is a technique in which a rigid frame is applied to the patient's head and images acquired. Because the frame and the lesion are visible in the images, the lesion can be localized relative to the frame. Devices may then be attached to the frame to direct surgical instruments

Conventional stereotactic neurosurgery remains a point by point process, conceptually little changed from the original devices which were designed for use with pneumoencephalograms. The exponential rise in amount of available imaging information over the past 15 years has not been matched by intrasurgical applications.

A new device will be presented which allows the intrasurgical position and trajectory to be displayed on preoperative images. This device has sub-millimetric accuracy and precision and is limited only by the image voxel size. The device can use both CT and MRI image sets concurrently or exclusively. Applications include surgical planning, biopsy, bone flap location and intracranial localization. Both phantom and clinical procedures will be shown.

1. PRESENT TECHNIQUES

1.1 Stereotactic Devices

Present day medical tomographic imaging can provide exquisite detection, localization and visualization of lesions within the head. Specific targets can be localized relative to other visualized anatomic landmarks with positional uncertainties limited only by pixel size and slice thickness. However, when the surgeon begins to operate that information is left on the light box. The relationship between the present surgical position, the lesion and objects of concern, such as major blood vessels, is bound by the accuracy of the surgeon's recall and training.

Present stereotactic devices arose from attempts to use the information available in medical images to guide the surgeon to the target.¹ The field is dominated by four systems; the Leksell, the Kelly-Goerss modification of the Todd-Wells, the Riechert-Mundinger and the Brown-Roberts-Wells (BRW). The BRW is notable in that it was the first apparatus to be developed based on tomographic images. The first three were initially developed when the primary form of neurological imaging was the ventriculogram. They all were later modified to use tomographic data^{2,5}.

In order to use these devices a frame such as the one shown in Figure 1 is attached to the skull by screws or pins. A set of N-shaped bars formed of a material perceptible on the desired imaging modality. When the images are made, the cross-section of the N-Bars are visible in the image frame. See Figure 2.

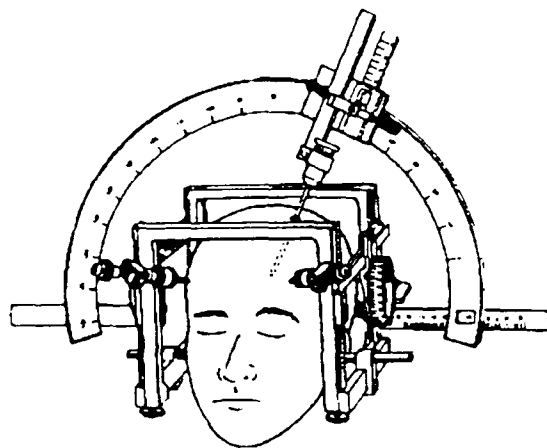


Figure 1. The Leksell Stereotactic device showing surgical target localization.

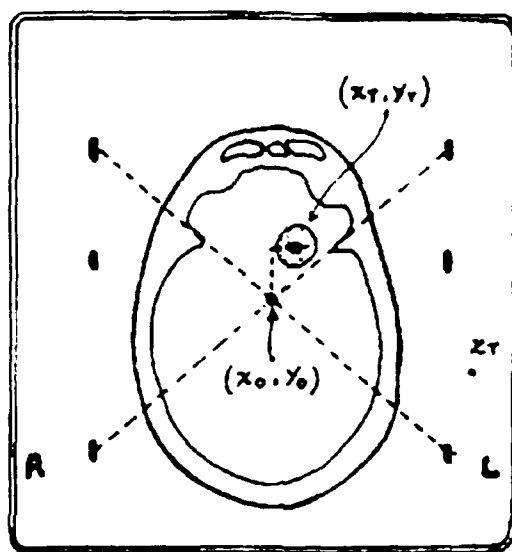


Figure 2. Axial image showing N-bar localization markers.

By making the frame visible in the images, lesions and other sites of surgical interest may be located relative to the frame as well as to other anatomic positions. Devices may then be attached to the frame to geometrically guide the surgeon to the site of interest. While this sort of guidance was a major surgical breakthrough, several factors limit its usefulness.

One problem is that, after the physician has located the desired target and entry points and planned the desired trajectory, all of the information available in the images is reduced to a series of parameters. The relationship between these parameters and the physical space of the head is non-intuitive. Therefore, at the time of surgery, should any change in the pre-planned process be desired, the entire procedure must be repeated. In addition, since the relationship between frame position and physical location is non-intuitive, it is difficult for the surgeon to detect any but the grossest errors.

One problem is that there is no feedback as to present physical position relative to imaged trajectory marker may be advanced to accompany the surgery but that places the frame in the surgeon's line of vision and only provides information regarding a single path.⁶

Articulated Arms

Articulated arms are flexible devices whose endpoint locations may be determined by a series of geometric calculations. A great deal of the scientific development of articulated arms arises from the field of robotics⁷, however, unless external mechanical power is provided for moving the articulated arm to a desired location, the device is not a robot. A drawing of a three-link, 6 degree of freedom articulated arm is provided in Figure 3.

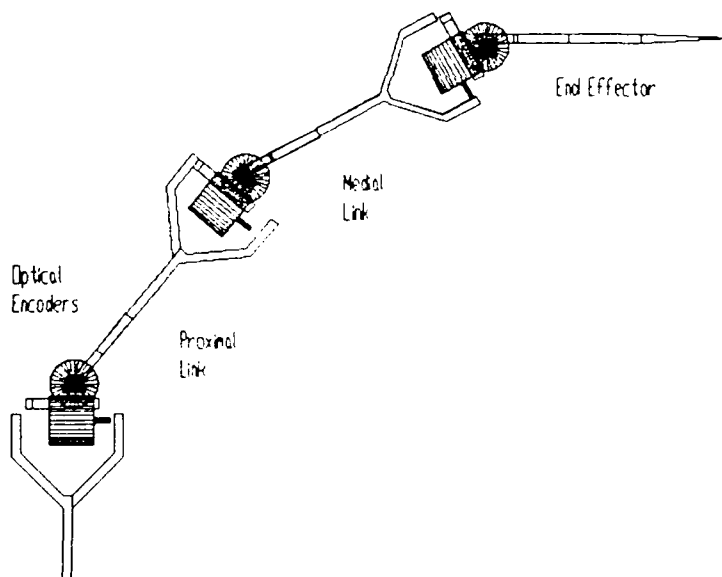


Figure 3 A three-link, six degree-of-freedom articulated arm.

The end effector's position, d , is calculated by use of the forward kinematic equation shown below.

$$d = T_1 T_2 T_3 T_4 T_5 \quad (1)$$

T_x represents a 4x4 rotational matrix for the Xth joint. An example of one such rotational matrix, in this case a rotation about Z and a translation in Y is shown in Equation 2.

$$T_X = \begin{bmatrix} \cos \theta & -\sin \theta & 0 & 0 \\ \sin \theta & \cos \theta & 0 & d \\ 0 & 0 & 1 & 0 \\ 0 & 0 & 0 & 1 \end{bmatrix} \quad (2)$$

Since the link lengths are fixed, and the matrices are sparse, the matrices are combined in a chaining operation to a single set of calculations in which the coefficients are changed as a function of the joint angles.

The accuracy of the endpoint determination is a combination of angular detection and machining precision. In a revolute articulated arm (all motion is angular), the perfect determination of the end position requires that all angular motion must be accounted for and exactly measured. In addition, the link lengths and geometries must be flawlessly known. Bends in the links and runout in the bearings cannot be accounted for and would be a source of error. Beyond these errors, accuracy questions are geometric; for a given set of link lengths, how accurately must the angles be known for a specific endpoint accuracy?

1.3 Required Accuracy

In any stereotactic or image-guided surgical system errors may arise from a number of places. Distortions in the imaging⁷, mechanical misadjustment or changes due to slippage of frames or markers between imaging and surgery or during surgery. In addition to errors there are a series of uncertainties. The ability of any imaging system to localize a single point in space is bound by the voxel size. Mechanical systems may be exactly adjusted yet the location of the tip is not a point but a volume in space described by the device's mechanical resolution.

Both the errors and the uncertainties between imaging and device are independent. Therefore, their effects form a vector addition. Overall system performance can only be described by the sum of each process's performance. Due to the vector nature of this sum, on any given operation errors may cancel each other and excellent precision be obtained, but the specifications must be made on the worst case.

The accuracy needed for surgical procedures is primarily dependent on location of the lesion. Lesions near the midbrain, optic nerves or major blood vessels require much more accuracy than other

However, the vector nature of the error requires that design error tolerances be specified. If the device moves 3 mm during surgery and the device localizes a target to within 3 mm, the error may be 0 or 6 mm. The difficulty is determining which case do you have.

2. METHODS

The design criteria were: submillimetric arm accuracy and sub-second image display. The first design goal was the design of the articulated arm.

2.1. Error Analysis

To determine the parameters required to realize the design goals, we performed a series of simulations. The method of analysis for the arm geometry consisted of determining a desirable physical configuration, solving the inverse kinematic equation using the Denavit-Hartenberg (D-H) method to obtain an analytic solution for each joint angle, and generating positional errors across the entire surgical volume. Modelling, error generation and analyses were accomplished through integration of existing robotics simulation procedures^{8,9}, modified procedures and original software. The error analysis involved the following steps:

- Generation of a model of the articulated arm, including link-lengths and joint configuration.
- Simulation of the moving of the endpoint to a target in the surgical volume.
- Each joint was then displaced one encoder least significant bit.
- The new endpoint position was compared to the initial position and the endpoint error calculated.

The results of the simulation studies suggested that a device which allowed access to the entire surgical field could be constructed using 16 bit angular encoders resulting in a worst-case endpoint positional error of much less than 1 mm.

2.3. Position Calculation and Image Handling

The second question to be addressed was one of data rates. In order to be truly interactive, we proposed a positional display refresh rate of 0.5 seconds. The position refresh rate is defined as the period required by the following chain of events:

- The pointing arm is moved from the present point in the surgical field to a new one.
- The new angular positions are captured and the new endpoint position determined.
- The appropriate image slice is determined and the new 512x512 image is displayed.

A 0.1 second end-to-end traversal of the surgical space of a 6 revolute-joint arm results in a slightly less than 10,000 bits/second data rate. Once the angular values are captured, the calculation of the new endpoint position (d) would take 588 floating point operations if each T_i was a general 4x4 matrix. However, since the matrices are sparse only 123 floating point operations are needed.

Assuming a modest 0.2 million floating point operations per second (MFlops), calculation of the registration matrix requires approximately 20 seconds.

1. Image Space - Arm Space Registration

In order to register the space described by motions of the arm with the image space, at least three points of commonality must be determined in each space. Once the three points are located in both spaces, a simple rotational matrix may be determined. This matrix is then the map for locating all the points within the surgical space on the images. This process presumes rigid rotation and requires that the points of commonality be well defined.

The points of commonality, called fiducial markers, can be determined in one of three ways. The first method is to use anatomic locations such as the tip of the nose, the nasion, the tragus or locations on the orbital rims which may be precisely located on both the scan and the patient. This form of marking is referred to as intrinsic fiducial markers. The difficulty with intrinsic fiducial markers is that it is very difficult to find locations which share the following characteristics: visibility on CT and MRI, rigid attachment to the rest of the head and well defined shapes for exact point location. Some authors^{10,11} have been using extrinsic markers such as small spheres or surgical staples attached to specific locations on the surface of the skin. We have resisted these techniques due to concerns about marker motion between imaging and surgery.

During the development of the articulated arm device, we have been using extrinsic fiducial markers, points on a stereotactic frame, for our registration process. This allows direct, application-based comparisons between the performances of the two devices.

2.5. Initial Arm Design

Based on our simulations and calculations, a prototype articulated arm was designed and constructed. The arm is a three-link, three joint, six degree of freedom articulated arm, primarily composed of stainless steel. Each joint consists of two rotational angles, mounted in a gimbal structure. This configuration leads to approximately 330° of free motion in each joint. The angular sensors are incremental optical encoders that generate 3,600 state changes per rotation which are interpolated into 72,000 pulses per rotation by hardware provided by the manufacturer. The angular position of the joint is transmitted to the angular sensors via quarter pitch spur gears. This arrangement allows for the transverse mounting of the angular sensors, reducing the total width of the arm. The spur gears are mounted at a 6° angle to minimize the gearing backlash.

2.6. Calculation and display system.

An 80386-based computer system is being used as the computational platform for the system. With the inclusion of a math co-processor, the computer has a rating of approximately 0.5 MFlop. The images are stored in the computer on a hard disk and can be read and displayed in less than a third of a second.

The arm endpoint position may be simultaneously displayed on 4 512x512 images on a 1280x1024 display. The display controller has a BITBLT rate of 100 million bits/second (12.5 million 8 bit pixels) which means it can place a new 512x512 image on the screen every 21 ms. The difference between this

performance and the present actual performance of 285 ms per image displayed is due to the hard disk and the system bus, not the display hardware. The display is composed of several scale windows displaying images from modalities such as CT and MR and one window presently showing a patient-specific wire frame model. The composite window displays the image handling and multimodality display are discussed in greater detail in the paper.¹²

Figure 3

3. Results

3.1 Accuracy

We made a series of measurements. Our initial attempt was to choose a point in space and return to it repeatedly, observing the variance of returned spatial coordinates. Our results showed we had an average error of 0.33 mm with a maximum error of 1.5 mm. This sort of measurement is the standard for evaluating the performance of the stereotactic systems. It is, however, merely a measure of precision not accuracy. It is especially poor for judging the performance of articulated arms, since their flexibility provides a vast number of paths to any given single location.

We devised a second technique in which we located a variety of points, distributed in three-dimensional space. Each point was located several times by different paths and by different users. We measured the distance between the points using electronic calipers and compared that to measured distance by the arm. The average error gives us a measure of the accuracy and the standard deviation a measure of the device's precision. Here the accuracy was 3.5 mm with a standard deviation of 2.5 mm.

Clearly, this performance was much poorer than the design values. Although we were intentionally choosing greatly divergent paths and some of the error could be ascribed to the user's ability to return the pointer to the same spot, the arm's performance was not what it could be.

3.2 Calibration

One source of error was the calibration of the arm. When you have the capability to measure angles to 1/200th of a degree it is difficult to initially position the links so that all of the encoders are at their zero position. We had confidence that we could hand-align the device to $\pm 2^\circ$ but anything more than that was uncertain. If you allow a 1/2 degree error in each joint of an articulated with link lengths similar to ours, worst case errors can go beyond 1 cm.

Two of the authors (CAE and RLG) devised a calibration technique which determined the initial angular offset and corrected for it at each joint. After this calibration was performed, the 3-D spatial targets were then relocated by each of the users. Now the points were located to with average errors of about 1 mm with standard deviations of less than 0.9mm. These errors may most likely be assigned to the operator's ability to return to the same location.

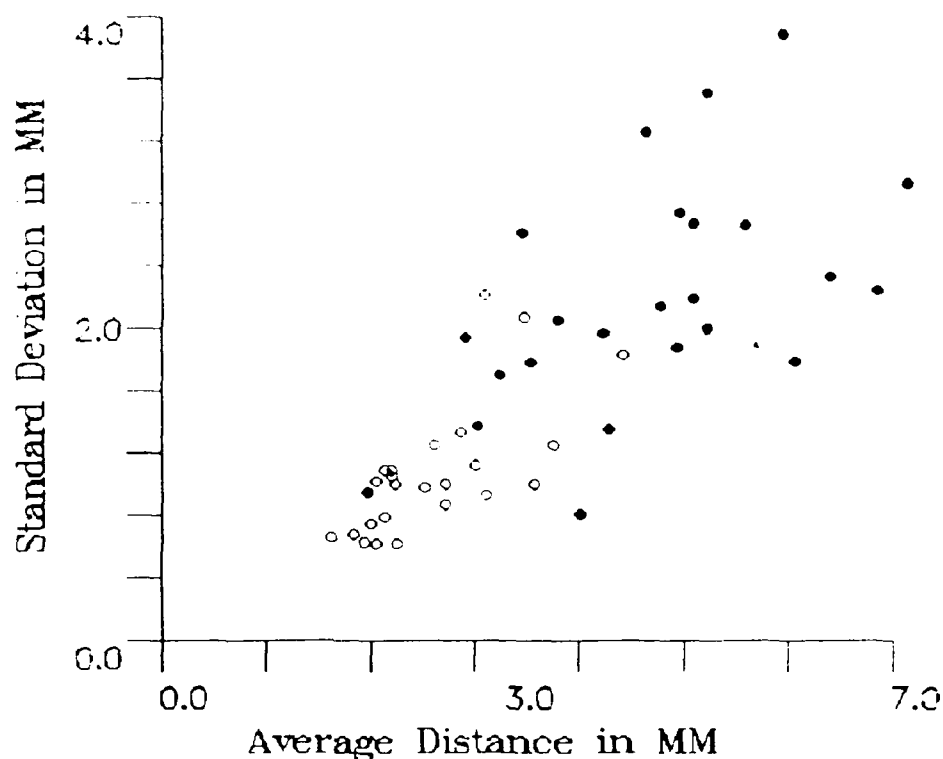


Figure 4. Pre and Post calibration results. Solid circles are precalibration, clear circles are post-calibration.

We lastly performed a study in which a single operator found points on a metal ruler placed arbitrarily in space. We located multiple points at distances ranging from 1 to 50 mms again using differing paths to the points. Our average error was 0.09 mm with a standard deviation of 0.22 mm. We should point out that these measurements are arm accuracy numbers only. Any error or positional uncertainty due to imaging would still be in the process. But what this really tells us is that it will take improvements in imaging devices such as CT and MR on the order of 8 fold before the arm error is the dominant term. This means with higher and higher resolution imaging our system accuracy will improve as well.

4. INTRAOPERATIVE PERFORMANCE

As stated earlier we have been using this device in conjunction with a standard stereotactic device. The presence of the stereotactic frame gives us a variety of easily identifiable targets. As of this writing we have used the IIG arm in 14 surgeries and in each the observed performance has been on the level of a very good stereotactic system. This sort of performance easily places the IIG surgery system performance on a par with the best of present stereotactic systems¹¹. Cases performed have included craniotomies, tumor biopsies, shunt placements, and cyst aspirations.

...olactic systems, the IIG surgical system makes all of the imaging information available on an interactive display of present surgical position. In one recent biopsy procedure, the patient was positioned and the skin was being closed when we realized that the films had never been developed in the box. They had never been missed because the information was available in a format accessible during the surgery.

5. ACKNOWLEDGEMENTS

We would like to acknowledge the invaluable contributions of the following people: George Jack Cannon, Susan Couch, R.N., Odie Lawrence, Bill Sh. Drake, Phillip Vermeulen and

This work was funded in part by grants from the Whitaker Foundation, DIO/T/TA and the National Institutes of Neurological Disorders and Stroke.

arily
hs to
that
iging
ining
eans

The
have
oxel.
:sent
, and

6. REFERENCES

- Heilbrun, M.P. Ed., Stereotactic Neurosurgery, Williams and Wilkins, Baltimore, 1988, 195.
1. Eklund, B. Jernberg, "Stereotaxis and tomography. A technical note", Acta Neurochir, Vol 52, p. 1, 1980.
 2. S. Goerss, P.J. Kelly, B. Kall, G.J. Alker, "A computed tomographic stereotactic adaptation system", Neurosurgery, Vol 10, p. 375, 1982.
 3. F. Munding, "CT-stereotactic biopsy of brain tumors", in Tumors of the Central Nervous System in Infancy and Childhood, Voth, D., Gutjahr, P., Langmaid, C. Eds. Springer, Berlin, 1982.
 4. R.A. Brown, "A computerized tomography-computer graphics approach to stereotaxic localization.", J Neurosurg, Vol 50, pp. 715-720, June 1979.
 5. Galloway, R.L., Maciunas, R.J. "Stereotactic Neurosurgery" CRC Critical Reviews in Biomedical Engineering, Vol 18, No. 3, Nov. 1990. pp 181-205.
 6. K.M. Ludeke, P. Roschmann, R. Tischler, "Susceptibility artifacts in NMR imaging", Magnetic Resonance Imaging, Vol 3, No.4, pp 329-343, 1985.
 7. K. Fernandez, ROBOSIM: A Software Tool for Robotic Simulation. Ph.D. Thesis Dissertation, Vanderbilt University, 1986.
 8. A.E. Balogh, J. Springfield, R.J. Maciunas, R.L. Galloway, "Simulation and Error Analysis for a Stereotactic Pointing System". Proceedings of the Annual International Conference of the IEEE Engineering in Medicine and Biology Society, Vol 11, p.925, Nov. 1989.
 9. E. Watanabe, T. Watanabe, S. Manaka, Y. Mayanagi, K. Takakura, "Three-dimensional digitizer (neuronavigator): new equipment for computed tomography-guided stereotaxic surgery", Surg-Neurol, Vol 27, p. 543, 1987.
 10. B. Guthrie, R. Kaplan, E. Laws, "Three-Dimensional Cranial Image Reconstruction for Interactive Freehand Stereotaxy". Proceedings of The American Association of Neurological Surgeons, p. 357, May 1990.
 11. Edwards, C.A., Galloway, R.L., Thomas, J.G., Schreiner, S., Maciunas, R.J., Simultaneous Graphics and Multislice Raster Image Display for Interactive, Image-Guided Surgery, SPIE, 1991, In Press.
 12. R.J. Maciunas, J.W. Latimer, C. Cobb, R.L. Galloway, "Accuracy Assessment for Stereotactic Frame Systems". Proceedings of The American Association of Neurological Surgeons, p.344, May 1990.

Simultaneous Graphics and Multislice Raster Image Display for Interactive, Image-Guided Surgery

VI-C

Charles A. Edwards, II¹, Robert L. Galloway Jr.^{1,2},
Judith G. Thomas¹, Steve Schreiner¹, Robert J. Maciunas²

1. Department of Biomedical Engineering
2. Department of Neurological Surgery
Vanderbilt University, Nashville, TN 37232

ABSTRACT

A surgeon typically uses information from a number of tomographic imaging methods (e.g., CT, MR, PET) during the course of a surgical procedure. These imaging techniques represent three-dimensional information as a set of two-dimensional images. To use this information, the surgeon is required to mentally construct a three-dimensional visualization from the set of two-dimensional images. The formation of the mental image becomes more complicated with the inclusion of multiple imaging modalities and multiple imaging planes.

We have developed a technique to enhance the mental three-dimensional visualization process through simultaneous graphics and multislice raster image display. The composite display, capable of displaying up to three raster images along with a patient-specific graphics model, is viewed on a 1280×1024 monitor. The raster images, displayed in a 512×512 format, may be any combination of imaging methods and imaging planes. The graphics model, determined from the imaging data, may be freely rotated as a depth-cued wireframe or shaded-surface model. Regions-of-interest may be incorporated into the graphics model for additional visual cues. Trajectory information may be obtained by moving a three-dimensional cursor in any raster image space or in the graphics model with instantaneous update of the remaining display area.

This design allows the surgeon to interactively obtain orientation and visualization information from the images in the operating room. Because the classic imaging planes are used, the surgeon is not required to deal with a new information format or a loss of resolution.

1. INTRODUCTION

Man has pursued the ability to view the unseen anatomical structure of the body for centuries. Detailed artistic drawings of anatomical structures done during dissections were the sole component of anatomical atlases for a long time. These drawings were used as educational tools and professional references. Artists/Scientists such as Aristotle, Galen, Leonardo da Vinci and Michelangelo were among those that wrestled with the problems of using two-dimensional drawings to depict three-dimensional structures (Fig. 1). Such line-drawings continue to be found in medical handbooks. In the early part of the 20th century,

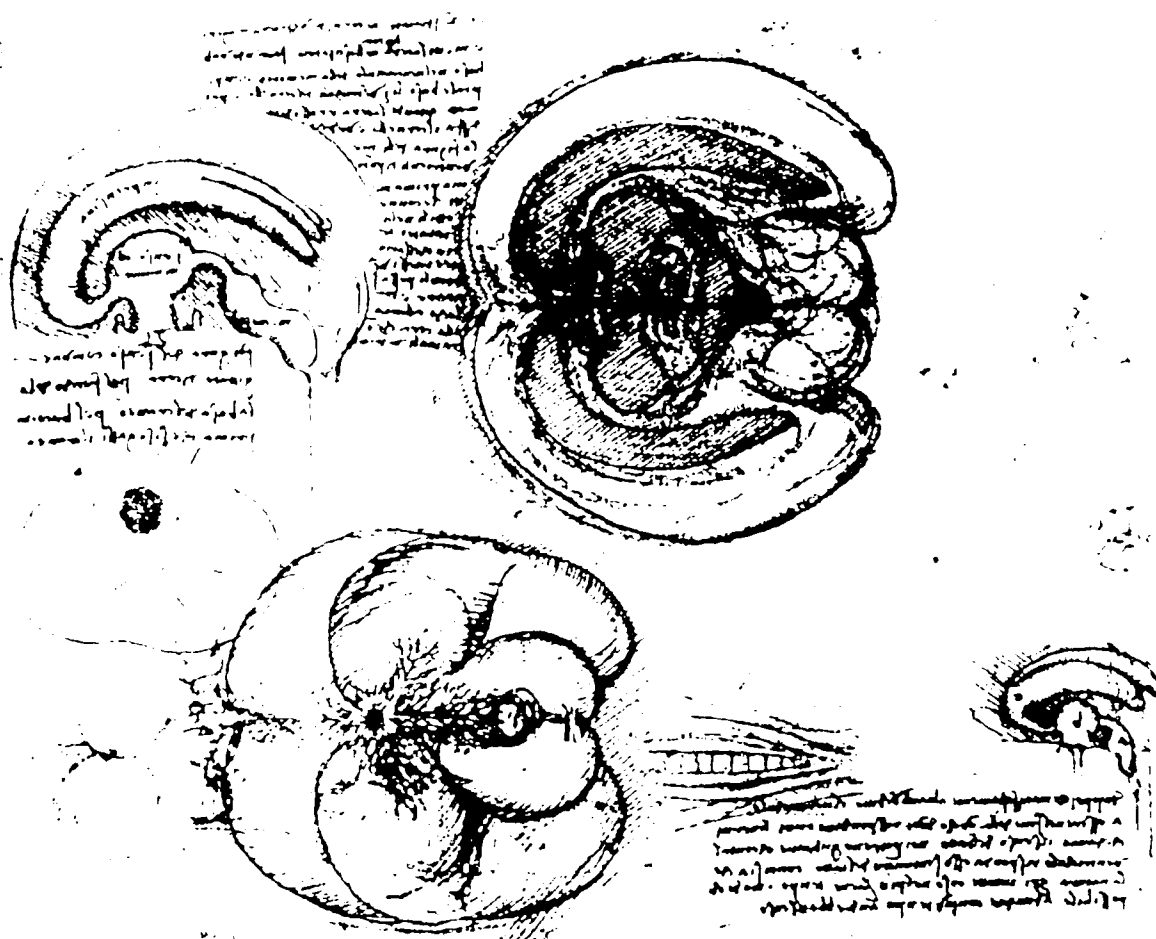


Figure 1. Leonardo da Vinci's drawing of cerebral ventricles modelled by a wax 'encephalogram'.

the shift from general to patient-specific atlases originated with W.C. Roentgen's first X-ray of his wife's hand. The introduction of computed tomography (CT) by G.N. Hounsfield in the 1970's tipped the balance in favor of the patient specific atlas. CT, in essence, allows non-invasive *in vivo* dissection from which a series of highly detailed imaging planes, or "slices", are obtained. These slices become an anatomical atlas for the patient. The 1980's saw the development of a number of tomographic imaging techniques including magnetic resonance (MR) and positron emission tomography (PET).¹ The rationale behind each of these imaging techniques is clear: provide the best representation of unseen anatomical structures and present them in a manner such that the maximum information content is conveyed for the task at hand. Over the years, great strides have been made in the visual representation of information, yet three dimensional structures must still be represented on two dimensional displays. The method used to visualize and interact with these representations remains a topic of research and debate.

From the first artistic renderings to the current sophisticated procedures, the way data is displayed and used interactively has suffered from the lack of understanding of how we

visualize information. A way to optimize the presentation of visual information still eludes us. As we continue to unravel the mysteries of the visual system, designers are attempting to display a maximum amount of information in the simplest form. The recent increases in computational power in addition to decreases in size and cost has brought about the union of scientific analysis and graphic display.² Computer platforms with supercomputer performance, high-performance graphics, large and fast disks, and large amounts of memory are now found in desktop models.

These developments are of special interest to one specialty in the field of neurosurgery, stereotaxy. Stereotaxy deals with the targeting of specific location within the brain prior to surgery by using pre-operative images. From the inception of stereotaxy, it has relied on the ability to use anatomic atlases whether they are artistic renderings or tomographic films.

In the present scenario, the surgeon uses the various film sheets (i.e., CT, MR, PET, etc.) as references during the operation. The surgeon mentally reconstructs the three-dimensional relationship between the slices shown on the film sheets. If, at any time during the procedure, additional information is required, the surgeon pauses in the operation and consults the film sheets (Fig. 2). The task becomes more difficult when the surgeon uses multiple imaging modalities and multiple imaging planes.

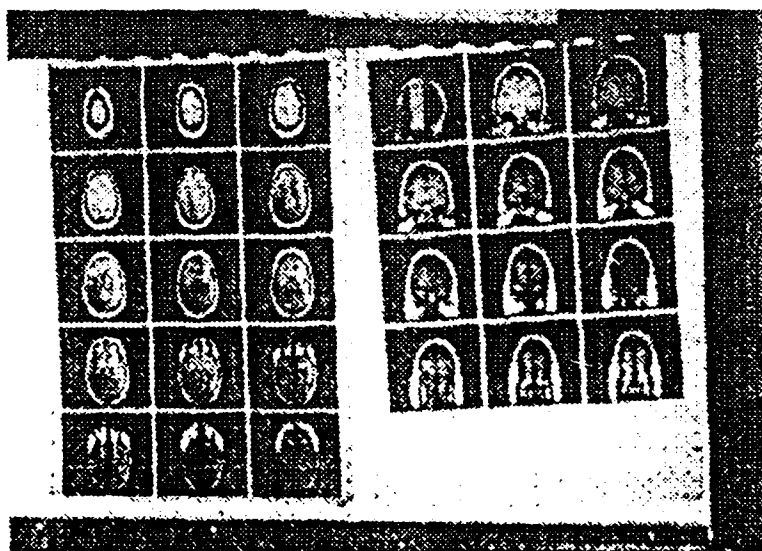


Figure 2. Medical image film sheets on an OR light box.

The computer is slowly finding its way into the operating room (OR). The recent advances in the computer industry have set the stage to bring the patient-specific atlas into the OR. We have developed an image display system that displays the patient-specific data from up to three different image sets along with a patient-specific graphics model. The system is interactively controlled by a three-dimensional pointing system held by the surgeon.

allows the surgeon to quickly access the patient's anatomical atlas and orient to the information.

2. METHODS

Obtaining Images

The imaging sets are obtained from one of the following:

- A) Siemens Somaton CT scanner
- B) 2.0 T Siemens Magnaton MR scanner operating at 1.5 T
- C) Siemens CTI 931 PET scanner

The imaging sets are obtained in their standard format on 9-track tape. The images are transferred either to a Sun Microsystems 4/490 or to a 25 MHz 80386-based computer. If the Sun Microsystems workstation is used, the images are transferred to the 80386-based platform via an Ethernet connection. Figure 3 illustrates the communication interfaces between the systems. The images are translated into the proper format for use by the 80386-based system and a header is added to the beginning of each image set.

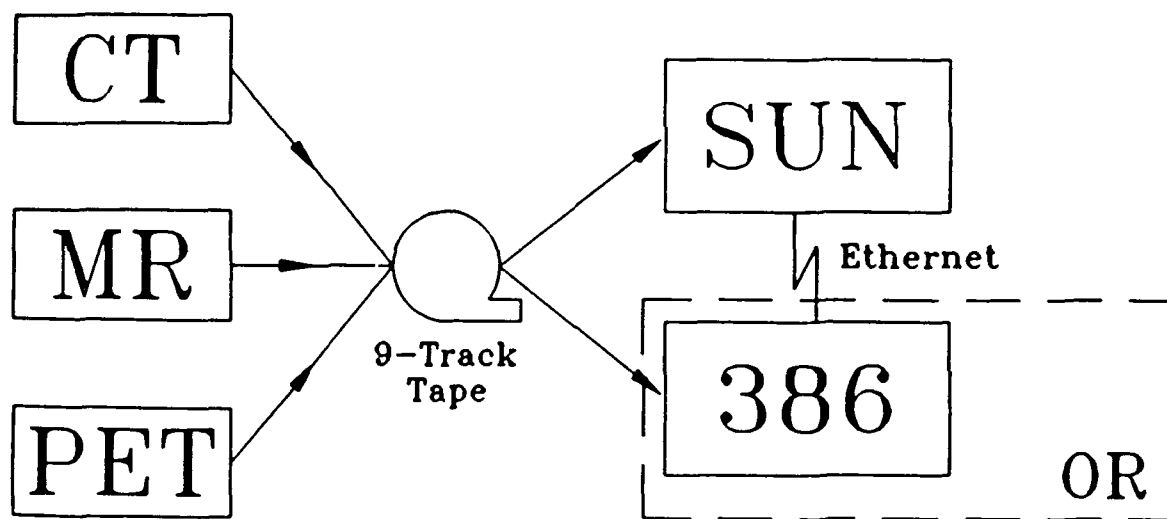


Figure 3. Images from CT, MR, and PET can be brought to the OR system by tape or Ethernet.

2.2 System Setup

The interactive, image-guided surgery system is constructed around a 25 MHz 80386-based computer (Everex STEP 386/25) equipped with 8 MBytes of random access memory (70 nsec RAM), a math coprocessor (Weitek 3167 Abacus) and a 383 MByte Winchester

disk (CDC Wren V 383H) with 15 msec average access time. The primary display (Amdek Video-410A) is driven by a monochrome graphics card (Hercules Graphics Card Plus).

In addition to a monochrome display, a high-performance, 3D solid visualization engine (Matrox SM-1281) is connected to a 19 inch RGB display (Mitsubishi HJ6905). The graphics engine has a resolution of 1280×1024 and can display 256 simultaneous colors from a true color palette of 16.7 million. Additional graphics capabilities include the ability to draw 80 000 three-dimensional vectors per second for almost instantaneously updated wireframe drawings, the ability to generate 20 000 Gourand-shaded polygons per second for rapid rendering of realistic models, and programmable light sources and depth cueing allowing realistic, real-time visual cues.

The combination of the above forms a 0.5 Mflops 3D workstation. High performance, relatively low cost, flexibility, and small size make the system the ideal solution for bringing patient-specific anatomical atlases to the OR in an electronic format.

2.3 Display

Graphics and raster images are displayed on a composite screen display. The display is composed of four 512×512 windows and a 250×1024 control panel. The four windows are used for the display of raster image and graphics, while the control panel will contain menu information (Fig. 4).

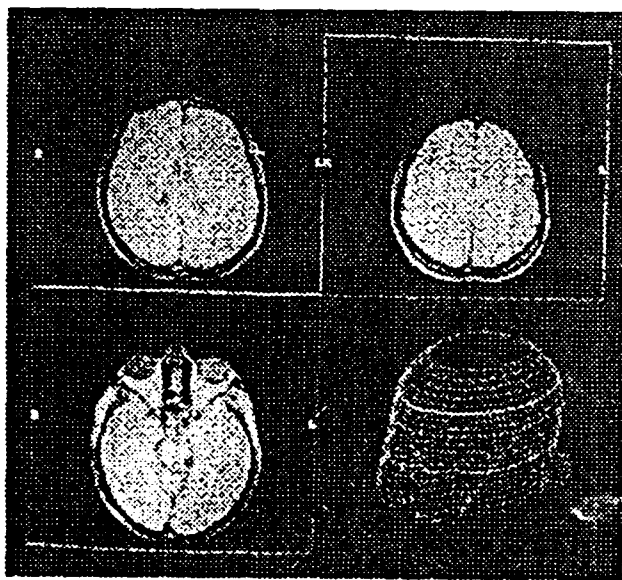


Figure 4. Graphics and raster images displayed on a composite screen display. Each image is 512×512 pixels.

The four 512×512 windows are capable of being used in a variety of schemes. Included in the possible permutations are:

- a) Multiple windows of a single scan
- b) Multiple scans from a single imaging modality
- c) Multiple imaging modalities simultaneously
- d) Multiple slice orientations
- e) Three-dimensional graphics (wireframe and shaded-surface models)
- f) Any combination of the above

2.3.1 Raster Images

Raster images (i.e., CT, MR, etc.) are compressed from their native 4096 gray values (12 bits) to 128 gray levels (7 bits) for display using an adaptive linear compression scheme. This compression procedure is designed to allow use of available color coding for depth cueing and shading of the graphics display. The compression of imaging data is unacceptable for diagnostic purposes; however, for an intrasurgical reference and target location the compressed images provide the required level of information (Fig. 5). The width and level used by the compression method may vary individually for each window.



Figure 5. A raster image with resection site and tumor.

A double-ended caching strategy is used to shuffle images from the disk to the memory. A caching system is necessary because a complete image set may be several times the size of the RAM. Two megabytes of RAM are assigned to each window.

2.3.2 Graphics

Patient-specific graphics models may be fashioned from information available in the medical images. The model of the patient's head is formed by thresholding combined with region connectivity analysis and region elimination³ (Fig. 6). The model assists the surgeon

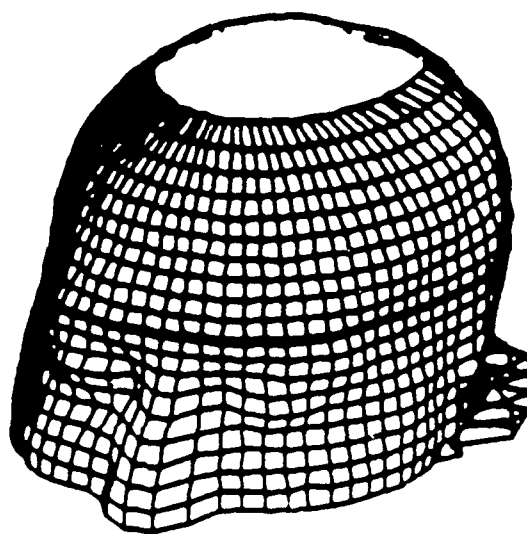


Figure 6. Patient-specific wireframe model.

in visual orientation between the surgical space and the imaging information being displayed. The model may be freely rotated to any position desired by the surgeon. Furthermore, areas of interest or concern may be modelled and displayed within the model of the head for additional visual cues.

2.4 Interactive Pointing System

An interactive pointing system described by Galloway *et al.*⁴ is incorporated with this display system to allow interactive surgical planning and, when imaging space is registered with surgical space, intrasurgical tracking of surgical position and trajectories is possible. The pointing device is an articulated arm with six degrees-of-freedom (Fig. 7). Movement of the pointer may be linked to any of the display windows allowing real-time interaction with both the raster images and graphics. Tracking is provided on "active" windows by a cursor if a raster image is displayed, or a representation of the articulated arm if a graphics model is present.

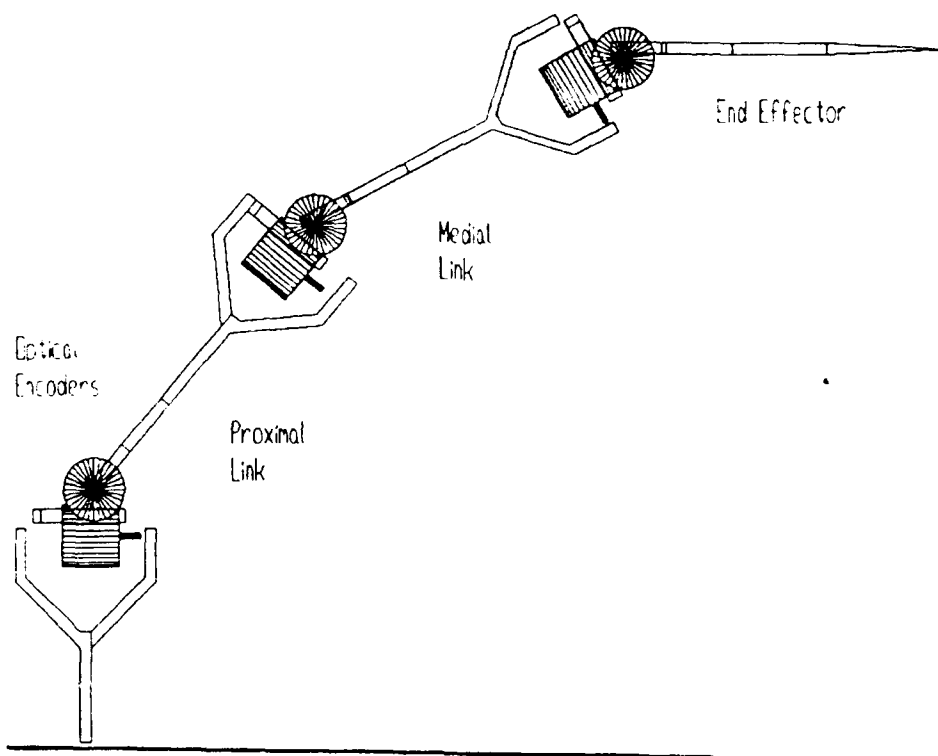


Figure 7. A six degree-of-freedom interactive pointing system.

3. DISCUSSION

The development of this system is an ongoing project. Initial reactions from the neurosurgical community have been positive. However, there remains work to be done. One area of concern is the lag time required by the caching system when the pointing device is moved an extended distance. Several solutions are possible. One solution is to increase the amount of RAM in the system, making it possible to increase the allotment assigned to each window. This has the effect of reducing or eliminating the number of calls to the cache. Another solution is the use of a caching controller for the disk drive. Several 80486-based systems currently available allow both solutions to be implemented. These systems have the capacity to hold large amounts of RAM (> 64 MBytes) and are equipped with caching controllers (with up to 8 MBytes of cache memory) for Small Computer System Interface (SCSI) disks with fast access times (< 15 msec).

While the present system is capable of displaying transverse, coronal, sagittal, and oblique planes for CT and MR images, PET images are lacking. The clinical use of PET is increasing steadily. Conceptually, there are no problems adding PET images. Among the modifications necessary to incorporate PET images are the ability to display color raster images and a method to register PET images to CT and/or MR images. Research is currently being conducted to allow the inclusion of PET and other imaging modalities such as MR angiography.

4. CONCLUSIONS

Stereotactic procedures have always relied on imaging space, be it general or patient-specific, for orientation guidance. A natural extension of this relationship is the "marriage" of image space to the physical stereotactic space. Recent advances in technology have, for the first time, provided the foundation on which such a system can be developed at a reasonable cost. The ability to display multislice raster images with graphics models simultaneously is an essential ingredient in successful implementation of an interactive, image-guided surgical system.

5. ACKNOWLEDGEMENTS

The authors gratefully acknowledge the assistance of Venky Mandava, Lewis Saettel, and Andy Richter.

The work was supported in part by grants from the Whitaker Foundation and the MFEL program of the SDIO/T/TA.

6. REFERENCES

1. Coatrieux, J.L. 1990. From the Guest Editor. *IEEE Engineering in Medicine and Biology*, 9: 4, 14.
2. Principe, J.C., D.G. Childers, and A.A. Arroyo. 1990. Guest Editorial: Special Issue on Visualization of and Interaction with Biomedical Data. *IEEE Transactions on Biomedical Engineering*, 37: 8, 741-743.
3. Thomas, J.G., R.L. Galloway, C.A. Edwards, G.L. Haden, and R.J. Maciunas. 1991. A Comparison of Three-Dimensional Surface Rendering Techniques. In *Medical Imaging V: Image Capture, Formatting, and Display, San Jose, California, February 24-26, 1991*, by the International Society for Optical Engineering, Vol 1444, In Press.
4. Galloway, R.L., C.A. Edwards, J.G. Thomas, S. Schreiner, and R.J. Maciunas. 1991. A New Device for Interactive, Image-Guided Surgery. In *Medical Imaging V: Image Capture, Formatting, and Display, San Jose, California, February 24-26, 1991*, by the International Society for Optical Engineering, Vol 1444, In Press.

A Comparison of Three-Dimensional Surface Rendering Techniques

VI-D

Judith G. Thomas¹, Robert L. Galloway Jr.^{1,2},
Charles A. Edwards, II¹, Gerald L. Haden³, Robert J. Maciunas²

1. Department of Biomedical Engineering
2. Department of Neurological Surgery
3. Department of Electrical Engineering
Vanderbilt University, 37232

ABSTRACT

To make use of the three-dimensional information contained in a series of computed tomography (CT) or magnetic resonance (MR) slices, one must either mentally reconstruct the data or generate a computer-aided rendering of the data on a computer display. Computer-aided rendering of a three-dimensional surface allows visualization of the model from different angles.

Creation of a three-dimensional model in wireframe or shaded surface format from tomographic slices requires identification of points along the surface of interest in each slice. This task can be accomplished (1) by manually outlining the surface in the images, or (2) by a computer algorithm designed to produce points along the surface of interest. In dealing with image sets of the head, structures outside the head (e.g., support structures, stereotactic frames, and noise) complicate the automatic detection of the perimeter of the head. This paper examines three methods of automatic wireframe generation from CT or MR slices of the head. The three approaches are based on the following techniques: traditional edge detection filters, neural networks, and thresholding combined with region connectivity analysis and region elimination. Results of the three approaches are presented along with a comparison of the relative advantages and disadvantages of each.

1. INTRODUCTION

Patient-specific three-dimensional surface models of the human anatomy are useful in surgical planning as well as in interactive, intraoperative use. Because the human brain is such a complex, critical structure enclosed by a rigid barrier, greater navigational assistance is needed than with other parts of the anatomy. Therefore, interactive guidance --using available imaging and computer technology-- during neurosurgery is especially important.

An interactive, image-guided (IIG) approach to stereotactic neurosurgery is under development by our group^{1,2}. This IIG system has a four-window high resolution computer display (Figure 1), up to three windows of which display preoperative scans (CT, MR or PET). Connected to the computer system is a pointing device used to locate surgical targets. In surgery, once physical space and image space have been registered, the three raster windows display the appropriate image slices corresponding to the pointer's current location within the patient's head. The actual endpoint location within the slices is also indicated in each window.

To provide three-dimensional orientation of the raster images for the surgeon, the fourth window displays a patient-specific three-dimensional surface rendering, or wireframe model, of the head (see Figure 2). Since this model is constructed from the edge points of the skin and scalp in the set of preoperative image slices, it is by definition registered to the set of image slices. The level of the wireframe corresponding to the level of the image slice displayed in the raster windows (which is the current level of the pointer) is highlighted, as shown in Figures 1 and 2. The wireframe model can be rotated interactively for viewing from the optimum perspective.

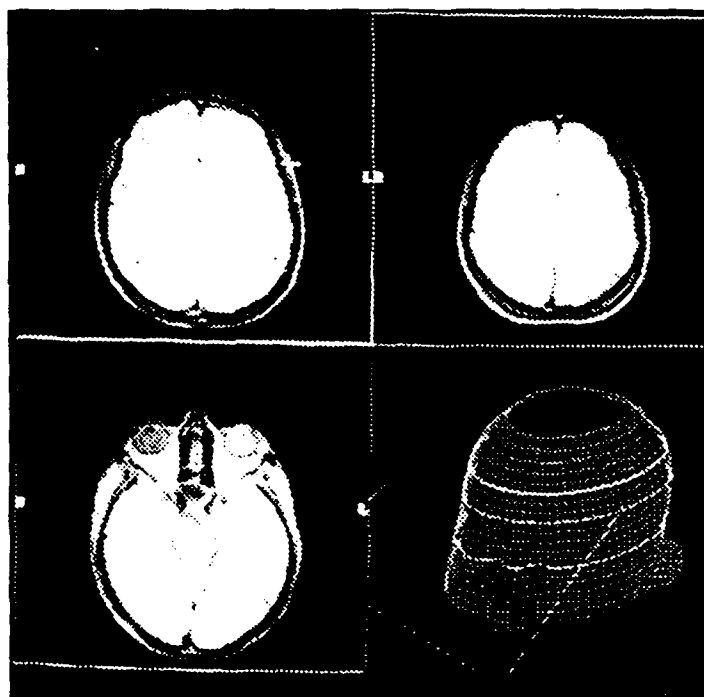


Figure 1. The 4-window display of the IIG system

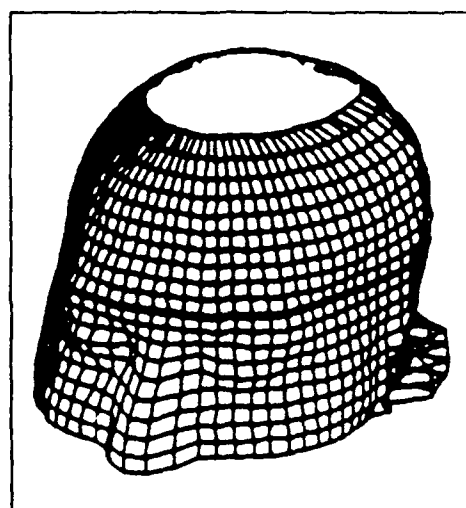


Figure 2. Patient-specific wireframe model

Three-dimensional surface models are often created by manually outlining the region of interest in each slice of the image set, which is a tedious and time-consuming process. Since our IIG system displays a patient-specific wireframe model, a more efficient method of extracting the perimeter of the head from an image set is required.

In evaluating possible image processing techniques for this application, the associated tasks and challenges must be understood. The automatic system should locate the boundary of the skin and scalp in each slice of an image set. (For discussion in this paper, CT image sets will be considered.) The presence of objects outside--and often adjacent to--the head must be eliminated or ignored by the system. Such objects include head support structures and cushioning as well as stereotactic frames. Stereotactic frames, used to locate targets within the brain, are screwed into the skull and have relatively bright image intensity (see Figure 3), making extraction of the true perimeter of the head difficult. It is also important to retain the features of the head which provide the visual cues for position orientation of the three-dimensional model. These features include the nose, ears, and eyes. In an image slice, the way in which the nose and ears protrude from the head may not differ much from that of other objects such as the stereotactic screws. This paper compares two new methods (developed by JGT) of accomplishing this task with a previously presented method³ (designed by GLH).

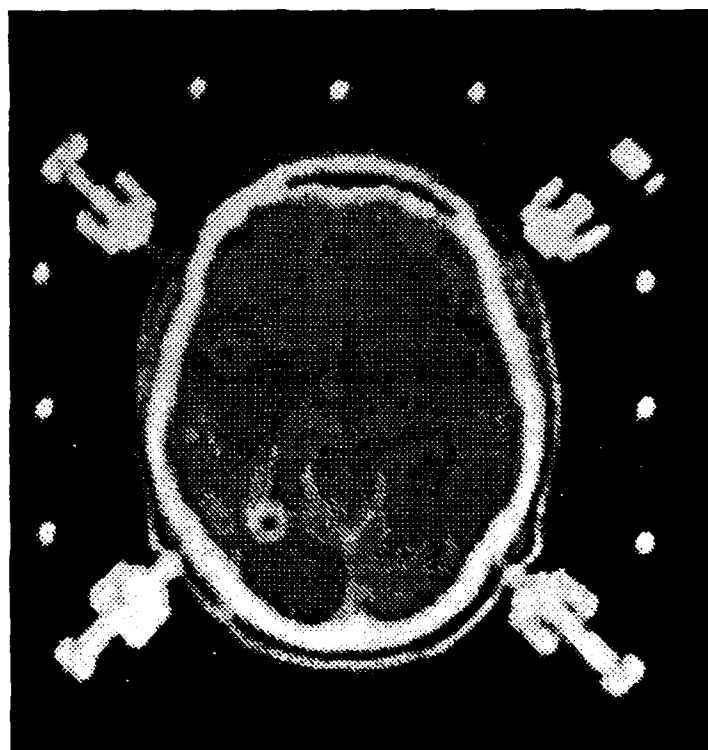


Figure 3. An image slice of a patient with a stereotactic frame attached

2. WIREFRAME CREATION METHODS

The wireframe model is not composed of continuous edge points around the perimeter of the head. Instead, it is made up of points at equal angular intervals around the head in each slice. These points are then connected as shown in Figure 2 to form the graphic model. An angular spacing of six degrees between edge points within a slice was determined to provide an adequately dense and recognizable model, while allowing for future visualization of regions of interest within the model.

All three wireframe methods investigated use the concept of "rays" to generate the sixty edge points per slice. First, for each image set, an image frame center is determined. The first method uses the actual center of the image frame size, while the latter two methods calculate a patient-specific center, by the following method: using the top slice of the image set, the x and y coordinates of the pixel corresponding to the centroid of the head in that slice are computed. (That x, y location will be referred to as the "ray center" in this paper.) From this center, radial lines at six degree intervals are constructed, extending to the outer edges of the image frame. This set of rays is used as a ray template: it is placed over each slice of the image set, as illustrated in Figure 4, and one pixel's x and y coordinates per ray are stored in the wireframe model. The z coordinate is constant for each slice, based on the slice number and the image set slice thickness.

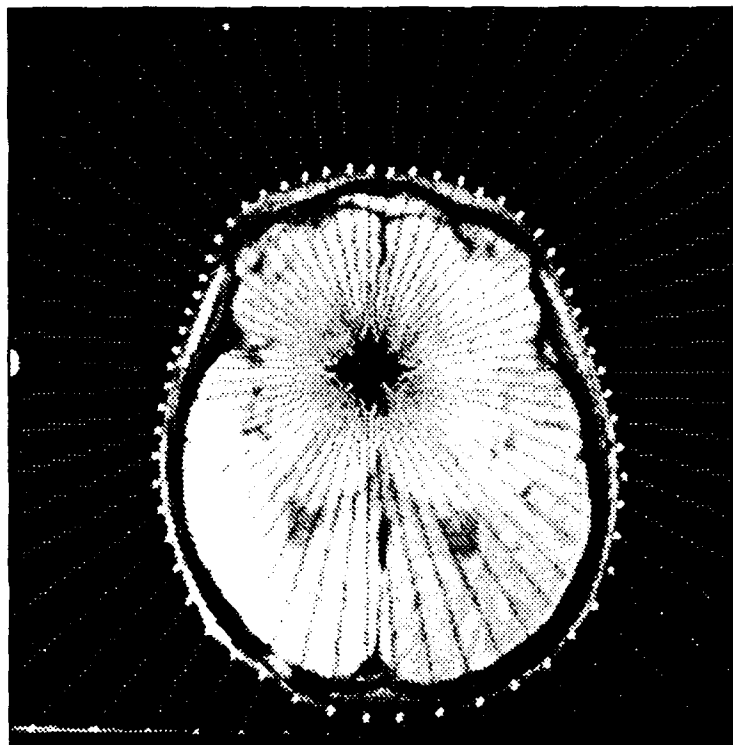


Figure 4. The patient-specific ray template overlaid onto one slice of the image set

2.1 Gradient-Based Edge Detection

For each slice of an image set, a 3x3 Sobel edge detection filter is applied, producing a gradient image. To reduce spurious gradients due to noise, median filtering of the gradient image is performed. The ray template is then placed over the gradient image. Beginning with the outer pixel of each ray, the algorithm then searches inward along the gradient image pixels corresponding to that ray until a pixel is found whose gradient value exceeds a predetermined threshold. The x and y coordinates of that pixel are passed to the wireframe model and the process continues with the next ray and eventually the next slice. During a second pass through the image set, the location of each wireframe point is compared with the corresponding point in the slice above. To smooth out incorrect points, if a given vertical slew limit is exceeded, the wireframe point is replaced by an average of its neighbors within the same slice.

The ray template used in this approach is identical for all images (of the same frame size); the center from which the rays are constructed is the center of the image frame size. As a result, the head region in all slices must contain the center of the frame so that edge points can be found on every ray.

2.2 Neural Network

Neural net theory has proven to be a good approach to inexact pattern classification applications. Therefore, a neural net program was designed to classify image pixels into two categories: one class being edge points of the head and all other points comprising the second category. The neural net topology used is the multi-layer perceptron network, with an input layer, one hidden layer, and an output layer consisting of a single node, with each layer connected by weighted links to the nodes of the next layer. (See Lippmann⁴ for a description of neural net models.) Training of the net employs a back-propagation algorithm which adjusts the weights between nodes based on the difference between actual and desired output node values.

Groups of pixel intensity values along one ray at a time are presented to the input layer of the trained net. One position in the input array always contains the current pixel of interest (POI). When the output node is high, the current POI is classified as an edge pixel of the head. The array of input values can be visualized as a sliding window. The window is "slid" along the intensity values of a ray, beginning with the outermost pixels. The output node of the net should be low when the pixel in the POI location of the input array does not lie on the edge of the head. When a true edge pixel does occupy the POI slot, the output node goes high and that pixel's coordinates are saved in the wireframe model.

The window presents an array of fourteen pixel intensities (from along the current ray) at time to the net: extending four pixels toward the outside of the image from the current POI and nine pixels toward the center. Figure 5 illustrates the layout of the net. This design allows the net to "look ahead" to better differentiate between external objects and the true edge of the head.

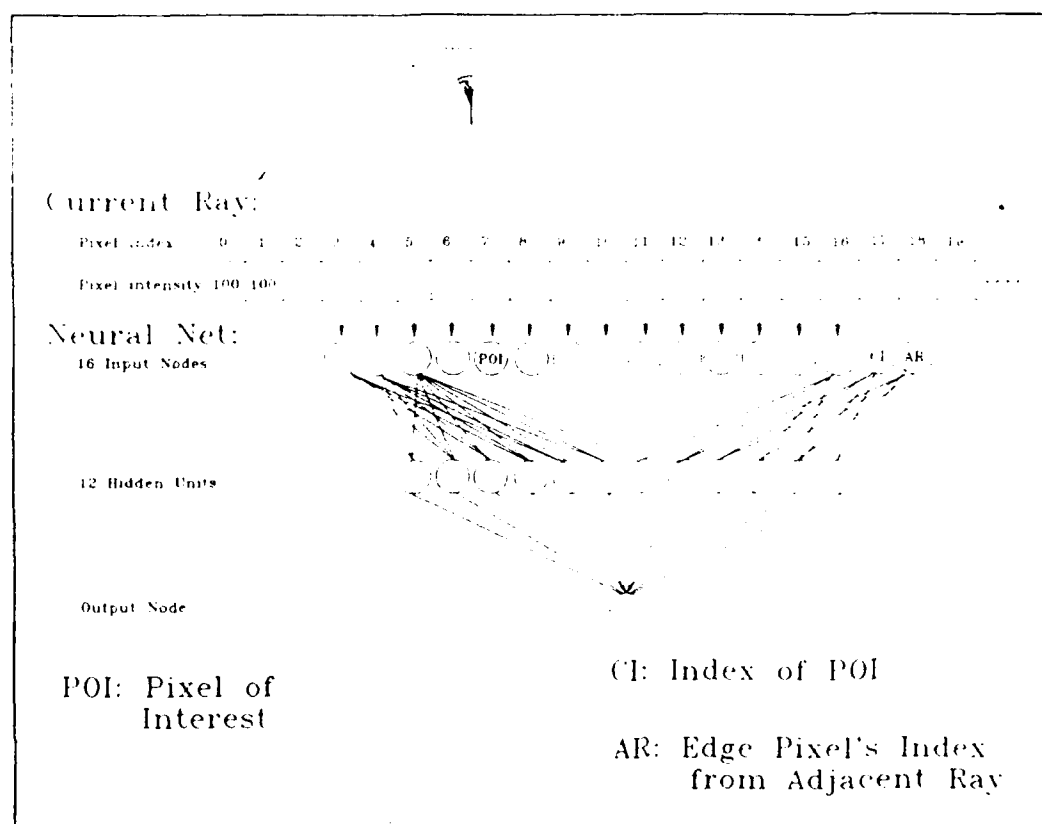


Figure 5. The neural net topology, illustrating an example in which pixel 7 is the current pixel of interest

To produce a smoother wireframe and to discourage large fluctuations in wireframe point location, two supplementary input nodes were added. Index values are assigned to each pixel along the current ray, with the outermost pixel being '0', the adjacent pixel labeled '1', etc. The two additional input nodes correspond to (1) the index value of the current POI, and (2) the index value of the edge pixel on the last (adjacent) ray. The input layer then has a total of sixteen nodes. Through experimentation with a range of numbers of hidden units, twelve was determined to be appropriate for this application.

To train the network, pairs of input arrays and their desired output values must be collected. The training data for this net was selected from five image slices. The input/output pairs are repeatedly presented to the net and the weights are updated according to the back-propagation algorithm. Once trained, the weights are saved and the net can be used in a feed-forward fashion to recognize edge pixels.

2.3 Region Analysis

To eliminate objects such as stereotactic frames while retaining the important facial features requires a robust technique, based on more information than image gradients. This third method of wireframe generation makes use of *a priori* knowledge of the typical range of image intensity values of the head as well as the usual range of head size, shape, and location in image slices.

First, the image is thresholded using an intensity value which retains all relevant features and potentially eliminates some noise and extraneous objects. (A threshold of 700 for 12-bit CT images is satisfactory.) This produces a binary image of the head and any other bright objects in the image.

Using a connectivity analysis algorithm such as that described in Rosenfeld and Kak⁵, each group of connected "on" pixels is assigned a different region number. The number of pixels in each region is tabulated. The head should be the largest region whose centroid is near the ray center (determined as described in Section 3). Therefore, beginning with the largest region in the slice, the centroid of the region is calculated. If the region's centroid is less than a specified distance from the ray center, that region is chosen as the head region. If not, the process continues with the next smaller region.

Once the head region is found, all other regions are removed from the binary image. Figure 6b shows the binary head region extracted by the algorithm from the slice in Figure 6a. The ray template can then be placed over the resulting binary image of the head region. The outermost "on" pixel along each ray is chosen as the wireframe point for that ray. A second pass is made on each slice to pull in points that are much further from the ray center than their neighbors.



Figure 6. (a) An image slice and (b) the binary "head region" extracted by the region analysis approach

3. RESULTS

Timing

The three methods were tested with several image sets, some with head holders present in the images, others with stereotactic frames. The table below compares the average time required by each method to locate wireframe points in one slice.

I. Edge Detection	II. Neural Network	III. Region Extraction
6 sec	7 sec	3 sec

Table: Average time required per slice

Accuracy

Although each technique demonstrates a high degree of accuracy in detecting the edge points of the head without any objects present external to the head, the ability to perform correctly in more complex situations varies. A wireframe editor is built in to all three methods that the points chosen from each slice can be examined and edited, if necessary. Accuracy of each method is evaluated by noting the percentage of points which lie on the true edge of the head, i.e., the points which do not require editing.

3.1 Method I

The edge detection approach is accurate only if nothing is present outside the head in the image slices. The first edge encountered along each ray is chosen as the edge point, whether or not that edge is actually part of a head holder or stereotactic frame. With nothing external to the head, however, this method is on average 99.9% accurate, meaning that in a typical image set of slices only one spurious edge point would need editing. But with either stereotactic frames and head holders, approximately 40% of the rays in each slice intersect the external object before intersecting the head. As a result, the best-case accuracy figure in the presence of external support structures is roughly 60%.

3.2.2 Method II

Training the neural net to accurately recognize the edge of the head with nothing external to the head is simple. The task of training the net to detect the edge of the head in the presence of external objects is much more difficult. First, a training set of 1690 correct input/output patterns was selected from 5 slices of a 79-slice image set which contained a head holder and cushioning external to the head. After 5100 iterations through the training set, the net could correctly classify every pattern in the training set. A graph of training progress is shown in Figure 7. The network then generalized to the other 74 slices with 99.1% accuracy.

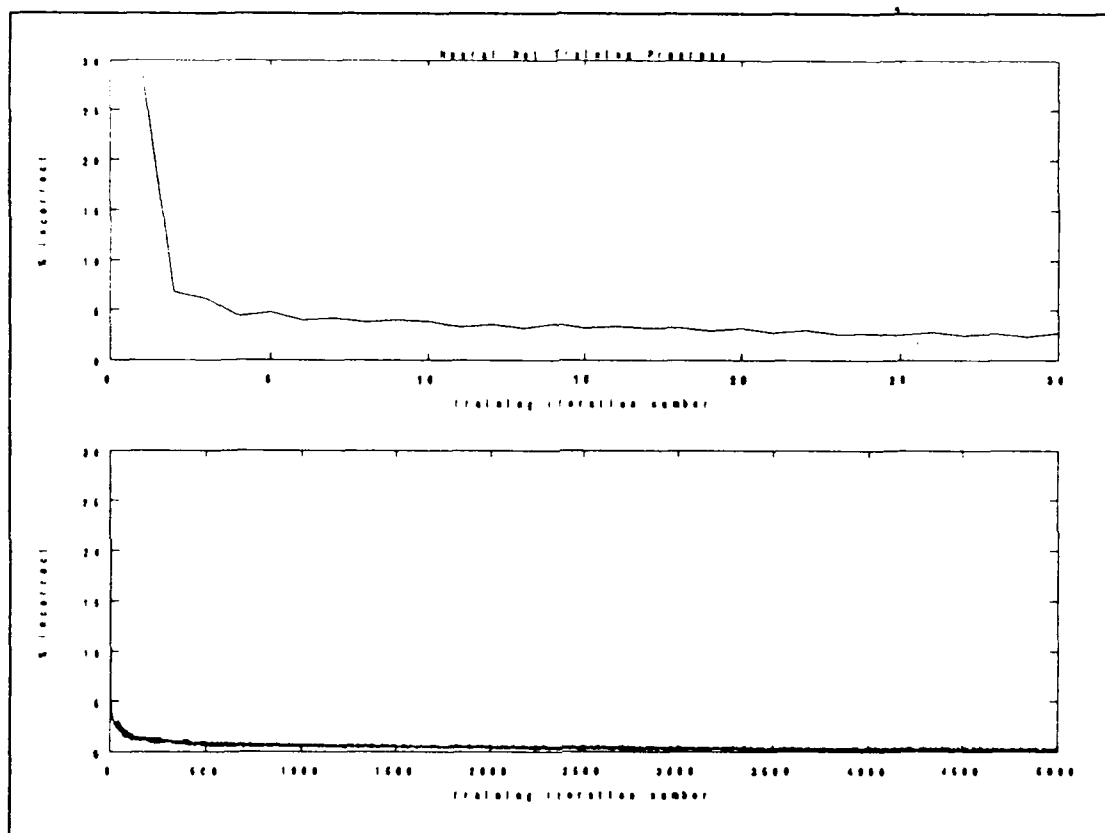


Figure 7. Neural net training progress showing the decrease in incorrectly classified patterns; the upper panel expands the first 30 iterations, while the lower shows the entire training process.

Since the way in which the stereotactic frame screws can protrude from the head is so similar to that of the nose and ears, it was difficult to train the net to discriminate between the two. The neural net as presented is not an adequate approach for images containing stereotactic frames.

4.2.3 Method III

The region extraction approach proves to be the most accurate for all cases. With nothing external to the head and with head holders, the system was found to be 100% accurate. Even in image sets containing a stereotactic frame, the system found correct wireframe edge points with 98.9% accuracy.

5. DISCUSSION AND CONCLUSIONS

The region labeling/extraction approach proves to be the most robust method of wireframe generation, as well as the most efficient. The performance of the neural net approach is quite impressive and deserves further investigation in applications of image edge detection. Enhancements of the network architecture, such as adding more input nodes, hidden layers, or possibly an additional output node to allow for more classes (e.g., a "stereotactic frame" class), may improve network performance and flexibility.

The two new techniques demonstrate a greater generality than the gradient technique. Problems with the gradient technique include the variation in appropriate gradient threshold choice as well as the sensitivity to objects outside the head.

6. ACKNOWLEDGEMENTS

The authors gratefully acknowledge the assistance of Steve Schreiner. This work was supported in part by a National Science Foundation Graduate Research Fellowship to JGT.

7. REFERENCES

1. R.L. Galloway, C.A. Edwards, J.G. Thomas, S. Schreiner, and R.J. Maciunas, "A New Device for Interactive, Image-Guided Surgery," *Medical Imaging V: Image Capture, Formatting, and Display*, Proc. SPIE 1444, in press, 1991.
2. C.A. Edwards, R.L. Galloway, J.G. Thomas, S. Schreiner, and R.J. Maciunas, "Simultaneous Graphics and Multislice Raster Image Display for Interactive, Image-Guided Surgery," *Medical Imaging V: Image Capture, Formatting, and Display*, Proc. SPIE 1444, in press, 1991.
3. R.L. Galloway, C.A. Edwards, G.L. Haden, and R.J. Maciunas, "Creation of a Wireframe Model for Three-Dimensional Registration of Raster Image Regions of Interest," *Medical Imaging V: Image Capture and Display*, Yongmin Kim, Editor, Proc. SPIE 1232, pp. 371-379, 1990.
4. R.P. Lippmann, "An Introduction to Computing with Neural Nets," *IEEE ASSP*, pp. 4-21, April 1987.
5. A. Rosenfeld and A. Kak, *Digital Picture Processing*, Academic Press, New York, 1976, pp. 347-349.

AN INTRA-OPERATIVE WORKSTATION FOR INTERACTIVE, IMAGE-GUIDED NEUROSURGERY

R. Galloway^{1,2}, C. Edwards¹, V. Mandava², R. Maciunas²

¹Department of Biomedical Engineering ²Department of Neurological Surgery
Vanderbilt University, Nashville, TN 37235

ABSTRACT

Interactive, image-guided (IIG) surgery is a technique by which the present surgical position and trajectory is tracked during the operation and displayed on pre-operatively obtained tomographic images. The manipulation of large data sets, high speed processing of real-time information and constraints imposed by function within an operating room represent considerable workstation design challenges. The system presently in use at Vanderbilt will be demonstrated and the design choices for the system explained.

INTRODUCTION

Modern tomographic imaging techniques such as computed tomography (CT), magnetic resonance (MR) and positron emission tomography (PET) provide an exquisite set of data for the three-dimensional visualization and localization of intracranial lesions. In most neurosurgical situations, that data is left on the lightbox during the surgery. The surgeon may step away from the patient and refer to the data during the operation, however, present surgical position relative to objects perceived in the image sets is a function of physician proprioception and identification of anatomic landmarks.

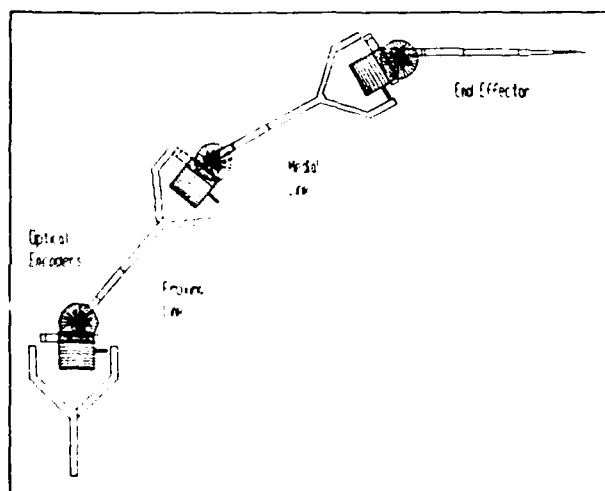


Figure 1. An articulated arm for neurosurgical localization. High resolution optical encoders give the arm a sub-millimeter application accuracy.

In order to provide interactive display of present surgical position, an articulated arm formed of revolute joints has been developed for intrasurgical use [1-3].

The arm, shown in Fig. 1, uses optical encoders to measure angular position and compute the position of the arm in arm-coordinate space. If three points, called fiducial points, can be found in the images and touched by the arm then a map can be created which allows the arm position to be mapped into image space. See Figure 2.



Figure 2. The optical encoders are read to determine the endpoint in arms space. This point is then mapped into image space and displayed on the proper image.

IMAGE SETS

One of the most daunting of the problems in implementing an IIG system is the size of the image set. A typical, neurosurgical CT set consists of 26 512x512 by 12bit (stored as two bytes) image planes or 13 megabytes (MB) of data. Adding MR and or PET data can push the total towards 20MB. If CT images are reformatted into sagittal and coronal views then the total image set size may pass 50MB.

Once the arm position has been calculated in image space, the appropriate image slices (as determined by a minimum euclidian distance) must be extracted from the sets and displayed. A cursor is then overlaid on the image to represent the end effector's position.

WORKSTATION DESIGN

The requirements for the computer system to implement an IIG device involved:

1. Real time management of optical encoder data.
 - a. Localization of end-effector in arm space.
 - b. Translation of arm space to image space.
2. Rapid determination and display of images
 - a. Image sizes range from 512² (CT) to 128² (PET).
 - b. Techniques for compression of image grayscale.
 - c. The display should be updated in less than 1 sec.
3. A technique for showing trajectory as well as location.

These requirements of high computational intensity, advanced graphics performance and large data set manipulation led us to workstation class machines.

The real time requirement for the arm operation proved to be the most constraining. Unix handles interrupts in a temporally statistical fashion. Although real-time Unix systems exist, they are generally dual processor systems and fail our cost and operating room constraints. DOS-based systems have the advantages of allowing real time operation and the huge installed base of systems keeps the costs acceptable but the operating system constrains both main memory and mass storage sizes.

We opted for a DOS-based solution with both software and hardware augmentation. The problem of the 640k barrier to DOS memory manipulation was solved by using a DOS-extender (Phar Lap). The extender, when coupled with an appropriate compiler, (NDP C-386) allowed the use of up to 4 gigabytes of RAM. We were limited to 16MB of memory by hardware considerations.

The mass storage requirements were addressed by the use of a TSR (WREN-Manager, On Track Systems). This utility allowed us to manage a 363MB hard disk with large data sets contiguously stored on a single virtual drive. The images can be imported to the hard disk either electronically from a network node or from archival storage on tape or optical disk. A system diagram is shown in Figure 3.

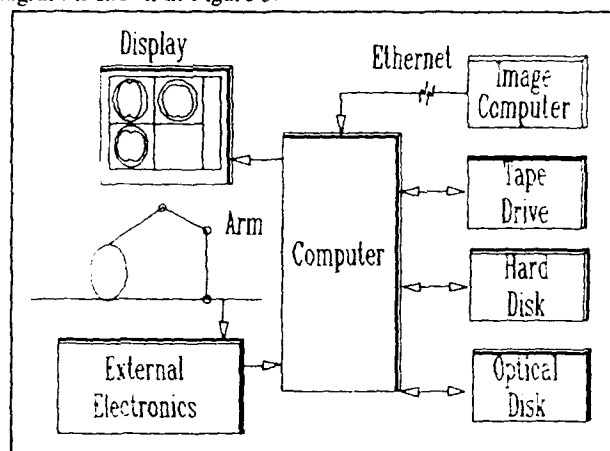


Figure 3. A 386-based workstation provides the platform for a IIG system.

The images are displayed on a 1280x1024 pixel monitor being driven by a SM1280 solid modelling display engine (Matrox Corp.) The display is broken into 4 512x512 windows with each window having its own window manager. This allows us to tag any image set to a window and individually map the arm endpoint into that image set.

Additionally, the solid modelling capabilities of the SM 1280 allow us to generate and display a patient-specific wireframe

or shaded-surface graphic image set. The graphic display may incorporate perspective and depth-cuing techniques to facilitate trajectory determination.

System Performance

In order to calculate the arm position in arm space, 64x4 matrices must be multiplied. Four of the elements of each matrix may be trigonometric functions. This could lead to long calculation times. Each matrix, however, is sparse and we were able to reduce time to solution by chaining the equations together and identifying common terms. We further improved the performance by creating a look-up table for trigonometric values at the program's start. Arm position can be calculated in less than 20 milliseconds and translated into image space microseconds later.

Once the location in image space is found, the appropriate image is pulled from disk and pumped to the window manager controlling the display. Images can be displayed at a rate of 12 per second, giving a complete screen update in 1/8 of a second. The graphics display is a vector recalculation in hardware on the SM 1280 board and so doesn't appreciably add to the update time.

The system has been used in numerous (>30) neurosurgical cases to date. The measured intraoperative system error is 0.93mm. The surgeons feel the display speed is adequate and a freeze frame has been added to allow extended study of any location.

REFERENCES

- [1] Galloway, R.L., Edwards, C.A., Haden, G.L., Maciunas, R.J., "Creation of a Wire-frame Model for Three-Dimensional Registration of Raster Image Regions of Interest". *Proc. SPIE, Medical Imaging IV*. Vol 1232, pp.371-379, Feb. 1990.
- [2] Maciunas, R.J., Galloway, R.L., Edwards, C. A., Haden, G.L., Allen, G.S., "Beyond Stereotaxy: A Computerized Articulated Localizing Arm for All Neurosurgical Procedures". *Proc.AANS*, p. 254, May 1990.
3. Edwards, C.A., Galloway, R.L., Thomas, J.G., Schreiner, S., Maciunas, R.J., "Simultaneous Graphics and Multislice Raster Image Display for Interactive, Image-Guided Surgery", *SPIE*, 1991, In Press.

Acknowledgements

This work was support in part by grants from the Whitaker Foundation, SDIO/T/TA and NIH grant #1 R29 NS28602-01A1.

The authors would also like to acknowledge the invaluable contributions of Judy Thomas and Steve Schreiner

Robert L. Galloway
Box 1653B Vanderbilt University
Nashville, TN. 37235

A WORKSTATION PLATFORM FOR STEREOTACTIC NEUROSURGICAL PLANNING

V.R. Mandava, R.J. Maciunas, J. M. Fitzpatrick, R.L. Galloway, C.R. Maurer

*Vanderbilt University
Nashville, Tennessee*

ABSTRACT

A software toolkit for a stereotactic neurosurgical workstation has been designed and is being developed. The toolkit is comprehensive in that it provides facilities for assisting surgeons across the entire spectrum of image related tasks including image importing from scanners, correlating/reformatting multimodal three dimensional stacks of images, surgical trajectory planning based on correlated images, and exporting correlated/reformatted images to an intraoperative image guided articulated arm.

INTRODUCTION

Stereotactic frames provide a means to physically reach any hidden anatomical location in the head with guidance from images. Early systems were guided by atlases and two dimensional projection images of the three dimensional head. A comprehensive review of stereotactic systems is given in [1]. The advances in computer technology and imaging technology have led to abilities for both acquiring and manipulating two dimensional cross sectional images of three dimensional objects. Imaging technologies such as CT and MRI provide structural information, while PET provides complementary functional information. Stereotactic technology has been accordingly thriving in providing apparatus that facilitate correlation between various image spaces and the physical space of the head. By virtue of these advances the need for a stereotactic neurosurgical workstation has been rapidly growing. In this paper we describe one such workstation with a wide spectrum of functionalities.

SYSTEM DESCRIPTION

Our workstation includes software tools: (i) to import CT, MRI, PET, and Digital Angiography (DA) images from the imaging scanners via magnetic tapes [6], (ii) to correlate the three dimensional stack of two dimensional images from CT, MRI, and PET, (iii) to reconstruct coronal and sagittal images from transverse images, (iv) to plan surgical trajectory based on correlated CT, MRI, and PET images, (v) to reconstruct oblique images passing through a surgical trajectory for serial biopsy and craniotomy, (vi) to measure distances and volumes of regions of interest, and (vii) to export correlated/reformatted CT, MRI, and PET images to an intraoperative image guided articulated arm [2].

Workstation platform: Our software tools are targeted for both the SUN-3 series and SUN-4/SPARC series workstations. However, the enormous memory and processing speed

requirements of typical image related tasks mandate SUN-4/SPARC series workstations for reasonable interactive response. The tools are window based and mouse driven.

Stereotactic frames: We use the COMPASS [3] [4] stereotactic frame in conjunction with our stereotactic workstation software. The modularity of our software makes the extensions to include other frames such as LEKSELL [5] less involved because only a few frame specific modules need to be developed, keeping the other modules that provide interactive surgical planning generic.

Surgical preplanning: "Neuroplanner", our surgical preplanning tool is shown in Figures 1 through 4. To the left of the menu a CT image and to the right of the menu three MRI images (proton density, T2-weighted, and T1-weighted) and a PET image of a patient are displayed in Figure 1. These images can be independently reviewed and points in any image can be correlated with anatomically corresponding points in other images. For instance points in the tumor region (left anterior) on the images indicated by cross marks correspond to the same anatomical location with in the accuracy of the stereotactic frame. The cross marks are displayed in white in the figure (we apologize for loosing the cross mark in the hot background on PET and in the enhanced background on CT, because the colored cross marks on the workstation screen are photographed in black and white). The number on the lower left corner of every image represents the serial number in the two dimensional image stack. The image number in all three MRI images is the same because the patient head is locked to the scanner bed and the images are acquired at exactly the same table position. However, our software does not take advantage of this fact but it can correlate points from arbitrarily oriented images. The correlated points can be used in computing a surgical trajectory. Coronal, sagittal, and oblique images passing through the trajectory can be reconstructed from any transverse CT or MRI or PET image volume. Four interactively reconstructed CT images are displayed to the right of the menu in Figure 2. The top left image is perpendicular to the trajectory at a selected depth. Depth can be interactively changed to display images at different depths. Top right and bottom right images are perpendicular to each other, passing through the trajectory. They appear as coronal and sagittal by virtue of the planned trajectory. A true coronal is displayed at bottom left. The trajectory can be interactively manipulated with the aid of transverse, coronal, sagittal, and oblique images. CT, MRI, and PET image volumes can be reformatted

regions of interest can be displayed on any of the images. 12 weighted MRI images is displayed left of the menu and reformatted PET images are displayed right of the menu. The 12 weighted MRI images are shown in Figure 3 and the PET image is shown in Figure 4. The menu is a list of regions of interest. The menu assigns identical three-dimensional coordinates to the same anatomical location in all the images. Hence, with the help of the menu, outlining of a region of interest in any of the images. The software can automatically outline such a region of interest in all the reformatted images. Outlines of the left side of brain and the right side of brain are shown in Figures 3 and 4 can be carefully examined for the accuracy of the segmentation.

Intraoperative guidance. Stereotactic coordinates of reformatted images are passed to an articulated arm. It guides the surgeon with the help of reformatted images to reach anatomical locations on the preplanned trajectories on an open craniotomy. Guidance is offered by stereotactic apparatus in the surgery.

References

- [1] R.L. Galloway, and R.J. Macinnis, "Stereotactic Neurosurgery", *Critical Reviews in Biomedical Engineering*, Vol. 18-3, pp. 207-243, 1990.
- [2] R.J. Galloway, Jr., C.A. Edwards, J.G. Thomas, S. Schreiner, and R.J. Macinnis, "A New Device for Interactive, Image Guided Surgery," *Proc. SPIE's Medical Imaging IV*, San Jose, CA, March 1991.
- [3] S.J. Goerss, P.J. Kelly, B.A. Kail, and G.L. Aiken, "A computerized tomographic stereotactic adaptation system", *Neurosurgery*, Vol. 10, pp. 375, 1982.
- [4] B.A. Kail, P.J. Kelly, S.J. Goerss, and L. Earnest, "Cross registration of points and regions from MR and CT", *Proc. of the Society for the Advancement of 3-D ILLUMBS*, pp. 946, Sept. 27-30, 1985.
- [5] L. Leksell, and B. Jernberg, "Stereotaxis and Tomography: A Technical Note", *Acta Neurochir.*, Vol. 52(1), 1980.
- [6] V.R. Mariani, Jr., M. Mariani, and J.M. Lippman, "LAP-1000: A microcomputer for processing and displaying images on a video computer. The image processing computer, *Computer Methods and Applications in Biology*, Vol. 13, pp. 213-220, 1980.

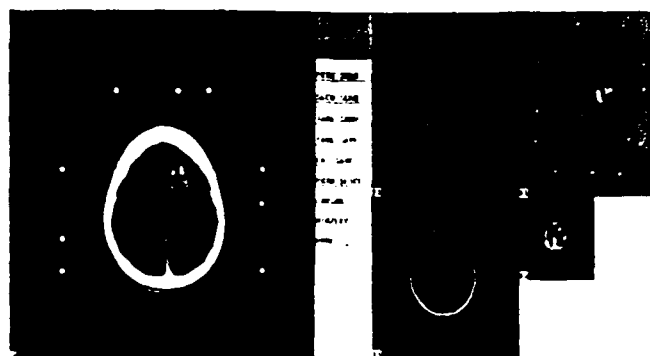


Fig. 1. Anatomical correlation between CT, MRI and PET images



Fig. 2. Trajectory planning with trajectories shown from CT, MRI, and PET



Fig. 3. Correlation images of 12 weighted MRI and reformatted PET

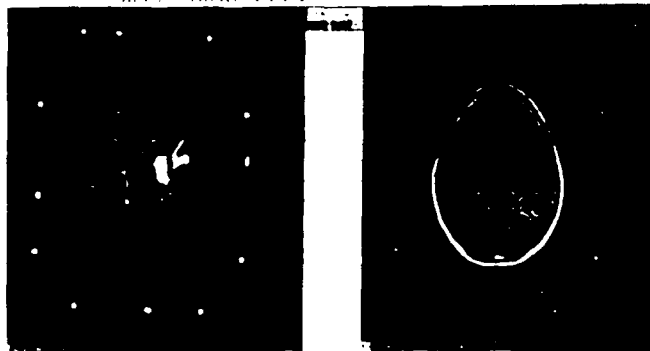


Fig. 4. Correlation images of 12 weighted MRI and reformatted PET

REAL-TIME ASSESSMENT OF LUNG MICROVASCULAR PERMEABILITY: USE OF A CO₂ LASER
AIDS MEASUREMENT OF 1,2-PROPANEDIOL CONCENTRATIONL.E. Olson¹, R.L. Galloway², and T.R. Harris³¹Department of Biomedical Engineering, ²Center for Lung Research, ³Department of Neurosurgery, Vanderbilt University, Nashville TN 37232

ABSTRACT

The feasibility of optical measurement of 1,2-propanediol as a multiple indicator dilution (MID) tracer of lung microvascular permeability has been demonstrated [1]. However, several complications were encountered making infrared optical densitometry measurements of propanediol concentrations in whole blood. A conventional, black-body emitter (Oriel glowbar 6363) was previously used as an infrared source. This measurement system was not sensitive enough to measure trace amounts of 1,2-propanediol. The use of a tunable CO₂ laser (Synrad 48-1g) was proposed as a new source to increase optical intensity of the device and ameliorate the signal-to-noise problems of the conventional system. In a steady state *in vitro* experiment, linear calibration of measured change in optical density versus propanediol concentration in ovine blood was achieved at concentrations typical of MID studies in animal models. This implies that the use of a CO₂ laser increases sensitivity by at least five hundred-fold for optical density measurements of 1,2-propanediol in whole blood.

INTRODUCTION

The use of radioactive MID techniques to measure the permeability-surface area product (PS) of the lung has been studied [2]. In this bolus technique, the diffusing tracer(s) which chromatographically separates from intravascular reference tracers provide information for calculating PS of the lung microvascular barrier. Small chain diols such as 1,2-propanediol and 1,4-propanediol as MID tracers give measures of lung microvascular permeability [3,4]. The infrared spectra of these compounds allow optical measurement in whole blood [1].

Optical MID techniques have also been examined [5,6]. In the work of Bassett *et al.* [5] and Neufeld and associates [6] have developed an optical assessment of extravascular lung water. Similar to these is the proposed optical MID technique to measure [1]. This technique depends on the successful measurement of optical density of the small chain diols.

BACKGROUND

Theory

Beer's theory applied to thin films of blood by Andersen and [7] gives optical density (O.D.) as:

$$O.D. = \epsilon C l - B(\lambda, H, \text{scattering}) \quad (1)$$

where ϵ is the extinction coefficient of propanediol at measured wavelength, C is propanediol concentration, and l is the optical path length. $B(\dots)$ is a complex function dependent on erythrocyte size, scattering, and other factors.

By separating propanediol concentration into plasma (p) and cellular (c) blood phases and accounting for oxygenation of hemoglobin (Hb), equation 2 becomes:

$$O.D. = (1-H) \epsilon_p C_p l + H \epsilon_c C_c l + \zeta - B(\lambda, H, \text{etc}) \quad (2)$$

where, ζ is the beersian absorbance of oxygenated and reduced Hb at the given wavelength. For optical MID studies, changes from baseline of propanediol concentration are used to calculate PS; thus, the difference in optical density from a baseline, $\Delta O.D.$, is:

$$\Delta O.D. = (1-H) (\epsilon_p \Delta C_p) l + H (\epsilon_c \Delta C_c) l + \Delta \zeta - \Delta B(\dots) \quad (3)$$

For use in a propanediol measurement device, the relationship between $\Delta O.D.$ and ΔC should be linear or at least predictable. Otherwise, the effects of scattering and blood oxygenation may confound the accurate optical measurement of propanediol.

Complications with Conventional Measurements

Shown in Figure 1 is our conventional optoelectronic measurement system for measuring propanediol concentration in whole blood.

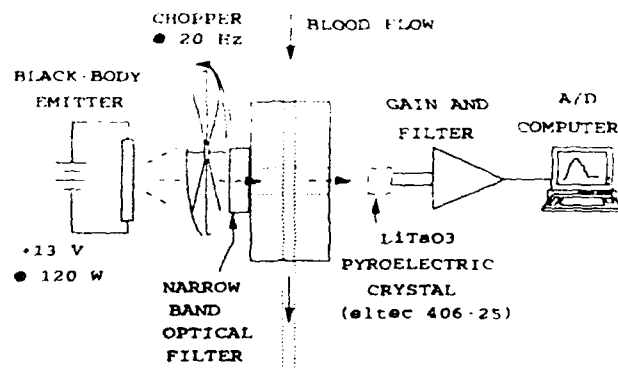


Figure 1: Conventional IR optoelectronic measurement system.

Parameters of the measurement system other than the light source were optimized. These included maximizing gain of the electronic measurement circuit, minimizing path length of the optical flow-through cell, and increasing to a maximum propanediol concentration used in MID bolus injectates. Optimization of each parameter had its own drawbacks. Minimizing path length--to approximately 100 μm --drastically increases hydraulic resistance of the optical flow-through cell. The electronic gain and filter circuit was optimized for frequency response and for gain (> 110 dB). Even after optimizing circuit elements and trying various configurations, the circuit was not adequately sensitive and noise-free. Maximizing propanediol concentration (to levels around 3 M) caused massive hemolysis. By making the blood hypertonic (2.3 g%) hemolysis was minimized; however, when hypertonic boluses were mixed with whole blood, hemolysis still occurred. The problems associated with these optimizations led to the selection of a CO_2 laser operating around 9.6 μm as a light source to increase total intensity, and retreat from the problematic optimum edge of the other design parameters.

METHODS AND MATERIALS

The laser optoelectronic system is quite similar to the conventional system shown in Figure 1. The only difference being the electronically chopped laser tuned to 9.55 μm --at P(20)--replacing the glowbar, mechanical chopper and optical filter. Steady-state calibration of the system was conducted *in vitro* by pumping ovine blood from a well-mixed 20 ml reservoir through the optical flow-through cell and returning to the reservoir. In this system, incremental levels of propanediol were sequentially added to the reservoir and observed on computer. Propanediol was mixed in a 1:1 ratio with saline to disperse the propanediol and minimize hemolysis. Hematocrits were taken of the blood throughout the experiment. Voltage output from the electronic circuit was stored digitally throughout the experiment.

RESULTS

Steady state values of $\Delta\text{O.D.}$ at four concentrations of propanediol were assessed by averaging time course data. Figure 2 shows $\Delta\text{O.D.}$ versus propanediol concentration for the steady-state calibrations. Linear regression of the data is also shown ($r^2 = 0.981$). Sensitivity of the measurement system to changes in propanediol concentration of 1 mM are arguably demonstrated. Hemolysis was insignificant throughout the course of this experiment.

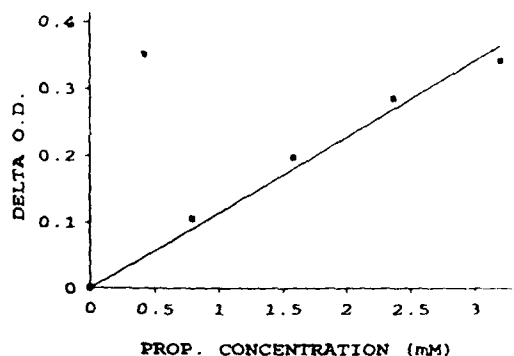


Figure 2: $\Delta\text{O.D.}$ versus propanediol concentration for our laser measurement system, $r^2 = 0.981$.

DISCUSSION

In the isolated dog lung preparation, typical nonhemolyzing concentrations of propanediol in MID studies are on the order of 1 mM. Although the noise level of the steady-state experiments are not exquisite, the sensitivity of this device appears adequate to measure such concentrations. Reasons for noise in this signal may include the lack of precise tuning of the laser to ensure mode stability, lack of adequate temperature control of the laser, and suboptimal electronic configuration. All of these problems can be explored and potentially optimized. Linear regression analysis demonstrates linearity between propanediol concentration and $\Delta\text{O.D.}$. This implies that scattering effects do not change with changes in propanediol concentrations of this magnitude. Analysis from steady-state tests using our conventional system reported previously [8] did show that the sensitivity of $\Delta\text{O.D.}$ measurements to propanediol concentration (slope of regression line) was 0.23 M^{-1} . In this experiment, the sensitivity of the laser system is 110 M^{-1} implying that the new system is almost 500 times more sensitive than the conventional one. The resolution of this measurement system may not be as increased, however, because of noise level considerations. This work is supported by PHS grant HL39155.

REFERENCES

- [1] R.L. Galloway, D.J. Staton, T.R. Harris, "The Optical Measurement of 1,2-Propanediol for the Determination of Lung Capillary Permeability-Surface Area", IEEE Trans. Biomed. Engr. Vol. 36, pp 591-597, 1989.
- [2] C. Crone, "The Permeability of Capillaries in Various Organs Determined by Use of the 'Indicator Diffusion' Method", Physiol. Scand., Vol. 58, pp 292-305, 1963.
- [3] T.R. Harris, R.J. Roselli, C.R. Maurer, R.E. Parker, and A. Pou, "Comparison of Labeled Propanediol and Urea as Markers of Lung Vascular Injury", J. Appl. Physiol. Vol. 64, pp 1852-1859, 1987.
- [4] L.E. Olson, A. Pou, and T.R. Harris, "Surface Area: An Independent Assessment of Lung Microvascular Permeability Using an Amphipathic Tracer", J. Appl. Physiol. Vol. 71, pp 1085-1096, 1991.
- [5] G. Basset, G. Mariet, F. Bouchonnet, J. Marsac, J. S. Botter and R. Capitini, "Simultaneous Detection of Deoxythymine Oxide and Indocyanine Green in Flowing Blood", J. Physiol. Vol. 50, pp 1367-1371, 1981.
- [6] L. G. Leksell, M.S. Schreiner, A. Sjlvestro and G.R. Sjolander, "Commercial Double Indicator-Dilution Densitometry with Heavy Water: Evaluation of Oleic-Acid Pulmonary Permeability", J. Clin. Monit. Vol. 6, pp 99-106, 1990.
- [7] N.M. Andersen and P. Sekely, "Light Absorbing and Scattering Properties of Nonhaemolysed Blood", Phys. Med. Biol. Vol. 12, pp 173-184, 1967.
- [8] L.E. Olson, R.L. Galloway, A. Pou and T.R. Harris, "Optical Measurements in Whole Blood of Tracer Diffusion and Microvascular Permeability", FASEB J. Vol. 5, pp 1085-1096, 1991.